Accrétion et différenciation de la Terre primitive : Évolution thermochimique jusqu'à aujourd'hui. Mémoire présenté en vue de l'obtention de l'Habilitation à Diriger des Recherches

Julien Monteux

Mémoire présenté en vue de l'obtention de l'Habilitation à Diriger des Recherches

Julien Monteux

Accrétion et différenciation de la Terre primitive : Évolution thermochimique jusqu'à aujourd'hui

Table des matières

Remerciements

Je souhaite remercier ici...

Les membres du jury qui ont accepté de juger les travaux résumés dans ce manuscrit, Anne Davaille, Chloé Michaut, Philippe Cardin, Denis Andrault, Maud Boyet et Gael Choblet.

Les personnes qui m'ont aidées dans le parcours scientifique qui m'a amené aujourd'hui à Clermont-Ferrand en particulier Riad Hassani, Jean-Luc Got, Nicolas Coltice, Yanick Ricard, Mark Jellinek, Catherine Johnson, Gabriel Tobie, Gaël Choblet, Laurent Husson.

Le Laboratoire Magmas et Volcans pour son accueil chaleureux.

Ma famille et mes amis.

Pauline, Martin, Valentine, Manon.

Contexte

La géodynamique occupe une place centrale dans la compréhension de la structure et de l'évolution thermique interne des planètes telluriques du système solaire puisqu'elle permet d'interpréter et de relier les différents types d'observations (sismique, géochimique, minéralogiques ...). L'activité de recherche que je mène est dédiée à la modélisation numérique de phénomènes géologiques et planétologiques.

Mon parcours scientifique m'a permis de réaliser mon stage de recherche de M2R dans l'équipe "Géophysique des Volcans" du Laboratoire de Géophysique Interne et de Tectonophysique à Chambéry (encadrants : J.L. Got et R. Hassani), puis ma thèse au Laboratoire de Sciences de la Terre de Lyon (encadrants : Y. Ricard et N. Coltice), suivi d'un stage postdoctoral au département Earth and Ocean Sciences de Vancouver (collaborateurs : M. Jellinek et C. Johnson). Ce parcours m'a mené ensuite au Laboratoire de Planétologie et de Géodynamique de Nantes où j'ai obtenu un financement A.N.R. Retour Post-Doctorant afin de développer le projet nommé ACCRETIS afin de contraindre la différenciation des satellites de glace (collaborateurs : G. Tobie, G. Choblet, B. Langlais, H. Amit). Aujourd'hui, je continue de développer des modèles numériques afin de caractériser l'évolution thermo-chimique de la Terre primitive au Laboratoire Magmas et Volcans de Clermont-Ferrand (collaborateurs : A. Bouhifd, M. Boyet, D. Andrault, G. Manthilake, S. Demouchy, M. Guitreau).

1 Introduction

La Terre est une formidable machine thermique qui tend à effacer les traces des évènements les plus anciens. Cependant, les données géochimiques, la présence de la Lune et certains observables géophysiques gardent encore aujourd'hui la mémoire d'évènements cruciaux pour l'évolution de la Terre qui se sont déroulés il y a plus de 4 milliards d'années. Notre connaissance de l'histoire de l'intérieur de la Terre a bénéficié de l'avènement de l'exploration planétaire, des outils de calcul numérique et d'analyse isotopique mais aussi des avancées importantes en pétrologie expérimentale.

Le bombardement météoritique à l'origine de la formation de la Terre et des autres objets du système solaire a eu lieu il y a environ 4.5 Ga. Ce phénomène d'accrétion s'est déroulé en peu de temps, quelques millions d'années après la formation des premiers solides (i.e. Calcium-Aluminium-rich Inclusions, C.A.I.) (Kleine and Rudge, 2011). Les impacts météoritiques ont ainsi joué un rôle crucial dans les étapes primitives d'évolution de la Terre gouvernant notamment son budget énergétique et chimique ainsi que les modalités de sa différenciation interne et de l'initiation de son champ magnétique. L'accumulation de matériel a formé des corps de plus en plus volumineux et ainsi de plus en plus rares qui ont eux même impacté des corps plus gros. Au bout de quelques millions d'années, les collisions ont impliqué des objets de plusieurs centaines de kilomètres de rayon (Agnor et al., 1999; Kokubo and Ida, 2000).

Au cours de l'accrétion de la Terre, les contributions des grands impacts entre planétésimaux et la désintégration des nucléïdes radioactifs à courte durée de vie ont induit des températures internes très élevées. Moins de 100 millions d'années plus tard, l'impact majeur qui a formé la Lune a fourni une énorme quantité d'énergie, faisant peut-être fondre entièrement la Terre. Ensuite, le refroidissement rapide de l'océan magmatique global a entraîné la cristallisation progressive du manteau et la formation d'une importante couche limite thermique à la base du manteau inférieur. Cette couche inférieure (souvent appelée couche "D") a toujours un impact important sur le bilan thermique de la Terre, car elle est étroitement liée au flux de chaleur à la limite noyau-manteau (CMB). Aujourd'hui, 4,5 milliards d'années (Ga) après sa formation, la Terre est toujours habitable, non seulement en raison des conditions clémentes qui règnent à sa surface, mais aussi grâce à son activité interne. La persistance du champ géomagnétique, en particulier, est essentielle pour protéger la vie des radiations solaires.

Il existe un consensus sur l'importance des premières étapes de formation des planètes et lunes du Système Solaire dans l'acquisition de leurs caractéristiques actuelles en termes de composition chimique, de dynamique interne et de formation de leur atmosphère (Kleine et al., 2002; Halliday, 2004). Cependant, les modalités d'évolutions primitives et les processus mis en jeu restent largement débattus. Pour répondre aux grandes questions et défis majeurs des Sciences de la Terre et de l'Univers, la planétologie comparée et les simulations numériques constituent des outils performants pour comprendre et reconstituer les phénomènes qui ont pu se dérouler il y a plus de 4.5 milliards d'années. Les planètes telluriques se sont formées

rapidement, dans les 100 premiers millions d'années après la formation des premiers solides du Système Solaire (Kleine et al., 2009), et les impacts géants étaient probablement fréquents durant les dernières étapes de l'accrétion (Canup and Agnor, 2000; Jacobson and Morbidelli, 2014). Le développement de méthodes d'analyses géochimiques a permis de contraindre la chronologie de la différenciation des planètes telluriques. Les grands événements de différenciation (formation du noyau, cristallisation de l'océan magmatique) se sont produits dans les premiers 100 Ma (Kleine et al., 2002; Boyet and Carlson, 2005).

L'intérieur de la Terre a ainsi subi une succession d'évènements majeurs depuis la formation de la Terre jusqu'à ce que nous en connaissons aujourd'hui notamment grâce à l'apport de la tomographie sismique. Ces évènements tels que les impacts géants, la séparation manteau/noyau ou la solidification du manteau primitif ont eu des conséquences non seulement thermiques avec des redistributions importantes de la chaleur primitive, dynamiques avec des transitions majeures au niveau des régimes d'écoulements mais aussi chimiques avec la mise en place de ségrégation plus ou moins complètes au sein du réservoir mantellique. Ces évènements ont aussi pu conditioner les modalités de démarrage du champ magnétique terrestre. Si le manteau constitue environ 85% du volume de la Terre, il n'en demeure pas moins mystérieux et son évolution primitive reste encore aujourd'hui largement débattue dans la communauté scientifique. Aujourd'hui l'essentiel du manteau est solide et son évolution thermo-chimique semble plutôt lente. Cependant il n'en a pas toujours été ainsi.

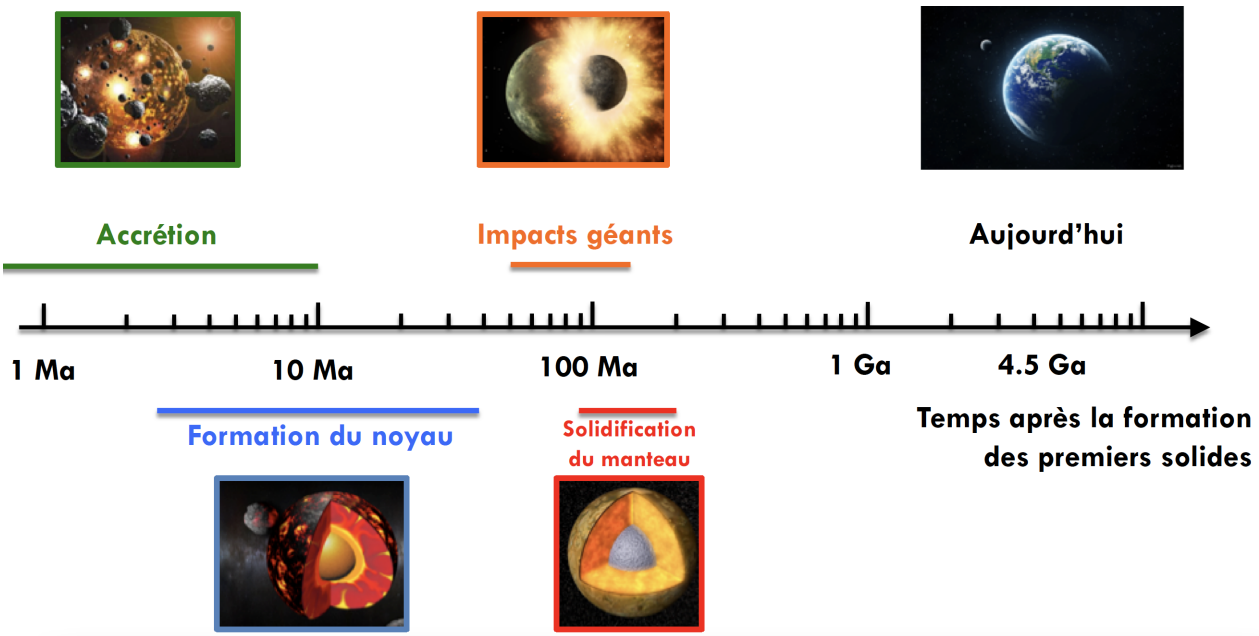

FIGURE 1 – Chronologie des grandes étapes de l'évolution interne de la Terre.

Au vu de la grande diversité des échelles caractéristiques de temps, de températures, de vitesses et de tailles, les simulations numériques sont des outils particulièrement adaptés pour

atteindre cet objectif et ainsi mieux comprendre :

- **Par quels processus les planètes ont-elles acquis leur structure interne ?**
- **Quel est le rôle des impacts dans l'évolution thermique des intérieurs planétaires ?**
- **Quelle a été l'influence des paramètres d'accrétion sur la composition des grands réservoirs à travers la formation du noyau et la cristallisation d'océans magmatiques ?**

Pendant mon parcours scientifique, j'ai étudié le rôle des impacts météoritiques et des grandes phases d'accrétion sur l'évolution de différents objets du Système Solaire : planètes telluriques, lunes, satellites de glace. Pour cela j'ai développé des outils de modélisation (numériques et analogiques) dans diverses géométries (1D, 2D, 3D, cartésien, cylindrique, sphérique). Ces modèles m'ont permis de mettre en évidence le rôle central des étapes primitives de formation et notamment des impacts géants dans l'acquisition des caractéristiques principales des objets du Système Solaire. Dans ce document, je propose de retracer l'évolution interne de la Terre depuis les dernières étapes de son accrétion jusqu'à la mise en place d'un champ magnétique, d'une convection mantellique et d'une tectonique des plaques (Figure 1). Nous verrons notamment le rôle central qu'ont joué les impacts météoritiques dans l'acquisition de ces caractéristiques et notamment sur le budget thermique primitif de la Terre, des planètes telluriques plus généralement mais aussi des satellites de glace.

2 Le rôle des impacts dans l'évolution thermique précoce des planètes

Les impacts météoritiques ont joué un rôle crucial dans les étapes primitives d'évolution de la Terre gouvernant notamment sa différenciation interne jusqu'à la formation de son atmosphère (Abe et al., 2000; Monteux et al., 2009; Ricard et al., 2009; Lebrun et al., 2013). Au cours de la dernière étape d'accrétion, l'essentiel de la masse des objets telluriques s'accumule et les protoplanètes deviennent des planètes. Cette étape a fait intervenir des phénomènes d'impact extrêmement énergétiques entre des embryons planétaires potentiellement différenciés. Ces impacts ont provoqué des phénomènes de fusion des roches terrestres à grandes échelle et la formation d'océans magmatiques au sein desquels le fer et les silicates se sont séparés pour former le noyau et le manteau (Tonks and Melosh, 1993). Malgré l'importance qu'ont eu les impacts météoritiques pour façonner la structure thermo-chimique interne de la Terre telle que nous la connaissons aujourd'hui, ces phénomènes sont encore peu contraints tant qualitativement que quantitativement et de nombreuses questions cruciales sont encore en suspens. Par exemple il est actuellement difficile de savoir comment est dissipée l'énergie cinétique de l'impacteur et quel est l'état thermique de la protoplanète après un impact. Les impacts météoritiques étant des phénomènes hautement complexes et énergétiques, mieux les comprendre pourrait permettre de mieux anticiper les différentes étapes de fusion et de recristallisation de la planète au cours de son accrétion et l'état thermique final auquel abouti la planète après des impacts répétés.

Un impact météoritique s'il se produit à des vitesses supérieures aux vitesses des ondes élastiques crée une onde de choc dans le matériel impacté ce qui provoque un changement de l'état thermodynamique du matériel impacteur et impacté. Le passage de l'onde de choc provoque une compression brutale qui se traduit par une addition irréversible d'énergie provoquant ainsi une hausse de la pression et de l'entropie (Figure 2). Après le passage de l'onde de choc, le matériel se décomprime jusqu'à pression ambiante de façon adiabatique. En connaissant les équations d'état et les caractéristiques thermodynamiques des matériaux mis en jeu (capacité calorifique, chaleur latente de fusion ...), on peut connaitre l'état thermodynamique (pression, température, taux de fusion ...) du matériel post-impacté.

2.1 Modélisation des impacts

Les impacts géants peuvent entraîner une augmentation significative de la pression et de la température sous le point d'impact et ainsi des déformations majeures au sein du corps impacté. En plus de la taille et de la vitesse des impacteurs, d'autres paramètres peuvent jouer un rôle important sur comment l'énergie cinétique de l'impacteur est transmise au corps impacté : la rhéologie, la porosité, la composition chimique des corps impliqués ou encore l'angle d'impact. Pour caractériser les effets de ces différents paramètres, il est désormais possible d'utiliser des modèles numériques pour simuler des impacts entre deux corps. Les hydrocodes (ou codes

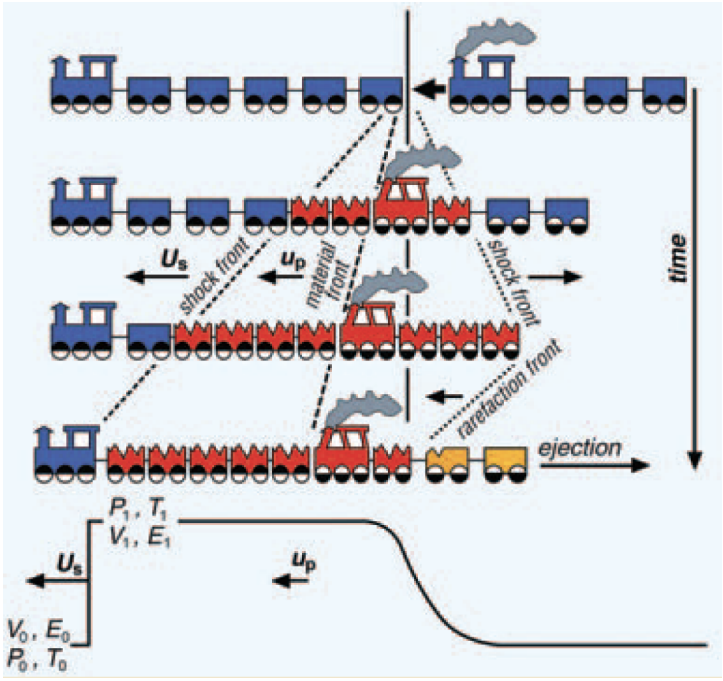

FIGURE 2 – *La formation et la propagation des ondes de choc et de raréfaction par analogie avec la collision de deux trains. P, T, E et V sont respectivement la pression, la température, l'énergie interne et le volume dans la matière non comprimée (état 0) et comprimée (état 1).* u_p *est la vitesse des particules derrière l'onde de choc et* U_s *la vitesse du choc (D'après Langenhorst and Deutsch (2012)).*

d'impacts) permettent de simuler numériquement des impacts météoritiques et le réajustement thermo-mécanique post-impact (ex. Jutzi and Asphaug (2011); Ćuk and Stewart (2012)).

Les simulations de processus dynamiques nécessitent la résolution des équations de conservation (masse, quantité de mouvement et énergie) pour un matériau donné. En plus de résoudre ces équations, les codes qui permettent de simuler les processus d'impact sont couplés à un modèle constitutif qui combine deux parties : la réponse volumétrique du matériau à l'onde de choc représentée par l'équation d'état du matériau (EOS) (eg. Tillotson, ANEOS...) , et la réponse aux déformations déviatoriques représentée par un modèle de résistance (Johnson-Cook, Ivanov, Collins...). La précision des prédictions du modèle dépend de la précision avec laquelle les modèles de matériaux (EOS + résistance) reproduisent le comportement du matériau, et de la connaissance des propriétés incluses dans ces modèles (Pierazzo et al., 2008; Stickle et al., 2020). Bien que les équations de conservation soient cohérentes entre les différents modèles numériques d'impact, la façon dont elles sont résolues peut varier. Il existe deux méthodes principales pour résoudre les équations du mouvement : une solution eulérienne et une solution lagrangienne. La solution eulérienne (ex. code CTH) traite les variables du domaine (ex. densité, température, pression) à partir d'un maillage fixe tandis que la méthode lagrangienne (ex. code Smooth Particle Hydrodynamic) traite les variables du domaine via un maillage qui se déplace dans l'espace et se déforme en même temps que le matériau. Une approche hybride

appelée Arbitrary Lagrangian Eulerian (ALE) permet d'utiliser un mélange de schémas lagrangiens et eulériens dans lesquels la solution d'un maillage lagrangien déformé est reportée sur un maillage eulérien fixé dans l'espace (Benson, 1992).

Ces codes d'impact (ou hydrocodes) se sont récemment avérés être des outils d'un grand intérêt pour la compréhension des phénomènes d'impacts géants et ont notamment permis de confirmer qu'un impact géant entre la Terre et un objet avec un rayon compris entre 3400 et 6370 km (nommé Théia) avait pu générer un champ de débris suffisant autour de la Terre pour former la Lune (Canup, 2004; Ćuk and Stewart, 2012). Ces codes permettent de modéliser l'impacteur et le corps impacté sous forme d'assemblage de plusieurs millions de blocs pluri-kilométriques et intègrent des équations d'état de plusieurs matériaux géologiques (ex. fer, basalte, dunite...) permettant ainsi de calculer précisément l'évolution Pression/Température de chaque matériau. Parmi eux, le code iSALE (Collins et al., 2008) est un hydrocode open-source (bénéficiant d'une version 2D et 3D) largement utilisé par la communauté scientifique de la planétologie. Il a été développé pour modéliser les écoulements de fluides à différentes vitesses. iSALE est ainsi particulièrement pertinent pour mesurer les conséquences internes de larges impacts météoritiques (Davison et al., 2010).

2.2 Augmentation de pression au cours d'un impact

Malgré la fréquence élevée des impacts à faibles vitesses ($<$10 km/s) pendant l'accrétion des corps telluriques du Système Solaire (Agnor et al., 1999), les caractéristiques de la propagation des ondes de choc lors de tels impacts étaient jusqu'à récemment peu contraintes (Pierazzo et al., 1997). Dans une étude développée en collaboration avec J. Arkani-Hamed, nous avons utilisé des simulations hydrocodes iSALE-2D afin de calculer l'évolution de la pression liée à l'impact et les vitesses de propagation de l'onde de choc sur un corps tellurique de la taille de Mars et pour des vitesses d'impact comprises entre 4 et 10 km/s (Figure 3) (Monteux and Arkani-Hamed, 2016). Nous avons considéré dans cette étude de gros impacteurs avec des diamètres compris entre 100 et 400 km comparables à ceux ayant généré des cratères d'impacts martiens comme Hellas ou Argyre. Nos résultats montrent que l'intensité de l'onde de choc se répartit en 3 zones sphériques dans le manteau autour du point d'impact et que cette intensité diminue avec l'éloignement au point d'impact. Nous avons caractérisé la répartition de la pression post-impact par des lois d'échelles ce qui représente une première étape primordiale pour déterminer l'intensité du chauffage lié à un impact sur une protoplanète en croissance.

Alors que les impacts majeurs lors de l'accrétion tardive d'une planète de type Mars se produisent sur un corps différencié, les caractéristiques de la propagation de l'onde de choc sont mal connues à l'intérieur de ces objets avec un manteau rocheux et un noyau liquide. Dans une deuxième étude (Monteux and Arkani-Hamed, 2019), nous avons utilisé d'autres simulations

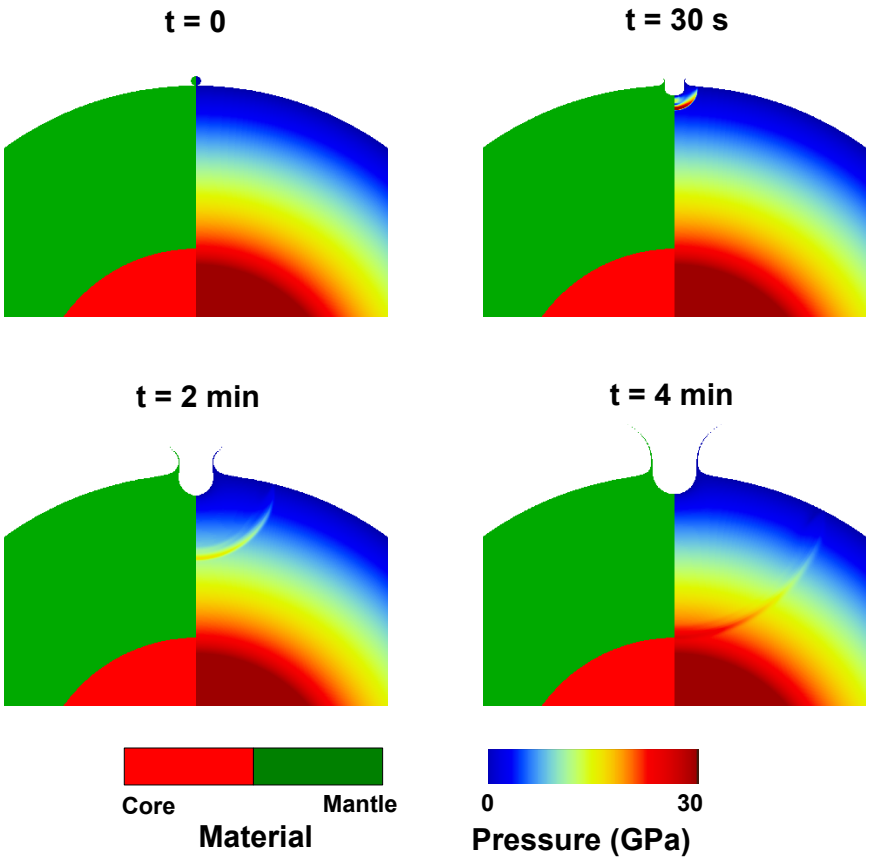

FIGURE 3 – *Évolution temporelle du champ de composition et de la pression lors du passage de l'onde de choc générée par un impact avec une vitesse* $V_{imp} = 10$ *km/s entre un impacteur avec un diamètre* $D_{imp} = 100$ *km et un corps de la taille de Mars (D'après Monteux and Arkani-Hamed (2016)).*

d'hydrocodes iSALE-2D pour calculer la pression de choc dans un corps différencié de type Mars pour des vitesses d'impact allant de 5 à 20 km/s, des rayons d'impacteur allant de 50 à 200 km et différentes rhéologies. Pour mieux représenter la distribution de la pression de choc en fonction de la distance du site d'impact à la surface, nous avons proposé deux régions distinctes dans le manteau : une région de champ proche qui s'étend jusqu'à 7-15 fois le rayon du projectile dans la cible, où la pression de choc maximale décroît de manière exponentielle avec l'augmentation de la distance du site d'impact, et une région de champ lointain où la pression décroît fortement avec la distance en suivant une loi de puissance. À la frontière entre le noyau et le manteau (CMB), la pression de choc maximale augmente du côté du manteau vers le côté du noyau. L'onde de choc réfractée se propage à l'intérieur du noyau où la pression de choc diminue en suivant une seconde loi de puissance.

2.3 Chauffage résultant d'un impact

L'énergie disponible lors d'un impact est l'énergie cinétique de l'impacteur. Ainsi elle est fonction de deux paramètres : la vitesse et la masse de l'impacteur. Lors de la collision, 10 à 20% est utilisée pour détruire l'impacteur, 40 à 50% de l'énergie d'impact permet de déformer le corps impacté et 30 à 40% est convertie en chaleur (O'Keefe and Ahrens, 1977). Au cours de la collision, une partie de l'énergie cinétique est donc dissipée sous forme de chaleur et permet une augmentation locale de la température en profondeur, en dessous du point d'impact dans une région sphérique à hémisphérique (Figure 4). L'évolution temporelle de la taille des impacteurs a probablement joué un rôle important dans l'évolution thermique primitive des planètes puisque la taille des impacteurs conditionne le taux d'accrétion mais aussi le volume de la région chauffée suite à un impact (Pierazzo et al., 1997).

Il est possible d'estimer au premier ordre l'augmentation de température en dessous du point d'impact en considérant que :

1. le volume chauffé est 3 fois le volume de l'impacteur
2. la vitesse de l'impacteur est au moins égale à la vitesse d'échappement de la planète impactée
3. une fraction γ de l'énergie cinétique de l'impacteur est dissipée sous forme de chaleur ($\gamma \approx 30\%$) le reste étant utilisé pour déformer et fragmenter l'impacteur et sa cible.

On aboutit ainsi à l'estimation suivante :

$$\Delta T \approx \frac{4\pi\gamma G\rho R^2}{9C_p} \tag{1}$$

avec G la constante gravitationnelle. Pour un corps de la taille de la Lune l'augmentation de température est d'environ 100 K alors que pour un corps de la taille de la Terre, cette augmentation de température est de l'ordre de 2000 K (Monteux et al., 2007).

Les vitesses d'impact sont généralement comprises entre 1 et 10 fois la vitesse d'échappement de la planète impactée (vitesse nécessaire pour échapper à l'attraction gravitationnelle du corps en croissance). Si les vitesses d'impact sont essentiellement fonction de la taille du corps impacté, l'apport d'énergie après impact augmentera donc au cours de l'accrétion (Figure 5). Les parties les plus externes des planètes en croissance seront ainsi plus susceptibles de fondre en premier (Kaula, 1979). Aussi lors des dernières étapes d'accrétion de grand volumes de manteau primitif sont susceptibles d'être chauffés par impact et de fondre si la température locale dépasse le solidus du manteau au cours de la croissance de la planète. Les énergies d'impact sont ainsi de plus en plus susceptibles de faire fondre le fer et les silicates du manteau. Cette énergie peut s'ajouter à la chaleur de désintégration radioactive des éléments à courtes périodes tels que ^{26}Al ou ^{60}Fe et entraîner des phénomènes de fusion significative au cours desquels se forment des océans magmatiques.

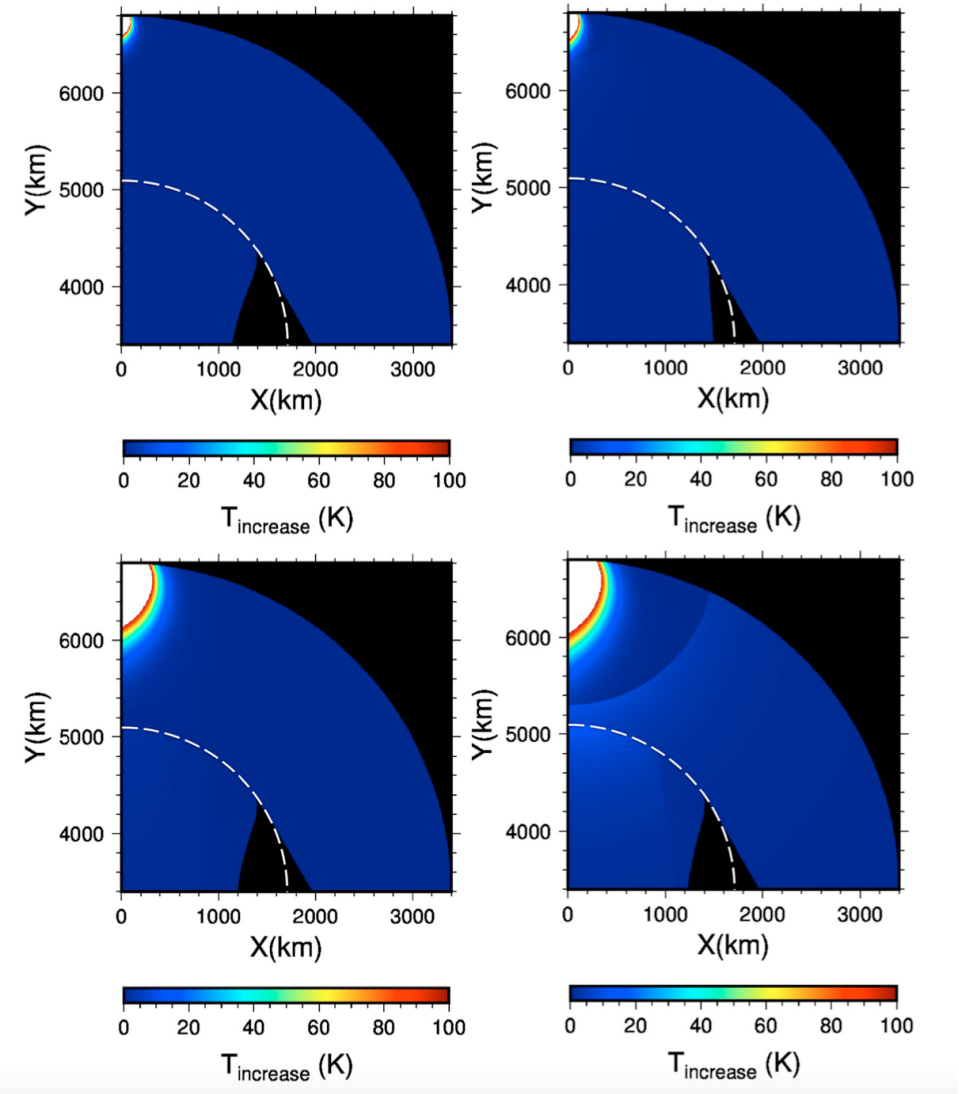

FIGURE 4 – *Augmentation de la température après un impact au sein d'une planète différenciée de la taille de Mars. La première ligne : $R_{imp} = 50$km et $V_{imp} = 10$ km/s, et la deuxième ligne : $R_{imp} = 150$ km et $V_{imp} = 10$ km/s (gauche : modèle constitutif avec résistance, droite : modèle hydrodynamique sans résistance). Les quatre figures représentent la combinaison des lois d'échelle obtenues à partir de codes iSALE avec le modèle d'augmentation de température induite par l'impact de Watters et al. (2009). La ligne blanche en pointillés représente le CMB (D'après Monteux and Arkani-Hamed (2019)).*

Grâce aux outils de modélisation disponibles (voir section 2.1), il est désormais possible d'estimer plus précisément la répartition du chauffage post-impact à l'intérieur du corps impacté. Dans l'étude évoquée précédemment (Monteux and Arkani-Hamed, 2019), à partir des résultats obtenus grâce aux simulations de l'hydrocode iSALE, nous avons dérivé des lois d'échelles qui illustrent l'influence de la rhéologie de la cible, de la taille de l'impacteur et de la vitesse de l'impact sur la propagation de l'onde de choc et la répartition de la pression au

cours d'un impact. En combinant les lois d'échelles obtenues avec un formalisme qui relie augmentation de température et pression de choc comme celui proposé par Watters et al. (2009), nous avons pu déterminer le chauffage induit par des impacts de diamètres supérieurs à 100 km au sein d'une planète différenciée. Nous avons ainsi pu comparer les champs de température post-impact obtenus avec l'hydrocode iSALE et les champs de température prédits par nos lois d'échelle. Ces résultats sont illustrés dans la Figure 4. Cette figure montre notamment l'importance de la taille de l'impacteur qui conditionne fortement le volume chauffé. Cette figure illustre aussi que la géométrie de la zone chauffée localisée en dessous du point d'impact n'est ni parfaitement hémisphérique (Tonks and Melosh, 1992) ni sphérique (Croft, 1982; Pierazzo et al., 1997).

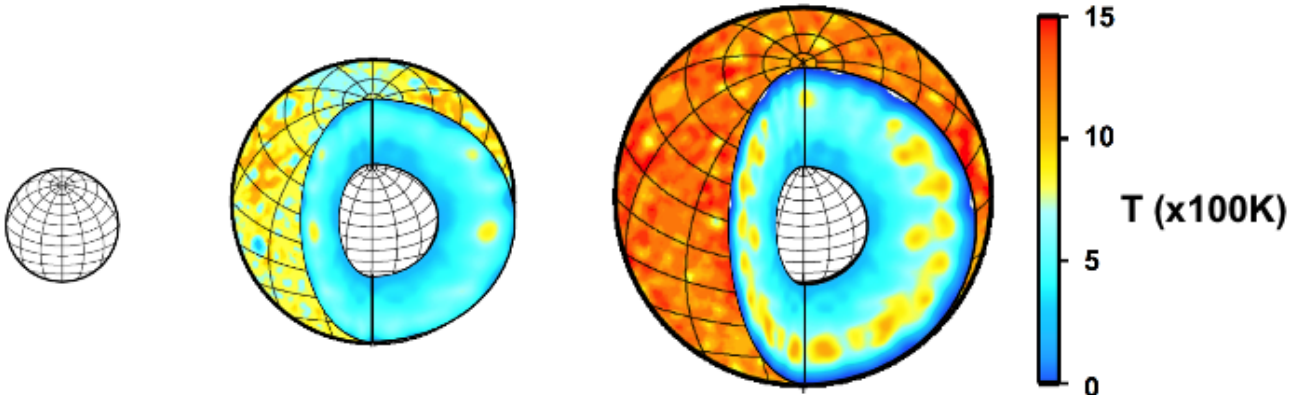

FIGURE 5 – *Représentation de l'évolution topographique et thermique d'une planète en croissance à partir d'un objet tellurique de rayon 500 km (gauche) jusqu'à l'accrétion d'un planète de 3000 km de rayon. Après chaque impact la protoplanète grossit et une partie de l'énergie cinétique est dissipée sous forme de chaleur en profondeur (centre). À la fin de l'accrétion, les vitesses d'impact étant plus élevées, l'intensité du chauffage par impact est plus grande dans les parties externes de la planète (droite).*

Une fois que l'anomalie thermique est formée en dessous du point d'impact, un réajustement mécanique à plus long terme va avoir lieu afin que le matériel chaud et moins dense puisse se refroidir. Au cours de mes travaux de thèse (Monteux et al., 2007), je me suis intéressé à la dynamique de relaxation de l'anomalie thermique engendrée par un impact météoritique sans fusion. J'ai développé un code numérique permettant de résoudre les équations de Navier-Stokes en différences finies, en géométrie axisymétrique cylindrique et en formulation en fonction de courant (Monteux et al., 2007). Nos résultats montrent que si l'impacteur est trop petit, l'anomalie thermique va seulement se refroidir par diffusion. Cependant, lorsque l'impacteur dépasse une taille critique, l'anomalie thermique subit d'abord une phase advective

isotherme puis refroidit par diffusion. L'épaisseur de l'anomalie thermique à la fin de l'étape advective ne dépend que des paramètres rhéologiques du corps impacté.

2.4 Impacts géants et fusion à grande échelle

Au cours des dernières étapes de la croissance des planètes telluriques, les collisions entre protoplanètes ne sont pas des évènements exceptionnels (Agnor et al., 1999). Les impacts géants sont maintenant connus pour être inévitables durant les étapes tardives de l'accrétion des planètes et ont pu avoir des conséquences majeures sur l'évolution tardive des planètes telluriques. Nous savons que certaines caractéristiques du Système Solaire peuvent être expliquées par les impacts géants. Les impacts géants sont ainsi invoqués pour expliquer la faible épaisseur du manteau de Mercure par rapport à la taille de son noyau (Benz et al., 1988), la dichotomie martienne (Marinova et al., 2008) ou encore les moments angulaires actuels des planètes (Kurosaki and Inutsuka, 2019).

La formation de la Lune est probablement due à un ou plusieurs impacts géants durant l'histoire primitive de la Terre. La faible taille du noyau métallique lunaire par rapport à l'épaisseur de son manteau et le fait que la Lune et la Terre présentent des similitudes de composition isotopique notamment en oxygène (Wiechert et al., 2001) supportent l'idée que, tôt dans l'histoire de la Terre, à un moment où la Terre était déjà différenciée (70-100 Ma après la formation des C.A.I.), la Terre a été impactée par un objet avec un rayon de plusieurs milliers de kilomètres (Théia). Le champ de débris suivant cet impact, essentiellement formé de matériel terrestre mantellique et donc appauvri en fer, s'est ensuite ré-accrété autour de la Terre permettant la formation de la Lune en orbite autour de la Terre. Les noyaux de l'impacteur et de la Terre se sont mélangés pour former le noyau terrestre (Hartmann and Davis, 1975). Les études du moment angulaire du système Terre-Lune menées par Cameron and Ward (1976) ont ensuite permis d'arriver à la même conclusion en donnant un ordre de grandeur de la taille de l'impacteur : entre 1/3 et 1/2 rayon terrestre. L'impact ayant formé le système Terre-Lune aurait eu lieu avec une vitesse de l'ordre de quelques $km.s^{-1}$. Cette théorie a inspiré de nombreux travaux de modélisation de cet impact notamment à l'aide des codes S.P.H. (Smoothed Particle Hydrodynamics) développés par Canup and Asphaug (2001). La similarité de composition isotopique en oxygène (Wiechert et al., 2001) et en tungstène (Touboul et al., 2007) laisse entrevoir deux possibilités. Soit la Lune s'est formée essentiellement à partir de matériel terrestre, soit les manteaux lunaire et terrestre se sont équilibrés à la suite de l'impact géant. Or, dans les modèles dynamiques (Canup, 2004), la majorité du matériel lunaire proviendrait de l'impacteur.

Pour expliquer la composition de la Lune et sa similarité isotopique avec la Terre, Lock et al. (2018) ont proposé un modèle faisant intervenir un impact géant, plus énergétique que dans le modèle traditionnel. Cet impact entraînerait la Terre dans un état de vaporisation et de

rotation rapide qui s'étend sur des dizaines de milliers de kilomètres. De tels états planétaires sont appelés "synestias". Lorsque la synestia se refroidit, la matière se condense et forme la Lune. Lock et al. (2018) ont constaté que la Lune se forme à l'intérieur de la synestia, entourée de vapeur de composition terrestre à des pressions de plusieurs dizaines de bars. La Lune orbite dans la synestia suffisamment longtemps pour s'équilibrer chimiquement avec la Terre vaporisée ce qui favoriserait les similitudes chimiques entre la Terre et la Lune.

Outre la formation de la Lune, cet impact géant a probablement eu des conséquences majeures sur l'état thermique du manteau terrestre. Le timing de l'impact (moins de 100 Ma après la formation des premiers solides) suppose qu'il a eu lieu sur une planète très chaude déjà significativement affectée par les précédents impacts, le chauffage radioactif et la formation du noyau (dont je discute dans la section suivante). Selon les modèles de Nakajima and Stevenson (2015), l'impact qui a formé le système Terre-Lune a entraîné la fusion complète du manteau terrestre et des processus de mélanges plus ou moins importants selon la taille de l'impacteur et la vitesse de rotation de la Terre avant impact.

L'idée que l'impact à l'origine du système Terre-Lune ait fondu et mélangé efficacement le manteau primitif est difficile à justifier géo-chimiquement notamment si on s'intéresse au système Hf-W. Les roches terrestres présentent en effet des rapport variés en $^{182}W/^{184}W$ notamment dans les roches anciennes (Lee and Halliday, 1996; Willbold et al., 2011; Touboul et al., 2012). Cette variété pourrait indiquer que le manteau primitif était hétérogène et que la signature de cette hétérogénéité a été préservée pendant plusieurs milliard d'années. Ainsi, moins de 1000 ans après l'impact géant (ce qui correspond au temps d'accrétion de la Lune), le manteau se résumerait à un océan magmatique de 2900 km de profondeur mais conservant potentiellement des hétérogénéités chimiques (Nakajima and Stevenson, 2015). La préservation à long terme de telles hétérogénéités indiquerait que la vigueur convective du manteau au cours des temps géologiques n'a pas été suffisante pour détruire tous les réservoirs mantelliques qui se sont formés au début de l'histoire de la Terre (Jackson et al., 2010). Des modèles dynamiques du manteau terrestre suggèrent que des parties vierges du manteau pourraient échapper à la différenciation au cours de l'âge de la Terre grâce à un isolement dans des tourbillons convectifs (Brandenburg et al., 2008). La question du mélange qui suit l'impact géant (1000 ans après l'impact) doit cependant être envisagée grâce à des modèles de convection adaptés à la caractérisation de processus turbulents (Solomatov, 2000)(voir Section 6).

2.5 Autres sources de chaleur

En plus du chauffage par impact, d'autres sources de chaleur ont pu participer au budget thermique primitif de la Terre. Ainsi, le chauffage par les éléments radioactifs à courte période ou la dissipation thermique liée à la formation du noyau terrestre ont pu jouer un rôle essentiel dans l'évolution des jeunes planètes.

2.5.1 Chauffage par les éléments radioactifs à courte période

La chaleur dégagée par la désintégration des éléments radioactifs à courtes périodes a probablement joué un rôle important sur les températures des planétésimaux primitifs. En effet, la désintégration radioactive de certains éléments s'accompagne d'un dégagement d'énergie sous forme de rayonnement (γ) ou de l'émission de particules α ou β dont la diffusion dans les matériaux environnants dégage d'importantes quantités de chaleur. Les éléments isotopiques (parents) à courtes demi-vies ont maintenant disparu mais un excès d'éléments (fils) issus de cette désintégration peut se retrouver dans les météorites intégrant des C.A.I.. L'étude de ces radioactivités maintenant "éteintes" dans les météorites donne des informations importantes sur l'environnement initial de formation des premiers corps et des étoiles (Meyer and Clayton, 2000).

Élémént père	$\tau_{1/2}$(Myr)	Élément fils	Production de chaleur par unité de masse (W/kg)
^{26}Al	0.7	^{26}Mg	1.5×10^{-7}
^{238}U	4468.3	^{206}Pb	9.17×10^{-5}
^{40}K	1248	^{40}Ar	2.97×10^{-5}
^{232}Th	14010	^{208}Pb	2.56×10^{-5}
^{60}Fe	1.5	^{60}Ni	$0.3 - 1.2 \times 10^{-8}$

TABLE 1 – Couples d'isotopes radioactifs ayant contribué au bilan thermique du manteau terrestre (selon Lebrun et al. (2013) et McDonough et al. (2020)).

Si l'on considère H le taux de production interne de chaleur par désintégration isotopique d'un planétésimal de rayon R. Ce chauffage prend le pas sur la diffusion thermique lorsque $\rho C_p H$ est supérieur à kT/R^2 avec k la conductivité thermique du planétésimal, T sa température, C_p sa capacité calorifique et ρ sa densité. $H \sim T/t$ donc lorsque $\rho C_p R^2/(kt) >> 1$, le planétésimal se réchauffe plus vite qu'il ne se refroidit par diffusion avec t l'âge du planétésimal. En 1 Ma et pour des objets avec des rayons inférieurs à 5 km, le refroidissement par diffusion était prépondérant. En 1 Ma, selon Kokubo and Ida (2000), les planétésimaux les plus volumineux auraient atteint des rayons de $\sim 10 - 100$ km. La chaleur associée à la désintégration était donc globalement retenue. La température maximale atteinte au centre d'un planétésimal de rayon $R = 30$ km aurait pu dépasser 1270 K (Schramm et al., 1970; Hutcheon and Hutchison, 1989). Les plus gros objets auraient ainsi pu subir une éventuelle différenciation associée à des phénomènes de fusion via la désintégration d'isotopes radioactifs à courte période puis évacuer leur chaleur par diffusion. Au moment où les protoplanètes commencent à atteindre des tailles importantes (~ 1000 km), elles ont évacué par diffusion une partie importante de leur chaleur issue de la désintégration radioactive des éléments à courte période.

Deux de ces radioactivités éteintes ont pu participer à l'état thermique initial des planétésimaux (Tableau 1) : la désintégration du ^{26}Al (principalement localisé dans la phase silicatée des planétésimaux) et la désintégration du ^{60}Fe (principalement localisé dans la phase métallique des planétésimaux). Des excès importants de ^{26}Mg ont été trouvés confinés dans des

C.A.I. dans des météorites carbonnées et dans chondrites ordinaires mais aussi dans du matériel météoritique non réfractaire (Hutcheon and Hutchison, 1989). Cette présence de ^{26}Mg en excès traduit la présence passée de ^{26}Al. Le ^{26}Al était ainsi présent en quantité significative pendant les premiers millions d'années du système solaire.

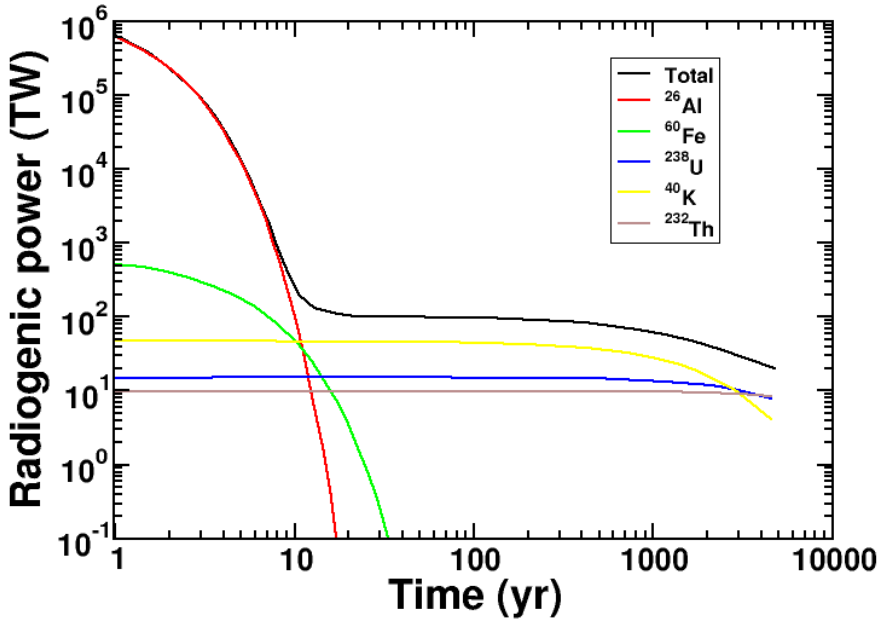

FIGURE 6 – *Évolution temporelle du chauffage radioactif pour les éléments chimiques qui ont le plus contribué au bilan thermique de la Terre depuis sa formation il y a plus de 4.5 Ga (à partir de McDonough et al. (2020)).*

Il est possible d'estimer la puissance dissipée par ce mode de chauffage en fonction du temps (Figure 6). Cette puissance est fonction de la composition chimique considérée en conditions initiales. McDonough et al. (2020) estiment qu'au cours des 20 premiers millions d'années apèrs la formation des C.A.I., le ^{60}Fe et le ^{26}Al ont été les éléments qui ont le plus contribué au chauffage radioactif dissipant une puissance allant jusqu'à 10^6 TW. Aujourd'hui, le chauffage radioactif est principalement fourni par la désintégration de ^{238}U, ^{40}K et ^{232}Th qui permettent de produire environ 20 TW de chauffage en profondeur principalement dans la lithosphère.

2.5.2 Dissipation thermique lors de la formation du noyau

Une autre source majeure de chaleur ayant fortement influencé l'état thermique primitif du manteau terrestre provient de la formation de son noyau. En effet si l'on imagine que le fer du noyau était initialement réparti uniformément au sein de la Terre après l'accrétion, la séparation fer/silicates et la chute du fer vers le noyau provoquent un transfert de masse important du fait que le fer du noyau est plus dense que les silicates du manteau. Ce transfert de masse diminue l'énergie potentielle du fer dans le manteau qui se convertit en chaleur à l'intérieur de la jeune Terre. Flasar and Birch (1973) estiment que cette conversion d'énergie potentielle en chaleur libérerait suffisamment d'énergie pour provoquer une augmentation de la température à l'intérieur de la Terre de plus de 2000 K.

La répartition de cette chaleur à l'intérieur de la Terre dépend fortement de la façon dont le fer va migrer vers son centre (Ke and Solomatov, 2009). Si le fer plonge en suivant de long chenaux, la chaleur ira principalement dans le noyau. Cependant si le fer plonge sous la forme de grosses gouttes ou de larges diapirs, l'énergie potentielle se dissipera principalement dans le manteau. Dépendamment des mécanismes de ségrégation, cela donnera lieu à des profils thermiques différents avec soit un noyau bien plus chaud que le manteau, soit un manteau très chaud voir fondu. Les modalités de différenciation et notamment les volumes caractéristiques de fer (gouttelettes centimétriques ou diapir pluri-kilométriques) mis en jeu lors de la séparation fer/silicates conditionnent donc l'état thermique primitif du manteau terrestre. Samuel et al. (2010) ont aussi montré qu'un grand nombre de petits diapirs de fer plongeant dans un océan magmatique favorise l'échange de chaleur fer/silicates et conduit à un noyau relativement chaud comme sur la Terre. À contrario, un petit nombre de grands diapirs a l'effet inverse et pourrait correspondre à une planète semblable à Mars. La séparation fer/silicates par diapirisme tend à laisser le manteau profond nettement plus chaud que sa partie supérieure, ce qui pourrait provoquer la fusion d'une fraction significative au dessus de la frontière manteau/noyau. Nous reviendrons plus en détail sur ce processus dans la section 3.

2.5.3 Chauffage par dissipation de marées

L'impact à l'origine de la formation du système Terre-Lune a probablement induit la formation d'un océan de magma terrestre profond et généré un disque de débris autour de la proto-Terre qui s'est rapidement ré-accrété pour former la Lune. À cette époque, la Lune était plus proche de la Terre qu'aujourd'hui, ce qui a pu avoir des conséquences importantes sur l'interaction entre les deux objets. En particulier, les interactions de marée qui ont suivi la formation de la Lune ont contrôlé l'évolution de la rotation et ont potentiellement influencé le refroidissement de la Terre et de la Lune primitives (Chen and Nimmo, 2016).

L'évolution de l'orbite lunaire dépend fortement de la manière dont l'énergie des marées a été dissipée sur la Terre primitive et est donc étroitement liée à son évolution thermique. La friction des marées associée aux mouvements de cisaillement dissipe une énorme quantité

d'énergie. Sur la Terre moderne, la dissipation des marées est dominée par les processus de dissipation océanique (Ray et al., 2001). Actuellement, la dissipation associée aux marées représente 3,5 TW, mais il y a 4,5 Ga, la puissance produite par la friction des marées pouvait être supérieure de plus de 2 ordres de grandeur (Farhat et al., 2022). Au cours de l'Hadéen, la fraction fondue du manteau silicaté de la Terre devait avoir un impact important sur les processus de dissipation des marées et, ainsi, sur l'ensemble de l'évolution du système Terre-Lune. En retour, l'énergie dissipée dans la Terre hadéenne a pu affecter sa structure thermique, sa dynamique convective et étendre la fraction interne en matériel fondu, conduisant à un régime thermique induit par les marées comparable à ce qui est observé sur Io, une des lunes de Jupiter (Kervazo et al., 2021). Même après la première étape de cristallisation de l'océan magmatique, une quantité importante de matière fondue peut être préservée dans le manteau hadéen (Ray et al., 2001) ce qui peut contrôler à la fois la production de chaleur par friction tidale et le transfert de chaleur par extraction de la matière fondue. Cette période de dissipation intense des marées (dépassant plusieurs centaines de TW) a pu durer pendant les premières dizaines de millions d'années suivant l'impact formant la Lune, ce qui pourrait avoir eu une influence significative sur la dynamique de refroidissement de la Terre partiellement fondue et sur la séquence de cristallisation.

Si l'état orbital et rotationnel récent du système Terre-Lune est bien documenté (Williams, 2000), les interactions du système Terre-Lune à ses débuts n'ont pas été étudiées et, en particulier, l'influence de la Lune primitive sur l'évolution thermique et la fusion de la Terre primitive reste encore inexplorée. Nous reviendrons plus en détails sur ce processus dans la section 6.4.

2.6 Perspectives : Le rôle des impacts dans l'évolution primitive de l'atmosphère terrestre (Thèse de T. Engels)

Les impacts météoritiques ont aussi participé à la formation de l'atmosphère terrestre :

1. en érodant l'atmosphère préexistante : Le long de sa trajectoire dans l'atmosphère, l'impacteur forme un canal de gaz chaud moins dense que l'atmosphère environnante. Ce gaz chaud migre à travers ce canal et est éventuellement éjecté dans l'espace (Shuvalov, 2009).
2. en apportant du matériel au corps impacté (Raymond et al. (2006), Engels et al. (in revision for Icarus)) : Ce matériel peut être soit dégazé lors de son impact à la surface du corps en croissance soit être dégazé ultérieurement après son dépôt sous forme solide à la surface du corps impacté.
3. en dégazant du matériel profond : Un impact entraîne la formation d'une atmosphère transitoire à haute température et riche en silicate, mais aussi la fusion de matériel rocheux dans lequel du gaz est emprisonné (Figure 7) (Marchi et al., 2016). Lors de son refroidissement rapide, l'atmosphère transitoire se condense, tandis que la masse fondue générée par l'impact se propage à la surface. Lorsque la roche fondue se propage, elle libère des gaz (CO, CO_2, H_2, SO_2, CH_4, H_2O, H_2S). Des études en laboratoire ont

permis de quantifier la quantité de volatils dégazés sur des matériaux impactés comme de la calcite ou de la serpentine (Lange and Ahrens, 1982, 1986). Ces études montrent notamment que la serpentine commence à dégazer son H_2O à des pressions de choc d'environ 20 GPa ou que la calcite commence à dégazer son CO_2 à 10–15 GPa. Au contact de la surface, un panache de gaz peut se développer au dessus du point d'impact où les molécules de gaz sont aussi chauffées et peuvent être accélérées vers le haut et échapper à la gravité du corps impacté.

La compétition de ces 3 phénomènes peut ainsi entraîner l'augmentation de l'épaisseur de l'atmosphère ou son érosion. L'efficacité du dégazage ou de l'érosion par impact est fonction de la vitesse d'impact (v_{imp}), de la taille de l'impacteur (R_{imp}), de la taille du corps impacté (R_p), de la composition chimique et des propriétés rhéologiques (porosité, viscosité) des matériaux mis en jeu.

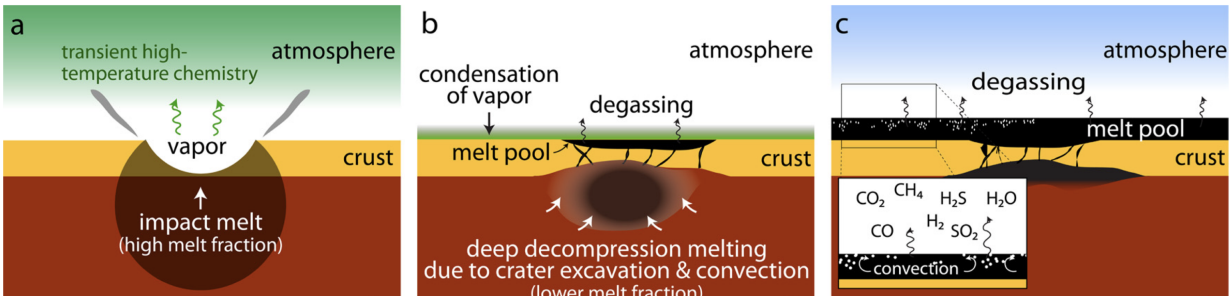

FIGURE 7 – *Représentation schématique d'un épisode de fusion et du dégazage provoqué par impact sur la Terre primitive (À partir de Marchi et al. (2016)).*

Le dégazage des éléments volatils est encore peu contraint et attribué à l'action combinée des hautes températures, à une amplification de la diffusion ou au développement de microfractures (Zhang, 2014). Comme la combinaison de ces mécanismes est peu connue, les lois d'échelles permettant d'obtenir la fraction de matériel dégazé par impact géant à partir d'expériences en laboratoires sur de petits volumes sont difficiles à obtenir. De plus, il existe encore de grandes incertitudes sur l'histoire accrétive des planètes et de la Terre notamment. Grâce à la modélisation numérique on connaît désormais mieux les conséquences internes des gros impacts météoritiques (Monteux and Arkani-Hamed, 2016, 2019). Les lois d'échelles obtenues à partir de modélisations hydrocodes montrent que la pression en dessous du point d'impact peut atteindre plusieurs dizaines de GPa sur des volumes comparables à celui de l'impacteur. Ensuite l'augmentation de pression subie lors de l'impact diminue rapidement en s'éloignant du point d'impact. Les paramètres d'accrétion ont ainsi pu jouer un rôle majeur sur l'évolution de l'épaisseur de cette atmosphère (Ahrens, 1993; Ahrens et al., 2004). Cependant, à l'heure actuelle, aucun modèle quantitatif ne permet d'intégrer l'effet du dégazage du manteau, des gaz initiaux et des composés volatils produits par l'impact lors de l'accrétion des planètes (Zhang, 2014).

Si globalement la taille des impacteurs va augmenter au cours de l'histoire primitive du

Système Solaire, cette taille n'est pas unique et obéit à une distribution où les gros corps sont plus rares que les petits. L'accrétion de petits planétésimaux va favoriser la formation d'une atmosphère alors que les impacts géants vont entrainer un dégazage massif mais surtout une érosion massive de l'atmosphère préexistante voir éventuellement sa disparition. Un impacteur de la taille de la Lune serait ainsi susceptible d'ôter 50% de l'atmosphère terrestre (Ahrens, 1993; Ahrens et al., 2004). Les objectifs de la thèse de Tristan Engels sont de contraindre l'évolution primitive de l'atmosphère terrestre lors des dernières étapes de son accrétion (i.e. après l'impact géant à l'origine du système Terre-Lune) et en particulier de :

1. Contraindre l'influence des paramètres d'accrétion (v_{imp}, R_{imp}, taux d'accrétion) sur l'évolution des atmosphères planétaires. La taille des impacteurs va gouverner non seulement la quantité de matériel potentiellement dégazé par impact mais aussi la fraction d'atmosphère érodée. La répartition temporelle des tailles d'impacteurs et des leurs vitesses a donc surement joué un rôle sur l'épaisseur finale de l'atmosphère primitive à la fin des grandes étapes d'accrétion. L'évolution de la taille du corps en croissance et ainsi son taux d'accrétion vont aussi contrôler sa capacité à retenir son atmosphère.
2. Quantifier l'importance de l'accrétion par rapport au dégazage profond. Au cours de son histoire primitive, la Terre a pu perdre son atmosphère de manière répétée. Les derniers impacts géants qui auraient chassé tout ou partie de l'atmosphère pourraient être le point de départ de la formation de l'atmosphère terrestre par dégazage du manteau ou dégazage par impact (Zhang, 2014). En apportant des contraintes sur les caractéristiques (épaisseur et composition) de l'atmosphère primitive et en comparant avec les caractéristiques de l'atmosphère actuelle, il est possible de contraindre l'importance du dégazage généré lors de l'accrétion par rapport au dégazage profond lié à des phénomènes plus tardifs comme le volcanisme ou le bombardement tardif « Late Heavy Bombardment » (LHB).

Nous testerons si un dégazage sélectif est un modèle viable pour expliquer le spectre des éléments volatils (C, H, N et S) (Marty, 2012) ou si d'autres processus doivent être pris en compte (formation du noyau, la nature des briques élémentaires ou bien l'érosion de la surface terrestre via les impacts). Il est à noter que ce projet est très complémentaire des expériences menées au LMV pour déterminer le partage des volatils entre le noyau et le manteau (ex. Clesi et al. (2016, 2018); Boujibar et al. (2014)). Nous développons actuellement avec le Laboratoire de Météorologie Physique de Clermont-Ferrand (L. Deguillaume, A. Bianco, L. Pailler) un modèle numérique dans lequel il sera possible de choisir les caractéristiques de l'accrétion de la Terre en termes de taille d'impacteurs, de vitesse d'impacts et de taux d'accrétion et de connaître les caractéristiques de l'atmosphère primitive générée par une telle accrétion. Les informations obtenues par ces modèles seront l'épaisseur mais aussi la composition de cette atmosphère en éléments tels que C, H, N, O et S.

Dans ce cadre, l'expertise du LaMP permettra d'aider à la compréhension des mécanismes de réactivité chimique avec l'objectif d'estimer l'évolution temporelle de l'atmosphère primitive générée par l'accrétion. Les composés chimiques (CO, CO_2, CH_4, H_2S, SO_2, ...) émis sont

des précurseurs à la formation de nouvelles espèces chimiques après réactions chimiques. Ces processus chimiques de transformations dépendent des conditions atmosphériques (pression, température,...) et du flux actinique solaire initiateur potentiel de réactions photochimiques. Des mécanismes chimiques devront être construits sur la base des précurseurs chimiques en évaluant les paramètres cinétiques importants (constantes de réactivité et leur dépendance à la température et à la densité de l'air, par exemple). Les travaux de recherche sur la réactivité chimique des panaches volcaniques pourront également servir à la création de ces mécanismes car les conditions de températures et les précurseurs sont similaires. Des mécanismes d'oxydation pourraient également aboutir à la formation de composés moins volatils et à la formation potentielle de particules solides (nucléation). Une fois ces transformations mieux appréhendées, des estimations de temps de vie de ces composés chimiques pourront être évaluées afin d'estimer l'évolution temporelle de l'atmosphère primitive. Les codes numériques de chimie atmosphérique développés par le LaMP sont en cours d'adaptation par T. Engels afin de simuler l'évolution chimique de l'atmosphère primitive.

Références personnelles

Monteux, J., *Coltice, N., Dubuffet, F., Ricard, Y., 2007, Thermo-mechanical adjustment after impacts during planetary growth, Geophys. Res. Lett., 34, 24201–24205.* **LIEN HAL**

Monteux, J., *Arkani-Hamed, J., 2016b, Scaling laws of impact induced shock pressure in planetary mantle, Icarus, 264, 246–256.* **LIEN HAL**

Monteux, J., *Arkani-Hamed J., 2019, Shock wave propagation in layered planetary interiors : Revisited. Icarus, 331, 238-256.* **LIEN HAL**

Engels T., **Monteux, J.**, *Boyet M., Bouhifd M.A., Large impacts and their contribution to the water budget of the Early Moon, in revision for Icarus.*

GEOPHYSICAL RESEARCH LETTERS, VOL. 34, L24201, doi:10.1029/2007GL031635, 2007

Thermo-mechanical adjustment after impacts during planetary growth

Julien Monteux,[1] Nicolas Coltice,[1] Fabien Dubuffet,[1] and Yanick Ricard[1]

Received 29 August 2007; accepted 7 November 2007; published 18 December 2007.

[1] The thermal evolution of planets during their growth is strongly influenced by impact heating. The temperature increase after a collision is mostly located next to the shock. For Moon to Mars size planets where impact melting is limited, the long term thermo-mechanical readjustment is driven by spreading and cooling of the heated zone. To determine the time and length scales of the adjustment, we developed a numerical model in axisymmetric cylindrical geometry with variable viscosity. We show that if the impactor is larger than a critical size, the spherical heated zone isothermally flattens until its thickness reaches a value for which motionless thermal diffusion becomes more effective. The thickness at the end of advection depends only on the physical properties of the impacted body. The obtained timescales for the adjustment are comparable to the duration of planetary accretion and depend mostly on the physical properties of the impacted body. **Citation:** Monteux, J., N. Coltice, F. Dubuffet, and Y. Ricard (2007), Thermo-mechanical adjustment after impacts during planetary growth, *Geophys. Res. Lett.*, *34*, L24201, doi:10.1029/2007GL031635.

1. Introduction

[2] Impacts have strongly influenced the evolution of planets: a collision of the Earth with a Mars-sized body is at the origin of the formation of the Moon [*Hartmann and Davis*, 1975] and the impact by a kilometer-sized body could be responsible for the mass extinction at the K-T boundary [*Alvarez et al.*, 1980]. It is during accretion that impacts played the most significant role, depositing and burying heat into growing planetary bodies.

[3] When the impact velocity becomes larger than the elastic velocities, a shock wave develops. The shock pressure, increasing with the size of the impacted body, is nearly uniform in a spherical region next to the impact (the isobaric core), and strongly decays away from it [*Croft*, 1982]. Following the adiabatic pressure release, the peak pressure being independent of impactor size, a temperature increase of several hundred degrees remains on Moon to Mars size bodies [*Senshu et al.*, 2002] (see equation (2)). Hence, the hotter temperatures are located close to the surface during planetary growth [*Kaula*, 1979] and large impacts have caused extensive melting and formation of magma oceans on Earth [*Tonks and Melosh*, 1993].

[4] The thermal anomaly caused by an impact generates a buoyant thermal anomaly that ultimately drives an isostatic adjustment. If the impact velocity is larger than 7.5 km.s^{-1}, a significant volume of the isobaric core is molten [*O'Keefe and Ahrens*, 1977] hence the adjustment is controlled by two-phase flow and probably hydrofracturation [*Solomatov*, 2000]. For smaller planets or planetesimals, melting is nearly absent therefore the thermo-mechanical adjustment is dominated by the slow viscous deformation and thermal diffusion of the hot thermal anomaly.

[5] In this study, we investigate the thermal relaxation and viscous deformation after the shock of an impactor on a small planet or planetesimal in order to derive scalings for the relevant length and time scales of the thermo-mechanical adjustment.

2. Model Description

2.1. Thermal State After an Impact

[6] Energy balance calculations and shock simulations suggest that the radius of the isobaric core R_{ic} is comparable or slightly larger than that of the impactor R_{imp} and we use $R_{ic} = 3^{1/3} R_{imp}$ [*Senshu et al.*, 2002; *Pierazzo et al.*, 1997]. Away from the isobaric core, the shock wave propagates and the peak pressure decays with the square of the distance r from the center of the isobaric core [*Pierazzo et al.*, 1997]. Just after the adiabatic pressure release, the thermal perturbation corresponds to an isothermal sphere of radius R_{ic} and temperature $T_0 + \Delta T$ that decays when $r > R_{ic}$ as

$$T(r) = T_0 + \Delta T \left(\frac{R_{ic}}{r}\right)^m, \quad (1)$$

with $m \sim 4.4$ as proposed by *Senshu et al.* [2002].

[7] The energy dissipated as heat following the shock is a fraction of the kinetic energy of the impactor. The impactor velocity v_{imp} should be comparable to the escape velocity $v_{imp} = \sqrt{2gR}$, where $g = 4/3\ G\pi\rho R$, ρ and R are the gravity, density and radius of the impacted growing planet [*Kokubo and Ida*, 1996]. Assuming $\rho \sim \rho_{imp} \sim \rho_{ic}$, the temperature increase ΔT is

$$\Delta T = \frac{4\pi}{9} \frac{\gamma}{f(m)} \frac{\rho G R^2}{C_p}, \quad (2)$$

where C_p is the heat capacity of the impacted body and G is the gravitational constant. The efficiency of kinetic to thermal energy conversion γ is close to 0.3 according to physical and numerical models [*O'Keefe and Ahrens*, 1977]. The function $f(m)$ represents the volume effectively heated normalized by the volume of the isobaric core (i.e., $f(m) = 1$ if only the isobaric core is heated). Assuming $R_{ic} \ll R$ and integrating equation (1) leads to $f(m) \sim 2.7$ and 37% of the impact heating is released within the isobaric core. The temperature increase does not depend on the size of the impactor but on the square of the radius of the impacted body.

[1] Laboratoire de Sciences de la Terre, UMR 5570, CNRS, Université de Lyon, Université Claude Bernard Lyon 1, Ecole Normale Supérieure de Lyon, Villeurbanne, France.

0094-8276/07/2007GL031635$05.00

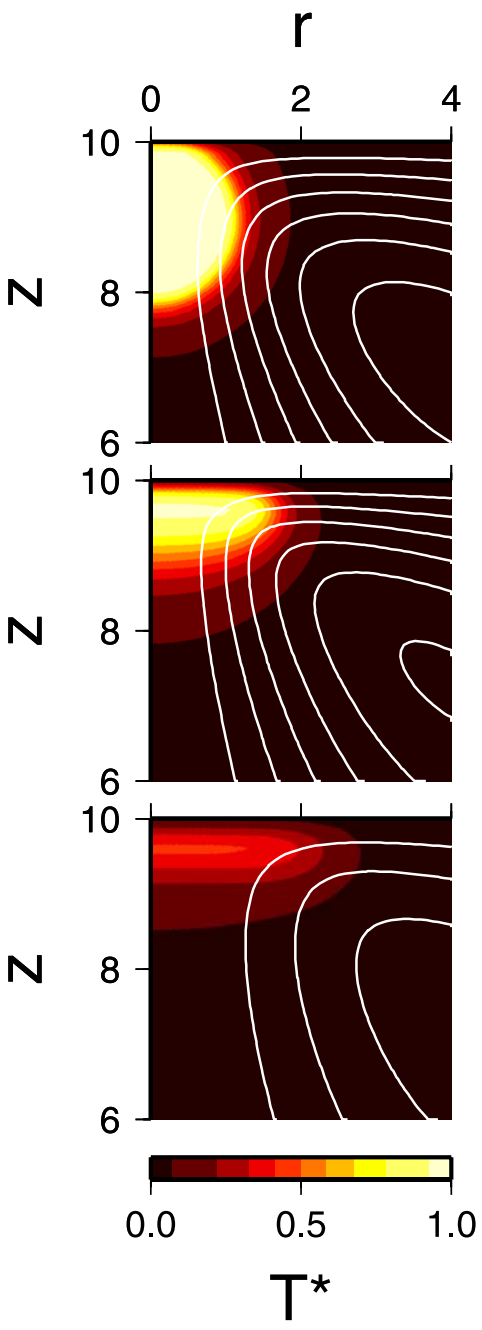

Figure 1. Close up view of the non dimensional temperature fields and streamlines computed for a temperature dependent viscosity at non-dimensionalized times (top) $t^* = 0$, (middle) $t^* = 3$ and (bottom) $t^* = 10$ (we use $\lambda = 10^{-2}$ and $Ra_{ic} = 10^2$ (see 2.2)).

[8] Immediately after the shock, a fraction of the isobaric core is removed during crater excavation. However, it is only for small impactors (less than 5 km of radius) and large planets (more than 3000 km of radius) that a significant fraction of the heated zone is redistributed [*Maxwell*, 1977]. Because our study is focused on large impacts (>10km) on small planets (<3000km), we can neglect the excavated heat or consider it as an additional uncertainty on the parameters γ or $f(m)$ (see equation (2)). Following excavation, reduction of the crater depth to at most few kilometers takes place through isostatic rebound. The total amount of vertical motion that occurs during the isostatic process (a few km), and its duration (typically a few 10^3y) are negligible compared to the length scales and timescales of thermal readjustment. After the crater formation, most of the initial energy still remains below the crater [*Turtle et al.*, 2003]. Modelling these processes of mass and energy redistribution is beyond the scope of this paper since we are interested in the long term consequences of shock heating as in work by *Reese et al.* [2002].

[9] The proposed thermal state following an impact sketched in Figure 1 (top) is that of a cold body of homogeneous temperature T_0 perturbed by the impact of a sphere of radius R_{ic} (the depth of the crater being negligible compared to the heated zone).

2.2. Thermo-Mechanical Model

[10] The governing non-dimensional equations for the extremely viscous flow of a cooling hot drop are

$$-\vec{\nabla}P^* + \vec{\nabla}\cdot\left(\frac{\eta(T^*)}{\eta_0}\vec{\nabla}\vec{v}^* + \left[\frac{\eta(T^*)}{\eta_0}\vec{\nabla}\vec{v}^*\right]^T\right) + T^*\vec{e_z} = 0, \tag{3}$$

$$\frac{\partial T^*}{\partial t^*} = \frac{\nabla^2 T^*}{Ra_{ic}} - \vec{v}^*.\vec{\nabla}T^*, \tag{4}$$

$$\vec{\nabla}.\ \vec{v}^* = 0, \tag{5}$$

where distances, temperature and velocity are normalized by R_{ic}, ΔT and the characteristic Stokes velocity v_s of the isobaric core

$$v_s = \frac{\alpha\rho g\Delta T R_{ic}^2}{\eta_0}, \tag{6}$$

where η_0 is the viscosity far from the impact and α the thermal expansivity of the impacted body. Ra_{ic} is the Rayleigh number based on the isobaric core radius:

$$Ra_{ic} = \frac{\alpha\rho g\Delta T R_{ic}^3}{\kappa\eta_0}. \tag{7}$$

We define a Rayleigh number based on the size of the isobaric core R_{ic} since in all our experiments, the radius of the planet R remains much larger than R_{ic} and thus does not affect the dynamics except through the gravity and the temperature increase (see equation (2)).

[11] For planets of Moon to Mars size the gravity and the temperature increase are not very large (e.g. $g \simeq 3$ m s^{-2}, $\Delta T \simeq 300$ K). We also consider impactors with radius small compared to the planet radius (e.g. $R_{ic} \simeq 300$ km). In this case, Ra_{ic} should remain moderate (say lower than 10^5) assuming that the coldest material of the growing planetesimal have a viscosity η_0 comparable to that of the present day Earth, say around 10^{21} Pa s (e.g. $Ra_{ic} \simeq 4700$ for $\kappa = 10^{-6}$ m^{2}s^{-1}, $\alpha = 5 \times 10^{-5}$ K^{-1}, $C_p = 1200$ J K^{-1} kg^{-1}, $\rho = 3870$ kg m^{-3}). The viscosity is temperature-dependent

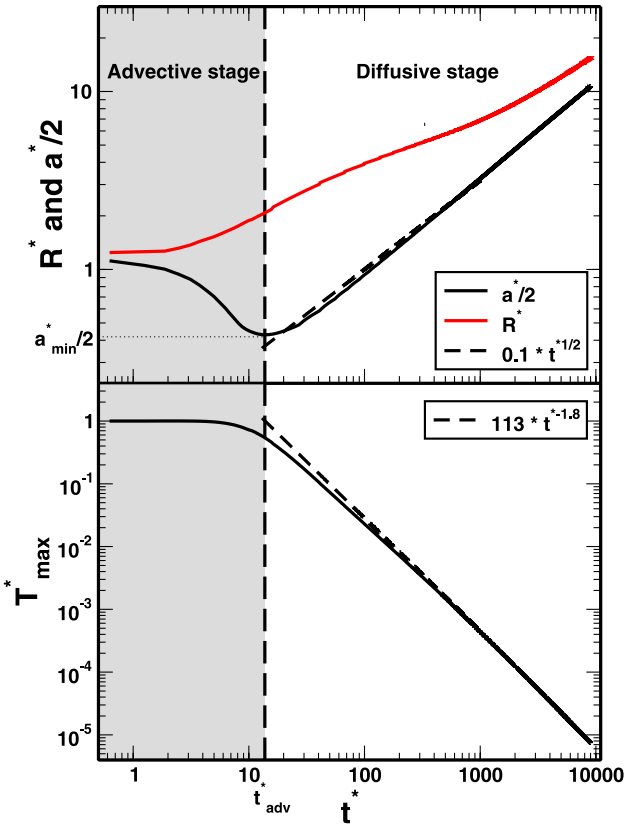

Figure 2. (top) Thickness $a^*/2$ (black solid line) and radial extent R^* (red solid line) and (bottom) maximal temperature at $r = 0$ as functions of time t^* for $Ra_{ic} = 10^2$. Power-law fits following a diffusive solution are depicted by dashed lines. The equilibrium between diffusive (gray field) and advective (white field) stages is obtained at $t^* = t^*_{adv}$.

$\eta(T^*) = \eta_0 \lambda^{T^*}$, λ being the viscosity ratio (lower than 1) between the hottest ($T^* = 1$) and the coldest ($T^* = 0$) material. This viscosity decreases sharply with temperature and its expression is simpler to implement than the usual Arrhenius law.

[12] We developed and benchmarked against analytical solutions a finite difference code to solve equations (3) and (5) in axisymmetric cylindrical geometry. We use a stream function formulation for the Stokes equation with a direct implicit inversion method [*Schubert et al.*, 2001]. The heat equation (4) is solved by an Alternating Direction Implicit (ADI) scheme. All the equations are discretized with a second order accuracy in space and time. Advection terms are calculated with a centered differences scheme. This scheme is known to produce numerical oscillations for grid Peclet numbers larger than $\simeq$20 (the grid Peclet number is $Ra\Delta x^2 v^*/\Delta t$ where Δx is the grid dimension and Δt the time step) [*Dubuffet et al.*, 2000] but in our simulations, the maximum Peclet number remains of order unity. We used at least 129 $\times$ 129 grid points and the dimensions of the calculation domain varies between $10R_{ic} \times 10R_{ic}$ and $100R_{ic} \times 100R_{ic}$. Boundary conditions are free-slip, isothermal at the surface and insulating on other walls. In order to keep a good accuracy in a large enough domain and with strong viscosity variations we run the simulations up to $Ra_{ic} = 10^4$ only, from which we fit scaling laws that can be extrapolated to higher Rayleigh numbers.

[13] The geometrical evolution of the post-impact thermal anomaly as a function of time is monitored by its nondimensional radial extent $R^*(t^*)$, its thickness $a^*(t^*)$ and its maximum temperature $T^*_{max}(t^*)$. $a^*(t^*)$ is the depth where the second derivative of the vertical temperature profile at $r^* = 0$ is zero. Along this profile the maximum temperature value $T^*_{max}(t^*)$ is reached at $z^* = z^*_{max}$. $R^*(t^*)$ is the distance where the second derivative of the horizontal temperature profile at $z^* = z^*_{max}$ is zero.

3. Results

[14] For large enough Rayleigh numbers, the thermal relaxation consists in an early advective stage corresponding to an isothermal flattening of the hot drop, followed by a later stage of diffusive cooling. For $Ra_{ic} \leq 4.9$, cooling is motionless.

3.1. Advective Stage and Diffusive Stage

[15] Figure 2 shows a first stage in the thermal relaxation corresponding to isothermal spreading of the buoyant hot region below the surface. This phenomenon of viscous gravity currents has been widely studied [*Bercovici and Lin*, 1996; *Koch and Koch*, 1995; *Huppert*, 1982; *Koch and Manga*, 1996]. The evolution of the shape is comparable to these works even though they were either designed to study mantle plumes fed by a deeper conduit [*Bercovici and Lin*, 1996] or compositional plumes [*Koch and Manga*, 1996]. Moreover, the analytical results and scaling laws given by *Koch and Koch* [1995] have been mostly derived in a regime where $R^* \gg a^*$ which is not really the case in our calculations.

[16] During the advective stage (see Figure 1 (middle)), the aspect ratio of the drop is increasing while the temperature and the volume of the thermal anomaly remain nearly constant, i.e.

$$\frac{a^*}{2} R^{*2} \sim 1. \tag{8}$$

The second stage of thermal relaxation is dominated by diffusion. After the hot drop stops flattening, heat is diffused in all directions and more efficiently through the top isothermal cold surface. As a consequence, R^* and a^* increase with time as seen in Figure 2. The evolution of $a^*(t^*)$ is rapidly consistent with a purely diffusive model: $a^*(t^*) \sim \sqrt{2\kappa t^*}$. The lateral extent, $R^*(t^*)$, evolves more slowly but reaches a similar diffusive behavior after a long time. The temperature decreases rapidly with the power of -1.8 (see Figure 1 (bottom) and Figure 2).

3.2. Time and Length Scales

[17] The transition from the advective to the diffusive stage happens when the diffusion velocity, κ/a overcomes the advection velocity which is of order $\alpha\rho g \Delta T a^2/\eta_0$. This simple balance implies that

$$\frac{a^*_{\min}}{2} = c_1 Ra_{ic}^{-1/3}, \tag{9}$$

where c_1 is a constant. The volume of the hot anomaly being constant, the radius of the thermal anomaly at the end

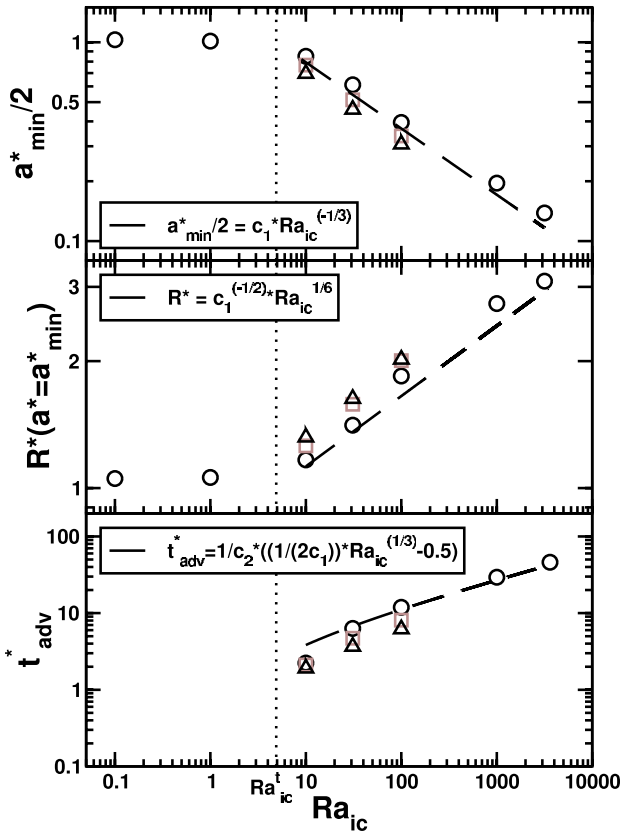

Figure 3. (top) Minimum thickness $a^*_{\min}/2$, (middle) radial extent R^* and (bottom) time of equilibrium t^*_{adv} as functions of Ra_{ic} for different viscosity contrasts (black circles for a uniform viscosity, brown squares and black triangles for $\lambda = 10^{-1}$ and $\lambda = 10^{-2}$). The dashed lines correspond to the predictions of equations (9),(10), and (12) (we use $c_1 = 1.7$, $c_2 = 0.2$).

of the advective stage, R^*_{adv} is easily obtained by combining equations (8) and (9):

$$R^*_{adv} = {c_1}^{-1/2} Ra_{ic}^{1/6}. \tag{10}$$

[18] The time t_{adv} at the end of the advection stage corresponds to the time needed to advect the bottom of the thermal anomal from its initial depth $2R_{ic}$ to its final depth $a_{\min}$. As the vertical velocity $\partial a/\partial t$ is of order of $-\alpha\rho g\Delta T a^2/\eta_0$, we get

$$\frac{\partial a}{\partial t} = -c_2 \frac{\alpha\rho g \Delta T a^2}{\eta_0}, \tag{11}$$

where c_2 is a geometrical factor.

[19] Integration of equation (11) from $a(0) = 2R_{ic}$ to $a(t_{adv}) = a_{\min}$ using equation (9) implies that the end of the advection phase occurs at

$$t^*_{adv} = \frac{1}{c_2}\left(\frac{1}{2c_1} Ra_{ic}^{1/3} - \frac{1}{2}\right). \tag{12}$$

[20] These scalings of equations (9), (10), and (12) are confirmed by fitting the results of the numerical experiments shown in Figure 3 with $c_1 \sim 1.7$ and $c_2 \sim 0.2$.

[21] Of course, the transition between advective and diffusive stages only occurs when the initial size of the isobaric core is larger than the minimum thickness given by equation (9). This threshold R^t_{ic} obtained when $a^*_{\min} = 2$ corresponds to the threshold Rayleigh number

$$Ra^t_{ic} = c_1^3 = 4.9. \tag{13}$$

For $Ra_{ic} < Ra^t_{ic}$, $a^*_{\min} = 2R_{ic}$ and t^*_{adv} is not defined. Below Ra^t_{ic} the heat is diffused out without advection.

[22] The previous scalings obtained for a uniform viscosity are also valid for large viscosity contrasts. Our simulations depicted in Figure 3 (squares for $\lambda = 10^{-1}$ and triangles for $\lambda = 10^{-2}$) show that large viscosity contrasts enable the drop an easier spreading below the surface in agreement with *Koch and Koch* [1995]. As the resistance to internal shearing decreases with λ, horizontal velocity contrasts are more important for low viscosities. As a result, the thickness decreases by about 10%, the radial extent increases by a similar amount and the advection time decreases by a factor ~2. The temperature dependence of the viscosity affects our results by a minor amount because the readjustment is mostly controlled by the viscosity far from the isobaric core.

[23] The scaling laws with physical dimensions can be easily expressed. Using equation (2) and assuming that the planet density remains uniform so that $g = 4/3\pi G\rho R$, the minimal thickness of the thermal anomaly and the time to reach this thickness are

$$a_{\min} = 2b_1 \frac{L^2}{R} \tag{14}$$

and

$$t_{adv} = b_2 \frac{L^2}{\kappa}\left(\frac{L}{R}\right)^2 \left(1 - b_1 \frac{L^2}{RR_{ic}}\right). \tag{15}$$

In these expressions, b_1 and b_2 are dimensionless constants,

$$b_1 = \frac{3}{2} c_1 \left(\frac{f(m)}{2\gamma\pi^2}\right)^{1/3} \sim 1.96, \qquad b_2 = \frac{b_1^2}{2c_1^3 c_2} \sim 1.96, \tag{16}$$

and the properties of the impacted planet appear through a characteristic length

$$L = \left(\frac{C_p \kappa \eta_0}{\alpha\rho^3 G^2}\right)^{1/6} \sim 212 \text{ km}. \tag{17}$$

4. Discussion and Conclusion

[24] We developed a thermo-mechanical model for the long term relaxation after an impact. In a first stage, the heated region spreads below the surface until diffusive cooling becomes more effective. The transition between the advective and diffusive stages is described by a thickness $a_{\min}$ and timescale t_{adv} for which we proposed scalings

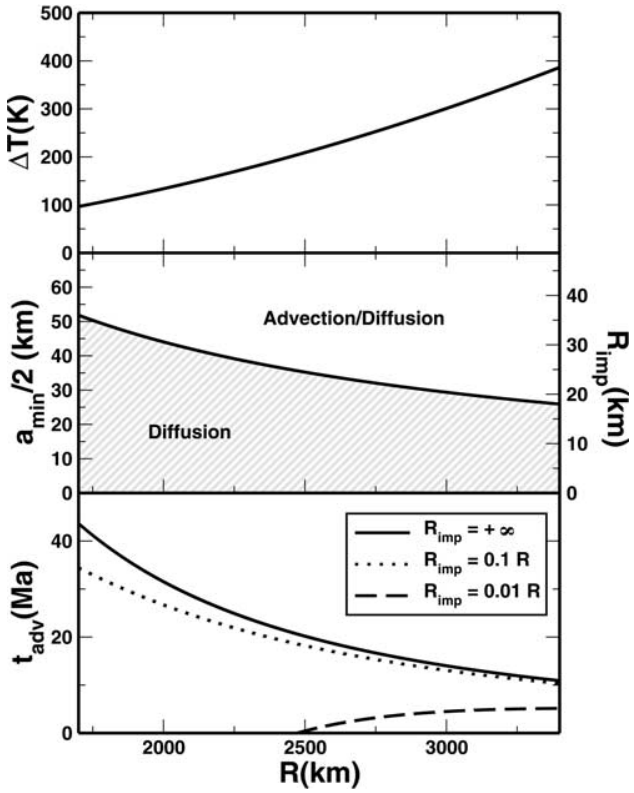

Figure 4. (top) Temperature increase ΔT, (middle) thickness $a_{\min}/2$ and (bottom) advection time t_{adv} as functions of the planetary radius. For too small impactors (right side label), advection does not occur. The advection time is plotted for different impactor radii.

laws. Hence we can predict geometrical and time evolution of the thermal anomaly caused by a meteoritical impact as functions of rheological parameters of the impacted planetesimal and impactor. All our results are summarized in Figure 4.

[25] The temperature increase (Figure 4, top) and the thickness of the thermal anomaly after advection (Figure 4, middle) do not depend on the initial size of the impactor but only on the properties of the impacted body (and therefore its radius assuming known its other properties, see equations (2) and (14)). As the volume of the isobaric core is proportional to that of the impactor the minimum thickness of the thermal anomaly corresponds also to the minimum radius of the impactor that can trigger advection (Figure 4, middle). For a Mars size planet (R = 3400 km), impacts increase the temperature by 390 K (in relative agreement with *Senshu et al.* [2002]) and post-impact advection only occurs for impactors with radius larger than 18 km. After advection, the final thickness of the thermal anomaly is 52 km. For smaller impactors, only heat diffusion occurs.

[26] The duration of advection depends on the impactor size (Figure 4, bottom). As shown in equation (15), the time of advection is lower than a threshold value obtained for an infinitely large impactor (which of course would disrupt the planet). For a Mars size planet impacted by bodies with 1/10 to 1/100 smaller radii, advection ends up after, 10 Myr, 5 Myr, respectively. After this advective stage, heat is slowly removed by diffusion in ~20 Myr.

[27] These timescales are of the same order as those for accretion and differentiation [*Yin et al.*, 2002]. Hence, until impact melting is efficient, heat brought by impacts is stored within the mantle even taking into account of the deformation of the heated region. The scalings proposed here could be used to compute more accurate one dimensional thermal evolution models of growing planets.

[28] **Acknowledgments.** The authors thank J. Schmalzl, H. Samuel and an anonymous reviewer for their useful comments about the manuscript. They also thank J. Melosh and M. Monnereau for helpful discussions. This project was funded by the A.N.R. ETHER.

References

Alvarez, L. W., W. Alvarez, F. Asaro, and H. V. Michel (1980), Extraterrestrial cause for the Cretaceous Tertiary extinction, *Science*, *208*, 1095–1108.

Bercovici, D., and J. Lin (1996), A gravity current model of cooling mantle plume heads with temperature-dependent buoyancy and viscosity, *J. Geophys. Res.*, *101*, 3291–3310.

Croft, S. K. (1982), A first-order estimate of shock heating and vaporization in oceanic impacts, in *Geological Implications of Impacts of Large Asteroids and Comets on Earth*, edited by T. L. Silver and P. H. Schultz, *Spec. Pap. Geol. Soc. Am.*, *90*, 143–152.

Dubuffet, F., M. Rabinowicz, and M. Monnereau (2000), Multiple scales in mantle convection, *Earth Planet. Sci. Lett.*, *178*, 351–366.

Hartmann, W. K., and D. R. Davis (1975), Satellite-sized planetesimals and lunar origin, *Icarus*, *24*, 504–514.

Huppert, H. E. (1982), The propagation of two-dimensional and axisymmetric viscous gravity currents over a rigid horizontal surface, *J. Fluid Mech.*, *121*, 43–58.

Kaula, W. M. (1979), Thermal evolution of Earth and Moon growing by planetesimal impacts, *J. Geophys. Res.*, *84*, 999–1008.

Koch, D. M., and D. L. Koch (1995), Numerical and theoretical solutions for a drop spreading below a free fluid surface, *J. Fluid Mech.*, *287*, 251–278.

Koch, D. M., and M. Manga (1996), Neutrally buoyant diapirs: A model for Venus coronae, *Geophys. Res. Lett.*, *23*, 225–228.

Kokubo, E., and S. Ida (1996), On runaway growth of planetesimals, *Icarus*, *123*, 180–191.

Maxwell, D. E. (1977), Simple Z model for cratering, ejection, and the overturned flap, in *Impact and Explosion Cratering: Planetary and Terrestrial Implications*, edited by D. J. Roddy, R. O. Pepin, and R. B. Merrill, pp. 1003–1008, Elsevier, New York.

O'Keefe, J. D., and T. J. Ahrens (1977), Impact-induced energy partitioning, melting, and vaporization on terrestrial planets, *Lunar Planet. Sci. Conf.*, *8th*, 3357–3374.

Pierazzo, E., A. M. Vickery, and H. J. Melosh (1997), A reevaluation of impact melt production, *Icarus*, 408–423.

Reese, C. C., V. S. Solomatov, and J. R. Baumgardner (2002), Survival of impact-induced thermal anomalies in the Martian mantle, *J. Geophys. Res.*, *107*(E10), 5082, doi:10.1029/2000JE001474.

Schubert, G., D. L. Turcotte, and P. Olson (2001), *Mantle Convection in the Earth and Planets*, Cambridge Univ. Press, New York.

Senshu, H., K. Kuramoto, and T. Matsui (2002), Thermal evolution of a growing Mars, *J. Geophys. Res.*, *107*(E12), 5118, doi:10.1029/2001JE001819.

Solomatov, V. S. (2000), *Fluid Dynamics of a Terrestrial Magma Ocean, Origin of the Earth and Moon*, edited by R. M. Canup et al., pp. 323–338, Univ. of Ariz. Press, Tucson.

Tonks, W. B., and H. J. Melosh (1993), Magma ocean formation due to giant impacts, *J. Geophys. Res.*, *98*, 5319–5333.

Turtle, E. P., E. Pierazzo, and D. P. O'Brien (2003), Numerical modeling of impact heating and cooling of the Vredefort impact structure, *Meteorit. Planet. Sci.*, *38*, 293–303.

Yin, Q., S. B. Jacobsen, K. Yamashita, J. Blichert-Toft, P. Télouk, and F. Albarède (2002), A short timescale for terrestrial planet formation from Hf-W chronometry of meteorites, *Nature*, *418*, 949–952.

N. Coltice, F. Dubuffet, J. Monteux, and Y. Ricard, Laboratoire de Sciences de la Terre, UMR 5570, CNRS, Université de Lyon, Université Claude Bernard Lyon 1, 2 rue R. Dubois, F-69622, Villeurbanne cedex, France. (nicolas.coltice@univ-lyon1.fr; fabien.dubuffet@univ-lyon1.fr; julien.monteux@univ-lyon1.fr; ricard@ens-lyon.fr)

Icarus 264 (2016) 246–256

Contents lists available at ScienceDirect

Icarus

journal homepage: www.journals.elsevier.com/icarus

Scaling laws of impact induced shock pressure and particle velocity in planetary mantle

J. Monteux [a,*], J. Arkani-Hamed [b,c]

[a] Laboratoire Magmas et Volcans, Clermont-Ferrand, France
[b] Department of Physics, University of Toronto, Toronto, Canada
[c] Department of Earth and Planetary Sciences, McGill University, Montreal, Canada

ARTICLE INFO

Article history:
Received 13 March 2015
Revised 24 September 2015
Accepted 24 September 2015
Available online 3 October 2015

Keywords:
Accretion
Impact processes
Thermal histories
Terrestrial planets
Interiors

ABSTRACT

While major impacting bodies during accretion of a Mars type planet have very low velocities (<10 km/s), the characteristics of the shockwave propagation and, hence, the derived scaling laws are poorly known for these low velocity impacts. Here, we use iSALE-2D hydrocode simulations to calculate shock pressure and particle velocity in a Mars type body for impact velocities ranging from 4 to 10 km/s. Large impactors of 100–400 km in diameter, comparable to those impacted on Mars and created giant impact basins, are examined. To better represent the power law distribution of shock pressure and particle velocity as functions of distance from the impact site at the surface, we propose three distinct regions in the mantle: a near field regime, which extends to 1–3 times the projectile radius into the target, where the peak shock pressure and particle velocity decay very slowly with increasing distance, a mid field region, which extends to ~4.5 times the impactor radius, where the pressure and particle velocity decay exponentially but moderately, and a more distant far field region where the pressure and particle velocity decay strongly with distance. These scaling laws are useful to determine impact heating of a growing protoplanet by numerous accreting bodies.

1. Introduction

Small planets are formed by accreting a huge number of planetesimals, a few km to a few tens of km in size, in the solar nebula (e.g. Wetherill and Stewart, 1989; Matsui, 1993; Chambers and Wetherill, 1998; Kokubo and Ida, 1995, 1996, 1998, 2000; Wetherill and Inaba, 2000; Rafikov, 2003; Chambers, 2004; Raymond et al., 2006). An accreting body may generate shock wave if the impact-induced pressure in the target exceeds the elastic Hugoniot pressure, ~3 GPa, implying that collision of a planetesimal with a growing planetary embryo can generate shock waves when the embryo's radius exceeds 150 km, assuming that impact occurs at the escape velocity of the embryo and taking the mean density of the embryo and projectile to be 3000 kg/m^3. Hundreds of thousands of collisions must have occurred during the formation of small planets such as Mercury and Mars when they were orbiting the Sun inside a dense population of planetesimal. Such was also the case during the formation of embryos that later were accreted to produce Venus and Earth. Terrestrial planets have also experienced large high velocity impacts after their formation. Over 20 giant impact basins on Mars with diameters larger than 1000 km (Frey, 2008), the Caloris basin on Mercury with a 1550 km diameter, and the South Pole Aitken basin on Moon with a 2400 km diameter are likely created during catastrophic bombardment period at around 4 Ga. The overlapping Rheasilvia and Veneneia basins on 4-Vesta are probably created by projectiles with an impact velocity of about 5 km/s within the last 1–2 Gyr (Keil et al., 1997; Schenk et al., 2012).

The shock wave produced by an impact when the embryo is undifferentiated and completely solid propagates as a spherical wave centered at the impact site until it reaches the surface of the embryo in the opposite side. Each impact increases the temperature of the embryo within a region near the impact site. Because impacts during accretion occur from different directions, the mean temperature in the upper parts of the embryo increases almost globally. On the other hand, the shock wave produced by a large impact during the heavy bombardment period must have increased the temperature in the mantle and the core of the planets directly beneath the impact site, enhancing mantle convection (e.g. Watters et al., 2009; Roberts and Arkani-Hamed, 2012, 2014), modifying the CMB heat flux which could in turn favor a hemispheric dynamo on Mars (Monteux et al., 2015), or crippling the core dynamo (e.g. Arkani-Hamed and Olson, 2010a).

* Corresponding author.

http://dx.doi.org/10.1016/j.icarus.2015.09.040
0019-1035/

The impact-induced shock pressure inside a planet has been investigated by numerically solving the shock dynamic equations using hydrocode simulations (e.g. Pierazzo et al., 1997; Wünnemann and Ivanov, 2003; Wünnemann et al., 2006; Barr and Citron, 2011; Kraus et al., 2011; Ivanov et al., 2010; Bierhaus et al., 2012) or finite difference techniques (e.g. Ahrens and O'Keefe, 1987; Mitani, 2003). However, these numerical solutions demand considerable computer capacity and time and are not practical for investigating the huge number of impacts that occur during the growth of a planet. Hence, the scaling laws derived from field experiments (e.g. Perret and Bass, 1975; Melosh, 1989) or especially from hydrocode simulations (Pierazzo et al., 1997) are of great interest when considering the full accretionary history of a planetary objects (e.g. Senshu et al., 2002; Monteux et al., 2014) or when measuring the influence of a single large impact on the long-term thermal evolution of deep planetary interiors (e.g. Monteux et al., 2007, 2009, 2013; Ricard et al., 2009; Roberts et al., 2009; Arkani-Hamed and Olson, 2010a; Arkani-Hamed and Ghods, 2011). Although the scaling laws provide approximate estimates of the shock pressure distribution, their simplicity and the small differences between their results and those obtained by the hydrocode simulations of the shock dynamic equations (that are likely within the numerical errors that could have been introduced due to the uncertainty of the physical parameters used in the hydrocode models) make them a powerful tool that can be combined with other geophysical approaches such as dynamo models (e.g. Monteux et al., 2015) or convection models (e.g. Watters et al., 2009; Roberts and Arkani-Hamed, 2012, 2014).

During the decompression of shocked material much of the internal energy of the shock state is converted into heat leading to a temperature increase below the impact site. The present study focuses on deriving scaling laws of shock pressure and particle velocity distributions in silicate mantle of a planet on the basis of several hydrocode simulations. The scaling laws of Pierazzo et al. (1997) were derived using impact velocities of 10–80 km/s, hence may not be viable at low impact velocities. For example, at an impact velocity of 5 km/s, comparable to the escape velocity of Mars, the shock pressure scaling law provides an unrealistic shock pressure that increases with depth. Here we model shock pressure and particle velocity distributions in the mantle using hydrocode simulations for impact velocities of 4–10 km/s and projectile diameters ranging from 100 to 400 km, as an attempt to extend Pierazzo et al.'s (1997) scaling laws to low impact velocities and reasonable impactor radii occurring during the formation of terrestrial planets. Hence, on the basis of our scaling laws it is possible to estimate the temperature increase as a function of depth below the impact site for impact velocities compatible with the accretionary conditions of terrestrial protoplanets. These scaling laws can easily be implemented in a multi-impact approach (e.g. Senshu et al., 2002; Monteux et al., 2014) to monitor the temperature evolution inside a growing protoplanet whereas it is not yet possible to adopt hydrocode simulations for that purpose.

The hydrocode models we have calculated are described in the first section, while the second section presents the scaling laws derived from the hydrocode models. The concluding remarks are relegated to the third section.

2. Hydrocode models of shock pressure distribution

The huge number of impacts during accretion makes it impractical to consider oblique impacts. Not only it requires formidable computer time, but more importantly because of the lack of information about the impact direction, i.e. the impact angle relative to vertical and azimuth relative to north. Therefore, we consider only head-on collisions (vertical impact) to model the thermo-mechanical evolution during an impact between a differentiated Mars size body and a large impactor. We use the iSALE-2D axisymmetric hydrocode, which is a multi-rheology, multi-material hydrocode, specifically developed to model impact crater formation on a planetary scale (Collins et al., 2004; Davison et al., 2010). To limit computation time, we use a 2 km spatial resolution (i.e. more than 25 cells per projectile radius, *cppr*) and a maximum time step of 0.05 s which is sufficient to describe the shockwave propagation through the entire mantle. The minimum post impact monitoring time is set to the time needed by the shockwave to reach the core–mantle boundary (≈5 min for the impact velocities studied here).

We investigate the shock pressure and particle velocity distributions inside a Mars size model planet for impact velocities V_{imp} of 4–10 km/s and impactors of 100–400 km in diameter. Such impactors are capable of creating basins of 1000–2500 km in diameter according to Schmidt and Housen (1987) and Holsapple (1993) scaling relationships between the impactor diameter and the resulting basin diameter. These basins are comparable with the giant impact basins of Mars created during the heavy bombardment period at around 4 Ga (Frey, 2008).

In our models, the impactor was simplified to a spherical body of radius R_{imp} with uniform composition while the target was simplified to a two layers spherical body of radius R and an iron core radius of R_{core}. The silicate mantle has a thickness of δ_m (see Table 1). We adopt physical properties of silicates (dunite or peridotite) for both the mantle and the impactor to monitor the shock pressure and the particle velocity in a Mars type body. We approximate the thermodynamic response of both the iron and silicate material using the ANEOS equation of state (Thompson and Lauson, 1972; Benz et al., 1989). To make our models as simple as possible we do not consider here the effects of porosity, thermal softening or low density weakening. However, as a first step towards more realistic models, we investigate the influence of acoustic fluidization and damage. All these effects can be accounted for in iSALE-2D and we will consider each effect in a separate study in near future.

Table 1
Typical parameter values for numerical hydrocode models.

Target radius	R	3400 km
Target core radius	R_{core}	1700 km
Silicate mantle thickness	δ_m	1700 km
Impactor radius	R_{imp}	50–200 km
Impact velocity	V_{imp}	4–10 km/s
Mantle properties (silicates)		
Initial density	ρ_m	3314 kg/m^3
Equation of state type		ANEOS
Poisson		0.25
Strength Model		Rock
(iSALE parameters)		(Y_{i0} = 10 MPa, μ_i = 1.2, Y_{im} = 3.5 GPa)
Acoustic Fluidization Model		Block
(iSALE parameters)		(t_{off} = 16 s, c_{vib} = 0.1 m/s, vib_{max} = 200 m/s)
Damage Model		Ivanov
(iSALE parameters)		($\varepsilon_{fb} = 10^{-4}$, $B = 10^{-11}$, $p_c = 3 \times 10^8$ Pa)
Thermal softening and porosity models		None
Core properties (iron)		
Initial density	ρ_c	7840 kg/m^3
Equation of state type		ANEOS
Poisson		0.3
Strength Model		Von Mises
(iSALE parameters)		(Y_0 = 100 MPa)
Acoustic Fluidization Model		Block
(iSALE parameters)		(t_{off} = 16 s, c_{vib} = 0.1 m/s, vib_{max} = 200 m/s)
Damage, thermal softening and porosity models		None

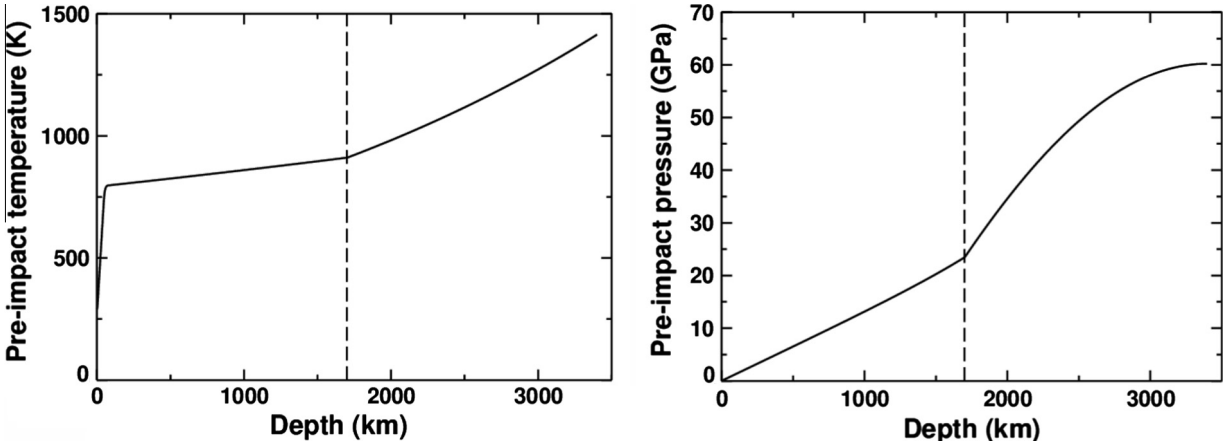

Fig. 1. Pre-impact temperature (left) and lithostatic pressure (right) as a function of depth. The dashed lines illustrate the core–mantle boundary.

The early temperature profile of a Mars size body is difficult to constrain because it depends on its accretionary history, on the amount of radiogenic heating and on the mechanisms that led to its core formation (e.g. Senshu et al., 2002). The uncertainties on the relative importance of these processes as well as the diversity of the processes involved in the core formation lead to a wide range of plausible early thermal states after the full differentiation of Mars. Since we do not consider here the thermal softening during the impact, we assumed the same radially dependent preimpact martian temperature field in all our simulations. Fig. 1 shows the pre-impact temperature profile as a function of depth. As the pre-impact pressure is governed by the material repartition and as we consider a differentiated Mars, the pre-impact pressure is more straightforward. Fig. 1 also shows the pre-impact hydrostatic pressure used in our models as a function of depth considering a 1700 km thick silicate mantle surrounding a 1700 km radius iron core. We emphasize that the peak pressure shown in our study does not include this hydrostatic pressure. However, the hydrostatic pressure is taken into consideration in calculating the hydrocode models. The peak pressure presents the shock induced pressure increase and is expected to depend on the physical properties of the target, but not on the size of the target as long as the size is large enough to allow shock wave propagates freely without interference with reflected waves. A scaling law should reflect the properties of the shock wave propagation in a uniform media. Fig. 2 shows the typical time evolution of the compositional and pressure fields after a 100 km diameter impact with V_{imp} = 10 km/s. Immediately after the impact, the shockwave propagates downward from the impact site. The shock front reaches the core–mantle boundary in less than 5 min while the transient crater is still opening at the surface. It is worth mentioning that the main goal is to derive a scaling law which is useful for numerous impacts during accretion where no information is available about the impact direction, i.e. the impact angle relative to vertical and azimuth relative to north. Moreover, the pressure reduction near the surface due to interference of the direct and reflected waves can easily be accommodated following the procedure by Melosh (1989), which is adapted to spherical surface by Arkani-Hamed (2005), when applying the scaling law to a particular accretion scenario.

In Fig. 3, we monitor the peak pressure as a function of the distance from the impact site d normalized by the impactor radius R_{imp} along the symmetry axis for the case illustrated in Fig. 2. In our iSALE models, the impact-induced pressure fields (as well as temperature and velocity fields) are extracted from a cell-centered Eulerian grid data. To validate our models, we have tested different spatial resolutions expressed here in terms of cells per projectile radius (*cppr*). In Fig. 3a, we represent the peak pressure

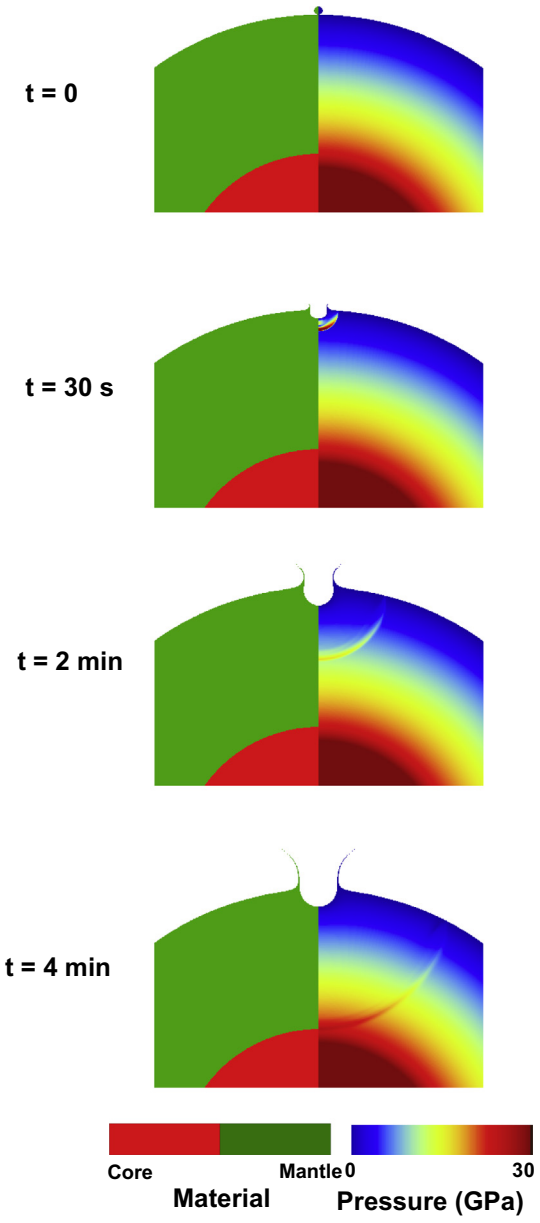

Fig. 2. A close up view of the material repartition (left column) and total pressure (right column) as functions of time (from top to bottom) in the model planet (for V_{imp} = 10 km/s and D_{imp} = 100 km). In this model, the grid resolution is 2 km in all directions. The silicate mantle and the impactor are made of dunite.

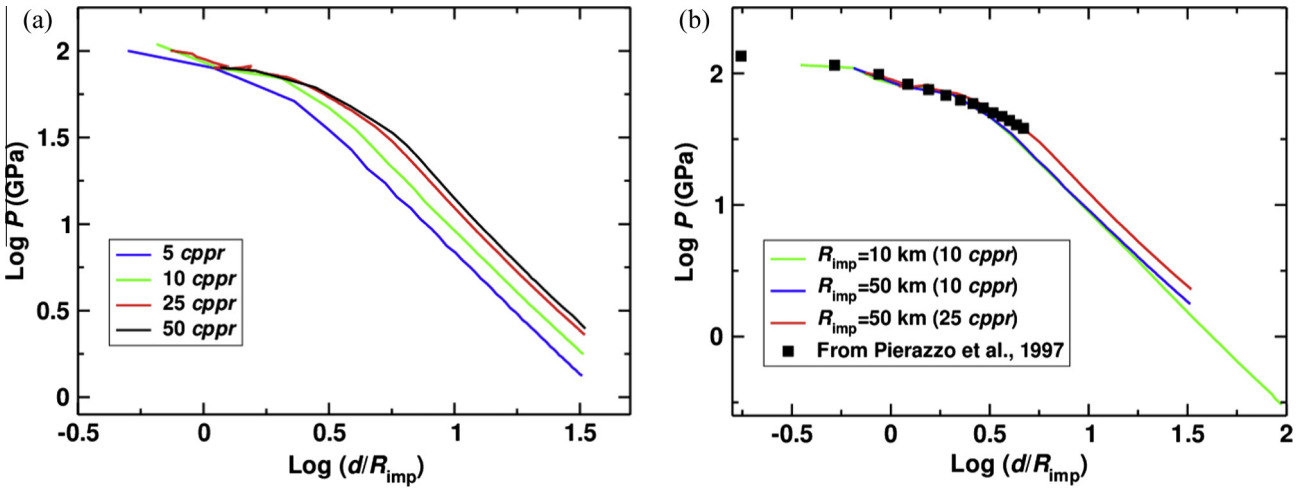

Fig. 3. Peak pressure decrease as a function of depth normalized by the radius of the impactor for the impact velocity of 10 km/s. The silicate mantle as well as the impactor are made of dunite. (a) Influence of the spatial resolution. Here we only consider the case with R_{imp} = 50 km. The results from our hydrocode models are shown by colored curves with a spatial resolution ranging from 5 to 50 *cppr* and (b) comparison of our results with R_{imp} = 50 km (red curve, 25 *cppr*) and R_{imp} = 10 km (green curve, 10 *cppr*) with the results from a similar model of Pierazzo et al. (1997) (black squares). (For interpretation of the references to color in this figure legend, the reader is referred to the web version of this article.)

decrease as a function of depth for *cppr* values ranging from 5 to 50, showing convergence for *cppr* values larger than 25. As illustrated in Fig. 3a, the difference between the results with 25 and 50 *cppr* is less than 10%. This resolution study is in agreement with Pierazzo et al. (2008) who have shown that the iSALE models converge for resolutions of 20 *cppr* or higher, although a resolution of 10 *cppr* still provides reasonable results (a resolution of 20 *cppr* appears to underestimate peak shock pressures by at most 10%). The resolution is 25 *cppr* or higher in our models.

In Pierazzo et al. (1997), the impactor radius ranged between 0.2 and 10 km. In Fig. 3b, we compare our results obtained with R_{imp} = 10 km, R_{imp} = 50 km and the results obtained by Pierazzo et al. (1997). Fig. 3b shows that even with a radius of 50 km, both our results and the results from Pierazzo et al. (1997) are in good agreement, confirming that the impactor size has minor effects on the peak pressure evolution with depth. The small differences between our results with different impactor radii (discussed further in more details) are plausibly the direct consequence of using increasing *cppr* values with increasing impactor radii. Consequently, we will use the normalized distance in all of our figures, as equations of motion should be invariant under rescaling of distance (Melosh, 1989; Pierazzo et al., 1997). However, to monitor the peak pressure evolution with R_{imp} = 10 km and to maintain a reasonable computational time, we have used only 10 *cppr*. This figure confirms that below 10 *cppr*, the spatial accuracy is insufficient and our results diverge from the results obtained by Pierazzo et al. (1997).

3. Shock pressure and particle velocity scaling laws at low impact velocities

A given hydrocode simulation may take on the order of 48 h to determine a 2D shock pressure and particle velocity distributions in the mantle of our model planet. The impact velocity is about 4 km/s for a protoplanet with a radius of 2860 km and mean density of 3500 kg/m^3, assuming that impacts occur at the escape velocity of the protoplanet. Mars is more likely a runaway planetary embryo formed by accreting small planetesimals and medium size neighboring planetary embryos. This indicates that the accreting bodies had velocities higher than 4 km/s when Mars was growing from 2860 km radius to its present radius of about 3400 km. Taking the mean radius of the impacting bodies to be 100 km, which is larger than that of a typical planetesimal, more than 15,000 bodies must have accreted at impact velocities higher than 4 km/s. Calculating the impact induced shock pressure and particle velocity inside the growing Mars would be formidable if hydrocode simulation is adopted for each impact. Because the impact-induced shock pressure P and particle velocity V_p inside a planetary mantle decease monotonically with distance from the impact side, simple exponential functions have been proposed to estimate peak pressure and particle velocity in the mantle of an impacted body. Solving the shock dynamic equations by a finite difference technique for silicate target and projectile, Ahrens and O'Keefe (1987) showed that pressure distribution in the target displays three regimes: an impedance match regime, Regime I, which extends to 1–3 times the projectile radius into the target where the peak shock pressure is determined by the planar impedance match pressure (McQueen et al., 1970); a shock pressure decay regime, Regime II, where the pressure decays exponentially as

$$P = P_o(d/R_{imp})^n, \quad \text{for } d > 1\text{–}3 \text{ times } R_{imp}, \text{ and}$$
$$n = -1.25 - 0.625\, Log(V_{imp}) \tag{1}$$

and the elastic regime, Regime III, where the shock pressure is reduced below the strength of target, the Hugoniot elastic limit, and the shock wave is reduced to an elastic wave with pressure decaying as d^{-3}. In Eq. (1) d is the distance from the impact site at the surface, R_{imp} is the projectile radius, and V_{imp} is the impact velocity in km/s. The peak pressure measurements in the nuclear explosions (Perret and Bass, 1975) led Melosh (1989) to propose a scaling low for the particle velocity distribution assuming conservation of momentum of the material behind the shock front which is taken to be a shell of constant thickness. Using several different target materials, and adopting hydrocode simulations Pierazzo et al. (1997) showed that the shock pressure P and particle velocity V_p decrease slowly in the near field zone, but rapidly in the deeper region,

$$P = P_{ic}(d_{ic}/d)^n, \quad n = -1.84 + 2.61\, Log(V_{imp}), \; d > d_{ic} \tag{2a}$$

$$V_p = V_{pic}(d_{ic}/d)^m \quad m = -0.31 + 1.15\, Log(V_{imp}), \; d > d_{ic} \tag{2b}$$

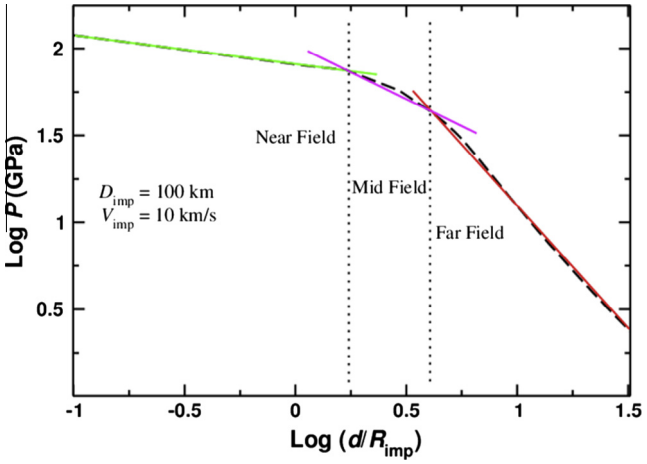

Fig. 4. Shock pressure versus normalized distance from the impact site at the surface produced by a 100 km diameter impactor with an impact velocity of 10 km/s. The dashed curve represents the hydrocode model, while the straight lines are fitted to three different parts of the hydrocode model.

The authors coined an isobaric zone of shock pressure P_{ic} and particle velocity V_{pic} for the near field of radius d_{ic}, about 1.5 R_{imp}. Eqs. (2a) and (2b) were derived by averaging results from many different materials and impactor sizes. The impact velocities adopted were 10–80 km/s and the projectile diameter ranged from 0.4 to 20 km.

In a log–log plot the peak shock pressure and the corresponding particle velocity are linear functions of distance from the impact site,

$$Log\ P = a + n\ Log(d/R_{imp}) \tag{3a}$$

$$Log\ V_p = c + m\ Log(d/R_{imp}) \tag{3b}$$

where a is the logarithm of pressure and c is the logarithm of particle velocity both at R_{imp} and n and m are decay factors. All parameters are impact velocity dependent:

$$a = \alpha + \beta\ Log(V_{imp}) \tag{4a}$$

$$c = \gamma + \Omega\ Log(V_{imp}) \tag{4b}$$

and

$$n = \lambda + \delta\ Log(V_{imp}) \tag{5a}$$

$$m = \eta + \zeta\ Log(V_{imp}) \tag{5b}$$

Fig. 4 shows the peak shock pressure inside the mantle of the model planet we obtained by hydrocode simulation and using a projectile of 100 km diameter at 10 km/s impact velocity. There is actually no isobaric region, rather the peak pressure decays slowly in the near field zone but much rapidly in the deeper parts, similar to the results by Ahrens and O'Keefe (1987). Although the regression lines fitted to the near field and far field are good representatives of the shock pressure distribution, they intersect at a much higher pressure than that of the hydrocode model and overestimate the pressure by as much as 30% in a large region located between the near field and the far field. Therefore, to better approximate the pressure distribution we fit the pressure curve by three lines, representing the near field, mid field and far field regions, which render a much better fit as seen in Fig. 4.

Fig. 5a shows the peak shock pressure versus distance from the impact site for impact velocities of 4–10 km/s and an impactor of 100 km in diameter. Because of different phenomenon such as excavation, melting, vaporization and intermixing between the target and projectile material, the shock front in near field is more difficult to characterize by our numerical models even for high *cppr*. Also, as the shock wave is not yet detached from the impactor, it cannot be treated as a single shock wave. Hence, the near field–mid field boundary and the scaling laws for the near field are less accurate than for the two other fields especially for large impact velocities (V_{imp} > 7 km/s). In Fig. 5, the larger dots show the intersections of the linear regression lines. For example a dot that separates near field from mid field is the intersection of the regression lines fitted to the near field and midfield. The regression lines are determined from fitting to the hydrocode data. Visually, we first divide the hydrocode data of a given model into three separate sections with almost linear trends, and then fit the regression lines to those three trends. Fig. 5a shows the hydrocode data, small dots, and the regression lines, demonstrating the tight fitting of the lines to the data. The large dots in the figure show the intersection of the regression lines of the adjacent regions. For example the dot that shows the near-field mid-field boundary is the intersection of the regression lines fitted to the near field and mid field hydrocode data. Note that a big dot does not necessarily coincide with the exact hydrocode result, a small dot. As the near field–mid field boundary is relatively less resolved, Fig. 5a shows a scatter of the dots separating those two fields and a slight slope change from V_{imp} > 7 km/s. In the average the near field–mid field boundary is at ~2.3 R_{imp} (~115 km) from the impact site. Fig. 5a shows that the depth to the mid field–far field boundary is almost independent of the pressure. It is at about 4.5 R_{imp} (~225 km) from the impact site.

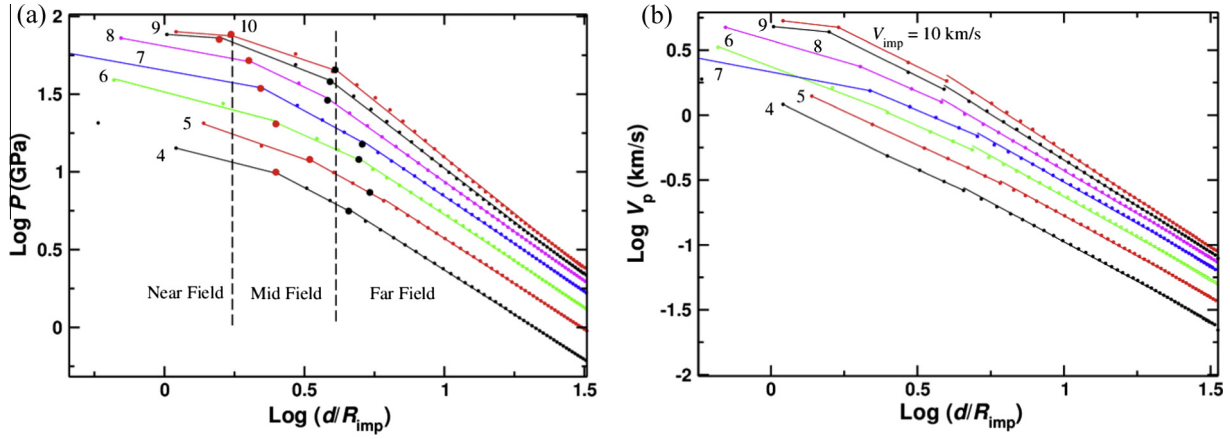

Fig. 5. (a) Shock pressure versus normalized distance from the impact site at the surface for an impactor of 100 km diameter and impact velocities ranging from 4 to 10 km/s. The numbers on the curves are the impact velocities. The hydrocode results are presented by dots, while the regression lines to the near field, mid field and far field regions are straight lines. The larger dots show the intersections of the linear regression lines. For example a dot that separates near field from mid field is the intersection of the regression lines fitted to the near field and mid field data and (b) shows the corresponding particle velocity.

We propose three scaling laws for shock pressure, and three for particle velocity:

$$Log\ P_i = a_i + n_i\ Log(d_i/R_{\rm imp}), \quad i = 1, 2, \text{ and } 3 \tag{6a}$$

$$Log\ V_{\rm pi} = c_i + m_i\ Log(d_i/R_{\rm imp}), \quad i = 1, 2, \text{ and } 3 \tag{6b}$$

For the near field $d_i < 2.3\ R_{\rm imp}$, mid field $2.3\ R_{\rm imp} < d_i < 4.5\ R_{\rm imp}$, and far field $d_i > 4.5\ R_{\rm imp}$. Table 2 lists the values of the parameters in the above equations as well as the misfits obtained from our regressions (smaller than 0.001 in all the regressions calculated here). Fig. 5a shows the three regression lines fitted to the near field, mid field, and far field of each model for shock pressure, and Fig. 5b displays those for particle velocity. The misfits from Table 2 are based on the fixed end points, shown as dots in Fig. 5.

The close agreement between Pierazzo et al. (1997) model for impact velocity of 10 km/s derived by averaging results of impactors with diameters 0.4–20 km, and our result for the same impact velocity but an impactor of 100 km in diameter indicates that the shock pressure distribution is less sensitive to impactor size in a log–log plot of pressure versus distance normalized to the impactor radius. To further investigate this point, we calculate models with impactor sizes of 100–400 km in diameter. Fig. 6a shows the hydrocode results for impact velocity of 10 km/s using different impactor size. The result obtained for $R_{\rm imp} = 10$ km is not included in the figure because of its low *cppr* value (see Fig. 3b). The curves have almost the same slope in the far field, and small deviations in the mid field and near field.

Pierazzo et al. (1997) used several different rock types for the solid mantle and concluded that their scaling laws are less sensitive to the rock types. Bearing in mind that dunite and peridotite are probably the most representative rocks for solid mantle, we run a hydrocode model using an impactor of 100 km in diameter, impact velocity of 10 km/s, and peridotite as a representative mantle and impactor rock. Fig. 6b compares the results for the dunite and peridotite models. They are indeed very similar, especially in the far field region, where the exponential factor n

Table 2
Parameters of the peak shock pressure distribution and the corresponding particle velocity in the mantle of the Mars size model planet. The pressure is expressed as:

$Log(P) = a + n\ Log(d/R_{\rm imp})$

and the particle velocity as:

$Log(V_p) = c + m\ Log(d/R_{\rm imp})$

where the pressure P is in GPa, the particle velocity V_p is in km/s, d is the distance from the impact site at the surface, and $R_{\rm imp}$ is the impactor radius. a and c are the logarithm of pressure and particle velocity at the distance $R_{\rm imp}$ from the impact site, and n and m are the decay exponents of pressure and particle velocity with distance from the impact site. a, c, n and m are impact velocity dependent:

$a = \alpha + \beta\ Log(V_{\rm imp})$
$n = \lambda + \delta\ Log(V_{\rm imp})$
$c = \gamma + \Omega\ Log(V_{\rm imp})$
$m = \eta + \zeta\ Log(V_{\rm imp})$

A misfit value is obtained by calculating the standard deviation of a line fitted to the hydrocode data within a given region: $\epsilon = 1/N\sqrt{\sum_1^N (Y_{\rm data} - Y_{\rm regression})^2}$, where N is the total number of points, $Y_{\rm data}$ is the hydrocode result and $Y_{\rm regression}$ denotes the value obtained by the linear regression. The zero misfit implies that the regression line is fitted to only 2 points, hence an exact fitting.

$V_{\rm imp}$ (km/s)	a	n	*misfit*	c	m	*misfit*
Near field						
4	1.1717	−0.4530	1.074E−07	0.1276	−1.1132	3.071E−08
5	1.3963	−0.6296	4.616E−03	0.2901	−1.0437	6.6837E−04
6	1.5137	−0.4713	8.429E−08	0.3722	−0.8573	0.000
7	1.6527	−0.3237	5.960E−08	0.3315	−0.4286	1.490E−08
8	1.8093	−0.3302	5.960E−08	0.5736	−0.6567	0.000
9	1.8853	−0.1228	8.429E−08	0.6817	−0.2156	4.214E−08
10	1.9072	−0.1364	1.332E−07	0.7354	−0.2622	8.411E−03
$\alpha = 0.040$, $\beta = 1.914$, $\lambda = -1.214$, $\delta = 1.058$						
$\gamma = -0.795$, $\Omega = 1.502$, $\eta = -2.602$, $\zeta = 2.368$						
Mid field						
4	1.3714	−0.9459	2.0576E−03	0.0917	−1.0211	3.8861E−04
5	1.5978	−0.9995	6.5599E−04	0.2911	−1.0402	7.3517E−04
6	1.6367	−0.8038	4.7266E−03	0.4143	−0.9942	8.0339E−04
7	1.8821	−0.9792	2.8677E−03	0.5141	−0.9563	1.8048E−03
8	1.9735	−0.8576	3.5979E−03	0.6750	−0.9888	6.5566E−05
9	2.0060	−0.7072	6.2120E−03	0.8611	−1.1259	2.0130E−03
10	2.0224	−0.6059	8.2497E−03	0.9317	−1.1190	1.3516E−03
$\alpha = 0.346$, $\beta = 1.736$, $\lambda = -1.469$, $\delta = 0.768$						
$\gamma = -1.206$, $\Omega = 2.114$, $\eta = -0.864$, $\zeta = -0.208$						
Far field						
4	1.5136	−1.1453	6.4139E−04	0.2397	−1.2158	1.1549E−03
5	1.7356	−1.1640	5.0752E−04	0.4635	−1.2389	1.0468E−03
6	1.9107	−1.1864	6.9751E−04	0.6248	−1.2531	1.2862E−03
7	2.0602	−1.2182	6.0862E−04	0.7628	−1.2783	1.3663E−03
8	2.2186	−1.2816	3.3932E−04	0.8936	−1.3220	1.0471E−03
9	2.4057	−1.3818	1.1730E−03	1.0620	−1.4091	8.7868E−04
10	2.5440	−1.4492	1.5957E−03	1.1887	−1.4687	1.3772E−03
$\alpha = -0.056$, $\beta = 2.558$, $\lambda = -0.647$, $\delta = -0.744$						
$\gamma = -1.177$, $\Omega = 2.333$, $\eta = -0.818$, $\zeta = -0.600$						

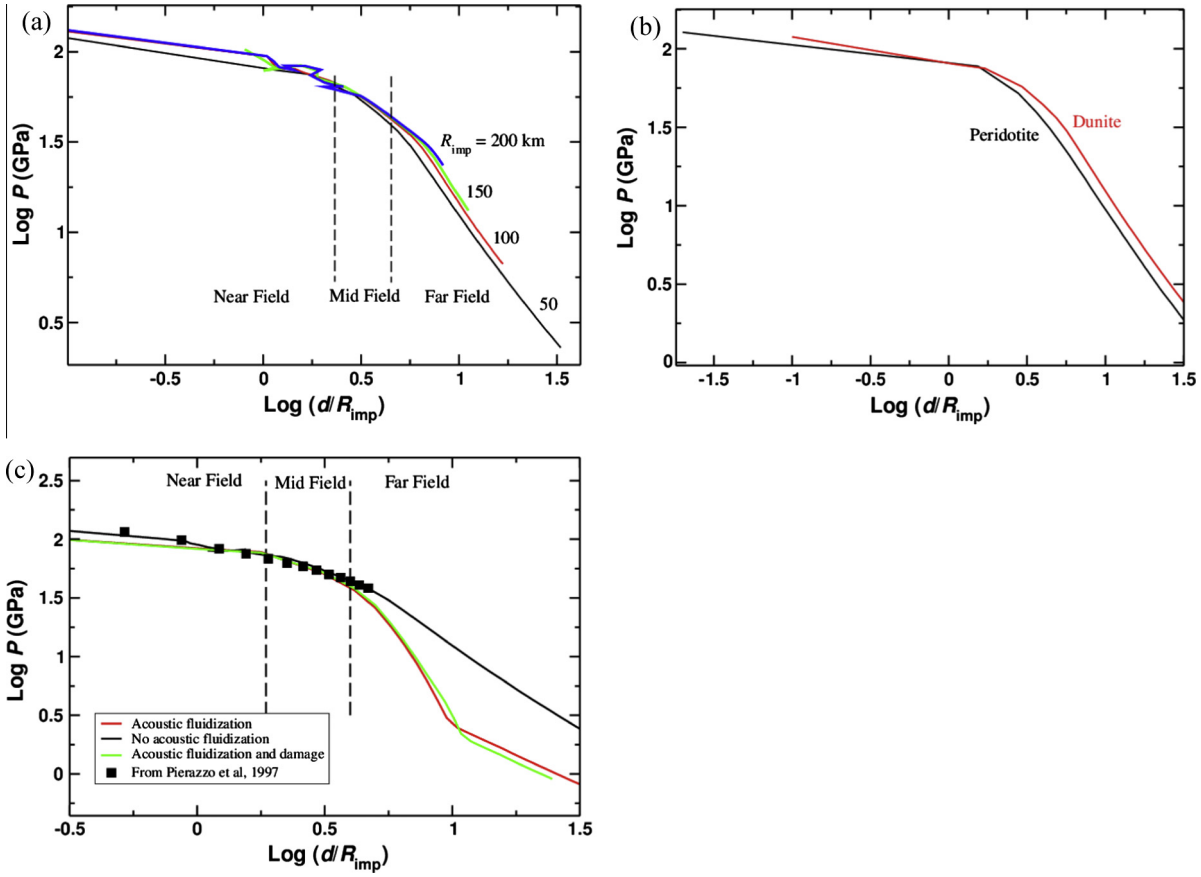

Fig. 6. (a) Shows the hydrocode results for impactors of 50–400 km diameter and impact velocity of 10 km/s, (b) compares the hydrocode results using dunite and peridotite as mantle rock types, for an impactor of 100 km diameter and impact velocity of 10 km/s and (c) illustrates the shock pressure as a function of d/R_{imp} with (red curve) and without (black curve) acoustic fluidization. The green curve represents the results considering an Ivanov damage model. (For comparison, the black squares represent the results from Pierazzo et al. (1997), which has not considered acoustic fluidization). (For interpretation of the references to color in this figure legend, the reader is referred to the web version of this article.)

in Eq. (3a) is −1.449 for dunite and −1.440 for peridotite. The major differences between the two models arise from the near field zone, hence propagates down to the deeper regions.

Among the other parameters and phenomenon that may influence the shockwave propagation (porosity, thermal softening...), accounting for the acoustic fluidization is required to accurately simulate the formation of a complex crater (e.g. Melosh, 1979; Bray et al., 2008; Potter et al., 2012). Indeed, acoustic fluidization is invoked to explain the collapse of complex craters by modifying the frictional strength of the damaged target. Fig. 6c compares the results obtained for R_{imp} = 50 km and V_{imp} = 10 km/s considering acoustic fluidization and an Ivanov damage model which prescribes damage as a function of plastic strain. This figure shows that for the near and mid fields, the results are similar. Pierazzo et al. (1997) did not include acoustic fluidization or damage in their models. Hence, our results without acoustic fluidization or damage model and the results from Pierazzo are in good agreement (Fig. 6c). As soon as the far field is reached, acoustic fluidization and damage tend to reduce the intensity of the shock pressure. This indicates that building more sophisticated models will be necessary in the near future. As the impact heating is mainly localized in the near- and mid-fields, including a damage model or acoustic fluidization should only weakly affect the thermal evolution of a growing protoplanet. However, it is worth mentioning that we are not concerned with the shape of the crater produced by a large impact, rather the main goal of our study is to extend the scaling laws of Pierazzo et al. (1997) to lower impact velocities which are more compatible with accretionary conditions.

Fig. 7 shows the impact velocity dependence of a, n, c, and m. Also included in Fig. 7b is the model by Ahrens and O'Keefe (1987) which was derived using impact velocities of 5 km/s and higher. Pierazzo et al. (1997) used impact velocities higher than those considered in the present study, except for their 10 km/s model. Hence, their results are shown in Fig. 7b by only one point, asterisk, at the impact velocity of 10 km/s.

The shock pressure along a non-vertical profile is not supposed to be the same as the one along a vertical profile, largely because of the pre-impact lithostatic pressure. As emphasized by Pierazzo et al. (1997, 2008) the shock front in deeper regions appears relatively symmetric around the impact point. Of course, it is not realistic in the case of an oblique impact (not studied here) and for the shallowest angles where the surface significantly affects the shock pressure decay. We have monitored the effect of the shockwave propagation angle θ with values varying between 90° (vertical profile) and 27° (Fig. 8). Similarly to Pierazzo et al. (1997), we did not find a significant angle dependence on our results especially when θ is ranging between 90° and 45°. For smaller values of θ, the surface effects appear to modify the shockwave propagation by reducing its intensity (Fig. 8a). Except in the mid field, where the n value decreases from −0.6 to −1.31, and in the far field, where the a value decreases from 2.54 to 1.93, the coefficients a and n from our scaling laws do not change significantly with the angle (Fig. 8b). This is particularly true in the near field where most of the impact heating occurs.

Scaling laws have been used by many investigators (e.g. Senshu et al., 2002; Tonks and Melosh, 1992, 1993; Watters et al., 2009;

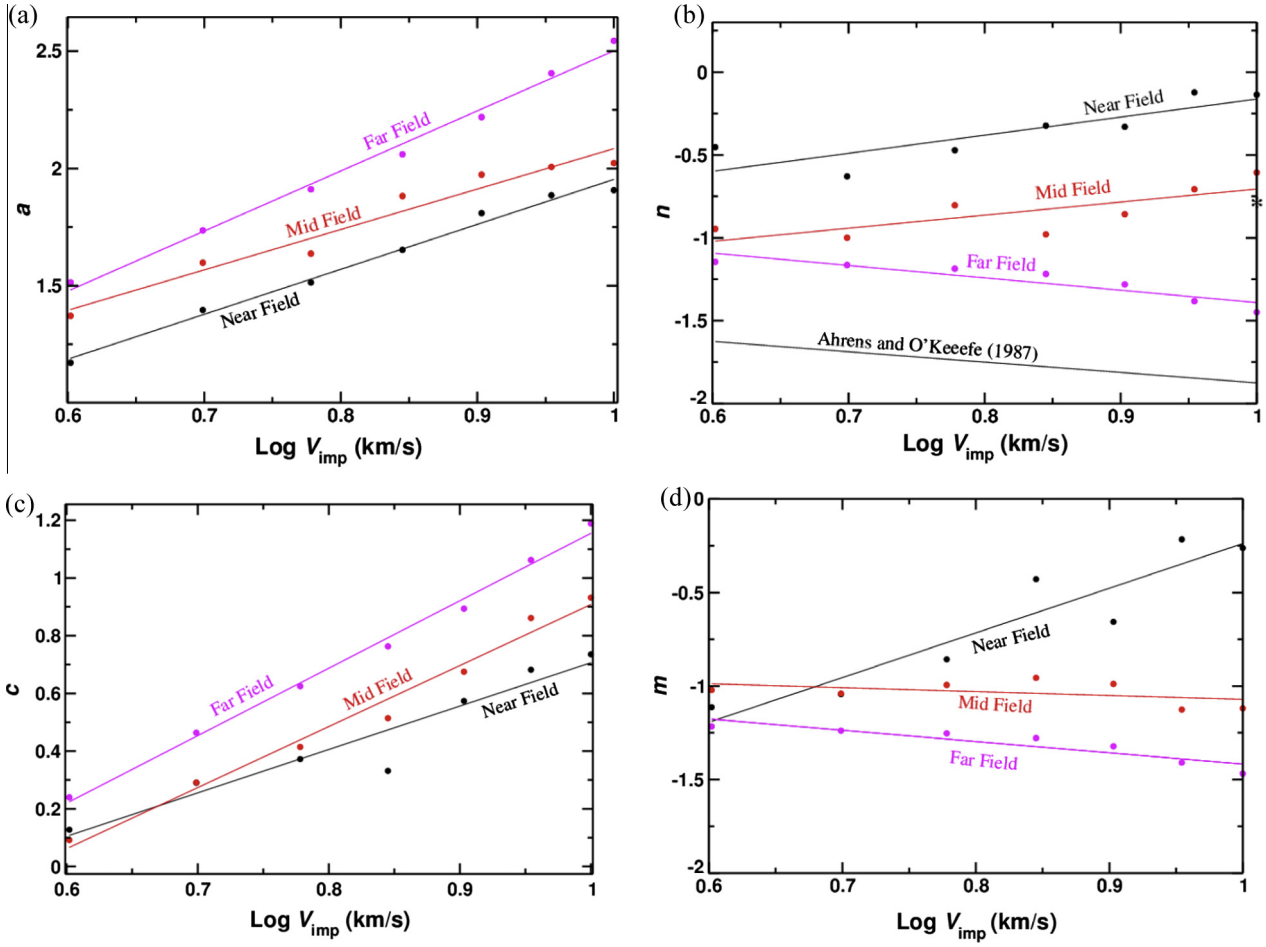

Fig. 7. Dependence of regression parameters *a*, *n*, *c*, and *m* from Eqs. (4) and (5) on the impact velocity. Dots are based on hydrocode models and lines are regression fits, see Table 2.

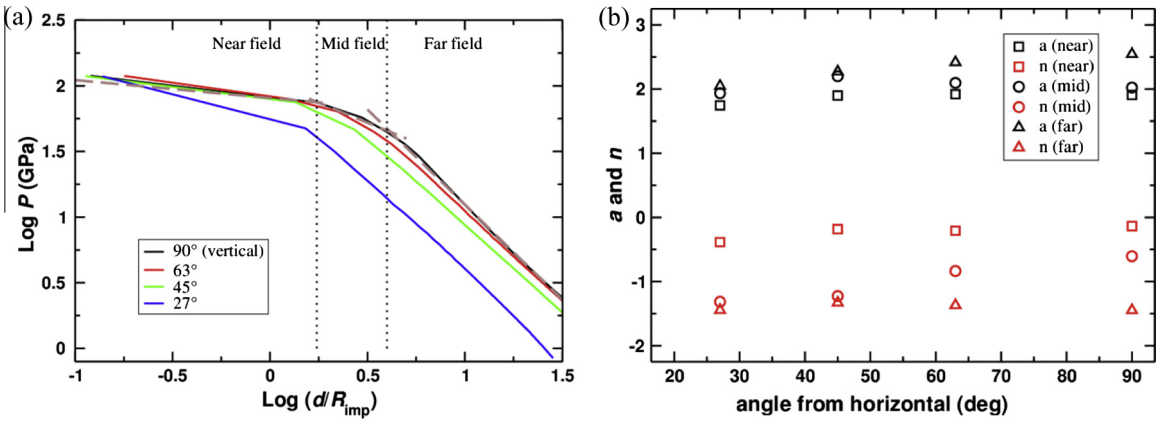

Fig. 8. The shockwave propagation as a function of the angle from the horizontal for the classical case (V_{imp} = 10 km/s and R_{imp} = 50 km). (a) Shock pressure decrease as a function of the distance to the impact site for propagation angles ranging between 27° and 90° and (b) dependence of regression parameters *a* and *n* (from Eqs. (4) and (5)) on the angle from horizontal.

Roberts et al., 2009; Arkani-Hamed and Olson, 2010a,b; Arkani-Hamed and Ghods, 2011), mainly because they require a much smaller computer and much less computer time and the difference between a hydrocode model and a corresponding scaling model is minute. For example, Fig. 9 shows the 2D distribution of the peak shock pressure determined for an impactor of 100 km in diameter and an impact velocity of 10 km/s calculated using our scaling laws in near field, mid field, and far field, and the parameter values from Table 2. The grid spacing is 2 km in radial direction and 0.03° in the colatitude direction. The entire computer time in a PC, CPU: 2.4 GHz, was only 16 s, which also calculated the 2D distribution of shock-induced temperature increase using Watters et al.'s (2009) foundering shock heating model. The computer time is substantially shorter than 48 h taken by our corresponding hydrocode

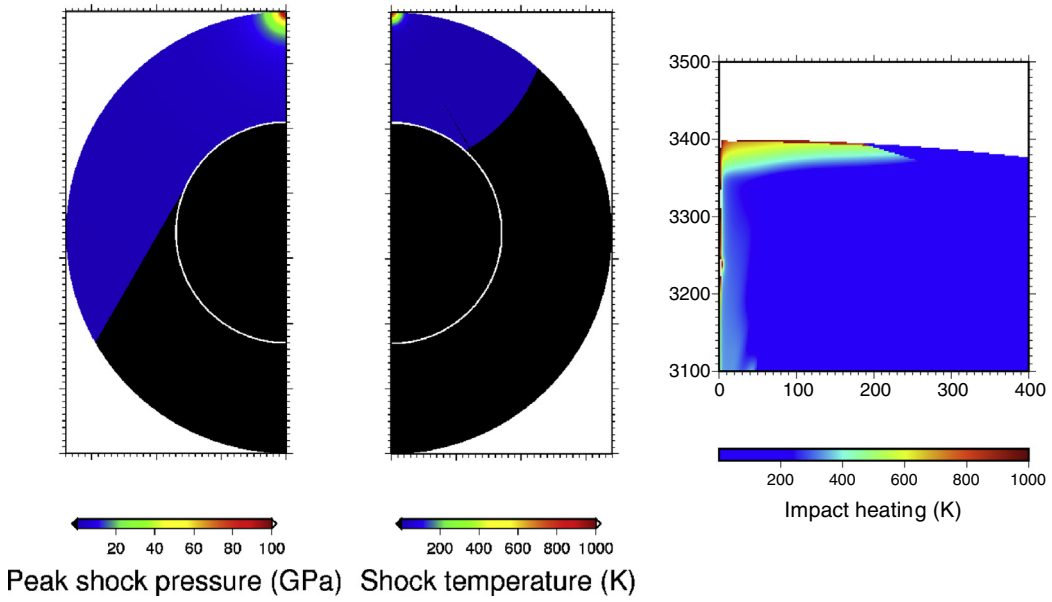

Fig. 9. 2D distribution of the peak shock pressure (left panel), and corresponding shock induced temperature increase (central panel) determined from our scaling laws for an impactor of 100 km in diameter and an impact velocity of 10 km/s calculated using the scaling laws in near field, mid field, and far field and the impact-induced temperature increase model from Watters et al. (2009) (see Eqs. (7)–(9)). The parameter values are based on regression lines from Fig. 7 and Table 2. The grid spacing is 2 km in radial direction and 0.03° in the colatitude direction. Only direct shock wave is considered. The black region in the mantle does not receive direct waves. The thin line extending from the impact site at the surface is the tangent line to the core. It shows that the part of the core receiving direct shock wave is not more than 25%. The color is saturated at higher values to better illustrate the regions with lower values. The right panel shows a close-up view of the corresponding temperature increase obtained from iSALE more than 30 min after the impact and illustrates the modifications that occur during the late stages of the impact process (excavation, central peak formation, slumping...). However, the intensity of impact heating is in agreement with our scaling laws. (For interpretation of the references to color in this figure legend, the reader is referred to the web version of this article.)

model using a CPU: 2.9 GHz laptop. This shows that it is feasible to determine impact heating during the accretion of a terrestrial planet using scaling laws, whereas it is almost impossible to adopt hydrocode simulations for that purpose.

During the decompression of shocked material much of the internal energy of the shock state is converted into heat (O'Keefe and Ahrens, 1977). Using thermodynamic relations, the waste heat used to heat up the impacted material can be estimated (Gault and Heitowit, 1963; Watters et al., 2009) and the corresponding temperature increase ΔT can be obtained. Hence, on the basis of our scaling laws it is possible to estimate the temperature increase as a function of depth below the impact site for impact velocities compatible with the accretionary conditions of terrestrial protoplanets. These scaling laws can easily be implemented in a multi-impact approach (e.g. Senshu et al., 2002; Monteux et al., 2014) to monitor the temperature evolution inside a growing protoplanet whereas it is not yet possible to adopt hydrocode simulations for that purpose. For example, included in Fig. 9 is the impact induced temperature increase corresponding to the shock pressure shown in the figure. The temperature increase is determined on the basis of foundering model of Watters et al. (2009) using constant values for the acoustic velocity C (6600 m/s) and the parameter S (0.86) in their expressions:

$$\Delta T(P) = \frac{P}{2\rho_0 S}(1 - f^{-1}) - (C/S)^2[f - \ln f - 1] \tag{7}$$

$$f(P) = -\frac{P}{\beta}\left(1 - \sqrt{\frac{2P}{\beta} + 1}\right)^{-1} \tag{8}$$

$$\beta = \frac{c^2 \rho_0}{2S} \tag{9}$$

with P the shock-increased pressure and ρ_0 the density prior to shock compression (see Table 1 for values).

Due to small size the impactor is not capable of increasing the lower mantle temperature of the model planet significantly, and only minor impact heating of the core has occurred. The thermal evolution model has to be combined to a topographical evolution model to account for the growth of the protoplanet as in Monteux et al. (2014). In these models, the impact angle (considered here as vertical) probably plays a key role because it influences both the morphology of the impact heating and the shape of the post-impact topography. A more elaborated scaling laws built upon 3D hydrocode models will be developed for that purpose in the near future.

It is worth emphasizing that our scaling laws, like those of others (Ahrens and O'Keefe, 1987; Pierazzo et al., 1997; Mitani, 2003), are derived from a few hydrocode models. Fig. 10 shows the profiles of the pressure along the axis of symmetry for comparison. The differences between the hydrocode model and the scaling law are small for the most part, but the exact scaling law differs by ~10 GPa for $d/R_{\mathrm{imp}} = 2$–3. This difference arises from the difficulty of correctly describe the near field as previously mentioned. Note that the interpolated model is in much better agreement with the hydrocode model.

A linear relationship has been proposed between the shock wave velocity V_s and particle velocity V_p on the basis of laboratory measurements (McQueen et al., 1967; Trunin, 2001)

$$V_s = C + SV_p \tag{10}$$

where C is the acoustic velocity and S is a constant parameter. We estimate the acoustic velocity in the mantle of the model planet on the basis of our hydrocode models (Fig. 5a and b) using Eq. (10) and the Hugoniot equation

$$P = \rho V_p V_s \tag{11}$$

where ρ (=3320 kg/m^3) is the pre-shock density. Fig. 11 shows the variations of C with depth for models with impact velocities of 4–10 km/s and an impactor of 100 km diameter, using $S = 1.2$ which

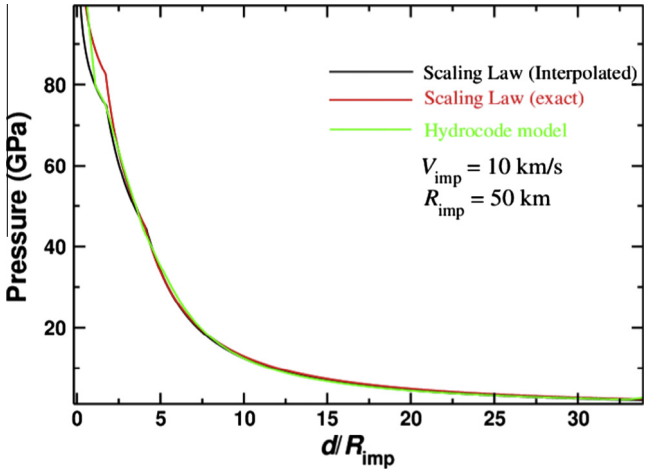

Fig. 10. Shock pressure versus distance from the impact site normalized to the impactor radius. The hydrocode model is the output of the hydrocode simulation. In the exact model we have used a and n, while α, β, λ and δ are used in the interpolated model, see Table 2.

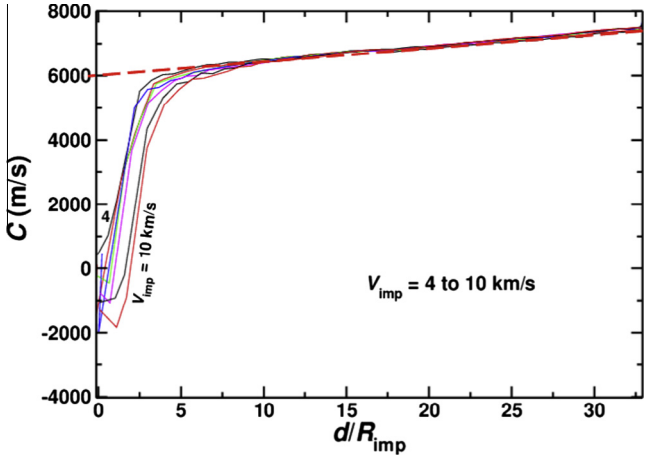

Fig. 11. The acoustic velocity determined using Eq. (10) for an impactor of 100 km diameter, and impact velocities ranging from 4 to 10 km/s. The S parameter in the equation is set to 1.2. The red dashed line is a line fit to C in the deeper region. (For interpretation of the references to color in this figure legend, the reader is referred to the web version of this article.)

is within the values proposed by the authors for dunite (e.g. Trunin, 2001). Adopting S = 0.86 (McQueen et al., 1967) does not change the results significantly, especially in the far field, where the acoustic velocity is less sensitive to particle velocity and linearly increases with depth. However C shows particle velocity dependence in the mid field and near field.

4. Conclusions

We have modeled the shock pressure and particle velocity distributions in the mantle of a Mars size planet using hydrocode simulations (iSALE-2D) for impact velocities of 4–10 km/s and projectile diameters ranging from 100 to 400 km. We have extended Pierazzo et al.'s (1997) scaling laws to low impact velocities and also considered large impactor radii occurring during the formation of terrestrial planets. We propose three distinct regions in the mantle: a near field region, which extends to 1–3 times the projectile radius into the target, where the peak shock pressure and particle velocity decay very slowly with increasing distance, a mid field region, which extends to ~4.5 times the impactor radius, where the pressure and particle velocity decay exponentially but moderately, and a more distant far field region where the pressure and particle velocity decay strongly with distance. The mid field–far field boundary is well constrained, whereas that of the near field–mid field is a relatively broad transition zone for the impact velocities examined.

Acknowledgments

This research was supported by Agence Nationale de la Recherche (Oxydeep decision No. ANR-13-BS06-0008) to JM, and by Natural Sciences and Engineering Research Council (NSERC) of Canada to JAH. We gratefully acknowledge the developers of iSALE (www.isale-code.de), particularly the help we have received from Gareth S. Collins. We are also grateful to the two reviewers for very helpful suggestions.

References

Ahrens, T.J., O'Keefe, J.D., 1987. Impact on the Earth, ocean and atmosphere. Int. J. Impact Eng. 5, 13–32, 122.
Arkani-Hamed, J., 2005. Magnetic crust of Mars. J. Geophys. Res. 110, E08005. http://dx.doi.org/10.1029/2004JE002397.
Arkani-Hamed, J., Ghods, A., 2011. Could giant impacts cripple core dynamos of small terrestrial planets? Icarus 212, 920–934.
Arkani-Hamed, J., Olson, P., 2010a. Giant impact stratification of the martian core. Geophys. Res. Lett. 37, L02201. http://dx.doi.org/10.1029/2009GL04141.
Arkani-Hamed, J., Olson, P., 2010b. Giant impacts, core stratification, and failure of the martian dynamo. J. Geophys. Res. 115, E07012.
Barr, A., Citron, R., 2011. Scaling of melt production in hypervelocity impacts from high-resolution numerical simulations. Icarus 211, 913–916.
Benz, W., Cameron, A.G.W., Melosh, H.J., 1989. The origin of the Moon and the single-impact hypothesis III. Icarus 81, 113–131.
Bierhaus, M., Wünnemann, K., Elbeshausen, D., 2012. Numerical modeling of basin-forming impacts: Implications for the heat budget of planetary interiors. Lunar Planet. Sci. 43. Abstract #2174.
Bray, V.J. et al., 2008. The effect of target properties on crater morphology: Comparison of central peak craters on the Moon and Ganymede. Meteorit. Planet. Sci. 43, 1979–1992.
Chambers, J.E., 2004. Planetary accretion in the inner Solar System. Earth Planet. Sci. Lett. 223, 241–252.
Chambers, J.E., Wetherill, G.W., 1998. Making the terrestrial planets: N-body integrations of planetary embryos in three dimensions. Icarus 136, 304–327.
Collins, G.S., Melosh, H.J., Ivanov, B.A., 2004. Modeling damage and deformation in impact simulations. Meteorit. Planet. Sci. 39 (2), 217–231. http://dx.doi.org/10.1111/j.1945-5100.2004.tb00337.x.
Davison, T.M., Collins, G.S., Ciesla, F.J., 2010. Numerical modeling of heating in porous planetesimal collisions. Icarus 208, 468–481. http://dx.doi.org/10.1016/j.icarus.2010.01.034.
Frey, H., 2008. Ages of very large impact basins on Mars: Implications for the late heavy bombardment in the inner Solar System. Geophys. Res. Lett. 35, L13203. http://dx.doi.org/10.1029/2008GL033515.
Gault, D.E., Heitowit, E., 1963. The partition of energy for hypervelocity impact craters formed in rock. Paper Presented at 6th Hypervelocity Impact Symposium. Firestone Tire and Rubber Co., Cleveland (30 Apr. to 2 May).
Holsapple, K.A., 1993. The scaling of impact processes in planetary sciences. Annu. Rev. Earth Planet. Sci. 21, 333–373.
Ivanov, B.A., Melosh, H.J., Pierazzo, E., 2010. Basin-forming impacts: Reconnaissance modeling. Geol. Soc. Am. Spec. Pap. 465, 29–49.
Keil, K. et al., 1997. Constraints on the role of impact heating and melting in asteroids. Meteorit. Planet. Sci. 32, 349–363.
Kokubo, E., Ida, S., 1995. Orbital evolution of protoplanets embedded in a swarm of planetesimals. Icarus 114, 247–257.
Kokubo, E., Ida, S., 1996. On runaway growth of planetesimals. Icarus 123, 180–191.
Kokubo, E., Ida, S., 1998. Oligarchic growth of protoplanets. Icarus 131, 171–178.
Kokubo, E., Ida, S., 2000. Formation of protoplanets from planetesimals in the solar nebula. Icarus 143, 15–27.
Kraus, R.G., Senft, L.E., Stewart, S.T., 2011. Impacts onto H_2O ice: Scaling laws for melting, vaporization, excavation, and final crater size. Icarus 214, 724–738.
Matsui, T., 1993. Early evolution of terrestrial planets: Accretion, atmospheric formation, and thermal history. In: Oya, H. (Ed.), Premitive Solar Nebula and Origin of Planets. Terra Scientific Publication Company, Tokyo, pp. 545–559.
McQueen, R.G., Marsh, S.P., Fritz, J.N., 1967. Hugoniot equation of state of twelve rocks. J. Geophys. Res. 72, 4999–5036.
McQueen, R.G. et al., 1970. The equation of state of solids from shock wave studies. In: Kinslow (Ed.), High Velocity Impact Phenomena. Academic, New York, pp. 294–491.
Melosh, H.J., 1979. Acoustic fluidization: A new geologic process? J. Geophys. Res. 84, 7513–7520.

Melosh, H.J., 1989. Impact Cratering: A Geologic Process. Oxford Univ. Press, New York.
Mitani, N.K., 2003. Numerical simulations of shock attenuation in solids and reevaluation of scaling law. J. Geophys. Res. 108 (E1), 5003. http://dx.doi.org/10.1029/2000JE001472.
Monteux, J. et al., 2007. Thermo-mechanical adjustment after impacts during planetary growth. Geophys. Res. Lett. 34, L24201. http://dx.doi.org/10.1029/2007GL031635.
Monteux, J. et al., 2009. A model of metal-silicate separation on growing planets. Earth Planet. Sci. Lett. 287, 353–362. http://dx.doi.org/10.1016/j.epsl.2009.08.020.
Monteux, J., Jellinek, M., Johnson, C.J., 2013. Dynamics of core merging after a martian mega-impact. Icarus 226 (1), 20–32. http://dx.doi.org/10.1016/j.icarus.2013.05.008.
Monteux, J. et al., 2014. Can large icy Moons accrete undifferentiated? Icarus 237, 377–387. http://dx.doi.org/10.1016/j.icarus.2014.04.041 (15 July 2014).
Monteux, J. et al., 2015. Giant impacts, heterogeneous mantle heating and a past hemispheric dynamo on Mars. Phys. Earth Planet. Int. 240, 114–124. http://dx.doi.org/10.1016/j.pepi.2014.12.005.
O'Keefe, J.D., Ahrens, T.J., 1977. Impact-induced energy partitioning, melting, and vaporization on terrestrial planets. Lunar Planet. Sci. 8, 3357–3374.
Perret, W.R., Bass, R.C., 1975. Free-Field Ground Motion Induced by Underground Explosions. Sandia Report SAND74-0252.
Pierazzo, E., Vickery, A.M., Melosh, H.J., 1997. A re evaluation of impact melt production. Icarus 127, 408–423.
Pierazzo, E. et al., 2008. Validation of numerical codes for impact and explosion cratering: Impacts on strengthless and metal targets. Meteorit. Planet. Sci. 43 (12), 1917–1938.
Potter, R. et al., 2012. Estimating transient crater size using the crustal annular bulge: Insights from numerical modeling of lunar basin-scale impacts. Geophys. Res. Lett. 39, L18203.
Rafikov, R.R., 2003. The growth of planetary embryos: Orderly, runaway, or oligarchic. Astron. J. 125, 942–961.
Raymond, S.N., Quinn, T., Lunine, J.I., 2006. High-resolution simulations of the final assembly of Earth-like planets, Terrestrial accretion and dynamics. Icarus 183, 265–282.
Ricard, Y., Srámek, O., Dubuffet, F., 2009. A multi-phase model of runaway core-mantle segregation in planetary embryos. Earth Planet. Sci. Lett. 284, 144–150.
Roberts, J.H., Arkani-Hamed, J., 2012. Impact-induced mantle dynamics on Mars. Icarus 218, 278–289.
Roberts, J.H., Arkani-Hamed, J., 2014. Impact heating and coupled core cooling and mantle dynamics on Mars. J. Geophys. Res. Planets 119, 729–744. http://dx.doi.org/10.1002/2013JE004603.
Roberts, J.H., Lillis, R.J., Manga, M., 2009. Giant impacts on early Mars and the cessation of the martian dynamo. J. Geophys. Res. 114, E04009.
Schenk, P. et al., 2012. The geologically recent impact basins at Vesta's south pole. Science 336, 694–697.
Schmidt, R.M., Housen, K.R., 1987. Some recent advances in the scaling of impact an explosion cratering. Int. J. Impact Eng. 5, 543–560.
Senshu, H., Kuramoto, K., Matsui, T., 2002. Thermal evolution of a growing Mars. J. Geophys. Res. 107 (E12), 5118. http://dx.doi.org/10.1029/2001JE001819.
Thompson, S., Lauson, H., 1972. Improvements in the CHART D Radiation-Hydrodynamic Code III: Revised Analytic Equations of State. Sandia National Laboratory Report SC-RR-71 0714. 113 p.
Tonks, W.B., Melosh, H.J., 1992. Core formation by giant impacts. Icarus 100, 326–346.
Tonks, W.B., Melosh, H.J., 1993. Magma ocean formation due to giant impacts. J. Geophys. Res. 98, 5319–5333.
Trunin, R.F., 2001. Experimental Data on Shock Compression and Adiabatic Expansion of Condensed Matter. RFNC-VNIIEF, Sarov, p. 446. ISBN: 5-85165-624-7.
Watters, W.A., Zuber, M.T., Hager, B.H., 2009. Thermal perturbations caused by large impacts and consequences for mantle convection. J. Geophys. Res. 114, E02001.
Wetherill, G.W., Inaba, S., 2000. Planetary accumulation with a continuous supply of planetesimals. Space Sci. Rev. 92, 311–320.
Wetherill, G.W., Stewart, G.R., 1989. Accumulation of a swarm of small planetesimals. Icarus 77, 330–357.
Wünnemann, K., Ivanov, B.A., 2003. Numerical modelling of impact crater depth-diameter dependence in an acoustically fluidized target. Planet. Space Sci. 51, 831–845.
Wünnemann, K., Collins, G.S., Melosh, H.J., 2006. A strain-based porosity model for use in hydrocode simulations of impacts and implications for transient-crater growth in porous targets. Icarus 180, 514–552.

Icarus 331 (2019) 238–256

Contents lists available at ScienceDirect

Icarus

journal homepage: www.elsevier.com/locate/icarus

Shock wave propagation in layered planetary interiors: Revisited

J. Monteux[a,*], J. Arkani-Hamed[b,c]

[a] Université Clermont Auvergne, CNRS, IRD, OPGC, Laboratoire Magmas et Volcans, F-63000 Clermont-Ferrand, France
[b] Department of Physics, University of Toronto, Toronto, Canada
[c] Department of Earth and Planetary Sciences, McGill University, Montreal, Canada

A B S T R A C T

While major impacts during late accretion of a Mars type planet occur on a differentiated body, the characteristics of the shockwave propagation are poorly known within these layered objects. Here, we use iSALE-2D hydrocode simulations to calculate shock pressure in a differentiated Mars type body for impact velocities ranging from 5 to 20 km/s, impactor radii ranging from 50 to 200 km, and different rheologies. To better represent the distribution of shock pressure as a function of distance from the impact site at the surface, we propose two distinct regions in the mantle: a near field region that extends to 7–15 times the projectile radius into the target, where the peak shock pressure decays exponentially with increasing the distance from the impact site, and a far field region where the pressure decays strongly with the distance following a power law. At the core-mantle boundary, the peak shock pressure increases from the mantle side to the core side. The refracted shockwave travels within the core where the shock pressure decreases following a second power law. In this study, we fit the output obtained from iSALE hydrocode simulations to determine scaling laws that illustrate the influence of the distance from the impact site, the ray angle, the target rheology, the impactor size and the impact velocity. Finally we combine these shock-pressure scaling laws with the formalism proposed by Watters et al. [2009] to determine the impact heating induced by large impacts within a differentiated Mars.

1. Introduction

Terrestrial planets are formed by accreting a huge number of planetesimals in the solar nebula [e.g., Chambers and Wetherill, 1998; Kokubo and Ida, 2000; Rafikov, 2003; Chambers, 2004; Raymond et al., 2006]. The ultimate goal is to investigate the thermal evolution of a growing terrestrial planet while taking into account the impact heating, heating by short-lived and long-lived radioactive elements, and by the core formation process. Because partial melting and core formation occur when a protoplanet's radius exceeds ~2700 km [e.g., Senshu et al., 2002], about 47% of Mars' and 90% of the Earth's and Venus' masses are expected to be accreted in the presence of a liquid core. To estimate the thermal state of a growing planet it is necessary to determine the impact heating of its solid mantle and liquid core by each impactor.

The impact-induced shock pressure and temperature increase inside a planet has been investigated using elaborated numerical models developed to better understand shock physics [e.g., Ahrens and O'Keefe, 1987; Pierazzo et al., 1997; Mitani, 2003; Wünnemann et al., 2006; Wünnemann et al., 2008; Ivanov et al., 2010; Barr and Citron, 2011; Kraus et al., 2011; Bierhaus et al., 2012; Leinhardt and Stewart, 2009]. However, the numerical solutions demand considerable computer capacity and time and are not practical for investigating a huge number of impacts that occur during the growth of a planet. For example, the formation of a planet like Mars requires about 3×10^5 planetesimals of ~100 km in diameter. On the other hand, the scaling laws derived on the basis of numerical solutions of the shock dynamic equations [e.g., Ahrens and O'Keefe, 1987; Pierazzo et al., 1997; Mitani, 2003; Monteux and Arkani-Hamed, 2016] require remarkably less computer power and time, and have been used by many investigators [e.g., Tonks and Melosh, 1992, 1993; Watters et al., 2009; Roberts et al., 2009; Arkani-Hamed and Olson, 2010a, 2010b; Ghods and Arkani-Hamed, 2011], mainly because of their simplicity and partly because the difference between their results and those obtained by the numerical simulations of the shock dynamic equations is likely within the tolerance of the errors introduced due to the uncertainty of pertinent physical parameters. We note that the existing scaling laws are applicable for uniform mantle models of terrestrial planets and cannot be used for planets consisting of a solid silicate mantle and a liquid iron core with drastically different physical properties. Extra formulations are required to relate the shock pressure and particle velocity at the base of the mantle to those at the top of the core. Arkani-Hamed and Ivanov [2014] derived the required boundary conditions at the core-mantle boundary (CMB) of a Mars type planet for a vertical impact on the basis of Hugoniot equations, the equality of the reflected and the refracted shock pressures, the continuity of the vertical component of particle velocity, and the Snell's law relating the incident angle to the refracted angle of a shock ray at the boundary. This resulted in a set of coupled 8

* Corresponding author.
E-mail address: j.monteux@opgc.univ-bpclermont.fr (J. Monteux).

https://doi.org/10.1016/j.icarus.2019.05.016
Received 20 September 2017; Received in revised form 1 February 2019; Accepted 13 May 2019
Available online 19 May 2019
0019-1035/

trigonometric equations to be solved simultaneously for each shock ray. At each point of the core mantle boundary, with spacing of 1° colatitude, the equations were solved iteratively until the difference between the two successive solutions were within a set error limit. Although such a simulation is much faster than the corresponding hydrocode simulation, it still takes considerable time to determine impact heating in a growing planet that requires several hundred thousand impacts during the accretion. Recently, Monteux and Arkani-Hamed [2016] derived scaling laws in the mantle of a Mars size planet on the basis of systematic hydrocode modeling, using impact velocities ranging from 4 to 10 km/s for impactor sizes ranging from 50 to 200 km in radius, and two different mantle rocks of dunite and peridotite overlying the iron core. The ANEOS type equations of state were used for the dunitic mantle rocks and the iron core.

In the present study, we adopt a new technique based on hydrocode models by Monteux and Arkani-Hamed [2016] while deriving a new scaling law for the iron core to assess shock pressure and the shock-related temperature increase in the entire Mars type planet. A given shock front propagates from the impact site at the surface of the planet down to the CMB. It then partly reflects back to the mantle, and partly enters the core and continues propagating until it impinges the CMB in the antipodal hemisphere, where it partly enters the antipodal mantle and partly reflects and propagates in the antipodal core. The second section characterizes the shockwave propagation within a differentiated Mars size planet for different sets of parameters (impactor radius, impact velocity, and mantle rheology). The third section compares the results from the scaling laws with those obtained using hydrocode simulations. In the fourth section, impact-heated models determined on the basis of the scaling laws to demonstrate the feasibility of the models derived by the scaling laws. Discussions and concluding remarks are relegated to the fifth, final section.

2. Shockwave propagation inside a Mars-type planet

Fig. 1 shows the 2D axi-symmetric total pressure (shock + lithostatic) distribution inside a Mars size body of radius 3400 km with a core radius of 1700 km, created by an impactor of 200 km in radius and at an impact velocity of 10 km/s obtained by hydrocode simulation. The shock pressure produced near the surface decays as the shock wave propagates downward until the wave impinges the CMB, where it partitions into two waves, a reflected wave that propagates outward in the mantle, and a refracted wave that enters the core and propagates downward. The reflected wave arriving at a given point in the mantle travels much longer, hence is always weaker than the direct wave that propagates directly from the impact site to that point. The peak pressure at the point is produced by the direct wave. The effects of the two reflected waves, one at the surface and the other at the CMB are not considered on the temperature of the mantle in this study (see below). An abrupt pressure jump is created at the top of the core by the refracted wave. The pressure then continues decreasing while the wave propagates in the core.

A total of 11 hydrocode models were simulated by Monteux and Arkani-Hamed [2016] that included impact velocities of 4 to 10 km/s at increments of 1 km/s for an impactor of 50 km in radius, and the impactor radii of 50 to 200 km at increments of 50 km for an impact velocity of 10 km/s. Two mantle rock types of dunite and peridotite were considered for a Mars-type planet. The authors considered shock wave propagation in the mantle of the impacted hemisphere. Here we extend the models allowing the wave enter the core, hence providing a means to estimate the characteristics of shock pressure and the related temperature increase throughout the mantle and the core.

2.1. The model set up

At the end of the planetary accretion, large impacts between planetesimals and protoplanets are frequent. The amount of energy dissipated during this regime of planetary evolution is large enough to significantly melt the growing planets and efficiently separate the metal phase from the silicate phase, resulting in the core formation. We consider a large impact between an undifferentiated bolide and a differentiated Mars size planet using numerical hydrocode simulations.

2.1.1. Physical model

We investigate the shock pressure inside a Mars size model planet for impact velocities V_{imp} of 5 to 20 km/s and impactors radii R_{imp} of 50 to 200 km. Such impactors are likely to create large impact basins with sizes comparable to the giant impact basins of Mars that were formed between 4.3 and 4 Ga [Frey, 2008; Robbins et al., 2013]. The impactors are large enough to have important consequences on their target. However the impactors might be too small to have experienced a complete melting and full metal/silicate separation before the impact unless they formed during the early Solar System evolution [Ricard et al., 2017] Impacts involving differentiated impactors will lead to the fragmentation of the impactor's core before sinking through the target's mantle [Kendall and Melosh, 2016]. In our models, an impactor is simplified by a spherical body of radius R_{imp} with uniform dunitic composition. Since we do not consider a realistic impactor with a metallic core, we underestimate the actual impactor mass and, as a consequence, the kinetic energy available for impact heating. In our models, the impactor and the impacted mantle have the same properties (composition, strength, rheology, and equation of state).

The ultimate goal is to determine the impact heating during the accretion of terrestrial planets such as Mars and the Earth. The huge number of impacts during accretion makes it impractical to consider oblique impacts for two main reasons: it requires formidable computer time, but more importantly because of the lack of information about the impact direction, i.e. the impact angle relative to vertical and azimuth relative to north. The peak shock pressure produced along the vertical direction beneath the impact site by an oblique impact appears to depend approximately on the sine of the impact angle relative to horizon (see Fig. 3 of Pierazzo and Melosh, 2000a, 2000b). This implies a shock pressure reduction by a factor of ~0.71 for the most probable impact angle of 45° [Shoemaker, 1962] compared to that of a vertical impact, assuming that all other parameters are equal. For example an oblique impact velocity of about 15 km/s produces almost the same shock pressures as that produced by a vertical impact velocity of about 11 km/s. The difference between these two velocities is well within the variations of the impact velocities of the N-body accretion models of terrestrial planets [e.g., Agnor et al., 1999; Chambers, 2013]. Studies of more realistic accretion scenarios, which take into account the oblique impacts and allow escape of material, conclude that the final state of an accreted body is less sensitive to the details of the collision [Agnor and Asphaug, 2004; Kokubo and Genda, 2010]. Therefore, we consider only head-on collisions (vertical impacts) to model the thermo-mechanical evolution during an impact between a differentiated Mars size body and a large uniform impactor.

As emphasized by Monteux and Arkani-Hamed [2016], the rheology of the impacted body plays a key role on the propagation of the shockwave and on the subsequent impact heating. However, the rheology of protoplanets is difficult to constrain precisely and is strongly governed by its thermal evolution. Depending on its accretion rate, on its composition in radiogenic elements and on the occurrence of large to giant impacts, growing Mars-sized protoplanets likely consist of a partially to fully molten mantle overlying a liquid metallic core [Kaula, 1979; Solomatov, 2000; Senshu et al., 2002; Ricard et al., 2009]. In the following study we consider that the rheology of the impacted protoplanets ranges between a “hydrodynamic model” with no-strength where both the dunitic mantle and the metallic core are inviscid materials, and a “model with strength” where the metallic core is an inviscid fluid while the dunitic mantle is treated using a pressure-, temperature-, and damage- dependent strength model.

Damage describes the transition from intact to fractured strength.

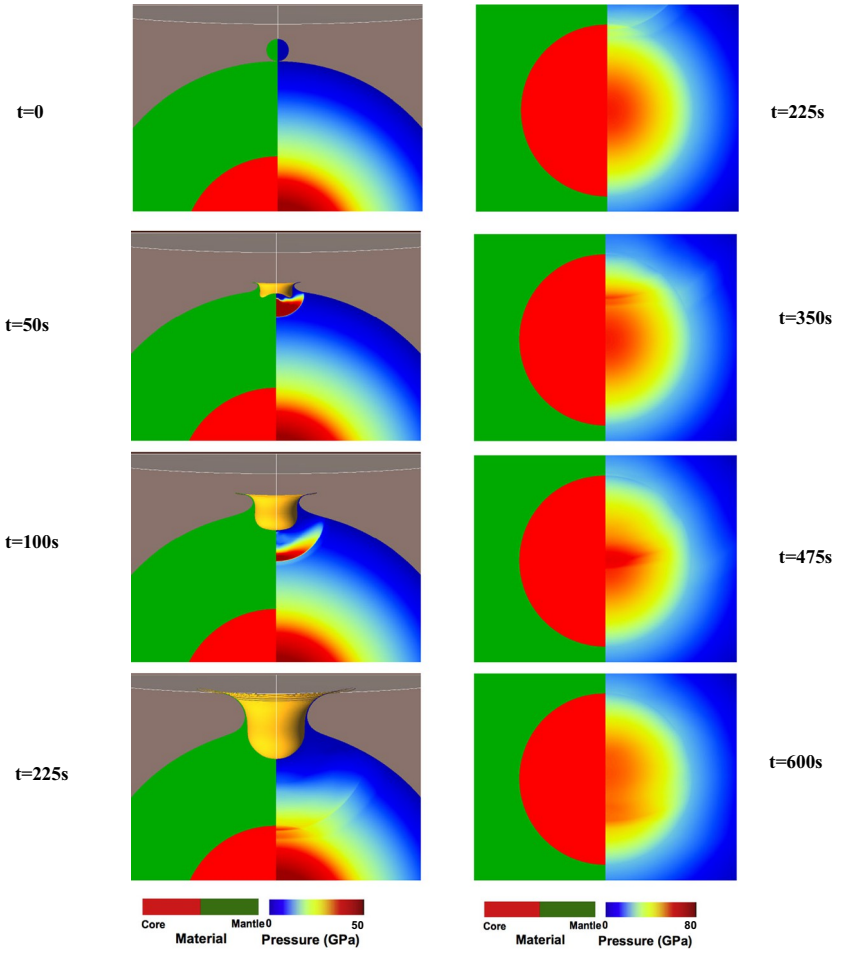

Fig. 1. Time evolution of the total pressure (shock + lithostatic) inside a differentiated Mars size body during the first 600 s after the impact, caused by a 200 km radius undifferentiated impactor at 10 km/s impact velocity. In our models, the Martian core is liquid. The lithostatic pressure is adopted from Monteux and Arkani-Hamed [2016] and the pre-impact temperature profile is illustrated in Fig. 4 (cold profile). The four left panels represent 4 specific times (from top to bottom): t = 0 s, t = 50s, t = 100 s and t = 225 s with a focus on the impacted mantle. The four right panels represent 4 times (from top to bottom): t = 225 s, t = 350 s, t = 475 s and t = 600 s with a focus on the impacted core. Note the change in the pressure scales between the left and right panels.

Under a constant pressure, damage begins to accumulate when the material begins to flow plastically. Damage is maximum when the material is completely fractured. Among the damage models available in iSALE, we adopt the Ivanov damage model [Ivanov et al., 1997], which prescribes damage as a function of plastic strain. In this model the plastic strain at failure is an increasing function of the total pressure P (lithostatic pressure plus the shock-induced pressure). This model allows rapid brittle failure in tensile and low-pressure modes, and semi-brittle failure at high pressures. The damage model from Ivanov et al. [1997] is simpler than the model developed by Collins and Melosh [2014] where the plastic strain at failure is a function of the brittle-ductile and brittle-plastic transition pressures, both these parameters being poorly constrained in the early protoplanets context.

The thermal softening is an efficient process for large-scale events [Potter et al., 2012]. Depending on the temperature and more specifically on the melt fraction, the impacted material can behave as a solid material or as fluid. The transition from solid-like to fluid-like behavior occurs at a critical melt fraction of ≈40% for early mantle material (Solomatov, 2000). As it depends on the temperature, the thermal softening process also strongly depends on the pre-impact temperature that is unfortunately poorly constrained in the Martian case. In our iSALE models, we use the Ohnaka thermal softening model where the shear strength of rocks depends on temperature, and reduces to zero at the melting temperature.

In the “model with strength”, we approximate the thermodynamic response of both the iron and dunitic material using the ANEOS equation of state [Thompson and Lauson, 1972; Benz et al., 1989]. To make our models as simple as possible we do not consider here the effects of porosity or low density weakening which are likely to be negligible in the deep interior of a planet. However, as a first step toward more realistic models, we investigate the influence of acoustic fluidization, thermal softening and damage. The simulation parameters are listed in Table 1.

2.1.2. Numerical model

We use the iSALE-2D axisymmetric hydrocode, which is a multi-rheology, multi-material hydrocode, specifically developed to model impact crater formation on a planetary scale [Amsden et al., 1980, Collins and Melosh, 2014, Davison et al., 2010]. To enable a comparison of our models, for all our simulations, we use a 2 km grid resolution computational domain. The horizontal and vertical number of cells per projectile radius (*cppr*) is maintained constant within the impacted mantle (=1700) and within the impacted core (=850) (see Table 2). The number of *cppr* varies only within the impactor when varying the impactor radius (*cppr* = 25 for R_{imp} = 50 km and *cppr* = 100 for R_{imp} = 100 km). Such spatial resolutions should lead to an underestimation of the peak shock pressure ranging between 5% (close to the impact site) and 10% (far from the impact site) according to resolution studies [e.g., Pierazzo et al., 2008; Wünnemann et al., 2008; Monteux and Arkani-Hamed, 2016].

iSALE requires the length of each time step (dt) and the maximum time step (dt_{max}). iSALE limits the time step by the speed of sound according to the Courant–Friedrichs–Lewy (CFL) condition while dt_{max} limits a timestep if it is smaller than the CFL-limited timestep. In our models, we use a dt_{max} value of 0.05 s. The minimum post impact monitoring time is set to the time needed by the shockwave to travel from the impact site through the entire core of the impacted planet.

In our iSALE models, we investigate the effects of the ray angle β relative to the symmetric axis (Fig. 2). To compare the shock wave propagation along each path illustrated in Fig. 2, we developed a

Table 1
Typical physical parameter values for numerical hydrocode models.

Target radius	R	3400 km (Rivoldini et al., 2011)
Target core radius	R_{core}	1700 km (Rivoldini et al., 2011)
Impactor radius	R_{imp}	50–200 km
Impact velocity	V_{imp}	5–20 km/s
Mantle properties (Dunite)		(Benz et al., 1989)
		Model with strength
Initial density	ρ_m	3314 kg/m^3
Heat capacity	c_p	1200 J/kg/m^3
Equation of state type		ANEOS for dunite (also stands for hydrodynamic models)
Poisson ratio		0.25
Strength Model		Rock
(iSALE parameters)		(Y_{i0} = 10 MPa, μ_i = 1.2, Y_{im} = 3.5 GPa)
Acoustic Fluidization Model		Block
(iSALE parameters)		(t_{off} = 16 s, c_{vib} = 0.1 m/s, vib_{max} = 200 m/s)
Damage Model		[Ivanov et al., 1997]
(iSALE parameters)		($\varepsilon_{fb} = 10^{-4}$, $B = 10^{-11}$, $P_c = 3 \times 10^8$ Pa)
Thermal softening model		[Ohnaka, 1995]
(iSALE parameters)	ξ	1.2
	T_m	1375 K [Davison, 2010]
Low density weakening and porosity models		None
Core properties (Iron)		(Thompson, 1990)
		All models
Initial density	ρ_c	7840 kg/m^3
Heat capacity	c_p	800 J/kg/m^3
Equation of state type		ANEOS for iron
Damage, low density weakening thermal softening and porosity models		None

Table 2
Typical numerical parameter values for numerical hydrocode models.

Horizontal cells	2000
Vertical cells	4000
Grid spacing	2 km
Cells per projectile radius (CPPR)	
Impactor	25 (*for* $R_{imp} = 50$ *km*) to 100 (*for* $R_{imp} = 200$ *km*)
Target mantle	1700
Target core	850
Maximum time step (dt_{max})	0.05 s

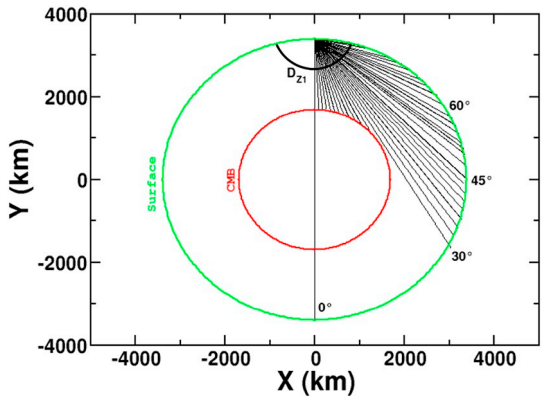

Fig. 2. The rays along which the shock pressure is monitored. The different rays illustrated here with thin solid lines correspond to different values of β ranging between 0° (vertical) and 80°. The black thick line at D_{Z1} represents the boundary between zones 1 and 2 (in this figure, the boundary is placed arbitrarily). Between the impact site and D_{Z1}, the pressure decreases exponentially while beyond D_{Z1}, the pressure decrease follows a power law (see Section 2.3). The numbers 30, 45, and 60 show the β values in degrees.

numerical method to extract the shock pressure and temperature at a fixed position from all our simulations. As a consequence, instead of using tracers, the impact-induced pressure and temperature fields are extracted from a cell-centered Eulerian grid points [Monteux and Arkani-Hamed, 2016]. Hence, the distance D corresponds to the straight-line distance between the impact site and the grid point where the peak pressure is located. It approximates the distance along a shock ray (see the Discussion section). Hence, we refer to the straight line as the ray from now on. We also investigate the effects of the angle β of the straight line, i.e., the so called ray, relative to the symmetric axis (Fig. 2). We emphasize that a ray does not enter the core when the ray angle β is larger than 30° in our model planet.

2.2. The reference models

Fig. 3 (left) shows the peak shock pressure distribution along the axis of symmetry ($\beta = 0°$) in a model with $R_{imp} = 50$ km and $V_{imp} = 10$ km/s. From Fig. 3, we can identify 2 zones of particular interest: Zone 1 where the peak shock pressure P_{Z1} decreases exponentially with the distance from the impact site, and Zone 2 where the peak shock pressure P_{Z2} still decreases significantly though less rapidly with the distance. As we will see later, these 2 zones are particularly distinguishable for small values of R_{imp}. Considering $V_{imp} = 10$ km/s is the average asteroid impact velocity on Mars [Bottke et al., 1994], we will define the case with $R_{imp} = 50$ km and $V_{imp} = 10$ km/s as our reference model. Fig. 3 (right) illustrates that considering a differentiated impactor (with a dunitic mantle and a liquid iron core) slightly increases the peak shock pressure magnitude during the propagation of the shockwave within the impacted planet because of the different mass repartition in the impactor. However, considering a differentiated impactor affects neither the pressure decay in 2 zones nor the position of the limit between the two zones.

The shock wave generated by an impactor propagates toward the center of the planet, while the shock pressure decays as the wave deposits energy in the form of irreversible work into the target [Ahrens and O'Keefe, 1987]. Hence, the ability of the impacted material to deform when experiencing large shock pressure is of the first importance for the characterization of the peak shock pressure evolution. Fig. 3 illustrates the influence of the mantle rheology on the shock wave propagation. The peak shock pressure experienced within the mantle decreases more rapidly in the model with strength than in the hydrodynamic model. In our models, the acoustic fluidization and the damage play minor roles on the shockwave propagation compared to that of the strength, because the lithostatic pressure is too high to allow fracturing of rocks.

If strength is present, shock waves attenuate faster because the rarefaction waves travel faster in material with strength and, therefore, cause a more rapid decay behavior [Curran et al., 1977; Bierhaus et al., 2013]. We note that the speed of sound in a strength-less material is given by $c = \sqrt{K/\rho}$ where K is the bulk modulus and ρ the density. If the material has some strength, the longitudinal wave speed is determined by $c_L = \sqrt{(K + 4/3\mu)/\rho}$ where μ is the shear modulus. Because $c_L > c$, the speed of the first, direct wave is larger when the strength is accounted for than in the hydrodynamic case, hence the shock waves attenuate faster in the models with strength [Curran et al., 1977; Bierhaus et al., 2013]. Ultimately, if the speed of the rarefaction wave depends on strength, then differences in strength should result in different attenuation behaviors. However this point is beyond the scope of our study. Outside Zone 1, the peak shock pressure continues to decrease with distance from the impact site and both models show a similar behavior: a power-law decrease followed by a pressure jump at the CMB. The more moderate decay in Zone 2 might be the consequence of a solid-state phase transformation that is considered in the ANEOS for dunite [Collins and Melosh, 2014]. This process does not occur in the hydrodynamic models, because the shock pressure does not drop below the critical pressure.

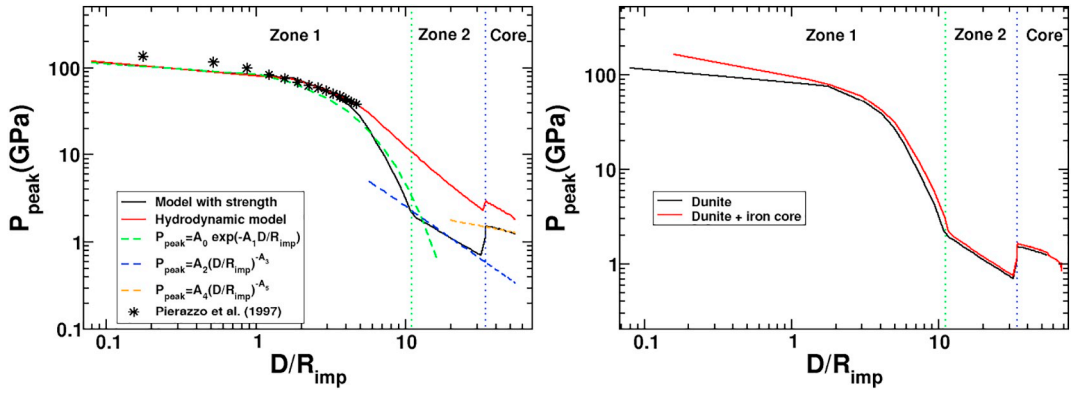

Fig. 3. Left: Shock pressure along the axis of symmetry ($\beta = 0°$) as a function of the distance from the impact site. In this (reference) case, $R_{imp} = 50$ km and $V_{imp} = 10$ km/s. The green, blue and orange dashed lines represent the fits obtained using Eqs. (1a), (1b) and (1c) respectively. Black stars represent the results from Pierazzo et al. [1997] for $V_{imp} = 10$ km/s and R_{imp} ranging between 0.4 and 10 km. Right: Same case as left panel (Model with strength) considering a dunitic (black solid line) impactor and a differentiated impactor with a 24 km core radius (red solid line). (For interpretation of the references to colour in this figure legend, the reader is referred to the web version of this article.)

Included in Fig. 3 are the results from Pierazzo et al. [1997] for $V_{imp} = 10$ km/s and R_{imp} ranging between 0.4 and 10 km, where the strength was not included. Our results for the hydrodynamic model, and the results from Pierazzo are in good agreement (Fig. 3). The small differences between our results and the results from Pierazzo et al. [1997] are plausibly the direct consequence of using different cppr values (for $R_{imp} = 50$ km, cppr = 25 while cppr = 20 for Pierazzo et al., 1997). Fig. 3 illustrates that accounting for strength significantly reduces the intensity of the shock pressure. This indicates that building more sophisticated models is necessary to estimate the shock pressure evolution after a large impact, as suggested by Monteux and Arkani-Hamed [2016].

For large impacts, the thermal softening is an efficient process that may influence the shockwave propagation. Indeed, accounting for thermal softening changes the strength and, thus, the speed of the rarefaction wave, which may result in a different attenuation behavior. This process strongly depends on the pre-shocked temperature profile that is still poorly constrained during the early evolution of terrestrial planets. To illustrate the influence of the thermal softening, we have run two models with different pre-impact spherically symmetric temperature distributions, characterized by a cold boundary layer at the surface overlying a convective-type, adiabatic temperature within the mantle. The difference between these two models is the surface temperature that is 293 K for the cold case and 500 K for the hot case. Fig. 4 shows that the thermal softening (as damage and acoustic fluidization) plays a minor role on the shockwave attenuation after a large impact. Accounting for thermal softening leads to a peak shock pressure decrease in Zone 1 and to an increase of the depth of Zone 1-Zone 2 transition. An initially hotter mantle only slightly enhances these 2 effects.

2.3. Scaling Laws

We have slightly modified the procedure by Monteux and Arkani-Hamed [2016]. By combining their near field and midfield, we reduce the number of parameters and make it easy to adopt the scaling laws in the impact heating of a terrestrial proto-plant during its accretion. We determine new scaling laws of shock pressure P for deriving universal scaling laws. From Fig. 3, we have identified 2 zones of particular interest: Zone 1 (associated to a peak shock pressure P_{Z1}) and Zone 2 (associated to a peak shock pressure P_{Z2}). This dichotomy is particularly pronounced in the models with strength.

We suggest two distinct scaling laws along the axis of symmetry to characterize the peak shock pressure in the model planet:

$$P_{Z1} = A_0 \exp(-A_1 D/R_{imp}) \quad (1a)$$

$$P_{Z2} = A_2 (D/R_{imp})^{-A_3} \quad (1b)$$

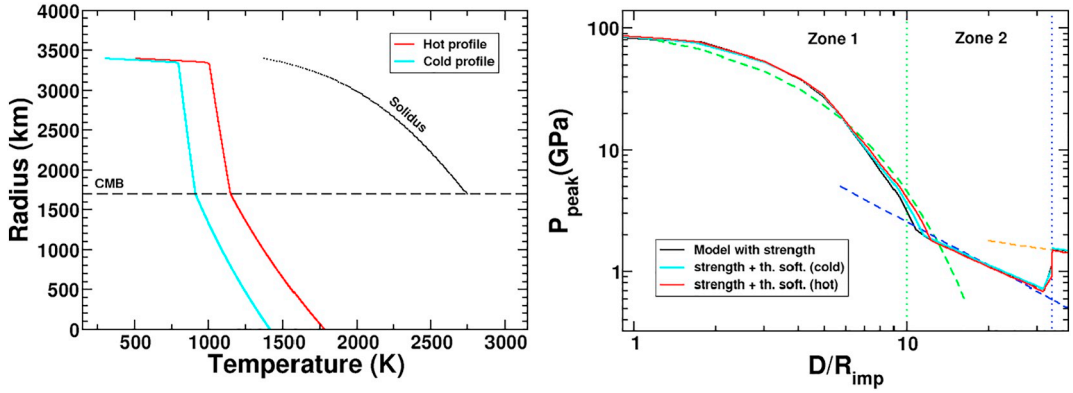

Fig. 4. Left: Pre-impact temperature profiles and solidus used for models including thermal softening. The cyan line represents the "cold" profile with a pre-impact surface temperature of 273 K while the red line represents the "hot" profile with a pre-impact surface temperature of 500 K. Right: Shock pressure along the axis of symmetry ($\beta = 0°$) as a function of the distance from the impact site. The black line represents the reference case (same as Fig. 3 for model with strength, $R_{imp} = 50$ km and $V_{imp} = 10$ km/s). The cyan and red lines represent the shock pressure decay for the models accounting for thermal softening considering the "cold" and the "hot" pre-impact temperature profile respectively illustrated on the left figure. The green, blue and orange dashed lines represent the fits obtained using Eq. (1a), 1b and 1c respectively. (For interpretation of the references to colour in this figure legend, the reader is referred to the web version of this article.)

where D is the distance from the impact site, R_{imp} is the impactor radius. A_0 is the maximum shock pressure and A_1, A_2, and A_3 are constant obtained by fitting the results from the hydrocode models. All these parameters are impact velocity and impactor radius dependent. They also depend on the ray angle β. Zone 1 corresponds to a hemisphere centered at the impact site with radius D_{Z1}. Zone 2 corresponds to the mantle shell beyond D_{Z1}. Zone 2 lies between D_{Z1} and the CMB for the ray angle $\beta < 30^{\circ}$. The zone is limited by the surface of the impacted planet for $\beta > 30^{\circ}$ (see Fig. 2).

The scaling law used to fit the peak shock pressure decay within Zone 1 is different from the classical power-law that usually uses other empirical or semi-empirical relations in impact studies [e.g. Ahrens et al., 1977]. However it has two advantages: 1) with this formalism the peak shock pressure does not go to infinity as D/R_{imp} goes to 0 compared to other power law forms [e.g., Ruedas, 2017], and 2) the peak shock pressure decays relatively slowly for $D/R_{imp} < 3$–4, which includes the "isobaric core" with slowly decaying shock pressure and the "pressure decay regime" regions proposed by Pierazzo et al. [1997]. On the other hand, the Zone 2 represents the far field region in the mantle where the shock pressure decays monotonically with distance from the impact site.

As the shock wave propagates in the mantle it creates a high pressure behind the shock front, which is determined on the basis of the Hugoniot equations. When the shockwave crosses the CMB, the peak shock pressure jumps from P_m (immediately above the CMB) to P_c (immediately below the CMB) because of the abrupt changes in the physical parameters, as previously identified [e.g., Ivanov et al., 2010; Arkani-Hamed and Ivanov, 2014]. After this sudden increase, the peak shock pressure continues to decrease as the wave propagates inside the core, which is characterized by a separate scaling law:

$$P_{core} = A_4 \, (D/R_{imp})^{-A_5} \tag{1c}$$

where A_4 and A_5 are constants. Fitting the peak shock pressure from our numerical models along the ray paths shown in Fig. 2 enables us to fully characterize the pressure increase experienced within the martian mantle and core. We note that a vertical impact on a spherically symmetric planet adopted in this study artificially enhances the shock pressure along the axis of symmetry in the core, hence Eq. (1c) overestimate the pressure near the axis of symmetry, while such an effect does not occur in the mantle (see the Discussion section below). Eqs. (1a), (1b) and (1c) will be used to fit the results from both the models with strength and the hydrodynamic models. The values of the different coefficients resulting from the corresponding fits are provided in the following sections. We would like to emphasize here that these scaling laws are only empirical and can be implemented in large-scale mantle models [e.g. Monteux and Arkani-Hamed, 2014] or in accretionary models [e.g. Monteux et al., 2014]. These scaling laws are determined by least square fitting to the results from the iSALE hydrocode models.

2.4. Shock wave propagation in the mantle: effects of the ray angle

During an impact, the maximum shock pressure is experienced at the impact site on the surface. Then the impact energy dissipates as the shockwave propagates within the model planet. Fig. 5 shows that the maximum shock pressure A_0, in either the models with strength or the hydodynamic models, increases with the impact velocity and the impactor radius. The peak shock pressure is nearly constant within an almost hemispheric region of a radius 1–2 times the impactor radius, centered at the impact site (see Fig. 3), which is coined as "isobaric core" by Pierazzo et al. [1997]. We note that A_0 is the shock pressure at the impact site and it remains the same for all of the ray angles considered. It is used in our scaling law (Eq. (1a)) to obtain the A_1 values from our models (Fig. 6). Fig. 5 shows the maximum shock pressure predicted from the planar impact model [Melosh, 1989]. As detailed by Osinski and Pierazzo [2012], the planar impact approximation yields an upper limit of the pressure expected during an impact event. Hence, it is not surprising that our A_0 values are slightly smaller than the results from the planar impact approximation.

Previous studies [Pierazzo et al., 1997; Monteux and Arkani-Hamed, 2016] monitored the influence of the ray angle β of the shock wave, and found no significant angle dependence in their results for β ranging between 0° (vertical) and 45°. Here we extend the investigation to β values up to 80°. A_1 is the exponential factor (Eq. (1a)), characterizing the ability of the upper mantle to attenuate the shockwave as it propagates. For large A_1 values, the peak shock pressure decreases rapidly with distance. Hence, higher A_1 values are expected for the models with strength than for the hydrodynamic models. In Fig. 6a and b, we present the A_1 values obtained by fitting the results from iSALE models to Eq. (1a) along different ray angles illustrated in Fig. 2. A_1 increases as a function of β, indicating that the peak shock pressure decreases more efficiently with distance at large ray angles. This behavior is common to both models with strength and hydrodynamics models. However, the increase is not significant for β values smaller than 45°, as also mentioned by Pierazzo et al. [1997]. We note that the rays impinging the core mantle boundary have β values smaller than 30°, indicating that propagation of shock waves inside the core is almost independent of the β values. Fig. 6a shows that A_1 is weakly affected by the impactor size for the range of impactors used in our study (i.e. 50 < Rimp < 200 km). For larger impactors (not studied here), one can expect an influence of the impacted protoplanet curvature on the shockwave propagation. However, Fig. 6b shows that A_1 is more sensitive to the impact velocity. Pierazzo et al. [1997] showed that the power-law exponent used to fit the angle dependency (for β ranging between 0° and 45°) was increasing with the velocity. From our results (for β ranging between 0° and 80°) it is difficult to extract such a tendency.

For the large ray angles, the path followed by the shockwave is shallower (Fig. 2). The shock wave propagating through shallower regions will cross material where the pressure and the uncompressed target density are smaller in average compared to shock wave propagating along the axis of symmetry. As a consequence, along small ray angle paths, the deformation is more difficult than along large ray angle paths. In addition, in shallower regions a significant part of the impact energy is dissipated during processes such as the excavation or the post-impact rebound. Finally, the interference of the direct pressure wave with the rarefaction wave that is reflected at the surface reduces the amplitude of the shock pressure [Melosh, 1989; Arkani-Hamed, 2005; Louzada and Stewart, 2009]. The consequence of these factors is that the isobaric surfaces are slightly elliptical with vertical major axis rather than spherical.

As previously mentioned, the shock wave decay rate with distance should be more rapid for the model with strength compared to the hydrodynamic models (as illustrated in Fig. 3). Fig. 6a and b confirm this point by showing that A_1 values are larger for models with strength than for hydrodynamic models for all β values. The correlation coefficients obtained by fitting our hydrocode data with the scaling laws from Eqs. (1a), (1b) and (1c) show that our choice is relevant. The correlation coefficients are close to 0.9 for all the range of impactor radii and impact velocities used in our models (except for $V_{imp} = 20$ km/s). The correlation coefficients are even higher for β values smaller than 65°. The correlation coefficients are also larger in the models with strength than in the hydrodynamic models because the dichotomy between Zone 1 and Zone 2 is more pronounced in the models with strength than in the hydrodynamic models (see Fig. 3).

In our study, the distance D from the impact site is normalized to the impactor radius R_{imp} to eliminate the dependence on the size of the projectile. Fig. 7 illustrates peak shock pressure profiles along a ray angle of $\beta = 36^{\circ}$ meaning that the ray does not cross the CMB (see Fig. 2). Fig. 7 shows that the boundary between Zone 1 and Zone 2 depends on both the impactor size and the impact velocity, hence the total pressure (shock plus lithostatic) through the Equation of State adopted in the hydrocode models. This suggests a relation between the

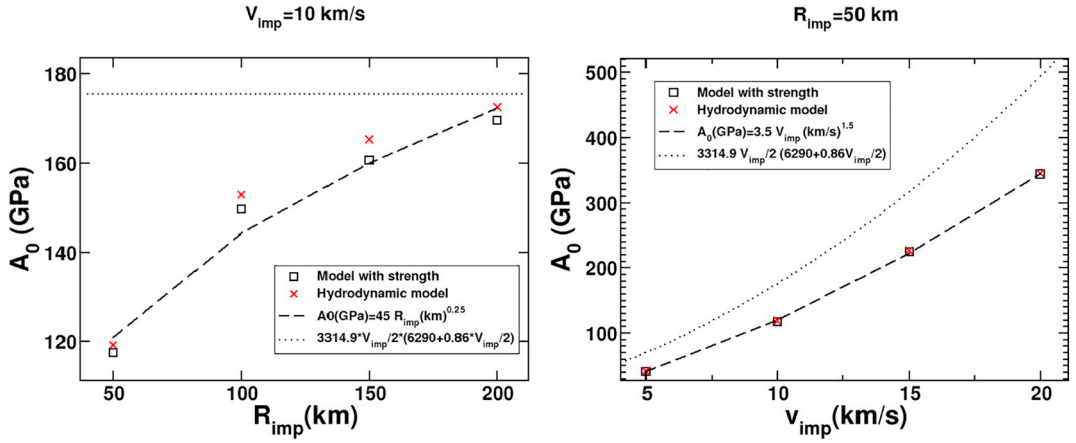

Fig. 5. The maximum peak shock pressure A_0 (Eq. (1a)) as a function of the impactor radius R_{imp} (left), and the impact velocity V_{imp} (right). The dotted lines represent the result from the planar impact approximation [Melosh, 1989] considering that both the impactor and the target are made of dunite (with $\rho_0 = 3314.9$, $C_0 = 6290$ m/s and $S = 0.86$ for both iSALE models and planar impact approximation).

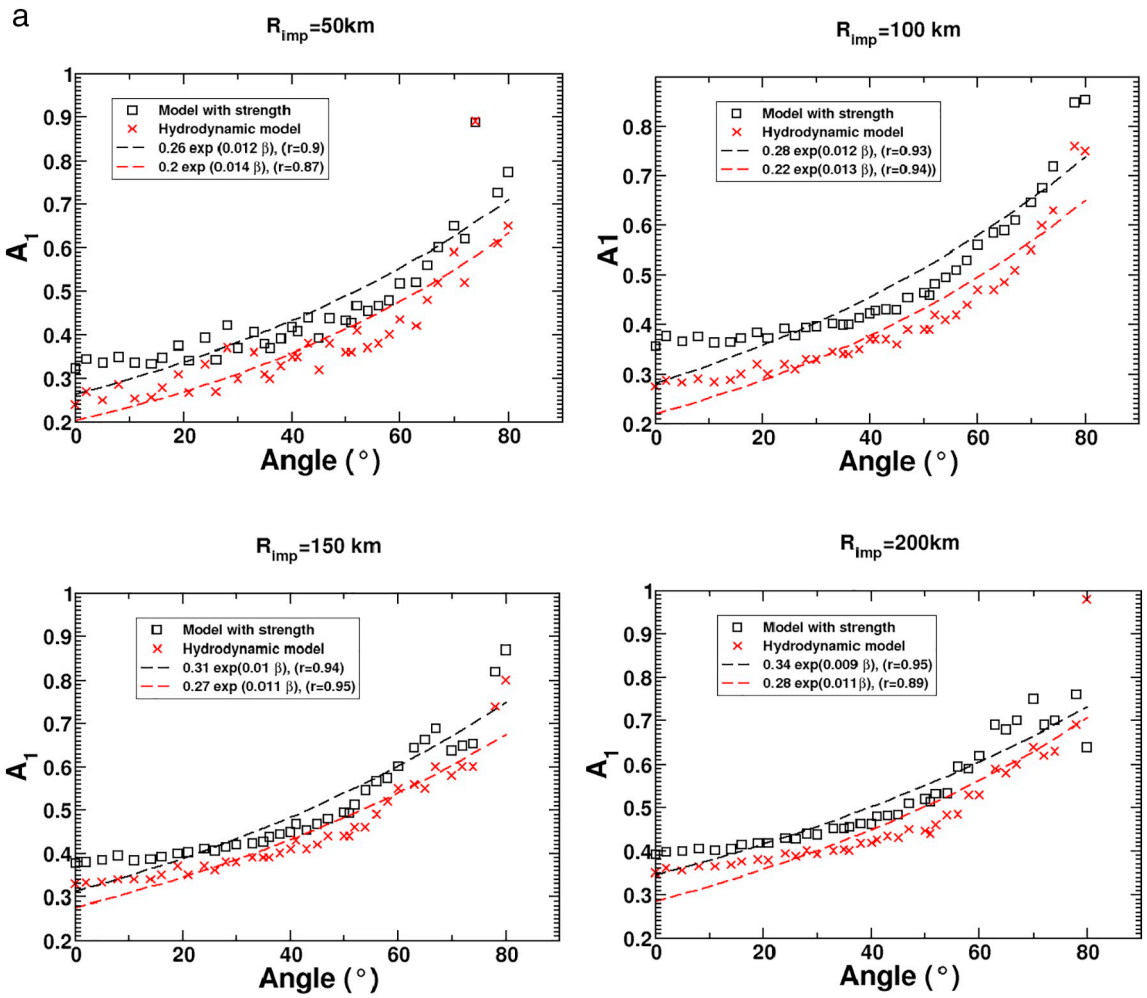

Fig. 6. a: A_1 as a function of the ray angle β (Eq. (1a): $P_{Z1} = A_0\, exp(-A_1\, D/R_{imp})$) for different impactor radii, but the same impact velocity ($V_{imp} = 10$ km/s). A_1 values are obtained by fitting the peak shock pressure in Zone 1 (close to the impact site) from iSALE models. The correlation coefficient (r), between the values obtained by the iSALE model and by the scaling law is mentioned in the legend box.
b: A_1 as a function of the ray angle β (Eq. (1a): $P_{Z1} = A_0\, exp(-A_1\, D/R_{imp})$) for different impact velocities ($R_{imp} = 50$ km). A_1 values are obtained by fitting the peak shock pressure in Zone 1 (close to the impact site) from iSALE models. The correlation coefficients (r), between the values obtained by the iSALE model and by the scaling law is mentioned in the legend box.

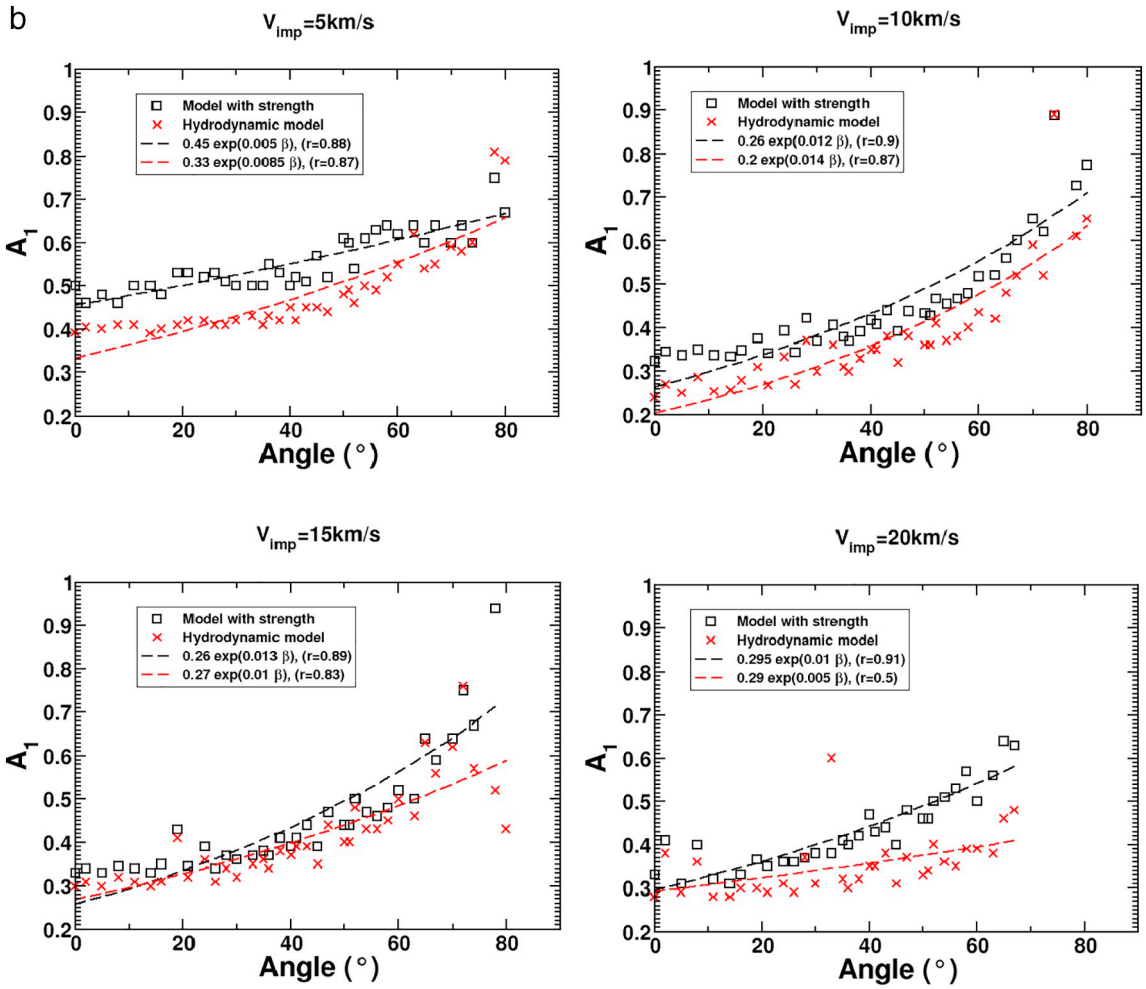

Fig. 6. (*continued*)

observed transition and a phase change in the Equation of State from our iSALE models. The Zone 1 - Zone 2 boundary occurs at a constant distance close to 10 times the radius of the impactor for the range of impactor sizes studied (Fig. 7, left). In the cases shown in Fig. 7, β is close to the critical value of 30° where the ray crosses the CMB (Fig. 2). As R_{imp} increases, the minimal value D/R_{imp} for which the shockwave crosses the CMB decreases from 34 (for R_{imp} = 50 km, black curve) to 8.5 (for R_{imp} = 200 km, blue curve). At this singular point (Fig. 7, left), a small jump of the peak pressure occurs because of the reflection of the shock waves with $\beta < 30°$ at the CMB. The ratio of the isobaric core radius to the projectile radius weakly depends on the impact velocity, as also concluded by Pierazzo et al. [1997]. For the range of impact velocities considered, the Zone 1 - Zone 2 boundary ranges between 7 and 15 times the radius of the impactor (Fig. 7, right). The small peak shock pressure jumps identified in Fig. 7 (left) for large impactors does not occur here because of the small, 50 km, impactor radius.

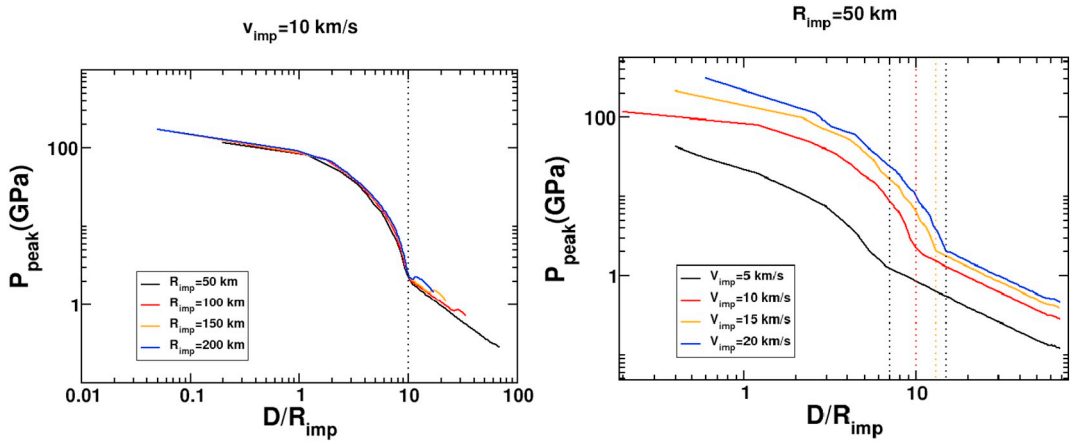

Fig. 7. Shock pressure along the ray angle $\beta = 36°$ as a function of the distance from the impact site for different impactor sizes with an impact velocity of 10 km/s (left) and different impact velocities for an impactor radius of 50 km (right). On the left panel, the vertical dotted line represents $D_{Z1} = 10\ R_{imp}$. On the right panel, the four vertical dotted lines represent different values of D_{Z1} corresponding to the different values of V_{imp}.

Once the shockwaves enter into Zone 2, the peak pressure continues to decrease. Fig. 8a and b show the dependency of A_2 on the ray angle (see Eq. (1b)). Because peak shock pressure decreases more rapidly with distance in the models with strength than in the hydrodynamic models (see Fig. 3), A_2 values are smaller in the models with strength than in the hydrodynamic models. Also, A_2 only slightly decreases with the ray angle β in both cases. For all impact velocities and impactor radii studied here, the A_2 values obtained from the models with strength are nearly constant up to the values of β close to 65°. For $\beta > 65°$, the data is more scattered (see Discussion at the end of the section). For the large impactor, $R_{imp} = 200$ km, the evolution of A_2 as a function of β is significantly different. This is probably due to the fact that, in that case, Zone 1 overlaps the CMB.

Fig. 9a and b show the relationship between A_3 (see Eq. (1b)) and the ray angle β. As for A_1, A_3 is smaller in the models with strength than in the hydrodynamic models. This feature is related to the higher shear strength in the models with strength, which consumes a portion of the impact energy to plastically deform the impacted material. Again, the more moderate decay in Zone 2 (i.e. smaller A_3 values) in models with strength compared to hydrodynamic models might be the consequence of a solid-state phase transformation that is considered in the ANEOS for dunite [Collins and Melosh, 2014]. Apart from this difference, both models behave similarly. Fig. 9a and b show that A_3 slightly increases with β up to $\beta \approx 65°$ indicating that the peak shock pressure decreases more efficiently with distance at large ray angles. From the results illustrated in Fig. 9b, the A_3 coefficient does not significantly depend on the impact velocity. However, Fig. 9a shows that the tendencies described earlier are completely different for $R_{imp} \geq 150$ km. Indeed, for large impactors, the size of Zone 2 is significantly reduced and the impacted hemisphere mainly consists of Zone 1 and the metallic core within the ray angle < 30°.

To illustrate the dependencies of A_1, A_2 and A_3 on β, we express them as $A_i = A_6 \exp(A_7 \beta)$ where i denotes 1, 2, or 3 (see legend boxes in the corresponding figures). Figs. 6, 8 and 9 show small values for A_7, typically ranging between 10^{-2} and 10^{-3}. This confirms that the shock wave propagation weakly depends on the ray angle that is ranging between 0° (vertical) and 45°, as already concluded by previous studies [Pierazzo et al., 1997; Monteux and Arkani-Hamed, 2016]. This can be extended for β up to 60° on the basis of Figs. 6, 8 and 9. For the hydrodynamic models the trend is similar although the iSALE data are more dispersed. Figs. 8 and 9 also show that for R_{imp} values larger than 150 km, the trend is less clear than for small impactors. As already mentioned, we attribute this feature to the overlap between Zone 1 and the CMB, which leads to the progressive disappearance of Zone 2 as R_{imp} increases. These differences are confirmed by the correlation coefficients that are larger for small impactors and are generally higher for

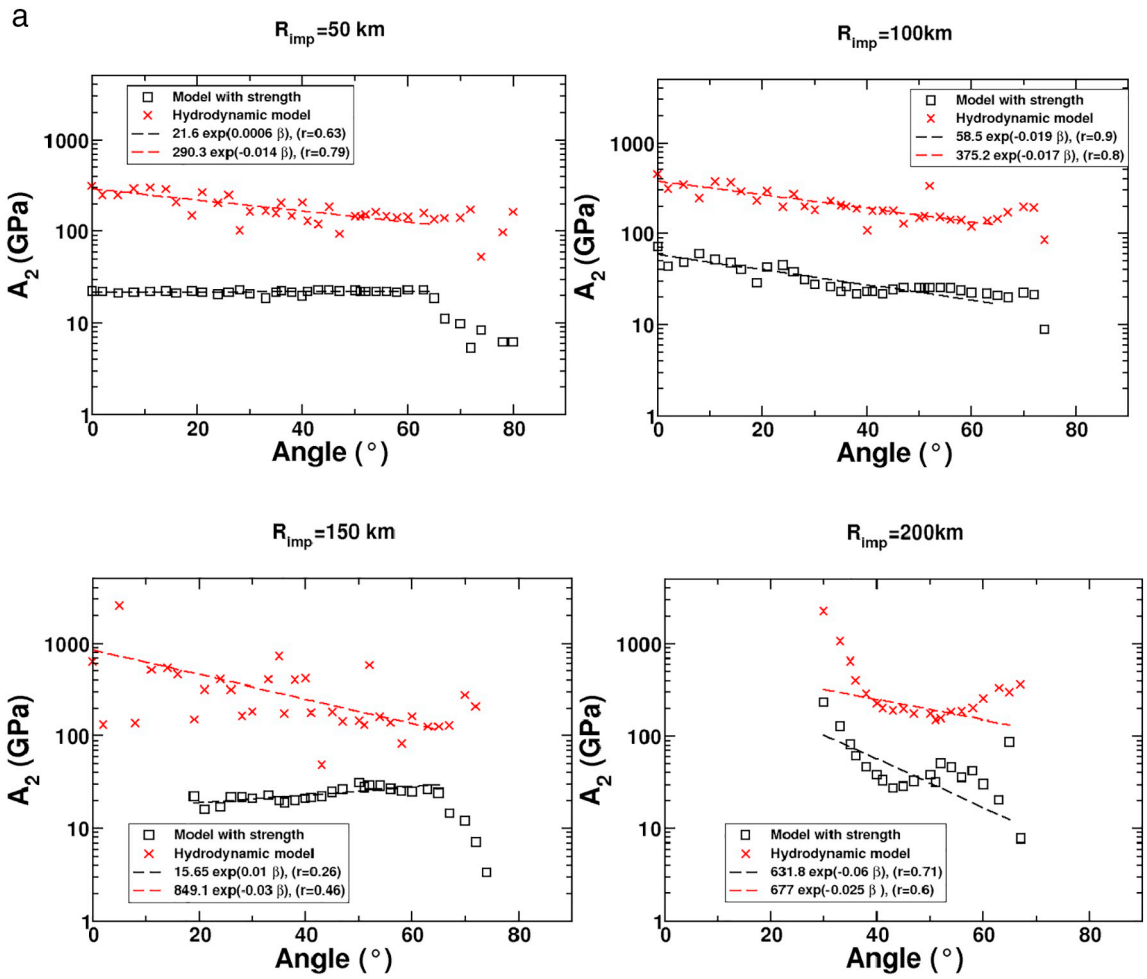

Fig. 8. a: A_2 as a function of the ray angle β (Eq. (1b): $P_{Z2} = A_2 (D/R_{imp})_3^A$) for different impactor radii, but an impact velocity of 10 km/s. A_2 values are obtained by fitting the shock pressure in Zone 2 (beyond D_{Z1}) from iSALE models. In these figures, $D_{Z1} = 10$. The correlation coefficient (r) for each scaling law is mentioned in the legend box (note that fits are restricted to $\beta \leq 65°$).
b: A_2 as a function of the ray angle β (Eq. (1b): $P_{Z2} = A_2 (D/R_{imp})_3^A$) for different impact velocities, but an impactor radius of 50 km. A_2 values are obtained by fitting the shock pressure in Zone 2 (beyond D_{Z1}) from iSALE models. In these figures, $D_{Z1} = 7$, 10, 13 and 15 for $V_{imp} = 5$, 10, 15 and 20 km/s respectively. The correlation coefficient (r) for each scaling law is mentioned in the legend box (note that fits are restricted to $\beta \leq 65°$).

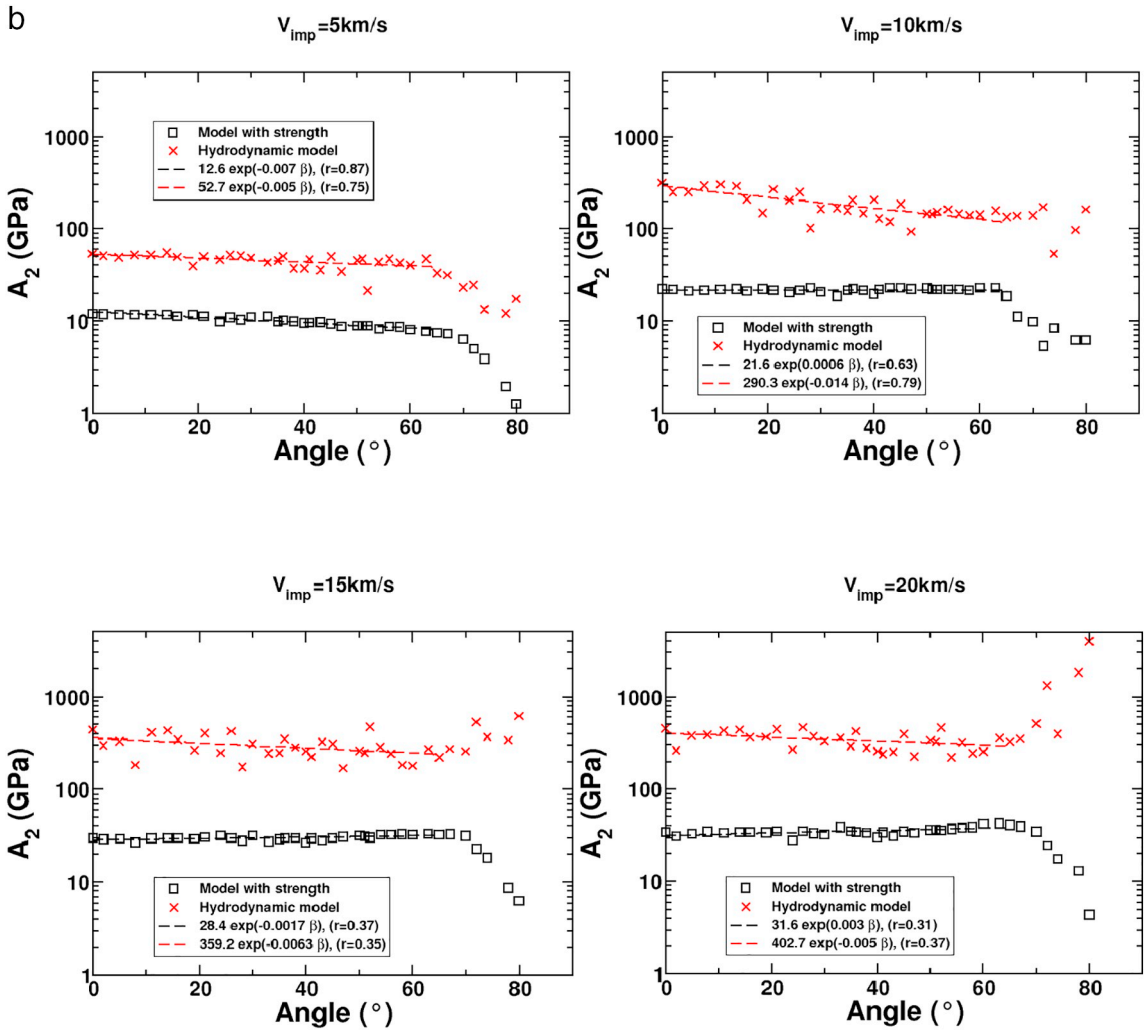

Fig. 8. (*continued*)

the models with strength than for the hydrodynamic models where the iSALE data is more dispersed.

Figs. 8 and 9 also exhibit a large variability for β values larger than 65°. For these large β values the shock waves propagate through shallower regions (see Fig. 2) where the total pressure is much smaller than that in the deep mantle. Moreover, in the shallowest region the largest initial impact is followed by multiple smaller impacts caused by ejecta fall back. Finally, the near surface region is also affected by the wave reflected at the surface that interferes with the direct wave and complicates the determination of the peak shock pressure [Melosh, 1989; Arkani-Hamed, 2005; Louzada and Stewart, 2009]. These 3 effects may explain the variability of the A_1, A_2, A_3 constants for large β values.

2.5. Effects of the CMB

The distinctly different physical properties of the mantle and the core have two major effects on the shock wave as it passes from the mantle to the core. The shock pressure increases abruptly as seen in Fig. 3, and a shock ray bends, obeying the Snell's law. Here we discuss each of these two effects.

Because the core radius is half the size of the impacted planet, the shock waves encounter the CMB only for β values smaller than 30 degrees (Fig. 2). Fig. 10 shows the ratio of the shock pressure immediately above the CMB, P_m, to that immediately below the CMB, P_c, in the impacted hemisphere. Both are calculated along a straight line determined by a ray angle and at the grid points of the hydrocode models immediately above and below the CMB, respectively. We note that P_m and P_c are actually the pressures slightly off the shock ray, hence are approximations to the actual pressures on the ray. A given shock ray bends toward the axis of symmetry as it crosses the CMB and the refraction angle determined through the Snell's law is smaller than the incident angle (see below). The bend is more pronounced at higher ray angles.

To connect the peak shock pressure between the mantle and the core we fit the ratio P_c/P_m as a function of the ray angle β with a quadratic expression for the models with strength:

$$P_c/P_m = b_1 + b_2\beta + b_3\beta^2 \quad (2a)$$

and a linear expression for the hydrodynamic models:

$$P_c/P_m = b_4 + b_5\beta \quad (2b)$$

where b_1, b_2, b_3, b_4 and b_5 are constant. The values of these constants for both models and as a function of R_{imp} and V_{imp} are listed in Table 3. The corresponding results are illustrated in Fig. 10a and b. We emphasize here that the Eqs. (2a) and (2b) used to fit the pressure jump as a function of the ray angle β are chosen empirically according to our results illustrated in Fig. 10 and b.

For all the impact velocities and impactor radii used in our models, the behavior is quite similar, although the shockwave that arrives at the CMB has much higher amplitude in the hydrodynamic case than in the models with strength (Fig. 3). Fig. 10 shows that the pressure jump at the CMB is more pronounced in the models with strength than in the

hydrodynamic models, regardless of the amplitude of the arriving shockwave. Because the pressure jump at the CMB is likely related to the amplitude of the arriving shockwave for a given model, our results emphasize the importance of the impacted material properties on the amplitude of the pressure jump.

For large impactors ($R_{imp} > 150$ km) and for β values smaller than 30°, we have shown that Zone 1 directly interferes with the impacted planet's core thus leading to a disappearance of Zone 2. Above this critical value of $\beta > 30°$, even if the direct shockwave does not cross the core (Fig. 2), one can expect that the transition from Zone 1 to Zone 2 would still be identified in our models. However, Fig. 8a (bottom panels) and Fig. 9a (bottom panels) also show a different behavior for large impactors for $\beta > 30°$. We attribute this phenomenon to the interaction of the direct shockwave with the core which produce a variety of diffracted and reflected shockwaves that affect the peak shock pressure far from the impact site and for $\beta > 30°$. As the shockwave behavior is completely different, our scaling laws for A_2, A_3 and P_c/P_m proposed in Eqs. (1b), (2a) and (2b) are less viable. The tendency for A_2 and A_3 is difficult to identify from our results (Figs. 8a and 9a (bottom panels)) and this complexity probably illustrate the complexity of the shockwave propagation far from the impact site.

The incident angle of a shock ray at the CMB increases from 0° to 90° as the ray angle β increases from 0° to 30°. The refraction angle of a given shock ray is determined on the basis of the Snell's law,

$$U_m/\sin\ \gamma_m = U_c/sin\ \gamma_c \quad (3)$$

where U_m and U_c are the shock wave velocities in the mantle and the core, γ_m is the incident angle, and γ_c is the refraction angle. U_m and U_c are determined from our numerical models (see the next section).

2.6. Shock wave propagation in the core

Fig. 11 shows the dependency of the coefficients A_4 and A_5 in Eq. (1c) on V_{imp} and R_{imp} determined along the axis of symmetry using the hydrocode models. A_4 shows a power-law behavior while A_5 shows almost linear dependency, especially those associated with the models with strength.

For a given ray angle β we calculate the incident and the refraction angles at CMB, hence the corresponding shock ray path in the core, assuming linear. The peak shock pressure decay along this ray path is determined from Eq. (1c), where D is the distance from the impact site to a point in the core measured along the ray path assuming that A_4 and A_5 are independent of the ray angle. Fig. 12 shows the distance of the peak shock pressure from the impact site in the impacted hemisphere of the mantle and the entire core versus the time since the impact. Table 4 lists the corresponding shock wave velocity in the mantle and the core.

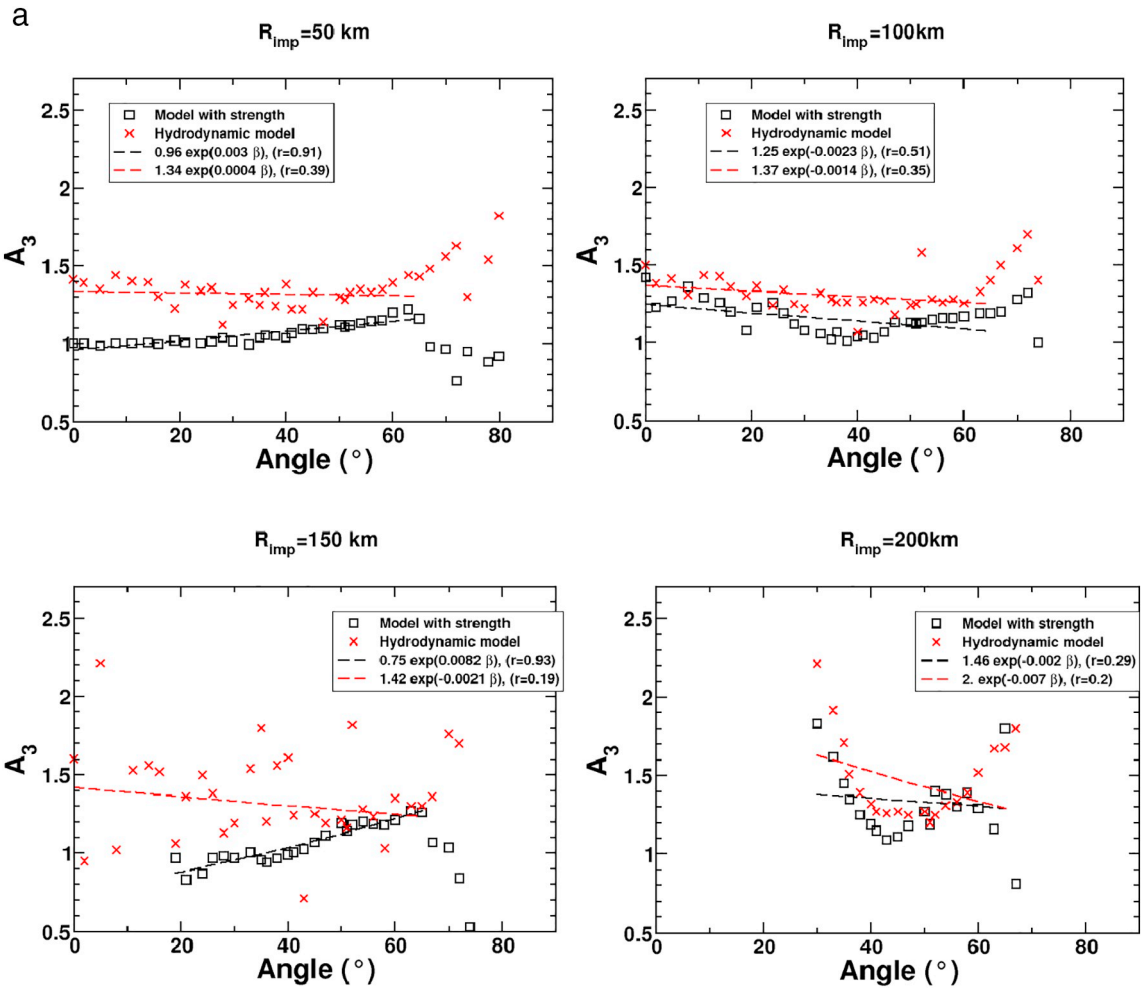

Fig. 9. a: A_3 as a function of the ray angle β (Eq. (1b): $P_{Z2} = A_2\ (D/R_{imp})^{A}_{3}$) for different impactor radii. A_3 values are obtained by fitting the shock pressure in Zone 2 (beyond D_{Z1}) from iSALE models. In these figures, $D_{Z1} = 10$. The correlation coefficient (r) for each scaling law is mentioned in the legend box (note that fits are restricted to $\beta \leq 65°$).
b: A_3 as a function of the ray angle β (Eq. (1b): $P_{Z2} = A_2\ (D/R_{imp})^{A}_{3}$) for different impact velocities. A_3 values are obtained by fitting the shock pressure in Zone 2 (beyond D_{Z1}) from iSALE models. In these figures, $D_{Z1} = 7$, 10, 13 and 15 for $V_{imp} = 5$, 10, 15 and 20 km/s respectively. The correlation coefficient (r) for each scaling law is mentioned in the legend box (note that fits are restricted to $\beta \leq 65°$).

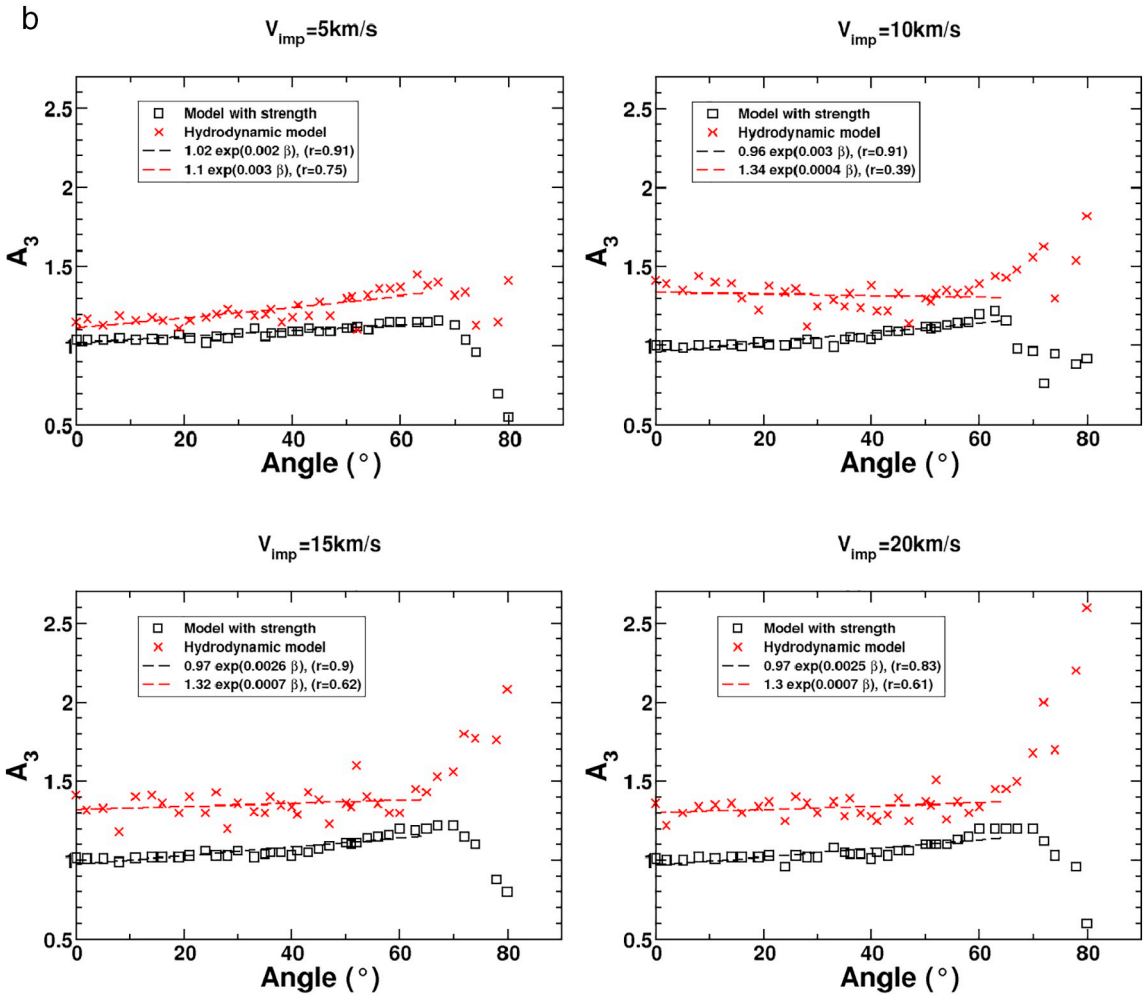

Fig. 9. (*continued*)

The shock wave velocities vary slightly among the models. More importantly, the velocity in the core is consistently lower than that in the mantle, indicating that the refracted ray angle is always smaller than the incident ray angle.

3. Comparison of the scaling law models with the iSALE models

Before implementing our scaling laws to the accretion of a planet it is required to compare the scaling law models with the iSALE models. Here we compare the hydrocode models and the models with strength to the corresponding models determined using our scaling laws for the impact velocity of 10 km/s and the impactor radius of 50 km (Fig. 13 a and b). In the scaling law models the refracted angles of the shock rays at the CMB are determined by the Snell's law. Hence, the shock pressure is not estimated in the equatorial region of the core where no refracted wave propagates. This results in the distinct lack of shock pressure in the equatorial part of the core and in the lower mantle beneath the shock ray that is tangent to the core mantle boundary. Several other features are not modeled by the scaling laws because we do not consider the reflection at the CMB and at the surface or the reflection and refraction at the antipodal CMB, which are included in solving the shock dynamic equation in the hydrocode models.

Fig. 13 (right panel) shows the relative difference between the two models. For the impacted hemisphere, the mean errors are 13% within the mantle and 14% within the core for the model with strength, and 10% within the mantle and 12% within the core for the hydrodynamic model. The fact that iSALE model combines both direct and indirect waves, while our model shows only the direct wave could contribute to the error between our scaling law parameterization and the iSALE data. The error pattern is similar in both the hydrodynamic and strength models. As mentioned above, the direct shock pressure within the core for β values larger than 30° is not determined by the scaling laws. The shock pressure of the hydrocode model in this region must be due to the secondary shock waves that are reflected at the surface and then refracted at the CMB. The scaling law models overestimate the peak shock pressure close to the impact site (Zone 1) where the error can locally reach 50%. However, despite the large peak shock pressure range in this region, our scaling laws provide a first order approximation to the hydrocode models.

An impact generates two compressional shockwaves, one propagates downward in the planet and the other propagates upward in the penetrating impactor. The latter reaches the top of the impactor, and reflects back and propagates downward as a rarefaction wave. The turbulence induced by the compressional wave in a given location inside the planet is diminished by the trailing rarefaction wave. This limits the thickness of the entire shock front with appreciable turbulence. The velocity of the rarefaction wave is higher than that of the original down going compressional wave, because the rarefaction wave propagates inside the penetrating impactor in the early times and then inside the planet that is already set in motion by the initially down going compressional wave. At a shock wave velocity of about 8 km/s, the passage of the entire shock front at a given location takes less than a minute for the largest impactor of 200 km considered in this study, and much shorter for other impactors. A given location in the mantle experiences more than one shock wave, such as the shock wave reflected at the surface and that reflected at the CMB. However, these shock

waves have low amplitudes because they travel longer distances than the direct wave and they arrive at much later times relative to the direct pressure wave. They rarely interfere with the direct wave except near the surface and near the CMB. In the case of the core, parts of the antipodal core is shocked twice, first by the direct wave that is refracted at the CMB of the impacted hemisphere beneath the impact site and second by the shock wave reflected at the CMB of the antipodal hemisphere. The first wave travels a shorter distance than the second one, hence passes a given location sooner than the arrival of the reflected wave. As in the case of the mantle, there is negligible interaction between these two waves, except for very close to the antipodal CMB. In general, a given location experiences multiple pressure increases due to the multiple reflected and refracted waves that travel through the planet's interior. However, the peak pressure is due to the direct shockwave.

4. Impact heating

During the decompression, a fraction of the energy is converted into heat [Bjorkman and Holsapple, 1987]. The temperature increase has been related to the shock pressure [e.g., Watters et al., 2009] as well as to the particle velocity [e.g., Gault and Heitowit, 1963]. The shock pressure in a given location diminishes within a time scale that is much shorter than the cooling timescale of the impact induced thermal anomaly. Although secondary shock waves lead to local pressure increase, the corresponding temperature increase is negligible compared to that of the direct shock wave. Here we only consider the direct shock heating in our estimation of the impact induced temperature increase.

The impact heating induced by the shockwave propagation is determined by implementing our scaling laws within the theoretical model proposed by Watters et al. [2009]

$$\Delta T(P_\delta) = \left(\frac{P_\delta}{2\rho_0 S}(1 - f^{-1}) - \left(\frac{C}{S}\right)^2 [f - \ln f - 1] \right) / c_p \tag{4}$$

$$f(P_\delta) = -\frac{P_\delta}{\beta}\left(1 - \sqrt{\frac{2P_\delta}{\beta} + 1}\right)^{-1} \tag{5}$$

$$\beta = \frac{C^2 \rho_0}{2S} \tag{6}$$

where P_δ is the shock-induced pressure, ρ_0 is the density prior to the shock compression and c_p is the heat capacity of the impacted material (see values in Table 1). The shock pressure implemented in Eqs. (4)–(6), is the shock-induced pressure predicted by our scaling laws (Eqs. (1a)–(1c) and (2a)–(2b)). Fig. 14 shows the temperature increase obtained using our scaling laws for both the hydrodynamic model and the

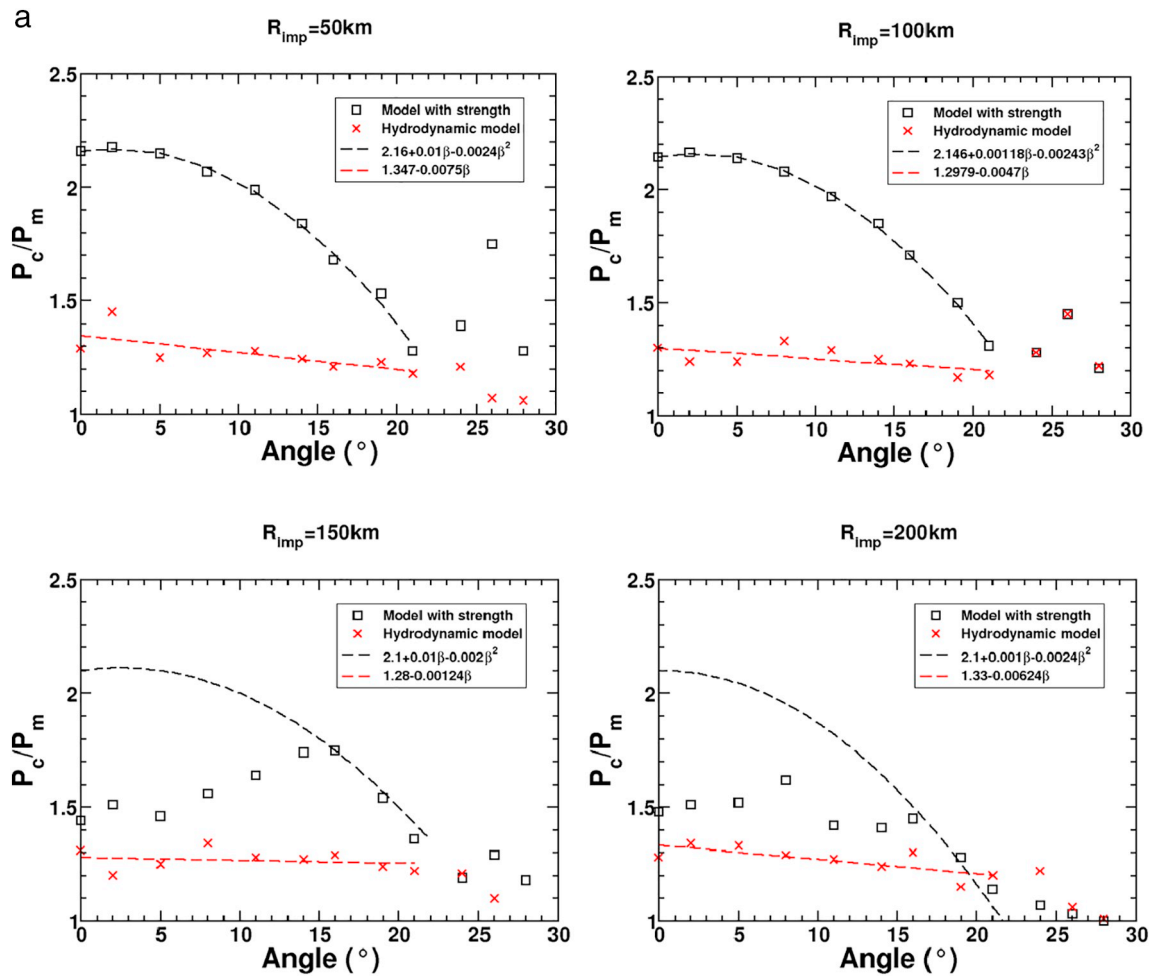

Fig. 10. a: Shock pressure jump P_c/P_m at the core mantle boundary as a function of the ray angle β for different impactor sizes, but a single impact velocity of 10 km/s. Data obtained from iSale models are shown with symbols while the analytical expression from Eq. (1c) is illustrated with dashed lines. For values of β larger than 30°, the rays do not cross the CMB.
b: Shock pressure jump P_c/P_m at the core mantle boundary as a function of the ray angle β for different impact velocities, but a single impactor radius of 50 km. Data obtained from iSale models are shown with symbols while the analytical expression from Eq. (1c) is illustrated with dashed lines. For values of β larger than 30°, the rays do not cross the CMB.

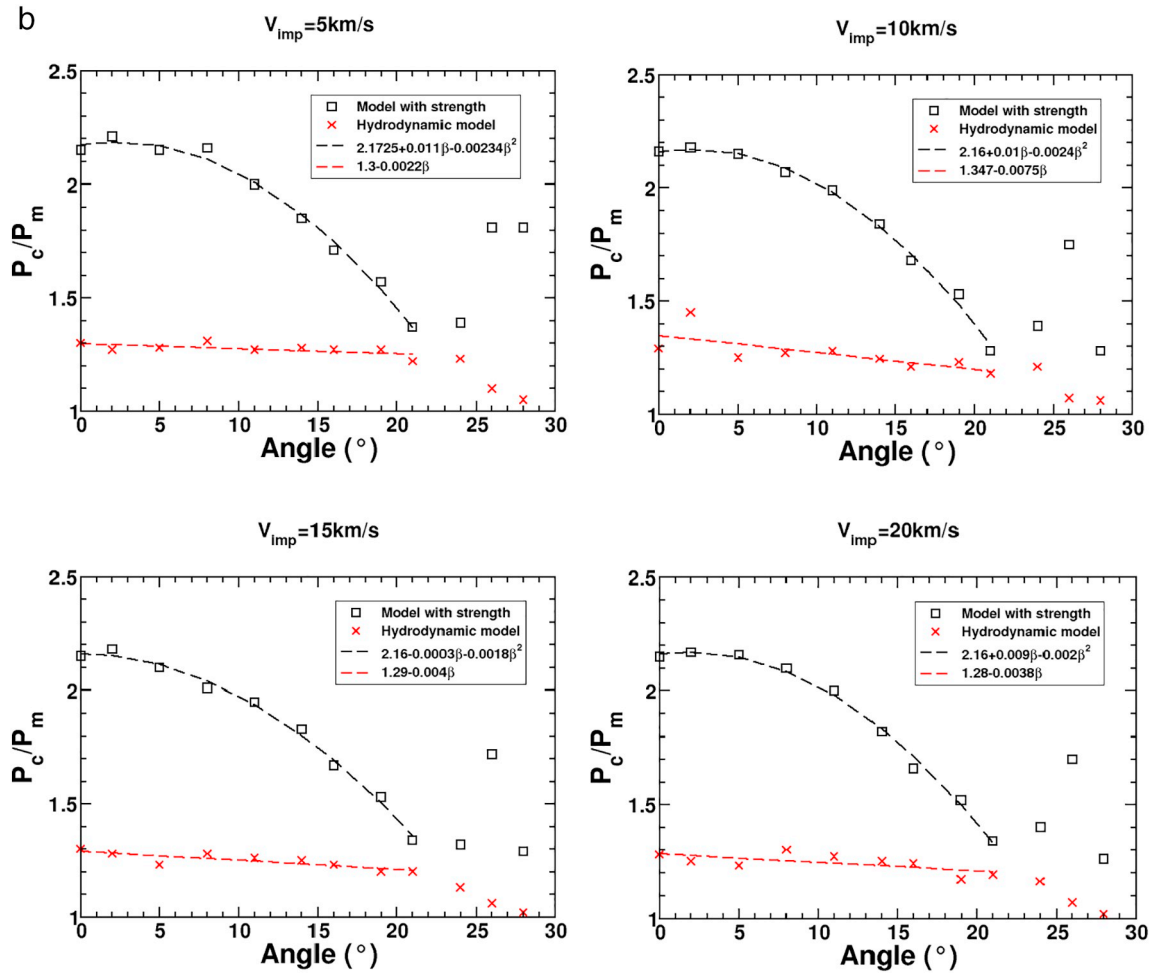

Fig. 10. (*continued*)

Table 3
Values of b_1, b_2, b_3, b_4 and b_5 obtained by fitting the results from the numerical models (Fig. 10a and b) with Eqs. (2a) and (2b). The values for models with strength are separated from those of hydrodynamic models with no strength and are shown as a function of R_{imp} and V_{imp}.

Models with strength	*b1*	*b2*	*b3*
R_{imp} = 50 km (V_{imp} = 10 km/s)	2.16	1×10^{-2}	-2.4×10^{-3}
R_{imp} = 100 km (V_{imp} = 10 km/s)	2.15	1.2×10^{-3}	-2.4×10^{-3}
R_{imp} = 150 km (V_{imp} = 10 km/s)	2.1	1×10^{-2}	-2×10^{-3}
R_{imp} = 200 km (V_{imp} = 10 km/s)	2.1	1×10^{-3}	-2.4×10^{-3}
V_{imp} = 5 km/s (R_{imp} = 50 km)	2.17	1.1×10^{-2}	-2.3×10^{-3}
V_{imp} = 10 km/s (R_{imp} = 50 km)	2.16	1×10^{-2}	-2.4×10^{-3}
V_{imp} = 15 km/s (R_{imp} = 50 km)	2.16	3×10^{-4}	-1.8×10^{-3}
V_{imp} = 20 km/s (R_{imp} = 50 km)	2.16	9×10^{-3}	$-2.$ x10^{-3}

Hydrodynamic models	*b4*	*b5*	
R_{imp} = 50 km (V_{imp} = 10 km/s)	1.35	-7.5×10^{-2}	–
R_{imp} = 100 km (V_{imp} = 10 km/s)	1.3	-4.7×10^{-3}	–
R_{imp} = 150 km (V_{imp} = 10 km/s)	1.28	-1.2×10^{-3}	–
R_{imp} = 200 km (V_{imp} = 10 km/s)	1.33	-6.2×10^{-3}	–
V_{imp} = 5 km/s (R_{imp} = 50 km)	1.3	-2.2×10^{-4}	–
V_{imp} = 10 km/s (R_{imp} = 50 km)	1.35	-7.5×10^{-2}	–
V_{imp} = 15 km/s (R_{imp} = 50 km)	1.29	-4×10^{-3}	–
V_{imp} = 20 km/s (R_{imp} = 50 km)	1.28	-3.8×10^{-3}	–

model with strength for V_{imp} = 10 km/s and R_{imp} = 50 km (top panels) and V_{imp} = 10 km/s and R_{imp} = 150 km (bottom panels). As mentioned before, the shock pressure is not estimated by the scaling laws where no refracted wave propagates (i.e. in the equatorial region of the core and the lower part of the mantle beneath the shock ray that is tangent to the CMB). Hence, we cannot estimate the post-impact temperature increase in these regions (illustrated by black areas in Fig. 14). This figure shows that for a 50 km radius impactor, the region with significant impact heating is localized in a small shallow volume. For a 150 km impactor, a larger fraction of the impacted mantle is affected. Below the impact site the temperature increase can reach ≈1900 K for both the hydrodynamic model and the model with strength. The largest temperature increase is localized in Zone 1 and the temperature increase in Zone 2 is weaker. The main difference between the two rheologies is the depth of the impact temperature increase, which is deeper in the hydrodynamic model than in the model with strength, because the pressure decay is more rapid in the model with strength (Fig. 6 a, bottom left panel). Moreover, the regions with increased temperature have shapes that are more prolate than spherical, because of the influence of the β angle on the pressure decay in Zone 1. The difference in the expression of the pressure decay between the two models as a function of β should lead to a difference in sphericity (Fig. 6 a). However, the difference is not significant in the cases illustrated in Fig. 14.

5. Discussion and conclusions

We have modeled the shock pressure distributions inside the impacted hemisphere of a differentiated Mars size planet using 2D axisymmetric hydrocode simulations (iSALE-2D) for vertical impacts with impact velocities of 5–20 km/s and impactor radii ranging from 50 to 200 km. From these hydrocode simulations, we have observed a distribution of the peak shock pressure within the impacted mantle and

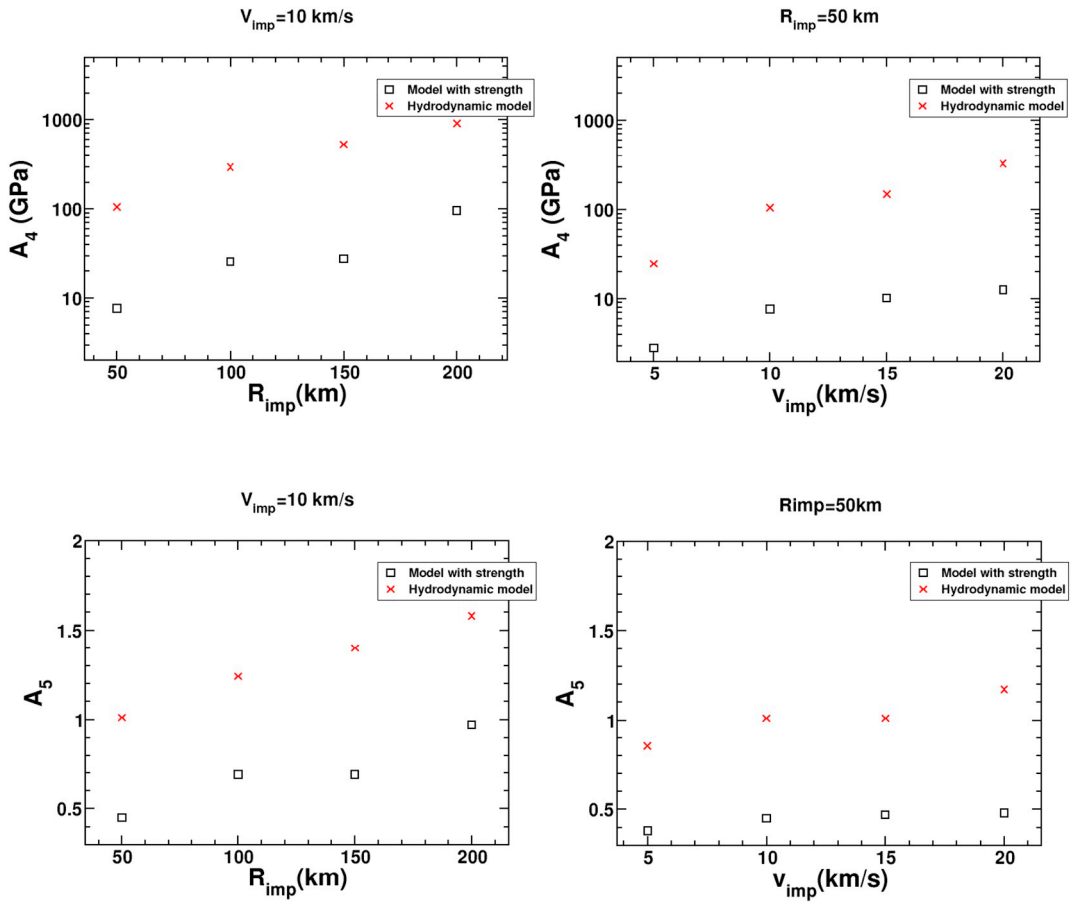

Fig. 11. A_4 and A_5 values (Eq. (1c): $P_{core} = A_4\ (D/R_{imp})^{-A_5}$) as functions of the impactor radius (left panels) and impact velocity (right panels).

proposed a mathematical formalism adapted to this distribution: a first zone (Zone 1) where the peak shock pressure decreases exponentially and a second zone (Zone 2) where the peak shock pressure decrease follows a power-law. With this formalism, the peak shock pressure does not go to infinity as D/R_{imp} goes to 0, and the peak shock pressure decays relatively slowly from the impact site to D/R_{imp} = 3–4, which includes the canonical "isobaric core" with slowly decaying shock pressure with distance from the impact site and the "pressure decay regime" region proposed by Pierazzo et al. [1997]. We have shown that the ray angle β has minor influence on the pressure decay pattern for $\beta < 65$–70°.

The most important contribution to the peak shock pressure distribution is related to the rheology of the material. Adopting a model where the impacted mantle is treated using models with strength can result in a significant decrease of the peak shock pressure compared to that of the hydrodynamic models. This difference in behavior occurs principally in the shallower zone (Zone 1) while in Zone 2 the behavior is similar in both models. We have shown that the peak shock pressure is about an order of magnitude smaller at the bottom of the Zone 1 in the models with strength compared to that in the hydrodynamic models.

The characteristic of the peak shock pressure in Zone 1 has important consequences on the peak shock pressure in Zone 2, since it determines the pressure in the upper part of Zone 2. Also, the mantle rheology affects the peak shock pressure at the CMB. We have combined our shock-pressure scaling laws with the formalism proposed by Watters et al. [2009] to determine the impact heating of a differentiated Mars model by a large impactor. Our results show that the mantle rheology governs the impact heating of a planet and the impact heating may be overestimated when the material strength is not accounted for.

The Martian rheology and its evolution since Mars formation are poorly constrained. However, the two models used in our study (hydrodynamic and with strength) enable us to cover a range of rheology models compatible with different stages of the Martian evolution. Our hydrodynamic models where the mantle is considered as an inviscid fluid may be an interesting proxy to characterize the impact heating during a magma ocean stage [Monteux et al., 2016]. On the other hand, our models with strength are more appropriate to characterize the large impact consequences within a solidified and cold Mars [Watters et al., 2009]. Our results show that the depth of the heated zone is different in the two cases (Fig. 14) with a larger thermal anomaly in the hydrodynamics models than in the models with strength as the pressure decay is more rapid in the latter case. In both cases, the shape of the impact-heated region is prolate because of the influence of β on the pressure decay. These effects need to be accounted for in accretionary models especially when about 3×10^5 planetesimals of ~100 km in diameter are needed to build a Mars size planet.

As illustrated in Fig. 13, our parameterized approach is associated to a mean error between our scaling laws and the direct results obtained by the iSALE models that ranges form 10 to 14% within the impacted hemisphere. As a consequence, the temperature increase derived from our scaling laws is also associated to this error range. Nonetheless, in the light of the incertitude that goes with our understanding of the early Solar System history and our knowledge of the effects of large impacts, our parameterized approach to calculate the temperature increase within a differentiated Mars-size protoplanet can be considered as a first order estimation.

As a consequence, the next step toward a better understanding of the early evolution of terrestrial planets is to implement more realistic rheological models in the hydrocode simulations. Such an effort would lead to more reliable scaling laws that could easily be implemented in accretion models to characterize the influence of large impacts on the

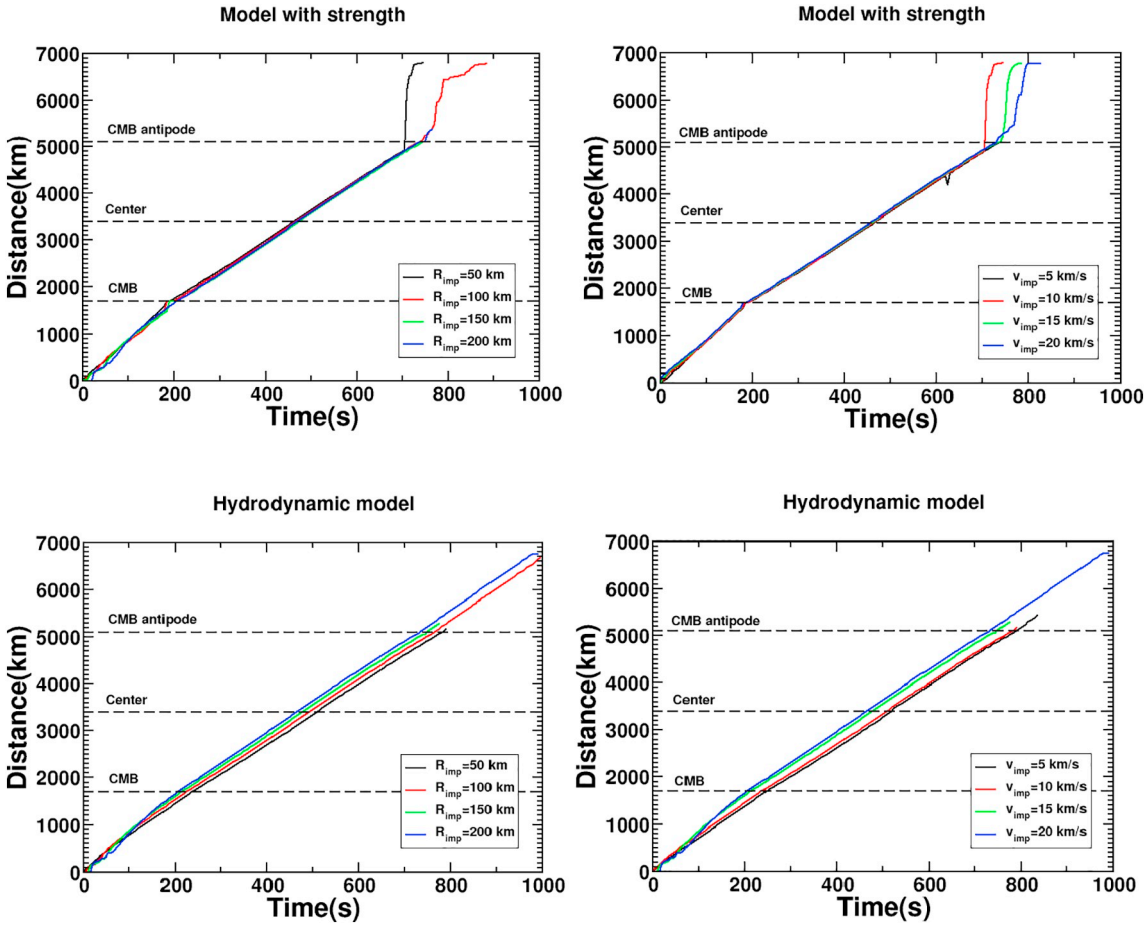

Fig. 12. Position of the peak shock pressure as a function of the time after the impact for the models with strength (top panels) and the hydrodynamic models (bottom panels).

Table 4
Velocity of the peak shock pressure propagation in the mantle and in the core for the models with strength and hydrodynamic models, obtained fitting the results from Fig. 12 with a linear expression.

	Target mantle	Target core
Models with strength		
R_{imp} = 50 km (V_{imp} = 10 km/s)	8.84 km/s	6.38 km/s
R_{imp} = 100 km (V_{imp} = 10 km/s)	8.52 km/s	6.44 km/s
R_{imp} = 150 km (V_{imp} = 10 km/s)	8.58 km/s	6.47 km/s
R_{imp} = 200 km (V_{imp} = 10 km/s)	8.93 km/s	6.50 km/s
V_{imp} = 5 km/s (R_{imp} = 50 km)	9.04 km/s	6.33 km/s
V_{imp} = 10 km/s (R_{imp} = 50 km)	8.84 km/s	6.38 km/s
V_{imp} = 15 km/s (R_{imp} = 50 km)	8.80 km/s	6.36 km/s
V_{imp} = 20 km/s (R_{imp} = 50 km)	8.60 km/s	6.38 km/s
Hydrodynamic models		
R_{imp} = 50 km (V_{imp} = 10 km/s)	6.96 km/s	6.36 km/s
R_{imp} = 100 km (V_{imp} = 10 km/s)	7.60 km/s	6.40 km/s
R_{imp} = 150 km (V_{imp} = 10 km/s)	8.33 km/s	6.46 km/s
R_{imp} = 200 km (V_{imp} = 10 km/s)	8.77 km/s	6.53 km/s
V_{imp} = 5 km/s (R_{imp} = 50 km)	6.76 km/s	6.41 km/s
V_{imp} = 10 km/s (R_{imp} = 50 km)	6.96 km/s	6.36 km/s
V_{imp} = 15 km/s (R_{imp} = 50 km)	8.33 km/s	6.46 km/s
V_{imp} = 20 km/s (R_{imp} = 50 km)	8.79 km/s	6.53 km/s

martian mantle dynamics [e.g. Roberts and Arkani-Hamed, 2012, 2017] or on other terrestrial planets [e.g. Roberts and Barnouin, 2012]. As large impacts are not isolated phenomena during the late regimes of planetary accretions, the scaling laws we have developed are suitable to be implemented in thermal evolution models that consider the accretion histories of growing planets [e.g. Monteux et al., 2014; Arkani-Hamed, 2017].

The followings are some shortcomings that require improvements of our scaling laws in the future to be better suited for shock waves travelling inside an actual planet, rather than the simple two-layered planet model where a uniform mantle overlies a uniform core.

- We have considered vertical impacts, whereas majority of impacts during the accretion of a planet is oblique. The peak shock pressure produced by an oblique impact along the vertical direction beneath the impact site depends on the sine of the impact angle relative to the local horizon (see Fig. 3 of Pierazzo and Melosh, 2000a, 2000b). This implies a shock pressure reduction by a factor of ~0.71 for the most probable impact angle of 45° [Shoemaker, 1962] compared to that of a vertical impact, assuming that all other parameters are equal. Moreover, a vertical impact on a spherically symmetric planet preserves the axial symmetry. Because the shock wave velocity in the core is smaller than that in the mantle, the axial symmetry results in the convergence of the refracted wave at the CMB of the impacted hemisphere toward the axis in the core, thus artificially increasing the shock pressure near the axis. However, the near axis enhancement of the shock pressure is negligible except very close to the antipodal CMB [Ivanov et al., 2010; Arkani-Hamed and Ivanov, 2014]. We also note that this artifact does not occur in the mantle because the shock rays are diverging away from the axis of symmetry. It is desirable to adopt oblique impacts in investigating the accretion of a planet. In an oblique impact, the axial symmetry is replaced by a plane symmetry, which avoids the convergence of the waves toward the axis in the expense of introducing more complex and computationally intensive three-dimensional (3D) calculations,

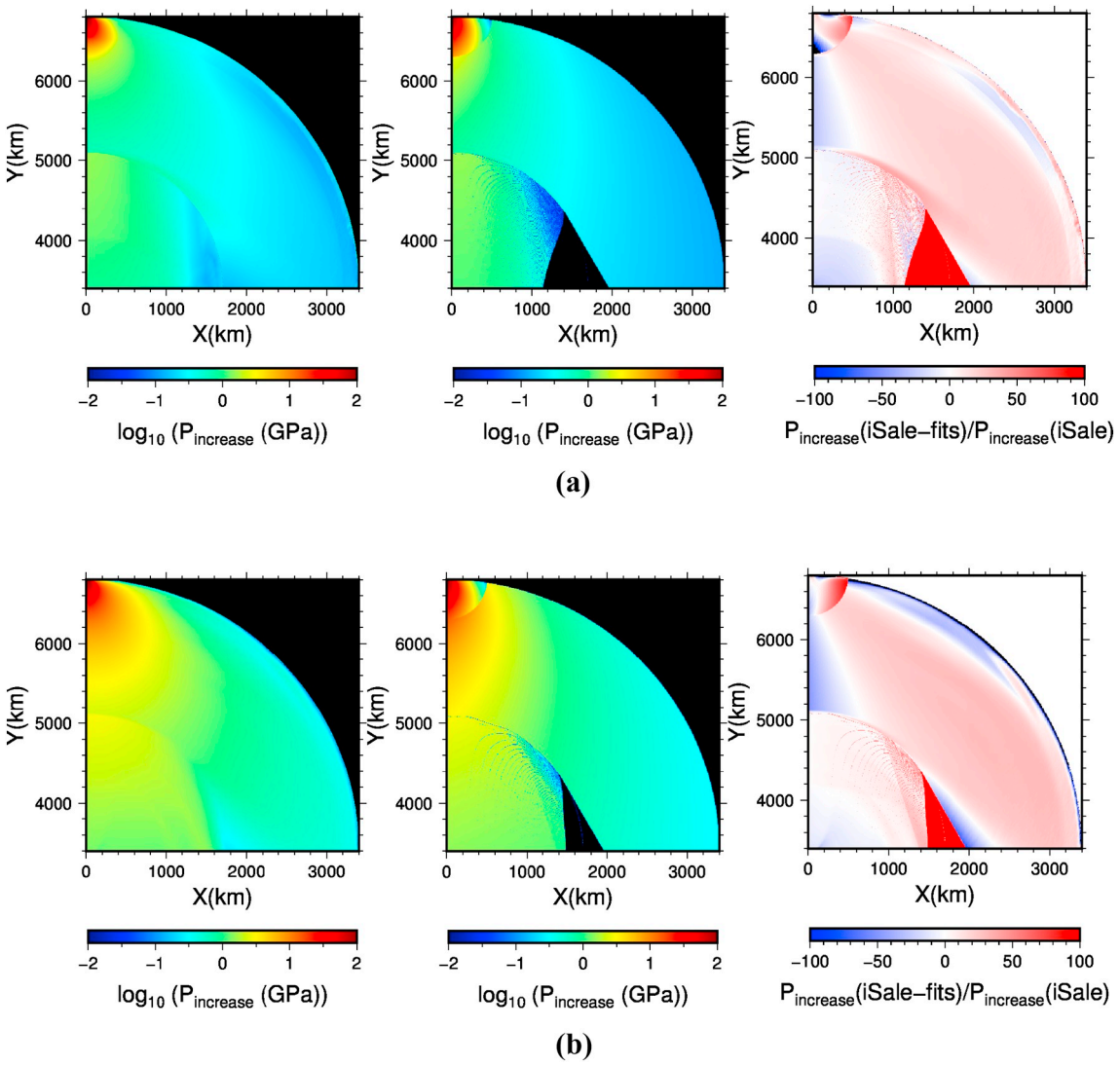

Fig. 13. Comparison of the maximum shock pressure experienced after an impact within a differentiated Mars size planet with R_{imp} = 50 km and V_{imp} = 10 km/s. (a) is for model with strength and (b) is for Hydrodynamic model. The left panel represents the result from the iSALE model and the middle panel represents the model obtained from our scaling laws (Eqs. (1a), (1b) and (1c)). The right panel shows the error relative to the iSALE model (in %). Note that only the impacted hemisphere is shown in this figure, because the scaling laws are derived for this hemisphere.

besides the substantial increase of the grid points in the computation domain.

- The distance travelled by a shock wave from the impact site to a given point in the planet is approximated by a straight line, D. In our simplified two-layered planet model with a uniform mantle overlying a uniform core, the first arrival shock wave travels in quiescent medium, hence the shock rays are straight lines until they interact with the core mantle boundary where they bend according to the Snell's law. Inside a real planet the rays are actually curved due to the pre-impact non-uniform density and temperature gradients in the interior of the planet. Because of the ray curvature a wave travels longer to reach an off axis location in the interior than D. Therefore, our model slightly over estimates the shock pressure experienced in that location. Moreover, because of the ray curvature an incident angle at the CMB and the corresponding refraction angle could be slightly different than those determined by the straight line approximation. However, the core radius is about one half of the planet radius, and the angle β is always smaller than 30°. Bearing in mind that the shock ray along the axis of symmetry is a straight line, the departure of the shock rays from the corresponding straight lines is negligible for these β values. As also mentioned above, the shock wave propagation weakly depends on the β angle that is ranging between 0° (vertical) and 45°, which is already concluded by previous studies [Pierazzo et al., 1997; Monteux and Arkani-Hamed, 2016]. More importantly, providing scaling laws along straight lines, rather than along shock rays, helps to easily determine the shock pressure in the entire region.

- We have considered only direct shock waves to determine our scaling laws. Because the laws are based on shock ray theory, they can be used to determine the pressure of secondary shock waves, such as those reflected at the surface and those reflected at the antipodal CMB of the core [Arkani-Hamed and Ivanov, 2014]. In general a reflect wave arriving at a location travels longer and is weaker than a direct wave. However, because of the zero pressure boundary condition at the surface the reflected wave is rarefaction and upon interference with the direct compressional wave effectively reduced the pressure experienced at a given location close to the surface [Melosh, 1989; Arkani-Hamed, 2005; Louzada and Stewart, 2009]. The interference of the direct and secondary waves is not considered in our present study.

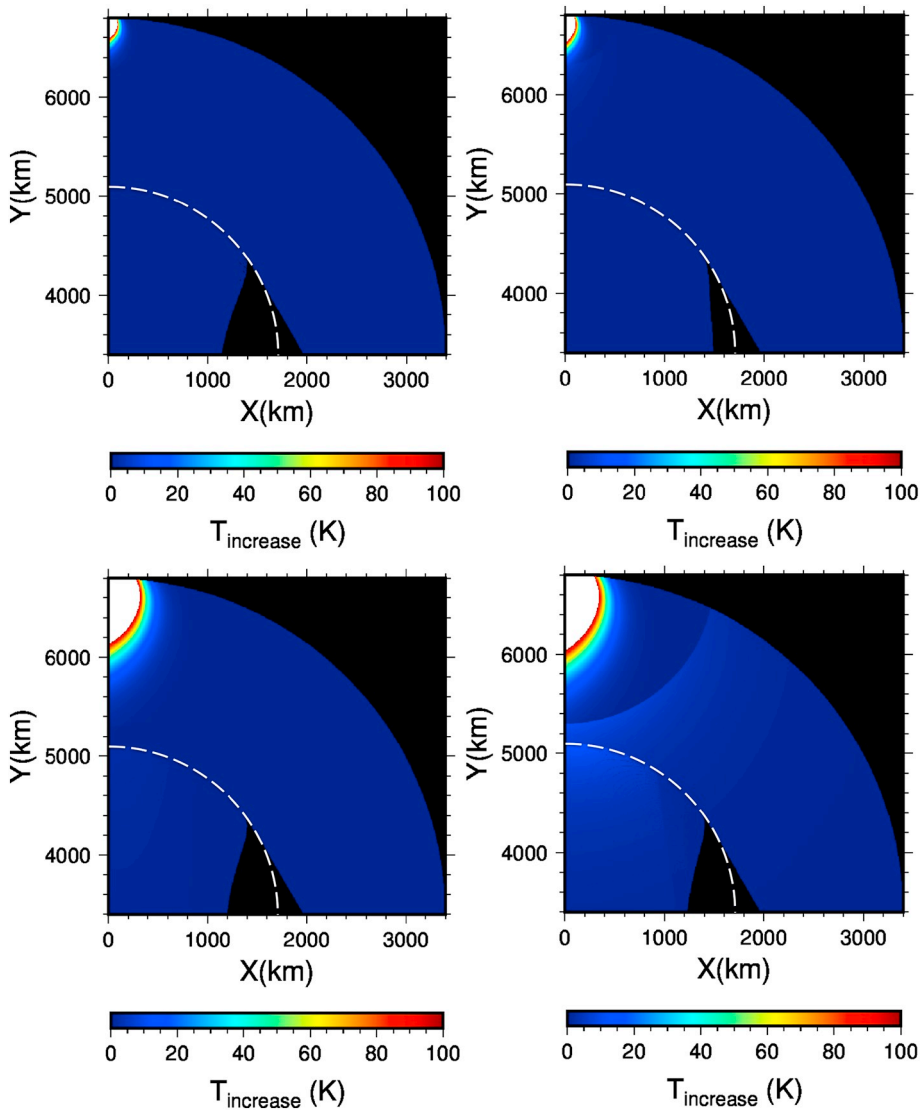

Fig. 14. Temperature increase after an impact within a differentiated Mars size planet. The first line: R_{imp} = 50 km and V_{imp} = 10 km/s, and the second line: R_{imp} = 150 km and V_{imp} = 10 km/s (Left: Model with strength, Right: Hydrodynamic model). All panels represents the model obtained from our scaling laws (Eqs. (1a), (1b) and (1c)) combined with the impact induced temperature increase model (Eqs. (4)–(6)) from Watters et al., (2009) (with C = 7.24 km/s, S = 1.25, $\rho = \rho_m$ for the mantle and C = 4 km/s, S = 1.6, $\rho = \rho_c$ for the core [Arkani-Hamed and Olson, 2010a, b]). The white dashed line represents the CMB.

- The size of the Zone 1 depends on the impactor size. For large impactors Zone 1 directly interferes with the core, and Zone 2 does not exist. For example, there is no Zone 2 for β values smaller than 15° when the impactor is larger than 150 km in radius. We propose the following procedure to estimate the shock pressure distribution inside the mantle and the core of a planet using our scaling laws. The impact-induced temperature increase may then be determined using, for example Watters et al. [2009] model.

- Consider a terrestrial planet with a radius R_p and a core radius R_c that is impacted by an impactor of radius R_{imp}. We assume that the Zone 1 is a hemisphere with a radius $R_1 = 10 \times R_{imp}$ centered at the impact site. There is no interaction of Zone 1 with the core for $R_1 < (R_p - R_c)$, and the equations provided in this paper are valid. This is also the case for any shock wave specified by a ray angle β when $\sin(\beta) > R_c/R_p$. For $R_1 > (R_p - R_c)$, Zone 1 may interact with the core. Because the shock wave velocity is greater than the particle velocity, it takes time for the CMB to deform, during which the shock wave has already entered the core, hence the incident shock wave impinges on a undeformed spherical core. Therefore, a Zone 2 exists for the colatitudes greater than θ_1, where $\cos(\theta_1) = (R_p^2 + R_c^2 - R_1^2)/2\,R_p\,R_c$, and the equations provided in this paper are still valid. Zone 1 interacts with the core only for the colatitudes smaller than θ_1.

Acknowledgements

This research was supported by the Auvergne Fellowship program to JM, and by the Natural Sciences and Engineering Research Council (NSERC) of Canada to JAH. We gratefully acknowledge the developers of iSALE (www.isale-code.de), particularly the help we have received from Gareth S. Collins. We also would like to thank the two anonymous reviewers for their constructive comments. This paper is Laboratory of Excellence ClerVolc contribution no. 350.

References

Agnor, C.B., Asphaug, E., 2004. Accretion efficiency during planetary collisions. Astrophys. J. 613, L157–L160.
Agnor, C.B., Canup, R.M., Leviston, H.F., 1999. On the character and consequences of large impacts in the late stage of terrestrial planet formation. Icarus 142, 219–237.

Ahrens, T.J., O'Keefe, J.D., 1987. Impact on the Earth, ocean and atmosphere. Int. J. Impact Eng. 5, 13–32.
Ahrens, T.J., O'Keefe, J.D., Merrill, R.B., 1977. Equations of State and Impact-Induced Shock-wave Attenuation on the Moon. Impact and Explosion Cratering. Pergamon Press, Elmsford, N.Y, pp. 639–656.
Amsden, A., Ruppel, H., Hirt, C., 1980. SALE: A Simplified ALE Computer Program for Fluid Flow at All Speeds. Los Alamos National Laboratories Report, LA-8095:101p. LANL, Los Alamos, New Mexico.
Arkani-Hamed, J., 2005. Magnetic crust of Mars. J. Geophys. Res. 110, E08005. https://doi.org/10.1029/2004JE002397.
Arkani-Hamed, J., 2017. Formation of a solid inner core during the accretion of Earth. J. Geophys. Res. Solid Earth 122. https://doi.org/10.1002/2016JB013601.
Arkani-Hamed, J., Ivanov, B., 2014. Shock wave propagation in layered planetary embryos. Phys. Earth Planet. Inter. 230, 45–59.
Arkani-Hamed, J., Olson, P., 2010a. Giant impact stratification of the Martian core. Geophys. Res. Lett. 37, L02201. https://doi.org/10.1029/2009GL04141.
Arkani-Hamed, J., Olson, P., 2010b. Giant impacts, core stratification, and failure of the Martian dynamo. J. Geophys. Res. 115, E07012.
Barr, A., Citron, R., 2011. Scaling of melt production in hypervelocity impacts from high-resolution numerical simulations. Icarus 211, 913–916.
Benz, W., Cameron, A.G.W., Melosh, H.J., 1989. The origin of the moon and the single-impact hypothesis III. Icarus 81, 113–131.
Bierhaus, M., Wünnemann, K., Elbeshausen, D., 2012. Numerical Modeling of Basin-forming Impacts: Implications for the Heat Budget of Planetary Interiors, Large Meteorite Impacts and Planetary Evolution V. LPI Contribution No. 1737.
Bierhaus, M., Wünnemann, K., Ivanov, B.A., 2013. Affect of Core Rheology on Shock Wave Propagation in Planetary Scale Impacts, 43rd Lunar and Planetary Science Conference. (Abstract # 2174.pdf).
Bjorkman, M.D., Holsapple, K.A., 1987. Velocity scaling impact melt volume. Int. J. Eng. 5, 155–163.
Bottke, W.F., Nolan, M.C., Greenberg, R., Kolvoord, R.A., 1994. Collisional lifetimes and impact statistics of near-Earth asteroids. In: Tucson, Gehrels T. (Ed.), Hazards Due to Comets and Asteroids. The University of Arizona Press, Arizona, pp. 337–357.
Chambers, J.E., 2004. Planetary accretion in the inner solar system. Earth Planet. Sci. Lett. 223, 241–252.
Chambers, J.E., 2013. Late-stage planetary accretion including hit-and-run collisions and fragmentation. Icarus 224, 43–56.
Chambers, J.E., Wetherill, G.W., 1998. Making the terrestrial planets: N-body integrations of planetary embryos in three dimensions. Icarus 136, 304–327.
Collins, G.S., Melosh, H.J., 2014. Improvements to ANEOS for multiple phase transitions. In: 45th Lunar and Planetary Science Conference, pp. 2664.
Curran, D.R., Shockey, D.A., Seaman, L., Austin, M., 1977. Mechanics and models of cratering in earth media. In: Roddy, D.J., Pepin, R.O., Merrill, R.B. (Eds.), Impact and Explosion Cratering. Pergamon, New York, pp. 1057–1087.
Davison, T.M., Collins, G.S., Ciesla, F.J., 2010. Numerical modelling of heating in porous planetesimal collisions. Icarus 208, 468–481. https://doi.org/10.1016/j.icarus.2010.01.034.
Frey, H., 2008. Ages of very large impact basins on Mars: implications for the late heavy bombardment in the inner Solar System. Geophys. Res. Lett. 35, L13203.
Gault, D.E., Heitowit, E., 1963. The partition of energy for hypervelocity impact craters formed in rock. In: Proceedings of the 6th Hypervelocity Impact Symposium. vol. 2. pp. 419–456.
Ghods, A., Arkani-Hamed, J., 2011. Effects of the Borealis impact on the mantle dynamics of Mars. Phys. Earth Planet. Inter. 188, 37–46.
Ivanov, B.A., Deniem, D., Neukum, G., 1997. Implementation of dynamic strength models into 2D hydrocodes: applications for atmospheric breakup and impact cratering. Int. J. Impact Eng. 20, 411–430.
Ivanov, B.A., Melosh, H.J., Pierazzo, E., 2010. Basin-forming impacts: reconnaissance modeling. Geol. Soc. Am. Spec. Pap. 465, 29–49.
Kaula, W.M., 1979. Thermal evolution of Earth and moon growing by planetesimal impacts. J. Geophys. Res. 84, 999–1008.
Kendall, J.D., Melosh, H.J., 2016. Differentiated planetesimal impacts into a terrestrial magma ocean: fate of the iron core. Earth Planet. Sci. Lett. 448, 24–33.
Kokubo, E., Genda, H., 2010. Formation of the terrestrial planets form protoplanets under a realistic accretion condition. Astrophys. J. Lett. 714, L21–L25.
Kokubo, E., Ida, S., 2000. Formation of protoplanets from planetesimals in the solar nebula. Icarus 143, 15–27.
Kraus, R.G., Senft, L.E., Stewart, S.T., 2011. Impacts onto H2O ice: scaling laws for melting, vaporization, excavation, and final crater size. Icarus 214, 724–738.
Leinhardt, Z.M., Stewart, S.T., 2009. Full numerical simulations of catastrophic small body collisions. Icarus 199, 542–559.
Louzada, K.L., Stewart, S.T., 2009. Effects of planet curvature and crust on the shock pressure field around impact basins. Geophys. Res. Lett. 36, L15203.
Melosh, H.J., 1989. Impact Cratering: A Geologic Process. Oxford Univ. Press, New York.
Mitani, N.K., 2003. Numerical simulations of shock attenuation in solids and reevaluation of scaling law. J. Geophys. Res. 108 (E1), 5003. https://doi.org/10.1029/2000JE001472.
Monteux, J., Arkani-Hamed, J., 2014. Consequences of giant impacts in early Mars: Core merging and Martian dynamo evolution. J. Geophys. Res. 119, 480–505.
Monteux, J., Arkani-Hamed, J., 2016. Scaling laws of impact induced shock pressure and particle velocity in planetary mantle. Icarus 264, 246–256.
Monteux, J., Tobie, G., Choblet, G., Le Feuvre, M., 2014. Can large icy moons accrete undifferentiated? Icarus 237, 377–387.
Monteux, J., Andrault, D., Samuel, H., 2016. On the cooling of a deep terrestrial magma ocean. Earth Planet. Sci. Lett. 448, 140–149.
Ohnaka, M., 1995. A shear failure strength law of rock in the brittle-plastic transition regime. Geophys. Res. Lett. 22, 25–28.
Osinski, G.R., Pierazzo, E., 2012. Impact Cratering: Processes and Products. Blackwell Publishing Ltd (330 pp.).
Pierazzo, E., Melosh, H.J., 2000a. Melt production in oblique impacts. Icarus 145, 252–261.
Pierazzo, E., Melosh, H.J., 2000b. Understanding oblique impacts from experiments, observations, and modeling. Annu. Rev. Earth Planet. Sci. 28, 141–167.
Pierazzo, E., Vickery, A.M., Melosh, H.J., 1997. A reevaluation of impact melt production. Icarus 127, 408–423.
Pierazzo, E., et al., 2008. Validation of numerical codes for impact and explosion cratering: impacts on strengthless and metal targets. Meteorit. Planet. Sci. 43 (12), 1917–1938.
Potter, R.W.K., et al., 2012. Constraining the size of the South Pole-Aitken basin impact. Icarus 220, 730–743.
Rafikov, R.R., 2003. The growth of planetary embryos: orderly, runaway, or oligarchic. Astron. J. 125, 942–961.
Raymond, S.N., Quinn, T., Lunine, J.I., 2006. High-resolution simulations of the final assembly of Earth-like planets, terrestrial accretion and dynamics. Icarus 183, 265–282.
Ricard, Y., Srámek, O., Dubuffet, F., 2009. A multi-phase model of runaway core-mantle segregation in planetary embryos. Earth Planet. Sci. Lett. 284, 144–150.
Ricard, Y., Bercovici, D., Albarède, F., 2017. Thermal evolution of planetesimals during accretion. Icarus 285, 103–117.
Rivoldini, A., Van Hoolst, T., Verhoeven, O., Mocquet, A., Dehant, V., 2011. Geodesy constraints on the interior structure and composition of Mars. Icarus 213, 451–472.
Robbins, S.J., Hynek, B.M., Lillis, R.J., Bottke, W.F., 2013. Large impact crater histories of Mars: the effect of different model crater age techniques. Icarus 225, 173–184.
Roberts, J.H., Arkani-Hamed, J., 2012. Impact-induced mantle dynamics on Mars. Icarus 218, 278–289.
Roberts, J.H., Arkani-Hamed, J., 2017. Effects of basin-forming impacts on the thermal evolution and magnetic field of Mars. Earth Planet. Sci. Lett. 478, 192–202. https://doi.org/10.1016/j.epsl.2017.08.031.
Roberts, J.H., Barnouin, O.S., 2012. The effect of the Caloris impact on the mantle dynamics and volcanism of Mercury. J. Geophys. Res. Planets 117, E02007.
Roberts, J.H., Lillis, R.J., Manga, M., 2009. Giant impacts on early Mars and the cessation of the martian dynamo. J. Geophys. Res. 114, E04009. https://doi.org/10.1029/2008JE003287.
Ruedas, T., 2017. Globally smooth approximations for shock pressure decay in impacts. Icarus 289, 22–33.
Senshu, H., Kuramoto, K., Matsui, T., 2002. Thermal evolution of a growing Mars. J. Geophys. Res. 107 (E12), 5118. https://doi.org/10.1029/2001JE001819.
Shoemaker, E.M., 1962. Interpretation of Lunar Craters. Academic Press, San Diego, pp. 283–359.
Solomatov, V.S., Canup, R.M., Righter, K., 69 collaborating authors, 2000. Fluid dynamics of a terrestrial Magma Ocean. In: Origin of the Earth and Moon. University of Arizona Press, Tucson, pp. 323–338.
Thompson, S.L., 1990. ANEOS analytic equations of state for shock physics codes input manual. In: Sandia National Laboratories Report SAND89-2951.
Thompson, S., Lauson, H., 1972. Improvements in the CHART D Radiation-Hydrodynamic Code III: Revised Analytic Equations of State. Sandia National Laboratory Report SC-RR-71 0714 (113 p).
Tonks, W.B., Melosh, H.J., 1992. Core formation by giant impacts. Icarus 100, 326–346.
Tonks, W.B., Melosh, H.J., 1993. Magma Ocean formation due to giant impacts. J. Geophys. Res. 98, 5319–5333.
Watters, W.A., Zuber, M.T., Hager, B.H., 2009. Thermal perturbations caused by large impacts and consequences for mantle convection. J. Geophys. Res. 114, E02001.
Wünnemann, K., Collins, G.S., Melosh, H.J., 2006. A strain-based porosity model for use in hydrocode simulations of impacts and implications for transient-crater growth in porous targets. Icarus 180, 514–552.
Wünnemann, K., Collins, G.S., Osinski, G.R., 2008. Numerical modelling of impact melt production in porous rocks. Earth Planet. Sci. Lett. 269 (3–4), 530–539.

3 Séparation manteau/noyau à l'intérieur de la Terre Primitive

La formation du noyau terrestre est un processus hautement énergétique qui s'est déroulé pendant ou juste après les principales étapes d'accrétion de la Terre (Stevenson, 1981). Ainsi cette phase primitive de la Terre est probablement intimement liée aux processus d'impacts. Lors de la collision avec un impacteur de rayon supérieur à 100 km, l'énergie apportée par la collision peut s'ajouter à l'énergie fossile issue des radioactivités des éléments à courte période et peut générer des zones de fusion à plus ou moins grandes échelles à l'intérieur desquelles le fer de l'impacteur est dispersé sous formes de gouttelettes (Figure 8). Lors des stades primitifs de formation des planètes, de tels évènements ont pu provoquer une ségrégation locale entre le fer dense et les silicates plus légers dans la zone chauffée (Tonks and Melosh, 1992; Deguen et al., 2011). Une fois rassemblés au fond du reservoir fondu par impact, de grands volumes de fer ont ensuite pu migrer vers le centre de la Terre et contribuer à la formation du noyau terrestre par percolation (Shannon and Agee, 1998) ou par diapirisme grâce à des instabilités de type Rayleigh-Taylor (Stevenson, 1981) (Figure 8).

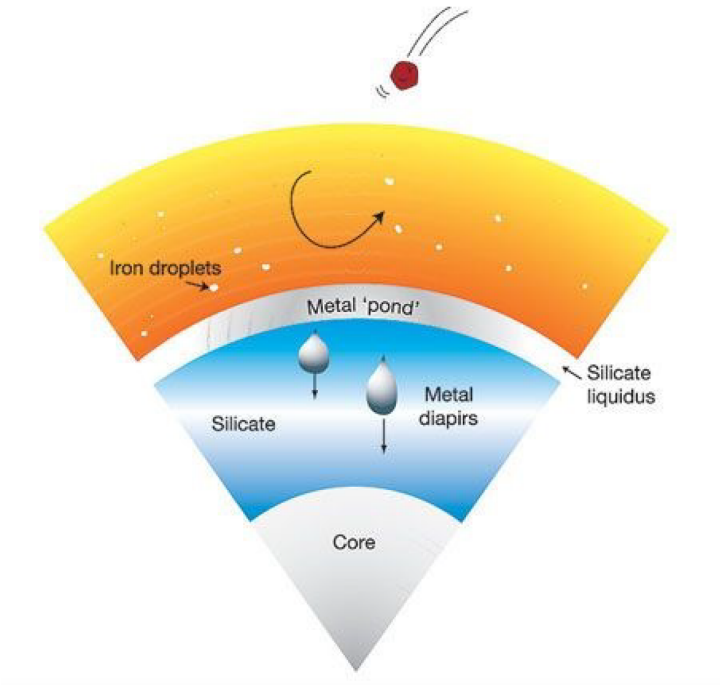

FIGURE 8 – *Modèle de formation du noyau terrestre à partir d'un océan magmatique profond (À partir de Wood (2011)).*

L'analyse géochimique des roches du manteau terrestre montre un excès en éléments sidé-

rophiles (ex. Ni, Co, Cu) par rapport à une différenciation à l'équilibre de matériel chondritique (Becker et al., 2006; Lorand et al., 2008, 2012). Les modalités de différenciation et notamment les volumes caractéristiques de fer (gouttelettes centimétriques ou diapir pluri-kilométriques) mis en jeu après impact entre deux corps différenciés conditionnent le degré d'équilibre chimique entre le manteau et le noyau terrestre (Rubie et al., 2003; Dahl and Stevenson, 2010). En effet si les volumes caractéristiques de fer en jeu lors de la formation du noyau sont importants (tailles kilométriques), les vitesses de séparation seront très élevées et l'équilibre thermo-chimique entre la phase métallique et la phase silicatée sera partiel. En revanche, si la séparation fer/silicates se fait via des gouttelettes de fer centimétriques, les échanges entre les deux phases seront facilités et l'équilibre thermo-chimique sera atteint. Une différenciation hors-équilibre est une hypothèse émise pour expliquer l'anomalie de concentrations en éléments sidérophiles dans les roches terrestres (Kleine and Rudge, 2011). Ainsi, les processus d'accrétion et de différenciation ont pu être enregistrés dans la composition chimique et isotopique du manteau des planètes telluriques. Cette composition chimique peut refléter comment le fer a plongé vers le noyau lors de la différenciation. Les processus de séparation fer/silicates à l'intérieur de la planète gouvernent la taille caractéristique de l'écoulement du fer dans le manteau. Ainsi, dans un océan magmatique turbulent, le fer plonge sous forme de gouttelettes centimétriques avant de s'accumuler à sa base. Ensuite, de larges volumes de fer peuvent être mobilisés par instabilités kilométriques, leur taille dépendant de la rhéologie du matériel sous-jacent. L'efficacité des échanges thermo-chimiques entre la phase métallique de l'impacteur et le manteau de l'impacté dépend fortement de la taille caractéristique du fer et des son temps de résidence dans le manteau. Ainsi, contraindre les processus de fragmentation siégeant dans le manteau primitif peut permettre de mieux comprendre les signatures géochimiques observées aujourd'hui .

3.1 Fragmentation du fer de l'impacteur dans un océan magmatique

Après un large impact, le noyau de métal de l'impacteur se disperse dans la zone fondue et plonge ensuite dans cet océan de magma moins dense sous la forme d'une pluie de fer ("Iron rain scenario"). Au cours de ce processus, deux fragmentations ont lieu : une fragmentation par impact (Kendall and Melosh, 2016) puis une fragmentation dans le réservoir fondu (Wacheul et al., 2014).

3.1.1 Fragmentation par impact

Lors d'un impact impliquant deux objets différenciés, l'impacteur va subir une déformation intense entraînant non seulement la fragmentation de son manteau silicaté mais aussi de son noyau métallique. Genda et al. (2017) ont modélisé les conséquences d'un impact avec un bolide différencié ($R = 1500$ km) après la formation du système Terre-Lune. Pour une collision oblique statistiquement probable (avec un angle d'impact de 45°), le noyau de l'impacteur

s'allonge et se désintègre ensuite en fragments de tailles décamétriques. Certains de ces fragments frappent la Lune en orbite, mais la plupart retombent sur Terre sous forme d'impacteurs secondaires entrainant une fragmentation supplémentaire. Genda et al. (2017) montrent qu'un seul impacteur oblique peut fournir une quantité suffisante d'éléments hautement sidérophiles (HSE) aux réservoirs de silicates terrestres primordiaux au début de l'Hadéen. Le processus d'impact permet aussi d'étirer la phase métallique favorisant ainsi la dispersion du fer liquide dans un volume beaucoup plus important dans la zone fondue par impact. Kendall and Melosh (2016) ont développé des modèles d'impact SPH (voir section 2) intégrant des traceurs lagrangiens qui suivent le noyau de fer initialement intact avec un rayon de 100 km au fur et à mesure que l'impact l'étire et le disperse. La distance de déplacement finale des paires de traceurs initialement les plus proches donne une mesure de l'étirement du noyau. Les statistiques d'étirement impliquent un mélange qui sépare le noyau de fer en feuillets, en ligaments et en fragments plus petits, sur une échelle de 10 km ou moins (Kendall and Melosh, 2016).

3.1.2 Fragmentation dans l'océan magmatique

Les fragments de noyau dispersés par l'impact dans les réservoirs terrestres subissent ensuite un nouveau mélange par entraînement turbulent lorsque les fragments de fer en fusion traversent l'océan de magma et se déposent plus profondément dans la planète. Une fois l'impact terminé soit environ une heure après la collision, cette deuxième fragmentation va former des gouttes de fer encore plus petites (avec des rayons inférieurs au mètre). Cette fragmentation a lieu dans le réservoir fondu par impact ce qui implique un milieu avec une viscosité très faible (0.01-100 Pa.s) sur des profondeurs pouvant aller jusqu'à la profondeur de la CMB dépendamment de l'angle d'impact et de la taille de l'impacteur (Nakajima et al., 2021).

Ainsi le réservoir fondu par impact est un milieu potentiellement très turbulent. La phase métallique a pu s'y déformer puis se fragmenter en gouttes de différentes tailles entraînant des échanges thermo-chimiques plus ou moins efficaces. Les fragmentations ont pu avoir lieu en cascade jusqu'à ce que les gouttelettes atteignent une taille caractéristique qui va dépendre essentiellement de la viscosité du milieu environnant. Pour les viscosités probables des liquides silicatés, le diamètre des gouttelettes stables est estimé à environ 1 cm (Rubie et al., 2003). C'est ce qui a amené à la formulation du "iron rain scenario", scénario largement utilisé pour quantifier l'efficacité des échanges thermo-chimiques entre le fer et les silicates dans un océan magmatique (Rubie et al., 2003).

Nous avons exploré ce scenario grâce à une série d'expériences en laboratoire dans le cadre de la thèse de J.B. Wacheul (Wacheul et al., 2014) (Figure 9). Nous avons utilisé le gallium liquide et des mélanges d'eau et de glycérol respectivement comme analogues du fer et des silicate fondus. Cela nous a notamment permis d'étudier l'influence du rapport de viscosité entre le fer et les silicates sur la dynamique de fragmentation. Alors que le scénario classique de la pluie de fer considère une population de gouttes purement sphériques avec un rayon caractéristique unique qui tombent vers le fond de l'océan magmatique à une vitesse unique, nos expériences ont montré une variété de formes stables pour les gouttes de métal liquide, une

large distribution de tailles et de vitesses, et une dynamique interne intense au sein du nuage avec la superposition de nouvelles fragmentations et d'assemblage de gouttes.

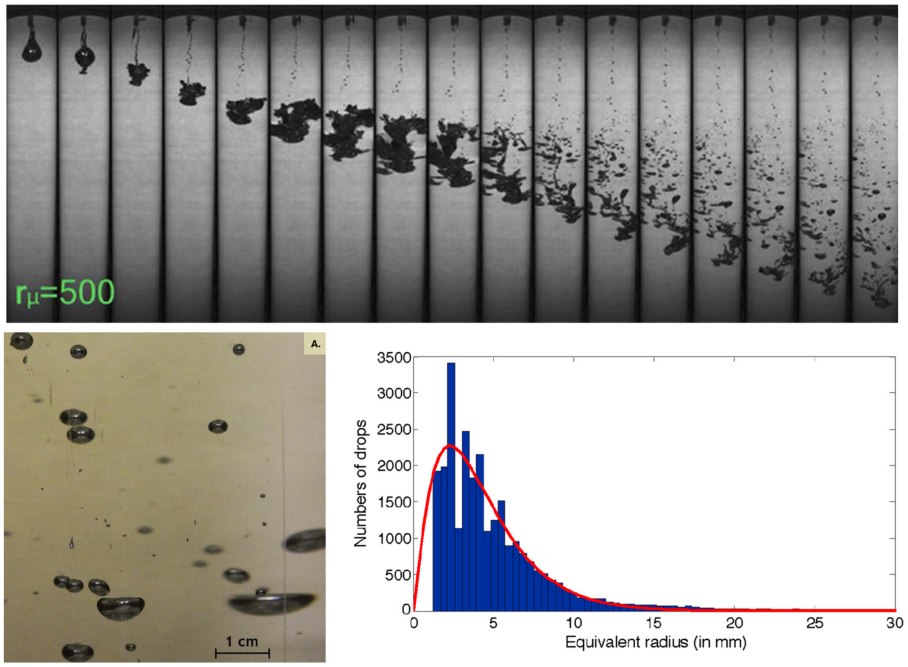

FIGURE 9 – *Haut : Modélisation analogique de la fragmentation d'un diapir de 31 mm de rayon initial. Nous représentons l'évolution temporelle (de la gauche vers la droite) pour un cas où le fluide ambiant est 500 fois plus visqueux que le diapir en fragmentation. Bas, gauche : gouttes de gallium liquide de différentes tailles tombant à travers du glycérol pur. Bas, droite : Histogramme du rayon équivalent des gouttelettes formées par la rupture d'un diapir de 30 mm de rayon initial tombant à travers un mélange de glycérol et d'eau (en bleu) et distribution Gamma la mieux ajustée (en rouge) (À partir de Wacheul et al. (2014)).*

Ces résultats ont notamment servi de précurseurs aux travaux de thèse de B. Qaddah dont M. Le Bars (I.R.P.H.E. Marseille) et moi étions les encadrants. Les premiers travaux de cette thèse portaient sur la modélisation de la dynamique de fragmentation d'une goutte de fer dans un océan magmatique (Qaddah et al., 2019). Nous avons pour cela développé des simulations numériques de la dynamique de descente d'une goutte de fer liquide initialement sphérique dans une phase de silicate en fusion, jusqu'à son éventuelle fragmentation. Nous avons considéré une géométrie 2D cylindrique axisymétrique. Nous avons fait varier la viscosité des silicates fondus entre 0.05 Pa.s et 100 Pa.s et le rayon initial de la goutte de fer entre 1 mm et 350 mm. Par conséquent, nous avons considéré des nombres de Reynolds compris entre 0.027 et 85600 et des nombre de Weber compris entre 0.073 et 7480. Notre modèle numérique a permis de contraindre la morphologie, la dynamique et la stabilité de la goutte de fer en fonction des nombres de Weber et de Reynolds sans dimension ainsi que du rapport de viscosité entre les silicates fondus et la goutte de fer liquide. En particulier, nous avons montré que le

rayon maximal de la goutte stable et le nombre de Weber critique sont des fonctions monotones croissantes de la viscosité de l'océan magmatique. L'épaisseur de la couche limite de quantité de mouvement dépend principalement du rayon de la goutte et légèrement de la viscosité de l'océan magmatique. L'augmentation de la viscosité de la phase silicatée empêche les oscillations de la phase métallique et limite la surface d'échange. A l'inverse, l'augmentation du rayon initial de la goutte de fer accroît sa déformation et augmente sa surface d'échange relative. Au-dessus du nombre de Weber critique, nous avons confirmé que la fragmentation du fer liquide se produit à une distance de chute comprise entre 3.5 et 8 fois le rayon initial de la goutte dans la gamme explorée du nombre de Weber modéré.

3.1.3 Évolution thermo-chimique des gouttelettes de fer

Nous avons ensuite développé des modèles numériques afin de suivre les échanges de chaleur entre une goutte de fer et l'océan magmatique pour différentes tailles initiales et viscosités ambiantes (Qaddah et al., 2020) (Figure 10). Nous avons exploré des nombres de Reynolds compris entre 0.05 et 48, des rapports de viscosité compris entre 50 et 4000, des nombres de Weber compris entre 0.04 et 5, et des nombres de Peclet compris entre 70 et 850. Nous avons montré que l'échange de chaleur entre les deux phases se produit principalement dans la partie avant de la goutte. Notre étude systématique et paramétrique a montré que l'épaisseur de la couche limite thermique, la profondeur et le temps d'équilibrage, le nombre de Nusselt et le volume de l'océan magmatique affecté par les échanges thermiques suivent tous des lois de puissance en fonction du nombre de Peclet. En raison des distorsions de la goutte, ces lois d'échelle s'écartent des bilans classiques qui ne considèrent que la diffusion de la chaleur à travers une couche limite thermique laminaire. Enfin, en considérant une viscosité du fluide ambiant dépendant de la température, nous avons montré qu'une couche de faible viscosité entoure la goutte, ce qui influence l'évolution thermique des gouttes non déformables à faible nombre de Reynolds uniquement et diminue la distance de rupture pour certains modes de rupture.

Enfin dans le cadre du post-doctorat de Vincent Clési que je co-supervisais avec A. Bouhifd, nous avons caractérisé les échanges chimiques lors la descente de gouttelettes métalliques dans un océan magmatique à l'aide de modèles numériques COMSOL Multiphysics (Clesi et al., 2020) (Figure 11). En faisant varier les viscosités du silicate et du métal (entre 0.1 et 1000 Pa.s pour chaque phase) ainsi que le coefficient de partage entre le métal et le silicate ($D_{met/sil}$ variant entre 1 et 1000), nous avons dérivé des relations permettant de quantifier le degré d'équilibre entre le métal et le silicate fondus, dans un régime caractérisé par de faibles nombres de Weber ($We < 10$) et de faibles nombres de Reynolds ($10^{-3} < Re < 10^{2}$). Nous avons montré que les principaux paramètres contrôlant l'équilibre pour un élément sidérophile sont la viscosité de la phase silicatée et le coefficient de partage de cet élément. Nous avons appliqué notre paramétrisation pour le Ni et le Co dans le contexte de l'accrétion tardive sur Terre afin de quantifier la variation du rapport Ni/Co après un large impact en fonction de la viscosité de l'océan magmatique, pour un scénario de pluie de gouttes de fer dans un océan

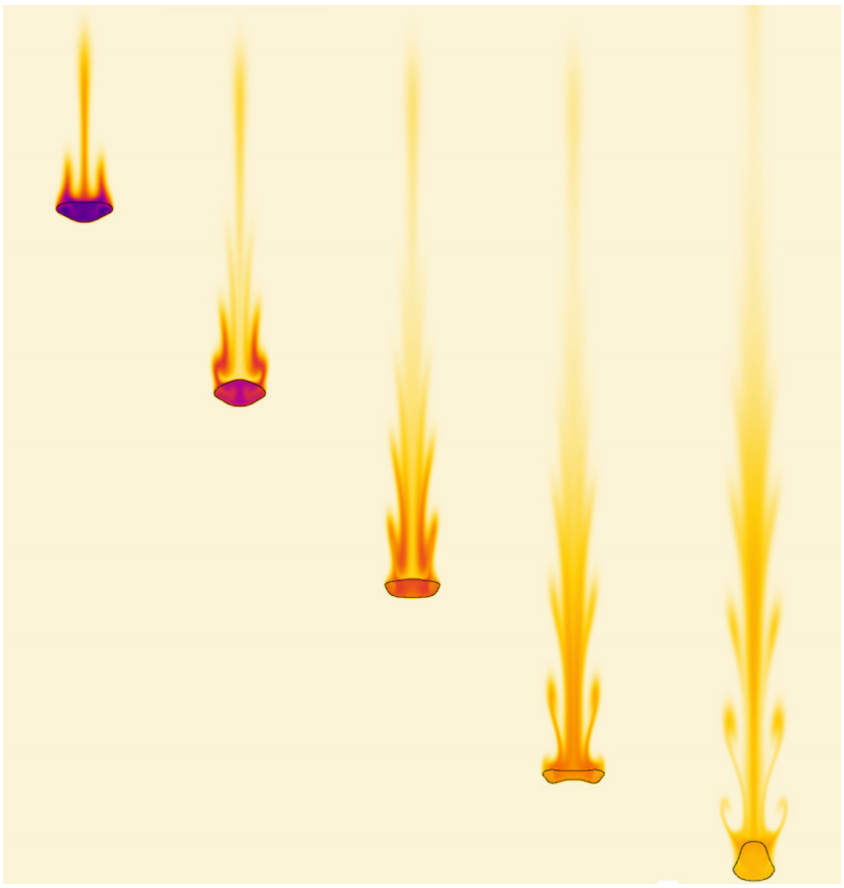

FIGURE 10 – *Évolution thermique d'une goutte de métal fortement déformable en fonction du temps. L'échelle de couleur représente l'anomalie de température normalisée par le contraste de température initial. La ligne noire continue représente la surface de la goutte de métal. (À partir de Qaddah et al. (2020)).*

magmatique. En considérant le modèle de Canup (2004), nous avons montré que la formation de la Lune avait un effet sur le rapport Ni/Co actuel. En fonction du rayon du noyau de Théia et de la viscosité de l'océan magmatique produit après l'impact entre la proto-Terre et Théia, la formation de la Lune pourrait être responsable de 0.45% à 3% du rapport Ni/Co actuel pour des viscosités d'océan magmatique de 0.1 à 100 Pa-s, respectivement.

3.2 Formation du noyau par diapirisme géant

Un impact géant peut entrainer la fusion d'importants volumes du manteau de la planète impacté formant ainsi des océan magmatiques localisés en dessous du point d'impact. Les réajustements mécaniques peuvent ensuite permettre à ces océans magmatiques de s'étaler et de

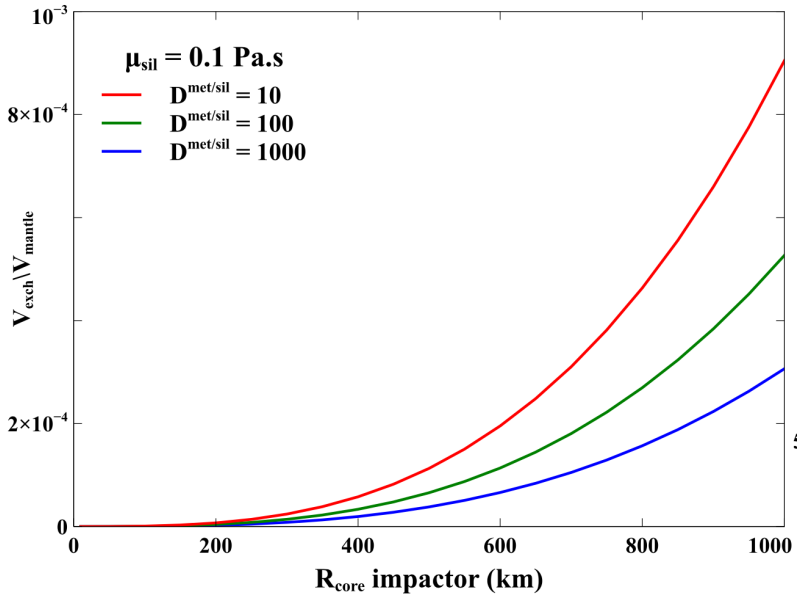

FIGURE 11 – *Fraction du manteau chimiquement contaminée par un élément modérément sidérophile (avec différentes valeurs de coefficient de partage $D^{met/sil}$) en fonction du rayon du noyau de l'impacteur. Dans cette figure, nous considérons que le noyau se fragmente en gouttelettes de fer avec un rayon $R_{Fe} = 1$ cm et que les viscosités du fer et des silicates fondus sont de 0.1 Pa.s. (À partir de Clesi et al. (2020)).*

recouvrir l'ensemble de la surface de la Terre primitive. Ce phénomène est amplifié lorsque plusieurs impacts géants se succèdent sur des intervalles de temps suffisamment courts pour que le matériel fondu n'ait pas le temps de recristalliser. Le fer va se rassembler à la base de ces océans magmatiques (voir section précédente) car il est plus dense que les silicates fondus desquels il se différencie. Ce fer peut soit provenir du noyau de l'impacteur, soit provenir du corps impacté lui même si la séparation fer/silicates n'avait pas encore eu lieu dans la zone fondue par impact.

Ces grands volumes de fer sont instables gravitairement car ils sont eux-mêmes plus denses que le matériel sous-jacent solide et composé de silicates (si la planète est différenciée) ou d'un mélange Fer/Silicates (si la planète est encore indifférenciée). Ainsi des instabilités de type Rayleigh Taylor peuvent se former provocant la chute de diapirs de fer de tailles kilométriques vers le centre de la Terre. Honda et al. (1993) a notamment modélisé la formation du noyau terrestre en considérant une couche de fer de plusieurs centaines de kilomètres d'épaisseur recouvrant l'intégralité d'un noyau indifférencié solide. D'après leurs modèles, Honda et al. (1993) ont montré que pour former le noyau en moins d'un milliard d'années, comme l'exigent diverses contraintes géophysiques et géochimiques, la viscosité du proto-noyau silicaté et indifférencié devrait être inférieure à 10^{26} Pa.s, ce qui est plus grand que la viscosité actuelle du

manteau, mais beaucoup plus petit que la viscosité estimée pour le proto-noyau silicaté à basse température et à haute pression. Cette étude a notamment mis en évidence que le chauffage du proto-noyau par l'énergie gravitationnelle libérée pendant la formation du noyau pouvait contribuer à l'accélération du processus de formation du noyau. Cependant il semble peu probable qu'une couche de fer aussi épaisse puisse se former et se stabiliser avant de plonger vers le centre de la Terre.

Senshu et al. (2002) a développé des modèles numériques 1D permettant de simuler l'histoire thermique au cours de l'accrétion de Mars à la manière de Kaula (1979). Il a cependant rajouté la contribution de la séparation métal-silicate dans cette planète en croissance. Dans leurs modèle, la perturbation thermique causée par les impacts de planétésimaux est calculée pour chaque événement d'impact et un diapir métallique est considéré à la base d'un bassin de magma si le site d'impact est chauffé au-dessus de la température de fusion. Le plongeon des diapirs métalliques est retracé en supposant une vitesse de Stokes. Leurs résultats numériques suggèrent que sur Mars, (1) aucun océan magmatique global n'est formé pendant l'accrétion, (2) la séparation métal-silicate a lieu sans fusion à l'échelle globale, et (3) au lieu d'un noyau métallique, une couche riche en métal se forme à la fin du processus d'accrétion. Ce modèle de formation de noyau planétaire a ensuite été développé en 3D par Golabek et al. (2009) afin de mettre en évidence l'influence des variations de viscosité au cours de ce processus.

Ces travaux m'ont amené à m'intéresser pendant ma thèse au plongeon d'un diapir de fer collecté dans la zone chauffée après un large impact météoritique (Figure 12). Pour étudier l'évolution d'un tel diapir métallique, nous avons proposé un modèle analytique de réajustement thermochimique que nous avons comparé à des simulations numériques en géométrie sphérique axisymétrique et à viscosité variable (Monteux et al., 2009). Pour cela, j'ai développé un code numérique permettant de résoudre les équations de Navier-Stokes en volumes finis et en formulation en fonctions de courant. Par rapport au modèle précédent (Monteux et al., 2007), ce modèle se place en géométrie axisymétrique sphérique dans l'approximation de Boussinesq étendu et permet de calculer la dissipation visqueuse ainsi que le chauffage par compression/décompression adiabatique. Ce nouveau modèle numérique permet non seulement de caractériser la dynamique de rééquilibrage thermique mais aussi l'évolution de la composition chimique en fonction du temps. Afin de pouvoir traiter le transport d'un champ de composition chimique, il est nécessaire de pouvoir résoudre convenablement (i.e. sans oscillation numérique) un champ purement advectif. Pour cela, mon code numérique inclut des schémas T.V.D. (Total Variation Diminishing) (Roe, 1986) parmi lesquels nous utilisons le schéma Superbee qui est non seulement non-oscillant mais permet aussi de limiter les flux diffusifs numériques.

Grâce à ces modèles, nous avons montré que la phase métallique s'enfonce avec une vitesse de l'ordre de la vitesse de Stokes comme considéré par Senshu et al. (2002). Autre point important que nous avons contraint : l'énergie thermique libérée par la ségrégation du métal

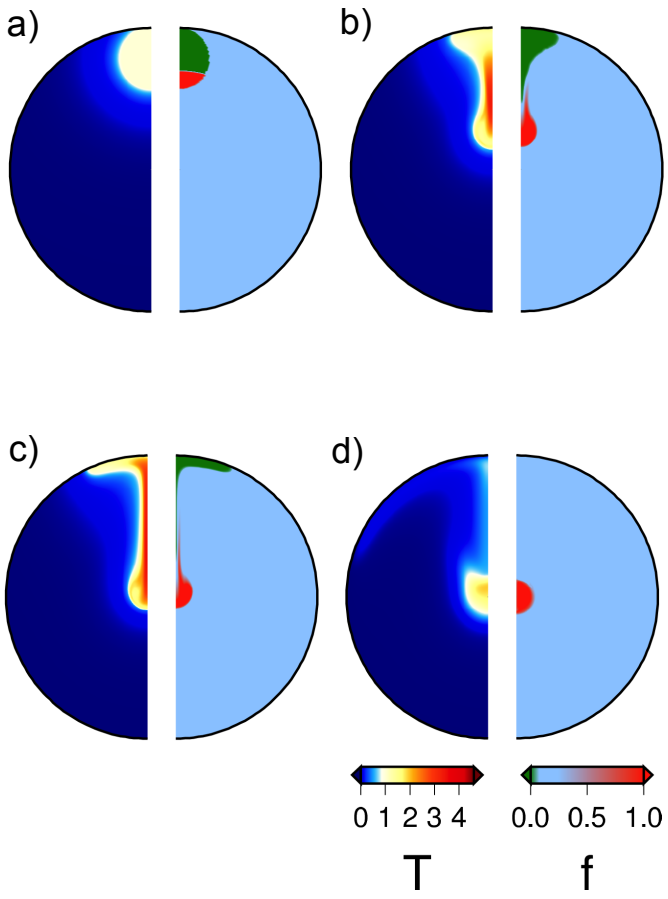

FIGURE 12 – *Température adimensionnée (demi-cercle gauche) et composition chimique (demi-cercle droite) (pour le fer* $f = 1$*, pour le matériel indifférencié* $f = 0.17$*, pour les silicates* $f = 0$*) au temps* $t = 0$ *(a),* $t = 1.4$ *Ma (b),* $t = 3.8$ *Ma (c) et* $t = 546$ *Ma (d) (dans un cas où la viscosité est uniforme,* $R = 4000$ *km,* $R_{imp} = 600$ *km et avec une résolution de* 200×200 *points de grille) (À partir de Monteux et al. (2009)).*

est comparable à l'énergie thermique dissipée lors de l'impact. Comme nous l'avons vu précédemment l'énergie de l'impact est distribuée potentiellement dans un grand volume de matériel indifférencié (Figure 4). L'énergie potentielle dissipée lors de la chute d'un important diapir de fer est quant à elle potentiellement libérée dans un volume beaucoup plus petit (le diapir de fer et ses environs proches). Un échauffement important du diapir métallique peut se produire lors de la chute, augmentant son excès de température d'un facteur 2 ou 3 au maximum. Lorsque l'on considère une viscosité de la phase métallique qui diminue avec la température, la proportion d'énergie thermique transférée à la matière indifférenciée environnante augmente au détriment de l'énergie dissipée dans la phase métallique. Ceci a pour effet de permettre d'une

part de former un proto-noyau à une température proche de celle de la zone d'impact et d'autre part de provoquer de la fusion et donc de la séparation Fer/silicates supplémentaire dans le manteau indifférencié environnant.

Ce processus pourrait ainsi être à l'origine d'une séparation Fer/silicates en cascade dans une planète initialement indifférenciée. En effet l'énergie potentielle dissipée en chaleur lors de la chute d'un importants volume de fer peut entraîner des phénomènes de fusion supplémentaires qui contribuent à séparer plus de fer et dissipent ainsi encore de l'énergie potentielle etc... Šrámek et al. (2010) ont développé des modèles bi-phasiques de simulations de la différenciation noyau-manteau montrant que le premier impact qui fait fondre la phase métallique près de la surface est potentiellement capable de déclencher toute la ségrégation noyau-manteau dans un phénomène d'emballement. Ils ont contraint le seuil de cette instabilité en fonction de la taille de l'impacteur et de la planète, ainsi que de la température initiale de la planète. La ségrégation du métal se produit par un mécanisme qui est intermédiaire entre l'instabilité diapir habituelle et une onde de porosité. Šrámek et al. (2010) ont contraint le rôle des paramètres les plus importants, tels que les viscosités du solide et du métal ou la dépendance en profondeur de la gravité.

Références personnelles

Monteux, J., *Ricard, Y., Coltice, N., Dubuffet, F., Ulvrova, M., 2009, A model of metal-silicate separation on growing planets, Earth Planet. Sci. Lett., 287, 353–362.* **LIEN HAL**

Wacheul, J.B., Le Bars, M., **Monteux, J.**, *Aurnou, J.M., 2014, Laboratory experiments on the breakup of liquid metal diapirs, Earth Planet. Sci. Lett., Volume 403, Pages 236-245.* **LIEN HAL**

Bouhifd A., Clesi V., Boujibar A., Bolfan-Casanova N., Cartier C., Hammouda T., Boyet M., Manthilake G., **Monteux J.**, *Andrault D., 2017, Silicate melts during Earth's core formation. Chemical Geology vol.461, p.128 - 139.* **LIEN HAL**

Qaddah B., **Monteux, J.**, *Clesi V., Bouhifd A., Le Bars M., 2019, Dynamics and stability of an iron drop falling in a magma ocean. Physics of the Earth and Planetary Interiors. vol.289, p.75-89.* **LIEN HAL**

Clesi V., **Monteux, J.**, *Qaddah B., Le Bars M., Wacheul J.B., Bouhifd A., 2020, Dynamics of core-mantle separation : Influence of viscosity contrast and metal/silicate partition coefficients on the chemical equilibrium. Physics of the Earth and Planetary Interiors, vol.306, p.106547.* **LIEN HAL**

Qaddah B., **Monteux, J.**, *Le Bars M., 2020, Thermal evolution of a metal drop falling in a less dense, more viscous fluid. Physical Review Fluids vol.5, p.053801.* **LIEN HAL**

Earth and Planetary Science Letters xxx (2009) xxx–xxx

Contents lists available at ScienceDirect

Earth and Planetary Science Letters

journal homepage: www.elsevier.com/locate/epsl

A model of metal–silicate separation on growing planets

J. Monteux *, Y. Ricard, N. Coltice, F. Dubuffet, M. Ulvrova

Université de Lyon, Lyon, F-69003, France
Université Lyon 1, Lyon, F-69003, France
Ecole Normale Supérieure de Lyon, Lyon, F-69364, France
CNRS, UMR5570, Laboratoire de Sciences de la Terre, Villeurbanne, F-69622, France

ARTICLE INFO

Article history:
Received 26 March 2009
Received in revised form 7 August 2009
Accepted 11 August 2009
Available online xxxx

Editor: T. Spohn

Keywords:
core formation
meteoritical impacts
early earth
numerical modeling
differentiation

ABSTRACT

The thermal evolution of planets during their accretionary growth is strongly influenced by impact heating. The temperature increase following a collision takes place mostly below the impact location in a volume a few times larger than that of the impactor. Impact heating depends essentially on the radius of the impacted planet. When this radius exceeds ~1000 km, the metal phase melts and forms a shallow and dense pool that penetrates the deep mantle as a diapir. To study the evolution of a metal diapir we propose a model of thermo-chemical readjustment that we compare to numerical simulations in axisymmetric spherical geometry and with variable viscosity. We show that the metallic phase sinks with a velocity of order of a Stokes velocity. The thermal energy released by the segregation of metal is smaller but comparable to the thermal energy buried during the impact. However as the latter is distributed in a large undifferentiated volume and the former potentially liberated into a much smaller volume (the diapir and its close surroundings) a significant heating of the metal can occur raising its temperature excess by at most a factor of 2 or 3. When the viscosity of the hot differentiated material decreases, the proportion of thermal energy transferred to the undifferentiated material increases and a protocore is formed at a temperature close to that of the impact zone.

1. Introduction

Core formation is the most important differentiation event that occurred during Earth's history. Metal/silicates separation is a rapid event (<60 My) (Kleine et al., 2002; Touboul et al., 2007; Yin et al., 2002) contemporaneous with Earth accretion and involving gravitational mechanisms such as percolation, negative diapirism and Rayleigh–Taylor instabilities (Honda et al., 1993; Stevenson, 1990). In the homogeneous accretion hypothesis, metal segregation and thereby core formation need significant heating to exceed the melting temperature of iron alloys or of silicates. During the early stages of planetesimals formation, heating by decay of short lived radionuclides is a potential energy source to enhance early differentiation (Yoshino et al., 2003). As a planetesimal grows, its gravity increases and it will increasingly attract the other surrounding planetesimals. The dissipation of the kinetic energy of the impacts provides a later shallow source of heat.

Impacts of large planetesimals have strongly influenced the late accretionary and thermal state of nearly fully-formed planetary bodies (Senshu et al., 2002; Tonks and Melosh, 1992). During an impact, when the relative velocity between a planet and an impactor overcomes the seismic velocities of the medium, a shock wave develops. The shock pressure is nearly uniform in a spherical region next to the impact (the isobaric core), and strongly decays away from it (Croft, 1982; Pierazzo et al., 1997). In this isobaric core, the kinetic energy of the impact is dissipated and leaves a temperature anomaly of several hundred degrees on Moon to Mars size bodies (Monteux et al., 2007; Senshu et al., 2002). The temperatures reached are mostly related to the properties (density and radius) of the impacted body, and only weakly to those of the impactor (Monteux et al., 2007). The melting temperature of iron alloys is lower than the silicates solidus (Agee, 1997; Fei et al., 1997; Ghosh and McSween, 1998). On large impacted planets, a local differentiation may occur between heavy metal and light silicates in the heated anomaly (Tonks and Melosh, 1992). Hence, a thermo-chemical readjustment follows, associated with the sinking of the metallic component toward the center of the impacted protoplanet (Fig. 1).

For large planets, gravitational energy release due to core formation can induce melting of the whole planet (Stevenson, 1989; Ricard et al., 2009). This subsequent melting depends on the mechanisms of the metal descent (Golabek et al., 2008; Samuel and Tackley, 2008). The aim of this study is to determine the thermal evolution of metal during descent and the thermal state of the core.

First, we propose analytical and numerical isoviscous models of segregation of a purely spherical iron diapir. As the viscosity contrast between molten metal and undifferentiated cold material can reach

* Corresponding author. Université de Lyon, Lyon, F-69003, France.
E-mail address: jmonteux@eos.ubc.ca (J. Monteux).

0012-821X/$ – see front matter © 2009 Elsevier B.V. All rights reserved.
doi:10.1016/j.epsl.2009.08.020

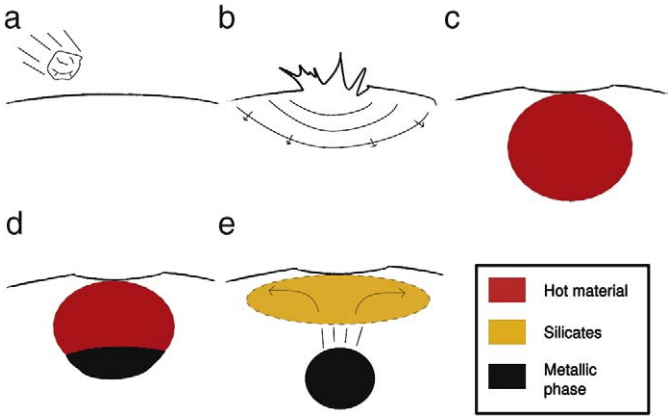

Fig. 1. Schematic view of the chemical equilibration following a large impact on an undifferentiated protoplanet. In the isobaric core resulting from the dissipation of the shock wave (a,b), the temperature increase melts the metal (c) that segregates rapidly (d), then sinks toward the planetary embryo center by a diapiric instability (e).

several orders of magnitude, we then focus on more realistic models of segregation of metal after a large impact with temperature dependent rheologies. We show that the size of impactors and viscosities involved largely determine the inner thermal state of a young planet.

2. Thermo-chemical state after large impact

2.1. Thermal state

After a meteoritical impact, heating is localized in a spherical region called the isobaric core just beneath the impact site. The radius of the isobaric core R_{ic} is comparable to the radius of the impactor R_{imp} and depends on energy conversion during the shock. With a minimal set of assumptions, we get $R_{ic} = 3^{1/3} R_{imp}$ following (Senshu et al., 2002) and (Pierazzo et al., 1997). Just after the adiabatic pressure release, the isobaric core is isothermal and we call ΔT_0 the shock induced temperature increase. The lower script 0 indicates that we consider this instant as the origin of our time variable. Outside the isobaric core, the temperature anomaly decays as $\Delta T_0(r) = \Delta T_0 (R_{ic}/r)^m$ with $m \sim 4.4$ as proposed by (Senshu et al., 2002). Assuming that the kinetic energy of the impactor is controlled by the escape velocity of the impacted body and that impactor and impacted body have the same densities (i.e., $\rho_{ic} = \rho_{imp} \equiv \rho_0$), a simple energy balance (Monteux et al., 2007), indicates that

$$\Delta T_0 = \frac{4\pi}{9} \frac{\gamma}{h(m)} \frac{\rho_0^2 G R^2}{\overline{\rho C_p}}, \quad (1)$$

where $\overline{\rho C_p}$ is the average heat capacity of the impacted body that is plausibly a mixture of silicate and metal, G is the gravitational constant, ρ_0 is the density of the undifferentiated material, R is the radius of the impacted planet and where the function $h(m)$ represents the volume effectively heated normalized by the volume of the isobaric core (typically $h(m) \sim 2$–3 (Monteux et al., 2007)). The empirical coefficient γ is the fraction of the kinetic energy of the impactor dissipated as heat. From shock experiments, γ ranges between 0.2 and 0.4 depending on material properties and shock velocities (O'Keefe and Ahrens, 1977) (i.e., 20 to 40% of the kinetic energy is buried at depth, the rest rapidly radiated away during or shortly after the impact). The shock-induced temperature excess, ΔT_0, strongly increases with the radius of the impacted body. According to the set of parameters of Table 1, $\Delta T_0(\mathrm{K}) = 4.7 \times 10^{-5} R^2(\mathrm{km})$; for a Moon size body ΔT_0 is 140 K while it is 1925 K for an Earth size body.

The thermal state of a protoplanet before an impact depends on its growth history and on its initial heating caused by short lived radionuclides like ^{26}Al and ^{60}Fe. This early radioactive heating can eventually cause melting and differentiation of planetesimals that have quickly grown (Yoshino et al., 2003). The impact heating superimposed to a sufficiently hot protoplanetary interior can trigger melting of the Fe–FeS system (the eutectic temperature is close to 1250 K at 1 bar) (Fei et al., 1997) and potentially of silicates (solidus temperature is around 1500 K at 1 bar) (Agee, 1997). In these cases, a fraction of the thermal energy is converted to latent heat during the phase transformations.

Table 1
Typical parameter values for numerical models.

Planet radius	R	1000–4000 km
Impactor radius	R_{imp}	100–400 km
Silicate density	ρ_{Si}	3500 kg m^{-3}
Iron density	ρ_{Fe}	8000 kg m^{-3}
Density difference	$\Delta\rho_0 = \rho_{Fe} - \rho_{Si}$	4500 kg m^{-3}
Average density	ρ_0	4270 kg m^{-3}
Heat capacity	$\overline{\rho C_p}$	4×10^3 kJ K^{-1} m^{-3}
Heat diffusivity	κ	10^{-6} m^2 s^{-1}
Thermal conductivity	k	4 W m^{-1} K^{-1}
Initial temperature	T_0	K
Metal content	f_0	0.17
Viscosity	η_0	10^{22} Pa s
Viscosity factor	λ	$2.5 \times 10^{-2} - 1$
Gravity	$g_0 = 4\pi G \rho_0 R/3$	m s^{-2}
Stokes velocity scale	$\Delta\rho_0 g_0 R^2/\eta_0$	~100 m yr^{-1}
Time scale	$\eta_0/\Delta\rho_0 g_0 R$	~20 kyr
Rayleigh number Ra_χ	$\overline{\rho C_p} \Delta\rho_0 g_0 R^3/\eta_0 k$	$\sim 10^8$
Buoyancy B	$\Delta\rho_0/\alpha\rho_0\Delta T_0$	25–250
Dissipation number D_χ	$\Delta\rho_0 g_0 R / \overline{\rho C_p} \Delta T_0$	36.6
Impact energy conversion coefficient	γ	0.3
Volume effectively heated by impact	$h(m)$	2.7
Stokes velocity coefficient	c_1	0.1–0.2
Heat diffusion coefficient	c_2	0.3–1.05

2.2. Compositional state

An impact on a large enough undifferentiated protoplanet composed of a mixture of metal alloys and silicates can trigger phase transformations and initiate differentiation. The first component that melts is the metal phase. In the region where metal melting occurs, the liquid metal can percolate through the solid silicate matrix. Percolation is only possible for small dihedral angles (<60°) or for large melt volume fraction above a percolation threshold. The dihedral angle of liquid iron alloy within silicates is large (~100°) in the upper mantle but decreases with increasing pressure (Shannon and Agee, 1996). However, the volume fraction of liquid alloy is typically larger than 10% if melting is complete, which overcomes the percolation threshold (Von Bargen and Waff, 1986). On Earth the core represents 17% of the volume of the planet, Mars has likely a slightly smaller core but Mercury's core is 43% of the planet. The metal is collected at the bottom boundary of the melted zone forming a diapir that ultimately sinks within the interior of the impacted protoplanet (Ricard et al., 2009).

If the temperature exceeds the silicate solidus and eventually the liquidus, the separation of metal and silicates can occur as a metal rainfall through a turbulent magma (Höink et al., 2005; Stevenson, 1990). Small droplets of heavy metal sediment at the bottom of the melted region. This scenario may not be the generic one, as it would imply that a planet embryo maintains a melted metal component without differentiating until the silicates start melting. It has been suggested that the metal may segregate per percolation, as soon as it melts, while the silicates are still mostly solid (Ricard et al., 2009). Locally, however, the impact of an undifferentiated planetesimal on an already differentiated large planetary embryo, may of course, be energetic enough to melt (or even vaporize) the silicate and metal contents of the impactor and the silicates of the impacted body inside the isobaric core.

The two processes (percolation or metal "rain") lead to a local differentiation within the melted region between light silicates and heavy metals on a short timescale compared to that of the slow viscous deformation (Tonks and Melosh, 1992). The melted region is as large as or a few times larger than the isobaric core (Pierazzo et al., 1997). Here, we identify the initially differentiated zone to the isobaric core, metal being overlaid by pure silicates shortly after the impact (see Fig. 1).

3. Dynamic model of differentiation

The setting described in the previous section is gravitationally unstable and the metal phase sinks toward the center of the impacted planetesimal while the silicates (lighter than undifferentiated material) spread underneath the surface. To study the global dynamics of this differentiation event, we develop a thermo-mechanical model in spherical axisymmetric geometry, of viscous flow with three chemical components. Using a viscous and linear rheology during the segregation of the core is clearly a large approximation. The large deviatoric stress generated by the metallic diapirs should lead to a non-linear rheology (Samuel and Tackley, 2008), elasto-plastic deformations (Gerya and Yuen, 2007) or even to hydrofracturation if they exceed the ultimate strength of rocks which is ~1–2 GPa (Davies, 1982). Pressure dependence of the rheology can also influence the metal sinking time but is not considered here since we focus on small growing planets. During the early stages of accretion, the interior of the growing planets may have been colder or hotter than the outer layers depending on the ratio of radioactive and impact heating and on the history of accretion. For simplicity, we assume in our models a homogenous temperature on the growing planet before the impact.

3.1. Physical model

Sinking occurs under the action of gravity in a spherical homogeneous protoplanetary body. We neglect for simplicity the changes of gravity during the differentiation. Hence gravitational acceleration $g(r)$ increases linearly with radius r:

$$g(r) = \frac{4}{3}G\pi\rho_0 r = g_0\frac{r}{R}, \tag{2}$$

where g_0 the surface gravity. The density of undifferentiated material is $\rho_0 = f_0\rho_{Fe} + (1-f_0)\rho_{Si}$ where f_0 is the volume fraction of metal and ρ_{Fe}, ρ_{Si}, the densities of the metallic phase and the pure silicates, respectively (see typical numerical values in Table 1.)

The dynamics of segregation potentially involves a series of multiscale physical processes, especially to take the effects of melting into account and a realistic multiphase dynamics (Golabek et al., 2008; Ricard et al., 2009). No numerical models can handle simultaneously all these complexities and as a consequence, we follow the approach of (Samuel and Tackley, 2008) and consider a thermo-chemical system with infinite Prandtl limit, with no possible subsequent phase separation within the undifferentiated material except that caused by the impact (e.g., the volumes of pure metal and pure silicates remain constant during the simulations and equal to 17% and 83% of the initial isobaric core).

The necessary approximations are somewhat different from the classic treatment of thermal convection (Ricard, 2007). We non-dimensionalize the lengths by the planetary radius R, the velocities by a Stokes velocity $\Delta\rho_0 g_0 R^2/\eta_0$ (where $\Delta\rho_0 = \rho_{Fe} - \rho_{Si}$ and η_0 is the reference viscosity of cold material far from the impact site), the temperature by ΔT_0 (see Eq. (1)). The governing mechanical non-dimensionnal equations are the conservation of mass

$$\nabla\cdot\mathbf{v} = 0, \tag{3}$$

and the conservation of momentum

$$-\nabla P + \nabla\cdot\left(\frac{\eta}{\eta_0}[\nabla\mathbf{v} + [\nabla\mathbf{v}]^T]\right) + \left(\frac{T}{B} - f\right)r\mathbf{e_r} = 0, \tag{4}$$

where $\mathbf{v}$, P, T and r are the non-dimensional velocity, pressure, temperature and radius, η the viscosity and $\mathbf{e_r}$ the radial unit vector. The buoyancy ratio B (Christensen and Yuen, 1985) is:

$$B = \frac{\Delta\rho_0}{\rho_0\alpha\Delta T_0}. \tag{5}$$

The downward buoyancy force that drives the flow increases with the volume fraction of metal f that varies between 0 (pure silicates) and 1 (pure metal), 0.17 being that of undifferentiated material. A depth dependent and constant in time gravity has been used in Eq. (4) although, in principle, gravity should have been computed self-consistently from the time-dependent density distribution. We assume a temperature dependent viscosity such as $\eta = \eta_0\lambda^T$ with λ being the viscosity factor (lower than 1) which is equivalent to the viscosity ratio between the hottest and coldest material at the start of the experiment. Such a viscosity decreases sharply with temperature and is simpler to implement than the usual Arrhenius law (Ratcliff et al., 1997; Ziethe and Spohn, 2007).

The conservation of energy writes

$$\frac{DT}{Dt} = \frac{\nabla^2 T}{Ra_\chi} + D_\chi\frac{\eta}{\eta_0}\Phi + \frac{1}{B}\frac{\Delta\rho}{\rho}\frac{T}{\Delta T_0}D_\chi\frac{DP}{Dt}. \tag{6}$$

The importance of diffusion is controlled by the compositional Rayleigh number Ra_χ,

$$Ra_\chi = \frac{\Delta\rho_0 g_0 R^3}{\kappa\eta_0}, \tag{7}$$

the chemical dissipation number is

$$D_\chi = \frac{\Delta\rho_0 g_0 R}{\overline{\rho C_p}\Delta T_0}, \tag{8}$$

considering for simplicity that $\overline{\rho C_p} = \rho_{Fe}C_p^{Fe} = \rho_{Si}C_p^{Si}$ (truly, see Table 1, $\rho_{Fe}C_p^{Fe} = 4\times10^3\,\mathrm{kJ\,K^{-1}m^{-3}}$, $\rho_{Si}C_p^{Si} = 3.85\times10^3\,\mathrm{kJ\,K^{-1}m^{-3}}$, and we use $\overline{\rho C_p} = 4\times10^3\ \mathrm{kJ\,K^{-1}m^{-3}}$). As g_0 is proportional to R and ΔT_0 to R^2, see Eq. (1), the chemical dissipation is independent of the planet radius and amounts to 36.6 (see Table 1).

An important energy source is provided by the dimensionless dissipation function Φ that expresses the conversion of potential energy into heat

$$\Phi = 2\,\underline{\epsilon} : \underline{\epsilon}. \tag{9}$$

where $\underline{\epsilon}$ is the dimensionless strain rate tensor. For simplicity, we make the approximation that the thermal conductivities of the metal, silicates and undifferentiated materials are the same (truly $k_{Fe} = 10\,\mathrm{W\,m^{-1}K^{-1}} > k_{Si} = 3\,\mathrm{W\,m^{-1}K^{-1}}$).

The metal volume fraction is then simply advected by the flow,

$$\frac{Df}{Dt} = 0. \tag{10}$$

3.2. Model approximations

The equations of momentum and energy conservations, Eqs. (4) and (6), are similar to those classically used for mantle convection simulations but a number of differences should be discussed. As the buoyancy number B is very large (the density difference between

metal and silicates is 40 to 620 times larger than the thermal density variations), the thermal buoyancy T/B can be safely neglected in the momentum equation.

Neglecting the terms in $1/B$ implies to omit the adiabatic heat transfer (the term in (DP/Dt)) in Eq. (6) but to keep the dissipation term $D_\chi(\eta/\eta_0)\Phi$. The differentiation of the planet liberates a large amount of potential energy converted into heat by the dissipation term but the adiabatic heating remains small. This is very different from the typical convection situation in which there is no time variation of the potential energy, and where the dissipation is on average balanced by the work due to compression and expansion over the convective cycle (Hewitt et al., 1975).

3.3. Numerical model

We implement a finite volume numerical model to solve Eqs. (3), (4), (6) and (10) in axi-symmetric spherical geometry. We use a stream function formulation for the equations of motion with a direct implicit inversion method (Schubert et al., 2001). Eqs. (6) and (10) are solved by an Alternating Direction Implicit (ADI) scheme (Douglas, 1955; Peaceman and Rachford, 1955).The stream function, temperature and compositional fields are described by a second-order approximation in space. To limit numerical diffusion when solving the transport equations, especially for the compositional field, we use a Total Variation Diminishing Superbee scheme (Laney, 1998; Roe, 1986) implemented in an implicit way (Sramek, 2007) which enables a high resolution of pure advective fields. We use at least 200×200 grid points. Velocity boundary conditions are free-slip at the surface and along the symmetry axis. Thermal boundary conditions are isothermal at the surface and insulating along the symmetry axis. We benchmark the viscous flow solver with variable viscosity and the transport scheme against several analytical solutions (Monteux, 2009).

4. Thermal evolution of sinking metallic diapir: analytical considerations

Before showing the results of complex numerical simulations with temperature dependent rheologies, we develop a simple model describing the thermal evolution of the sinking metal diapir, by approximating the metal diapir by a spherical drop falling into undifferentiated medium of uniform viscosity with a Stokes-like velocity. The radius of the metal drop R_{Fe} can be related to the radius R_{ic} of the volume initially differentiated after impact heating by $R_{\mathrm{Fe}}^3 = f_0 R_{\mathrm{ic}}^3$ and to the radius of the impactor by $R_{\mathrm{Fe}}^3 = 3 f_0 R_{\mathrm{imp}}^3$.

4.1. Sinking velocity

The velocity V of the metallic diapir in an undifferentiated medium is comparable to the Stokes velocity of a sphere of similar volume. The density difference between the metal and the undifferentiated material is a function of temperature and composition but the temperature contribution is minor. Hence, we consider $\Delta\rho = (1-f_0)\Delta\rho_0$. Because gravity is a linear function of depth, the velocity of the sphere decreases during sinking as

$$V = \frac{dr}{dt} = -c_1(1-f_0)\frac{\Delta\rho_0 g_0 R_{\mathrm{Fe}}^2}{\eta_S}\frac{r}{R}. \tag{11}$$

In Eq. (11), the dimensionless constant c_1 depends on the geometry of the system and on the viscosity contrast between the falling sphere and the surrounding medium.

The viscosity of the surrounding undifferentiated material η_S controls the sinking velocity. In the case of a sphere sinking in an infinite medium, the coefficient c_1 is given by the Hadamard–Rybczynski equation and varies from $4/15 = 0.27$ (isoviscous) to $1/3 = 0.33$ for an inviscid sphere (Hadamard, 1911; Rybczynski, 1911). In the situation described in this paper, the boundary conditions are applied at a finite distance (the planetary surface) and the Hadamard and Rybczynski equation is thus only an approximation (Honda et al., 1993; Samuel and Tackley, 2008). The exact value of the constant c_1 will be obtained later through numerical experiments.

The position of the metallic drop obtained by solving Eq. (11) varies from an initial position r_0 ($r_0 = R - R_{\mathrm{Fe}} \sim R$) as

$$r(t) = r_0 \exp\left(-\frac{t}{\tau_S}\right), \tag{12}$$

with a characteristic time equal to

$$\tau_S = \frac{\eta_S R}{c_1 \Delta\rho_0 g_0}\frac{1}{(1-f_0)}\frac{1}{R_{\mathrm{Fe}}^2}. \tag{13}$$

As g_0 is proportional to the planetary radius R (Eq. (2)), the time τ_S is independent of the planetary radius but depends only on the diapir size R_{Fe}. Of course, no segregation occurs, i.e., $\tau_S \to +\infty$, for a planet of pure silicates ($f_0 = 0$ which means $R_{\mathrm{Fe}} = 0$) or of pure metal ($f_0 = 1$). This characteristic sinking time is strongly dependent of the viscosity of the surrounding undifferentiated material which is poorly constrained. With the typical values of Table 1, this time can be computed from the size R_{imp} of the impactor and we find $\tau_S(\mathrm{kyr}) = 2.7\times10^9(\eta_S/\eta_0)R_{\mathrm{imp}}^{-2}(\mathrm{km})$.

4.2. Global energy conversion

As we assume that gravity remains constant with time (albeit non-uniform), the energy equation Eq. (6) integrated over the whole planet with the use of the momentum equation Eq. (4) and neglecting the adiabatic decompression of the planet during the core segregation is simply

$$\frac{d}{dt}(\Delta E_p + \Delta E_T) = F, \tag{14}$$

where the total potential and thermal energies changes are

$$\Delta E_p = \int_\Omega \frac{1}{2}[\rho(\mathbf{r},t) - \rho(\mathbf{r},0)] g_0 \frac{r^2}{R} dV, \tag{15}$$

(Ω is the planetary volume),

$$\Delta E_T = \int_\Omega \overline{\rho C_p}[T(\mathbf{r},t) - T(\mathbf{r},0)] dV, \tag{16}$$

and the heat flux F is

$$F = \int_\Sigma k \frac{\partial T}{\partial r} dS, \tag{17}$$

(Σ is the planetary surface).

As we neglect the term in $1/B$ in the energy equation Eq. (4), the Eq. (14) misses the energy variation ΔE_a due to the changes in pressure (the subscript a means that this term is related to changes in adiabatic compression)

$$\frac{d\Delta E_a}{dt} = \int_\Omega \alpha T \frac{\partial P}{\partial t} dV \sim \alpha T_0 \frac{d}{dt}\int_\Omega [P(\mathbf{r},t) - P(\mathbf{r},0)] dV \tag{18}$$

where the last approximation assumes that the temperature remains close to T_0. The difference of pressure between a homogeneous and a differentiated planet is easy to compute analytically and is of order $\alpha T_0 \Delta E_p$, i.e., a few percent of the changes in potential energy. This confirms that the energy change due to pressure changes is a minor effect.

4.3. Maximum temperature

The maximum temperature that the sinking metal can reach can be estimated by assuming that the whole variation of potential energy is only used to heat up the metal, without any heat transfer to the surrounding material.

Let us consider a melted zone of radius R_{ic} underneath and tangent to the planetary surface that differentiates ultimately forming a metallic core of volume V_{Fe} and radius R_{Fe} (with $R_{Fe}^3 = f_0 R_{ic}^3$) and a silicate layer of volume V_{Si} within a shell surrounding the whole planet with inner shell radius R_S and outer shell radius R i.e., $R_S^3 = R^3 - (1-f_0)R_{ic}^3$. The change of potential energy is according to Eq. (15) (Flasar and Birch, 1973):

$$\Delta E_p = \frac{2\pi}{5R} g_0((\rho_{Fe}-\rho_0)R_{Fe}^5 + (\rho_{Si}-\rho_0)(R^5-R_S^5)). \quad (19)$$

Assuming $R_{ic} \ll R$, a Taylor expansion of Eq. (19) leads to

$$\Delta E_p \sim -\frac{1}{2}\Delta\rho_0 g_0 R f_0 (1-f_0) V_{ic} = -\frac{1}{2}(\rho_{Fe}-\rho_0) g_0 R V_{Fe} = -\frac{1}{2}(\rho_0-\rho_{Si}) g_0 R V_{Si}, \quad (20)$$

where V_{ic} is the volume of the isobaric core. The change of potential energy is thus equivalent to that released by the sinking of the isobaric volume V_{ic} and excess density $f_0(1-f_0)\Delta\rho_0$. Alternatively it corresponds to the energy released by a metal sphere of volume V_{Fe} sinking, or of a silicate sphere rising, through undifferentiated material. If only the metal heats up, the change of thermal energy according to Eq. (16) is $\Delta E_T = \overline{\rho C_p} f_0 \Delta\Theta V_{ic}$ where $\Delta\Theta$ is the temperature increase (just after the impact, the metal temperature is $T_0 + \Delta T_0$, then it reaches at most $T_0 + \Delta T_0 + \Delta\Theta$). A scaling value for the temperature increase during segregation is thus

$$\Delta\Theta = \frac{1-f_0}{2}\frac{1}{\overline{\rho C_p}}\Delta\rho_0 g_0 R. \quad (21)$$

As g_0 is proportional to R (Eq. (2)), the core segregation can increase the temperature by a quantity proportional to R^2 (Flasar and Birch, 1973; Ricard et al., 2009). The ratio of $\Delta\Theta$ to the post impact temperature ΔT_0 is, according to Table 1 and Eq. (1),

$$\frac{\Delta\Theta}{\Delta T_0} = \frac{3h(m)}{2\gamma}(1-f_0)\frac{\Delta\rho_0}{\rho_0} \sim 11.8 \quad (22)$$

or, $\Delta\Theta(K) = 11.8\Delta T_0(K) = 5.6\times10^{-4}R^2(\mathrm{km})$ which rapidly becomes a large quantity as R increases. Of course, in a real situation not all energy will remain within the metal, and we will see that, when the metal diapir is too small, the metal can even cool off rather than warm up during its motion.

4.4. Thermal regime of the metallic sphere

While the hot metallic sphere is sinking, it warms up by shear heating but it also cools down by diffusion. In the reference frame of the sinking drop, the conservation of energy integrated over the volume V_{Fe} of the metallic drop (or through its surface S_{Fe}) indicates that

$$\overline{\rho C_p} V_{Fe}\frac{d\Delta T}{dt} = -k\frac{\Delta T}{\delta}S_{Fe} + \underline{\underline{\tau}} : \nabla\mathbf{v}\, V_{Fe}, \quad (23)$$

where we assume that the temperature and the dissipation are at first order uniform in the metal. The difference ΔT is the difference between the diapir and the undifferentiated material. We assume that $\Delta T = T - T_0$, i.e., that the hot diapir sinks into a medium that keeps its initial temperature outside the boundary thickness δ. Even when the diapir viscosity is low and when the dissipation occurs significantly outside it, our numerical simulations show that the maximum temperature is reached inside the diapir.

The thickness δ over which the temperature diffuses should be written as R_{Fe} times a dimensionless function c_2 of the various parameters of the problem. The thickness of the diffusive boundary layer, c_2, should decrease with the sinking velocity of the diapir (i.e., with the Peclet number VR_{Fe}/κ) as a power law with exponent $-1/2$ or $-1/3$, depending on the viscosity ratio between the metal and the undifferentiated material (see e.g., Ribe, 2007). We can also write the dissipation $\underline{\underline{\tau}}:\nabla\mathbf{v} = \eta_e V^2/R_{Fe}^2$ where η_e is the effective viscosity of the region where dissipation occurs. In this case, Eq. (23) using the expressions of the time dependent position, Eq. (12), and of the maximum temperature increase, Eq. (21), can be recast as

$$\frac{d\Delta T}{dt} = -\frac{\Delta T}{\tau_D} + 2a\left(\frac{r_0}{R}\right)^2\frac{\Delta\Theta}{\tau_S}\exp\left(-2\frac{t}{\tau_S}\right), \quad (24)$$

where the dimensionless constant

$$a = c_1\frac{\eta_e}{\eta_S} \quad (25)$$

characterizes the proportion of heat effectively dissipated in the metal and τ_D the characteristic time of diffusion

$$\tau_D = \frac{c_2 R_{Fe}^2}{3\kappa}, \quad (26)$$

where c_2, measuring in terms of R_{Fe} the thickness of the thermal boundary layer around the metal, $\delta = c_2 R_{Fe}$, is a dimensionless number.

Eq. (24) cannot be used predictively in a complex situation as it requires the knowledge of various parameters c_1, c_2 and a. The dependences of these parameters with more fundamental quantities (mostly with the temperature dependence of the viscosity) have to be determined empirically. We will see however, that for a given choice of the rheology, Eq. (24) captures the evolution of the metallic diapir temperature as a function of time and the dependence of this temperature with the diapir size. For example, Eq. (24) suggests that the diffusion term decreases with R_{Fe} (as R_{Fe}^{-2} if one considers c_2 as a constant) while the dissipation term increases with R_{Fe}^2. We can also use Eq. (24) qualitatively by assuming $a \sim c_1 \sim 4/15$ (using Stokes law) and $c_2 \sim 1$.

Eq. (24) shows that the temperature is not necessarily an increasing function of time. More precisely, according to Eq. (24) the metal temperature increases just after the impact ($t \sim 0$), if

$$-\frac{\Delta T_0}{\tau_D} + 2a\left(\frac{r_0}{R}\right)^2\frac{\Delta\Theta}{\tau_S} = 0 \quad (27)$$

Using the expressions for the temperature increase upon impact ΔT_0 (see Eq. (1)), the maximum temperature increase during segregation $\Delta\Theta$ (see Eq. (21)) and for the two time constants τ_S and τ_D (see Eqs. (13) and (26)), this condition implies that dissipative heating overcomes the conductive diffusion when

$$R_{Fe} > R_{Fe,min} \quad 28$$

where $R_{Fe,min}$ involves the properties of the planet, but not its radius since ΔT_0 is proportional to R^2

$$R_{Fe,min}^4 = \frac{9}{8\pi}\left(\frac{r_0}{R}\right)^2\frac{1}{c_1 c_2 a}\frac{\Delta T_0}{\Delta\Theta}\frac{\eta_S\kappa}{G\rho_0(1-f_0)\Delta\rho_0}. \quad 29$$

According to the set of parameters shown in Table 1, $R_{Fe,min} \sim 45$ km (using $c_1 \sim a \sim 4/15$, $r_0 \sim R$ and $c_2 \sim 1$). However, using values fitted from experiments does not change this radius very much for the moderate

level of viscosity variations used in our simulations hereafter. Such a diapir corresponds to an impactor of radius R_{imp}~60 km ($R_{imp}=R_{ic}/3^{1/3}=R_{Fe}/(3f_0)^{1/3}$). Therefore, only impactors larger than $R_{imp}=$ 60 km generate metallic diapirs that heat up during sinking, although their initial temperature set by the impact is not dependent on the size of the impactor.

Integration of Eq. (24) leads to

$$\Delta T=\Delta T_0 exp\left(-\frac{t}{\tau_D}\right)+a\left(\frac{r_0}{R}\right)^2\Delta\Theta\frac{2\tau_D}{2\tau_D-\tau_S}\left(exp\left(-\frac{t}{\tau_D}\right)-exp\left(-2\frac{t}{\tau_S}\right)\right). \quad (30)$$

The initial temperature anomaly ΔT_0 decreases exponentially with time while the interplay between diffusion and dissipation controls the general temperature evolution. For the diapir to heat up, the heating time $\tau_S/2$ must be shorter than the diffusive time τ_D. Typically r_0~R and in the regime where the diapir heats up, the dissipation occurs before the diffusion, $\tau_S/2 \ll t \ll \tau_D$; the temperature rapidly increases to $\Delta T=\Delta T_0+a(r_0/R)^2\Delta\Theta$, and the physical interpretation of a is therefore the percentage of heat dissipated inside the metal. According to Eq. (25), a should be lower than the coefficient c_1 of the Rybczinski–Hadamard velocity as the effective viscosity of the hot diapir η_{le} is likely lower than the average viscosity η_{ls}. For a numerical application we take however $a \sim c_1=4/15 \sim 0.27$ as obtained for the isoviscous Rybczinski–Hadamard velocity. As $\Delta\Theta$ and ΔT_0 are simultaneously proportional to R^2, the maximum temperature of the diapir is at most $\Delta T=4.2\Delta T_0$ and is independent of the planet size.

Dissipation decreases as $\exp(-2t/\tau_s)=(r/r_0)^2$ according to Eq. (12). Hence, the dissipation term in Eq. (24) decreases with depth. When a diapir heats up, its temperature increases therefore to the maximum ΔT_{max} reached at the radius r that satisfies $d\Delta T/dt=0$ or

$$0=-\frac{\Delta T_{max}}{\tau_D}+2a\frac{\Delta\Theta}{\tau_S}\left(\frac{r}{R}\right)^2, \quad (31)$$

which implies

$$\left(\frac{r}{r_0}\right)^2=\frac{\Delta T_{max}}{\Delta T_0}\left(\frac{R_{Fe,\,min}}{R_{Fe}}\right)^4. \quad 32$$

The factor $\Delta T_{max}/\Delta T_0$ varies between 1 (no heating) and 4.2 (maximum estimated temperature). As an example, an impactor of radius 120 km, generates a metallic diapir of 96 km (two times $R_{Fe,min}$) that heats up until it reaches half the radius of the impacted planet. The expression Eq. (32) is only valid when $R_{Fe}>R_{Fe,min}$, otherwise the diapir temperature simply decreases.

5. Numerical simulations

We compare the predictions of the analytical model to spherical axisymmetric calculations of a sinking metallic drop, especially to extract the diffusive and sinking times τ_D and τ_S and the fraction of heat trapped in the metallic phase (e.g., the constants c_1, c_2 and a, that we expect to be close to 4/15, 1 and 4/15). We then compare these results to more complex numerical experiments where a compositional anomaly is generated in the isobaric core after a large impact. The effect of variable viscosity is also studied in these models.

5.1. Numerical models of sinking metallic drops

5.1.1. Sinking velocity

We solve numerically a set of problems in which we introduce metallic spheres ($f_0=1$) of different sizes, tangent to the surface, in undifferentiated planets ($f_0=0.17$) of various radii. From this set of experiments, we compare the temporal evolution of the sphere position to what is predicted by Eq. (12). The calculations presented here are isoviscous for simplicity but variable viscosity will be introduced in more complex cases. Fig. 2 shows that the values of τ_S obtained by fitting the center of the diapir position to an exponential in the numerical models, vary as $1/R_{Fe}^2$ as expected from the analytical model, with $c_1=0.187$ (almost 70% of the Hadamard–Rybczynski velocity for a homogenous viscosity $4/15=0.27$). For large sphere radii, boundary effects are stronger and the sinking times are slightly larger.

5.1.2. Temperature evolution

Large sinking diapirs heat up before cooling down by diffusion when the velocity of the metal decreases sufficiently towards the center. Our theoretical predictions given by Eq. (30) are in good agreement with the computed evolutions using the value c_1 obtained previously. Fig. 3 shows the consistency between the numerical results and the theory when the parameters c_2 and a are fitted ($c_2=0.72$, $a=0.2$ which is reasonably close to $c_1=0.187$). The value of a, indicates that 20% of the released heat is trapped in the metal. The maximum temperature value, $2.2\Delta T_0$, is in rough agreement with the estimate $\Delta T=\Delta T_0+a(r_0/R)^2\Delta\Theta=2.88\Delta T_0$. This value is obtained for sufficiently large impactors (>200 km) since smaller ones can cool off very early upon sinking as seen from Eq. (32).

We monitor the temperature evolution for various diapir radii. Fitting the temperature evolution with Eq. (30) leads to values of τ_D and a for each diapir radius. The corresponding characteristic diffusive times are plotted in Fig. 4. These times are consistent with analytical

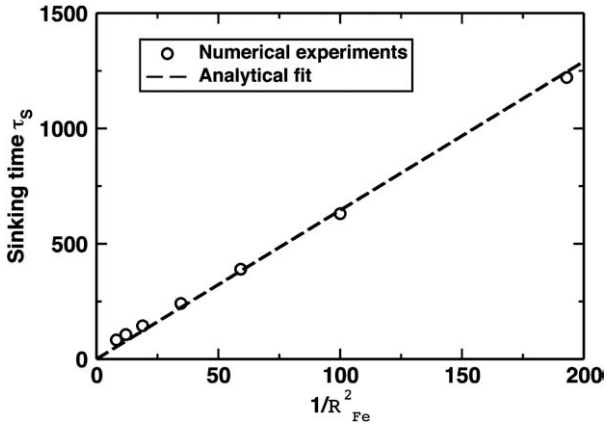

Fig. 2. Characteristic sinking time τ_S as a function of $1/R_{Fe}^2$ normalized with the impacted planet radius.. Results from numerical experiments (with uniform viscosity $\eta_{ls}=10^{22}$ and $R=1000$ km) are represented with black circles. Theoretical fit from Eq. (13) is shown by the dashed line with $c_1=0.187$.

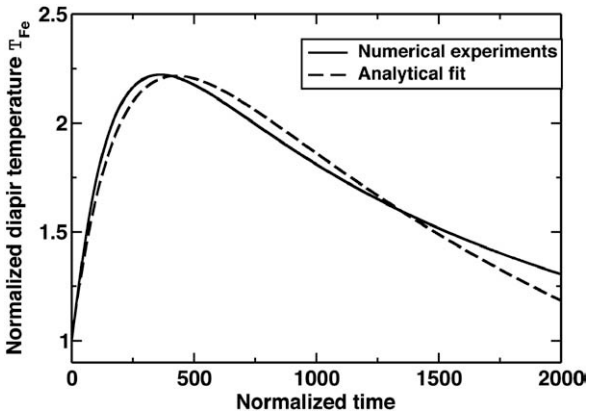

Fig. 3. Temperature evolution (black line) of a metallic sphere ($R_{Fe}=130$ km) falling in an undifferentiated planet with $R=1000$ km. Theoretical evolution from Eq. (30) is shown with a dashed line ($c_1=0.187$, $c_2=0.72$ and $a=20\%$).

predictions from Eq. (26) and increase with the square of the diapir size. For all the experiments, the fraction of heat a trapped in the metal is therefore reasonably constant ($\sim 22 \pm 5\%$) and close to c_1.

To verify Eq. (32) that predicts the radius for which dissipation overcomes diffusion, we computed the rate of heating or cooling of metallic spheres as a function of their radius and depths. Various planetary radii have been used and, as predicted, the heating always occur in the external part of the planet (filled symbols). Near the center of the impacted planet, when the gravity decreases, diffusion dominates (open symbols) and the temperature of the sinking metallic phase decreases. As shown in Fig. 5, the transition between heating and cooling occurs consistently within the shaded area predicted by the analytical expressions Eq. (32). For small diapirs (i.e. for $R_{Fe} \leq 45$ km), diffusion dominates and prevents heating. Large diapirs reach their maximum temperature and start cooling near the high temperature estimate of the analytical model.

5.2. Application to global evolution after an impact

The thermo-chemical initial conditions after an impact differ from a simple hot metallic sphere sinking within an undifferentiated material. Indeed, the denser metallic pond collected at the bottom of the isobaric core is not spherical and above it, a volume of light silicates rises and spreads underneath the surface until it covers the entire surface of the planet. These deviations from our analytical model potentially modify the results obtained from the sinking metallic drop model. Here we show numerical simulations of segregation after an impact and compare them to the analytical model previously developed.

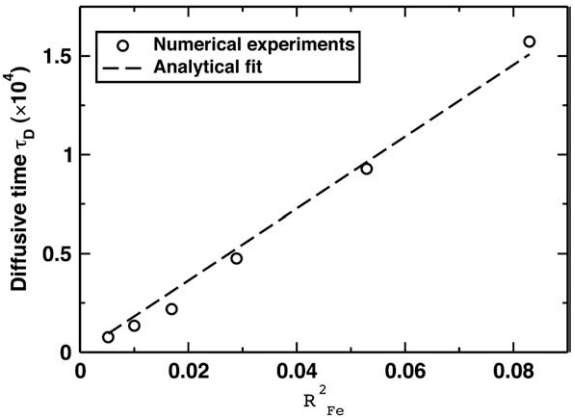

Fig. 4. Non-dimensional characteristic time of diffusion τ_D as a function of the non-dimensionalized metallic sphere radius. Results from numerical experiments (with a uniform viscosity and $R = 1000$ km) are represented with black circles. Theoretical fit from Eq. (26) is shown in dashed line with $c_2 = 1.01$.

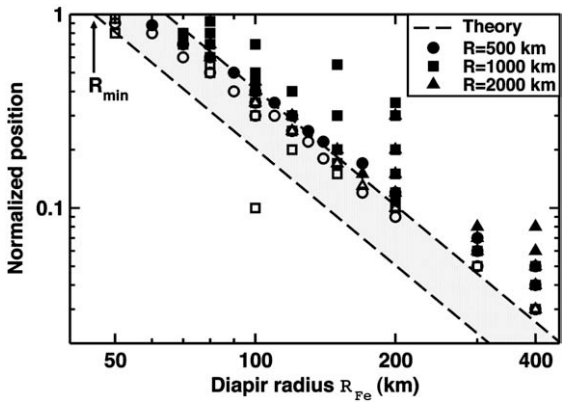

Fig. 5. Thermal behaviour of a sinking metal sphere in an undifferentiated media as function of position and sphere radius. Each symbol represents the instantaneous thermal behaviour of a hot metallic sphere with radius R_{Fe} for a given initial position. Filled symbols represent numerical experiments with viscous heating and open symbols represent numerical experiments with only cooling. Different symbols characterize different planets radii. The analytical transition between heating and cooling is predicted within the shaded area and the boarders of this area are defined with $\Delta T_{max}/\Delta T_0$ between 1 (no heating) and 4.2 (maximum heating) (see, Eq. (32)).

Fig. 6 depicts the thermal and compositional evolution after an impact of a large impactor ($R = 4000$ km, $R_{imp} = 600$ km and $R_{Fe} = 480$ km). The four rows correspond to real time snapshots at 0, 1.4, 3.8 and 546 Myrs. The temperature field is depicted in the left column, and the composition in the right column (undifferentiated material in light blue, metal in red, silicates in green). The metallic pond sinks towards the center of the planet while heating. This heating is in agreement with our previous findings that dissipation is larger than diffusion for large impacts. However, the metal develops a tail through sinking and is significantly deformed. In the meantime, the light silicates rise upward and heat up as well, while stretching laterally to cover the whole surface of the planet. Of course, the diffusion of heat out of the silicate layer near the surface, is much faster than that out of the deep protocore and this shallow hot silicate layer cools rapidly. On a much longer time scale (assuming unrealistically that no other impact occurs, hot thermal plumes should start from the proto core–mantle boundary and deliver the protocore heat to the surface (Behounkova and Choblet, 2009).

Fig. 7 illustrates the evolution of the conversion from potential to thermal energy with time. During the thermo-chemical reequilibration, the potential energy (thick line) decreases as the metal approaches the center and as the silicates spread beneath the surface. Viscous heating induces an increase of thermal energy (grey line). Once the metal has reached the center of the impacted protoplanet, the thermal energy can only decrease. During this whole process, heat

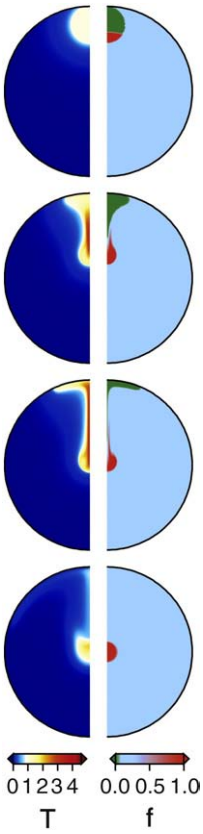

Fig. 6. Non-dimensional temperature (left) and composition (right) at times $t = 0$ (first line), $t = 1.4$ Myr (second line), $t = 3.8$ Myr (third line) and $t = 546$ Myr (fourth line) (computed for a uniform viscosity with $R = 4000$ km, $R_{imp} = 600$ km and 200×200 grid points).

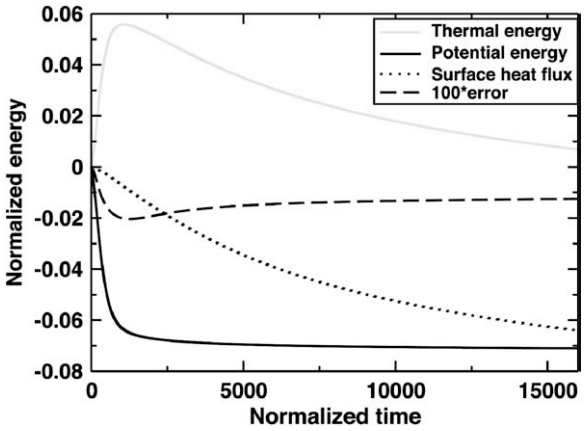

Fig. 7. Non-dimensionalized potential (solid black line) and thermal (solid grey line) energies and time integrated surface heat flow (dotted black line) as functions of time. The sum of these three quantities times 100 is shown in dashed black line. Its difference to zero is indicative of the accuracy of the energy conservation of the numerical code (for $R=2000$ km, $R_{imp}=300$ km and $R_{Fe}=240$ km and uniform viscosity).

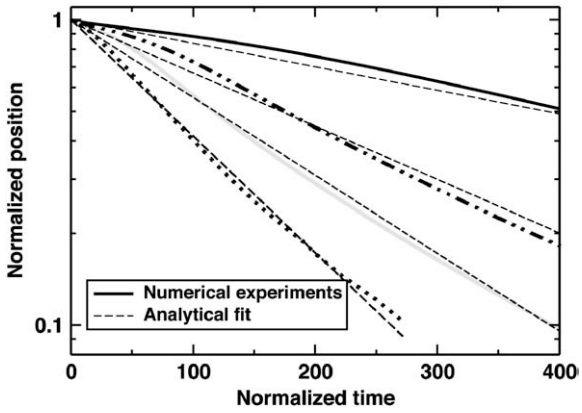

Fig. 9. Position of the inertia center of the metal phase as a function of time for a uniform viscosity (black line) and for temperature-dependent viscosities with $\lambda=0.25$ (dashed dotted line), $\lambda=0.1$ (grey line) and $\lambda=2.5\times10^{-2}$ (dotted line) ($R=2000$ km and $R_{imp}=300$ km). Thin dashed lines correspond to simple exponential fittings from which the sinking times are extracted (see Table 2).

is slowly removed by diffusion through the surface of the planet and the cumulative heat flux (dotted line) balances the total energy budget. This global balance (sum of potential energy, thermal energy and cumulative heat flux (see Eq. (14)) is closely satisfied which illustrates the good accuracy of the numerical code.

We now introduce a temperature-dependence of the viscosity in the calculations. Experimental results suggest that the viscosity contrast between melt iron and solid silicates can reach 20 orders of magnitude (Vocadlo et al., 2000). Such a viscosity contrast is difficult to handle numerically and we use much smaller values.

In our models, the viscosity varies as $\eta=\eta_0\lambda^T$ and as the temperature of metal may increase while sinking by a factor up to 2, it implies maximum viscosity contrasts up to $1/\lambda^2$ orders of magnitude between cold and hot materials. Using a composition dependent viscosity would have been more realistic but viscous fronts are too difficult to handle numerically. We compare the thermo-chemical states at the same time, $t=3.2$ Myr for different viscosity factors in Fig. 8. We use $\lambda=0.25$ (Fig. 8 second row), $\lambda=0.1$ (Fig. 8 third row) and $\lambda=2.5\times10^{-2}$ (Fig. 8 bottom row), the top row being the reference isoviscous case.

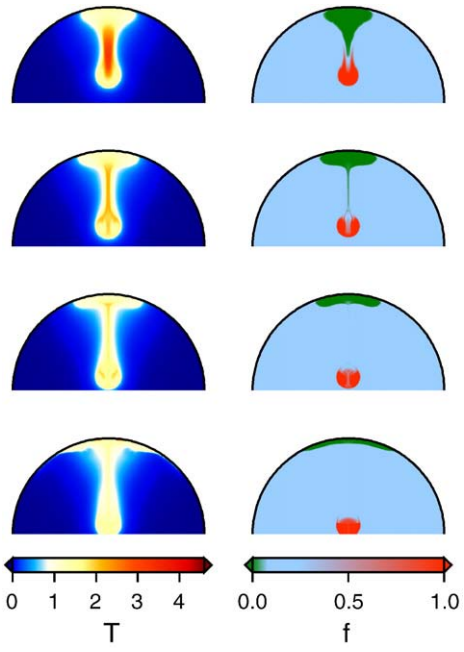

Fig. 8. The four rows depict the temperature (left) and the composition (right) at $t=3.2$ Myr (with $R=2000$ km and $R_{imp}=300$ km), for a uniform viscosity (top) and for variable viscosities (contrast of ~16 (second row), ~100 (third row) and ~1600 (bottom row)). As expected, the sinking velocity of the metallic diapir and the rising velocity of the silicates, both increase when their viscosity is decreased.

Increasing the temperature-dependence of the viscosity softens the surrounding material around the metallic drop and the metallic diapir, at a given time, is closer to the center when its viscosity is decreased, as shown in Fig. 8. However, this effect remains small. Because the metallic pond becomes less viscous, its shape becomes more spherical and the tail developed in isoviscous experiments becomes thinner. Increasing the sinking velocity increases the rate of shear heating but not the total release of thermal energy which is only related to the change in gravitational energy. Lowering the viscosity in the surrounding material and within the metallic pond has also the effect of diminishing η_e. The dissipation is therefore increased in the undifferentiated material and decreased in the hot and less viscous metallic diapir. This effect combined with the faster spreading of the hot silicate that removes the heat more rapidly lead to lower maximum temperatures (see Fig. 8).

We monitor the position of the inertia center of the metallic diapir as a function of time and compute the sinking times τ_S (see Fig. 9). The position of the diapir obeys reasonably the exponential law predicted by Eq. (12). In the isoviscous case, the observed normalized time is $\tau_S=563$ which is twice longer than what is predicted by Eq. (13). This is due to the fact that the initial diapir shape is not spherical and to the presence of the rising volume of silicates. When the viscosity decreases with temperature the sinking is faster, $\tau_S=249$, 170 and 114, for $\lambda=0.25$, 0.1 and 2.5×10^{-2} (see Fig. 9 and Table 2). This is due to two effects: the reduction of viscosity inside the metal (the Rybczinski–Hadamard formula predicts an increase of the velocity factor c_1 from 0.27 to 0.33 when the interior viscosity of the diapir decreases) and the decrease of viscosity of the heated surrounding material.

In the experiments depicted in Figs. 6 and 8, the metal temperature increases and reaches a value close to twice the initial temperature of the isobaric core (Fig. 10). However, heating within the metal is less

Table 2
Values obtained by fitting numerical experiments with theoretical predictions (Eqs. (12) and (30)) for different values of λ (with $R=2000$ km and $R_{imp}=300$ km).

	$\lambda=1$	$\lambda=0.25$	$\lambda=0.1$	$\lambda=2.5\times10^{-2}$
τ_S	563	249	170	114
τ_D	20054	16520	13316	8974
a	19%	14.7%	11%	7%

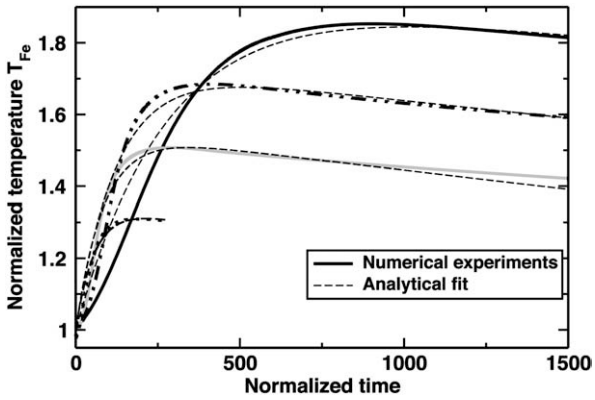

Fig. 10. Temperature evolution of the metal phase as a function of time for a uniform viscosity (solid black line) and for temperature-dependent viscosities with $\lambda = 0.25$ (dashed dotted line), $\lambda = 0.1$ (grey line) and $\lambda = 2.5 \times 10^{-2}$ (dotted line) ($R = 2000$ km and $R_{imp} = 300$ km). Thin dashed lines correspond to theoretical results from Eq. (30) from which the diffusive times and the proportion of energy heating the metal diapir are extracted (see Table 2).

pronounced with variable viscosity and decreases with the viscosity contrast. Fitting the computed temperature evolutions in the metallic diapirs with our theoretical model gives values of c_2 in the isoviscous case and the variable viscosity cases (see Table 2 and Fig. 10). The thickness of the thermal boundary measured by c_2 decreases with the sinking velocity (the Peclet number). The values of c_2 and of τ_D are therefore related to $Pe^{-n} \propto \tau_S^n$ with an exponent ~1/3 in the range of values, $n = 1/2 - 1/3$ predicted in Ribe (2007).

When the temperature dependence of the viscosity increases, the proportion of energy heating the metal diapir, a, decreases (see Table 2). As a consequence, the heat release of the gravitational energy becomes increasingly efficient in the surrounding undifferentiated material. This suggests that a diapir of very small viscosity does not heat much during its motion while most of the release of gravitational energy occurs in the undifferentiated materials. A low viscosity diapir keeps basically its initial temperature because its characteristic diffusive time is larger than its sinking time and also because of the buffering effect of the temperature dependent viscosity (i.e., a too large cooling would increase the viscosity and would bring back the dissipation within the diapir itself).

6. Discussion and conclusion

Core formation events induced by meteoritical impacts play a major role in determining the early thermo-chemical state of growing planets. Large meteoritical impacts can trigger a local differentiation between metal and silicates in a spherical zone above the surface called the isobaric core. The segregation of dense and light phases through the undifferentiated material of the impacted protoplanet induces a large viscous heating.

We followed the dynamics of the metal phase after a large impact with numerical experiments in axisymmetrical spherical geometry. The sinking velocity of the metal phase is Stokes-like and is function of the viscosity contrast between the metal phase and the undifferentiated crossed media. The velocity increases when viscous heating decreases the viscosity of the surrounding material. A stress dependent viscosity (not considered here) would also increase this velocity (Samuel and Tackley, 2008). The sinking process in a planet with a cold interior compared to its surface would eventually imply higher viscosity contrasts between the metal and the surrounding material and would lead to longer sinking times.

The gravitational energy release during the segregation is converted into viscous heating in the metal and in the silicates. Our results show that a net viscous heating of the metallic phase only occurs for large metallic diapirs ($R_{Fe} > 45$ km). This metallic volume at the bottom of the isobaric core would be produced by an impactor of order $R_{imp} > 60$ km. This result underlines the importance of accretion conditions on the inner thermal state of planetary bodies. Small metallic diapirs cool while sinking and may ultimately bring the metal in a solid state to the core of the impacted planet.

The heat repartition between the metal phase, the silicates and the undifferentiated material is not only a function of the size of the metallic diapir but also of the rheology of the various phases. For low viscosity of the metal and of the sheared zone around the metallic diapir, the metal phase is weakly heated. Hence, gravitational energy release will mainly lead to the heating of the surrounding undifferentiated material and ultimately to its differentiation.

The viscosity variations that we explore in our simulations are of order $\lambda^{\Delta T_{max}}$ which in the most extreme cases reach about four orders of magnitude over very short distances. This is certainly modest relative to the viscosity contrasts of 20 orders of magnitude that exist between liquid metal and solid silicates (Vocadlo et al., 2000). Viscosity contrasts based on composition rather than temperature would be more realistic but would have occurred on even shorter distances (the computation grid itself) that could not be resolved with classical numerical methods. Our model is therefore an end-member of possible models on heating modes during core formation. However, the description of the physics of the processes would still be valid for larger viscosity contrasts.

As soon as a growing planet reaches a few thousand kilometers in radius R, the heating by impacts becomes significant (the temperature increase varies as R^2 and reaches 400 K for $R = 3000$ km, (Monteux et al., 2007)). This temperature increase superimposed on the fossil temperature T_0 from short half-life radionucleides (^{26}Al and ^{60}Fe) and previous impacts can lead to a temperature larger than the melting temperature of the metallic phase. Our analytical models confirmed by numerical experiments show that the metallic drop reaches the planet center in a time depending on the size of the metallic drop and the background viscosity of the planet but not of its radius (see Eq. (13)). Even in the case where the impacted planet is relatively cold and with a high viscosity of 10^{22} Pa s, this time is smaller than a few million years for an impactor of 300 km. The sinking timescales obtained in our models are comparable to those obtained with an Arhenius rheology (Ziethe and Spohn, 2007) and within the timeframe required for an early core formation (<60 My). The temperature increase in the undifferentiated material localized along the sinking path of the metallic diapir could provide a preferential low viscosity channel for the following differentiation events.

Proposing predictive models for the thermal consequences of differentiation after an impact is fundamental in order to understand the thermal state of the interior of growing planets. As shown in Ricard et al. (2009), core formation of terrestrial protoplanets could be the consequence of a runaway segregation induced by a large enough impact on undifferentiated material. These results also underline the importance of accretionary conditions (size and temporal repartition of impacts) on the thermal energy repartition and, hence, on the magnetic history of growing planets (Elkins-Tanton et al., 2005).

Acknowledgements

The authors thank H. Samuel, S. Labrosse and M. Jellinek for helpful discussions. The authors also thank H. Schmeling, T. Spohn and anonymous reviewers for constructive comments. This project was funded by the A.N.R. ETHER.

References

Agee, C.B., 1997. Melting temperatures of the Allende meteorite: implications for a Hadean magma ocean. Phys. Earth Planet. Int. 100, 41–47.
Behounkova, M., Choblet, G., 2009. Onset of convection in a basally heated spherical shell, application to planets. Earth Planet. Sci. Lett., submitted.
Christensen, U.R., Yuen, D.A., 1985. Layered convection induced by phase transitions. J. Geophys. Res. 90, 10291–10300.

Croft, S.K., 1982. A first-order estimate of shock heating and vaporization in oceanic impacts. Geological Implications of Impacts of Large Asteroids and Comets on Earth: In: Silver, T.L., Schultz, P.H. (Eds.), Spec. Pap. Geol. Soc. Am., vol. 190.

Davies, G.F., 1982. Ultimate strength of solids and formation of planetary cores. Geophys. Res. Lett. 9, 1267–1270.

Douglas, J., 1955. On the numerical integration of $\frac{\partial^2 u}{\partial x^2} + \frac{\partial^2 u}{\partial y^2} = \frac{\partial u}{\partial t}$ by implicit methods. J. Soc. Ind. Appl. Math. 3, 42–65.

Elkins-Tanton, L.T., Zaranek, S.E., Parmentier, E.M., Hess, P.C., 2005. Early magnetic field and magmatic activity on Mars from magma ocean cumulate overturn. Earth Planet. Sci. Lett. 236, 1–12.

Fei, Y., Bertka, C.M., Finger, L.W., 1997. High-pressure iron–sulfur compound, Fe_3S_2, and melting relations in the FeFeS system. Science 275, 1621–1623.

Flasar, F.M., Birch, F., 1973. Energetics of core formation: a correction. J. Geophys. Res. 78, 6101–6103.

Gerya, T.V., Yuen, D.A., 2007. Robust characteristics method for modelling multiphase visco-elastic thermo-mechanical problems. Phys. Earth Planet. Int. 163, 83–105.

Ghosh, A., McSween, H.Y., 1998. A thermal model for the differentiation of asteroid 4 vesta, based on radiogenic heating. Icarus 134, 187–206.

Golabek, G.J., Schmeling, H., Tackley, P.J., 2008. Earth's core formation aided by flow channelling instabilities induced by iron diapirs. Earth Planet. Sci. Lett. 271, 24–33.

Hadamard, J., 1911. Mouvement permanent lent d'une sphère liquide et visqueuse dans un liquide visqueux. C. R. Acad. Sci. 152, 1735–1738.

Hewitt, J.M., McKenzie, D.P., Weiss, N.O., 1975. Dissipative heating in convective flows. J. Fluid Mech. 68, 721–738.

Höink, T., Schmalzl, J., Hansen, U., 2005. Formation of compositional structures by sedimentation in vigorous convection. Phys. Earth Planet. Int. 153, 11–20.

Honda, R., Mizutani, H., Yamamoto, T., 1993. Numerical simulation of Earth's core formation. J. Geophys. Res. 98, 2075–2090.

Kleine, T., Münker, C., Mezger, K., Palme, H., 2002. Rapid accretion and early core formation on asteroids and the terrestrial planets from Hf-W chronometry. Nature 418, 952–955.

Laney, C.B., 1998. Computational gasdynamics. Cambridge University Press, Cambridge.

Monteux, J., 2009. Modélisation numérique de la formation du noyau terrestre : contribution des impacts météoritiques. Ph.D. thesis, Université Claude Bernard Lyon 1.

Monteux, J., Coltice, N., Dubuffet, F., Ricard, Y., 2007. Thermo-mechanical adjustment after impacts during planetary growth. Geophys. Res. Lett. 34, 24201–24205.

O'Keefe, J.D., Ahrens, T.J., 1977. Impact-induced energy partitioning, melting, and vaporization on terrestrial planets. In: Merril, R.B. (Ed.), Lun. Planet. Sci. Conf., vol. 8, pp. 3357–3374.

Peaceman, D.W., Rachford, H.H., 1955. The numerical solution of parabolic and elliptic differential equations. J. Soc. Ind. Appl. Math. 3, 28–41.

Pierazzo, E., Vickery, A.M., Melosh, H.J., 1997. A reevaluation of impact melt production. Icarus 127, 408–423.

Ratcliff, J.T., Tackley, P.J., Schubert, G., Zebib, A., 1997. Transitions in thermal convection with strongly variable viscosity. Phys. Earth Planet. Int. 102, 201–212.

Ribe, N.M., 2007. In: Schubert, G. (Ed.), Analytical Methods in Mantle Dynamics, Treatise of Geophysics, vol. 7. Elsevier.

Ricard, Y., 2007. In: Schubert, G. (Ed.), Physics of Mantle Convection, Treatise of Geophysics, vol. 7. Elsevier.

Ricard, Y., Sramek, O., Dubuffet, F., 2009. A multi-phase model of runaway core–mantle segregation in planetary embryos. Earth Planet. Sci. Lett., in press.

Roe, P.L., 1986. Characteristic-based schemes for the Euler equations. Annu Rev Fluid Mech 18, 337–365.

Rybczynski, W., 1911. über die fortschreitende bewegung einer flüssigen kugel in einen medium. Bull. Acad. Sci. Cracovie 1, 40–46.

Samuel, H., Tackley, P.J., 2008. Dynamics of core formation and equilibration by negative diapirism. Geochem. Geophys. Geosyst. 9, 6011–6026.

Schubert, G., Turcotte, D.L., Olson, P., 2001. Mantle convection in the Earth and planets. Cambridge University Press. Sep.

Senshu, H., Kuramoto, K., Matsui, T., 2002. Thermal evolution of a growing Mars. J. Geophys. Res. 107, 1–13.

Shannon, M.C., Agee, C.B., 1996. High pressure constraints on percolative core formation. Geophys. Res. Lett. 23, 2717–2720.

Sramek, O., 2007. Modèle d'écoulement biphasé en sciences de la terre: Fusion partielle, compaction et différenciation,. Ph.D. thesis, Ecole Normale Supérieure de Lyon.

Stevenson, D.J., 1989. Formation and early evolution of the Earth. In: Peltier, W.R. (Ed.), Mantle convection and plate tectonics.

Stevenson, D.J., 1990. Fluid dynamics of core formation. In: Newsom, H.E., Jones, J.H. (Eds.), Origin of the Earth. Oxford Univ, New York.

Tonks, W.B., Melosh, H.J., 1992. Core formation by giant impacts. Icarus 100, 326–346.

Touboul, M., Kleine, T., Bourdon, B., Palme, H., Wieler, R., 2007. Late formation and prolonged differentiation of the Moon inferred from W isotopes in lunar metals. Nature 450, 1206–1209.

Vocadlo, L., Alfè, D., Price, G.D., Gillan, M.J., 2000. First principles calculations on the diffusivity and viscosity of liquid Fe–S at experimentally accessible conditions. Phys. Earth Planet. Int. 120, 145–152.

Von Bargen, N., Waff, H.S., 1986. Permeabilities, interfacial areas and curvatures of partially molten systems: results of numerical computations of equilibrium microstructures. J. Geophys. Res. 91, 9261–9276.

Yin, Q., Jacobsen, S.B., Yamashita, K., Blichert-Toft, J., Télouk, P., Albarède, F., 2002. A short timescale for terrestrial planet formation from Hf-W chronometry of meteorites. Nature 418, 949–952.

Yoshino, T., Walter, M.J., Katsura, T., 2003. Core formation in planetesimals triggered by permeable flow. Nature 422, 154–157.

Ziethe, R., Spohn, T., 2007. Two-dimensional stokes flow around a heated cylinder: a possible application for diapirs in the mantle. J. Geophys. Res. 112, 1–13.

Please cite this article as: Monteux, J., et al., A model of metal–silicate separation on growing planets, Earth Planet. Sci. Lett. (2009), doi:10.1016/j.epsl.2009.08.020

Earth and Planetary Science Letters 403 (2014) 236–245

Contents lists available at ScienceDirect

Earth and Planetary Science Letters

www.elsevier.com/locate/epsl

Laboratory experiments on the breakup of liquid metal diapirs

Jean-Baptiste Wacheul [a,b], Michael Le Bars [a,c,*], Julien Monteux [d], Jonathan M. Aurnou [a]

[a] Department of Earth, Planetary and Space Sciences, University of California, Los Angeles, CA 90095-1567, USA
[b] Ecole Normale Supérieure, Paris, France
[c] CNRS, Aix-Marseille Université, École Centrale Marseille, IRPHE UMR 7342, Marseille, France
[d] Laboratoire de Planétologie et de Géodynamique, LPG Nantes, CNRS UMR 6112, Université de Nantes, France

ARTICLE INFO

Article history:
Received 21 January 2014
Received in revised form 14 May 2014
Accepted 26 June 2014
Available online 24 July 2014
Editor: C. Sotin

Keywords:
metal diapir
breakup
core formation
magma ocean
metal–silicate equilibration
laboratory experiments

ABSTRACT

The validity of the iron rain scenario, i.e. the widely accepted model for the dynamics of iron sedimentation through a magma ocean during the latest stage of the Earth's accretion, is explored via a suite of laboratory experiments. Liquid gallium and mixtures of water and glycerol are used as analogs of the iron and the molten silicate respectively. This allows us to investigate the effects of the viscosity ratio between iron and silicate and to reproduce the relevant effects of surface tension on the fragmentation dynamics. While the classical iron rain scenario considers a population of purely spherical drops with a single characteristic radius that fall towards the bottom of the magma ocean at a unique velocity without any further change, our experiments exhibit a variety of stable shapes for liquid metal drops, a large distribution of sizes and velocities, and an intense internal dynamics within the cloud with the superimposition of further fragmentations and merging events. Our results demonstrate that rich and complex dynamics occur in models of molten metal diapir physics. Further, we hypothesize that the inclusion of such flows into state of the art thermochemical equilibration models will generate a similarly broad array of complex, and likely novel, behaviors.

1. Introduction

Differentiation of Earth into a core and a mantle was likely completed within the first tens million years after its accretion (e.g. Stevenson, 1990; Boyet et al., 2003; Boyet and Carlson, 2005). Numerical simulations (Neumann et al., 2012) and geochemical data on meteorites (Yoshino et al., 2003) also show that small planetesimals could have differentiated even earlier when accounting for heating by decay of short-lived radionuclides. There is also strong evidence that the Earth's late accretion is due to collisions with large planetesimals (a tenth to a third of Earth mass), when both the impactor and the proto-Earth were already differentiated (Morbidelli et al., 2012). During accretion, the Earth and other planets in formation underwent several mechanisms of heating: 1) the decay of relatively abundant radioactive elements with short half-life (Merk et al., 2002; Walter and Tronnes, 2004), 2) the conversion of gravitational potential energy by viscous forces during differentiation (Rubie et al., 2007; Monteux et al., 2009; Samuel, 2012), 3) the collisions themselves with the conversion of huge amount of kinetic energy (Safronov, 1978; Kaula, 1979; Reese and Solomatov, 2006; Monteux et al., 2007), these impacts alone being able to generate a local melting resulting in a shallow magma ocean (Tonks and Melosh, 1992). In addition, the primitive atmosphere was certainly much more opaque to IR radiation, so the effect of thermal blanketing was highly efficient (Abe and Matsui, 1985). Thus, according to the simulations, Earth has probably had one or several episodes of global magma ocean, with depths possibly reaching thousands of kilometers (Tonks and Melosh, 1993). In this context, further impacts of differentiated planetesimals would require, in order for the cores of the Earth and the meteorites to merge, that the latter flows through the magma ocean (Fig. 1). This process can be seen as a secondary step of mixing between core and mantle, since it could lead to partial or complete thermo-chemical equilibration between the sinking metal and the molten surrounding silicates, depending on the characteristics of the flow of the core material through the mantle.

The importance of this exchange is an issue for the interpretation of numerous geochemical proxies, such as the tungsten 182 signal. Hafnium (^{182}Hf) disintegrates in tungsten (^{182}W) with a relatively short half-life of 9 My, comparable with the time scale of core differentiation. They are both refractory but tungsten is siderophile whereas hafnium is lithophile. This is why the

* Corresponding author at: CNRS, Aix-Marseille Université, École Centrale Marseille, IRPHE UMR 7342, Marseille, France. Tel.: +33 4 13552020; fax: +33 4 13552001.
E-mail address: lebars@irphe.univ-mrs.fr (M. Le Bars).

http://dx.doi.org/10.1016/j.epsl.2014.06.044
0012-821X/

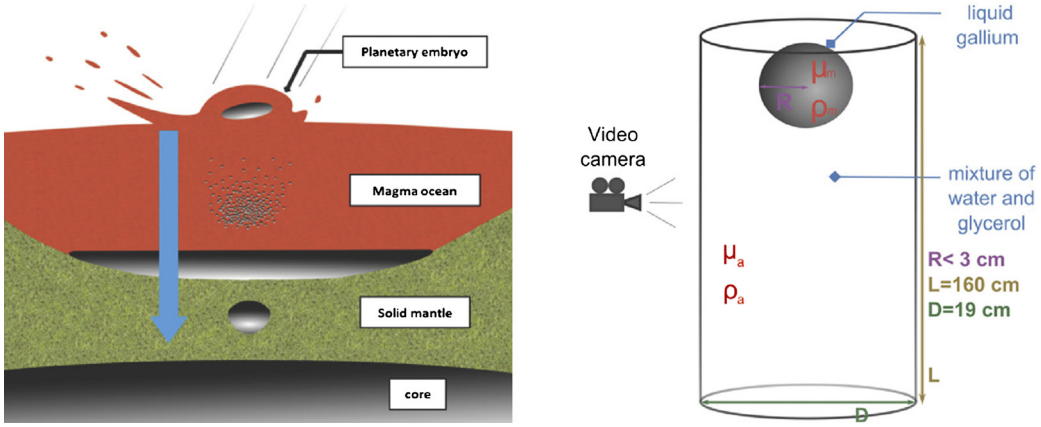

Fig. 1. Left: schematic of the metal/silicate separation after the impact of a differentiated planetesimal with the early Earth in reference to the work of Stevenson (1990). The equilibration by diffusion between the impactor's core and the magma ocean during the metal rainfall and later when sinking through the solid mantle as a large diapir is poorly constrained, and strongly depends on the fluid dynamics of the iron sedimentation. Right: schematic of our experiment.

^{182}Hf–^{182}W system has been used in multiple studies to approximate the age of terrestrial bodies' core (Lee and Halliday, 1996; Harper and Jacobsen, 1996; Kleine et al., 2004). However due to the late impacts and possible mixing that could occur, there are very poor constraints on which event – late impacts or core differentiation – is relevant for the interpretation of the ratio ^{182}W/^{184}W. Then the age given by this proxy could be any intermediary between the initial differentiation of the proto-Earth and the most recent giant impact that it endured, depending on how much ^{182}W has been absorbed by the asteroid's core during its passing through the mantle (Kleine et al., 2004). The same kind of interrogation can be held against interpretations of the U/Pb proxy, and for the coefficients of partition between metal and silicate, which strongly depend on the details of the small-scale processes at the iron–silicate interface during sedimentation. Actually, these interfacial dynamics influence every mechanism of equilibration by diffusion, such as diffusion of heat and diffusion of momentum by viscosity, both leading to indetermination on the initial thermal state of the mantle and the core, and on the repartition of the energy between these two (Monteux et al., 2009; Samuel et al., 2010). Thus, in order to model the evolution of both Earth's core and mantle, it is important to understand the fluid dynamics at the drop scale during the iron sedimentation (Solomatov, 2000). Towards this goal, we present here novel laboratory experiments investigating the fluid dynamics of sedimenting liquid metal droplets.

2. Parameters controlling the fluid dynamics of the iron sedimentation

The equilibration between the iron and molten silicate strongly depends on the typical size of the metal entities. Indeed, for a given volume of metal, a single large diapir would fall rapidly through the magma ocean with a relatively small surface of exchanges, while the fragmentation of the same volume of iron through a large number of small structures broadens the surface area of exchanges and slows down the falling velocity, hence extending the time during which iron and silicate equilibrate. Note that in the present paper, we generically use the term diapir to designate any large blob of fluid moving through an ambient fluid via the action of buoyancy forces.

Several approaches have been developed in order to give a physically coherent description of what happens when a liquid iron diapir falls through a magma ocean, and ultimately to provide a time scale for the equilibration. At first order, the shape of the falling diapir is dominated by two forces. The surface tension tends to stabilize a spherical shape, while the dynamic pressure deforms the diapir and tears it apart. Let us assume for instance, a typical diapir with a radius $R_0 = 10$ km falling at the inviscid, free fall Newtonian velocity V valid for a rigid sphere

$$V \simeq \sqrt{\frac{\Delta\rho}{\rho_a} g R_0}, \tag{1}$$

where ρ_a is the silicate density ("a" standing for "ambient"), $\Delta\rho$ is the density difference between iron and silicate, and g is the gravitational acceleration. Assuming an Earth with more than half its final mass, V is close to 1 km/s. The Re number for the flow in the mantle, which estimates the ratio of the inertial and viscous forces, is

$$Re_a = \frac{\rho_a V R_0}{\mu_a} \gtrsim 10^{10}, \tag{2}$$

where μ_a is the silicate dynamic viscosity. This large Re value provides an *a posteriori* validation of the inviscid velocity estimate provided by Eq. (1). It also implies that dynamic pressure scales as the inertia. On the other hand, the characteristic strength of surface tension is directly linked to the radius of curvature of the surface, so its order of magnitude roughly depends on the radius of the spheroid diapir R_0. A good estimation of the stability of a diapir is given by the Weber number, which is the ratio of the inertial and surface tension forces:

$$We_a = \frac{\rho_a V^2 R_0}{\sigma}, \tag{3}$$

where σ is the coefficient of surface tension. For $We \gg 1$, diapirs are unstable and break-up. Below some threshold of order 1 (e.g. $We_c = 6$ for rain drops, see Villermaux and Bossa, 2009), surface tension and inertia compensate, and the diapir is stable. This widely used breakup criterium (e.g. Tonks and Melosh, 1992; Rubie et al., 2003; Dahl and Stevenson, 2010; Deguen et al., 2011) allows a calculation of the maximal radius for stable diapirs, given some hypothesis regarding its falling speed. For the simple Newtonian velocity scaling given by (1), the maximal radius corresponds to

$$R_{cap} \simeq \sqrt{We_c \frac{\sigma}{\Delta\rho g}}, \tag{4}$$

which is about 1 to 2 cm for the Earth's iron–silicate system. Such a criterium is well known in the case of water drops in the air, for which it has been confirmed by experiments (Villermaux and Bossa, 2009). It has also been supported by a recent numerical study designed for the case of an iron diapir in molten

silicate (Samuel, 2012). In this study, the initial spherical diapir flattens, then breaks up within a distance of no more than 10 diapir radii. The diapir's sons keep breaking up, cascading downward to the scale R_{cap} where surface tension compensates the pressure forces. However, in these axisymmetric simulations, the breakup is not actually computed, but is supposed to occur shortly after the topological change from pancake to torus. Thus, the size of the resulting drops remains unknown. According to this scenario, there is no way for a 10 km radius diapir corresponding to a Weber number above 10^{14} to remain entirely intact during its fall. It should rapidly break up into a cloud of drops of radius R_{cap}, *i.e.* the so-called "iron rain". Then, most models of metal–silicate equilibration (e.g. Rubie et al., 2003; Ulvrová et al., 2011; Samuel, 2012) assume that all iron drops have an identical and fixed spherical shape with a radius equal to R_{cap} and a unique sedimentation velocity based on free fall models.

On the other hand, for diapirs with a radius of 10 km and above, the Weber number is so large (above 10^{14}) that its dynamics are controlled by the inertia of the flow only, allowing one to completely ignore the effects of surface tension. The resulting miscible models lead to interesting findings. For instance, Deguen et al. (2011) supposed that the diapir rapidly becomes a cloud of drops that then evolves in a coherent manner as a buoyant thermal, whose radius grows linearly with depth because of turbulent mixing with the outside. They found that for a shallow magma pond created by an impact as for a deep magma ocean (Deguen et al., 2014), there should be enough dilution between metal and silicate for them to reach chemical equilibration. On the contrary, Dahl and Stevenson (2010) considered a diapir with an almost constant shape eroded by Raleigh–Taylor and Kelvin Helmholtz instabilities. Their conclusions were very different: erosion was found to be insufficient to allow for full equilibration for diapirs with a radius above 10 km.

Open questions thus remain on all stages of the iron sedimentation, from the large-scale dynamics to the behavior at the smallest scales, where surface tension modifies the modalities of diffusive exchanges. In this context, the numerical study by Ichikawa et al. (2010), in agreement with the results for water drops in the air (Villermaux and Bossa, 2009), pointed out that the cloud of drops contains a whole distribution of sizes and not just a single one (Karato and Murthy, 1997). Furthermore, the distribution of speeds and the relation between size and speed of drops are not trivial, supporting the idea that the iron rain scenario with a single size and speed may be inaccurate. However, the conclusions of Ichikawa et al. (2010) are supported mostly by 2D numerical simulations, where surface tension is not properly rendered. Hence they still need confirmation.

In addition, it is worth noting that all previous studies of the stability of diapirs have neglected the influence of the viscosity ratio between the ambient fluid and the metal

$$r_\mu = \frac{\mu_a}{\mu_m}. \tag{5}$$

When the magma ocean cools down, or as the diapir goes deeper into the mantle, the magma becomes closer to the solidus and contains more crystals. Therefore, the viscosity of the magma is expected to increase from 10^{-3} to 10^{2} Pa s, corresponding to r_μ ranging from 1 to 10^5 (Deguen et al., 2011; Samuel, 2012). Such a large viscosity ratio is known to have a significant effect on the shape of falling drops (e.g. Bonometti and Magnaudet, 2006; Ohta et al., 2010). Indeed, from the continuity of the velocity and the stress tensor at the drop interface, a large r_μ in a large Reynolds number flow implies intense internal recirculations inside the drop, which then deforms and may be dynamically stabilized. This has not been investigated in a geophysical context.

Table 1
List of relevant parameters and typical Earth's and experimental values.

Symbol	Parameter	Value for the Earth	Value in our experiment
ρ_a	ambient fluid density	3000 kg m^{-3}	997–1260 kg m^{-3}
ρ_m	liquid metal density	7000 kg m^{-3}	6095 kg m^{-3}
μ_a	ambient fluid viscosity	10^{-3}–10^{2} Pa s	10^{-3}–1 Pa s
μ_m	liquid metal viscosity	10^{-3} Pa s	1.9×10^{-3} Pa s
r_μ	viscosity ratio	1 to 10^5	0.5 to 500
σ	surface tension	1 J m^{-2}	0.7 J m^{-2}

Here we report the first experiments designed to simulate the last stages of the fragmentation process with realistic values of the iron–silicate viscosity ratio and relevant behaviors regarding the effects of surface tension on the fragmentation dynamics. The set-up is presented in Section 3. In Section 4, we investigate the variety of stable shapes for iron drops, as well as their mutual interactions and dynamics after the initial breakup. The measured distributions of size and velocity are presented in Sections 5 and 6, highlighting the influence of the viscosity ratio. The relevance of the complex fluid dynamics shown by our experiments to the Earth is illustrated in Section 7 by a simple equilibration model based on our results. Conclusions and open questions are given in Section 8.

3. Set-up and methods

Our experimental set-up is sketched in Fig. 1. As an analogue for the magma ocean, we use a 160 cm high cylindrical tank, with a diameter of 19 cm, filled with a mixture of water and glycerol. The glycerol (resp. water) has a dynamic viscosity of 1.08 Pa s (resp. 0.00093 Pa s) at room temperature (23 °C): the mixture of the two allows us to explore a range of 3 orders of magnitude for the viscosity of the ambient fluid μ_a, with a density ranging from $\rho_a = 1260$ kg m^{-3} for pure glycerol to $\rho_a = 997$ kg m^{-3} for pure water. As an analogue for the liquid iron diapir, we use liquid gallium. It has a viscosity $\mu_m = 1.9 \times 10^{-3}$ Pa s and a density $\rho_m = 6095$ kg m^{-3} (King and Aurnou, 2013). The gallium is initially contained in a latex balloon at the top of the set-up; the ballon is then popped by a syringe needle at the beginning of the experiment. This method has two advantages: the amount of gallium is precisely known by weighing the balloon, and since the retraction of the balloon occurs within about 1/50 s, the diapir has no initial speed and its initial shape is the one imposed by the balloon. The fall of the diapir is then recorded by a high speed USB camera at 136 frames per second, with a resolution of 196 × 1280 pixels (examples of these videos can be viewed at https://www.youtube.com/watch?v=g-AmGmWWK1o&list=UU7u8FUioww0nKsdXPO6emhA). In addition to this camera, higher resolution videos of the lower part of the experiment are taken at 60 frames per second with a resolution of 1280 × 720 pixels. Beyond direct visualization, the videos are used to recover the shape and velocity of the droplets, after removing the background and after binarization. Each droplet in a selected frame is detected using the Matlab Image Processing toolbox, and an equivalent radius is retrieved by measuring its apparent area A and applying the formula $r = \sqrt{A/\pi}$. This is a lower estimate since the drops are oblate at different degrees. We also construct space–time diagrams by extracting the same horizontal line from all frames of a chosen video. The resulting image then gives us the horizontal radius of each droplet reaching the selected depth as well as its arrival time, hence its mean fall velocity.

Relevant parameters are listed in Table 1 in comparison with Earth's values. Experiments were run with 6 different sizes of the initial diapir ranging from an equivalent radius of 14 mm to 30 mm, and with 4 viscosities of the ambient fluid 0.001, 0.01, 0.1 and 1 Pa s. In the inertial regime, the characteristic velocity of the

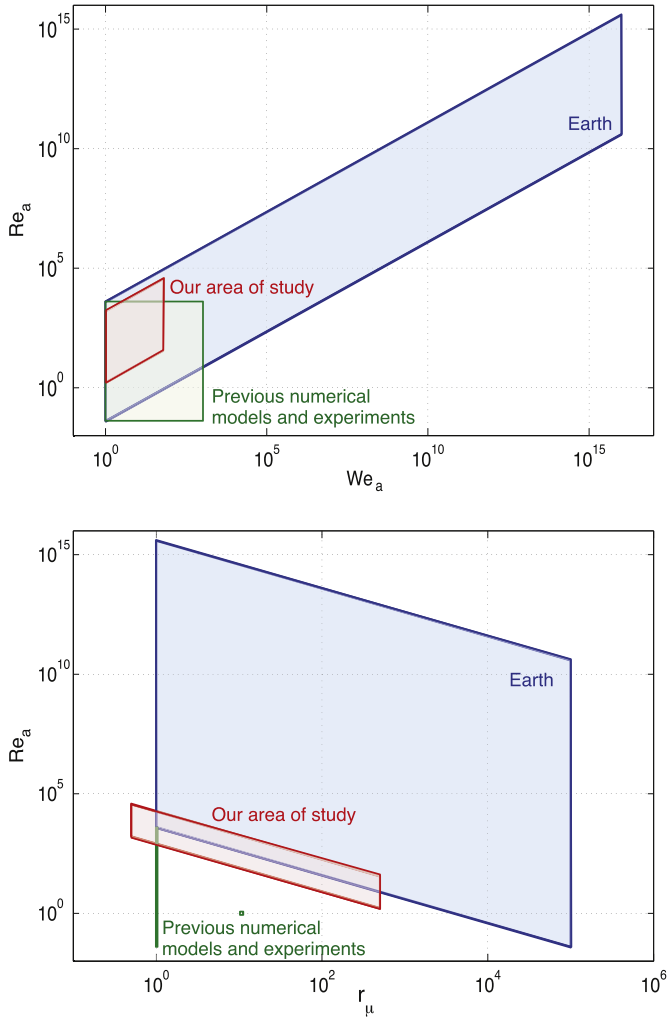

Fig. 2. In blue, area of the parameter space associated with the fall of iron diapirs in the context of Earth's accretion. Variations are due to changes in the viscosity of the magma ocean and in the diapir radius, ranging from its initial value to the radius corresponding to a Weber number of 1. For comparison, the area explored by previous studies (Ichikawa et al., 2010; Samuel, 2012; Deguen et al., 2014) is shown in green, whereas the parameter space explored by the present study is shown in red. (For interpretation of the references to color in this figure legend, the reader is referred to the web version of this article.)

flow scales as the Newtonian velocity introduced in Eq. (1). Then, the dynamics is entirely characterized by four dimensionless parameters: the density ratio $\Delta\rho/\rho_a$, the viscosity ratio $r_\mu = \mu_a/\mu_m$, and the Newtonian Reynolds and Weber numbers Re_a and We_a (based on the Newtonian velocity). In our experiment, $\Delta\rho/\rho_a$ remains almost constant at about 5 (the ambient density only marginally varies with the proportion of water), which means that as in the geophysical setting, density changes are of order 1, such that the Boussinesq approximation cannot be applied. With the accessible range of initial diapir radii, we are able to produce initial Reynolds numbers from 10 to 4×10^4 and initial Newtonian Weber numbers from 14 to 64. As shown in Fig. 2, this is obviously limited compared to the possible geophysical values, especially for diapirs with large initial radius. But even if the dynamic similitude between the experiment and reality is not exact, the experiments are capable of reaching the relevant dynamical regime, with a fully turbulent flow and a Weber number above the critical value for breakup. Furthermore, the similitude is exact for diapir radii around the decimeter scale, hence for the final stages of the fully-developed iron rain. Note finally that our experiment is the first one to take into account the effects of the viscosity ratio, which spans the range 0.5–500 in our set-up.

4. Zoology of the breakup

The results of 3 experiments in pure glycerol with different initial radius of the diapir are shown in Figs. 3A, 3B and 4. Fig. 5 shows a closer look of the various possible shapes of gallium drops obtained in the experiment presented in Fig. 4. According to the classical iron rain scenario applied to our experimental set-up, any diapir with a Weber number larger than 6 should rapidly give rise to a cloud of spherical drops with a single characteristic radius $R_{cap} = 1$ cm that should fall with a Newtonian velocity $V = 74\ \mathrm{cm\,s^{-1}}$, without any further dynamical change. This is not the case.

For the lowest initial radius (Fig. 3A), the diapir is stable even if its Weber number is above the known threshold 6 (note that the effective Weber number is $\simeq$9, calculated using the measured falling velocity instead of the scaling given by Eq. (1)). One can also notice that its equilibrium shape is not spherical: the drop takes the form of a cap, where the intense internal recirculation driven by viscous coupling with the ambient fluid stabilizes the non-spherical shape of the molten metal droplet (see also the sketch in Fig. 5B). The viscosity ratio strongly influences the shape and the condition for stability of a single structure, as found in the studies of Bonometti and Magnaudet (2006), Ohta et al. (2010) using axisymmetric numerical simulations. There is a clear tendency for large viscosity ratios to stabilize the drops, and the diapir shown in Fig. 3A is indeed unstable for r_μ below 50 (not shown here). According to results in Bonometti and Magnaudet (2006), Ohta et al. (2010), which are coherent with our experimental observations, the critical Weber number can actually be more than one order of magnitude larger than the classically used value $We_c = 6$, depending on the viscosity ratio and the initial shape of the drop.

The slightly larger diapir shown in Fig. 3B rapidly breaks up into three large caps plus some smaller drops. A striking point here is that after this initial break-up, the dynamics is not frozen: the three caps interact and two of them finally merge to re-build a larger diapir. For comparison, the same experiment but with an ambient viscosity 100 times less viscous is shown in Fig. 3C. The initial behavior of the diapir is similar but the breakup dynamics is clearly different, even if the Weber number is the same in both experiments. The Reynolds number is greater in Fig. 3C because of the smaller ambient viscosity; but comparing both series of pictures, one can notice that the falling velocities are close in the two experiments: both cases are in the Newtonian regime, and changes in Re_a cannot explain changes in the fragmentation behavior. Thus, we argue that the differences between Figs. 3B and 3C are due to viscosity ratio effects, which allow for the dynamical stabilization of larger drops by strong internal recirculations in case 3B.

The dynamics of initially large diapirs systematically follows the series of stages illustrated in Fig. 4: after a short acceleration, we observe waves forming on the surface of the diapir, qualitatively similar to the description of Dahl and Stevenson (2010). But almost simultaneously, the diapir flattens as the wave amplitudes rise: it evolves towards a thin wavy sheet where the axisymmetry is fully broken. It breaks up shortly after this stage: holes appear in the sheet, the transient ligaments retract and break-up. The drops resulting from this burst have various sizes and shapes, and the biggest ones continue to break up in the same way until a steady-state is reached. The whole process can be seen as a downward cascade toward small scales where surface tension is important. However, we also observe multiple coalescence of droplets several times in a row, corresponding to a non-linear inverse cascading process. From the experimental videos, we see that

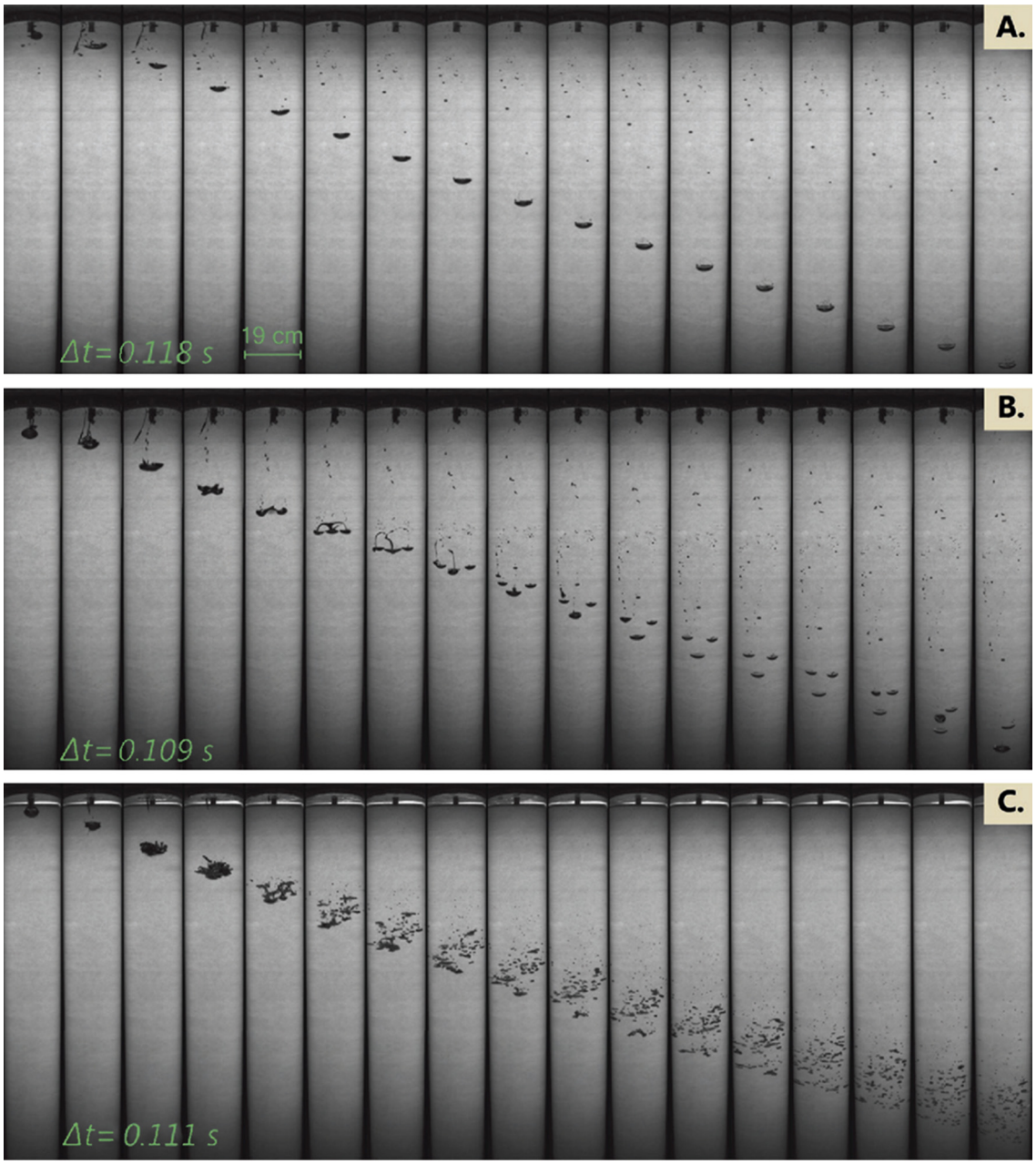

Fig. 3. Successive snapshots with a fixed time interval for 3 experiments. A: Fall of a 14 mm initial radius diapir in pure glycerine, corresponding to $Re_a = 12$, $We_a = 14$ and a viscosity ratio of 500. The diapir has a stable cap shape. B: same as A but for a 23 mm initial radius diapir, corresponding to $Re_a = 24$ and $We_a = 37$. The diapir breaks up in 3 main cap-shaped stable drops of close sizes. C: same as B but for an ambient fluid 100 times less viscous, corresponding to $Re_a = 2400$, $We_a = 37$ and a viscosity ratio of 5.

small drops accelerate and merge when they are near bigger drops whose rear recirculation engulfs them. One can argue that the narrowness of our experiment limits the spreading of the metallic droplet cloud, thereby enhancing the typical frequency of droplet collisions. But as noted above, coalescence happens even if there are very few drops. We thus believe that this inverse cascade process is also relevant in larger domains, as for instance in magma oceans.

Fig. 5A shows a closer instantaneous view of the droplet cloud once the steady-state is reached. A whole distribution of shapes and sizes is observed. Large drops have a cap shape stabilized by internal recirculation (see Fig. 5B), and the smallest drops adopt a spherical shape; a continuity of flattened ellipsoidal shapes is observed in between.

We have also observed a novel metastable structure (Fig. 5C) formed during the breakup of the biggest diapirs. These structures look like a hot air balloon and fall slowly relative to other droplets of comparable size. From slow motion videos of their formation and disappearance, we have inferred that they are bubbles of gallium enclosing glycerol (see Fig. 5D), similar to bubbles of soapy water in air. This bubble structure explains their relative stability as well as their anomalously low settling velocity for their rather large size.

5. Distribution of sizes and influence of the viscosity ratio

Fig. 6 shows the cumulative distribution of droplets sized obtained from the breakup of the largest class of diapir for a viscosity ratio of $r_\mu = 50$. This corresponds to $Re_a = 368$ and $We_a = 64$. Taking into account the resolution of the video ($9.0\ \text{pixels}\,\text{cm}^{-1}$), we are able to detect the size of drops larger than 0.6 mm in radius, the smaller ones being detected as drops of 0.6 mm. The

Fig. 4. Successive snapshots with a fixed time interval $\Delta t = 0.18$ s for a 30 mm initial radius diapir falling through pure glycerol, corresponding to $Re_a = 37$, $We_a = 64$ and a viscosity ratio of 500. One can notice that the mean speed of the front of the diapir is rather constant.

breakup of metal diapirs does not create droplets of one single size but a whole distribution of equivalent radii, in agreement with the simulations of Ichikawa et al. (2010). Because the formation of drops results from the generic process of ligament rupture, their size distribution is well fitted by a Gamma distribution, whose probability density function p writes:

$$p(x) = \frac{x^{k-1} e^{-x/\theta}}{\theta^k \Gamma(k)}, \tag{6}$$

where k is the shape of the Gamma distribution, θ its scale, and $\Gamma(k)$ is the Gamma function evaluated at k. Such a Gamma distribution of droplet sizes is similar to the one obtained in the case of water drops in the air (Villermaux and Bossa, 2009). Note however that in this last case, the viscosity ratio is reverse (i.e. the more viscous fluid is inside) and the shapes of the obtained drops are very different. Our distribution is tightened around a mean radius of 4 mm. This value can be related to a breakup criterion, now understood in a statistical sense: surface tension sets the characteristic length scale of the distribution, the mean radius. Using our experimental results, the critical Weber number corresponding to this radius is $We_c \simeq 1$. The distributions obtained for diapirs with different initial sizes are similar to the one shown in Fig. 6, and so is the measured mean radius, provided that these diapirs are large enough to create a distribution of sizes that converges statistically. This condition is verified for the 4 biggest classes of diapirs that we have produced.

Fig. 7 shows series of snapshots from 4 experiments with the same initial diapir but different viscosity ratios. With our present set-up, because a large number of drops are superimposed on the video images, it was not possible to detect their individual contours for a viscosity ratio smaller than 50. Hence we could not perform a systematic quantitative study of the sizes distribution as a function of r_μ. But relying on direct observation, we see that there is a clear tendency for large viscosity ratios to stabilize bigger drops, as already noticed in Section 4 for single structures. In all cases, we expect to systematically recover a Gamma-type distribution for the equivalent radii. This means that the distributions always have the same shape, with a peak at a small scale corresponding to $We_c \simeq 1$, and an exponential tail. But we expect the slope of this tail to be significantly more gentle when the viscosity ratio increases. This corresponds to a decreasing value of the shape of the Gamma distribution: for instance, Villermaux and Bossa (2009) found a shape value of 4 for the breakup of water in the air (viscosity ratio 2×10^{-2}), while we find a shape of 2.2 for a viscosity ratio of 50, as shown in Fig. 6.

6. Simultaneous distributions of sizes and velocities

The interactions between the droplets lead to a wide range of sizes and velocities in our experiments. Fig. 8 shows the distribution of sizes and speeds for a viscosity ratio $r_\mu = 50$ and a diapir with an initial radius of 23 mm, using the values obtained from a space–time diagram at a distance of 140 cm from the initial position of the center of mass of the diapir. It is plotted in the same way as in Ichikawa et al. (2010). The fact that velocities are calculated from the travel time through the tank averages out a large part of the variability due to raw turbulence and allows us to then consider the mean structure of the flow. Interestingly, the drops' velocities do not follow a Newtonian scaling based on their individual radius, even when adjusting the pre-factor (see Fig. 8). This result seems to validate the entrainment hypothesis described by Deguen et al. (2011, 2014): after the breakup, the drops fall as an interacting cloud whose velocity is determined by the inertia of the whole flow, related to the initial mass of the diapir. Additional fluctuations are related to the turbulent mixing and interactions between drops.

7. Typical equilibration length

We can estimate a rough length scale of equilibration following the same reasoning as in Samuel (2012), but using the distribution

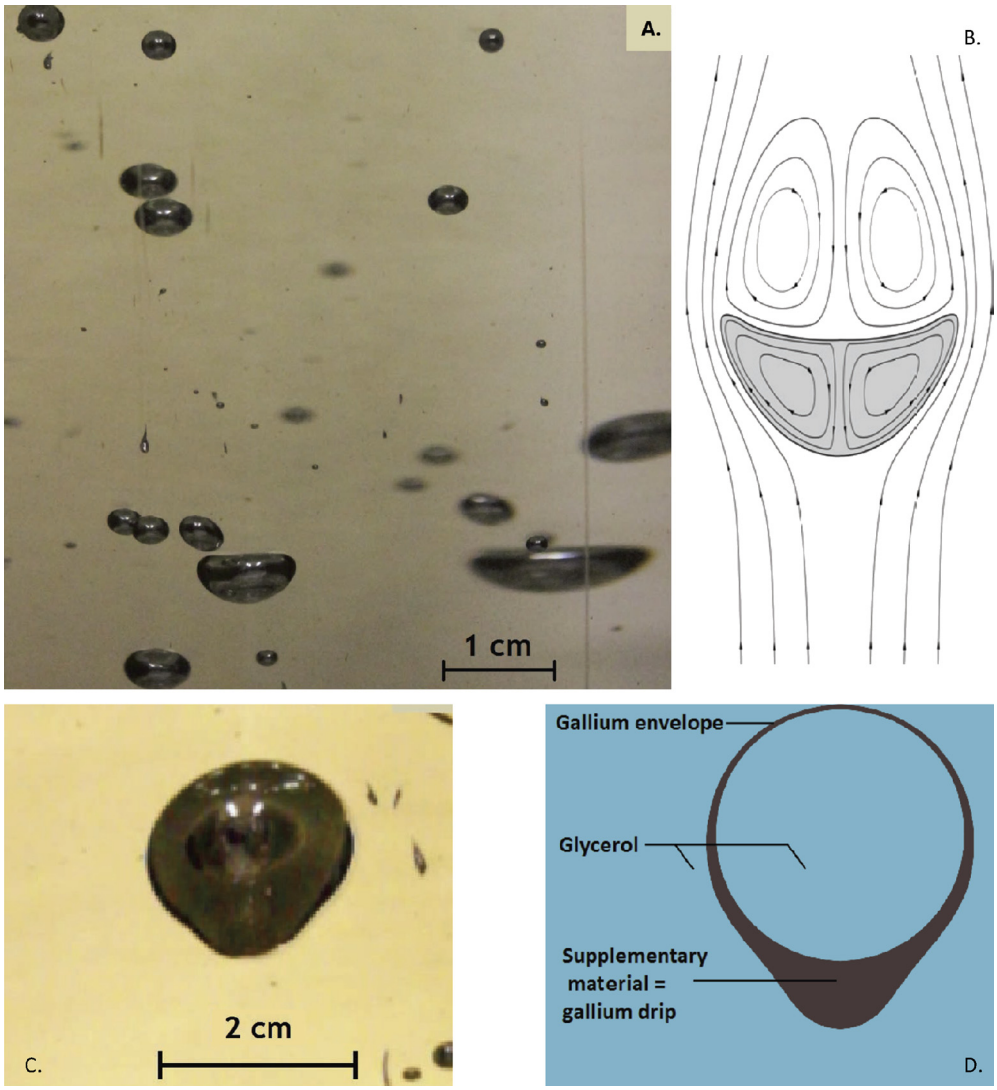

Fig. 5. A: drops of liquid gallium of various sizes falling through pure glycerol. Several intermediates between cap shape and spherical shape are present. B: expected streamlines of the relative flow within and around a falling diapir with a cap shape (shown in gray). C: gallium bubble enclosing glycerol formed during the breakup of a 30 mm radius diapir in pure glycerol. Due to its reduced buoyancy compared to full gallium drops, it falls slowly. These structures last from one tenth of a second to several minutes. D: schematic of a gallium bubble.

of sizes and velocities found in our experiments. Note that the relatively simple equilibration models shown below are meant only for illustration of potential consequences of the complex dynamics exhibited in our experiments. The question of geochemical equilibration clearly deserves more detailed studies.

In our model, we neglect the breakup distance and consider that the distribution of sizes and speeds has reached a steady state. From our observations, from simulations (Samuel, 2012) as well as from previous experiments (Deguen et al., 2014), breakup occurs within a typical length scale of a few initial radii, so the previous hypothesis is valid for initial entities at least 10 times smaller than the mantle depth: we choose here an initial diapir of radius 10 km sedimenting in a magma ocean with a minimum depth of 100 km. We suppose that the metal concentration C_m in a chemical element of interest (e.g., Ni, Co, W, Hf) is uniform inside each drop and that it evolves following a simple Fick's law

$$\frac{4\pi}{3} r^3 \frac{dC_m}{dt} = -4\pi r^2 \kappa \frac{C_m - C_{m,eq}}{\delta_{BL}}, \tag{7}$$

where r is the drop radius, κ the chemical diffusivity coefficient of typical order 10^{-8} m^2 s^{-1}, and $C_{m,eq}$ the equilibrium concentration. We further assume that the thickness of the chemical boundary layer δ_{BL} scales as $\delta_{BL} = \sqrt{2\kappa r/v}$, where v is the local speed

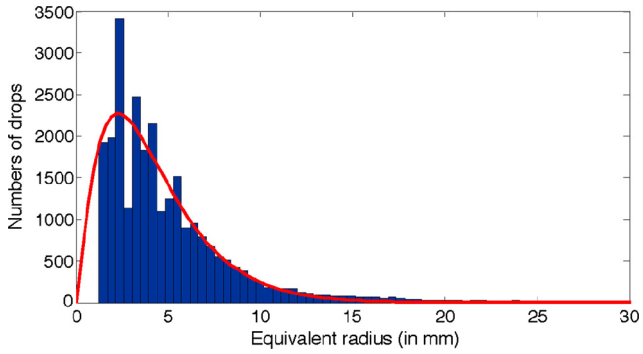

Fig. 6. Histogram of the equivalent radius of the droplets created by the breakup of a 30 mm initial radius diapir falling through a mixture of glycerol and water (in blue) and best fitting Gamma distribution (in red, with shape 2.2 and scale 1.9). Dimensionless parameters of the experiment are $Re_a = 368$, $We_a = 64$ and $r_\mu = 50$. The low cutoff radius is set by the resolution of the video to 0.6 mm. A large number of measurements is necessary for obtaining converged statistics. This cumulative distribution was thus constructed from 6 runs of the same experiment and using the last 10 frames of each video, i.e. once a statistically steady state is reached and before the fastest droplet touches the bottom of the tank. (For interpretation of the references to color in this figure legend, the reader is referred to the web version of this article.)

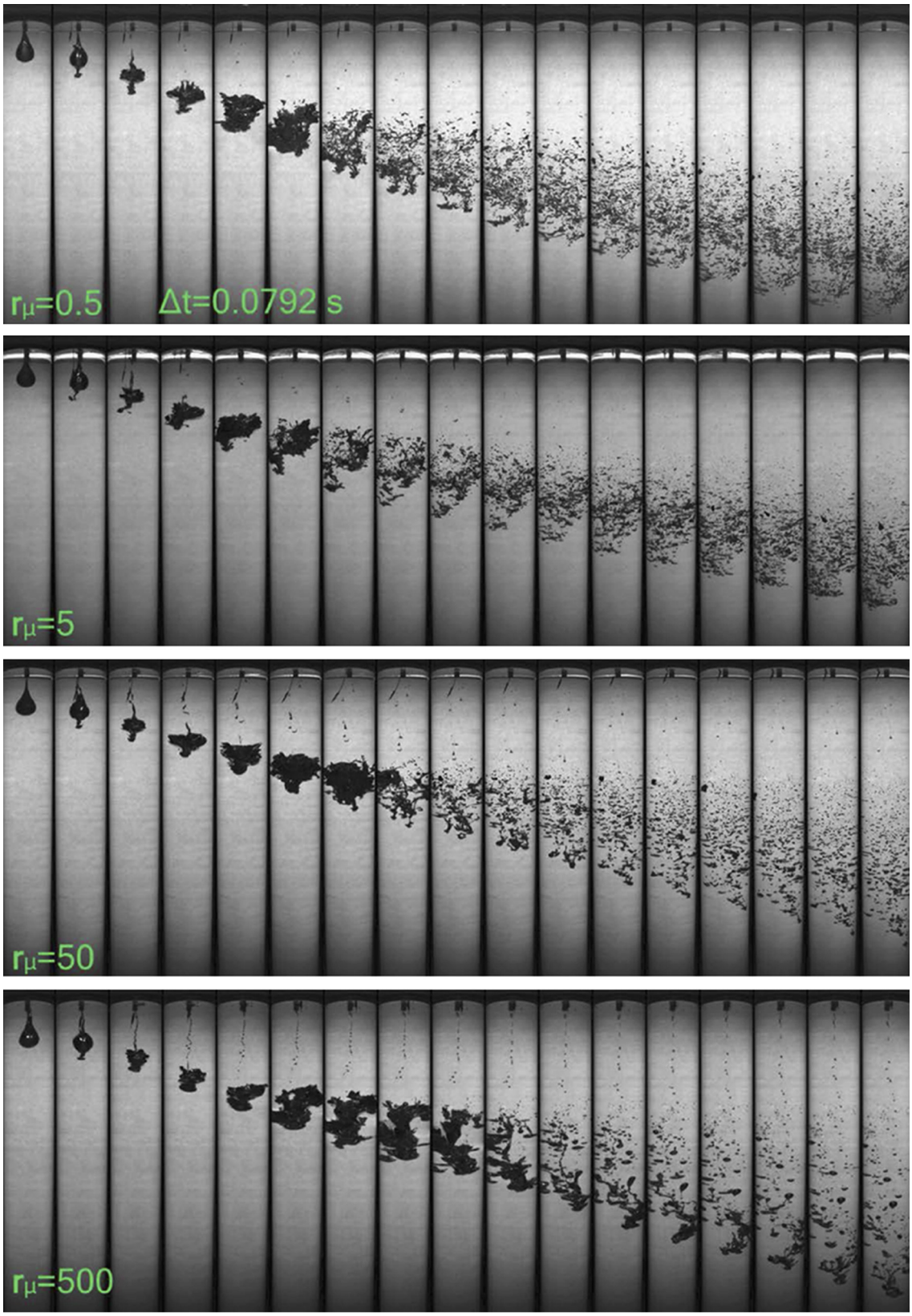

Fig. 7. Series of snapshots of the diapirs evolution for 4 runs of the experiment with a 31 mm initial radius diapir. From top to bottom, only the viscosity of the ambient fluid increases; the corresponding viscosity ratios are 0.5, 5, 50, and 500. Rigorously, changing the ambient viscosity also changes the Reynolds number. But it may be noticed from the snapshots that the mean sedimentation velocities in the four cases are comparable, and, hence, largely independent of the ambient fluid viscosity, as expected in the Newtonian limit. We argue then that the various observed dynamics are primarily related to changes in the viscosity ratio.

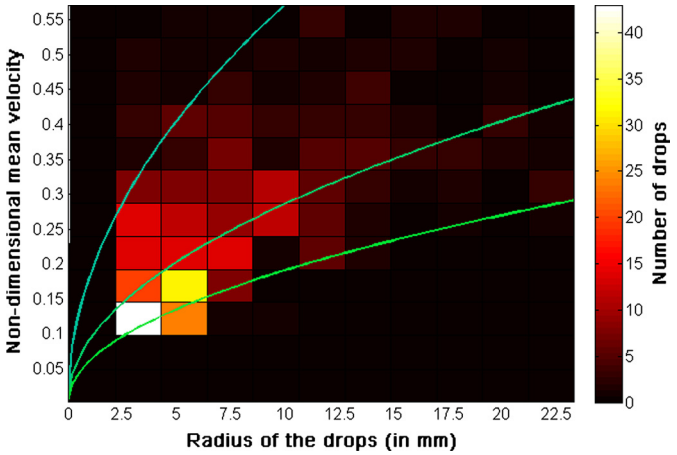

Fig. 8. Distribution of the drops equivalent radii (in mm, along the x-axis) and speeds (non-dimensionalized by the Newtonian speed of the initial diapir, along the y-axis). The initial radius of the diapir is 23 mm and the viscosity ratio is 50, which gives $Re_a = 244$ and $We_a = 37$. Three curves of the corresponding Newtonian velocity scaling (1) with a prefactor respectively equal to 1, 1/2 and 1/3 from top to bottom, are shown in green. (For interpretation of the references to color in this figure legend, the reader is referred to the web version of this article.)

of the flow around the droplet, assumed to be constant (following Samuel, 2012). We define the degree of equilibration as

$$C^*(t) = \frac{C_m(t) - C_m(t=0)}{C_{m,eq} - C_m(t=0)}. \tag{8}$$

Eq. (7) then leads to an exponential solution

$$C^*(t) = 1 - e^{-t/\tau} \quad \text{where } \tau = \frac{r^{3/2}}{3}\sqrt{\frac{2}{\kappa v}}. \tag{9}$$

Following our experimental results, we evaluate the degree of equilibration using three different values for the local speed of the drops and the speed at which the cloud of drops is entrained. The reference case corresponds to the standard iron rain scenario with a cloud of drops with a uniform radius R_{cap}, and where the local and global speeds are the corresponding Newtonian speed. Two other scenarios based on our experimental results are investigated. The local speed is given in one case by the Newtonian speed for each drop whose radius follows a Gamma distribution, and in the other case by the size-speed distribution results presented in Fig. 8, where we are assuming that the distribution does not depend on the large scale parameters such as the mean diameter and velocity of the drop cloud. In both cases, the global speed is the Newtonian velocity of the initial 10 km radius diapir. This estimate agrees with our present experimental results, as shown, for example, in Fig. 7. The global sedimentation speed, however, probably decreases over time because of the progressive entrainment of ambient fluid, as shown by Deguen et al. (2011, 2014). This effect is not seen here, possibly because of the limited size of our container. Corresponding equilibration results for the three models are shown in Fig. 9.

In all cases, the entire distribution of drops fully equilibrates before reaching the bottom of the magma ocean. However, the predicted depth of equilibration is 1 to 3 orders of magnitude larger when considering the scenarios derived from our fluid mechanics experiments compared to the idealized iron rain. This is the result of two combined effects highlighted by our laboratory experiments: droplet velocities are significantly larger than in the classical iron rain, and the drop size distribution puts a significant fraction of the metal phase in drops larger than R_{cap}, which implies a smaller surface of exchange between iron and silicate. As a result, equilibration will integrate a broader range of conditions regarding pressure and temperature, and the energy and

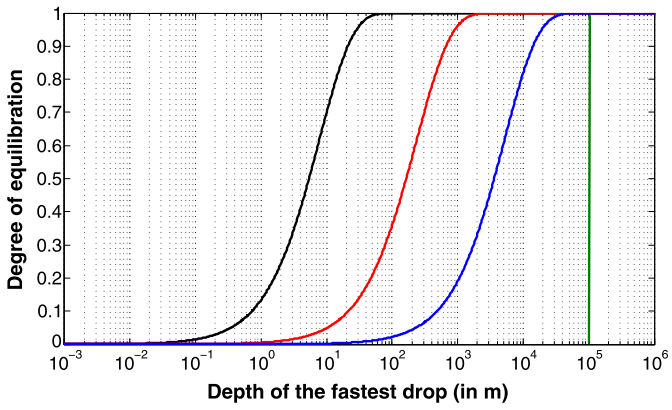

Fig. 9. Degree of equilibration of a cloud of droplets resulting from the fragmentation of an initially 10 km radius diapir and falling through a magma ocean. The classical iron rain scenario is shown in black for reference. Two scenarios derived from the statistics of our experiments with an initial radius $R = 30$ mm and $r_\mu = 50$ are also shown, where the global speed of the drop cloud is taken as the Newtonian velocity of the initial 10 km radius diapir. In red, the local speed of the drops is derived from the distributions shown in Fig. 8. In blue, the local speed is given by the Newtonian scaling law for each drop radius. Note that the present model neglects the breakup distance of the initial diapir. For an initial diapir of radius 10 km, this implies a minimum depth of the magma ocean of 100 km, shown by the vertical green line. (For interpretation of the references to color in this figure legend, the reader is referred to the web version of this article.)

mass exchanged by diffusion during the sinking of a particular metal droplet can occur substantively deeper within the magma ocean. Besides, for several elements, the partition coefficient depends on the pressure of equilibration. Expected changes in the depth of equilibration will also change their final repartition between core and mantle.

8. Conclusions and open questions

Our laboratory experiments on the fragmentation of gallium drops falling through glycerol shed new light on the dynamics of the iron sedimentation process that likely occurs during a terrestrial body's final accretionary stages. The classical iron rain scenario considers a population of spherical drops with a single characteristic radius that fall towards the bottom of the magma ocean at a unique velocity without any further change. In contrast, here we find that the fragmentation of an initially large diapir actually gives rise to a variety of stable shapes, a large distribution of sizes and velocities, and an intense internal dynamics within the cloud with the superimposition of further fragmentations and merging. Thus, we argue that previous models of chemical and thermal equilibration processes can only be accurate in a statistical mean sense (e.g. Rubie et al., 2003; Samuel et al., 2010). On the basis of our simple equilibration model, we still predict a complete equilibration before reaching the core, but at a significantly deeper depth. One should also keep in mind that the probability of a "strange" event, i.e. an anomalously large diapir or an anomalously slow falling velocity, is statistically possible, especially for large viscosity ratios.

Additional experiments are necessary to complement the conclusions drawn here, notably with a larger tank to avoid confinement effects and to allow for initially larger diapirs. Also it now appears necessary to take into account, in more evolved models of equilibration, the complex internal dynamics between drops inside the clouds, including the observed inverse cascade and the global sedimentation dynamics. It is also necessary, in addition to the first study for fixed-shape spherical drops by Ulvrová et al. (2011), to account for the very intense internal dynamics inside and outside large drops, which both stabilizes and deforms them, and should increase the equilibration process by advection.

All these effects clearly deserve further studies that are beyond the scope of this paper. Finally, our experiments have highlighted the importance of the viscosity ratio on the fluid dynamics of the fragmentation and sedimentation processes. As in Earth, the heat brought by the conversion of gravitational and kinetic energy during accretion is not negligible (see e.g. Tonks and Melosh, 1992; Samuel et al., 2010), it would now be interesting to study the strong coupling between the heating by viscous damping of the intense flows caused by the fall of iron diapirs, the changes in the ambient viscosity induced by this thermal evolution, and the corresponding evolution of the drop size distribution.

Acknowledgements

We thank Professor E. Villermaux for helpful discussions. M.L.B. acknowledges financial support from the European Commission, Research Executive Agency, Marie Curie Actions (project FP7-PEOPLE-2011-IOF-298238). J.M. is funded by Agence Nationale de la Recherche (Accretis decision No. ANR-10-PDOC-001-01). J.M.A. and the UCLA SpinLab are supported by the NSF Geophysics Program.

References

Abe, Y., Matsui, T., 1985. The formation of an impact-generated H_2O atmosphere and its implications for the thermal history of the Earth. J. Geophys. Res. 90, 545–559.

Bonometti, T., Magnaudet, J., 2006. Transition from spherical cap to toroidal bubbles. Phys. Fluids 18, 052102.

Boyet, M., Carlson, R.W., 2005. ^{142}Nd evidence for early (>4.53 Ga) global differentiation of the silicate Earth. Science 309, 576–581.

Boyet, M., Blichert-Toft, J., Rosing, M., Storey, M., Télouk, P., Albarède, F., 2003. ^{142}Nd evidence for early Earth differentiation. Earth Planet. Sci. Lett. 214, 427–442.

Dahl, T.W., Stevenson, D.J., 2010. Turbulent mixing of metal and silicate during planet accretion and interpretation of the Hf–W chronometer. Earth Planet. Sci. Lett. 295, 177–186.

Deguen, R., Landeau, M., Olson, P., 2014. Turbulent metal–silicate mixing, fragmentation, and equilibration in magma oceans. Earth Planet. Sci. Lett. 391, 274–287. http://dx.doi.org/10.1016/j.epsl.2014.02.007.

Deguen, R., Olson, P., Cardin, P., 2011. Experiments on turbulent metal–silicate mixing in a magma ocean. Earth Planet. Sci. Lett. 310, 303–313.

Harper, C., Jacobsen, S., 1996. Evidence for ^{182}Hf in the early solar system and constraints on the timescale of terrestrial accretion and core formation. Geochim. Cosmochim. Acta 60, 1131–1153.

Ichikawa, H., Labrosse, S., Kurita, K., 2010. Direct numerical simulation of an iron rain in the magma ocean. J. Geophys. Res. 115, B01404.

Karato, S.-I., Murthy, V., 1997. Core formation and chemical equilibrium in the Earth—I. Physical considerations. Phys. Earth Planet. Inter. 100, 61–79.

Kaula, W.M., 1979. Thermal evolution of Earth and moon growing by planetesimal impacts. J. Geophys. Res. 84, 999–1008.

King, E.M., Aurnou, J.M., 2013. Turbulent convection in liquid metal with and without rotation. Proc. Natl. Acad. Sci. USA 110 (17), 6688–6693.

Kleine, T., Mezger, K., Münker, C., Palme, H., Bischoff, A., 2004. ^{182}Hf–^{182}W isotope systematics of chondrites, eucrites, and martian meteorites: chronology of core formation and early mantle differentiation in Vesta and Mars. Geochim. Cosmochim. Acta 68, 2935–2946.

Lee, D.-C., Halliday, A.N., 1996. Hf–W isotopic evidence for rapid accretion and differentiation in the early solar system. Science 274, 1876–1879.

Merk, R., Breuer, D., Spohn, T., 2002. Numerical modeling of ^{26}Al-induced radioactive melting of asteroids considering accretion. Icarus 159, 183–191.

Monteux, J., Coltice, N., Dubuffet, F., Ricard, Y., 2007. Thermo-mechanical adjustment after impacts during planetary growth. Geophys. Res. Lett. 34, L24201.

Monteux, J., Ricard, Y., Coltice, F., Dubuffet, N., Ulvrová, M., 2009. A model of metal–silicate separation on growing planets. Earth Planet. Sci. Lett. 287, 353–362.

Morbidelli, A., Lunine, J., O'Brien, D., Raymond, S., Walsh, K., 2012. Building terrestrial planets. Annu. Rev. Earth Planet. Sci. 40, 251–275.

Neumann, W., Breuer, D., Spohn, T., 2012. Differentiation and core formation in accreting planetesimals. Astron. Astrophys. 543, A141.

Ohta, M., Yamaguchi, S., Yoshida, Y., Sussman, M., 2010. The sensitivity of drop motion due to the density and viscosity ratio. Phys. Fluids 22, 072102.

Reese, C., Solomatov, V., 2006. Fluid dynamics of local martian magma oceans. Icarus 184, 102–120.

Rubie, D.C., Melosh, H., Reid, J., Liebske, C., Righter, K., 2003. Mechanisms of metal–silicate equilibration in the terrestrial magma ocean. Earth Planet. Sci. Lett. 205, 239–255.

Rubie, D.C., Nimmo, F., Melosh, H.J., 2007. Formation of Earth's core. In: Treatise on Geophysics. Elsevier, pp. 51–90.

Safronov, V.S., 1978. The heating of the Earth during its formation. Icarus 33, 3–12.

Samuel, H., 2012. A re-evaluation of metal diapir breakup and equilibration in terrestrial magma oceans. Earth Planet. Sci. Lett. 313, 105–114.

Samuel, H., Tackley, P., Evonuk, M., 2010. Heat partitioning during core formation by negative diapirism in terrestrial planets. Earth Planet. Sci. Lett. 290, 13–19.

Solomatov, V.S., 2000. Fluid dynamics of a terrestrial magma ocean. In: Origin of the Earth and Moon. University of Arizona Press, pp. 323–338.

Stevenson, D.J., 1990. Fluid dynamics of core formation. In: Origin of the Earth. Oxford University Press, pp. 231–249.

Tonks, B., Melosh, J., 1992. Core formation by giant impacts. Icarus 100, 326–346.

Tonks, B., Melosh, J., 1993. Magma ocean formation due to giant impacts. J. Geophys. Res. 98, 5319–5333.

Ulvrová, M., Coltice, N., Ricard, Y., Labrosse, S., Dubuffet, F., Velimský, J., Srámek, O., 2011. Compositional and thermal equilibration of particles, drops, and diapirs in geophysical flows. Geochem. Geophys. Geosyst. 12, 1–11.

Villermaux, E., Bossa, B., 2009. Single-drop fragmentation determines size distribution of raindrops. Nat. Phys. 5, 697–702.

Walter, M., Tronnes, R., 2004. Early Earth differentiation. Earth Planet. Sci. Lett. 225, 253–269.

Yoshino, T., Walter, M., Katsura, T., 2003. Core formation in planetesimals triggered by permeable flow. Nature 422, 154–157.

Chemical Geology xxx (2016) xxx–xxx

Contents lists available at ScienceDirect

Chemical Geology

journal homepage: www.elsevier.com/locate/chemgeo

Silicate melts during Earth's core formation

M.A. Bouhifd [a,*], V. Clesi [a], A. Boujibar [b], N. Bolfan-Casanova [a], C. Cartier [c], T. Hammouda [a], M. Boyet [a], G. Manthilake [a], J. Monteux [a], D. Andrault [a]

[a] Laboratoire Magmas et Volcans, Université Blaise Pascal, CNRS UMR 6524, Campus Universitaire des Cézeaux, 6 Avenue Blaise Pascal, 63178 Aubière Cedex, France
[b] NASA Johnson Space Center, 2101 Nasa Parkway, Houston, TX 77058, USA
[c] Department of Geology (B20), Université de Liège, B-4000 Sart Tilman, Belgium

ARTICLE INFO

Article history:
Received 3 March 2016
Received in revised form 17 December 2016
Accepted 21 December 2016
Available online xxxx

Keywords:
Magma ocean
Earth's core
Magma ocean crystallization
Bridgmanite
Liquidus
Helium
Nb-Ta paradox
Redox state

ABSTRACT

Accretion from primordial material and its subsequent differentiation into a planet with core and mantle are fundamental problems in terrestrial and solar system. Many of the questions about the processes, although well developed as model scenarios over the last few decades, are still open and much debated. In the early Earth, during its formation and differentiation into rocky mantle and iron-rich core, it is likely that silicate melts played an important part in shaping the Earth's main reservoirs as we know them today.

Here, we review several recent results in a deep magma ocean scenario that give tight constraints on the early evolution of our planet. These results include the behaviour of some siderophile elements (Ni and Fe), lithophile elements (Nb and Ta) and one volatile element (Helium) during Earth's core formation. We will also discuss the melting and crystallization of an early magma ocean, and the implications on the general feature of core-mantle separation and the depth of the magma ocean. The incorporation of Fe^{2+} and Fe^{3+} in bridgmanite during magma ocean crystallization is also discussed. All the examples presented here highlight the importance of the prevailing conditions during the earliest time of Earth's history in determining the composition and dynamic history of our planet.

1. Introduction

Silicate melts have played an important role in Earth's evolution from the core formation 4.5 billion years ago to present-day volcanic activity. Modern planetary formation models show that terrestrial planets likely formed through three modes of growth that were ordered in time in the protoplanetary disk. In step I, km-sized planetesimals formed by the coagulation of gas and dust in less than ~10^4 years. In step II, the collisional evolution of the planetesimals population led to the growth of Moon to Mars-sized planetary embryos formed by runaway growth through collisions among the planetesimals in $<10^6$ years. In step III, giant collisions among the planetary embryos resulted in the formation of a few terrestrial planets that swept up all the other bodies. This stage may have taken up to ~10^8 years (e.g. Chambers, 2004; Morbidelli et al., 2012). At least step II and step III were energetic enough to have likely melted a large fraction of the silicate Earth (e.g. Canup, 2012). Theory and observations point in fact to the occurrence of magma oceans in the early evolution of terrestrial planets and in many planetesimals (e.g. Greenwood et al., 2005; Elkins-Tanton, 2012). In addition a magma ocean scenario provides a favorable environment in which metal-silicate segregation can occur rapidly and efficiently (e.g. Stevenson, 1990).

It is now well established that for metal and silicate to segregate rapidly on a planetary scale requires that at least the metal is molten (Stevenson, 1990). On the other hand, when the silicate is also largely molten, liquid metal can segregate extremely efficiently (e.g. Rubie et al., 2003). The short time scale of Earth's core formation, ranging from 30 to 100 Ma after the beginning of solar system accretion (e.g. Kleine et al., 2009) can be also used as an indirect evidence for large scale melting during the first 100 Ma of Earth's history. There are three main sources of energy that can produce the melting that is required for core formation: (1) the decay of short-lived radioactive nuclides (^{26}Al and ^{60}Fe) during the first 1–3 Ma of the solar system evolution (Yoshino et al., 2003); (2) the energy delivered by impacts that can generate local or global melting especially during the late stages of Earth accretion (Tonks and Melosh, 1993); (3) the conversion of potential energy into heat via viscous dissipation during the segregation of the metallic phase that can increase the silicate temperature by 1000–3000° (Ke and Solomatov, 2009; Monteux et al., 2009; Samuel et al., 2010; more details can be found in the review paper by Rubie et al., 2015b).

Melting events are common in the first stages of Solar System history and start very rapidly after the beginning of solar nebula condensation, dated at 4.567–4.568 Ga, age of refractory inclusions, known as CAIs (see Amelin et al., 2002; Bouvier and Wadhwa, 2010; Connelly et al., 2012). Oldest ages measured in iron meteorites show that metal-silicate separation began on planetesimals within 1 to 1.5 Ma of the start of

* Corresponding author.
E-mail address: A.Bouhifd@opgc.univ-bpclermont.fr (M.A. Bouhifd).

http://dx.doi.org/10.1016/j.chemgeo.2016.12.035
0009-2541/

Solar System formation (Kruijer et al., 2012, 2014). The study of basaltic achondrites (angrites, eucrites) coming from different parent bodies shows that small planetesimals have experienced magma ocean stages during the first million years of their history (e.g. Brennecka and Wadhwa, 2012; Touboul et al., 2015). This chronology shows that the building blocks of forming planets implied mainly differentiated objects instead of primitive and undifferentiated materials. In planets, the last stages of accretion end with very large collisions. The most spectacular event for Earth corresponds to the Moon-forming giant impact event. The study of short-lived systematics in terrestrial samples gives evidence for successive magma-ocean stages on Earth. Noble gas systematics trace the mantle's degassing and the Xenon isotope signature is consistent with extensive loss of volatile elements within the first 100 Ma of Earth's existence (Allègre et al., 1983; Yokochi and Marty, 2005; Mukhopadhayay, 2012). The high $^{3}He/^{22}Ne$ fractionation observed in the Earth's mantle suggests at least two separate magma ocean steps during the Earth's accretion (Tucker and Mukhopadhyay, 2014). Excesses in ^{182}W (produced by the decay of ^{182}Hf) measured in 2.7 Ga-old komatiites are explained by a large-scale magmatic differentiation during the first 30 Ma of the Solar System's history (Touboul et al., 2012). Since the giant Moon-forming impact is dated between 40 and 200 Ma (Boyet et al., 2015 and references therein), this collision may not have induced a complete homogenization of the Earth's mantle. The combined measurements of $^{146,147}Sm$-$^{142,143}Nd$ systematics of undisturbed Eoarchean metabasalts (from the southwestern part of Greenland, Isua Supracrustal Belt) suggest differentiation of the mantle source at ~4.47 Ga (Rizo et al., 2011). Chemical fractionation would have occurred during the crystallization of a large magma ocean which extended down into the lower mantle. This chronology is consistent with the presence of zircon formed in a terrestrial crust at ~4.4 Ga (Wilde et al., 2001; Valley et al., 2014).

Concerning the Earth one of the most important events during the first 100 Ma is the segregation of the metallic core. Among the several uncertainties about the formation of the Earth and other planets, the physical conditions upon which Earth differentiated are important questions that remain much debated. Evidence on the earliest times on Earth comes mainly from two sources: (1) The concentrations of core-forming elements left behind in the silicate part provide a fingerprint on the conditions under which this segregation occurs. (2) The Moon is the second important source of evidence, it is believed to have formed after the Earth's core formation as a result of a giant impact between Earth and a Mars-size body (named Theia) (Hartmann and Davis, 1975; Tonks and Melosh, 1993). The magma oceans were reservoirs where partial to complete equilibrium and segregation of the metallic phase from the impactor and the silicate phase from the target were likely to occur (Rubie et al., 2003). The thermo-chemical exchanges that occurred in the magma oceans have strongly influenced the geochemical signature within the current deepest parts of the Earth. Hence they play a key role on how we constrain the differentiation processes in terms of characteristic timescales, P - T conditions or redox conditions. The metal silicate separation processes and especially the characteristic volumes that are involved (cm-droplets to km-diapirs) during the core formation govern the degree of chemical equilibration between the mantle and the core of the Earth (Samuel, 2012; Wacheul et al., 2014). During the latest stages of planetary accretions the large impactors were probably differentiated. After a collision, the impactor's core is assimilated into the partially to completely molten mantle leading to a first fragmentation due to the impact itself. This first fragmentation is poorly constrained but it is the starting point of the second fragmentation that is likely to occur within the turbulent magma ocean. During these two stages of fragmentation, the impactor's core was potentially fragmented down to cm-size droplets (Rubie et al., 2003). If the impactor's core was completely emulsified in droplets ("iron rain scenario"), the thermo-chemical exchanges between the metallic phase from the impactor and the silicates from the magma ocean were extremely efficient (Rubie et al., 2003). Many geochemical models are based on this "iron rain scenario". However, after a large impact, the emulsification of the impactor's core might be incomplete and large volumes of iron may sink without experiencing a complete equilibration with the mantle they are passing through (Dahl and Stevenson, 2010). In this case, a limited fraction of the mantle could equilibrate with the metallic phase. This could explain the relatively high abundance of highly siderophile elements of the terrestrial mantle that should have efficiently segregated into the core. Recently, laboratory experiments have constrained the mixing (Deguen et al., 2011, 2014) and the fragmentation dynamics (Wacheul et al., 2014) during the sinking of a metallic volume within a magma ocean. Wacheul et al. (2014) showed that there was a wide range of metallic droplet sizes and shapes as well as important interactions within the sinking metal cloud in which fragmentation and coalescence events are superimposed. For the first time, Wacheul et al. (2014) have estimated the influence of the viscosity contrast between liquid iron and the liquid silicates and showed that a large viscosity contrast favors large-scale diapirs. The characteristic size (that governs the sinking velocity) and the shape of the metallic droplets (that governs the exchange surface) are both key parameters to anticipate the degree of equilibration of any chemical element within a magma ocean (Rubie et al., 2003). This degree of equilibration is a strong function of the partition coefficient of each element considered (Deguen et al., 2014).

In summary, the Earth accreted over a period of at least 100 Ma with several magma ocean episodes. During this period the main part of core formation process occurred. In this paper we will review results involving exchanges between molten silicate and metal liquid during the first 100 Ma that give rise to strong constraints on the evolution of our planet. This review includes the conditions of the Earth's core formation determined from the behaviour of some siderophile elements (Ni and Fe) and lithophile elements (Nb and Ta). Recent results also show that the early core could have incorporated enough helium to supply deep-rooted plumes with high $^{3}He/^{4}He$ ratios throughout the age of the Earth. We will discuss the melting and crystallization of an early magma ocean, and the implications on the general feature of core-mantle separation and the depth of the magma ocean. We will also discuss the incorporation of Fe^{2+} and Fe^{3+} in bridgmanite during magma ocean crystallization.

2. Conditions during Earth's core formation

2.1. Constraints from siderophile elements

The knowledge of the pressure, temperature and oxygen fugacity (f_{O2}) conditions prevailing during Earth's core formation is derived mainly from the behaviour of the siderophile elements (iron loving elements) that are depleted in the mantle. In this context, the behaviour of Ni and Co has been considered to provide an important clue, both being refractory elements and present in the Earth's mantle in a near-chondritic Ni to Co ratio (Newsom, 1990). In addition, Ni and Co are almost identical to Fe in cosmochemical volatility (Grossman, 1972; O'Neill and Palme, 1998). By using all existing data of metal – silicate partitioning of Ni and Co the consensus at the present time is that metal-silicate equilibration at high pressures, in the range of 40–60 GPa (corresponding to depths of 1000–1500 km), was required to produce the observed Ni and Co depletions in the mantle (see: Bouhifd and Jephcoat, 2011; Righter, 2011; Fischer et al., 2015; Siebert et al., 2012; for the most recent studies). Similar conclusions were reached based on the metal-silicate partitioning of lithophile and weakly-siderophile elements (Mann et al., 2009; Siebert et al., 2011). One should note here that the conditions of Earth's core formation derived from metal-silicate partitioning of siderophile elements cannot be used as arguments for single-stage core formation as this is highly unlikely considering that Earth's core formation occurred during a series of large impact events (e.g. Canup, 2008; O'Brien et al., 2006; Morbidelli et al., 2012; Wetherill, 1985). Such impacts added Fe-rich

metal which segregated to the Earth's proto-core. The experimental results of metal – silicate partitioning of Ni and Co suggest only that some impactor must re-equilibrate in the deep magma ocean above 40 GPa, presumably as a result of emulsification (Rubie et al., 2003) before reaching the center of our planet to form the core, and leaving the observed mantle abundances of siderophile elements.

2.1.1. Silicate melts structure control on metal-silicate partitioning of Ni

As noted above, Ni is the most studied element to constraint the conditions of Earth's core formation. The available experimental data of molten metal – silicate liquid partitioning of Ni that range from about 1 GPa up to 100 GPa (e.g. Li and Agee, 1996, 2001; Thibault and Walter, 1995; Ohtani and Yurimoto, 1996; O'Neill et al., 1998; Gessmann and Rubie, 2000; Bouhifd and Jephcoat, 2003, 2011; Chabot et al., 2005; Siebert et al., 2012; Fischer et al., 2015; and references therein) show a decrease of metal-silicate partition coefficients of Ni (D_{Ni}) with increasing pressure (at roughly constant oxygen fugacity and temperature following the liquidus of chondritic mantle). Another important feature of D_{Ni} versus pressure is its marked slope change for pressures higher than 35 GPa. As noted by Sanloup et al. (2013), this slope change coincides with a change in the coordination of silicon (in a basaltic melt composition) from 4-fold coordination under ambient conditions to 6-fold coordination at about 35 GPa. One can note that similar results were obtained by studying the structure of basaltic melt at high pressures using first-principles simulations (Bajgain et al., 2015). The similarity of the transition pressure from 4- to 6-fold coordination of Si and the pressure of the marked change in the D_{Ni} coefficients indicates that melt compressibility controls siderophile-element partitioning – at least for Ni (Sanloup et al., 2013). For other siderophile elements, like Cr, V or Mn, metal-silicate partition coefficients versus pressure do not show any slope change at around 35 GPa (see Fischer et al., 2015 for experiments up to 100 GPa). We reported in Fig. 1 a compilation of D_{Fe} versus pressure up to about 55 GPa that shows no slope change at around 35 GPa (the reported experiments in Fig. 1 are at f_{O2} varying between IW-1 and IW-2). These examples show that melt compressibility is not affecting all siderophile elements partitioning in the same way.

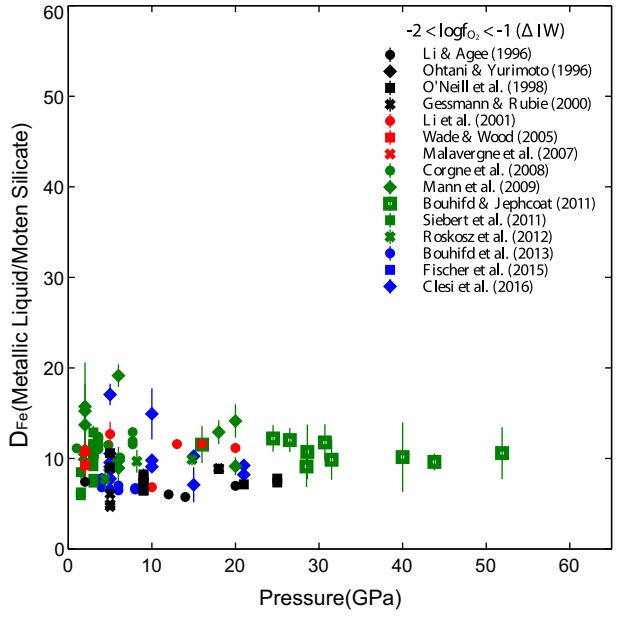

Fig. 1. Molten metal – silicate liquid partition coefficients of Fe as a function of pressure (GPa). The temperatures of the experiments were above the liquidus of a chondritic composition, and the oxygen fugacity ranges between IW-2 and IW-1. The compiled data are taken from the authors reported in the figure.

2.2. Constraints from refractory lithophile elements

How elements are distributed between the main reservoirs (core, magma ocean, atmosphere) during planetary differentiation depends on their chemical affinity. Geochemists and cosmochemists have divided the chemical elements into groups, such as the iron-loving siderophile elements, the silicate-loving lithophile elements, the gas phase-loving atmophile elements, and the sulfur-loving chalcophile elements (Goldschmidt, 1937). This classification has been constructed based on the form in which the elements are encountered at the Earth's surface, i.e. under ambient pressure and temperature, and oxidizing conditions. However, each element behaviour is likely to be modified by intensive parameters variations. This is illustrated in the following for the case of Nb and Ta distribution between molten metal and silicate, this pair of elements giving important clues on oxygen fugacity prevailing during early Earth history.

2.2.1. Oxygen fugacity effect on metal – Silicate partitioning of Nb and Ta

The variation of the partitioning with the oxygen fugacity (f_{O2}) of any cation in silicate liquid informs on its electronic charge in the silicate melt. In fact, metal-silicate partitioning of an element M between silicate and metal involves exchange between oxidized species ($MO_{n/2}$) in the silicate and reduced species in the metal (M). This exchange reaction must depend on oxygen fugacity and the oxidation state *n* of the element M in the silicate melt as reported in the following equation:

$$MO_{n/2} = M + n/4\ O_2 \quad (2)$$

Working with trace elements, some simplifying assumptions can be made to express their activities and the equilibrium constant can be approximated to the Nernst partition coefficient, yielding the following equation:

$$D_M = \frac{X_M^{alloy}}{X_M^{silicate}} \approx \frac{a_M^{alloy}}{a_M^{silicate}} = exp\left(-\frac{\Delta G^0}{RT}\right) - \frac{n}{4}(fO_2) \quad (3)$$

with X representing the weight fractions, *a* the activities, ΔG^0 the Gibbs free energy change at the standard state and fO_2 the oxygen fugacity. According to the Eq. (3) the metal-silicate partition coefficient for any cation is inversely related to the oxygen fugacity. Additionally, it is also a function of the element valence state in the silicate melt. It can also be predicted that, in theory, any element should become siderophile, provided that the conditions are sufficiently reducing. The most reducing conditions recorded in the solar system are those of calcium aluminium refractory inclusions (CAIs) of carbonaceous chondrites, about 7 log units below Fe-FeO equilibrium (IW-7) (Grossman et al., 2008). (Note that enstatite chondrite conditions may have been even lower, of the order of IW-10 (Larimer and Buseck, 1974).

2.2.2. The "Nb paradox"

As the Earth accreted and differentiated, metallic materials segregated from silicates to form the iron-rich core. Because they were excluded from the core, the proportions of the refractory lithophile elements left over in the silicate part of the Earth are thought to have remained identical to those of chondritic meteorites throughout accretion (Kargel and Lewis, 1993). Niobium and tantalum, two refractory elements, have been classified as high field strength elements (HFSE), because their ionic charge over ionic radius ratio is high. This electronic feature mostly defines Nb and Ta behaviour in magmatic systems: as their sizes differ significantly from that of the available lattices in most of the common minerals, both elements tend to partition into the liquid phase during melting (Hofmann, 1988). Moreover Nb and Ta are described as "geochemical twins": they are known to occur only in pentavalent state and octahedrally coordinated (VI-fold) in geological systems, and share the same ionic radius (0.64 Å, Shannon, 1976). For those reasons,

Nb and Ta should behave similarly during the extraction of the core. However, the Nb/Ta ratio of the bulk silicate Earth (BSE) is significantly lower ($Nb/Ta_{(BSE)} = 14 \pm 0.3$) than the chondritic value ($Nb/Ta_{(chondrites)} = 19.9 \pm 0.6$), as well as lunar rocks ($Nb/Ta_{(Moon)} = 17.0 \pm 0.8$ (Münker et al., 2003)). This observation is quoted as the "niobium paradox". To resolve this paradox, three main explanations have been proposed: the Earth has a hidden silicate reservoir characterized by a superchondritic Nb/Ta that originated from the subduction of refractory eclogite through Earth's history (Rudnick et al., 2000); early storage of the late stage residual melt from the magma ocean (Nebel et al., 2010); the `missing Nb'' has been sequestrated into the core (Cartier et al., 2014; Wade and Wood, 2001).

2.2.3. Nb and Ta partitioning between metal and silicate melts

Various experimental studies support the idea that the core may be the "missing Nb" reservoir. The results are based on Nb and Ta metal-silicate melts partition coefficients, which appear to be mainly dependent on oxygen fugacity, compared to pressure, temperature or silicate composition (Cartier et al., 2014). When plotted as a function of oxygen fugacity (Fig. 2), partition coefficients describe lines which slopes that depend directly on the cation valence state in the silicate melt.

Under moderately reducing conditions (IW to IW-3) data are consistent with Nb_2O_5 and Ta_2O_5 in the silicate melt, i.e. Nb and Ta are mainly 5+ in the silicate liquid. More surprisingly, Nb and Ta describe different slopes under very reducing conditions (for f_{O2} > IW-3), consistent with NbO and Ta_2O_3 in the silicate melts. This contrasting valence change of Nb and Ta under reducing conditions is responsible for the two elements decoupling in metal – silicate systems. One can note here that the observed behaviour above for Nb and Ta is not a general feature for all lithophile elements as for Sm and Nd for example we did not observe any slope break of D_{Sm} and D_{Nd} as a function of oxygen fugacity in the range of IW-5 and IW-1. The reported results for Sm and Nd for S-free systems are consistent with Sm and Nd being dissolved in the silicate melt as Sm^{3+} and Nd^{3+} in reducing conditions between IW-5 and IW-1 (Bouhifd et al., 2015). Thus, partitioning data is a good tool to reveal element valence states. However the uncertainty on the element valence state is quite large, because of experimental and analytical error, coupled with significant uncertainties on experimental samples intrinsic oxygen fugacity estimation. The slope is also a function of the interaction coefficient of the element which can vary as Si enters the metal at low f_{O2} - this is another good reason to independently constrain the valence through spectroscopy with direct valence probing in the samples.

2.2.4. Nb and Ta speciation in silicate melts

In a recent study, XANES spectra have been acquired in silicate glasses equilibrated under moderately and highly reducing conditions (Fig. 2) (Cartier et al., 2015). Under moderately reducing conditions, the studied silicate glasses mainly contain Nb and Ta in the 5+ state. Under highly reducing conditions, silicate glasses contain Nb^{2+} and Ta^{3+}. These results confirm the information about Nb and Ta valence obtained with partition coefficients. Thus Nb and Ta behaviour in metal – silicate melts systems is mainly controlled by redox conditions, which simplifies the modeling of their partition coefficients as a function of oxygen fugacity.

2.2.5. Nb/Ta ratio as an fO_2 proxy during core formation

The results presented here show that Nb/Ta ratio in the primitive magma ocean depends mainly on the prevailing oxygen fugacity. Additionally, the experiments show that pressure has no effect (Cartier et al., 2014), meaning that Nb-Ta systematics cannot be used to estimate the depth of the magma ocean, in contrast to Ni and Co for example. Nb-Ta systematics, however, can be used to shed light on the oxidation state of the planet primitive building blocks.

For this, planet growth from planetesimals has been modeled in light of Nb/Ta evolution in the magma ocean during core formation. As noted above, when observed, Nb depletion is likely due to its trapping in the metallic core. Therefore, present day Earth's mantle bears the evidence of a reduced stage at some early stage of our planet history. By applying the metal-silicate partitioning data to a heterogeneous accretion scenario (such as proposed by Rubie et al., 2011) it is possible to reach the observed subchondritic Nb/Ta ratio (14 ± 0.3) of the bulk silicate Earth (Fig. 3). According to this scenario, the first ~70 wt% of the Earth accreted from reduced material, similar to enstatite chondrites, except for its lower volatile content, yielding extremely low Nb/Ta in the silicate mantle. The last 30% consist of more oxidized material, allowing for Nb/Ta to increase, until it reaches its present day value.

In the case of the Moon, the Nb/Ta estimate is of 17.0 ± 0.8 (Münker et al., 2003). It is higher than the Earth's value, but still subchondritic. Noting that the Moon's core is very small and has a negligible effect on Nb budget, the Nb/Ta of the Moon mantle is necessarily the result of the mixing of the proto-Earth mantle with the impactor Theia. Considering that terrestrial and lunar samples are isotopically similar, a successful scenario is that at the time of impact, the Moon may have inherited the chemical signature of the Earth's upper mantle, whose Nb/Ta was higher than the modern value due to the crystallization of bridgmanite. This signature would have been subsequently erased due to the homogenization of the whole Earth's mantle. Nb/Ta ratio is

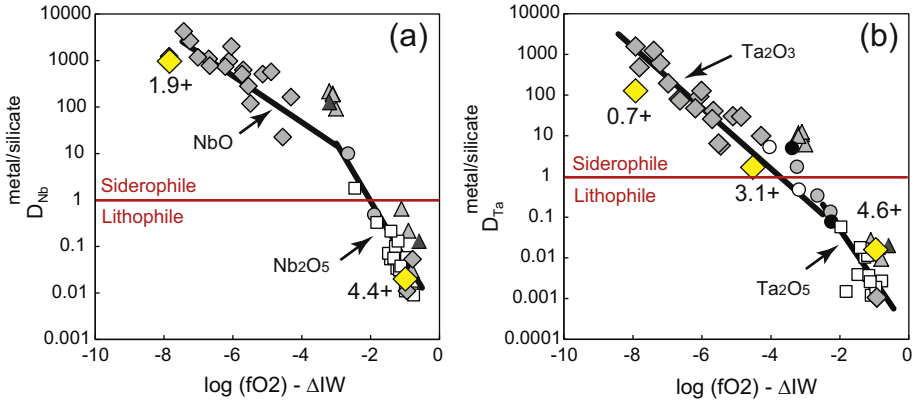

Fig. 2. Experimentally determined metal-silicate partition coefficients for Nb (a) and Ta (b) as a function of oxygen fugacity, expressed in log units relative to Fe-FeO (IW) equilibrium (open, gray and closed symbols; compilation after Cartier et al., 2014). The data have been obtained over a range of pressure between 0 and 20 GPa. The red lines delineate the domain where lithophile behaviour is observed from that of siderophile behaviour). The black lines illustrate the slope of data alignment with suggested valence state in the silicate melt (Nb: 5+ and 2+; Ta: 5+ and 3+). Yellow diamonds represent experiments, for which Nb and Ta valence states have been directly measured by x-ray spectroscopy (Cartier et al., 2015). In this case, estimated errors on valence states are ±0.6 and ±1.3 for Nb and Ta, respectively. (For interpretation of the references to colour in this figure legend, the reader is referred to the web version of this article.)

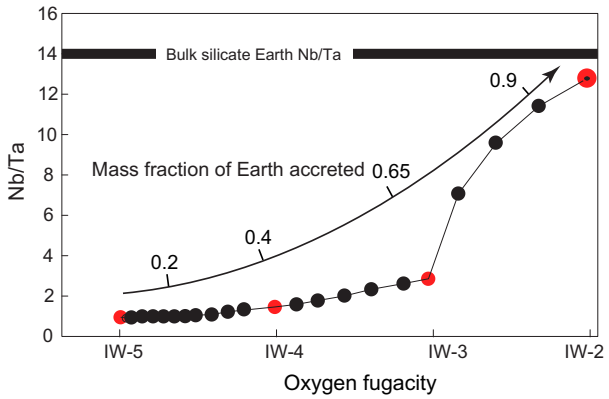

Fig. 3. Evolution of the Earth's mantle Nb/Ta ratio during the planet growth as a function of oxygen fugacity (after Cartier et al., 2014). The model considers the accumulation of impactors, starting with reduced and small-sized bodies, followed by less reduced and larger objects (Rubie et al., 2011). This accretion model also considers the degree of mixing (core – mantle equilibration) after each impact. The first stages are characterized by very low Nb/Ta ratios, due to massive core uptake. The last bodies accreted are more oxidized and their metallic parts do not fully equilibrate with the mantle, yielding to an increase of the Nb/Ta ratio, up to the current estimated value of 14. The arrow indicates the corresponding mass fraction accumulated as accretion progresses.

therefore a good fO_2 proxy during core formation. Mars and Vesta-4, for example, are considered to have differentiated under only moderately reducing conditions (IW and IW-1.5, respectively). This explains why SNC and HED meteorites display an almost chondritic Nb/Ta.

In summary, realistic Earth's core formation models are now in our reach that include a combination of a multistage core-mantle differentiation with N-body accretion simulations, or a continuous Earth's core formation where pressure, temperature and oxygen fugacity vary as the Earth's accretion proceed (e.g. Rubie et al., 2015a). In these models, we consider that the accretion of the Earth occurred during a series of large impact events (e.g. Canup, 2008; Wetherill, 1985; O'Brien et al., 2006; Monteux et al., 2009; Nakajima and Stevenson, 2015). The pressure and temperature of metal-silicate equilibrium likely increased as accretion progressed and core formation was therefore a continuous process. Other geochemical arguments based on ^{107}Pd-^{107}Ag and ^{182}Hf-^{182}W (e.g. Halliday and Wood, 2009) provide support for continuous core formation. In addition, Wade and Wood (2005) completed the deep magma ocean model by presenting a model in which the magma ocean deepened in proportion to the size of the proto-Earth, and in which the Earth became more oxidized at the last accretion stages during the first 100 Ma. Results of both models suggest that accretion of Earth was heterogeneous with the initial 60–70% of Earth's mass forming from reducing material and the final 30–40% from relatively oxidized material. These models also give results for metal-silicate partitioning of a significant number of siderophile elements that are consistent with observed mantle abundances provided the oxygen fugacity increases from about IW-5 to IW-2 (5 to 2 log units lower than the Iron-Wüstite buffer) during core separation. This conclusion is consistent with *N*-body simulations of terrestrial planet formation, which show that the Earth accreted material from farther from the sun at later times (e.g. Raymond et al., 2006; Morbidelli et al., 2012; Fischer and Ciela, 2014; Rubie et al., 2015a). Consequently, Earth began to accrete with a low FeO content in its mantle (in the range of 0.2–0.5 wt% consistent with the reduced chondritic bodies as enstatite chondrites), and at the final stages of accretion we can assume that the Earth's core is 85 wt% Fe and the mantle about 8 wt% FeO (McDonough and Sun, 1995). Finally, for Earth the reducing material can be similar to enstatite chondrites as it is consistent with the ^{17}O, ^{48}Ca, ^{50}Ti, ^{62}Ni and ^{90}Mo isotopic study by Dauphas et al. (2014). Enstatite chondrites being the main building blocks of the Earth are also consistent with a recent collisional erosion model (Boujibar et al., 2015) or the separation of the core from a hydrous magma ocean (Clesi et al., 2016).

Other model suggests that the Earth's mantle can start in a highly oxidized state and becomes more reduced as FeO enters the core (Rubie et al., 2004; Siebert et al., 2013). However this type of model is only valid when no Si partitions into the Earth's core. Recent experiments show in fact the simultaneous incorporation of Si and O at the Earth's core formation conditions (Bouhifd and Jephcoat, 2011; Siebert et al., 2012; Tsuno et al., 2013; Fischer et al., 2015). Every mole of silicon that enters into the core releases two moles of FeO that partition into the mantle following the reaction (1), as proposed by Javoy (1995) and Javoy et al. (2010) to argue for an enstatite chondrite model for the Earth:

$$2Fe_{(metal)} + SiO_{2\ (silicate)} = Si_{(metal)} + 2FeO_{(silicate)} \quad (1)$$

Consequently the initially oxidized mantle cannot be reduced to its present state when mass balance is taken into account (e.g. Rubie et al., 2015a).

3. Incorporation of highly volatiles in an early magma ocean

Highly volatile elements are defined as elements with low 50% condensation temperature (lower than about 800 K at 10^{-4} atm – McDonough and Sun, 1995) and can include hydrogen, carbon, nitrogen, sulfur and noble gases. In the following we will only focus on helium, and how the solubility and partitioning of this element during Earth's core formation places strong constraints on the formation and evolution of our planet. For the other elements their behaviour during the earliest time of our planet can be found in recent papers – even if the origins and abundances of these elements are still much debated – (e.g. Albarède, 2009; Armytage et al., 2013; Bergin et al., 2015; Boujibar et al., 2014; Dasgupta et al., 2013; Gaillard and Scaillet, 2014; Gaillard et al., 2015; Halliday, 2013; Hirschmann, 2016; Hirschmann and Dasgupta, 2009; Hirschmann et al., 2012; Jephcoat et al., 2008; Kadik et al., 2015; Li et al., 2016; Marty, 2012; Marty et al., 2013; Moreira, 2013; Mukhopadhayay, 2012; Roskosz et al., 2013; Wood et al., 2013; and references therein).

3.1. Helium in early magma ocean

To simulate Earth's core formation under conditions of segregation from a deep magma ocean, helium partitioning was determined in a mixture of a molten CI-chondrite model composition and Fe-Ni metal alloy liquid (Bouhifd et al., 2013). The results presented in this study show that the concentrations of He in a CI-chondrite melt increase with increasing pressure up to ~3 GPa, remain roughly constant in the range of 3 to 8 GPa and drop from 2000 ppm to about 500 ppm and again remain constant to the maximum pressure reached of that work (of ~16 GPa). One can note that the shape of He solubility in CI-chondrite melt versus pressure is similar to that observed for Ar with similar silicate composition (Bouhifd and Jephcoat, 2006). We reported in Fig. 4a–b the Ar and He solubilities in CI-chondrite melt at high pressures. Both studies indicate that below 8 GPa (pressure corresponding to a drop of Ar and He solubilities in CI-chondrite melt and corresponding to depths <300 km in the Earth's mantle), Ar and He may dissolve in silicate melts formed by partial melting in the Earth's interior. In a study up to 8 GPa, the partition coefficient of Ar between clinopyroxene and its melt was found to be between 10^{-3} and 10^{-4}, implying that He and Ar would be partitioned in melt and also ultimately degassed (Brooker et al., 2003). This behaviour indicates that Ar and He maintain their geochemically assumed incompatible behaviour with crystalline phases. Similar conclusion can be drawn from experiments at 0.1 GPa where all noble gases show an incompatible behaviour for olivine and clinopyroxene (Heber et al., 2007). However, the high-pressure step decrease of Ar and He in CI-chondrite melt observed at about 8 GPa implies that there may be an increase in compatibility with the crystalline phase (assuming that the crystalline phase does not undergo similar drop in solubility at high pressures). At depths for pressures >8 GPa (~300 km

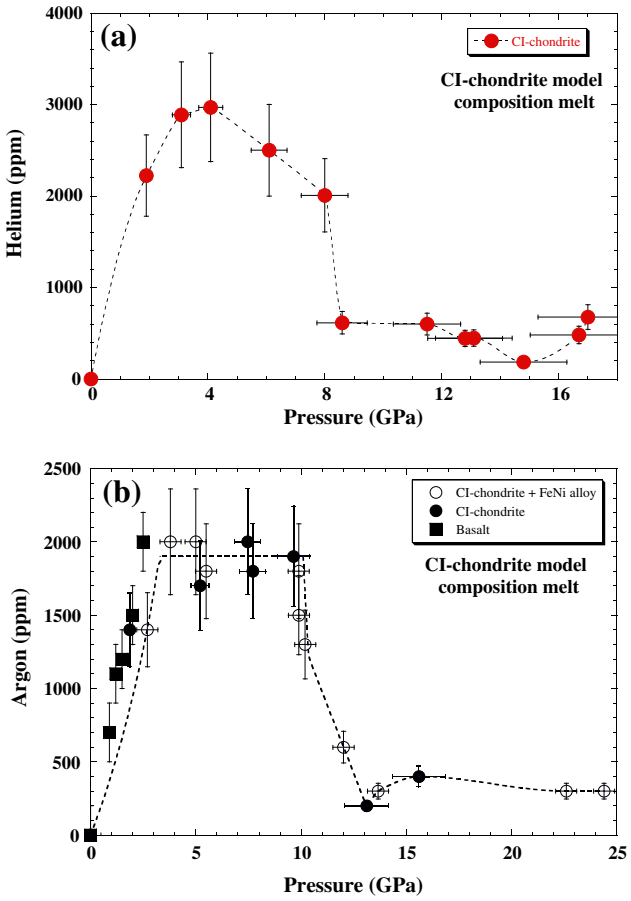

Fig. 4. **(a)** Helium concentrations (ppm) in CI-chondrite melt as a function of pressure (GPa). Figure taken from Bouhifd et al. (2013). **(b)** Argon concentrations (ppm) in CI-chondrite melt as a function of pressure (GPa). Data are taken from Bouhifd and Jephcoat (2006), Bouhifd et al. (2008) and White et al. (1989). For both figures error bars correspond to 1σ (ranging from 7 to 25%) of the average of the chemical analysis and to 10% of the nominal pressures reported. The dashed lines are used as a guide line only.

in the Earth's mantle) the Ar and He solubility in CI-chondrite melt indicates that it would be possible for primordial and radiogenic Ar and He to be preferentially retained deep in the Earth. One can note here that the solubility of Ar in silicate melts at high pressure is an ongoing debate as the solubility drop of Ar in SiO_2 melt at about 5 GPa (Chamorro-Perez et al., 1996; Bouhifd et al., 2008) was not reproduced in a recent study by Niwa et al. (2013), who instead show a slight decrease of Ar solubility in the range of 5–12 GPa. For basaltic melt, molecular dynamic simulations show also a slight decrease of Ar solubility in the range of 5 to 20 GPa (Guillot and Sator, 2012), but such calculations present large uncertainties. In any case, for silicate melts, it is widely accepted that noble gases dissolve into the interstitial sites, meaning that their solubility is related to the concentration of holes able to accommodate atoms of particular size (Doremus, 1966; Studt et al., 1970; Shackelford et al., 1972; Shelby, 1976). Increasing pressure causes a continuous densification of melts leading to changes in the silicate units/species distribution within the silicate melt. In their molecular dynamics simulations of molten anorthite, Nevins and Spera (1998) show that near 5 GPa the activation volumes of all species present in the melt are higher in absolute value than the partial molar volume of Ar, meaning that Ar can still be accommodated in molten anorthite at this pressure. However, above 20 GPa the activation volumes of all melt species drop below the partial molar volume of argon. This pressure is very consistent with the onset pressure of Ar solubility drop for anorthite liquid of about 17 GPa (Bouhifd and Jephcoat, 2006). Thus, a first-order interpretation of the drop in Ar solubility data is that they represent a closing of a characteristic void space in melts at high pressures and temperatures.

3.2. Earth's core as a reservoir for primordial helium

The question now is whether the Earth's core could plausibly be a reservoir for helium, knowing that a large impact that formed the Moon may have depleted the mantle as well as the atmosphere from the noble gases by about 2 orders of magnitude. In fact, Xe isotopes indicate that extensive loss (>97%) occurred from the mantle and atmosphere at two episodes of major mantle degassing, presumably driven by giant impacts, respectively at 20–50 Ma and about 100 Ma after the formation of the solar system which is consistent with the timing of Moon formation derived from Hf-W systematics and simulations of the giant impact (Pepin and Porcelli, 2006; Porcelli et al., 2001). Helium concentration in the early Earth's core was controlled by the initial He abundance in the early mantle at the time of core formation. High mantle concentrations of noble gases may have existed in the early mantle even if the mechanism by which early Earth acquired its noble gases is still debated. Noble gases in the early Earth's mantle can have two main origins: (1) the first origin/mechanism is the dissolution of gases from a dense, gravitationally captured atmosphere (assuming the Earth reached much of its present mass before dissipation of the solar nebula) and convected into the mantle. In this scenario, noble gases of solar composition, in particular solar-type helium and neon are dissolved from the atmosphere (e.g. Harper and Jacobsen, 1996; Honda et al., 1991; Mizuno et al., 1980). (2) The second scenario is that mantle noble gases are already present in the parent bodies of the Earth, due to irradiation by the solar wind of refractory grains (e.g. Moreira, 2013; Moreira and Charnoz, 2016; Porcelli and Halliday, 2001; and references therein). Such mechanisms can provide at a minimum 7×10^{12} atoms ^{3}He g^{-1} in the mantle (Mizuno et al., 1980; Porcelli and Ballentine, 2002; Porcelli and Halliday, 2001; Trieloff and Kunz, 2005). Considering this value as the initial ^{3}He abundance during the Earth's core formation, and the measured molten metal – silicate liquid partition coefficients of He (D_{He}) that range from about 5×10^{-3} to 2×10^{-2} at high pressure and high temperature (Bouhifd et al., 2013; Zhang and Yin, 2012), the early Earth's core would contains between 3×10^{10} and 1.2×10^{11} ^{3}He atoms g^{-1}. 1. On the other hand, the ^{3}He flux from Oceanic Island Basalts (OIB) ranges from about 38 to 1000 mol yr^{-1} equivalent to values from about 2.3×10^{25} to ~6×10^{26} atoms ^{3}He yr^{-1} (e.g. Lupton and Craig, 1975; Porcelli and Ballentine, 2002). The ratio of ^{3}He flux from OIB to the concentrations of ^{3}He in the Earth's core requires that 0.8 to 3% of the mass of the core should have released its primordial helium (Bouhifd et al., 2013). The range of ^{3}He/^{4}He ratios observed in the present day OIB samples would then be the result of mixing from the core with radiogenic ^{4}He and residual ^{3}He from the mantle. In addition, the early core would probably have formed with a high He/U ratio because U is a highly lithophile element (Wheeler et al., 2006; Malavergne et al., 2007; Bouhifd et al., 2013), and the core probably maintained a high, throughout Earth's history, ^{3}He/^{4}He ratio. The mantle reservoir debate (at least for helium – more similar work is needed for other noble gases) must now include exchange processes that operate at the core-mantle boundary, especially when molten metal – silicate melt reactions are involved (e.g. Herzberg et al., 2013), and knowing, as reported by Macpherson et al. (1998) that high ^{3}He/^{4}He coincides with a domain of ULZV usually associated with partial melting of silicates directly above a molten core. Finally, even if the core helium budget is actually sufficient to provide all mantle ^{3}He, it is reasonable to expect that only OIBs originating from the core-mantle boundary can carry the high ^{3}He-^{4}He core signature, making the Earth's core a plausible reservoir for these high ^{3}He-^{4}He ratios.

4. Magma ocean crystallization after core formation

After the core-mantle separation, a second major chemical differentiation event occurred during the magma ocean crystallization. Indeed, during the cooling and the subsequent solidification of the magma

ocean, compatible elements (e.g. Mg, Cr) were preferentially collected in the solid phase while the incompatible elements (e.g. Al, Na, Fe) selectively partitioned into melts. Depending on the density contrast between the solid and the ambient liquid, a major chemical separation occurred within the early mantle. This differentiation event was strongly influenced by the cooling processes that governed the rheology, the melt fraction and hence the efficiency of chemical exchanges within the solidifying early mantle. As the melt fraction depends on the distance between the solidus and liquidus of the mantle, the melting curves of the primitive mantle have major consequences on the cooling dynamics of the early mantle, on the existence of chemical heterogeneities and on their lifetime within primitive mantle reservoirs. Until recently, the determination of melting properties of samples was rather limited in pressure. Now systematic experimental determinations of the solidus and liquidus of geological materials are determined up to the core-mantle boundary (CMB) using the laser-heated diamond anvil cell technique (LHDAC) (e.g. Fiquet et al., 2010; Andrault et al., 2011, 2014; Nomura et al., 2014; Tateno et al., 2014; Pradhan et al., 2015). In Fig. 5 we report the liquidus and solidus of chondritic mantle (the details about the determination of the liquidus and solidus of chondritic material – that are beyond the scope of the present work – are reported in Andrault et al., 2011).

In vigorously convecting systems such as magma oceans, the temperature distribution is nearly adiabatic and isentropic and the crystallization is supposed to start as soon as the adiabatic profile is crossing the liquidus (e.g. Solomatov, 2007). In one-phase systems, such as a completely molten or a completely solid layer, the equation for an adiabat is

$$\left(\frac{\partial T}{\partial r}\right)_S = -\frac{\alpha g}{C_p} T \tag{4}$$

where T is the temperature, r is radius and g is the gravitational acceleration. ρ, α and C_p are respectively the density, the coefficient of volumetric thermal expansion and the specific heat of the considered one phase material at a given depth.

In two-phase systems, the effects of phase changes need to be considered (Solomatov, 2007). For a zone of partial melting, the density ρ', the coefficient of volumetric thermal expansion α' and the specific heat C'_p of the partially molten material are given as follows:

$$\frac{1}{\rho'} = \frac{1-\phi}{\rho_s} + \frac{\phi}{\rho_m} \tag{5}$$

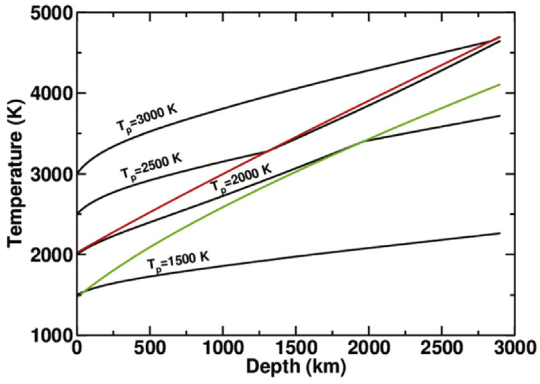

Fig. 5. Adiabatic profiles (black solid lines computed from Thomas and Asimow, 2013), solidus (green) and liquidus (red) (from Andrault et al., 2011) considering a chondritic composition for the early mantle. In this context, as the adiabats are steeper than the liquidus in the whole mantle, an initially fully molten mantle will start to solidify from the core-mantle boundary toward the Earth's surface. (For interpretation of the references to colour in this figure legend, the reader is referred to the web version of this article.)

$$\alpha' = \alpha + \frac{\Delta\rho}{\rho'(T_{liq} - T_{sol})} \tag{6}$$

$$C'_p = C_p + \frac{\Delta H}{T_{liq} - T_{sol}} \tag{7}$$

where ϕ is the melt fraction at a given depth, ρ_s is the density of the solid phase, ρ_m is the density of the molten phase, $\Delta\rho$ is the density difference between solid and liquid. T_{liq} and T_{sol} are the liquidus and solidus temperature at a given depth. ΔH is the latent heat released during solidification. The equation for such adiabats is given by:

$$\left(\frac{\partial T}{\partial r}\right)_S = -\frac{\alpha' g}{C'_p} T \tag{8}$$

The thermodynamical parameters for the molten magma ocean are closely related to its chemical composition. Volume and elastic parameters of silicate liquids have been recently characterized up to 140 GPa using shock compression experiments (Mosenfelder et al., 2007, 2009; Thomas et al., 2012; Thomas and Asimow, 2013). In Fig. 5 we also reported the adiabats computed from Thomas and Asimow (2013) considering a chondritic composition for the early mantle. The adiabatic temperature profiles are calculated by numerical integration of Eqs. (1) and (5) using a fourth-order Runge–Kutta method (Press et al., 1993). We assumed here a multi-component system with a chondritic composition (62% enstatite + 24% forsterite + 8% fayalite + 4% anorthite + 2% diopside). Using fourth-order Birch-Murnaghan/Mie-Grüneisen equation of state fits for molten silicate liquids from Thomas and Asimow (2013), we obtained the melt density ρ_m, the volumetric thermal expansion α as a function of pressure as well as the specific heat C_p of the molten material for this multicomponent assemblage (see Monteux et al., 2016 for more details). Fig. 5 illustrates that a chondritic two-phase adiabat is steeper than the purely liquid or solid one-phase chondritic adiabats (Solomatov, 2007).

Depending on the slope difference between the adiabats and the liquidus, the crystallization will occur either from the bottom toward the surface or from the top toward the bottom (e.g. Solomatov, 2007; Labrosse et al., 2007; Monteux et al., 2016). Hence, determining precisely the adiabatic profiles within the magma ocean is also a key aspect to constrain the thermo-chemical evolution of the early terrestrial mantle (Thomas and Asimow, 2013). When the melt fraction of the magma ocean decreases down to a critical value of 40% the cooling dynamics are not governed by the liquid phase but by the solid phase (Abe, 1997). Upon cooling, both the solid and liquid compositions will diverge from the early mantle composition. The density contrast between the liquid and solid phases may lead to a separation between the two phases as a consequence of crystal sedimentation and/or transcrystalline migration of the liquid (e.g. Schiano et al., 2006). This differentiation may lead to the separation between compatible elements that will easily reach the solid phase (e.g. Mg, Cr) while the incompatible elements will remain in the liquid phase (e.g. Al, Na, Fe). The density contrast will affect the chemical segregation and, hence, the geodynamical consequences will differ depending if the buoyancy between the two phases is positive or negative even if the vigor of the convection will potentially erase the chemical contrasts. The ascent or descent of the liquid phase within the partially molten mantle will either contribute to early volcanism or to the formation of a dense basal magma ocean. This aspect is currently under debate: Nomura et al. (2011) suggest an iron rich liquid phase denser than the mantle while Andrault et al. (2012) suggest a buoyant liquid phase that, as a consequence, leads to the formation of a deep residual layer enriched in compatible elements.

4.1. Implications for the magma ocean during accretion

The observations of a high liquidus temperature for a chondritic mantle as well as a large gap between its solidus and liquidus temperatures have important implications for the properties of the magma ocean during accretion. As reported in Fig. 5, a fully molten chondritic mantle that would extend to a pressure range of 40–60 GPa (pressure/depth of magma ocean range derived from siderophile elements) exhibits temperatures in the range of 3000–3500 K (e.g. Bouhifd and Jephcoat, 2011; Righter, 2011; Siebert et al., 2012; Fischer et al., 2015). Such conditions correspond to a surface potential temperature of about 2500 K (e.g. Andrault et al., 2011). Such a hot surface is not stable and is only compatible with a transient magma ocean. In fact, surface temperatures higher than 1800 K prevent formation of an (H_2O-CO_2)-rich atmosphere required to produce an efficient thermal blanket to the magma ocean (Abe and Matsui, 1988; Zahnle et al., 1988). Above 1800 K, it appears that significant silicate vaporization occurs, and such rock vapor atmosphere conducts heat easily so that the magma ocean would cool down in a few thousand years (Nagahara and Ozawa, 1996; Sleep et al., 2001). A conclusion of transient magma ocean during the first 100 Ma of Earth's history drawn from melting curves of chondritic mantle is consistent with geochemical evidence (Tucker and Mukhopadhyay, 2014). In this latter study, the authors present evidence for at least two separate magma ocean episodes on early Earth based on the ratio of primordial ^{3}He and ^{22}Ne in the present-day mantle.

4.2. Role on mantle chemical heterogeneities

As noted above the abundance of moderately siderophile elements in the Earth's mantle are better explained with scenarios where the pressure and temperature of core-mantle equilibration increase with time (e.g. Wood et al., 2006; Fischer et al., 2015), hence where the magma ocean's floor deepened throughout Earth's accretion. In the majority of these core-segregation models, the magma ocean floor is located at half or 2/3 of the depth of the core-mantle boundary, which increases progressively on the course of the accretion (e.g. Wade and Wood, 2005; Rubie et al., 2015a; Fischer et al., 2015). This implies that as soon as the Earth achieved about ~30% of its present-day mass, the floor of the magma ocean reached a pressure sufficient to enter the stability domain of bridgmanite (Al-bearing (Mg,Fe)SiO_3 with perovskite-type structure, Bg). Therefore, the equilibration between magma-ocean, Bg-rich solid mantle and segregating metallic phases, may have had an important role during Earth's differentiation.

Archean rocks show anomalies of ^{142}Nd in comparison to modern samples, which suggests an early differentiation of the primitive mantle through early decay of the extinct radionuclide ^{146}Sm (Boyet and Carlson, 2006; Caro et al., 2006; Rizo et al., 2013). The strong fractionation between Sm and Nd required for explaining these isotopic anomalies support a scenario of a magma ocean at ~4.47 Ga (Rizo et al., 2011). The modern terrestrial samples show relatively homogeneous ^{142}Nd/^{144}Nd ratios, resulting from efficient mantle convection and mixing of the early-formed enriched and depleted reservoirs. This constant isotopic ratio recorded by samples from the surface is however higher than those measured in the majority of chondrites, with the exception of some enstatite chondrites (Gannoun et al., 2011). The question of the starting material for modeling the long-term evolution of the silicate Earth is essential. Although none of the chondrite group known so far seems to reproduce exactly the terrestrial composition, enstatite chondrites are closest to Earth's composition when looking at the abundance of ^{142}Nd and of many other refractory elements (Warren, 2011). The stable Nd isotopic composition of terrestrial samples is different from that of carbonaceous and ordinary chondrites (Carlson et al., 2007; Burkhardt et al., 2016). This suggests that the ^{142}Nd difference is not due to the ^{146}Sm decay but was caused by isotopic variation imparted during the formation of Solar System. For enstatite chondrites, the difference is more elusive since their stable Nd isotopic composition are within the terrestrial field considering the analytical error and that they have 10 ppm deficit in ^{142}Nd relative to the Earth. If Earth is mainly made by enstatite chondrites, the calculated ^{147}Sm/^{144}Nd ratio of the silicate Earth would be 0.200, which is 2% higher than the average chondritic ^{147}Sm/^{144}Nd ratio and within the range of values previously measured for whole-rock chondrites. Bouvier and Boyet (2016) have also identified primitive Solar System material (calcium-aluminium-rich refractory inlcusions) without isotopic anomalies in Nd compared to the terrestrial composition but this type of material cannot have formed Earth. Therefore, the preservation of an unsampled or hidden reservoir due to early differentiation from magma ocean crystallization is still a conceivable hypothesis but the volume is probably more reduced than estimates proposed by Boyet and Carlson (2005). As a matter of fact, seismic tomography showed the presence of anomalously high seismic velocities at the D" layer, that can be interpreted in several ways, including the occurrence of partial melts, enriched in incompatible elements and representing leftovers from an ancient basal magma ocean, in a scenario where the magma ocean is crystallizing from the mid-lower mantle (Labrosse et al., 2007). The recent discovery of large excesses of ^{182}W that seems to be correlated to high ^{3}He/^{4}He ratios in modern flood basalts indicates long-term preservation of W isotopic signatures formed in the first 50 Ma of Earth's history (Rizo et al., 2016). The notoriety of this undegassed hidden reservoir hypothesis is typically due to the fact that it can resolve several geochemical paradoxes such as the noble gas isotopic signatures (Coltice et al., 2011).

In fact, a remarkable feature of the core-mantle boundary is the existence of ULVZs (Ultra Low Velocity Zones). The ULVZs are characterized by *S*- and *P*- seismic velocity reductions and are usually associated with partial melting of silicates directly above the core (Williams and Garnero, 1996; Revenaugh and Meyer, 1997; Vidale and Hedlin, 1998; Lay et al., 2004; Rost et al., 2005) although alternative interpretations are possible: solid-state origin (Fe-enriched (Mg,Fe)O) (e.g. Wicks et al., 2010; Bower et al., 2011; Brown et al., 2015) or accumulated sediments on top of the Earth's core (Buffett et al., 2000). More details on the origin of the ULVZs can also be found in the review papers by Tackley (2012) or Carlson et al. (2014).

In order to trap and isolate enriched melts deep at the CMB, their density should stay higher than the solid mantle. Two recent experimental studies aimed at determining the density contrast between Bg and silicate melt by measuring the partition coefficients of Fe between Bg and melt ($D_{Fe}^{Bg/melt}$) at various pressures, down to CMB conditions (Andrault et al., 2012; Nomura et al., 2011). These studies provided contrasting results where $D_{Fe}^{Bg/melt}$ was of 0.2–0.3 in Nomura et al. (2011) and Tateno et al. (2014) and 0.5–0.6 in Andrault et al. (2012), leading to contradictory interpretations for the fate of deep silicate melts, which are either denser or more buoyant than the solid silicate. A recent study conducted at fixed pressure (25 GPa) has proposed another explanation to this controversy, showing that the degree of melting (F) can significantly vary $D_{Fe}^{Bg/melt}$ (Boujibar et al., 2016). This study shows that at 25 GPa, $D_{Fe}^{Bg/melt}$ is close to 1 at extremely low degree of melting and becomes constant and equaling 0.3 ± 0.1 when F is higher than 10%. Therefore, the degree of melting is another parameter that should be taken into account in order to address mantle dynamics and the fate of a molten enriched reservoir at the base of the lower mantle.

4.3. Role on the redox state of the mantle

Several studies have previously proposed that Bg crystallization had major effects on the redox state of the mantle (Frost et al., 2004; Wood et al., 2006). Bg has the ability to integrate high levels of Fe^{3+} in its structure. In particular, it was previously shown that the presence of Al enhances the incorporation of Fe^{3+}, owing to the coupled substitution of Al and Fe^{3+} for Mg and Si in their respective dodecahedral and octahedral sites (Andrault et al., 2007; Lauterbach et al., 2000). This

substitution mechanism is so stable that it was suggested to force Fe^{2+} to disproportionate into Fe^{3+} and Fe^0 through the reaction:

$$3\ Fe^{2+} = Fe^0 + 2\ Fe^{3+} \quad (2)$$

Therefore, since the magma ocean's floor reached a depth sufficiently high to crystallize Bg, the magma ocean/solid mantle boundary was presumably acting as an oxygen pump, where Fe^{3+} was stabilized in Bg and progressively released to the magma ocean, while Fe^0 was systematically trapped in the solid lower mantle and subsequently falling to the core. Therefore the crystallization of the magma ocean was considered as a plausible mechanism for raising the oxygen state of the Earth's mantle (Wade and Wood, 2005). This idea was based on the fact that Al-content increases the solubility of Fe^{3+} in Bg independently from the oxygen fugacity (Frost et al., 2004; Frost and Langenhorst, 2002). However recent experimental studies showed that the oxygen fugacity (nature of the starting composition or capsule material) has an important effect on Fe^{3+} incorporation in Bg (Nakajima et al., 2012; Boujibar et al., 2016). In particular, recent experimental data on equilibrium between Bg, silicate melt and liquid metal showed that at an f_{O2} of ~IW-2 (2 log units below IW buffer), the Fe^{3+}-content in Bg is relatively low (~20%) and weakly dependent on the Al-content. Aluminium starts having an important positive effect on Fe^{3+} in Bg only when the oxygen fugacity is higher than ~IW-1 to IW (Fig. 6) (Boujibar et al., 2016). These results are challenging previous planetary differentiation models and imply that Bg crystallization during the cooling of the magma ocean can only have a substantial effect on the redox state of the mantle after the end of core segregation. Given that the final fO_2 equilibration between core and mantle is about IW-2 (based on present-day FeO content of the mantle of ~8 wt% and on the 85 wt% Fe of the core, estimated from the Earth's core density deficit), one can conclude that any increase of the Earth's redox state before the completion of core segregation should originate from other mechanisms than Bg crystallization from the magma ocean.

5. Concluding remarks

Earth's core formation models that include a combination of a multistage core-mantle differentiation with N-body accretion simulations lead to coherent view of the early history of our planet. The actual models suggest that accretion of Earth was heterogeneous with the initial 60–70% of Earth's mass forming from reducing material and the final 30–40% from relatively oxidized material. In addition, the available observations point to the occurrence of magma oceans in the early evolution of terrestrial planets. By applying this scenario we found that the Earth's core is a plausible reservoir for primordial helium. It is also possible to match the observed subchondritic Nb/Ta ratio of the bulk silicate Earth, highlighting that planetary accretion of reduced materials played an important role in the chemical evolution of Earth, and more generally, that Nb/Ta ratio can be used to trace prevailing oxygen fugacities during the segregation of planetary cores.

The available experiments of a high liquidus temperature for a chondritic mantle, as well as observations based on the ratio of primordial helium and neon isotopes, lead to a conclusion of transient magma ocean during the first 100 Ma of Earth's history. At least two separate magma ocean episodes on early Earth are suggested from noble gases isotopes.

To solve the existing controversy about the partitioning of Fe between bridgmanite and silicate melt, it seems that the degree of melting should be taken into account in order to address mantle dynamics and the fate of a molten enriched reservoir at the base of the lower mantle.

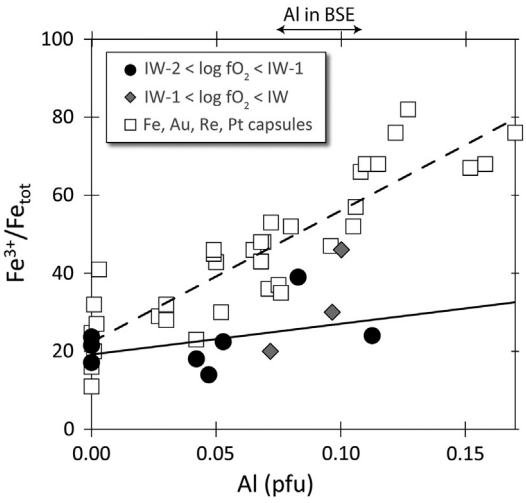

Fig. 6. $Fe^{3+}/\sum Fe$ in bridgmanite as a function of Al-content for different f_{O2} conditions ranging from IW-2 to IW-1 (black circles) (Boujibar et al., 2016; Terasaki et al., 2007; Frost et al., 2004), IW-1 to IW (gray diamonds) (Frost et al., 2004) and close or higher than IW buffer (where capsule material was metallic Fe, Au, Re or Pt) (Frost and Langenhorst, 2002; Frost et al., 2004; Lauterbach et al., 2000; McCammon et al., 2004; Saikia et al., 2009).

Acknowledgments

This paper was presented in the 10th Silicate Melt Worshop – La Petite Pierre. We thank Don Dingwell, Kai Uwe Hess and Pascal Richet for the organization of the workshop and for being the guest editors of this special issue. Part of this work was funded by the CNRS-INSU (program: PNP), ANR (project: Oxy-Deep), and ERC (project: ISOREE). This research was also financed by the French Government Laboratory of Excellence initiative n°ANR-10-LABX-0006, the Région Auvergne and the European Regional Development Fund. This is Laboratory of Excellence ClerVolc contribution number 231.

References

Abe, Y., 1997. Thermal and chemical evolution of the terrestrial magma ocean. Phys. Earth Planet. Inter. 100, 27–39.
Abe, Y., Matsui, T., 1988. Evolution of an impact-generated H_2O–CO_2 atmosphere and formation of a hot proto-ocean on Earth. J. Atmos. Sci. 45, 3081–3101.
Albarède, F., 2009. Volatile accretion history of the terrestrial planets and dynamic implications. Nature 461, 1227–1233.
Allègre, C.J., Staudacher, T., Sarda, P., Kurz, M., 1983. Constraints on evolution of Earth's mantle from rare gas systematics. Nature 303, 762–766.
Amelin, Y., Krot, A.N., Hutcheon, I.D., Ulyanov, A.A., 2002. Lead isotopic ages of chondrules and calcium-aluminium-rich inclusions. Science 297, 1678–1683.
Andrault, D., Bolfan-Casanova, N., Bouhifd, M.A., Guignot, N., Kawamoto, T., 2007. The role of Al-defects on the equation of state of Al-(Mg,Fe)SiO_3 perovskite. Earth Planet. Sci. Lett. 263, 167–179.
Andrault, D., Bolfan-Casanova, N., Lo Nigro, G., Bouhifd, M.A., Garbarino, G., Mezouar, M., 2011. Solidus and liquidus profiles of chondritic mantle: implication for melting of the Earth across its history. Earth Planet. Sci. Lett. 304, 251–259.
Andrault, D., Petitgirard, S., Lo Nigro, G., Devidal, J.-L., Veronesi, G., Garbarino, G., Mezouar, M., 2012. Solid-liquid iron partitioning in Earth's deep mantle. Nature 487, 354–357.
Andrault, D., Pesce, G., Bouhifd, M.A., Bolfan-Casanova, N., Hénot, J.-M., Mezouar, M., 2014. Melting of subducted basalt at the core–mantle boundary. Science 344, 892–895.
Armytage, R., Jephcoat, A.P., Bouhifd, M.A., Porcelli, D., 2013. Metal-silicate partitioning of iodine at high pressures and temperatures: implications for the Earth's core and ^{129}Xe budgets. Earth Planet. Sci. Lett. 373, 140–149.
Bajgain, S., Ghosh, D.B., Karki, B.B., 2015. Structure and density of basaltic melts at mantle conditions from first-principles simulations. Nat. Commun. 6:8578. http://dx.doi.org/10.1038/ncomms9578.
Bergin, E.A., Blake, G.A., Ciesla, F., Hirschmann, M.M., Li, J., 2015. Tracing the ingredients for a habitable Earth from interstellar space through planet formation. Proc. Natl. Acad. Sci. 112, 8965–8970.
Bouhifd, M.A., Jephcoat, A.P., 2003. The effect of pressure on partitioning of Ni and Co between silicate and iron-rich metal liquids: a diamond-anvil cell study. Earth Planet. Sci. Lett. 209, 245–255.
Bouhifd, M.A., Jephcoat, A.P., 2006. Aluminium control of argon solubility in silicate melts under pressure. Nature 439, 961–964.
Bouhifd, M.A., Jephcoat, A.P., 2011. Convergence of Ni and Co metal-silicate partition coefficients in the deep magma-ocean and light-elements core solubility at high pressures. Earth Planet. Sci. Lett. 307, 341–348.
Bouhifd, M.A., Jephcoat, A.P., Kelley, S.P., 2008. Argon solubility drop in silicate melts at high pressures: a review of recent experiments. Chem. Geol. 256, 252–258.
Bouhifd, M.A., Jephcoat, A.P., Heber, V.S., Kelley, S.P., 2013. Helium in an early Earth's core. Nat. Geosci. 6, 982–986.

Bouhifd, M.A., Boyet, M., Cartier, C., Hammouda, T., Bolfan-Casanova, N., Devidal, J.L., Andrault, D., 2015. Superchondritic Sm/Nd ratio of the Earth: impact of Earth's core formation. Earth Planet. Sci. Lett. 413, 158–166.

Boujibar, A., Andrault, D., Bouhifd, M.A., Bolfan-Casanova, N., Devidal, J.L., Trcera, N., 2014. Metal-silicate partitioning of sulfur, new experimental and thermodynamical constraints on planetary accretion. Earth Planet. Sci. Lett. 391, 42–54.

Boujibar, A., Andrault, D., Bolfan-Casanova, N., Bouhifd, M.A., Monteux, J., 2015. Cosmochemical fractionation by collisional erosion during the Earth's accretion. Nat. Commun. 6:8295. http://dx.doi.org/10.1038/ncomms9295.

Boujibar, A., Bolfan-Casanova, N., Andrault, D., Bouhifd, M.A., Trcera, N., 2016. Incorporation of Fe^{2+} and Fe^{3+} in bridgmanite during magma ocean crystallization. Am. Mineral. 101, 1560–1570.

Bouvier, A., Boyet, M., 2016. Primitive solar system materials and Earth share a common initial ^{142}Nd abundance. Nature 537, 399–402.

Bouvier, A., Wadhwa, M., 2010. The age of the solar system redefined by the oldest Pb-Pb age of a meteoritic inclusion. Nat. Geosci. 3, 637–641.

Bower, D.J., Wicks, J.K., Gurnis, M., Jackson, J.M., 2011. A geodynamic and mineral physics model of a solid-state ultralow-velocity zone. Earth Planet. Sci. Lett. 303, 193–202.

Boyet, M., Carlson, R.W., 2005. ^{142}Nd evidence for early (>4.53 Ga) global differentiation of the silicate Earth. Science 309, 576–581.

Boyet, M., Carlson, R.W., 2006. A new geochemical model for the Earth's mantle inferred from ^{146}Sm-^{142}Nd systematics. Earth Planet. Sci. Lett. 250, 254–268.

Boyet, M., Carlson, R.W., Borg, L.E., Horan, M., 2015. Sm-Nd systematics of lunar ferroan anorthositic suite rocks: constraints on lunar crust formation. Geochim. Cosmochim. Acta 148, 203–218.

Brennecka, G.A., Wadhwa, M., 2012. Uranium isotope compositions of the basaltic angrite meteorites and the chronological implications for the early Solar System. Proc. Natl. Acad. Sci. U. S. A. 109, 9299–9303.

Brooker, R.A., Du, Z., Blundy, J.D., Kelley, S.P., Allan, N.L., Wood, B.J., Chamorro, E.M., Wartho, J.A., Purton, J.A., 2003. The "zero charge" partitioning behaviour of noble gases during mantle melting. Nature 423, 738–741.

Brown, S.P., Thorne, M.S., Miyagi, L., Rost, S., 2015. A compositional origin to ultralow velocity zones. Geophys. Res. Lett. 42:1039–1045. http://dx.doi.org/10.1002/2014GL062097.

Buffett, B.A., Garnero, E.J., Jeanloz, R., 2000. Sediments at the top of Earth's core. Science 290, 1338–1342.

Burkhardt, C., Borg, L.E., Brennecka, G.A., Shollenberger, Q.R., Dauphas, N., Kleine, T., 2016. A nucleosynthetic origin for the Earth's anomalous ^{142}Nd composition. Nature 537, 394–398.

Canup, R.M., 2008. Accretion of the Earth. Phil. Trans. R. Soc. A 366, 4061–4075.

Canup, R.M., 2012. Forming a Moon with an Earth-like composition via a giant impact. Science 338, 1052–1055.

Carlson, R.W., Boyet, M., Horan, M., 2007. Chondrite barium, neodymium, and samarium isotopic heterogeneity and early Earth differentiation. Science 316, 1175–1178.

Carlson, R.W., et al., 2014. How did early Earth become our modern world? Annu. Rev. Earth Planet. Sci. 42, 151–178.

Caro, G., Bourdon, B., Birck, J.L., Moorbath, S., 2006. High precision $^{142}Nd/^{144}Nd$ measurements in terrestrial rocks: constraints on the early differentiation of the Earth's mantle. Geochim. Cosmochim. Acta 70, 164–191.

Cartier, C., Hammouda, T., Boyet, M., Bouhifd, M.A., Devidal, J.L., 2014. Redox control on Nb/Ta fractionation during planetary accretion. Nat. Geosci. 7, 573–576.

Cartier, C., Hammouda, T., Boyet, M., Mathon, O., Testemale, D., Moine, B.N., 2015. Evidence for Nb^{2+} and Ta^{3+} in silicate melts under highly reducing conditions: A XANES study. Am. Mineral. 100, 2152–2158.

Chabot, N.L., Draper, D.S., Agee, C.B., 2005. Conditions of core formation in the Earth: Constraints from nickel and cobalt partitioning. Geochim. Cosmochim. Acta 69, 2141–2151.

Chambers, J.E., 2004. Planetary accretion in the inner solar system. Earth Planet. Sci. Lett. 223, 241–252.

Chamorro-Perez, E., Gillet, P., Jambon, A., 1996. Argon solubility in silicate melts at very high pressures. Experimental set-up and preliminary results for silica and anorthite melts. Earth Planet. Sci. Lett. 145, 97–107.

Clesi, V., Bouhifd, M.A., Bolfan-Casanova, N., Manthilake, G., Fabbrizio, A., Andrault, D., 2016. Effect of H_2O on metal-silicate partitioning of Ni, Co, V, Cr, Mn and Fe: implications for the oxidation state of the Earth and Mars. Geochim. Cosmochim. Acta 192, 97–121.

Coltice, N., Moreira, M., Herlund, J., Labrosse, S., 2011. Crystallization of a basal magma ocean recorded by helium and neon. Earth Planet. Sci. Lett. 308, 193–199.

Connelly, J.N., Bizzarro, M., Krot, A.N., Nordlund, A., Wielandt, D., Ivanova, M.A., 2012. The absolute chronology and thermal processing of solids in the Solar protoplanetary disk. Science 338, 651–655.

Dahl, T.W., Stevenson, D.J., 2010. Turbulent mixing of metal and silicate during planet accretion and interpretation of the Hf–W chronometer. Earth Planet. Sci. Lett. 295, 177–186.

Dasgupta, R., Chi, H., Shimizu, N., Buono, A.S., Walker, D., 2013. Carbon solution and partitioning between metallic and silicate melts in a shallow magma ocean: implications for the origin and distribution of terrestrial carbon. Geochim. Cosmochim. Acta 102, 191–212.

Dauphas, N., Chen, J.H., Zhang, J., Papanastassiou, D.A., Davis, A.M., Travaglio, C., 2014. Calcium-48 isotopic anomalies in bulk chondrites and achondrites: Evidence for a uniform isotopic reservoir in the inner protoplanetary disk. Earth Planet. Sci. Lett. 407, 96–108.

Deguen, R., Olson, P., Cardin, P., 2011. Experiments on turbulent metal–silicate mixing in a magma ocean. Earth Planet. Sci. Lett. 310, 303–313.

Deguen, R., Landeau, M., Olson, P., 2014. Turbulent metal–silicate mixing, fragmentation, and equilibration in magma oceans. Earth Planet. Sci. Lett. 391, 274–287.

Doremus, R.H., 1966. Physical solubility of gases in fused silica. J. Am. Ceram. Soc. 49, 461–462.

Elkins-Tanton, L.T., 2012. Magma oceans in the inner solar system. Annu. Rev. Earth Planet. Sci. 40, 113–139.

Fiquet, G., Auzende, L., Siebert, J., Corgne, A., Bureau, H., Ozawa, H., Garbarino, G., 2010. Melting of peridotite to 140 GPa. Science 329, 1516–1518.

Fischer, R.A., Ciela, F.J., 2014. Dynamics of the terrestrial planets from a large number of *N*-body simulations. Earth Planet. Sci. Lett. 392, 28–38.

Fischer, R.A., Nakajima, Y., Campbell, A.J., Frost, D.J., Harries, D., Langenhorst, F., Miyajima, N., Pollok, K., Rubie, D.C., 2015. High pressure metal-silicate partitioning of Ni, Co, V, Cr, Si, and O. Geochim. Cosmochim. Acta 167, 177–194.

Frost, D.J., Langenhorst, F., 2002. The effect of Al_2O_3 on Fe-Mg partitioning between magnesiowüstite and magnesium silicate perovskite. Earth Planet. Sci. Lett. 199, 227–241.

Frost, D.J., Liebske, C., Langenhorst, F., McCammon, C.A., Tronnes, R.G., Rubie, D.C., 2004. Experimental evidence for the existence of iron-rich metal in the Earth's lower mantle. Nature 428, 409–412.

Gaillard, F., Scaillet, B., 2014. A theoretical framework for volcanic degassing chemistry in a comparative planetology perspective and implications for planetary atmospheres. Earth Planet. Sci. Lett. 403, 307–316.

Gaillard, F., Scaillet, B., Pichacant, M., Iacono-Marziano, G., 2015. The redox geodynamics linking basalts and their mantle sources through space and time. Chem. Geol. 418, 217–233.

Gannoun, A., Boyet, M., Rizo, H., El Goresy, A., 2011. ^{146}Sm-^{142}Nd systematics measured in enstatite chondrites reveals a heterogeneous distribution of ^{142}Nd in the solar nebula. PNAS 108, 7693–7697.

Gessmann, C.K., Rubie, D.C., 2000. The origin of the depletions of V, Cr and Mn in the mantles of the Earth and Moon. Earth Planet. Sci. Lett. 184, 95–107.

Goldschmidt, V.M., 1937. The principles of distribution of chemical elements in minerals and rocks. The Seventh Hugo Müller Lecture, Delivered before the Chemical Society on March 17th, 1937.

Greenwood, R.C., Franchi, I.A., Jambon, A., Buchanan, P.C., 2005. Widespread magma oceans on asteroidal bodies in the early solar system. Nature 435, 916–918.

Grossman, L., 1972. Condensation in the primitive solar nebula. Geochim. Cosmochim. Acta 36, 597–619.

Grossman, L., Beckett, J.R., Fedkin, A.V., Simon, S.B., Ciesla, F.J., 2008. Redox conditions in the solar nebula: observational, experimental, and theoretical constraints. Rev. Mineral. Geochem. 68, 93–140.

Guillot, B., Sator, N., 2012. Noble gases in high-pressure silicate liquids: a computer simulation study. Geochim. Cosmochim. Acta 80, 51–69.

Halliday, A.N., 2013. The origins of volatiles on the terrestrial planets. Geochim. Cosmochim. Acta 105, 146–171.

Halliday, A.N., Wood, B.J., 2009. How did Earth accrete? Science 325, 44–45.

Harper, C.L., Jacobsen, S.B., 1996. Noble gases and Earth's accretion. Science 273, 1814–1818.

Hartmann, W.K., Davis, D.R., 1975. Satellite-sized planetesimals and lunar origin. Icarus 24, 504–514.

Heber, V.S., Brooker, R.A., Kelley, S.P., Wood, B.J., 2007. Crystal–melt partitioning of noble gases (helium, neon, argon, krypton, and xenon) for olivine and clinopyroxene. Geochim. Cosmochim. Acta 71, 1041–1061.

Herzberg, C., et al., 2013. Nickel and helium evidence for melt above the core-mantle boundary. Nature 493, 393–397.

Hirschmann, M.M., 2016. Constraints on the early delivery and fractionation of Earth's major volatiles from C/H, C/N, and C/S ratios. Am. Mineral. 101, 540–553.

Hirschmann, M.M., Dasgupta, R., 2009. The H/C ratios of Earth's near-surface and deep reservoirs, and consequences for deep Earth volatile cycles. Chem. Geol. 262, 4–16.

Hirschmann, M.M., Withers, A.C., Ardia, P., Foley, N.T., 2012. Solubility of molecular hydrogen in silicate melts and consequences for volatile evolution of terrestrial planets. Earth Planet. Sci. Lett. 345-348, 38–48.

Hofmann, A.W., 1988. Chemical differentiation on the Earth: the relationship between mantle, continental crust, and oceanic crust. Earth Planet. Sci. Lett. 90, 297–314.

Honda, M., McDougall, I., Patterson, D.B., Doulgeris, A., Clague, D.A., 1991. Possible solar noble-gas component in Hawaiian basalts. Nature 349, 149–151.

Javoy, M., 1995. The integral enstatite chondrite model of the Earth. Geophys. Res. Lett. 22, 2219–2222.

Javoy, M., et al., 2010. The chemical composition of the Earth: enstatite chondrite models. Earth Planet. Sci. Lett. 293, 259–268.

Jephcoat, A.P., Bouhifd, M.A., Porcelli, D., 2008. Partitioning experiments in the laser-heated diamond anvil cell: volatile content in the Earth's core. Phil. Trans. R. Soc. A 366, 4295–4314.

Kadik, A.A., Koltashev, V.V., Kryukova, E.B., Plotnichenko, V.G., Tsekhonya, T.I., Kononkova, N.N., 2015. Solubility of nitrogen, carbon, and hydrogen in FeO-Na_2O-Al_2O_3-SiO_2 melt and liquid iron alloy: influence of oxygen fugacity. Geochem. Int. 53, 849–868.

Kargel, J.S., Lewis, J.S., 1993. The composition and early evolution of Earth. Icarus 105, 1–25.

Ke, Y., Solomatov, V.S., 2009. Coupled core–mantle thermal evolution of early Mars. J. Geophys. Res. Planets 114 (13), 1–12.

Kleine, T., Touboul, M., Bourdon, B., Nimmo, F., Mezger, K., Palme, H., Jacobsen, S.B., Yin, Q.-Z., Halliday, A.N., 2009. Hf-W chronology of the accretion and early evolution of asteroids and terrestrial planets. Geochim. Cosmochim. Acta 73, 5150–5188.

Kruijer, T.S., Sprung, P., Kleine, T., Leya, I., Burkhardt, C., Wieler, R., 2012. Hf-W chronometry of core formation in planetesimals inferred from weakly irradiated iron meteorites. Geochim. Cosmochim. Acta 99, 287–304.

Kruijer, T.S., Fischer-Gödde, M., Kleine, T., Burkhardt, C., Wieler, R., 2014. Nucleosynthetic W isotope anomalies and the Hf-W chronometry of Ca–Al-rich inclusions. Earth Planet. Sci. Lett. 403, 317–327.

Labrosse, S., Hernlund, J.W., Coltice, N., 2007. A crystallizing dense magma ocean at the base of the Earth's mantle. Nature 450, 866–869.
Larimer, J.W., Buseck, P.R., 1974. Equilibration temperatures in enstatite chondrites. Geochim. Cosmochim. Acta 38, 471–477.
Lauterbach, S., McCammon, C.A., van Aken, P., Langenhorst, F., Seifert, F., 2000. Mössbauer and ELNES spectroscopy of $(Mg,Fe)(Si,Al)O_3$ perovskite: a highly oxidized component of the lower mantle. Contrib. Mineral. Petrol. 138, 17–26.
Lay, T., Garnero, E.J., Williams, Q., 2004. Partial melting in a thermo-chemical boundary layer at the base of the mantle. Phys. Earth Planet. Inter. 146, 441–467.
Li, J., Agee, C.B., 1996. Geochemistry of mantle–core differentiation at high pressure. Nature 381, 686–689.
Li, J., Agee, C.B., 2001. The effect of pressure, temperature, oxygen fugacity and composition on partitioning of nickel and cobalt between liquid Fe–Ni–S and liquid silicate: implications for the Earth's core formation. Geochim. Cosmochim. Acta 65, 1821–1832.
Li, Y., Dasgupta, R., Tsuno, K., Monteleone, B., Shimizu, N., 2016. Carbon and sulfur budget of the silicate Earth explained by accretion of differentiated planetary embryos. Nat. Geosci. 7, 781–785.
Lupton, J.E., Craig, H., 1975. Excess ^3He in oceanic basalts; evidence for terrestrial primordial helium. Earth Planet. Sci. Lett. 26, 133–139.
Macpherson, C.G., Hilton, D.R., Sinton, J.M., Poreda, R.J., Craig, H., 1998. High $^3He/^4He$ ratios in the Manus backarc basin: Implications for mantle mixing and the origin of plumes in the western Pacific Ocean. Geology 26, 1007–1010.
Malavergne, V., Tarrida, M., Combes, R., Bureau, H., Jones, J., Schwandt, C., 2007. New high-pressure and high-temperature metal/silicate partitioning of U and Pb: implications for the cores of the Earth and Mars. Geochim. Cosmochim. Acta 71, 2637–2655.
Mann, U., Frost, D.J., Rubie, D.C., 2009. Evidence for high pressure core-mantle differentiation from the metal-silicate partitioning of lithophile and weakly-siderophile elements. Geochim. Cosmochim. Acta 73, 7360–7386.
Marty, B., 2012. The origins and concentrations of water, carbon, nitrogen and noble gases on Earth. Earth Planet. Sci. Lett. 313-314, 56–66.
Marty, B., Alexander, C.M.O.'.D., Raymond, S.N., 2013. Primordial origins of Earth's carbon. Rev. Mineral. Geochem. 75, 149–181.
McCammon, C.A., Lauterbach, S., Seifert, F., Langenhorst, F., van Aken, P.A., 2004. Iron oxidation state in lower mantle mineral assemblages. I. Empirical relations derived from high-pressure experiments. Earth Planet. Sci. Lett. 222, 435–449.
McDonough, W.F., Sun, S.-S., 1995. The composition of the Earth. Chem. Geol. 120, 223–253.
Mizuno, H., Nakazawa, K., Hayashi, C., 1980. Dissolution of the primordial rare gases into the molten Earth's material. Earth Planet. Sci. Lett. 50, 202–210.
Monteux, J., Ricard, Y., Coltice, N., Dubuffet, F., Ulvrova, M., 2009. A model of metal– silicate separation on growing planets. Earth Planet. Sci. Lett. 287, 353–362.
Monteux, J., Andrault, D., Samuel, H., 2016. On the cooling of a deep terrestrial magma ocean, Earth and planet. Sci. Lett. 448, 140–149.
Morbidelli, A., Lunine, J.I., O'Brien, D.P., Raymond, S.N., Walsh, K.J., 2012. Building terrestrial planets. Annu. Rev. Earth Planet. Sci. 40, 251–275.
Moreira, M., 2013. Noble gas constraints on the origin and evolution of Earth's volatiles. Geochem. Perspect. 2, 229–403.
Moreira, M., Charnoz, S., 2016. The origin of the neon isotopes in chondrites and on Earth. Earth Planet. Sci. Lett. 433, 249–256.
Mosenfelder, J.L., Asimow, P.D., Ahrens, T.J., 2007. Thermodynamic properties of Mg_2SiO_4 liquid at ultra-high pressures from shock measurements to 200 GPa on forsterite and wadsleyite. J. Geophys. Res. Solid Earth 112:B06208. http://dx.doi.org/10.1029/2006JB004364.
Mosenfelder, J.L., Asimow, P.D., Frost, D.J., Rubie, D.C., Ahrens, T.J., 2009. The MgSiO3 system at high pressure: thermodynamic properties of perovskite, postper- ovskite, and melt from global inversion of shock and static compression data. J. Geophys. Res. Solid Earth 114:B01203. http://dx.doi.org/10.1029/2008JB005900.
Mukhopadhayay, S., 2012. Early differentiation and volatile accretion recorded in deep-mantle neon and xenon. Nature 486, 101–104.
Münker, C., Pfänder, J.A., Weyer, S., Büchl, A., Kleine, T., Mezger, K., 2003. Evolution of planetary cores and the Earth-Moon system from Nb/Ta systematics. Science 301, 84–87.
Nagahara, H., Ozawa, K., 1996. Evaporation of forsterite in H-2 gas. Geochim. Cosmochim. Acta 60, 1445–1459.
Nakajima, M., Stevenson, D.J., 2015. Melting and mixing states of the Earth's mantle after the Moon-forming impact. Earth Planet. Sci. Lett. 427, 286–295.
Nakajima, Y., Frost, D.J., Rubie, D.C., 2012. Ferrous iron partitioning between magnesium silicate perovskite and ferropericlase and the composition of perovskite in the Earth's lower mantle. J. Geophys. Res. 117, 1–12.
Nebel, O., van Westrenen, W., Vroon, P.Z., Wille, M., Raith, M.M., 2010. Deep mantle storage of the Earth's missing niobium in late-stage residual melts from a magma ocean. Geochim. Cosmochim. Acta 74, 4392–4404.
Nevins, D., Spera, F.J., 1998. Molecular dynamics simulations of molten $CaAl_2Si_2O_8$: dependence of structure and properties on pressure. Am. Mineral. 83, 1220–1230.
Newsom, H.E., 1990. Accretion and core formation in the Earth: evidence from siderophile elements. In: Newson, H.E., Jones, J.H. (Eds.), Origin of the Earth. Oxford University Press, New York, pp. 273–288.
Niwa, K., Miyakawa, C., Yagi, T., Matsuda, J., 2013. Argon solubility in SiO_2 melt under high pressures: a new experimental result using laser-heated diamond anvil cell. Earth Planet. Sci. Lett. 363, 1–8.
Nomura, R., Ozawa, H., Tateno, S., Hirose, K., Hernlund, J.W., Muto, S., Ishii, H., Hiraoka, N., 2011. Spin crossover and iron-rich silicate melt in the Earth's deep mantle. Nature 473, 199–202.
Nomura, R., Hirose, K., Uesugi, K., Ohishi, Y., Tsuchiyama, A., Miyake, A., Ueno, Y., 2014. Low core–mantle boundary temperature inferred from the solidus of pyrolite. Science 343, 522–525.
O'Brien, D.P., Morbidelli, A., Levison, H.F., 2006. Terrestrial planet formation with strong dynamical friction. Icarus 184, 39–58.
Ohtani, E., Yurimoto, H., 1996. Element partitioning between metallic liquid, magnesiowustite, and silicate liquid at 20 GPa and 2500 °C: a secondary ion mass spectrometric study. Geophys. Res. Lett. 23, 1993–1996.
O'Neill, H.S.C., Palme, H., 1998. Composition of the silicate Earth: implications for accretion and core formation. In: Jackson, I. (Ed.), The Earth's Mantle, Composition, Structure, and Evolution. Cambridge University Press, pp. 3–126.
O'Neill, H.S.C., Canil, D., Rubie, D.C., 1998. Oxide-metal equilibria to 2500 °C and 25 GPa: Implications for core formation and the light component in the Earth's core. J. Geophys. Res. 103, 12239–12260.
Pepin, R.O., Porcelli, D., 2006. Xenon isotope systematics, giant impacts, and mantle degassing on the early Earth. Earth Planet. Sci. Lett. 250, 470–485.
Porcelli, D., Ballentine, C.J., 2002. Models for the distribution of terrestrial noble gases and evolution of the atmosphere. Rev. Mineral. Geochem. 46, 411–480.
Porcelli, D., Halliday, A.N., 2001. The core as a possible source of mantle helium. Earth Planet. Sci. Lett. 192, 45–56.
Porcelli, D., Woolum, D., Cassen, P., 2001. Deep Earth rare gases: initial inventories, capture from the solar nebula, and losses during Moon formation. Earth Planet. Sci. Lett. 193, 237–251.
Pradhan, G.K., Fiquet, G., Siebert, J., Auzende, A.-L., Morard, G., Antonangeli, D., Garbarino, G., 2015. Melting of MORB at core-mantle boundary. Earth Planet. Sci. Lett. 431, 247–255.
Press, W.H., Teukolsky, S.A., Vetterling, W.T., Flannery, B.P., 1993. Numerical Recipes in FORTRAN the Art of Scientific Computing. second ed. Cambridge University Press, New York, NY, USA.
Raymond, S.N., Quinn, T., Lunine, J.I., 2006. High-resolution simulations of the final assembly of Earth-like planets I. Terrestrial accretion and dynamics. Icarus 183, 265–282.
Revenaugh, J., Meyer, R., 1997. Seismic evidence of partial melt within a possibly ubiquitous low-velocity layer at the base of the mantle. Science 277, 670–673.
Righter, K., 2011. Prediction of metal–silicate partition coefficients for siderophile elements: an update and assessment of PT conditions for metal–silicate equilibrium during accretion of the earth. Earth Planet. Sci. Lett. 304, 158–167.
Rizo, H., Boyet, M., Blichert-Toft, J., Rosing, M., 2011. Combined Nd and Hf isotope evidence for deep-seated source of Isua lavas. Earth Planet. Sci. Lett. 312, 267–279.
Rizo, H., Boyet, M., Blichert-Toft, J., Rosing, M.T., 2013. Early mantle dynamics inferred from Nd-142 variations in Archean rocks from southwest Greenland. Earth Planet. Sci. Lett. 377, 324–335.
Rizo, H., et al., 2016. Preservation of Earth-forming events in the tungsten isotopic composition of modern flood basalts. Science 352, 809–812.
Roskosz, M., Bouhifd, M.A., Jephcoat, A.P., Marty, B., Mysen, B.O., 2013. Nitrogen solubility in molten metal and silicate at high pressure and temperature. Geochim. Cosmochim. Acta 121, 15–28.
Rost, S., Garnero, E.J., Williams, Q., 2005. Seismological constraints on a possible plume root at the core-mantle boundary. Nature 435, 666–669.
Rubie, D.C., Melosh, H.J., Reid, J.E., Liebske, C., Righter, K., 2003. Mechanisms of metal– silicate equilibration in the terrestrial magma ocean. Earth Planet. Sci. Lett. 205, 239–255.
Rubie, D.C., Gessmann, C.K., Frost, D.J., 2004. Partitioning of oxygen during core formation on the Earth and Mars. Nature 429, 58–61.
Rubie, D.C., Frost, D.J., Mann, U., Asahara, Y., Nimmo, F., Tsuno, K., Kegler, P., Holzheid, A., Palme, H., 2011. Heterogeneous accretion, composition and core–mantle differentiation of the Earth. Earth Planet. Sci. Lett. 301, 31–42.
Rubie, D.C., et al., 2015a. Accretion and differentiation of the terrestrial planets with implications for the compositions of early-formed solar system bodies and accretion of water. Icarus 248, 89–108.
Rubie, D.C., Nimmo, F., Melosh, H.J., 2015b. Formation of the Earth's core. treatise on geophysics, second edition. In: Stevenson, D. (Ed.), Evolution of the Earth 9. Elsevier, Amsterdam, pp. 43–79.
Rudnick, R., Barth, M., Horn, I., McDonough, W., 2000. Rutile-bearing refractory eclogites: missing link between continents and depleted mantle. Science 287, 278–281.
Samuel, H., 2012. A re-evaluation of metal diapir breakup and equilibration in terrestrial magma oceans. Earth Planet. Sci. Lett. 313, 105–114.
Samuel, H., Tackley, P.J., Evonuk, M., 2010. Heat partitioning in terrestrial planets during core formation by negative diapirism. Earth Planet. Sci. Lett. 290, 13–19.
Saikia, A., Boffa Ballaran, T., Frost, D.J., 2009. The effect of Fe and Al substitution on the compressibility of MgSiO3-perovskite determined through single-crystal X ray diffraction. Phys. Earth Planet. Inter. 173, 153–161.
Sanloup, C., et al., 2013. Structural change in molten basalt at deep mantle conditions. Nature 503, 104–107.
Schiano, P., Provost, A., Clocchiatti, R., Faure, F., 2006. Transcrystalline melt migration and Earth's mantle. Science 314, 970–974.
Shackelford, J.F., Studt, P.L., Fulrath, R.M., 1972. Solubility of gases in glass II. He, Ne, and H_2 in fused silica. J. Appl. Phys. 43, 1619–1626.
Shannon, R.D., 1976. Revised effective ionic radii and systematic studies of interatomic distances in halides and chalcogenides. Acta Crystallogr. Sect. A: Cryst. Phys. Diffr. Theor. Gen. Crystallogr. 32, 751–767.
Shelby, J.E., 1976. Pressure dependence of helium and neon solubility in vitreous silica. J. Appl. Phys. 47, 135–139.
Siebert, J., Corgne, A., Ryerson, F.J., 2011. Systematics of metal–silicate partitioning for many siderophile elements applied to Earth's core formation. Geochim. Cosmochim. Acta 75, 1451–1489.
Siebert, J., Badro, J., Antonangeli, D., Ryerson, F.J., 2012. Metal-silicate partitioning of Ni and Co in a deep magma ocean. Earth Planet. Sci. Lett. 321-322, 189–197.
Siebert, J., Badro, J., Antonangeli, D., Ryerson, F.J., 2013. Terrestrial accretion under oxidizing conditions. Science 339, 1194–1197.

Sleep, N.H., Zahnle, K.J., Neuhoff, P.S., 2001. Initiation of clement surface conditions on the earliest Earth. Proc. Natl. Acad. Sci. 98, 3666–3672.
Solomatov, V.S., 2007. Magma oceans and primordial mantle differentiation. In: Schubert, G. (Ed.)first ed. Treatise on Geophysics v. 9. Elsevier, pp. 91–119.
Stevenson, D.J., 1990. In: Newsom, H.E., Jones, J.H. (Eds.), Fluid dynamics of core formation, in the *Origin of the Earth*. Oxford University Press.
Studt, P.L., Shackelford, J.F., Fulrath, R.M., 1970. Solubility of gases in glass: a monoatomic model. J. Appl. Phys. 44, 2777–2780.
Tackley, P.J., 2012. Dynamics and evolution of the deep mantle resulting from thermal, chemical, phase and melting effects. Earth Sci. Rev. 110, 1–25.
Tateno, S., Hirose, K., Ohishi, Y., 2014. Melting experiments on peridotite to lowermost mantle conditions. J. Geophys. Res. Solid Earth 119, 4684–4694.
Terasaki, H., Frost, D.J., Rubie, D.C., Langenhorst, F., 2007. Interconnectivity of Fe–O–S liquid in polycrystalline silicate perovskite at lower mantle conditions. Phys. Earth Planet. Inter. 161, 170–176.
Thibault, Y., Walter, M.J., 1995. The influence of pressure and temperature on the metal–silicate partition coefficients of nickel and cobalt in a model C1 chondrite and implications for metal segregation in a deep magma ocean. Geochim. Cosmochim. Acta 59, 991–1002.
Thomas, C.W., Asimow, P.D., 2013. Direct shock compression experiments on premolten forsterite and progress toward a consistent high-pressure equation of state for CaO-MgO-Al_2O_3-SiO_2-FeO liquids. J. Geophys. Res. Solid Earth 118, 5738–5752.
Thomas, C.W., Liu, Q., Agee, C.B., Asimow, P.D., Lange, R.A., 2012. Multi-technique equation of state for Fe2SiO4 melt and the density of Fe-bearing silicate melts from 0 to 161 GPa. J. Geophys. Res. Solid Earth 117:B10206. http://dx.doi.org/10.1029/2012JB009403.
Tonks, W.B., Melosh, H.J., 1993. Magma ocean formation due to giant impacts. J. Geophys. Res. 98, 5319–5333.
Touboul, M., Puchtel, I.S., Walker, R.J., 2012. ^{182}W evidence for long-term preservation of early mantle differentiation products. Science 335, 1065–1069.
Touboul, M., Sprung, P., Aciego, S.M., Bourdon, B., Kleine, T., 2015. Hf–W chronology of the eucrite parent body. Geochim. Cosmochim. Acta 156, 106–121.
Trieloff, M., Kunz, J., 2005. Isotope systematics of noble gases in the Earth's mantle: possible sources of primordial isotopes and implications for mantle structure. Phys. Earth Planet. Inter. 148, 13–38.
Tsuno, K., Frost, D.J., Rubie, D.C., 2013. Simultaneous partitioning of silicon and oxygen into the Earth's core during early Earth differentiation. Geophys. Res. Lett. 40, 66–71.
Tucker, J.M., Mukhopadhyay, S., 2014. Evidence for multiple magma ocean outgassing and atmospheric loss episodes from mantle noble geases. Earth Planet. Sci. Lett. 393, 254–265.
Valley, J.W., et al., 2014. Hadean age for post-magma-ocean zircon confirmed by atom-probe tomography. Nat. Geosci. 7, 219–223.
Vidale, J.E., Hedlin, M.A.H., 1998. Evidence for partial melt at the core–mantle boundary north of Tonga from the strong scattering of seismic waves. Nature 391, 682–685.
Wacheul, J.B., Le Bars, M., Monteux, J., Aurnou, J.M., 2014. Laboratory experiments on the breakup of liquid metal diapirs. Earth Planet. Sci. Lett. 403, 236–245.
Wade, J., Wood, B.J., 2001. The Earth's "missing" niobium may be in the core. Nature 409, 75–78.
Wade, J., Wood, B.J., 2005. Core formation and the oxidation state of the Earth. Earth Planet. Sci. Lett. 236, 78–95.
Warren, P.H., 2011. Stable-isotopic anomalies and the accretionary assemblage of the Earth and Mars: a subordinate role for carbonaceous chondrites. Earth Planet. Sci. Lett. 311, 93–100.
Wetherill, G.W., 1985. Occurrence of giant impacts during the growth of terrestrial planets. Science 228, 877–879.
Wheeler, K.T., Walker, D., Fei, Y., Minarik, W.G., McDonough, W.F., 2006. Experimental partitioning of uranium between liquid iron sulfide and liquid silicate: implications for radioactivity in the Earth's core. Geochim. Cosmochim. Acta 70, 1537–1547.
White, B.S., Brearly, M., Montana, A., 1989. Solubility of argon in silicate liquids at high pressures. Am. Mineral. 74, 513–529.
Wicks, J.K., Jackson, J.M., Sturhahn, W., 2010. Very low sound velocities in iron-rich (Mg,Fe)O: Implications for the core–mantle boundary region. Geophys. Res. Lett. 37, L15304. http://dx.doi.org/10.1029/2010GL043689.
Wilde, S.A., Valley, J.W., Peck, W.H., Graham, C.M., 2001. Evidence from detritical zircons for the existence of continental crust and oceans on the Earth 4.4 Gyr ago. Nature 409, 175–178.
Williams, Q., Garnero, E.J., 1996. Seismic evidence for partial melt at the base of Earth's mantle. Science 273, 1528–1530.
Wood, B.J., Walter, M.J., Wade, J., 2006. Accretion of the Earth and segregation of its core. Nature 441, 825–833.
Wood, B.J., Li, J., Shahar, A., 2013. Carbon in the core: influence on the properties of core and mantle. Rev. Mineral. Geochem. 75, 231–250.
Yokochi, R., Marty, B., 2005. Geochemical constraints on mantle dynamics in the Hadean. Earth Planet. Sci. Lett. 238, 17–30.
Yoshino, T., Walter, M., Katsura, T., 2003. Core formation in planetesimals triggered by permeable flow. Nature 422, 154–157.
Zahnle, K.J., Kastings, J.F., Pollack, J.B., 1988. Evolution of a steam atmosphere during Earth's accretion. Icarus 74, 62–97.
Zhang, Y., Yin, Q.Z., 2012. Carbon and other light element contents in the Earth's core based on first-principles molecular dynamics. Proc. Natl. Acad. Sci. U. S. A. 109, 16579–16583.

Physics of the Earth and Planetary Interiors 289 (2019) 75–89

Contents lists available at ScienceDirect

Physics of the Earth and Planetary Interiors

journal homepage: www.elsevier.com/locate/pepi

Dynamics and stability of an iron drop falling in a magma ocean

B. Qaddah[a,b,*], J. Monteux[a], V. Clesi[a], M.A. Bouhifd[a], M. Le Bars[b]

[a] Université Clermont Auvergne, CNRS, IRD, OPGC, Laboratoire Magmas et Volcans, F-63000 Clermont-Ferrand, France
[b] CNRS, Aix Marseille Univ, Centrale Marseille, IRPHE, Marseille, France

ARTICLE INFO

Keywords:
Core formation
Fluid dynamics
Numerical modeling
Metal drop
Magma ocean

ABSTRACT

The latest stages of planetary accretion involved large impacts between differentiated bodies, hence large scale melting events. Consequently, the iron brought by the impactors sank within a deep magma ocean, before reaching the proto-core. Yet the fluid dynamics of this process remains poorly known. Here, we report numerical simulations of the sinking dynamics of an initially spherical liquid iron drop within a molten silicate phase, up to its possible fragmentation. We consider a 2D cylindrical axisymmetric geometry. We vary the viscosity of the molten silicates in the range of 0.05 Pa.s–100 Pa.s and the initial radius of the iron drop in the range of 1 mm–350 mm. Hence, we investigate Reynolds number in the range of [0.027–85600] and Weber number in the range of [0.073–7480]. Our numerical model constrains the morphology, dynamics and stability of the iron drop as a function of the dimensionless Weber and Reynolds numbers as well as of the viscosity ratio between the molten silicates and the liquid iron drop. In particular, we show that the maximal stable drop radius and the critical Weber number are monotonically increasing functions of the magma ocean viscosity. The momentum boundary layer thickness depends mainly on the drop radius and slightly on the magma ocean viscosity. Increasing the viscosity of the silicate phase prevents oscillations of the iron phase and limits the exchange surface. Oppositely, increasing the initial radius of the iron drop enhances its deformation and increases its relative exchange surface. Above the critical Weber number, we confirm that the fragmentation of the liquid iron occurs within a falling distance equal to 3.5–8 times the drop initial radius in the explored range of moderate Weber number, and we describe a variety of fragmentation regimes. Consequences for Earth's formation models are briefly assessed.

1. Introduction

The Earth core formation is a complex process which remains actively debated theoretically, experimentally, and numerically (e.g. Stevenson, 1990; Tonks and Melosh, 1992; Chambers, 2004; O'Brien et al., 2006; Wood et al., 2006; Morbidelli et al., 2012; Deguen et al., 2014; Wacheul et al., 2014; Bouhifd et al., 2017). The core formation is highly dependent on accretion as both processes are contemporaneous (Kleine et al., 2002; Touboul et al., 2007). In the latest stages of planetary accretion, giant impacts have occurred [Fig. 1], leading for instance to the formation of the Moon following the collision between a large differentiated body of Mars size and the proto-Earth (Hartmann and Davis, 1975). The enormous amount of kinetic energy brought in by these collisions (Tonks and Melosh, 1992; Monteux et al., 2007; Samuel, 2012), the decay of short-lived radio-elements (^{26}Al and ^{60}Fe) causing radioactive heating (Walter and Tronnes, 2004), and the heat dissipation from the conversion of potential energy (Monteux et al., 2009; Samuel, 2012) probably led to the formation of deep magma oceans (Tonks and Melosh, 1992). Following the impact, the liquid iron from the impactor core spread and then sank into this less dense magma ocean as an immiscible fluid, leading to thermo-chemical exchanges between the two phases, before merging with the proto-core. This dynamical process may involve deformation of the initial drops coming from the primary breakup at impact, and possibly their breakup into even smaller droplets [Fig. 1] (Samuel, 2012).

Three scenarios have been proposed to characterise the motion of liquid iron within the magma ocean and the thermo-chemical equilibration between the two phases. In the first scenario, i.e. the so-called iron rain model (Stevenson, 1990; Karato and Rama Murthy, 1997; Rubie et al., 2003), it is suggested that an impactor's core with a diameter of [10–100] km immediately fragments into small droplets with a single characteristic diameter of the order of 1 cm, corresponding to the capillary size. All droplets descend independently towards the bottom of the magma ocean at the same velocity and without any further change in shape, leading to an efficient chemical equilibration at a distance of less than 200 m within the magma ocean. In contrast, Dahl

* Corresponding author.
E-mail address: qaddah@irphe.univ-mrs.fr (B. Qaddah).

https://doi.org/10.1016/j.pepi.2019.02.006
Received 16 October 2018; Received in revised form 8 February 2019; Accepted 14 February 2019
Available online 06 March 2019
0031-9201/

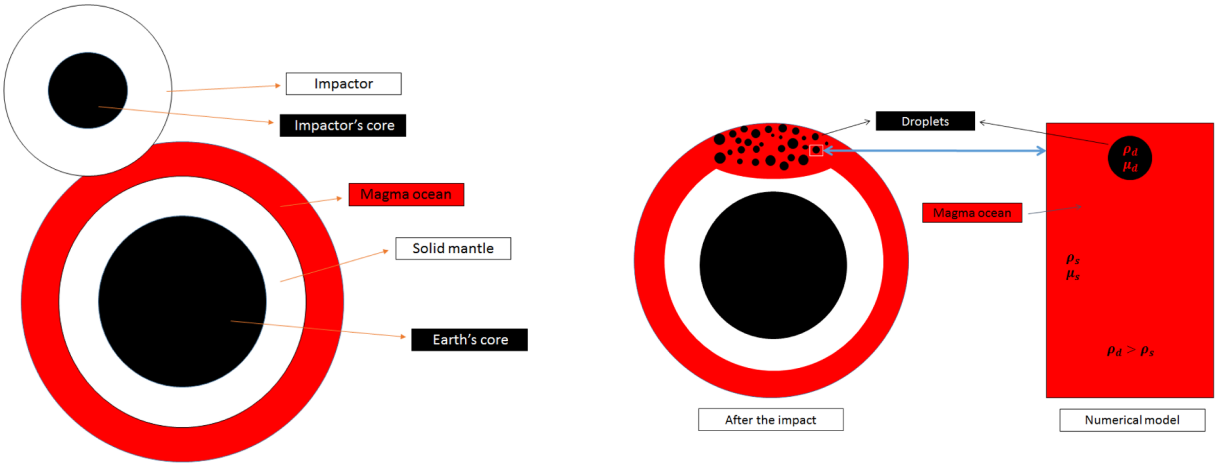

Fig. 1. Schematic of the metal/silicate separation during an impact between a differentiated planetesimal and the early Earth with a schematic of our computational domain.

and Stevenson (2010) proposed a theoretical model where the large liquid iron impactor's core does not break up into the magma ocean if its initial size is large enough; it is only eroded by Rayleigh-Taylor and Kelvin-Helmholtz instabilities. Such a core formation episode would be far from thermo-chemical equilibrium between the impactor's core and the magma ocean. More recently, Deguen et al. (2011) and Deguen et al. (2014) used fluid dynamics experiments to show that a large core always breaks and forms a cloud of droplets with different sizes. But before doing so, it first evolves from its initial state as a turbulent thermal with strong entrainment and mixing, leading to rapid equilibration even before fragmentation.

In these previous studies, the influence of the viscosity ratio between the molten silicates and the liquid iron is neglected. Wacheul et al. (2014) developed analog experiments using gallium to mimic the liquid iron and a mixture of water and glycerol to mimic molten silicates. They found that the value of the viscosity ratio is very important and changes significantly the flow morphology. Later on, Wacheul and Le Bars (2018) validated the turbulent thermal model proposed by Deguen et al. (2014) using global temperature measurements of the liquid metal equilibration. However, numerous questions remain regarding the local dynamics at the scale of one drop, including: What is the maximum stable size of a drop as a function of the viscosity ratio? How is the exchange surface between iron drops and molten silicates influenced by the viscosity ratio? What is the size of the dynamical boundary layer across which the thermal and chemical exchanges occur? Answering those questions is fundamental for a better estimate of the equilibration length in planets, hence for relevant models of planet initial thermochemical state.

Several works have already investigated the dynamics of a buoyant bubble or drop in a viscous environment. For instance, a seminal experimental study of rising bubbles of hydrogen in aqueous sugar solutions is reported by Bhaga and Weber (1981) to determine the shape of the bubble, its terminal velocity, the geometry of its wake, and the flow streamline around it. Several experimental investigations of drop breakup in gas-liquid and liquid-liquid systems are reviewed by Pilch and Erdman (1987). An axisymmetric numerical model of a secondary breakup of a spherical liquid drop falling from rest due to gravity in another immiscible liquid is presented in Han and Tryggvason (1999) for different density and viscosity ratios, showing large drop deformation and various breakup modes. Another axisymmetric numerical investigation of the evolution of a large bubble rising by buoyancy in the presence of both capillary and viscous effects was carried out by Bonometti and Magnaudet (2006), in particular to determine the transition from a spherical cap to a toroidal shape. The influence of viscosity and density ratios is investigated systematically by Ohta et al. (2009), Ohta et al. (2010), Ohta et al. (2014), Ohta and Sussman (2012). Finally, the first systematics on the asymmetric motion and the fragmentation modes of a bubble of gas rising in a liquid using three-dimensional numerical simulations are reported in Tripathi et al. (2015). However, previous works on the effects of viscosity contrast were motivated by industrial applications mainly, apart from 2 cases in Ichikawa et al. (2010) exploring the relative dynamical changes for viscosity ratios 0.1 and 10 between iron and a magma ocean. In the context of the core formation, the viscosity of the magma ocean strongly depends on its evolving temperature and pressure (Karki and Stixrude, 2010). Hence, the viscosity contrast between the metallic and silicate phases can differ by several orders of magnitude. We thus propose here to constrain the influence of the viscosity contrast between the metallic phase and the magma ocean focusing on the sinking of a unique iron droplet. We also investigate the influence of the droplet radius and derive scaling laws to characterise this fluid dynamics.

The study is organised as follows. Section 2 introduces the physical and numerical model, including the governing equations, the relevant non-dimensional parameters, the numerical model description, and our computational domain and mesh. Section 3 then presents our main numerical results including systematic studies of the drag coefficient, fragmentation modes, characteristic time and distance before breakup, and maximum stable radius before breakup. In Section 4, we discuss possible planetary applications, focusing on the potential efficiency of thermo-chemical exchanges around the drop which depends on the boundary layer thickness and the exchange surface between iron drop and molten silicates. Conclusions and future works are detailed in the final Section 5.

2. Physical and numerical model

2.1. Governing equations

We consider the sinking dynamics of an initially spherical iron drop, falling in a less dense and more viscous fluid under the action of gravity. We assume that both the liquid iron drop and the surrounding molten silicates behave as Newtonian, incompressible, and immiscible fluids with uniform surface tension, and constant density and viscosity within each fluid. We note here that we do not consider the thermo-chemical exchanges that may occur between the two phases. This point will be the subject of a separated study. Hence, the fluid dynamics is governed by the Navier-Stokes equations to characterize:

1. the conservation of mass

$$\nabla . \boldsymbol{u} = 0, \tag{1}$$

2. the conservation of momentum

$$\rho\left(\frac{\partial \boldsymbol{u}}{\partial t} + \boldsymbol{u}.\nabla\boldsymbol{u}\right) = \nabla.[-P\boldsymbol{I} + \mu(\nabla\boldsymbol{u} + (\nabla\boldsymbol{u})^T)] + \rho\boldsymbol{g} + \boldsymbol{F}_{st} \quad (2)$$

with $\boldsymbol{u}$ the fluid velocity vector (m/s), ρ the fluid density (kg/m^3), μ the fluid viscosity (Pa.s), t the time (s), P the fluid pressure (Pa), $\boldsymbol{g}$ the gravitational acceleration (m/s^2), $\boldsymbol{F}_{st}$ the surface tension force (N/m^3) and $\boldsymbol{I}$ the identity matrix.

We monitor the interface between the liquid iron drop and the molten silicates using the Level Set method, an Eulerian and implicit method frequently used in multiphase flow problems (e.g. Luo et al., 2006). It consists in defining a level set function ϕ, equal to 1 in iron and 0 in the surrounding silicates, and rapidly changing through the interface, whose position is determined by the isocontour $\phi = 0.5$. The equation governing the transport and reinitialization of ϕ is:

$$\frac{\partial \phi}{\partial t} + \boldsymbol{u}.\nabla\phi = \gamma\nabla.[\epsilon\nabla\phi - \phi(1-\phi)\frac{\nabla\phi}{|\nabla\phi|}] \quad (3)$$

with γ (m/s) and ϵ (m) the reinitialization parameters. ϵ determines the thickness of the layer around the interface, and is typically chosen equal to half the size of the characteristic mesh in the region explored by the interface. γ determines the amount of reinitialization: a suitable value for γ is the maximum velocity magnitude experienced in the model.

The density and dynamical viscosity are evaluated using the level set function:

$$\rho = \rho_s + (\rho_d - \rho_s)\phi \quad (4)$$

$$\mu = \mu_s + (\mu_d - \mu_s)\phi \quad (5)$$

where subscripts “s” and “d” stand for the molten silicates and the liquid iron drop respectively.

The surface tension force is determined by:

$$\boldsymbol{F}_{st} = \nabla.\boldsymbol{T} = \nabla.(\sigma[\boldsymbol{I} + (-\boldsymbol{n}\boldsymbol{n}^T)]\Delta) \quad (6)$$

with σ (N/m) the surface tension coefficient, I the identity matrix, $\boldsymbol{n}$ the interface normal unit vector, and Δ the Dirac delta function, nonzero only at the fluid interface. The interface normal unit vector is calculated as

$$\boldsymbol{n} = \frac{\nabla\phi}{|\nabla\phi|}. \quad (7)$$

The level set parameter ϕ is also used to approximate the delta function by a smooth function (Hu et al., 2014) defined by

$$\Delta = 6|\phi(1-\phi)||\nabla\phi|. \quad (8)$$

2.2. Physical and non-dimensional parameters

According to the Buckingham Π theorem, in our study, there are 6 dimensionless numbers based on the control parameters (see Figs. 1 and 2). One could for instance choose the two aspect ratios related to the drop vs. the computational domain sizes, the density ratio, the viscosity ratio, and then define *a priori* Weber and Reynolds numbers based on the Newton theoretical velocity (see e.g. Wacheul et al., 2014). A complete dynamical study would then necessitate to explore the influence of those 4 later parameters in a computational box sufficiently large such that boundary conditions do not influence the dynamics. Here, we are interested in determining the dynamics of metal drops sinking into a magma ocean: we thus vary only the drop radius and the magma ocean viscosity, which are the main variables in the geophysical situation of interest, while we keep all the other dimensioned parameters fixed at their expected geophysical values (see Table 1).

In each simulation, starting from rest, the drop accelerates until reaching a constant terminal velocity, possibly with small oscillations around it. We monitor this mean terminal velocity V for each case. We end up our simulations when either the drop reaches a stable regime before the bottom of the domain or the drop fragments. In the later case the axisymmetric approximation is not relevant anymore. Each run is thus characterised by the 4 dimensionless numbers:

- the Reynolds number compares inertia and viscous effects: $Re = \frac{\rho_s V D}{\mu_s}$, with $D = 2R$ the drop initial diameter (R is the initial radius). The Reynolds number determines the falling drop dynamical regime: $Re < 1$ implies a Stokes regime where the viscous effects dominate; Re = 1–500 implies an intermediate regime where both viscous effects and inertial forces are important; and $Re > 500$ implies a Newtonian regime where the inertial forces are dominant

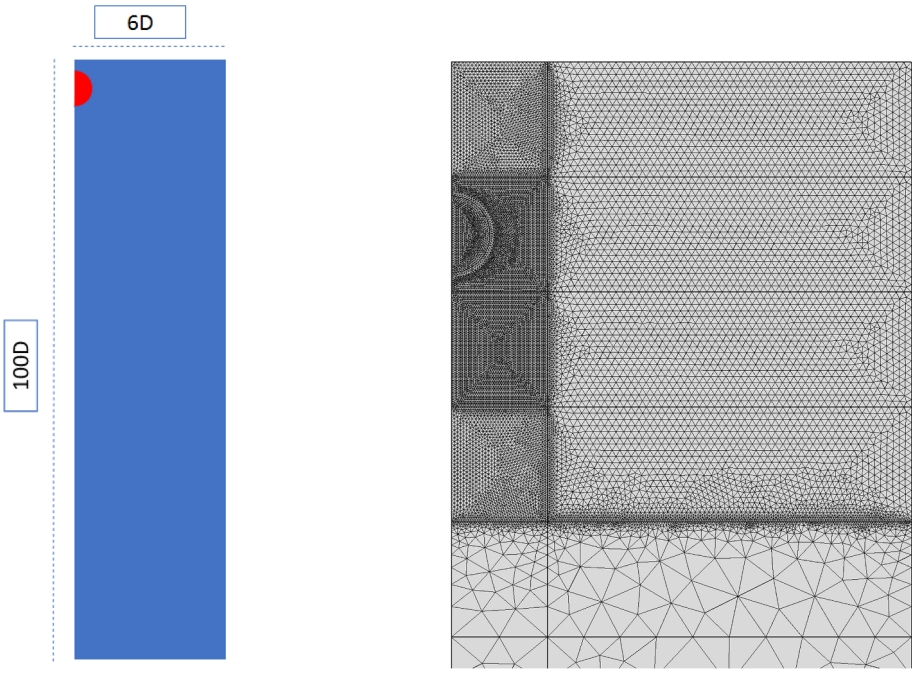

Fig. 2. Global view of our geometry with the initial drop at the top (left), and a zoom illustrating our manual method for adaptive mesh (right).

Table 1
Symbol definitions and values of the physical and non-dimensional parameters used in this study. Reynolds and Weber numbers are defined *a posteriori* using the relevant terminal velocity, measured in each run.

	Symbol	Value or range
Silicates density	ρ_s	3500 kg/m^3
Iron drop density	ρ_d	7500 kg/m^3
Density ratio	R_ρ	2.14
Iron drop viscosity	μ_d	0.005 Pa.s
Magma ocean viscosity	μ_s	0.05–100 Pa.s
Viscosity ratio	R_μ	10–20,000
Initial drop radius	R	1–350 mm
Surface tension coefficient	σ	1 N/m
Reynolds number	Re	0.027–85,600
Weber number	We	0.073–7480

(see Samuel, 2012).

- the Weber number measures the relative importance of inertia over surface tension: $We = \frac{\rho_s V^2 D}{\sigma}$. It controls and governs the deformation and breakup of the drop (Pilch and Erdman, 1987). Indeed inertia forces aim at deforming and fragmenting the iron drop, while the surface tension force prevents it from deformation and disruption. When $We \gg 1$, the inertia forces dominate leading to strong deformation and rapid fragmentation (e.g. Wacheul et al., 2014).
- the viscosity ratio is defined as the ratio of the silicates viscosity over the iron drop viscosity: $R_\mu = \frac{\mu_s}{\mu_d}$. The viscosity of liquid iron weakly depends on pressure and $\sim 5 \times 10^{-3}$ Pa.s at both inner core boundary pressure conditions (Poirier, 1988) and at the Earth surface (Assael et al., 2006). Oppositely, the magma ocean viscosity varies between 10^{-4} and 100 Pa.s depending on the thermal and dynamic conditions (Karki and Stixrude, 2010; Rubie et al., 2003; Samuel, 2012). In our model, we fix the viscosity of the metallic phase and the viscosity contrast ranges between 10 and 20000.
- the density ratio compares the iron drop density over the silicates density: $R_\rho = \frac{\rho_d}{\rho_s}$. The densities of liquid iron and molten silicates depend on the temperature and pressure conditions (Assael et al., 2006; de Wijs et al., 1998; Samuel, 2012). In our models, for simplicity, we fix $\rho_d = 7500\ \mathrm{kg.m^{-3}}$ and $\rho_s = 3500\ \mathrm{kg.m^{-3}}$. As a consequence, in this study, the density ratio is constant and equals to 2.14.

After a large collision involving two differentiated protoplanets, the core of the impactor is first fragmented in large scale iron structures (Kendall and Melosh, 2016). In the magma ocean, these structures overcome a second fragmentation resulting in the formation of a cloud of droplets with typical size ranging between a few millimetres to several centimetres (Deguen et al., 2014; Wacheul et al., 2014). In our study, we characterize the dynamics of a droplet in the iron cloud and determine the influence of the viscosity contrast on this droplet. For that, we vary the initial radius of the drop from 1 to 350 mm, exploring a large range of expected sizes in the iron rain cloud.

All the parameters used in this paper are listed in Table 1.

2.3. Numerical method

In this work, we solve Eqs. (1)–(3) using the COMSOL Multiphysics software, based on the finite element method. We study a 2D axisymmetric geometry with no-slip boundary conditions at the lateral boundary and open boundary conditions at the top and bottom boundaries. To avoid the wall effects, the computational domain must be large enough. For instance, Bonometti and Magnaudet (2006) considered a computational domain of $5.5D \times 12.6D$ to avoid contamination of the results. Their computations are stopped before the bubble arrives too close to the domain boundary. Ohta et al. (2010) used a computational domain of $4D \times 6D$, and considered a levitating drop with an entering inflow at the top boundary equal to its terminal velocity. Samuel (2012) also considered a levitating drop but with a square computational domain of $5D \times 5D$, and the inflow velocity is self-adjusting at the instantaneous velocity of the center of mass of the drop. Here, we have checked the convergence of our results as a function of the domain size, and we do not see any significant difference once the domain is larger than $4D$ and longer than $7.5D$. As sketched in Figs. 1 and 2, our computational domain is an axisymmetric cylinder of size $(r \times z) = (6D \times 100D)$.

The drop dynamics requires a fine mesh to capture all its details while conserving the overall mass of iron. Especially, the level set method has a tendancy to diffuse numerical artifacts on the interface and then gives incorrect results. Since our computational domain is very large, we need an adaptive mesh strongly refined in the drop vicinity, which we have implemented manually. To do so, we divide our domain in several regions, as shown in Fig. 2. We mesh the region that the drop crosses over a given time interval with a very fine mesh of size $h_x = 0.025R$, small enough to capture all the dynamics on the interface without any significant error or numerical diffusion. We mesh the region behind the drop with a thin mesh $h_x = 0.07R$ to correctly capture the physics of the wake, which also influences the dynamics. The mesh around the drop gradually widens in the radial direction until reaching $h_x = 0.2R$, from where it remains fixed until the wall. Finally, our mesh in front of the drop in the vertical direction first increases in an intermediate region to $h_x = 0.07R$, and then keeps increasing until reaching a very large value $h_x = 5000R$. When the drop approaches the bottom of the finer mesh region, the simulation is stopped, the whole pattern is translated, and the simulation is restarted on this new grid. We have tested this procedure and found that the dynamics of the falling drop doesn't change significantly when using smaller h_x (see Appendix). Also the overall iron mass during the course of each complete computation does not change by more than 0.7%, hence showing good numerical convergence. This method is relatively inexpensive in term of calculation time, and allows for a systematic study, with runs taking from 7 h to one week on a bi-processor, 3.2–3.6 GHZ, computer.

3. Systematic numerical study

We performed 84 simulations, whose dimensionless parameters are given in Table 2. In the following sections, we discuss our obtained numerical results in terms of drag coefficient, fragmentation modes, time and distance before breakup, and maximum stable drop radius. A particular attention is paid to the influence of the viscosity contrast between the metallic and silicate phases. The influence of the initial drop shape is shortly addressed at the end of this section; everywhere else, we start from a spherical drop.

3.1. Drag coefficient

The drag coefficient is a dimensionless number that quantifies the drag or resistance of the sinking drop into the magma ocean. It strongly depends on the viscosity ratio, density ratio, and surface tension, all of which control the interface conditions. In our case where the driving force is buoyancy and the initial geometry is spherical, we classically define the drag coefficient as

$$C_D = \frac{8}{3}\frac{(\rho_d - \rho_s)gR}{\rho_s V^2}, \tag{9}$$

with V the measured terminal velocity. Below, we first rapidly review the different theroretical models for the drag coefficient, and then compare with our numerical measurements.

3.1.1. For small Reynolds numbers

Several previous studies focused on the analytical determination of the drag coefficient for spherical fluid particles (e.g. Clift and Gauvin,

Table 2
Non-dimensional parameters for all performed simulations used in this study. In all our simulations, $R_\rho = 2.14$.

Simulation	Re	We	R_μ	$R(mm)$
#1	19.7	0.139	10	1
#2	315	7.09	10	5
#3	372	8.22	10	6
#4	426	9.27	10	7
#5	553	10.9	10	10
#6	1610	37.0	10	25
#7	3280	95.8	10	40
#8	73.9	8.13	50	6
#9	93.0	9.64	50	8
#10	106	11.1	50	9
#11	108	10.4	50	10
#12	202	24.2	50	15
#13	322	37.0	50	25
#14	638	91.0	50	40
#15	1510	290	50	70
#16	14.3	1.82	100	6
#17	35.3	7.43	100	8
#18	44.2	8.74	100	10
#19	51.8	9.58	100	11
#20	66.0	13.5	100	11.5
#21	71.4	15.2	100	12
#22	92.4	20.3	100	15
#23	154	33.9	100	25
#24	314	87.8	100	40
#25	750	287	100	70
#26	11.9	3.35	200	6
#27	19.7	6.90	200	8
#28	25.1	9.02	200	10
#29	30.4	11.0	200	12
#30	36.4	14.6	200	13
#31	38.7	15.3	200	14
#32	42.5	17.2	200	15
#33	76.1	33.1	200	25
#34	146	75.7	200	40
#35	363	268	200	70
#36	637	580	200	100
#37	1.53	1.05	1000	8
#38	2.70	2.61	1000	10
#39	6.49	10.0	1000	15
#40	11.2	22.4	1000	20
#41	15.4	33.9	1000	25
#42	19.7	46.4	1000	30
#43	26.0	68.8	1000	35
#44	28.8	74.3	1000	40
#45	38.5	106	1000	50
#46	52.1	161	1000	60
#47	68.6	240	1000	70
#48	122	530	1000	100
#49	0.027	0.073	20000	15
#50	0.127	0.927	20000	25
#51	0.509	9.27	20000	40
#52	0.952	25.9	20000	50
#53	1.22	38.7	20000	55
#54	1.54	56.6	20000	60
#55	2.27	105	20000	70
#56	5.15	379	20000	100
#57	24.4	26.5	500	20
#58	7.56	42.5	2500	30
#59	8.42	49.5	2500	35
#60	9.82	61.2	2500	40
#61	12.3	84.7	2500	45
#62	2670	636	50	100
#63	24100	1380	10	150
#64	37100	2460	10	200
#65	67800	5480	10	300
#66	85600	7480	10	350
#67	4770	1350	50	150
#68	7360	2420	50	200
#69	13400	5380	50	300
#70	16960	7330	50	350
#71	2380	1350	100	150
#72	3660	2400	100	200
#73	6700	5340	100	300
#74	8430	7290	100	350
#75	1180	1330	200	150
#76	1820	2370	200	200
#77	3360	5360	200	300
#78	4221.35	7273.386	200	350
#79	231	1270.5	1000	150
#80	502.25	3603.643	1000	250
#81	667.8	5309.01	1000	300
#82	837.9	7164.045	1000	350
#83	28.35	17.22	300	15
#84	24.57	19.2	400	18

1970; Hadamard, 1911; Mei et al., 1994) and for deformed fluid particles (e.g. Moore, 1965; Darton and Harrison, 1974; Clift et al., 1978; Loth, 2008). For spherical drops, the internal circulation is supposed to prevent forming any wake separation of the external flow. This in turn helps to prevent any change in shape and keeps the droplet spherical. Hadamard (1911) proposed an analytical relation at finite but low Reynolds $Re \ll 1$. An asymptotic solution was derived by Harper and Moore (1968) for intermediate Reynolds numbers but remains limited to $Re < 100$ at finite values of the viscosity ratio. To fill the gap between Harper and Moore (1968) and Hadamard (1911), an empirical mixed Stokes correction factor resulting from the internal circulation was proposed by Mei et al. (1994) in the limit $R_\mu \to 0$:

$$C_{D_{R_\mu \to 0}} = \frac{16}{Re}\left[1 + \left[\frac{8}{Re} + \frac{1}{2}\left(1 + \frac{3.315}{\sqrt{Re}}\right)\right]^{-1}\right]. \tag{10}$$

3.1.2. For moderate and large Reynolds numbers

For intermediate but increasing Reynolds numbers ($0.1 < Re < 2000$), the drop begins to distort, leading to changes in the wake from an attached laminar wake (spherical drop), to a separated laminar wake (deformable drop), to an unsteady transitional wake (breakup into droplets) and finally to a turbulent wake (catastrophic breakup) (Loth, 2008). The wake actually depends on the interplay between surface tension and hydrodynamic pressure stresses, hence on *We*. Davies and Taylor (1950) found a converged value $C_D = \frac{8}{3}$ for gas bubbles in a liquid at infinite Reynolds and Weber numbers. In order to encompass the influence of viscosity and a wide range of small to large Reynolds numbers, an empirical correlation was proposed by Darton and Harrison (1974) and Clift et al., 1978 for infinitely large *We*:

$$C_{D_{We \to \infty}} = \frac{8}{3} + \frac{24}{Re}\left(\frac{2 + 3R_\mu}{3 + 3R_\mu}\right). \tag{11}$$

To capture the drag in the intermediate range of *Re* and *We* values (of interest here), Loth (2008) proposed the following expression by combining Eqs. (10) and (11) and adding a functional dependence $(\Delta(C_D)^*)$ on *We*, where $\Delta(C_D)^*$ increases monotonically with Weber number:

$$C_D = C_{D_{We \to 0}} + \Delta(C_D)^*[C_{D_{We \to \infty}} - C_{D_{We \to 0}}] \tag{12}$$

$$\Delta(C_D)^* = \tanh(0.021We^{1.6}). \tag{13}$$

Here $C_{D_{We \to 0}}$ is given by Eq. (10), the imposed spherical shape being related to an infinite surface tension, hence to $We \to 0$. Experimentally, several investigations partly tackled the relevant limit of a metal drop in a more viscous environment, including: the fragmentation of liquid mercury drops sinking within water reported by Patel (1978) and Patel and Theofanous (1981), who found a drag coefficient equal to 2.5–3; the fragmentation of gallium drops in water by Kim et al. (1983), who found that the drag coefficient depends on the Reynolds number; and the analog model of Wacheul and Le Bars (2018), who reported a convergence value of the drag coefficient at large Reynolds equal to

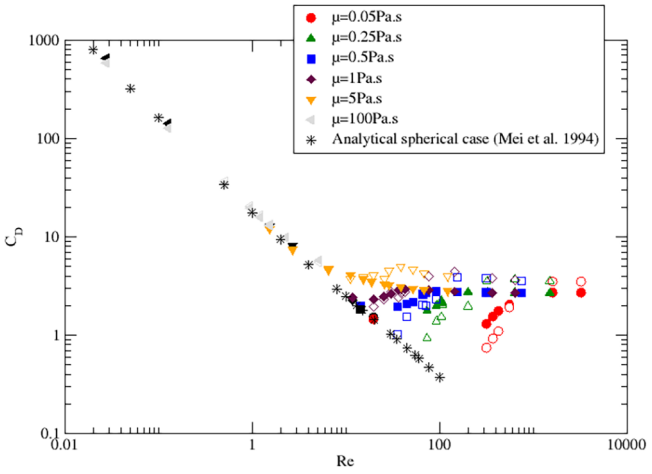

Fig. 3. Drag coefficient as a function of the Reynolds number for various values of the silicates viscosity. Filled symbols are the analytical results given by Eq. (12), while empty symbols show our numerical results from the first 62 simulations in Table 2. Filled black symbols show numerical results for an undeformable sphere $R_\mu = 0$, and black stars are the analytical results from Eq. (10).

3.7 ± 1.

3.1.3. Results and discussion

We have monitored the velocity V of the sinking metallic drop in our simulations and obtained the corresponding values for C_D from Eq. (9). Fig. 3 presents our measured C_D as a function of the Reynolds number for various viscosity ratios, and the comparison of our results with the analytical solutions of Mei et al. (1994) (Eq. (10) and Loth (2008) (Eq. (12)). For $We < 1$ and low Reynolds numbers (up to $Re = 20$ depending on R_μ), the droplet remains spherical and our results agree with the analytical model proposed by Mei et al. (1994): C_D is inversely proportional to Re and barely depends on the viscosity ratio. When flow separation occurs (i.e. when the Weber number exceeds unity), this expression is not valid anymore because the drop deforms: it takes the shape of an ellipsoid, a disc or a cup. This deformation increases the frontal area and leads to a transient increase of C_D with Re, depending on R_μ. Qualitative agreement between our simulations and Eq. (12) is satisfactory, but small quantitative differences exist. This is not surprising, since the empirical formula Eq. (12) was calibrated on gas bubbles rising in a liquid, which are more sensitive to deformation than the liquid drops studied here. But no equivalent to Eq. (12) is yet available for liquid-liquid systems, and one has thus to rely on numerical results. Finally, for large Re, C_D converges towards a constant value 3.5 ± 0.5, independently of R_μ. This value is above the analytical estimate of 8/3, but is compatible with the results of Wacheul and Le Bars (2018) who found a mean value of C_D equal to 3.7 ± 1.

3.2. Fragmentation modes

The breakup mechanism is very sensitive to the Weber number, as well as to the viscosity ratio between the metal and the silicates. Two main fragmentation modes have been documented in previous experimental and numerical studies, namely the “bag breakup” just above the critical Weber number, and the “shear breakup” at large Weber number (see the limit cases in Fig. 4) (Krzeczkowski, 1980; Pilch and Erdman, 1987; Dai and Faeth, 2001). Several authors have tackled the description of the different breakup mechanisms in the intermediate range of Weber number, leading to a complex situation. Examples include (Krzeczkowski, 1980), who developed series of experiments for liquid droplets of water, methanol, ethanol, butanol and glycerine in an external air stream, and documented two breakup modes independent of the viscosity ratio: the “bag-jet” and the “transition” modes. Pilch and

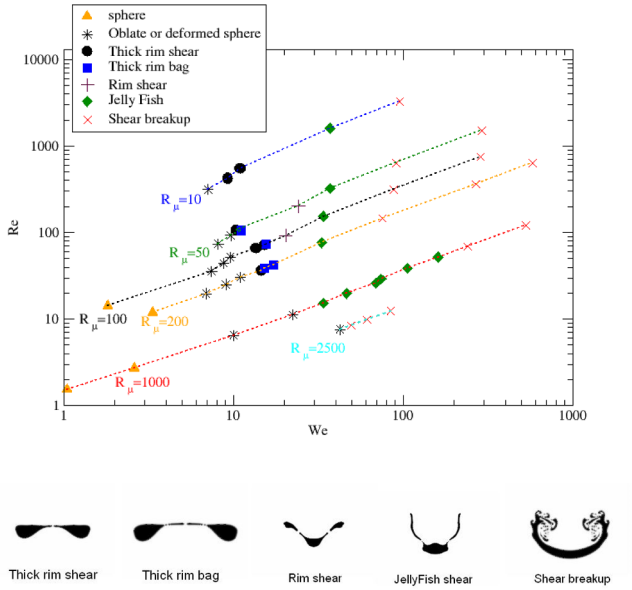

Fig. 4. Regime diagram of the fragmentation modes as a function of Re and We numbers for various viscosity ratios: $R_\mu = 10$ (blue dotted line), $R_\mu = 50$ (green dotted line), $R_\mu = 100$ (black dotted line), $R_\mu = 200$ (orange dotted line), $R_\mu = 1000$ (red dotted line), and $R_\mu = 2500$ (turquoise dotted line). Our numerical results come from the first 62 simulations in Table 2. (For interpretation of the references to colour in this figure legend, the reader is referred to the web version of this article.)

Erdman (1987) introduced two breakup modes for a single liquid drop within an external gas flow: the “bag-stamen” mode and the “sheet stripping” mode. Dai and Faeth (2001) used droplets of water and ethanol and defined a “bag-plume” mode, close to the “bag-jet” and “bag-stamen”, and a “plume-shear” mode, close to the “shear breakup”. Cao et al. (2007) pursued this experimental investigation and presented a new “dual-bag” breakup mode for $We = 28$–41. Recently, 3D numerical simulations of liquid droplets levitating in a gas flow with a uniform velocity have been performed by Kékesi et al. (2014), changing the viscosity and density ratios for a fixed Weber number value ($We = 20$). They identified 5 breakup regimes, as shown in Fig. 4: “thick rim shear” and ”thick rim bag” (both close to “bag breakup”), ”rim shear”, ”jellyfish shear”, and ”shear” breakup respectively. In our study, we use their classification.

For each mode of fragmentation, we describe below the temporal evolution of a typical spherical drop starting from rest at $t = 0$, until its breakup at $t = t_{bk}$.

- Thick rim shear (Fig. 5): the initial sphere rapidly deforms into a spherical cap ($t = 0.13$ s), then the hydrodynamic pressure force concentrates on the middle of the drop leading to the formation of a small bag ($t = 0.2$ s). Surface tension then prevents breakup and the drop returns to form a half-sphere ($t = 0.355$ s), before a second oscillation starts. Then, as the inertial forces and associated pressure are reinforced, the vertical thickness decreases even more, and a thin film forms near the symmetry axis, with a thicker rim ($t = 0.55$ s). The rim extends radially and drains out the liquid film ($t = 0.6$ s), until a hole occurs at the symmetry axis ($t = 0.62$ s). At this stage, the metal phase actually forms a ring that might persist for a longer time before fragmentation of Rayleigh-Plateau type, to which we cannot have access with our axisymmetic simulation. Kékesi et al. (2014) showed in 3D simulations that this last stage is actually rapid, i.e. a few milliseconds. Note also that thick rim shear seems marginal in the parameter space explored here, and is replaced rapidly by thick rim bag, except for cases with the smaller viscosity ratio $R_\mu = 10$ (see Fig. 4).

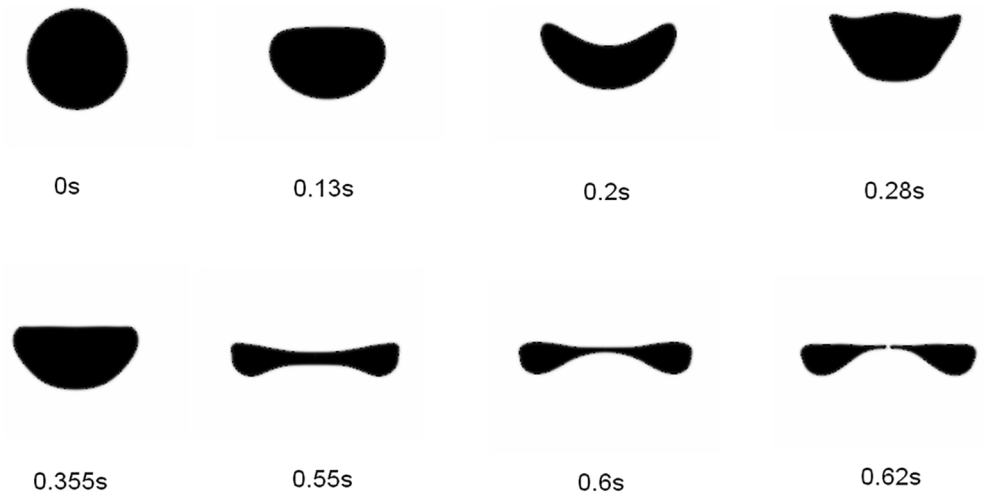

Fig. 5. Deformation and thick rim shear breakup of an iron drop within a magma ocean. In this model, $Re = 36.4$, $We = 14.6$, $R_\mu = 200$ (simulation #30 in Table 2).

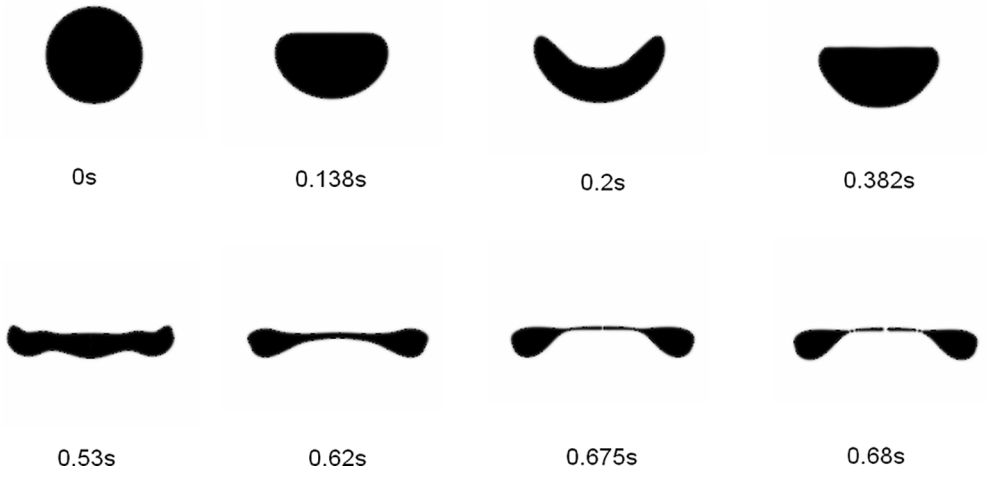

Fig. 6. Deformation and thick rim bag breakup of an iron drop within a magma ocean. In this model, $Re = 42.5$, $We = 17.2$, $R_\mu = 200$ (simulation #32 in Table 2).

- Thick rim bag (Fig. 6): this breakup process is similar to the thick rim shear, until fragmentation. Then, breakup appears almost simultaneously in the center of the drop ($t = 0.675$ s) and at the connection between the film and the rim, forming satellite droplets ($t = 0.68$ s).
- Rim shear (Fig. 7): again the initiation of the breakup is similar to the two processes described above, with the formation of a spherical cap ($t = 0.131$ s), followed by a bag ($t = 0.2$ s), and back ($t = 0.37$ s). Then, the drop extends in both radial and vertical directions, forming a sheet ($t = 0.48$ s and 0.51 s) under the action of the strong vorticity in the wake. Finally, surface tension drains the iron both into the center and into the rim ($t = 0.57$ s), while the sheet

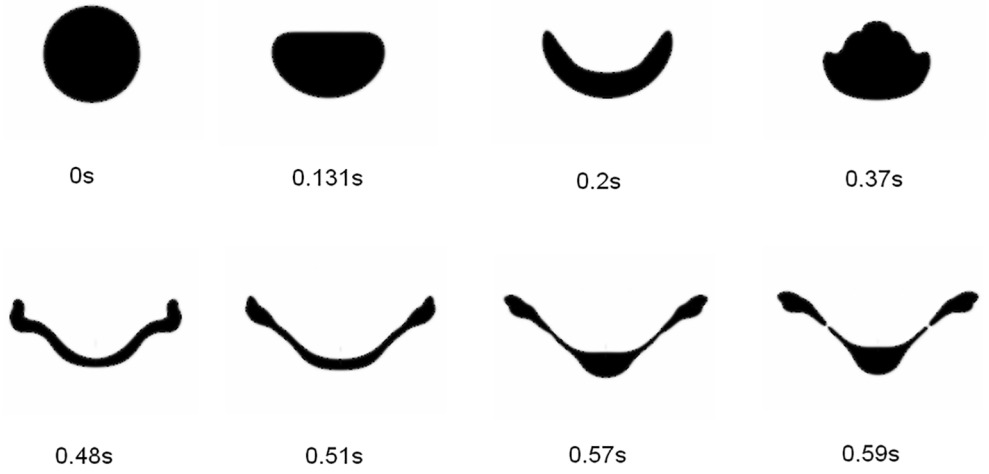

Fig. 7. Deformation and rim shear breakup of an iron drop within a magma ocean. In this model, $Re = 92.4$, $We = 20.3$, $R_\mu = 100$ (simulation #22 in Table 2).

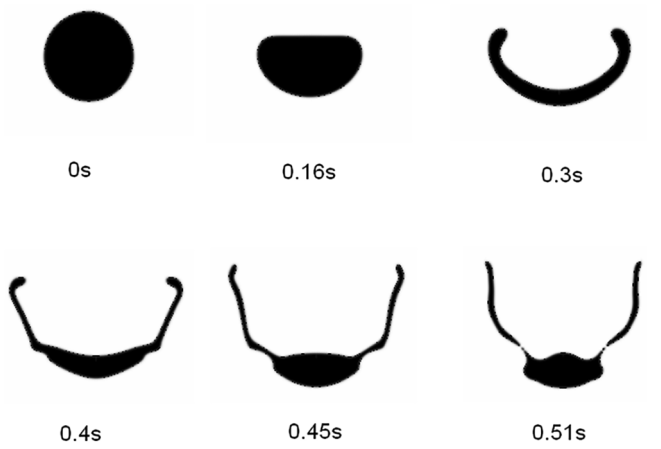

Fig. 8. Deformation and jellyfish shear breakup of an iron drop within a magma ocean. In this model, $Re = 76.1$, $We = 33.1$, $R_\mu = 200$ (simulation #33 in Table 2).

connecting the two thins, and finally breaks ($t = 0.59$ s).

- Jellyfish shear (Fig. 8): in this mode, no rim forms. Instead, a thin skirt forms while iron is mostly localized along the symmetry axis ($t = 0.4$ s and $t = 0.45$ s). Oscillations develop in the thin membrane, whose ends fold in and out. The velocity is concentrated in the wake of the silicates which accelerates the drop center relative to its membranes, leading to a rapid fragmentation in the connecting region ($t = 0.51$ s).
- Shear breakup (Fig. 9): the drop shape deforms first into a spherical cap ($t = 0.24$ s) and second into a skirt. Then, the rim does not thicken, but folds inside and turns around itself through the action of vorticity, leading to its thinning ($t = 0.4$ s). Rapidly, this thin sheet breaks into small droplets ($t = 0.42$ s). No oscillations are observed here, and the rapid fragmentation is mainly due to the vorticity in the wake behind the drop that is two to three times larger than the vorticity in the drop.

The deformation of the droplet depends on the viscosity of the external flow, the density ratio, the surface tension and the drop size. When *Re* and *We* are both small, the drop remains spherical without any deformation, due to the internal circulation within the drop that prevents forming any separated wake. When the hydrodynamic pressure force increases, a separated laminar wake and an external circulation behind the drop occur, leading to shape deformation. Increasing the Reynolds number, the drop first deforms to an ellipsoid, and possibly

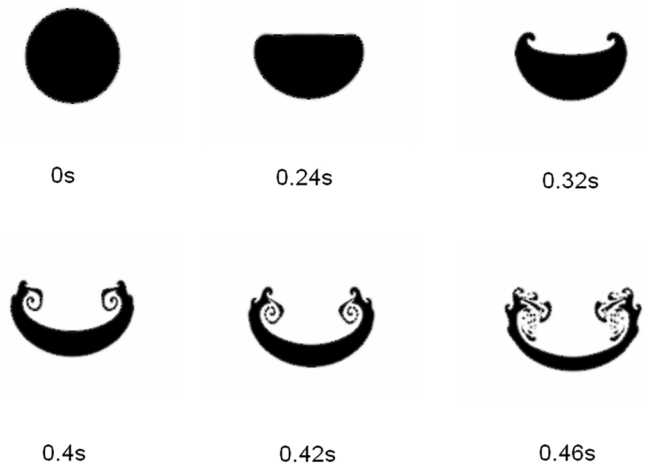

Fig. 9. Deformation and shear breakup of an iron drop within a magma ocean. In this model, $Re = 2670$, $We = 636$, $R_\mu = 50$ (simulation #62 in Table 2).

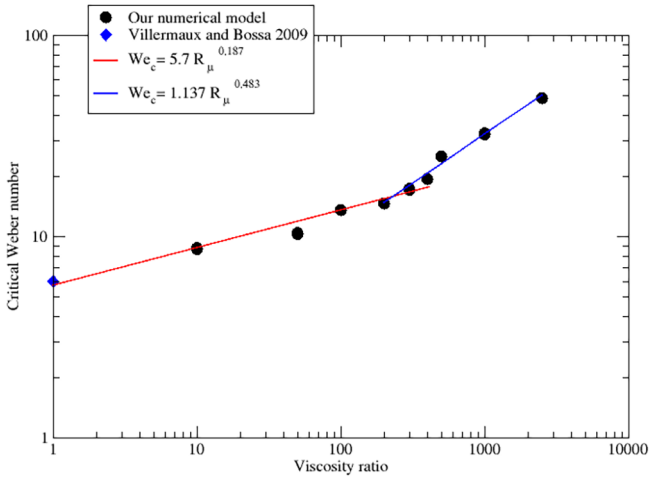

Fig. 10. Critical Weber number as a function of the viscosity ratio. The blue diamond is the critical Weber number when the viscosity ratio equal to 1, as obtained by Villermaux and Bossa (2009). The red and blue lines represent the scaling laws derived from our data. (For interpretation of the references to colour in this figure legend, the reader is referred to the web version of this article.)

gives rise to oscillations from oblate to prolate shapes. For a viscosity ratio less than 100, the drop keeps oscillating until the end of the domain, while for a viscosity ratio greater than 100, the velocity of the drop exceeds the oscillation velocity, leading to rapid damping of the initially excited oscillation. Further increasing the Reynolds number, the drop takes the shape of a spherical cap. And once hydrodynamic pressure overcomes surface tension (i.e. large enough Weber number), one of the five fragmentation modes occurs, depending also on the viscosity ratio. From our systematic study for different viscosity ratios, we built up a fragmentation regime diagram in terms of Reynolds and Weber numbers shown in Fig. 4. For a viscosity ratio $R_\mu = 1000$, we observe only two modes, and drop oscillations are prevented by the high silicates viscosity. On the contrary for $R_\mu = 50$, we observe the five different modes and strong drop oscillations. One should also notice that the critical Weber number depends on the viscosity ratio: for $R_\mu = 10$, the breakup begins at $We \approx 9$ while for $R_\mu = 1000$, it starts at $We \approx 34$. Systematic estimate of the critical Weber number is shown in Fig. 10. We consider in this figure that fragmentation occurs as soon as the first volume of iron separates from the main drop. The increase in the viscosity ratio leads to an increase in the critical Weber number following two empirical scaling laws depending on first-breakup regime. When the viscosity ratio is rather low (i.e. <300 typically), the drop fragments quickly as a thick rim shear after only one or two oscillations along a short drop path. In this case, critical Weber is defined as a low power law of the viscosity ratio by the following scaling law

$$We_c = 5.7 R_\mu^{0.187}. \tag{14}$$

On the other hand, at a viscosity ratio of ~ 300, a Jellyfish behaviour takes place, and between $R_\mu = 300$ and $R_\mu = 500$, the drop first breakup becomes slow and transitions from thick rim shear to Jellyfish. In this region and above, where shear breakup takes place, the critical Weber number depends more significantly on the viscosity ratio and is given by the following scalling law

$$We_c = 1.137 R_\mu^{0.483}, \tag{15}$$

valid at least in the range $R_\mu = [300;2500]$ explored here.

From our simulation #41, we also report a new fragmentation mode illustrated in Fig. 11. This mode is initially similar to the jellyfish shear breakup except that the membrane fold is so important that it finally closes at the back, encapsulating the silicates within a bubble of iron (Fig. 11, $t = 3.7$ s). Then, the next oscillation of the membrane tears the

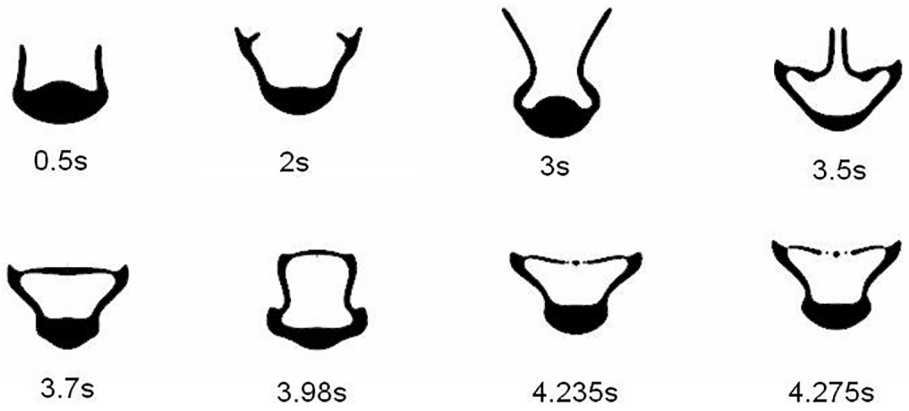

Fig. 11. The path of a new fragmentation mode where the iron structure encloses the silicates.

glued back which breaks from the center, forming one central droplet and two satellites droplets. Note that Wacheul et al. (2014) observed in their experiments similar bubbles of metal enclosing the viscous ambiant fluid and exhibiting a lower velocity that pure iron droplets. While being dynamically intriguing, this mode remains very marginal.

3.3. Time and distance before breakup

After an impact, large drops deform and fragment at a distance and time that depend on the sinking dynamics. We define these time and distance as the breakup time t_{bk} and distance d_{bk}. Deguen et al. (2014) predicted that for large Weber numbers, t_{bk} and d_{bk} reach an asymptotic regime. In this section we test this prediction. From our models, we determine t_{bk} and d_{bk} as the time and location where the first droplet or ligament of iron separates from the main drop. We then define the dimensionless breakup time t^*_{bk} as Pilch and Erdman (1987):

$$t^*_{bk} = \frac{t_{bk} V}{D}\sqrt{\frac{\rho_d}{\rho_s}} \tag{16}$$

where the break up time is normalized by the characteristic time of drop breakup by Kelvin-Helmholtz instability. We define the dimensionless breakup distance as:

$$d^*_{bk} = \frac{d_{bk}}{R}. \tag{17}$$

Fig. 12 shows the variations of t^*_{bk} as a function of the Weber number for various viscosity ratios. From Fig. 12, we see that t^*_{bk} decreases with the increase of *We*. We note that, for large *We*, t^*_{bk} converges towards a constant value ranging between 1 and 1.8. This result is consistent with

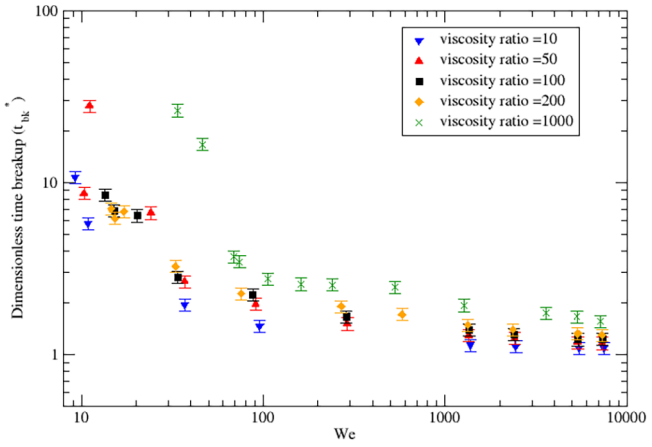

Fig. 12. Non-dimensional break-up time as a function of Weber number for viscosity ratios R_μ ranging between 10 and 1000.

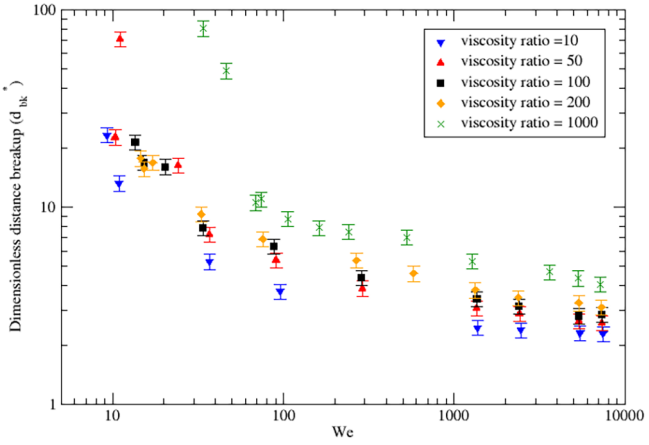

Fig. 13. Non-dimensional break-up distance d^*_{bk} as a function of the Weber number for viscosity ratios R_μ ranging between 10 and 1000.

the result of Pilch and Erdman (1987) who found $t^*_{bk} = 1.25$ for $We > 350$. A dependence on the viscosity ratio is also present, especially at $We \leqslant 80$, with a tendency for large R_μ to stabilise the drops.

The non-dimensionalised breakup distance d^*_{bk} is reported in Fig. 13. It also shows a dependence on the viscosity ratio, especially at low *We*, and a possible convergence towards an asymptotic value ranging between 2 and 4 at large *We*. For comparison, Deguen et al. (2014) found a breakup distance equal to 6–8 times the drop radius for *We* up to 3000 and $R_\mu = 0.5$. Landeau et al. (2014) found a value equal to 3.5–7.5 times the radius for $25 < We < 1000$ and $0.45 < R_\mu < 1.25$. Hence our results are in correct agreement with those experimental observations. This is all the more noticeable that Landeau et al. (2014) observed 3D turbulence in lab experiments at $We > 600$, effects that are missing from our axisymmetric simulations. Note finally that Wacheul and Le Bars (2018) found a breakup distance $(13 \pm 2)R$ for $10 < We < 50$ and $0.4 < R_\mu < 700$, but their breakup criteria actually detected a "significant" and well-advanced breakup, thus implicitly leading to an overestimation of d^*_{bk} compared to other results. Fig. 13 illustrates the influence of the viscosity ratio on the breakup distance. For low *We*, d^*_{bk} ranges between 10 and 80 for the whole range of viscosity ratios used in our study. For large *We*, d^*_{bk} ranges between 2 and 4.5. Increasing the viscosity ratio generically increases the breakup distance and as a consequence, the potential depth of equilibrium between iron drops and silicates.

3.4. Maximum stable drop radius

After an impact, the impactor's iron core disrupts into large scale drops (Kendall and Melosh, 2016). After this first fragmentation, a

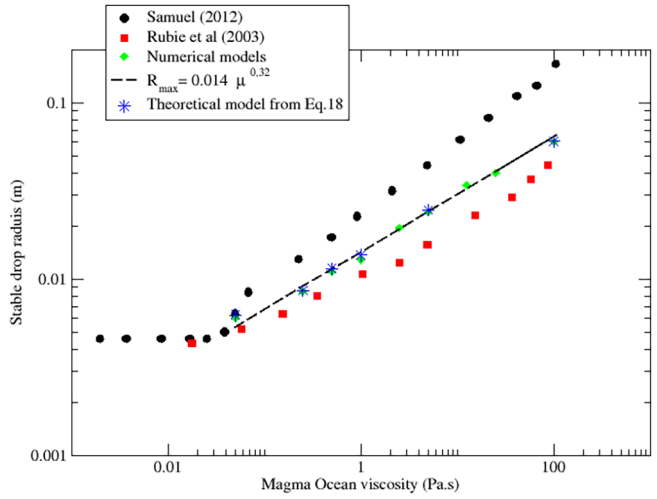

Fig. 14. Stable drop radius as a function of plausible magma ocean viscosities. The green diamonds present our numerical results, the red squares correspond to the results of Rubie et al. (2003), the black circles display the results of Samuel (2012), the blue stars correspond the analytical results of the Eq. (18) and the black dash line presents the scaling law proposed by this study. (For interpretation of the references to colour in this figure legend, the reader is referred to the web version of this article.)

second fragmentation occurs within the magma ocean resulting in the formation of a cloud of droplets (Deguen et al., 2014; Wacheul et al., 2014). At the end of this second fragmentation, iron droplets reach a maximum stable radius R_{max}. Following Wacheul et al. (2014) and using the Newtonian velocity scale accounting for the drag coefficient (Eq. (9)), R_{max} is simply related to the critical Weber number by

$$R_{max} = \sqrt{We_c \frac{3C_D}{16} \frac{\sigma}{\Delta\rho g}}. \quad (18)$$

Numerical data from Fig. 14 show the last drop radius for which deformation may occur but without fragmentation. According to Fig. 14, the maximal stable drop radius increases with the magma ocean viscosity. From our numerical data, we propose a scaling law to determine the maximum stable radius as a power function of magma ocean viscosity, valid for magma viscosities larger than ~ 0.1 Pa.s up to 100 Pa.s:

$$R_{max} = 0.014\mu_s^{0.32}(m). \quad (19)$$

Our results are in agreement with the analytical Eq. (18), confirming the self-consistency of our numerical results. Fig. 14 also shows the comparison of our results with the model of Rubie et al. (2003) and the model of Samuel (2012). Differences come from different values of C_D, where we use our effective numerical values rather than any theoretical estimation. It should also be noted that Rubie et al. (2003) and Samuel (2012) do not consider the dynamical influence of the viscosity contrast between metal and silicates in their models.

3.5. The influence of initial conditions

After an impact, the impactor's core is likely fragmented in metallic diapirs with a large range of shapes (spherical, oblate or prolate) (Kendall and Melosh, 2016). This deformation process is likely to affect the post-impact sinking dynamics of the metallic phase as we envision in our study by modifying our initial shape conditions. Bonometti and Magnaudet (2006) found that their final bubble topology and features vary with the initial shape of the bubble. Without trying to be exhaustive on this subject that would deserve a dedicated study on its own, we have thus investigated the behavior of a drop at the critical Weber number for two viscosity ratios ($R_\mu = 200$ and $R_\mu = 1000$),

Fig. 15. The final shape of the iron droplets for different initial conditions. Spherical case (left), prolate form (middle) and oblate form (right).

starting from a spherical, oblate or prolate form with an ellipticity ranging between 0.59 and 0.82, maintaining the total volume of iron constant. Results for $R_\mu = 1000$ are shown in Fig. 15, reporting a significant sensitivity to initial conditions. For the initial oblate form, the drop does not fragment and converges to a skirt shape. On the contrary, the initial prolate shape disrupts more rapidly than the spherical case, the time and distance before breakup being respectively 27.4% and 28.3% smaller than the corresponding values for the spherical case. The shape is also different, with an increase of the surface in the prolate case of 10.9% compared to the spherical case. For the other viscosity ratio $R_\mu = 200$, we find that the fragmentation modes are identical for the three initial conditions, but differences on the order of 10% exist in the breakup time, distance before breakup, and surface. Among the three initial cases, the spherical initial condition always leads to a less rapid fragmentation and to a smaller surface.

4. Implications for the metal/silicate exchanges

In the present study, we focus on the dynamics of the two phase flow only, without considering neither the thermal evolution of the metallic droplet nor chemical exchanges that could occur between the metallic and silicate phases. Our results nevertheless enable to constrain two fundamental parameters for thermochemical equilibration, namely the thickness of the boundary layer at the iron/ silicates interface, and the surface of the metallic droplet across which thermochemical exchanges are likely to occur. Those two points are addressed below. We then propose some first order estimates of the equilibration of an initially 10 km metallic core sinking and fragmenting within a magma ocean and compare our results with the classical iron-rain model (Rubie et al., 2003).

4.1. Boundary layer thickness

During the sinking of an iron drop, three boundary layers can form at the interface between the metalic and silicate phases: the dynamical, thermal and chemical boundary layers. The thickness of each boundary layer may have a strong influence on the thermo-chemical exchanges. In this study, we focus on the dynamical boundary layer Δ. We thus consider a velocity profile along the normal to the drop interface at the front of the drop, as shown in [Fig. 16]: Δ is defined as the distance from the drop interface to the point where the velocity is equal to 10% the drop terminal velocity. In the case of a rigid sinking sphere, the thickness of the boundary layer scales as $Re^{-1/2}$ (Ulvrová et al., 2011). In our models, the metallic droplet is deformable and three parameters *a priori* control the flow, hence Δ: R_μ, *Re* and *We*. Here, we seek a power law for the boundary layer thickness in terms of the two varied parameters in our study, namely the drop radius and the magma ocean viscosity.

Our numerical results are shown in Fig. 17. A good fit is found with the empirical scaling law

$$\Delta = 1.442R^{0.916}\mu_s^{0.062}(m). \quad (20)$$

Hence, the boundary layer thickness depends mainly on the drop radius and only slightly on the magma ocean viscosity. For a standard viscous boundary layer in the vicinity of a solid sphere, one would expect a scaling $\propto \mu_s^{0.5}$. This surprisingly low dependence on the ambient viscosity is probably due to the drop deformation and to the

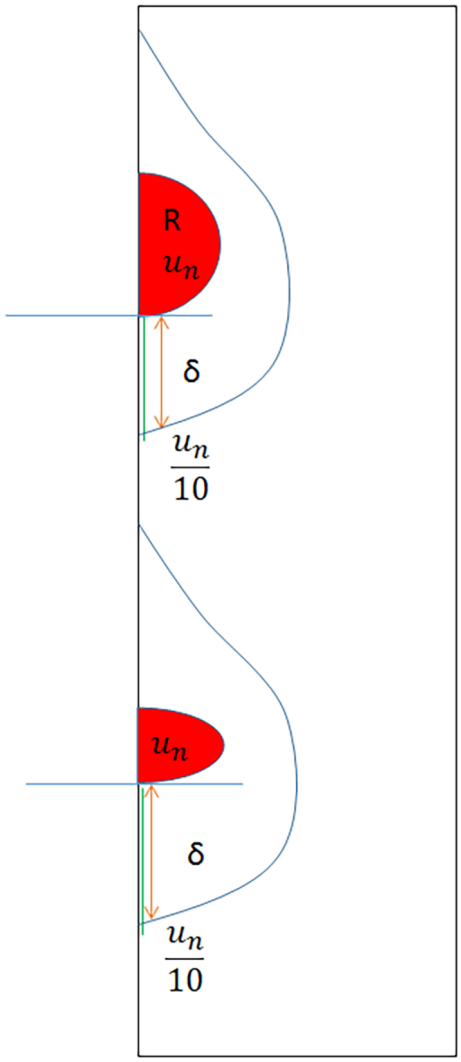

Fig. 16. Schematic representation of the geometry used for the determination of the boundary layer thickness Δ at the drop surface: spherical case (top) and deformed drop (bottom).

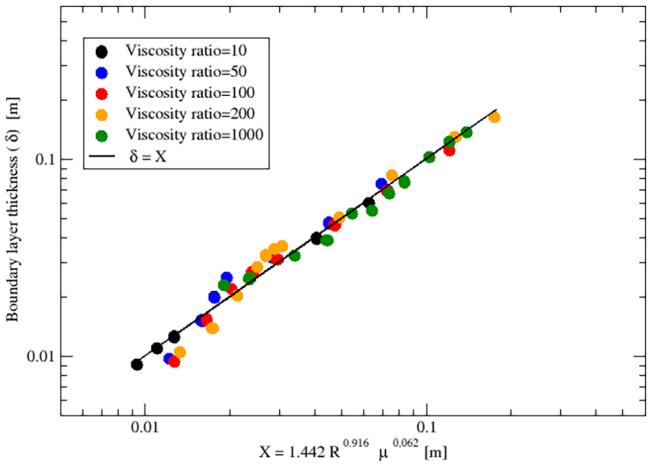

Fig. 17. Boundary layer thickness as a function of the varied parameters in this study (drop radius and magma ocean viscosity) for viscosity ratios R_μ ranging between 10 and 1000. Our numerical results come from the first 62 simulations in Table 2).

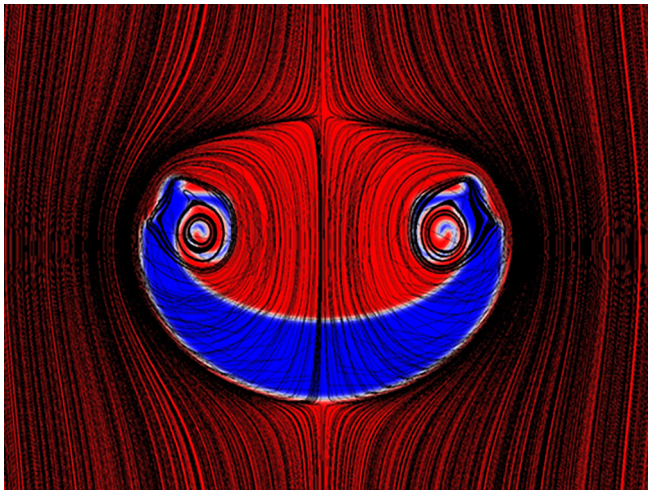

Fig. 18. The streamlines around a large drop. In this model, $Re = 2670$, $We = 636$, $R_\mu = 50$ (simulation #62 in Table 2). The black lines are the streamlines, the red region represents the molten silicates and the blue region represents the deformable iron drop. (For interpretation of the references to colour in this figure legend, the reader is referred to the web version of this article.)

associated internal circulations and wake. It presumably affects the equilibration. Note however that Eq. (20) is valid in the frontal section of the drop, but the boundary layer size is not constant along the drop surface. Also, the generated wake might encapsulate silicates that are entrained with the falling iron, as shown in Fig. 18 and observed numerically (Monteux and Arkani-Hamed, 2014) and experimentally (Fleck et al., 2018), for an even more viscous surrounding fluid. This also influences equilibration. Clearly, the equilibration process is complex, global, and deserves a study on its own.

4.2. Time evolution of the droplet surface

The exchange surface between two fluids qualifies the surface through which thermo-chemical transfers occur. As shown in the Figs. 5–9 and 11, the spherical drop deforms and oscillates during its sinking. This leads to variations in the potential exchange surface between the liquid iron and the molten silicates.

We monitored the surface S of each drop from its initial position until reaching a stationary regime or until breakup. We normalized S by the corresponding spherical surface ($S^* = S/(4\pi R^2)$). Fig. 19 shows the evolution of S^* as a function of time for an initial radius $R = 10$ mm. Fig. 19 illustrates the influence of the viscosity contrast R_μ. For $R_\mu = 1000$, the drop remains spherical and its normalised surface is constant ($S^* = 1$). When the magma ocean viscosity decreases, the deformation of the drop becomes significant and the oscillations of the drop lead to oscillations of its surface. For $R_\mu = 100$, the drop deforms and oscillates several times, but the surface tension is large enough to prevent the drop from breaking up, and a steady state is reached after 1.5 s. For $R_\mu = 10$ and $R_\mu = 50$, the drop surface oscillations are followed by a fragmentation (at 0.393 s and 0.6 s respectively). These large deformation processes significantly increase the droplet surface, which can increase by up to 200% before the fragmentation. Our results show that the viscosity ratio between the liquid iron and silicate phases strongly influences the shape of the metallic drops. As a consequence, considering a purely spherical drop when calculating the transfers across the exchange surface provides only a lower bound estimate which might be significantly off, especially for $R_\mu < 100$.

4.3. Application to a 10 km metal diapir

In the previous sections, we studied the dynamical properties of

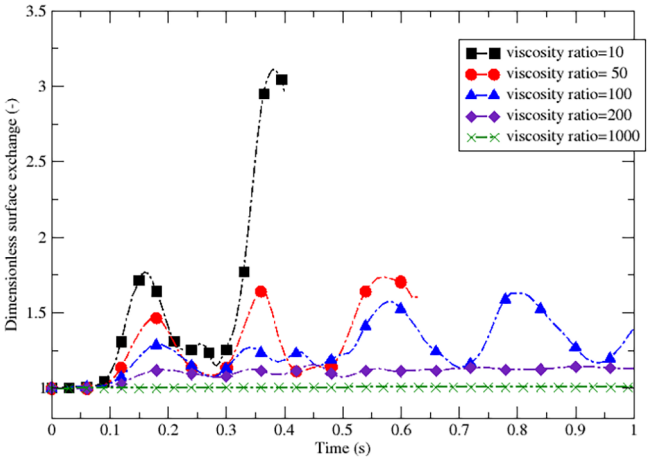

Fig. 19. Non-dimensional surface exchange as a function of time for viscosity ratios R_μ ranging between 10 and 1000. Here, we consider a drop of initial radius $R = 10$ mm. For viscosity ratio = 10 (black line), $Re = 553$ and $We = 10.9$. For viscosity ratio = 50 (red line), $Re = 108$ and $We = 10.4$. For viscosity ratio = 100 (blue line), $Re = 44.2$ and $We = 8.74$. For viscosity ratio = 200 (purple line), $Re = 25.1$ and $We = 9.02$. For viscosity ratio = 1000 (green line), $Re = 2.70$ and $We = 2.61$. (For interpretation of the references to colour in this figure legend, the reader is referred to the web version of this article.)

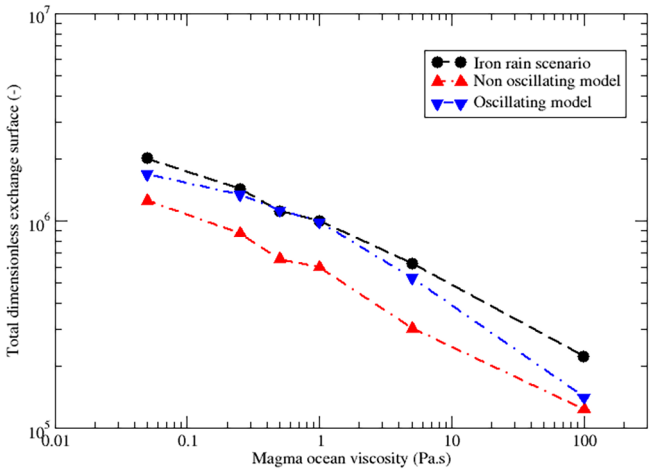

Fig. 20. Normalised exchange surface S^* as a function of magma ocean viscosity after the breakup of a 10 km metal diapir. In the sinking droplet population, no cut-off is considered at $R = R_{max}$.

sinking droplets as a function of the viscosity ratio between the iron droplet and the magma ocean. We showed that, within an iron cloud, each droplet is associated to a boundary layer thickness and an exchange surface that both depend on the droplet size and viscosity ratio. In our numerical models we do not solve the equations governing the thermo-chemical transfers between the metallic droplets and the magma ocean. However, we can estimate the efficiency of the potential thermo-chemical equilibration by determining the total potential exchange surface within a metallic cloud composed of small droplets and resulting from the fragmentation of a 10 km radius metallic diapir, which is the typical lengthscale of iron fragments dispersed after a large impact (Kendall and Melosh, 2016). We consider in these estimations that the 10 km metallic diapir is fragmented in a population of small droplets that compose a larger scale metallic cloud sinking through the magma ocean (Deguen et al., 2014).

To characterize the size of the droplets within the cloud, we used the analytical law for the distribution of droplets sizes obtained from the fragmentation of a large analog diapir with a viscosity ratio $R_\mu = 50$ derived experimentally by Wacheul et al. (2014). We assume here that this analytical law is valid for any system with the same viscosity ratio once it is normalised by the characteristic radius of the system, i.e. the maximal stable radius R_{max}. The number of drops $n(R)$ for a given radius R resulting from the breakup of a 10 km iron core is then associated to a gamma distribution:

$$n(R) = NR^{k-1}e^{-\frac{R}{\theta}} \tag{21}$$

where N is a multiplicative constant determined by volume conservation of iron, k is the shape of the gamma distribution, and θ is the scale of the gamma distribution normalised by R_{max}. Wacheul et al. (2014) explicitly mentioned that the shape and scale might depend on the viscosity ratio. In the absence of any further data, we assume constant values with $\theta = 1.9$ and $k = 2.2$ for viscosity ratios ranging between 10 and 1000. Note that R_{max} is nearly constant in the study of Wacheul et al. (2014) and Eq. (21) is obtained from a snapshot at a given time relatively shortly after the primary breakup, where transient large radius drops are still present. In our study, we have shown that R_{max} is a function of the magma ocean viscosity (Fig. 14). Hence, for each magma ocean viscosity, we use R_{max} from our numerical study (Fig. 14) and determine N by volume conservation from a initially 10 km iron diapir radius. We then compute the number of drops of each size, and their relative surface of exchange normalised by their corresponding spherical surface.

We have shown in our numerical models that shape oscillations might influence the surface of the drops (Fig. 19), especially for the largest radii and smallest viscosity ratio. We consider here three models of droplet population within the cloud:

1. a non oscillating population of droplets with a constant radius for a fixed viscosity corresponding to the classical iron rain scenario (Rubie et al., 2003),
2. a non oscillating droplet population derived from our models with variable radii where the droplets remain spherical,
3. an oscillating population derived from our models with variable radii where the droplets deform.

Fig. 20 shows the total dimensionless surface within the fragmenting cloud for the three different cases. In all cases, the exchange surface decreases when increasing the magma ocean viscosity because the maximum stable drop radius also increases when increasing the magma ocean viscosity (see Fig. 14). In the iron rain scenario, the population is composed of droplets smaller than in the two cases derived from our models (oscillating and non oscillating) where large drops are allowed in the distribution. Hence the potential exchange surface is larger (up to 60%) in the iron rain scenario and the equilibration should be more efficient. For the population composed of oscillating droplets, the deformation leads to an increase of the surface of the sinking droplets especially for low magma ocean viscosities where R_{max} is smaller than for large magma ocean viscosities. The total exchange surface in the oscillating case is larger than in the non-oscillating case (by 13–43%) but remains smaller than in the iron rain scenario (by 7–37%). For large magma ocean viscosity (i.e. large viscosity contrasts), the droplets do not oscillate and the exchange surface value is close for both oscillating and non oscillating populations. For low magma ocean viscosities (i.e. small viscosity contrasts), the deformations are so important in the oscillating population that the total surface is close to the surface obtained in the iron rain scenario.

It is to be noted that large metallic drops (with $R > R_{max}$) are allowed in the populations used to obtain Fig. 20. Such large drops are not stable but are likely to exist during the second phase of the fragmentation following an impact that occurs in the shallow magma ocean (Wacheul et al., 2014). Within a deep magma ocean, transient drops with radii $R > R_{max}$ will fragment in smaller droplets and disappear from the populations used in Fig. 20. We can thus redo our calculation

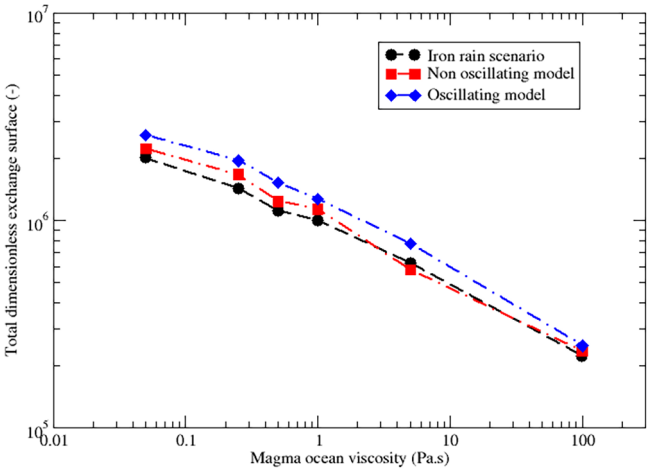

Fig. 21. Normalised exchange surface S^* as a function of magma ocean viscosity after the breakup of a 10 km metal diapir. In the sinking droplet population, a cut-off is considered at $R = R_{max}$.

by imposing a cut-off at R_{max} using the values from our numerical models (Fig. 14). Fig. 21 illustrates the total potential exchange surface within a sinking cloud of metallic droplets as a function of the magma ocean viscosity considering the same initial volume as in Fig. 20. Imposing a cut-off at R_{max} generates a population of smaller droplets than in Fig. 20. In the oscillating and non oscillating populations used in Fig. 21 many droplets are even smaller than the maximum stable drop radius of the iron rain model. Hence Fig. 21 shows that the total surface of the metallic droplets for both the oscillating and non oscillating populations is larger than the total surface derived from the iron rain scenario. Still, the non oscillating model will be less efficient for thermo-chemical equilibrium than the oscillating model and large magma ocean viscosities (i.e. large viscosity contrasts) significantly reduce (by a factor 10) the potential exchange surface between the silicate and metallic phases.

Results from Figs. 20 and 21 both underline the competition between (1) the deformation processes at the scale of the droplet that enhance the equilibration between the iron and silicate phases and (2) the viscosity contrast that limits the potential exchange surface by allowing large drops. In the shallow part of the magma ocean where large transient metallic drops are likely to exist, the thermo-chemical equilibration will be less efficient than in the deepest part of the magma ocean. However, this conclusion needs to be constrained by implementing thermo-chemical transfers in our dynamical models and using realistic partition coefficients and conductivities that should vary with pressure and temperature.

5. Conclusions and future works

During the late stages of planetary accretion, large impacts between differentiated protoplanets have strongly influenced the thermo-chemical state of the future terrestrial planets. Following the impact and the formation of a deep magma ocean, the metallic phase from the impactor has overcome strong deformation and fragmentation processes before reaching the deepest part of the magma ocean. The dynamics of this fragmentation probably played a key role on the equilibration efficiency between the metallic phase from the impactor and the impacted proto-mantle.

We have performed axisymmetric numerical simulations to model the sinking dynamics of an initially spherical liquid iron drop within a molten silicate phase. We have explored a large range of relevant parameters, considering initial drop radii in the range of [1–350] mm resulting from the breakup of an initially larger metallic diapir, and magma ocean viscosities in the range [0.05–100] Pa.s. This large range of viscosity is meant to encompass all relevant geophysical situations, depending on pressure, depth, temperature, composition and impact history.

For large Reynolds numbers, we have showed that the drag coefficient for all viscosity ratios converges towards a unique value on the order of 3.5 ± 0.5. We have found that the maximum stable drop radius increases as a function of the magma ocean viscosity following a power law that scales with $\mu_s^{0.32}$. The corresponding critical Weber number increases as a function of the viscosity ratio following two power laws depending on the breakup regime, that scale with $R_\mu^{0.187}$ and $R_\mu^{0.483}$ for the range of low and large magma ocean viscosity respectively. We have identified five breakup mechanisms depending on the Weber and Reynolds numbers and on the viscosity ratio between silicates and iron phases. We have also shown that the initial shape of the metallic drop (spherical, prolate or oblate) strongly influences its subsequent dynamics by modifying its final shape before breakup, its potential exchange surface, and the time and distance before breakup. We have emphasized the effect of the viscosity contrast on the potential exchange surface between the iron phase and the molten surrounding silicates. Indeed, an increase of the viscosity ratio decreases the potential exchange surface between the iron drop and the molten silicates while it increases the time and distance before breakup. We have shown that the dynamical boundary layer thickness increases as a function of the drop radius and the magma ocean viscosity following power law that scales with $R^{0.916}$ and $\mu_s^{0.062}$. Finally, we have implemented our numerical results in a first order model to characterise the ability of an initially 10 km metallic diapir to exchange with its surrounding environment while fragmenting. Our dynamical model predicts that potential thermo-chemical equilibration within a fragmenting cloud depends on the depth at which the cloud is fragmenting: thermo-chemical equilibration should be less efficient in the shallowest part of the magma ocean than in the deepest part.

The next step is now to implement in our models the resolution of the equations governing the thermo-chemical exchanges between the metallic phase and the magma ocean. The chemical and thermal diffusion of a sinking undeformable sphere has been extensively studied in the chemical/heat transfer literature (Levich, 1962; Clift et al., 1978). In their numerical models, Ulvrová et al. (2011) evaluated time scales of chemical equilibration within an undeformable metallic droplet sinking through a deformable medium. If the exchange dynamics in the case of a sinking sphere is strongly constrained, the dynamics of thermo-chemical equilibration between a deformable droplet and its environment and the influence of the viscosity contrast between the two phases still deserve extensive studies.

As shown in our study, the depth of the magma ocean could also influence the fragmentation dynamics. As large transient droplets are more likely in the early fragmentation regime, full thermo-chemical equilibration could be achieved deeper in the magma ocean. The transfer parameters governing the equilibration rate are also pressure/temperature dependent. The viscosity of the molten silicates (Karki and Stixrude, 2010), the partition coefficient of lithophile/siderophile elements (Bouhifd and Jephcoat, 2003) and the thermal conductivity of iron (de Koker et al., 2012) are all affected by pressure changes with depth. An exhaustive study accounting for realistic parameters in the context of a deep magma ocean will surely help to constrain the thermo-chemical signature at the end of the core-mantle separation.

Acknowledgements

The authors acknowledge funding by the ERC under the European Union's Horizon 2020 research and innovation program through Grant No. 681835- FLUDYCO-ERC-2015-CoG. This research also received funding from the French PNP program (INSU-CNRS), the French Government Laboratory of Excellence initiative No. ANR-10-LABX-0006 and the Région Auvergne. This paper is Laboratory of Excellence ClerVolc contribution No. 338.

Appendix A. Computational resolution and convergence

In order to confirm that our mesh correctly captures the dynamics of the falling drop within the magma ocean and to determine the quality and limits of our numerical model, we performed systematics tests on two representative cases.

In the first case, we focus on the dynamics of a strongly oscillating drop that does not converge to a single shape and remains in oscillation (simulation #18 in Table 2). This corresponds to a worst case scenario from a numerical point of view. Fig. 22(left) shows the normalised boundary layer thickness on the drop radius as a function of different grid sizes $h_x = R/15,\ R/25,\ R/33.4,\ R/40,\ R/50,\ R/66.7$. We observe a reasonable convergence of the numerical results from $h_x = R/40$, with changes limited to 1.4%. To quantify the dynamic difference between $h_x = R/40$ and the finest mesh $h_x = R/66.7$, we calculate the normalised exchange surface as a function of time in Fig. 22(Right). We note that the first two drop oscillations have the same dynamics; then, differences occur. Yet the dynamical times remain close, and the evolution of the exchange surface is almost the same between the two mesh sizes, with a relative maximum error $\simeq 3.5\%$.

In this paper, we are also interested in the fragmentation modes. To confirm that these fragmentation modes don't depend on the mesh size and don't come from any numerical artifact, we calculate an extremely distorted drop which breaks up after a few oscillations in a second test case (simulation #83 in Table 2). Fig. 23 shows the final drop shape just after the breakup for the grid sizes $h_x = R/40$ and $h_x = R/66.7$. This figure confirms that from $h_x = R/40$, the fragmentation mode and the final drop shape do not change significantly with the grid resolution.

We finally compare the cost (CPU) for one second of simulation of the first test case with different mesh sizes in Table 3. The finest mesh is 4 times more expensive than $h_x = R/40$. The purpose of this article being to perform a systematic study to capture the drop dynamics for a large range of radius and ambient viscosity, we have chosen the mesh size of $h_x = R/40$, which is a good compromise between simulation costs and global dynamical results.

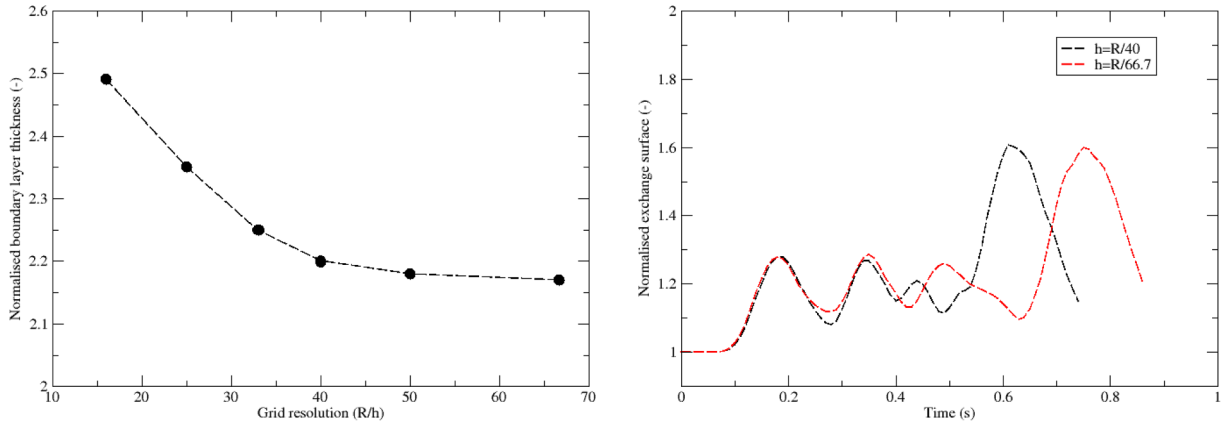

Fig. 22. Comparison of different mesh sizes of a strongly oscillating drop (simulation #18 in Table 2). Left: Normalised boundary layer thickness as a function of grid sizes. Right: Normalised exchange surface as a function of time.

Fig. 23. Comparison of the final shape of the fragmented drop for two different mesh sizes. (simulation #83 in Table 2).

Table 3
Comparison of the cost of one simulation for three different grid sizes.

Grid size (h_x)	CPU
$R/40$	51h15
$R/50$	121h5
$R/66.7$	205h

References

Assael, M.J., Kakosimos, K., Banish, R.M., Brillo, J., Egry, I., Brooks, R., Quested, P.N., Mills, K.C., Nagashima, A., Sato, Y., Wakeham, W.A., 2006. Reference data for the density and viscosity of liquid aluminum and liquid iron. J. Phys. Chem. Ref. Data 35, 285–300.

Bhaga, D., Weber, M.E., 1981. Bubbles in viscous liquids: shapes, wakes and velocities. Fluid Mech. 105, 61–85.

Bonometti, T., Magnaudet, J., 2006. Transition from spherical cap to toroidal bubbles. Phys. Fluids 18, 052102 .

Bouhifd, A., Clési, V., Boujibar, A., Bolfan-Casanova, N., Cartier, C., Hammouda, T., Boyet, M., Manthilake, G., Monteux, J., Andrault, D., 2017. Silicate melts during earth's core formation. Chem. Geol. 461, 128–139.

Bouhifd, M., Jephcoat, A., 2003. The effect of pressure on partitioning of ni and co between silicate and iron-rich metal liquids: a diamond-anvil cell study. Earth Planet. Sci. Lett. 209, 245–255.

Cao, X.K., Sun, Z.G., Li, W.F., Liu, H.F., Yu, Z.H., 2007. A new breakup regime of liquid

drops identified in a continuous and uniform air jet flow. Phys. Fluids 19, 057103 .
Chambers, J.E., 2004. Planetary accretion in the inner solar system. Earth Planet. Sci. Lett. 223, 241–251.
Clift, R., Gauvin, W.H., 1970. The motion of particles in turbulent gas streams. 1, 14–28.
Clift, R., Grace, J.R., Weber, M.E., 1978. Bubbles, Drops and Particles. Academic Press, New York.
Dahl, T.W., Stevenson, J., 2010. Turbulent mixing of metal and silicate during planet accretion and interpretation of the hf-w chronometer. Earth Planet. Sci. Lett. 295, 177–186.
Dai, Z., Faeth, G.M., 2001. Temporal properties of secondary drop breakup in the multimode breakup regime. Multiph. Flow 27, 217–236.
Darton, R.C., Harrison, D., 1974. The rise of single gas bubbles in liquid fluidized beds. Trans. Inst. Chem. Eng. 52, 301–306.
Davies, R., Taylor, G.I., 1950. The mechanics of large bubbles rising through extended liquids and through liquids in tubes. Proc. R. Soc. London 200.
de Koker, N., Steinle-Neumann, G., Vlček, V., 2012. Electrical resistivity and thermal conductivity of liquid fe alloys at high p and t, and heat flux in earth's core. Proc. Natl. Acad. Sci. U.S.A. 109, 4070–4073.
de Wijs, G.A., Kresse, G., Vocadlo, L., Dobson, D., Alfè, D., Gillan, M.J., Price, G.D., 1998. The viscosity of liquid iron at the physical conditions of the earth's core. Nature 392, 805–807.
Deguen, R., Landeau, M., Olson, P., 2014. Turbulent metal – silicate mixing, fragmentation, and equilibration in magma oceans. Earth Planet. Sci. Lett. 391, 274–287.
Deguen, Renaud, Olson, Peter, Cardin, Philippe, 2011. Experiments on turbulent metal-silicate mixing in a magma ocean. Earth Planet. Sci. Lett. 310 (3–4), 303–313.
Fleck, J.R., Rains, C.L., Weeraratne, D.S., Nguyen, C.T., Brand, D.M., Klein, S.M., McGehee, J.M., Rincon, J.M., Martinez, C., Olson, P.L., 2018. Iron diapirs entrain silicates to the core and initiate thermochemical plumes. Nat. Commun.
Hadamard, J.S., 1911. Mouvement permanent lent d'une sphere liquide et visqueuse dans un liquide visqueux. C. R. Acad. Sci. 152, 1735–1738.
Han, J., Tryggvason, G., 1999. Secondary breakup of axisymmetric liquid drop. Phys. Fluids 11.
Harper, J.F., Moore, D.W., 1968. The motion of a spherical liquid drop at high reynolds number. Fluid Mech. 32, 367–391.
Hartmann, W.K., Davis, D.R., 1975. Satellite-sized planetesimals and lunar origin. Icarus 24, 504–514.
Hu, J., Jia, R., Wan, K.T., Xiong, X., 2014. Simulation of droplet impingement on a solid surface by the level set method. COMSOL Conference in Boston.
Ichikawa, H., Labrosse, S., Kurita, K., 2010. Direct numerical simulation of an iron rain in the magma ocean. Geophys. Res. 115, B01404.
Karato, S.I., Rama Murthy, V., 1997. Core formation and chemical equilibrium in the earth physical considerations. Phys. Earth Planet. Int. 100, 61–79.
Karki, B.B., Stixrude, L.P., 2010. Viscosity of mgsio3 liquid at earths mantle conditions: implications for an early magma ocean. Science 328, 740–742.
Kékesi, T., Amberg, G., Wittberg, L.P., 2014. Drop deformation and breakup. Int. J. Multiph. Flow 66, 1–10.
Kendall, J.D., Melosh, H., 2016. Differentiated planetesimal impacts in a terrestrial magma ocean: fate of the iron core. Earth Planet. Sci. Lett. 448, 24–33.
Kim, D.S., Burger, M., Frohlich, G., Unger, H., 1983. Experimental investigation of hydrodynamic fragmentation of gatliunm drops in water flows. Int. Mtg on Light Water Reactor Severe Accident Evaluation, Cambridge, Mass.
Kleine, T., Münker, C., Mezger, K., Palme, H., 2002. Rapid accretion and early core formation on asteroids and the terrestrial planets from Hf-W chronometry. Nature 418, 952–955.
Krzeczkowski, S.A., 1980. Measurements of liquid droplet disintegration mechanism. Multiph. Flow 6, 227–239.
Landeau, M., Deguen, R., Olson, P., 2014. Experiments on the fragmentation of a buoyant liquid volume in another liquid. Fluid Mech. 749, 478–518.
Levich, V., 1962. Physicochem. Hydrodyn.
Loth, E., 2008. Quasi-steady shape and drag of deformable bubbles and drops. Multiph. flow 34, 523–546.
Luo, X.-Y., Ni, M.-J., Ying, A., Abdou, M., 2006. Application of the level set method for multi-phase flow computation in fusion engineering. Fusion Eng. Des. 81, 1521–1526.
Mei, R., Klausner, J.F., Lawrence, C.J., 1994. A note on the history force on a spherical bubble at finite reynolds number. Phys. Fluid 6, 418–420.
Monteux, J., Arkani-Hamed, J., 2014. Consequences of giant impacts in early Mars: core merging and Martian dynamo evolution. J. Geophys. Res. (Planets) 119, 480–505. https://doi.org/10.1016/j.icarus.2013.05.008.
Monteux, J., Coltice, N., Dubuffet, F., Ricard, Y., 2007. Thermo-mechanical adjustment after impacts during planetary growth. Geophys. Res. Lett. 34, 24201–24205.
Monteux, J., Ricard, Y., Coltice, N., Dubuffet, F., Ulvrova, M., 2009. A model of metal-silicate separation on growing planets. Earth Planet. Sci. Lett. 287, 353–362. https://doi.org/10.1016/j.epsl.2009.08.020.
Moore, D.W., 1965. The velocity of rise of distorted gas bubbles in a liquid of small viscosity. Fluid Mech. 23, 749–765.
Morbidelli, A., Lunine, J.I., O'Brien, D.P., Raymond, S.N., Walsh, K.J., 2012. Building terrestrial planets. Earth Planet. Sci. 40, 451–475.
O'Brien, David P., Morbidelli, Alessandro, Levison, Harold F., 2006. Terrestrial planet formation with strong dynamical friction. Icarus 184, 39–58. https://doi.org/10.1016/j.icarus.2006.04.005.
Ohta, M., Sussman, M., 2012. The buoyancy-driven motion of a single skirted bubble or drop rising through a viscous liquid. Phys. Fluids 24, 112101 .
Ohta, M., Akama, Y., Yoshida, Y., Sussman, M., 2009. Three-dimensional simulations of vortex ring formation from falling drops in an immiscible viscous liquid. Chem. Eng. Jpn. 42, 648–655.
Ohta, M., Yamaguchi, S., Yoshida, Y., Sussman, M., 2010. The sensitivity of drop motion due to the density and viscosity ratio. Phys. Fluids 22, 072102 .
Ohta, M., Akama, Y., Yoshida, Y., Sussman, M., 2014. Influence of the viscosity ratio on drop dynamics and breakup for a drop rising in an immiscible low-viscosity liquid. Fluid Mech. 752, 383–409.
Patel, P.D., 1978. Hydrodynamic fragmentation of drops (Ph.D. Dissertation). Purdue Univ. West Lafayette, Ind.
Patel, P.D., Theofanous, T.G., 1981. Hydrodynamic fragmentation of drops. Fluid Mech. 103, 207–223.
Pilch, M., Erdman, C.A., 1987. Use of breakup time data and velocity history data to predict the maximum size of stable fragments for acceleration-induced breakup of a liquid drop. Multiph. Flow 13, 741–757.
Poirier, J.P., 1988. Transport properties of liquid metals and viscosity of the earth's core. Geophys. J. 92, 99–105.
Rubie, D.C., Melosh, H.J., Reid, J.E., Liebske, C., Righter, K., January 2003. Mechanisms of metal-silicate equilibration in the terrestrial magma ocean. Earth Planet. Sci. Lett. 205, 239–255.
Samuel, H., 2012. A re-evaluation of metal diapir breakup and equilibration in terrestrial magma oceans. Earth Planet. Sci. Lett. 313–314, 105–114.
Stevenson, D.J., 1990. Fluid dynamics of core formation. Origin of the Earth 231–249.
Tonks, W.B., Melosh, H.J., 1992. Core formation by giant impacts. Icarus 100, 326–346.
Touboul, M., Kleine, T., Bourdon, B., Palme, H., Wieler, R., 2007. Late formation and prolonged differentiation of the Moon inferred from W isotopes in lunar metals. Nature 450, 1206–1209.
Tripathi, M.K., Sahu, K.C., Govindarajan, R., 2015. Dynamics of an initially spherical bubble rising in quiescent liquid. Nat. Commun.
Ulvrová, M., Coltice, N., Ricard, Y., Labrosse, S., Dubuffet Velìmskì, F., Šràmek, M., 2011. Compositional and thermal equilibration of particles, drops, and diapirs in geophysical flows. Geochem. Geophys. Geosyst. 12.
Villermaux, E., Bossa, B., 2009. Single – drop fragmentation determines size distribution of rain drops. Nat. Phys. 5, 697–702.
Wacheul, J.B., Le Bars, M., 2018. Experiments on fragmentation and thermo-chemical exchanges during planetary core formation. Phys. Earth Planet. Int. 276, 134–144.
Wacheul, J.B., LeBars, M., Monteux, J., Aurnou, J.M., 2014. Laboratory experiments on the breakup of liquid metal diapirs. Earth Planet. Sci. Lett. 403, 236–245.
Walter, M.J., Tronnes, R.G., 2004. Early earth differentiation. Earth Planet. Sci. Lett. 225, 253–269.
Wood, B.J., Walter, M.J., Wade, J., 2006. Accretion of the earth and segregation of its core. Nature 441, 825–833.

Physics of the Earth and Planetary Interiors 306 (2020) 106547

Contents lists available at ScienceDirect

Physics of the Earth and Planetary Interiors

journal homepage: www.elsevier.com/locate/pepi

Dynamics of core-mantle separation: Influence of viscosity contrast and metal/silicate partition coefficients on the chemical equilibrium

V. Clesi[a,*], J. Monteux[a], B. Qaddah[a,b], M. Le Bars[b], J.-B. Wacheul[b], M.A. Bouhifd[a]

[a] Université Clermont Auvergne, CNRS, IRD, OPGC, Laboratoire Magmas et Volcans, F-63000 Clermont-Ferrand, France
[b] CNRS, Aix Marseille Université, Centrale Marseille, Institut de Recherche sur les Phénomènes Hors Equilibre, UMR 7342, 49, Rue F. Joliot-Curie - B.P. 146, 13384 Marseille Cedex 13, France

A B S T R A C T

The composition of the Earth's core and mantle is set by the chemical equilibrium between metals and silicates during core/mantle segregation. The metallic core separated from the mantle by gravitational descent in the form of diapirs in a magma ocean, and therefore the dynamics of the diapir's downward movement has an influence on the chemical equilibrium. In this study, we characterize the descent of metallic droplets into a molten silicate using numerical models. By varying the silicate and metal viscosities (between 0.1 and 1000 Pa·s for each phase) as well as the partition coefficient between metal and silicate ($D^{met/sil}$, varying between 1 and 1000), we obtained quantifying parametrizing equations for the degree of equilibrium between molten metal and molten silicate, in a regime characterized by low *We* ($We < 10$) and low *Re* ($10^{-3} < Re < 10^{2}$). We showed that the main parameters controlling the equilibrium for a siderophile element are the viscosity of the silicate and the partition coefficient. We applied our parameterization for Ni and Co in the context of late accretion on Earth so as to quantify the variation of the Ni/Co ratio after a large impact as a function of the magma ocean viscosity, for an iron-rain scenario of metal/silicate segregation. Using previous models (Canup, 2004) of the Moon–forming impact, we showed that the Moon formation had an effect on the current Ni/Co ratio. Depending on the radius of Theia's core and the viscosity of the magma ocean produced after the impact between the proto-Earth and Theia, the Moon formation could account for 0.45% to 3% of the current Ni/*Co* ratio for magma ocean viscosities of 0.1 to 100 Pa·s, respectively.

1. Introduction

The main process occurring on Earth during the first 100–150 million years was the segregation of its metallic Fe-rich core (e.g. Bouhifd et al., 2017; Rubie et al., 2015; Wood et al., 2006; and references therein). One major consequence of this segregation is the depletion of the Earth's mantle in the siderophile elements relative to primitive solar system abundances (e.g. Jones and Drake, 1986).

The most recent Earth core formation models include a combination of multistage core-mantle differentiation with N-body accretion simulations, combined with continuous Earth core formation where pressure, temperature, oxygen fugacity and chemical composition of both the mantle and core vary during accretion of the Earth (e.g. Rubie et al., 2015, and references therein). These models consider that the accretion of the Earth occurred during a series of large impact events (e.g. Canup, 2008; Wetherill, 1985; O'Brien et al., 2006; Monteux et al., 2009; Nakajima and Stevenson, 2015). More importantly, these models provide results for the metal-silicate partitioning of a significant number of siderophile elements, which are consistent with observed mantle abundances given that the oxygen fugacity increases from about IW-5 to IW-2 (5 to 2 log units lower than the Iron-Wüstite buffer) during core segregation (e.g. Cartier et al., 2014; Rubie et al., 2015; Wade and Wood, 2005).

In this context, the behavior of Ni and Co (two refractory and moderately siderophile elements) has been considered to provide an important indication of the conditions of Earth core formation. The consensus is now that metal-silicate equilibration at high pressure, in the range of 40–60 GPa (corresponding to depths of 1000–1500 km), was required to produce the observed Ni and Co depletions in the mantle (Bouhifd and Jephcoat, 2011; Siebert et al., 2012; Righter, 2011; Fischer et al., 2015; Clesi et al., 2016, for some of the most recent studies). Similar conclusions were reached based on the metal-silicate partitioning of lithophile and weakly-siderophile elements (e.g. Mann et al., 2009). One can note here that the conditions of Earth core formation as derived from metal-silicate partitioning of several elements cannot be used as an argument for single-stage core formation. This is highly unlikely given that Earth core formation occurred over a series of large impact events.

Most core formation models are based on metal-silicate partitioning experiments where both phases are fully molten and both thermodynamic and kinetic equilibrium are reached. This type of scenario favors rapid core - mantle segregation, which is confirmed by isotopic

* Corresponding author at: Laboratoire de Géologie de Lyon- Terre, Planètes, Environnement, CNRS UMR 5276, ENS de Lyon, Université Lyon 1, Campus de la Douà, Batiment Geode, 2 Rue Raphaël Dubois, 69622, Villeurbanne Cedex, France.
E-mail address: vincent.clesi@univ-lyon1.fr (V. Clesi).

https://doi.org/10.1016/j.pepi.2020.106547
Received 6 September 2019; Received in revised form 18 May 2020; Accepted 24 June 2020
Available online 04 July 2020
0031-9201/

studies on Hf/W and short lived isotopes (Kleine et al., 2002; Jacobsen et al., 2008; Kleine et al., 2009; Kleine and Rudge, 2011). If the kinetic equilibrium is well constrained, the extent to which the mantle and core equilibrate with each other is model dependent. So we know that if the metal were to segregate by forming large diapirs descending through the silicate magma ocean, the timescale for the equilibration would be too long to explain the isotopic ratios of Hf/W (Rubie et al., 2003). Therefore, the metal could have segregated by forming smaller diapirs, or droplets, whose radius varied between 0.1 and 10 cm, forming a cloud of iron in the magma ocean (Deguen et al., 2014; Wacheul et al., 2014). An intermediate scenario combining iron-rain mingling for the first part of segregation in the magma ocean, followed by creation of large descending diapirs also exists, which can explain the equilibrium in a deep magma ocean. In such a scenario, the metal falls through the molten silicate in the form of droplets, and then forms a metallic pond at the base of the magma ocean. Gravitational instability then allows metal to form large diapirs which descend through the solid layer of the mantle into the proto-core (e.g. Stevenson, 1981; Monteux et al., 2015; Fleck et al., 2018). This study focuses on the iron-rain phase of core-mantle segregation, during which chemical equilibrium is reached (Rubie et al., 2003, 2011), as large diapirs have less chemical interaction with the surrounding fluid (Ulvrová et al., 2011; Wacheul et al., 2014). In the scenario of segregation by iron rain (Fig. 1), the extent to which the magma ocean is in equilibrium with the core depends on the properties of the metallic flow. The physics of the fluid flow is dependent on various parameters, one of the most important being the viscosity of the surrounding fluid (Ke and Solomatov, 2009; Monteux et al., 2009; Ricard et al., 2009). Numerical and analog simulations of a metallic diapir descending through a surrounding fluid with different viscosities have shown that the diapir is more stable when surrounding viscosity increases from low values ($\sim 10^{-1}$ Pa·s) to high values (~100 Pa·s), (Samuel, 2012; Wacheul et al., 2014). This has an impact on chemical equilibrium, since break–up of the diapir increases the surface of exchange between metal and silicate and small droplets sink more slowly than large diapirs (Ulvrová et al., 2011; Wacheul et al., 2014). The efficiency of equilibrium is also increased when internal convection favors homogenization of concentrations in the metallic droplets (Ulvrová et al., 2011).

The goal of the present study is to characterize the influence of viscosity (metal and silicate phases) and chemical equilibrium on the global equilibrium rate in a magma ocean. To do that, the most relevant methods are analog and numerical modeling (e.g. Samuel and Tackley, 2008; Šrámek et al., 2010; Deguen et al., 2011; Wacheul et al., 2014). Numerical simulations are more practical than analog ones for studying the effects of different phenomena happening simultaneously. In addition, it is difficult to find analogs for both metal and silicate which will react exactly like these two phases, and even more complicated to find analogs that behave chemically and physically in the same way as molten metal and molten silicate. Given the limitations of analog experiments for multiple physical modeling, we chose to perform numerical simulations of a falling metallic sphere into a molten silicate using COMSOL Multiphysics 5.0 modeling software. This approach allows the chemical equilibrium for different types of siderophile elements to be determined. In our simulations we combined chemical diffusion calculations with different types of flow. In particular, these simulations led us to explore the contamination of a silicate column by an excess of a siderophile element initially present in the diapir. Since viscosity influences the type of flow, which in turn is crucial in core-mantle equilibrium modeling (Rubie et al., 2003, 2011; Samuel, 2012), viscosity must have an influence on the extent of core-mantle equilibrium. Furthermore, the equilibrium depends on the partition coefficients of the elements between metal and silicate ($D^{met/sil}$), which depend on pressure, temperature, oxygen fugacity and composition of metal and silicate. Therefore, we tested the contamination of silicate by generic siderophile elements using four different values of $D^{met/sil}$ (1, 10, 100, 1000).

Since major chemical transfers likely occurred during the iron rain process (Rubie et al., 2003) our simulations looked at the equilibrium of droplets with the surrounding silicate. In general, large diapirs in a turbulent environment tend to break into small droplets, forming a cloud in which each droplet moves at the same speed (Wacheul and Le Bars, 2017, 2018). In this study, we look at how one droplet of a given radius (R_{Fe} = 1 cm), which can be deformed but cannot break (see Wacheul et al., 2014), interacts with the surrounding silicate. Then this behavior is extrapolated to the entire droplet cloud, and we can estimate the extent to which equilibrium is reached between the magma ocean and the falling metal during planetary accretion.

As a result of these simulations, we constrain the chemical exchanges between a small metallic diapir and a silicate volume as a function of silicate viscosity (varying from 0.1 Pa·s to 1000 Pa·s), the viscosity ratio between metal and silicate, and time. We thus parameterize the effect of varying viscosity on metal-silicate equilibration, and we use this parameterization to re-evaluate models of core-mantle segregation. Moreover, we characterize the effect of changing the magma ocean viscosity on the chemical composition of the mantle. Finally, we discuss the potential consequences of giant impacts such as the Moon-forming impact on the chemical composition of the Earth's mantle.

2. Physical model

To model the sinking of a metallic droplet into a silicate liquid, we

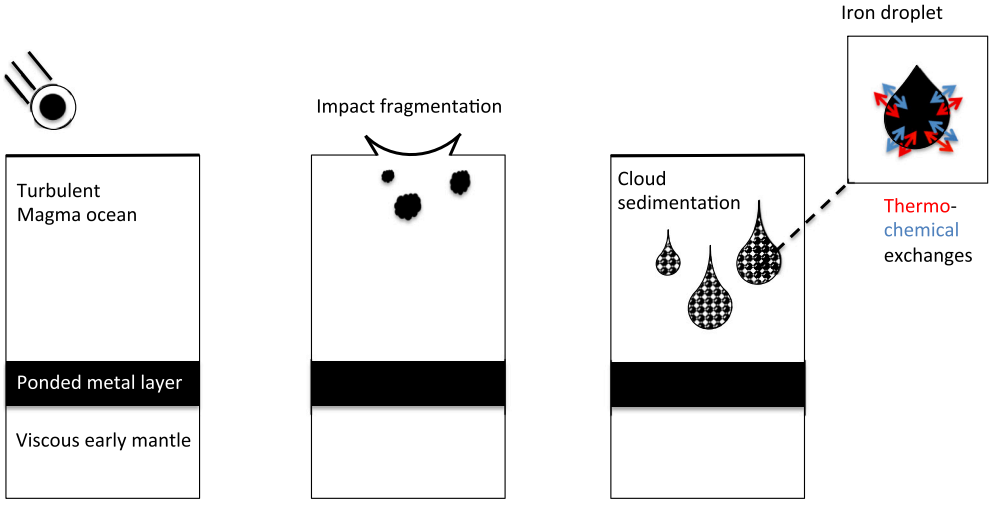

Fig. 1. Schematics of core-mantle segregation. First, the impactor (metal + silicate) enters a turbulent magma ocean. The impactor is fragmented and melted on impacting the surface of the proto-planet. The metallic phase then forms a diapir which, if the magma ocean is turbulent enough, fragments into a cloud of droplets ranging in size from a few millimeters to 10 cm maximum (Rubie et al., 2011; Deguen et al., 2014; Wacheul et al., 2014; Wacheul and Le Bars, 2017, 2018). Each droplet interacts with the surrounding silicate, exchanging heat and chemical elements, until it reaches thermo-chemical equilibrium with its environment.

Table 1
Parameters and variables used in this study. When values are not given, the variable is calculated later in the text (according to the specific case).

Parameter	Name	Values in this study
All models		
ρ	Density of the fluid	Silicate: 3300 - metal: 8000 kg.m^{-3}
t	Time	0.6–125 s
u	Velocity vector	m·s^{-1}
R_{Fe}	Radius of the diapir	1 cm
h_{max}	Maximum unit cell size	0.1 × R_{Fe}
Two-phase flow		
P	Dynamic Pressure of the fluid	1 atm
μ	Dynamic viscosity of the fluid	10^{-1}–10^{3} Pa·s
g	Acceleration of gravity	9.81 m·s^{-2}
l	Distance fluid - initial interface	m
F_{st}	Surface tension force	Calculated for σ = 1 N.m^{-1}, in N.m^{-3}
Φ	Volume fraction of the fluid	Silicate: Φ = 0 metal: Φ = 1 no unit
ϵ_{ls}	Parameter controlling interface reinitialization	$h_{max}/2$
γ	Parameter controlling velocity reinitialization	0.001–0.3 m·s^{-1}
Transport of diluted species		
c_i	Concentration of element i	mol·m^{-3}
k_c	Diffusion coefficient of element i	10^{-6} m^2·s^{-1}
R_i	Reaction rate for element i	mol·m^{-3}.s^{-1}
N_i	Molar flux of element i	0 mol·m^{-2}·s^{-1}
Scaling of the study		
Re	Reynolds number	2.5 × 10^{-5} to 110
We	Weber number	2.3 × 10^{-5} to 3.5
R_μ	Viscosity ratio (=μ_{met}/μ_{sil})	10^{-4} to 10^{4}
R_C	Ratio of the silicate volume reacted	See Section 3

used the software COMSOL Multiphysics, and in particular the modules "Computational Fluids Dynamics" and "Chemical Reaction Engineering". In each module, a set of equations is defined and solved at each time step. These equations are described in the following subsections. The parameters we used for these equations are listed in Table 1.

2.1. Two-phase flow model

In our study, the fluid dynamics are governed by the Navier-Stokes equations that characterize:

- Conservation of mass

$$\nabla \cdot \boldsymbol{u} = 0 \tag{1}$$

- Conservation of momentum

$$\rho\frac{\partial \boldsymbol{u}}{\partial t} + \rho(\boldsymbol{u}\cdot\nabla)\boldsymbol{u} = -\nabla P\boldsymbol{I} + \nabla\cdot[\mu(\nabla\boldsymbol{u} + (\nabla\boldsymbol{u})^T)] + \rho\boldsymbol{g} + \boldsymbol{F_{st}} \tag{2}$$

Eq. (1) is the conservation of mass for an incompressible fluid with $\boldsymbol{u}$ the flow velocity vector. Eq. (2) describes the conservation of momentum, with acceleration of the fluid ($\frac{\partial \boldsymbol{u}}{\partial t}$) and an inertia term ($\rho(\boldsymbol{u}\cdot\nabla)\boldsymbol{u}$) where ρ is fluid density. The first term on the right-hand side of Eq. (2) ($-\nabla P$) is the effect of the dynamic pressure P on the fluid. The second term ($\nabla\cdot[\mu(\nabla\boldsymbol{u} + (\nabla\boldsymbol{u})^T)]$) is the component representing the effect of viscous forces on the fluid with μ the fluid viscosity. The third term ($\rho\boldsymbol{g}$) is the gravitational force that applies to the whole domain with $\boldsymbol{g}$ the gravitational acceleration vector. The fourth term $\boldsymbol{F_{st}} = \nabla\cdot(\sigma(\boldsymbol{I} - \boldsymbol{nn}^T)\delta)$ is the surface tension force with σ the surface tension coefficient, **I** the identity matrix, $\boldsymbol{n}$ a unit vector normal to the surface of interest and δ a smeared out Dirac function located at the interface. Since the volume of metal is small, we ignored the Coriolis forces in Eq. (2).

We monitored the interface between the liquid iron droplet and the molten silicates using the Level Set method, a Eulerian and implicit method used in multiphase flow problems (e.g. Qaddah et al., 2019). For that, we defined a function Φ, characterizing the silicate when Φ = 0 and the metal when Φ = 1. The boundary between the two phases was then set at Φ = 0.5. These values were obtained by modifying the level set field using a smeared out Heaviside function (Olsson and Kreiss, 2005), which allows direct calculation of the volume fraction of a given phase by integration of the variable Φ on the volume considered. The equation governing the transport of Φ is:

$$\frac{\partial\Phi}{\partial t} + \boldsymbol{u}\cdot\nabla\Phi = \gamma\nabla\left(\epsilon_{ls}\nabla\Phi - \Phi(1-\Phi)\frac{\nabla\Phi}{|\nabla\Phi|}\right) \tag{3}$$

with γ (m/s) and ϵ_{ls} (m) the reinitialization parameters. The γ parameter limits the numerical diffusion of the metallic phase during the simulation and needs to be adjusted empirically when the viscosity varies. Indeed, γ is a parameter that determines the amount of reinitialization or stabilization and must be carefully adjusted for each specific problem. If γ is too low, the thickness of the interface might not remain constant, and oscillations in Φ could appear because of numerical instabilities. On the other hand, if γ is too high, the interface moves incorrectly. The ideal value of γ was given by the maximum velocity reached by the diapir during its descent, as detailed in Section 3. The range of values for γ is given in Table 1. ϵ_{ls} is the parameter controlling the width of the interface between fluids during reinitialization. This equation (Eq. (3)) is a combination of the equations presented in Olsson and Kreiss (2005), modified for the COMSOL inbuilt solver. This solver allows the advection (on the left-hand side of the equation) and the reinitialization parameter (right-hand side of the equation) to be solved at the same time. The dynamic viscosity and the density are evaluated using the level set function and are defined by $\mu = \mu_{sil} + \Phi(\mu_{met} - \mu_{sil})$ and $\rho = \rho_{sil} + \Phi(\rho_{met} - \rho_{sil})$, respectively (subscript *met* refers to metal and *sil* to silicates). The resolution of the level set equation without using the COMSOL Multiphysics module is detailed in Olsson and Kreiss, 2005. Furthermore, this method has been already validated and applied to a similar problem in Qaddah et al., 2019.

The temperature of both the metallic droplets and the surrounding molten silicates is difficult to constrain. It is related to the history of both phases before the merging and involves radioactive heating, viscous dissipation and accretionary heating. In our study we consider that the impact that precedes the iron droplet sinking homogenizes the temperature of both phases. Hence, we do not consider heat conservation in the equations solved in our models, and focus instead on the chemical equilibration processes alone.

2.2. Chemical model

The chemical diffusion and reactions of elements are described by transport equations including an advective term to account for the movement of the phase and conservation of mass, a diffusion term (Fick's law) to account for diffusive transfer, and a reaction term to account for the chemical transfer based on the partition coefficient between metal and silicate. In our models we solve the following equation:

$$\frac{\partial c_i}{dt} + \nabla\cdot(-k_c\nabla c_i) + \boldsymbol{u}\cdot\nabla c_i = R_i \tag{4}$$

Eq. (4) is the transport equation for diluted species including Fick's law for the diffusion of an element ($\nabla\cdot(-k_c\nabla c_i)$) with the addition of an advective term ($u\cdot\nabla c_i$) to account for motions within the fluids. c_i is the concentration of element i in the phase of interest, k_c the diffusion coefficient and R_i the reaction rate for element i.

In our case, there are no external sources of elements (N_i = 0, Fig. 2).

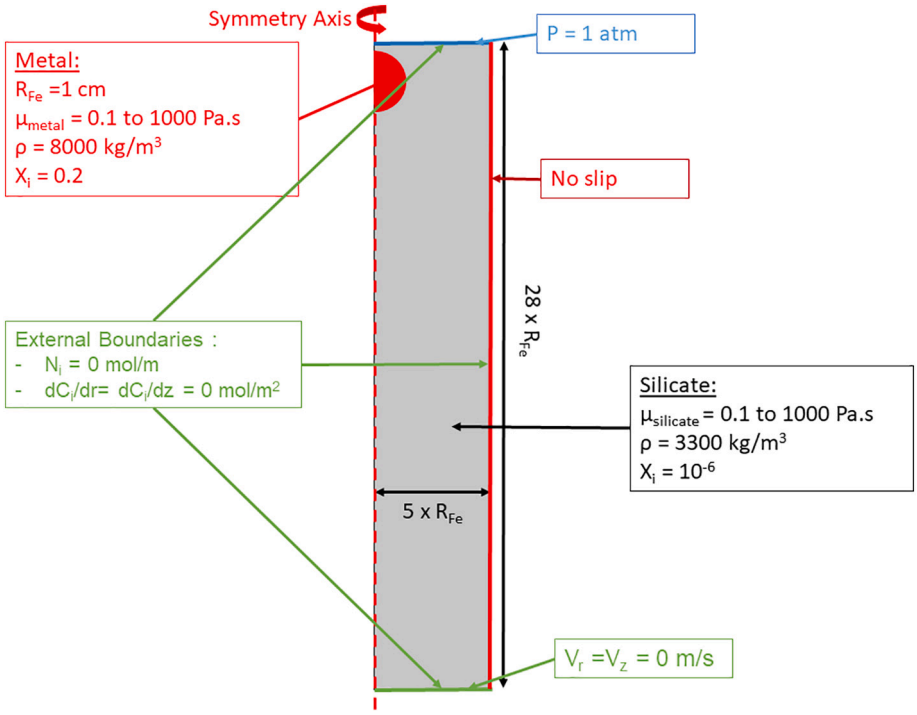

Fig. 2. Schematic representation of the initial conditions and geometry of our models. The characteristics of the metal and silicate phases are listed respectively in red and black. The boundary conditions are detailed in blue (top), solid red line (side), green (bottom and global conditions). The red arrow illustrates the symmetry axis (red dotted line) used to define the 3D output. (For interpretation of the references to color in this figure legend, the reader is referred to the web version of this article.)

We assumed the diffusion coefficient (k_c) to be the same for both phases, and independent of the partition coefficient (D_i). Therefore we defined two functions to describe the behavior of element i in each phase. One function (X_i^{sil}) describes the behavior of element i in the silicate, and therefore tends toward 0 when $\Phi = 1$, the other (X_i^{met}) described the behavior of element i in the metal and tends toward 0 when $\Phi = 0$. The combination of the two functions give us the global concentration of element i in our computational domain. The link between the two functions, the partitioning coefficient and the phase field is made by defining a reaction at the interface between the metal and silicate (i.e. when $\Phi = 0.5$): R_i is the reaction rate necessary to reach the chemical equilibrium defined by the metal-silicate partition coefficient of element i (D_i). D_i is the Nernst partition coefficient given by $D_i = \frac{X_i^{met}}{X_i^{sil}}$, where X_i^{met} is the mass fraction of element i in the metallic phase, and X_i^{sil} the mass fraction of the same element in the silicate phase at equilibrium. R_i is given by Eq. (5):

$$\frac{dc_i}{dt} = R_i \tag{5}$$

where c_i is the concentration in either silicate or metal in mol·m^{-3}, obtained from the density of the phase where the element is ρ^{phase} (for either a metal or silicate phase), the molar mass of the element (M_i) and the mass fraction of the element i in the phase considered is represented by $c_i = X_i^{phase} \rho^{phase} \Big/ M_i$. R_i is automatically calculated in a stationary state from the initial conditions and a given partition coefficient so as to reach equilibrium using COMSOL's in-built solver before the simulation. The reaction rate is high enough to maintain the equilibrium between two calculation steps: the typical time for equilibration is 10^{-5} s, which is less than the time step solved by solver. R_i is negative when removing siderophile elements from the metallic phase, and positive when creating the same element in the silicate phase. The reaction function is only defined for the metal/silicate boundary, given by the condition $\Phi = 0.5$. The higher the value of $D_i^{met/sil}$, the closer the conditions are to equilibrium, and the lower the reaction rate (R_i) will be. For the domain where $\Phi = 0$ or 1, the equilibrium is set to 0, and therefore the reaction rate is 0. For a given time step, the in-built COMSOL Multiphysics 5.0 solver calculate the Navier-Stokes equations (Eqs. (1) and (2)) using finite element method, yielding the velocity field. Then the level-set equation is computed at the same time the advection-diffusion (Eq. (4)) equation is solved by finite-element methods on the entire computational domain, with the reaction R_i only defined where $\Phi = 0.5$. The results of the calculation are then used as starting condition for the next time step.

2.3. Geometry, mesh and initial conditions

First, we defined a geometry for the simulation, using one of the defined boundaries for the eulerian solver available with COMSOL Multiphysics 5.0 software geometries. The best choice for our type of simulation would have been be a 3-D model with a falling sphere inside it, so as to compare our simulation to analog simulations (Deguen et al., 2011, 2014; Wacheul et al., 2014). Since this type of simulation is very costly in terms of computational time, especially for fluid flow simulations, we used a 2D-axisymetric geometry, which solves the equation on a 2D surface, and uses the symmetry conditions to give a 3D output. This is a good compromise between a 2D and 3D simulation when the diapir is not fragmented. Our simulations focused on a weakly deformable falling sphere (i.e. no break up) with a radius of 1 cm in a cylinder whose diameter was set during the calibration of the simulation.

The geometry and boundary conditions used in this study are presented in Fig. 2. In this geometry, a rotational symmetry axis is defined. For the fluid flow, the boundaries of our calculation domain are characterized as follows:

- on the top boundary, the condition is given by $P = 1$ atm,
- on the bottom boundary, the condition is set to be a null velocity field
- on the side boundary, the condition is a no slip condition
- on all the boundary there is a no flow condition for the level set equation.

The conditions for chemical diffusion is a constant budget in chemical elements throughout the numerical simulation, i.e. no elemental flux ($N_i = 0$), inward or outward, is allowed on all the external boundaries.

For our calculation domain we used a fixed mesh of triangles, with three main parameters: h_{max}, h_{min} and a curving parameter. The h_{max} parameter gives the maximum size of the triangle side, h_{min} gives the minimum size and the curving parameter gives the arc interception for curving triangles at spherical boundaries. The parameter controlling the accuracy and the computation time for the calculation is h_{max}. The best value for this parameter was determined in the resolution study, see Section 2.4.

The initial conditions are described in Fig. 2. The viscosities were varied for each simulation, but the geometry of the set-up, the initial concentrations, the densities and the droplet radius were kept constant. To avoid numerical instabilities inherent in $X_{sil}^0 = 0$%wt, the initial concentration was set to $X_{sil}^0 = 10^{-4}$%wt for the silicate with a density $\rho_{sil} = 3300$ kg.m^{-3}; and $X_{met}^0 = 20$% wt for the metal with a density $\rho_{met} = 8000$ kg.m^{-3}. The radius of the droplet was $R_{Fe} = 1$ cm, falling in a cylinder with a 5 cm radius and a 28 cm height, with the center of the droplet placed initially at 26 cm height.

2.4. Tests of the COMSOL simulation

To correctly set up the computational domain in terms of size and mesh, two effects need to be accounted for:

(1) Grid resolution, which has to be sufficient to capture the physics of small droplet deformation.
(2) Boundary effects, to avoid a major influence of the outer border of the domain on the flow and the generation of artifacts in the velocity field.

To minimize the numerical diffusion of iron during the diapir's descent, we tested several maximum sizes for the mesh grid component h_{max}. Fig. 3 illustrates the time evolution of the ratio between the calculated volume over the theoretical volume of one droplet (given by $V_{theoretical} = \frac{4}{3}\pi R_{Fe}^3$ with $R_{Fe} = 1$ cm) for h_{max} values ranging between 0.06 and 0.2 cm. The simulations were performed using the same initial geometry as in Fig. 2, with a silicate and a metal viscosity of 100 Pa·s (corresponding to a Reynolds number of ~2. 10^{-3}, see Eq. (6)) and no chemical component to solve. The precision of the calculation increased as the mesh size decreased, especially when there was deformation. On the other hand, the smaller the mesh grid components were, the longer it took to complete the calculation. As can be seen in Fig. 3, the precision is better for a mesh component size of 0.1 cm than for smaller (0.06 and 0.08 cm) or larger (0.2 cm) mesh component sizes. In addition, a maximum component size allowed a calculation time of a few hours (~6 h), whereas a mesh grid size of 0.06 cm yielded calculation times from a dozen hours to 2 days for the less viscous flows. Therefore, for the rest of the study, we used a maximum size of 0.1 cm for the mesh grid (i.e. $R_{Fe}/10$). The mesh size could be adapted to the type of flow for each simulation: for example, for a higher degree of diapir deformation during the simulation (typically for less viscous flows), the mesh size had to be decreased to avoid numerical artifacts. To increase the precision, COMSOL also made it possible to set a minimum size for the mesh grid component so as to get an adapted mesh, with smaller elements at the interfaces between the two phases, and larger elements as the distance from the interface increases. Varying the parameter h_{min} did not affect the simulation for a given value of h_{max}, so it was kept at a constant value of $h_{min} = h_{max}/40$.

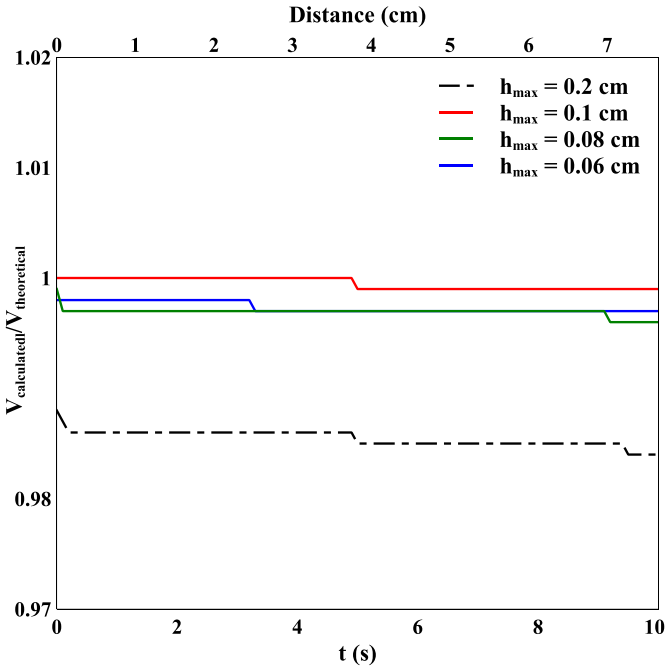

Fig. 3. Evolution of the metallic volume ratio ($V_{calculated}/V_{theoretical}$) during a simulation for different h_{max} values, for a silicate viscosity of 100 Pa·s. The colored and dashed line represent the evolution of $V_{calculated}/V_{theoretical}$ for different mesh sizes with time. The scale at the top shows the distance traveled by the diapir over a given time.

The second point was to avoid boundary effects on the fluid flow during the simulation. We tested several domain sizes and checked the different velocity field components (r- and z- components). We chose a height equal to $28xR_{Fe}$ and a width equal to $5xR_{Fe}$ which was sufficient to avoid the recirculating flow associated to the descending diapir having a large effect on the velocity field (Fig. 4), while keeping computational time within reasonable bounds. This size of domain still affected the velocity of the diapir (Chang, 1961 and Fig. 4). Fig. 4 shows that increasing the width to $6\times R_{Fe}$ changed the velocity field, albeit very slightly, which indicates a diminution of the wall effect: the mean velocity of the diapir increased by 8% compared to the mean velocity for a width of $5xR_{Fe}$. However, increasing the width of the domain from $5xR_{Fe}$ to $6xR_{Fe}$ led to a significant increase in computational time (by at least 46%). Given the limited effect of increasing the domain width and the significant effects on the computational time, we considered this smaller width to be suitable for the study. We applied the same reasoning to choose the height of our domain. To test the resolution of the diffusion in Eq. (4), we benchmarked the validity of the COMSOL solver against steady and unsteady analytical solutions for diffusion problems (Crank, 1975). To test the advective part, we compared the flow velocities from our models with those velocities obtained by Samuel (2012) (see Section 3.2). Our results showed an acceptable agreement, despite a large discrepancy between theoretical results and observed velocities (45% for the largest one) for flows with the largest velocities, i.e. in the intermediate regime. To explain the observed differences, we calculated the mesh Peclet number Pe_{mesh} after each simulation with $Pe_{mesh} = \frac{vh_{max}}{k_c}$, where v is the velocity of the diapir, h_{max} is the mesh size and k_c is the diffusion coefficient (10^{-6} m^2·s^{-1}, which is higher than a typical chemical diffusion, but high enough to limit numerical diffusion, see Qaddah et al., accepted manuscript). In the reference case and for the other cases within the Stokes regime, the value of Pe_{mesh} was sufficiently low ($Pe_{mesh} < 10$) meaning that numerical diffusion was negligible (see Mittal and Jain, 2012). For the cases within the intermediate regime, Pe_{mesh} was higher ($Pe_{mesh} > 50$), which indicates possible numerical diffusion that likely affected our results. To correct this effect a much smaller mesh size would have been necessary. However, the mesh size necessary to prevent numerical diffusion in our models would have led to unreasonable computational times. Therefore, for the lowest viscosity used in our models some error calculations might have occurred in our results, but are negligible in the final model (see Sections 5 and 6).

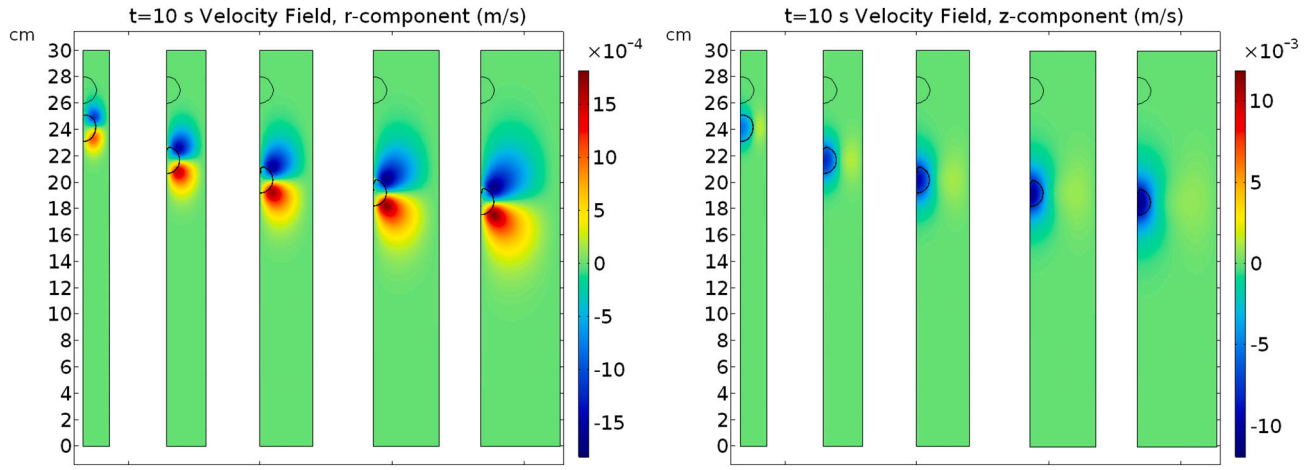

Fig. 4. Evolution of the velocity field, r-component (on the left) and z-component (on the right), for different widths of computational domain. Widths vary from 2× R_{Fe} to 6× R_{Fe}. The chosen width for the simulations is 5xR_{Fe}. Note that the results presented here are calibration runs, with a height of 30xR_{Fe}. The same simulations have been performed at varying heights, leading to a final height of 28× R_{Fe} (see Fig. 2 for the calibrated geometry).

3. Results

In this section we present the results of our simulations as well as a definition of the non-dimensional numbers and parameters used to interpret the results of the simulation in terms of degree of equilibrium. A reference run was arbitrarily defined to set a reference time evolution for the non-dimensional parameters. Then we varied the viscosity of the silicate and metallic phase for a given partition coefficient value, and finally we varied the value of the partition coefficient for a given viscosity.

3.1. Reference case and characteristic non-dimensional numbers

In this section we present the results for a reference case, where $\mu_{sil} = \mu_{met} = 100$ Pa·s. The temporal evolution of the reference case flow is presented in Fig. 5. This figure shows that for this case both the diapir deformation and the numerical diffusion are weak. The metallic droplet moves a distance of 10 × R_{Fe} (10 cm) in 12.1 s.

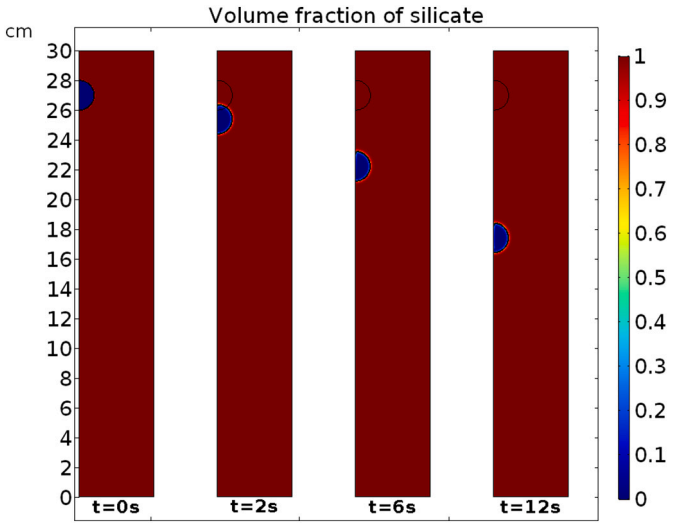

Fig. 5. Evolution of the volume fraction of the silicate during the simulation. When equal to 1 (red), the fluid is a silicate, when equal to 0 (blue) the fluid is a metal. The limit between metal and silicate is the black line between the red and blue parts ($\Phi_{ls} = 0.5$). The time necessary for the diapir to reach the distance of 10R_{Fe} is 12.1 s. (For interpretation of the references to color in this figure legend, the reader is referred to the web version of this article.)

To compare this flow to other flows with different viscosities, we need to use non-dimensional numbers. Since this study focuses on the viscosity variations and the characteristics of the flow, the Reynolds number (*Re*) is the more adequate non-dimensional number, which is given by Eq. (6):

$$Re = \frac{\rho_{sil} R_{Fe} v_{diapir}}{\mu_{sil}} \tag{6}$$

where ρ_{sil} is the density of the surrounding silicate, R_{Fe} is the initial radius of the diapir, v_{diapir} is the velocity of the diapir and μ_{sil} is the silicate viscosity (see Table 1). This number expresses the ratio of inertial forces to viscous forces. When $Re < 1$, the flow is considered to be a Stokes flow, which means that diapir deformation is limited during the descent. When $1 < Re < 500$, the flow is an intermediate flow between Newtonian and Stokes flow (Samuel, 2012). In our study, we did not investigate the case of $Re > 500$, which is a highly turbulent Newtonian flow.

The velocity of the diapir is strongly governed by the viscosity of the surrounding silicate, which affects the value of *Re* (e.g. Samuel, 2012, and references therein). In order to compare different values of the viscosity ratio $R_\mu = \mu_{met}/\mu_{sil}$, we defined the reference time for each calculation as the time necessary for a metallic droplet with radius R_{Fe} to move through a distance d = 10 × R_{Fe}.

The other non-dimensional number which controls the flow is the Weber number (*We*), which is the ratio of the inertial forces on the surface tension:

$$We = \frac{\rho_{sil} v_{diapir}^2 R_{Fe}}{\sigma} \tag{7}$$

with σ the surface tension (see Table 1 for value). The break-up of the diapir is controlled by the Weber number (Wacheul et al., 2014). When $We < 6$ the diapir is stable in Stokes and intermediate flows, and when $We > 6$ the surface tension is no longer high enough to prevent the diapir breaking up (Wacheul and Le Bars, 2017). In this case and in the rest of the present study, the diapirs are always stable with $We < 6$. For the reference case, the diapir velocity is about $v_{diapir} \approx 8 \times 10^{-3}$ m·s^{-1}. This velocity yields low values of *Re* and *We* (2.2×10^{-3} and 1.2×10^{-3}, respectively), which explains the diapir's stability during its descent (see Fig. 5).

To study the chemical equilibrium between metal and silicate, we calculated a non-dimensional concentration, or more precisely a non-dimensional mass fraction termed *X′*. This non dimensional mass fraction was calculated so as to satisfy three conditions:

(i) If there is no change in the initial concentration in the silicate, X' is equal to 0 (no equilibrium at all)
(ii) If equilibrium is reached, X' is equal to 1.
(iii) X' is proportional to the concentration in the silicate ($X' \propto X$)

The first condition is reached if $X = X_{sil}^0$. Therefore $X' = 0$ implies a null numerator for X', i.e. $X' \propto X - X_{sil}^0$. For the second condition, it is reached if $X = {X_{met}^{eq}}/{D^{met/sil}}$, by definition of the partition coefficient, where X_{met}^{eq} is the concentration of the element in the metallic phase at equilibrium. In our case, the element is a siderophile ($D^{met/sil} \geq 1$) and the initial concentration is high ($X_{met}^0 = 0.2$). Therefore, at the end of the simulation we could approximate the equilibrium concentration by $X_{met}^{eq} \sim X_{met}^0$.Satisfying the condition $X' = 1$, with $X' \propto X - X_{sil}^0$ and the non-dimensionality of X' yield to the following formula given in Eq. (8):

$$X' = \frac{X - X_{sil}^0}{X_{met}^0/D^{met/sil} - X_{sil}^0} \tag{8}$$

X' is a useful parameter for tracking the evolution of concentration in a particular case, but it is not enough to quantify how much of the silicate is affected by a change in concentration. Moreover, this parameter is not suitable for comparing different studies, because it is strongly affected by the duration of the sinking. The evolution of the non-dimensional concentration, X', in the reference case is shown in Fig. 6. Equilibrium in the silicate is reached when $X' = 1$ (area in red). This area forms a very narrow zone around the diapir, and most of the silicate is not chemically equilibrated with the metal, because the simulation run time is not long enough.

The parameter R_C is the ratio of the silicate volume that has reacted with the metal to the total volume of silicate. The definition is $R_c = V_{reacted}^{sil}/V_{total}^{sil}$, where $V_{reacted}^{sil}$ is the volume of silicate where $X > \boldsymbol{X_{sil}^0}$; meaning R_C is the volume fraction of silicate that has reacted with the metal. To visualize how the ratio is calculated, a representation of the integrated volume is shown in Fig. 7. In this figure, the areas colored in red represent the volume of silicate that has evolved in terms of chemical composition, while the areas in blue represent that which has not been contaminated by the diapir's descent.

For each simulation, the volume chemically affected by the diapir's descent increases with time. The time evolution of the R_C value for the reference case is shown in Fig. 8. R_C is increasing with time following

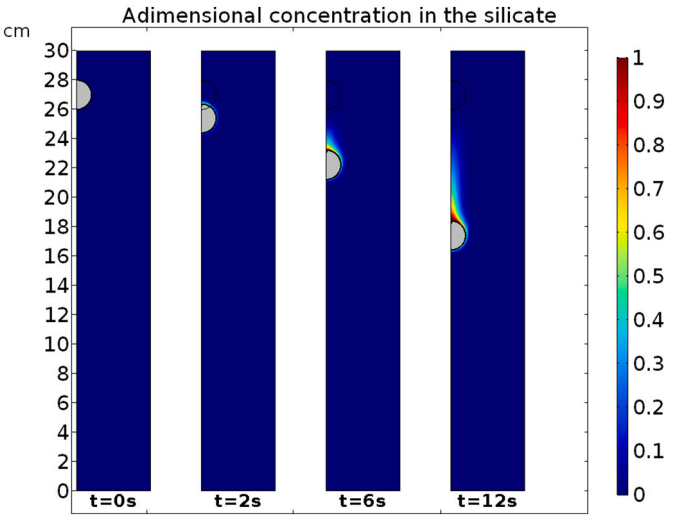

Fig. 6. Evolution of adimensional concentration of the siderophile element in the silicate, for a partition coefficient $D^{met/sil} = 1$. For clarity purposes the metal is shown by the grey area surrounded by a black line. The black line is the boundary between metal and silicate and defines the surface where the exchange reaction happens. The adimensional concentration is given by the following formula given in Eq. (9). In this case $X_{sil}^0 = 10^{-5}$, $X_{met}^0 = 0.2$ and $D^{met/sil} = 1$, and the chemical Peclet number is $Pe \sim 800$.

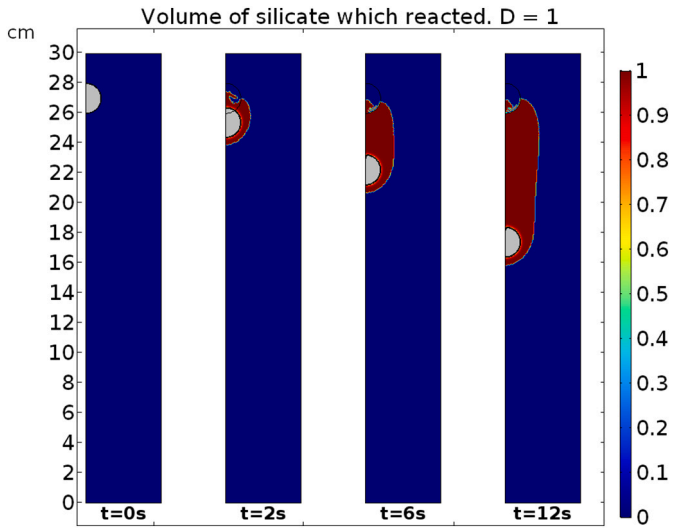

Fig. 7. Evolution of the volume of silicate undergoing reaction during the simulation. In red, the volume of silicate affected chemically. In blue, the volume of silicate unaffected by the passage of the diapir. The metal is colored in grey. The ratio R_C defined in the study corresponds to the volume of the red areas divided by the total volume of silicate (red + blue areas). (For interpretation of the references to color in this figure legend, the reader is referred to the web version of this article.)

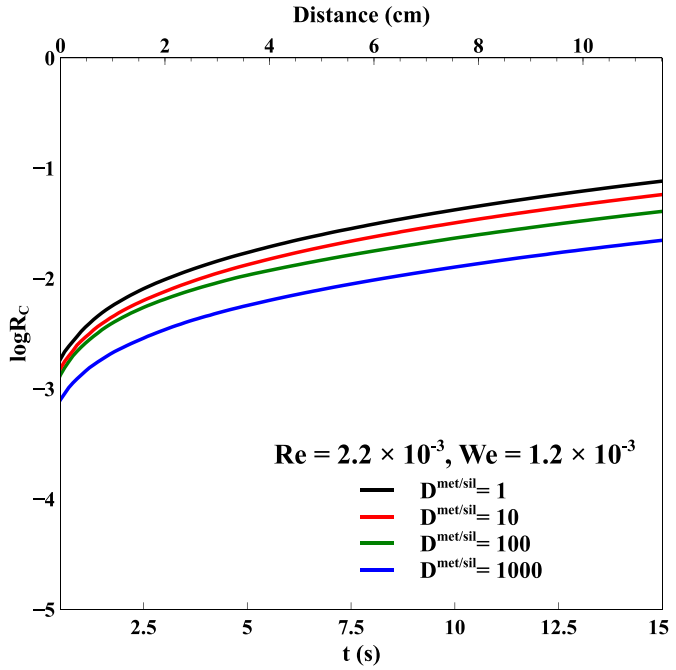

Fig. 8. Evolution of R_C as a function of time in the reference case defined in the text ($\mu_{sil} = \mu_{met} = 100$ Pa·s). The four lines illustrate four different values of $D^{met/sil}$ ranging from 1 (black) to 10^3 (blue). (For interpretation of the references to color in this figure legend, the reader is referred to the web version of this article.)

the same trend in each case. The difference is in the absolute values of $D^{met/sil}$: the more elevated the value is, the closer the initial conditions are to equilibrium conditions, which leads to a lower reaction rate.

3.2. Range of Re and We values

The aim of our models was to constrain the influence of the viscosity contrast between the silicate and metallic phases. This led to a wide

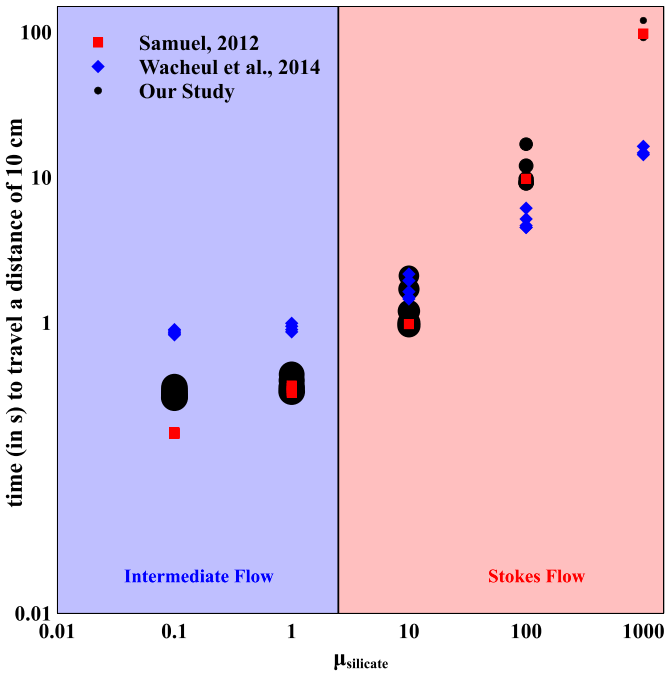

Fig. 9. Evolution of the time necessary for the diapir to move through $10R_{Fe}$ as a function of the silicate viscosity. Black points are the values corresponding to each study. The red area corresponds to Stokes flows, and the blue area to intermediate flows. The clusters of black points correspond to the variation in velocity due to the variation in metal viscosity. The theoretical values are plotted in red and derived from Eqs. (9) and (10). Typical times of diapir equilibrium, from Wacheul et al. (2014), are shown in blue. The size of the marker is scaled logarithmically on the chemical Peclet number, ranging from 8 (smallest) to 3000 (largest). (For interpretation of the references to color in this figure legend, the reader is referred to the web version of this article.)

range of *Re* and *We* values in our numerical simulations. The viscosity of the silicates surrounding the metal droplet controls the flow regime and the sinking velocity. The evolution of the time necessary to reach the distance of $10 \times R_{Fe}$, which depends mostly on the silicate viscosity (Samuel, 2012 and references therein), is presented in Fig. 9. The higher the viscosity of the silicate, the longer it takes for the diapir to reach a set distance. The changes in flow regime result in different expressions for the diapir velocity. In our study, the range of *Re* values only allows Stokes regime flows ($Re < 1$) or intermediate regime flows ($1 < Re < 500$), with two different expressions for the diapir's velocity. In a Stokes flow the velocity is given by:

$$v_{Stokes} = \frac{2}{9}\frac{(\rho_{met} - \rho_{sil})gR_{Fe}^2}{\mu_{sil}} \quad (9)$$

For intermediate flows, the sinking velocity is given by:

$$v_{intermediate} = \sqrt[2]{\frac{(\rho_{met} - \rho_{sil})gR_{Fe}}{\rho_{sil}C_D}} \quad (10)$$

with C_D the drag coefficient. In our case, the drag coefficient is approximated by $\boldsymbol{C_D = \frac{12}{Re} + 0.3}$, following Samuel (2012). From Eq. (10), we can also calculate the velocity in each drop flow regime: Stokes, intermediate, and Newton (e.g. Qaddah et al., 2019). The theoretical times associated with the velocity are compared to the actual times observed in simulations in Fig. 9. It shows a good agreement between theoretical and observed diapir velocity, despite some scatter. This scatter is consistent with the wall effect of our simulations: the variation in velocity observed in the Stokes flow is of the order of 10%, which is consistent with the variation expected if the wall effect is negligible (see Section 2.4). Comparison with the typical equilibrium time from Wacheul et al. (2014) in Fig. 9 shows that, except for the intermediate flows, the fall time chosen in our study is long enough to reach full equilibrium (or more than 90% of equilibrium in some cases) inside the metal, leaving the silicate as the limiting phase for equilibrium. The dispersion of the obtained reference time (Eqs. (8) and (9)) in Fig. 9 for

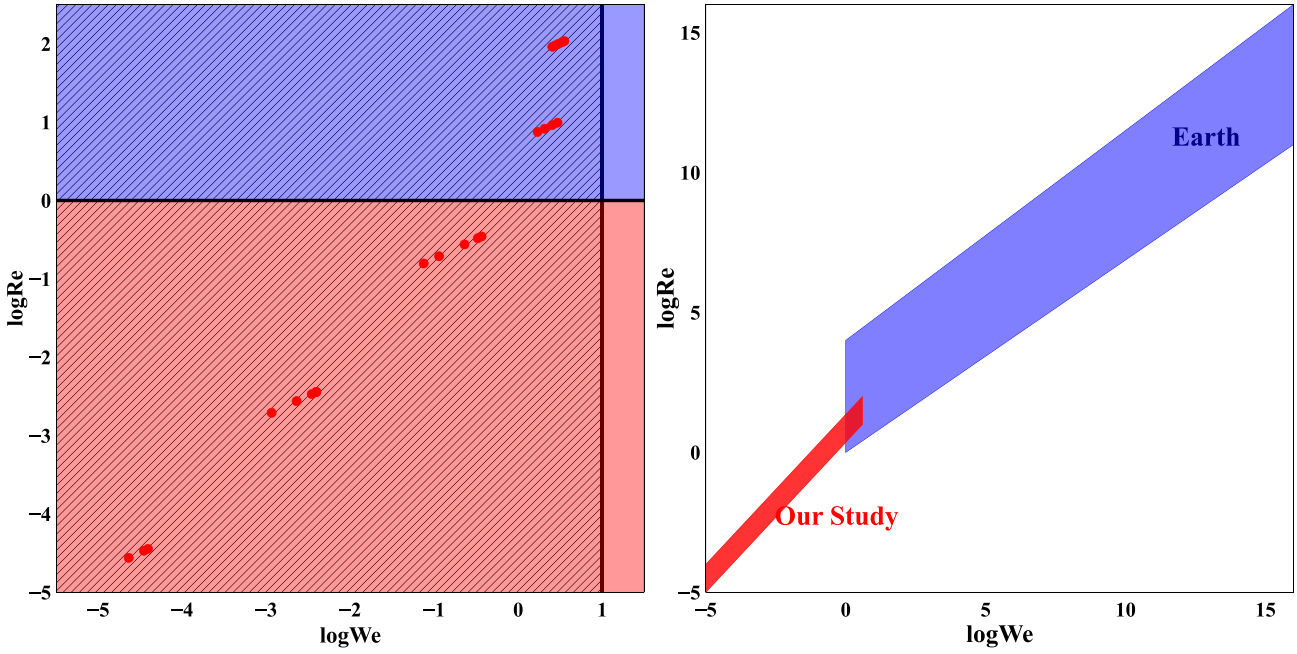

Fig. 10. On the left: *Re* as a function of *We* obtained from our numerical simulations (one red circle for each calculation). The blue area shows the Intermediate regime flow, and the red area the Stokes regime flow. The dashed area illustrates the domain where diapirs are stable. On the right: Comparison between the geologically plausible values of *We* and *Re* for the Earth's magma ocean and the values covered by our study. (For interpretation of the references to color in this figure legend, the reader is referred to the web version of this article.)

a chosen value of μ_{sil} is considered therefore as a negligible discrepancy in the rest of the study.

In Fig. 10 we plot the *Re* values as a function of the *We* values for each simulation (i.e. for each viscosity contrast used in our calculations). The velocity of the diapir (v_{diapir}) used to calculate *Re* and *We* is determined from our numerical models by the time necessary for the diapir to move through a distance of 10 × R_{Fe}. This time is dependent on the viscosity and illustrated in Fig. 9. Fig. 10 (left) shows that in all our numerical simulations, the metallic droplet is stable (i.e. no break up occurs) even though some models are in the Stokes regime and others are in the Intermediate flow regime. In Fig. 10 (right) we compare the range of values with the range of *We* and *Re* values relevant to the geological context of a liquid metallic droplet sinking through a terrestrial magma ocean (Wacheul et al., 2014). As shown in Fig. 10 (right), our range of values is limited compared to possible geophysical values. Larger diapirs leading to high *Re* and *We* values are not considered in our study, which focuses on small droplets in the iron rain scenario.

3.3. Influence of the viscosity ratio

The viscosity ratio is an important parameter controlling the dynamics of diapir descent, both its shape (Qaddah et al., 2019) and stability (Wacheul et al., 2014). In this section, we focus on the influence of the viscosity ratio R_μ ($=\mu_{met}/\mu_{sil}$) by varying the value of the silicate viscosity for a given metal viscosity. Changing the viscosity of metal affects its ability to deform and, hence, its terminal velocity, but this effect is not as strong as the change in velocity implied by a change in ambient viscosity. This behavior is consistent with the equation of diapir velocity in Stokes and intermediate flows (Eqs. (9) and (10)), and is strongly dependent on the silicate viscosity. It is visible in Fig. 9, where a decrease in silicate viscosity from 1000 Pa·s to 10 Pa·s (Stokes flows) leads to an increase in sinking velocity from 10^{-3} m·s^{-1} to 0.1 m·s^{-1} for a metal viscosity of 1 Pa·s. For a constant silicate viscosity of 10 Pa·s, a decrease of the metallic viscosity from 1000 Pa·s to 0.1 Pa·s only increases the velocity from 0.05 to 0.1 m·s^{-1}. The viscosity ratio influences the sinking velocity and, hence, affects the *Re* number and the flow regime, but not as strongly as the silicate viscosity.

Fig. 11 illustrates the influence of the *Re* number on the silicate volume chemically contaminated during the sinking of a metallic droplet with R_{Fe} = 1 cm. For each case, the evolution of R_C is shown as a function of *Re*, and for a distance of 10 cm (10 × R_{Fe}). The time corresponding to this distance is shown in Fig. 5 as a function of viscosity. Except for the case with $D^{met/sil} = 10^3$, there is no linear correlation between log(R_C) and log(*Re*). However, we clearly show a transition between the Stokes regime and the Intermediate regime. In the Stokes regime flow, an increasing *Re* (i.e. a decreasing value of μ_{sil}) leads to a significant decrease of R_C, while R_C values seem to reach a plateau when the flow reaches the intermediate flow regime. Fig. 11 also shows that the approximation made by Rubie et al. (2003) to achieve an analytical solution for equilibrium is only valid for low *Re* flows (high silicate viscosity). As the density of the silicate is not significantly altered by the reaction, the parameter R_c (volume ratio of silicate equilibrated) can be compared to their parameter F_s (mass ratio of silicate equilibrated). For the lowest *Re* value, there is good agreement between our numerical data and the analytical calculation. However, extrapolating the analytical solution to higher *Re* flows leads to an overestimation of the equilibrated volume.

The R_C ratio is presented in Fig. 12 as a function of R_μ. A decrease in R_C is observed with an increase in R_μ (i.e. a decrease of μ_{sil}) for a given viscosity of the metallic phase. For the five parts of Fig. 12, which correspond to the five values of μ_{met}, the trend and the magnitude of the values of R_c are quite similar, meaning that the effect of the viscosity ratio is less important than the ambient viscosity, which governs the flow regime. For high values of R_μ, the same plateau phenomenon as seen in Fig. 11 is observed, which corresponds to lower silicate viscosity values (intermediate flow). In the Stokes regime, the sinking velocity

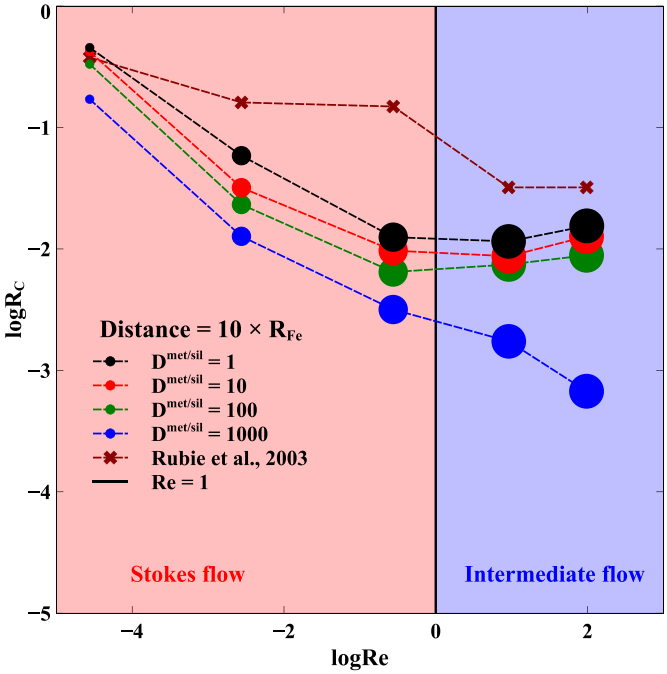

Fig. 11. Evolution of R_C as a function of *Re* during the sinking of a 1 cm-radius droplet for an adimensional time of 1. The Stokes flow regime (red area) and intermediate flow regime (blue area) are separated by a black vertical line at *Re* = 1. The dot color characterizes different values for $D^{met/sil}$ ranging from 1 to 10^3. The size of the marker is scaled logarithmically on the chemical Peclet number, ranging from 8 (smallest) to 3000 (largest). (For interpretation of the references to color in this figure legend, the reader is referred to the web version of this article.)

scales with μ_{sil}^{-1} (Eq. (9)) while in the intermediate regime, the sinking velocity scales with C_D^{-1}. Given the expression of the drag coefficient (derived from Samuel, 2012; see Section 3.2), and the expression of *Re* (Eq. (6)), the sinking velocity in the intermediate regime scales with $(\rho_{sil}\mu_{sil})^{-0.5}$, as given by Eq. (10). Hence, R_μ has a greater effect on Stokes flows than intermediate flows, because the changes in diapir velocity are more pronounced for Stokes flows, as shown in Fig. 5.

Although the evolutions of R_C as a function of R_μ are quite similar in the five panels of Fig. 12, some differences are noticeable. For the lowest values of μ_{met}, the R_C ratio increases at high R_μ values while for high values of μ_{met}, the R_C ratio is nearly constant or decreases with high R_μ (except for $D^{met/sil} = 1000$). This could be explained by the fact that a higher viscosity ratio tends to stabilize the diapir and slow down its descent (Wacheul et al., 2014). In a Stokes regime, it leads to an increase in the time necessary to reach the same distance, in other words a longer reaction time; but in intermediate regimes this time does not change significantly, while the diapir is less deformed, leading to a smaller surface of exchange between metal and silicate. We illustrate this point in Fig. 13, for a silicate viscosity of 0.1 Pa·s: the normalized surface of the diapir varies from 1 to 2.3 with decreasing values of R_μ, which means that low R_μ for high *Re* (~100) values lead to an increase of exchange surface by 130% relatively to the initial diapir surface. The same effect is observed for μ_{sil} = 1 Pa·s (*Re* ~ 10), to a lesser degree: for low metallic viscosity (R_μ = 0.1) the diapir surface increases by 20%. This leads to an increase in R_c value for all partition coefficients except for $D^{met/sil} = 1000$, for which an increase in diapir surface has a negligible effect, the deformation occurring over a short timescale at a low reaction rate. This effect is weak in our study compared to the effect of *Re* and $D^{met/sil}$ (see Section 3.4), because the *We* range of our study does not allow major diapir deformation. For the deformation rate to have a strong impact on chemical equilibrium, the *We* values have to be much higher (*We* > 10, see Lherm and Deguen, 2018).

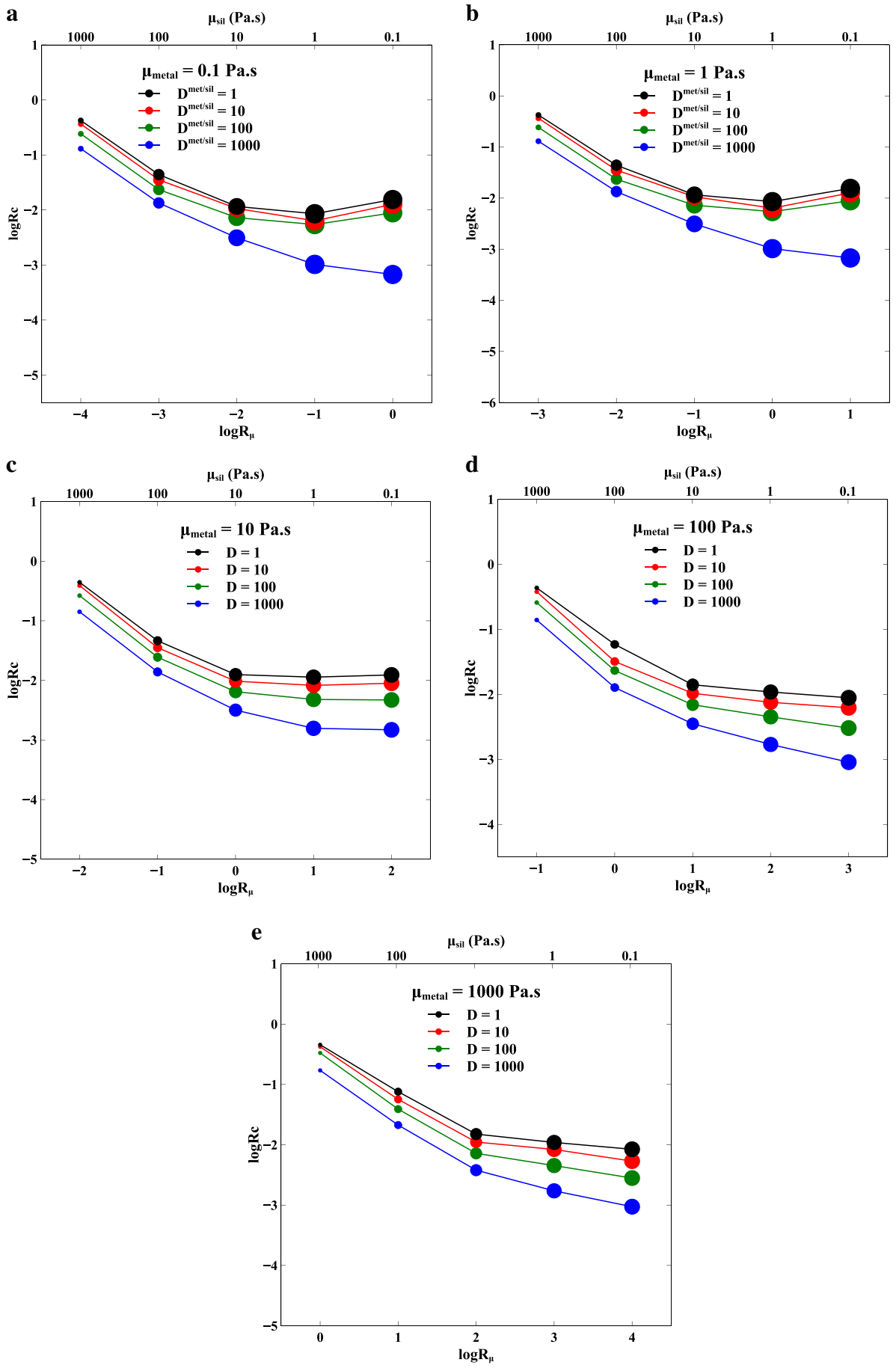

(caption on next page)

Fig. 12. Evolution of R_C as a function of R_μ for 5 different metallic viscosities (shown in the 5 boxes), different values of $D^{met/sil}$ and obtained at a distance of $10R_{Fe}$. From top left to bottom panel the metallic viscosity increases from 0.1 Pa·s to 1000 Pa·s. The silicate viscosities corresponding to R_μ are indicated on the top x-axis. The size of the marker is scaled logarithmically with the chemical Peclet number, ranging from 8 (smallest) to 3000 (largest).

3.4. Influence of the partition coefficient

We have shown in Figs. 11 and 12 that chemical equilibration was less efficient when the value of the viscosity ratio between the iron and silicate phases was higher. This conclusion also stands for the whole range of partition coefficients used in our models. As detailed in Section 2.2, the higher the value of $D^{met/sil}$, the closer the conditions are to equilibrium conditions, and the lower the reaction rate (R_i) will be. However, the thermodynamical equilibrium is reached faster, which limits the amount of exchange between the metallic droplet and the surrounding silicate. Therefore, the contaminated volume represented by R_C decreases when $D^{met/sil}$ increases (see Figs. 11 and 12). This effect is relatively small: an increase of 3 orders of magnitude decreases *Rc* by less than one order of magnitude.

3.5. Parameterization of the chemical contamination

As shown in the previous sections, the contamination of silicate by a siderophile element depends on the Reynolds number, viscosity ratio, and the values of metal-silicate partition coefficients. To use our results in an iron rain scenario following an impact during planetary formation, it is necessary to quantify the relative effect of each parameter on chemical contamination. In Section 3.1 and 3.2 we chose a distance of $10 \times R_{Fe}$ and the relevant time (Fig. 5) at which R_C is considered to have reached a stationary value. With this assumption the error is limited, since R_C tends to reach a plateau in all our simulations (see Fig. 8). Therefore, we consider the R_C values obtained from our models at a distance of $10 \times R_{Fe}$ in our parameterization.

We show in Sections 3.2 and 3.3 that increasing the Reynolds number and viscosity ratio both tend to decrease R_C. In Figs. 11 and 12, $\log(R_c)$ decreases linearly with both $\log(Re)$ and $\log(R_\mu)$ independently of the value of $D^{met/sil}$ with a small error in the prediction ($R^2 > 0.85$–0.9). Concerning the effect of partition coefficients, (Section 3.4), all the curves in Figs. 11 and 12 are parallel, showing that there is a linear relationship between $\log(R_c)$ and $\log(D^{met/sil})$. We parameterize the evolution of $\log(R_C)$ as a function of $logRe$, $logR_\mu$ and $logD^{met/sil}$. The method used here is a multi-linear regression fit on all the data retrieved from the simulations:

$$logR_C = a \times logD^{met/sil} + b \times logRe + c \times logR_\mu + d \quad (11)$$

where a, b, c and d are constants fitted to the data by least-square regressions. The values of the parameters are presented in Table 2. As shown in Fig. 14, the parameterization of Eq. (11) shows a relatively good fit to the data retrieved from calculations. This kind of fit is not perfect, and could certainly be improved by including non-linear dependencies. It is also worth noting that this parameterization is valid for a narrow range of Re and We values, and its precision is lower at high Re values (see Section 2.4). For instance, different results can be found in turbulent cases (high Re, Deguen et al., 2014) and/or with deformed diapirs (high We, Lherm and Deguen, 2018). However, this form of equation (Eq. (11)) is practical to use in models of planetary formation with limited error on the value of R_C, therefore we chose this form to simplify the calculations in Sections 5 and 6.

This parameterization shows that the main parameters controlling the contamination of a liquid silicate reservoir by a siderophile element during the sinking of a metallic droplet are the Reynolds number and the metal-silicate partition coefficients. The higher the $D^{met/sil}$ is, the less the silicate will be contaminated, which reflects the fact that we consider here a siderophile element. The Reynolds number has the same effect as $D^{met/sil}$: the higher Re is, the lower R_C will be. This high absolute value of b reflects the importance of the silicate viscosity, which controls the diapir velocity, as well as the type of flow and the deformation of the diapir. The fact that the parameter b is negative shows that increasing the value of the Reynolds number will decrease R_C. Indeed, decreasing the viscosity increases the Reynolds number (Eq. (6)) as well as the diapir velocity (e.g. Samuel, 2012; Wacheul et al., 2014, and Fig. 5).

4. From a single droplet to the large impact context

In the previous section, we derived a parameterization (Eq. (11)) to estimate the volume fraction of a magma ocean contaminated by a unique 1 cm-radius metallic droplet. In this section we apply this parameterization to large impacts in the context of late accretion.

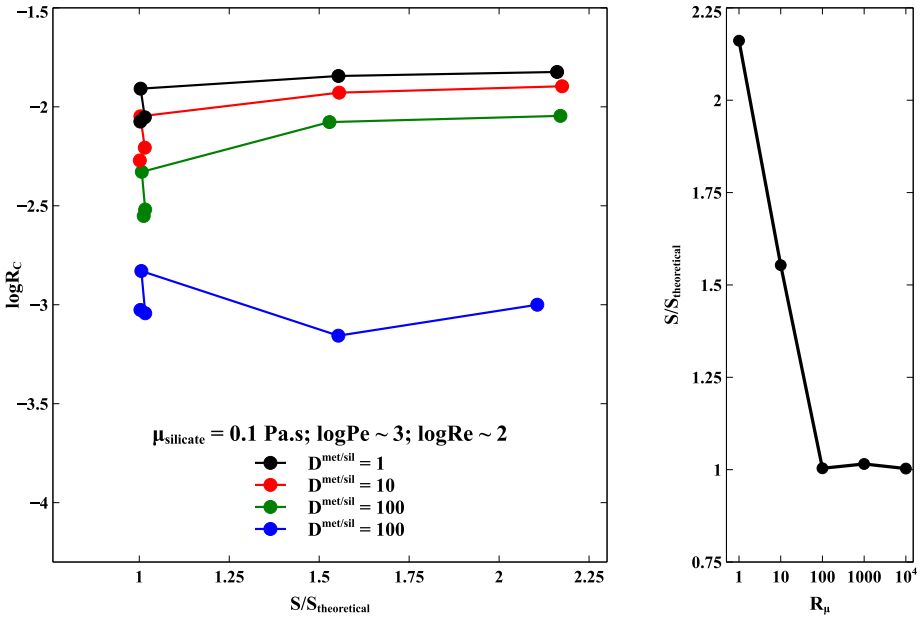

Fig. 13. Evolution of log R_C as a function of the normalized surface (left panel) and evolution of the normalized surface as a function of R_μ (right panel) for models with $\mu_{silicate} = 0.1$ Pa·s for the reference time defined in Fig. 9. The normalized surface of the diapir is the surface of the diapir in the simulation divided by $S_{theoretical} = 4\pi R_{Fe}^2$ (initial surface of the sphere).

Table 2
Values of fitted parameters for Eq. (11) using the least-square methods. The errors associated with the value are given by the 1σ error value. The data used for parameterization are the same as the data presented in Sections 3.3 and 3.4. The comparison between calculated values from Eq. (11) and the values obtained after simulation is presented in Fig. 13.

Parameters	a (*Dmet/sil*)	b (*Re*)	c (R_μ)	d
Values	−0.235	−0.283	0.011	−1.686
1σ	0.02	0.03	0.001	0.07

The parameterization was calculated for a pertinent range of metallic and silicate viscosities. Numerical simulations and laboratory experiments estimated the viscosity of silicate melts at high pressure within the range of 0.01 Pa·s to 1 Pa·s. (Liebske et al., 2005; Karki and Stixrude, 2010; Karki et al., 2018). This range is stable because the viscosity tends to increase with pressure, but decrease with increasing temperature. As for the viscosity of metallic liquid, few experiments have been made, but the experimental results also show that the range of viscosity for liquid iron alloy is stable, at around 0.01–0.1 Pa·s (Kono et al., 2015). Therefore, the effect of viscosity on the equilibrium rate calculated in our simulation can be extrapolated for a high pressure context in an entirely liquid magma ocean. The higher values (10–1000 Pa·s) of μ_{sil} tested in our simulation can also be applied at the end of the magma ocean stage when the silicate liquid is starting to crystallize (but before the mushy stage where the flow dynamics is governed by the viscosity of the solid silicate phase).

A more limiting factor to the extrapolation of our parameterization to planetary formation is the size of our computational domain. However, it is possible under certain conditions, which are listed below.

When a differentiated impactor collides with a growing planet, two fragmentation mechanisms of its metallic core occur. The first fragmentation is induced by the impact itself that stretches and disperses the impactor's core (Kendall and Melosh, 2016). The lunar crater observations showed that the most probable impact angle is $\alpha = 45^\circ$ (Shoemaker, 1962). When considering an impactor with a metallic core radius of R_{core} impacting a magma ocean at an angle $\alpha = 45^\circ$, it is possible to apply our parameterization: the dispersion of the impactor's core material becomes the same as our study computational domain. The mantle fraction affected by the impact (i.e. the volume of mantle into which the metallic droplets are initially spread out) can be approximated by the volume of a cylindrical portion with an angle α, a thickness h and a radius L. The volume of mantle affected is then $V_{affected} = \alpha h L^2/2$. For $R_{imp} = 100$ km, $R_{core} = 50$ km, and $\alpha = \pi/4$, Kendall and Melosh (2016) give $h = 200$ km, $L = 2000$ km: we can then estimate $V_{affected} = 3.14 \times 10^{17}$ m^3. After the first fragmentation induced by the impact, a second rapid fragmentation occurs leading to the formation of much smaller droplets of different sizes. Wacheul et al. (2014) showed that metallic diapirs will fragment into droplets with a mean radius of between 4 mm and 20 mm. Assuming an average droplet radius of 1 cm (Rubie et al., 2003) and that all the impactor's core diapir is fragmented into these cm-radius droplets, an impactor's core with radius $R_{core} = 50$ km will fragment into $\approx 10^{20}$ cm-radius droplets. This yields a concentration of 400 droplets/m^3, or 1 droplet per 2.5 l, which yields a metal/silicate volume ratio of 0.0016 within $V_{affected}$. Currently, no scaling law describes the relation between (L, h, α) and R_{imp} (and as a consequence R_{core}). According to Kendall and Melosh (2016), for $R_{core} = 50$ km, $L \approx 40 R_{core}$ and $h \approx 4 R_{core}$ and by making the assumption that these two relations are also valid for different R_{core} values, we can infer that the ratio of the impactor's core volume over the affected volume is constant for any impactor size.

In the numerical models described in the previous sections, we consider a metallic droplet sinking into a large volume of molten silicates to avoid boundary effects. In our study the ratio between the volume of the iron droplet and the volume of the computational domain is 0.0019, which is relatively close to the volume ratio of 0.0016 expected after an impact.

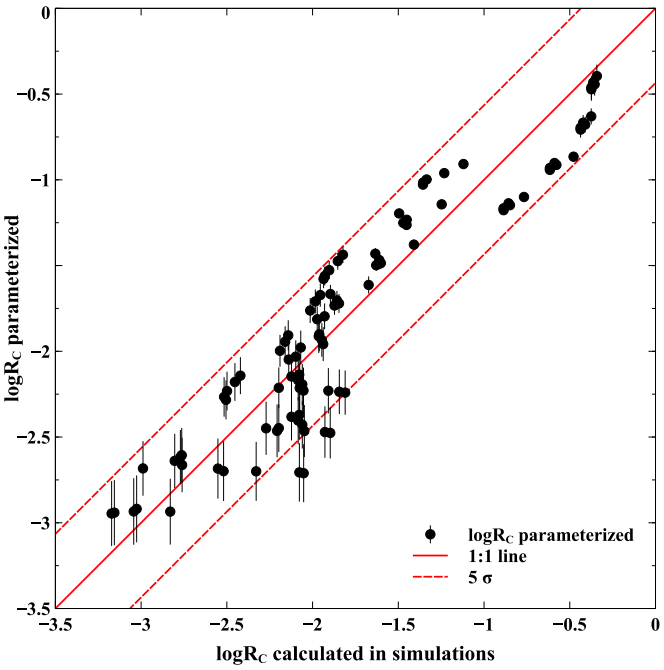

Fig. 14. logRc calculated from the parameterization of Eq. (11) vs logRc obtained from the simulations. The red line is the 1:1 line (perfect fit), and the dashed lines bound the 5σ confidence interval. (For interpretation of the references to color in this figure legend, the reader is referred to the web version of this article.)

After a large impact, the impactor's core is dispersed within a volume $V_{affected} = \alpha h L^2/2$. Assuming the formation of a cloud of cm-radius droplets with an iron fraction $\chi_{Fe} = 0.0016$ within $V_{affected}$, the volume where chemical exchange between the droplets and the magma ocean will occur is:

$$V_{exch} = R_c V_{affected} \tag{12}$$

Using Eq. (11), Table 2 and considering $L = 40 R_{core}$ and $h = 4 R_{core}$ (Kendall and Melosh, 2016), we can calculate the fraction of the volume of the Earth's mantle V_{exch}/V_{mantle} in which chemical exchange is likely to occur. Fig. 15 shows V_{exch}/V_{mantle} as a function of the impactor radius and illustrates the influence of the partition coefficient and the viscosity contrast between the magma ocean and the liquid iron on this ratio.

As the impactor size increases, the mantle volume chemically affected by the impact increases by ${R_{imp}}^3$. This relation is constrained by the simple formula we have used to relate $V_{affected}$ to R_{core}. Given the current knowledge of the impact-induced fragmentation mechanisms of an iron core on a planetary scale, this simplification is a first step toward a global understanding of the chemical equilibration occurring after a large impact. Fig. 15 (left) illustrates that an increase in partition coefficient leads to a decrease in the ratio V_{exch}/V_{mantle} in agreement with Eq. (11) and the values from Table 2. Fig. 15 (left) shows that for $R_{core} = 1000$ km, increasing the partition coefficient by 2 orders of magnitude decreases the value of the ratio V_{exch}/V_{mantle} by a factor of 3. This effect is significant but less important than the influence of the viscosity ratio. Fig. 15 (right) shows that increasing the magma ocean viscosity relative to a constant liquid iron viscosity of 0.1 Pa·s from 0.1 Pa·s to 100 Pa·s leads to an increase in V_{exch}/V_{mantle} by a factor of more than 5. According to Fig. 15, a very large impact such as that which led to the formation of the Moon-Earth system, involving a highly viscous magma ocean, would strongly enhance the chemical equilibration between the impactor's core and the Earth's mantle. This result needs to be nuanced, since a large impact is likely to increase

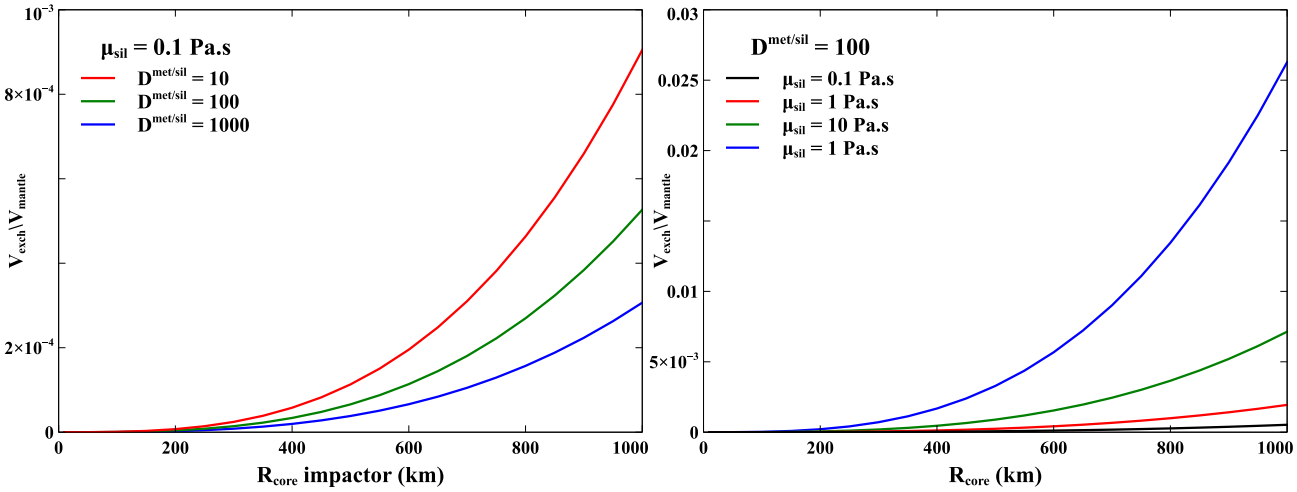

Fig. 15. Mantle fraction chemically contaminated by a moderately siderophile element after metallic core fragmentation as a function of the impactor size. In these figures we compute Eqs. (6), (11) and (12) using $R_{Fe} = 1$ cm, $v_{diapir} = v_{stokes}$ and $\mu_{met} = 0.1$ Pa·s. The left panel shows the influence of the partition coefficient for a fixed viscosity ratio $R_{\mu} = 1$. The right panel shows the influence of the viscosity ratio for a fixed partition coefficient $D^{met/sil} = 100$.

temperature and therefore lower the viscosity of the magma ocean.

5. Signature of a large impact on the mantle composition

This section aims at improving previous accretion models (e.g. Fischer et al., 2015; Siebert et al., 2012; Wood et al., 2008) by accounting for a possible chemical disequilibrium at a given depth. Previous models assumed that at a given step in accretion, equilibrium is reached throughout the entire mantle (Wood et al., 2008; Siebert et al., 2012; Boujibar et al., 2014; Clesi et al., 2016). This equilibrium is set by the final pressure on reaching equilibrium, usually at a depth corresponding to 50% of the core mantle boundary depth (or close to this depth, for instance in Rubie et al., 2015), in order to fit the Ni and Co partitioning behavior (Bouhifd and Jephcoat, 2003, 2011; Fischer et al., 2015).

In this section and the following one, the hypothesis is the same as in previous models of accretion, but with the notable exception that not all of the mantle reaches equilibrium. The amount of mantle equilibrated is defined using Eqs. (11) and (12), i.e. our parameterization is applied directly to a classical model of equilibration in a magma ocean, thus adding one step of complexity to previous models.

5.1. Geochemical elements of interest

To estimate the chemical equilibrium between the impactor's core and the impacted mantle, we focus our calculations on the chemical behavior of moderately siderophile elements such as Ni and Co for which $D^{met/sil}$ is strongly dependent on pressure (Bouhifd and Jephcoat, 2003, 2011; Siebert et al., 2012; Fischer et al., 2015). These two elements are important, since the models of deep magma ocean are designed to explain their relatively high abundances in the BSE (Drake and Righter, 2002). The maximum depth of the magma ocean (around 50% the CMB depth throughout accretion) is derived from the pressure for which the partitioning behavior of Ni and Co yields a 19.05 ± 2 ratio in the BSE (Bouhifd and Jephcoat, 2003, 2011). In the previous sections, we considered a generic, moderately siderophile element with a metal/silicate partition coefficient ranging from 1 to 1000. This range is large enough to extrapolate the trend derived from our simulations to the behavior of Ni and Co at high pressure. For Ni, this partition coefficient ranges between ≈400 for $P = 1$ GPa, and ≈ 20 for $40 < P < 60$ GPa. For *Co*, the partition coefficient ranges between ≈ 100 for P = 1 GPa and ≈ 20, for 40 < P < 60 GPa (Bouhifd and Jephcoat, 2011 and references therein). In the models presented below, we assume that the pressure of equilibrium after an impact corresponds to the last stages of equilibrium in a deep magma ocean, at between 50 and 60 GPa (see Appendix B in Clesi et al., 2016 for the corresponding calculations and the full evolution of pressure, temperature and f_{O2} during the accretion) with values of Ni and Co partition coefficients of between 20 and 80 for the corresponding f_{O2}. In the following section, we consider that the iron content of the mantle is close to the BSE content (8% wt) and is not affected by the impact. The f_{O2} is then considered constant relatively to the iron-wüstite buffer and its value is $\log f_{O2} \approx -2$ ΔIW. In this case, the Ni and Co partition coefficients have converged toward the same value: $D^{met/sil} \approx 20$, which is used in the following calculations.

5.2. Chemical signature of a large impact on the Ni/Co ratio

Here we characterize the effect of a single impactor on the Ni/Co ratio in the mantle. We consider an initially fully accreted Earth. The reference composition of the impacted mantle is set to the BSE composition defined in McDonough and Sun (1995) (Ni/Co = 19.05, 2000 ppm of Ni and 105 ppm of Co in the mantle). We consider that the silicate fraction of the impactor is lost during impact and that only its metallic core is trapped within the impacted mantle. The impactor has a radius of between 10 km and 1000 km and the same composition as the Earth's core (McDonough, 2003). Given the range of impactor size, the mass accreted is negligible compared to the Earth's mass: with a mean density of 9400 $kg.m^{-3}$, a metallic impactor of 1000 km radius adds a total mass of $\sim 3.10^{22}$ kg, which is 0.5% of the Earth's mass. This choice of size and composition for the impactor allows us to focus on the change in mantle concentration, without changing the final core concentration, especially the light element (Si and S) content, in the core. Furthermore, this impactor composition, and its relatively low mass, would not significantly change the oxygen fugacity and thus does not affect the partitioning behavior of Ni and Co.

This section aims at characterizing the partitioning behavior of Ni and Co as a function of the impactor radius and the viscosity contrast R_{μ} computing Eqs. (11) and (12). The first term of Eq. (11) illustrates the influence of the partition coefficients for Ni and Co. These partition coefficients are controlled mainly by pressure and temperature, as well as the composition of the metallic phase, and oxygen fugacity (Bouhifd and Jephcoat, 2003, 2011; Siebert et al., 2012; Fischer et al., 2015). To obtain partitioning behavior independent of oxygen fugacity, we use the exchange partition coefficient K_d, which is the thermodynamical constant of the reaction:

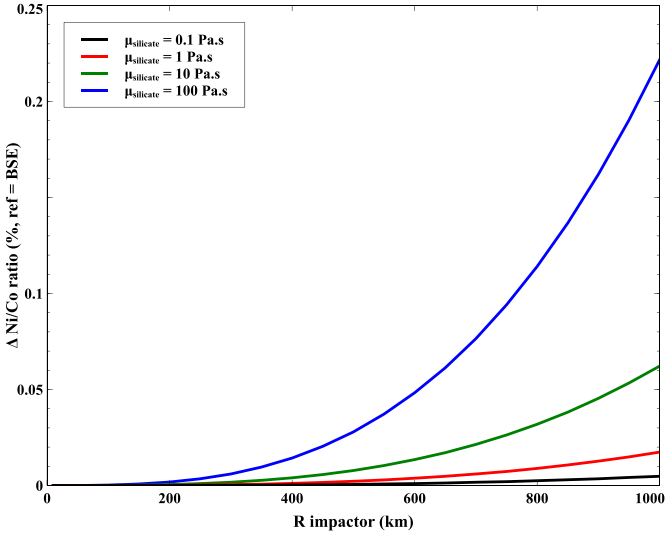

Fig. 16. Evolution of Ni/Co ratio in the mantle after an impact as a function of the impactor size for different silicate viscosities (0.1 to 100 Pa·s). We represent here the variation of the Ni/*Co* ratio after the impact relative to the initial BSE concentration: $\Delta\left(\frac{Ni}{Co}\right) = 100 \times \frac{\left(\frac{Ni}{Co}\right)_{Final} - \left(\frac{Ni}{Co}\right)_{BSE}}{\left(\frac{Ni}{Co}\right)_{BSE}}$. Since the impact happens on the BSE, the more the Ni/Co ratio is different to that of the BSE, the more the impactor has reached equilibrium.

$$MO_{n/2} + \frac{n}{2}Fe \rightarrow \frac{n}{2}FeO + M \tag{13}$$

where M is the element considered (in our case Ni or Co), and n is the valence of the element M (in our case, $n = 2$). In reaction (13), the oxides are in the silicate phase, while the reduced element is in the metallic phase. The exchange partition coefficient is given by $K_d = \frac{c_M}{c_{MO_{n/2}}} \times \left(\frac{c_{FeO}}{c_{Fe}}\right)^{n/2}$ where c_M and c_{Fe} are the molar fractions of M and Fe in the metallic phase, and c_{FeO} and $c_{MOn/2}$ are the molar fractions of FeO and $MO_{n/2}$ in the silicate phase. To estimate the values of the partition coefficients, we use the parameterization of K_d from Clesi et al. (2016), where we ignore the effect of water, as well as the carbon content in the metallic phase. The exchange partition coefficient, K_d, is given by:

$$log\, K_d^{element} = \frac{b_{el}}{T} + c_{el}\frac{P}{T} + e_{el}\, log\,(1 - \chi_{Si}^{metal}) + g_{el}\, log\,(1 - \chi_S^{metal}) + h_{el} \tag{14}$$

The parameters b_{el}, c_{el}, e_{el}, g_{el} and h_{el} are detailed in Clesi et al. (2016), and are different for each element studied. *P* and *T* are the pressure (in GPa) and temperature (in Kelvin) of equilibrium, respectively, corresponding to the pressure at 50% of CMB depth (i.e., 1450 km), and the liquidus temperature associated with it (Andrault et al., 2011). We assume here an equilibrium pressure of 63 GPa, and an equilibrium temperature of 3450 K. χ_{Si}^{metal} and χ_S^{metal} are the mass fractions of silicon and sulfur in the impactor. We assume here that $\chi_{Si}^{metal} = 0.06$ and $\chi_S^{metal} = 0.019$ (McDonough, 2003). K_d is then converted into a Nernst partition coefficient (mass ratio) following:

$$D^{met/sil} = \frac{M_{oxide} \times M_{Fe}}{M_{FeO} \times M_{element}} \times K_d^{element} \times D_{Fe}^{met/sil} \tag{15}$$

where $M_{element}$ is the molar mass of Ni or Co, M_{oxide} is the molar mass of NiO or CoO, and M_{Fe} and M_{FeO} are the molar masses of Fe and FeO respectively. $D_{Fe}^{met/sil}$ is the partition coefficient of iron and equals 13.65 in the BSE model. We consider that the impactor does not significantly change the oxygen fugacity and therefore does not influence the $D_{Fe}^{met/sil}$ value.

The second term in Eq. (11) characterizes the influence of the Reynolds number, which is given by Eq. (6). As stated in Section 4, we consider that the metal fragments into droplets with a radius of 1 cm. The sinking velocity of these droplets is given by Eq. (9). We assume here a silicate density of $\rho_{mantle} = 4500$ kg.m^{-3} (mean density of the Earth's mantle), a metallic density of $\rho_{metal} = 9400$ kg.m^{-3}, which is consistent with iron rich liquid alloys at these pressures (Morard et al., 2013) and the current Earth's value for the acceleration of gravity (i.e., 9.81 m·s^{-2}). The viscosity of the silicate phase in our calculations ranges from 0.1 to 100 Pa·s. The third term in Eq. (11) measures the influence of the viscosity ratio $R_\mu = \mu_{met}/\mu_{sil}$. In our calculations, we consider a constant value for the metallic viscosity (= 0.1 Pa·s), consistent with iron liquid viscosity at high pressure (Kono et al., 2015).

Once the parameter *Rc* is calculated for Ni and Co, the impactor equilibrates with a volume of mantle defined by Eq. (12) in Section 4, considering that $V_{impactor}/V_{affected} = 0.0016$, independent of the size of the impactor. As R_C expresses the volume fraction of the silicate that has reacted with the metal, it may overestimate the volume of the mantle that has equilibrated with the metal phase. Hence the parameter R_C should be considered as a first-order approximation of the volume equilibrated. Therefore, for Eq. (12), the mass of mantle that is equilibrated is obtained by simple multiplication by ρ_{mantle}. In this mass of mantle, the concentration of Ni or *Co* is in equilibrium and is given by $\chi_{eq}^{silicate} = \frac{\chi_{impactor}^{metal}}{D^{met/sil}}$. The final mass fraction of Ni or Co is given by:

$$\chi_{final}^{silicate} = \chi_{initial}^{silicate} + (\chi_{eq}^{silicate} - \chi_{initial}^{silicate})\frac{m_{equilibrated}}{m_{mantle}} \tag{16}$$

where, $\chi_{final}^{silicate}$ is the concentration of Ni or *Co* in the final mantle, $\chi_{initial}^{silicate}$ is the initial concentration of Ni or *Co* in the mantle, $\chi_{eq}^{silicate}$ is the concentration at equilibrium, $m_{equilibrated}$ is the mass that is equilibrated and m_{mantle} is the mass of the Earth's mantle. The final Ni/*Co* ratio is then derived from $\chi_{final}^{silicate}$ for Ni and Co. The results of calculations for different viscosities as a function of the impactor radius are presented in Fig. 16.

Fig. 16 shows that a single impactor, even a large one, does not significantly affect the Ni/Co ratio in the mantle. The maximum variation is 0.25%, and is obtained for a large impactor (1000 km radius) for a relatively high viscosity of the magma ocean (100 Pa·s). For low viscosities (0.1 and 1 Pa·s), a metallic impactor weakly affects the Ni/Co ratio in the mantle (less than 0.1% change for a 1000 km radius impactor). Such a small variation confirms that high spatial resolution models are not necessary even for large Pe_{mesh} values obtained for low viscosities. For a relative error of 100% in the values of R_c, at a viscosity of 0.1 Pa·s, it would only induce a variation in Ni/Co of between 0 and 0.2% within the final model.

Eq. (16) shows that the final concentration is proportional to the volume equilibrated if $\chi_{eq}^{silicate}$ is higher than $\chi_{initial}^{silicate}$. In this case, late accretion of a metallic impactor, which yields a high metallic concentration in Ni and *Co* (similar to the Earth core concentration given in McDonough, 2003); with a high equilibrium pressure, which yields low partition coefficient values for Ni and *Co*, $(\chi_{eq}^{silicate} - \chi_{initial}^{silicate})$ is positive. The impactor is metallic and rich in Ni and Co (5.2%wt and 0.24%wt, respectively), and impacts a silicate mantle with a BSE composition. Therefore, when the mass of mantle equilibrated is higher, the variation in Ni or Co concentration compared to the BSE in the mantle is higher. If the disequilibrium is high, the $m_{equilibrated}$ is low, and therefore there is less variation in the Ni/Co ratio. As shown in Fig. 16, the amount of disequilibrium is higher for a low viscosity magma ocean, as well as for small metallic impactors, and therefore there is no change in the moderately siderophile element concentrations in the mantle under these conditions. This means that, to have a significant effect on the moderately siderophile element concentrations in the BSE, late accretion impactors need to be large and impact a viscous magma ocean in order to increase the degree of equilibrium. Even in this case, if the amount of Ni and Co in the

impactor is not significantly higher than that in the Earth's core, the change in BSE composition will not be significant, as illustrated in Fig. 16.

6. Discussion

6.1. Earth accretion models and magma ocean properties

In the previous section we characterized the effects of a late impact, negligible in mass, composed only of a metallic phase. However, most of the disequilibrium happens during accretion. Therefore, Eq. (16) is not relevant, at least not in this form, in the context of a growing planet. Assuming that the mantle of the impactor and of the growing Earth is well mixed before equilibration with the metallic fraction, we can define the concentration of the post-impact mantle, $\chi_{post-impact}^{silicate}$.By modifying Eq. (16), and knowing the composition of the impactor's metallic phase it is possible to calculate the composition of a growing planetary mantle before it equilibrates with the metallic phase of the impactor. It is given by:

$$\chi_{post-impact}^{silicate} = \frac{m_{mantle}}{m_{mantle} - m_{equilibrated}} \left(\chi_{final}^{silicate} - \frac{m_{equilibrated}}{m_{mantle}} \chi_{equilbrated}^{silicate} \right) \quad (17)$$

Since $m_{equilibrated}$ is dependent on the size of the impactor core and magma ocean viscosity, it is possible to calculate the composition of the mantle for a 90% accreted Earth hit by a Mars-sized impactor (Moon-forming impact) as a function of the impactor's core radius and viscosity of the magma ocean. Fig. 17 shows the corresponding results for comparison with Fig. 16: in this case, the greater the degree of equilibrium, the lower the initial Ni/Co ratio.

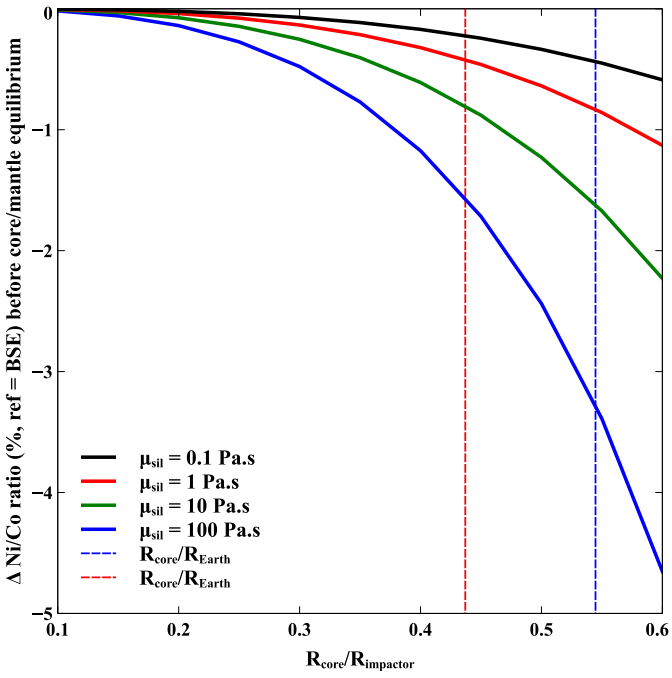

Fig. 17. Ni/Co ratio in the Earth's mantle before equilibration with the core of an impactor corresponding to 10% of the Earth's mass as a function of the radius of the impactor's core normalized to the impactor size and for different magma ocean viscosities. The R_{core}/R_{Earth} current ratio is shown by the blue dashed line, and the R_{core}/R_{Mars} ratio by a red dashed line. In the calculation, the impactor is the same size as Mars ($R_{impactor}$ = 3390 km), and the impactor core radius ranges from 340 km to 2040 km. We represent here the variation in Ni/*Co* ratio before the impact relative to the BSE concentration but for a well-mixed mantle after impact: $\Delta\left(\frac{Ni}{Co}\right) = 100 \times \frac{\left(\frac{Ni}{Co}\right)_{post-impact} - \left(\frac{Ni}{Co}\right)_{BSE}}{\left(\frac{Ni}{Co}\right)_{BSE}}$. (For interpretation of the references to color in this figure legend, the reader is referred to the web version of this article.)

The results displayed in Fig. 17 show that it is possible to reach the same final Ni/Co ratio for the Earth's mantle with drastically different properties of the impactor and the magma ocean. From Fig. 17, two post-impact models can be derived:

- A model with a low $R_{core}/R_{impactor}$ ratio and low magma ocean viscosity, which yields a lower degree of equilibrium between metal and silicate. In this kind of model, the composition of the Earth's mantle is more dependent on the equilibrium conditions between the metallic phase and the silicate phase than on the composition of the impactor. For instance, the models presented in e.g. Burbine and O'Brien (2004), Rai and van Westrenen (2013) or Dauphas et al. (2014) are based on mixing different chondritic compositions where the main parameter fitted is the isotopic consistency, and they are therefore predominantly compositionally-derived models. For these models to be consistent, the impactor's core needs to be small ($R_{core}/R_{impactor} < 0.4$, left-hand side of Fig. 17), and the magma ocean viscosity low ($\mu_{magma\ ocean} \approx 0.1$–1 Pa·s), so as to achieve a low equilibrium rate between metal and silicate.
- A model with a high $R_{core}/R_{impactor}$ ratio, and high viscosity of the magma ocean, which yields greater equilibrium between metal and silicate. In this kind of model, the main changes in Earth mantle composition are due more to the composition of the impactor and less to the chemical reactions between metal and silicate. For instance, the models presented in e.g. Wood et al., 2008, Siebert et al., 2012 and Boujibar et al., 2014 are based on the metal-silicate partitioning behavior, where the discriminating parameter is the relative core/mantle abundances of siderophile elements, and they are therefore predominantly equilibrium-derived models. In this kind of model, a minimal equilibrium needs to be reached, and therefore the impactor's core needs to be large ($R_{core}/R_{impactor} > 0.4$, right-hand side of Fig. 17), and/or the magma ocean viscosity needs to be high ($\mu_{magma\ ocean} \approx$ 10–100 Pa·s).

To summarize, our results cannot constrain the viscosity of the magma ocean (especially given the error in our calculations for low viscosity calculations, see Section 2.4), but for a given model, our results can constrain the range of magma ocean viscosities in order to reach the BSE concentrations for moderately siderophile elements.

However, this work needs to be done for each accretion step or impact, and for each element, which would increase the number of plausible scenarios to accrete the Earth, but could also provide compositional constraints on irreconcilable scenarios, and therefore allow some impactor compositions to be excluded from a given model.

6.2. Effect of Moon formation on the Ni/Co ratio in the Earth's mantle

In the previous section we showed that the properties of the magma ocean are model dependent: they have to be inferred from the impactor properties and the final BSE content chosen as a control of the model output. In this section, we infer the viscosity of a magma ocean for one particular model: the Moon formation by an impact with a Mars-sized impactor (Canup, 2004). The Moon forming impactor (named Theia) is believed to be a large Mars-sized impactor which hit the proto-Earth at the end of accretion with an oblique trajectory (Canup and Asphaug, 2001; Canup, 2004). In a simulation of this kind of impact, most of the metal and silicate of the impactor merges with the Earth (Canup, 2004). If we consider mass of the Moon to be negligible compared to that of Theia, and ignore the loss of particles due to the impact, we can determine that the final 10% mass accreted to the Earth was due to the impact with Theia. The core of this impactor is 30% of the total mass of the impactor (Canup, 2004), with the same mean density as the Earth,

so it is not improbable that the ratio $R_{core}/R_{impactor}$ is comparable to that of the Earth or Mars today (given by the red and blue vertical lines in Fig. 17). In that case, Eq. (17) and Fig. 17 shows that some equilibrium occurred between the magma ocean formed by the impact and the impactor's core sinking into the Earth's core. For every magma ocean viscosity tested here, it is necessary to have interaction between Theia's core and the proto-Earth's mantle to get the final BSE concentration. For a magma ocean viscosity of 0.1 Pa·s, the proto-Earth's Ni/Co ratio is between 0.25% and 0.45% lower than the BSE values for a $R_{core}/R_{impactor}$ comparable to those of Mars and the Earth respectively. For a magma ocean viscosity of 100 Pa·s, the proto-Earth Ni/Co ratio is between 1.45% and 3.00% lower than the BSE values for a $R_{core}/R_{impactor}$ comparable to those of Mars and the Earth, respectively.

This means that the Moon forming impact had a significant effect on the BSE Ni/Co ratio, which can be high if the magma ocean formed after the impact was viscous (100 Pa·s) and the core radius of Theia was around 1850 km.

7. Conclusion

We developed numerical models to characterize the effects of viscosity and partition coefficients on the metal/silicate equilibrium for moderately siderophile elements. We showed that the volume of silicate equilibrated with a small volume of metal is mostly controlled by the partition coefficients and the viscosity of the silicate. The viscosity ratio between metal and silicate is a second order parameter but still has a significant effect.

The scope of this study does not include other elements that have different partitioning behavior (V, Cr, Mn etc.) and future models of equilibrium between metal and silicate will have to integrate these elements to get a clearer view of chemical exchanges within the Early Earth. Furthermore, the range of *Re* and *We* covered in this study does not cover the whole range of *Re* and *We* numbers during the accretion event (Fig. 10). Therefore, in the future, we will need to model more complex flows (such as shown in Samuel, 2012 or Wacheul et al., 2014), to widen the scope of our interpretations (see Section 4 for the extrapolation conditions). Future models should also account for the thermal equilibration during metal/silicate separation (Wacheul and Le Bars, 2018) to characterize the effects of temperature on the partition coefficient values. Other phenomena, while important, are ignored due to being beyond the scope of the study, for instance the effect of the droplet size and shape (Qaddah et al., 2019), or stretch-enhancing diffusion (Lherm and Deguen, 2018), or the possibility of large core-merging events (Landeau et al., 2016). All these phenomena are beyond the scope of this study and should be taken into account in further work and models of accretion.

Nevertheless, we proposed a parameterization of the disequilibrium between a silicate magma ocean and a metallic droplet for moderately siderophile element behavior. Using this parameterization on Ni and Co behavior at the end of accretion, it is possible to define some constraints on the viscosity of the magma ocean. For a given model of accretion to fit the current BSE concentrations, the viscosity of the magma ocean and the impactor composition need to be changed accordingly: large impactors with large metallic cores ($R_{core} > 1100$ km) and high magma ocean viscosity (10–100 Pa·s) favor a high degree of metal/silicate equilibrium; while metal/silicate disequilibrium models can be achieved with moderately small metallic cores ($R_{core} \approx$ 300–1000 km) and low viscosity (0.1–1 Pa·s) magma ocean.

When applying our results to the Moon-forming impact, we showed that the current Ni/Co ratio in the BSE is affected by the Moon's formation, depending on the viscosity of the magma ocean formed after the impact. The Moon's formation can account for 0.25 to 0.45% of the final BSE Ni/Co ratio for a low viscosity (0.1 Pa·s) magma ocean, and for 1.45% to 3% of the final BSE Ni/Co ratio for a high viscosity (100 Pa·s) magma ocean.

CRediT authorship contribution statement

V. Clesi: Conceptualization, Methodology, Investigation, Formal analysis, Data curation, Visualization, Writing - original draft, Writing - review & editing.**J. Monteux:**Conceptualization, Writing - review & editing, Resources, Visualization, Supervision, Funding acquisition.**B. Qaddah:**Methodology, Investigation, Visualization, Writing - review & editing.**M. Le Bars:**Supervision, Validation, Writing - review & editing.**J.-B. Wacheul:**Validation, Writing - review & editing.**M.A. Bouhifd:**Conceptualization, Supervision, Funding acquisition, Writing - review & editing.

Declaration of competing interest

The authors declare that they have no known competing financial interests or personal relationships that could have appeared to influence the work reported in this paper.

Acknowledgments

This research received funding from the French PNP program (INSU-CNRS), the French Government Laboratory of Excellence initiative No. ANR-10-LABX- 0006 and the Région Auvergne. This paper is Laboratory of Excellence ClerVolc contribution No. 421. This project has received funding from the European Research Council (ERC) under the European Union's Horizon 2020 research and innovation programme (grant agreement 681835 FLUDYCO-ERC-2015-CoG). This project has received funding from the European Research Council (ERC) under the European Union's Horizon 2020 research and innovation programme (grant agreement 716429). We thank Renaud Deguen for his fruitful comments.

References

Andrault, D., Bolfan-Casanova, N., Lo Nigro, G., Bouhifd, M.A., Garbarino, G., Mezouar, M., 2011. Solidus and liquidus profiles of chondritic mantle: implication for melting of the Earth across its history. Earth Planet. Sci. Lett. 304 (1–2), 251–259.

Bouhifd, M.A., Jephcoat, A.P., 2003. The effect of pressure on partitioning of Ni and Co between silicate and iron-rich metal liquids: a diamond-anvil cell study. Earth Planet. Sci. Lett. 209 (1–2), 245–255.

Bouhifd, M.A., Jephcoat, A.P., 2011. Convergence of Ni and Co metal-silicate partition coefficients in the deep magma-ocean and coupled silicon-oxygen solubility in iron melts at high pressures. Earth Planet. Sci. Lett. 307 (3–4), 341–348.

Bouhifd, M.A., Clesi, V., Boujibar, A., Bolfan-Casanova, N., Cartier, C., Hammouda, T., Boyet, M., Manthilake, G., Monteux, J., Andrault, D., 2017. Silicate melts during Earth's core formation. Chem. Geol. 461, 128–139.

Boujibar, A., Andrault, D., Bouhifd, M.A., Bolfan-Casanova, N., Devidal, J.-L., Trcera, N., 2014. Metal-silicate partitioning of sulphur, new experimental and thermodynamic constraints on planetary accretion. Earth Planet. Sci. Lett. 391, 42–54.

Burbine, T.H., O'Brien, K.M., 2004. Determining the possible building blocks of the Earth and Mars. Meteorit. Planet. Sci. 39 (5), 667–681.

Canup, R.M., 2004. Simulations of a late lunar-forming impact. Icarus 168 (2), 433–456.

Canup, R.M., 2008. Accretion of the Earth. Philos. Trans. R. Soc. A Math. Phys. Eng. Sci. 366 (1883), 4061–4075.

Canup, R.M., Asphaug, E., 2001. Origin of the Moon in a giant impact near the end of the Earth's formation. Nature 412 (6848), 708.

Cartier, C., Hammouda, T., Boyet, M., Bouhifd, M.A., Devidal, J.-L., 2014. Redox control of the fractionation of niobium and tantalum during planetary accretion and core formation. Nat. Geosci. 7 (8), 573.

Chang, I.D., 1961. On the wall effect correction of the Stokes drag formula for axially symmetric bodies moving inside a cylindrical tube. Z. Angew. Math. Phys. 12 (1), 6–14.

Clesi, V., Bouhifd, M.A., Bolfan-Casanova, N., Manthilake, G., Fabbrizio, A., Andrault, D., 2016. Effect of H2O on metal-silicate partitioning of Ni, Co, V, Cr, Mn and Fe: implications for the oxidation state of the Earth and Mars. Geochim. Cosmochim. Acta 192, 97–121.

Crank, J., 1975. The Mathematics of Diffusion, 2nd ed. Clarendon Press, Oxford viii, 414 p.

Dauphas, N., Chen, J.H., Zhang, J., Papanastassiou, D.A., Davis, A.M., Travaglio, C., 2014. Calcium-48 isotopic anomalies in bulk chondrites and achondrites: evidence for a uniform isotopic reservoir in the inner protoplanetary disk. Earth Planet. Sci. Lett. 407, 96–108.

Deguen, R., Olson, P., Cardin, P., 2011. Experiments on turbulent metal-silicate mixing in a magma ocean. Earth Planet. Sci. Lett. 310 (3–4), 303–313.

Deguen, R., Landeau, M., Olson, P., 2014. Turbulent metal-silicate mixing, fragmentation,

and equilibration in magma oceans. Earth Planet. Sci. Lett. 391, 274–287.
Drake, M.J., Righter, K., 2002. Determining the composition of the Earth. Nature 416 (6876), 39.
Fischer, R.A., Nakajima, Y., Campbell, A.J., Frost, D.J., Harries, D., Langenhorst, F., Miyajima, N., Pollok, K., Rubie, D.C., 2015. High pressure metal-silicate partitioning of Ni, Co, V, Cr, Si, and O. Geochim. Cosmochim. Acta 167, 177–194.
Fleck, J.R., Rains, C.L., Weeraratne, D.S., Nguyen, C.T., Brand, D.M., Klein, S.M., McGehee, J.M., Rincon, J.M., Martinez, C., Olson, P.L., 2018. Iron diapirs entrain silicates to the core and initiate thermochemical plumes. Nat. Commun. 9 (1), 71.
Jacobsen, B., Yin, Q.-Z., Moynier, F., Amelin, Y., Krot, A.N., Nagashima, K., Hutcheon, I.D., Palme, H., 2008. 26Al-26Mg and 207Pb-206Pb systematics of Allende CAIs: Canonical solar initial 26Al/27Al ratio reinstated. Earth Planet. Sci. Lett. 272 (1–2), 353–364.
Jones, J.H., Drake, M.J., 1986. Geochemical constraints on core formation in the Earth. Nature 322 (6076), 221.
Karki, B.B., Stixrude, L.P., 2010. Viscosity of MgSiO3 liquid at Earth's mantle conditions: implications for an early magma ocean. Science 328 (5979), 740–742.
Karki, B.B., Ghosh, D.B., Bajgain, S.K., 2018. Simulation of silicate melts under pressure. In: Magmas Under Pressure, pp. 419–453.
Ke, Y., Solomatov, V.S., 2009. Coupled core-mantle thermal evolution of early Mars. J. Geophys. Eng. Planets 114 (E7).
Kendall, J.D., Melosh, H.J., 2016. Differentiated planetesimal impacts into a terrestrial magma ocean: fate of the iron core. Earth Planet. Sci. Lett. 448, 24–33.
Kleine, T., Rudge, J.F., 2011. Chronometry of meteorites and the formation of the Earth and Moon. Elements 7 (1), 41–46.
Kleine, T., Munker, C., Mezger, K., Palme, H., 2002. Rapid accretion and early core formation on asteroids and the terrestrial planets from Hf-W chronometry. Nature 418 (6901), 952–955.
Kleine, T., Touboul, M., Bourdon, B., Nimmo, F., Mezger, K., Palme, H., Jacobsen, S.B., Yin, Q.-Z., Halliday, A.N., 2009. Hf–W chronology of the accretion and early evolution of asteroids and terrestrial planets. Geochim. Cosmochim. Acta 73 (17), 5150–5188.
Kono, Y., Kenney-Benson, C., Shibazaki, Y., Park, C., Shen, G., Wang, Y., 2015. High-pressure viscosity of liquid Fe and FeS revisited by falling sphere viscometry using ultrafast X-ray imaging. Phys. Earth Planet. Inter. 241, 57–64.
Landeau, M., Olson, P., Deguen, R., Hirsh, B.H., 2016. Core merging and stratification following giant impact. Nat. Geosci. 9 (10), 786.
Lherm, V., Deguen, R., 2018. Small-scale metal/silicate equilibration during core formation: the influence of stretching enhanced diffusion on mixing. J. Geophys. Res. Solid Earth 123 (12), 10,496–10,516.
Liebske, C., Schmickler, B., Terasaki, H., Poe, B.T., Suzuki, A., Funakoshi, K.I., Funakochi, K.i., Ando, R., Rubie, D.C., 2005. Viscosity of peridotite liquid up to 13 GPa: implications for magma ocean viscosities. Earth Planet. Sci. Lett. 240 (3–4), 589–604.
Mann, U., Frost, D.J., Rubie, D.C., 2009. Evidence for high-pressure core-mantle differentiation from the metal–silicate partitioning of lithophile and weakly-siderophile elements. Geochim. Cosmochim. Acta 73 (24), 7360–7386.
McDonough, W.F., 2003. 3.16–Compositional model for the Earth's core. In: Treatise on Geochemistry, pp. 547–568.
McDonough, W.F., Sun, S.-S., 1995. The composition of the Earth. Chem. Geol. 120, 223–253.
Mittal, R.C., Jain, R.K., 2012. Redefined cubic B-splines collocation method for solving convection–diffusion equations. Appl. Math. Model. 36 (11), 5555–5573.
Monteux, J., Ricard, Y., Coltice, N., Dubuffet, F., Ulvrova, M., 2009. A model of metal–silicate separation on growing planets. Earth Planet. Sci. Lett. 287 (3–4), 353–362.
Monteux, J., Amit, H., Choblet, G., Langlais, B., Tobie, G., 2015. Giant impacts, heterogeneous mantle heating and a past hemispheric dynamo on Mars. Phys. Earth Planet. Inter. 240, 114–124.
Morard, G., Siebert, J., Andrault, D., Guignot, N., Garbarino, G., Guyot, F., 2013. F. and D. Antonangeli. The Earth's core composition from high pressure density measurements of liquid iron alloys. Earth Planet. Sci. Lett. 373, 169–178.
Nakajima, M., Stevenson, D.J., 2015. Melting and mixing states of the Earth's mantle after the Moon-forming impact. Earth Planet. Sci. Lett. 427, 286–295.
O'Brien, D.P., Morbidelli, A., Levison, H.F., 2006. Terrestrial planet formation with strong dynamical friction. Icarus 184 (1), 39–58.
Olsson, E., Kreiss, G., 2005. A conservative level set method for two phase flow. J. Comput. Phys. 210 (1), 225–246.
Qaddah, B., Monteux, J., Clesi, V., Bouhifd, M.A., Le Bars, M., 2019. Dynamics and stability of an iron drop falling in a magma ocean. Phys. Earth Planet. Inter. 289, 75–89.
Qaddah, B., Monteux, J., Le Bars, M., April 2020. Thermal Evolution of a Metal Drop Falling in a less Dense, more Viscous Fluid. Physical Review Fluids Accepted manuscript.
Rai, N., van Westrenen, W., 2013. Core-mantle differentiation in Mars. J. Geophys. Eng. Planets 118 (6), 1195–1203.
Ricard, Y., Šrámek, O., Dubuffet, F., 2009. A multi-phase model of runaway core-mantle's segregation in planetary embryos. Earth Planet. Sci. Lett. 284 (1–2), 144–150.
Righter, K., 2011. Prediction of metal-silicate partition coefficients for siderophile elements: an update and assessment of P-T conditions for metal-silicate equilibrium during accretion of the Earth. Earth Planet. Sci. Lett. 304 (1–2), 158–167.
Rubie, D.C., Melosh, H.J., Reid, J.E., Liebske, C., Righter, K., 2003. Mechanisms of metal-silicate equilibration in the terrestrial magma ocean. Earth Planet. Sci. Lett. 205 (3–4), 239–255.
Rubie, D.C., Frost, D.J., Mann, U., Asahara, Y., Nimmo, F., Tsuno, K., Kegler, P., Holzheid, A., Palme, H., 2011. Heterogeneous accretion, composition and core-mantle differentiation of the Earth. Earth Planet. Sci. Lett. 301 (1–2), 31–42.
Rubie, D.C., Jacobson, S.A., Morbidelli, A., O'Brien, D.P., Young, E.D., de Vries, J., Nimmo, F., Palme, H., Frost, D.J., 2015. Accretion and differentiation of the terrestrial planets with implications for the compositions of early-formed Solar System bodies and accretion of water. Icarus 248, 89–108.
Samuel, H., 2012. A re-evaluation of metal diapir breakup and equilibration in terrestrial magma oceans. Earth Planet. Sci. Lett. 313-314, 105–114.
Samuel, H., Tackley, P.J., 2008. Dynamics of core formation and equilibration by negative diapirism. Geochem. Geophys. Geosyst. 9 (6).
Shoemaker, E.M., 1962. Interpretation of lunar craters. In: Physics and Astronomy of the Moon, pp. 283–359.
Siebert, J., Badro, J., Antonangeli, D., Ryerson, F.J., 2012. Metal-silicate partitioning of Ni and Co in a deep magma ocean. Earth Planet. Sci. Lett. 321–322, 189–197.
Šrámek, O., Ricard, Y., Dubuffet, F., 2010. A multiphase model of core formation. Geophys. J. Int. 181 (1), 198–220.
Stevenson, D.J., 1981. Models of the Earth's core. Science 214 (4521), 611–619.
Ulvrová, M., Coltice, N., Ricard, Y., Labrosse, S., Dubuffet, F., Velímský, J., Šrámek, O., 2011. Compositional and thermal equilibration of particles, drops, and diapirs in geophysical flows. Geochem. Geophys. Geosyst. 12 (10).
Wacheul, J.-B., Le Bars, M., 2017. Fall and fragmentation of liquid metal in a viscous fluid. Physical Review Fluids 2 (9), 090507.
Wacheul, J.-B., Le Bars, M., 2018. Experiments on fragmentation and thermo-chemical exchanges during planetary core formation. Phys. Earth Planet. Inter. 276, 134–144.
Wacheul, J.-B.-, Le Bars, M., Monteux, J., Aurnou, J.M., 2014. Laboratory experiments on the breakup of liquid metal diapirs. Earth Planet. Sci. Lett. 403, 236–245.
Wade, J., Wood, B.J., 2005. Core formation and the oxidation state of the Earth. Earth Planet. Sci. Lett. 236 (1–2), 78–95.
Wetherill, G.W., 1985. Occurrence of giant impacts during the growth of the terrestrial planets. Science 228 (4701), 877–879.
Wood, B.J., Walter, M.J., Wade, J., 2006. Accretion of the Earth and segregation of its core. Nature 441 (7095), 825–833.
Wood, B.J., Wade, J., Kilburn, M.R., 2008. Core formation and the oxidation state of the Earth: additional constraints from Nb, V and Cr partitioning. Geochim. Cosmochim. Acta 72 (5), 1415–1426.

Thermal evolution of a metal drop falling in a less dense, more viscous fluid

B. Qaddah,[1,2,*] J. Monteux,[2] and M. Le Bars[1]
[1]*CNRS, Aix Marseille Université, Centrale Marseille, IRPHE, 13013 Marseille, France*
[2]*Université Clermont Auvergne, CNRS, IRD, OPGC, Laboratoire Magmas et Volcans, F-63000 Clermont-Ferrand, France*

(Received 20 December 2019; accepted 16 April 2020; published 15 May 2020)

The initial state of terrestrial planets was partly determined, during accretion, by the fall of metal drops in a liquid magma ocean. Here we perform systematic numerical simulations in two-dimensional cylindrical axisymmetric geometry of these falling dynamics and associated heat exchanges at the scale of one single drop for various initial sizes and ambient viscosities. We explore Reynolds number in the range 0.05–48, viscosity ratios in the range 50–4000, Weber number in the range 0.04–5, and Peclet number in the range 70–850. We show that heat exchange between the two phases occurs predominantly at the front section of the drop. Our systematic, parametric study shows that the thermal boundary layer thickness, the depth and time for equilibration, the Nusselt number, and the magma ocean volume affected by thermal exchanges all scale as power laws of the Peclet number. Because of drop distortions, these scaling laws deviate from the classical balances considering only heat diffusion through a laminar thermal boundary layer. Finally, when considering a temperature-dependent viscosity of the ambient fluid, we show that a low-viscosity layer surrounds the drop, which influences the thermal evolution of nondeformable, low-Reynolds-number drops only and decreases the breakup distance for some limited breakup modes.

DOI: 10.1103/PhysRevFluids.5.053801

I. INTRODUCTION

Core formation of terrestrial planets is a complex process contemporaneous with planetary accretion [1,2]. Its fluid dynamics and thermodynamics have been addressed in numerous studies (e.g., Refs. [3–8]). During the last stages of, e.g., Earth accretion, giant impacts likely occurred between the proto-Earth and up to Mars-sized differentiated bodies [9]. The kinetic energy released during such collisions [10,11], the radioactive heating caused by the disintegration of short-lived radio elements [12], and the heat dissipation resulting from the conversion of potential energy during core formation and core/mantle separation [13], melt part or all of the Earth mantle [11]. Following each impact, the iron core of the impactor thus spread and sank into a deep magma ocean. There, the metal further fragmented into blobs of different sizes, ranging from millimeter drops up to kilometer diapirs before assembling with the Earth protocore ([4,8,14,15]). Thermochemical exchanges occurred between the fragmented metal drops and the liquid magma ocean during their sinking, determining the initial thermal and chemical state of the planet ([4,16–18]). Past studies have provided many scenarios to characterize and quantify the thermochemical exchanges. References [17] and [19] modelled the diffusive equilibration through a laminar thermal boundary layer of, respectively, a cloud of uniform drops and a large diapir of iron. Reference [18] further evaluated the influence of drop deformations in Ref. [17]

*Corresponding author: qaddah@irphe.univ-mrs.fr

scenario. Reference [20] solved the fully coupled dynamical and thermal/chemical equations, but for a fixed spherical geometry only. Reference [4] used experiments where a large volume of immiscible fluid falls into a less dense ambient to show that the smallest scale of turbulence—rather than diffusion through a laminar boundary layer—leads to rapid thermochemical equilibration, even before fragmentation. Reference [7] confirmed this conclusion in their analog model, measuring the global cooling of a large volume of hot Galinstan after its fall through a deep tank of viscous oil. Yet a systematic temporal description of heat exchanges at the scale of one falling, freely evolving drop, is still missing.

Importantly, the magma ocean viscosity highly depends on its evolving temperature and pressure [21]. Therefore, the viscosity ratio between the magma ocean and iron drops can vary by several orders of magnitude as a function of depth, of time after impact, etc. Following and extending an abundant literature in different contexts (e.g., Refs. [22–26]), analog experiments in Refs. [7,8] and numerical simulations at the scale of one metal drop in Ref. [27] showed that the viscosity contrast indeed plays an important role in iron drops shape, velocity, and fragmentation. Reference [27] predicted that thermochemical exchanges should increase with drop deformation and oscillations; but they did not explicitly solve for the fully coupled dynamical and thermal equations. This is the purpose of the present paper. Open questions include the following: How and where do heat exchanges occur? Do the drop deformation/oscillations indeed favor heat exchanges? What are the characteristics time and depth needed to reach equilibration between the two phases? And what is the influence of a temperature-dependent viscosity of the magma?

The paper is organized as follows. Section II introduces the physical and numerical models, with the governing equations, the nondimensional parameters, and the numerical method. Section III presents in detail a reference case, describing its mechanical and thermal behavior, average temperature evolution, heat transfer at the drop interface, and the magma ocean volume heated during the drop sinking. In Sec. IV, we present the main numerical results from our systematic parametric study and derive generic scaling laws for the above detailed parameters. Section V then focuses on changes induced by a temperature-dependent viscosity in the magma ocean. Conclusions and future works are outlined in Sec. VI.

II. PHYSICAL AND NUMERICAL MODELS

A. Governing equations

We consider an initially spherical, liquid metal drop of radius R, falling in an initially motionless, less dense and more viscous surrounding fluid (i.e., a magma ocean) under the action of gravity. The initial temperature of the liquid drop and of the magma ocean strongly depends on the growth history of the protoplanet before the impact and on its initial heating caused by short lived elements [13]. Here we consider that the liquid metal drop is hotter than the magma ocean, with uniform initial temperatures in both phases. Both phases behave as Newtonian, incompressible, and immiscible fluids with uniform surface tension and constant density and viscosity within each fluid at first. In Sec. V, we also consider a temperature-dependent magma ocean viscosity. The dynamical and thermal evolution of the falling drop and ambient liquid is governed by the Navier-Stokes and heat transfer equations, describing

(i) The mass conservation:

$$\boldsymbol{\nabla} \cdot \boldsymbol{u} = 0, \tag{1}$$

with $\boldsymbol{u}$ the fluid velocity vector (m s^{-1}).

(ii) The momentum conservation:

$$\rho\left(\frac{\partial \boldsymbol{u}}{\partial t} + \boldsymbol{u} \cdot \boldsymbol{\nabla}\boldsymbol{u}\right) = \boldsymbol{\nabla} \cdot \left\{ -P\boldsymbol{I} + \mu[\boldsymbol{\nabla}\boldsymbol{u} + (\boldsymbol{\nabla}\boldsymbol{u})^T] \right\} + \rho\boldsymbol{g} + \boldsymbol{F}_{\text{st}}, \tag{2}$$

with ρ the fluid density (kg m^{-3}), μ the fluid dynamic viscosity (Pa s), t the time (s), P the fluid pressure (Pa), $\boldsymbol{g}$ the gravitational acceleration (m s^{-2}), $\boldsymbol{F}_{\rm st}$ the surface tension force (N m^{-3}) and $\boldsymbol{I}$ the identity matrix.

(iii) The heat conservation:

$$\rho C_p\left[\frac{\partial T}{\partial t}+\boldsymbol{u}\cdot\boldsymbol{\nabla}T\right]+\boldsymbol{\nabla}\cdot[-k\boldsymbol{\nabla}T]=0, \tag{3}$$

with C_p the heat capacity at constant pressure (J kg^{-1} K^{-1}), T the fluid temperature (K), and k the fluid thermal conductivity (W m^{-1} K^{-1}). No heat source is considered in our model. In this work, we ignore the effect of viscous heating. Viscous heating during km-scale metal diapir sinking can significantly increase the temperature of the diapir and of the surrounding material depending on the viscosity contrast between the metal and silicate phases [13,28]. When considering the full mantle/core separation within terrestrial planets, viscous heating should be accounted for in the heat budget [29]. In this study we focus on small droplets (millimeters to centimeters in radius) falling over short distances (up to 200 times their radius). Our results (not shown here) confirm that thermal contribution from viscous heating is negligible at such small scales.

To monitor the interface between the falling drop and the magma ocean, we use the level set method, a Eulerian and implicit method frequently used in multiphase flow problems (e.g., Ref. [30]). The level set function ϕ equals to 1 in the metal drop and 0 in the ambient liquid and rapidly changes through the interface, whose position is determined by the isocontour $\phi = 0.5$. The transport and reinitialization of the level set function ϕ are governed by:

$$\frac{\partial\phi}{\partial t}+\boldsymbol{u}\cdot\boldsymbol{\nabla}\phi=\gamma\boldsymbol{\nabla}\cdot\left[\epsilon\boldsymbol{\nabla}\phi-\phi(1-\phi)\frac{\boldsymbol{\nabla}\phi}{|\,\boldsymbol{\nabla}\phi\,|}\right], \tag{4}$$

with γ (m/s) and ϵ (m) the reinitialization parameters. γ determines the reinitialization amount: A suitable value for γ is the maximum velocity magnitude experienced in the model. ϵ determines the layer thickness around the interface and is equal to half the size of the characteristic mesh in the region explored by the interface. The density and dynamical viscosity are evaluated using the level set function:

$$\rho=\rho_m+(\rho_d-\rho_m)\phi, \tag{5}$$

$$\mu=\mu_m+(\mu_d-\mu_m)\phi, \tag{6}$$

where subscripts "m" and "d" denote the magma ocean and the liquid metal drop, respectively. The surface tension force is determined by:

$$\boldsymbol{F}_{\rm st}=\boldsymbol{\nabla}\cdot\boldsymbol{T}=\boldsymbol{\nabla}\cdot\{\sigma[\boldsymbol{I}+(-\boldsymbol{n}\boldsymbol{n}^T)]\delta\}, \tag{7}$$

with σ (N/m) the surface tension coefficient, I the identity matrix, $\boldsymbol{n}$ the interface normal unit vector, and δ the Dirac δ function, nonzero only at the fluid interface. The interface normal unit vector is calculated as

$$\boldsymbol{n}=\frac{\boldsymbol{\nabla}\phi}{|\,\boldsymbol{\nabla}\phi\,|}. \tag{8}$$

The level set parameter ϕ is also used to approximate the δ function by a smooth function [31] defined by

$$\delta=6\,|\,\phi(1-\phi)\,||\,\boldsymbol{\nabla}\phi\,|\,. \tag{9}$$

Note that in this work, we focus on thermal exchanges only and do not calculate the chemical exchanges between the two phases, which are also extremely interesting from a geological point of view (see, e.g., Ref. [32]). Indeed, the main difficulties in solving for chemical exchanges are (i) the small value of the chemical diffusivities and (ii) the presence of a partition coefficient at the

TABLE I. Symbol definitions and values of the physical and nondimensional parameters used in this study.

	Symbol	Value or range
Magma ocean density	ρ_m	3500 kg m^{-3}
Metal drop density	ρ_d	7500 kg m^{-3}
Metal drop viscosity	μ_d	0.005 Pa s
Magma ocean viscosity	μ_m	0.25–20 Pa s
Initial drop radius	R	4–25 mm
Surface tension coefficient	σ	1 N m^{-1}
Magma ocean heat capacity	Cp_m	667 J kg^{-1} K^{-1}
Metal heat capacity	Cp_d	800 J kg^{-1} K^{-1}
Magma ocean conductivity	k_m	10 W m^{-1} K^{-1}
Metal conductivity	k_d	100 W m^{-1} K^{-1}
Viscosity ratio	R_μ	50–4000
Density ratio	R_ρ	2.14
Reynolds number	Re	0.05–48
Weber number	We	0.04–5
Peclet number	Pe	70–850
Nusselt number	Nu	1–6

metal/magma interface, meaning that species concentration at the moving interface is discontinuous [32]. Such challenges are at present beyond the scope of our numerical study. We nevertheless argue that the main conclusions shown here for heat exchanges also give some clues for chemical exchanges and hence should be accounted for in geochemical models of planet building [33].

B. Physical and nondimensional parameters

The main parameters that characterize the dynamical and thermal evolution of a falling drop in a more viscous medium are the viscosity, density, thermal conductivity, heat capacity, and initial temperature of the two fluids; the initial drop size; the gravity; and the surface tension between the two phases. In the geophysical problem of interest (i.e., core formation), the magma ocean viscosity and the metal drop initial radius vary over a wide range of values, while the other parameters are roughly constant (even if rigorously, the thermal conductivity and heat capacity of a magma ocean moderately depend on its composition (e.g., Refs. [34,35]), and the thermal conductivity and heat capacity of metal drops moderately depend on temperature and pressure (e.g., Refs. [36,37]). Hence in this study, we vary these two parameters R and μ_m, in the accessible, relevant ranges 4–25 mm and 0.25–20 Pa s, respectively, while we keep all the other parameters fixed at their representative geophysical values (see Table I).

In our simulations, the drop falls from rest, accelerates until reaching a constant terminal velocity, possibly with small oscillations around it, and exchanges heat with the ambient liquid. We continue our simulations until the drop reaches a stable dynamical regime and its temperature contrast with the ambient reaches less than 20% of its initial value. During the fall, we monitor the average velocity V and the average temperature T of the drop (minus the initial ambient temperature). The dynamical and thermal evolution of each drop is then characterized by the following output dimensionless numbers, where we use the terminal average velocity (note that if it has not yet reached a steady value by the end of the computation, we use estimate from our previous study [27]):

(i) The Reynolds number ($\mathrm{Re} = \frac{\rho_m V R}{\mu_m}$) is the ratio of inertial to viscous forces. Three different regimes are possible: The Stokes regime corresponds to $\mathrm{Re} < 1$ where the viscous effects dominate; the intermediate regime corresponds to $\mathrm{Re} = 1 - 500$ where both viscous and inertial forces are important; and the Newtonian regime corresponds to $\mathrm{Re} > 500$ where the inertial forces are

TABLE II. Dimensional and nondimensional parameters for all performed simulations used in this study. Pe_h is the grid Peclet number (see Sec. II C).

Simulation	R (mm)	μ_m (Pa s)	R_μ	Re	We	Pe	Pe_h	ΔT (K)
no. 1	8	20	4000	0.05	0.04	70	0.43	100
no. 2	8	10	2000	0.2	0.15	137.26	0.84	100
no. 3	8	5	1000	0.76	0.52	254	1.55	100
no. 3a (T-dependent μ_m)	8	5	1000	0.81	0.59	271	1.65	100
no. 3b (T-dependent μ_m)	8	5	1000	0.98	0.85	327	2	1000
no. 4	8	1	200	9.5	3.23	635	3.89	100
no. 5	8	0.5	100	21.8	4.26	728.36	4.46	100
no. 5a (T-dependent μ_m)	8	0.5	100	22.4	4.48	747.6	4.57	100
no. 5b (T-dependent μ_m)	8	0.5	100	23.52	4.94	785	4.8	1000
no. 6	8	0.25	50	47.6	5	793.73	4.86	100
no. 6a (T-dependent μ_m)	8	0.25	50	47.6	5	793.73	4.86	100
no. 6b (T-dependent μ_m)	8	0.25	50	47.6	5	793.73	4.86	1000
no. 7	4	1	200	2.2	0.34	145.67	0.89	100
no. 8	6	1	200	5.67	1.53	378.19	2.32	100
no. 9	10	1	200	12.7	4.61	847.42	5.2	100
no. 10	25	1	200	45	23.2	3008	18.45	100
no. 10a (T-dependent μ_m)	25	1	200	41.13	19.5	2745	16.8	1000

dominant. Here the Reynolds number ranges from 0.05 to 48, and hence our drops are in the Stokes to intermediate regimes.

(ii) The Weber number ($\mathrm{We} = \frac{\rho_m V^2 R}{\sigma}$) compares the inertial and surface tension forces. It governs the deformation, breakup, and terminal shape of a drop (see, e.g., Refs. [27,38]). When $\mathrm{We} < O(1)$, the drop remains spherical without any change of its morphology, while increasing Weber number leads to stronger and stronger deformation, then to fragmentation above a threshold which increases with the viscosity ratio, starting from $\sim$3 for viscosity ratio $\leqslant$1 (see, e.g., Refs. [27,39]). Here the Weber number ranges from 0.04 to 5, considering stable, potentially deformable drops only.

(iii) The Peclet number ($\mathrm{Pe} = \frac{\rho_m C p_m V R}{k_m}$) compares the rate of heat advection to diffusion at the drop scale. Here the Peclet number ranges from 70 to 850, so heat transfer is strongly affected by advection.

(iv) The Nusselt number [$\mathrm{Nu} = \frac{R\overline{\nabla T}.\boldsymbol{n}}{(\overline{T_{\mathrm{int}}} - T_m)}$] compares the measured, averaged heat transfer at the drop interface to a purely conductive case, with $\overline{T_{\mathrm{int}}}$ the mean temperature at the interface and T_m the magma ocean temperature far from the drop. Here the Nusselt number ranges from 1 to 6, hence confirming the important role of advection in heat transfer.

All relevant parameter values are given in Table I.

C. Numerical model

We solve Eqs. (1)–(4) using axisymmetric simulations with COMSOL Multiphysics software, based on the finite-element method. The details of our 17 runs for this study are listed in Table II. Each run represents 2 to 4 weeks' computation time on a biprocessor, eight-core, 3.2- to 3.6-GHz workstation. The axisymmetric geometry assumption is validated in Ref. [40] for a Weber number up to 120. For the dynamics, we use open conditions at the top and bottom boundaries and no-slip conditions at the lateral boundary. For the temperature, we consider no flux conditions at all boundaries. The computational domain must be large enough to allow for convergence without any wall effects. Here we chose an axisymmetric cylinder of size $(r \times z) = (12R \times 200R)$, which is sufficiently large to reach a statistically steady motion (see our previous study [27]) and to follow equilibration up to a 80% decrease of the initial temperature anomaly.

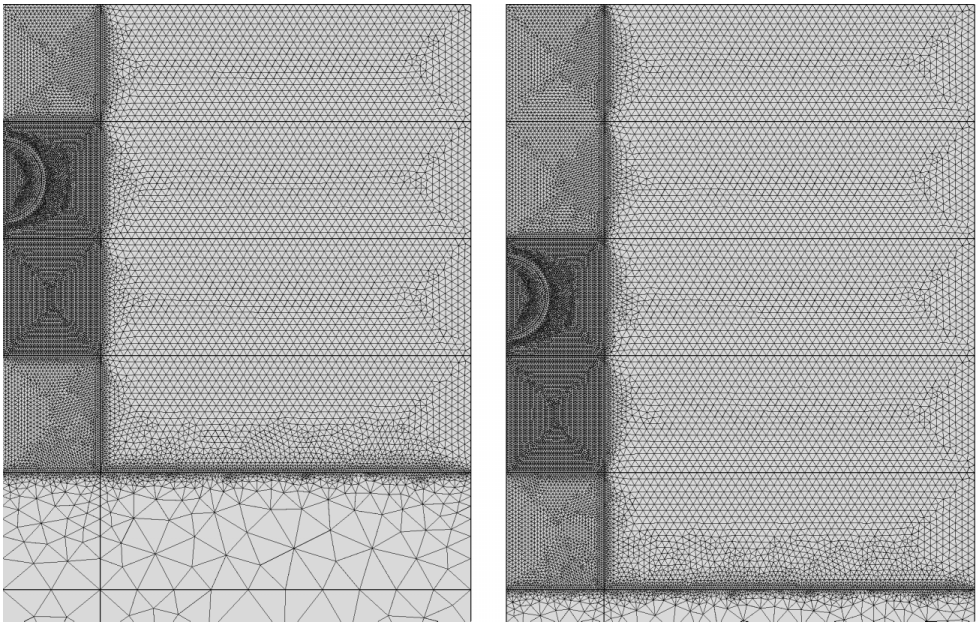

FIG. 1. A zoom illustrating our adaptive mesh (left) and the method for mesh evolution over time when the drop reaches the bottom of the finest mesh region (right).

To capture precisely the dynamical and thermal evolution of the drop, a fine mesh is required. For that, we use an adaptive mesh with a high resolution in the drop vicinity. As shown in Fig. 1, we divide our domain into several regions where the cell sizes vary between $h = 0.015R$ and $h = 1.5R$. As detailed in Ref. [27], the simulation is programed to stop when the drop reaches the bottom of the finest mesh region: The whole mesh pattern is then translated and the simulation is restarted on this new grid [see Fig. 1 (right)].

Mesh convergence has been checked, always using standard Lagrange mesh elements of type P2-P3 (quadratic for the pressure and temperature fields and cubic for the velocity field). In Ref. [27], we showed that a mesh size $h = 0.025R$ (or smaller) allows us to capture the falling drop dynamics. Here we further performed two tests for the resolution of thermal transfers. In the first one, we compare the numerical and analytical heat transfers by thermal diffusion from a motionless spherical drop. The analytical solution for the radial temperature profile from the drop center to a given distance (r) is given by [41]

$$T = 0.5T_0\left[\operatorname{erf}\frac{R+r}{2\sqrt{Dt}} + \operatorname{erf}\frac{R-r}{2\sqrt{Dt}}\right] - \frac{T_0}{r}\sqrt{\frac{Dt}{\pi}}\left[e^{\frac{-(R-r)^2}{4Dt}} - e^{\frac{-(R+r)^2}{4Dt}}\right] \tag{10}$$

with T the temperature anomaly (T_0 its initial value) and D the thermal diffusivity ($m^2\ s^{-1}$). Figure 2 (left) shows the excellent agreement of our numerical results.

For the second test, we calculated, for different minimum grid sizes $h = 0.05R$, $0.035R$, $0.025R$, $0.015R$, $0.01R$, the normalized average drop temperature as a function of normalized time for our reference case no. 4 in Table II (see details in next section). Figure 2 (right) shows a reasonable convergence of the numerical results from $h = 0.015R$, with a relative maximum error $\simeq 3.5\%$, while the drop mass during the course of this simulation does not change by more than 0.4% from its initial mass. Therefore, we confirm that our mesh $h = 0.015R$ captures correctly the thermal evolution of the metal drop.

Finally, the grid Peclet number $\mathrm{Pe}_h = \frac{Vh}{D_{\mathrm{int}}}$, with $D_{\mathrm{int}} = \frac{D_d + D_m}{2}$ the mean thermal diffusivity, is an appropriate parameter in the convection-diffusion equation to determine whether the heat transfer in the system corresponds to numerical artifacts or not. Reference [42] found very accurate solutions for grid Peclet number up to 10. As shown in Table II, our runs in this study remain below this

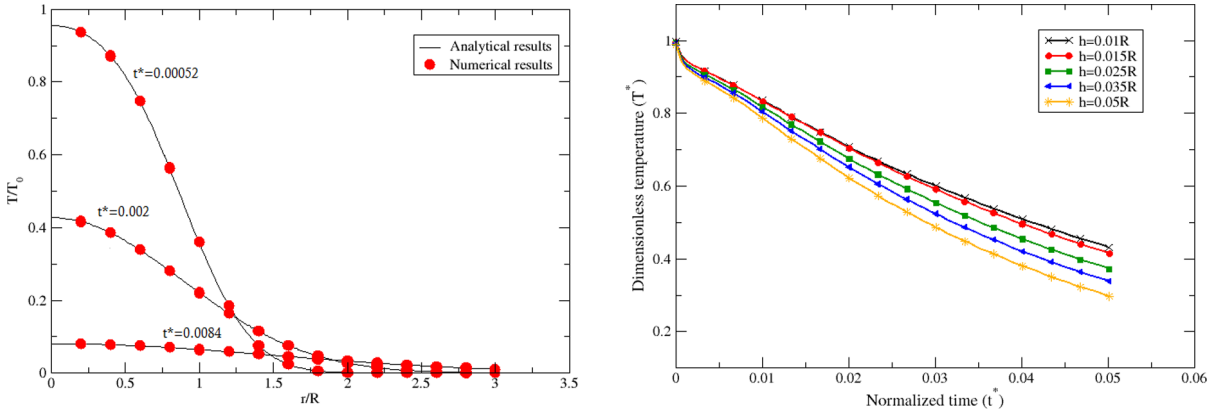

FIG. 2. Left: Comparison of our numerical results with the analytical results in Ref. [41] for the radial profile of the normalized temperature anomaly for a nondeformable and immobile drop. Right: Comparison of the time evolution of the normalized mean temperature anomaly determined with different mesh sizes for a deformable and mobile drop (simulation no. 4 in Table II).

criterion for stability, except for run no. 10, which we hence do not consider for heat transfer studies in the following sections.

III. REFERENCE CASE

In this section, we present our reference case, from which, in the next section, we then change the drop size keeping the viscosity ratio constant, and the magma ocean viscosity keeping the drop size constant. This reference case corresponds to simulation no. 4 in Table II: The drop initial radius is 8 mm, the magma ocean viscosity is 1 Pa s, the metal viscosity is 0.005 Pa s (viscosity contrast 200), and the initial temperature difference between the metal drop and the magma ocean is 100 K.

The drop motion from rest and its thermal evolution are shown in Fig. 3. The spherical drop accelerates due to gravity and rapidly deforms into a spherical cap. Then, surface tension equilibrates inertia at the drop interface and prevents any further change in morphology. Higher temperatures are concentrated at the front of the drop, while the thermal wake behind the drop expands as a function of time. To characterize this dynamics, we define and compute the following quantities.

A. Average drop velocity

During its fall, the drop mean velocity varies with time depending on the drop morphology. In our simulations, we compute it as:

$$V(t) = \frac{\int_v U(r,z,t)[\phi(r,z,t) \geqslant 0.5]dv}{\int_v [\phi(r,z,t) \geqslant 0.5]dv}, \tag{11}$$

with $U(r,z,t)$ the local velocity magnitude (m/s), $dv = 2\pi r dr dz$ accounting for axisymmetric cylindrical geometry, and $[\phi(r,z,t) \geqslant 0.5]$ the Boolean operator allowing to only capture the iron drop volume. Note that we use the mean magnitude velocity of the drop, which is actually very close to its average falling velocity (change of less than 3% in our reference case) because vertical motions largely predominate. We normalize $V(t)$ by the free fall Newton velocity $U_N = \sqrt{\frac{\Delta\rho g R}{\rho_m}}$ and time by the diffusion time $t_{\rm dif} = \frac{R^2 \rho_m C p_m}{k_m}$. Figure 4 shows the result for our reference case. The drop rapidly accelerates from rest up to $t^* = 0.02$, then several small oscillations occur before converging toward its asymptotic terminal fall velocity, which we use to compute the output dimensionless numbers.

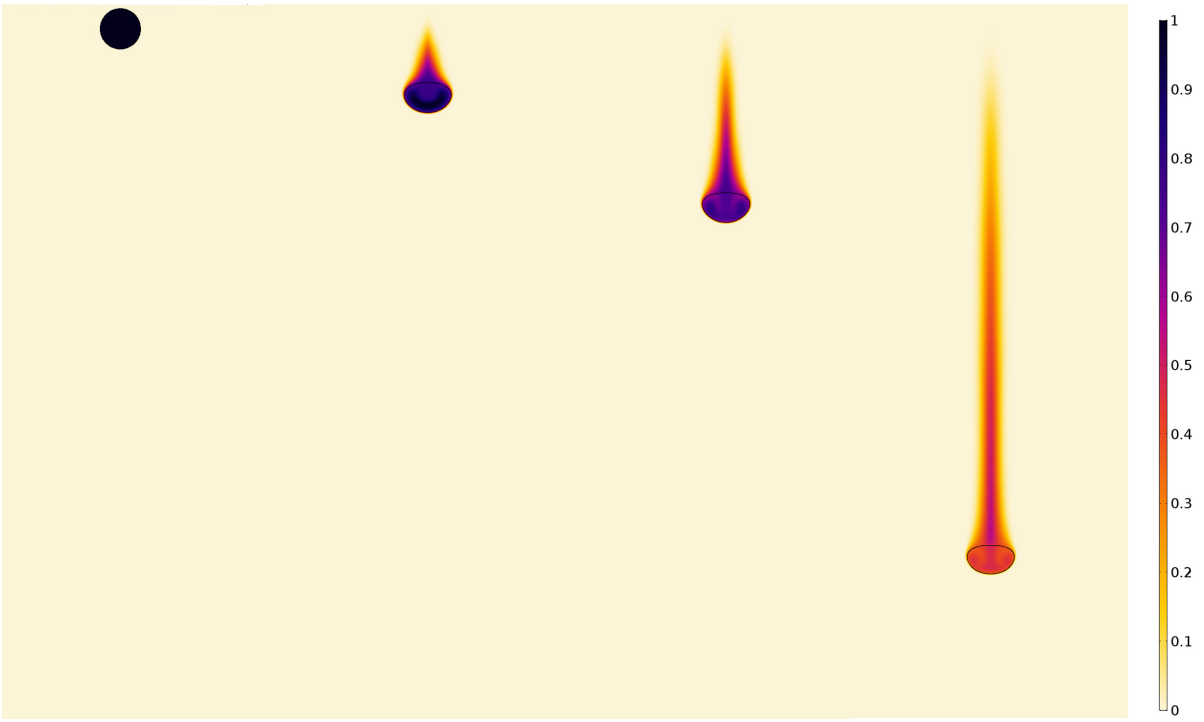

FIG. 3. Dynamical and thermal evolutions of the metal drop as a function of time for simulation no. 4 in Table II. The color presents the temperature anomaly normalized by its initial value T^*. The black solid line separates the metallic material from the magma ocean. From left to right, the time normalized by the thermal diffusion time is $t^* = 0$, 0.01, 0.02, and 0.05.

B. Average temperature evolution of the metal drop

As shown in Fig. 3, the liquid drop exchanges heat with the liquid magma ocean and loses its heat as a function of time and depth. We determine the mean average temperature anomaly of the drop compared to the magma ocean as:

$$T(t) = \frac{\int_v T(r,z,t)[\phi \geqslant 0.5]dv}{\int_v [\phi \geqslant 0.5]dv}. \tag{12}$$

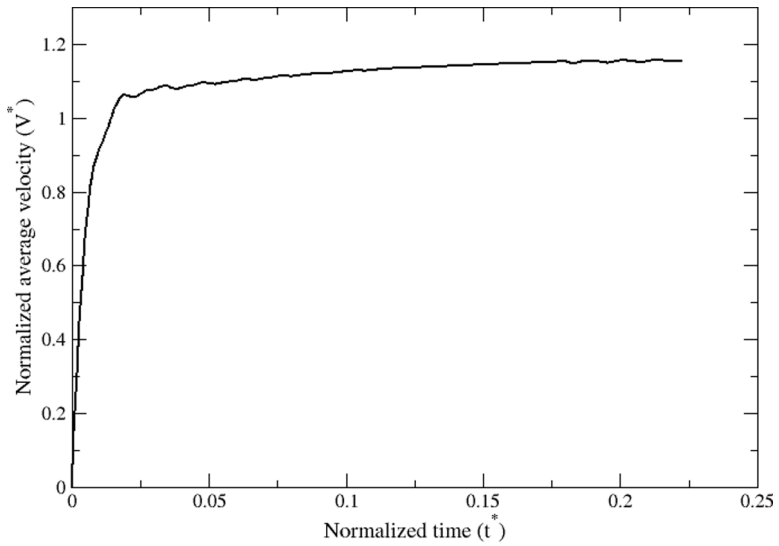

FIG. 4. Normalized average velocity of the metal drop as a function of normalized time for simulation no. 4 in Table II.

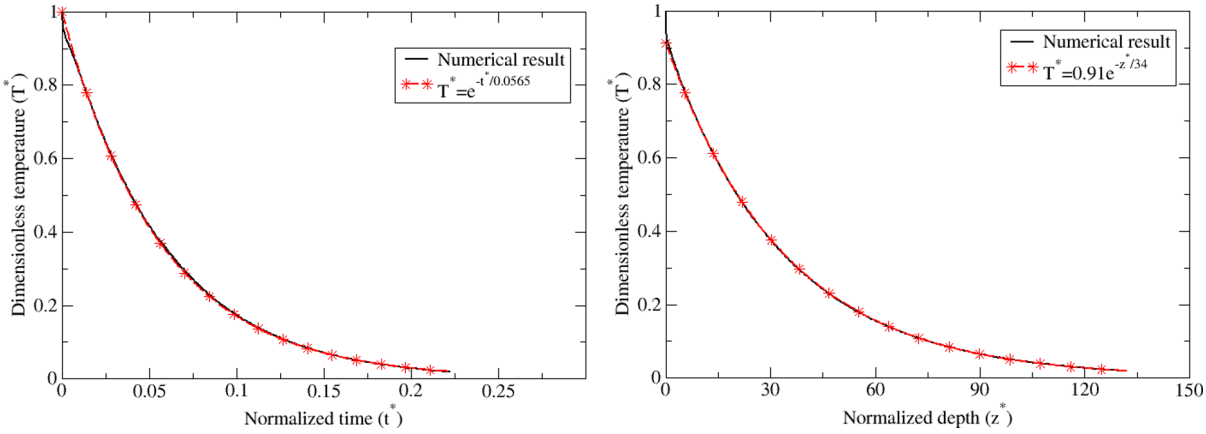

FIG. 5. Normalized average temperature anomaly of the metal drop as a function of normalized time (left) and depth (right) for simulation no. 4 in Table II. The black lines represent our numerical results and the red dashed lines with stars represent the exponential fits from Eq. (13). The correlation coefficient for the two fits is 0.9999.

We normalize $T(t)$ by its initial value, giving $T^*(t)$. Its evolution for the reference case as a function of time or as a function of depth of its center of mass (normalized by the initial radius R) is shown in Fig. 5. After a rapid adjustment of the initial temperature jump at the interface, T^* decreases exponentially toward equilibrium. We determine the best exponential fits according to

$$T^* = e^{(-t/t_c)} \quad \text{and} \quad T^* = C_z e^{(-z/l_c)}, \tag{13}$$

where C_z is a constant (see Fig. 5 in red with stars). In geophysical science, the characteristic time (t_c) and length (l_c) for equilibration are very important parameters [7], used to set the degree of equilibration between iron and silicate of magma ocean in planet building models [33]. Note that chemical equilibrium is more difficult to reach than thermal equilibrium because of the lower value of the chemical diffusivity. The chemical equilibration between the metallic phase and the magma ocean is a key process and constraints on this dynamics contribute to our understanding of the core formation in terms of timing. However, it is also a process that is complicated to compute because of the presence of a partition coefficient at the interface. The results shown below for thermal equilibrium may be considered as first-order trends for chemical equilibrium that will nevertheless deserve a dedicated study.

C. Volume of heated magma during the drop sinking

The magma ocean temperature increases during the fall of the drop, especially in its wake. It is important in geophysics to quantify how much of the magma is contaminated (here, thermally affected) by the formation of the iron core: This would for instance affect the initial structure and heat budget of the Earth's mantle. In our simulations, we calculate the volume of magma ocean affected by thermal exchange as:

$$\mathrm{Vo} = \int_v [T > T_C][\phi \leqslant 0.5] dv, \tag{14}$$

with T_C a chosen temperature anomaly (K) and $[\phi \leqslant 0.5]$ the Boolean operator allowing to only capture the magma ocean volume. An example of the captured volume of heated magma ocean is shown in Figure 6 (left). We performed tests with several T_C corresponding to 0.1, 1, and 10 K. Results of the volume normalized by the initial drop volume as a function of the drop depth are shown in Figure 6 (right). The three curves corresponding to different equilibrium degrees are parallel, until a depth equals to $50R$ where $T_C = 10\,\mathrm{K}$ is strongly affected by thermal diffusion in the magma ocean. The same behavior would of course take place at longer time/depth for the

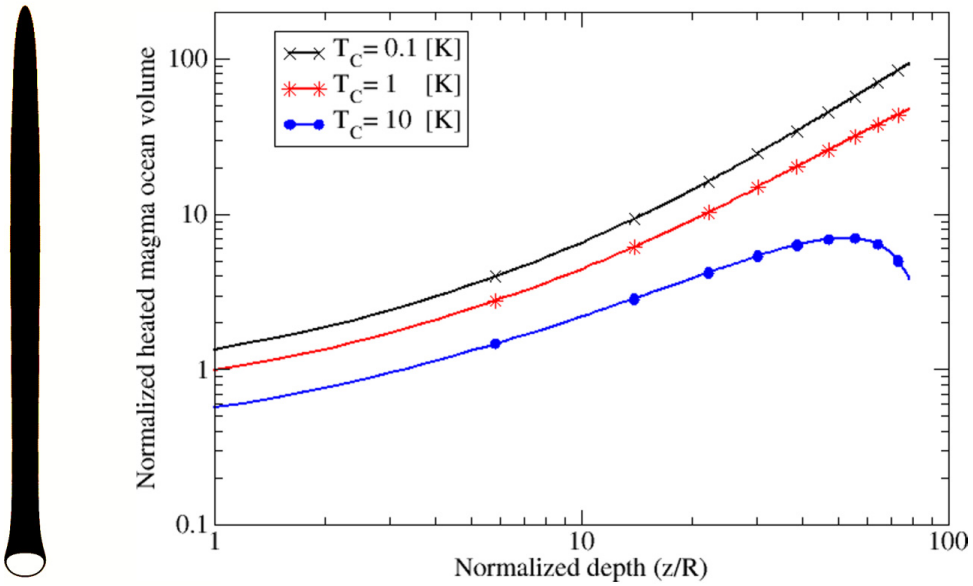

FIG. 6. Left: Volume of heated magma ocean ($T_C = 1$ K) once the drop reaches a time $t^* = 0.067$ and a depth $z = 37R$ in our simulation no. 4 in Table II. Right: Normalized heated magma volume as a function of normalized depth for different values of T_C.

other T_C. But our purpose here is to look at the relative initial behavior before the diffusion effect dominates, depending on the drop radius and magma viscosity. In the following, for our parametric study, we thus compare heated volumes considering $T_C = 1$ K at three different depths: $10R$, $20R$, and $30R$.

D. Heat transfer at the drop interface

To evaluate the Nusselt number, we compute the mean temperature anomaly and the mean temperature gradient at the interface, using, respectively,

$$\overline{T_{\text{int}}} = \frac{\int_v T\phi(1-\phi)dv}{\int_v \phi(1-\phi)dv}, \tag{15}$$

$$\overline{\nabla T_{\text{int}}} = \frac{\int_v \nabla T\phi(1-\phi)dv}{\int_v \phi(1-\phi)dv}, \tag{16}$$

where $\phi(1-\phi)$ allows us to capture only the interface region between the two phases. Figure 7 shows the temperature gradient in and around the drop at a given time for our reference simulation. Most heat transfer between the metal drop and the magma ocean occurs at the drop front side, while the back half only accounts for about 15% of the total. The existence of a hot thermal wake and the external recirculation behind the drop that encapsulates and entrains magma with the sinking drop are the main reasons limiting back thermal exchanges [27,43].

A close view of the temperature field and of the thermal boundary layer is shown in Fig. 8. We define the thermal boundary layer thickness as the distance from the drop interface to a point where the temperature anomaly reaches 1% of its interfacial value. The boundary layer is very thin at the drop front section, where most thermal exchanges are carried out. It significantly increases behind the drop. An example of thickness measurement is shown in Fig. 8 (right) at the thinnest position, i.e., at the front of the drop. In order to give a global estimate around the drop, we also define the average boundary layer thickness as

$$\delta_{T_{\text{av}}} = \frac{\overline{T_{\text{int}}}}{\overline{\nabla T_{\text{int}}}}. \tag{17}$$

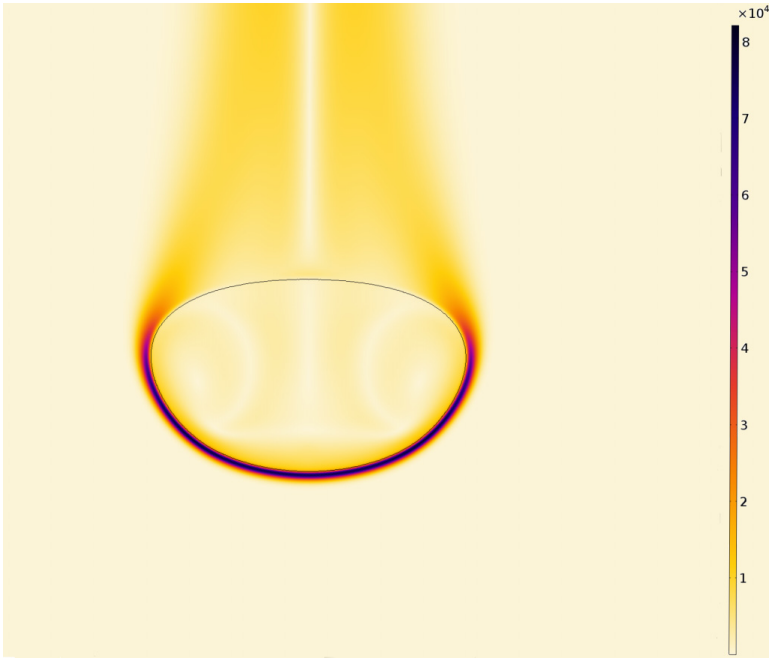

FIG. 7. Temperature gradient (K/m) in and around the drop for our reference simulation no. 4 in Table II at time $t^* = 0.055$.

IV. PARAMETRIC STUDY AND SCALING ANALYSIS

We now present our systematic exploration of the parameter space, changing the magma ocean viscosity or the drop initial radius as shown in Table II, from our reference simulation no. 4. We then analyze our results in terms of scaling laws. In particular we determine the influence of the Peclet number on the dimensionless parameters defined in the previous section: the time and length of equilibration, the normalized thermal boundary layer thickness, the Nusselt number, and the dimensionless magma ocean volume affected by thermal exchanges.

A. Time and length of equilibration

As expected from previous studies of drop dynamics, but largely neglected in geophysical applications (see, e.g., discussions in Refs. [8,27]), the characteristic time and length of equilibrium depend on the viscosity contrast between the metal drop and the magma ocean. As presented in Fig. 9, increasing the viscosity ratio increases the required time for thermal equilibration (Fig. 9,

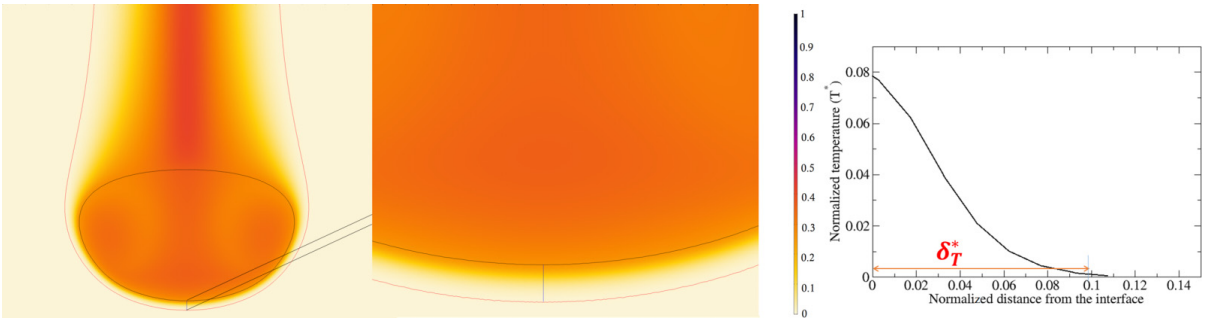

FIG. 8. Left: Temperature anomaly (color scale) and contour of the thermal boundary layer (red line) around the drop (black line) for our reference simulation no. 4 in Table II at time $t^* = 0.067$. Middle: zoom at the drop front. Right: Temperature profile of the thermal boundary layer in front of the drop and determination of the local boundary layer thickness.

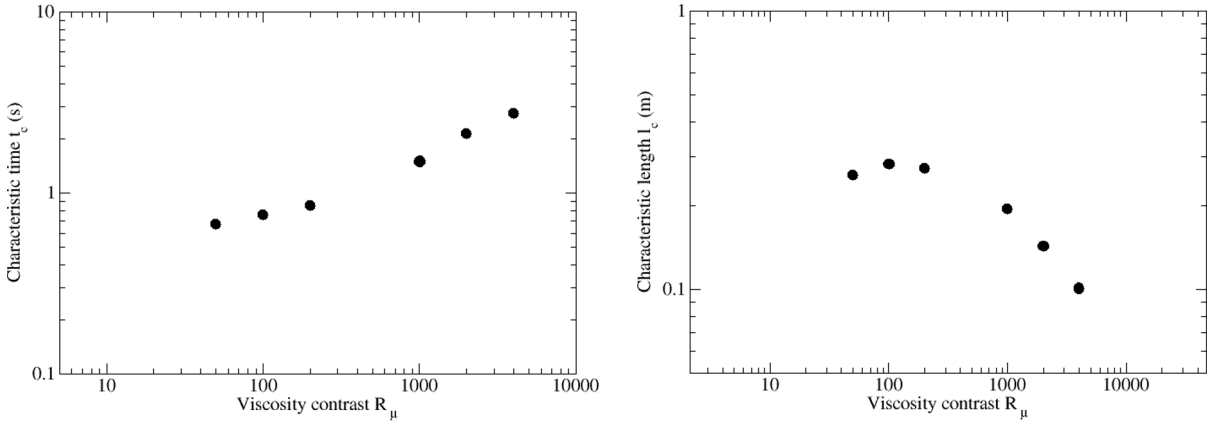

FIG. 9. Characteristic time (left) and length (right) of equilibration as a function of the viscosity contrast [see Eq. (13)].

left), mostly because a larger ambient viscosity limits advective heat exchanges. We can further observe in Fig. 9 (left) two different slopes corresponding to two different dynamical regimes of the drop: For $R_\mu > 1000$, the drop remains spherical and the equilibration characteristic time is highly dependent on the viscosity ratio, while for $R_\mu < 200$, the drop deforms which limits the influence of R_μ. The evolution of the equilibration length is nonmonotonic (Fig. 9, right), because the magma ocean viscosity also influences the falling velocity. Globally, with a more viscous ambient fluid, the thermal equilibrium between the two phases occurs less deeply in the magma ocean once the stable drop is formed, as we predicted in our previous work [27].

The drop size at a given viscosity ratio also influences the thermochemical equilibration (for a fixed spherical shape, see Ref. [20]). Increasing the initial radius of the liquid metal drop decreases the surface of exchange over volume initial ratio and increases the drop falling velocity: We thus expect an increase of both the characteristic time and length, as confirmed in Fig. 10. In Ref. [27], we predicted that increasing the drop initial radius also leads to surface extension due to drop distortion, hence to faster equilibration compared to a purely spherical drop: This effect is, however, limited, because drop deformation mostly occurs at the back of the drop, while heat exchange takes place mostly at the front.

Those two series of results can be rationalized by considering dimensionless properties as a function of the Peclet number. Here we normalize the equilibrium time by the thermal diffusion time and the equilibrium length by the initial drop radius. Results are shown in Fig. 11. The thermal equilibrium time for a high Peclet, spherical drop theoretically scales as $\mathrm{Pe}^{-0.5}$ (see, e.g., Ref. [32]).

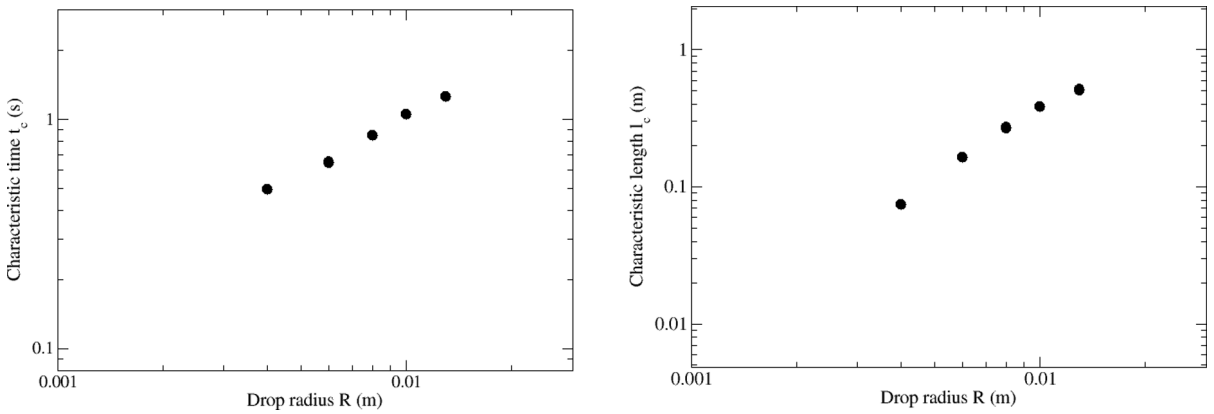

FIG. 10. Characteristic time (left) and length (right) of equilibration as a function of the drop initial radius [see Eq. (13)].

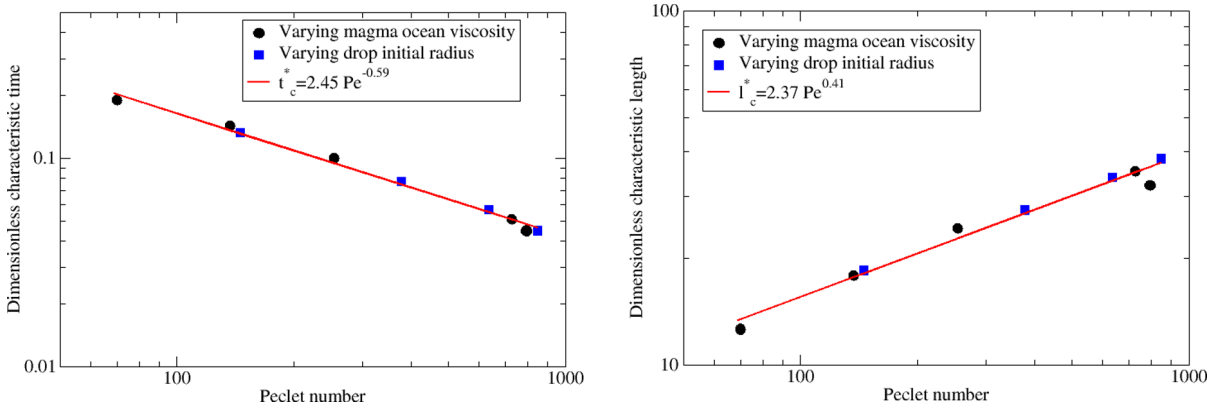

FIG. 11. Dimensionless equilibrium time (left) and length (right) as a function of the Peclet number.

Here we find

$$t_c^* = 2.45\mathrm{Pe}^{-0.59\pm0.01}, \tag{18}$$

where the shown uncertainty in the exponent comes from considering separately numerical simulations performed while changing the viscosity ratio and those performed while changing the initial sphere radius. This acceleration of the equilibration compared to the theoretical model may be a signature of the drop deformation at large Peclet. Indeed, performing the same fit only on the subset of data points where the drop remains spherical gives an exponent 0.51 ± 0.01.

Correspondingly, the length needed to reach the equilibration increases monotonically with Peclet number following

$$l_c^* = 2.37\mathrm{Pe}^{0.41\pm0.01}, \tag{19}$$

in agreement with a quasiconstant falling velocity, i.e., $l_c = V \times t_c$. In conclusion, when the flow advection measured by the Peclet number increases, thermal equilibration occurs faster but deeper in the magma ocean (after drop formation), which is of importance for Earth's building models [33].

B. Heat exchanges

Simply equilibrating large-scale heat advection along the drop surface with heat diffusion through the thermal boundary layer perpendicular to it, the theoretical size of the thermal boundary layer normalized by the drop radius classically scales as $\mathrm{Pe}^{-0.5}$: This was verified numerically in Ref. [20] for a rigid falling sphere. As shown in Fig. 12 (left), we also recover this scaling at the drop front, where most heat exchange occurs: The best fit gives

$$\delta_T^* = 2.53\mathrm{Pe}^{-0.5\pm0.01}. \tag{20}$$

With the deformable drops considered here, however, the boundary layer thickness strongly varies around the metal drop: We thus compute a characteristic average value $\delta_{T_{\mathrm{av}}}$ from Eq. (17), normalized by the initial radius. Results are shown in Fig. 12 (right), with the best-fit scaling law

$$\delta_{T_{\mathrm{av}}}^* = 10.7\mathrm{Pe}^{-0.6\pm0.01}. \tag{21}$$

Over the explored range, the average thickness is at least three times larger than the front one. The larger-than-expected 0.6 exponent might again be a signature of drop distortion at large Peclet number.

Then, by definition, the Nusselt number averaged over the drop surface should scale as $1/\delta_{T_{\mathrm{av}}}^*$. This is indeed recovered, as shown in Fig. 13 with the best-fit scaling law

$$\mathrm{Nu} = 0.08\mathrm{Pe}^{0.63\pm0.02}. \tag{22}$$

Note that Nu varies over time in many cases in this study: We consider here its time-averaged value.

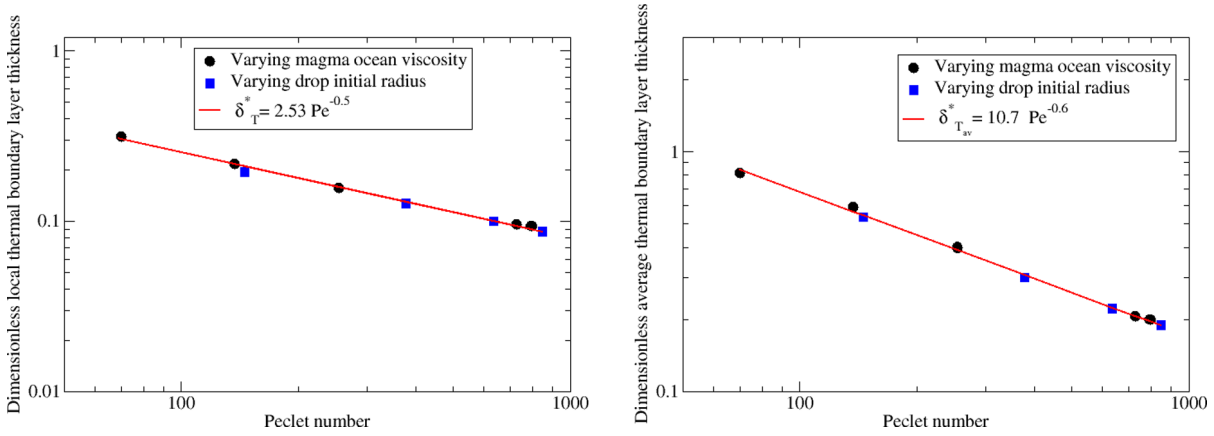

FIG. 12. Dimensionless thickness of the thermal boundary layer at the drop front as a function of Peclet number (left). Dimensionless average thickness of the thermal boundary layer around the drop as a function of Peclet number (right).

Comparing this result with the one obtained in the previous section, we also recover that the typical dimensionless time for equilibration t_c^* scales like $1/\mathrm{Nu}$, as expected. This proves the self-consistency of our measurements.

C. Volume of heated magma ocean

In the wake of the drop, the magma ocean is thermally affected by its passage. Because of heat diffusion within the magma ocean, the affected volume widens with time. But on the short times, at a given depth of the drop z, it can be estimated by simply balancing the heat that has passed through the drop interface with the heat accumulated in this volume of magma ocean, whose temperature has increased by a given amount larger or equal to T_C. We then predict

$$\mathrm{Vo}^* = \frac{\text{Volume of heated magma}}{\text{Initial drop volume}} \sim 3\frac{\mathrm{Nu}}{\mathrm{Pe}}\frac{z}{R}\frac{\Delta T_0}{T_C}, \tag{23}$$

with ΔT_0 the initial temperature difference between the two phases. Results in Fig. 14 show a good agreement with a small relative error for various depths $z = 10R$, $20R$, $30R$ and temperature

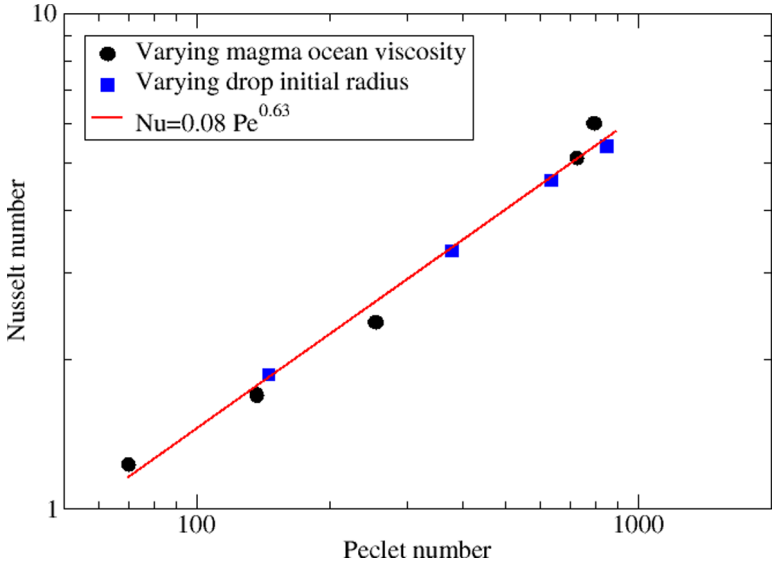

FIG. 13. Nusselt number as a function of Peclet number

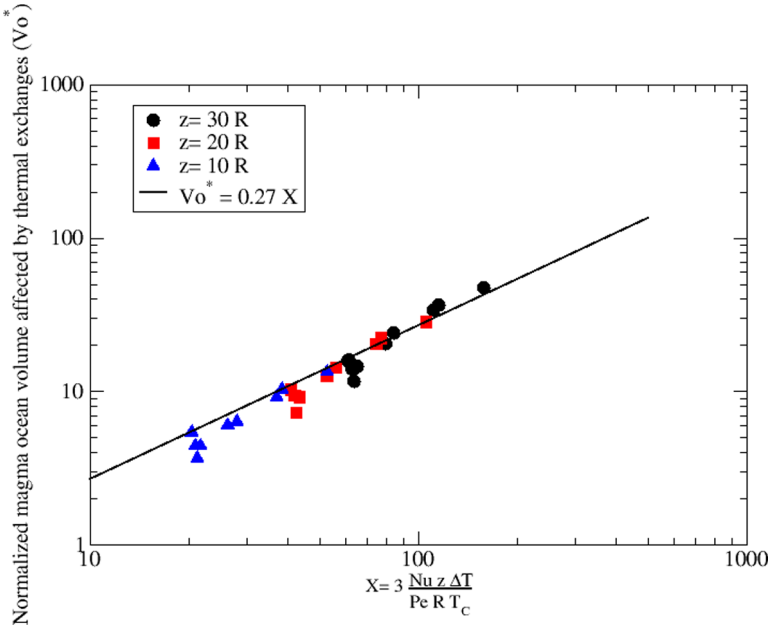

FIG. 14. Dimensionless heated magma ocean volume as a function of X, and comparison with our scaling law (23). Our numerical results are represented with different symbols for different given depths.

contrast $T_C = 1K$, using the previously determined scaling for Nu. This volume can be compared to the volume crossed by the falling drop, which writes in its dimensionless form

$$V^*_{\text{crossed}} = \frac{\pi R^2 z}{4/3\pi R^3} = \frac{3z}{4R}, \tag{24}$$

which also scales linearly with depth. Our result does not exhibit any strong increase of the volume effectively contaminated vs. this simple geometrical estimate: this is because, even in our most turbulent cases, the falling drop encapsulates in its wake a small volume of silicate and entrains it toward the deep, while the rest of the ambient fluid remains largely motionlesss or laminar. No additional mixing is generated. Our conclusion should nevertheless be re-evaluated in the presence of global magma motions, coming, e.g., from turbulent convection, depending on the typical excited time- and length scales. But this is beyond the scope of the present paper. Our conclusion should also be re-evaluated while considering large-scale viscous heating which, for a turbulent wake of a large diapir or a large cloud of drops, might generate strong additional heating long after the iron fall.

V. INFLUENCE OF A TEMPERATURE-DEPENDENT VISCOSITY

The magma ocean viscosity increases from the surface to the base of the magma ocean because of the combined effects of temperature and pressure [21]. Those large-scale variations are irrelevant in the context of our local study; nevertheless, during the drop fall over the typical length of $\sim 200R$ considered here, the temperature of the liquid magma ocean increases because of heat exchanges with the drop, therefore its viscosity decreases at a given pressure (i.e., depth) following the equation in Ref. [21] for anhydrous liquid

$$\mu_T = 0.00033 e^{[6400/(T-1000)]} \text{Pa s}. \tag{25}$$

Here we investigate the influence of such a temperature-dependent viscosity on the dynamics, stability, and thermal evolution of a drop. For a given initial viscosity ratio, the initial magma ocean temperature is computed using (25), and we then consider an initial temperature difference with the hot metal drop of $\Delta T = 100\,\text{K}$ or $\Delta T = 1000\,\text{K}$. We focus on three reference cases, only changing

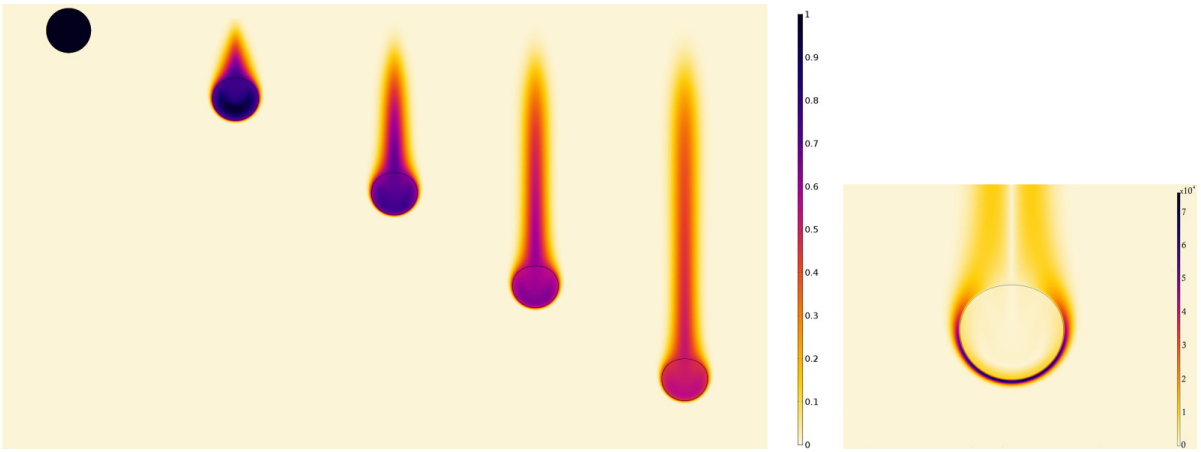

FIG. 15. Thermal evolution of the nondeformable metal drop as a function of normalized time (left). The color scale presents the temperature anomaly normalized by its initial value T^*, and the black solid line shows the surface of the metal drop. From left to right, $t^* = 0$, 0.0167, 0.033, 0.05, and 0.067. The right figure shows the temperature gradient (K/m) in and around the spherical drop. In this model, Re = 0.76, Pe = 254, and $R_\mu = 1000$ (simulation no. 3 in Table II).

the viscosity ratio (see Table II). Those cases are first presented in the absence of temperature-dependent viscosity:

(i) The nondeformable drop case (simulation no. 3 in Table II, Re = 0.76 and Pe = 254) is presented in Fig. 15. Drop's shape remains mostly constant. The temperature is close to uniform inside the drop because of internal recirculation and progressively decreases in the wake. Most heat transfer takes place at the front.

(ii) The weakly deformable drop case (simulation no. 5 in Table II, Re = 21.8 and Pe = 728.36) is presented in Fig. 16. The drop quickly deforms toward a spherical cap, associated with a strong release of heat in its wake. The system then reaches a quasi-steady state, with the most surprising feature being a more rapid temperature decrease in the drop than in the wake, leading to a positive heat transfer from the silicate to the iron in the drop's back. Nevertheless, most heat transfer still takes place at the front.

(iii) Finally, the strongly deformable drop case (simulation no. 6 in Table II, Re = 47.6 and Pe = 793.73) is presented in Fig. 17. Here the drop shape keeps oscillating over the whole depth because of competing surface tension and inertial forces. This induces oscillatory temperature changes in the wake, associated to periodic thermal plumes emitted from the drop sides and strong inhomogeneous fluxes within the magma ocean. Nevertheless, heat transfers between iron and silicate are still largely focused at the drop's front, explaining that this case is not associated with any specific signature in the previous section.

We now rerun those three cases using the previously defined temperature-dependent viscosity.

A. Drop dynamics

Figure 18 shows the normalized average velocity of each drop as a function of the normalized time for constant magma ocean viscosity in black lines and for temperature-dependent viscosity with $\Delta T = 100$ K ($\Delta T = 1000$ K) in red (blue) dashed lines. The normalized average velocity for the nondeformable drop (Fig. 18, left) with $\Delta T = 100$ K increases moderately by about 4.8% compared to the constant viscosity case, keeping the spherical shape without change in the morphology. For $\Delta T = 1000$ K, the drop deforms from the back side and its velocity strongly increases by about 26%; concomitantly, the average viscosity around the drop decreases by 93%, explaining this significant dynamical change. Such significant changes of the drag in the Stokes regime for an underformable drop were already addressed in Refs. [44,45].

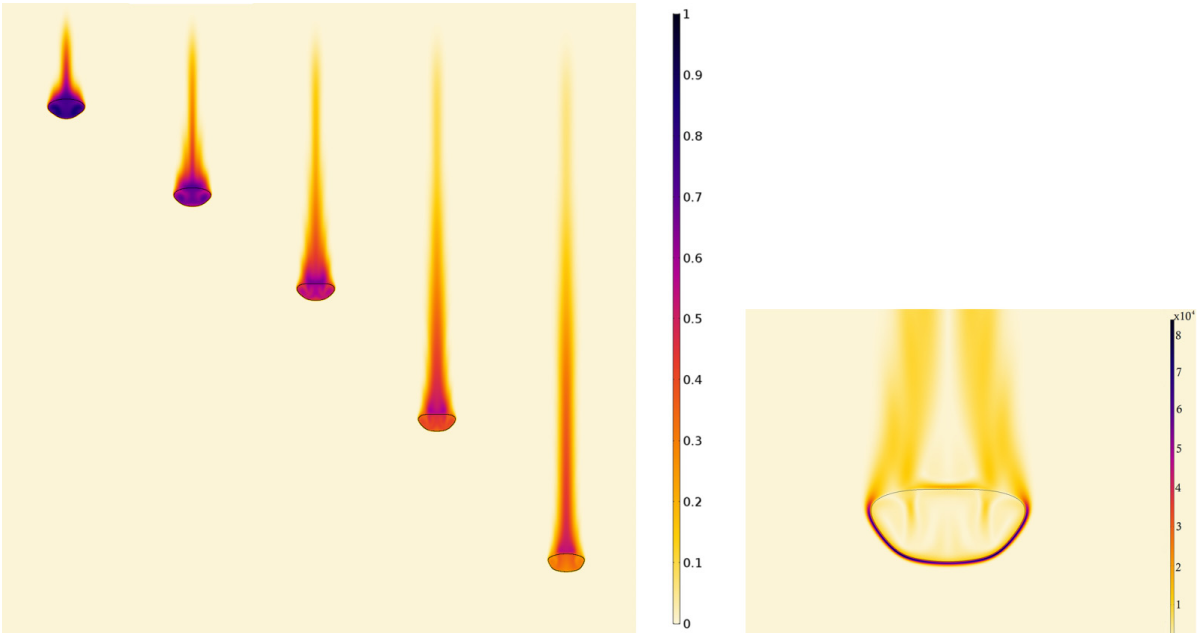

FIG. 16. Thermal evolution of the weakly deformable metal drop as a function of normalized time (left). The color scale presents the temperature anomaly normalized by its initial value T^*, and the black solid line shows the surface of the metal drop. From left to right, $t^* = 0.015$, 0.024, 0.033, 0.047, and 0.06. The right figure shows the temperature gradient (K/m) in and around the deformable drop. In this model, Re = 21.8, Pe = 728.36, and $R_\mu = 100$ (simulation no. 5 in Table II).

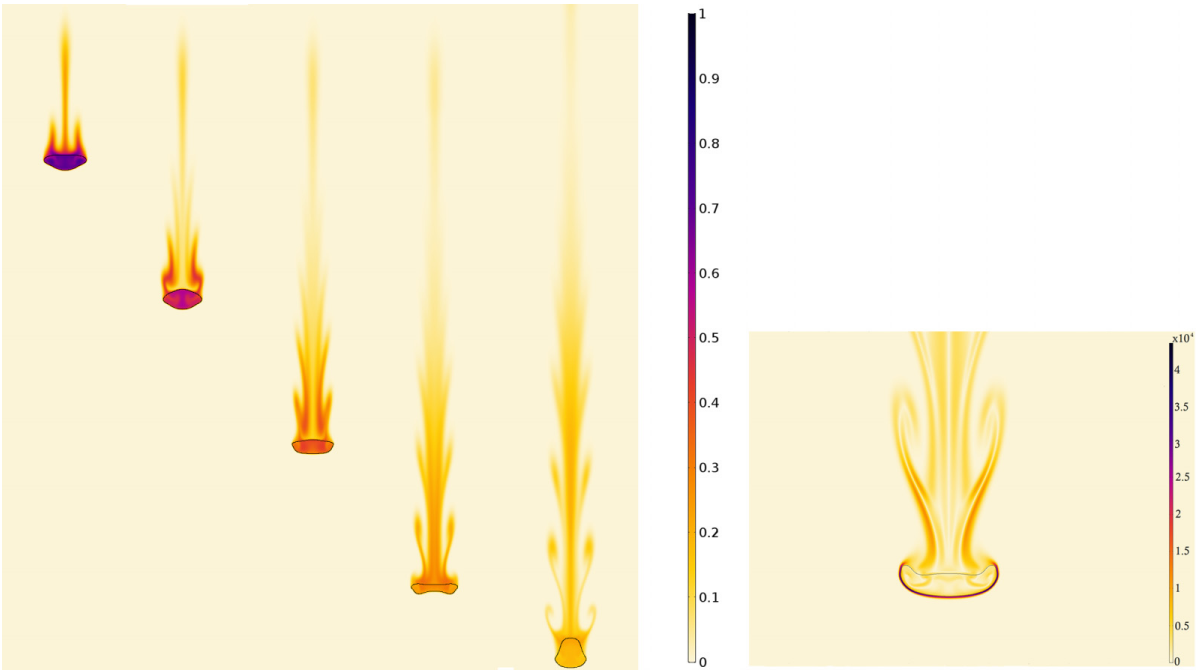

FIG. 17. Thermal evolution of the strongly deformable metal drop as a function of normalized time (left). The color scale presents the temperature anomaly normalized by its initial value T^*, and the black solid line shows the surface of the metal drop. From left to right, $t^* = 0.02$,0.033,0.047,0.06, and 0.077. The right figure shows the temperature gradient (K/m) in and around the deformable drop. In this model, Re = 47.6, Pe = 793.73, and $R_\mu = 50$ (simulation no. 6 in Table II).

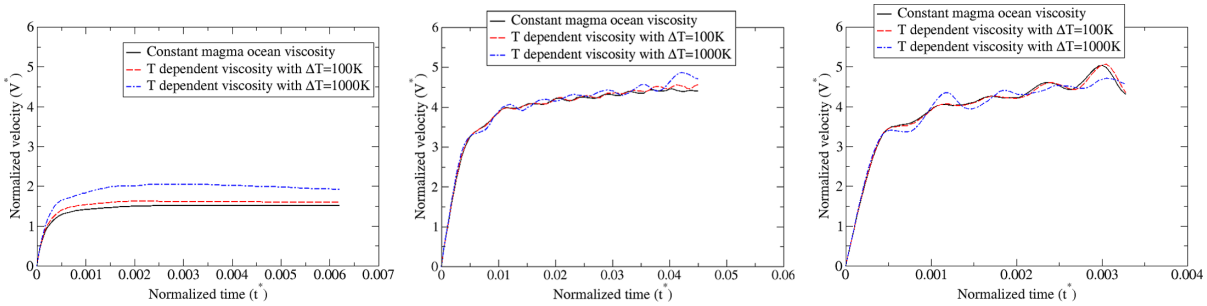

FIG. 18. Comparison of the normalized average velocity field as a function of normalized time to show the influence of a temperature-dependent viscosity for a nondeformable spherical drop (left), a weakly deformable drop (middle) and a strongly deformable drop (right). The black lines present the constant magma ocean viscosity. The red (blue) dashed lines present the temperature-dependent viscosity with $\Delta T = 100\,\mathrm{K}$ ($\Delta T = 1000\,\mathrm{K}$).

On the contrary, for the weakly deformable drop (Fig. 18, middle) and the strongly deformable drop (Fig. 18, right), no significant dynamical change is observed, despite a large viscosity decrease in the associated thermal boundary layer (by 76% and 92%, respectively, for $\Delta T = 1000$ K; see also Fig. 19). This indicates that the drop dynamics is already mostly inviscid in the absence of temperature-dependent viscosity, as can be guessed from the corresponding values of the Reynolds number (see caption of Figs. 16 and 17).

B. Drop fragmentation

In the most extreme previous case (the strongly deformable drop with $\Delta T = 1000\,\mathrm{K}$), Fig. 19 indicates that the hot silicate layer surrounding the drop has a viscosity value of the order 0.05 Pa s: Assuming such a viscosity uniformly in the ambient magma ocean, our previous study [27] predicts a rapid fragmentation, which is not observed here. Actually, the viscosity constrast at the interface does not influence the drop stability, because the thermal boundary layer where the low viscosity is localized is very thin in front of the drop, compared to any relevant dynamical length scale; besides, the wake has no influence on the drop. Temperature-dependent viscosity only affects the drop's

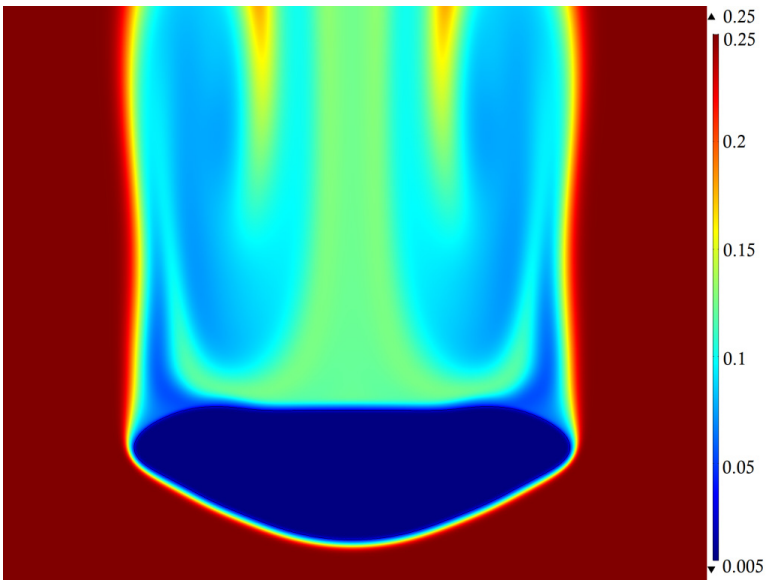

FIG. 19. View of the viscosity field (in Pa s) around the strongly deformable drop when a temperature-dependent viscosity is considered.

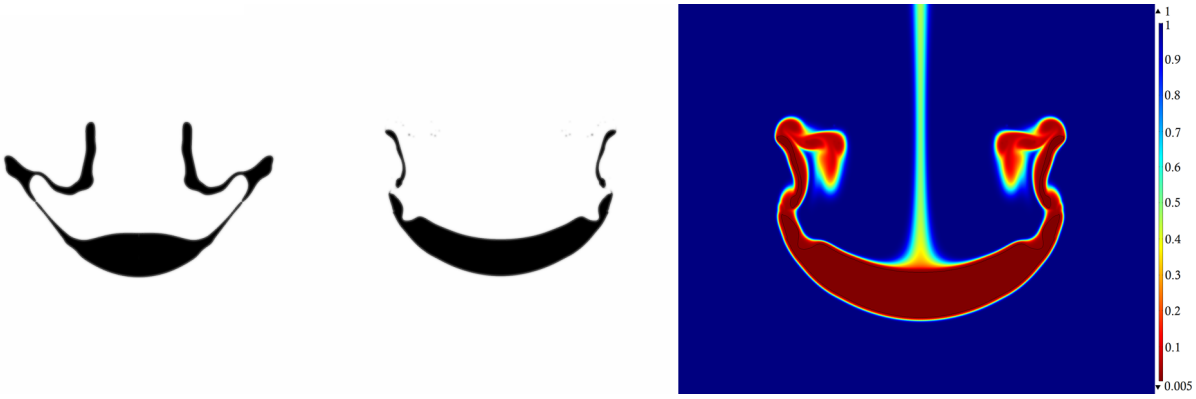

FIG. 20. Final form at breaking of the drop for a constant viscosity magma ocean (left) and a temperature-dependent viscosity magma ocean with $\Delta T = 1000$ K (middle). On the right, view of the viscosity field (in Pa.s) around the drop in the later case. In this model, Re = 50, Pe = 3330, and $R_\mu = 200$ (simulation no. 10 in Table II).

dynamics and fragmentation when flows and temperature change on comparable scales in upfront or sides locations.

To further prove this, we performed a simulation with a drop radius of 25 mm and a viscosity ratio of 200 for constant magma ocean viscosity first and then for $\Delta T = 1000$ K–dependent magma ocean viscosity (simulation no. 10 in Table II). Figure 20 (left) shows the jellyfish fragmentation mode when constant magma ocean viscosity is considered (more details can be found in Ref. [27]). The normalized time ($t^*_{bk} = \frac{t_{bk}V}{2R}\sqrt{\frac{\rho_d}{\rho_m}}$) and distance ($d^*_{bk} = \frac{d_{bk}}{R}$) of breakup equal 3.8 and 10.7, respectively. For temperature-dependent viscosity (Fig. 20, middle), another jellyfish fragmentation mode is observed, with time and distance of breakup equal to 2.3 and 5.6, respectively. Actually, here the extended jellyfish membranes form filaments, where thermal effects are very important. These membranes sink into a less-viscous medium whose thickness is comparable to the membranes thickness (see Fig. 20, right). Thus, the filaments move freely in this zone with low viscous constraints and finally separate from the drop volume, leading to fragmentation.

Note finally that the local dimensionless numbers, taken at the mean temperature (and associated viscosity) of the thermal boundary layer, become Re = 1000, We = 19, and $R_\mu = 10$. From Figs. 4, 12, and 13 of our previous study [27], we find consistent results for the fragmentation mode of the drop, as well as for its time and distance of breakup, accounting for these dimensionless numbers (to compare with our previous study, Re and We should be multiplied in this study by a factor 2 because in Ref. [27], Re and We were calculated using the drop diameter).

Hence, temperature-dependent magma ocean viscosity influences the drop fragmentation in the filament forming regimes only. In such regimes, the results in Ref. [27] as a function of Re, We, and R_μ already allow predicting fragmentation mode, breaking time and distance by considering local values of the dimensionless numbers.

C. Thermal evolution

In Fig. 21, we compare the normalized mean iron temperature for each case as a function of normalized time. For a nondeformable drop (Fig. 21, left), the average temperature for $\Delta T = 100$ K (red dashed lines) and $\Delta T = 1000$ K (blue dashed lines) temperature-dependent viscosity decreases by about 6.1% and 20.8% with respect to the constant viscosity case (black line). As a consequence, it significantly changes the characteristic time and length of equilibration (see Table III). For a weakly deformable drop (Fig. 21, middle), the average temperature evolution with $\Delta T = 1000$ K changes only by about 13.6%; no difference is measured for a strongly deformable drop (Fig. 21, right). As for the fall velocity, temperature-dependent viscosity influences significantly the thermal

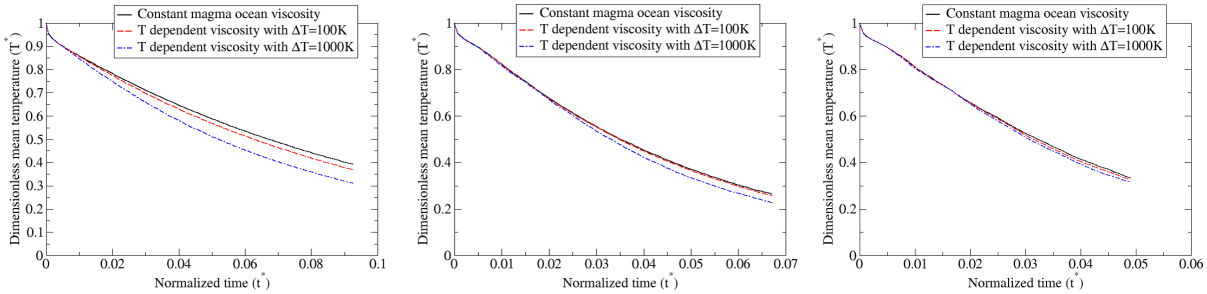

FIG. 21. Comparison of the dimensionless temperature as a function of normalized time for a nondeformable drop (left), a weakly deformable drop (middle) and a strongly deformable drop (right). The black lines present the constant magma ocean viscosity. The red (blue) dashed lines present the temperature-dependent viscosity with $\Delta T = 100\,\mathrm{K}$ ($\Delta T = 1000\,\mathrm{K}$).

evolution of nondeformable drops only (i.e., the drops in the Stokes regime). Note, finally, that in the intermediate regime, the characteristics time and length of equilibration decrease slightly with a temperature-dependent viscosity compared to the constant magma ocean viscosity case, whereas in the Stokes regime, the equilibrium characteristic length increases with a temperature-dependent viscosity, in contrast to the characteristic time of equilibration (see Table III).

Regarding the volume of heated magma ocean shown in Fig. 22, no significant change is observed for all cases with $\Delta T = 100\,\mathrm{K}$ (red dashed lines). The volume of heated magma ocean increases by about 1.5 to 2 times compared to the constant viscosity case (black line) for $\Delta T = 1000\,\mathrm{K}$ (blue dashed lines) due to the initial larger temperature difference; but the curves remain parallel, hence exhibiting no specific dynamical signature.

Finally, we have measured the heat transfer between the two phases for all drops with a temperature-dependent viscosity. As shown in Table IV, in agreement with our previous observations, we do not notice any significant change compared to our scaling law for constant viscosity, except maybe for the less deformable drop: Indeed, heat transfer is mostly due to diffusive exchanges through a thin thermal boundary layer at the drop front, which are not affected by temperature-dependent viscosity. The same conclusion was reached experimentally in Ref. [45] in his study of diapiric magma transport through the lithosphere, hence in the limit of small Reynolds number, nondeformable drop, and using an exponential form of the temperature-dependent viscosity law. Associated numerical simulations in Ref. [44] in the limit of infinite Prandtl number exhibited a very weak dependence on the total viscosity variation. Additional systematic studies, both experimental and numerical, are necessary to explore the parameter range relevant to

TABLE III. The change in characteristics time and length for cases also studied with a temperature-dependent viscosity.

Simulation	ΔT	t_c^*	l_c^*
no. 3 (constant magma ocean viscosity)	100	0.1	24.25
no. 3a (T-dependent μ_m)	100	0.0975	25.6
no. 3b (T-dependent μ_m)	1000	0.082	27
no. 5 (constant magma ocean viscosity)	100	0.05	35.14
no. 5a (T-dependent μ_m)	100	0.0496	33.33
no. 5b (T-dependent μ_m)	1000	0.045	31.25
no. 6 (constant magma ocean viscosity)	100	0.045	32
no. 6a (T-dependent μ_m)	100	0.044	29.4
no. 6b (T-dependent μ_m)	1000	0.042	27.7

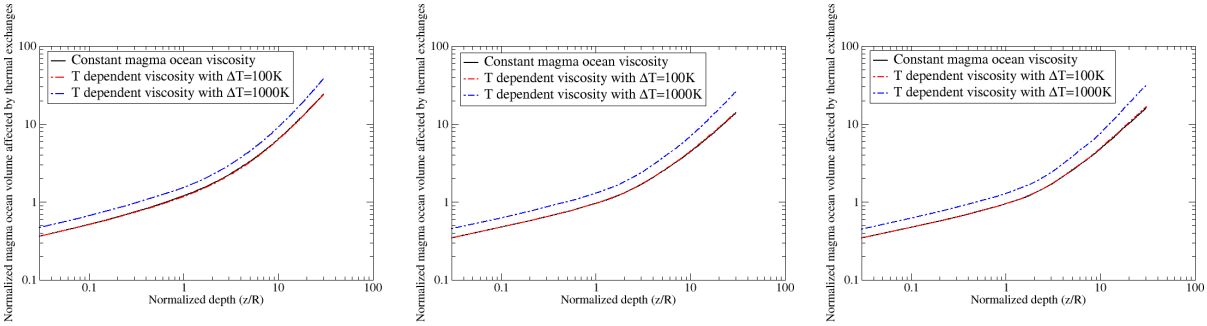

FIG. 22. Comparison of normalized heated magma ocean volume as a function of normalized time for a nondeformable drop (left), a weakly deformable drop (middle) and a strongly deformable drop (right). The black lines present the constant magma ocean viscosity. The red (blue) dashed lines present the temperature-dependent viscosity with $\Delta T = 100\,\mathrm{K}$ ($\Delta T = 1000\,\mathrm{K}$).

our configuration. In the meantime, we suggest that using our scaling law [Eq. (22)] is the most acceptable solution.

VI. CONCLUSIONS AND FUTURE WORK

We have carried out series of numerical simulations to characterize the thermal exchanges between a falling drop and a viscous ambient fluid, exploring a new parameter range relevant for the geophysical application of a hot liquid iron drop falling in a magma ocean. We have shown that because of drop distortions, thermal equilibration properties slightly change from the theoretical predictions based on diffusive heat exchanges through a laminar thermal boundary layer. We have also tested that accounting for a temperature-dependent viscosity in the magma ocean barely influences the obtained results, except for limited cases like nondeformable, low-Reynolds-number drops or jellyfish fragmentation mode. Our most relevant results for geophysical application are the scaling laws for the normalized length of equilibration and for the Nusselt number, which both increase monotonically with the Peclet number as $\mathrm{Pe}^{0.41\pm0.01}$ and $\mathrm{Pe}^{0.63\pm0.02}$, respectively.

Future work should now consider (i) the presence of convection in the ambient magma ocean, which could affect our conclusions providing the associated velocity at the drop scale is at least of similar order as the falling drop velocity, hence requiring extremely turbulent regimes, and (ii) chemical exchanges between iron and silicates, which will determine the initial chemical state of the considered planet (see, e.g., Ref. [46]). Chemical and thermal constitutive equations being similar, similar equilibration scaling laws and dynamics are nevertheless expected.

TABLE IV. Comparison of the Nusselt numbers for cases of temperature-dependent viscosity between our numerical results and our scaling law for constant viscosity Eq. (22).

Simulation	Nu: measured	Nu: Eq. (22)	Relative error (%)
no. 3a	2.65	2.72	2.6
no. 3b	2.95	3.07	4.1
no. 5a	5.15	5.17	0.4
no. 5b	5.21	5.33	2.3
no. 6a	5.28	5.36	1.5
no. 6b	5.35	5.36	0.2

ACKNOWLEDGMENTS

The authors acknowledge funding by the European Research Council under the European Union's Horizon 2020 research and innovation program through Grant No. 681835-FLUDYCO-ERC-2015-CoG. This research also received funding from the French PNP program (INSU-CNRS), the French Government Laboratory of Excellence initiative No. ANR-10-LABX-0006, and the Région Auvergne. This paper is Laboratory of Excellence ClerVolc Contribution No. 406. We are grateful to the Mésocentre Clermont Auvergne University for providing help as well as computing and storage resources.

[1] T. Kleine, C. Münker, K. Mezger, and H. Palme, Rapid accretion and early core formation on asteroids and the terrestrial planets from Hf-W chronometry, Nature **418**, 952 (2002).
[2] M. Touboul, T. Kleine, B. Bourdon, H. Palme, and R. Wieler, Late formation and prolonged differentiation of the Moon inferred from W isotopes in lunar metals, Nature **450**, 1206 (2007).
[3] R. Deguen, P. Olson, and P. Cardin, Experiments on turbulent metal-silicate mixing in a magma ocean, Earth Planet. Sci. Lett. **310**, 303 (2011).
[4] R. Deguen, M. Landeau, and P. Olson, Turbulent metal-silicate mixing, fragmentation, and equilibration in magma oceans, Earth Planet. Sci. Lett. **391**, 274 (2014).
[5] M. Landeau, R. Deguen, and P. Olson, Experiments on the fragmentation of a buoyant liquid volume in another liquid, Fluid Mech. **749**, 478 (2014).
[6] D. J. Stevenson, Fluid dynamics of core formation, *Origin of the Earth* (Oxford University Press, 1990), pp. 231–249.
[7] J. B. Wacheul and M. Le Bars, Experiments on fragmentation and thermo-chemical exchanges during planetary core formation, Phys. Earth Planet. Int. **276**, 134 (2018).
[8] J. B. Wacheul, M. LeBars, J. Monteux, and J. M. Aurnou, Laboratory experiments on the breakup of liquid metal diapirs, Earth Planet. Sci. Lett. **403**, 236 (2014).
[9] W. K. Hartmann and D. R. Davis, Satellite-sized planetesimals and lunar origin, Icarus **24**, 504 (1975).
[10] J. Monteux, N. Coltice, F. Dubuffet, and Y. Ricard, Thermo-mechanical adjustment after impacts during planetary growth, Geophys. Res. Lett. **34**, 24201 (2007).
[11] W. B. Tonks and H. J. Melosh, Core formation by giant impacts, Icarus **100**, 326 (1992).
[12] M. J. Walter and R. G. Tronnes, Early earth differentiation, Earth Planet. Sci. Lett. **225**, 253 (2004).
[13] J. Monteux, Y. Ricard, N. Coltice, F. Dubuffet, and M. Ulvrova, A model of metal-silicate separation on growing planets, Earth Planet. Sci. Lett. **287**, 353 (2009).
[14] H. Genda, R. Brasser, and S. J. Mojzsis, The terrestrial late veneer from core disruption of a lunar-sized impactor, Earth Planet. Sci. Lett. **480**, 25 (2017).
[15] J. D. Kendall and H. Melosh, Differentiated planetesimal impacts in a terrestrial magma ocean: Fate of the iron core, Earth Planet. Sci. Lett. **448**, 24 (2016).
[16] H. Ichikawa, S. Labrosse, and K. Kurita, Direct numerical simulation of an iron rain in the magma ocean, Geophys. Res. **115**, B01404 (2010).
[17] D. C. Rubie, H. J. Melosh, J. E. Reid, C. Liebske, and K. Righter, Mechanisms of metal-silicate equilibration in the terrestrial magma ocean, Earth Planet. Sci. Lett. **205**, 239 (2003).
[18] H. Samuel, A re-evaluation of metal diapir breakup and equilibration in terrestrial magma oceans, Earth Planet. Sci. Lett. **313–314**, 105 (2012).
[19] T. W. Dahl and J. Stevenson, Turbulent mixing of metal and silicate during planet accretion and interpretation of the hf-w chronometer, Earth Planet. Sci. Lett. **295**, 177 (2010).
[20] M. Ulvrová, N. Coltice, Y. Ricard, S. Labrosse, F. Dubuffet, J. Velìmský, and M. Šràmek, Compositional and thermal equilibration of particles, drops, and diapirs in geophysical flows, Geochem. Geophys. Geosyst **12**, Q10014 (2011).
[21] B. B. Karki and L. P. Stixrude, Viscosity of mgsio3 liquid at earth's mantle conditions: Implications for an early magma ocean, Science **328**, 740 (2010).

[22] T. Bonometti and J. Magnaudet, Transition from spherical cap to toroidal bubbles, Phys. Fluids **18**, 052102 (2006).
[23] M. Ohta and M. Sussman, The buoyancy-driven motion of a single skirted bubble or drop rising through a viscous liquid, Phys. Fluids **24**, 112101 (2012).
[24] M. Ohta, Y. Akama, Y. Yoshida, and M. Sussman, Three-dimensional simulations of vortex ring formation from falling drops in an immiscible viscous liquid, Chem. Eng. Jpn. **42**, 648 (2009).
[25] M. Ohta, S. Yamaguchi, Y. Yoshida, and M. Sussman, The sensitivity of drop motion due to the density and viscosity ratio, Phys. Fluids **22**, 072102 (2010).
[26] M. Ohta, Y. Akama, Y. Yoshida, and M. Sussman, Influence of the viscosity ratio on drop dynamics and breakup for a drop rising in an immiscible low-viscosity liquid, Fluid Mech. **752**, 38 (2014).
[27] B. Qaddah, J. Monteux, V. Clesi, A. Bouhifd, and M. Le Bars, Dynamics and stability of an iron drop falling in a magma ocean, Phys. Earth Planet. Int. **289**, 75 (2019).
[28] H. Samuel, P. J. Tackley, and M. Evonuk, Heat partitioning in terrestrial planets during core formation by negative diapirism, Earth Planet. Sci. Lett. **290**, 13 (2010).
[29] F. M. Flasar and F. Birch, Energetics of core formation: A correction, J. Geophys. Res. **78**, 6101 (1973).
[30] X-Y. Luo, M.-J. Ni, A. Ying, and M. Abdou, Application of the level set method for multi-phase flow computation in fusion engineering, Fus. Eng. Des. **81**, 1521 (2006).
[31] J. Hu, R. Jia, K. T. Wan, and X. Xiong, Simulation of droplet impingement on a solid surface by the level set method, in *Proceedings of the COMSOL Conference in Boston* (COMSOL, Boston, 2014).
[32] V. Lherm and R. Deguen, Small-scale metal/silicate equilibration during core formation: The influence of stretching enhanced diffusion on mixing, J. Geophys. Res.: Solid Earth **123**, 10,496 (2018).
[33] D. C. Rubie, F. Nimmo, and H. J. Melosh, *Formation of the Earth's Core, Treatise on Geophysics – Evolution of the Earth* (2nd ed.) (Elsevier, Amsterdam, 2015), pp. 43–79.
[34] A. M. Hofmeister, Mantle values of thermal conductivity and the geotherm from phonon lifetimes, Science **283**, 1699 (1999).
[35] C. W. Thomas and P. D. Asimow, Direct shock compression experiments on premolten forsterite and progress toward a consistent high-pressure equation of state for cao-mgo-al2o3-sio2-feo liquids, J. Geophys. Res.: Solid Earth **118**, 5738 (2013).
[36] N. de Koker, G. Steinle-Neumann, and V. Vlček, Electrical resistivity and thermal conductivity of liquid fe alloys at high p and t, and heat flux in earth's core, Proc. Natl. Acad Sci. USA **109**, 4070 (2012).
[37] H. Ichikawa, T. Tsuchiya, and Y. Tange, The p-v-t equation of state and thermodynamic properties of liquid iron, J. Geophys. Res.: Solid Earth **119**, 240 (2014).
[38] M. Pilch and C. A. Erdman, Use of breakup time data and velocity history data to predict the maximum size of stable fragments for acceleration-induced breakup of a liquid drop, Multiphase Flow **13**, 741 (1987).
[39] E. Villermaux and B. Bossa, Single-drop fragmentation determines size distribution of rain drops, Nat. Phys. **5**, 697 (2009).
[40] S. S. Jain, N. Tyagi, R. S. Prakash, R. V. Ravikrishna, and G. Tomar, Secondary breakup of drops at moderate Weber numbers: Effect of Density ratio and Reynolds number, Int. J. Multiphase Flow **117**, 25 (2019).
[41] J. Crank, *The Mathematics of Diffusion* (2nd ed.) (Clarendon Press, Oxford, 1975).
[42] R. C. Mittal and R. K. Jain, Redefined cubic b-splines collocation method for solving convection–diffusion equations, Appl. Math. Model. **36**, 5555 (2012).
[43] J. R. Fleck, C. L. Rains, D. S. Weeraratne, C. T. Nguyen, D. M. Brand, S. M. Klein, J. M. McGehee, J. M. Rincon, C. Martinez, and P. L. Olson, Iron diapirs entrain silicates to the core and initiate thermochemical plumes, Nat. Commun. **9**, 71 (2018).
[44] S. F. Daly and A. Raefsky, On the penetration of a hot diapir through a strongly temperature-dependent viscosity medium, Geophys. J. Int. **83**, 657 (1985).
[45] N. M. Ribe, Diapirism in the earth's mantle: Experiments on the motion of a hot sphere in a fluid with temperature-dependent viscosity, J. Volcanol. Geotherm. Res. **16**, 221 (1983).
[46] M. Bouhifd and A. Jephcoat, The effect of pressure on partitioning of ni and co between silicate and iron-rich metal liquids: A diamond-anvil cell study, Earth Planet. Sci. Lett. **209**, 245 (2003).

4 Impacts géants et évolution primitive des dynamos planétaires

Le champ magnétique terrestre est la conséquence de mouvements rapides du fer dans la partie liquide du noyau terrestre (voir ex. Jones (2015)). L'état du noyau (liquide ou solide) est gouverné par l'efficacité du transport de chaleur dans le manteau et par l'énergie thermique accumulée dans le noyau au cours de son histoire. Comprendre l'état thermique du noyau terrestre et son évolution au cours du temps permet donc aussi de mieux comprendre l'évolution du champ magnétique des objets du système solaire et ainsi comprendre pourquoi certaines planètes en ont un et d'autres non (Buffett, 2002).

Parmi les planètes telluriques et les lunes du système solaire, Ganymède, Mercure et la Terre possèdent actuellement un champ magnétique. Les données paléo-magnétiques les plus anciennes retrouvées à la surface de la Terre étant datées à 3.45 Ga, l'initiation de la géodynamo a potentiellement eu lieu peu de temps après la formation du noyau (Tarduno et al., 2010). Vénus possède un noyau liquide mais ne montre pas de signe de dynamo (Langlais et al., 2010). Mars et probablement la Lune ont enregistré dans leur croûte des preuves d'un champ magnétique interne transitoire (Dyal et al., 1974; Acuña et al., 1999). Les dynamos lunaire et martienne auraient été initiées tôt dans l'histoire de ces objets pour s'arrêter ensuite entre 4.1 et 3.75 Ga (Acuña et al., 1999; Lillis et al., 2008). Bien qu'il y ait aujourd'hui une recrudescence des preuves de ces dynamos transitoires, leur chronologie et les mécanismes de leur initiation et de leur arrêt restent des énigmes majeures.

Pour savoir si une dynamo planétaire peut être générée dans le noyau, il est nécessaire de connaitre l'état thermique interne de la planète et notamment la différence de température entre le noyau et le manteau environnant (i.e. le flux de chaleur). En effet, la génération d'un champ magnétique requiert trois ingrédients : un fluide métallique liquide avec une grande conductivité électrique, une source d'énergie apportée par la convection thermo-chimique et une dynamique favorable au sein du noyau (principalement de l'hélicité induite par de la rotation) (Moffatt, 1978; Olson, 2007). Pour des corps où le noyau est plus petit (ex. la Lune), d'autres mécanismes que la convection doivent être invoqués (Dwyer et al., 2011; Le Bars et al., 2011). Généralement, si nous considérons que le noyau est composé essentiellement de fer et que la planète tourne suffisamment vite sur elle-même, la deuxième condition peut être caractérisée en suivant l'évolution du flux de chaleur à la frontière manteau/noyau (CMB). Plus la convection au sein du noyau sera vigoureuse et complexe, plus la probabilité d'avoir une dynamo sera grande (Kutzner and Christensen, 2002; Christensen and Aubert, 2006). Une convection vigoureuse se traduira aussi par un flux de chaleur important à la CMB.

De nombreux modèles se sont intéressés à l'influence d'impacts géants à la fin de l'accrétion des planètes sur les dynamos primitives (Roberts et al., 2009; Arkani-Hamed and Olson, 2010; Monteux et al., 2011). En effet, ces impacts géants déposent non seulement une quantité importante de chaleur dans le manteau susceptible de réduire considérablement l'efficacité de refroidissement du noyau et ainsi d'arrêter la dynamo, mais ils apportent aussi potentiellement

une quantité importante de fer via le noyau de l'impacteur qui peut se réchauffer pendant sa chute et modifier le bilan thermique du noyau.

Les cadres temporels des activités magnétiques des satellites et planètes du Système Solaire, et notamment le fait que ces activités aient pu exister durant les premiers millions d'années de leur histoire, suggèrent que ces dynamos sont peut-être liées aux étapes d'accrétion et de différenciation primitives lors de la formation des planètes (Stevenson, 2003). Grâce aux modèles développés au cours de mon parcours, j'ai proposé de nouveaux mécanismes d'initiation de dynamos planétaires, j'ai relié ces mécanismes aux processus de différenciation et j'ai apporté des contraintes quant aux temps, tailles et rhéologies nécessaires pour la génération de tels champs magnétiques.

4.1 Initiation des dynamos au sein des proto-planètes indifférenciées

Il est difficile de contraindre comment le champ magnétique d'une planète se met en marche. Dans la section suivante, je propose de détailler les conditions d'initiation de ce champ magnétique selon deux modalités : (1) au cours de la chute d'un important volume de fer et (2) une fois cet important volume de fer au centre de la planète

4.1.1 Au cours de la chute d'un diapir de fer

Qu'ils aient pour origine des phénomènes de séparation locale suite à un impact ou l'assemblage de deux noyaux après impact entre deux protoplanètes différenciées ou d'autres processus de différenciation (percolation, gouttelettes de fer au sein d'un océan magmatique, instabilités Rayleigh-Taylor ...), les diapirs de fer ont fortement influencé la formation du noyau des planètes telluriques et ce pendant les premiers millions d'années de leur histoire (Stevenson, 1981). La variété des processus de différenciation implique une large gamme de tailles caractéristiques de ces diapirs de fer qui peut varier entre quelques centimètres et plusieurs centaines de kilomètres. La vitesse de chute de la phase métallique dépend essentiellement de la taille des diapirs et de la rhéologie du manteau dans lequel ils plongent. La large gamme possible de ces deux paramètres (Karato and Murthy, 1997) implique donc des vitesses de chute variées qui peuvent atteindre dans les cas les plus favorables plusieurs kilomètres par seconde.

Lors de la chute du diapir de fer fondu, les interactions avec le manteau environnant plus visqueux vont engendrer un champ de vitesse axisymétrique au sein du diapir. J'ai déterminé si l'écoulement au sein d'un diapir de fer pouvait générer un champ magnétique lors de sa chute vers le centre d'une planète en rotation (Monteux et al., 2012). Les résultats des modèles numériques que j'ai développés en collaboration avec H. Amit (CR LPGNantes), N. Schaeffer et P. Cardin (ISTerre Grenoble) montrent que l'écoulement produit dans le diapir peut générer un champ magnétique seulement s'il plonge dans une planète en rotation et si les forces inertielles dans le diapir sont suffisamment importantes (Monteux et al., 2012). Les effets de la

rotation et des forces inertielles produisent de l'hélicité dans l'écoulement ce qui est nécessaire pour générer une dynamo (Moffatt, 1978). L'initiation d'une dynamo est plus facile pour un diapir qui plonge à partir de l'équateur que pour un diapir qui plonge au pôle en suivant l'axe de rotation de la planète. Nos modèles ont permis d'apporter des contraintes sur les tailles de diapir et les viscosités du manteau nécessaires pour initier de telles dynamos mais aussi sur l'importance de la rotation et de la turbulence dans le diapir (Figure 13). Nous avons aussi caractérisé l'intensité et la morphologie de ce champ magnétique.

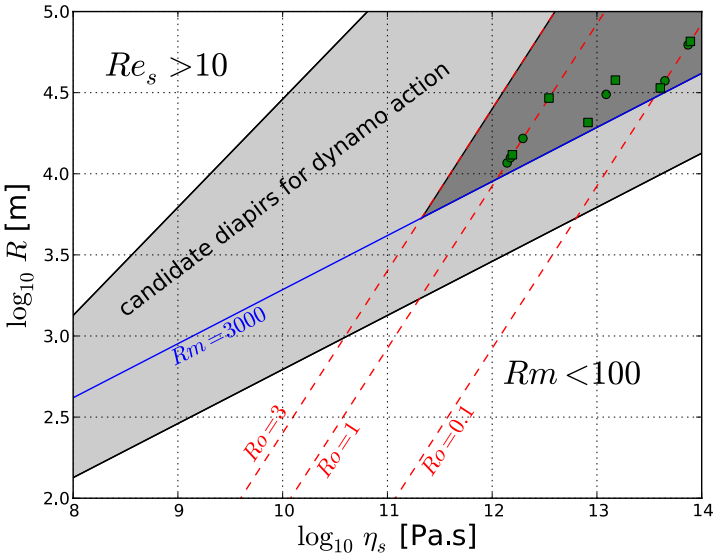

FIGURE 13 – *Caractéristiques des diapirs pouvant engendrer un champ magnétique pendant leur chute en fonction de leur taille R et de la viscosité du manteau dans lequel ils plongent η_s. Les symboles verts représentent les dynamos cinématiques produites numériquement (les cercles pour des diapirs plongeant le long de l'axe de rotation de la planète et les carrés pour les diapirs plongeant à l'équateur). La ligne bleue représente la plus petite valeur du nombre de Reynolds magnétique pour laquelle une dynamo est obtenue dans nos modèles. La ligne en trait tiretés rouge $Ro = 1$ représente la limite du nombre de Rossby étudiée dans nos modèles (régime rotationnel). Pour des valeurs de Ro plus grandes (non étudiées), une dynamo pourrait être générée. Pour de gros diapirs ($R > 10$ km) et de faibles viscosités du manteau ($\eta_s < 10^{10}$ Pa.s), le nombre de Reynolds du manteau $Re_s > 10$ et le diapir est susceptible de se dissocier (Monteux et al., 2012).*

Nos modèles apportent une explication alternative (et/ou complémentaire) aux dynamos classiques lunaire et martienne engendrées par de la convection dans le noyau (Stegman et al., 2003; Stanley et al., 2008; Amit et al., 2011) qui étaient considérées jusqu'ici comme le seul modèle possible de génération de champ magnétique. Le mécanisme que nous propo-

sons s'ajoute aux modèles de dynamos par forçage mécanique provoquée par des mouvements différentiels entre le manteau et le noyau lunaire (Le Bars et al., 2011; Dwyer et al., 2011). Si nous plaçons nos résultats dans un contexte à n-diapirs lors de la différenciation d'une planète, nos modèles constituent une explication complémentaire des champs magnétiques fossiles observés à la surface de Mars et de la Lune (Hood et al., 2001; Langlais et al., 2004).

4.1.2 Une fois au centre de la protoplanète

Les mouvements convectifs et la génération d'une dynamo dans un noyau planétaire métallique dépendent de son état thermique et de la différence de température avec le manteau environnant. L'état thermique de la phase métallique séparée de la phase silicatée après impact météoritique une fois qu'elle a atteint le centre d'une planète en croissance dépend fortement du volume de diapir de fer et des contrastes de viscosité entre les phases métalliques et silicatées. Comme discuté précédemment (voir section 3), pour des rayons de diapir de fer suffisamment grands (supérieurs à 70 km), la dissipation thermique résultant de la déformation visqueuse du manteau environnant engendre une augmentation de la température du diapir métallique par rapport à sa température juste après l'impact (Monteux et al., 2009). Un protonoyau initialement plus chaud que le manteau environnant peut expliquer la présence d'une dynamo primitive au sein des planètes telluriques (Williams and Nimmo, 2004). Savoir si la différence de température entre le protonoyau et le manteau est suffisante pour générer une dynamo est fonction de la rhéologie du manteau et du volume du diapir métallique.

J'ai utilisé le modèle numérique développé durant ma thèse (Monteux et al., 2009) pour identifier les tailles caractéristiques de planètes, de diapir métallique et les contrastes de viscosité nécessaires à une dynamo primitive générée au sein d'un protonoyau différencié après un impact météoritique. Mes résultats montrent notamment que ce sont les conditions d'accrétion qui contrôlent l'existence du champ magnétique primitif (Monteux et al., 2011). En effet, j'ai montré que si une planète peut atteindre une taille significative sans subir de différenciation majeure, un impact géant à la fin de son accrétion peut différencier un protonoyau suffisamment chaud pour initier une dynamo interne pendant plusieurs millions d'années (Figure 14). Ainsi, si un corps avec un rayon d'environ 500 km impacte une planète indifférenciée de la taille de Mars ($R = 3400$ km), une dynamo sera initiée (Figure 14). La durée de cette dynamo évoluera entre quelques milliers d'années et plusieurs millions d'années selon les modes de transfert thermique à la frontière protonoyau/manteau.

4.2 Influence des impacts géants sur les dynamos planétaires

En plus d'être des hypothèses plausibles pour expliquer de nombreuses caractéristiques du système solaire comme le système Terre-Lune (Canup, 2004), les dichotomies magnétique et

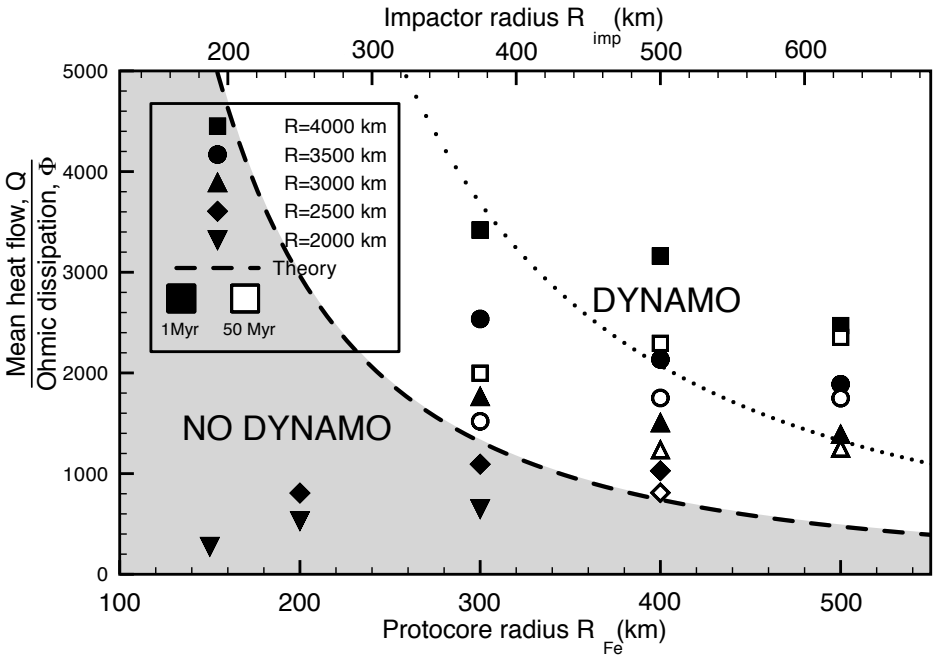

FIGURE 14 – *Flux de chaleur à la frontière du protonoyau en fonction de la taille du protonoyau (symboles noirs) (Monteux et al., 2011). Ce protonoyau est formé par un épisode de différenciation suite à un impact géant. La forme des symboles est liée à la taille de la planète impactée. La ligne en traits tiretés représente la valeur seuil à dépasser pour générer une dynamo dans un cas où le protonoyau et le manteau ont la même viscosité. La ligne pointillée correspond au même seuil mais en considérant que le protonoyau est beaucoup moins visqueux que le manteau. Si le flux de chaleur est supérieur à la valeur seuil pendant plus de 50 Ma, un deuxième symbole blanc représente la valeur du flux de chaleur correspondant.*

topographique martiennes (Marinova et al., 2008; Nimmo et al., 2008) et le faible volume du manteau de Mercure par rapport à son noyau (Benz et al., 1988), les impacts météoritiques géants sont de plus en plus évoqués pour expliquer l'initiation ou l'arrêt de la dynamo des planètes telluriques (Roberts et al., 2009; Arkani-Hamed and Olson, 2010; Reese et al., 2010). Dans les modèles proposés, les impacts font intervenir des corps avec des rayons typiquement compris entre 100 et 1000 km. Au moment de ces impacts, le bolide impacteur et la cible impactée étaient probablement différenciés. Si la vitesse d'impact est faible (de l'ordre de la vitesse d'échappement) l'efficacité de l'accrétion est proche de 100 % et tout le matériel de l'impacteur se combine à la planète impactée (Asphaug, 2010). Ainsi, de grands volumes de fer ont potentiellement pu être apportés au sein de la planète impactée et influencer la génération d'une dynamo. Au vu des différences de viscosité et ainsi de temps caractéristique de réajustement thermique qu'il existe entre le manteau et le noyau, le chauffage par impact géant a pu jouer un rôle à plus long terme sur les dynamos planétaires que le chauffage du

noyau.

4.2.1 Impacts géants et assemblages de noyaux

Lors d'un impact géant, la quasi totalité du noyau de l'impacteur s'est assemblée avec le noyau déjà existant (Canup, 2004). Une partie, voire la totalité du plongement de la phase métallique, a pu se faire par diapirisme d'importants volumes de fer. Les études montrent que les impacts géants et l'assemblage des deux noyaux ont pu avoir des conséquences importantes d'un point de vue thermique (Arkani-Hamed and Olson, 2010), d'un point de vue chimique (Dahl and Stevenson, 2010) et du point de vue de l'histoire magnétique de l'objet impacté (Reese et al., 2010). Ces études se sont intéressées aux conséquences thermo-mécaniques d'un impact géant sur une planète différenciée. Cependant, aucune d'entre elles ne considère correctement l'assemblage entre le noyau de l'impacteur et le noyau du corps impacté. De tels phénomènes ont pu avoir des conséquences importantes sur l'activité magnétique de la planète impactée.

J'ai développé avec M. Jellinek, C. Johnson (UBC, Vancouver) (Monteux et al., 2013) et avec J. Arkani-Hamed (University of Toronto) (Monteux and Arkani-Hamed, 2014)) des modèles numériques afin de caractériser la dynamique d'assemblage des deux noyaux et notamment l'accommodation par déformation du noyau préexistant ainsi que la modification du flux de chaleur au niveau de la CMB (Figure 15). Après un impact géant, une quantité importante de l'énergie cinétique de l'impact est convertie en chaleur au sein du manteau de la planète impactée. En augmentant la température dans le manteau, cet effet a tendance à diminuer le flux de chaleur à la CMB mais aussi à créer une stratification thermique sous la CMB qui arrête la dynamo (Arkani-Hamed and Olson, 2010). Cependant, lors de la chute du noyau de l'impacteur, le chauffage visqueux convertissant l'énergie potentielle du diapir en chaleur peut potentiellement augmenter la température du noyau plongeant. Ce deuxième effet augmenterait ainsi la température dans le noyau de la planète et modifierait la capacité du noyau à se refroidir par convection et ainsi son activité magnétique. Si la planète impactée ne possédait pas de dynamo avant l'impact géant, l'assemblage des noyaux pourrait en initier une.

Nos résultats montrent que les paramètres tels que le volume du noyau de l'impacteur retenu au sein de la planète impactée ainsi que la profondeur à laquelle est enseveli ce matériel gouvernent le temps caractéristique d'assemblage des deux noyaux mais aussi l'intensité de la dissipation visqueuse dans le noyau plongeant. Nos résultats montrent aussi qu'augmenter significativement le contraste de viscosité entre le noyau de l'impacteur et le manteau peut réduire la durée de l'assemblage des noyaux à moins de 1000 ans mais n'affecte pas la température d'assemblage (Monteux and Arkani-Hamed, 2014). De plus, quelque soit l'efficacité du mélange thermique à l'intérieur du noyau martien, l'assemblage des noyaux ne fait que retarder le redémarrage de la dynamo préalablement arrêtée par la stratification thermique post-impact (Monteux et al., 2013; Monteux and Arkani-Hamed, 2014). Le temps nécessaire pour redémarrer la dynamo après impact géant et assemblage des noyaux est de l'ordre de $150 - 200$ Ma (Monteux and Arkani-Hamed, 2014).

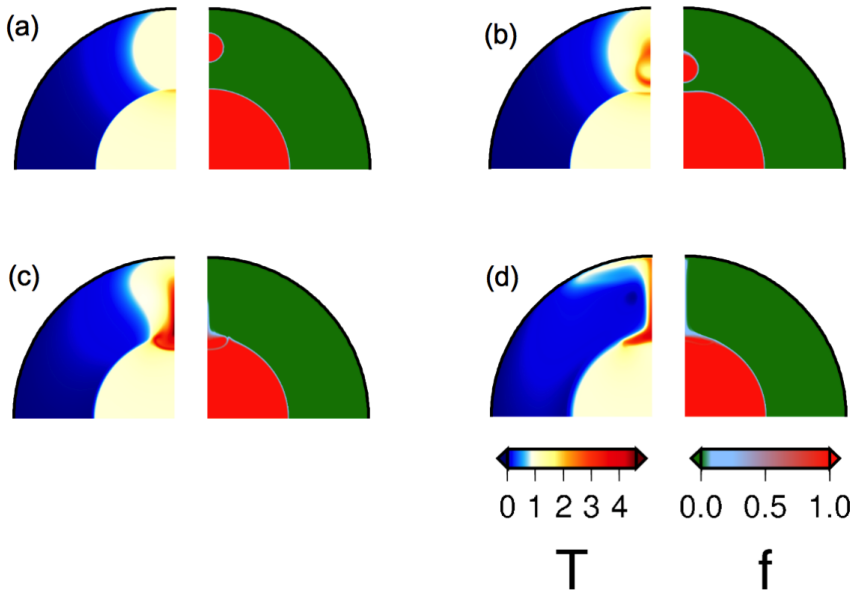

FIGURE 15 – *Température normalisée (gauche) et composition (droite) (pour le fer $f = 1$, pour les silicates $f = 0$) aux temps t = 0 (a), t = 0.6 Ma (b), t = 6 Ma (c) and t = 38.8 Ma (d) (résultats obtenus avec une viscosité uniforme, $R_{planete} = 3400$ km et $R_{impacteur} = 600$ km) (Monteux et al., 2013).*

4.2.2 Influence de l'état thermique post-impact du manteau sur la dynamo

Les propriétés thermiques du manteau jouent un rôle majeur sur la capacité du noyau sous-jacent à se refroidir et donc sur sa propension à générer un champ magnétique. Ainsi, la présence d'anomalies thermiques à la base du manteau peuvent engendrer des variations locales du flux de chaleur à la frontière manteau noyau. Si localement le manteau inférieur est chaud, le flux de chaleur à la CMB sera faible alors que des zones mantelliques profondes plus froides peuvent favoriser des flux de chaleur importants. Ces variations locales de flux de chaleur plus ou moins étendues peuvent avoir des conséquences importantes sur les mouvements convectifs à l'intérieur du noyau et sur la structure du champ magnétique généré.

Le contrôle du manteau sur les dynamos planétaires est souvent étudié en imposant des flux de chaleur hétérogènes à la limite noyau-manteau sur la frontière extérieure des simulations numériques de dynamo. Ces modèles entrent généralement dans deux catégories principales : Soit ils sont proportionnels aux modèles de tomographie sismique du manteau inférieur de la Terre pour simuler des conditions réalistes, soit ils sont représentés par des harmoniques sphériques simples pour une compréhension physique fondamentale. Cependant, en réalité,

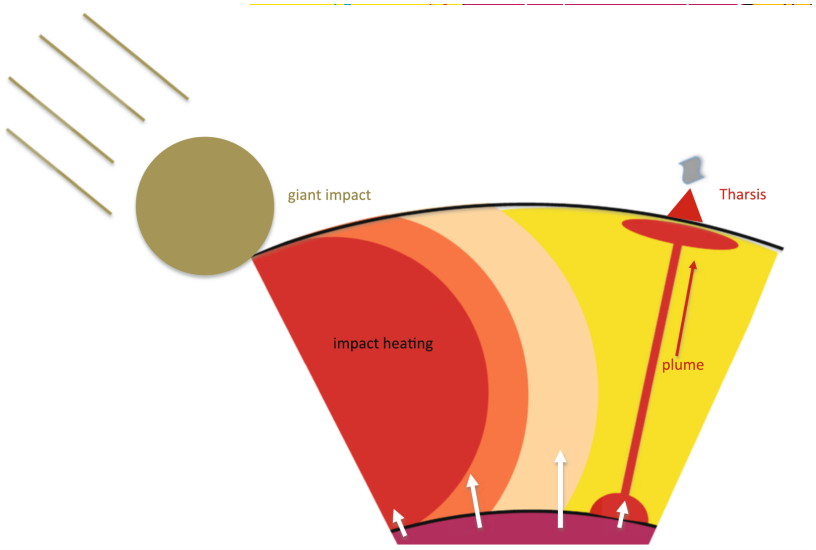

FIGURE 16 – *Representation schématique illustrant la complexité dynamique possible dans le manteau inférieur de Mars et pouvant motiver des modèles alternatifs de flux de chaleur à la CMB (À partir de Amit et al. (2015)).*

la dynamique du manteau inférieur est beaucoup plus compliquée et ces modèles de flux de chaleur à la CMB peuvent être un peu trop simplistes. Pour Mars, des modèles alternatifs ont été développés en considérant un chauffage localisé du manteau induit par un panache mantellique (Sreenivasan and Mark Jellinek, 2012) ou un impact géant (Kuang et al., 2014). En effet, lors d'un impact géant, le manteau se réchauffe significativement ce qui entraîne une modification du flux de chaleur à la frontière manteau/noyau (Figure 16). Ceci a pour effet de modifier les modalités de refroidissement du noyau et donc sa capacité à générer un champ magnétique (Buffett, 2002).

J'ai modélisé l'effet d'un impact géant sur le champ magnétique de Mars en considérant une anomalie thermique-post impact dans le manteau martien. J'ai déterminé les variations latérales de flux de chaleur ainsi que la réduction du flux de chaleur moyen à la CMB en fonction de la position géographique et de la taille de l'impact. J'ai ainsi pu imposer un flux de chaleur hétérogène à la frontière manteau/noyau comme condition aux limites dans un code de dynamo numérique (code MAGIC) et suivre l'évolution du champ magnétique martien après impact géant (Monteux et al., 2015). Un impact polaire (i.e. sur l'axe de rotation) entraîne une dichotomie magnétique Nord/Sud qui est plus forte que la dichotomie Est/Ouest générée par un impact à l'équateur. L'amplitude de la dichotomie est contrôlée par la vigueur de la convection elle-même fonction des variations latérales du flux de chaleur à la CMB. Nos résultats montrent qu'une hétérogénéité de flux de chaleur générée par un impact géant est plus efficace qu'une anomalie synthétique de degré 1 du flux de chaleur pour générer des dichotomies magnétiques hémisphériques. Nos résultats montrent qu'un impact entre Mars et un objet avec un rayon de ~ 1000 km a même pu enregistrer la dichotomie magnétique observée dans le champ crustal

martien si le refroidissement de l'océan magmatique post-impact a été suffisamment rapide (avec des temps inférieurs à 100 kyr).

Références personnelles

Monteux, J., Jellinek, A. M., Johnson, C. L., 2011, Why might planets and moons have early dynamos ?, Earth Planet. Sci. Lett., 310, 349–359. **LIEN HAL**

Monteux, J., Schaeffer, N., Amit, H., Cardin, P., 2012, Can a sinking metallic diapir generate a dynamo ?, J. Geophys. Res. (Planets), 117 (16), 10005. **LIEN HAL**

Monteux, J., Jellinek, A. M., Johnson, C. L., 2013. Dynamics of core merging after a mega-impact with applications to Mars' early dynamo ? Icarus 226, 20–32. **LIEN HAL**

Monteux, J., J., Arkani-Hamed, 2014. Consequences of giant impacts in early Mars : Core merging and Martian dynamo evolution, J. Geophys. Res. (Planets), Volume 119, Issue 3, pages 480–505. **LIEN HAL**

Monteux, J., Amit, H., Choblet, G., Langlais, B., Tobie, G., 2015, Giant impacts, heterogeneous mantle heating and a past hemispheric dynamo on Mars, Phys. Earth Planet. Int., 240, 114-124. **LIEN HAL**

Amit, H., Choblet, G., Olson, P., **Monteux, J.**, Deschamps, F., Langlais, B., Tobie, G., 2015 Towards more realistic core-mantle boundary heat flux patterns : a source of diversity in planetary dynamos, Prog. Earth. Planet. Sci., 2-26. **LIEN HAL**

(This is a sample cover image for this issue. The actual cover is not yet available at this time.)

Earth and Planetary Science Letters 310 (2011) 349–359

Contents lists available at SciVerse ScienceDirect

Earth and Planetary Science Letters

journal homepage: www.elsevier.com/locate/epsl

Why might planets and moons have early dynamos?

J. Monteux [a,*], A.M. Jellinek [a], C.L. Johnson [a,b]

[a] Department of Earth and Ocean Sciences, University of British Columbia, Canada
[b] Planetary Science Institute, Tucson, AZ, United States

ARTICLE INFO

Article history:
Received 17 September 2010
Received in revised form 5 August 2011
Accepted 9 August 2011
Available online xxxx

Editor: T. Spohn

Keywords:
early dynamos
growing planets
meteoritic impacts
numerical modeling

ABSTRACT

Remanent crustal magnetization of martian and lunar crustal rocks plausibly records magnetic fields related to core dynamos active during the first few hundred Myr of evolution of these bodies. Such early fields suggest that core dynamos may occur during or as a result of accretion. We investigate whether the processes governing the segregation and sinking of metallic Fe after a large impact can yield thermal conditions in the core that favor dynamo action on growing planets. Depending on the sizes of the impactor and planet, as well as the temperature-dependence of the viscosity, we identify conditions in which an early transient core dynamo is possible. We also consider the effect of a molten layer surrounding the protocore on the duration of this early dynamo. Our results suggest that dynamos can be initiated in bodies with a radius of 3500 km radius or greater under Earth-like conditions for ohmic dissipation in the core, and in smaller bodies if a less restrictive critical magnetic Reynolds number condition is applied. These dynamos may persist for several kyr to several Myr depending on the heat transfer regime at the protocore–mantle boundary.

1. Introduction

Among the terrestrial planets and moons of the inner Solar System, Mars and possibly the Moon record evidence for early and short-lived (a few hundred Myr) internally generated magnetic fields. Mars Global Surveyor and Lunar Prospector magnetometer data (Acuña et al., 1999; Hood et al., 2003) confirm the presence of ancient magnetized crust on these bodies. Although later dynamo fields (beginning around or after 3.9 Ga) have been suggested for both bodies (Cisowski et al., 1983; Schubert et al., 2000), most evidence points to earlier dynamos, that ceased by ~3.9 Ga (Garrick-Bethell et al., 2009; Johnson and Phillips, 2005; Lawrence et al., 2008; Lillis et al., 2008). Moreover, recent analyses of paleomagnetism in angrite meteorites suggest that an early and internally generated dynamo occurred within the angrite parent body (Weiss et al., 2008). Although there is increasing evidence for the occurrence of these transient dynamos, their origin and timing remain a major enigma. Here we investigate a plausible temporal link between early dynamos and the large impacts that characterize the late accretion histories of terrestrial bodies in our solar system. Assuming chondritic bulk compositions, these impacts can lead to extensive mantle melting, iron–silicate separation, iron segregation and ultimately core formation (Monteux et al., 2009; Ricard et al., 2009; Srámek et al., 2010; Tonks and Melosh, 1992). If dynamo action depends primarily on the rate of core heat loss (Buffett, 2002), then a crucial issue for explaining early dynamos is to understand the thermal states of both the impacted planet and the nascent core: under what conditions will the resulting core cooling be sufficiently large to favor dynamo action?

Large meteorite impacts can govern the early stages of planetary formation. Fig. 1 shows a schematic temporal evolution of our impact-induced dynamo model from time t_1 (impact time) to time t_5 (dynamo is initiated). A collision between an impactor and an undifferentiated protoplanet leads to an increase in mass of the impacted body, the formation of an impact basin, the propagation of shock waves (Fig. 1, t_1) and a localized temperature increase, ΔT_0, in a spherical region below the impact site (Fig. 1, t_2). All these processes are very fast compared to the following thermo-chemical re-equilibration. The temperature increase is constant within a spherical volume V_{ic} called isobaric core with radius R_{ic} and rapidly decreases away from it (Monteux et al., 2007; Pierazzo et al., 1997; Senshu et al., 2002). Assuming that meteorites impact at the escape velocity of the impacted body, this temperature increase scales with the size of the impacted planet and is superimposed on the initial mean temperature, T_0, of the planet before impact. For sufficiently large planets, the temperature increase can overcome the melting temperature of the metallic phase leading to metal–silicate separation (Monteux et al., 2009) (Fig. 1, t_3). The dense metallic phase sinks toward the center of the impacted body. How this occurs is debated. Proposed mechanisms include percolation through a solid mantle (Shannon and Agee, 1996; Stevenson, 1990), settling of cm-sized droplets in a magma ocean [e.g. (Rubie et al., 2003)] and to large mantle diapirs [e.g. (Ricard et al., 2009; Senshu et al., 2002; Tonks and Melosh, 1992)]. In addition, it has been proposed that metallic diapirs can sink toward the center of the planet via fracturation and diking (Solomatov, 2000; Stevenson, 2003b; Tonks and Melosh, 1992) or

* Corresponding author.
E-mail address: jmonteux@eos.ubc.ca (J. Monteux).

0012-821X/$ – see front matter © 2011 Elsevier B.V. All rights reserved.
doi:10.1016/j.epsl.2011.08.014

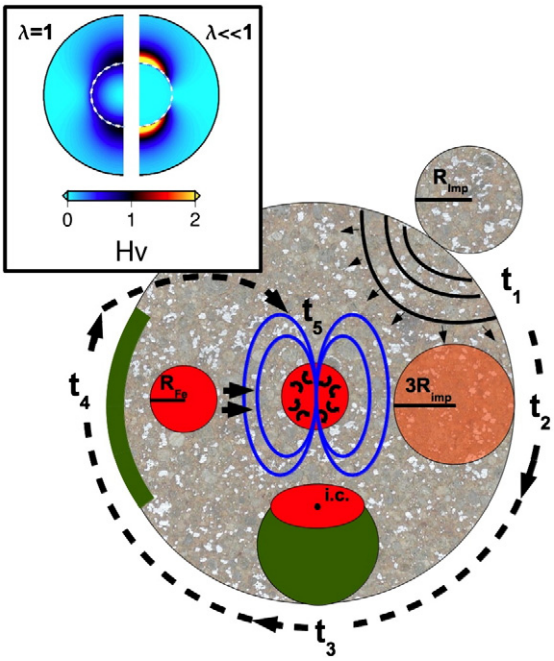

Fig. 1. Schematic view of the chemical equilibration following a large impact on an undifferentiated protoplanet. Within the isobaric region that results from the dissipation of the shock wave (time step t_1), the temperature increase (orange circle, t_2) melts the metal (red) that segregates rapidly from silicates (green) (t_3). The initial position of the inertial center of the iron diapir is indicated with a black dot (i.c.). Then the metallic phase sinks by a diapiric instability (t_4). Subsequent convection within the protocore can initiate an early magnetic field (t_5). The top left panel shows where viscous heating (H_v) occurs for a spherical density anomaly (i.e. a metallic protocore) outlined by the white dashed line within a Rybczynski–Hadamard analytical velocity field (see text for details). $H_v \sim \bar{\varepsilon}^2$ where $\bar{\varepsilon}$ is the dimensionless strain rate tensor. The viscous heating is shown for 2 viscosity ratios, λ, between the hot protocore and the cold undifferentiated material. For $\lambda = 1$ (uniform viscosity), viscous heating can occur within the sphere, while for $\lambda \ll 1$, viscous heating only occurs outside the sphere. Here, H_v is normalized by the maximum value of H_v when $\lambda = 1$. (For interpretation of the references to color in this figure legend, the reader is referred to the web version of this article.)

viscous deformation (Honda et al., 1993; Monteux et al., 2009) depending on the thermal state of the planet. Here, we consider a simplified scenario in which a single large impact into an initially undifferentiated planet leads to a single Fe-diapir that sinks through an effectively viscous mantle at a Stokes velocity (Fig. 1, t_4).

Whether convection and dynamo generation can occur in a liquid iron protocore depends on the temperature difference between the protocore and the surrounding mantle. A protocore sufficiently hotter than the surrounding silicate mantle is one way to explain the presence of an early dynamo on terrestrial planets and moons. Previous studies have examined the following possible causes of an early hot protocore and dynamo: radioactive heating (Nimmo, 2009; Williams and Nimmo, 2004; Yoshino et al., 2003), strong cooling by mantle convection (Breuer and Spohn, 2003; Elkins-Tanton et al., 2005; Nimmo and Stevenson, 2000; Stegman et al., 2003) or impact heating (Monteux et al., 2009; Reese and Solomatov, 2010). Here we focus on whether the thermal conditions resulting from a single large impact and the subsequent differentiation event are also favorable to dynamo initiation. In this case, the temperature difference between the protocore and the overlying mantle depends on the thermal evolution of the metallic diapir as it sinks through a colder mantle toward the center of the planet (Fig. 1, t_5). Because the heat content and buoyancy of the diapir depend on its volume, one critical parameter will be the radius of the metallic diapir R_{Fe}. An additional potentially important contribution to the initial core–mantle temperature difference will be the extent to which the gravitational potential energy released on sinking is converted into heat in the metallic diapir and in the surrounding mantle via viscous dissipation. The importance of this effect, and where it occurs (i.e., primarily in the diapir or surrounding mantle), will depend critically on the strongly temperature-dependent viscosity $\eta(T)$ of the rocks composing the protoplanetary mantle. For impacted planets of given radii R we use the numerical model of Monteux et al. (2009) to identify $R_{Fe} - R - \eta(T)$ conditions favoring dynamo action. In addition, we investigate the dependence of the dynamo duration on the protocore size, and on conditions that lead to melting of the overlying mantle material.

2. Thermo-chemical model

2.1. Initial state

The initial structure and thermal state of a growing planet depend particularly on the characteristics of its accretion (Kaula, 1979; Safronov, 1978). Indeed, differentiated terrestrial planets probably formed rapidly from accumulation of chondritic material (Agee, 1997). In more detail, during accretion, heating driven by a combination of the dissipation of impact energy and the decay of short lived radionuclides such as ^{26}Al and/or ^{60}Fe (Monteux et al., 2007; Senshu et al., 2002; Yoshino et al., 2003) increases the mean internal temperature and gives rise to a radial temperature gradient that depends on the accretion rate relative to the rate of radiative cooling to space. Where this growth rate is very high in comparison to surface cooling, this heating can ultimately cause partial or complete melting (Yoshino et al., 2003) and extensive internal differentiation. In contrast, where the growth rate is very low in comparison to surface cooling, little additional heating occurs (Wood et al., 2006) and the growing planet remains an undifferentiated mechanical mixture of the accreted impactors. Hence, depending on its growth rate, the frequency of impacts and the size of the impactors, a protoplanet can potentially grow to a Mars size radius in ≈1 Myr without undergoing any significant episodes of melting and any subsequent global differentiation processes (Senshu et al., 2002). Short-lived isotopic constraints restrict the timing of core formation on terrestrial planets to be within the first tens of Myr following accretion (Kleine et al., 2002; Touboul et al., 2007; Yin et al., 2002). From these models, the martian core formation occurred faster (within 30 Myr) than the Earth's core formation (within 50 Myr). Consequently, between 1 Myr (the growing planet reaches a Mars size radius with no or little differentiation) and 50 Myr (the core is fully formed), large impacts can lead to episodic large differentiation events. Depending on the thermal states of the resulting protocore and surrounding mantle, subsequent cooling may drive a core dynamo that generates a magnetic field observable at the surface.

Whether an impact onto an undifferentiated planet leads to melting and core formation depends critically on the fraction γ of the initial kinetic energy E_{kin} of the impactor that is dissipated within the planet itself as a result of work done by shock waves (Monteux et al., 2009; Tonks and Melosh, 1992). E_{kin} is proportional to the impact velocity v_{imp}^2, which can be decomposed into two contributions:

$$v_{imp}^2 = v_{esc}^2 + v_\infty^2. \quad (1)$$

Here, v_{esc} is the escape velocity of the impacted planet and v_∞ is the velocity of the impactor at a distance much greater than that over which the gravitational attraction of the impacted planet is important. A conservative and well-constrained estimate of E_{kin} is possible if we take $v_\infty = 0$ and assume $v_{imp} = v_{esc}$. We note that in the case of an impact on a moon orbiting around a larger central body, the gravitational attraction of the central body can increase this impact velocity and we address this issue in Section 5. Laboratory experiments and modeling studies suggest that the energy released within the planet is mainly dissipated by frictional heating and melting within a spherical region (an "isobaric core") with a volume V_{ic} that is at most 3 times larger than the volume of the impactor V_{imp} (Croft, 1982; O'Keefe and Ahrens, 1977; Pierazzo et al.,

1997; Senshu et al., 2002). Within this region the temperature increases uniformly from T_0 to $T_0+\Delta T_0$ where T_0 is the temperature of the impacted body before the impact and ΔT_0 is the temperature increase due to impact heating. Experiments suggest also that there is an additional thin spherical shell of damaged and heated material outside the isobaric core. Assuming that the work done by shock waves in this shell causes no melting, the excess temperature ΔT_0 decreases rapidly and smoothly with distance r across the shell as approximately $\Delta T_0(R_{ic}/r)^m$. Following Senshu et al. (2002), and fitting the decay of peak pressure with distance away from the edge of the isobaric core $m\approx 4.4$ (Monteux et al., 2007). Hence, the amount of energy E_{ext} dissipated as heat outside the isobaric core is:

$$E_{ext} = 2\pi\overline{\rho_0 C_p}\int_0^{\pi}\int_{R_{ic}}^{+\infty}\Delta T_0\left(\frac{R_{ic}}{r}\right)^m r^2\sin\theta d\theta dr \quad (2)$$

with θ as the zenith angle from the impact site and $\overline{\rho_0 C_p}$ is the average specific heat of the impacted body. For the axisymmetric geometry of the isobaric core, the previous equation can be reduced to:

$$E_{ext} = \overline{\rho_0 C_p} V_{ic}\Delta T_0\left(\frac{3(2m-5)}{2(m-3)(m-2)}\right). \quad (3)$$

Assuming that $v_{imp}=v_{esc}$ (Kokubo and Ida, 1996) and that $v_{ic}=3v_{imp}$ (Senshu et al., 2002), a balance between the kinetic energy delivered to heat the growing planet (γE_{kin}) and the energy used to heat up and melt the isobaric core and to heat up the surrounding material without melting is

$$\frac{4\pi}{9}\gamma G\rho_0^2 V_{ic}R^2 = \overline{\rho_0 C_p}\Delta T_0 V_{ic} + E_{ext} + V_{ic}(\rho_{Fe}f_0 L_{Fe} + \rho_{Si}(1-f_0)L_{Si}). \quad (4)$$

After some algebra we obtain the temperature increase at the impact site as a function of the impacted planet radius (Monteux et al., 2007)

$$\Delta T_0 = \frac{1}{h_m\overline{\rho_0 C_p}}\left[\frac{4\pi}{9}\gamma\rho_0^2 GR^2 - (\rho_{Fe}f_0 L_{Fe} + \rho_{Si}(1-f_0)L_{Si})\right]. \quad (5)$$

Here, G is the gravitational constant, ρ_0 is the density of the undifferentiated planetary material, R is the radius of the impacted planet. L_{Fe} and L_{Si} are the latent heat required for melting respectively the metallic and the silicate phases. f_0 is the volume fraction of metal in the impacted planet. From Eqs. (3), (4), and (5), h_m represents the amount of heat that is used to increase the temperature inside and outside the isobaric core relative to the amount of heat used to increase the temperature by ΔT_0 within the core and (Monteux et al., 2007)

$$h_m = 1 + \frac{3(2m-5)}{2(m-3)(m-2)} \approx 2.7. \quad (6)$$

Because ΔT_0 depends on γ, the value for γ requires some discussion. O'Keefe and Ahrens (1977) show that γ depends on the impact velocity and that the fraction of energy converted into heat increases with impact velocity. Our assumption that $v_{imp}=v_{esc}$ implies that our modeled impactors are in a "slow impactor regime". From the measurements of O'Keefe and Ahrens (1977) a reasonable value for γ is 0.3. We apply this value in our calculations and discuss the influence of the uncertainty of this choice in Section 5. An additional issue that requires mention is the assumption that there is no melting in the spherical shell around the isobaric core. For $\gamma=0.3$, calculation of ΔT_0 as a function of planet radius shows that this approximation is strictly appropriate for planetary radii less than about 4000–4500 km. For larger planets, latent heat may be consumed outside the isobaric core and so ΔT_0 calculated with Eq. 5 may be overestimated. The magnitude of the overestimate is, however, unclear because the effect of melting on the presence and structure of the spherical shell region bounding the isobaric core is unknown. Nevertheless, assuming that the geometry of the region is similar to the case without melting, calculations show that the uncertainty in the value for γ will have a greater influence on our estimates for ΔT_0.

The magnitude of the temperature increase in Eq. 5 depends on the two terms in square brackets: the left-hand term describes the kinetic energy released to heat the mantle on impact and the right-hand term is the latent heat consumed to melt the silicate and iron components of the mantle. For iron–silicate segregation to occur in the heated volume, ΔT_0 must be positive and a sketch of the thermal state following impact is shown in Fig. 1 (t_2). Thus, equating the two terms in parentheses in Eq. 5 gives a critical impacted planet radius above which segregation is possible:

$$R_{crit} > \left[\frac{\rho_{Fe}f_0 L_{Fe} + \rho_{Si}(1-f_0)L_{Si})}{4\pi/9\gamma\rho_0^2 G}\right]^{1/2}. \quad (7)$$

For parameter values listed in Table 1, $R_{crit}=$ 1620 km. Hence, impact heating on a Moon to a Mars-sized body will result in the separation of the dense iron phase from the silicate phase as a metallic diapir (Fig. 1). We note that whereas our assumption that $v_{imp}=v_{esc}$ is appropriate for most planets, for moons this simplification underestimates the impact velocity, which will be governed by the gravitational potential of the central body and leads to a lower bound on ΔT_0.

This temperature increase is superimposed on the pre-impact thermal regime of the protoplanet. The background thermal state depends on the accretionary process, which can lead to a temperature profile that increases with radius toward the surface (Senshu et al., 2002), and on the strong early rate of radiogenic heating, which augments the mean internal temperature of the planet (Yoshino et al., 2003). For simplicity we assume that T_0 is uniform and close to the eutectic temperature of the Fe–FeS system at 1 bar (Fei et al., 1997) and that the impacted body before the impact is a homogenous mixture of silicate and metal.

For a given initial bulk composition, the radius of the diapir separated after a large impact R_{Fe} is a function of the impactor size R_{imp} and f_0 in the impacted planet and scales as $R_{Fe}=(3f_0)^{1/3}R_{imp}$

Table 1
Typical parameter values for numerical models.

Planet radius	R	2000–4000 km
Diapir (protocore) radius	R_{Fe}	150–500 km
Density difference	$\Delta\rho_0$	4500 kg m^{-3}
Average density	ρ_0	4270 kg m^{-3}
Iron density	ρ_{Fe}	8000 kg m^{-3}
Silicate density	ρ_{Si}	3500 kg m^{-3}
Mean thermal expansion	α	4.4×10^{-5} K^{-1}
Iron thermal expansion	α_{Fe}	1.5×10^{-5} K^{-1}
Silicate thermal expansion	α_{Si}	5×10^{-5} K^{-1}
Iron heat capacity	$C_{p,Fe}$	800 J K^{-1} kg^{-1}
Silicate heat capacity	$C_{p,Si}$	1000 J K^{-1} kg^{-1}
Average specific heat of the impacted body	$\overline{\rho_0 C_p}$	4×10^6 J K^{-1} m^{-3}
Initial temperature	T_0	1250 K
Iron melting temperature	$T_{melt,Fe}$	1250 K
Silicate melting temperature	$T_{melt,Si}$	1650 K
Iron latent heat	L_{Fe}	4×10^5 J kg^{-1}
Silicate latent heat	L_{Si}	2.7×10^5 J kg^{-1}
Thermal diffusivity	κ	10^{-6} m^2 s^{-1}
Mean thermal conductivity	$k=k_{Si}$	4 W m^{-1} K^{-1}
Iron thermal conductivity	k_{Fe}	40 W m^{-1} K^{-1}
Metal content	f_0	0.17
Reference viscosity	η_0	10^{22} Pa s
Impact energy conversion coefficient	γ	0.3–0.5
Volume effectively heated by impact	h_m	2.7
Gravitational constant	G	6.67×10^{-11}m^3 kg^{-1} s^{-2}
Average magnetic field strength	$\overline{B}$	2.5 mT
Magnetic diffusivity	ν	2 m^{2}s^{-1}
Magnetic permeability	μ	$4\pi\times10^{-7}$ H m^{-1}

(Monteux et al., 2009). The metal diapir sinks toward the center of the planet over time-scales from several kyr to several Myr depending on the rheology of the protoplanetary mantle. Once at the center of the undifferentiated planet, this "metallic diapir" will be referred to as a "protocore".

2.2. Heat partitioning during the sinking of the diapir

The initial thermal state of the protocore is governed by its volume and the rate and location of viscous dissipation during its sinking, which depends on the viscosity ratio λ (lower than 1) between the hot protocore and the relatively cold undifferentiated surrounding mantle (Ke and Solomatov, 2009). For a given λ the rate of viscous dissipation depends on the shear strain rate $\dot{\varepsilon}^2$, where $\dot{\varepsilon} \sim V_S / R_{Fe}$ and V_S is the sinking velocity. Monteux et al. (2009) showed that for small diapirs (i.e., $R_{Fe}<70$ km), the rate of viscous dissipation is negligible and the metallic phase only cools during its sinking. In contrast, for $R_{Fe}>70$ km and for mantle and diapir viscosities that are equal (uniform viscosity), viscous deformation within the diapir and the surrounding mantle leads to dissipation that can increase the temperature of the metal diapir over its initial value from T_0 to $T_{core}>T_0+\Delta T_0$.

Fig. 1 (top left panel) shows where the viscous heating occurs when a spherical metallic diapir sinks within a Rybczynski–Hadamard analytical velocity field (Hadamard, 1911; Rybczynski, 1911) for 2 different viscosity ratios λ. For a uniform viscosity (λ=1), viscous coupling between the metallic diapir and the surrounding material occurs and a fraction of gravitational energy is converted to heat up the diapir. However, for small viscosity ratios ($\lambda<\mathcal{O}(10)^{-2}$), viscous heating is restricted to the surrounding mantle and is concentrated at the diapir's poles where strain rates are greatest (Fig. 1, top left panel and Samuel et al., 2010). In this case, the initial temperature of the protocore is lower than in the isoviscous case and remains close to the initial temperature of the diapir (i.e. $T_{core}=T_0+\Delta T_0$).

2.3. Dynamical model for the sinking of an iron diapir

2.3.1. Physical model

To investigate the dynamics of the metallic diapir separated after a large impact, we adapt the numerical finite volume model in spherical axisymmetric geometry of Monteux et al. (2009). In particular, neglecting the effects of adiabatic compression, conservation of energy applied to an undifferentiated planet of radius R leads to

$$\frac{DT}{Dt} = \frac{\nabla^2 T}{Ra_\chi} + D_\chi \frac{\eta}{\eta_0}\Omega. \tag{8}$$

where T and t are dimensionless temperature and time (T and t are respectively normalized by ΔT_0 and by a Stokes time $t_{Stokes}=\eta_0/\Delta\rho g_0 R$). $Ra_\chi = \frac{\Delta\rho_0 g_0 R^3}{\kappa\eta_0}$ is the compositional Rayleigh number and $D_\chi = \frac{\Delta\rho_0 g_0 R}{\rho_0 C_p \Delta T_0}$ is the dissipation number (with κ the heat diffusivity and $\rho_0 C_p$ the average specific heat of the impacted body). $\Delta\rho_0$ is the density difference between metal and silicates. g_0 is the gravity at the surface of the impacted protoplanet. ΔT_0 is the density difference between metal and silicates. g_0 is the gravity at the surface of the impacted protoplanet. ΔT_0 is the initial impact induced temperature increase below the impact site. Ω is the dimensionless dissipation function and expresses the conversion of potential energy into heat:

$$\Omega = \tau : \nabla \mathbf{v} \tag{9}$$

where τ is the dimensionless deviatoric stress tensor and $\mathbf{v}$ is the non-dimensional velocity (normalized with $v_{Stokes}=R/t_{Stokes}$). Prior to impact, we assume a homogenous temperature T_0 of the growing planet. The viscosity is $\eta=\eta_0\lambda^T$ where $\eta_0=\eta(T_0)$ is the viscosity of the cold undifferentiated material at the start of the experiment (Ratcliff et al., 1997; Ziethe and Spohn, 2007).

Assuming that the protoplanet is incompressible, the other dimensionless governing equations are continuity

$$\nabla \cdot \mathbf{v} = 0, \tag{10}$$

and momentum conservation assuming infinite Prandtl number

$$-\nabla P + \nabla \cdot \left(\frac{\eta}{\eta_0}\left[\nabla\mathbf{v} + [\nabla\mathbf{v}]^T\right]\right) + \left(\frac{T}{B} - f\right) r\mathbf{e_r} = 0, \tag{11}$$

where P and r are the non-dimensional pressure and radius (P and r are respectively normalized by η_0/t_{Stokes} and R). $\mathbf{e_r}$ is the radial unit vector and f represents the volume fraction of metal. Following Monteux et al. (2009), we introduce the buoyancy ratio $B=\Delta\rho_0/(\rho_0\alpha\Delta T_0)$ where ρ_0 and α are the density and thermal expansion of the undifferentiated material (see Table 1 for values). Gravity depends on the radial position r and $g(r) = \frac{4}{3}G\pi\rho_0 r = g_0\frac{r}{R}$.

After an impact and the subsequent differentiation, the metallic phase and the purely silicate phase are separated within the thermal anomaly (Fig. 1, t_3). Hence a chemical readjustment occurs leading to the sinking of the dense iron though the lighter undifferentiated material. The buoyancy force that drives the flow of the diapir toward the center of the protoplanet increases with the volume fraction of metal f. In our models, we consider only two chemical phases meaning that f varies between 1 (pure metal) and 0.17 (undifferentiated material with chondritic composition). During sinking, chemical diffusion is negligible. The metal volume fraction f is then simply advected by the flow:

$$\frac{\partial f}{\partial t} + v \cdot \nabla f = 0. \tag{12}$$

2.3.2. Simplifications of the governing equations

We make a number of approximations to simplify the analysis of the initial thermal state of the protocore. We neglect the thermal buoyancy T/B in the momentum equation as the buoyancy number B is very large (the density difference between metal and silicates is 140 to 560 times larger than the thermal density variations). In addition, in treating the metal–silicate separation, our model neglects multi-phase dynamics associated with core–mantle segregation (Golabek et al., 2008; Srámek et al., 2010).

Prior to the impact, the planet is undifferentiated meaning that the impact and the subsequent local differentiation lead to the first episode of core formation. Moreover, as this study focuses on the thermal state of the metallic phase once at the center of the planet, we do not consider the dynamical effects of the purely silicate phase that spreads beneath the impacted planet surface while the diapir sinks to the center of the planet (Monteux et al., 2009; Reese and Solomatov, 2006).

2.3.3. Numerical model

We implement a finite volume numerical model to solve Eq. 8, Eq. 10, Eq. 11 and Eq. 12 in axisymmetric spherical geometry in a 200×400 grid. We use a stream function formulation for the equations of motion with a direct implicit inversion method (Schubert et al., 2001). Eq. 8 and Eq. 12 are solved by an Alternating Direction Implicit (ADI) scheme (Peaceman and Rachford, 1955; Douglas, 1955). The stream function, temperature and compositional fields are described by a second-order approximation in space. To limit numerical diffusion when solving the transport equations, especially for the compositional field, we use a Total Variation Diminishing Superbee scheme (Laney, 1998; Roe, 1986) implemented in an implicit way (Srámek et al., 2010) which enables high resolution of purely advective fields. Mechanical boundary conditions are free-slip at the surface and along the symmetry axis. Thermal boundary conditions are isothermal at the surface and insulating along the symmetry axis.

3. Magnetic field considerations

3.1. Temperature of the protocore

Once at the center of the planet, core cooling depends on the temperature of the protocore and the thermal state and melting temperature of the silicate at the protocore–mantle boundary. As discussed above, the temperature of the protocore depends on the post-impact temperature difference ΔT_0 (cf. Eq. 5). The maximal temperature increase after sinking is (Monteux et al., 2009):

$$\Delta T \approx \Delta T_0 \left(1 + a(\lambda)\left(\frac{r_0}{R}\right)^2 \frac{\Delta\Theta}{\Delta T_0}\right), \tag{13}$$

where $a(\lambda)$ is the fractional amount of viscous dissipation in the metal during the sinking of the iron toward the center of the planet. r_0 is the initial distance between the inertial center of the metallic diapir (noted i.c. in (Fig. 1, t_3)) and the center of the planet before the diapir starts to sink. $\Delta\Theta$ is the maximum temperature increase in the unrealistic case in which all the potential energy released by the diapir is used to heat up the metal phase. Assuming the impact velocity is the escape velocity of the planet (cf., Section 2) then $\Delta\Theta/\Delta T_0$ is constant, independent of the planet size and equal to 11.8 (Monteux et al., 2009) and the temperature of the metallic phase at the end of the sinking is

$$T_{core} \approx T_0 + \Delta T = T_0 + \Delta T_0 \left(1 + a(\lambda)\left(\frac{r_0}{R}\right)^2 \frac{\Delta\Theta}{\Delta T_0}\right). \tag{14}$$

During the sinking of the metallic diapir, its pressure increases and leads to additional heating by compressional effects. This heating process is inversely proportional to the buoyancy ratio B (Monteux et al., 2009). In our models, B is large enough to consider that this thermal effect is negligible compared to viscous heating (Samuel and Tackley, 2008).

3.2. Conditions for an early magnetic field

Three conditions are required to drive a dynamo on a growing planet:

1. The heat flow Q out of the core must exceed the adiabatic value Q_A such that convection can occur (Stevenson et al., 1983). This condition is

$$Q > Q_A = \frac{k_{Fe}\alpha_{Fe}g_c T_{Fe}}{C_{p,Fe}} 4\pi R_{Fe}^2 \tag{15}$$

where k_{Fe}, α_{Fe}, T_{Fe} and $C_{p,Fe}$ are respectively the thermal conductivity, the thermal expansion, the temperature and the heat capacity of the metallic phase and g_c is the gravity at the surface of the protocore (see Table 1 for values). In our model, once the metallic phase has reached the center of the impacted planet, T_{Fe} decreases monotonically with time due to heat conduction to the surrounding mantle.

2. The ratio of the rate at which gravitational potential energy is released by convection to the rate of ohmic dissipation, Φ, must exceed a critical value (Buffett, 2002):

$$\frac{Q}{\Phi} > \frac{1}{\epsilon_T}. \tag{16}$$

Here, ϵ_T is the Carnot-style efficiency for thermal convection. We note that a dynamo can be generated even with a subadiabatic heat flow if the compositional convection is important (Buffett, 2002; Christensen and Wicht, 2008). However, here we consider neither this mechanism or effects related to the presence of an inner core. Assuming that the characteristic length scale of the flow leading to magnetic field generation is the radius of the protocore, Φ can be approximated as (Buffett, 2002):

$$\Phi = \left(\frac{\nu\overline{B}^2}{\mu}\right) \frac{4}{3}\pi R_{Fe}, \tag{17}$$

where $\overline{B}$ is the average strength of the magnetic field within the core, ν is the magnetic diffusivity and μ is the magnetic permeability (see Table 1 for values). In the absence of constraints on $\overline{B}$ for early planets, we assume a current Earth-like value of 2.5 mT (Kuang and Bloxham, 1997) that is independent of the protocore size or the planetary radius. The efficiency of thermal convection is then given by (Buffett, 2002)

$$\epsilon_T = \frac{0.8\pi}{3}\frac{\alpha_{Fe}G\rho_{Fe}R_{Fe}^2}{C_{p,Fe}}\left(1-\frac{Q_A}{Q}\right), \tag{18}$$

where ρ_{Fe} is the density of the metallic phase and G is the gravitational constant.

3. The structure of the convective motions carrying magnetic field lines must be sufficiently complicated to favor self-sustaining dynamo action. A measure of this complexity is that the magnetic Reynolds number (Christensen and Aubert, 2006)

$$Re_m = \frac{UL}{\nu} > Re_m^{crit} = O\left(10-10^2\right). \tag{19}$$

Here, L and U are the characteristic length and velocity scales for the flow within the protocore and ν is the magnetic diffusivity of the metal phase. Whereas the natural length scale in the problem is the depth of the convecting iron layer, the choice of an appropriate velocity scale depends on the leading order force balance (Christensen, 2010). As the rotation rate of growing planets is potentially time-dependent and poorly constrained a convenient and reasonable choice is based on a balance between inertial and buoyancy forces and is (Stevenson, 2003a):

$$U \sim \left(\frac{q\alpha_{Fe}g_c R_{Fe}}{\rho_{Fe}C_{p,Fe}}\right)^{1/3}, \tag{20}$$

where q is the heat flux out of the core ($q = Q/(4\pi R_{Fe}^2)$). Taking $L = R_{Fe}$, $g_c = 4/3\pi G\rho_{Fe}R_{Fe}$, the combination of Eqs. 19 and Eq. 20 leads to the condition

$$Re_m = \left(\frac{4\pi G q\alpha_{Fe}R_{Fe}^2}{3C_{p,Fe}}\right)^{1/3}\frac{R_{Fe}}{\nu} > O\left(10-10^2\right) \tag{21}$$

Among the three criteria above, the first is typically considered a necessary condition for a thermally-driven dynamo. (Subadiabatic dynamos are possible if e.g., compositional gradients also drive convection.). As we shall see in Section 4, this condition ($Q > Q_A$) is easily met in our models. However it is not a sufficient condition for dynamo action, as indicated by the other two conditions. The second condition assumes an Earth-like dynamo: in particular it assumes an Earth-like value for the root mean square magnetic field in the core, a particular efficiency for conversion of gravitational potential energy into magnetic energy and a particular toroidal-to-poloidal field conversion efficiency. The third condition is a more general criterion for dynamo action, and whereas scalings other than Eq. 20 for the velocity field are possible, we have chosen one that does not depend upon knowing the early rotation rate of the planet or moon.

3.3. Heat flow across the protocore: analytic considerations

The three conditions required for an early dynamo (Eq. 15, Eq. 16 and Eq. 21) all impose conditions on the heat flow out of the protocore. At the protocore–mantle boundary there are two asymptotic heat transfer regimes. The first is a conductive transfer across a thermal boundary layer growing on the mantle side where the corresponding heat flow Q_{cond} is:

$$Q_{cond} \sim \frac{4\pi k \Delta T R_{Fe}^2}{\delta} \tag{22}$$

where $\delta \approx 2\sqrt{\kappa t}$ is the thickness of the conductive boundary layer at any time t. As t becomes large $\delta = c_2 R_{Fe}$ (where c_2 is an order 1 constant (Monteux et al., 2009)). k is the thermal conductivity of the surrounding material. For computational reasons, in our numerical models, we make the approximation that thermal conductivities for metallic and undifferentiated material are the same (i.e., $k = k_{Fe} = k_{Si}$, Table 1). In reality, the thermal conductivity of the core material is ≈ 10 times bigger than the conductivity for the silicates. Hence, this simplification underestimates the protocore heat flow and our criteria for dynamo action is more restrictive than in the more realistic case of unequal silicate and metal thermal conductivities.

As illustrated in Fig. 2, the temperature of the protocore might overcome the solidus temperature of the surrounding material depending on its chemical composition and on the impacted planetary radius. Hence, a melt layer may form above the protocore (see also Section 5.2). As this melt layer grows in thickness with time (and assuming it is greater than a few tens of meters thick), vigorous convection will enhance core cooling over the conductive case and lead to a heat flow that is independent of the thickness of the melt layer and of the form (Turner, 1973):

$$Q_{conv} \sim 0.8\pi R_{Fe}^2 \left(\frac{\rho_{Si}^2 g_c \alpha_{Si} k^2 C_{p,Si}}{\mu_{melt}} \right)^{1/3} \left(T_{core} - T_{melt,Si} \right)^{4/3} \tag{23}$$

where ρ_{Si}, α_{Si}, $C_{p,Si}$ and μ_{melt} are respectively the density, the thermal expansion, the heat capacity and the viscosity of the molten silicate layer (see Table 1 for typical values). Eventually, the heat flux out of the core will, of course, become balanced by the heat flux across the overlying solid mantle and the melt layer will have a quasi-steady thickness.

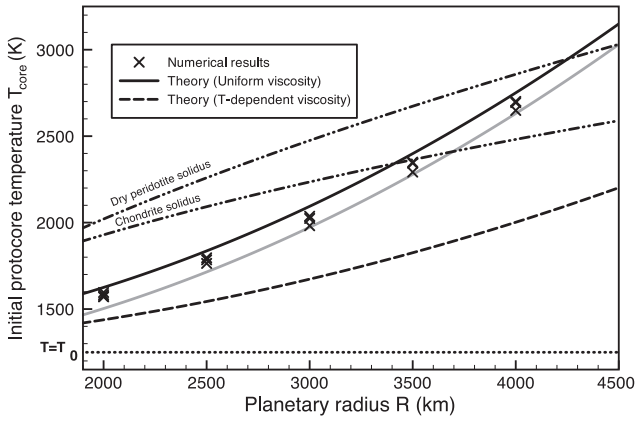

Fig. 2. Initial temperature of the protocore once at the center of the planet as a function of the planetary radius. Each symbol represents a numerical result for a given R_{Fe} (R_{Fe} in the range of 150–500 km) for a uniform viscosity. Theoretical predictions for T_{core} from Eq. 14 are given for uniform viscosity (black solid line, $a(\lambda) = 15\%$) and temperature dependent viscosity (black dashed line, $a(\lambda) = 0\%$). The black solid line is without melting and the gray one is with melting. The region in between defines the range of initial protocore temperature (see Eq. 5). The dotted line shows $T = T_0$. The chondritic solidus (Agee, 1997) and the dry peridotite solidus (Zerr and Boehler, 1994) at $P = P_{CMB}$ are represented with dashed-double-dotted lines (see Section 5.2 for calculation details).

4. Numerical results

4.1. Diapir descent: the initial protocore temperature

In our models, where we specify the viscosity of the impacted planet as $\eta_0 = 10^{22}$ Pas, metallic diapirs descend to the center of the planet relatively quickly (e.g. in less than 10 Myr for $R_{Fe} = 400$ km) (Monteux et al., 2009). During the sinking of the diapir the temperature difference between the protocore and the mantle increases rapidly in response to viscous heating depending on the fraction of gravitational energy converted into heat ($a(\lambda)$). Then this temperature difference decreases as the diapir cools once it reaches the center of the planet.

We investigate T_{core} for diapirs in the range of 150–500 km and planet radii in the range of 2000–4000 km. For the diapir radii range studied here, the protocore temperature at the end of sinking is given by Eqs. 13 and 14. The results from our numerical models for uniform viscosity contrasts are shown in Fig. 2 and are in agreement with Eq. 14. Theoretical predictions of T_{core} are represented in Fig. 2 with and without taking into account the effect of melting in the isobaric core after impact (gray and black solid lines respectively). The region in between defines the range of initial temperature and the difference between these two theoretical models is within the range of uncertainties of γ. For a uniform viscosity, viscous coupling between metal and undifferentiated mantle material is important and $a(\lambda) \approx 15\%$ (Monteux et al., 2009). As the viscosity contrast between the hot metallic phase and the surrounding mantle increases, the fraction of gravitational potential energy converted into heat in the metallic phase decreases (see Section 2.2). That is, as the mantle/core viscosity ratio becomes very large $a(\lambda) \to 0$ and viscous dissipation is concentrated in the mantle (Monteux et al., 2009). In this limit, the initial temperature of the protocore after the sinking is $T_{core} = T_0 + \Delta T_0$. The predictions of Eq. 14 for this asymptotic case are shown in Fig. 2 (dashed line). As expected, the reduced dissipation in the metallic diapir leads to a lower predicted T_{core}.

A high temperature contrast between the protocore and the surrounding undifferentiated mantle can eventually lead to the formation of a molten layer above the protocore-mantle boundary. In Fig. 2, we include the chondrite solidus temperature from Agee (1997) and the dry peridotite solidus from Zerr and Boehler (1994) at the center of the impacted planet as a function of the planetary radius. This effect will be more precisely discussed in Section 5.2.

Because of the practical difficulty in obtaining accurate solutions for very large viscosity variations, we restrict our numerical studies to the isoviscous case, which is well-explained by our theory. The agreement between our isoviscous theory and the numerical solutions gives us confidence that application of the theory for the variable viscosity case is justified. From Fig. 2 these isoviscous solutions will overestimate the core temperature by $\approx 10-40\%$, depending on the protoplanetary radius. Thus, quantitatively, the uncertainties of this enhanced heat flow for predicting dynamo action are not so large. From Eq. 13, assuming $a(\lambda) = 15\%$, the temperature difference between the protocore and the cold surrounding material in the isoviscous model is overestimated by a factor ≈ 2.8. From Eq. 21 $Re_m \propto Q^{1/3} \propto \Delta T^{1/3}$ and, thus, the magnetic Reynolds number will be a factor of about 1.4 too large (i.e., it is still accurate to $O(1)$).

4.2. Dynamo initiation in a conductive heat transfer case

To determine whether or not a dynamo is initiated in the protocore, we monitor the average heat flow Q across the protocore–mantle boundary as a function of time for a wide range of $R - R_{Fe}$ conditions. We stop calculations 50 Myr after the impact because at this time the

core is probably fully formed and because of the potential onset of mantle convection, the thermal consequences of which are beyond the scope of this paper (Behounkova and Choblet, 2009).

For all the $R-R_{Fe}$ range studied here, conditions studied, we find that $Q>>Q_A$ after impact, which means that core convection can occur (see Eq. 15). For example, once a metallic diapir with $R_{Fe}=300$ km has reached the center of a planet with radius $R=3500$ km, it starts to cool and over the 50 Myr period studied, Q/Q_A decreases from 32.5 to 20. For $R=2000$ km, Q/Q_A decreases from 15 to 10 over the same time interval (in the calculation of Q_A we consider that $k_{Fe}=40\ \mathrm{W\ m^{-1}\ K^{-1}}$). Assuming that the thickness of the thermal boundary layer around the protocore scales with the size of the protocore, this corresponds to a temperature difference of ≈300 to 2700 K between the metallic phase and the overlying mantle material (see Fig. 2). However, as discussed in Section 3, this condition alone does not guarantee dynamo action, and so we next examine the additional requirements for a dynamo.

In the special case of the impacted planet being Earth-like from a magnetic perspective, convection within the protocore has to be sufficiently vigorous to supply energy at a rate that compensates for the loss due to ohmic decay. We monitor the ratio of the heat flow to the ohmic dissipation as a function of time. Assuming a conductive heat transfer across the protocore mantle boundary, $k=k_{Si}$ and $\delta\sim R_{Fe}$, from Eq. 13, Eq. 17 and Eq. 22 we obtain

$$\left(\frac{Q_{cond}}{\Phi}\right)\sim\frac{3\mu k\Delta T_0}{\nu\overline{B}^2}\left(1+a(\lambda)\frac{\Delta\theta}{\Delta T_0}\right), \tag{24}$$

which is a conservative bound on whether a dynamo will occur (we consider here that $r_0/R\approx 1$). $a(\lambda)$ and $\Delta\theta/\Delta T_0$ are independent of R. However, from Eq. 5, $\Delta T_0\propto R^2$. Hence, (Q_{cond}/Φ) varies with R^2. Fig. 3 shows Q/Φ as a function of the planet radius for different iron diapir sizes and different times (1 Myr and 50 Myr), after the diapir reaches the center of the impacted planet. The dashed line is the theoretical prediction from Eq. 24 for a uniform viscosity case (i.e., $a(\lambda)=15\%$). Numerical results are consistent with Eq. 24 at very early time (just after the metallic diapir has reached the center of the planet). At larger times, the protocore cools down and Q/Φ decreases. The temperature of the metallic phase after sinking and hence the initial heat flow across the protocore is a sensitive function of the viscosity contrast between the metallic phase and the surrounding mantle (see Section 3.2). The theoretical value of the initial conductive heat flow when the viscosity of the hot metallic fraction is much smaller than the viscosity of the relatively cold undifferentiated material is given by Eq. 13 and Eq. 22 with $a(\lambda)=0\%$. The black dotted line in Fig. 3 shows the corresponding theoretical prediction for (Q_{cond}/Φ) immediately after sinking as a function of R for $a(\lambda)=0\%$. In this case, the theoretical value for (Q_{cond}/Φ) is different by a factor of 2.8 compared with the uniform viscosity case, consistent with expectations from Rybczynski–Hadamard effects.

In all sets of planetary and metallic diapir radii studied here $Q>>Q_A$. Consequently, the condition for the presence of a dynamo from the combination of Eq. 16 and Eq. 18 simplifies to:

$$\frac{Q}{\Phi}>\frac{3}{0.8\pi}\frac{C_{p,Fe}}{G\alpha_{Fe}\rho_{Fe}R_{Fe}^2} \tag{25}$$

Fig. 4 shows Q/Φ as a function of the protocore radius resulting from a single impact for different planet sizes in uniform viscosity cases. For $t=1$ Myr after the end of the sinking (black filled symbols), and for a given planetary radius, different trends appear as a function of R_{Fe}. The ratio Q/Φ is initially larger for larger bodies because $Q\propto\Delta T_o\propto R^2$. However, as mentioned in Section 2.2 when $R_{Fe}<70$ km, no viscous heating occurs during the sinking (Monteux et al., 2009) as cooling by diffusion overwhelms viscous heating. As R_{Fe} increases from 70 km radius, viscous heating becomes more and more efficient and leads to an increase of the initial heat flux and as a consequence of Q/Φ. When R_{Fe} reaches a critical value (≈300 km), the simplification $r_0/R=1$ is less and less valid since the diapir is initially buried deeper. Hence, for a given R, as R_{Fe} increases r_0/R decreases so the initial temperature of the protocore, the heat flux and Q/Φ also decrease. With subsequent cooling, the reduction in core temperature over a given time period Δt, say, scales as $Q\Delta t\,/\left(\overline{\rho C_p}R_{Fe}^3\right)$. Because heat flow will decline with the core–mantle temperature difference, and the incremental change in core temperature $\propto(1/R_{Fe}^3)$, small protocores cool faster than big ones. Hence, for a given R, and for $t=50$ Myr after the end of the sinking (white filled symbols), Q/Φ increases as a function of R_{Fe}.

In Fig. 4, the black dashed line represents the condition required to get a dynamo from Eq. 25. Results show that a dynamo is difficult to initiate with a small protocore (i.e. small impactors). Once the protocore

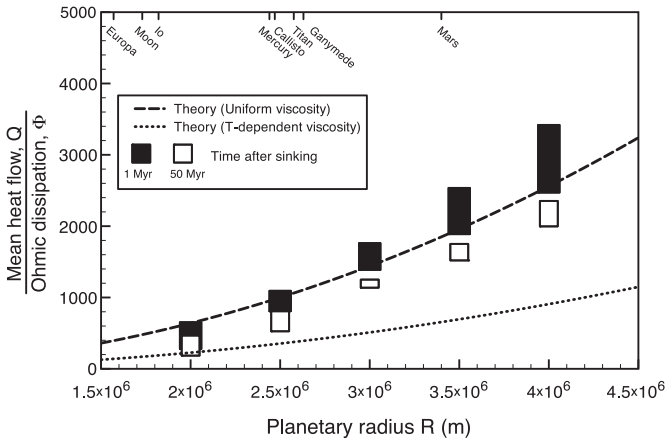

Fig. 3. Temporal evolution (symbols from black to white) of the ratio Q/Φ as a function of the planetary radius. For each planetary radius, we investigated several diapir sizes at times $t=1$ and 50 Myr for a uniform viscosity. The length of the rectangles represents the variation of Q/Φ for the range of diapir sizes. The width of each rectangle is arbitrary. Theoretical predictions for (Q_{cond}/Φ) at $t=0$ Myr from Eq. 24 for uniform viscosity (black dashed line, $a(\lambda)=15\%$) and temperature dependent viscosity (black dotted line, $a(\lambda)=0\%$) are shown. Planetary and moon radii of small solar system objects are indicated on the top x-axis.

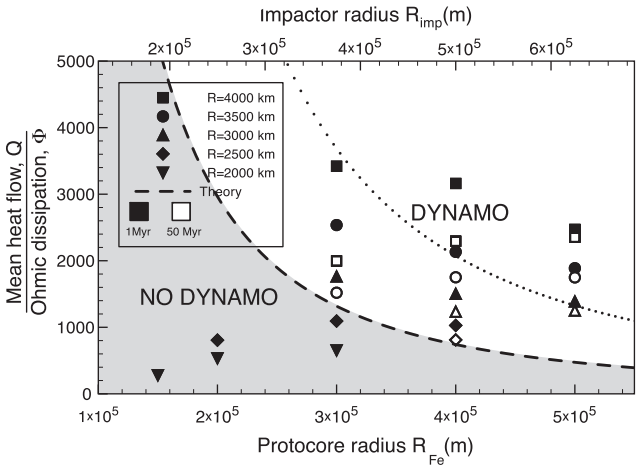

Fig. 4. Q/Φ 1 Myr after the diapir reaches the center of the impacted planet as a function of the metallic diapir radius (black symbols). The protocore radius differentiated after a single impact corresponds to an impactor radius indicated on the top x-axis. The symbol shape is related to the radius of the impacted planet. The black dashed line represents the threshold expression from Eq. 25 in the isoviscous case ($a(\lambda)=15\%$). Above this dashed line (white domain) a dynamo is plausible, while below it no dynamo is generated. The dotted line corresponds to the same threshold but assuming a protocore less viscous than the surrounding mantle ($a(\lambda)=0\%$). If Q/Φ after 50 Myr is within the dynamo domain, a second white filled symbol represents Q/Φ at this time.

radius is larger than 400 km km (i.e. R_{imp}>500 km), however, an early dynamo can be initiated in the first 50 Myr in a planet with a radius greater than 2500 km and in the absence of a molten layer surrounding the protocore. As the planet size increases, the initial protocore temperature increases and the duration of the early dynamo is longer (over 50 Myr). As the protocore size increases, its characteristic cooling time increases and the duration of the early dynamo is also longer. However, a large viscosity contrast between hot iron and cold undifferentiated material will decrease the initial heat flow by a factor of 2.8 (see Fig. 3), and increase the dynamo threshold from Eq. 25. The dotted line in Fig. 4 illustrates this theoretical effect. Fig. 4 shows that a dynamo can still be initiated after an impact, but an increase of the impactor and impacted planet radii are needed relative to the isoviscous case. Hence an impact with R_{imp}>625 km (i.e. R_{Fe}>500 km) on a Mars size body (i.e. $R\sim3500km$) can initiate an early magnetic field. The duration of this early dynamo increases with the size of the impactor.

Dynamo generation requires a magnetic Reynolds number larger than a critical value (see Eq. 21). We monitored the mean heat flux q as a function of time and calculated the corresponding magnetic Reynolds numbers. Fig. 5 shows the results for the two extreme planetary radii (i.e. $R=2000$ km and $R=4000$ km) and the range of protocore sizes studied here. The two lines (solid and dashed) correspond to $q=q_A=Q_A/(4\pi R^2)$ with $R=2000$ km and $R=4000$ km respectively. Three regimes emerge. Below, the solid line $q<q_A$ and no convection occurs. Above the solid line and below Re_m^{crit}, convection occurs but no dynamo is generated. Above these criteria, the thermally-driven convective flow within the protocore can generate a dynamo. As mentioned above, the magnetic Reynolds number will be a factor of about 1.4 too large in the isoviscous compared with the temperature-dependent viscosity case. The dotted line represents the values for Re_m expected from the temperature-dependent viscosity model (i.e. Re_m from isoviscous models divided by a factor 1.4). This figure illustrates three results. First, temperature-dependent viscosity has a weak influence on the Re_m values obtained in this study. Second, as the heat flux out of the protocore obtained from our numerical models is ~20 larger than the adiabatic heat flux q_A (see Eq. 15 and discussion above), then $Re_m(q)\gg Re_m(q_A)$. Third, Re_m easily exceeds the critical value needed to generate a dynamo in the whole range of planet and protocore radii studied here.

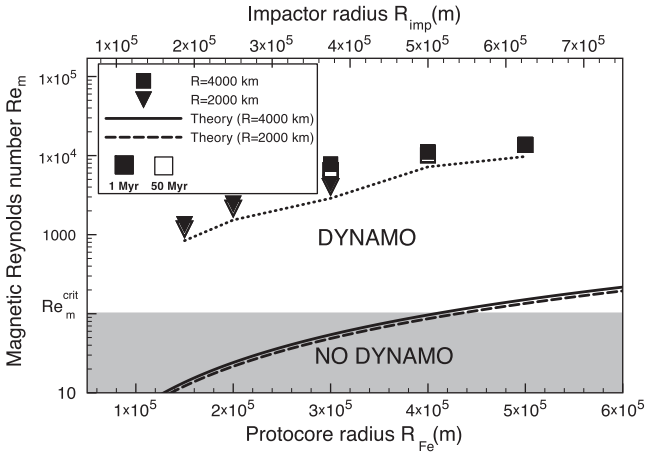

Fig. 5. Magnetic Reynolds number of the protocore as a function of its size from our numerical models. The protocore radius differentiated after a single impact corresponds to an impactor radius indicated on the top x-axis. The symbol shape is related to the radius of the impacted planet and its color (black or white) to the time after the diapir reaches the center of the impacted planet. The dotted line represents the numerical results expected from a temperature-dependent viscosity model (i.e., R_{em} from isoviscous models divided by a factor 1.4). The theoretical Reynolds number values obtained from Eq. 21 are represented with a solid line (with ΔT_0 corresponding to R=4000 km) and a dashed line (with ΔT_0 corresponding to R=2000 km). The gray domain illustrates Re_m^{crit} above which a dynamo is plausible.

5. Discussion

These results provide an important link between the accretion and differentiation histories of the terrestrial planets and their potential for early magnetic fields. They suggest that the presence or absence of an early magnetic field on a planet could be related to its accretionary history.

5.1. Application to Solar System objects

Our results indicate that for bodies in the range of $R=2000$–4000 km and protocore radii in the range of 300–650 km, the core heat flow exceeds the adiabatic heat flow, and Re_m easily exceeds Re_m^{crit} for 50 Myr after the iron diapir reaches the center of the planet and in the absence of additional mantle melting at the protocore–mantle boundary. These conditions suggest that for the range of $R-R_{Fe}$ conditions studied, dynamo action is possible. A more restrictive criterion is that the heat flow must also exceed the ohmic dissipation under Earth-like conditions. In this case, and assuming no mantle melting, we find that a large impact (a 625 km radius impactor, or $R_{Fe}=500$ km) onto a Mars-size (i.e., $R=3500$ km or greater) undifferentiated planet is needed to initiate a dynamo that would persist at least for ~50 Myr (Fig. 4).

As noted earlier the ohmic dissipation criterion has several underlying assumptions about the dynamo action. In particular, we note that the Earth-like value of the magnetic field in the core $\overline{B}$ may not be applicable to other bodies. For example, Mercury, the only other inner solar system body to have a present-day dynamo, has a magnetic field at its surface that is 100 times weaker than Earth's surface field. While the origin of this weak field is not well understood, it is at least reasonable to propose that Mercury's core field could be weaker than Earth's. A factor of two decrease in the core field results in a factor of four increase in Q/Φ, allowing dynamo action for smaller impactors and impacted bodies.

Independent of its mode of formation, such a scenario is more difficult to envision for the Moon for two reasons. First, the Moon is smaller ($R=1700$ km), and in our models, the heat flow across the core mantle boundary does not reach the critical value required to overcome ohmic dissipation. Second, its volumetric metallic fraction is only 1−2% meaning that the impactor size needed to differentiate a large volume of metal is unrealistically large. However, our models do not consider any contribution of the central body to the impact velocity. v_{esc} for the Earth is 4–5 times bigger than v_{esc} for the Moon. Considering that the impact velocity on the Moon is equal to the escape velocity on the Earth can increase the initial temperature of the Moon's protocore and the protocore–mantle boundary heat flow by a factor ≈20. Moreover, our choice of γ provides a lower bound on ΔT_0. If V_∞ is not zero, heating within and outside the core will increase. Finally, radiogenic heating (Nimmo, 2009; Williams and Nimmo, 2004), latent heat release and compositional convection within the core (Labrosse et al., 1997) can also lead to a significant increase of the heat flow across the core–mantle boundary. The solidification of a 100 km radius inner core can release ~10^{10} W which is 1000 times larger than Φ for a 200 km core radius planet. Under the assumption that a heat flow high enough to overcome Earth-like ohmic dissipation is required, these sources of heat and/or compositional buoyancy could explain an early dynamo on the Moon or on small radii objects.

5.2. The effect of a molten lower mantle layer on dynamo duration

If the rocks at the protocore–mantle boundary are at sufficiently high temperature and pressure to be close to their melting temperature, heat

transfer from the protocore can cause the progressive growth of a mantle melt layer (see Eq. 5 and Fig. 2). Assuming that the undifferentiated mantle surrounding the protocore is homogenous, that gravity decreases linearly with depth and that $(R_{Fe}/R)^2 << 1$, the pressure at the core mantle boundary is:

$$P_{CMB} \approx \frac{2}{3}\pi G \rho_0^2 R^2 \tag{26}$$

For the impacted planet radii range in our models, P_{CMB} ranges from 10 to 50 GPa. The formation of a molten layer then depends on the initial temperature of the protocore which is governed by the impacted planet radius R (see Eq. 5). Melting occurs when the initial protocore temperature is larger than the solidus of the surrounding material. In the isoviscous case, Fig. 2 shows that the protocore temperature overcome the solidus temperature of the surrounding mantle only when R>3500 km with a chondritic composition (Agee, 1997) or when R>4500 km with a dry peridotite composition (Zerr and Boehler, 1994). When the viscosity of the diapir is smaller than the surrounding undifferentiated solid mantle, the initial temperature of the protocore is smaller and it is more difficult to form a molten layer unless the pre-impact temperature T_0 at the center is increased by ≈500 K. As mentioned in Section 2.1, the pre-impact temperature is a function of the accretion rate and of the early radiogenic heating. In our models the pre-impact thermal state is homogenous and $T_0 = 1250$ K. Hence, in our single impact scenario, the formation of a molten layer at the top of the protocore without additional silicate differentiation would require a pre-impact temperature that increases with depth.

The conductive heat flux applied to Eq. 25 is not appropriate if heat transfer from the core melts the lower mantle. Vigorous convection within a growing melt layer will enhance the heat transfer from the protocore. Thus, mantle melting can increase the likelihood of dynamo action over the conditions identified in Fig. 4 but, in return, can decrease the duration of an early dynamo as heat will be removed more quickly. Hence, a key issue is to know whether convection in the melt layer will cause the core to freeze. In the case of a molten layer, the duration of a dynamo is limited by the time needed to remove the excess heat (the specific heat plus the latent heat of crystallization) from the protocore with a heat flow Q. In that case, the duration of the dynamo is:

$$t_{dynamo} \approx \frac{4\pi R_{Fe}^3 \rho_{Fe}\left[C_{p,Fe}\left(T_{core} - T_{melt,Fe}\right) + L_{Fe}\right]}{3Q} \tag{27}$$

where $T_{melt,Fe}$ and L_{Fe} are the melting temperature and the latent heat of the metallic phase (see Table 1 for typical values). Fig. 6 shows the time needed to remove the heat excess as a function of the planetary radius for 3 different heat transfer types: solid state conduction, time-dependent conduction and convection within a molten layer. Our results show that this time can vary with several orders of magnitude. In the case of a conductive layer, the time to remove the heat excess is very long ($\approx 10^9$ yr) and the duration of an early dynamo is essentially governed by the time during which vigorous convection occurs within the protocore ($\approx 10^6 - 10^7$ yr). However, in the case where a molten convecting layer forms above the protocore, core freezing occurs in $10^3 - 10^4$ yr, potentially limiting the duration of the dynamo to <10 ky. As underlined in Fig. 2, the extent of melting depends on the composition of the surrounding rocks and on the easiness to cross the solidus. Hence, the composition of the early mantle is also a key parameter in the duration of the early dynamo.

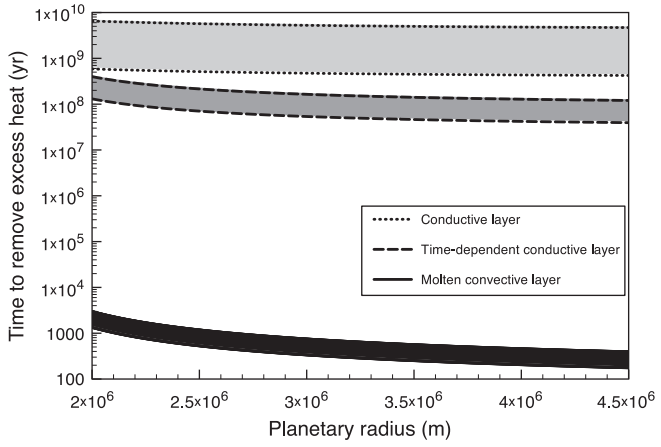

Fig. 6. Time to remove the excess heat from the protocore for 3 different protocore–mantle boundary heat transfers as a function of the planetary radius. The dotted line represents the case of a conductive boundary layer (Eq. 22, $\delta = R_{Fe}$ and Eq. 27) and the dashed line represents the case of a time dependent conductive boundary layer (Eq. 22, $\delta = 2\sqrt{\kappa t}$ and Eq. 27). The black line shows the case where a molten layer surrounds the protocore (Eq. 23, $\eta_{melt} = 100$ Pa.s and Eq. 27). This time also depends on the size of the protocore. For each case, 2 lines delimit a domain from $R_{Fe} = 150$ km (lower line) to 500 km (upper line).

5.3. Future investigations

This dynamo initiation model is a first step toward a more general model of core formation. From the results of our models, several questions need to be addressed:

1. How do hyper-velocity impacts affect the heat repartition after an impact and how does this in turn enhance an impact-induced early dynamo? The fraction of kinetic energy (γ) that is retained as heat below the impact site and the spatial heat repartition after an impact (h_m) are key parameters to characterize the early inner thermal state of growing planets. Better constraints on these parameters would greatly assist any models that investigate the thermal consequences of impacts early in a planet's history.
2. How will multiple diapirs from multiple impacts affect the early protocore thermal state? The sinking of multiple metallic diapirs will strongly affect the thermal state of both the core and the mantle and may play a key role on the temperature contrast between these two reservoirs (Golabek et al., 2009). This prospect is currently beyond the scope of this study because of the geometry used in our numerical models (axisymmetric spherical). However, our study gives a parametrization of the inner thermal consequences after a single large metallic diapir sinking. The scalings proposed here could be used to compute more accurate one dimensional thermal evolution models of growing planets.
3. What is the influence of the timescale between two successive impacts? If a second impact occurs shortly after the first (i.e., within, say, three thermal diffusion timescales RFe^2/κ.), then the thermal effect of the first impact will still be present within the mantle and the second diapir will sink into a warmer and less viscous mantle. The second diapir will descend more quickly. Moreover, the viscosity contrast between the second diapir and the hotter mantle will decrease and viscous heating will be relatively enhanced within the second metallic diapir (see Section 2.2).
4. In the framework of a late giant impact between two differentiated bodies, what is the effect of the core merging on the dynamo activity? The thermal effect of giant impact on dynamos has been recently studied (Reese and Solomatov, 2010; Roberts et al., 2009) but the dynamics of merging between the preexisting core and the impactor's core and the thermal consequences have also to be considered in future models. Within the framework of our model, a giant impact might kill a preexisting dynamo depending on size of the impactor as the thermal effect of both the impact and the

viscous heating during the sinking may reduce the total heat flow across the CMB.

5. How would a second large impact or merging phenomenon change the Hf–W systematics? Depending on the efficiency of equilibration between the impactor's core and the impacted body's mantle, this merging phenomenon may be a major feature of the current W isotopes composition of planets and influence the Hf–W chronology of accretion (Jacobsen, 2005).

6. Conclusions

The dynamics of terrestrial planetary accretion governs their differentiation histories and their potential for early magnetic fields. We have shown that under Earth-like conditions for ohmic dissipation in the core impactors (with R_{imp}>625 km) leading to major differentiation events during early stages of planetary formations can initiate early dynamos. If the ohmic dissipation criterion is relaxed, allowing dynamo action simply if the critical magnetic Reynolds number in the core is exceeded, we find that dynamo action is possible for a larger range of impactors and planets (notably smaller impactors and smaller impacted bodies). Such early dynamos can persist for several kyr to several Myr depending on the size of both the impactor and the impacted body and depending on the heat transfer regime across the protocore. The duration of the early dynamo is also a strong function of the rheology of the early mantle of the impacted body. This rheology determines the sinking velocity of the metallic diapir, the amount of viscous heating during the sinking and the ease to remove the heat from the protocore in the case of a molten layer.

Acknowledgments

The authors thank Laboratoire de Sciences de la Terre de Lyon for its computing time and R. Pawlowicz for useful discussions. We also thank three anonymous reviewers for thoughtful and constructive comments. This project was funded by a Lavoisier fellowship and the Canadian Institute for Advanced Research. A.M. Jellinek and C.L. Johnson acknowledge support from NSERC and C.L. Johnson from NASA's Planetary Geology and Geophysics Program.

References

Acuña, M., et al., 1999. Global distribution of crustal magnetization discovered by the mars global surveyor MAG/ER experiment. Science 284, 790–793.
Agee, C.B., 1997. Melting temperatures of the Allende meteorite: implications for a Hadean magma ocean. Phys. Earth Planet. Int. 100, 41–47.
Behounkova, M., Choblet, G., 2009. Onset of convection in a basally heated spherical shell, application to planets. Phys. Earth Planet. Int. 176, 157–173.
Breuer, D., Spohn, T., 2003. Early plate tectonics versus single-plate tectonics on Mars: evidence from magnetic field history and crust evolution. J. Geophys. Res. (Planets) 108, 5072–5085.
Buffett, B.A., 2002. Estimates of heat flow in the deep mantle based on the power requirements for the geodynamo. Geophys. Res. Lett. 29 (12), 1–4.
Christensen, U.R., 2010. Dynamo scaling laws and applications to the planets. Space Sci. Rev. 152, 565–590.
Christensen, U.R., Aubert, J., 2006. Scaling properties of convection-driven dynamos in rotating spherical shells and application to planetary magnetic fields. Geophys. J. Int. 166, 97–114.
Christensen, U.R., Wicht, J., 2008. Models of magnetic field generation in partly stable planetary cores: applications to Mercury and Saturn. Icarus 196, 16–34.
Cisowski, S.M., Collinson, D.W., Runcorn, S.K., Stephenson, A., Fuller, M., 1983. A review of lunar paleointensity data and implications for the origin of lunar magnetism. J. Geophys. Res. 88, 691–704.
Croft, S.K., 1982. A first-order estimate of shock heating and vaporization in oceanic impacts. In: Silver, T.L., Schultz, P.H. (Eds.), Geological Implications of Impacts of Large Asteroids and Comets on Earth: Spec. Pap. Geol. Soc. Am., 190, pp. 143–152.
Douglas, J., 1955. On the numerical integration of $\frac{\partial^2 u}{\partial x^2} + \frac{\partial^2 u}{\partial y^2} = \frac{\partial u}{\partial t}$ by implicit methods. J. Soc. Ind. Appl. Math. 3, 42–65.
Elkins-Tanton, L.T., Zaranek, S.E., Parmentier, E.M., Hess, P.C., 2005. Early magnetic field and magmatic activity on Mars from magma ocean cumulate overturn. Earth Planet Sci. Lett. 236, 1–12.
Fei, Y., Bertka, C.M., Finger, L.W., 1997. High-pressure iron–sulfur compound, Fe3S2, and melting relations in the FeFeS system. Science 275, 1621–1623.
Garrick-Bethell, I., Weiss, B.P., Shuster, D.L., Buz, J., 2009. Early lunar magnetism. Science 323, 356–359.
Golabek, G.J., Schmeling, H., Tackley, P.J., 2008. Earth's core formation aided by flow channelling instabilities induced by iron diapirs. Earth Planet Sci. Lett. 271, 24–33.
Golabek, G.J., Gerya, T.V., Kaus, B.J.P., Ziethe, R., Tackley, P.J., 2009. Rheological controls on the terrestrial core formation mechanism. Geochem. Geophys. Geosyst. 10, Q11007. doi:10.1029/2009GC002552.
Hadamard, J., 1911. Mouvement permanent lent d'une sphère liquide et visqueuse dans un liquide visqueux. C. R. Acad. Sci. 152, 1735–1738.
Honda, R., Mizutani, H., Yamamoto, T., 1993. Numerical simulation of Earth's core formation. J. Geophys. Res. 98, 2075–2090.
Hood, L.L., Richmond, N.C., Pierazzo, E., Rochette, P., 2003. Distribution of crustal magnetic fields on Mars: shock effects of basin-forming impacts. Geophys. Res. Lett. 30 (6), 1–4.
Jacobsen, S.B., 2005. The Hf–W isotopic system and the origin of the Earth and Moon. Ann. Rev. of Earth and Planet. Sci. 33, 531–570.
Johnson, C.L., Phillips, R.J., 2005. Evolution of the Tharsis region of Mars: insights from magnetic field observations. Earth and Planet Sci. Lett. 230, 241–254.
Kaula, W.M., 1979. Thermal evolution of earth and moon growing by planetesimal impacts. J. Geophys. Res. 84, 999–1008.
Ke, Y., Solomatov, V.S., 2009. Coupled core–mantle thermal evolution of early Mars. J. Geophys. Res. (Planets) 114 (13), 1–12.
Kleine, T., Münker, C., Mezger, K., Palme, H., 2002. Rapid accretion and early core formation on asteroids and the terrestrial planets from Hf–W chronometry. Nature 418, 952–955.
Kokubo, E., Ida, S., 1996. On runaway growth of planetesimals. Icarus 123, 180–191.
Kuang, W., Bloxham, J., 1997. An Earth-like numerical dynamo model. Nature 389, 371–374.
Labrosse, S., Poirier, J., Le Mouel, J., 1997. On cooling of the Earth's core. Phys. of the Earth and Planet. Int. 99, 1–17.
Laney, C.B., 1998. Computational Gasdynamics. Cambridge University Press, Cambridge.
Lawrence, K., Johnson, C., Tauxe, L., Gee, J., 2008. Lunar paleointensity measurements: implications for lunar magnetic evolution. Phys. Earth Planet. Int. 168, 71–87.
Lillis, R.J., Frey, H.V., Manga, M., 2008. Rapid decrease in Martian crustal magnetization in the Noachian era: implications for the dynamo and climate of early Mars. Geoph. Res. Lett. 35, 14,203–14,209.
Monteux, J., Coltice, N., Dubuffet, F., Ricard, Y., 2007. Thermo-mechanical adjustment after impacts during planetary growth. Geophys. Res. Lett. 34, 24201–24205.
Monteux, J., Ricard, Y., Coltice, N., Dubuffet, F., Ulvrova, M., 2009. A model of metal–silicate separation on growing planets. Earth and Planet Sci. Lett. 287, 353–362.
Nimmo, F., 2009. Energetics of asteroid dynamos and the role of compositional convection. Geoph. Res. Lett. 36, 10,201–10,207.
Nimmo, F., Stevenson, D.J., 2000. Influence of early plate tectonics on the thermal evolution and magnetic field of Mars. J. Geophys. Res. 105, 11,969–11,980.
O'Keefe, J.D., Ahrens, T.J., 1977. In: Merril, R.B. (Ed.), Impact-induced Energy Partitioning, Melting, and Vaporization on Terrestrial Planets: Lun. Planet. Sci. Conf., 8, pp. 3357–3374.
Peaceman, D.W., Rachford, H.H., 1955. The numerical solution of parabolic and elliptic differential equations. J. Soc. Ind. Appl. Math. 3, 28–41.
Pierazzo, E., Vickery, A.M., Melosh, H.J., 1997. A reevaluation of impact melt production. Icarus 127, 408–423.
Ratcliff, J.T., Tackley, P.J., Schubert, G., Zebib, A., 1997. Transitions in thermal convection with strongly variable viscosity. Phys. Earth Planet. Int. 102, 201–212.
Reese, C.C., Solomatov, V.S., 2006. Fluid dynamics of local martian magma oceans. Icarus 184, 102–120.
Reese, C.C., Solomatov, V.S., 2010. Early martian dynamo generation due to giant impacts. Icarus 207, 82–97.
Ricard, Y., Srámek, O., Dubuffet, F., 2009. A multi-phase model of runaway core-mantle segregation in planetary embryos. Earth Planet Sci. Lett. 284, 144–150.
Roberts, J.H., Lillis, R.J., Manga, M., 2009. Giant impacts on early Mars and the cessation of the Martian dynamo. J. Geophys. Res. (Planets) 114 (13), 4009–4019.
Roe, P.L., 1986. Characteristic-based schemes for the Euler equations. Annu. Rev. Fluid Mech. 18, 337–365.
Rubie, D.C., Melosh, H.J., Reid, J.E., Liebske, C., Righter, K., 2003. Mechanisms of metal–silicate equilibration in the terrestrial magma ocean. Earth Planet Sci. Lett. 205, 239–255.
Rybczynski, W., 1911. über die fortschreitende bewegung einer flüssigen kugel in einen medium. Bull. Acad. Sci. Cracovie 1, 40–46.
Safronov, V.S., 1978. The heating of the earth during its formation. Icarus 33, 3–12. doi:10.1016/0019-1035(78)90019-2.
Samuel, H., Tackley, P.J., 2008. Dynamics of core formation and equilibration by negative diapirism. Geochem. Geophys. Geosyst. 9, 6011–6026.
Samuel, H., Tackley, P.J., Evonuk, M., 2010. Heat partitioning in terrestrial planets during core formation by negative diapirism. Earth and Planet Sci. Lett. 290, 13–19.
Schubert, G., Russell, C.T., Moore, W.B., 2000. Geophysics: timing of the Martian dynamo. Nature 408, 666–667.
Schubert, G., Turcotte, D.L., Olson, P., 2001. Mantle Convection in the Earth and Planets. Cambridge University Press.
Senshu, H., Kuramoto, K., Matsui, T., 2002. Thermal evolution of a growing Mars. J. Geophys. Res. 107, 1–13.
Shannon, M.C., Agee, C.B., 1996. High pressure constraints on percolative core formation. Geophys. Res. Lett. 23, 2717–2720.
Solomatov, V.S., 2000. Fluid Dynamics of a Terrestrial Magma Ocean. In: Canup, R.M., Righter, K., 69 collaborating authors (Eds.), Origin of the earth and moon. University of Arizona Press, Tucson, pp. 323–338.

Srámek, O., Ricard, Y., Dubuffet, F., 2010. A multiphase model of core formation. G. J. Int. 181, 198–220.
Stegman, D.R., Jellinek, A.M., Zatman, S.A., Baumgardner, J.R., Richards, M.A., 2003. An early lunar core dynamo driven by thermochemical mantle convection. Nature 421, 143–146.
Stevenson, D.J., 1990. Fluid dynamics of core formation. In: Newsom, H.E., Jones, J.H. (Eds.), Origin of the Earth. Oxford Univ, New York. 231–249 pp.
Stevenson, D.J., 2003a. Planetary magnetic fields. Earth Planet Sci. Lett. 208, 1–11.
Stevenson, D.J., 2003b. Planetary science: mission to Earth's core — a modest proposal. Nature 423, 239–240.
Stevenson, D.J., Spohn, T., Schubert, G., 1983. Magnetism and thermal evolution of the terrestrial planets. Icarus 54, 466–489.
Tonks, W.B., Melosh, H.J., 1992. Core formation by giant impacts. Icarus 100, 326–346.
Touboul, M., Kleine, T., Bourdon, B., Palme, H., Wieler, R., 2007. Late formation and prolonged differentiation of the Moon inferred from W isotopes in lunar metals. Nature 450, 1206–1209.
Turner, J.S., 1973. Buoyancy Effects in Fluids. Cambridge University Press, Cambridge.
Weiss, B.P., Berdahl, J.S., Elkins-Tanton, L., Stanley, S., Lima, E.A., Carporzen, L., 2008. Magnetism on the angrite parent body and the early differentiation of planetesimals. Science 322, 713–716.
Williams, J., Nimmo, F., 2004. Thermal evolution of the Martian core: implications for an early dynamo. Geol. 32.
Wood, B.J., Walter, M.J., Wade, J., 2006. Accretion of the Earth and segregation of its core. Nature 441, 825–833.
Yin, Q., Jacobsen, S.B., Yamashita, K., Blichert-Toft, J., Télouk, P., Albarède, F., 2002. A short timescale for terrestrial planet formation from Hf–W chronometry of meteorites. Nature 418, 949–952.
Yoshino, T., Walter, M.J., Katsura, T., 2003. Core formation in planetesimals triggered by permeable flow. Nature 422, 154–157.
Zerr, A., Boehler, R., 1994. Constraints on the melting temperature of the lower mantle from high-pressure experiments on MgO and magnetite. Nature 371, 506–508. doi:10.1038/371506a0.
Ziethe, R., Spohn, T., 2007. Two-dimensional stokes flow around a heated cylinder: a possible application for diapirs in the mantle. J. Geophys. Res. 112, 1–13.

Can a sinking metallic diapir generate a dynamo?

Julien Monteux,[1] Nathanaël Schaeffer,[2] Hagay Amit,[1] and Philippe Cardin[2]

Received 5 March 2012; revised 21 August 2012; accepted 21 August 2012; published 10 October 2012.

[1] Metallic diapirs may have strongly contributed to core formations during the first million years of planetary evolutions. The aim of this study is to determine whether the dynamics induced by the diapir sinking can drive a dynamo and to characterize the required conditions on the size of the diapir, the mantle viscosity and the planetary latitude at which the diapir sinks. We impose a classical Hadamard flow solution for the motion at the interface between a spherical sinking diapir and a viscous mantle on dynamical simulations that account for rotational and inertial effects in order to model the flow within the diapir. The flows are confined to a velocity layer with a thickness that decreases with increasing rotation rate. These 3D flows are is then used as input for kinematic dynamo simulations to determine the critical magnetic Reynolds number for dynamo onset. Our results demonstrate that the flow pattern inside a diapir sinking into a rotating planet can generate a magnetic field. Large diapirs ($R > 10$ km) sinking in a mantle with a viscosity ranging from 10^9 to 10^{14} Pa.s provide plausible conditions for a dynamo. Equatorial sinking diapirs are confined to a thicker velocity layer and are thus possibly more favorable for dynamo generation than polar sinking diapirs. In addition equatorial sinking diapirs produce stronger saturated magnetic fields. However, for the range of parameters studied here, estimation of the intensity of diapir-driven magnetic fields suggests that they could not have contributed to the lunar or Martian crustal paleomagnetic fields.

Citation: Monteux, J., N. Schaeffer, H. Amit, and P. Cardin (2012), Can a sinking metallic diapir generate a dynamo?, *J. Geophys. Res.*, *117*, E10005, doi:10.1029/2012JE004075.

1. Introduction

[2] Episodic migration of large volumes of iron may have strongly contributed to core formations during early planetary evolution [*Stevenson*, 1981]. Complete separation of the metallic phase from the silicate chondritic material may occur within only several million years on terrestrial planets [*Kleine et al.*, 2002; *Yin et al.*, 2002; *Touboul et al.*, 2007]. Such a fast process necessarily involves melting of the metallic phase which requires a large amount of energy. This energy can be provided by radiogenic heating [*Yoshino et al.*, 2003], impact processes [*Tonks and Melosh*, 1993] or gravitational energy release during metal-silicate separation [*Šrámek et al.*, 2010]. Once molten, the dense metallic phase can sink toward the center of the planet via various phenomena such as percolation through a solid matrix [*Shannon and Agee*, 1996], settling of metallic droplets within a convecting magma ocean [*Rubie et al.*, 2003; *Höink et al.*, 2006], two-phase flow dynamics [*Ricard et al.*, 2009; *Šrámek et al.*, 2010] or Rayleigh-Taylor instabilities [*Stevenson*, 1981; *Honda et al.*, 1993]. These various processes may lead to a wide range of characteristic length scales [*Karato and Murthy*, 1997]. Percolation and metal rainfall occur at small length scales ($\sim 10^{-2}$ m) and can ultimately form a dense metallic layer at the bottom of a magma ocean. Then, depending on the thickness of this accumulated metallic layer, Rayleigh-Taylor instabilities can mobilize up to 100-km sized diapirs [*Honda et al.*, 1993].

[3] Large scale metallic volumes can also be separated from silicates by differentiation events following a large impact on an undifferentiated planet [*Tonks and Melosh*, 1993; *Monteux et al.*, 2009]. Indeed, after a large impact a fraction of the kinetic energy is transferred at depth to thermal energy via shock waves propagation and may separate locally the metallic phase from the silicate phase. Then, the dense metallic phase overcomes viscous heating during its sinking toward the center of the planet. If the separated metallic volume is hot enough, vigorous convection occurs within the metallic phase once it has reached the center of the planet, and a dynamo can be generated [*Monteux et al.*, 2011a]. Ultimately, large iron cores of planetesimals could even have directly sunk into the pre-existing core just after an impact [*Benz et al.*, 1987; *Monteux et al.*, 2011b]. In this study, we term *metallic diapir* every volume of iron that sinks toward the center of the growing planet independently of its size or sinking process.

[1]Laboratoire de Planétologie et de Géodynamique, UMR 6112, CNRS, Université de Nantes, Nantes Atlantiques Universités, Nantes, France.
[2]ISTerre, Université de Grenoble 1, CNRS, Grenoble, France.

Corresponding author: J. Monteux, Laboratoire de Planétologie et de Géodynamique, UMR 6112, CNRS, Université de Nantes, Nantes Atlantiques Universités, 2 rue de la Houssinière, FR-44000 Nantes, France. (julien.monteux@univ-nantes.fr)

0148-0227/12/2012JE004075

[4] Large metallic diapirs lead to a large deviatoric stress that deforms the surrounding material and accommodates the sinking of the diapir toward the center of the planet. Depending on the rheology of the surrounding mantle, negative metallic diapirism may lead to viscous deformation [*Monteux et al.*, 2009], non-linear rheology [*Samuel and Tackley*, 2008], elasto-plastic deformation [*Gerya and Yuen*, 2007] or even to fracturing if the ultimate strength of solid rocks is exceeded [*Davies*, 1982; *Stevenson*, 2003]. During the early times of planetary formation extinct radioactivities (^{26}Al and ^{60}Fe) and large impact heating have played a major role in the thermal budget of the planets. This early heating was retained in the internal part of the planet, leading to a hot proto-mantle and favoring sinking via viscous deformation. Hence, large metallic diapirs potentially sank toward the center of the planet in a Hadamard-regime [*Hadamard*, 1911] with a timescale that is a function of the viscosity of the proto-mantle [*Karato and Murthy*, 1997]. This Hadamard flow constrains the internal dynamics of the diapir.

[5] Can a sinking metallic diapir generate a dynamo? Dynamo theory requires three main conditions for the generation of magnetic field: a fluid with large electrical conductivity, large velocities and some favorable flow pattern. In large-scale dynamos operating in planetary outer cores, the energy source generating large velocities is typically thermo-chemical convection driven by secular cooling and light element release due to a freezing inner core [*Olson*, 2007]. However, non-convective energy sources may also drive dynamos, for example precession [*Tilgner*, 2005], tidal distortion of the core-mantle boundary (CMB) [*Le Bars et al.*, 2011] or heterogeneous mechanical boundary conditions [*Guervilly and Cardin*, 2010].

[6] Kinematic dynamos provide vital information about the efficiency of magnetic field generation for different flow morphologies [*Gubbins et al.*, 2000a, 2000b]. Very simple laminar flows often lack significant helicity which is an important ingredient for a dynamo [*Moffatt*, 1978]. They are therefore inefficient in generating a magnetic field, which requires the magnetic Reynolds number to exceed large critical values [*Gailitis*, 1970; *Dudley and James*, 1989; *Moss*, 2008]. Even if the helicity is not indispensable in the dynamo process, these kinematic dynamo models have shown that it is a favorable factor. Self-consistent 3D numerical dynamo models show a hemispheric anti-symmetric pattern of helicity associated with the α^2 dynamo mechanism [*Olson et al.*, 1999]. In these models helicity is generated by the action of the Coriolis force that yields positive/negative radial vorticity correlated with downwelling in the northern/southern hemisphere respectively [*Olson et al.*, 2002; *Amit et al.*, 2007].

[7] We use kinematic dynamo simulations to determine the critical magnetic Reynolds number above which the flow strength (for a given flow pattern) is sufficient to amplify a magnetic seed field. To resolve the flow inside the diapir, we impose the simple flow pattern of a viscous bubble as a mechanical outer boundary condition on a dynamical simulation. Because the diapir is in a rotating planetary reference frame and its low viscosity may accommodate inertial effects, we take into account Coriolis and inertial forces. These rotational and inertial effects may help dynamo action by introducing helicity to the dynamics within the interior of the sinking diapir.

[8] The aim of this study is to determine whether such sinking dynamics can drive a dynamo, and to constrain the required conditions for the size of the diapir and the mantle viscosity of the planet. In addition, we also investigate the importance of the planetary latitude at which the diapir sinks on the conditions for obtaining a dynamo. In section 2, we show that there exists a considerable range of parameters in which large metallic diapirs are stable. The theory and method are described in section 3. We present the results of our models in section 4. In section 5 we discuss the diapir driven magnetic field growth rate and intensity from an initial interplanetary magnetic seed field. In section 6 we discuss the feasibility of obtaining diapir driven dynamos in geophysical conditions. Conclusions and possible planetary implications are highlighted in section 7.

2. Stability of Large Metallic Diapirs

[9] In the laminar flow regime, the sinking velocity of a metallic diapir obeys a Hadamard velocity [*Hadamard*, 1911; *Batchelor*, 1967; *Monteux et al.*, 2009]

$$U = \frac{2}{9}\left(\frac{\eta+\eta_s}{\eta+\frac{2}{3}\eta_s}\right)\frac{\Delta\rho g R^2}{\eta_s} \simeq \frac{1}{3}\frac{\Delta\rho g R^2}{\eta_s} \quad (1)$$

where η is the viscosity inside the diapir, η_s is the viscosity of the surrounding mantle (with $\eta_s \gg \eta$), $\Delta\rho$ is the density difference between the metallic diapir and the silicate mantle, g is the gravitational acceleration at the depth of the diapir and R is the radius of the metallic diapir. For early partially molten planetary mantles, $\Delta\rho \sim 5000$ kg/m^3 and $\eta_s \sim 10^7$–10^{13} Pa.s [*Karato and Murthy*, 1997]. Actually, the gravity and the sinking velocity decrease with depth. For simplicity however, we fix the gravity in the partially molten zone to a constant value of $g \sim 5$ m/s^2 (intermediate value between the Moon's and the Earth's surface gravities). The sinking velocity from equation (1) is related to the Stokes velocity by $U_{Stokes} = 2U/3$ which is the velocity of a solid sphere sinking in a viscous medium (i.e. $\eta_s \ll \eta$).

[10] Whether a large metallic diapir will break depends on the stability of the surrounding flow, which is depicted by the Reynolds number Re_s based on the sinking velocity U and the fluid properties of the surrounding mantle:

$$Re_s = \frac{\rho_s U R}{\eta_s} = \frac{\rho_s \Delta\rho g R^3}{3\eta_s^2} \quad (2)$$

where $\rho_s \sim 5000$ kg/m^3 is the estimated density of the mantle. For $Re_s \gtrsim 10^3$, viscous forces are negligible compared to inertia and diapir break-up occurs. When $1 \lesssim Re_s \lesssim 10^3$, the diapir may or may not break depending on the importance of inertia over surface tension forces. For $Re_s \lesssim 1$, inertia is negligible and no break-up occurs [*Samuel*, 2012]. In Figure 1, we represent the stability domain for large metallic diapirs as a function of diapir size R and mantle viscosity η_s. The conservative upper bound $Re_s = 10$ plotted in Figure 1 provides a limit on candidate diapirs for dynamo action. Figure 1 shows that even very large diapirs can sink without break-up if the molten mantle viscosity is sufficiently large.

[11] Because the mantle viscosity is strongly dependent on the temperature, the thermal evolution of the protoplanet is a

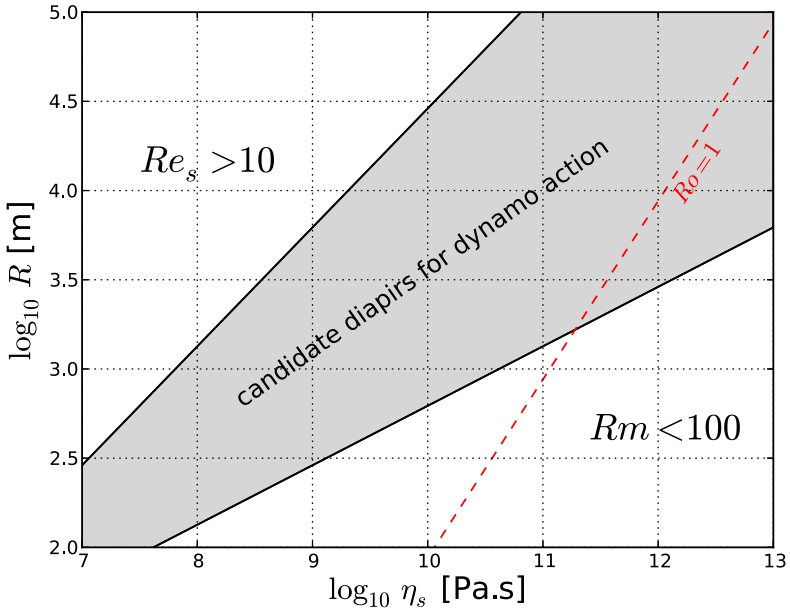

Figure 1. Candidate diapirs for possible dynamo action (shaded region) must have $Re_s \lessapprox 10$ to be stable and $Rm \gtrsim 100$ for magnetic induction to be possible. The $Ro = 1$ contour shows that larger η_s gives more dominant rotational effects in the fluid dynamics inside the diapir (above this line $Ro > 1$). For definitions of Re_s, Rm and Ro see equations (2), (3) and (7).

key parameter to define the plausible metal diapir sinking regimes. In the early stages of planetary formation and before the dissipation of potential energy associated with the full core formation, the growing planets were schematically divided in three domains: a completely molten shallow magma ocean, a partially molten deep magma ocean and a solid core [*Karato and Murthy*, 1997].

[12] The most superficial layer of a growing planet was probably completely molten forming a several hundred kilometers thick magma ocean. In this magma ocean, the viscosity ranges 10^{-4}–10^{2} Pa.s. In the shallow magma ocean and considering $R > 1$ km, $Re_s \gg 10^5$ and turbulent effects lead to emulsification and to rapid break-up of the metallic diapir until it reaches a cm size [*Rubie et al.*, 2003; *Samuel*, 2012]. However, *Dahl and Stevenson* [2010] have shown that diapirs with radii larger than 10 km can survive complete erosion and preserve most of their initial volume as they reach the bottom of a 1000 km thick magma ocean. In the turbulent magma ocean, the metallic material rapidly segregates from silicates and forms a layer above the rheological transition separating the fully molten magma ocean to the partially molten magma ocean [*Höink et al.*, 2005]. From the iron layer cumulated at the bottom of the molten magma ocean, Rayleigh-Taylor instabilities can mobilize large volume of iron by diapirism [*Stevenson*, 1981; *Honda et al.*, 1993].

[13] From the bottom of the outermost magma ocean, temperature and melting fraction decrease with depth [*Safronov*, 1978; *Kaula*, 1979; *Senshu et al.*, 2002] and the viscosity rapidly increases to 10^{7}–10^{13} Pa.s [*Karato and Murthy*, 1997] (see Table 1). Assuming that U is a Stokes velocity, for a 100 km radius diapir the typical value of Re_s within this partially molten reservoir ranges between 10^{9} and 10^{-3}, while for a 1 km radius diapir Re_s ranges between 10^{3} and 10^{-9}. Hence, in this zone and with a favorable diapir size and viscosity regime, diapirs can potentially settle in a laminar flow regime (see Figure 1). Within the solid deep core, the viscosity was probably larger than 10^{18} Pa.s thus also leading to a laminar Stokes flow regime.

[14] Severe heatings associated with large impacts are phenomena that often occur especially at the end of planetary accretion. In a local volume deep below the impact site, the temperature dramatically increases up to the solidus temperature of silicates which results in massive melting. If the molten volume is not differentiated before the impact, a local separation occurs in a nearly spherical volume [*Tonks and Melosh*, 1992; *Monteux et al.*, 2009]. The impactor's core material can eventually be collected in the impact-produced magma pool where the local $Re_s \gg 1$ [*Deguen et al.*, 2011]. Then, the sinking of this large collected volume is governed by the rheology of the surrounding material and may occur in a laminar Stokes flow regime depending on the viscosity of the mantle. We restrict our study to the laminar flow regime

Table 1. Reference Values for Some Diapirs of Radius R Sinking in a Mantle of Viscosity η_s, Which Are Possible Candidates for Driving a Dynamo

R (km)	η_s (Pa.s)	U (m/s)	Re_s	Rm	E	Ro
0.1	10^{7}	8	0.4	400	10^{-6}	10^{3}
1	10^{7}	800	400	4×10^{5}	10^{-8}	10^{4}
1	10^{9}	8	0.04	4×10^{3}	10^{-8}	100
10	10^{9}	800	40	4×10^{6}	10^{-10}	10^{3}
10	10^{11}	8	$\ll 1$	4×10^{4}	10^{-10}	10
10	10^{13}	0.08	$\ll 1$	400	10^{-10}	0.1
100	10^{11}	800	4	4×10^{7}	10^{-12}	100
100	10^{13}	8	$\ll 1$	4×10^{5}	10^{-12}	1

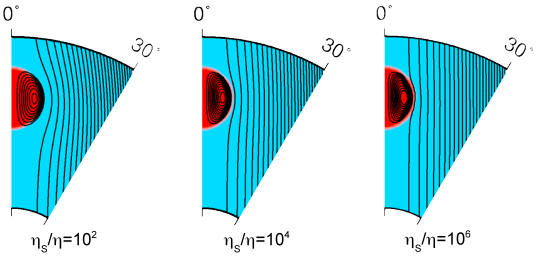

Figure 2. Streamlines of a sinking metallic sphere (red) in an undifferentiated planet (blue). The streamlines are in the moving frame of the sinking diapir. The ratio between the diapir radius to the planetary radius is 0.125. The three images show the flows for three different ratios between the mantle viscosity η_s and the diapir viscosity η. These results were obtained using the thermo-chemical convection code developed by *Monteux et al.* [2009] in spherical axisymmetric geometry.

where the diapir does not break. Hence, we particularly focus on the dynamics of a diapir sinking in the deep and partially molten magma ocean.

3. Theory and Method

[15] The growth or decay of a magnetic seed field B_i depends on the diapir magnetic Reynolds number Rm which represents the ratio of advection of magnetic field by the flow to magnetic diffusion

$$Rm = \frac{UR}{\lambda} = \frac{\Delta\rho g R^3}{3\eta_s \lambda} \tag{3}$$

with $\lambda \sim 1$ m^2/s being the magnetic diffusivity of liquid iron inside the diapir [*Olson*, 2007]. Numerical dynamo simulations of rotating convection in a spherical shell show that $Rm \gtrsim 100$ is a necessary condition for magnetic field generation [*Christensen and Aubert*, 2006]. Figure 1 shows the limit $Rm = 100$ as a function of diapir radius R and mantle viscosity η_s. Combining the conditions on Re_s and Rm, we find a considerable range of diapirs (with $R \gtrsim 100$ m and the full estimated range of η_s) that are both stable against break-up as well as sufficiently fast for significant magnetic induction. It is not clear however whether the particular flow pattern inside the diapir is capable of generating a magnetic field. The goal of this study is to verify the feasibility of dynamo action by a diapir sinking flow.

[16] The laminar flow pattern within a sinking diapir in a non-rotating system is well known from theoretical [*Hadamard*, 1911; *Batchelor*, 1967] and experimental [*Spells*, 1952] studies. This circulation pattern consists of a purely poloidal one-roll axisymmetric velocity field [*Batchelor*, 1967]:

$$U_r(r,\theta) = U\left(R^2 - r^2\right)\cos\theta \tag{4}$$

$$U_\theta(r,\theta) = -U\left(R^2 - 2r^2\right)\sin\theta \tag{5}$$

where r and θ are the radial and co-latitude spherical coordinates in the reference frame of the diapir. During its sinking, a spherical diapir might deform depending on the rheological properties of both the metallic and the silicate phases [*Monteux et al.*, 2009; *Ulvrová et al.*, 2011]. For simplicity we assume that the diapir maintains a spherical shape during its sinking. Figure 2 shows the internal circulation obtained using the thermo-chemical convection code developed by *Monteux et al.* [2009]. The flow pattern is in good agreement with both the theoretical and the experimental results and weakly depends on the viscosity ratio between the sinking metallic diapir and the surrounding mantle.

[17] When the planet is rapidly rotating and the viscosity of the diapir is sufficiently small, the Coriolis and inertial forces must be taken into account. Two non-dimensional numbers characterize the dynamical system: the ratio of viscous to Coriolis forces is measured by the Ekman number

$$E = \frac{\nu}{\Omega R^2} \tag{6}$$

where $\nu = \eta/\rho$ is the kinematic viscosity of the molten iron and Ω is the rotation rate of the planet. The ratio of inertial to Coriolis forces is characterized by the Rossby number

$$Ro = \frac{U}{\Omega R} \tag{7}$$

where U is the amplitude of the sinking diapir velocity field (equation (1)). The rotation rate Ω has probably decreased during the early stages of planetary accretion from a couple of hours [*Agnor et al.*, 1999]. For simplicity, we consider in our study a constant Ω equal to the current Earth value (see Table 2).

[18] We solve numerically the non-dimensional Navier-Stokes equation including Coriolis and inertial forces in a spherical container representing the sinking diapir:

$$\frac{\partial \mathbf{u}}{\partial t} + \mathbf{u}\cdot\nabla\mathbf{u} + 2\mathbf{e_z}\times\mathbf{u} = -\nabla\pi + E\nabla^2\mathbf{u} \tag{8}$$

where $\mathbf{u}$ is the velocity field (in units of $R\Omega$), t is time (in units of Ω^{-1}), $\mathbf{e_z}$ is the unit vector in the direction of the planetary rotation axis and π the reduced pressure. The Hadamard velocity field (equations (4) and (5)) scaled by Ro is imposed at the spherical outer boundary and drives the flow within the diapir. When the hydrodynamic diapir Reynolds number $Re = Ro/E \ll 10^3$ (not to be confused with Re_s),

Table 2. Estimated Parameters and Non-dimensional Numbers for Present Earth's Outer Core, a Candidate Sinking Diapir, and Input Non-dimensional Numbers Used in Our Models[a]

	Earth	Diapir	Models
ν	10^{-6}	10^{-6}	-
λ	1	1	-
R	3×10^6	10^2–10^5	-
Ω	7×10^{-5}	7×10^{-5}	-
U	5×10^{-4}	10^{-5}–10^3	-
E	10^{-15}	10^{-12}–10^{-6}	10^{-5}–10^{-2}
Ro	10^{-6}	10^{-3}–10^4	10^{-3}–1
Rm	10^3	10^2–10^8	10^3–10^5
Pm	10^{-6}	10^{-6}	10^{-1}–10^5

[a]All parameters are given in SI units. All values for Earth's core are from *Olson* [2007]. Diffusivities and rotation rate for diapirs are assumed to be as for the Earth's core. Note that in calculating the non-dimensional number ranges for the diapir not all combinations of R and U are admissible, since U depends on R (equation (1)). For the candidate sinking diapir, see Figure 1.

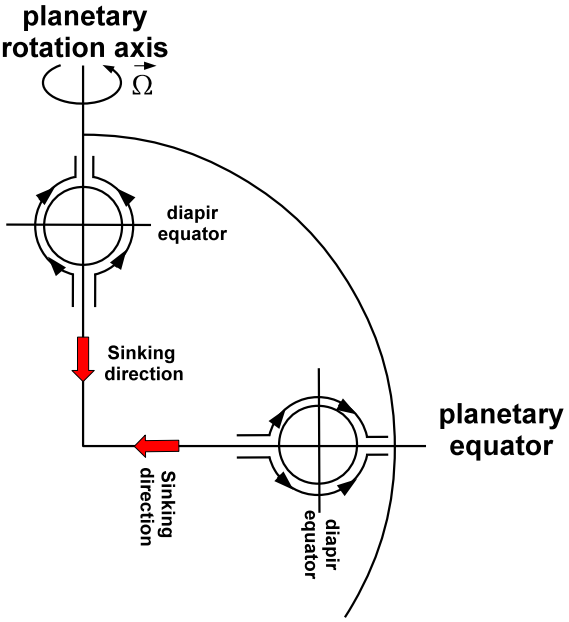

Figure 3. Schematic illustration of the geometries of the two end-member sinking diapirs. In polar sinking (top) the local gravity is parallel to the rotation vector, whereas in equatorial sinking (right) the local gravity is perpendicular to the rotation vector.

the expected flow pattern equations (4) and (5) is recovered in the whole volume to a very good accuracy. Details of the numerical method can be found in Appendix A.

[19] If the resulting three-dimensional flow **u** is stationary, it is then used as input to a kinematic dynamo code, which solves the induction equation

$$\frac{\partial \mathbf{B}}{\partial t} = \nabla \times (\mathbf{u} \times \mathbf{B}) + \frac{E}{Pm}\nabla^2 \mathbf{B} \tag{9}$$

where the magnetic field **B** is in units of $\sqrt{\mu_0 \rho_{Fe}} R\Omega$, and $Pm = \nu/\lambda$ is the magnetic Prandtl number. μ_0 is the magnetic permeability of free space ($\mu_0 = 4\pi \times 10^{-7}$ H.m^{-1}) and ρ_{Fe} is the diapir density ($\rho_{Fe} = 10^4$ kg.m^{-3}). Note that Rm (equation (3)) can be rewritten as $Rm = RoPm/E$. A growing magnetic field indicates the presence of a dynamo.

[20] If the Navier-Stokes simulation leads to a time-dependent flow (as it is the case for high Ro and Re), we resort to a much slower fully self-consistent dynamo code, which solves the induction equation (9) coupled with the Navier-Stokes equation (8) with the addition of the Lorentz force $(\nabla \times \mathbf{B}) \times \mathbf{B}$. We denote the critical magnetic Reynolds number for the onset of a dynamo by Rm_c. To characterize the efficiency of the flow pattern in generating a magnetic field, we also examine the helicity $H = \mathbf{u} \cdot (\nabla \times \mathbf{u})$.

[21] The relevant parameters and non-dimensional numbers are listed in Table 2, including their typical values for Earth's outer core, the possible ranges for the sinking diapir, as well as values used in our numerical models. The most significant variability and uncertainty appears in the size of the diapir R and the viscosity of the surrounding mantle η_s. It is therefore worth-while writing the control parameters of the models in terms of these two quantities. For example, substituting equation (1) into equation (7) allows rewriting the Rossby number as

$$Ro = \frac{1}{3}\frac{\Delta \rho g R}{\eta_s \Omega} \tag{10}$$

Using fixed values for $\Delta\rho$, g, Ω, ν and λ, the input control parameters E, Ro and Rm are given in terms of the diapir size R and the mantle viscosity η_s in Tables 1 and 2. For a successful dynamo ($Rm > Rm_c$) to be considered geophysical, it is required to have E, Ro and Rm within the (rather broad) estimated range for candidate diapirs (see Figure 1), but also the magnetic Prandtl number must have the value of molten iron, that is $Pm \sim 10^{-6}$ [*Olson*, 2007]. We limit our dynamical models to the rotational regime of $Ro \leq 1$ but we also investigate the ability of the simple laminar Hadamard flow without rotation and inertia to generate a magnetic field.

[22] Two end-member scenarios are examined, one in which the diapir falls on the geographic pole of the planet, the other in which the diapir falls on the equator of the planet. In the first the Hadamard flow forcing is parallel to the planetary rotation axis, in the second the Hadamard flow forcing is perpendicular to the planetary rotation axis (see Figure 3). The consequences of these two end-member scenarios for the dynamo are compared.

4. Results

4.1. Fluid Flow Inside the Diapir

[23] We begin by reporting the velocity fields within the diapir obtained by our dynamical model. Figure 4a shows a solution for a large Ekman number of $E = 10^{-2}$ and a Rossby number of $Ro = 10^{-1}$ for a polar sinking diapir. The meridional flow consists of a single poloidal roll anti-symmetric with respect to the equator and axisymmetric with respect to the rotation axis, as in the classical Hadamard flow solution without rotation and inertia (equations (4) and (5)). However, in addition the solution contains an azimuthal axisymmetric toroidal flow component anti-symmetric with respect to the equator, which is due to the Coriolis force. Compared to Figure 2, the streamlines are distorted toward the outer part of the sphere in response to the rotational effect. Note that the radial flow is much weaker than the tangential flow. In the rotational regime where $Ro \ll 1$ the flow pattern is weakly dependent on Ro. In this regime, the main difference between flow models of two different Ro values is that the magnitude scales linearly with Ro. For $Ro \sim 1$ and hence large Reynolds numbers $Re = Ro/E$, the flow is no longer stationary.

[24] For smaller Ekman numbers (Figures 4b and 4c), the flow pattern is qualitatively similar but is now confined to a thinner layer below the boundary of the diapir. Figure 5 shows the thickness of the velocity layer h normalized by the diapir's radius as a function of E^{-1} for $Ro = 10^{-2}$. The decrease in h with decreasing E obeys a power law

$$\frac{h}{R} = AE^x \tag{11}$$

For a polar sinking diapir the prefactor is $A_p \sim 4$ and the power is $x_p \sim 0.5$ (Figure 5, red). The 1/2 power is suggestive of an Ekman boundary layer control [e.g. *Pedlosky*, 1987], as may be expected in a system governed by rotational effects. The same results are found for all $Ro < 1$ values (not shown).

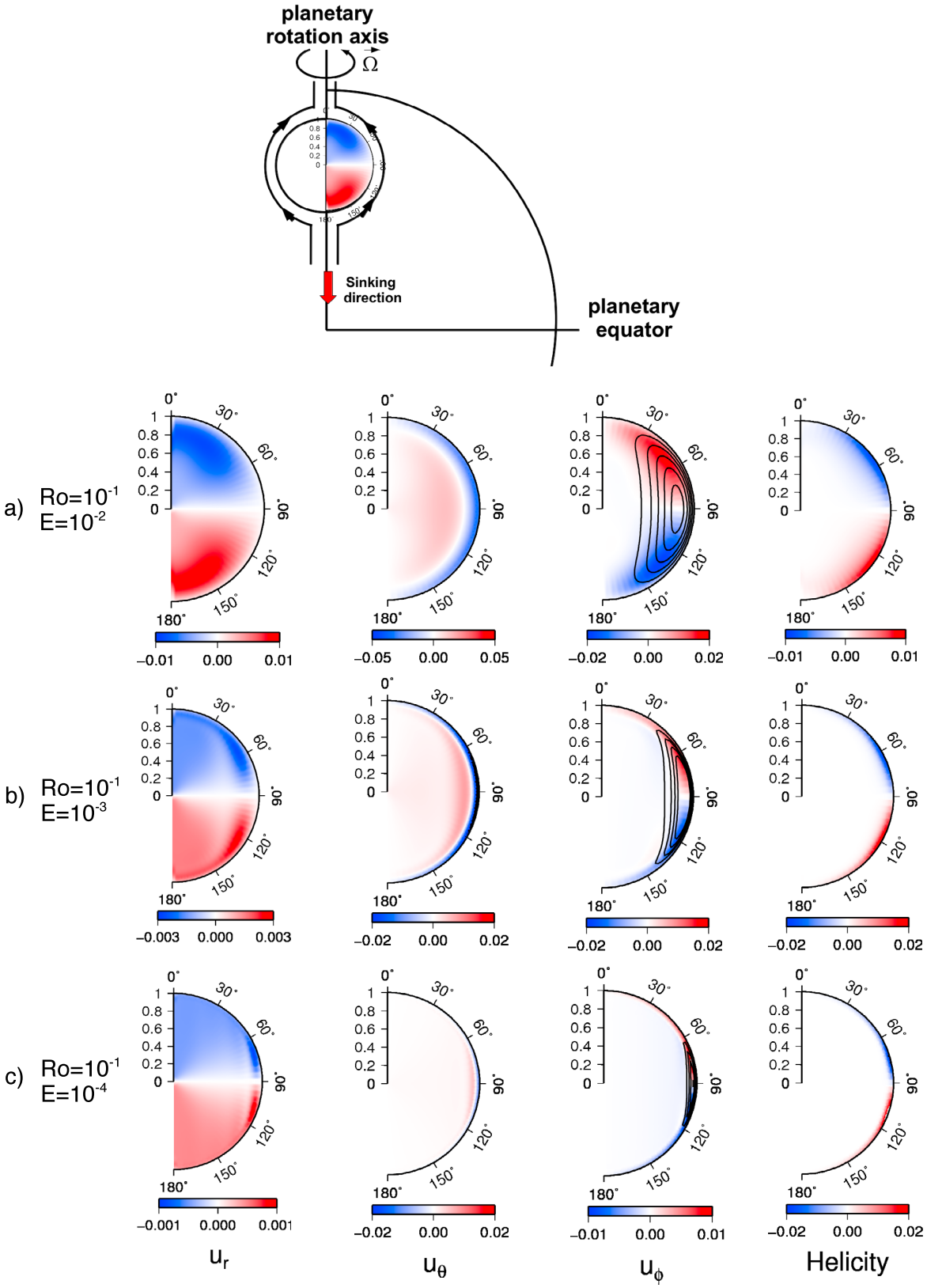

Figure 4. Flow components and helicity for three different E values and $Ro = 10^{-1}$ in the case of a polar sinking diapir. The streamlines with black solid contours (representing counter-clockwise circulation) are superimposed on the u_ϕ subplots. The sinking geometry is illustrated at the top of the figure where u_r is represented. The mean flow is axisymmetric.

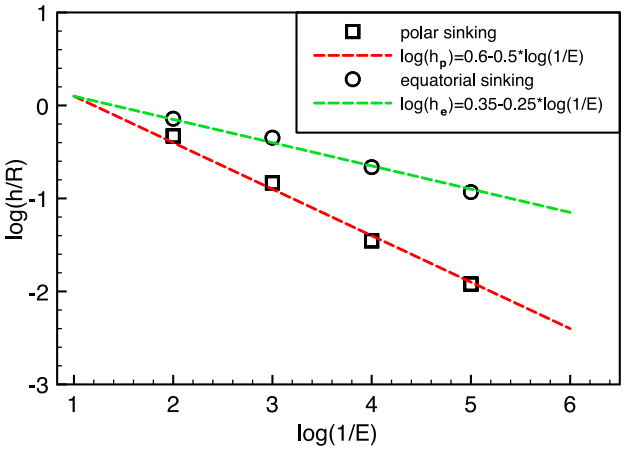

Figure 5. The non-dimensional thickness of the velocity layer h/R as a function of E^{-1} for $Ro = 10^{-2}$ in log-log scale. The depth is defined where the azimuthal velocity drops to 10% of its maximum value at colatitude 60° (for polar sinking diapir, red) or at co-latitude 90° (for equatorial sinking diapir, green).

[25] We repeat the flow analysis for equatorial sinking diapirs. Note that the visualization is in the planetary reference frame, so the north pole points in the direction of the rotation rate (and not in the diapir sinking latitude). Here the flow is symmetric with respect to the equator (Figure 6). In this configuration, the rotation and sinking axes are perpendicular, so that the axisymmetry of the flow is lost. Indeed, in the equatorial plane, the stationary flow is dominated by an $m = 1$ spiral (see Figure 7), and the effect of the Coriolis force tends to make the flow invariant along the rotation axis (Figure 6). The analysis of the thickness of the velocity layer for equatorial sinking diapir leads to the prefactor $A_e \sim 2$ and a power of $x_e \sim 0.25$ (equation (11) and Figure 5, green), reminiscent of a Stewartson internal layer control [*Stewartson*, 1957; *Schaeffer and Cardin*, 2005].

[26] Because helicity favors dynamo action, we examine the pattern of helicity and its dependence on E and Ro. For a polar sinking diapir, the helicity is hemispheric anti-symmetric negative/positive in the northern/southern hemisphere respectively (Figure 4). This helicity pattern is governed by the interaction between the latitudinal flow and the radial shear of the azimuthal flow. As with the flow pattern, the thickness of the layer of significant helicity decreases with decreasing E. For equatorial sinking diapirs the helicity is also hemispheric anti-symmetric (Figure 6). Here the hemispheric anti-symmetric helicity pattern is obtained by the interaction between the azimuthal flow and the radial shear of the latitudinal flow.

4.2. Magnetic Field Generation

[27] First, we used the analytic Hadamard flow solution without rotation and inertia (equations (4) and (5)). We found no dynamo. Next, we accounted for the effect of rotation: for each flow solution obtained by different combinations of E and Ro, we search for the critical magnetic Reynolds number Rm_c above which dynamo action takes place. Figure 8 shows the results of such a parametric study for a polar sinking diapir. The smallest Rm_c values (most favorable flow morphologies for dynamo action) appear for $E = 10^{-3}$. Weaker rotation yields weaker helicity and subsequent field generation, whereas stronger rotation confines the flow to a thinner layer and thus dynamo action is once again less efficient. In the rotational regime where $Ro \ll 1$, Rm_c does not depend on Ro. This is expected because the flow pattern is almost independent of Ro for $Ro \ll 1$. On approach to $Ro \sim 1$, the flow pattern changes and some non-trivial dependence of Rm_c on Ro emerges.

[28] The results of the parametric study for the equatorial sinking diapirs (Figure 9) are similar to those for the polar sinking diapirs. Because the flow of equatorial sinking diapirs is not axisymmetric, one must compute the velocity and magnetic fields with many coupled azimuthal modes, leading to much higher computation times (10 to 30 times longer) than in the polar sinking dynamos. Hence, we decided to focus on $E \leq 10^{-3}$ and $0.1 \leq Ro < 1$. The smallest Rm_c for equatorial sinking diapir was found for $E = 10^{-4}$. From Figures 8 and 9 we can see that Rm has to be at least larger than 3000 to envision a diapir driven dynamo generation which restricts the candidate diapir domain (Figures 1 and 10).

[29] Figure 11 shows images of the magnetic field for a diapir sinking from the equator for two sets of parameters (($E = 10^{-5}$, $Ro = 0.3$), top; ($E = 10^{-4}$, $Ro = 0.1$), bottom). The magnetic field is characterized by small scale features as the flow within the diapir becomes more turbulent (Figure 11, bottom). Note that in the equatorial sinking case, even at small Ekman number, the magnetic field is strong in a significant volume fraction, despite the confinement of the flow to a narrower layer.

5. Magnetic Seed Field Growth Rate and Saturation

[30] We have demonstrated that a sinking diapir can generate a dynamo. Next we estimate the intensity of the magnetic field, in particular whether the sinking time is long enough for the magnetic field to reach saturation before arriving at the bottom of the partially molten mantle. This requires the computation of the non-linear dynamo problem, i.e. the simultaneous solution of the coupled momentum and induction equation. As initial condition, we consider a uniform interplanetary magnetic seed field $B_i = 3 \times 10^{-9}$ T [*Riedler et al.*, 1989]. We monitor the intensity of the dipolar component of the magnetic field at the diapir surface as a function of time from a successful dynamo model of equatorial sinking diapir. We have computed several such dynamos, all of them exhibiting a similar behavior: strong small scale magnetic field within the diapir (Figure 11), with relatively weak dipolar field at its surface. In Figure 12, the time is non-dimensionalized by the time a diapir with radius R needs to travel a distance R. The magnetic field is saturated before a 10 km diapir reaches the bottom of a 200 km depth partially molten mantle. For polar diapirs (not shown), the saturated field is slightly weaker and the growth rate is slower compared with the equatorial case.

[31] We also monitor the corresponding magnetic field intensity at the surface of the planet as a function of time (Figure 12, red line). The intensity of the magnetic field

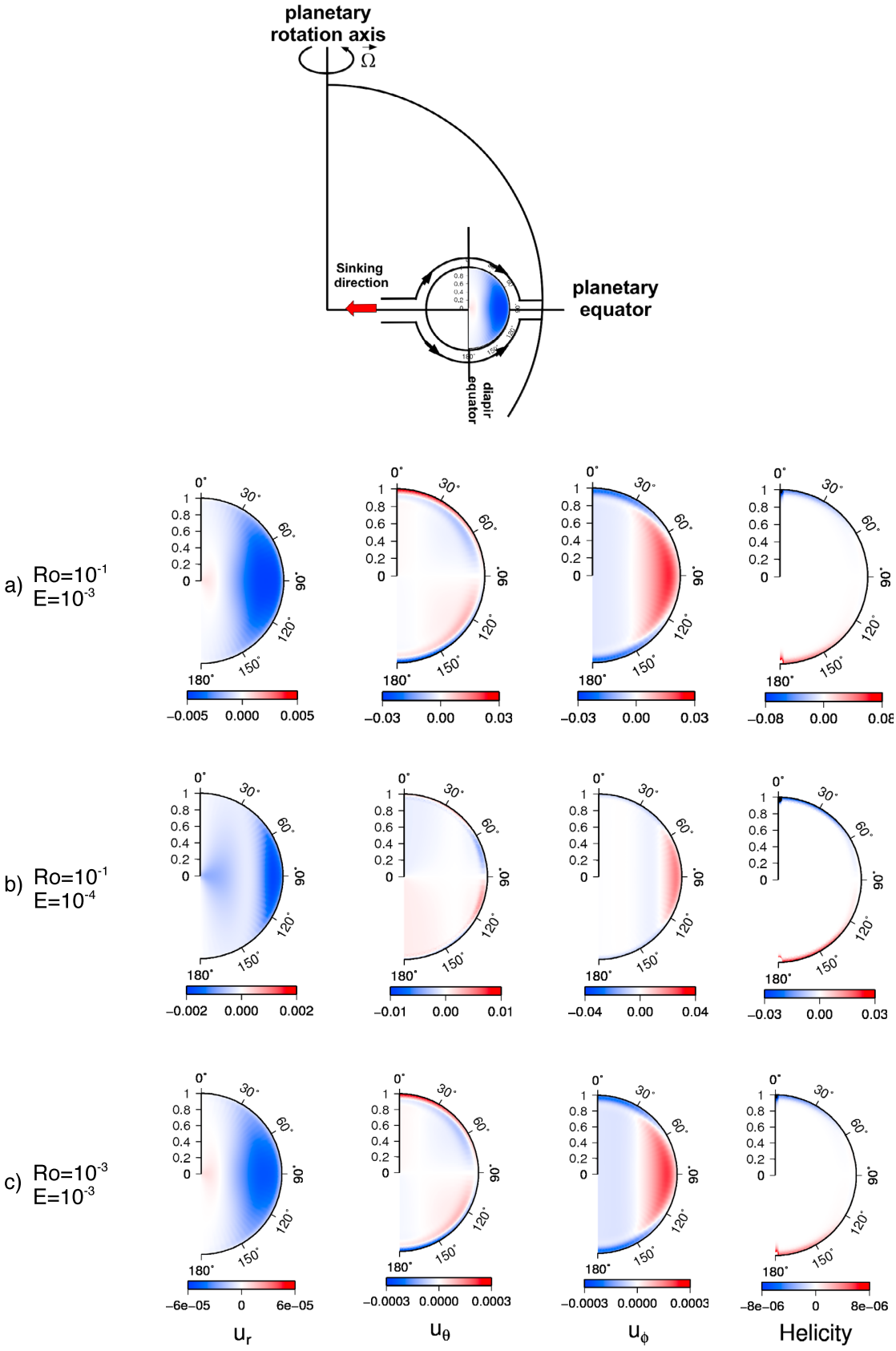

Figure 6. As in Figure 4 for equatorial sinking diapirs. As in Figure 4, the vertical direction points to the rotation axis of the planet.

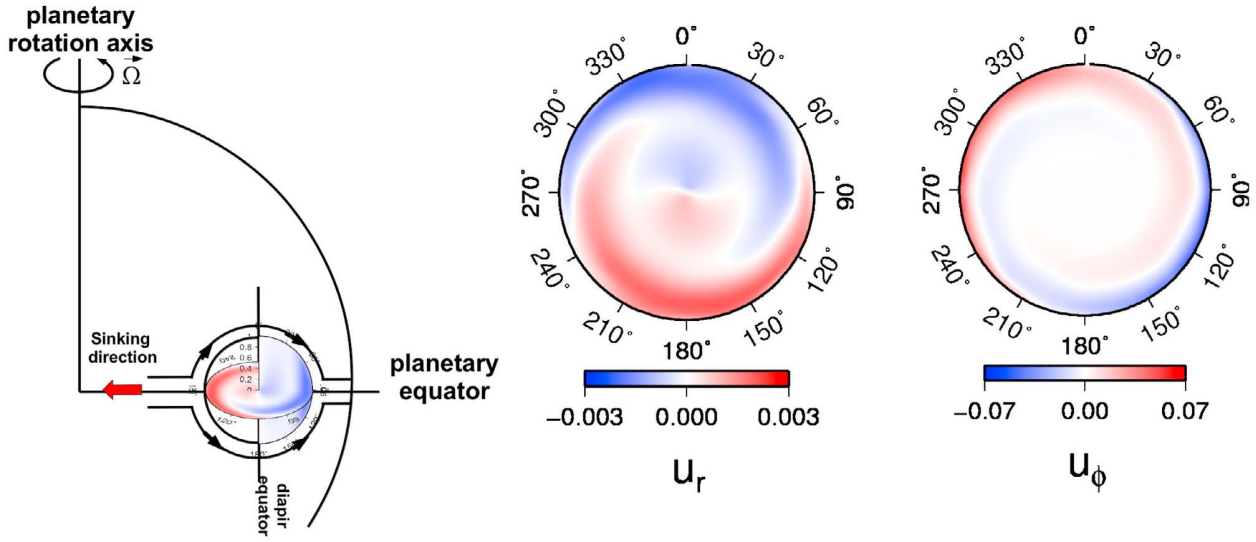

Figure 7. Illustration of the geometry and flow components in the equatorial plane of the planet for $E = 10^{-4}$ and $Ro = 10^{-1}$ for an equatorial sinking diapir.

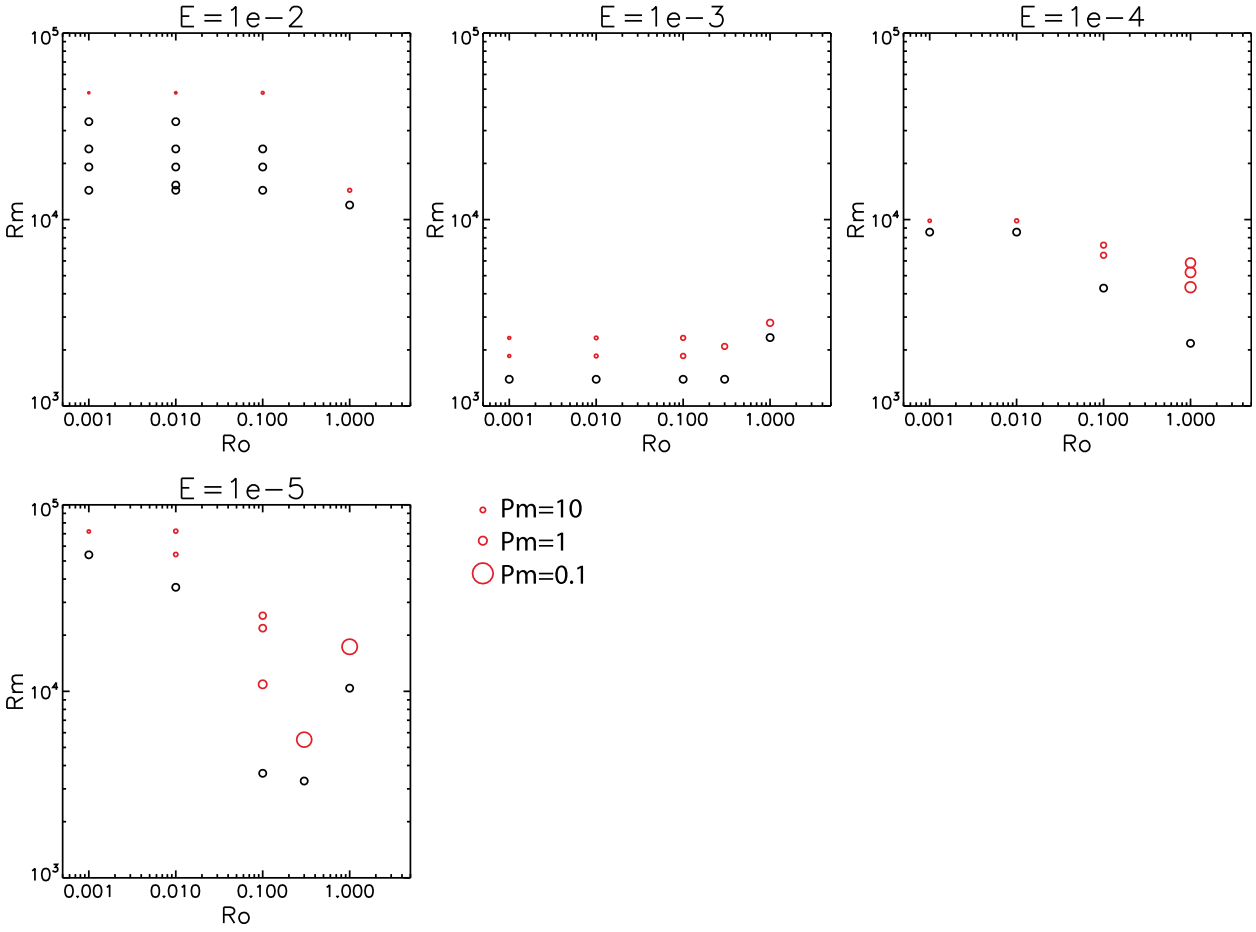

Figure 8. Regime diagram of kinematic dynamos for polar sinking diapirs. Black circles are no dynamos, red circles are dynamos. The values of *Pm* for the dynamo cases in log-scale are represented by the size of the red circles (see legend).

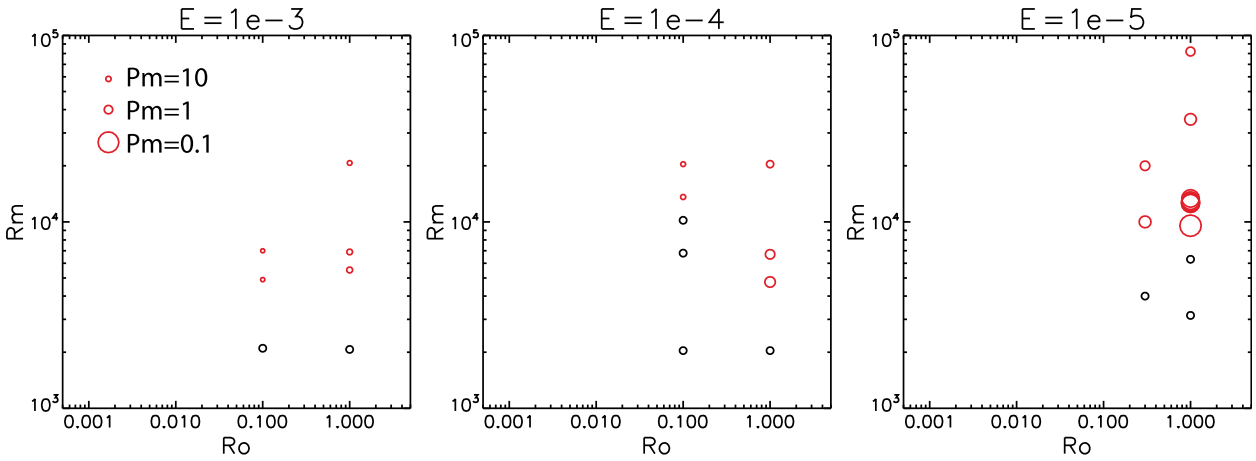

Figure 9. As in Figure 8 for equatorial sinking diapirs.

decreases with the distance d from the surface of the diapir:

$$B \sim B_0 \frac{d}{R}^{-\ell-2} \tag{12}$$

where ℓ is the spherical harmonic degree. We consider the dipolar component of the magnetic field (i.e. $\ell = 1$) which is the strongest contribution far from the generating region. The magnetic field intensity generated by the diapir deep in the mantle never overcomes the initial magnetic seed field intensity. This means that within the range of parameters of our study ($Ro \leq 1$, $Ek \geq 10^{-5}$ and $Pm \geq 10^{-1}$), a dynamo generated by a sinking metallic diapir is unlikely to leave a footprint on the surface paleomagnetic field of a growing planet.

6. Discussion

[32] We studied dynamos generated by 3D circulation driven by Hadamard flow on the outer boundary under the influence of the Coriolis force ($Ro \lesssim 1$, $E \ll 1$). This is an important constraint, which restricts the candidate diapirs from our models to the region below the $Ro \simeq 3$ line of Figure 10, where rotational effects are important. In the highly rotational regime of $Ro \ll 1$ the flow morphology as

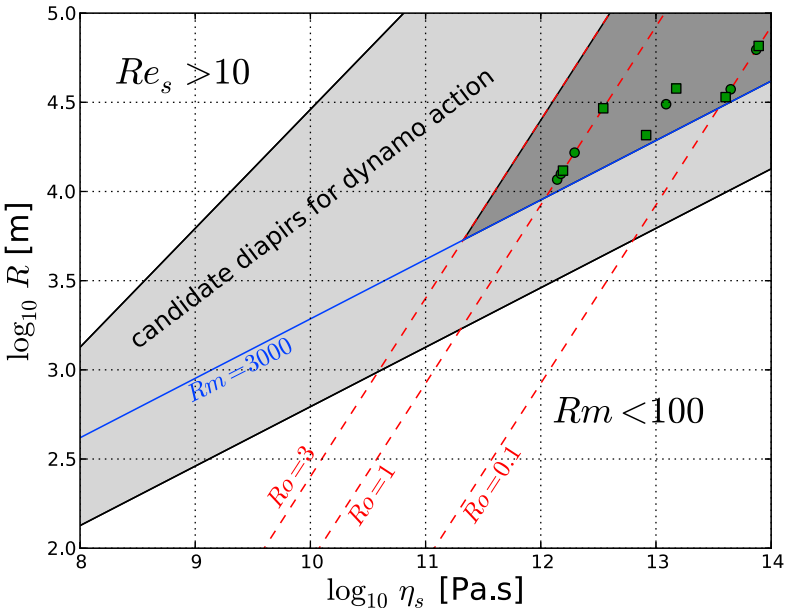

Figure 10. A refined diagram of candidate diapirs for dynamo action. We constrain the candidate diapirs from the results of our models to the dark shaded zone. Successful dynamos are represented with green symbols (squares for polar and circles for equatorial sinking diapirs). The blue solid line for $Rm = 3000$ represents the minimum value for a successful dynamo from our models. The red dashed line for $Ro = 1$ represents the limit of the rotational regime investigated in our study. We also represent the $Ro = 0.1$ value. Larger but moderate Ro values marked by the $Ro = 3$ line (not studied here) may possibly lead to dynamo action. We extend the domain to $\eta_s = 10^{14}$ Pa.s where dynamos were observed in our models.

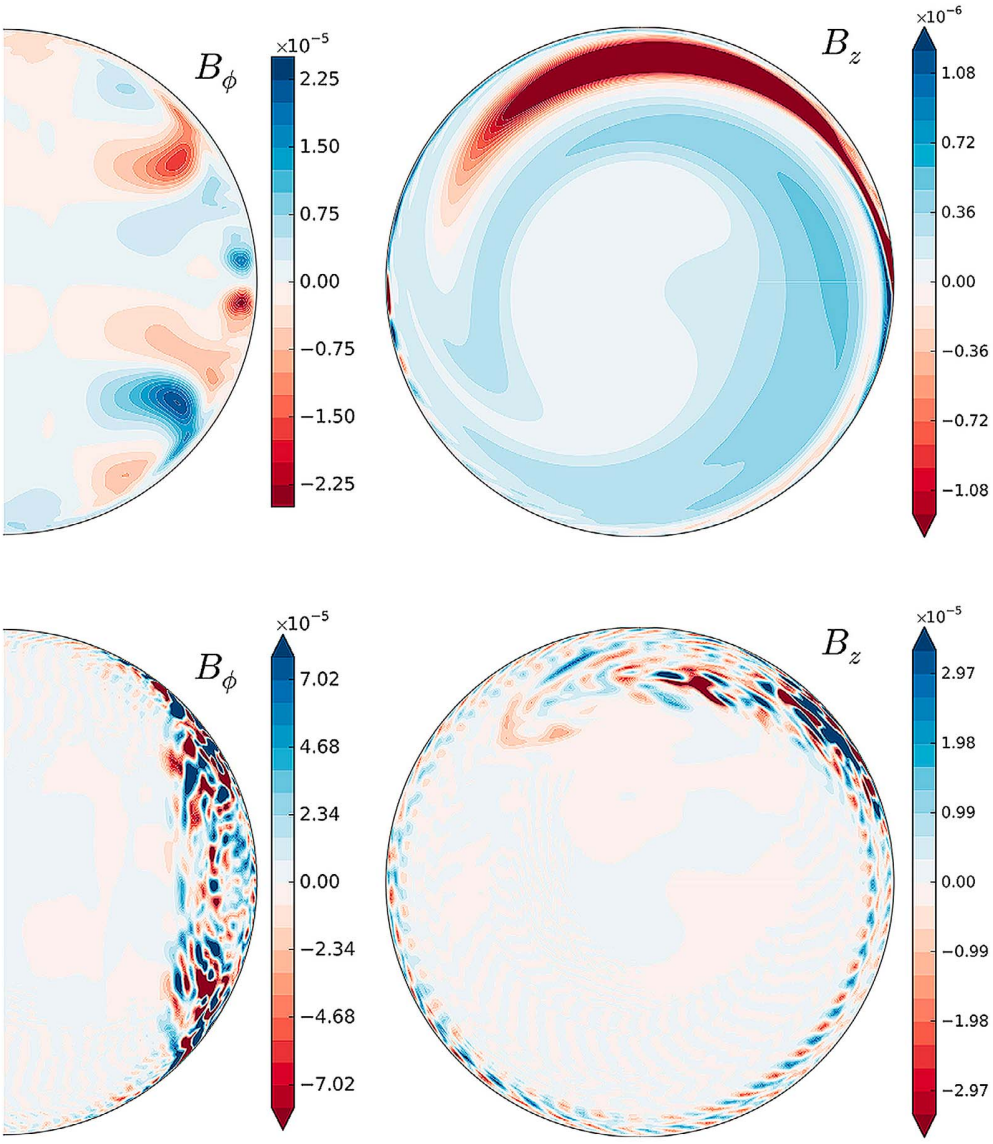

Figure 11. Example of dynamo magnetic fields for an equatorial sinking diapir. (left) The ϕ-component of the magnetic field in an arbitrary meridional cross-section and (right) the Z-component of the magnetic field in the equatorial plane. (top) $E = 10^{-4}$, $Ro = 0.1$, $Pm = 20$, $Re = 10^3$ and (bottom) $E = 10^{-5}$, $Ro = 0.3$, $Pm = 0.5$, $Re = 3 \times 10^4$.

well as Rm_c do not depend on Ro. The behavior of the system for $Ro \sim 1$ is complicated to investigate due to computational limitations. In these systems turbulence becomes important, the flow is unsteady and temporal fluctuations dominate the dynamics. This regime can eventually lead to more complex flows and favor dynamo generation, although it is unlikely [*Peyrot et al.*, 2007; *Ponty and Plunian*, 2011].

[33] Can sinking diapirs produce dynamos in nature? In our numerical simulations, all physical parameters are in the geophysical range except for the liquid iron viscosity, which influences both Ekman and magnetic Prandtl number. Unfortunately, simulations with lower E are computationally very costly. In Figures 8 and 9 the magnetic Prandtl number Pm is represented by the size of the circles in the dynamo cases, so that larger circles represent smaller Pm, closer to the geophysical value. Both these figures show that we have obtained dynamos at smaller Pm values when decreasing E. In the regime which is accessible for our simulations, the lowest Pm values are on the order of 0.1, five orders of magnitude too large. Such computational problems of obtaining Earth-like E and Pm values are ubiquitous to all numerical dynamo studies [*Christensen and Aubert*, 2006; *Christensen and Wicht*, 2007].

[34] From Figures 8 and 9, we obtain the critical magnetic Reynolds number Rm_c for each combination of E and Ro values. This global Rm_c scales with R^3 (equations (1) and (3)). Lowering the Ekman number confines the flow to a narrow velocity layer at the outer part of the diapir, which results in larger Rm_c. This motivates defining a local critical

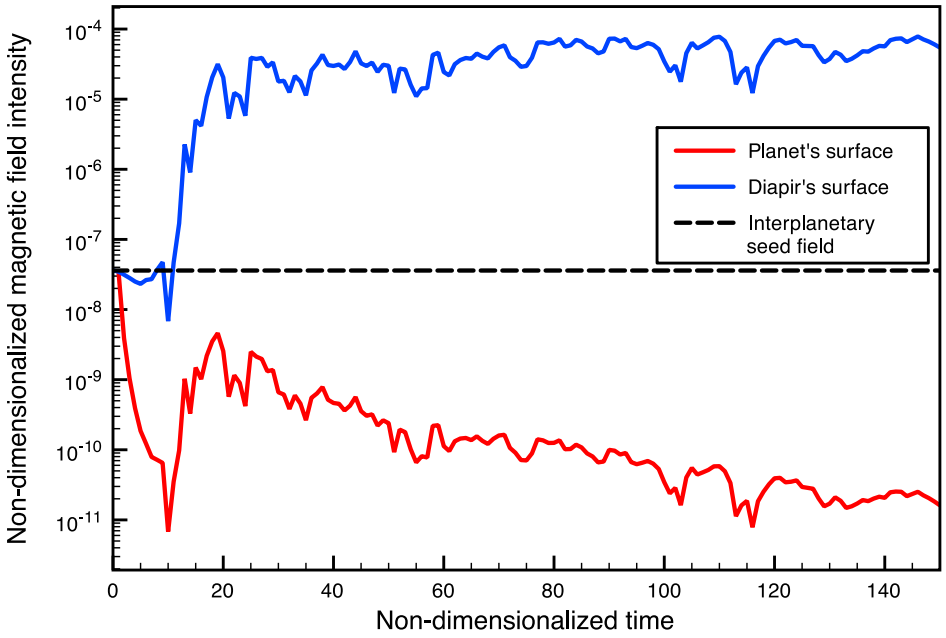

Figure 12. Intensity of the dipolar magnetic field generated by an equatorial sinking diapir as a function of time with $Ro = 1$, $E = 10^{-5}$, $Rm = 10^5$, $Pm = 1$. The intensity of the magnetic field is non-dimensionalized by $\sqrt{\mu_0 \rho_{Fe}} R\Omega$ $\rho_{Fe} = 10^4$ kg.m^{-3} and $R = 10$ km. The blue line represents the evolution of the dipolar magnetic field at the surface of the diapir, and the red line at the surface of the planet.

magnetic Reynolds number Rm_c^L based on the thickness of the velocity layer h:

$$Rm_c^L = \frac{h}{R} Rm_c \tag{13}$$

[35] Using the best fits to h from Figure 5, we plot Rm_c^L as a function of E^{-1} in Figure 13. It is difficult to extrapolate a relation between Rm_c^L and E. Based on this figure, Rm_c^L appears to have an asymptotic behavior with decreasing E, with polar sinking dynamos seeming to be favorable. However, the thickness h of that layer is much larger in the equatorial sinking case ($h \sim E^{1/4}$) than in the polar sinking case ($h \sim E^{1/2}$). It thus appears that dynamo generation from a sinking diapir could be favored by equatorial sinking diapirs for realistic Ekman numbers. Even in the very pessimistic case, where $Rm_c \sim 10^5$ (two orders of magnitude larger than our optimal model) for realistic Ekman numbers, giant diapirs (radius from 30 to 100 km) can still produce strong magnetic fields during their sinking. In addition, the turbulent fluctuations may limit the decrease of h with decreasing E (Figure 5), leading to the decrease of Rm_c at low E (equation (13)). However, lowering the Ekman number will lead to smaller scale magnetic field generation (as suggested by Figure 11), leading to a possibly lower magnetic field at the surface of the planet.

7. Conclusions and Perspectives

[36] Our results show that the flow pattern driven by a diapir sinking through a partially molten mantle within a rotating planet can generate a magnetic field. This dynamo generation seems more favorable for a diapir sinking from the equator than from the planet's rotational pole. Large diapirs ($R > 10$ km) sinking in a mantle with a viscosity ranging from 10^9 to 10^{14} Pa.s (see Table 1) provide plausible conditions to generate a transient dynamo that may have occurred in the early history of terrestrial planets or immediately after a giant impact and the subsequent core merging process. However, the magnetic field generated by a single diapir in our models is too weak to contribute to the paleomagnetic field recorded on Mars or on the Moon.

[37] Several questions arise from our results:

[38] 1. What is the influence of the intensity of the magnetic seed field on the feasibility of a diapir driven dynamo? We have considered in this study the very weak homogeneous interplanetary magnetic seed field. However, magnetic fields are expected to be generated in planetary cores during the early evolution of planets and moons [*Monteux et al.*, 2011a]. The presence of a stronger magnetic field during early planetary evolutions may change the flow inside the diapir, leading to faster and stronger magnetic field amplification.

[39] 2. How will multiple diapirs affect the early planetary magnetic fields? Large diapirs are not isolated events during planetary differentiations. The presence of multiple diapirs may influence the sinking dynamics of each diapir [*Manga and Stone*, 1993] and hence the dynamo generation.

[40] 3. Can the magnetic field of the sinking diapirs help to start the planetary dynamo? If the convective planetary dynamo is subcritical [*Christensen et al.*, 2001], i.e. the dynamo cannot start without a strong initial field, the core

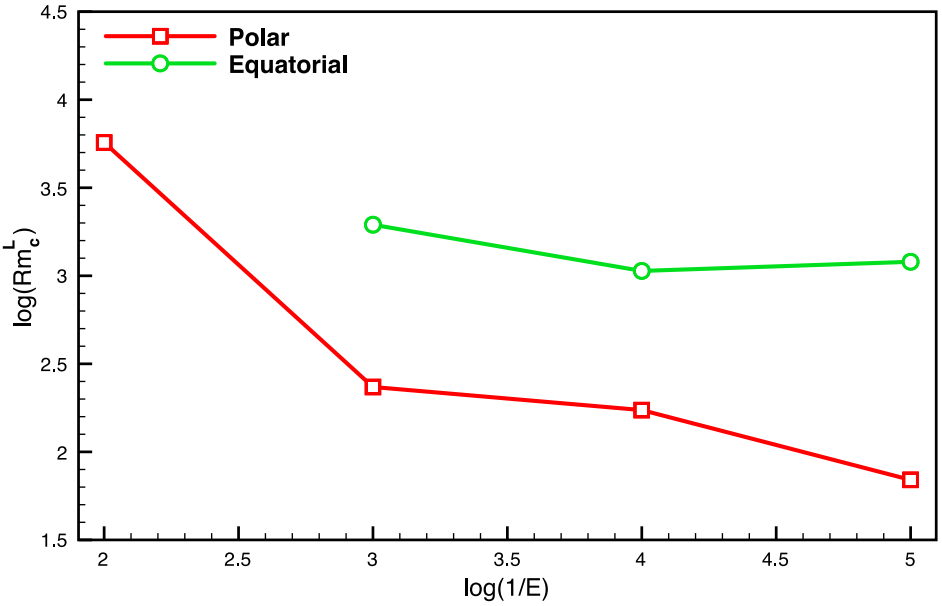

Figure 13. Local magnetic Reynolds number Rm_c^L as a function of E^{-1}. Rm_c^L is obtained by combining the results for Rm_c from Figures 8 and 9 (choosing the most favorable Ro value for each value of E) and the fits for h from Figure 5.

merging process could bring the required magnetic field intensity inside the planetary core to trigger a dynamo.

Appendix A: Numerical Method

[41] Our three-dimensional spherical code uses a second order finite differences scheme in the radial direction and pseudo-spectral spherical harmonic expansion in the tangential direction using the high performance SHTns library (N. Schaeffer, Efficient spherical harmonic transforms aimed at pseudo-spectral numerical simulations, preprint, 2012, arXiv:1202.6522). The time stepping uses a semi-implicit Crank-Nicholson scheme for the diffusive terms, while the non-linear terms are handled by an Adams-Bashforth scheme (second order in time). To calculate the 3D flow, the momentum equation is time stepped in the spherical fluid shell with imposed velocity field at the spherical outer boundary. For kinematic dynamo simulations the induction equation is solved with an insulator outside the outer boundary and an imposed stationary 3D velocity field. The full dynamo problem can also be solved with coupled induction and momentum equations.

[42] We want to emphasize that there is no solid inner core: our code supports fluid that fills the whole sphere. The method to overcome numerical instability near $r = 0$ is based on the fact that the minimum length-scale resolved by a spherical harmonic expansion truncated at degree $\ell_{\max}$ is about $\pi r/\ell_{\max}$. Hence when $r \to 0$, we resolve smaller and smaller angular length-scale, which is at best useless, and can lead to numerical instabilities. We overcome this limitation with a spherical harmonic truncation ℓ_{tr} that depends on r. Specifically, we use

$$\ell_{tr}(r) = 1 + (\ell_{\max} - 1)\frac{r}{r_{\max}} \qquad \text{(A1)}$$

Although the finite difference scheme has a theoretical error that scales like $1/r$, the numerical solutions of the velocity field and magnetic field are perfectly smooth near $r = 0$, with flow and magnetic field that are allowed to cross $r = 0$. We use $\ell_{\max}$ ranging from 20 to 90 and the number of radial grid points ranges from 100 to 300 depending on the strength of inertial effects (measured by the hydrodynamic Reynolds number $Re = Ro/E$).

[43] In the case of a diapir falling on the planetary pole, the boundary conditions are symmetric by rotation around the rotation axis of the planet. This implies that the stationary flow is axisymmetric (when there are no instabilities). When computing the kinematic dynamo problem with an axisymmetric flow, the various azimuthal wave numbers m of the magnetic field are independent. Moreover, it is known from the Cowling theorem that the magnetic field must include non-axisymmetric ($m > 1$) terms [*Cowling*, 1934]. Hence we search for magnetic field with $m = 1$, $m = 2$ and $m = 3$ separately. We find that most often the first growing magnetic field mode is the one with $m = 2$.

[44] In the case of a diapir falling on the planetary equator, the boundary conditions are not symmetric by rotation around the rotation axis of the planet. However, they are purely $m = 1$, and we find that the stationary flow, without inertial effects (small Ro/E) is mainly a spiralling $m = 1$ flow. When inertial effects are not negligible, all azimuthal wave numbers are present in the flow, leading to longer computations, where we usually set $m_{\max} = \ell_{\max}/2$, which seems to be a reasonable truncation scheme when looking at the resulting spectra. The kinematic dynamo computation also requires all azimuthal wave numbers to be computed at once because they are coupled by the $m > 0$ flow. We use the same truncation as for the flow, and for some cases we verified that larger truncations did not change the dynamo onset threshold significantly.

[45] **Acknowledgments.** The authors thank B. Langlais and T. Seon for useful discussions. The authors also thank the anonymous reviewers for constructive comments. J.M. is funded by Agence Nationale de Recherche (Accretis decision ANR-10-PDOC-001-01). Part of the numerical simulations were run at the Service Commun de Calcul Intensif de l'Observatoire de Grenoble (SCCI).

References

Agnor, C. B., R. M. Canup, and H. F. Levison (1999), On the character and consequences of large impacts in the late stage of terrestrial planet formation, *Icarus*, *142*, 219–237, doi:10.1006/icar.1999.6201.

Amit, H., P. Olson, and U. Christensen (2007), Tests of core flow imaging methods with numerical dynamos, *Geophys. J. Int.*, *168*, 27–39.

Batchelor, G. (1967), *An Introduction to Fluid Dynamics*, Cambridge Univ. Press, Cambridge, U. K.

Benz, W., W. L. Slattery, and A. G. W. Cameron (1987), The origin of the Moon and the single-impact hypothesis., *Icarus*, *71*, 30–45, doi:10.1016/0019-1035(87)90160-6.

Christensen, U., and J. Aubert (2006), Scaling properties of convection-driven dynamos in rotating spherical shells and application to planetary magnetic fields, *Geophys. J. Int.*, *166*, 97–114.

Christensen, U., and J. Wicht (2007), Numerical dynamo simulations, in *Core Dynamics*, *Treatise Geophys.*, vol. 8, edited by P. Olson, pp. 245–282, Elsevier, Oxford, U. K.

Christensen, U. R., et al. (2001), A numerical dynamo benchmark, *Physics Earth Planet. Inter.*, *128*(1–4), 25–34, doi:10.1016/S0031-9201(01)00275-8.

Cowling, T. (1934), The magnetic field of sun spots, *Mon. Not. R. Astron. Soc.*, *94*, 39–48.

Dahl, T. W., and D. J. Stevenson (2010), Turbulent mixing of metal and silicate during planet accretion and interpretation of the Hf-W chronometer, *Earth and Planet. Sci. Lett.*, *295*, 177–186, doi:10.1016/j.epsl.2010.03.038.

Davies, G. F. (1982), Ultimate strength of solids and formation of planetary cores, *Geophys. Res. Lett.*, *9*, 1267–1270.

Deguen, R., P. Olson, and P. Cardin (2011), Experiments on turbulent metal-silicate mixing in a magma ocean, *Earth Planet. Sci. Lett.*, *310*, 303–313, doi:10.1016/j.epsl.2011.08.041.

Dudley, M., and R. James (1989), Time-dependent kinematic dynamos with stationary flows, *Proc. R. Soc. London, Ser. A*, *425*, 407–429.

Gailitis, A. (1970), Self-excitation of a magnetic field by a pair of ring vortices [in Russian], *Mag. Gidrodin.*, *6*, 19–22. [*Magnetohydrodynamics*, Engl. Transl., *6*, 14–17.]

Gerya, T. V., and D. A. Yuen (2007), Robust characteristics method for modelling multiphase visco-elastic thermo-mechanical problems, *Phys. Earth Planet. Inter.*, *163*, 83–105.

Gubbins, D., C. Barber, S. Gibbons, and J. Love (2000a), Kinematic dynamo action in a sphere: I. Effects of differential rotation and meridional circulation on solutions with axial dipole symmetry, *Proc. R. Soc. London, Ser. A*, *456*, 1333–1353.

Gubbins, D., C. Barber, S. Gibbons, and J. Love (2000b), Kinematic dynamo action in a sphere: II. Symmetry selection, *Proc. R. Soc. London, Ser. A*, *456*, 1669–1683.

Guervilly, C., and P. Cardin (2010), Numerical simulations of dynamos generated in spherical Couette flows, *Geophys. Astrophys. Fluid Dyn.*, *104*, 221–248, doi:10.1080/03091920903550955.

Hadamard, J. (1911), Mouvement permanent lent d'une sphére liquide et visqueuse dans un liquide visqueux, *C. R. Acad. Sci.*, *152*, 1735–1738.

Höink, T., J. Schmalzl, and U. Hansen (2005), Formation of compositional structures by sedimentation in vigorous convection, *Phys. Earth Planet. Inter.*, *153*, 11–20.

Höink, T., J. Schmalzl, and U. Hansen (2006), Dynamics of metal-silicate separation in a terrestrial magma ocean, *Geochem. Geophys. Geosyst.*, *70*, Q09008, doi:10.1029/2006GC001268.

Honda, R., H. Mizutani, and T. Yamamoto (1993), Numerical simulation of Earth's core formation, *J. Geophys. Res.*, *98*, 2075–2089.

Karato, S.-I., and V. Murthy (1997), Core formation and chemical equilibrium in the Earth—I. Physical considerations, *Phys. Earth Planet. Inter.*, *100*, 61–79.

Kaula, W. M. (1979), Thermal evolution of Earth and Moon growing by planetesimal impacts, *J. Geophys. Res.*, *84*, 999–1008.

Kleine, T., C. Münker, K. Mezger, and H. Palme (2002), Rapid accretion and early core formation on asteroids and the terrestrial planets from Hf-W chronometry, *Nature*, *418*, 952–955.

Le Bars, M., M. Wieczorek, O. Karatekin, D. Cébron, and M. Laneuville (2011), An impact-driven dynamo for the early Moon, *Nature*, *479*, 215–218.

Manga, M., and H. A. Stone (1993), Buoyancy-driven interactions between two deformable viscous drops, *J. Fluid Mech.*, *256*, 647–683, doi:10.1017/S0022112093002915.

Moffatt, H. (1978), *Magnetic Field Generation in Electrically Conducting Fluids*, Cambridge Univ. Press, Cambridge, U. K.

Monteux, J., Y. Ricard, N. Coltice, F. Dubuffet, and M. Ulvrova (2009), A model of metal-silicate separation on growing planets, *Earth Planet. Sci. Lett.*, *287*, 353–362.

Monteux, J., A. M. Jellinek, and C. L. Johnson (2011a), Why might planets and moons have early dynamos?, *Earth. Planet. Sci. Lett.*, *310*, 349–359, doi:10.1016/j.epsl.2011.08.014.

Monteux, J., M. Jellinek, and C. L. Johnson (2011b), Core merging after the Martian giant impact, *Lunar Planet. Sci. Conf.*, *XLII*, Abstract 1665.

Moss, D. (2008), Simple laminar dynamos: From two rolls to one, *Geophys. Astrophys. Fluid Dyn.*, *102*, 195–203.

Olson, P. (2007), Overview on core dynamics, in *Core Dynamics*, *Treatise Geophys.*, vol. 8, edited by P. Olson, pp. 1–30, Elsevier, Oxford, U. K.

Olson, P., U. Christensen, and G. Glatzmaier (1999), Numerical modeling of the geodynamo: Mechanisms of field generation and equilibration, *J. Geophys. Res.*, *104*, 10,383–10,404.

Olson, P., I. Sumita, and J. Aurnou (2002), Diffusive magnetic images of upwelling patterns in the core, *J. Geophys. Res.*, *107*(B12), 2348, doi:10.1029/2001JB000384.

Pedlosky, J. (1987), *Geophysical Fluid Dynamics*, Springer, New York.

Peyrot, M., F. Plunian, and C. Normand (2007), Parametric instability of the helical dynamo, *Phys. Fluids*, *19*, 054109, doi:10.1063/1.2734118.

Ponty, Y., and F. Plunian (2011), Transition from large-scale to small-scale dynamo, *Phys. Rev. Lett.*, *106*, 154502, doi:10.1103/PhysRevLett.106.154502.

Ricard, Y., O. Šrámek, and F. Dubuffet (2009), A multi-phase model of runaway core-mantle segregation in planetary embryos, *Earth Planet. Sci. Lett.*, *284*, 144–150.

Riedler, W., K. Schwingenschuh, D. Moehlmann, V. N. Oraevskii, E. Eroshenko, and J. Slavin (1989), Magnetic fields near Mars—First results, *Nature*, *341*, 604–607, doi:10.1038/341604a0.

Rubie, D., H. Melosh, J. Reid, C. Liebske, and K. Righter (2003), Mechanisms of metal-silicate equilibration in the terrestrial magma ocean, *Earth Planet. Sci. Lett.*, *205*, 239–255.

Safronov, V. S. (1978), The heating of the Earth during its formation, *Icarus*, *33*, 3–12, doi:10.1016/0019-1035(78)90019-2.

Samuel, H. (2012), A re-evaluation of metal diapir breakup and equilibration in terrestrial magma oceans, *Earth Planet. Sci. Lett.*, *313*, 105–114, doi:10.1016/j.epsl.2011.11.001.

Samuel, H., and P. Tackley (2008), Dynamics of core formation and equilibration by negative diapirism, *Geochem. Geophys. Geosyst.*, *9*, Q06011, doi:10.1029/2007GC001896.

Schaeffer, N., and P. Cardin (2005), Quasigeostrophic model of the instabilities of the stewartson layer in flat and depth-varying containers, *Phys. Fluids*, *17*(10), 104111, doi:10.1063/1.2073547.

Senshu, H., K. Kuramoto, and T. Matsui (2002), Thermal evolution of a growing Mars, *J. Geophys. Res.*, *107*(12), 5118, doi:10.1029/2001JE001819.

Shannon, M. C., and C. B. Agee (1996), High pressure constraints on percolative core formation, *Geophys. Res. Lett.*, *23*, 2717–2720.

Spells, K. (1952), A study of circulation patterns within liquid drops moving through a liquid, *Proc. Phys. Soc. B*, *65*, 541–546.

Šrámek, O., Y. Ricard, and F. Dubuffet (2010), A multiphase model of core formation, *Geophys. J. Int.*, *181*, 198–220, doi:10.1111/j.1365-246X.2010.04528.x.

Stevenson, D. (1981), Models of the Earth's core, *Science*, *214*, 611–619.

Stevenson, D. J. (2003), Planetary science: Mission to Earth's core—A modest proposal, *Nature*, *423*(6937), 239–240, doi:10.1038/423239a.

Stewartson, K. (1957), On almost rigid rotations, *J. Fluid Mech.*, *3*(01), 17–26, doi:10.1017/S0022112057000452.

Tilgner, A. (2005), Precession driven dynamos, *Phys. Fluids*, *17*(3), 034104, doi:10.1063/1.1852576.

Tonks, W. B., and H. J. Melosh (1992), Core formation by giant impacts, *Icarus*, *100*, 326–346.

Tonks, W. B., and H. J. Melosh (1993), Magma ocean formation due to giant impacts, *J. Geophys. Res.*, *98*, 5319–5333.

Touboul, M., T. Kleine, B. Bourdon, H. Palme, and R. Wieler (2007), Late formation and prolonged differentiation of the Moon inferred from W isotopes in lunar metals, *Nature*, *450*, 1206–1209.

Ulvrová, M., N. Coltice, Y. Ricard, S. Labrosse, F. Dubuffet, J. Velímský, and O. Šrámek (2011), Compositional and thermal equilibration of particles, drops, and diapirs in geophysical flows, *Geochem. Geophys. Geosyst.*, *121*, Q10014, doi:10.1029/2011GC003757.

Yin, Q., S. B. Jacobsen, K. Yamashita, J. Blichert-Toft, P. Télouk, and F. Albarède (2002), A short timescale for terrestrial planet formation from Hf-W chronometry of meteorites, *Nature*, *418*, 949–952.

Yoshino, T., M. J. Walter, and T. Katsura (2003), Core formation in planetesimals triggered by permeable flow, *Nature*, *422*, 154–157.

Icarus 226 (2013) 20–32

Contents lists available at SciVerse ScienceDirect

Icarus

journal homepage: www.elsevier.com/locate/icarus

Dynamics of core merging after a mega-impact with applications to Mars' early dynamo

J. Monteux [a,b,*], A.M. Jellinek [b], C.L. Johnson [b,c]

[a] Laboratoire de Planétologie et de Géodynamique de Nantes, UMR CNRS, Université de Nantes, France
[b] Department of Earth, Ocean and Atmospheric Sciences, University of British Columbia, Canada
[c] Planetary Science Institute, Tucson, AZ, United States

ARTICLE INFO

Article history:
Received 3 October 2012
Revised 23 April 2013
Accepted 9 May 2013
Available online 18 May 2013

Keywords:
Mars, Interior
Magnetic fields
Impact processes
Planetary dynamics

ABSTRACT

A giant impact occurring within the first 500 Myr of martian history may have been responsible for the dichotomy between the northern lowlands and the southern highlands and may have influenced the initiation or cessation of early and short-lived core dynamo. We hypothesize that a significant volume of metallic iron from a differentiated impactor merged with a preexisting martian core. We investigate the dynamics and thermal effects of this core merging, assuming that the impactor's core sank as a single metallic diapir through a solid mantle. We explore the consequences of this process for dynamo action and for Mars' magnetic field history. For large impacts (with radii larger than 100 km) and plausible mantle viscosities, merging is expected to occur in less than 1 Myr. Depending on the temperature-dependence of the mantle viscosity, viscous dissipation within the diapir may be very large. Where thermal mixing of the hot diapir into a preexisting core is complete, merging can increase the temperature gradient to the surrounding mantle and consequently drive a dynamo until this additional heat is transferred to the mantle, which takes on the order of 100 Myr. If merging leads to strong thermal stratification in the core, however, dynamo action may be inhibited.

1. Introduction

Mega impacts (with an impactor/target radius ratio between one tenth and 1) probably played an important role in the late history of terrestrial planetary accretion. An impact between the proto-Earth and a Mars-size protoplanet can, for example, explain the Earth–Moon system (Hartmann and Davis, 1975) and a large impact removing part of the silicate mantle is a hypothesis for the high iron/silicate ratio on Mercury (Smith, 1979; Benz et al., 1988). Among the hypotheses for the origin of the martian dichotomy including an endogenic origin (Elkins-Tanton et al., 2003; Roberts and Zhong, 2006; Citron and Zhong, 2012) or a plate-tectonics feature (Sleep, 1994), an exogenic origin by a mega impact that displaced crustal material from the northern to the southern hemisphere seems to be the most plausible candidate (Wilhelms and Squyres, 1984; Nimmo et al., 2008; Andrews-Hanna et al., 2008; Marinova et al., 2008, 2011). Models for the martian impact suggest that the impactor was 800–1300 km in radius and hit the planet with a speed comparable to or larger than the martian escape velocity (i.e. $v_{imp} > 5$ km s^{-1}) within the first 500 Myr of martian history (Frey, 2006). Such a dramatic event can generate a debris disk around Mars that could have re-accreted and formed the martian moons (Rosenblatt, 2011).

In addition to a history of large impacts, Earth, Mercury and Mars have, or have had, an internally generated magnetic field. Mercury and the Earth have active core dynamos, whereas widespread crustal magnetism strongly suggest that Mars had an early internally-generated magnetic field (Acuña et al., 1999; Hood et al., 2003; Lillis et al., 2008a) that ceased by around 4.0 Ga (Acuña et al., 1999; Johnson and Phillips, 2005; Lillis et al., 2008b). The timing of the initiation of the martian dynamo is difficult to constrain and strongly depends on the differentiation processes that occurred during the first million years of martian history (Monteux et al., 2011). The cause of the cessation of the martian dynamo is also still currently debated. Recent models explore the effects of large impacts on the dynamo generation process, and in particular on the cessation of dynamo action as a result of a reduction of the core–mantle boundary (CMB) heat-flux (Roberts et al., 2009; Watters et al., 2009; Roberts and Arkani-Hamed, 2012). Shock heating within the core can also increase the CMB heat flow and create a thermal stratification that prevents heat loss from the inner part of the core, inhibiting core convection (Arkani-Hamed and Olson, 2010). Alternatively, other models show that the thermal anomaly induced by a large impact and the formation of a hot molten iron layer from the impactor's core at the CMB can favor dynamo generation (Reese and Solomatov, 2010).

* Corresponding author at: Laboratoire de Planétologie et de Géodynamique de Nantes, UMR CNRS, Université de Nantes, France.
E-mail address: julien.monteux@univ-nantes.fr (J. Monteux).

0019-1035/$ - see front matter © 2013 Elsevier Inc. All rights reserved.
http://dx.doi.org/10.1016/j.icarus.2013.05.008

At the time of the proposed giant impact, both Mars and the impactor were probably differentiated (Yoshino et al., 2003). Models suggest that although some material was ejected far from Mars, the majority of the mass of the impactor's core was retained within the planet and merged with the pre-impact martian core (Canup, 2004; Ćuk and Stewart, 2012). The aim of this study is to characterize the dynamics of core merging as a result of a diapiric descent of molten iron (Monteux et al., 2009) on a Mars-size planet. In addition, we investigate how the processes of impact and core merging might influence the thermal regime of Mars' core and, in turn, magnetic field generation (cf., Monteux et al., 2011).

2. Thermo-chemical state before the martian mega-impact

2.1. Pre-impact interior of Mars

The initial structure and thermal state of a growing planet is determined by the characteristics of its accretion from chondritic material (Safronov, 1978; Kaula, 1979; Agee, 1997). During accretion, heating driven by a combination of the dissipation of impact energy and the decay of short lived radionuclides such as ^{26}Al and/or ^{60}Fe (Yoshino et al., 2003; Monteux et al., 2007) increases the mean internal temperature and gives rise to a radial temperature gradient that depends on the accretion rate relative to the rate of radiative cooling to space (Kaula, 1979; Senshu et al., 2002). If the growth rate is very high in comparison to surface cooling, this heating can ultimately cause partial or complete melting of the chondritic material (Yoshino et al., 2003) and lead to extensive metal/silicate separation (Tonks and Melosh, 1992; Senshu et al., 2002; Monteux et al., 2009).

Hf/W chronology suggests that core formation happened during the first 10–30 myr of Mars' history (Lee and Halliday, 1997; Nimmo and Kleine, 2007). Such a rapid process involves extensive melting potentially enhanced by radiogenic heating as a result of the decay of short-lived radionuclides (Yoshino et al., 2003), impact heating (Tonks and Melosh, 1992; Senshu et al., 2002; Monteux et al., 2009) and gravitational energy conversion during metal/silicate separation (Stevenson, 1989; Ricard et al., 2009). Metal/silicate separation can occur via a wide range of phenomena such as percolation (Shannon and Agee, 1996), the sedimentation of metallic rain through a magma ocean (Rubie et al., 2003; Höink et al., 2005) or a large diapir sinking through a solid mantle after an impact (Tonks and Melosh, 1992; Monteux et al., 2009). Whatever the mechanism, Mars' internal structure characterized by a ~1700 km diameter Fe-core was mostly established within ~10 Myr of the planet's formation (Yoder et al., 2003) (cf., Fig. 1a).

The gravitational heat released during martian core formation was partitioned between the planet's core and mantle. The fraction of gravitational heat taken up by the metal or the silicate fraction depends strongly on the rheology of the planet and on the segregation mechanisms (Samuel and Tackley, 2008; Monteux et al., 2009; Ke and Solomatov, 2009). The combined processes leading to core formation yield a wide range of possible early thermal states, depending on the nature and timescale of the core formation process and the heat transfer properties of Mars' early mantle. In particular, the core could initially have had a temperature close to the deep mantle temperature if thermal equilibration was efficient. Alternatively, it could have been hotter than the mantle if the gravitational potential energy released during core formation was largely retained within the core itself, a situation which would lead to potentially strong cooling to the mantle (Fig. 1a).

2.2. Interior structure of the impactor

In this study, we consider impactors with a radius in the range 200–800 km. The lower bound for our range is motivated by the impactor size needed to create large impact basins such as Hellas or Utopia, and the upper bound is motivated by the minimum impactor radius needed in exogenic models for the dichotomy boundary (Marinova et al., 2008). Assuming that both the impactor and the target body had chondritic compositions, their volumetric metal fractions, f_0, should be similar (we consider that the impactor has the same metal content as Mars and we use f_0 = 12.5% (Stevenson, 2001)). Hence, for 200–1300 km diameter impactors, an additional volume of core material with a radius between 100 km and 700 km merges with the preexisting core (Fig. 1).

3. Thermo-chemical state after a mega-impact

3.1. Mantle heating and melting

Kinetic energy of the impactor is dissipated as a result of the irreversible work done by shock waves in damaging crustal rocks (Senshu et al., 2002; Monteux et al., 2011) as well as heating and melting the target material. This dissipation process is a complex mechanism that is still poorly constrained specially for giant impact events. In our models, we consider that post-impact heating and melting mostly occurs within a spherical region with a volume V_{ic} (and a radius R_{ic}) that is typically taken to be 3 times larger than the volume V_{imp} of the impactor itself (O'Keefe and Ahrens, 1977; Croft, 1982; Pierazzo et al., 1997). The energy available to heat and melt the target planet is $\Delta E = \gamma m_{imp} v_{imp}^2/2$, where γ is the fraction of the kinetic energy of the impactor ultimately dissipated to heat up the mantle (O'Keefe and Ahrens, 1977), m_{imp} is the impactor mass and v_{imp} is the impact velocity. The energy needed to melt a silicate volume V_{ic} is $\Delta E_{m,Si} = \rho_{Si} V_{ic} L_{Si}$, where ρ_{Si} and L_{Si} are the density and latent heat of the silicate material. The energy needed to melt the impactor core is $\Delta E_{m,Fe} = \rho_{Fe} f_0 V_{imp} L_{Fe}$ with L_{Fe} and ρ_{Fe} are the density and latent heat of the impactor's core.

In the heated region the temperature increases uniformly from an initial value T_0 by an amount ΔT_0 (Fig. 1c). The excess temperature ΔT_0 decreases rapidly and smoothly with distance r from the boundary of the isothermal anomaly as approximately $\Delta T_0 (R_{ic}/r)^m$ (Fig. 1c). Following Senshu et al. (2002), and fitting the decay of peak pressure with distance away from the edge of the isobaric core $m \approx 4.4$ (Monteux et al., 2007). The energy needed to increase the temperature inside and outside the isobaric core is $\Delta E_{th} = h_m \rho_{Si} V_{ic} C_{p,Si} \Delta T_0$, where $C_{p,Si}$ is the specific heat of the silicate material and h_m is a geometric parameter representing the amount of heat that is used to increase the temperature inside and outside the isobaric core relative to the amount of heat used to increase the temperature by ΔT_0 within the isobaric core (Senshu et al., 2002; Monteux et al., 2011) and

$$h_m = 1 + \frac{3(2m-5)}{2(m-3)(m-2)} \approx 2.7 \quad (1)$$

Hence, from the following energy balance:

$$\Delta E = \Delta E_{th} + \Delta E_{m,Si} + \Delta E_{m,Fe} \quad (2)$$

and using $m_{imp} = \rho_0 V_{imp} = \rho_0 V_{ic}/3$, we obtain:

$$\Delta T_0 = \frac{1/6 \gamma \rho_0 v_{imp}^2 - L_{Si}\rho_{Si} - f_0/3 L_{Fe}\rho_{Fe}}{h_m \rho_{Si} C_{p,Si}} \quad (3)$$

Assuming that the impact velocity is equal to the escape velocity of the planet we obtain a minimum estimate for the kinetic energy where $v_{imp} = v_{esc} = \sqrt{2gR}$ with $g = 4/3\pi G \rho_0 R$, G the gravitational constant and R the radius of the target planet. After some algebra:

$$\Delta T_0 = \frac{4/9\pi\gamma\rho_0^2 G R^2 - L_{Si}\rho_{Si} - \frac{f_0}{3} L_{Fe}\rho_{Fe}}{h_m \rho_{Si} C_{p,Si}}, \quad (4)$$

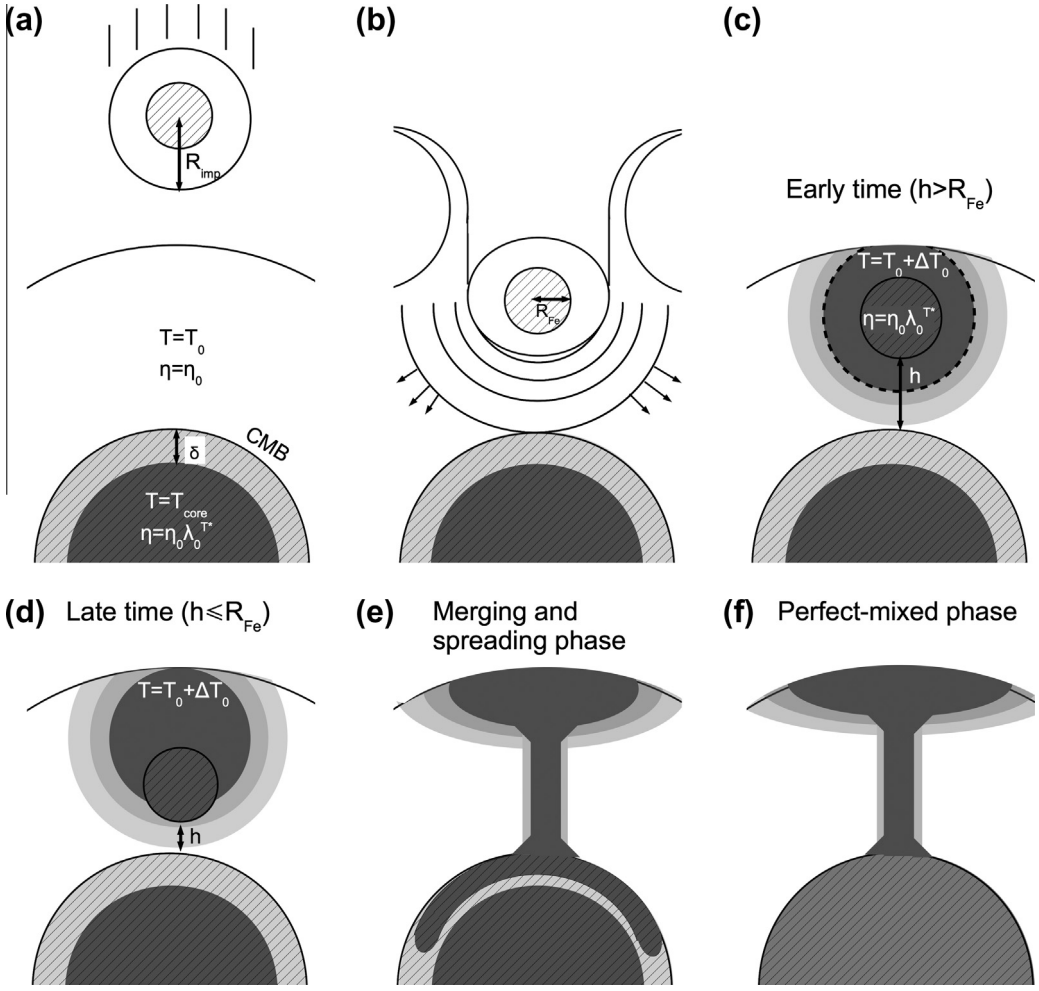

Fig. 1. Schematic representation of the thermo-chemical evolution following a mega-impact on a Mars-size body. After the impact (a) and the subsequent shockwave propagation (b), the impactor's core, radius R_{Fe}, is buried within the martian mantle and a large thermal anomaly remains (c). The post-impact temperature increase is constant within a volume delimited by the dashed line and rapidly decreases away from it. The dense metallic material from the impactor rapidly sinks towards the pre-impact martian core. During the sinking, potential energy is converted into heat in the mantle via viscous dissipation. Two sinking regimes occur (c and d) depending on the distance h between the impactor and the martian core (see Section 4). Finally the intruded metallic material merges with the preexisting core, spreads at its top (e) and eventually mixes with it later (f). The hatched volumes represent the metallic material from the martian core and the impactor. Gray shading represents temperature of the silicate (unhatched) or metallic (hatched) material and shows schematically the evolution of the thermal anomaly in the mantle during the sinking and merging phases (see also Fig. 5, left column).

For a Mars-sized planet with a mantle temperature close to its solidus the impact heating is always sufficiently large to completely melt the impacted mantle volume V_{ic} (i.e., $\Delta T_0 > 0$). For smaller or much colder planets, impact heating may only partially melt the impacted region, depending on the slope of the mantle solidus in temperature-composition space (Ernst et al., 2010; Roberts and Barnouin, 2012).

Noting that f_0 is O (10^{-1}), the term representing the energy needed to melt the impactor's core has a minor influence compared to the mantle melting term in Eq. (4). Hence, Eq. (4) can be simplified to give:

$$\Delta T_0 \approx \frac{4/9\pi\gamma\rho_0^2 GR^2 - L_{Si}\rho_{Si}}{h_m \rho_{Si} C_{p,Si}}, \quad (5)$$

Indeed using the set of parameters in Table 1 and making the assumption that the martian mantle before the impact is solid and close to its solidus, $\Delta T_0 \sim 400$ K. Including the impactor's core melting term in Eq. (4) would only reduce ΔT_0 by $\sim$10 K.

3.2. The fate of the impactor's material

During the mega-impact, a significant fraction of the impactor's silicate mantle is ejected far from the impact site to form a disk of debris, but most of the impactor's core is retained within the target planet (Canup, 2004; Ćuk and Stewart, 2012) (cf., Fig. 1b and c). For simplicity we assume that the full volume of the impactor's core is retained within the martian mantle after the giant impact. This assumption is reasonable for impact velocities close to the escape velocity of the target planet (Asphaug, 2010). We assume a solid mantle prior to impact, and that the impactor core sinks as a single, spherical diapir.

4. Dynamic models of diapir sinking

Once buried below the surface, the dense metallic core of the impactor sinks towards the center of the target planet (Fig. 1). Dissipation of the work done by buoyancy forces driving motion of this diapir occurs by a combination of viscous, viscoplastic (Samuel and Tackley, 2008), elasto-plastic (Gerya and Yuen, 2007) and fracturing (Davies, 1982; Stevenson, 2003) processes and causes heating in the mantle and/or the diapir, depending on the deformation regime. Where the effective mantle viscosity is very large in comparison to that of the diapir dissipation is concentrated in the mantle. As viscosity variations decline in response to heat transfer from the diapir to the mantle, however, dissipation will increasingly oc-

Table 1
Typical parameter values for numerical models.

Mars radius	R	3400 km
Mars core radius	R_c	1700 km
Thickness of the core thermal boundary layer	δ	0–0.4R_c
Impactor radius	R_{imp}	200–800 km
Impactor core radius (=diapir size)	R_{Fe}	100–400 km
Initial gap thickness	h_0	580 km
Average density of the planet	ρ_0	4060 kg m^{-3}
Iron density	ρ_{Fe}	8000 kg m^{-3}
Silicate density	ρ_{Si}	3500 kg m^{-3}
Density difference (=$\rho_{Fe} - \rho_{Si}$)	$\Delta\rho_0$	4500 kg m^{-3}
Average coefficient of thermal expansion	α	4.5×10^{-5} K^{-1}
Iron coefficient of thermal expansion	α_{Fe}	1.5×10^{-5} K^{-1}
Silicate coefficient of thermal expansion	α_{Si}	5×10^{-5} K^{-1}
Iron heat capacity	$C_{p,Fe}$	800 J K^{-1} kg^{-1}
Silicate heat capacity	$C_{p,Si}$	1000 J K^{-1} kg^{-1}
Average specific heat of the target body	$\overline{\rho_0 C_p}$	4×10^6 J K^{-1} m^{-3}
Buoyancy ratio	Γ	94
Iron latent heat	L_{Fe}	2.7×10^5 J kg^{-1}
Silicates latent heat	L_{Si}	4×10^5 J kg^{-1}
Pre-impact mantle temperature	T_0	1600 K
Pre-impact core temperature	T_c	2000 K
Heat diffusivity	χ	10^{-6} m^2 s^{-1}
Thermal conductivity	$k = k_{Si} = k_{Fe}$	4 W m^{-1} K^{-1}
Metal content	f_0	12.5%
Reference viscosity	η_0	10^{20}–10^{22} Pa s
Viscosity ratio between the hot metallic diapir and the surrounding mantle	λ_0	10^{-2}–1
Impact energy conversion coefficient	γ	0.3
Volume effectively heated by impact over the impactor volume	h_m	2.7
Surface gravity	g_0	3.85 m s^{-2}
Core surface gravity	g_c	=g_0
Gravitational constant	G	6.67×10^{-11} m^3 kg^{-1} s^{-2}
Average magnetic field strength	$\overline{B}$	2.5 mT
Magnetic diffusivity	ν	2 m^2 s^{-1}
Magnetic permeability	μ	$4\pi \times 10^{-7}$ H m^{-1}
Stokes regime geometrical constant	a_0	4/15–1/3
"Early time" regime geometrical constant	a_1	1/9
"Late time" regime parameter	a_2	1.3×10^{-9} m s$^{1/3}$

cur in both the mantle and the diapir (Section 4.4.3) (Samuel and Tackley, 2008; Monteux et al., 2009).

4.1. Physical model: Descent of a single diapir

To investigate the dynamics of the metallic diapir, we adapt the numerical finite volume model in spherical axisymmetric geometry of Monteux et al. (2009). We assume that the mantle is deforming in a diffusion creep limit. Conservation of energy applied to a planet of radius R then leads to

$$\frac{DT}{Dt} = \frac{\nabla^2 T}{Ra_\chi} + Di\left(\frac{\eta}{\eta_0}\Gamma\Omega - v_r\left(T + \frac{T_0}{\Delta T_0}\right)r\right), \quad (6)$$

where T, t and r are dimensionless temperature, time and radius. v_r is the dimensionless radial velocity. $Ra_\chi = \frac{\Delta\rho_0 g_0 R^3}{\chi\eta_0}$ is the compositional Rayleigh number, $Di = \frac{\alpha\rho_0 g_0 R}{\rho_0 C_p}$ is the dissipation number and $\Gamma = \Delta\rho_0/(\rho_0\alpha\Delta T_0)$ is the buoyancy ratio (Table 1). Within the target planetary mantle gravity is set equal to a constant: $g_0 = \frac{4}{3}G\pi\rho_0 R$. Within the planetary core, however, gravity is proportional to r, where $g(r) = g_0\frac{r}{R_c}$. Last, Ω is the dimensionless dissipation function and expresses the conversion of potential energy into heat through viscous dissipation:

$$\Omega = 2\underline{\varepsilon} : \underline{\varepsilon}. \quad (7)$$

where $\underline{\varepsilon}$ is the dimensionless shear strain rate tensor. Prior to impact, we assume a homogenous temperature, T_0, in the martian mantle. The viscosity is $\eta = \eta_0\lambda_0^T$, where λ_0 is the ratio (<1) of the viscosity of the hottest material (iron or silicates) to that of the colder, surrounding solid silicate mantle far from the impact site where $T = T_0$ (see value in Table 1). This viscosity decreases sharply with temperature and its expression is simpler to implement than the usual Arrhenius law (Ratcliff et al., 1997; Ziethe and Spohn, 2007). We neglect the compositional dependence of the viscosity as this effect will be much smaller than the temperature-dependence. η_0 is the reference viscosity of mantle material far from the impact site (see value in Table 1). The viscosity contrast between molten iron and mantle under martian conditions may exceed 10–20 orders of magnitude, depending on the mantle temperature. Such viscosity variations are impossible to resolve with our numerical method. However, experiments show that the dynamic influence of these large viscosity variations on diapir sinking are similar to viscosity variations of order 10^2 (Jellinek et al., 2003; Thayalan et al., 2006), the effects of which we can explore parametrically.

The other dimensionless governing equations are continuity

$$\nabla \cdot \mathbf{v} = 0, \quad (8)$$

and momentum conservation, assuming infinite Prandtl number

$$-\nabla P + \nabla \cdot \left(\frac{\eta}{\eta_0}[\nabla\mathbf{v} + [\nabla\mathbf{v}]^T]\right) + \left(\frac{T}{\Gamma} - f\right)r\mathbf{e_r} = 0, \quad (9)$$

where $\mathbf{v}$ and P are the non-dimensional velocity and pressure and $\mathbf{e_r}$ is the radial unit vector. Coupling core and mantle convection models is a difficult problem, given the different timescales and material properties for each layer. We assume here that Eq. (9) is also valid in the core. The core and the mantle are both treated as highly viscous materials. In reality, the viscosity of the core is much smaller than the mantle viscosity and the assumption that Prandtl number is

infinite is no longer valid. We will return to this issue in the conclusion.

The buoyancy force that drives the flow of the diapir towards the center of the protoplanet increases with the metallic volume fraction f that varies between 0 (pure silicates) and 1 (pure metal). The metal volume fraction f is then simply advected by the flow:

$$\frac{Df}{Dt} = 0. \tag{10}$$

4.2. Numerical model

We implement a finite volume numerical model to solve Eqs. (6), (8), (9) and (10) in axisymmetric spherical geometry. We use a stream function formulation for the equations of motion with a direct implicit inversion method (Schubert et al., 2001). Eqs. (6) and (10) are solved by an Alternating Direction Implicit (ADI) scheme (Peaceman and Rachford, 1955; Douglas, 1955). The stream function, temperature and compositional fields are described by a second-order approximation in space. To limit numerical diffusion when solving the transport equations, especially for the compositional field, we use a Total Variation Diminishing Superbee scheme (Roe, 1986; Laney, 1998) implemented in an implicit way (Srámek et al., 2010) which enables high resolution of pure advective fields. To avoid any singularity at the center of the planet, we use a staggered grid mesh (see Patankar (1980) for details) where the steam function is calculated at the corners and the temperature and compositional fields are calculated at the center of the grid cells. We use at least 200 grid points along the r-direction (i.e. the resolution $dr = 17$ km) and 400 grid points along the θ direction (i.e. the resolution $d\theta = 0.45°$). Hence the grid-point density is slightly larger towards the center of the planet. Velocity boundary conditions are free-slip at the surface and along the symmetry axis. Thermal boundary conditions are isothermal at the surface and insulating along the symmetry axis.

4.3. Analytical model of the core merging process

Buoyancy-driven interactions between two deformable viscous drops has been widely studied both experimentally and numerically (Davis et al., 1989; Yiantsios and Davis, 1990; Manga and Stone, 1993). Building on this body of work, we characterize the interaction between the preexisting core and the sinking diapir by monitoring the gap thickness, h, which is the thickness of the mantle layer between the base of the diapir and the CMB, measured along the axis of symmetry of the diapir (Fig. 2). We compare the results from our numerical models with analytical predictions. We consider the initial time t_0 to be the time at which the impact occurs.

During sinking, a diapir will deform the surrounding mantle over a radial distance that depends on the diameter of the diapir, the effective viscosities of the mantle and core, the gap thickness and the density difference across the CMB. When the diapir is small in comparison with the mantle depth and far from the core–mantle boundary, interactions with the core are negligible (Fig. 2, left). If we also neglect deformation of the density interface forming the upper boundary of the mantle the diapir sinks in the "Stokes regime" with a velocity given by Hadamard (1911) and Rybczynski (1911)

$$v = -\frac{dh}{dt} = \frac{a_0 \Delta\rho_0 g_0 R_{Fe}^2}{\lambda_0 \eta_0}, \tag{11}$$

where a_0 is a geometrical constant. In the case of a diapir sinking in an infinite medium, a_0 is given by the Hadamard–Rybczynski equation and varies from $4/15 = 0.27$ (isoviscous) to $1/3 = 0.33$ for an inviscid sphere (Hadamard, 1911; Rybczynski, 1911).

Integrating Eq. (11) with h_0 as the initial gap thickness,

$$h(t) = h_0\left(1 - \frac{t}{t_s}\frac{R_{Fe}}{h_0}\right). \tag{12}$$

Here t_s is the characteristic time for diapir descent in this regime and is given by

$$t_s = \frac{R_{Fe}}{v} = \frac{\lambda_0 \eta_0}{a_0 \Delta\rho_0 g_0 R_{Fe}} \tag{13}$$

For the impactor size range studied here, the diapir is not necessarily small in comparison to the mantle and the Stokes regime described above is not valid. As the diapir descends and $h \sim R_{Fe}$, mantle flow interacts increasingly with the CMB (Fig. 2, middle). The sinking velocity in this "Early time" regime is modified from Eq. (11) and has the form (Yiantsios and Davis (1990)):

$$v(t) = -\frac{dh}{dt} = \frac{a_1 \Delta\rho_0 g_0 R_{Fe}^{3/2} h(t)^{1/2}}{\lambda_0 \eta_0} \tag{14}$$

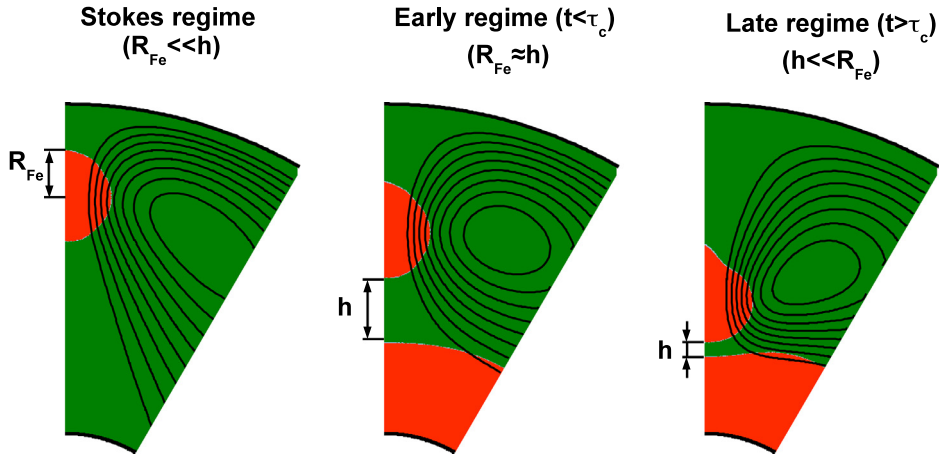

Fig. 2. Dynamics of core merging for the three regimes described in Section 4.3 and computed for $R_{Fe} = 300$ km sinking in an isoviscous differentiated Mars size planet (silicate material is represented in green and metallic material is represented in red). These results are obtained from the numerical model described in the article. Solid black lines illustrate the streamlines resulting from the diapir sinking. In the left figure, the planetary core is not present to illustrate its negligible influence on the sinking dynamics when the diapir is far from it. In this case, the viscous stress scales with $1/R_{Fe}$ (Hadamard, 1911; Rybczynski, 1911). In the middle figure, the interaction with the core results in viscous stresses that scale with $1/h$. In the right figure where $h < R_{Fe}$, interactions between the diapir and the merging core increase and the lubrication force scales with $1/h$ (Yiantsios and Davis, 1990). (For interpretation of the references to color in this figure legend, the reader is referred to the web version of this article.)

where a_1 is a geometrical constant that we determine from our numerical models. Integration of Eq. (14) with the same initial condition leads to

$$h(t) = h_0\left(1 - \frac{t}{t_c}\right)^2 \tag{15}$$

and identifies a characteristic time for diapir descent that is governed primarily by the mantle viscosity (Yiantsios and Davis, 1990):

$$t_c = \frac{2\lambda_0\eta_0}{a_1\Delta\rho_0 g_0 R_{Fe}}\left(\frac{h_0}{R_{Fe}}\right)^{1/2}. \tag{16}$$

In contrast to Eq. (13), this sinking time depends on the ratio (R_{Fe}/h_0). When $h \to 0$, $v \to 0$ (Eq. (14)) and the merging time increases towards infinity as a result of the large lateral pressure gradients required to drive viscous mantle out of the way of the sinking diapir. Indeed, Eq. (15) is strictly valid only where $t \leqslant t_c$. At "Late time" $(t/t_c \to \infty)$ the gap becomes very thin and is expected to evolve with a form (Jones and Wilson (1978) and Yiantsios and Davis (1990)):

$$h(t) = a_2 t^{-1/3} \tag{17}$$

where a_2 is a function of λ_0 and the density difference across the CMB. We obtain a_2 from our numerical results. Comparison of Eqs. (12), (15) and (17) shows that as the diapir approaches and deforms the CMB, the rate of descent will steadily decline.

4.4. Numerical results

For the range of plausible martian impactors, R_{Fe} ranges from 100 km to about 650 km. In this range, the smallest values of R_{Fe} lead to an initial Stokes regime, after which the diapir motion or gap evolution is successively described by the Early Time and Late Time regimes. Intermediate and large values of R_{Fe} lead to an initial state described by the Early Time regime, after which the motion of the diapir is described by Late Time regime. As the diapir size increases, the relative amount of time spent in the Late Time regime increases. Because the motion of the diapir in the Stoke's regime is very fast, we consider an initial gap thickness h_0 that is independent of the size of the impactor, and we model only the Early Time and Late Time regimes. We set $h_0 = 580$ km, which allows us to consider R_{Fe} in the range 100 km to a maximum value of $(R_{Mars} - R_c - h_0)/2 = 560$ km. Finally, we note that for small diapirs ($R_{Fe} < 100$ km), the Stokes regime dominates during the sinking, and conversely for very large diapirs ($R_{Fe} > 650$ km) the Late Time Regime may be the only sinking regime. Neither of these two cases is considered here.

4.4.1. Initial setup

We use the numerical model to characterize the dynamics of core merging after a giant impact on a Mars size body. First, we consider the initial martian core temperature to be homogeneous (i.e. the thickness of the thermal boundary layer $\delta = 0$) and we use the estimated present-day temperature value $T = T_{core} = 2000$ K (Williams and Nimmo, 2004). The initial thermo-chemical conditions are shown schematically in Fig. 3 in which the hatched regions represent the metallic phase from the impactor and from Mars. The initial temperature is represented with a gray scale.

4.4.2. Evolution of the gap thickness

We first monitor the thermal evolution following an impact in the absence of core merging (i.e. we consider only the thermal re-equilibration since no core merging occurs). This unphysical case is used as a control case to separate the influence of the impact heating from the diapir merging on the thermal evolution of the planet. Fig. 4 shows the thermal evolution after a 600 km impact on a Mars size body with homogeneous viscosity ($\eta_0 = 10^{22}$ Pa s). After the impact heating, the hot anomaly advects and spreads beneath the planetary surface in a few million years. Then, the hot anomaly and the target planet's core cool by diffusion.

We now consider the impactor's core. Fig. 5 shows the thermal and chemical evolution after a 600 km impact (i.e. $R_{Fe} = 300$ km) on a differentiated Mars with homogeneous viscosity ($\eta_0 = 10^{22}$ Pa s). Following the impact, a metallic diapir from the impactor forms rapidly and sinks towards the pre-existing core, while undergoing significant viscous heating. Motion of the diapir displaces surrounding mantle and deforms the CMB (Figs. 2 and 5). Merging and thermal mixing of the hot diapir into the core occurs eventually, causing the average temperature of the core to rise (Fig. 5), leading in turn, to an enhanced CMB heat flux that causes the formation and rise of a plume (Fig. 5d). The plume rising from the CMB is not the result of the onset of thermal convection in the mantle to remove the heat from the core. It is a consequence of the diapir sinking and especially of the viscous dissipation that occurs along the sinking path and generates a localized hot channel.

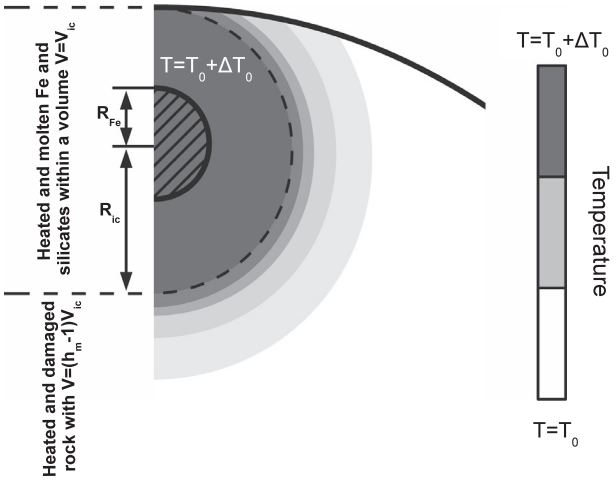

Fig. 3. Sketch to show repartitioning of the post impact heating in the martian mantle. The solid black line represents the planetary surface. Melting is restricted to the material limited by the dashed line. The impactor's core is represented by hatched lines.

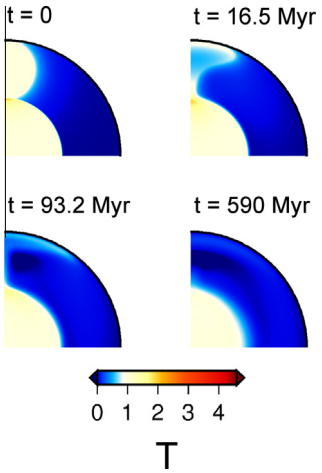

Fig. 4. Non-dimensional temperature evolution as a function of time. In this control case, we do not consider the impactor's core (computed for a uniform viscosity with $R = 3400$ km, $R_{imp} = 600$ km, $\eta_0 = 10^{22}$ Pa s and 300×600 grid points). To convert this temperature field in Kelvin, $T(K) = T_0 + T\Delta T_0$.

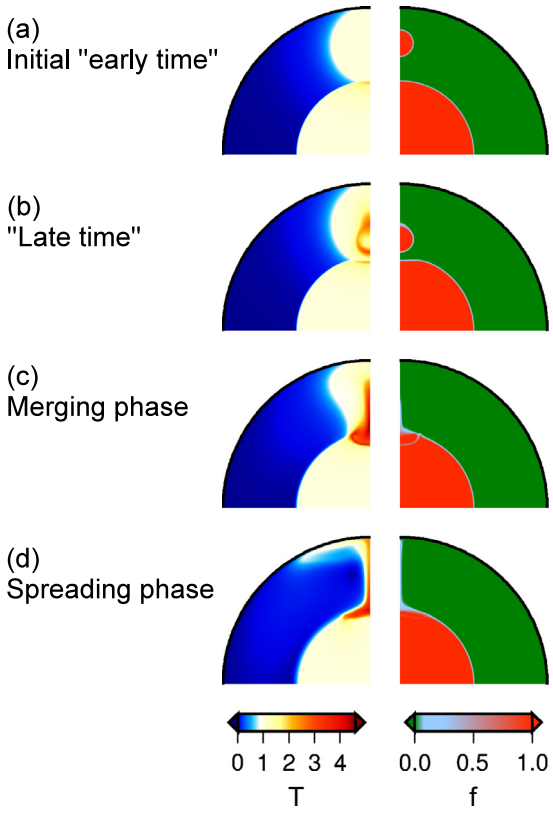

Fig. 5. Non-dimensional temperature (left) and composition (right) at times $t = 0$ (a), $t = 0.6$ Myr (b), $t = 6$ Myr (c) and $t = 38.8$ Myr (d) (computed for a uniform viscosity with $R = 3400$ km, $R_{imp} = 600$ km, $R_{Fe} = 300$ km, $\eta_0 = 10^{22}$ Pa s, $h_0 = 580$ km and 300×600 grid points). As the diapir sinks, its velocity decreases because of the increasing influence of the pre-existing core on the dynamics (see Section 4.3 for details). After the merging (c), the hot metallic fraction from the impactor spreads at the top of the martian core (d). To convert this temperature field in Kelvin, $T(K) = T_0 + T\Delta T_0$.

The plume rising does not happen in the absence of the diapir sinking (Fig. 4).

In Fig. 6, we show the temporal evolution of the gap thickness after a 600 km impact and compare it with theoretical predictions from Eqs. (15) and (17) to obtain characteristic coalescence times t_c

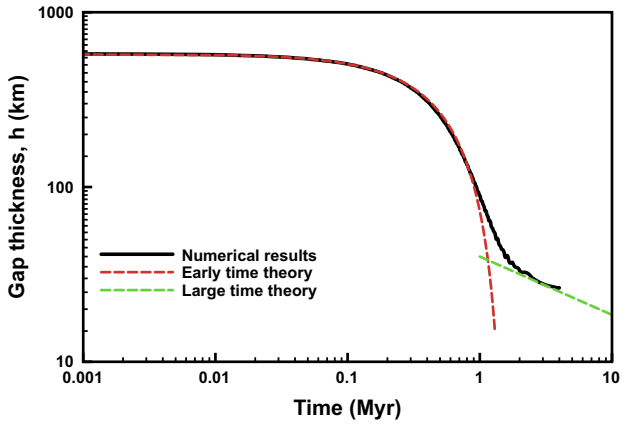

Fig. 6. Evolution of the gap thickness between the merging core and the CMB with $R_{imp} = 600$ km (i.e. $R_{Fe} = R_{imp}/2 = 300$ km). Theoretical evolutions for early times from Eq. (15) and late times from Eq. (17) are shown with red and green dashed lines respectively. From this model, we obtain a coalescence time, $t_c = 1.55$ Myr and $a_2 \sim 1.3 \times 10^9$ m s$^{1/3}$. (For interpretation of the references to color in this figure legend, the reader is referred to the web version of this article.)

and values for a_2. We repeat this for a range of plausible impactor sizes. Consistent with Eq. (16), our numerical values for t_c decrease in proportion to $R_{Fe}^{-3/2}$ (red circles, Fig. 7). In Fig. 7, we fit the numerical t_c values with the analytical prediction (black dashed line, Fig. 7) from Eq. (16) and obtain $a_1 = 1/9$.

4.4.3. Influence of the temperature-dependence of the mantle viscosity on the core merging timescale

The viscosity contrast between the sinking diapir and its environment is a key parameter in understanding the core merging dynamics. Qualitatively, as the metallic diapir sinks, shear heating occurs at the interface of the diapir (Samuel et al., 2010) and both the temperature of the diapir and the surrounding mantle can increase. Depending on the effective viscosity contrast between the metallic diapir and the mantle, the mean temperature increase within the sinking diapir can reach a maximum value $\approx 2\Delta T_0$ (Monteux et al., 2009). This temperature excess drives a heat flux from the diapir to the surrounding mantle, leading to the progressive growth of a thermal boundary layer (Fig. 5). Because the mantle viscosity declines exponentially with increasing temperature, mantle shear will be increasingly concentrated within the hottest, low viscosity part of this thermal boundary layer (Morris, 1982; Thayalan et al., 2006). Thus, heat transfer from the diapir will reduce both the effective viscosity retarding diapir motion and the radial length scale over which viscous deformation in the mantle occurs. The timescale for merging will consequently decline as a result of two processes. First, the lubricating effect of an enveloping layer of low mantle viscosity will cause metallic diapirs to descend more rapidly (cf. Eq. (14)). Second, localization of shear within only the narrow, hottest part of the thermal boundary layer will enable diapirs to more closely approach the CMB before interacting with the core.

We explore these effects quantitatively in Fig. 8, which shows analytical and numerical solutions for the evolution of the gap thickness h for a range of background mantle viscosities and diapir/mantle viscosity ratios. In the isoviscous case ($\lambda_0 = 1$), when the average viscosity decreases in the mantle (from $\eta_0 = 10^{22}$ Pa s, black solid line to $\eta = 10^{20}$ Pa s, gray solid line), the diapir sinks faster (see Eq. (14)). Consequently, the sinking time values obtained by fitting our numerical results with Eq. (15) decrease by two orders of magnitude (see Table 2).

Theoretical, experimental and numerical models (Morris, 1982; Jellinek et al., 2003; Thayalan et al., 2006) show that whereas in the isoviscous case radial mantle deformation scales with the size of the diapir, R_{Fe}, in the temperature-dependent case deformation is confined to the hottest, low viscosity part of the thermal boundary layer with a length scale typically $\sim 0.1 R_{Fe}$. As a consequence, the value of a_1 obtained by fitting our numerical results with Eq. (16) increases (see Table 2) and the sinking time value for ($\eta_0 = 10^{22}$ Pa s, $\lambda_0 = 0.01$) is smaller than for ($\eta_0 = 10^{20}$, $\lambda_0 = 1$).

5. Effect on a preexisting dynamo

We now discuss the consequences of a giant-impact and the subsequent core merging process on the martian dynamo. We first revisit the core heat flux conditions required for dynamo generation. Next, we explore the influence of core merging on the efficiency of core cooling, and thus dynamo action, for different pre-impact mantle thermal regimes.

5.1. Conditions required for dynamo generation

As discussed in Monteux et al. (2011), three conditions are required to generate a dynamo on a growing planet:

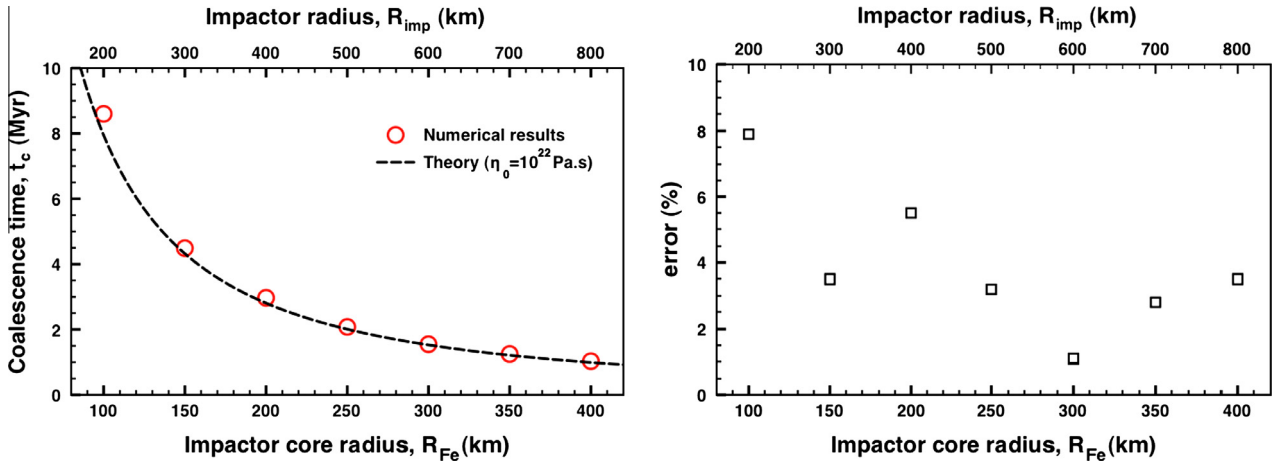

Fig. 7. Characteristic coalescence time, t_c (left panel) as a function of the impactor core radius R_{Fe}. Results from numerical experiments (with uniform viscosity $\eta_0 = 10^{22}$ Pa s and $h_0 = 580$ km) are represented with red circles. Theoretical fit from Eq. (16) is shown with the black dashed line ($a_1 = 1/9$). The corresponding errors between the numerical and theoretical models are plotted in the right panel. (For interpretation of the references to color in this figure legend, the reader is referred to the web version of this article.)

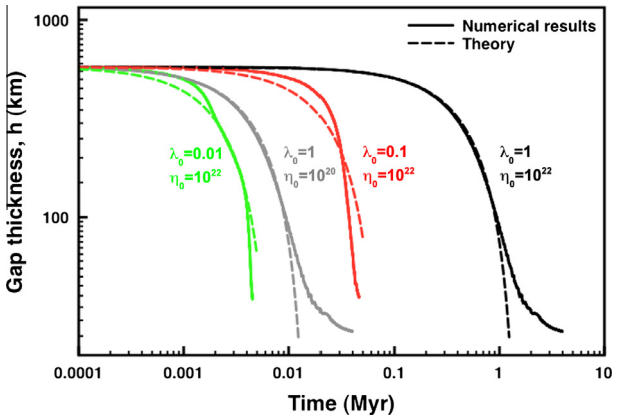

Fig. 8. Time evolution of the gap thickness between the sinking core and the pre-existing core for four different rheologies. Solid black line and solid gray line represent results from uniform viscosity models with $\eta_0 = 10^{22}$ Pa s and $\eta_0 = 10^{20}$ Pa s respectively. Solid red line and solid green line represent results from temperature dependent viscosities with $\lambda_0 = 0.1$ and $\lambda_0 = 0.01$ respectively (with $\eta = \eta_0 \lambda_0^T$ and $\eta_0 = 10^{22}$ Pa s). Theoretical predictions are shown in the corresponding color with dashed lines for the coalescence theory (Eq. (15)). (For interpretation of the references to color in this figure legend, the reader is referred to the web version of this article.)

Table 2
Sinking time values obtained fitting numerical experiments with theoretical predictions (Eq. (15)) for different values of η_0 and λ_0 (with $R_{imp} = 600$ km, $h_0 = 580$ km).

	$\eta_0 = 10^{22}$ Pa s $\lambda_0 = 1$	$\eta_0 = 10^{20}$ Pa s $\lambda_0 = 1$	$\eta_0 = 10^{22}$ Pa s $\lambda_0 = 0.1$	$\eta_0 = 10^{22}$ Pa s $\lambda_0 = 0.01$
t_c	1.56×10^3 kyr	15.6 kyr	79 kyr	7.5 kyr
a_1	0.11	0.11	0.21	0.23

1. The mean heat flux q_{CMB} out of the core must exceed the adiabatic value q_A such that convection can occur (Stevenson et al., 1983). This condition is

$$q_{CMB} > q_A = \frac{k_{Fe}\alpha_{Fe}g_c T_c}{C_{p,Fe}} \tag{18}$$

where k_{Fe}, α_{Fe}, T_c and $C_{p,Fe}$ are respectively the thermal conductivity, the coefficient of thermal expansion, the temperature and the heat capacity of the metallic phase and g_c is the gravity at the surface of the protocore. The largest uncertainties in the calculation of q_A are related to T_c and k_{Fe}. Assuming reasonable values, convection in the martian core should start once $q_{CMB} > q_A = 5 - 19$ mW m^{-2} (Nimmo and Stevenson, 2000) (see Table 1 for values).

2. The ratio of the rate at which gravitational potential energy is released by convection to the rate of ohmic dissipation, Φ, must exceed a critical value (Buffett, 2002):

$$\frac{4\pi R_c^2 q_{CMB}}{\Phi} > \frac{1}{\epsilon_T}. \tag{19}$$

where ϵ_T is the Carnot-style efficiency for thermal convection. Here, we do not consider the effect of compositional convection or the presence of an inner core. Assuming that the characteristic scale of core flow leading to magnetic field generation is the radius of the protocore, Φ can be approximated as (Buffett, 2002):

$$\Phi = \frac{4}{3}\pi R_c \left(\frac{\nu \bar{B}^2}{\mu}\right), \tag{20}$$

where $\bar{B}$ is the average strength of the magnetic field within the core, ν is the magnetic diffusivity and μ is the magnetic permeability (see Table 1 for values). In the absence of constraints on $\bar{B}$ for early planets, we assume a current Earth-like value of 2.5 mT (Kuang and Bloxham, 1997) that is independent of the protocore size or the planetary radius. The efficiency of thermal convection is given by Buffett (2002)

$$\epsilon_T = \frac{0.8\pi}{3}\frac{\alpha_{Fe} G \rho_{Fe} R_c^2}{C_{p,Fe}}\left(1 - \frac{q_A}{q_{CMB}}\right), \tag{21}$$

with ρ_{Fe} the density of the metallic phase and G the gravitational constant.
Hence Eqs. (19)–(21) along with values from Table 1 lead to:

$$q_{CMB} - q_A > \frac{\nu \bar{B}^2 C_{p,Fe}}{0.8\pi G \mu \alpha_{Fe} \rho_{Fe} R_c^3} \approx 8 \times 10^{-2} \text{ mW m}^{-2} \tag{22}$$

3. The structure of the convective motions carrying magnetic field lines must be sufficiently complicated to favor self-sustaining dynamo action. A measure of this complexity is that the magnetic Reynolds number (Christensen and Aubert, 2006) must exceed a critical value:

$$Re_m = \frac{UL}{\nu} > Re_m^{crit} = O(10 - 10^2) \tag{23}$$

Here, L and U are the characteristic length and velocity scales for the flow within the protocore and v is the magnetic diffusivity of the metal phase. The natural length scale in the problem is the depth of the convecting iron layer, however the velocity scale depends on the leading order force balance (Christensen, 2010). As the rotation rate of growing planets is potentially time-dependent and poorly constrained, a convenient and reasonable choice is based on a balance between inertial and buoyancy forces and is (Stevenson, 2003):

$$U \sim \left(\frac{(q_{CMB} - q_A)\alpha_{Fe} g_c R_c}{\rho_{Fe} C_{p,Fe}}\right)^{1/3}, \quad (24)$$

Taking $L = R_c$ and $Re_m^{crit} = 10^2$, the combination of Eqs. (23) and (24) leads to the condition

$$q_{CMB} - q_A > \frac{\rho_{Fe} C_{p,Fe}}{\alpha_{Fe} g_c R_c}\left(Re_m^{crit}\frac{v}{R_c}\right)^3 \approx 10^{-4}\ \text{mW m}^{-2} \quad (25)$$

Among the three criteria above, the first is typically considered a necessary condition for a thermally-driven dynamo (subadiabatic dynamos are possible if compositional buoyancy effects enter the problem). It is not a sufficient condition for dynamo action, as indicated by the other two conditions. However, conditions 2 and 3 require that the heat flux q_{CMB} at the CMB be only about 1% greater than the adiabatic heat flux q_A. Thus, we take q_A to be a reasonable critical value for dynamo generation (Stevenson et al., 1983; Nimmo and Stevenson, 2000; Williams and Nimmo, 2004).

5.2. Thermal consequences of the core merging

5.2.1. CMB cooling

To understand the influence of the merging process on thermally-driven dynamo action, we first specify the thermal structure and cooling regime of the core prior to merging, which depends on the previous accretion and core formation histories (Monteux et al., 2009; Samuel et al., 2010). Two end-member models for the initial interior thermal state of Mars are the isothermal case with the core and the mantle having the same temperature, and a situation where the core is much hotter than the mantle. In the case of a pre-impact core hotter than the mantle, the thickness δ of the thermal boundary layer (TBL), across which temperature declines linearly from the core to the mantle value is governed by the mode of heat loss to the mantle. Strong cooling to the mantle leads to thin thermal boundary layers and vigorous convection, weak cooling leads to relatively more sluggish flow or no convection at all. To simplify this problem we consider three pre-impact core thermal states: an isothermal core and mantle (uniform temperature), and two models where the core is hotter than the mantle with $\delta = 0.1R_c$ (strong core cooling) and $\delta = 0.4R_c$ (weak core cooling and no core convection).

Our results show that one major consequence of large impacts is to heat the mantle and reduce the temperature difference between the core and mantle (where there is one initially) and, thus the CMB heat flux (Roberts et al., 2009). Where a metallic diapir forms and descends such that it becomes hotter than the pre-existing core, merging can lead to the spread of a thin, hot, gravity current along the CMB. If the timescale for spreading t_{spread} is much smaller than the timescale for thermal diffusion t_{diff} across the current then this stratification can insulate the core against the mantle. This can in turn drive a heat flux into the core itself and inhibit dynamo action (Arkani-Hamed and Olson, 2010).

In the uniform temperature case, following merging and coalescence (Fig. 9, top-left panel, solid circles) an increase in the CMB heat flux occurs at $\sim 10t_c$ because the production of thermal stratification increases the temperature difference to the mantle. The magnitude of this temperature difference increases with rate of spreading relative to the rate at which thermal diffusion smoothes temperature variations. Thus, the largest diapirs spreading in the lowest viscosity cores are characterized by the greatest increases in CMB heat flux (green curve). By contrast, in the weak and strong core cooling cases, initial mantle heating causes a reduction in the CMB heat flux following coalescence that is followed, in turn, by an increase in this heat flux until $t/t_{diff} \to 1$. The magnitude of this increase is in proportion to the strength of the resulting thermal stratification. As in the uniform temperature case, the greatest CMB heat fluxes then correspond with the largest diapirs and lowest viscosity cores (green curves). Notably, the smallest and most slowly spreading diapir in the strong cooling regime (Fig. 9, red curve) produces no significant stratification because $t_{spread}/\ t_{diff} \gg 1$.

5.2.2. Merging, stratification and thermal mixing: Potential effect on an early Mars dynamo

Material from our lowest viscosity and largest diapirs spreads along the CMB as a thin, axisymmetric gravity current. In the limit that this spreading is under the zero Reynolds number conditions of our numerical simulations, the radius of the current will increase at a rate that is approximately proportional to time $t^{1/8}$ (Huppert, 1982) to form a hot, stratified layer that insulates the core and inhibits core convection and dynamo action (Fig. 9, green curves) (Arkani-Hamed and Olson, 2010). This thermal stratification persists until the thermal anomaly introduced by the gravity current has diffused into the overlying mantle and underlying core. Where weak or no stratification is produced, merging and spreading weakens core convection as a result of mantle heating but will not necessarily destroy a pre-existing dynamo (Fig. 9, blue and red curves).

In reality, the gravity current driven as a result of the merging of a ~400 km radius diapir carrying ~800 K temperature variations can spread in a very low viscosity core under finite-or even high-Re conditions. In the high-Re limit, at large times where the current is thin in comparison to its radius, the radius of the current will increase in proportion to $t^{1/2}$ (Kotsovinos, 2000) and may involve extensive mixing across the density interface forming the base of the flow, depending on the magnitude of the temperature difference, the thickness of the flow and the rotation rate of Mars (Linden, 1977; Linden, 1979; Fleury et al., 1991; Kotsovinos, 2000).

A careful consideration of the efficiency of thermal mixing across this density interface requires a different numerical model and is beyond the scope of this paper. However, it is useful to explore the end-member case of perfect thermal mixing in order to determine the maximum core heat flux that is likely to occur after merging, spreading and thorough mixing. To obtain a crude estimate of the effects of complete thermal mixing of the hot gravity current into the underlying core, we stir in the gravity current at $t = t_{spread}$ and then determine the mean temperature of the core $\overline{T_c}$ and the corresponding CMB heat flux (Fig. 10, solid square). Because spreading and mixing in a high-Re limit will occur on a timescale that is much smaller than t_{diff} (i.e., for $t_{spread} \ll t_{diff}$), we explore only the effect of stirring in the stratified layer corresponding to the largest, lowest viscosity diapir in Fig. 9 (Fig. 10). In Fig. 10, the discontinuity in the heat flux evolution is the consequence of imposing a new thermal state. The main effect of an imposed mixing event at $t = t_{spread}$ is to reduce the average core temperature to a value intermediate between the initial and fully stratified cases (Fig. 10). Whereas the peak in the CMB heat flux corresponds to stratification that would likely destroy the dynamo (cf., Fig. 9), the lower, post-mixing, heat flux can drive a dynamo for several diffusion times, which corresponds to a few hundred million years.

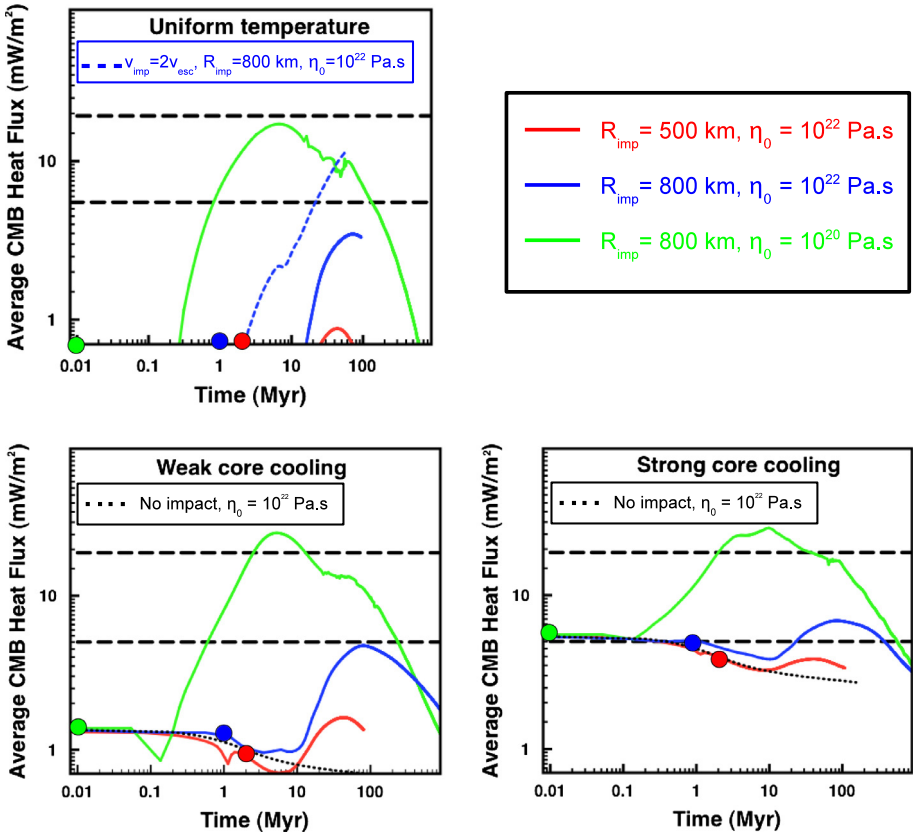

Fig. 9. Time evolution of the mean CMB heat flux in the stratified case as a function of the viscosity and impactor size. The characteristic diffusion time $t_{diff} = d^2/\kappa$, where the steady-state thickness d is defined where the spreading gravity current extends over 25% of the CMB. In the three panels different initial thermal states before impact are considered. The two horizontal black dashed lines represent the theoretical dynamo criterion for q_{CMB} ($q_{CMB} > q_A = 5 - 19$ mW m^{-2}). In the top-left panel, pre-impact temperature is assumed to be constant ($T = T_0$). In the bottom panels, the core is initially hotter than the mantle $T = T_{core} > T_0$. The black dotted lines represent q_{CMB} in the absence of an impact. In the bottom left panel the CMB thermal boundary layer thickness $\delta = 0.4R_{Fe}$ and in the bottom right panel $\delta = 0.1R_{Fe}$. Red, blue and green solid lines represent the evolution with ($R_{imp} = 500$ km, $\eta_0 = 10^{22}$ Pa s), ($R_{imp} = 800$ km, $\eta_0 = 10^{22}$ Pa s), and ($R_{imp} = 800$ km, $\eta_0 = 10^{20}$ Pa s) respectively. In the top-left panel, the blue dashed line is the result of the same model as the solid blue line but with $v_{imp} = 2v_{esc}$ (i.e. the post-impact temperature increase is ≈4 times larger). Filled circles represent the coalescence times t_c/t_{diff} from Eq. (16). In the weak and strong core cooling cases, the mean heat flux decreases for $t_c/t_{diff} < t/t_{diff} < 10t_c/t_{diff}$ because of the post-impact mantle thermal anomaly that inhibits the CMB heat loss. The combination of the spreading and cooling mantle thermal anomaly, and of the thermal core stratification leads to an increase of the CMB heat flux after $t \sim 10t_c/t_{diff}$. The maximum average heat flux increase at the CMB is reached when $R_{imp} = 800$ km and when $\eta_0 = 10^{20}$ Pa s. (For interpretation of the references to color in this figure legend, the reader is referred to the web version of this article.)

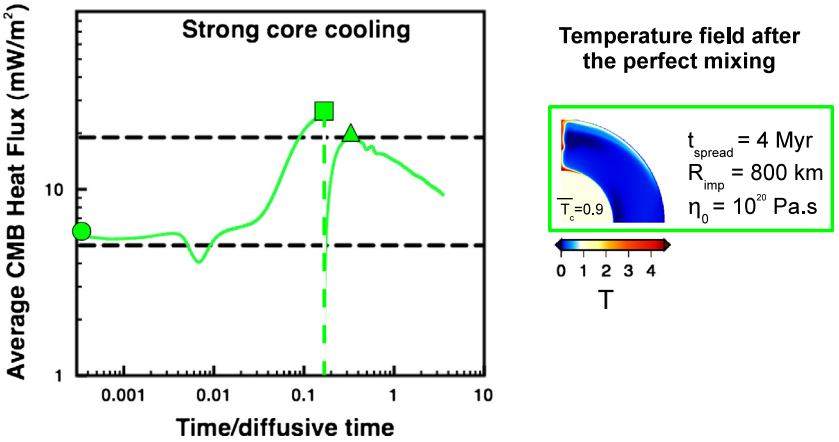

Fig. 10. Time evolution of the mean CMB heat flux in the perfect mixing case as a function of the viscosity and impactor size. The characteristic diffusion time $t_{diff} = d^2/\kappa$, where the steady-state thickness d is defined where the spreading gravity current extends over 25% of the CMB. Here $t_{diff} = 27.8$ Myr. Perfect thermal mixing is imposed within the core when $t = t_{spread}$ (vertical dashed line). The two horizontal black dashed lines represent the theoretical dynamo criterion for q_{CMB} ($q_{CMB} > q_A = 5 - 19$ mW m^{-2}). The green solid line represent the evolution with ($R_{imp} = 800$ km, $\eta_0 = 10^{20}$ Pa s, $t_{spread} = 4$ Myr). The filled circle represents the coalescence times (t_c/t_{diff}) from Eq. (16), the filled square represents the spreading time (t_{spread}/t_{diff}) and the filled triangle represents the relevant mean heat flux after thermal mixing. The right panel shows the corresponding non-dimensional temperature field right after the perfect mixing. To convert this temperature field in Kelvin, $T(K) = T_0 + T\Delta T_0$. (For interpretation of the references to color in this figure legend, the reader is referred to the web version of this article.)

6. Conclusions

Giant impacts may have played an important role in the thermal and magnetic evolutions of terrestrial planets. The giant impact potentially forming the martian dichotomy could have supplied a significant volume of iron that merged with the preexisting core. We model the dynamics of the sinking of a large metallic diapir within a silicate mantle and the influence of the deformation of the preexisting core on the merging process. We obtain characteristic timescales of the coalescence time between the two cores as a function of the viscosity of the mantle and the size of the sinking diapir. Our results are in agreement with theoretical and experimental models of buoyancy-driven motions sinking toward a deformable surface. We also show that the thermal consequences of the merging process can influence the generation of a martian dynamo. Assuming perfect thermal mixing, the dynamo generation might be favored by large impacts, low viscosity of the preexisting core and strong preexisting core cooling. The dynamo can last as long as several hundred million years depending on the mixing process within the core.

The novelty of our models is that we characterize and understand theoretically the sinking of a large volume of iron through a silicate mantle as well as the interactions between the two cores during the merging. Our thermal models also include the dissipation of energy via viscous heating which allows us to characterize the thermal consequences of the impactor's core sinking within the mantle and the pre-existing core. The results illustrate that the core merging is a process with a characteristic time that is essentially governed by the mechanical properties of the mantle. The dynamics and thermal consequences of the core merging process are important aspects of the giant impacts that potentially delivered large volumes of iron during the late accretionary history of terrestrial planets.

The heating induced by the impact within the mantle and the viscous dissipation during diapir sinking enhances a thermal anomaly within the mantle. These processes strongly affect the heat budget of the mantle and may have long term consequences on a planet's thermal evolution. The impact heating within the mantle leads to a dichotomy of the core cooling: the core heat flux at the CMB below the impact site is different than the CMB heat flux on the opposite side of the core. This mantle heterogeneity might affect the dynamo and the resulting paleomagnetic field recorded at the surface (Stanley et al., 2008; Sreenivasan and Jellinek, 2012). Moreover, recent dynamo simulations show that the efficiency of a mantle heterogeneity centered at the geographical pole in producing a south-north dichotomy is much higher than that of an heterogeneity centered at the equator in producing an east–west dichotomy (Amit et al., 2011). Hence, our models may have interesting implications for the understanding of the structure of the past martian dynamo.

We illustrate the importance of better constraining the thermal states of the cores, the size of the largest metallic diapir that remains after a giant impact, and the depth at which the impactor's core is buried before experiencing viscous deformation and the core merging process. We assume that the impact occurs with the martian escape velocity which is the minimum impact velocity; larger impact velocities can substantially increase the post-impact temperature in the mantle and in the merging core prior to its sinking. Hence, in this respect our results provide a lower bound on the temperature increase in the planetary core after the diapir merging and on the CMB heat flux increase (see Fig. 9, top left panel).

In our models, we make the strong assumption that the sinking impactor's core, the target silicate mantle and the target iron core are in the infinite Prandtl number regime. In reality, both the molten metallic cores have viscosities that are 10–20 orders of magnitude smaller than the mantle viscosity. Accounting for such large realistic viscosity contrasts may have consequences on both the sinking and the merging dynamics. Indeed, considering a more realistic viscosity contrast between the sinking metallic diapir and the silicate mantle may affect the heat dissipation during the sinking. Viscous heating will preferentially occur in the surrounding mantle reducing the maximal temperature reached within the merging diapir and the energy brought to the preexisting core (Monteux et al., 2009, 2011; Samuel et al., 2010). However, considering an inviscid sinking metallic diapir should not change significantly the diapir sinking velocity which is mainly governed by the mantle viscosity (Hadamard, 1911; Rybczynski, 1911; Yiantsios and Davis, 1990). Inertial and Coriolis forces can even favor dynamo generation during the sinking of the molten metallic diapir (Monteux et al., 2012). Concerning the merging dynamics, the injection of a large volume of molten iron in a turbulent and rotating preexisting core is a process that is difficult to handle numerically. To the first order, the merging dynamics is probably bounded between two extreme cases. In the infinite Prandtl number approximation, the stratification at the end of the merging is unavoidable and the core merging process will stop the preexisting dynamo. However, turbulence and rotational forces may enhance efficient thermal mixing within the preexisting core which may reactivate a dynamo previously killed by the impact heating.

Future missions will provide important additional constraints on interior structure and remanent crustal magnetic field of Mars that will help constrain interior thermal evolution and dynamo models. The MAVEN mission will provide low-altitude vector magnetic field observations at locations other than those sampled at low altitudes by Mars Global Surveyor. The InSight mission will provide constraints on the outer core radius, mantle seismic velocity structure (and hence on temperature and composition), and heat flow at a single lander location. The inference (from seismology) of any thermal dichotomy between the northern hemisphere and the southern hemisphere could be the consequence of a large core merging event. Another key to testing such models may consist of measurements of the degree of equilibration between the mantle and the core material of Mars. During the core merging following a giant impact, the metal may sink as unequilibrated blobs (Dahl and Stevenson, 2010; Kleine and Rudge, 2011). Hence, some memory of the core merging process might have been recorded in the martian mantle. An inferred dichotomy in the chemical composition of the martian mantle between the northern lowlands and the southern highlands could also be the consequence of a giant impact and of the subsequent core merging process.

Acknowledgments

J. Monteux is funded by Agence Nationale de la Recherche (Accretis decision No. ANR-10-PDOC-001-01). M. Jellinek and C.L. Johnson acknowledge support from the Natural Science and Engineering Research Council of Canada. We thank J. Roberts and anonymous reviewer for thoughtful and constructive comments.

References

Acuña, M. et al., 1999. Global distribution of crustal magnetization discovered by the Mars Global Surveyor MAG/ER experiment. Science 284, 790–793.
Agee, C.B., 1997. Melting temperatures of the Allende meteorite: Implications for a Hadean magma ocean. Phys. Earth Planet. Inter. 100, 41–47.
Amit, H., Christensen, U.R., Langlais, B., 2011. The influence of degree-1 mantle heterogeneity on the past dynamo of Mars. Phys. Earth Planet. Inter. 189, 63–79. http://dx.doi.org/10.1016/j.pepi.2011.07.008.
Andrews-Hanna, J.C., Zuber, M.T., Banerdt, W.B., 2008. The Borealis basin and the origin of the martian crustal dichotomy. Nature 453, 1212–1215. http://dx.doi.org/10.1038/nature07011.
Arkani-Hamed, J., Olson, P., 2010. Giant impact stratification of the martian core. Geophys. Res. Lett. 370 (L02), 201. http://dx.doi.org/10.1029/2009GL041417.

Asphaug, E., 2010. Similar-sized collisions and the diversity of planets. Chem. Erde/Geochem. 70, 199–219. http://dx.doi.org/10.1016/j.chemer.2010.01.004.
Benz, W., Slattery, W.L., Cameron, A.G.W., 1988. Collisional stripping of Mercury's mantle. Icarus 74, 516–528. http://dx.doi.org/10.1016/0019-1035(88)90118-2.
Buffett, B.A., 2002. Estimates of heat flow in the deep mantle based on the power requirements for the geodynamo. Geophys. Res. Lett. 29 (12), 1–4.
Canup, R.M., 2004. Simulations of a late lunar-forming impact. Icarus 168, 433–456. http://dx.doi.org/10.1016/j.icarus.2003.09.028.
Christensen, U.R., 2010. Dynamo scaling laws and applications to the planets. Space Sci. Rev. 152, 565–590.
Christensen, U.R., Aubert, J., 2006. Scaling properties of convection-driven dynamos in rotating spherical shells and application to planetary magnetic fields. Geophys. J. Int. 166, 97–114.
Citron, R.I., Zhong, S., 2012. Constraints on the formation of the martian crustal dichotomy from remnant crustal magnetism. Phys. Earth Planet. Inter. 212, 55–63. http://dx.doi.org/10.1016/j.pepi.2012.09.008.
Croft, S.K., 1982. A first-order estimate of shock heating and vaporization in oceanic impacts. In: Silver, T.L., Schultz, P.H. (Eds.), Geological Implications of Impacts of Large Asteroids and Comets on Earth, vol. 190. Spec. Pap. Geol. Soc. Am., pp. 143–152.
Ćuk, M., Stewart, S.T., 2012. Making the Moon from a fast-spinning Earth: A giant impact followed by resonant despinning. Science 338, 1047–1052. http://dx.doi.org/10.1126/science.1225542.
Dahl, T.W., Stevenson, D.J., 2010. Turbulent mixing of metal and silicate during planet accretion and interpretation of the Hf-W chronometer. Earth Planet. Sci. Lett. 295, 177–186. http://dx.doi.org/10.1016/j.epsl.2010.03.038.
Davies, G.F., 1982. Ultimate strength of solids and formation of planetary cores. Geophys. Res. Lett. 9, 1267–1270.
Davis, R.H., Schonberg, J.A., Rallison, J.M., 1989. The lubrication force between two viscous drops. Phys. Fluids 1, 77–81. http://dx.doi.org/10.1063/1.857525.
Douglas, J., 1955. On the numerical integration of $\frac{\partial^2 u}{\partial x^2}+\frac{\partial^2 u}{\partial y^2}=\frac{\partial u}{\partial t}$ by implicit methods. J. Soc. Ind. Appl. Math. 3, 42–65. http://dx.doi.org/10.1137/0103004.
Elkins-Tanton, L.T., Parmentier, E.M., Hess, P.C., 2003. Magma ocean fractional crystallization and cumulate overturn in terrestrial planets: Implications for Mars. Meteorit. Planet. Sci. 38, 1753–1771.
Ernst, C.M. et al., 2010. Exposure of spectrally distinct material by impact craters on Mercury: Implications for global stratigraphy. Icarus 209, 210–223. http://dx.doi.org/10.1016/j.icarus.2010.05.022.
Fleury, M., Mory, M., Hopfinger, E.J., Auchere, D., 1991. Effects of rotation on turbulent mixing across a density interface. J. Fluid Mech. 223, 165–191. http://dx.doi.org/10.1017/S0022112091001386.
Frey, H.V., 2006. Impact constraints on the age and origin of the lowlands of Mars. Geophys. Res. Lett. 33, L08S02. http://dx.doi.org/10.1029/2005GL024484.
Gerya, T.V., Yuen, D.A., 2007. Robust characteristics method for modelling multiphase visco-elastic thermo-mechanical problems. Phys. Earth Planet. Inter. 163, 83–105.
Hadamard, J., 1911. Mouvement permanent lent d'une sphère liquide et visqueuse dans un liquide visqueux. C.R. Acad. Sci. 152, 1735–1738.
Hartmann, W.K., Davis, D.R., 1975. Satellite-sized planetesimals and lunar origin. Icarus 24, 504–514.
Höink, T., Schmalzl, J., Hansen, U., 2005. Formation of compositional structures by sedimentation in vigorous convection. Phys. Earth Planet. Inter. 153, 11–20.
Hood, L.L., Richmond, N.C., Pierazzo, E., Rochette, P., 2003. Distribution of crustal magnetic fields on Mars: Shock effects of basin-forming impacts. Geophys. Res. Lett. 30 (6), 1–4.
Huppert, H.E., 1982. The propagation of two-dimensional and axisymmetric viscous gravity currents over a rigid horizontal surface. J. Fluid Mech. 121, 43–58.
Jellinek, A.M., Gonnermann, H.M., Richards, M.A., 2003. Plume capture by divergent plate motions: Implications for the distribution of hotspots, geochemistry of mid-ocean ridge basalts, and estimates of the heat flux at the core–mantle boundary. Earth Planet. Sci. Lett. 205, 361–378. http://dx.doi.org/10.1016/S0012-821X(02)01070-1.
Johnson, C.L., Phillips, R.J., 2005. Evolution of the Tharsis region of Mars: Insights from magnetic field observations. Earth Planet. Sci. Lett. 230, 241–254.
Jones, A.F., Wilson, S.D.R., 1978. The film drainage problem in droplet coalescence. J. Fluid Mech. 87, 263–288. http://dx.doi.org/10.1017/S0022112078001585.
Kaula, W.M., 1979. Thermal evolution of Earth and Moon growing by planetesimal impacts. J. Geophys. Res. 84, 999–1008.
Ke, Y., Solomatov, V.S., 2009. Coupled core–mantle thermal evolution of early Mars. J. Geophys. Res. (Planets) 114 (13), 1–12.
Kleine, T., Rudge, J.F., 2011. Chronometry of meteorites and the formation of the Earth and Moon. Elements 7, 41–46. http://dx.doi.org/10.1016/j.gca.2006.06.004.
Kotsovinos, N.E., 2000. Axisymmetric submerged intrusion in stratified fluid. J. Hydraul. Eng. 126, 446–456. http://dx.doi.org/10.1061/(ASCE)0733-9429(2000)126:6(446).
Kuang, W., Bloxham, J., 1997. An Earth-like numerical dynamo model. Nature 389, 371–374.
Laney, C.B., 1998. Computational Gasdynamics. Cambridge University Press, Cambridge.
Lee, D.C., Halliday, A.N., 1997. Core formation on Mars and differentiated asteroids. Nature 388, 854–857.
Lillis, R.J., Frey, H.V., Manga, M., 2008a. Rapid decrease in martian crustal magnetization in the Noachian era: Implications for the dynamo and climate of early Mars. Geophys. Res. Lett. 35 (L14), 203.
Lillis, R.J., Frey, H.V., Manga, M., Mitchell, D.L., Lin, R.P., Acuña, M.H., Bougher, S.W., 2008b. An improved crustal magnetic field map of Mars from electron reflectometry: Highland volcano magmatic history and the end of the martian dynamo. Icarus 194, 575–596.
Linden, P.F., 1977. The flow of a stratified fluid in a rotating annulus. J. Fluid Mech. 79, 435–447. http://dx.doi.org/10.1017/S0022112077000251.
Linden, P.F., 1979. Mixing in stratified fluids. Geophys. Astrophys. Fluid Dyn. 13, 3–23. http://dx.doi.org/10.1080/03091927908243758.
Manga, M., Stone, H.A., 1993. Buoyancy-driven interactions between two deformable viscous drops. J. Fluid Mech. 256, 647–683. http://dx.doi.org/10.1017/S0022112093002915.
Marinova, M.M., Aharonson, O., Asphaug, E., 2008. Mega-impact formation of the Mars hemispheric dichotomy. Nature 453, 1216–1219. http://dx.doi.org/10.1038/nature07070.
Marinova, M.M., Aharonson, O., Asphaug, E., 2011. Geophysical consequences of planetary-scale impacts into a Mars-like planet. Icarus 211, 960–985. http://dx.doi.org/10.1016/j.icarus.2010.10.032.
Monteux, J., Coltice, N., Dubuffet, F., Ricard, Y., 2007. Thermo-mechanical adjustment after impacts during planetary growth. Geophys. Res. Lett. 34, 24201–24205.
Monteux, J., Ricard, Y., Coltice, N., Dubuffet, F., Ulvrova, M., 2009. A model of metal-silicate separation on growing planets. Earth Planet. Sci. Lett. 287, 353–362.
Monteux, J., Jellinek, A.M., Johnson, C.L., 2011. Why might planets and moons have early dynamos? Earth Planet. Sci. Lett. 310, 349–359. http://dx.doi.org/10.1016/j.epsl.2011.08.014.
Monteux, J., Schaeffer, N., Amit, H., Cardin, P., 2012. Can a sinking metallic diapir generate a dynamo? J. Geophys. Res. (Planets) 117 (16), E10005. http://dx.doi.org/10.1029/2012JE004075.
Morris, S., 1982. The effects of a strongly temperature-dependent viscosity on slow flow past a hot sphere. J. Fluid Mech. 124, 1–26. http://dx.doi.org/10.1017/S0022112082002389.
Nimmo, F., Kleine, T., 2007. How rapidly did Mars accrete? Uncertainties in the Hf W timing of core formation. Icarus 191, 497–504. http://dx.doi.org/10.1016/j.icarus.2007.05.002.
Nimmo, F., Stevenson, D.J., 2000. Influence of early plate tectonics on the thermal evolution and magnetic field of Mars. J. Geophys. Res. 105, 11969–11980.
Nimmo, F., Hart, S.D., Korycansky, D.G., Agnor, C.B., 2008. Implications of an impact origin for the martian hemispheric dichotomy. Nature 453, 1220–1223. http://dx.doi.org/10.1038/nature07025.
O'Keefe, J.D., Ahrens, T.J., 1977. Impact-induced energy partitioning, melting, and vaporization on terrestrial planets. In: Merril, R.B. (Ed.), Lun. Planet. Sci. Conf., vol. 8, pp. 3357–3374.
Patankar, S.V., 1980. Numerical Heat Transfer and Fluid Flow. Series in Computational Methods in Mechanics and Thermal Sciences. Hemisphere Publishing Corp., Washington, DC, 210p..
Peaceman, D.W., Rachford, H.H., 1955. The numerical solution of parabolic and elliptic differential equations. J. Soc. Ind. Appl. Math. 3, 28–41. http://dx.doi.org/10.1137/0103003.
Pierazzo, E., Vickery, A.M., Melosh, H.J., 1997. A reevaluation of impact melt production. Icarus 127, 408–423.
Ratcliff, J.T., Tackley, P.J., Schubert, G., Zebib, A., 1997. Transitions in thermal convection with strongly variable viscosity. Phys. Earth Planet. Inter. 102, 201–212.
Reese, C.C., Solomatov, V.S., 2010. Early martian dynamo generation due to giant impacts. Icarus 207, 82–97. http://dx.doi.org/10.1016/j.icarus.2009.10.016.
Ricard, Y., Šrámek, O., Dubuffet, F., 2009. A multi-phase model of runaway core–mantle segregation in planetary embryos. Earth Planet. Sci. Lett. 284, 144–150.
Roberts, J.H., Arkani-Hamed, J., 2012. Impact-induced mantle dynamics on Mars. Icarus 218, 278–289. http://dx.doi.org/10.1016/j.icarus.2011.11.038.
Roberts, J.H., Barnouin, O.S., 2012. The effect of the Caloris impact on the mantle dynamics and volcanism of Mercury. J. Geophys. Res. (Planets) 117, E02007. http://dx.doi.org/10.1029/2011JE003876.
Roberts, J.H., Zhong, S., 2006. Degree-1 convection in the martian mantle and the origin of the hemispheric dichotomy. J. Geophys. Res. (Planets) 111 (10), E06013. http://dx.doi.org/10.1029/2005JE002668.
Roberts, J.H., Lillis, R.J., Manga, M., 2009. Giant impacts on early Mars and the cessation of the martian dynamo. J. Geophys. Res. (Planets) 114 (13), E04009. http://dx.doi.org/10.1029/2008JE003287.
Roe, P.L., 1986. Characteristic-based schemes for the Euler equations. Ann. Rev. Fluid Mech. 18, 337–365.
Rosenblatt, P., 2011. The origin of the martian moons revisited. Astron. Astrophys. Rev. 19, 44. http://dx.doi.org/10.1007/s00159-011-0044-6.
Rubie, D.C., Melosh, H.J., Reid, J.E., Liebske, C., Righter, K., 2003. Mechanisms of metal–silicate equilibration in the terrestrial magma ocean. Earth Planet. Sci. Lett. 205, 239–255.
Rybczynski, W., 1911. über die fortschreitende bewegung einer flüssigen kugel in einen medium. Bull. Acad. Sci. Cracovie 1, 40–46.
Safronov, V.S., 1978. The heating of the Earth during its formation. Icarus 33, 3–12. http://dx.doi.org/10.1016/0019-1035(78)90019-2.
Samuel, H., Tackley, P.J., 2008. Dynamics of core formation and equilibration by negative diapirism. Geochem. Geophys. Geosyst. 9, 6011–6026.
Samuel, H., Tackley, P.J., Evonuk, M., 2010. Heat partitioning in terrestrial planets during core formation by negative diapirism. Earth Planet. Sci. Lett. 290, 13–19.
Schubert, G., Turcotte, D.L., Olson, P., 2001. Mantle Convection in the Earth and Planets. Cambridge University Press.

Senshu, H., Kuramoto, K., Matsui, T., 2002. Thermal evolution of a growing Mars. J. Geophys. Res. 107, 1–13.
Shannon, M.C., Agee, C.B., 1996. High pressure constraints on percolative core formation. Geophys. Res. Lett. 23, 2717–2720.
Sleep, N.H., 1994. Martian plate tectonics. J. Geophys. Res. 99, 5639. http://dx.doi.org/10.1029/94JE00216.
Smith, J.V., 1979. Mineralogy of the planets: A Voyage in space and time. Mineral. Mag. 43, 1–89.
Srámek, O., Ricard, Y., Dubuffet, F., 2010. A multiphase model of core formation. Geophys. J. Int. 181, 198–220. http://dx.doi.org/10.1111/j.1365-246X.2010.04528.x.
Sreenivasan, B., Jellinek, A., 2012. Did the Tharsis plume terminate the martian dynamo? Earth Planet. Sci. Lett. 349, 209–217. http://dx.doi.org/10.1016/j.epsl.2012.07.013.
Stanley, S., Elkins-Tanton, L., Zuber, M.T., Parmentier, E.M., 2008. Mars' paleomagnetic field as the result of a single-hemisphere dynamo. Science 321, 1822–1825. http://dx.doi.org/10.1126/science.1161119.
Stevenson, D.J., 1989. Formation and early evolution of the Earth. In: Peltier, W.R. (Ed.), Mantle Convection and Plate Tectonics, pp. 818–868.
Stevenson, D.J., 2001. Mars' core and magnetism. Nature 412, 214–219.
Stevenson, D.J., 2003. Planetary magnetic fields. Earth Planet. Sci. Lett. 208, 1–2.
Stevenson, D.J., Spohn, T., Schubert, G., 1983. Magnetism and thermal evolution of the terrestrial planets. Icarus 54, 466–489.
Thayalan, V., Jellinek, A.M., Lenardic, A., 2006. Recycling the lid: Effects of subduction and stirring on boundary layer dynamics in bottom-heated planetary mantle convection. Geophys. Res. Lett. 33, L20318. http://dx.doi.org/10.1029/2006GL027668.
Tonks, W.B., Melosh, H.J., 1992. Core formation by giant impacts. Icarus 100, 326–346.
Watters, W.A., Zuber, M.T., Hager, B.H., 2009. Thermal perturbations caused by large impacts and consequences for mantle convection. J. Geophys. Res. (Planets) 114, E02,001. http://dx.doi.org/10.1029/2007JE002964.
Wilhelms, D.E., Squyres, S.W., 1984. The martian hemispheric dichotomy may be due to a giant impact. Nature 309, 138–140. http://dx.doi.org/10.1038/309138a0.
Williams, J., Nimmo, F., 2004. Thermal evolution of the martian core: Implications for an early dynamo. Geology 32, 97–100.
Yiantsios, S.G., Davis, R.H., 1990. On the buoyancy-driven motion of a drop towards a rigid surface or a deformable interface. J. Fluid Mech. 217, 547–573. http://dx.doi.org/10.1017/S0022112090000842.
Yoder, C.F., Konopliv, A.S., Yuan, D.N., Standish, E.M., Folkner, W.M., 2003. Fluid core size of Mars from detection of the solar tide. Science 300, 299–303. http://dx.doi.org/10.1126/science.1079645.
Yoshino, T., Walter, M.J., Katsura, T., 2003. Core formation in planetesimals triggered by permeable flow. Nature 422, 154–157.
Ziethe, R., Spohn, T., 2007. Two-dimensional stokes flow around a heated cylinder: A possible application for diapirs in the mantle. J. Geophys. Res. 112, 1–13.

AGU PUBLICATIONS

JGR

Journal of Geophysical Research: Planets

RESEARCH ARTICLE
10.1002/2013JE004587

Key Points:
- Following a giant impact, the impact parameters govern the merging temperature
- For plausible viscosity contrasts the merging time occurs in less than 1 kyr
- Core merging only delays the re-initiation of the dynamo for a very short time

Correspondence to:
J. Monteux,
julien.monteux@univ-nantes.fr

Citation:
Monteux, J., and J. Arkani-Hamed (2014), Consequences of giant impacts in early Mars: Core merging and Martian dynamo evolution, *J. Geophys. Res. Planets*, *119*, 480–505, doi:10.1002/2013JE004587.

Received 28 NOV 2013
Accepted 29 JAN 2014
Accepted article online 6 FEB 2014
Published online 6 MAR 2014

Consequences of giant impacts in early Mars: Core merging and Martian dynamo evolution

Julien Monteux[1] and Jafar Arkani-Hamed[2]

[1]Laboratoire de Planétologie et de Géodynamique, Université de Nantes, Nantes, France, [2]Department of Physics, University of Toronto, Toronto, Ontario, Canada

Abstract A giant impact is an increasingly popular explanation for the formation of the northern lowland on Mars. It is plausible that at the impact time both Mars and the impactor were differentiated with solid silicate mantles and liquid iron cores. Such a large impact likely resulted in merging of the cores of both bodies, a process which will have implications on the thermal state of the planet. We model the evolution of the Martian mantle following a giant impact and characterize the thermochemical consequences of the sinking of an impactor's core as a single diapir. The impact heating and the viscous heating induced during the core merging may affect the early thermal state of Mars during several tens of million years. Our results show that large viscosity contrasts between the impactor's core and the surrounding mantle silicates can reduce the duration of the merging down to 1 kyr but do not modify the merging temperature. When the viscosity contrast between the diapir and the surrounding silicates is larger than a factor of 1000, the descent of the diapir can lead to some entrainment of the relatively shallow silicates to deepest regions close to the core-mantle boundary. Finally, the direct impact heating of Martian core leads to thermal stratification of the core and kills the core dynamo. It takes on the order of 150–200 Myr to reinitiate a strong dynamo anew. The merging of the impactor's core with the Martian core only delays the reinitiation of the dynamo for a very short time.

1. Introduction

Giant impacts were common in the later stage of accretion of terrestrial planets. The Earth is likely formed by accretion of a few dozen moons to Mars-size planetary embryos (see the review by *Chambers* [2004]). A Mars-size impact on Earth may have resulted in the formation of the Moon [*Hartmann and Davis*, 1975; *Cameron and Benz*, 1991; *Canup*, 2004]. An oblique collision of a large body with a mass about one sixth of the Mercury's has likely stripped away a significant part of Mercury's mantle [*Smith*, 1979; *Benz et al.*, 1988]. As an alternative to endogenic formation models [e.g., *Zhong and Zuber*, 2001; *Reese and Solomatov*, 2006], an 800–1300 km size impact has been proposed to explain the formation of northern lowland of Mars [*Wilhelms and Squyres*, 1984; *Nimmo et al.*, 2008; *Andrews-Hanna et al.*, 2008; *Marinova et al.*, 2008], and the lunar farside highlands were likely formed by accretion of a companion moon [*Jutzi and Asphaug*, 2011].

Part of an impactor may be retained by the planet, depending on the impact angle, impact velocity and the impactor to planet mass ratio. The accretion efficiency is close to 1 for impacts occurring at low velocities (i.e., the impact velocity v_{imp} < twice the escape velocity of the planet v_{esc}) with impact angles of ~45° or less relative to the local vertical direction, whereas for impacts occurring at higher velocities (i.e., $v_{imp} > 2v_{esc}$) and at higher impact angles the efficiency is negligible [*Asphaug*, 2010]. The impact-induced shock wave propagation heats the planet and results in a large thermal anomaly buried deep in the mantle of the planet with a volume comparable to the volume of the impactor [e.g., *Tonks and Melosh*, 1993; *Pierazzo et al.*, 1997; *Arkani-Hamed*, 2005; *Monteux et al.*, 2007; *Arkani-Hamed and Ghods*, 2011]. This thermal energy added to the preimpact temperature of a planet may result in melting and iron-silicate segregation in the mantle.

Recent studies have explored the effects of large impacts on the Martian mantle dynamics [e.g., *Watters et al.*, 2009; *Ghods and Arkani-Hamed*, 2011; *Roberts and Arkani-Hamed*, 2012] and on the cessation of dynamo action [e.g., *Roberts et al.*, 2009; *Arkani-Hamed and Olson*, 2010a, 2010b; *Arkani-Hamed*, 2012]. At the time of a giant impact, both Mars and the impactor were probably differentiated [*Yoshino et al.*, 2003; *Neumann et al.*, 2012]. It is likely that the entire impactor's iron core merged with the preexisting core of Mars. The processes involved in the merging dynamics are strongly dependent on the rheology of the impacted mantle where the iron core of the impactor sinks and on the characteristic size of the sinking core. These processes can involve sedimentation of metallic rain at the base of a magma ocean [*Rubie et al.*, 2003; *Höink et al.*, 2005]

followed by a large diapir, which sinks through the underlying solid mantle [*Tonks and Melosh*, 1992]. The impact heating can have severe consequences on the thermal state of the planet and on the cessation of the core dynamo [e.g., *Arkani-Hamed and Olson*, 2010a, 2010b]. Also, the hot and molten iron brought by the merging of an impactor's core can envelop the preexistent core and generate dynamo if the layer is thicker than about 30 km [*Reese and Solomatov*, 2010].

Monteux et al. [2013] investigated the dynamics and the thermal effects of the core merging by monitoring the evolution of a spherical diapir sinking through a solid mantle. The authors used some idealized models of Mars and the impact heating as first-order estimates. For example (1) the iron diapir is assumed to start as a spherical body. During the impact process, the molten iron of the impactor is mixed with the partially molten parts of the impactor's and planet's silicates. However, due to its higher density compared to the silicates, the molten iron segregates and pounds at the bottom of the partially molten zone in the mantle while conforming to the shape of the zone. Hence, the initial shape of the iron diapir is a thin spherical cap with a flat top and an almost spherical bottom, certainly far from being spherical. Because the dynamics of a sinking body is strongly affected by its shape the spherical shape assumption has significant effects on the sinking time of the diapir. (2) The impact creates a spherical isobaric zone with an almost constant temperature, and temperature decays exponentially outside this zone. By choosing the decay scaling factor of $\sim (r_o/r)^{4.4}$, where r_o and r denote the radius of the isobaric sphere and the distance from the center of the sphere, the authors severely underestimated the impact-induced temperature increase outside the isobaric core. This resulted in much colder thus higher viscosity lower mantle beneath the impact site in their temperature-dependent viscosity models, hence hampering the sinking of the iron diapir. (3) The mantle viscosity was assumed either constant (isoviscous) or temperature dependent. The mantle viscosity is actually temperature and pressure dependent, decreases with increasing temperature and increases with increasing pressure. Also the viscosity reduces substantially upon partial melting. Moreover, in reality, the rheology also depends on the strain rate and plasticity can occur [*Golabek et al*., 2009]. The latter is not taken into account here.

The aim of the present study is to monitor the thermal evolution of the Martian mantle following a giant impact and, in particular, the dynamics of the sinking iron diapir of the impactor. We relax the assumptions made by *Monteux et al*. [2013] by using more realistic models. This provides a means to assess the adverse effects of the assumptions. For example, (1) we start with the molten iron of the impactor as an almost spherical cap, numerically determined by the shape of the partially molten impact-heated region in the upper mantle of the Mars models, (2) we use a more realistic scaling law for the decay of temperature outside the isobaric zone derived on the basis of hydrocode numerical simulations of an impact [*Pierazzo et al*., 1997; *Watters et al*., 2009], and (3) we use not only constant and temperature-dependent viscosity models but also incorporate the pressure- and melt-dependent viscosity models. Furthermore, we investigate the effects of other factors such as (1) the higher viscosity contrast between the iron diapir and the surrounding mantle, (2) the higher impact velocity of 10 km/s which is within the range of impact velocities of Mars [*Neukum and Wise*, 1976] (on Mars, $v_{esc} = 5$ km/s), (3) different physical properties of Martian mantle which control the Equation Of State (EOS) for propagation of shock waves, hence the ability of the mantle to convert the energy from the impact-induced shock wave to internal heating, and (4) the influence of melting on the heat budget and mantle dynamics. In comparison with the models from *Monteux et al*. [2013], the preimpact thermal state, the postimpact thermal state, the postimpact chemical repartition of the impactor's core, and the mantle viscosity are considered more realistically. We also investigate in detail the effect of an impact on the core dynamo of Mars. This includes two aspects: (1) the direct heating of the core by the impact-induced shock wave, and (2) the impactor core merging on the Martian core. The first aspect, which is the most important factor, was not considered by *Monteux et al*. [2013], but the second aspect was also investigated by the authors.

The second section deals with the preimpact Martian model, while the third section presents the postimpact temperature and chemical repartitions. The core merging dynamics is described in the fourth section, and the results are presented in the fifth, sixth, and seventh sections. The effects of impacts on the core dynamo of Mars are investigated in the following section. The concluding remarks are relegated to the last section.

2. Preimpact Martian Model

This section describes the preimpact models of Mars considered in this study. The models are spherically symmetric with radially dependent physical parameters.

2.1. Pressure and Gravity Profiles

The Martian topographic dichotomy is one of the oldest features on Mars, formed sometime between 4.5 and 3.7 Ga [*McGill and Dimitriou*, 1990; *Frey et al*., 2002; *Solomon et al*., 2005]. Hence, at the time of the giant impact that might be responsible for the Martian dichotomy, both the impactor and Mars were probably differentiated. Hf/W chronology suggests that core formation happened during the first 10–30 Myr of Mars' history [*Lee and Halliday*, 1997; *Kleine et al*., 2002; *Nimmo and Kleine*, 2007; *Dauphas and Pourmand*, 2011]. Such a rapid process involves extensive melting, which is potentially enhanced by radiogenic heating as a result of the decay of short-lived radionuclides ^{26}Al and ^{60}Fe [*Yoshino et al*., 2003; *Neumann et al*., 2012], impact heating [*Tonks and Melosh*, 1992; *Senshu et al*., 2002; *Monteux et al*., 2009], and gravitational energy conversion during the core formation resulting in metal/silicate separation [*Stevenson*, 1989; *Ricard et al*., 2009]. The metal/silicate separation can occur via a wide range of phenomena such as percolation [*Shannon and Agee*, 1996; *Walte et al*., 2007; *Bagdassarov et al*., 2009; *Walte et al*., 2011], the sedimentation of metallic rain through a magma ocean [*Rubie et al*., 2003; *Höink et al*., 2005] or a large diapir sinking through a solid mantle [*Tonks and Melosh*, 1992; *Monteux et al*., 2009]. Whatever the mechanism, Mars' internal structure, characterized by a $\approx$1700 km radius liquid iron core [*Yoder et al*., 2003], was mostly established within $\approx$10 Myr of the planet's formation [*Kleine et al*., 2002].

Considering a simple two-layered density model, ρ_{Fe} for the core (with radius R_{core}) and ρ_{Si} for the mantle, the integration of

$$dP = -\rho g dr \tag{1}$$

leads to the following gravity and pressure profiles in the core,

$$g(r) = \frac{4}{3}\pi G \rho_{Fe} r \tag{2}$$

$$\begin{aligned} P(r) = {} & \frac{2}{3}\pi G \rho_{Fe}^2 \left(R_{core}^2 - r^2\right) + \frac{2}{3}\pi G \rho_{Si}^2 \left(R^2 - R_{core}^2\right) \\ & + \frac{4}{3}\pi G \rho_{Si} R_{core}^3 \left(\rho_{Fe} - \rho_{Si}\right)\left(\frac{1}{R_{core}} - \frac{1}{R}\right) \end{aligned} \tag{3}$$

and in the mantle,

$$g(r) = \frac{4}{3}\pi G \left(r\rho_{Si} + \frac{R_{core}^3}{r^2}\left(\rho_{Fe} - \rho_{Si}\right)\right) \tag{4}$$

$$P(r) = \frac{2}{3}\pi G \rho_{Si}^2 \left(R^2 - r^2\right) + \frac{4}{3}\pi G \rho_{Si} R_{core}^3 \left(\rho_{Fe} - \rho_{Si}\right)\left(\frac{1}{r} - \frac{1}{R}\right) \tag{5}$$

where ρ_{Fe} and ρ_{Si} are assumed constant, g is the gravitational acceleration, r is the distance to the center of the planet, and G is the gravitational constant. Figure 1 presents the density, gravity, and pressure profiles used in our models.

2.2. Temperature Field

The preimpact thermal state of Mars strongly depends on the short-lived radiogenic heating, the accretion processes and the dissipation of potential energy during the core formation [e.g., *Senshu et al*., 2002; *Golabek et al*., 2009; *Šrámek et al*., 2010]. The uncertainties on the relative importance of these processes as well as the diversity of the processes involved in the core formation lead to a wide range of plausible early thermal states after the full differentiation of Mars.

The preimpact Martian temperature field is assumed only radially dependent. From the surface, the temperature increases rapidly through the top thermal boundary layer and then increases adiabatically and gradually down to the bottom thermal boundary layer, where it again increases rapidly toward the core-mantle boundary (CMB). We use the temperature profile from *Roberts and Arkani-Hamed* [2012] with the CMB temperature of $T_{CMB} = 2000$ K as the preimpact temperature profile (see Figure 1). The temperature increases adiabatically in the core as

$$\frac{dT}{dr} = -\frac{\alpha_{Fe} g(r) T}{c_{p,Fe}} \tag{6}$$

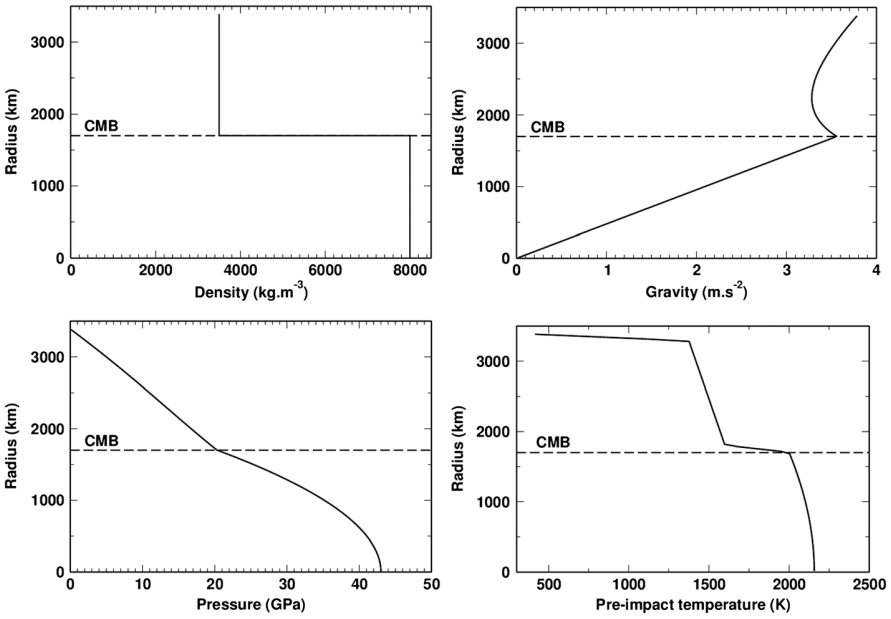

Figure 1. The preimpact density, gravity, pressure, and temperature profiles of the Mars model.

With the linear increase of gravity in the core (equation 2) and assuming constant thermal expansion coefficient α_{Fe} and heat capacity $c_{p,Fe}$, the integration of equation 6 leads to [e.g., *Coradini et al.*, 1983]

$$T_{core}(r) = T_{CMB} \exp\left(\left(\frac{2\pi\alpha_{Fe} G\rho_{Fe}}{3c_{p,Fe}}\right)\left(R_{core}^2 - r^2\right)\right) \tag{7}$$

Included in Figure 1 is the preimpact temperature profile used in our models.

3. Postimpact Temperature and Chemical Repartition

After a giant impact, the shock wave propagation results in a large thermal anomaly in the upper mantle of the planet [e.g., *Tonks and Melosh*, 1993; *Senshu et al.*, 2002; *Monteux et al.*, 2007; *Watters et al.*, 2009; *Arkani-Hamed and Olson*, 2010a, 2010b; *Roberts and Arkani-Hamed*, 2012]. Depending on the impact velocity and the efficiency of conversion from the kinetic energy to heat, the subsequent temperature increase may exceed the melting temperature of the mantle material [*Pierazzo et al.*, 1997; *Ghods and Arkani-Hamed*, 2011; *Monteux et al.*, 2011]. In the following section we describe our model of large impact heating of the Martian mantle and core.

3.1. The Impact-Induced Temperature Increase

Following a giant impact, a nearly uniform shock pressure P_s is generated inside the so-called isobaric sphere of radius r_c, [*Croft*, 1982; *Melosh*, 1989]

$$P_s = \rho_{Si}(C_0 + S\, u_o)\, u_o \tag{8}$$

where ρ_{Si} and C_0 are the preshock density and acoustic velocity of the silicate mantle, u_o is the particle velocity in the isobaric sphere, which is taken to be one half the impact velocity v_{imp} assuming similar target and impacting materials, and S is a constant. D_{imp} is the impactor diameter and v_{imp} is in km/s [*Arkani-Hamed and Olson*, 2010a, 2010b] of $r_c = 0.0525\, D_{imp}\, v_{imp}$. The shock pressure decays with distance from the impact site outside the isobaric region. Several different models have been proposed for the shock pressure distribution outside the isobaric region [*Ahrens and O'Keefe*, 1987; *Melosh*, 1989; *Pierazzo et al.*, 1997; *Mitani*, 2003]. In this study, we adopt the average model of *Pierazzo et al.* [1997]. Accordingly, the shock pressure P_s at a distance d from the isobaric center is calculated by

$$P_s(d) = P_s(r_c)\cdot(r_c/d)^n \qquad d > r_c; n = -1.84 + 2.61 \log v_{imp} \tag{9}$$

The axisymmetric shock pressure in the Martian interior is calculated at 1 × 1 km grid intervals in a spherical coordinate system with the symmetry axis passing through the impact site and the planet's center. The

Table 1. C_0 and S Values for the Dunite

C_0 (m/s)	S	Reference
6600	0.86	*McQueen et al.* [1967], $P < 44$ GPa
5600	1.2	*McQueen et al.* [1967], $P > 45$ GPa
5500	1.80	*Ahrens and Johnson* [1995]
5140	1.12	*Trunin* [2001], $29.8 < P < 102.1$ GPa
5120	1.27	*Trunin* [2001], $30.6 < P < 223.7$ GPa
7800	0.2	*Melosh* [1989], $44 < P < 73$ GPa
4400	1.5	*Melosh* [1989], $P > 73$ GPa

pressure reduction near the surface due to interference of the direct and reflected waves is taken into consideration after modifying *Melosh*'s [1989] rectangular coordinate algorithm to a spherical coordinate algorithm [*Shahnas and Arkani-Hamed*, 2007; *Louzada and Stewart*, 2009]. At the core-mantle boundary the incident pressure wave is partly reflected to the mantle and partly transmitted to the core [*Arkani-Hamed and Ghods*, 2011]. The interference of the direct and reflected waves in the mantle near the core-mantle boundary has only minor effects on the shock pressure and is neglected.

As the impact-induced shock wave propagates in the planet it creates a high pressure behind the shock front and sets the material in motion. The pressure behind the shock front is determined using the conservation of momentum across the front,

$$P_s - P_o = \rho_o u\, U. \tag{10}$$

where u and U are the particle and shock wave velocities, respectively. P is the total pressure (shock pressure plus the preshock lithostatic pressure) behind the shock front. P_o and ρ_o are the preshock lithostatic pressure and density ahead of the shock front, which are radially dependent (Figure 1). We also use an empirical, linear Equation of State (EOS) to relate the shock wave velocity to the particle velocity,

$$U = C_0 + S\, u. \tag{11}$$

The acoustic velocity C_0 (= $(K/\rho_o)^{1/2}$, K is the bulk modulus) and the parameter S are pressure and temperature dependent in general. We assume they are constant in our models, with different values in the core and the mantle. Table 1 is a list of measurements for dunite, which is probably a reasonable candidate for the mantle material. The S values of 1.8 by *Ahrens and Johnson* [1995] and 0.2 by *Melosh* [1989] are well off compared to the others. In our models C_0 ranges between 5140 and 6965 m/s and S between 0.8 and 1.12. The $C_0 = 6965$ (m/s) is the average value in the upper mantle of the Earth, from the base of the crust down to 670 km transition zone which is comparable to Martian interior as far as temperature and pressure is concerned, determined using the PREM model of the Earth [*Dziewonski and Anderson*, 1981].

The shock-induced temperature increase ΔT is determined following the "foundering" model of *Watters et al.* [2009] (see Figure 2, bottom left),

$$\Delta T = \left\{ P_\delta (1 - 1/f)/(2\,\rho_o S) - (C_0/S)^2 (f - ptln\, f - 1) \right\} / C_p, \tag{12}$$

where

$$f = -P_\delta / \left(\beta \left\{ 1 - \left[(2\,P_\delta/\beta) + 1^{1/2} \right] \right\} \right), \tag{13}$$

$$P_{\delta =} P_s - P_o, \tag{14}$$

$$\beta = \left(C_0{}^2 \rho_o \right) / (2\,S), \tag{15}$$

P_o is the preshock lithostatic pressure, ρ_o stands for the preshock density, and C_p is the specific heat of the mantle.

3.2. Postimpact Melting and Thermal Mixing

The temperature field below the impact site and before the core merging is obtained by adding the preimpact temperature profile $T_0(r)$ and the impact-induced temperature increase $\Delta T(r,\theta)$. Considering that the preimpact mantle is solid, the postimpact temperature can exceed the solidus temperature of silicates within the Martian mantle, consume latent heat, and generate a large partially to completely molten zone. The latent heat of melting is accounted for in the heat budget. For simplicity, we consider that the solidus (T_{sol}) and the liquidus (T_{liq}) temperatures of silicates are constant with depth and $T_{sol} = 1800$ K and $T_{liq} = 2300$ K [*Ghods and Arkani-Hamed*, 2007]. Truly, T_{sol} and T_{liq} are also pressure dependent [*Katz et al.*, 2003; *Roberts and Barnouin*, 2012]. The iron core of the impactor is assumed to be molten prior to the impact and no latent heat is consumed to melt it.

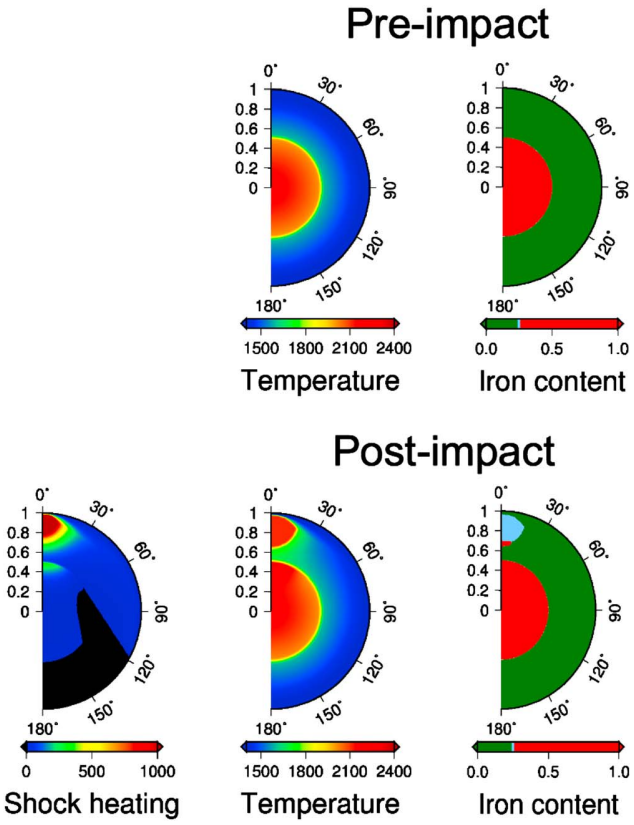

Figure 2. Preimpact temperature (in K)/compositional fields, shock-induced temperature increase (in K), and postimpact temperature (in K)/compositional fields after a 750 km diameter impact with $C_0 = 6000$ m/s and $S = 0.86$ (Reference case). In the right bottom figure, the blue colored material represents partially molten silicates.

For a given mantle volume, the potential temperature $T(r, \theta) = T_0(r) + \Delta T(r, \theta)$ must be modified to take into account the latent heat of melting. The fraction of melt f_{melt} is calculated as follows. For a potential temperature larger than $(T_{liq} + L_{Si}/C_{pSi})$ melting is complete ($f_{melt} = 1$) and the latent heat consumption leads to a temperature reduction from T to T' following

$$T'(r, \theta) = T(r, \theta) - L_{Si}/C_{pSi}. \quad (16)$$

For a potential temperature lower than the T_{sol}, $f_{melt} = 0$ and no latent heat is consumed

$$T'(r, \theta) = T(r, \theta). \quad (17)$$

Where the potential temperature T ranges between T_{sol} and $T_{liq} + L_{Si}/C_{pSi}$, the latent heat consumption linearly increases within the partially molten region and

$$T'(r, \theta) = \left[C_p T(r, \theta)\left(T_{liq} - T_{sol}\right) + T_{sol} L_{Si}\right] / \left[C_{pSi}\left(T_{liq} - T_{sol}\right) + L_{Si}\right] \quad (18)$$

After the impact heating and melting, mechanical mixing due to segregation of iron occurs within the partially molten region leading to a homogenization of the temperature where partial melting occurs [*Senshu et al.*, 2002; *Deguen et al.*, 2011]. The efficiency of mixing increases with the size of the planet and gravitational energy released per impactor mass [*Pierazzo et al.*, 1997; *Deguen et al.*, 2011]. Hence, in the partially to completely molten volume, called hereafter the segregation volume, both silicates and iron are in thermal equilibrium. As a rough estimate we determine the temperature inside the segregation volume by volume averaging the temperatures of the partially and completely molten material.

The final postimpact temperature field strongly depends on D_{imp}, C_0 and S (see Table 2). Figure 2 (second column) shows the preimpact and postimpact temperature fields for $D_{imp} = 750$ km, $C_0 = 6000$ m/s, and $S = 0.86$ model,

Table 2. Free Parameters Range Studied in Our Models

Parameter	Description	Value
C_0	Acoustic velocity of the mantle	5140, 6000, and 6965 m/s
	Acoustic velocity of the core	3800 m/s
S	EOS Constant of the mantle	0.8, 0.86, and 1.12
	EOS Constant of the core	1.6
v_{imp}	Impact velocity	10 km/s
D_{imp} (=2 R_{imp})	Impactor diameter	500, 750, and 1000 km
η_0	Reference viscosity	10^{20}–10^{22} Pa s
ρ_0	Mean density	4060 kg m^{-3}
ρ_{Si}	Mantle density	3500 kg m^{-3}
ρ_{Fe}	Core density	7500 kg m^{-3}
c_T	Temperature-induced viscosity contrast	10–1000
c_Z	Pressure-induced viscosity contrast	10
c_1	Temperature-induced viscosity contrast (if $f_{melt} = 0$)	10–1000
c_2	Melt-induced viscosity contrast (if $f_{melt} > 0$)	30–3000

which is designated as our reference model for the rest of the study. The impact angle should also influence the shape of the postimpact thermal anomaly and, hence, the shape of the segregation volume where melting occurs [*Pierazzo and Melosh*, 2000]. Indeed, increasing the impact angle from 0° (head-on impact) to larger values (oblique impacts) reduces the volume of the impact melt. Here we consider the upper limit case of a vertical impact where the efficiency of melt production is optimal.

3.3. Postimpact Chemical Repartition

Assuming that the bulk chemistry of the impactor is the same as Martian (12.5% volume of the metallic phase), a metallic volume with an equivalent radius $R_{Fe} = R_{imp}/2$ is retained when the planet is hit by an impactor with a radius R_{imp}. The retained impactor's core is denser than the silicates and rapidly sinks and fills the bottom of the segregation volume [*Monteux et al.*, 2009; *Deguen et al.*, 2011]. This leads to the formation of a complex shape diapir that starts to sink toward the Martian core while deforming the relatively colder and more viscous surrounding mantle (see Figure 2, third column).

4. Dynamic Model of Core Merging

Once buried below the surface, the dense metallic core of the impactor sinks toward the center of the target planet. Dissipation of the work done by buoyancy forces driving motion of this diapir occurs and causes heating in the mantle and/or the diapir.

4.1. Physical Model

To investigate the dynamics of the metallic diapir, we follow the procedure adopted by *Monteux et al.* [2009] and assume that the mantle deforms in a diffusion creep limit. Briefly, the conservation of energy leads to

$$\frac{DT}{Dt} = \frac{\nabla^2 T}{Ra_\chi} + Di\left(\frac{\eta}{\eta_0} B\Omega - v_r\left(T + \frac{T_0(r)}{\Delta T_0}\right)r\right) \quad \text{with} \quad \frac{D}{Dt} = \frac{\partial}{\partial t} + (v\cdot\nabla) \tag{19}$$

T, t, r, and v_r are dimensionless temperature, time, radius, and radial velocity, respectively. $Ra_\chi = \frac{\Delta\rho_0\ g_0\ R^3}{\kappa\eta_0}$ is the compositional Rayleigh number and $Di = \frac{\alpha\rho_0 g_0 R}{\rho_0 C_p}$ is the dissipation number (with κ the heat diffusivity and $\overline{\rho_0 C_p}$ the average volume specific heat of the impacted body). $B = \frac{\Delta\rho_0}{\rho_0 \alpha \Delta T_0}$ is the chemical/thermal buoyancy ratio, where ρ_0 and α are the average density and thermal expansion of the planet. The density difference, which drives the flow, is a function of temperature and chemical composition. Because $B >> 1$, the influence of the chemical difference between iron and silicates is preponderant in the density difference. The temperature-, pressure-, and melt-dependent viscosity is η, and η_o is a constant reference viscosity. The dimensionless dissipation function Ω expresses the conversion of potential energy into heat through viscous dissipation,

$$\Omega = 2\underline{\varepsilon} : \underline{\varepsilon} \tag{20}$$

where $\underline{\varepsilon}$ is the dimensionless shear strain rate tensor. The preimpact temperature $T_0(r)$ is radially dependent.

Assuming an incompressible medium with an infinite Prandtl number, the conservation of mass and momentum are expressed as

$$\nabla\cdot v = 0 \tag{21}$$

and

$$-\nabla P + \nabla\cdot\left(\frac{\eta}{\eta_0}[\nabla v + [\nabla v]\right) + \left(\frac{T}{B} - f\right)re_r = 0 \tag{22}$$

where v and P are the nondimensional velocity and pressure and e_r is the radial unit vector. The buoyancy force that drives the diapir toward the center of the planet increases with the volume fraction of metal f that varies between 1 (pure metal) and 0 (pure silicates). The f is simply advected by the flow

$$\frac{Df}{Dt} = 0. \tag{23}$$

4.2. Viscosity Model

After ponding at the bottom of the segregation zone, the dense metallic phase sinks toward the core of the impacted planet. How this occurs is debated. Proposed mechanisms include percolation through a solid mantle [*Shannon and Agee*, 1996; *Stevenson*, 1990], settling of centimeter-sized droplets in a magma ocean

[*Rubie et al*., 2003] and large mantle diapirs [*Ricard et al*., 2009; *Senshu et al*., 2002; *Tonks and Melosh*, 1992]. In addition, it has been proposed that metallic diapirs can sink toward the centers of the planets via fracturing and diking [*Tonks and Melosh*, 1992; *Solomatov*, 2000; *Stevenson*, 2003] or via viscous deformation [*Honda et al*., 1993; *Monteux et al*., 2009] depending on the thermal state of the planets' mantle. In the frame of the impactor's core sinking as a single large metallic diapir, the rheology of the Martian mantle plays a key role since it governs its ability to deform during the merging. Under the conditions of a massive iron diapir sinking through solid mantle the large deviatoric stress generated by the diapir could lead to a nonlinear rheology [*Samuel and Tackley*, 2008; *Golabek et al*., 2009], elastoplastic deformations [*Gerya and Yuen*, 2007] or even to fracturing if they exceed the ultimate strength of rocks which is ~1–2 GPa [*Davies*, 1982].

However, several lines of evidence suggest the viscous deformation considered in the present study to be a more likely mechanism: (1) Detailed study of the distance from Mars to Phobos, the motion of the shadow of Phobos on the surface of Mars measured by Mars Orbiter Laser Altimeter, and the Viking I Lander observation of the motion of the shadow of Phobos passing over it led *Bills et al*. [2005] to suggest that the mantle of Mars at present is more deformable than that of the Earth, (2) in its early history, because of the combination of the heating from accretion and short-lived radioisotopes, and from conversion of potential energy during core formation, the Martian mantle was probably much hotter and softer than today [*Senshu et al*., 2002; *Breuer et al*., 2010], and more importantly (3) the iron diapir sinks through the already impact-heated region of the mantle below the segregation zone. Included in Figure 2 (second row, middle) is the temperature field immediately after a 750 km diameter impact (other temperature fields obtained from the different impact parameters investigated in this study will be represented later in Figures 5, 7, and 8). The temperature directly beneath the segregation zone is much closer to the solidus of the mantle, implying that the metallic core likely sinks via diffusional flow deformation (Newtonian flow) [*Honda et al*., 1993; *Monteux et al*., 2013]. Hence, excluding power law rheologies and plasticity seems to be reasonable as a first-order approximation. However, as the mantle viscosity in early Mars may be sufficiently large to support large stresses, more sophisticated models considering these two effects might be envisioned. Due to the numerical limitations of our model, this is currently beyond the scope of the present study.

To account for the viscosity contrast between the hot molten material and the cold solid material, we adopt a temperature-, melt-, and pressure-dependent viscosity model:

$$\eta\,(T,P)/\eta_0(T_0,P_0) = \exp(-c_T T + c_Z P). \tag{24}$$

where $\eta_0 = \eta(T_0,P_0)$ is the viscosity of the cold and shallow undifferentiated material at the start of the experiment, c_Z is a constant, and c_T depends on the melt fraction of the material. For completely solid, c_T equals c_1, and c_2 for completely molten regions (see Table 2). In the partially molten region c_T is linearly interpolated between c_2 and c_1,

$$c_T = (c_2 - c_1)/\left(T_{\mathrm{liq}} - T_{\mathrm{sol}}\right)T(r,\theta) + c_1 - (c_2 - c_1)/\left(T_{\mathrm{liq}} - T_{\mathrm{sol}}\right)\,T_{\mathrm{sol}}. \tag{25}$$

This type of viscosity model decreases sharply with temperature and its expression is simpler to implement than the usual Arrhenius law [*Ratcliff et al*., 1997; *Ziethe and Spohn*, 2007]. We neglect the compositional dependency of the viscosity for two reasons. First, the compositional contrasts are sharp and may lead to steep viscosity fronts, difficult to handle numerically. Second, among the parameters that might affect the viscosity (composition, temperature, melting degree, and pressure) experimental results suggest that the viscosity contrast is more sensitive to the melting degree and temperature. Ultimately, the viscosity contrast between hot molten iron (or fully molten silicates) and solid cold silicates can reach 20 orders of magnitude [*Vocadlo et al*., 2000].

To model the influence of the viscosity contrast between hot molten iron and cold solid silicates on the core merging dynamics, we use much smaller contrast. This approach is encouraged by the fact that the viscosity of the surrounding silicate material mainly governs the merging velocity [*Hadamard*, 1911; *Batchelor*, 1967]. Diapirs more than 10 times less viscous than the wall rock will behave like inviscid diapirs [*Weinberg and Podladchikov*, 1994]. However, shear-heating partitioning is strongly dependent on the viscosity contrast between the two media [*Ke and Solomatov*, 2009; *Monteux et al*., 2009]. In our study we consider two end-member viscosity models: models where the viscosity remains uniform and constant and models where the hot diapir is initially 10^3 times less viscous than the coldest mantle. Further viscous heating during the core merging can eventually increase the viscosity contrasts up to 10^4. Incorporating larger viscosity contrasts leads to numerical instabilities.

4.3. Numerical Model

The above dynamic equations are solved in an axisymmetric spherical geometry using 200×400 to 400×800 grid points in the r and θ directions. An implicit inversion method [*Schubert et al*., 2001] is adopted for the momentum equation and an Alternating Direction Implicit scheme [*Peaceman and Rachford*, 1955; *Douglas*, 1955] for the energy and mass conservation. The numerical diffusion in solving the transport equations, especially for the compositional field, is constrained using total variation diminishing Superbee scheme [*Roe*, 1986; *Laney*, 1998] in an implicit procedure [*Šrámek et al*., 2010], which enables a high resolution of pure advective fields. Free-slip velocity is imposed at the surface and along the axis of symmetry. The core-mantle boundary is a mobile interface that can deform in response to the merging of the impactor's core. Thermal boundary conditions are isothermal at the surface and insulating along the symmetry axis. The spherically symmetric boundary conditions are applied at the center of the planet.

4.4. Simplifications

A number of approximations are made in the numerical models to simplify the analysis of the core merging process:

1. We assume that the heat capacities per unit volume of iron and silicates are equal and representative of a mixture: $\overline{\rho C_p} = \rho_{\mathrm{Fe}} C_{p,\mathrm{Fe}} = \rho_{\mathrm{Si}} C_{p,\mathrm{Si}}$. Actually, $\rho_{\mathrm{Fe}} C_{p,\mathrm{Fe}} = 4500$ kJ K^{-1} m^{-3} and $\rho_{\mathrm{Si}} C_{p,\mathrm{Si}} = 4200$ kJ K^{-1} m^{-3}. We use $\overline{\rho C_p} = 4312$ kJ K^{-1} m^{-3}.
2. The characteristic diffusion time ($\propto R_{\mathrm{Fe}}^2/\kappa$) during the core merging is much larger than the characteristic sinking time $\left(\propto \frac{\eta_0}{\Delta\rho_0 g R_{\mathrm{Fe}}}\right)$ even with the metallic thermal conductivity k_{Fe} (= 40 W m^{-1} K^{-1}) [*Stacey and Anderson*, 2001] larger than the silicate thermal conductivity k_{Si} (= 3–4 W m^{-1} K^{-1}) [*Hofmeister*, 1999]. Hence, the heat diffusion during the sinking is negligible and the thermal conductivities for metallic and silicate material are assumed to be equal.
3. The heat partitioning during the metal/silicate separation is strongly dependent on the mechanisms of iron segregation. If liquid iron is transported to the center of the planet through channels, the potential energy related to core formation would largely go into the core [*Ke and Solomatov*, 2009]. However, when the liquid metal is transported via a large diapir and depending on the viscosity contrast between the diapir and the surrounding silicates, the potential energy of the diapir that is released via viscous heating heats the surrounding silicates causing further melting [*Ke and Solomatov*, 2009; *Monteux et al*., 2009; *Samuel et al*., 2010]. Also, crystallization of the molten silicate occurs especially near the cold Martian surface. These two processes can influence the heat budget and affect the temperature evolution. Moreover, the viscous heating can have consequences on the rheology of the material surrounding the diapir and modify the sinking dynamics. In our dynamic model of core merging, we do not consider any *consumption* or release of latent heat during the sinking of the diapir. However, in the melt-dependent viscosity models, the viscosity increases abruptly by a factor of c_2 when temperature within a grid cell decreases below the solidus. On the opposite, when the temperature within a grid cell exceeds T_{liq} its viscosity is reduced abruptly by a factor c_2 (see Table 2 for values).
4. During the sinking of the large volume of the impactor's iron core, the gravity field locally and temporally changes slightly. We neglect the changes of the gravity during the sinking.
5. The impactor's iron core, the silicate mantle, and the iron core of the planet are considered in the infinite Prandtl number regime. In reality, the molten metallic cores have viscosities that are about 20 orders of magnitude smaller than the mantle viscosity. Such large but realistic viscosity contrasts may have consequences on both the sinking and the merging dynamics and may affect the heat dissipation during the sinking [*Ke and Solomatov*, 2009; *Monteux et al*., 2009, 2011; *Samuel et al*., 2010]. However, in the case of Newtonian rheology as considered here, increasing the viscosity contrast between the hot liquid diapir and the surrounding silicates may not significantly change the sinking velocity of the diapir which is mainly controlled by the mantle viscosity [*Hadamard*, 1911; *Rybczynski*, 1911; *Yiantsios and Davis*, 1990]. Diapirs more than 10 times less viscous than the wall rock will behave like inviscid bubbles and further decrease in viscosity will not alter the behavior [*Hadamard*, 1911; *Rybczynski*, 1911; *Weinberg and Podladchikov*, 1994]. When considering a power law rheology, a large viscosity contrast between the diapir and the mantle might affect the terminal velocity of the diapir and induce differences with the theoretical velocities predicted with a Newtonian rheology [*Weinberg and Podladchikov*, 1994].

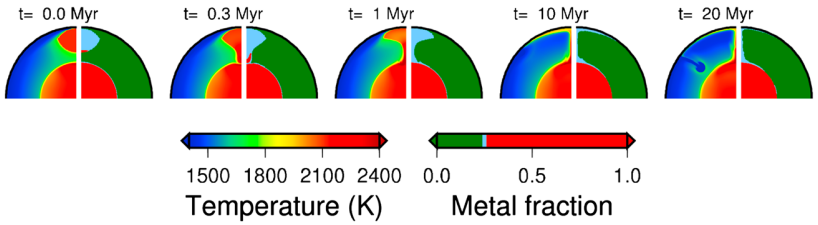

Figure 3. (left to right) Thermochemical readjustment for the model with $D_{imp} = 750$ km, $C_0 = 6000$ m s^{-1}, $S = 0.86$, and $\eta_0 = 10^{21}$ Pa s (isoviscous) at certain times after the impact. In each panel the left part shows the temperature distribution, and the right part shows the iron fraction. The blue colored material in the right part represents partially molten silicates.

5. Reference Model (Influence of the Initial Shape)

Figure 3 shows the thermochemical evolution for the reference model where $D_{imp} = 750$ km, $C_0 = 6000$ m s^{-1}, $S = 0.86$, and $\eta = 10^{21}$ Pa s (isoviscous). The dense iron diapir rapidly sinks toward the planet's core. During the sinking, the potential energy of the diapir is converted into heat via viscous dissipation and heats both the mantle and the diapir. The diapir becomes slightly hotter than the Martian core and spreads on the core in a short time. However, because of the small density difference between the molten and solid silicates, it takes much longer time for the hot and molten silicates to ascend and spread beneath the rigid lithosphere of the planet, potentially forming a magma ocean. The spreading is followed by the initiation of convection in the Martian mantle where a cold slab sinks toward the CMB from the edge of the hot magma ocean.

During sinking, the metallic diapir deforms the surrounding mantle over a radial distance that depends on the diameter of the diapir, the effective viscosities of the mantle and the diapir, the distance between the diapir and the planet's core (i.e., the gap thickness), and the density difference across the CMB. The core of the planet has a minor effect on the dynamics of the diapir at a large gap thickness and the diapir sinks with a Stokes-like velocity [*Batchelor*, 1967; *Monteux et al*., 2013]. When the gap thickness is small, the mantle flow that enables the diapir sinking is confined between two mechanical boundary layers, one at the bottom of the diapir and the other at the top of the core. The horizontal shear stress in these boundary layers hampers the sinking of the diapir, and the sinking velocity decreases.

In Figure 4 (top, black lines), we monitor the gap thickness for our reference case. The gap thickness is calculated using the composition profile along the symmetry axis and particularly the difference in positions where the second derivative is zero. Because of some numerical diffusion of the compositional field, the final gap thickness of our models is slightly larger than the vertical spatial resolution of our models. As illustrated also in Figure 4 (top, black lines), the final gap thickness decreases for higher numerical resolutions. We consider that the time when the final gap thickness is reached corresponds to the "merging time" $t = t_m$ (i.e., the two cores are about to enter physically in contact). The characteristic coalescence time t_c in case of a spherical diapir is [*Monteux et al*., 2013]

$$t_c = \frac{2\lambda_0 \eta_0}{a_1 \Delta\rho_0 g_0 R_{Fe}} \left(\frac{h_0}{R_{Fe}}\right)^{1/2} \tag{26}$$

where λ_0 is the mantle viscosity/diapir viscosity ratio, h_0 is the initial gap thickness, and a_1 is a geometrical constant that is typically on the order of 0.1 for the isoviscous case and 0.2 for the T-dependent viscosity [*Monteux et al*., 2013]. Calculating the characteristic coalescence time from equation 26, we obtain a characteristic sinking time $t_c = 0.36$ Myr. From Figure 4 (top, black lines), we observe that our numerical results (where the merging time $\approx$ 0.36–0.47 Myr) are in agreement with the theoretical coalescence time of the spherical diapir and that the initial shape of the diapir does not significantly affect the sinking time [*Weinberg and Podladchikov*, 1994]. An elongated diapir could increase the surface contact between the iron and the silicated material, potentially increasing the chemical degree of equilibration. However, the sinking time is too short for such a chemical equilibration.

6. Influence of C_0, S, and D_{imp}

This section characterizes the influence of C_0, S, D_{imp} for different viscosity models. The characteristics of these models and the main results are listed in Table 3. In particular we monitor the merging temperature T_m which is

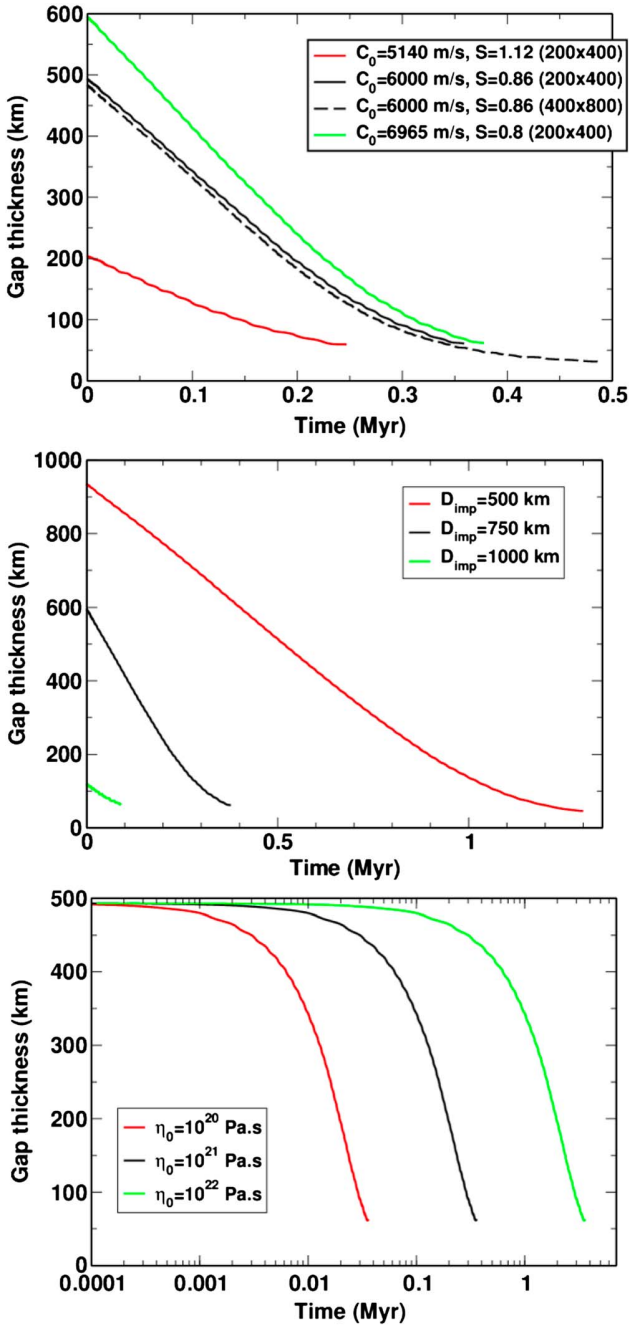

Figure 4. Gap thickness evolution for models with different (C_0, S) sets of (top) parameters, (middle) impactor diameters D_{imp}, and (bottom) reference viscosities η_0.

the average temperature within the sinking diapir when $t = t_m$. The initial gap thickness is a function of the postimpact segregation volume. Hence, it depends on the (C_0, S) set of parameters and on the impactor size. We monitor the thermochemical evolution after a large impact on Mars using different sets of parameters C_0, S, and D_{imp}.

Figure 5 (first column) illustrates the influence of C_0 and S on the postimpact segregation volume and hence on the thermochemical state before the merging process. For the three sets of (C_0, S) examined, the initial temperature within the segregation volume slightly varies and is $\approx 2100 \pm 10$ K. When C_0 increases and S decreases a smaller segregation volume is generated after the impact. On the other hand, when C_0 decreases and S increases, the size of the segregation volume increases. Hence, the impactor's core is initially closer to the CMB (Figure 5, top). Consequence, the core merging occurs in a short time (Figure 4, top). Within the range of C_0, S studied here the sinking time (i.e., the time needed for the two cores to enter in contact) can decrease by $\approx 35\%$ (from 0.38 Myr for ($C_0 = 6965$ m s^{-1}, $S = 0.8$) to 0.25 Myr for ($C_0 = 5140$ m s^{-1}, $S = 1.12$)) (Figure 6, right). As C_0 and S control the shape of the segregation volume and especially the initial gap thickness between the two cores, these parameters play also a significant role on the temperature of the diapir immediately before merging. Within the range of C_0, S studied here the merging temperature can increase by $\approx 10\%$ (from 2130 K for ($C_0 = 5140$ m s^{-1}, $S = 1.12$) to 2350 K for ($C_0 = 6965$ m s^{-1}, $S = 0.8$)) which can have important consequences on the preexisting core cooling after merging (Figure 6, left).

The Martian topographic dichotomy is related to an impact ranging from 800 to 1300 km in diameter [*Marinova et al.*, 2008; *Andrews-Hanna et al.*, 2008; *Nimmo et al.*, 2008]. In our models, we consider that the impactor's core is collected at the bottom of the segregation volume. When the impactor is too large ($D_{imp} > 1000$ km), the segregation volume is in contact with the Martian core, and the merging dynamics is governed by the viscosities of the molten silicates and the liquid iron. Hence, the merging dynamics involves turbulent flows and our models are no more valid. Therefore, we limit our study to impactor diameters ranging from 500 km to 1000 km. Moreover, as detailed above, decreasing C_0 and increasing S would increase the size of the segregation volume, and for $D_{imp} = 1000$ km, $C_0 < 6965$ m s^{-1} and $S > 0.8$, the

Table 3. Model Specifics

Model	Impactor Diameter (Shell Thickness) (km)	C_0 (m/s)	S	Reference Viscosity (Pa s)	Viscosity Contrast	Merging Time (Myr)	Merging Temperature (K)
M0 (ref.)	750 (0.8)	6000	0.86	10^{21}	1	0.36	2286.7
M1	750 (0.8)	6965	0.8	10^{21}	1	0.37	2352.5
M2	750 (0.8)	5140	1.12	10^{21}	1	0.24	2137.6
M3	1000 (1.8)	6965	0.8	10^{21}	1	$8.9\ 10^{-2}$	2127.7
M4	500 (0.2)	6965	0.8	10^{21}	1	1.3	2392.9
M5	750 (0.8)	6000	0.86	10^{20}	1	$3.6\ 10^{-2}$	2287.3
M6	750 (0.8)	6000	0.86	10^{22}	1	3.6	2280.5
M7	750 (0.8)	6000	0.86	10^{21}	10 (*T-P*)	0.1	2281.6
M8	750 (0.8)	6000	0.86	10^{21}	10 (*T-P* melt)	$6.3\ 10^{-2}$	2290.1
M9	750 (0.8)	6000	0.86	10^{21}	100 (*T-P*)	$1.3\ 10^{-2}$	2277.4
M10	750 (0.8)	6000	0.86	10^{21}	100 (*T-P* melt)	$7.5\ 10^{-3}$	2323.2
M11	750 (0.8)	6000	0.86	10^{21}	1000 (*T-P*)	$1.5\ 10^{-3}$	2292.5
M12	750 (0.8)	6000	0.86	10^{21}	1000 (*T-P* melt)	$1.0\ 10^{-3}$	2301.3

segregation volume also overlaps the CMB. Hence, to measure the influence of the impactor size, we only consider $C_0 = 6965$ m s^{-1} and $S = 0.8$. Figure 7 shows the merging dynamics for three impactor diameters. When D_{imp} increases, the segregation volume and the metallic volume of the impactor increase. However, the mean temperature of the segregation volume is not significantly affected (differences of ≈ 10 K between $D_{imp} = 500$ km and $D_{imp} = 1000$ km) (Figure 6, left). The major difference resides in the volume of the postimpact segregation zone of the planet which is much more significant for $D_{imp} = 1000$ km (see Figure 7, third row). When the impactor diameter increases, the volume of the segregation zone and the size of the merging diapir increase, resulting in the reduction of h_0 and in the increase of R_{Fe}, which reduce the sinking time from ≈ 1 Myr for $D_{imp} = 500$ km to ≈ 0.1 Myr for $D_{imp} = 1000$ km (Figure 6, right). As D_{imp} controls the initial distance between the two cores, it also influences the temperature of the diapir before merging [*Monteux et al.*, 2009]. Hence, when D_{imp} increases from 500 to 1000 km, the impactor's core becomes initially closer to the CMB and h_0 decreases from 935 km to 120 km (Figure 4, middle). Hence, its available potential energy decreases, and the merging temperature decreases by ≈ 12 % (from 2400 to 2130 K) (see Figure 6, left).

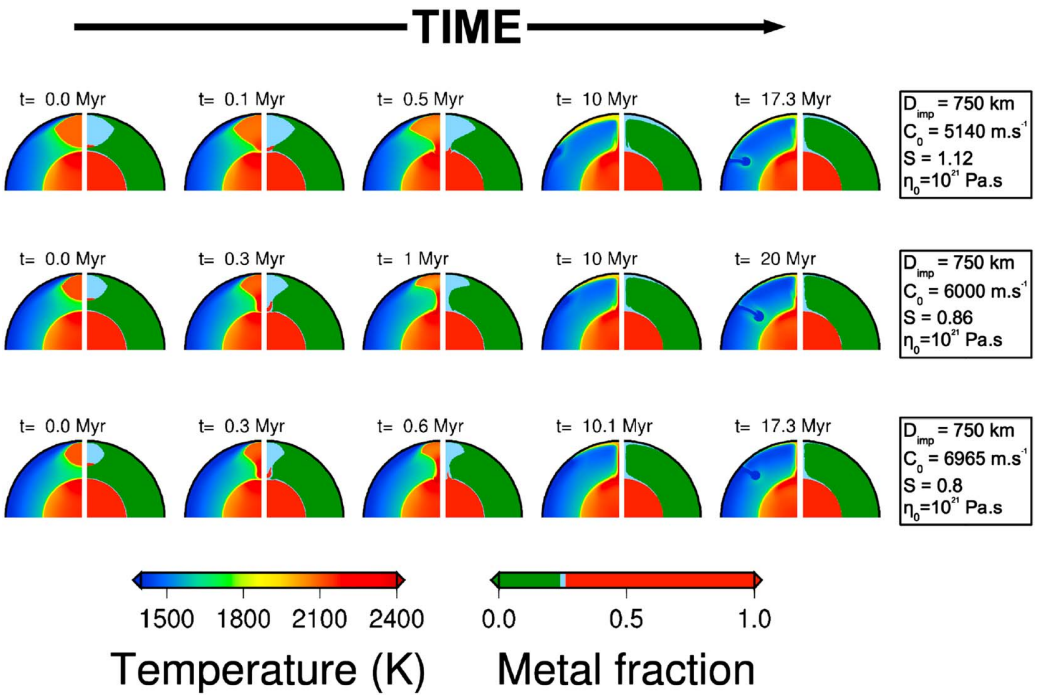

Figure 5. Thermochemical readjustment as a function of time for models with three (C_0, S) sets of parameters. We consider here that the viscosity η_0 is uniform and constant.

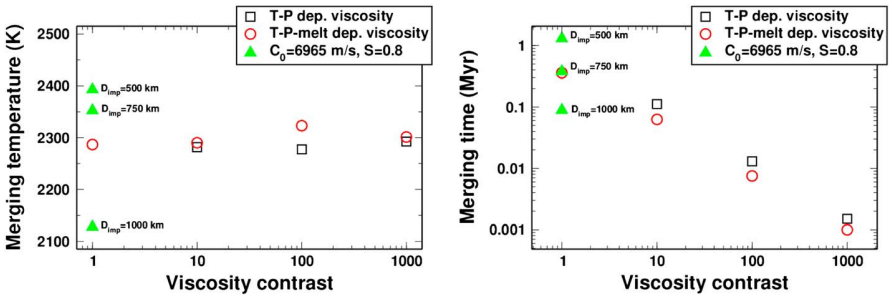

Figure 6. (left) Merging temperatures and (right) merging times as a function of the viscosity contrast. Green filled solid triangles represent results for uniform viscosities, with $C_0 = 6965$ m/s and $S = 0.8$ and for different impactor diameters (indicated close to the corresponding symbol). The open symbols represent the values obtained with $C_0 = 6000$ m/s and $S = 0.86$ for *T-P* dependent viscosities (black squares) and for *T-P* melt-dependent viscosities (red circles).

Finally, by controlling the segregation volume D_{imp}, C_0 and S indirectly control the final radial extension of the magma ocean spreading, and the position of the cold slab that sinks from the surface toward the CMB (see Figures 5 and 7).

7. Influence of the Viscosity Model

7.1. Influence of the Average Viscosity

The mantle viscosity is a key parameter in the core merging process that governs the ability of the mantle to deform and accommodate the metallic diapir sinking, while deforming at farther distances to compensate for the accommodation. The viscosity also governs the spreading of the hot silicate material in the upper mantle. When consider dynamical models with uniform viscosities (i.e., η_0 is constant and $c_T = c_Z = 0$), modifying the mean viscosity does change the heat repartitioning at the end of the merging and affects the characteristic

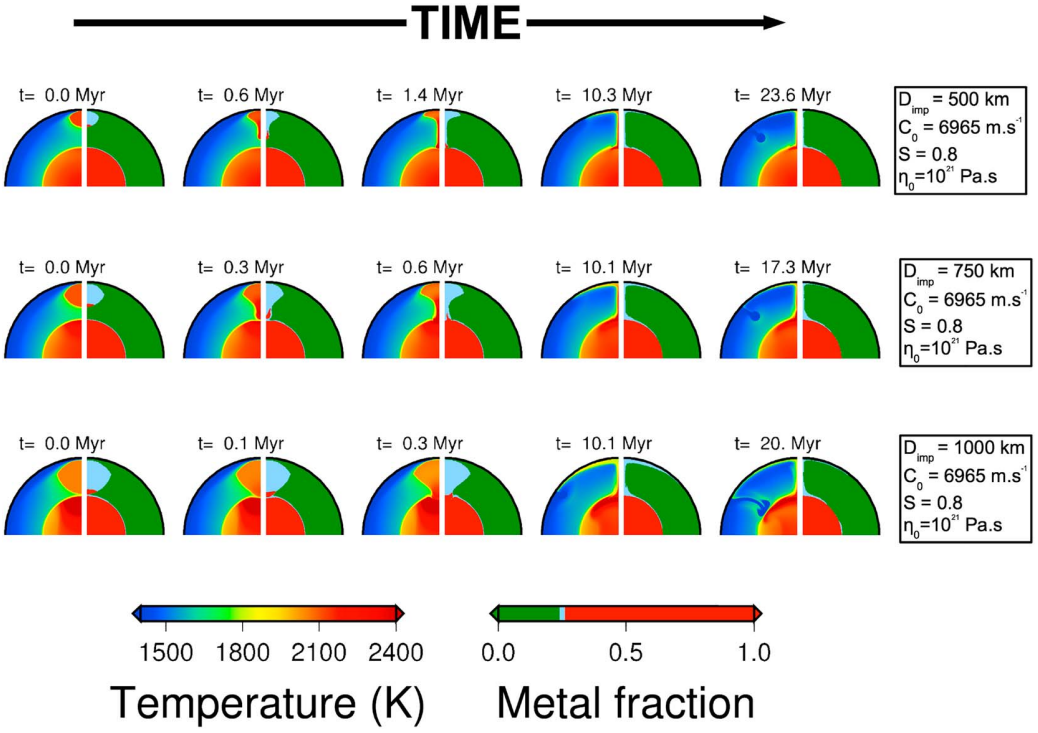

Figure 7. Thermochemical readjustment as a function of time for models with three impactor sizes. We consider here that the viscosity η_0 is uniform and constant. $C_0 = 6965$ m s^{-1} and $S = 0.8$.

merging and spreading times. In the laminar flow regime, the terminal sinking velocity U of a metallic diapir sinking in an infinite media obeys the Hadamard velocity law [*Hadamard*, 1911; *Batchelor*, 1967; *Monteux et al*., 2009]. As a consequence

$$U = \frac{2}{9}\left(\frac{\eta_d + \eta_s}{\eta_d + \frac{2}{3}\eta_s}\right)\frac{\Delta\rho_0 g {R_{\mathrm{Fe}}}^2}{\eta_s} \tag{27}$$

where η_d is the viscosity inside the diapir and η_s is the viscosity of the surrounding material. In the isoviscous case (Figure 4, bottom) when the average viscosity of the mantle decreases the diapir sinks faster (see equation 27), and the sinking time is significantly reduced. For example, in an isoviscous model, $\eta_d = \eta_s$, increasing the viscosity from 10^{20} Pa s (Figure 4, bottom, red line) to 10^{22} Pa s (Figure 4, bottom, green line) leads to an increase of the sinking times from ≈ 0.1 Myr to ≈ 10 Myr (Table 3). Similarly, an increase of the average viscosity by 2 orders of magnitude increases the spreading time of the hot mantle thermal anomaly from ≈ 1 Myr to ≈ 100 Myr, even if the thermal anomaly cools by diffusion. However, the changes in the average uniform viscosity have less effects on the merging temperatures that range between 2280 and 2290 K at $t = t_m$ (Table 3). For large viscosities, as the characteristic merging and spreading times are longer, heat diffusion plays a significant role and smoothes the temperature contrasts between the hot merging channel and the surrounding silicates, at the CMB, and between the sinking slab and the colder surrounding mantle.

7.2. Influence of Varying Viscosity

The viscosity contrast between the sinking diapir and its surroundings is a key parameter in the core merging dynamics and the repartitioning of the viscous heating [*Ke and Solomatov*, 2009; *Samuel et al*., 2010; *Monteux et al*., 2011, 2013]. Qualitatively, as the metallic diapir sinks, shear heating occurs at the interface of the diapir and the surroundings [*Samuel et al*., 2010; *Monteux et al*., 2011], leading to the temperature increase of both the diapir and the surrounding mantle. Depending on the effective viscosity contrast between the metallic diapir and the mantle, the mean temperature of the diapir sinking in a Mars-size planet can increase by a few hundred Kelvins [*Monteux et al*., 2009]. This temperature increase is maximal when the diapir and the surrounding mantle are isoviscous [*Monteux et al*., 2009]. The viscosity contrast between molten iron and mantle under Martian conditions may exceed 10–20 orders of magnitude, depending on the mantle temperature. Such viscosity variations are impossible to resolve with our numerical method. However, experiments show that the dynamic influence of these large viscosity variations on diapir sinking is similar to viscosity variations of order 10^2 [*Jellinek et al*., 2003; *Thayalan et al*., 2006], the effects of which we can explore parametrically.

To characterize the influence of a variable viscosity, we monitor the thermochemical readjustment following a 750 km diameter impact and the subsequent core merging for three viscosity models: isoviscous, *T-P* dependent and *T-P* melt dependent. During the impactor's core sinking the viscous heating enhances the temperature and decreases the viscosity of the material immediately surrounding the diapir. The viscosity decrease is mainly localized in the sinking channel where the highest temperatures are reached. In this region, the temperature of the already impact-heated mantle beneath the segregation zone can exceed the solidus temperature and lead to partial melting and a significant viscosity decrease. For the *T-P* melt-dependent viscosity model (Figure 8, third row) and using a reference viscosity $\eta_0 = 10^{21}$ Pa s, the core merging is much faster than for the isoviscous model and occurs in less than 1 kyr when the viscosity contrast is 1000 between the hottest and the coldest material (see Table 3 for values). The spreading of the hot silicate mantle beneath the lithosphere is also facilitated by the increasing viscosity contrast. However, it is achieved within a much longer timescale that is governed by the surrounding mantle viscosity.

The radial deformation of the mantle in the isoviscous case scales with the size of the diapir [e.g., *Morris*, 1982; *Jellinek et al*., 2003; *Thayalan et al*., 2006], whereas in the temperature-dependent case the deformation is confined to the hottest, lowest viscosity material surrounding the diapir with a length scale typically ≈ 0.1 R_{Fe}. Moreover, the horizontal shear stress in the boundary layer between the diapir and the CMB that retards the sinking of the diapir is very small for the *T-P* and *T-P* melt-dependent viscosity. Both these effects increase the sinking velocity when increasing the viscosity contrast between the diapir and the surrounding mantle. Figure 9 shows the evolution of the gap thickness for three viscosity models, isoviscous (with $\eta_0 = 10^{21}$ Pa s), *T-P* dependent (with $c_Z = 10$ and $c_T = 10$–1000), and *T-P* melt dependent (with $c_Z = 10$, $c_1 = 10$–1000, and $c_2 = 30$–3000). The highest viscosity contrasts between the hot diapir and the surrounding mantle are obtained in the *T-P* melt-dependent viscosity model (Figure 8); hence, the coalescence time is shortest (see Figure 6, right).

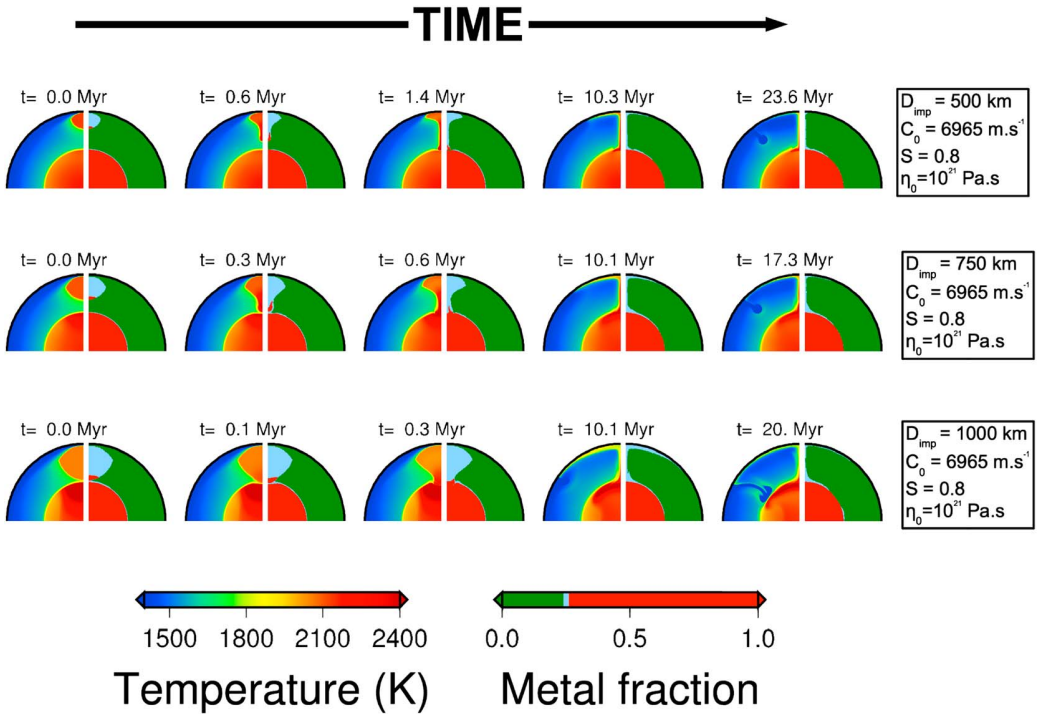

Figure 8. Thermochemical readjustment as a function of time for an isoviscous, a *T-P* dependent (with a viscosity contrast of 100) and a *T-P* melt-dependent (with a viscosity contrast of 100 to 300) viscosity models. (rows 2 and 3) The right part of each panel shows the evolution of the viscosity during the core merging process.

Figure 6 summarizes the influence of the viscosity contrast on the merging times (right) and the temperature of the merging diapir (left) (see values in Table 3). This figure emphasizes the weak influence of the viscosity contrast on the temperature of the impactor's core before merging with the Martian core. The temperature ranges between 2280 and 2330 K while the viscosity contrast increases by 3 orders of magnitude. As detailed above and illustrated in Figure 6 (left) the merging temperature is much more sensitive to the impactor size, while the viscosity contrast is a key parameter when considering the merging time. Figure 6 (right) shows that an increase of the viscosity contrast by 3 orders of magnitude decreases the merging time from 0.36 Myr to ≈ 1 kyr. Here the influence of the impactor size is weaker according to the results of our models.

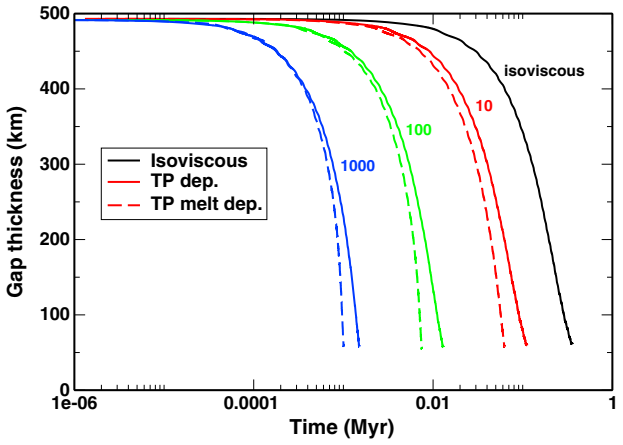

Figure 9. Gap thickness evolution for three different viscosities: uniform (black solid line), *T-P* dependent (colored solid lines), and *T-P* melt dependent (colored dashed lines). For *T-P* and *T-P* melt-dependent viscosities, three viscosity contrasts are represented: 10 (red), 100 (green), and 1000 (blue).

8. Thermochemical Consequences of the Core Merging

This section addresses the consequences of the core merging in terms of thermochemical equilibration.

8.1. The Core-Mantle Equilibrium

After the impact and the formation of the segregation volume, mechanical mixing due to segregation of iron occurs within the partially molten region and can enhance thermochemical equilibrium between the iron from the impactor and molten silicates. The degree of

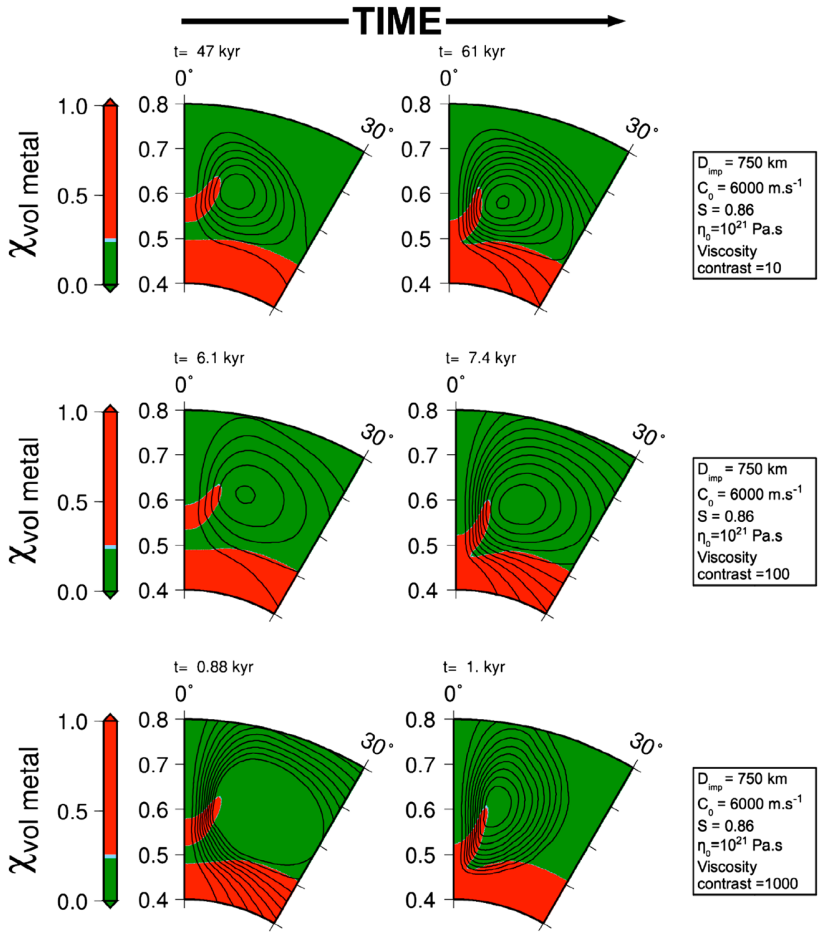

Figure 10. (left to right) Close-up view of the time evolution of the compositional field within the core merging area using the *T-P* melt viscosity model with a viscosity contrast of (top) 10, (middle) 100, and (bottom) 1000. Solid lines represent the streamlines in the reference frame of Mars.

equilibration decreases with increasing characteristic size of the metallic diapirs [*Ulvrová et al.*, 2011; *Deguen et al.*, 2011; *Samuel*, 2012]. For centimeter-sized droplets sinking through a turbulent magma ocean, the thermochemical equilibration is efficient and rapidly achieved [*Samuel*, 2012]. However, during the core merging, the metallic phase may sink as blobs and lead to metal/silicate disequilibrium [*Dahl and Stevenson*, 2010; *Kleine and Rudge*, 2011]. In our models, the impactor's metallic phase is sinking as a large single diapir and chemical equilibrium should depend on the complexity of the flow structure within and outside the diapir [*Ulvrová et al.*, 2011]. However, from the sinking times obtained in our models ($<$ 1 kyr for the most realistic viscosity contrast) (see Table 3), it seems difficult to envision any chemical reequilibration during the diapir sinking. As detailed above, increasing the viscosity contrast between the hot sinking diapir and the surrounding material drastically reduce the merging time but also leads to an elongation of merging core's tail because of the large-scale mantle flow and of the increase in the ability of the diapir to deform (Figure 10). If any chemical equilibration might occur, this thin tail is a good candidate.

The flow induced in the mantle during the sinking can also lead to some entrainment of the silicates from the upper to the lower mantle. This entrainment increases with the diapir size (i.e., with the impactor size) and with the viscosity contrast between the metallic diapir and the mantle (Figure 10). Once the two cores have fully merged, the flow induced by the thermal readjustment within the mantle tends to bring the deep silicate material upward. The accuracy of this phenomenon increases as the viscosity contrast between the diapir and the silicates increases (Figure 10). However, according to the streamlines shown in Figure 10 (right column) the molten silicate material entrained downward during the diapir sinking does not seem to be

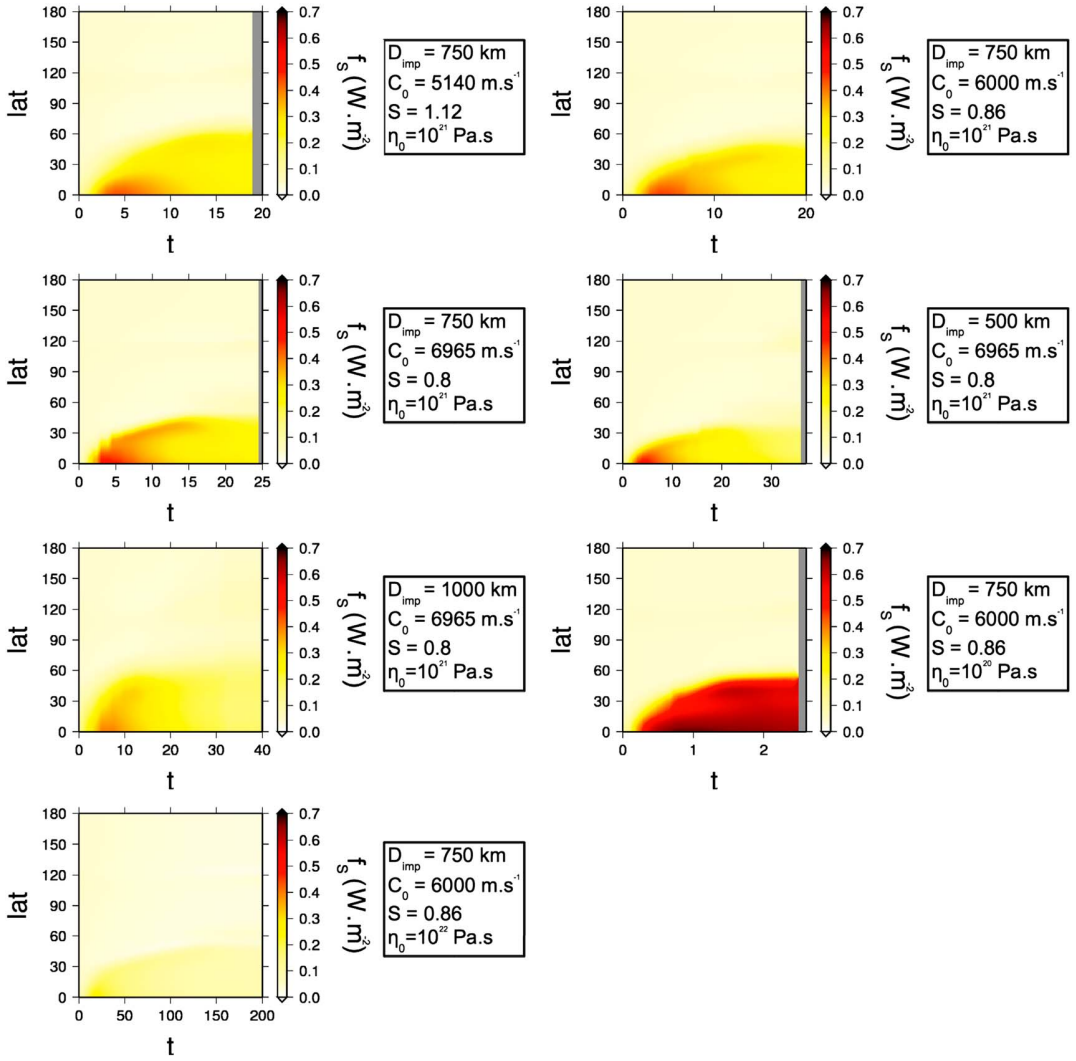

Figure 11. Surface heat flux as a function of time and latitude for different impact properties and average viscosities.

reentrained upward after the merging. Hence, core merging subsequent to a giant impact results in the mixing of silicate material in the mantle.

8.2. Consequences for the Martian Cooling

8.2.1. Mantle Cooling

The impact heating and the viscous dissipation associated with the impactor's core sinking modify the thermal state of the Martian mantle. During and after the merging, a thermal readjustment occurs in the mantle modifying the surface heat flux. The readjustment of the postimpact thermal anomaly within the mantle and its spreading beneath the Martian lithosphere leads to an increase of the surface heat flux. During the early advective stage, corresponding to the flattening of the hot mantle anomaly, the radial extent of the high heat flux patch increases with time. This early advective stage is followed by a later stage of motionless diffusive cooling where the surface heat flux progressively decreases and the mantle thermal anomaly diminishes [*Monteux et al.*, 2007]. The radial extent of the thermal anomaly, its thickness and the duration of the advective stage are strongly dependent on the size of the thermal anomaly and on the physical properties of the planet. Figure 11 shows the time evolution of the surface heat flux (f_S), as a function of the colatitude for different C_0, S, D_{imp}, and η_0 models. Low viscosities and large thermal anomalies favor the spreading of the anomaly over large distances. Hence, the largest sizes for theses patches ($\theta \approx 60°$) are reached for small

viscosities ($\eta_0 = 10^{20}$ Pa s) and large impactor sizes ($D_{imp} = 1000$ km). The time of the transition between the advective and the diffusive stages strongly depends on the mantle viscosity. For $\eta_0 = 10^{21}$ Pa s this time is typically on the order of 10 Myr which is comparable with the models from *Monteux et al.* [2007].

T-P and *T-P* melt-dependent viscosities also influence the evolution of the surface heat flux. Large viscosity contrasts between the hot anomaly and the relatively colder mantle enable easier spreading of the anomaly below the surface [*Koch and Koch*, 1995; *Monteux et al*., 2007]. As the resistance to internal shearing decreases with increasing viscosity contrast, the horizontal velocity becomes more significant for low viscosities. As a result, for the *T-P* and *T-P* melt-dependent viscosity models, the radial extent increases by ≈ 10%, while the advection time decreases by a factor of ≈ 2 compared to the isoviscous models [*Monteux et al*., 2007]. Long-term monitoring of the surface heat flux can be very time consuming especially when considering large viscosity contrasts. Hence, we did not monitor the long-term surface heat flux in the nonuniform viscosity cases. However, the temperature dependence of the viscosity should affect our results by a minor amount because the readjustment is mostly controlled by the viscosity far from the segregation volume.

8.2.2. Core Cooling

During the sinking, viscous heating leads to a temperature increase in both the diapir and the surrounding mantle. For a uniform viscosity and for diapir larger than ≈ 70 km in diameter, viscous coupling between the metallic diapir and the surrounding material occurs and a fraction of the gravitational energy of the diapir is converted to heat up the diapir [*Monteux et al*., 2009]. However, when the diapir is less viscous than the mantle, viscous heating is restricted to the surrounding mantle and is concentrated at the diapir's poles where strain rates are greatest [*Samuel et al*., 2010; *Monteux et al*., 2011]. In this case, the temperature of the impactor's core does not increase significantly during the sinking and remains close to its initial presinking temperature at the base of the segregation zone [*Monteux et al*., 2009].

The temperature of the diapir when merging with the Martian core is also dependent on the distance traveled during the sinking and increases with the initial distance between the diapir (i.e., the initial depth of the segregation zone) and the CMB [*Monteux et al*., 2009]. Hence, the merging temperature of the diapir may be larger or smaller than the core temperature, depending on the size of the diapir, the distance traveled by the diapir, and the viscosity contrast with the surrounding mantle. For instance, when the segregation volume is large (Figure 5, first row and Figure 7, third row), the initial distance between the diapir and the CMB is not large enough for the diapir to heat up significantly, and the merging diapir is colder than the Martian core. For other sets of parameters the merging core is hotter than the Martian core (Table 3).

Following the merging, the impactor's core is trapped between the hot impacted core material and the hot mantle material from the channel where the diapir has sunk. The positive buoyancy of these two materials between which the impactor's core is trapped tends to spread the impactor's core beneath the CMB (Figure 12). However, the mixing dynamics that occurs within the Martian core after the merging has to be considered here with caution. The injection of a large volume of molten iron of the impactor in a rotating core of the planet is a process that involves Coriolis and inertial forces that are neglected here, because of our infinite Prandtl number approximation. We address this issue in section 10.

9. Effects on the Core Dynamo

A giant impact not only excavates the near surface and heats the upper mantle of a planet as discussed above but also heats the core of the planet in two distinct stages. In the first stage, the shock wave created by the impact propagates in the core, heating it differentially within about 1 h. In the second stage, the merging of the impactor iron diapir modifies the thermal state of the planet's core. Here we investigate the effects of these two stages on the core dynamo of Mars.

The first stage has been studied by many investigators [e.g., *Arkani-Hamed and Olson*, 2010a, 2010b; *Ghods and Arkani-Hamed*, 2011]. Here we follow the procedure adopted by *Arkani-Hamed and Olson* [2010b]. Briefly, the shock wave leads to a temperature increase within the core of the planet, much stronger in the region directly beneath the impact site (Figure 2, bottom left). The low-viscosity rotating liquid core cannot sustain lateral variations of temperature and the core overturns, resulting in a stably stratified temperature which increases with radius. The thermal stratification diminishes the possible preexisting core convection, hence the core dynamo, within a few kyr [*Arkani-Hamed and Olson*, 2010a]. Here we assume it occurs immediately after the impact. Shortly after, the juxtaposition of the superheated stratified core to the relatively colder

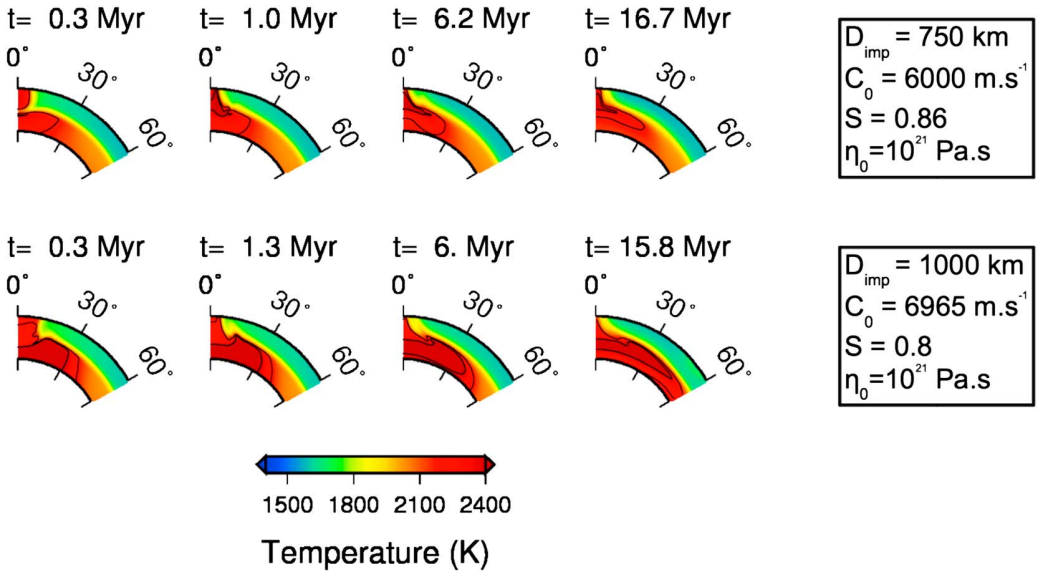

Figure 12. Close-up view of the temperature field within the core merging area for two impactor sizes, two sets of C_0 and S, and viscosity of 10^{21} Pa s.

mantle results in convection in the outer part of the core which generates a dynamo as it thickens over time. Here we first present the results for our reference model ($D_{imp} = 750$ km, $C_0 = 6000$ m s^{-1}, $S = 0.86$ and $\eta = 10^{21}$ Pa s) in some detail and then provide the major results for the other models.

Included in Figure 2 (bottom left) is the impact-induced temperature increase inside our reference model, showing the differentially heated mantle and core. We note that the temperature in the uppermost part of the core directly beneath the impact site is higher than that in the adjacent mantle. This is partly due to shock pressure jump as the shock wave inters the core and partly because of low-specific heat of the iron core, 600 J/kg/K, compared to that of the silicate mantle, 1200 J/kg/K. Also, the impact heating of the core is appreciable only within ~40° colatitude relative to the symmetric axis passing the impact site and the center of the planet, the area which covers only 12% of the core's surface. About 88% of the core is juxtaposed to the base of the mantle with preimpact temperature. Once the core stratifies and the hottest part of the core is placed directly beneath the core-mantle boundary, the core essentially cools almost globally. The thermal evolution of the core is calculated by numerically solving the 1-D enthalpy equation and following the procedure adopted by *Arkani-Hamed and Olson* [2010b]. The radial grid interval is taken to be 100 m to allow accurate determination of the thickness of the thermal boundary layer in the convecting outer core. The domain of calculation includes the entire core plus a 100 km thick thermal boundary layer at the base of the mantle. The preimpact temperature is assumed adiabatic inside the core with 2000 K at the core-mantle boundary. It linearly decreases in the overlying mantle layer to 1500 K at the top of the layer. The spherically symmetric temperature distribution inside the core immediately after the impact is obtained by first adding the preimpact temperature to the impact-induced temperature increase and then allowing the thermal stratification. The liquid core has a kinetic viscosity of 10^4 m^2/s and it rotates with a 24 h period (see Table 2 for physical properties of the core). The core viscosity must be much smaller. However, reducing the viscosity by 8 orders of magnitude has only minor effects on the core cooling [*Arkani-Hamed and Olson*, 2010b], because the core cooling is mainly controlled by the overlying solid mantle.

To illustrate the effects of the impactor core merging on the Martian core dynamo two scenarios are calculated for each models listed in Table 3: one without considering the merging and the other with merging. Figure 13 shows the thermal evolution of the core and the overlying mantle for 300 Myr after the impact where no merging is considered. The positive temperature gradient deep in the core retains stable condition, prohibiting convection, while the upper most part of the core convects and maintains adiabatic temperature as it thickens and penetrates to deeper parts of the core. Although the very high temperature at the top of the stratified core diminishes rapidly, the impact heating remains appreciable for much longer time. Figure 14 shows the time variations of the thickness of the convecting outer core, the heat flux at the core-mantle boundary, the magnetic

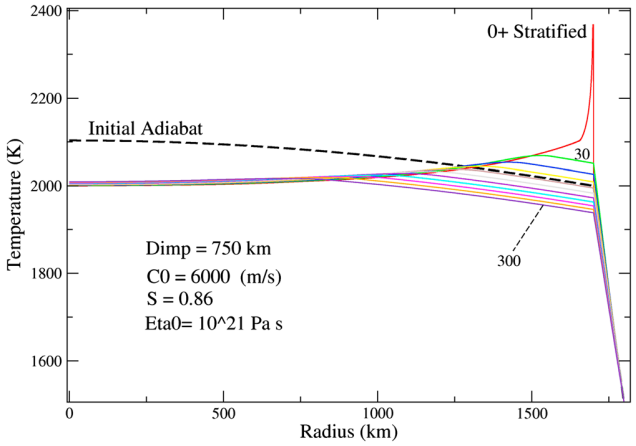

Figure 13. Thermal evolution of Martian core after an impact, where no core merging is considered. The temperature is shown at 30 Myr intervals. The numbers on the curves denote time after the impact in Myr. The curve "Initial Adiabat" is the preimpact temperature, and "0+ Stratified" denotes the temperature after the first stage of stratification. D_{imp} is the impactor diameter in kilometer, C_0 is the acoustic velocity of the mantle in m/s, S is the constant in the EOS, and η_0 is the mantle viscosity assumed isoviscous mantle.

Reynolds number and the mean magnetic intensity inside the convecting outer core for 300 Myr after the impact. Similar to the results obtained by other investigator [e.g., *Arkani-Hamed and Olson*, 2010b; *Arkani-Hamed and Ghods*, 2011], the impact certainly cripples the possible preimpact core dynamo and it takes around 150–200 Myr for the convecting outer core to generate a strong core dynamo, taking the threshold value of 20 for the magnetic Reynolds number. We note that the outer core is not thick enough to generate an appreciable dynamo within the first ~20 Myr after the impact, despite very high heat flux at the core-mantle boundary.

Due to the positive buoyancy relative to the core of Mars, the impactor diapir spreads on the core (Figure 12) and creates a super-heated iron layer of ~0.8 km thickness. Figure 15 compares the thermal evolution of the core for the first 10 Myr with and without the diapir merging. At the time of merging the iron diapir is about 100 K hotter than the uppermost part of Mars' core. However, the iron layer cools very rapidly such that the difference between the two models almost disappears within less than 2 Myr. This is better illustrated in Figure 16 where the thickness of the convecting outer core, the heat flux at the core-mantle boundary, and the magnetic Reynolds number and the mean magnetic field intensity of the convecting outer core are displayed within the first 1 Myr after the impact for both models. The merging iron layer reinitiates convection at about 0.37 Myr, and its effects diminish rapidly within the first 1 Myr.

The effects of physical parameters of the mantle and the size of the impactor are also estimated for both scenarios, with and without merging. Figures 17 and 18 show the effects of the diapir merging on the core dynamo for different viscosity models of the mantle, different C_0 and S values as well as different size of the impactor. The

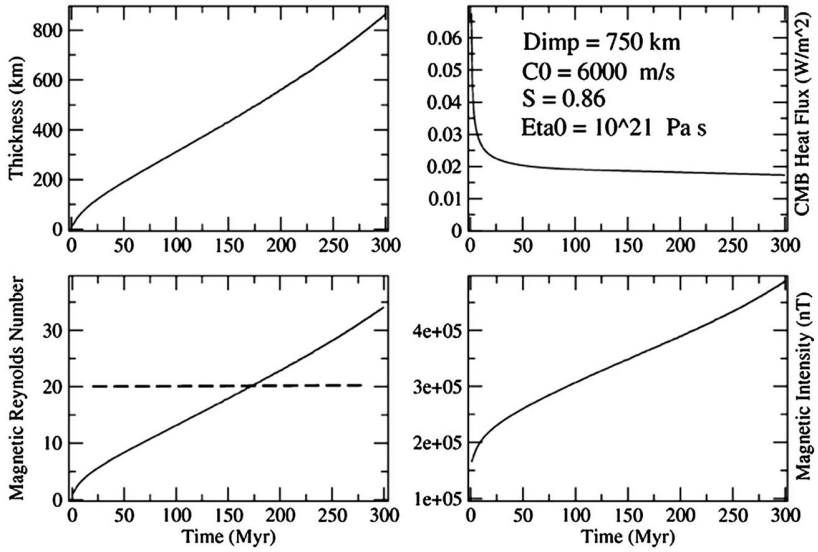

Figure 14. The evolution of the thickness of the convecting outer core, the heat flux at the core-mantle boundary, the magnetic Reynolds number, and the mean magnetic intensity in the convecting zone corresponding to the thermal evolution of the core shown in Figure 13.

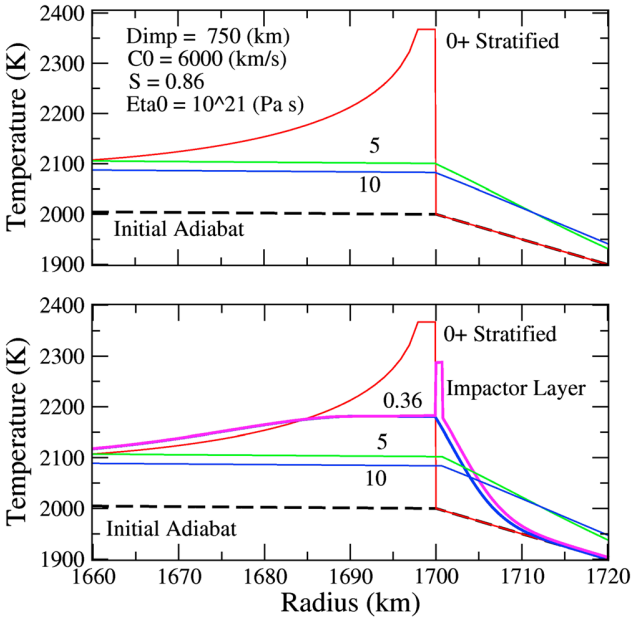

Figure 15. Thermal evolution of Martian core within 10 Myr after an impact. (top) With no core merging and (bottom) with core merging that occurs at 0.36 Myr after the impact. The blue and magenta curves in Figure 15 (bottom) show the temperature distribution immediately before and immediately after the core merging. See Figure 13 for details.

isoviscous mantle with a viscosity of 10^{22} Pa s, and to a lesser extent 10^{21} Pa s, delays the merging time and has appreciable effects on the dynamo. It takes longer time for the iron diapir of the smaller impactor ($D_{imp} = 500$ km), which initiates at the base of a smaller segregation zone, to sink through the mantle before merging to the core, hence has appreciable effect on the core dynamo because the Martian core cools prior to the merging. The $C_0 = 6965$ (m/s) and $S = 0.8$ model results in an appreciable merging effects. However, the effects diminish within a few Myr in all models. It is plausible to conclude that the main effect of an impact on the core dynamo is due to direct heating of the core (see Figure 14), which was not considered by *Monteux et al.* [2013], and diapir merging has almost negligible effects. This is largely because the iron layers produced on the Martian core by the diapirs are very thin, and no dynamo can be generated inside the layers. It requires a thickness of about 30 km for an iron layer to generate dynamo [e.g., *Reese and Solomatov*, 2010]. The iron layers can only delay the initiation of the dynamo for a very short time.

10. Limitations of Our Models

The stratification of the differentially heated Martian core occurs while the impactor's core diapir is still descending in the mantle. The core merging incorporates some new material within the Martian core with a

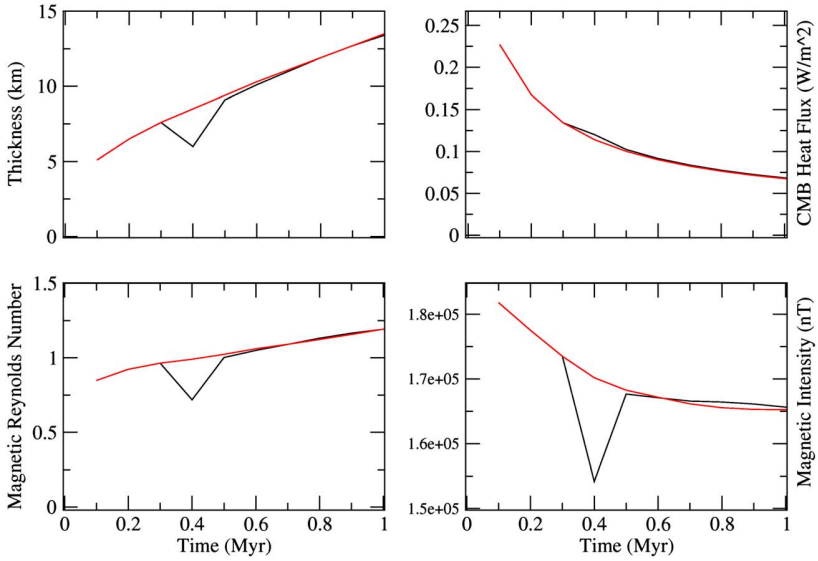

Figure 16. The evolution of the thickness of the convecting outer core, the heat flux at the core-mantle boundary, the magnetic Reynolds number, and the mean magnetic intensity in the convecting zone within the first 1 Myr. The red curves are for the no merging scenario, and the black ones are for the merging scenario.

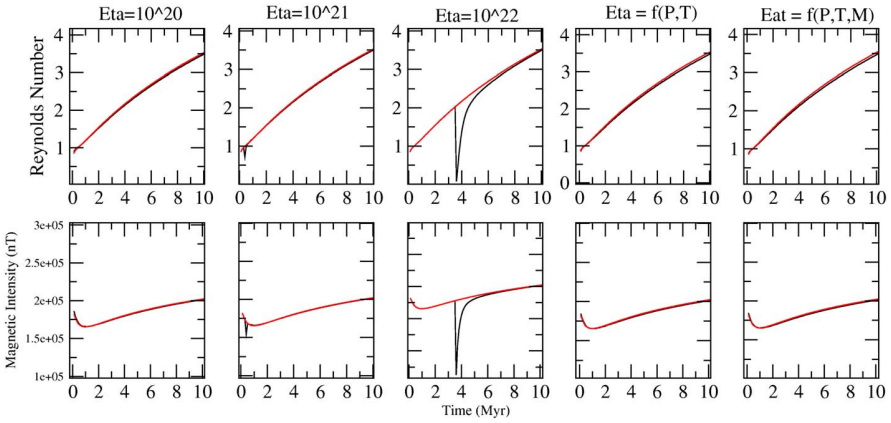

Figure 17. Effects of the mantle viscosity on the Reynolds number and the mean magnetic intensity in the convecting outer core for a model with 750 km impactor diameter, $C_0 = 6000$ m/s, and $S = 0.86$. *Eta* at the top denotes the mantle viscosity: either isoviscous with 10^{20}, 10^{21}, or 10^{22} Pa s, or temperature- and pressure-dependent (f(*P*,*T*)), or temperature, pressure, and melt dependent (f(*P*,*T*,*M*)) with a viscosity contrast of 1000. The red curves are for the no merging scenario, and the black ones are for the merging scenario.

temperature that depends on the size of the impactor, the segregation volume and the viscosity contrast between the diapir and the mantle. In any case, the core merging leads to lateral temperature variations and may initiate restratification of the core.

Our present numerical model of spreading the iron diapir on the Martian core does not include the rotation effect (i.e., no Coriolis forces) and assumes an infinite Prandtl number (i.e., no inertial forces) in the momentum equation. Hence, we do not obtain the stratification that likely occurs immediately after the impact as discussed in the previous section, and the second restratification that would occur after the complete core merging. Consequently, materials from our lowest viscosity and largest diapir spread beneath the CMB as a thin, axisymmetric gravity current (see Figure 12). The spreading of the hot core anomaly stops when diffusive cooling overcomes advective transport leading to a partial stratification of the core [*Monteux et al.*, 2013]. This thermal stratification persists until the thermal anomaly introduced by the gravity current diffuses into the overlying mantle and the underlying part of the core. The dynamics of thermal mixing under realistic core viscosities will be the subject of a separated study.

11. Conclusions

Giant impacts may have significantly influenced the mantle dynamics of Mars. We investigated the postimpact thermochemical readjustment after one single giant impact occurring during the early stages of

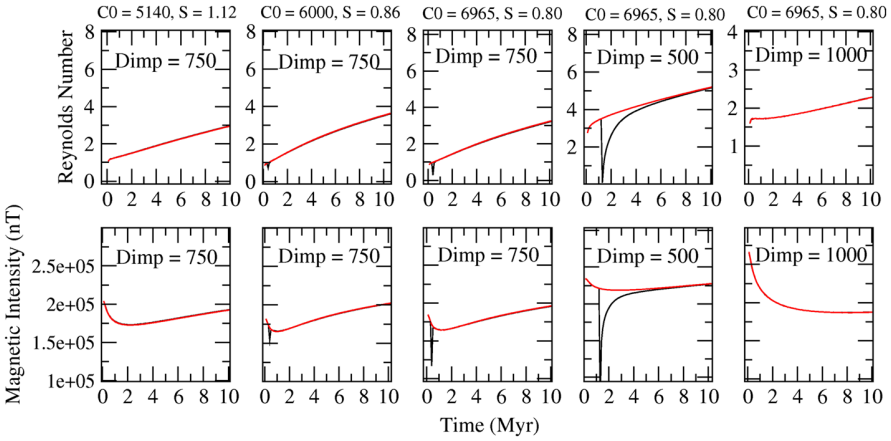

Figure 18. Effects of the acoustic velocity, C_0, and EOS constant, *S*, of the mantle on the magnetic Reynolds number and mean magnetic intensity of the convecting outer core. The mantle has a constant viscosity of 10^{21} Pa s. *D* denotes the impactor diameter in kilometer. The red curves are for the no merging scenario, and the black ones are for the merging scenario.

the Martian history. In particular, we studied the thermal consequences of the sinking of an impactor's core in the Martian mantle as a function of the impactor size and for different mantle viscosity models. Our results show that the core merging is a fast process that occurs in a time mainly governed by the mantle viscosity. Although this study is the continuation of the study by *Monteux et al*. [2013], several improvements have been achieved in the characterization of the impact heating, the initial postimpact geometry of the impactor's core and the viscosity models. Indeed, from our results we can now separate the influences of the impactor size (D_{imp}), the ability of the impacted mantle to be shock heated (C_0 and S) and the mantle viscosity (type and viscosity contrast) on the time required for sinking and on the temperature of the impactor's core when merging with the Martian one. We can now conclude that the viscosity does not play a key role in the thermal evolution during the merging (only modifying the merging temperature by ≈ 1 % for the range of viscosities adopted here). However, it plays an important role on the sinking time which is very sensitive to the viscosity contrast between the sinking diapir and the surrounding material that can decrease from 0.3 Myr to 1 kyr. From the range of parameters considered here (with viscosity contrast up to 3 orders of magnitude), the merging time is probably too short to envision any chemical equilibration during the sinking. Concerning the thermal evolution, the impactor diameter D_{imp} and the (C_0, S) values seem to be the key parameters that govern both the merging time (by controlling the diapir size and initial depth) and the merging temperature that can vary by 10% in the range of parameters studied here (from 2130 to 2350 K). In our models, we assume that the impact occurs with a moderate impact velocity (about twice the Martian escape velocity); larger impact velocities can substantially increase the postimpact temperature in the merging core prior to its sinking which strengthen the importance of the impact parameters on the merging temperature.

Our study also highlights that, even if the core merging processes could reduce the efficiency of chemical equilibration during the core formation in terrestrial planets [*Kleine and Rudge*, 2011], the flow dynamics generated within the mantle during the merging process for large viscosity contrasts could enhance some mixing between upper and deep silicate material even in the absence of mantle convection. Because the characteristic timescales of thermal readjustment within the mantle are long, the hot postimpact mantle anomaly creates a surface heat flux anomaly as it spreads below the Martian surface. The spreading stage lasts ≈ 10 Myr and is followed by a diffusive cooling that occurs within a longer timescale. More importantly, we can now make a better estimate of the influence of the core merging process on the Martian dynamo. The main effect of a large impact on the core dynamo is due to direct heating of the core, and diapir merging has almost negligible effects. The spreading of the merging diapir as a hot and thin layer surrounding the preexisting Martian core can only delay the initiation of the dynamo for a very short time.

In our models, the impact angle is vertical which maximizes the postimpact melt volume, hence the segregation volume in which the metal/silicates separation occurs [*Pierazzo and Melosh*, 2000]. Oblique impacts could influence the core merging dynamics by reducing the initial position of the metallic diapir and modifying the shape of the postimpact mantle thermal anomaly. The asymmetry introduced in the thermal state of the mantle by an oblique impact cannot be included in our current axisymmetric model and has to be modeled in a 3-D model in the future. However, an oblique impact has less effect on the cessation and reactivation of the core dynamo, except for the amount of impact heating of the core. This is because the core stratifies almost immediately after the impact and retains a spherically symmetric temperature distribution.

Acknowledgments

J.M. is funded by Agence Nationale de la Recherche (Accretis decision ANR-10-PDOC-001-01), and J.A.H. is supported by the Natural Sciences and Engineering Research Council (NSERC) of Canada. We also thank the two anonymous reviewers and the Associate Editor for valuable comments, which helped to improve the manuscript significantly.

References

Ahrens, T. J., and M. L. Johnson (1995), Shock wave data for rocks, in *Mineral Physics and Crystallography, A Handbook of Physical Constants*, vol. 3, edited by T. J. Ahrens, pp. 35–44, Amer. Geophys. Union, Washington, D. C.

Ahrens, T. J., and J. D. O'Keefe (1987), Impact on the Earth, ocean and atmosphere, *Int. J. Impact Eng.*, *5*, 13–32.

Andrews-Hanna, J. C., M. T. Zuber, and W. B. Banerdt (2008), The Borealis basin and the origin of the Martian crustal dichotomy, *Nature*, *453*, 1212–1215, doi:10.1038/nature07011.

Arkani-Hamed, J., and A. Ghods (2011), Could giant impacts cripple core dynamos of small terrestrial planets?, *Icarus*, *212*, 920–934.

Arkani-Hamed, J. (2005), Magnetic crust of Mars, *J. Geophys. Res.*, *110*, E08005, doi:10.1029/2004JE002397.

Arkani-Hamed, J. (2012), Life of the Martian dynamo, *Phys. Earth Planet. Inter.*, *196-197*, 83–96.

Arkani-Hamed, J., and P. Olson (2010a), Giant impact stratification of the Martian core, *Geophys. Res. Lett.*, *370*, L02201, doi:10.1029/2009GL041417.

Arkani-Hamed, J., and P. Olson (2010b), Giant impacts, core stratification, and failure of the Martian dynamo, *J. Geophys. Res.*, *115*, E07012, doi:10.1029/2010JE003579.

Asphaug, E. (2010), Similar-sized collisions and the diversity of planets, *Chemie der Erde / Geochem.*, *70*, 199–219, doi:10.1016/j.chemer.2010.01.004.

Bagdassarov, N., G. Solferino, G. J. Golabek, and M. W. Schmidt (2009), Centrifuge assisted percolation of Fe–S melts in partially molten peridotite: Time constraints for planetary core formation, *Earth Planet. Sci. Lett.*, *288*(1–2), 84–95, doi:10.1016/j.epsl.2009.09.010.

Batchelor, G. (1967), *An Introduction to Fluid Dynamics*, Cambridge Univ. Press, Cambridge, U. K.
Benz, W., W. L. Slattery, and A. G. W. Cameron (1988), Collisional stripping of Mercury's mantle, *Icarus*, *74*, 516–528, doi:10.1016/0019-1035(88)90118-2.
Bills, B. G., G. A. Neumann, D. E. Smith, and M. T. Zuber (2005), Improved estimate of tidal dissipation within Mars from MOLA observations of the shadow of Phobos, *J. Geophys. Res.*, *110*, E07004, doi:10.1029/2004JE002376.
Breuer, D., S. Labrosse, and T. Spohn (2010), Thermal evolution and magnetic field generation in terrestrial planets and satellites, *Space Sci. Rev.*, *152*, 449–500.
Cameron, A. G. W., and W. Benz (1991), The origin of the Moon and the single impact hypothesis IV, *Icarus*, *92*, 204–216.
Canup, R. M. (2004), Simulations of a late lunar-forming impact, *Icarus*, *168*, 433–456, doi:10.1016/j.icarus.2003.09.028.
Chambers, J. E. (2004), Planetary accretion in the inner solar system, *Earth Planet. Sci. Lett.*, *223*, 241–252.
Coradini, A., C. Federico, and P. Lanciano (1983), Earth and Mars—Early thermal profiles, *Phys. Earth Planet. Inter.*, *31*, 145–160.
Croft, S. K. (1982), A first-order estimate of shock heating and vaporization in oceanic impacts, in *Geological Implications of Impacts of Large Asteroids and Comets on Earth*, vol. 190, edited by T. L. Silver and P. H. Schultz, pp. 143–152, *Spec. Pap. Geol. Soc. Am.*, Boulder, Colo.
Dahl, T. W., and D. J. Stevenson (2010), Turbulent mixing of metal and silicate during planet accretion and interpretation of the Hf-W chronometer, *Earth Planet. Sci. Lett.*, *295*, 177–186.
Dauphas, N., and A. Pourmand (2011), Hf-W-Th evidence for rapid growth of Mars and its status as a planetary embryo, *Nature*, *473*, 489–493.
Davies, G. F. (1982), Ultimate strength of solids and formation of planetary cores, *Geophys. Res. Lett.*, *9*, 1267–1270.
Deguen, R., P. Olson, and P. Cardin (2011), Experiments on turbulent metal–silicate mixing in a magma ocean, *Earth Planet. Sci. Lett.*, *310*, 303–313.
Douglas, J. (1955), On the numerical integration of $\partial^2 u/\partial x^2 + \partial^2 u/\partial y^2 = \partial u/\partial t$ by implicit methods, *J. Soc. Ind. Appl. Math.*, *3*, 42–65, doi:10.1137/0103004.
Dziewonski, A. M., and D. L. Anderson (1981), Preliminary reference Earth model, *Phys. Earth Planet. Inter.*, *25*, 297–356.
Frey, H. V., J. H. Roark, K. M. Shockey, E. L. Frey, and S. E. H. Sakimoto (2002), Ancient lowlands on Mars, *Geophys. Res. Lett.*, *29*(10), 1384, doi:10.1029/2001GL013832.
Gerya, T. V., and D. A. Yuen (2007), Robust characteristics method for modelling multiphase visco-elastic thermo-mechanical problems, *Phys. Earth Planet. Inter.*, *163*, 83–105.
Ghods, A., and J. Arkani-Hamed (2007), Impact-induced convection as the main mechanism for formation of mare basalts, *J. Geophys. Res.*, *112*, E03005, doi:10.1029/2006JE002709.
Ghods, A., and J. Arkani-Hamed (2011), Effects of the Borealis impact on the mantle dynamics of Mars, *Phys. Earth Planet. Inter.*, *188*, 37–46.
Golabek, G. J., T. V. Gerya, B. J. P. Kaus, R. Ziethe, and P. J. Tackley (2009), Rheological controls on the terrestrial core formation mechanism, *Geochem. Geophys. Geosyst.*, *10*, Q11007, doi:10.1029/2009GC002552.
Hadamard, J. (1911), Mouvement permanent lent d'une sphère liquide et visqueuse dans un liquide visqueux, *C.R. Acad. Sci.*, *152*, 1735–1738.
Hartmann, W. K., and D. R. Davis (1975), Satellite-sized planetesimals and lunar origin, *Icarus*, *24*, 504–514.
Hofmeister, A. M. (1999), Mantle values of thermal conductivity and the geotherm from phonon lifetimes, *Science*, *283*, 1699–1706.
Höink, T., J. Schmalzl, and U. Hansen (2005), Formation of compositional structures by sedimentation in vigorous convection, *Phys. Earth Planet. Inter.*, *153*, 11–20.
Honda, R., H. Mizutani, and T. Yamamoto (1993), Numerical simulation of Earth's core formation, *J. Geophys. Res.*, *98*, 2075–2090.
Jellinek, A. M., H. M. Gonnermann, and M. A. Richards (2003), Plume capture by divergent plate motions: Implications for the distribution of hotspots, geochemistry of mid-ocean ridge basalts, and estimates of the heat flux at the core-mantle boundary, *Earth Planet. Sci. Lett.*, *205*, 361–378, doi:10.1016/S0012-821X(02)01070-1.
Jutzi, M., and E. Asphaug (2011), Forming the lunar farside highlands by accretion of a companion moon, *Nature*, *476*, 69–72.
Katz, R. F., M. Spiegelman, and C. H. Langmuir (2003), A new parameterization of hydrous mantle melting, *Geochem. Geophys. Geosyst.*, *4*(9), 1073, doi:10.1029/2002GC000433.
Ke, Y., and V. S. Solomatov (2009), Coupled core–mantle thermal evolution of early Mars, *J. Geophys. Res.*, *114*, E07004, doi:10.1029/2008JE003291.
Kleine, T., and J. F. Rudge (2011), Chronometry of meteorites and the formation of the Earth and Moon, *Elements*, *7*, 41–46.
Kleine, T., C. Münker, K. Mezger, and H. Palme (2002), Rapid accretion and early core formation on asteroids and the terrestrial planets from Hf–W chronometry, *Nature*, *418*, 952–955.
Koch, D. M., and D. L. Koch (1995), Numerical and theoretical solutions for a drop spreading below a free fluid surface, *J. Fluid Mech.*, *287*, 251–278.
Laney, C. B. (1998), *Computational Gas Dynamics*, Cambridge University Press, Cambridge.
Lee, D. C., and A. N. Halliday (1997), Core formation on Mars and differentiated asteroids, *Nature*, *388*, 854–857.
Louzada, K. L., and S. T. Stewart (2009), Effects of planet curvature and crust on the shock pressure field around impact basins, *Geophys. Res. Lett.*, *36*, L15203, doi:10.1029/2009GL037869.
Marinova, M. M., O. Aharonson, and E. Asphaug (2008), Mega-impact formation of the Mars hemispheric dichotomy, *Nature*, *453*, 1216–1219, doi:10.1038/nature07070.
McGill, G. E., and A. M. Dimitriou (1990), Origin of the Martian global dichotomy by crustal thinning in the Late Noachian or early Hesperian, *J. Geophys. Res.*, *95*, 12,595–12,605.
McQueen, R. G., S. P. Marsh, and J. N. Fritz (1967), Hugoniot equation of state of twelve rocks, *J. Geophys. Res.*, *72*, 4999–5036.
Melosh, H. J. (1989), *Impact Cratering: A Geologic Process*, Oxford Univ. Press, New York.
Mitani, N. K. (2003), Numerical simulations of shock attenuation in solids and reevaluation of scaling law, *J. Geophys. Res.*, *108*(E1), 5003, doi:10.1029/2000JE001472.
Monteux, J., N. Coltice, F. Dubuffet, and Y. Ricard (2007), Thermo-mechanical adjustment after impacts during planetary growth, *Geophys. Res. Lett.*, *34*, L24201, doi:10.1029/2007GL031635.
Monteux, J., Y. Ricard, N. Coltice, F. Dubuffet, and M. Ulvrová (2009), A model of metal-silicate separation on growing planets, *Earth Planet. Sci. Lett.*, *287*, 353–362.
Monteux, J., A. M. Jellinek, and C. L. Johnson (2011), Why might planets and moons have early dynamos?, *Earth Planet. Sci. Lett.*, *310*, 349–359, doi:10.1016/j.epsl.2011.08.014.
Monteux, J., A. M. Jellinek, and C. L. Johnson (2013), Dynamics of core merging after a mega-impact with applications to Mars' early dynamo, *Icarus*, *226*, 20–32.
Morris, S. (1982), The effects of a strongly temperature-dependent viscosity on slow flow past a hot sphere, *J. Fluid Mech.*, *124*, 1–26, doi:10.1017/S0022112082002389.

Neukum, G., and D. V. Wise (1976), Mars: A standard crater curve and possible new time scale, *Science*, *194*, 1381–1387.
Neumann, W., D. Breuer, and T. Spohn (2012), Differentiation and core formation in accreting planetesimals, *Astron. Astrophys.*, *543*, A141, 23.
Nimmo, F., and T. Kleine (2007), How rapidly did Mars accrete? Uncertainties in the Hf/W timing of core formation, *Icarus*, *191*, 497–504, doi:10.1016/j.icarus.2007.05.002.
Nimmo, F., S. D. Hart, D. G. Korycansky, and C. B. Agnor (2008), Implications of an impact origin for the Martian hemispheric dichotomy, *Nature*, *453*, 1220–1223, doi:10.1038/nature07025.
Peaceman, D. W., and H. H. Rachford (1955), The numerical solution of parabolic and elliptic differential equations, *J. Soc. Ind. Appl. Math.*, *3*, 28–41, doi:10.1137/0103003.
Pierazzo, E., and H. J. Melosh (2000), Melt production in oblique impacts, *Icarus*, *145*, 252–261.
Pierazzo, E., A. M. Vickery, and H. J. Melosh (1997), A reevaluation of impact melt production, *Icarus*, *127*, 408–423.
Ratcliff, J. T., P. J. Tackley, G. Schubert, and A. Zebib (1997), Transitions in thermal convection with strongly variable viscosity, *Phys. Earth Planet. Inter.*, *102*, 201–212.
Reese, C. C., and V. S. Solomatov (2006), Fluid dynamics of local Martian magma oceans, *Icarus*, *184*, 102–120.
Reese, C. C., and V. S. Solomatov (2010), Early Martian dynamo generation due to giant impacts, *Icarus*, *207*, 82–97, doi:10.1016/j.icarus.2009.10.016.
Ricard, Y., O. Šrámek, and F. Dubuffet (2009), A multi-phase model of runaway core-mantle segregation in planetary embryos, *Earth Planet. Sci. Lett.*, *284*, 144–150.
Roberts, J. H., and J. Arkani-Hamed (2012), Impact-induced mantle dynamics on Mars, *Icarus*, *218*, 278–289, doi:10.1016/j.icarus.2011.11.038.
Roberts, J. H., and O. S. Barnouin (2012), The effect of the Caloris impact on the mantle dynamics and volcanism of Mercury, *J. Geophys. Res.*, *117*, E02007, doi:10.1029/2011JE003876.
Roberts, J. H., R. J. Lillis, and M. Manga (2009), Giant impacts on early Mars and the cessation of the Martian dynamo, *J. Geophys. Res.*, *114*, E04009, doi:10.1029/2008JE003287.
Roe, P. L. (1986), Characteristic-based schemes for the Euler equations, *Annu. Rev. Fluid Mech.*, *18*, 337–365.
Rubie, D. C., H. J. Melosh, J. E. Reid, C. Liebske, and K. Righter (2003), Mechanisms of metal-silicate equilibration in the terrestrial magma ocean, *Earth Planet. Sci. Lett.*, *205*, 239–255.
Rybczynski, W. (1911), Über die fortschreitende Bewegung einer flüssigen Kugel in einem Medium, *Bull. Acad. Sci. Cracovie*, *1*, 40–46.
Samuel, H. (2012), A re-evaluation of metal diapir breakup and equilibration in terrestrial magma oceans, *Earth Planet. Sci. Lett.*, *313*, 105–114, doi:10.1016/j.epsl.2011.11.001.
Samuel, H., and P. J. Tackley (2008), Dynamics of core formation and equilibration by negative diapirism, *Geochem. Geophys. Geosyst.*, *9*, Q06011, doi:10.1029/2007GC001896.
Samuel, H., P. J. Tackley, and M. Evonuk (2010), Heat partitioning in terrestrial planets during core formation by negative diapirism, *Earth Planet. Sci. Lett.*, *290*, 13–19.
Schubert, G., D. L. Turcotte, and P. Olson (2001), *Mantle convection in the Earth and planets*, Cambridge University Press, New York.
Senshu, H., K. Kuramoto, and T. Matsui (2002), Thermal evolution of a growing Mars, *J. Geophys. Res.*, *107*(E12), 5118, doi:10.1029/2001JE001819.
Shahnas, H., and J. Arkani-Hamed (2007), Viscous and impact demagnetization of Martian crust, *J. Geophys. Res.*, *112*, E02009, doi:10.1029/2005JE002424.
Shannon, M. C., and C. B. Agee (1996), High pressure constraints on percolative core formation, *Geophys. Res. Lett.*, *23*, 2717–2720.
Smith, J. V. (1979), Mineralogy of the planets: A voyage in space and time, *Mineral. Mag.*, *43*, 1–89.
Solomatov, V. S. (2000), Fluid dynamics of a terrestrial magma ocean, in *Origin of the earth and moon*, edited by R. M. Canup et al., pp. 323–338, University of Arizona Press, Tucson.
Solomon, S. C., et al. (2005), New perspectives on ancient Mars, *Science*, *307*, 1214–1220.
Šrámek, O., Y. Ricard, and F. Dubuffet (2010), A multiphase model of core formation, *Geophys. J. Int.*, *181*, 198–220, doi:10.1111/j.1365-246X.2010.04528.x.
Stacey, F. D., and O. L. Anderson (2001), Electrical and thermal conductivities of Fe-Ni-Si alloy under core conditions, *Phys. Earth Planet. Inter.*, *124*, 153–162.
Stevenson, D. J. (1989), Formation and early evolution of the Earth, in *Mantle Convection and Plate Tectonics*, edited by W. R. Peltier, pp. 818–868 Routledge, Abingdon, U. K.
Stevenson, D. J. (1990), Fluid dynamics of core formation, in *Origin of the Earth*, edited by H. E. Newsom and J. H. Jones, pp. 231–249, Oxford Univ, New York.
Stevenson, D. J. (2003), Planetary science: Mission to Earth's core—A modest proposal, *Nature*, *423*, 239–240.
Thayalan, V., A. M. Jellinek, and A. Lenardic (2006), Recycling the lid: Effects of subduction and stirring on boundary layer dynamics in bottom heated planetary mantle convection, *Geophys. Res. Lett.*, *33*, L20318, doi:10.1029/2006GL027668.
Tonks, W. B., and H. J. Melosh (1992), Core formation by giant impacts, *Icarus*, *100*, 326–346.
Tonks, W. B., and H. J. Melosh (1993), Magma ocean formation due to giant impacts, *J. Geophys. Res.*, *98*, 5319–5333.
Trunin, R. F. (2001), Experimental data on shock compression and adiabatic expansion of condensed matter, *Academic Publication*, *RFNC-VNIIEF*, *SAROV*.
Ulvrová, M., N. Coltice, Y. Ricard, S. Labrosse, F. Dubuffet, J. Velímský, and O. Šrámek (2011), Compositional and thermal equilibration of particles, drops, and diapirs in geophysical flows, *Geochem. Geophys. Geosyst.*, *12*, Q10014, doi:10.1029/2011GC003757.
Vocadlo, L., D. Alfè, G. D. Price, and M. J. Gillan (2000), First principles calculations on the diffusivity and viscosity of liquid Fe–S at experimentally accessible conditions, *Phys. Earth Planet. Inter.*, *120*, 145–152.
Walte, N. P., J. K. Becker, P. D. Bons, D. C. Rubie, and D. J. Frost (2007), Liquid-distribution and attainment of textural equilibrium in a partially-molten crystalline system with a high-dihedral-angle liquid phase, *Earth Planet. Sci. Lett.*, *262*(3-4), 517–532.
Walte, N. P., D. C. Rubie, P. D. Bons, and D. J. Frost (2011), Deformation of a crystalline aggregate with a small percentage of high-dihedral-angle liquid; implications for core-mantle differentiation during planetary formation, *Earth Planet. Sci. Lett.*, *305*, 1–2.
Watters, W. A., M. T. Zuber, and B. H. Hager (2009), Thermal perturbations caused by large impacts and consequences for mantle convection, *J. Geophys. Res.*, *114*, E02001, doi:10.1029/2007JE002964.
Weinberg, R. F., and Y. Podladchikov (1994), Diapiric ascent of magmas through power law crust and mantle, *J. Geophys. Res.*, *99*, 9543–9559, doi:10.1029/93JB03461.
Wilhelms, D. E., and S. W. Squyres (1984), The Martian hemispheric dichotomy may be due to a giant impact, *Nature*, *309*, 138–140, doi:10.1038/309138a0.

Yiantsios, S. G., and R. H. Davis (1990), On the buoyancy-driven motion of a drop towards a rigid surface or a deformable interface, *J. Fluid Mech.*, *217*, 547–573, doi:10.1017/S0022112090000842.
Yoder, C. F., A. S. Konopliv, D. N. Yuan, E. M. Standish, and W. M. Folkner (2003), Fluid core size of Mars from detection of the solar tide, *Science*, *300*, 299–303, doi:10.1126/science.1079645.
Yoshino, T., M. J. Walter, and T. Katsura (2003), Core formation in planetesimals triggered by permeable flow, *Nature*, *422*, 154–157.
Zhong, S. J., and M. T. Zuber (2001), Degree-1 mantle convection and the crustal dichotomy on Mars, *Earth Planet. Sci. Lett.*, *189*, 75–84.
Ziethe, R., and T. Spohn (2007), Two-dimensional stokes flow around a heated cylinder: A possible application for diapirs in the mantle, *J. Geophys. Res.*, *112*, *B09403*, doi:10.1029/2006JB004789.

Physics of the Earth and Planetary Interiors 240 (2015) 114–124

Contents lists available at ScienceDirect

Physics of the Earth and Planetary Interiors

journal homepage: www.elsevier.com/locate/pepi

Giant impacts, heterogeneous mantle heating and a past hemispheric dynamo on Mars

Julien Monteux [a,b,c,*], Hagay Amit [a], Gaël Choblet [a], Benoit Langlais [a], Gabriel Tobie [a]

[a] Laboratoire de Planétologie et Géodynamique, Université de Nantes, CNRS, UMR-6112, 2 rue de la Houssinière, 44322 Nantes Cedex, France
[b] ISTerre, Université de Grenoble 1, CNRS, Grenoble, France
[c] Laboratoire Magmas et Volcans, Université Blaise Pascal – CNRS – IRD, OPGC, 5 rue Kessler, 63038 Clermont Ferrand, France

ARTICLE INFO

Article history:
Received 22 July 2014
Received in revised form 12 November 2014
Accepted 16 December 2014
Available online 12 January 2015

Keywords:
Mars
Dynamo
Magnetic field
Core-mantle boundary
Impact
Heat flux

ABSTRACT

The martian surface exhibits a strong dichotomy in elevation, crustal thickness and magnetization between the southern and northern hemispheres. A giant impact has been proposed as an explanation for the formation of the Northern Lowlands on Mars. Such an impact probably led to strong and deep mantle heating which may have had implications on the magnetic evolution of the planet. We model the effects of such an impact on the martian magnetic field by imposing an impact induced thermal heterogeneity, and the subsequent heat flux heterogeneity, on the martian core-mantle boundary (CMB). The CMB heat flux lateral variations as well as the reduction in the mean CMB heat flux are determined by the size and geographic location of the impactor. A polar impactor leads to a north–south hemispheric magnetic dichotomy that is stronger than an east–west dichotomy created by an equatorial impactor. The amplitude of the hemispheric magnetic dichotomy is mostly controlled by the horizontal Rayleigh number Ra_h which represents the vigor of the convection driven by the lateral variations of the CMB heat flux. We show that, for a given Ra_h, an impact induced CMB heat flux heterogeneity is more efficient than a synthetic degree-1 CMB heat flux heterogeneity in generating strong hemispheric magnetic dichotomies. Large Ra_h values are needed to get a dichotomy as strong as the observed one, favoring a reversing paleodynamo for Mars. Our results imply that an impactor radius of ~1000 km could have recorded the magnetic dichotomy observed in the martian crustal field only if very rapid post-impact magma cooling took place.

1. Introduction

Giant impacts have strongly influenced the internal structure and dynamics of the terrestrial planets during the primordial stages of their evolutions (Hartmann and Davis, 1975; Benz et al., 1988; Asphaug et al., 2006; Andrews-Hanna et al., 2008; Marinova et al., 2008; Nimmo et al., 2008; Jutzi and Asphaug, 2011). These events are plausible explanations for remarkable features of the solar system such as the small volume of Mercury's mantle relative to its core (Benz et al., 1988; Gladman and Coffey, 2009), the Earth–Moon system (Canup, 2004) and the topographic martian and lunar hemispheric dichotomies (Marinova et al., 2008; Nimmo et al., 2008; Jutzi and Asphaug, 2011). Giant impacts have also been invoked to explain the initiation or cessation of the dynamos of the terrestrial planets and moons (Roberts et al., 2009; Arkani-Hamed and Olson, 2010; Reese and Solomatov, 2010; Monteux et al., 2013; Monteux and Arkani-Hamed, 2014). In these models, the impactors' radii typically range between 100 and 1000 km. These impacts deliver a large amount of heat to the deep mantle, which is likely to strongly affect the efficiency of core cooling and in turn the dynamo activity. Although there is a higher probability that a giant impact will fall on low-latitudes of the planetary surface (Le Feuvre and Wieczorek, 2011), true polar wander events can ultimately place the resulting thermal anomaly at high-latitudes of the Core Mantle Boundary (CMB). Moreover, large impacts could be responsible for significant resurfacing and reset the magnetization of the pre-impact material (Langlais and Thébault, 2011; Lillis et al., 2013).

On Earth, the influence of lower mantle thermal heterogeneity on core magnetohydrodynamics has been extensively studied

* Corresponding author at: Laboratoire Magmas et Volcans, Université Blaise Pascal – CNRS – IRD, OPGC, 5 rue Kessler, 63038 Clermont Ferrand, France.
E-mail address: j.monteux@opgc.univ-bpclermont.fr (J. Monteux).

http://dx.doi.org/10.1016/j.pepi.2014.12.005
0031-9201/

using numerical dynamos with imposed non-uniform outer boundary conditions. It has been shown that heterogeneous CMB heat flux causes a deviation from axisymmetry in the core flow (Aubert et al., 2007), in the time-average paleomagnetic field (Olson and Christensen, 2002) and in locations of intense magnetic flux patches on millennial time-scales (Bloxham, 2002; Amit et al., 2010). It may also explain the emergence of intense magnetic flux patches in the equatorial region (Amit and Choblet, 2012) and may even yield field locking (Gubbins et al., 2007; Willis et al., 2007). Heterogeneous CMB heat flux may also recover the lateral variations in the inner-core boundary seismic properties (Aubert et al., 2008; Amit and Choblet, 2009). Finally, reversal frequency and the trajectory of the paleomagnetic dipole axis during reversals may also be governed by the heterogeneous lower mantle (Glatzmaier et al., 1999; Kutzner and Christensen, 2004; Olson et al., 2010, 2013; Olson and Amit, 2014).

Heterogeneous mantle control has also been proposed to explain some features of planetary magnetic fields. Cao et al. (2014) found that high equatorial CMB heat flux breaks the core flow symmetry and produces north–south asymmetric magnetic fields which may explain the observed field of Mercury (Anderson et al., 2012). Stanley (2010) argued that temperature differences in the surrounding envelope of the convective zone of Saturn axisymmetrize its magnetic field. It has also been proposed that CMB heterogeneity may have controlled the shape of the current Martian magnetic field (Stanley et al., 2008). Mars is characterized by a striking magnetic field dichotomy, which is correlated with the topographic dichotomy. The Northern Lowlands are mostly devoid of significant magnetic fields. In contrast the southern highlands exhibit large and in some places intense magnetic field anomalies, up to 1500 nT at 90 km altitude as measured by Mars Global Surveyor (Acuña et al., 1998). This is two orders of magnitude larger than the crustal magnetic field on Earth. In terms of magnetized material, this suggests a thick (40 km) and intensely magnetized (up to 12 A/m) lithosphere to produce the observed magnetic field (Langlais et al., 2004), or any combination of a thinner lithosphere and a more intense magnetization (e.g., Parker, 2003).

The martian magnetic dichotomy can be explained using two end-members scenarios. In the external scenario, the dynamo was equally strong in both hemispheres, and the resulting magnetization was equally strong in both hemispheres. Then the magnetization of the northern hemisphere was removed or erased after the dynamo cessation, e.g., by a giant impact (Nimmo et al., 2008) or volcanic activity (Lillis et al., 2008). Alternatively a significant magnetization was never recorded in the northern hemisphere because surface conditions, lithological or alteration processes were different from those in the southern hemisphere (Rochette, 2006; Quesnel et al., 2009; Chassefière et al., 2013). In the internal scenario, the magnetization is strong only in the southern hemisphere because the dynamo was hemispheric to begin with (Langlais and Amit, 2008; Stanley et al., 2008; Amit et al., 2011).

Such an hemispheric dynamo could have been driven by CMB heat flux heterogeneity possibly caused by a very large-scale mantle convection pattern (Harder and Christensen, 1996; Zhong and Zuber, 2001; Elkins-Tanton et al., 2003, 2005; Ke and Solomatov, 2006; Roberts and Zhong, 2006) or by a giant impact (Roberts et al., 2009). In this study we propose a model for the magnetic field dichotomy in which the dynamo hemisphericity (internal origin) is related to a large impact (external origin). For that purpose, we model heterogeneous CMB heat flux resulting from giant impact heating and investigate its influence on the core dynamo by imposing it as a static, laterally-varying outer boundary condition on numerical dynamo models. In this approach, the CMB heat flux pattern and amplitude, as well as the reduction in the mean heat flux with respect to a reference pre-impact value, are determined by the impactor size, using a synthetic description of the impact heating zone. In Section 2 we describe our method. The results are presented in Section 3. Discussion, post-impact time evolution and applicability of our results to Mars are given in Section 4. Conclusions and possible planetary applications are highlighted in Section 5.

2. Method

2.1. Impact heating at the Core Mantle Boundary

Large impacts brought to Mars a formidable amount of energy that is a function of the impactor mass and velocity, the latter strongly depending on the impacted planet radius R. After a large collision on a Mars-size body, a significant fraction of this energy is deeply buried as heat within the mantle and leads to a local temperature increase ΔT_0 below the impact site. The size and the shape of the post-impact thermal anomaly depend on several parameters such as the size of the impactor, the impact velocity and angle, and the structure of the martian mantle. Increasing the size of the impactor leads to an increase of the heated volume while increasing the impact angle from 0 (head-on impact) to larger values (oblique impacts) reduces the maximal depth reached by the post-impact thermal anomaly (Pierazzo et al., 1997; Pierazzo and Melosh, 2000). Here for simplicity, we consider that the volume of the thermal anomaly only scales with the size of the impactor and we consider the case of a head-on impact. Hence, the post-impact thermal anomaly in our models is approximately uniform within a spherical volume (termed isobaric core) with radius R_{ic} that is 1 to 1.44 times larger than the radius of the impactor R_{imp} (Pierazzo et al., 1997; Senshu et al., 2002; Monteux et al., 2013).

On Mars, the impactor size invoked to explain the topographic dichotomy ranges between 320 and 1350 km (Marinova et al., 2008; Nimmo et al., 2008). This has to be compared to the size of the martian mantle. Based on solar tidal deformations, the martian core radius has been estimated between 1520 and 1840 km (Yoder et al., 2003). For simplicity, we assume a core radius of 1700 km, which implies a mantle thickness of about 1700 km. Hence, considering that $R_{ic} = 1.44R_{imp}$, the post-impact spherical thermal anomaly is likely to overlap the CMB for $R_{imp} > 500$ km. For an impactor radius of $R_{imp} = 1200$ km, the disruption of the impacted planet will only occur when the impact velocity reaches values of $\sim$100 km/s which is much larger than the impact velocity v_{imp} considered here ($v_{imp} = 5$ km/s) (Tonks and Melosh, 1992; Reese et al., 2010). In our models, we consider that the impactor radius ranges between 600 and 1000 km bearing in mind that larger impactors with larger impact angles could have similar thermal consequences at the CMB (Pierazzo et al., 1997; Pierazzo and Melosh, 2000).

As the volume of the isobaric core is governed by the size of the impactor, the magnitude of the temperature increase can be directly related to the impact velocity. Making the conservative hypothesis that the impact velocity is close to the martian escape velocity and that the volume of the isothermal sphere is 3 times larger than the impactor (Senshu et al., 2002; Monteux et al., 2013), the energy balance accounting for heating and melting of both the impactor and impacted material may lead to a uniform spherical temperature increase of $\sim$400 K in the martian mantle (Monteux et al., 2013). Away from the isothermal sphere, the temperature decreases rapidly with distance r as $(R_{ic}/r)^m$ with m typically ranging between 4 and 5 (Senshu et al., 2002; Monteux et al., 2007).

Geochemical evidence and crater densities indicate that the martian topographic dichotomy could have formed within the first 50 Myr of Solar System formation and that the martian northern

hemisphere has been low and stable for nearly all of Mars' history (Zuber, 2001; Frey et al., 2002; Solomon et al., 2005; Marinova et al., 2008). Hence, the impact-driven temperature increase is superimposed to the pre-impact thermal state of the martian mantle that strongly depends on the short-lived radiogenic heating, the accretion processes and the dissipation of gravitational energy during the core formation (Senshu et al., 2002; Golabek et al., 2009; Šrámek et al., 2010). The uncertainties on the relative importance of these processes as well as the diversity of the processes involved in the core formation lead to a wide range of plausible early thermal states after the full differentiation of Mars. For simplicity, we assume here a 1D radially dependent pre-impact mantle temperature field. The choice of this specific temperature field is not crucial as long as the impact heating of the mantle is predominant. As shown later, the main parameter affecting the dynamo is the amplitude of the heat-flux heterogeneity at the CMB. Before the impact heating, we consider a simplified temperature profile as in Monteux et al. (2013) with a CMB temperature of $T = 2000$ K and a convective mantle temperature of ~ 1600 K (Roberts and Arkani-Hamed, 2012). It should be noted that in reality, the pre-impact thermal state of the martian mantle was probably much more complicated than the one used in our models, with lateral heterogeneities as well as radial variations (including thermal boundary layers and pressure dependence). For simplicity, we do not consider the changes of mantle properties with depth such as the pressure increase and the corresponding adiabatic heating. Because we consider here that the mantle temperature above the CMB is uniform and equal to 1600 K while the core temperature is 2000 K, adding more complexity should slightly decrease the amplitude of the heat flux heterogeneity. However, since the early martian thermal state is poorly constrained, our simple model may be considered as a reasonable first step to understand the influence of giant impacts on planetary dynamos.

The superposition of the large impact-driven temperature increase leads to a significant perturbation of the pre-impact homogeneous CMB mean heat flux q_0^h. To obtain the post-impact heat flux at the martian CMB for a given impactor radius, we used an impact heating model similar to the one described in Monteux et al. (2013). A uniform spherical temperature anomaly rapidly decreasing with distance is superimposed on the martian pre-impact temperature field. The impact heating is followed by a thermal re-adjustment within a characteristic time that is governed by the rheology of the mantle surrounding the impact-induced thermal anomaly. This characteristic time is $\tau_{\text{imp}} \sim 10$ Myr (Monteux et al., 2007). The characteristic magnetic diffusion time is $\tau_\lambda = r_o^2/\lambda$ where r_o is the core radius and λ is the magnetic diffusivity (e.g., Bloxham and Jackson, 1991). For Mars $r_o = 1700$ km and combined with updated estimates of the electrical conductivity of molten iron in Earth's core conditions of $\lambda \sim 0.5$ m^2/s (Pozzo et al., 2012), these estimates give $\tau_\lambda \sim 180$ kyr. Since $\tau_{\text{imp}} \gg \tau_\lambda$, the post impact mantle temperature field may be considered constant in our numerical dynamo models.

The shock wave also leads to a temperature increase within the core of the impacted planet, much stronger in the region directly beneath the impact site. The low-viscosity rotating liquid core cannot sustain lateral variations of temperature and the core overturns, resulting in a stably stratified temperature which increases with radius. In the case of a homogeneous CMB heat flux, the thermal stratification occurs within a few kyr (Arkani-Hamed and Olson, 2010). This stratification kills the possible pre-existing core convection, and hence the core dynamo. Then it can take up to several tens of Myr to remove this stratification by conductive core heat loss (Arkani-Hamed and Olson, 2010). However, a significant fraction of the mantle right above the CMB may have experienced melting which facilitated the core cooling. The time needed to remove the core excess heat by convection is 10^3–10^4 years when considering a molten layer above the CMB (Monteux et al., 2011). It is therefore likely that after the impact the martian dynamo died during the time needed to generate and remove the post-impact core stratification (i.e., $\sim 10^3$–10^4 years). Then, the dynamo probably re-started, while the impact-driven lower mantle anomaly was still in place (during $\tau_{\text{imp}} \sim 10$ Myr). For simplicity, we do not consider here the core impact heating and the subsequent rapid thermal readjustment. Our dynamo models are convectively unstable throughout the shell, corresponding to the state of the system after core stratification has been removed and while the CMB heterogeneity was still in place. We discuss this aspect in the conclusion section.

As the post-impact mantle temperature reaches the temperature of the core, the heat flux q is nearly zero where the isobaric core overlaps with the CMB. Away from the isobaric core and along the CMB, the heat flux increases rapidly to its pre-impact mean value q_0^h (Fig. 1). The reduction in the mean CMB heat flux due to the impact corresponds to the relative CMB surface that is heated by the impactor and is defined by q_0^r as

$$q_0^r = \frac{q_0^h - q_0}{q_0^h} \tag{1}$$

where q_0 is the post-impact mean heat flux. The amplitude of the heat flux heterogeneity is commonly given by q^* (Olson and Christensen, 2002) with

$$q^* = \frac{q_{\max} - q_{\min}}{2q_0} \tag{2}$$

where $q_{\max}$ and $q_{\min}$ are the maximal and minimal values of the post-impact heat flux, respectively. In Fig. 1, we show q_0^r and q^* obtained from our post-impact heating model as a function of the impactor size. As the impactor size increases, the extension of the isobaric core on the CMB increases, i.e., q_0 decreases and therefore q_0^r and q^* increase. An impactor with a radius smaller than $R_{\text{imp}} \sim 500$ km has a negligible effect on the heated surface of the CMB. For small impactors a small portion of the CMB is heated so $q_0 \simeq q_0^h$, and since $q_{\max} = q_0^h$ and $q_{\min} = 0$ always hold, for small impactors $q^* \simeq 0.5$. An impactor radius of $R_{\text{imp}} \sim 1000$ km decreases the mean CMB heat flux by 26.5% and produces an heterogeneity with amplitude $q^* \sim 0.67$. In our models, we limit the impactor radius to 1000 km and consider a head-on impact which may represent cases with larger impactors and smaller impact angles (Pierazzo et al., 1997; Pierazzo and Melosh, 2000).

Next we expand the impact-driven CMB heat flux pattern in terms of spherical harmonic coefficients (Fig. 2). In order to use it as an outer boundary condition for heat flux in our dynamo models, we performed a spherical harmonic expansion truncated at $\ell_{\max} = 20$ (see Fig. 2 for $R_{\text{imp}} = 800$ km). First we fit the CMB heat flux with the following analytical expression in terms of the angular distance ω from the impactor's center:

$$q_\omega = \exp\left[-\frac{1}{n}\left(\frac{\omega}{\omega_0}\right)^n\right] \tag{3}$$

The Gauss-like function (3) avoids undesirable Gibbs effects associated with discontinuous gradients on the edge of the imprint of the isobaric core on the CMB. The best fit parameters found for the three impactor radii are $\omega_0 = 15^\circ$ and $n = 3$ for $R_{\text{imp}} = 600$ km, $\omega_0 = 30^\circ$ and $n = 7$ for $R_{\text{imp}} = 800$ km and $\omega_0 = 48^\circ$ and $n = 7$ for $R_{\text{imp}} = 1000$ km.

2.2. Numerical dynamo models

We solve the set of self-consistent non-dimensional Boussinesq magnetohydrodynamics equations for dynamo action due to thermal convection of an electrically conducting fluid in a rotating

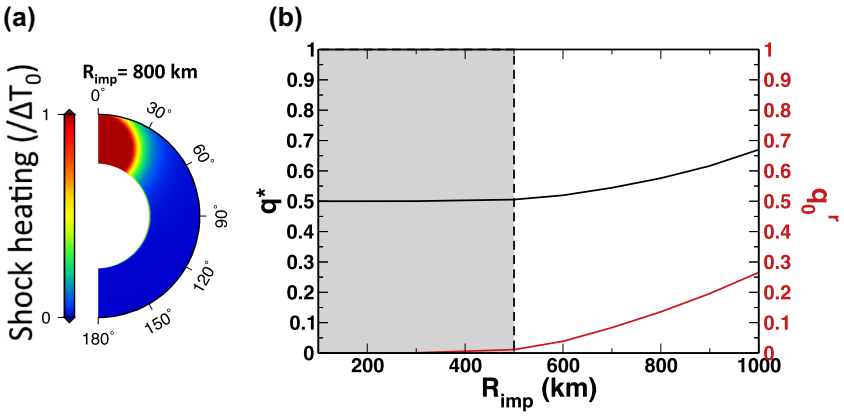

Fig. 1. (a) martian mantle post-impact temperature increase for $R_{imp} = 800$ km. (b) Conventional amplitude of heat flux heterogeneity on the CMB q^* (black line, Eq. (2)) and the mean heat flux reduction q_0^r (red line, Eq. (1)) vs. impactor size R_{imp}. In the grey domain ($R_{imp} < 500$ km), the impactor is too small for isobaric core to reach the CMB. (For interpretation of the references to color in this figure legend, the reader is referred to the web version of this article.)

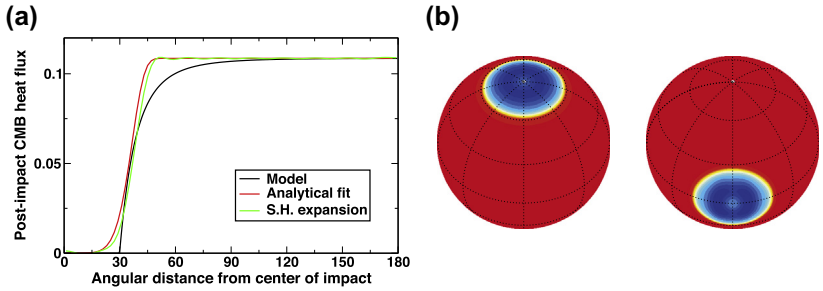

Fig. 2. (a) Post-impact CMB heat flux (black line), analytical fit (red line) and spherical harmonic expansion (green line) vs. angular distance from the center of the impact driven heated area. (b) Imposed CMB heat flux anomalies resulting from an impactor of radius 800 km falling on the north pole (left) or the equator (right). (For interpretation of the references to color in this figure legend, the reader is referred to the web version of this article.)

spherical shell (for governing equations and more details see Amit et al., 2011). We use the code MAGIC by Wicht (2002). We analyze numerical dynamos with rigid insulating boundary conditions. The models differ in the imposed outer boundary heat flux pattern and the amplitude of its variation. A summary of model parameters, outer boundary heat flux patterns and main results is given in Table 1.

It is likely that Mars has no solid inner core up to the present day (e.g., Schubert and Spohn, 1990; Breuer et al., 2010) and, as a consequence, convection in the early martian dynamo was purely thermal (Amit et al., 2011; Dietrich and Wicht, 2013), driven by secular cooling and perhaps by radioactive heating. This convection mode is highly sensitive to CMB heat flux heterogeneity and may thus break internal dynamo symmetries with relatively moderate heterogeneity amplitudes (Hori et al., 2014). Due to numerical singularity at the center of the planet, we retain in our dynamo models a small inner core with a radius $r_i/r_o = 0.2$ of the outer core radius. We impose zero heat flux on the inner boundary so that the inner core is convectively passive. Overall, results by Aubert et al. (2009) and Hori et al. (2010) suggest that such a relatively small and passive inner core has little effect on the dynamo models.

Four internal non-dimensional parameters control the dynamo action. The heat flux Rayleigh number (Olson and Christensen, 2002) represents the strength of buoyancy force driving the convection relative to retarding forces

$$Ra = \frac{\alpha g_0 q_0 D^4}{k\kappa\nu} \tag{4}$$

where α is thermal expansivity, g_0 is gravitational acceleration on the outer boundary at radius r_o, q_0 is the mean heat flux across the outer boundary, D is shell thickness, k is thermal conductivity, κ is thermal diffusivity and ν is kinematic viscosity. The Ekman number represents the ratio of viscous and Coriolis forces

$$E = \frac{\nu}{\Omega D^2} \tag{5}$$

The Prandtl number is the ratio of kinematic viscosity to thermal diffusivity

$$Pr = \frac{\nu}{\kappa} \tag{6}$$

and the magnetic Prandtl number is the ratio of kinematic viscosity to magnetic diffusivity λ

$$Pm = \frac{\nu}{\lambda} \tag{7}$$

A fifth non-dimensional number is the amplitude of the outer boundary heat flux heterogeneity which is expressed by q^* (see Eq. (2)).

In all cases a volumetric homogeneous heat source ϵ compensates for the loss of heat through the outer boundary according to

$$-4\pi r_o^2 Pr\left[\frac{\partial T}{\partial r}(r_o)\right] = \frac{4}{3}\pi(r_o^3 - r_i^3)\epsilon \tag{8}$$

where $[\ldots]$ denotes averaging over the outer boundary surface S. In terms of the non-dimensional variables $\left[\frac{\partial T}{\partial r}(r_o)\right] = 1$, so for $r_i/r_o = 0.2$ (the geometry used in the study) the source term is $\epsilon \simeq 2.42$. We use moderate amplitudes of CMB heat flux heterogeneity to avoid violation of the Boussinesq approximation on which the dynamo code relies.

Table 1
Summary of numerical dynamo models parameters and resulted magnetic hemispheric dichotomies. In all cases $r_i/r_o = 0.2$, $Pr = 1$ and $Pm = 3$. The upper part includes reversing dynamos with $E = 3 \cdot 10^{-4}$; The lower part includes non-reversing dynamos with $E = 1 \cdot 10^{-4}$. The imposed CMB heat flux patterns are either degree-1 single harmonics (Y_1^0 or Y_1) denoted as cases Y, or impact driven centered at the pole or at the equator denoted as cases I. All Y cases are from Amit et al. (2011) except cases Y2 and Y3 which are from this study. The radius of the impactor is R_{imp}. The conventional amplitude of the heat flux anomaly q^* is defined as the ratio of the peak-to-peak difference to twice the mean (Olson and Christensen, 2002). The reduction in the mean heat flux due to the impact is q_0^r. *Rm* is the magnetic Reynolds number based on the rms velocity in the volume of the shell. *SN* and *EW* denote *south–north* and *east–west*, 'cnt' and 'rnd' subscripts denote *continuous* and *random* crust formation. East–west ratios are calculated with respect to the hemisphere centered at longitude 0° (center of large heat flux anomaly for Y_1^1 and equatorial *I* cases) to the hemisphere centered at longitude 180°. For reversing cases only ratios based on random crust formation are given, for Y_1^0 or polar I cases only south–north ratios are given, for Y_1^1 or equatorial I cases only east–west ratios are given. As reference cases, the homogeneous CMB heat flux models from Amit et al. (2011) give *SN* and *EW* values of unity. The average chron duration τ_{ch} is given in kyrs for the reversing cases.

Case	Pattern	R_{imp} [km]	*Ra*	q^*	q_0^r	*Rm*	SN_{cnt}	SN_{rnd}	EW_{cnt}	EW_{rnd}	τ_{ch}
I1	Polar	600	$2.90 \cdot 10^7$	0.51	0.04	386	–	1.18	–	–	40.9
I2	Polar	800	$2.69 \cdot 10^7$	0.56	0.13	423	–	1.54	–	–	22.6
I3	Polar	1000	$2.21 \cdot 10^7$	0.66	0.26	439	–	2.25	–	–	18.3
Y1	Y_1^0	–	$3 \cdot 10^7$	0.8	–	488	–	2.54	–	–	12.2
I4	Polar	1000	$4 \cdot 10^7$	0.66	0.26	572	–	2.58	–	–	15.4
Y2	Y_1^0	–	$2 \cdot 10^7$	0.8	–	412	–	2.35	–	–	14.9
I5	Equatorial	800	$2.69 \cdot 10^7$	0.56	0.13	350	–	–	–	1.22	28.2
Y3	Y_1^0	–	$1 \cdot 10^7$	0.8	–	303	–	1.68	–	–	26.3
Y4	Y_1^1	–	$3 \cdot 10^7$	0.8	–	405	–	–	–	1.14	17.5
I6	Polar	800	$8.97 \cdot 10^6$	0.56	0.13	99	1.12	1.13	–	–	∞
I7	Polar	1000	$7.35 \cdot 10^6$	0.66	0.26	182	1.59	1.57	–	–	∞
Y5	Y_1^0	–	$1 \cdot 10^7$	0.3	–	114	1.16	1.16	–	–	∞
Y6	Y_1^0	–	$1 \cdot 10^7$	0.5	–	157	1.49	1.50	–	–	∞
I8	Equatorial	800	$8.97 \cdot 10^6$	0.56	0.13	104	–	–	1.01	1.01	∞
Y7	Y_1^1	–	$1 \cdot 10^7$	0.5	–	133	–	–	1.01	1.01	∞

Most dynamo models fall into two categories. In the first, the radial field on the CMB is dominated by an axial dipole component, but the field does not reverse. In the second, the field is multipolar and dipole reversals occur (Kutzner and Christensen, 2002). Earth-like models that are both dipole-dominated and reversing are only found in a narrow transitional regime of parameters space (Olson, 2007; Wicht et al., 2009). Following Amit et al. (2011), we consider cases from both regimes.

2.3. Hemispheric magnetic dichotomy monitoring

The kinetic energy of the impactor is dissipated as a result of the irreversible work done by shock waves in damaging crustal rocks as well as heating and melting the target material (Pierazzo et al., 1997; Senshu et al., 2002; Reese and Solomatov, 2006; Monteux et al., 2011). After the excavation process, a significant fraction of the material molten by impact is redistributed heterogeneously at the surface of the impacted planet (Marinova et al., 2008, 2011). The distribution of the molten material is governed by the impact parameters such as the impact velocity and angle. At low impact velocities (6–10 km/s) and oblique impact angles (30–60°), 50–70% of the impact-induced melt distribution might be contained within the area of impact and 25–30% might be deposited at the antipode of the impact site (Marinova et al., 2008). The impact-induced molten material might be redistributed over a thickness that ranges between 30 and 50 km (Marinova et al., 2008, 2011). The cooling and the crystallization of the molten material leads to the formation of the impact induced crust potentially recording the anomalous dynamo.

We consider two end member crust formation scenarios (Amit et al., 2011; Langlais and Thébault, 2011) as illustrated in Fig. 3. In the case of continuous and homogeneous crust formation, each part of the martian crust is formed by a large number of incremental and superposed additions (e.g., lava flows, sills, dykes) over an extended period of time. Each new layer records the magnetic field at its time of cooling below the Curie Temperature, and the present crustal field at a specific location results from the vertical superposition of the magnetization vectors of the various layers (Fig. 3, bottom line). If this crust formation scenario occurs while the dynamo reverses (Fig. 3, bottom right), the present local crustal field would thus represent the intensity of a long-term time-average martian paleomagnetic field. In the extreme case of periodic inversions and layers with equal thicknesses, the superposed opposite sign magnetization vectors could eventually cancel each other. The other end-member model assumes a random crust formation where crustal units are formed in relatively rapid events (Fig. 3, top line). Individual crustal blocks are created randomly both in space and time and each block acquires a magnetization which only depends on the dynamo field at the time of cooling. The present local field in this scenario thus results from adjacent magnetization vectors, or in a probabilistic way, from the time-average of the paleofield intensity. It is likely that neither one of these end-member scenarios represent what actually occurred on Mars, and rather that the actual way in which the magnetized part of the martian crust formed may be intermediate between the two scenarios.

We follow the statistical measures proposed by Amit et al. (2011) corresponding to these two end-member crust formation scenarios. In the context of a continuous homogeneous crust formation scenario, we calculate the ratio of intensities of the time-average field at the planet surface

$$SN_{cnt} = [| < \vec{B} > |]_{sh}/[| < \vec{B} > |]_{nh} \quad (9)$$

where *SN* denotes the ratio between the rms surface average in the southern and northern hemispheres and the subscript 'cnt' denotes *continuous* crust formation. In the context of a random crust formation scenario, we calculate the magnetic dichotomies based on the time-average of the magnetic field intensity

$$SN_{rnd} = [< |\vec{B}| >]_{sh}/[< |\vec{B}| >]_{nh} \quad (10)$$

where the subscript 'rnd' denotes *random*. Eqs. (9) and (10) are applied for the east–west dichotomies EW_{cnt} and EW_{rnd} by replacing the summations with the appropriate hemispheres.

The relevance of the continuous or random crust formation scenario depends on the relation between the cooling time of the Impact Induced Molten Material (IIMM) and the typical magnetic

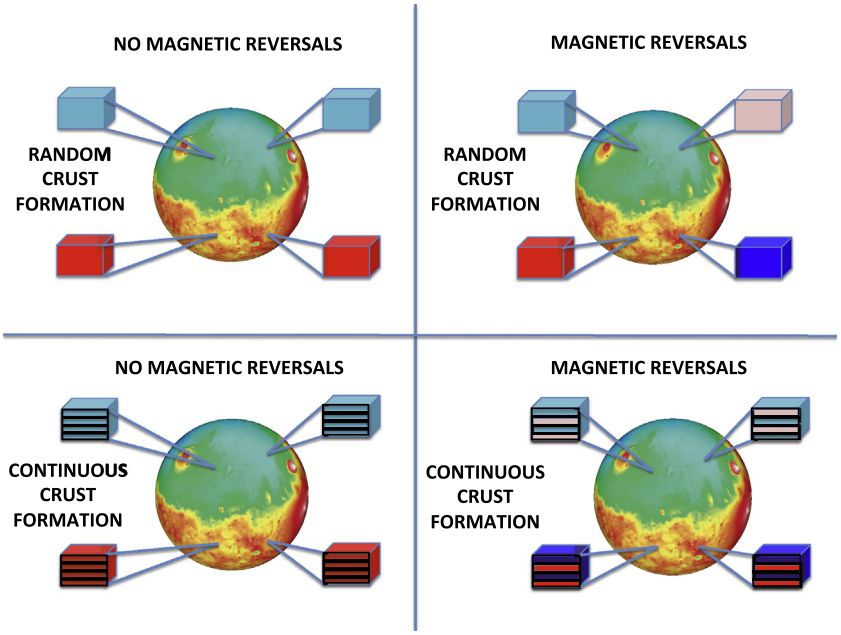

Fig. 3. Schematic illustration of the random (top) and continuous (bottom) crust formation scenarios and the corresponding recorded magnetization without (left) or with (right) magnetic reversals. Blue/red denotes negative/positive radial magnetic paleofields, respectively, so alternating colors correspond to paleomagnetic reversals. Cubes represent a vertical cut through the martian crust that has recorded strong (deep blue or deep red) or weak (light red or light blue) magnetic paleofields. The weak magnetic paleofield is restricted to the impacted pole while the strong magnetic paleofield is restricted to the opposite one. The current magnetic field observed at the surface results from the vertically integrated magnetization over the cube. (For interpretation of the references to color in this figure legend, the reader is referred to the web version of this article.)

timescales. The cooling time of the IIMM strongly depends on the presence of an atmosphere that may prevent the IIMM from rapid cooling (e.g., Lebrun et al., 2013). In the case of molten material induced by a giant impact, a significant fraction of the atmosphere (if any) can be eroded from the impacted body (Shuvalov, 2009) which strongly enhances the excess heat removal and decreases the cooling and solidification times. Hence, the duration of the partially molten stage decreases from more than 1 million years with an atmosphere to ~1000 years when no atmosphere is present (Lebrun et al., 2013). The two crust formation scenarios give identical dichotomies for non-reversing dynamos (Amit et al., 2011). In the reversing case, if the crust was formed over a period much longer than a typical magnetic timescale, the continuous scenario is relevant (Dietrich and Wicht, 2013). Conversely, if the crust was formed faster than a typical magnetic timescale (i.e., without any atmosphere), the random scenario is relevant (see Fig. 3).

3. Influence of impact heating on core dynamo

Various CMB heat flux models corresponding to varying impactor sizes were examined. We considered two extreme geographic locations of the impactor, with a center falling on the geographical pole or on the equator. The impactor introduces warm material to the lower mantle, thus locally decreases the CMB heat flux. Apart from pattern dependence, the reduction in mean CMB heat flux (expressed by the *Ra* number compared to its reference homogeneous case) as well as the amplitude of the heat flux heterogeneity q^* are all dependent in a self-consistent manner on the radius of the impactor. A larger impactor warms a larger part of the CMB, thus reduces the mean CMB heat flux q_0 more and produces larger q^* (see Table 1).

Fig. 4 shows the time-average rms radial field at the CMB and the time-average field intensity at the surface of Mars for case I2 with an impactor of radius 800 km falling on the north geographic pole. Here and elsewhere all magnetic field values are given in units of $\sqrt{\rho\mu_0\lambda\Omega}$ where ρ is the fluid density and μ_0 is permeability of free space. The impactor yields an hemispheric field similar to those obtained with synthetic Y_1^0 CMB heat flux patterns (Stanley et al., 2008; Amit et al., 2011; Dietrich and Wicht, 2013).

Fig. 5 shows the time-average zonal temperature and flow in case I2. The reduced CMB heat flux in the north pole region caused by the impactor results in a relatively warmer fluid there. The colder fluid in the more vigorously convecting southern hemisphere is associated with fluid downwelling at high-latitudes that concentrates the magnetic field. This produces a south–north magnetic hemispheric dichotomy. In addition, the boundary driven thermal wind flow exhibits a large one cell meridional circulation with surface flow going southward, carrying weak magnetic flux from north to south. These dynamical features are also in agreement with those obtained with a synthetic Y_1^0 CMB heat flux pattern (Stanley et al., 2008; Amit et al., 2011).

When the impactor is falling on the equatorial plane, some magnetic dichotomy may be expected between eastern and western hemispheres. Indeed Fig. 6 shows that in case I5 such a dichotomy is obtained. Note that the east–west dichotomy in this case is significantly weaker than the south–north dichotomy in the corresponding polar impactor case I2 with the same impactor radius of 800 km. However, compared to the east–west dichotomy obtained with a synthetic Y_1^1 CMB heat flux pattern (Amit et al., 2011), the impactor driven east–west dichotomy is significantly stronger (compare cases I5 and Y4 in Table 1).

Fig. 7 shows two snapshots of the radial field at the CMB and the intensity at the surface of Mars for case I3 with the largest impactor studied here (radius of 1000 km) falling on the north geographic pole as well as the corresponding long term time-average surface intensity. The differences between the two snapshots attest to the chaotic time dependence of this model. Nevertheless, in both snapshots the relatively small-scale radial field at the CMB is strongest at high latitudes of the southern hemisphere. The surface

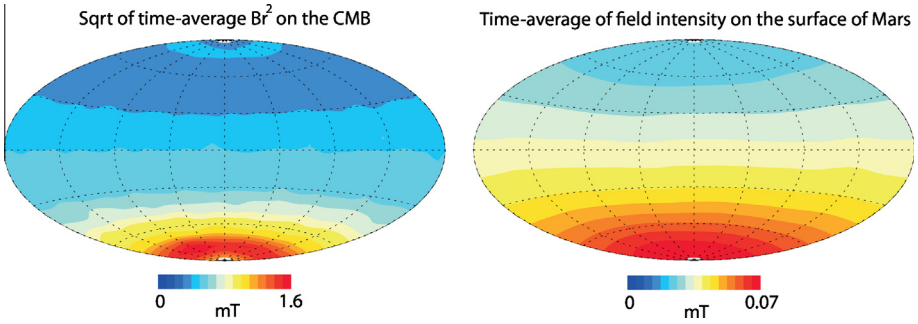

Fig. 4. Time-average magnetic field properties on the CMB (left) and on the surface of Mars (right) in case I2. The CMB field is upward continued to the surface of Mars as a potential field.

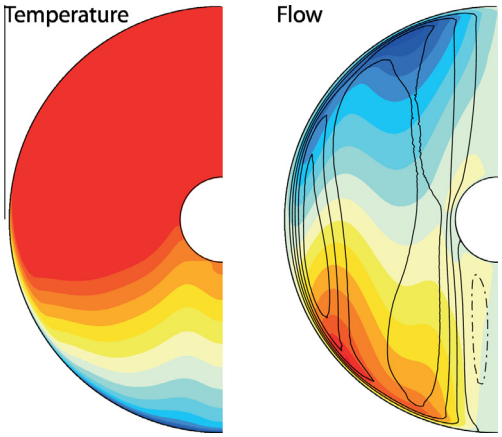

Fig. 5. Time-average zonal temperature (left) and flow (right) in case I2. In the right subplot colors denote azimuthal flow and streamlines denote meridional circulation (solid/dashed are anti-clockwise/clockwise, respectively). (For interpretation of the references to color in this figure legend, the reader is referred to the web version of this article.)

intensity is large scale, and also peaks at the polar region of the southern hemisphere. In this case, the time-average south–north dichotomy is 2.25 (see Table 1), very close to the lower bound estimation of 2.4 obtained by Amit et al. (2011) based on observations of the martian crustal magnetic field (Langlais et al., 2004).

Finally we examine the influence of the strength of the internal core convection. Case I4 is identical to case I3 except for its Ra value which is larger. The south–north magnetic dichotomy in this case is 2.58 (Table 1), demonstrating that more vigorous core convection produces more hemispherical fields.

Our models show that a polar impactor leads to a stronger north–south hemispheric magnetic dichotomy than an equatorial impactor to an east–west dichotomy. We also find that in the non-reversing regime of parameters, the magnetic field dichotomy that can be recorded in the cooling IIMM is independent of the crust formation scenario (random or continuous). Reversing dynamos that convect stronger produce stronger magnetic dichotomies than non-reversing dynamos. These results are in agreement with those obtained by Amit et al. (2011) for degree-1 heat flux patterns.

The amplitude of the CMB heat flux heterogeneity (Fig. 2) is commonly measured by the peak to peak lateral variation (Olson and Christensen, 2002). However, when the pattern is not smooth and very localized, with imbalance between areas of positive and negative anomalies, q^* is inadequate. This is exactly the case in the impact driven heat flux patterns considered here. For example, for very small impacts the amplitude is negligible but q^* approaches 0.5 (Fig. 1b). We quantify the impact driven heterogeneity amplitude by q_0^r (Eq. (1)) which measures the extent of the CMB surface affected by the impact heating. Therefore, in order to compare the efficiency of magnetic hemispheric dichotomy generation by impact driven patterns with the efficiency by synthetic degree-1 patterns, q_0^r in the first must be compared with q^* in the latter. In addition we propose that the governing parameter controlling the amplitude of the hemispheric magnetic dichotomy is the horizontal Rayleigh number Ra_h (Willis et al., 2007). We define Ra_h as:

$$Ra_h = \begin{cases} q^* Ra & \text{in Y cases} \\ q_0^r Ra & \text{in I cases} \end{cases} \tag{11}$$

To adequately compare the synthetic Y_1^0 CMB heat flux cases from Amit et al. (2011) and the polar impact driven CMB heat flux cases from this study, we plot in Fig. 8 the increase of the south–north dichotomy $SN-1$ as a function of Ra_h (11). This figure shows that for a given lateral forcing, an impact induced CMB heat flux heterogeneity is significantly more efficient than a synthetic Y_1^0 CMB heat

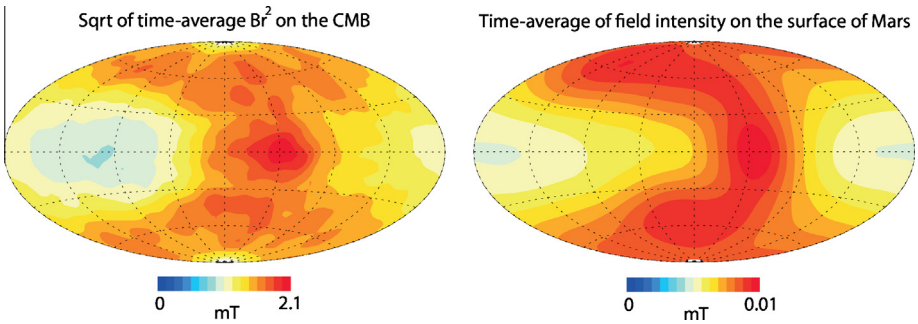

Fig. 6. As in Fig. 4 for case I5 (note different color scales). (For interpretation of the references to color in this figure legend, the reader is referred to the web version of this article.)

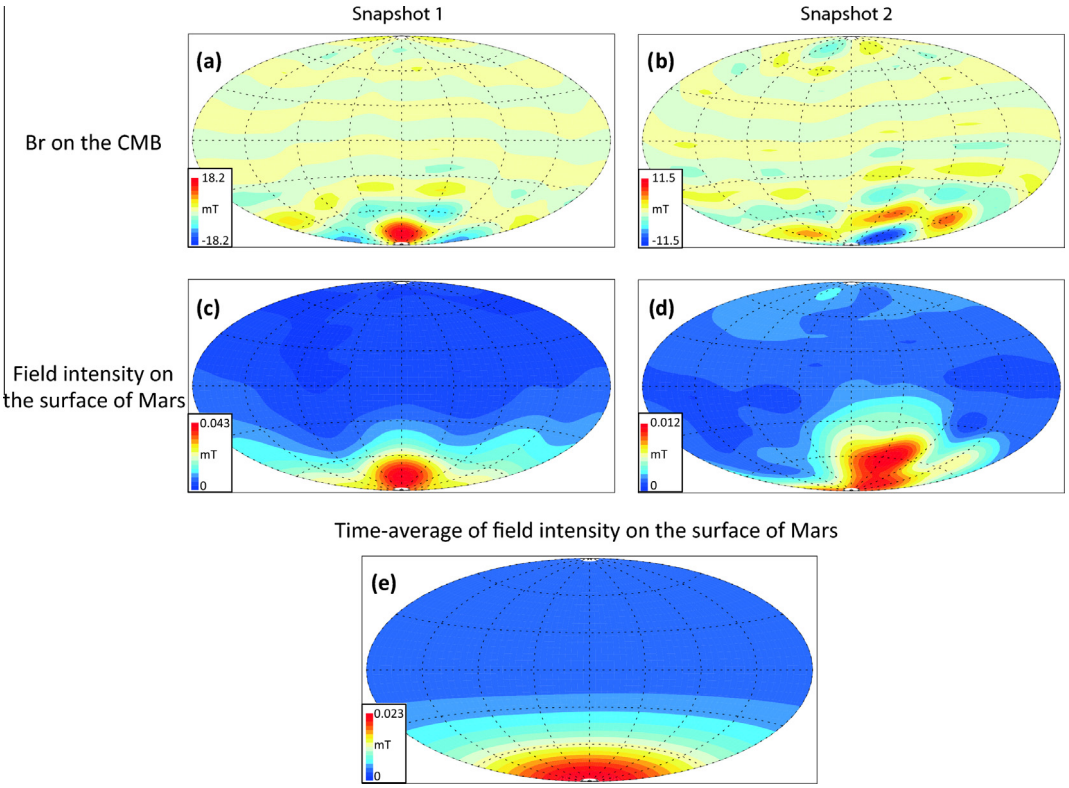

Fig. 7. Two arbitrary snapshots of the radial magnetic field B_r on the CMB (a and b) and surface intensity of the magnetic field (c and d) in case I3. The time-average surface intensity is shown in (e). Here the spherical harmonic expansion is truncated at $\ell_{max} = 10$. Note differences in color scales among the maps. The CMB field is upward continued to the surface of Mars as a potential field. (For interpretation of the references to color in this figure legend, the reader is referred to the web version of this article.)

flux heterogeneity in generating hemispheric magnetic dichotomies. Note that the curve of the impact cases is elevated with respect to that of the Y_1^0 cases, although the slopes of both curves seem comparable. Fig. 8 also shows that the impactor size needed to generate the observed martian dichotomy (Amit et al., 2011) is about 1000 km, which is within the estimated range of impactor sizes (Marinova et al., 2008). The better efficiency of impact driven hemispheric dynamos over the synthetic cases is even more pronounced in the equatorial cases (see Table 1).

4. Implication for crustal magnetic dichotomy

Our results show that large Ra_h (and therefore large Ra) are needed in order to get a dichotomy as strong as the observed. As large Ra are likely to be associated with reversing dynamos (e.g., Kutzner and Christensen, 2002), the possibility to record a dichotomy in the crust depends on the duration of a chron relative to the duration of the crystallization of the IIMM induced by the impact. If a slow crystallization rate was coupled with short magnetic chrons (Dietrich and Wicht, 2013), then our models cannot explain the observed martian dichotomy. However, if a relatively rapid magma cooling was coupled with a relatively low reversal frequency then the impact induced magnetic dichotomy may have been recorded within the martian crust and explain the observed signal. Hence, the relevant magnetic timescale is a duration of a typical chron.

In our non-reversing dynamo models the chron duration is effectively infinite and the hemispheric magnetic dichotomies may be recorded by the crustal magnetization (Fig. 3, left). However, the amplitudes of the dichotomies in these cases are too low to explain the observed hemispheric crustal magnetic dichotomy on Mars (Table 1). Dynamo models with large amplitude hemispheric dichotomies tend to reverse frequently, in agreement with the findings of Dietrich and Wicht (2013). For example, in case I3 a typical chron persists for ∼18 kyr. In order for such a model to record an hemispheric magnetic dichotomy at the crust, very fast crust formation is required.

Dietrich et al. (2013) studied hemispherical dynamos in the framework of classical mean field theory. For $q^* > 0.6$ Dietrich and Wicht (2013) found hemispheric $\alpha\Omega$ dynamos with fast oscillations over periods of ∼10 kyrs. In our models the amplitude of CMB heat flux heterogeneity is moderate with $q^* \sim 0.6$, and more importantly $q_0^r \ll 0.6$. Our dynamos are therefore of the α^2-type with chaotic (reversing or non-reversing) behavior. In addition, the moderate q_0^r does not change the dynamo regime from stable to reversing. In these dynamos the duration of a chron (or the reversal frequency) depends on the level of turbulence in the core (Olson and Amit, 2014), which is in general unknown (even for the Earth). Chron duration varied immensely over Earth's history between 40 kyrs and 40 Myrs (Merrill et al., 1998).

Fig. 9 illustrates the interplay between the relevant time-scales: the crystallization time τ_c, the spreading time τ_{imp} and the duration of a chron. In the context of a martian giant impact, the associated molten thickness δ ranges between 30 and 50 km and the melt fraction is ∼20% (Marinova et al., 2008). Hence, the crystallization and cooling times of the shallow IIMM induced by one impact should be rapid: even if the complete solidification timescale ultimately depends on the poorly constrained evolution of the post-impact transient atmosphere (Abe, 1997), crystallization of this local molten material should occur in less than 1000 years (Reese and Solomatov, 2006). The subsequent evolution of the partially molten material could involve isostatic readjustment of a deep, initially hemispheric, retained melt region and lateral spreading as a gravity current (Reese et al., 2011). Overall, the surface

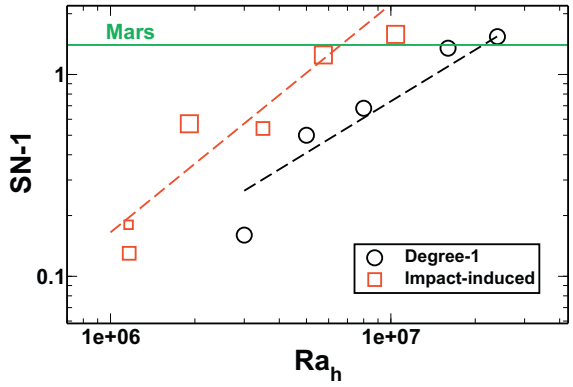

Fig. 8. South–north dichotomy as a function of the horizontal Rayleigh number Ra_h (Eq. (11)). The black symbols are the values obtained (with $r_i/r_o = 0.2$) for the synthetic Y_1^0 CMB heat flux patterns (with $Ra_h = q^* Ra$). The red symbols are the values obtained in cases of polar impact driven CMB heat flux patterns (with $Ra_h = q_0^r Ra$). The size of the red symbols increases with the size of the impactor. The corresponding power law fits are plotted with dashed lines. The green horizontal line represents the martian value of $SN-1$ from Amit et al. (2011) based on observations of the martian crustal magnetic field (Langlais et al., 2004). All degree-1 cases are from Amit et al. (2011) except cases Y2 and Y3 from this study (see also Table 1). (For interpretation of the references to color in this figure legend, the reader is referred to the web version of this article.)

temperature of the IIMM falls below the Curie temperature in a timescale that strongly depends on factors such as the characteristics of the above atmosphere or the viscosity of the solid mantle if isostatic rebound is involved. This instant characterizes the beginning of the time interval when the solidified crust starts to record the magnetic field. The cold front then propagates downwards from the surface and a secondary front most probably develops at the base of the IIMM whose nature depends on the thermal state of the pre-impact crust on top of which the IIMM is superimposed (Fig. 9). The crustal material originating in the impact event stops recording the magnetic field precisely when the innermost region is cooler than the Curie temperature. In summary, given these somewhat overlapping ranges of timescales for the crust formation and magnetic chrons, we argue that both end-member crust formation scenarios are in principle possible, bearing in mind that reality may be somewhere in between.

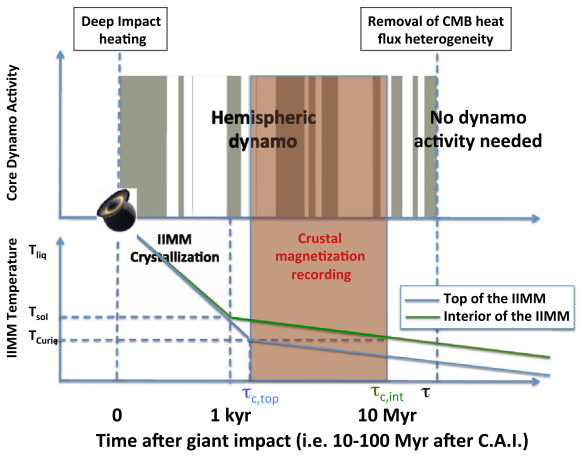

Fig. 9. Schematic illustration of temporal evolution of core dynamo activity (top panel) and of the IIMM temperature (bottom panel) after a giant impact. The C.A.I. (Calcium-Aluminium rich Inclusions) are the oldest objects in the solar system. In the bottom panel, the blue line represents the temperature evolution at the interior of the IIMM while the green line represents the top of the IIMM (i.e., the post impact martian surface). (For interpretation of the references to color in this figure legend, the reader is referred to the web version of this article.)

Our study also emphasizes the importance of the duration of the post-impact thermal anomaly at the CMB (τ_{imp}). If this timescale is shorter than the time needed by the IIMM to cool down to temperatures smaller than the Curie temperature τ_c, the hemispheric dynamo has ended before the crust was able to record it. However, if τ_{imp} is larger than τ_c, the post-impact magnetic field can be recorded within the crust. The beginning of this record starts at $\tau_{c,top} \sim 1$ kyr and ends at $\tau_{c,int} \sim 10$—100 Myr, this time interval being mostly controlled by heat diffusion. The deep post-impact thermal re-adjustment occurs within a characteristic time that is governed by the rheology of the mantle surrounding the post-impact thermal anomaly. For a mantle viscosity comparable to that of the present day Earth, say around 10^{21} Pa.s, this characteristic spreading time is $\tau_{imp} \sim 10$—100 Myr (Monteux et al., 2007; Watters et al., 2009) which is much larger than the characteristic magnetic diffusion time $\tau_\lambda \sim 30$ kyrs (e.g., Bloxham and Jackson, 1991) or the time needed by the top of the IIMM to reach the Curie temperature $\tau_{c,top}$ (Fig. 9).

5. Conclusion

Can the observed martian hemispheric magnetic dichotomy be the consequence of a giant impact that has led to an internal hemispheric magnetic field? Our results show that a ~1000 km radius impactor can generate a sufficiently large scale thermal anomaly at the CMB so that a hemispheric dichotomy comparable to the observed is generated. An impact induced CMB heat flux heterogeneity is more efficient than a synthetic degree-1 CMB heat flux heterogeneity in generating strong hemispheric magnetic dichotomies. This magnetic dichotomy is stronger for a polar impact than for an equatorial impact. This result reconciles the giant impact induced scenario evoked to explain the martian topographic dichotomy (Andrews-Hanna et al., 2008; Marinova et al., 2008; Nimmo et al., 2008) and the heterogeneous CMB heat flux scenario proposed to explain why the magnetization is strong only in the southern hemisphere (Stanley et al., 2008) via a more realistic CMB heat flux pattern than the previously used synthetic degree-1. Hence, we propose here that an external event at the martian surface may have produced an internal hemispheric dynamo.

From our results, three relevant timescales arise: the cooling time of the impact induced molten material, the duration of a magnetic chron and the duration of the post-impact thermal anomaly at the CMB. The first is mainly governed by the characteristics of the martian atmosphere, the second is governed by the core dynamics while the third is governed by the mantle dynamics. If a relatively rapid magma cooling was coupled with a relatively low reversal frequency and with a stable CMB heat flux heterogeneity, then the impact induced magnetic dichotomy may have been recorded within the martian crust and explain the observed signal.

According to some studies (e.g., Arkani-Hamed and Olson, 2010), a giant impact might have led to a thermal stratification at the top of the core that terminated the dynamo. However, core stratification can be removed much faster by convection of molten material, over a timescale orders of magnitude shorter than the longevity of mantle thermal anomalies. Hence our scenario of giant impact leading to heterogenous mantle heating and to a hemispheric dynamo on Mars may follow an episode of dynamo shutdown.

Our impact driven CMB heat flux heterogeneity model may also be applied to model dynamos of other planets. Indeed, giant impacts were common in the later stage of accretion of terrestrial planets. The Earth is likely formed by accretion of a few dozen moon to Mars-size planetary embryos (see review by Chambers

(2004)). A Mars-size impact on Earth may have resulted in the formation of the Moon (Hartmann and Davis, 1975; Cameron and Ward, 1976; Canup, 2004). The Moon was also probably hit by a large planetesimal at the end of its formation (Jutzi and Asphaug, 2011). Finally, an oblique collision of a large body with a mass about one sixth of Mercury's has likely stripped away a significant part of its mantle (Smith, 1979; Benz et al., 1988). Furthermore, these three terrestrial objects have or have had an internally generated magnetic field (Stevenson, 2003). Hence, giant impacts have potentially strongly influenced their internal dynamics and dynamo activities.

Acknowledgments

J. Monteux was funded by Agence Nationale de la Recherche (Accretis Decision No. ANR-10-PDOC-001-01). We thank Johannes Wicht for providing the MAGIC code. We thank two anonymous reviewers for their careful and insightful reviews that greatly improve the manuscript. The authors also thank N. Mangold and J.P. Lorand for useful discussions.

References

Abe, Y., 1997. Thermal and chemical evolution of the terrestrial magma ocean. Phys. Earth Planet. Inter. 100, 27–39.
Acuña, M., Connerney, J., Wasilewski, P., Lin, R., Anderson, K., Carlson, C., McFadden, J., Curtis, D., Mitchell, D., Reme, H., Mazelle, C., Sauvaud, J., d'Uston, C., Cros, A., Medale, J., Bauer, S., Cloutier, P., Mayhew, M., Winterhalter, D., Ness, N., 1998. Magnetic field and plasma observations at Mars: initial results of the Mars global surveyor mission. Science 279 (5357), 1676–1680.
Amit, H., Choblet, G., 2009. Mantle-driven geodynamo features – effects of post-Perovskite phase transition. Earth Planets Space 61, 1255–1268.
Amit, H., Choblet, G., 2012. Mantle-driven geodynamo features – effects of compositional and narrow D" anomalies. Phys. Earth Planet. Inter. 190, 34–43.
Amit, H., Aubert, J., Hulot, G., 2010. Stationary, oscillating or drifting mantle-driven geomagnetic flux patches? J. Geophys. Res. 115, B07108.
Amit, H., Christensen, U., Langlais, B., 2011. The influence of degree-1 mantle heterogeneity on the past dynamo of Mars. Phys. Earth Planet. Inter. 189, 63–79.
Anderson, B.J., Johnson, C.L., Korth, H., Winslow, R.M., Borovsky, J.E., Purucker, M.E., Slavin, J.A., Solomon, S.C., Zuber, M.T., McNutt Jr., R.L., 2012. Low-degree structure in Mercury's planetary magnetic field. J. Geophys. Res. (Planets) 117.
Andrews-Hanna, J.C., Zuber, M.T., Banerdt, W.B., 2008. The Borealis basin and the origin of the martian crustal dichotomy. Nature 453, 1212–1215.
Arkani-Hamed, J., Olson, P., 2010. Giant impact stratification of the Martian core. Geophys. Res. Lett. 37, L02201.
Asphaug, E., Agnor, C.B., Williams, Q., 2006. Hit-and-run planetary collisions. Nature 439, 155–160.
Aubert, J., Amit, H., Hulot, G., 2007. Detecting thermal boundary control in surface flows from numerical dynamos. Phys. Earth Planet. Inter. 160, 143–156.
Aubert, J., Amit, H., Hulot, G., Olson, P., 2008. Thermo-chemical wind flows couple Earth's inner core growth to mantle heterogeneity. Nature 454, 758–761.
Aubert, J., Labrosse, S., Poitou, C., 2009. Modelling the paleo-evolution of the geodynamo. Geophys. J. Int. 179, 1414–1428.
Benz, W., Slattery, W.L., Cameron, A.G.W., 1988. Collisional stripping of Mercury's mantle. Icarus 74, 516–528.
Bloxham, J., 2002. Time-independent and time-dependent behaviour of high-latitude flux bundles at the core-mantle boundary. Geophys. Res. Lett. 29, 1854.
Bloxham, J., Jackson, A., 1991. Fluid flow near the surface of the Earth's outer core. Rev. Geophys. 29, 97–120.
Breuer, D., Labrosse, S., Spohn, T., 2010. Thermal evolution and magnetic field generation in terrestrial planets and satellites. Space Sci. Rev. 152, 449–500.
Cameron, A.G.W., Ward, W.R., 1976. The origin of the Moon. Lun. Planet. Inst. Conf. Abs. 7, 120–122.
Canup, R.M., 2004. Simulations of a late lunar-forming impact. Icarus 168, 433–456.
Cao, H., Aurnou, J.M., Wicht, J., Dietrich, W., Soderlund, K.M., Russell, C.T., 2014. A dynamo explanation for Mercury's anomalous magnetic field. Geophys. Res. Lett. 41, 4127–4134.
Chambers, J.E., 2004. Planetary accretion in the inner Solar System. Earth Planet. Sci. Lett. 223, 241–252.
Chassefière, E., Langlais, B., Quesnel, Y., Leblanc, F., 2013. The fate of early Mars' lost water: the role of serpentinization. J. Geophys. Res. (Planets) 118, 1123–1134.
Dietrich, W., Wicht, J., 2013. A hemispherical dynamo model: implications for the Martian crustal magnetization. Phys. Earth Planet. Int. 217, 10–21.
Dietrich, W., Schmitt, D., Wicht, J., 2013. Hemispherical Parker waves driven by thermal shear in planetary dynamos. Europhys. Lett., 104
Elkins-Tanton, L.T., Parmentier, E.M., Hess, P.C., 2003. Magma ocean fractional crystallization and cumulate overturn in terrestrial planets: implications for Mars. Meteorit. Planet. Sci. 38, 1753–1771.
Elkins-Tanton, L.T., Zaranek, S.E., Parmentier, E.M., Hess, P.C., 2005. Early magnetic field and magmatic activity on Mars from magma ocean cumulate overturn. Earth Planet. Sci. Lett. 236, 1–12.
Frey, H.V., Roark, J.H., Shockey, K.M., Frey, E.L., Sakimoto, S.E.H., 2002. Ancient lowlands on Mars. Geophys. Res. Lett. 29, 1384.
Gladman, B., Coffey, J., 2009. Mercurian impact ejecta: Meteorites and mantle. Meteorit. Planet. Sci. 44, 285–291.
Glatzmaier, G., Coe, R., Hongre, L., Roberts, P., 1999. The role of the Earth's mantle in controlling the frequency of geomagnetic reversals. Nature 401, 885–890.
Golabek, G.J., Gerya, T.V., Kaus, B.J.P., Ziethe, R., Tackley, P.J., 2009. Rheological controls on the terrestrial core formation mechanism. Geochem. Geophys. Geosyst. 10, Q11007.
Gubbins, D., Willis, P.W., Sreenivasan, B., 2007. Correlation of Earth's magnetic field with lower mantle thermal and seismic structure. Phys. Earth Planet. Inter. 162, 256–260.
Harder, H., Christensen, U., 1996. A one-plume model of Martian mantle convection. Nature 380, 507–509.
Hartmann, W.K., Davis, D.R., 1975. Satellite-sized planetesimals and lunar origin. Icarus 24, 504–514.
Hori, K., Wicht, J., Christensen, U., 2010. The effect of thermal boundary conditions on dynamos driven by internal heating. Phys. Earth Planet. Inter. 182, 85–97.
Hori, K., Wicht, J., Dietrich, W., 2014. Ancient dynamos of terrestrial planets more sensitive to core-mantle boundary heat flows. Planet. Space. Sci. 98, 30–40.
Jutzi, M., Asphaug, E., 2011. Forming the lunar farside highlands by accretion of a companion moon. Nature 476, 69–72.
Ke, Y., Solomatov, V.S., 2006. Early transient superplumes and the origin of the Martian crustal dichotomy. J. Geophys. Res. (Planets) 111, 10001.
Kutzner, C., Christensen, U., 2002. From stable dipolar towards reversing numerical dynamos. Phys. Earth Planet. Inter. 131, 29–45.
Kutzner, C., Christensen, U.R., 2004. Simulated geomagnetic reversals and preferred virtual geomagnetic pole paths. Geophys. J. Int. 157, 1105–1118.
Langlais, B., Amit, H., 2008. The past martian dynamo. Science 321, 1784–1785.
Langlais, B., Thébault, E., 2011. Predicted and observed magnetic signatures of martian (de)magnetized impact craters. Icarus 212, 568–578.
Langlais, B., Purucker, M., Mandea, M., 2004. Crustal magnetic field of Mars. J. Geophys. Res. 109, E02008.
Lebrun, T., Massol, H., Chassefière, E., Davaille, A., Marcq, E., Sarda, P., Leblanc, F., Brandeis, G., 013. Thermal evolution of an early magma ocean in interaction with the atmosphere. J. Geophys. Res. (Planets) 118, 1155–1176.
Le Feuvre, M., Wieczorek, M.A., 2011. Nonuniform cratering of the Moon and a revised crater chronology of the inner Solar System. Icarus 214, 1–20.
Lillis, R.J., Frey, H.V., Manga, M., 2008. Rapid decrease in Martian crustal magnetization in the Noachian era: implications for the dynamo and climate of early Mars. Geophys. Res. Lett. 35, 14203.
Lillis, R.J., Stewart, S.T., Manga, M., 2013. Demagnetization by basin-forming impacts on early Mars: contributions from shock, heat, and excavation. J. Geophys. Res. (Planets) 118, 1045–1062.
Marinova, M.M., Aharonson, O., Asphaug, E., 2008. Mega-impact formation of the Mars hemispheric dichotomy. Nature 453, 1216–1219.
Marinova, M.M., Aharonson, O., Asphaug, E., 2011. Geophysical consequences of planetary-scale impacts into a Mars-like planet. Icarus 211, 960–985.
Merrill, R., McElhinny, M., McFadden, P., 1998. The Magnetic Field of the Earth: Paleomagnetism, the Core, and the Deep Mantle. Academic Press, San Diego, California, USA.
Monteux, J., Arkani-Hamed, J., 2014. Consequences of giant impacts in early Mars: core merging and Martian dynamo evolution. J. Geophys. Res. (Planets) 119, 480–505.
Monteux, J., Coltice, N., Dubuffet, F., Ricard, Y., 2007. Thermo-mechanical adjustment after impacts during planetary growth. Geophys. Res. Lett. 34, 24201–24205.
Monteux, J., Jellinek, A.M., Johnson, C.L., 2011. Why might planets and moons have early dynamos? Earth Planet. Sci. Lett. 310, 349–359.
Monteux, J., Jellinek, A.M., Johnson, C.L., 2013. Dynamics of core merging after a mega-impact with applications to Mars' early dynamo. Icarus 226, 20–32.
Nimmo, F., Hart, S.D., Korycansky, D.G., Agnor, C.B., 2008. Implications of an impact origin for the martian hemispheric dichotomy. Nature 453, 1220–1223.
Olson, P., 2007. Gravitational dynamos and the low frequency geomagnetic secular variation. Proc. Natl. Acad. Sci. 104, 20159–20166.
Olson, P., Amit, H., 2014. Magnetic reversal frequency scaling in dynamos with thermochemical convection. Phys. Earth Planet. Inter. 229, 122–133.
Olson, P., Christensen, U., 2002. The time averaged magnetic field in numerical dynamos with nonuniform boundary heat flow. Geophys. J. Int. 151, 809–823.
Olson, P., Coe, R.S., Driscoll, P.E., Glatzmaier, G.A., Roberts, P.H., 2010. Geodynamo reversal frequency and heterogeneous core-mantle boundary heat flow. Phys. Earth Planet. Inter. 180, 66–79.
Olson, P., Deguen, R., Hinnov, L.A., Zhong, S., 2013. Controls on geomagnetic reversals and core evolution by mantle convection in the Phanerozoic. Phys. Earth Planet. Inter. 214, 87–103.
Parker, R., 2003. Ideal bodies for Mars magnetics. J. Geophys. Res. Planets 108 (E1).
Pierazzo, E., Melosh, H.J., 2000. Melt production in oblique impacts. Icarus 145, 252–261.
Pierazzo, E., Vickery, A.M., Melosh, H.J., 1997. A reevaluation of impact melt production. Icarus 127, 408–423.
Pozzo, M., Davies, C., Gubbins, D., Alfè, D., 2012. Thermal and electrical conductivity of iron at Earth's core conditions. Nature 485, 355–358.

Quesnel, Y., Sotin, C., Langlais, B., Costin, S., Mandea, M., Gottschalk, M., Dyment, J., 2009. Serpentinization of the martian crust during Noachian. Earth Planet. Sci. Lett. 277, 184–193.
Reese, C.C., Solomatov, V.S., 2006. Fluid dynamics of local martian magma oceans. Icarus 184, 102–120.
Reese, C.C., Solomatov, V.S., 2010. Early martian dynamo generation due to giant impacts. Icarus 207, 82–97.
Reese, C.C., Orth, C.P., Solomatov, V.S., 2010. Impact origin for the Martian crustal dichotomy: Half emptied or half filled? J. Geophys. Res. (Planets) 115 (14), 5004–+.
Reese, C.C., Orth, C.P., Solomatov, V.S., 2011. Impact megadomes and the origin of the martian crustal dichotomy. Icarus 213, 433–442.
Roberts, J.H., Arkani-Hamed, J., 2012. Impact-induced mantle dynamics on Mars. Icarus 218, 278–289.
Roberts, J., Zhong, S., 2006. Degree-1 convection in the Martian mantle and the origin of the hemispheric dichotomy. J. Geophys. Res. 111, E06013.
Roberts, J.H., Lillis, R.J., Manga, M., 2009. Giant impacts on early Mars and the cessation of the Martian dynamo. J. Geophys. Res. (Planets) 114 (13), E04009.
Rochette, P., 2006. Crustal magnetization of Mars controlled by lithology or cooling rate in a reversing dynamo? Geophys. Res. Lett. 33, 2202.
Schubert, G., Spohn, T., 1990. Thermal history of Mars and the sulfur content of its core. J. Geophys. Res. 95, 14095–14104.
Senshu, H., Kuramoto, K., Matsui, T., 2002. Thermal evolution of a growing Mars. J. Geophys. Res. 107, 1–13.
Shuvalov, V., 2009. Atmospheric erosion induced by oblique impacts. Meteorit. Planet. Sci. 44, 1095–1105.
Smith, J.V., 1979. Mineralogy of the planets: a voyage in space and time. Mineral. Mag. 43, 1–89.
Solomon, S.C., Aharonson, O., Aurnou, J.M., Banerdt, W.B., Carr, M.H., Dombard, A.J., Frey, H.V., Golombek, M.P., Hauck, S.A., Head, J.W., Jakosky, B.M., Johnson, C.L., McGovern, Neumann, G.A., Phillips, R.J., Smith, D.E., Zuber, M.T., 2005. New Perspectives on Ancient Mars. Science 307, 1214–1220.
Šrámek, O., Ricard, Y., Dubuffet, F., 2010. A multiphase model of core formation. Geophys. J. Int. 181, 198–220.
Stanley, S., 2010. A dynamo model for axisymmetrizing Saturn's magnetic field. Geophys. Res. Lett. 37, 5201.
Stanley, S., Elkins-Tanton, L., Zuber, M.T., Parmentier, E.M., 2008. Mars' paleomagnetic field as the result of a single-hemisphere dynamo. Science 321, 1822–1825.
Stevenson, D.J., 2003. Planetary magnetic fields. Earth Planet. Sci. Lett. 208, 1–2.
Tonks, W.B., Melosh, H.J., 1992. Core formation by giant impacts. Icarus 100, 326–346.
Watters, W.A., Zuber, M.T., Hager, B.H., 2009. Thermal perturbations caused by large impacts and consequences for mantle convection. J. Geophys. Res. (Planets) 114, E02001.
Wicht, J., 2002. Inner-core conductivity in numerical dynamo simulations. Phys. Earth Planet. Inter. 132, 281–302.
Wicht, J., Stellmach, S., Harder, H., 2009. Numerical models of the geodynamo: from fundamental Cartesian models to 3D simulations of field reversals. In: Glassmeier, H., Soffel, H., Negendank, J. (Eds.), Geomagnetic Field Variations – Space-time Structure, Processes, and Effects on System Earth. Springer, Berlin, pp. 107–158.
Willis, A.P., Sreenivasan, B., Gubbins, D., 2007. Thermal core mantle interaction: exploring regimes for locked dynamo action. Phys. Earth Planet. Inter. 165, 83–92.
Yoder, C.F., Konopliv, A.S., Yuan, D.N., Standish, E.M., Folkner, W.M., 2003. Fluid core size of Mars from detection of the solar tide. Science 300, 299–303.
Zhong, S., Zuber, M.T., 2001. Degree-1 mantle convection and the crustal dichotomy on Mars. Earth Planet. Sci. Lett. 189, 75–84.
Zuber, M.T., 2001. The crust and mantle of Mars. Nature 412, 220–227.

Amit *et al. Progress in Earth and Planetary Science* (2015) 2:26
DOI 10.1186/s40645-015-0056-3

Progress in Earth and Planetary Science
a SpringerOpen Journal

REVIEW Open Access

Towards more realistic core-mantle boundary heat flux patterns: a source of diversity in planetary dynamos

Hagay Amit[1*], Gaël Choblet[1], Peter Olson[2], Julien Monteux[3], Frédéric Deschamps[4], Benoit Langlais[1] and Gabriel Tobie[1]

Abstract

Mantle control on planetary dynamos is often studied by imposing heterogeneous core-mantle boundary (CMB) heat flux patterns on the outer boundary of numerical dynamo simulations. These patterns typically enter two main categories: Either they are proportional to seismic tomography models of Earth's lowermost mantle to simulate realistic conditions, or they are represented by single spherical harmonics for fundamental physical understanding. However, in reality the dynamics in the lower mantle is much more complicated and these CMB heat flux models are most likely oversimplified. Here we term *alternative* any CMB heat flux pattern imposed on numerical dynamos that does not fall into these two categories, and instead attempts to account for additional complexity in the lower mantle. We review papers that attempted to explain various dynamo-related observations by imposing alternative CMB heat flux patterns on their dynamo models. For present-day Earth, the alternative patterns reflect non-thermal contributions to seismic anomalies or sharp features not resolved by global tomography models. Time-dependent mantle convection is invoked for capturing past conditions on Earth's CMB. For Mars, alternative patterns account for localized heating by a giant impact or a mantle plume. Recovered geodynamo-related observations include persistent morphological features of present-day core convection and the geomagnetic field as well as the variability in the geomagnetic reversal frequency over the past several hundred Myr. On Mars the models aim at explaining the demise of the paleodynamo or the hemispheric crustal magnetic dichotomy. We report the main results of these studies, discuss their geophysical implications, and speculate on some future prospects.

Keywords: Magnetic field; Dynamo; Core-mantle boundary; Heat flux

Introduction

General

Various geophysical observations have been recovered by imposing heterogeneous heat flux patterns on the outer boundary of numerical dynamo simulations. For the Earth, the most popular prescribed heat flux patterns are either proportional to seismic velocity anomalies obtained from tomography models of the lowermost mantle to mimic realistic conditions, or spherical harmonic degree and order 2 which is the dominant term in these tomography models (Aubert et al. 2007, 2008; Bloxham 2002; Christensen and Olson 2003; Davies et al. 2008; Glatzmaier et al. 1999; Gubbins et al. 2007, 2011; Heimpel and Evans 2013; Kutzner and Christensen 2004; Olson and Amit 2014; Olson and Christensen 2002; Olson et al. 2010; Sreenivasan 2009; Sreenivasan and Gubbins 2011; Takahashi et al. 2008). For other planets, various single harmonics are often used, for example degree-1 for Mars (Amit et al. 2011a; Dietrich and Wicht 2013; Stanley et al. 2008) and degree-2 for Mercury and Saturn (Cao et al. 2014; Stanley 2010, respectively), reflecting the low-resolution information on planetary deep interiors. Various single harmonics were imposed for the geodynamo as well in order to obtain fundamental physical understanding of the complex dynamo simulations (e.g., Glatzmaier et al. 1999).

*Correspondence: Hagay.Amit@univ-nantes.fr
[1] CNRS UMR 6112, Université de Nantes, Laboratoire de Planétologie et de Géodynamique, 2 rue de la Houssinière, Nantes, F-44000, France
Full list of author information is available at the end of the article

Inferring core-mantle boundary (CMB) heat flux from tomography models relies on the assumption that seismic and thermal anomalies in the lowermost mantle are highly correlated. However, this idealized linear relation may not hold in reality. Observational and numerical studies of the lower mantle suggest that the structures and dynamics there are far more complex. First, non-thermal contributions (e.g., compositional, phase changes) perturb the idealized linear seismic-thermal mapping (Bull et al. 2009; Deschamps et al. 2012; Lay et al. 2008; Nakagawa and Tackley 2008; Tackley 2011; Trampert et al. 2004). Second, while the spatial resolution inherent to tomographic models in the lowermost mantle (e.g., Lekic et al. 2012) exceeds the resolution of the observed core field, strong lateral gradients of shear wave velocities are not captured. As revealed by detailed waveform analyses at several locations, boundaries of large low shear-wave velocity provinces (LLSVPs) might however be very sharp (e.g., Ni et al. 2005; To et al. 2005). Similarly, synthetic single harmonic patterns for planetary mantle heterogeneity, for example for the CMB conditions that prevailed during the paleo dynamo of Mars, are oversimplified. Even if the Martian anomaly was indeed large-scale (Elkins-Tanton et al. 2005; Harder and Christensen 1996; Ke and Solomatov 2006; Roberts and Zhong 2006; Roberts et al. 2009), it was likely more complex than a single harmonic pattern. Note finally that simulating the geodynamo at earlier times requires information about the time-dependent mantle convection pattern, which is not witnessed by present-day tomography (Yoshida and Santosh 2011; Zhang and Zhong 2011; Zhang et al. 2010; Zhong et al. 2007).

Here we term any CMB heat flux pattern that is neither tomographic nor single harmonic as *alternative*. For the Earth, the alternative patterns include those that account for non-thermal effects or non-resolved small scales in various ways (Amit and Choblet 2009, 2012; Amit et al. in press) and those that model the mantle heterogeneity in the past hundreds of Myr in various ways (Amit and Olson 2015; Olson et al. 2013). For Mars, the alternative patterns are obtained by modeling localized mantle heating induced by a mantle plume (Sreenivasan and Jellinek 2012) or a giant impact (Kuang et al. 2014; Monteux et al. 2015).

Figure 1a illustrates some proposed dynamical scenarios of Earth's lower mantle that result in alternative CMB heat flux patterns (see also, e.g., Lay et al. 2008). Subducting slabs bring cold material to the CMB and locally increase the heat flux. Time-dependent plate motions therefore change the location of these large CMB heat flux regions. Further complications arise from the presence of post-perovskite phase transition (or even its double crossing) in the slab reservoirs of the lowermost mantle. LLSVPs may represent thermochemical piles of a not only hot but also compositionally different material (e.g., Trampert et al. 2004). Growth and collapse of these thermochemical piles, as observed in analog experiments (Davaille 1999), may yield temporal changes in the total heat loss through the CMB and the amplitude of the lateral heterogeneity. Ultra low velocity zones (ULVZs) at the edges of LLSVPs (McNamara et al. 2010) form hot regions that are too narrow to be captured by global large-scale tomography models.

Figure 1b illustrates the effects of localized mantle heating on Mars' CMB heat flux. Giant impacts heat the mantle and reduce the CMB heat flux right below the impact site. Likewise, mantle plumes that originate at the lowermost mantle and may have produced extensive volcanism such as Tharsis are also potential zones of reduced CMB heat flux. It may also be naively expected that core heating by impacts would yield a CMB heat flux increase. However, core impact heating leads to the formation of a hot layer at the top of the core (within 10 kyr) which prevents the core from cooling (Arkani-Hamed 2012; Arkani-Hamed and Olson 2010; Roberts and Arkani-Hamed 2014). Thus, core impact heating could inhibit the dynamo generation during a timescale that is governed by the efficiency of the surrounding mantle to extract the impact induced core thermal anomaly (from several kyr up to 100 Myr).

Numerical simulations of mantle convection may shed light on the relation between the observed seismic anomalies and the CMB heat flux heterogeneity. Nakagawa and Tackley (2008) assumed a linear equation of state to relate their models' thermal, mineral, and chemical anomalies with seismic anomalies. Their purely thermal case gives nearly perfect linear relation between seismic and thermal anomalies, whereas adding post-perovskite effects breaks the linearity but maintains a unique relation (Fig. 2a). The situation is more complicated when chemical anomalies are accounted for; when the density contrast is large enough, a parallel branch appears and the thermal-seismic relation becomes non-unique (Fig. 2b). Implementation of the results of Nakagawa and Tackley (2008) might be problematic because due to limited vertical resolution global tomographic models do not sample precisely the CMB but rather a vertically averaged region above it.

The outline of this review paper is as follows. In the "Alternative models of core-mantle boundary heat flux" subsection, we introduce motivations for alternative CMB heat flux models. Related dynamo properties inferred from observations are listed in subsection "Relevant observed planetary dynamo properties" . In the section "Methods" , we recall the governing equations and control parameters of numerical dynamo simulations. We describe the incorporation of mantle control effects by imposing an outer thermal boundary condition. In the section "Review" , we describe the results of papers that

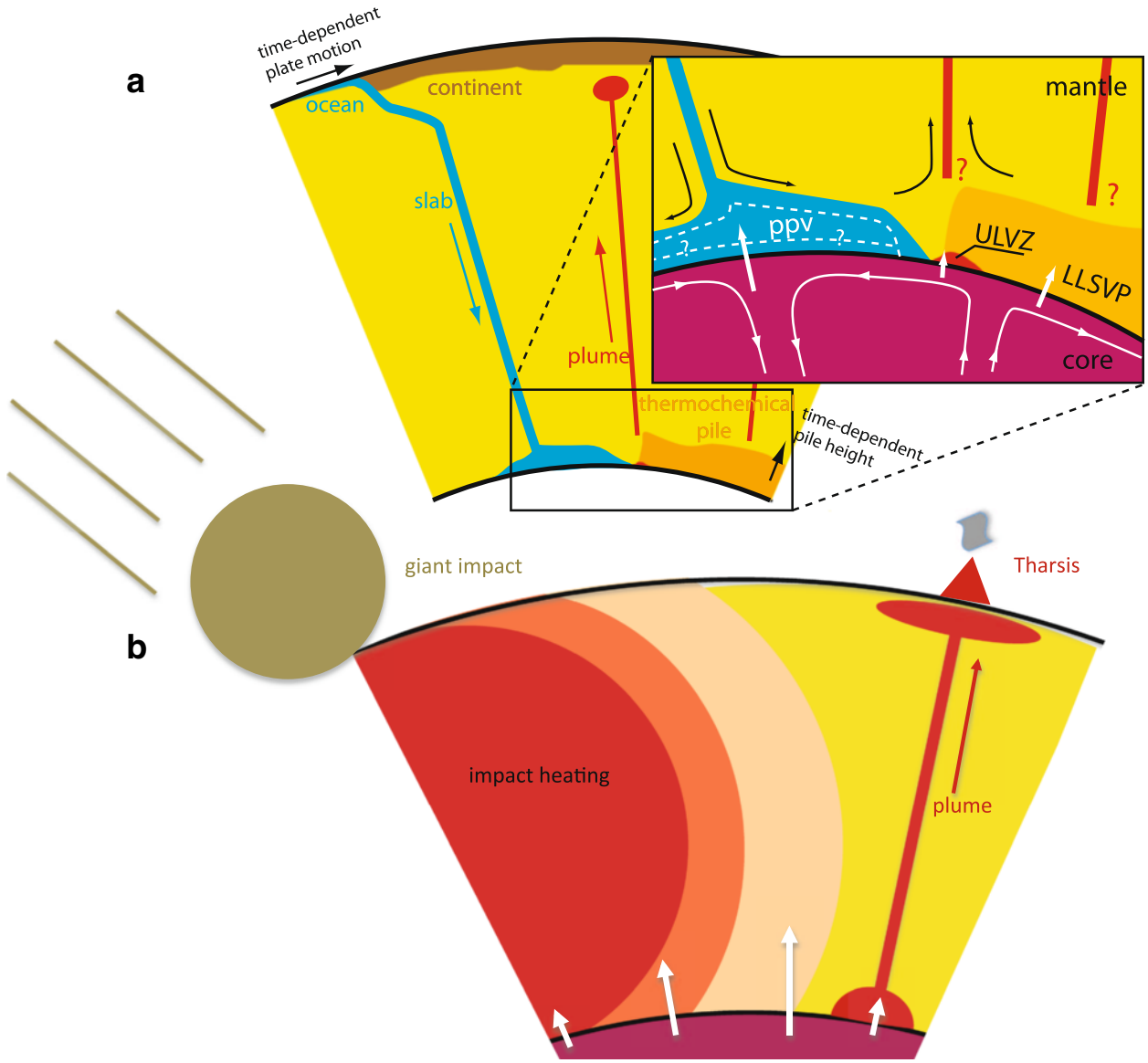

Fig. 1 Cartoons showing various possible dynamical complexities in the Earth's **a** and Mars' **b** lowermost mantles that may motivate modeling of alternative CMB heat flux models

imposed alternative outer boundary conditions on numerical dynamos. For each of these papers, we specify the procedure used to construct the alternative CMB heat flux model and we report how the perturbation from the conventional reference pattern affected the resulting planetary dynamo features. We discuss the results in the subsection "Discussion", and we propose some future prospects in subsection "Future prospects".

Alternative models of core-mantle boundary heat flux

The existence of the post-perovskite phase transition (Murakami et al. 2004; Oganov and Ono 2004) was invoked to explain the seismic heterogeneity of the lowermost mantle (Lay et al. 2006). Post-perovskite is needed to explain core-reflected (Hernlund et al. 2005) and diffracted (Cobden et al. 2012) waves. It may also be a good candidate for the D" discontinuity, at least in regions where P- and S-waves have opposite signs (Cobden and Thomas 2013). In contrast, in probabilistic tomography models the thermal distribution is similar with and without post-perovskite (Mosca et al. 2012). Mantle convection simulations that incorporate post-perovskite effects indicate that its presence affects mantle dynamics (Cizkova et al. 2010; Nakagawa and Tackley 2011) and distorts the thermal-seismic relation from its linearity (Nakagawa and Tackley 2008).

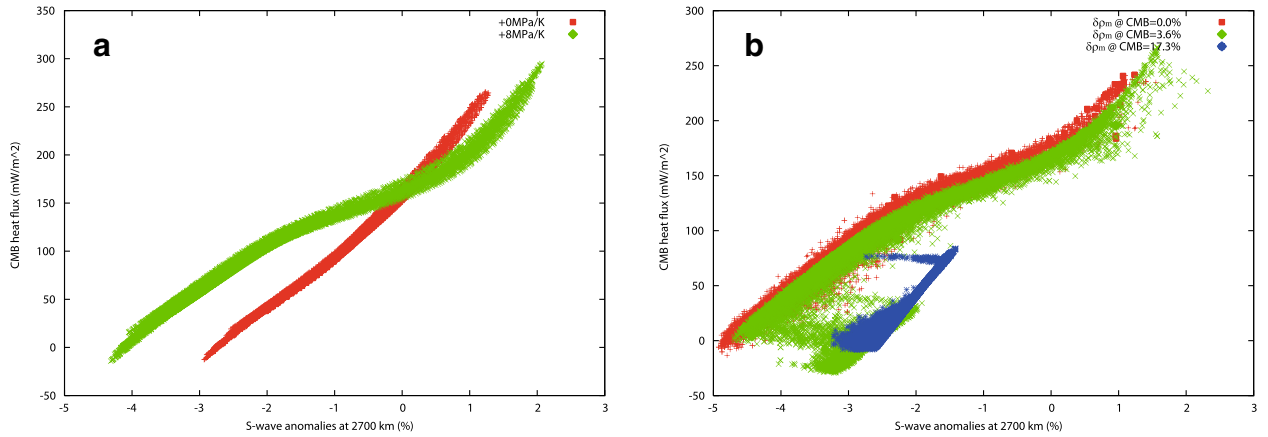

Fig. 2 Scatter plots of CMB heat flux anomalies vs. seismic shear velocity anomalies at the lowermost mantle based on mantle convection simulations. **a** Isochemical cases without (*red*) and with (*green*) post-perovskite. **b** Thermochemical cases with various density contrasts $\delta\rho_m$ at the CMB. From Nakagawa and Tackley (2008)

Sharp margins of LLSVPs were suggested by local studies of the lowermost mantle (Ni et al. 2002; To et al. 2005; Wang and Wen 2007). Dynamical models indicate that ULVZs likely correspond to the hottest regions of LLSVPs (McNamara et al. 2010). Thin hot narrow regions on the edges of the LLSVPs were identified in two end-member models of lower mantle dynamics (Bull et al. 2009). The low spatial resolution of global tomography models excludes such short wavelength features (e.g., Ritsema et al. 2007).

LLSVPs are better explained if a compositional component is also present (Deschamps et al. 2012; Mosca et al. 2012; Trampert et al. 2004). These structures could be primitive or may consist of recycled crustal material, although the seismic sensitivity of mantle material indicates that the latter is less likely (Deschamps et al. 2012). By taking into account seismic normal modes, Ishii and Tromp (1999) provided an independent constraint on mantle density distributions, which can be used to resolve thermal and compositional contributions to seismic anomalies, as done by probabilistic tomography studies (Mosca et al. 2012; Trampert et al. 2004).

One obvious motivation to consider alternative CMB heat flux patterns is the time-dependence of mantle dynamics. Global plate motion models indicate that the distribution of continents has evolved from a spherical harmonic degree-1 heterogeneity before the breakup of supercontinent Pangea to its present-day degree-2 structure (Seton et al. 2012). Some mantle convection models constrained by reconstructed time-dependent plate motions suggest that the supercontinent formation and breakup was accompanied by substantial change in mantle convection pattern (Zhang and Zhong 2011; Zhang et al. 2010; Zhong et al. 2007). According to these dynamical models, the low seismic velocity structures below the Pacific and Africa predate and postdate, respectively, the Pangea breakup (McNamara and Zhong 2005; Zhang et al. 2010). These time-dependent mantle convection patterns would inevitably correspond to time-dependent CMB heat flux with patterns distinctively different from that inferred from present-day tomography models.

In contrast, the pattern of LLSVPs has been interpreted as a root mantle structure that prevailed for several hundreds of Myr (Burke 2011; Burke et al. 2008; Dziewonski et al. 2010). Evidence for long-lived mantle structure comes from hotspot reconstructions (Torsvik et al. 2006) and paleomagnetic pole locations that indicate substantial true polar wander in the Mesozoic (Courtillot and Besse 1987). The dynamical origin of this (stationary) degree-2 pattern may be two mantle superplumes (Romanowicz and Gung 2002; Torsvik et al. 2010), plume clusters (Schubert et al. 2004) or dense chemical piles above the CMB (McNamara and Zhong 2005; Tackley 2002; Tan and Gurnis 2007). Permanent or not, the thermochemical piles are clearly dynamic and respond to changes in the global mantle circulation, through variations in their footprints above the CMB and their height in the lower mantle. Variations in either or both of these would affect the mean CMB heat flux and the amplitude of its heterogeneity.

Alternative CMB heat flux models were also constructed for planets other than the Earth. It has been argued that the emergence of the Tharsis volcanic complex coincided with the termination of the Martian dynamo (Jellinek et al. 2008; Johnson and Phillips 2005; Lillis et al. 2008). Mars' mantle may contain a single huge plume (Harder and Christensen 1996; Srámek and Zhong 2010). If Tharsis emerged from such a deep mantle plume, then it may indeed have affected the thermal heterogeneity on Mars' CMB.

Another possible scenario is localized mantle heating by giant impacts. This process enhances the iron/silicate separation and modifies the heat repartition between the mantle and the core. Thus, large impacts potentially affected the efficiency of core cooling and dynamo activity during (Monteux et al. 2011, 2012) or after terrestrial core formation (Glenn Sterenborg and Crowley 2013; Ke and Solomatov 2009; Monteux and Arkani-Hamed 2014; Monteux et al. 2013; Reese and Solomatov 2010). This large-scale heating also strongly influences mantle dynamics (Reese et al. 2002; Roberts and Arkani-Hamed 2012; Roberts and Barnouin 2012; Watters et al. 2009) and hence the heat repartition in the deepest part of terrestrial bodies. The onset or demise of terrestrial dynamos were modeled by giant impacts (Arkani-Hamed and Olson 2010; Kuang et al. 2014; Monteux and Arkani-Hamed 2014; Monteux et al. 2013; Roberts et al. 2009). Large impacts heated Mars' mantle below the impact site, with the heated volume depending mostly on the impactor's size and velocity (Pierazzo et al. 1997; Tonks and Melosh 1993). The impact-driven heating may be modeled by a uniform spherical temperature increase with rapid temperature decrease away from the isothermal sphere (Monteux et al. 2007, 2013; Senshu et al. 2002). Hence, for large impacts, the CMB heat flux may be affected.

Giant impacts may also have affected the morphology of the Martian paleomagnetic field. These events were invoked to explain the Martian and lunar topographic hemispheric dichotomies (Jutzi and Asphaug 2011; Marinova et al. 2008; Nimmo et al. 2008). Numerical dynamos with a synthetic Y_1^0 heat flux pattern lead to magnetic fields concentrated at the large heat flux hemisphere (Amit et al. 2011a; Dietrich and Wicht 2013; Stanley et al. 2008). Giant impacts may produce a similar effect with a more realistic CMB heat flux pattern (Monteux et al. 2015).

Relevant observed planetary dynamo properties

Alternative (or any) heterogeneous CMB heat flux is expected to influence the dynamo on very long timescales (Olson and Christensen 2002), but some statistical preference can already be detected on shorter timescales (Amit et al. 2010a; Bloxham 2002). Stronger heat flux heterogeneity amplitudes increase the probability of a high correlation between a dynamo property and its mantle-driven long-term average (Aubert et al. 2007). If the heterogeneity amplitude is very large compared to the mean superadiabatic CMB heat flux, locking may occur and a mantle signature may appear in a snapshot (Willis et al. 2007).

Because neither the dynamo equations nor the geometry of planetary outer cores contain any special longitude, any persistent deviation of a dynamo property from axisymmetry can only be explained by boundary heterogeneity. In contrast there are special latitudes, obviously the geographic equator and poles, but also the latitude of the tangent cylinder (Aurnou et al. 2003). However, there is no preferred hemisphere (neither in the dynamo equations nor in the geometry of planetary outer cores), so any persistent deviation of a dynamo property from equatorial symmetry may also require boundary heterogeneity. Below we list the main dynamo-related observations that motivated imposing heterogeneous CMB heat flux, in particular alternative patterns.

The primary dynamo observation is the observed magnetic field at the surface, from which a truncated (or large-scale) part can be downward continued to model the radial magnetic field on the CMB. Many studies attempted to reproduce the locations of high-latitude intense geomagnetic flux patches. The existence of two of these prominent geomagnetic field features at each hemisphere (Jackson et al. 2000) is consistent with the Y_2^2 dominance of the lowermost mantle seismic heterogeneity (e.g., Masters et al. 2000). The longitudes of the flux patches and the large seismic shear velocity structures seem to be correlated (Gubbins 2003), although some patches exhibit significant mobility (Amit et al. 2011b; Korte and Holme 2010). The time-average radial field of the dynamo model of Aubert et al. (2008) decently reproduces the longitudes of the flux patches in the paleomagnetic field (Kelly and Gubbins 1997). However, a shift between the locations of the large heat flux structures and the patches was observed, with the shift value depending on the dynamo internal parameters (Aubert et al. 2007; Olson and Christensen 2002; Takahashi et al. 2008). Alternatively, some geomagnetic (or paleomagnetic) spectral information, e.g., the number of patches at each hemisphere (corresponding to the dominant order), may be used as an observational constraint (Amit and Choblet 2009).

While high-latitude intense flux patches near the edge of the tangent cylinder (Aurnou et al. 2003) are a robust feature of dipole-dominated numerical dynamos (Christensen et al. 1998), the observed intense geomagnetic flux patches at low-latitude (Jackson 2003) are less characteristic of these models. The morphological criteria for Earth-like dynamos proposed by Christensen et al. (2010) identify well magnetic field models that resemble the geomagnetic field, but these criteria contain no information about the latitudinal distribution of magnetic flux. Alternative CMB heat flux heterogeneity offers a ready explanation for localized low-latitude intense flux patches (Amit and Choblet 2012; Amit et al. in press). However, such flux patches are not necessarily connected to boundary heterogeneity. Mobile low-latitude flux patches are seen in numerical dynamos without boundary heterogeneity when a strong enough influence

of rotation on outer core convection is present (Wicht et al. 2011).

Other geodynamo properties apart from the magnetic field may also be used as observational constraints to dynamo models with heterogeneous CMB heat flux. For example, core flow models inverted from the geomagnetic secular variation (Holme 2007) show active Atlantic vs. quiet Pacific hemispheres (Amit and Olson 2006; Aubert et al. 2013; Gillet et al. 2009; Holme and Olsen 2006; Hulot et al. 2002). In addition, the seismic velocity, anisotropy, and attenuation of the inner core exhibit an east-west hemispheric dichotomy (Tanaka and Hamaguchi 1997), although these three seismic properties may sample different parts of the inner core (Deuss 2014; Irving and Deuss 2011). Aubert et al. (2008) recovered the observed patterns of the paleomagnetic field and the inner core hemispheric dichotomy in the corresponding time-average quantities of their dynamo model. The inner core hemispheric dichotomy may indeed be mantle-driven (Aubert et al. 2008; Gubbins et al. 2011), or alternatively independent inner core dynamics (Alboussiére et al. 2010; Monnereau et al. 2010) may produce anomalous bouyancy flux that would affect the outer core dynamics and the properties of the CMB (Aubert et al. 2013; Olson and Deguen 2012).

On much longer timescales of hundreds of Myr, the enigmatic variability of the geomagnetic reversal frequency may constrain changes in mantle conditions. In particular, the existence of long superchrons of tens of Myr in which no reversal was found in the paleomagnetic record in contrast to periods of hyper-reversing behavior (Gradstein et al. 2012; Merrill et al. 1998) is difficult to reconcile without time-dependent CMB conditions (Amit and Olson 2015; Biggin et al. 2012; Olson et al. 2013). In mantle convection simulations constrained by reconstructed plate motions the timing of the Kiaman Reversed Superchron (KRS) at around 270–315 Ma coincides with the low mean and equatorial CMB heat flux (Zhang and Zhong 2011). However, fast plate motions during the most recent Cretaceous Normal Superchron (CNS) may result in large CMB heat flux and frequent reversals (Olson et al. 2013).

Strong crustal magnetic field measured by Mars Global Surveyor is suggestive of a core dynamo that ceased at some time during the Noachian (Acuña et al. 2001; Langlais and Purucker 2007; Lillis et al. 2008; Milbury et al. 2012). Localized mantle heating may have affected the efficiency of the dynamo generation on Mars. A strong mantle plume rooted at the CMB could have terminated the Martian dynamo (Sreenivasan and Jellinek 2012). Alternatively, if the Martian dynamo was subcritical (Kuang et al. 2008), a moderate CMB heat flux anomaly induced by a giant impact could have stopped the dynamo (Kuang et al. 2014).

It has been proposed that the hemispheric dichotomy in Mars' crustal magnetic field was caused by heterogeneous CMB heat flux when the Martian paleo dynamo operated (Stanley et al. 2008). The magnitude of this dichotomy (Amit et al. 2011a) is recovered only with strongly convecting reversing dynamo models (Dietrich and Wicht 2013). Thus, in order to record hemispheric magnetization, the Martian crust should have cooled over a shorter period than the typical chron time (Lebrun et al. 2013), which poses a constraint on the feasibility of the hemispherical dynamo scenario for explaining the hemispheric dichotomy in Mars' crustal magnetic field (Dietrich and Wicht 2013; Monteux et al. 2015).

Methods

The following set of self-consistent non-dimensional Boussinesq (i.e., incompressible) magnetohydrodynamics equations for dynamo action due to thermochemical convection of an electrically conducting fluid in a rotating spherical shell were solved (e.g., Olson et al. 1999):

$$E\left(\frac{\partial \vec{u}}{\partial t}+\vec{u}\cdot\nabla\vec{u}-\nabla^2\vec{u}\right)+2\hat{z}\times\vec{u}+\nabla P = Ra\frac{\vec{r}}{r_o}T+\frac{1}{Pm}(\nabla\times\vec{B})\times\vec{B} \tag{1}$$

$$\frac{\partial \vec{B}}{\partial t}=\nabla\times(\vec{u}\times\vec{B})+\frac{1}{Pm}\nabla^2\vec{B} \tag{2}$$

$$\frac{\partial T}{\partial t}+\vec{u}\cdot\nabla T=\frac{1}{Pr}\nabla^2 T+\epsilon \tag{3}$$

$$\nabla\cdot\vec{u}=0 \tag{4}$$

$$\nabla\cdot\vec{B}=0 \tag{5}$$

where $\vec{u}$ is the velocity, $\vec{B}$ is the magnetic field, T is co-density (Braginsky and Roberts 1995), t is time, $\hat{z}$ is a unit vector in the direction of the rotation axis, P is modified pressure which contains centrifugal effects, $\vec{r}$ is the position vector, r_o is the core radius, and ϵ is co-density source or sink. Four internal non-dimensional parameters in (1)–(5) control the dynamo action. The Ekman number represents the ratio of viscous and Coriolis forces

$$E=\frac{\nu}{\Omega D^2} \tag{6}$$

where ν is kinematic viscosity. The Prandtl number is the ratio of kinematic viscosity to thermal diffusivity κ

$$Pr=\frac{\nu}{\kappa} \tag{7}$$

and the magnetic Prandtl number is the ratio of kinematic viscosity to magnetic diffusivity λ

$$Pm=\frac{\nu}{\lambda} \tag{8}$$

The strength of buoyancy force driving the convection relative to retarding forces is represented by the

Rayleigh number. When the CMB heat flux is strongly superadiabatic, *Ra* can be defined based on the mean CMB heat flux q_0 as (Olson and Christensen 2002)

$$Ra = \frac{\alpha g_0 q_0 D^4}{k\kappa\nu} \tag{9}$$

where α is thermal expansivity, g_0 is gravitational acceleration on the outer boundary at radius r_o, D is shell thickness, and k is thermal conductivity. The heat flux based *Ra* (9) was used with either generic thermochemical convection (Amit and Choblet 2009; Amit et al. in press; Amit and Choblet 2012) or purely thermal convection (Monteux et al. 2015). Alternatively, when convection is dominantly chemical, *Ra* can be defined based on the rate of light elements release into the outer core due to inner core freezing as (Olson 2007a)

$$Ra = \frac{\beta g_0 D^5 \dot{\chi}}{\kappa\nu^2} \tag{10}$$

where $\dot{\chi}$ is the time rate of change of the light element concentration (mixing ratio) in the outer core due to inner core growth. The mixing ratio based *Ra* (10) was invoked with dominantly (or purely) chemical convection (Amit and Olson 2015; Olson et al. 2013). The final internal control parameter is ϵ, the sink (or source) term that appears in the co-density equation (Christensen and Wicht 2007), which parameterizes the effects of mixing of light elements in the outer core due to inner core freezing, secular cooling of the outer core, and radioactivel heat sources.

Various alternative CMB heat flux models were imposed on the outer boundary of the dynamo models. In the "Review" section below, we describe in details the procedures for their constructions. The non-dimensional heat flux anomaly amplitude is classically defined in numerous studies by the peak-to-peak difference normalized by twice the mean value (e.g., Olson and Christensen 2002) as

$$q^* = \frac{q_{\max} - q_{\min}}{2q_0} \tag{11}$$

When the CMB heat flux is localized (11) appears to be inappropriate, hence various alternative measures were proposed. Sreenivasan and Jellinek (2012) proposed their control parameter f as the peak-to-background difference normalized by the background heat flux H_B

$$f = \frac{q_B - q_{\min}}{q_B} \tag{12}$$

They also defined the ratio of the average heat flux, either over the plume footprint or over the entire CMB, to the background heat flux, i.e. $\bar{q}_{\text{plume}}/q_B$ or $\bar{q}_{CMB}/q_B$, respectively (Sreenivasan and Jellinek 2012). Kuang et al. (2014) defined their control parameter ϵ_l as the relative post-impact heterogeneity amplitude, as in (12). In contrast, according to the model of mantle heating by impact of Monteux et al. (2015), in the vicinity of the impact, the lower mantle is heated to the core temperature and the CMB heat flux becomes zero, whereas away from it the lower mantle temperature is unchanged. Therefore, the control parameter q_0^r of Monteux et al. (2015) is based on the portion of the CMB heated by the impact

$$q_0^r = \frac{q_0^h - q_0}{q_0^h} \tag{13}$$

where q_0^h and q_0 are the pre- and post-impact mean CMB heat flux values, respectively.

To dimensionalize the dynamo models output, D, D^2/ν, and $\sqrt{\rho\mu_0\lambda\Omega}$ were used to scale length, time, and magnetic field, respectively, where ρ is the fluid density and μ_0 the permeability of free space. Co-density is scaled either by Dq_0/k when (9) is used or by $\rho\beta D^2\dot{\chi}/\nu$ when *Ra* is defined by (10). For studying the present-day geodynamo an Earth-like inner-outer core radii ratio of $r_i/r_o = 0.35$ was applied (Amit and Choblet 2009, 2012; Amit et al. in press). A smaller ratio of $r_i/r_o = 0.2$ was applied for Mars (Monteux et al. 2015) to approach no inner core conditions while avoiding numerical instability. The past geodynamo was modeled with a variable aspect ratio based on thermal history modeling (Olson et al. 2013). Numerical dynamos with rigid insulating boundary conditions were analyzed. Overall, the models differ in the imposed outer boundary heat flux pattern, the amplitude of its variation and the convection vigor and style—all of these choices depend on the particular geophysical application.

Parametric studies of numerical dynamos found two main types of solutions: non-reversing dipole-dominated and reversing multipolar (Christensen and Aubert 2006; Kutzner and Christensen 2002; Olson and Christensen 2006). Careful choice of control parameters may yield some "Earth-like" overlap of dipole-dominated reversing dynamos (Olson 2007a; Wicht et al. 2009). In this review, studies that focus on morphological features of the present-day field had dipole-dominated non-reversing models as a reference state, whereas in studies of reversal frequency either reversing dynamos or models of both types were analyzed. Both types of solutions were examined in the context of the paleo dynamo of Mars. Table 1 summarizes the control parameters, convection styles, inner to outer core ratios, and dynamo types in the papers reviewed here.

Review

To our best knowledge, only eight papers have examined the effects of alternative (i.e., neither tomographic nor single harmonic) CMB heat flux on planetary dynamos (Amit and Choblet 2009, 2012; Amit and Olson 2015; Amit et al. in press; Kuang et al. 2014; Monteux et al. 2015; Olson et al. 2013; Sreenivasan and Jellinek

Table 1 Summary of dynamo models control parameters, geometry, convection styles and reversibility in the following papers: AC09 (Amit and Choblet 2009), AC12 (Amit and Choblet 2012), ADC15 (Amit et al. in press), ODHZ13 (Olson et al. 2013), AO15 (Amit and Olson 2015), SJ12 (Sreenivasan and Jellinek 2012), KJRF14 (Kuang et al. 2014) and MACLT15 (Monteux et al. 2015). In all papers $Pr = 1$. Control parameters correspond to the definitions in this paper (see "Methods" section), so the values may differ from the original papers if different definitions were used (in particular for the Ekman number). Alternative definitions of CMB heat flux heterogeneity amplitudes q^*_{eff} (termed here *effective*) include f of SJ12 (12), ϵ_l of KJRF14 (also 12) and q'_0 of MACLT15 (13). The Rayleigh number for SJ12 and KJRF14 is given in terms of the critical value for the onset of convection Ra_c. The time-dependent inner core size in ODHZ13 is determined based on a core evolution model

Paper	E	Ra	Pm	q^*	q^*_{eff}	r_i/r_o	*Conv*	*Rev?*
AC09	$3 \cdot 10^{-4}$	10^6	3	0.5	–	0.35	TC	No
AC12	$3 \cdot 10^{-4}$	$(0.5-1) \cdot 10^6$	$3-7$	$0.5-0.8$	–	0.35	TC	No
ADC15	$3 \cdot 10^{-4}$	$(1-3) \cdot 10^6$	$3-10$	$0.7-1.34$	–	0.35	TC	No
ODHZ13	$5.75 \cdot 10^{-3}$	$(1.5-4) \cdot 10^4$	20	$0.67-1.1$	–	Variable	C	Both
AO15	$(1-6) \cdot 10^{-3}$	$(0.6-18) \cdot 10^5$	20	$0.65-2.22$	–	0.35	C	Both
SJ12	$5 \cdot 10^{-5}$	$12Ra_c$	1	–	$4-29$	0.35	TC	No
KJRF14	$2.6 \cdot 10^{-5}$	$\sim Ra_c$	1	–	$0.05-0.3$	0.31	T	Yes
MACLT15	$(1-3) \cdot 10^{-4}$	$(0.735-4) \cdot 10^7$	3	$0.3-0.8$	$0.04-0.26$	0.2	T	Both

Conv convection type, *T* thermal, *TC* thermochemical, *C* chemical, *Rev?* reversibility

2012). Here we describe for each of these papers the CMB heat flux models that were imposed as outer boundary conditions on the dynamo simulations. Then, for each paper, we compare the results with those obtained with a reference heat flux model (Table 2) and we report the consequences for the resulting dynamo properties.

Lower mantle thermal-chemical-phase heterogeneity and geodynamo morphological features

Here we review the papers by Amit and Choblet (2009), Amit and Choblet (2012), and Amit et al. (in press). As in previous studies, a reference CMB heat flux anomaly of purely thermal origin δq_T was assumed to be linearly proportional to the lowermost mantle seismic shear velocity anomaly δv_s:

$$\frac{\delta q_T}{q_T} \propto \frac{\delta v_s}{v_s} \tag{14}$$

Figure 3a shows the CMB heat flux based on the tomography model of Masters et al. (2000) and (14). Nakagawa and Tackley (2008) found that when incorporating post-perovskite phase transition in their mantle convection models, the δq to δv_s relation becomes an inclined step function (Fig. 2a), with the spreading effect well approximated by a tanh function. Following equation (B8) of Nakagawa and Tackley (2008), Amit and Choblet (2009) attempted to parameterize the thermal-phase interpretation δq_{Tp} as

$$\frac{\delta q_{Tp}}{q_{Tp}} = \frac{\delta q_T}{q_T} + A\left[0.5\left(\tanh\left(-\frac{1}{B}\frac{\delta q_T}{q_T}\right)-1\right)\right] + D \tag{15}$$

Table 2 Summary of dynamo models imposed outer boundary heat flux patterns in AC09 (Amit and Choblet 2009), AC12 (Amit and Choblet 2012), ADC15 (Amit et al. in press), ODHZ13 (Olson et al. 2013), AO15 (Amit and Olson 2015), SJ12 (Sreenivasan and Jellinek 2012), and MACLT15 (Monteux et al. 2015). For each paper, the reference and alternative patterns are given. Tomographic always refers to present-day, HF1 is the time-dependent model of Zhang and Zhong (2011). For more details, see text

Paper	Reference	Alternative
AC09	Tomographic	Thermal + post-perovskite
AC12	Y_2^2	Y_2^2 + ridges
ADC15	Tomographic	Probabilistic tomography
ODHZ13	Tomographic	HF1
AO15	Homogeneous	Rotated Y_2^0
SJ12	Homogeneous	Plume-induced
KJRF14	Homogeneous	Impact-induced
MACLT15	Degree-1	Impact-induced

The non-dimensional parameters in (15) are the amplitude A, the tanh spreading factor B, and the offset D. For a given amplitude A, the spreading factor B is constrained by reaching the tanh asymptote while maintaining an inclined step function (rather than Z-like curve).

Figure 3b shows a heat flux anomaly map that accounts for post-perovskite according to (15). The patterns in Fig. 3a, b are similar, but the relative magnitudes of the positive/negative heat flux structures vary. When the post-perovskite effect is included, the positive structures weaken and spread over larger areas, whereas the negative structures remain strong and more localized (Fig. 3b). This is due to the particular pattern of the tomographic model that contains larger amplitude narrower regions of negative seismic velocity anomalies ($\delta v_s, \delta q_T < 0$) as opposed to broader regions of weaker positive anomalies (Fig. 3a). The tanh function strongly reduces intermediate δv_s while it reduces extreme δv_s more mildly, resulting in a spreading effect acting stronger on the positive δq_T.

Following Aubert et al. (2008), Amit and Choblet (2009) compared three long-term time-average properties of their dynamo models with relevant observations: the radial magnetic field on the outer boundary with the time-average paleomagnetic field over the past 5 Myr (Kelly and Gubbins 1997), the flow at the top of the shell with the core flow model of Amit and Christensen (2008) obtained from inversions of the historical geomagnetic secular variation (Jackson et al. 2000) and averaged over the period 1840–1990, and the inner boundary buoyancy flux with seismic anomalies of the upper inner core (Tanaka and Hamaguchi 1997). As an example, we highlight here the latter comparison (Fig. 4). The inner boundary buoyancy flux is characterized by two isolated positive low-latitude structures both in the thermal case (Fig. 4a, denoted as T) as well as when accounting for post-perovskite (Fig. 4b, denoted as Tp1). In addition, however, the ICB buoyancy fluxes contain other orders. More vigorous convection leads to stronger filtering of the CMB order 2 content and the ICB pattern remains dominantly order 1 (Aubert et al. 2008), whereas slightly supercritical convection leaves the ICB pattern with nearly non-distorted order 2 (Gubbins et al. 2011). Amit and Choblet (2009) found that the ratio of order 1 to order 2 in Fig. 4b is significantly larger than that in 4a. This suggests that accounting for post-perovskite improves the agreement of the dynamo models with the order 1 dominance in seismic properties of the upper inner core (Tanaka and Hamaguchi 1997), although the phase may vary substantially from one dynamo model to another. Amit and Choblet (2009) argued that accounting for post-perovskite also improves the recovery of the Atlantic/Pacific hemispheric dichotomy in core flow activity (Amit and Christensen 2008; Gillet et al. 2009) and the single intense

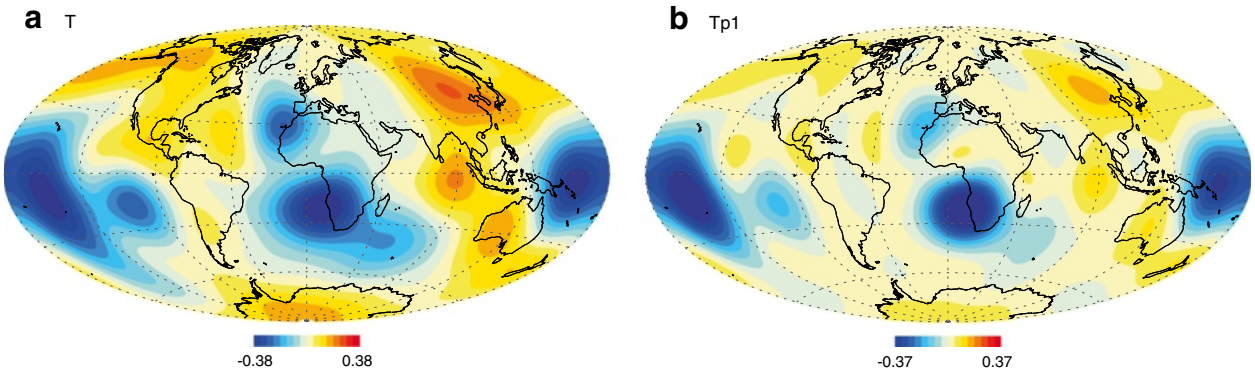

Fig. 3 Non-dimensional CMB heat flux patterns based on the mantle tomography model of Masters et al. (2000): **a** Thermal linear interpretation T and **b** interpretation including a post-perovskite effect Tp1. From Amit and Choblet (2009)

paleomagnetic flux patch in the southern hemisphere (Kelly and Gubbins 1997).

Next, narrow features that are not captured by global tomography models were considered. Lower mantle tomography models are dominated by a Y_2^2 component (e.g., Masters et al. 2000), which is classically interpreted as the largest scale temperature anomaly. Such a pattern was imposed by many authors as heat flux on the outer boundary of their numerical dynamo models (e.g., Aubert et al. 2007; Bloxham 2002; Olson and Christensen 2002; Sreenivasan 2009). Amit and Choblet (2012) used the Y_2^2 pattern as a reference case and superimposed on it low heat flux ridges at the four margins of hot and cold large-scale structures (Table 2). The ridges were modeled using a Gaussian geometry with an amplitude equal to that of the hot large-scale features (Fig. 5).

Figure 6 presents two close-ups of the time-average dynamo model velocity and magnetic field, one on the center of Fig. 5 (i.e., center of a ridge with a positive heat flux anomaly to its east), the other centered on a ridge with a positive heat flux anomaly to its west. In places where a positive heat flux anomaly appears east of the ridge (Fig. 6 left), the poloidal flow dominates and the fluid diverges from the hot ridge. Stronger field appears east of the ridge where cold fluid downwelling concentrates magnetic flux. In contrast, in places where a positive heat flux anomaly appears west of the ridge (Fig. 6 right), the upwelling associated with this ridge is broken at the equator, westward toroidal flow dominates, and the magnetic field exhibits patches of comparable intensity on both sides of the ridge. Note that the fluid upwellings appear very close to the longitudes of the hot CMB heat flux ridges, in contrast to previous studies of numerical dynamos with a Y_2^2 CMB heat flux pattern in which a phase shift was found between the heat flux and the flow structures (Aubert et al. 2007; Olson and Christensen 2002; Takahashi et al. 2008).

Amit and Choblet (2012) interpreted the low-latitude dynamics around the ridge locations by a combined effect of westward drift in the time-average homogeneous dynamo (Aubert 2005) and the steady boundary-driven flow that roughly goes from hot to cold regions (Gubbins 2003). When cold material is east of the ridge the two flows counteract and the ridge acts as a flow barrier, whereas when cold material is west of the ridge both flows are westward and the barrier effect is diminished. Applying these inferences to the tomography model of

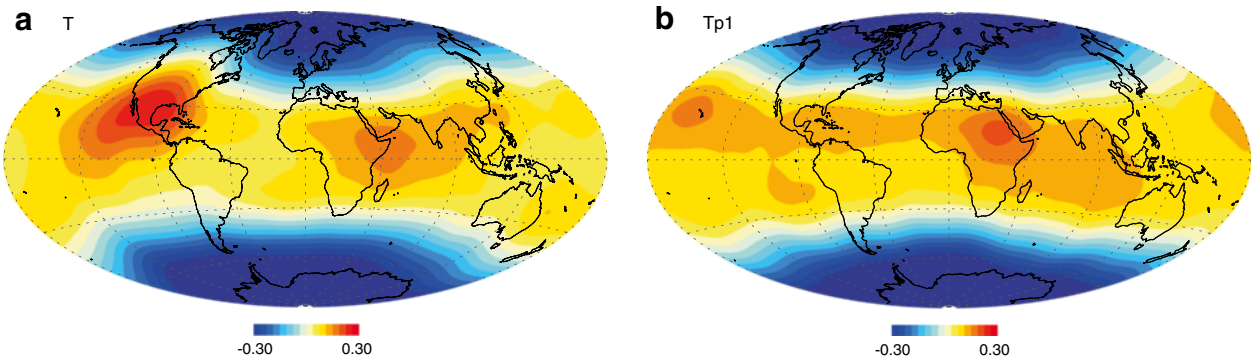

Fig. 4 Time-average inner-core boundary buoyancy flux anomalies normalized by the mean buoyancy flux: **a** Model T and **b** Model Tp1. From Amit and Choblet (2009)

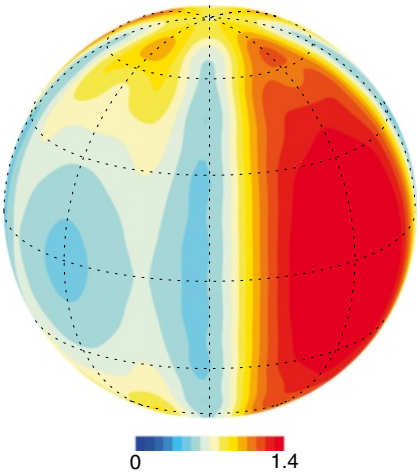

Fig. 5 Non-dimensional CMB heat flux based on a Y_2^2 pattern with narrow hot ridges superimposed on the boundaries between large-scale hot and cold structures. From Amit and Choblet (2012)

Masters et al. (2000), Amit and Choblet (2012) predicted (in a statistical sense) fluid upwelling at the top of the core and a barrier for azimuthal flow below central Asia and the Indian Ocean and below the American Pacific coast. Below east Asia and Oceania and below the Americas they predicted persistent intense low-latitude geomagnetic flux patches. These predictions are in agreement with preferred longitudes of virtual geomagnetic poles during reversals both in paleomagnetic data (Hoffman 1996; Love 1998; Merrill and McFadden 1999) and in tomographic reversing dynamo models (Coe et al. 2000; Kutzner and Christensen 2004). It also resonates with the persistent production of low-latitude geomagnetic flux patches below Indonesia during the historical era (Jackson et al. 2000).

Finally, probabilistic tomography may be used to isolate the thermal component of the observed seismic anomalies. A limitation of the probabilistic tomography models published so far is that only even spherical harmonic degrees are included (Mosca et al. 2012; Trampert et al. 2004). To overcome this problem, Amit et al. (in press) mapped the ratio between shear-wave velocity δlnV_s^e (even degrees) and thermal anomalies δT^e (even degrees) in probabilistic tomography and applied this mapping to a conventional lower mantle seismic tomography model δlnV_s^C (even and odd degrees) to obtain a rescaled thermal anomaly distribution δT^P with both even and odd degrees. Mathematically they wrote

$$\delta T^P = \frac{\delta T^e}{\delta lnV_s^e}\delta lnV_s^C \tag{16}$$

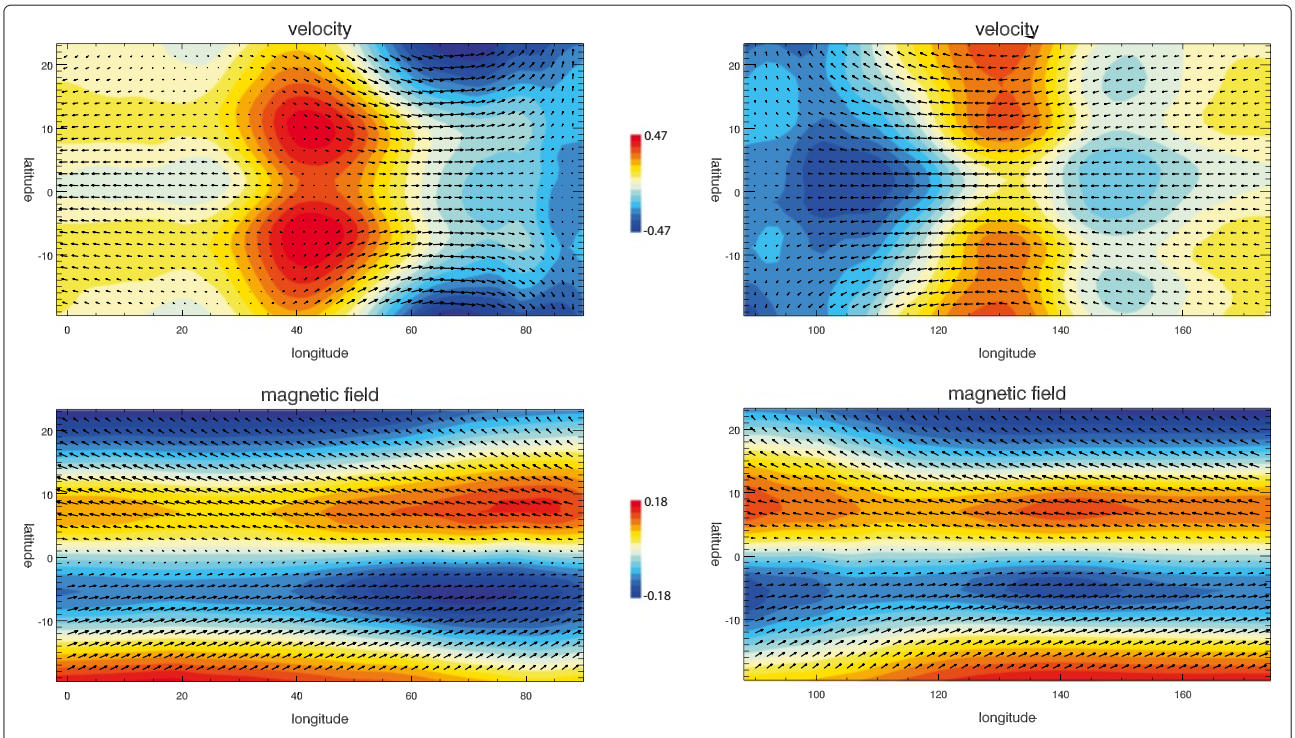

Fig. 6 Zoom into two ridges at low-latitude of the time-average of a dynamo case with imposed CMB heat flux as in Fig. 5, with a positive heat flux anomaly to the east (*left*, where Fig. 5 is centered) and with a positive heat flux anomaly to the west (*right*). Non-dimensional velocity at the *top* of the free stream is shown in the *top* panel, non-dimensional magnetic field in the *bottom* panel. Radial components are in *colors*, tangential components in *arrows*. From Amit and Choblet (2012)

To avoid numerical instabilities at regions where $\delta ln V_s^e$ is low, at each node of the probabilistic tomography model δT^e and $\delta ln V_s^e$ were sampled according to their full probability distribution functions (PDFs) rather than their mean values, resulting in a full PDF of the ratio $\delta T^e / \delta ln V_s^e$. Amit et al. (in press) applied the above procedure on the conventional seismic tomography model of Masters et al. (2000) and the probabilistic tomography model of Mosca et al. (2012) for the seismic and thermal anomalies. The resulting CMB heat flux pattern inferred from probabilistic tomography (Fig. 7) exhibits positive structures mostly concentrated at low latitude.

The dynamo models with an imposed probabilistic tomography heat flux pattern are characterized by stronger magnetic and convective activity at low-latitude than the dynamo models with conventional tomography heat flux. The timeseries of the ratio of RMS low-latitude magnetic flux to RMS high-latitude magnetic flux as well as the ratio of maximum low-latitude magnetic flux to maximum high-latitude magnetic flux (Fig. 8) show larger mean values and much larger temporal fluctuations in the probabilistic dynamo models (Fig. 8b) than those obtained with conventional tomography (Fig. 8a). For comparison, Amit et al. (in press) found that the historical geomagnetic field model *gufm1* (Jackson et al. 2000) exhibits for the period 1840–1990 average RMS and maxima ratios of 0.675 and 0.725, respectively. The higher resolution model *CHAOS-4* (Olsen et al. 2014) for the period 2000–2010 is characterized by somewhat larger average ratios of 0.797 and 0.882, and the average ratios in the lower resolution archeomagnetic field model *Cals3k.3* (Korte et al. 2009) for the past three millennia are 0.470 and 0.648. Accounting for the temporal fluctuations in the dynamo models with the CMB heat flux pattern inferred from probabilistic tomography, any of these models may occasionally recover the observed low- to high-latitude geomagnetic flux ratios.

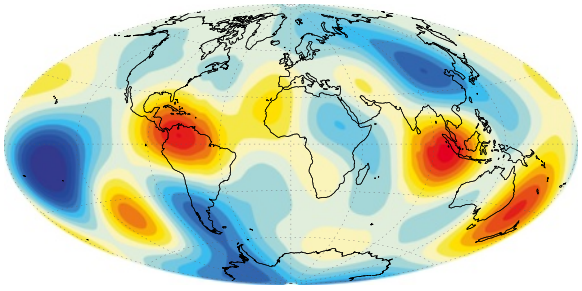

Fig. 7 Non-dimensional normalized CMB heat flux pattern inferred from probabilistic tomography. The same pattern was used for different q^* values (see Table 1), hence the absence of a *color bar*. *Red/blue* denotes positive/negative heat flux anomalies, respectively. From Amit et al. (in press)

Lower mantle history and geomagnetic reversal frequency

Here we review the papers by Olson et al. (2013) and Amit and Olson (2015). Zhang and Zhong (2011) imposed a reconstructed plate tectonics model for the period 0–120 Ma (Lithgow-Bertelloni and Richards 1998) and Atlantic hemisphere continent reconstructions for older periods (Scotese 2001) as a time-dependent mechanical upper boundary condition on their mantle thermochemical convection model to infer the time-dependent CMB heat flux. According to one of the CMB heat flux models of Zhang and Zhong (2011), termed HF1, relatively large/low mean CMB heat flux corresponds to fast/slow plate reconstructions (Lithgow-Bertelloni and Richards 1998; Scotese 2001), respectively. In addition, HF1 includes temporal changes in the heat flux pattern (Fig. 9) and amplitude (Table 1), most notably a transition from degree-1 dominance during Pangea to degree-2 dominance at present.

Olson et al. (2013) imposed snapshots of HF1 (Fig. 9) on chemical convection dominated numerical dynamos. In addition, they accounted for the time-dependent core evolution that is controlled by the mean CMB heat flux. Using thermal history modeling (Labrosse 2003), Olson et al. (2013) determined the time-dependent CMB heat flux and consequently the time-dependent inner core size and inner core boundary buoyancy flux. According to these models, a few tens of Myrs after inner core nucleation outer core convection indeed becomes dominantly chemical. Very high core thermal conductivity (e.g., Pozzo et al. 2012) implies that higher CMB heat flux, radiogenic heating, or some presently unknown form of chemical differentiation in the core would be needed to power the geodynamo prior to inner core nucleation. However, the debate on core thermal conductivity is still ongoing (Zhang et al. 2015). Finally, Olson et al. (2013) also accounted for the observed nearly linear increase in length of day (Williams 2000) to derive a time-dependent rotation rate. Overall, they established the relative temporal evolution of the Rayleigh and Ekman numbers for the period corresponding to the HF1 model.

Olson et al. (2013) compared the time-dependent reversal frequency of two types of dynamo models, one with time-dependent and another with fixed present-day CMB heat flux (both cases include time-dependent core evolution). This comparison allows distinguishing between the direct effects of the CMB heterogeneity and the effects of the core evolution. Figure 10 shows comparison of the reversal frequency of the dynamo models of Olson et al. (2013) with the observed paleomagnetic reversal frequency record (Gradstein et al. 2012). The dynamo model with fixed CMB heat flux is characterized by weaker temporal variability in reversal frequency. In contrast, the dynamo model with time-dependent CMB heat

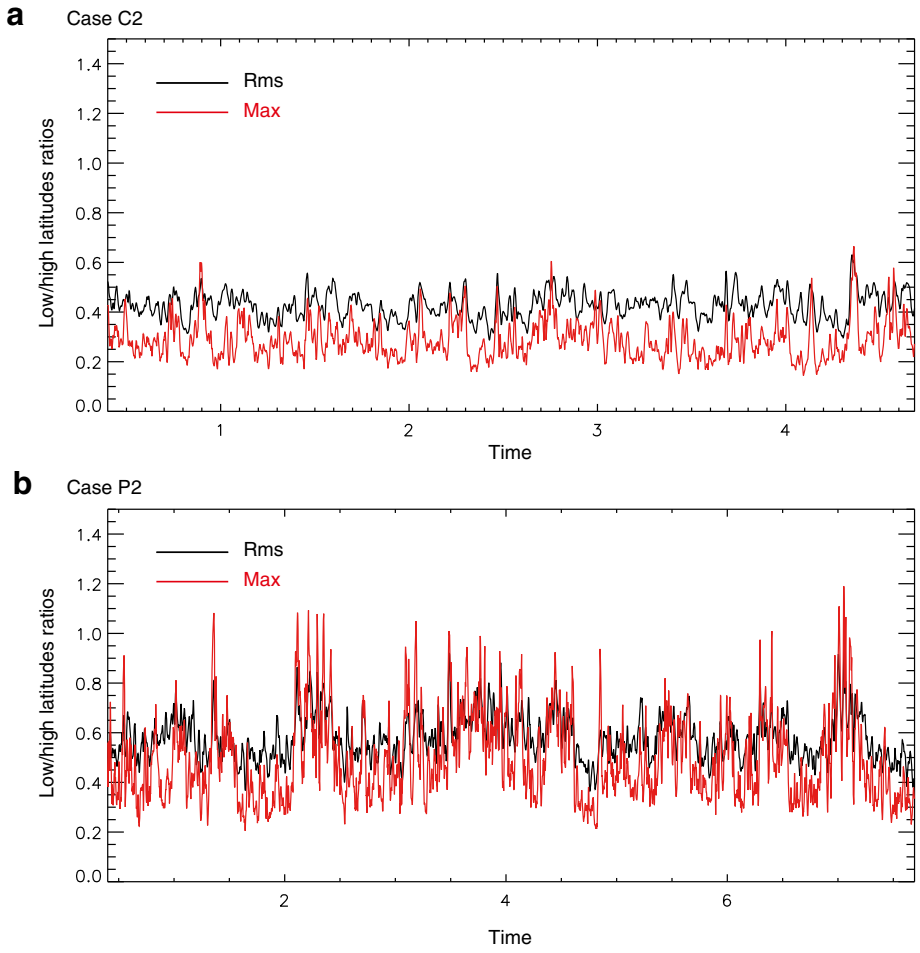

Fig. 8 Timeseries of low/high-latitude magnetic flux ratios for dynamo models with the same control parameters but different outer boundary heat flux patterns, one with a pattern from conventional tomography (**a**, case C2 of Amit et al. in press) and the other with a pattern inferred from probabilistic tomography (**b**, case P2 of Amit et al. in press). *Black/red curves* are RMS/maxima ratios, respectively. From Amit et al. (in press)

flux shows larger reversal frequency fluctuations including superchrons and rather hyper-reversing periods. In particular, at 275 Ma when Pangea was at its height and prior to it, the dynamo model with time-dependent CMB heat flux recovers the low reversal frequency, whereas that is not the case for the dynamo model with fixed CMB heat flux. Olson et al. (2013) argued that the transition from low to high reversal frequency is driven by the supercontinent cycle. Both dynamo models fail to reproduce the robust Cretaceous Normal Superchron at 120 Ma. However, Olson et al. (2013) demonstrated that the reversal frequency is strongly sensitive to mild changes in the CMB heat flux (mean, pattern, and its amplitude).

In contrast, the lower mantle may exhibit a quasi-stationary pattern. Amit and Olson (2015) proposed that the extreme variability in the recorded geomagnetic reversal frequency, from hyper-reversing periods to superchrons, may be explained by lower mantle piles with a fixed lateral pattern but time-dependent height. Amit and Olson (2015) proposed a simple model of the D" layer with fixed temperature difference, conserved volume with time, and a conductive equilibrium. Based on these assumptions, they derived analytically the dependence of the mean CMB heat flux and the amplitude of its lateral heterogeneity on the pile height. They showed that superplume growth increases both the mean CMB heat flux and the amplitude of its lateral heterogeneity, whereas pile collapse decreases these two quantities.

Figure 11 shows the rotated Y_2^0 CMB heat flux pattern based on the model of lower mantle seismic heterogeneity by Dziewonski et al. (2010). The mean heat flux was assumed to be close to the core adiabat, i.e., the dynamo models are dominated by chemical convection. The heterogeneity pattern was generated using spherical harmonics Y_2^0, Y_2^2, and Y_1^1, with relative amplitudes of 10 : 10 : 1, respectively. Amit and Olson (2015) determined the

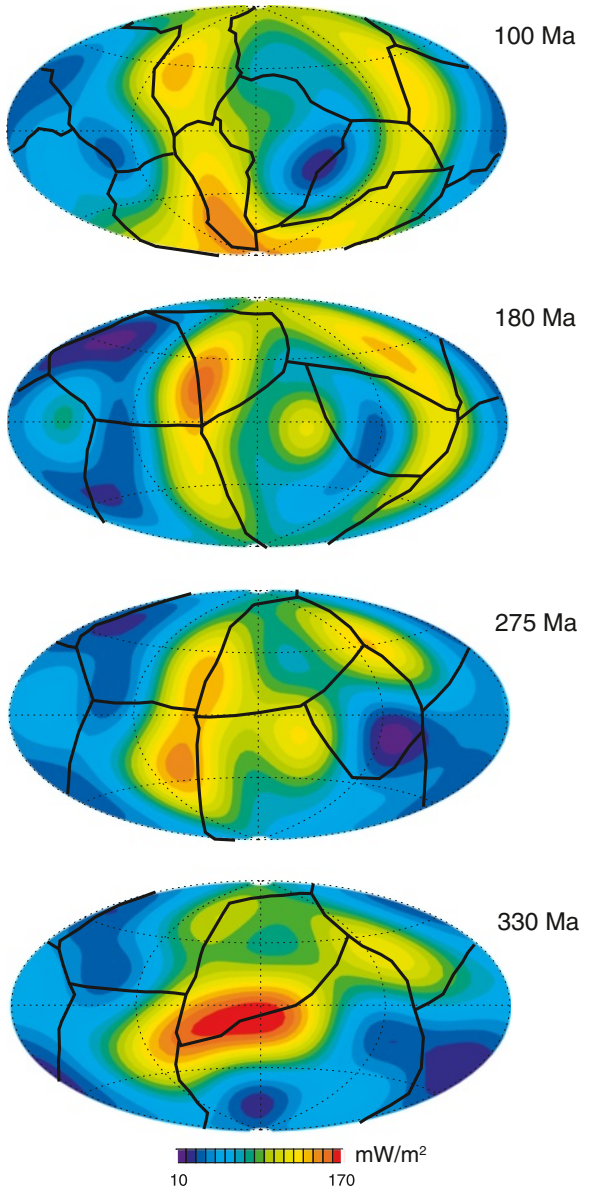

Fig. 9 Snapshots of CMB heat flux (*colors*) and plate boundaries (*solid black lines*) from the mantle history model HF1 of Zhang and Zhong (2011). From Olson et al. (2013)

amplitudes of mean heat flux and heterogeneity in their dynamo models based on their analytical piles model as functions of pile height. In addition, they set the Rayleigh number based on the mean heat flux from their analytical piles model.

Figure 12 shows the non-dimensional reversal frequency as functions of pile height and mean outer boundary heat flux for the rotated Y_2^0 (Fig. 11) dynamos. The error bars correspond to $\sqrt{N}/\tau_d$ (where N is the reversal frequency and τ_d is the dipole free decay time), consistent with a Poisson distribution (Lhuillier et al. 2013). The reversal frequency increases approximately linearly beyond onset. There is a fairly small window separating the pile height that would produce magnetic superchrons and the pile height that would produce hyper-reversing dynamos. A relatively moderate increase of ∼35 % in CMB heat flux corresponds to a transition from dynamo models exhibiting superchrons to those in a hyper-reversing state. Amit and Olson (2015) concluded that pile growth may stimulate polarity reversals, whereas pile collapse may inhibit reversals.

Localized mantle heating and the paleo dynamo of Mars

Here we review the papers by Sreenivasan and Jellinek (2012), Kuang et al. (2014), and Monteux et al. (2015). Sreenivasan and Jellinek (2012) simulated the localized CMB anomaly induced by the mantle plume that produced Tharsis by

$$q = q_{\min} exp\left(-\left[\left(\theta-\theta_p\right)^2/\delta_\theta^2 + \left(\phi-\phi_p\right)^2/\delta_\phi^2\right]\right) \tag{17}$$

where θ and ϕ are latitude and longitude, θ_p and ϕ_p are the corresponding coordinates of the plume center, and δ_θ^2 and δ_ϕ^2 are the corresponding exponential decay coefficients, set to be 15° at the equator. The localized CMB plume-induced heat flux heterogeneity is visualized in the inlet of Fig. 13a.

The dynamo models of Sreenivasan and Jellinek (2012) are strongly supercritical (Table 1), requiring large heterogeneity amplitudes to terminate the dynamo (Fig. 13a). Increasing heterogeneity amplitude attenuates the field and eventually leads to the dynamo failure (Fig. 13b). In addition, it is easier to kill the dynamo if the mantle plume is centered at low-latitude (Fig. 13a).

The underlying mechanism for the demise of the dynamo due to the localized CMB heating is visualized in Fig. 14. The boundary heterogeneity weakens the axial flow and reverses its direction. As a result, the kinetic helicity also weakens significantly. The weakening of helicity reduces the field generation efficiency (Moffatt 1978) and leads to the demise of the dynamo (Sreenivasan and Jellinek 2012).

Kuang et al. (2014) also studied the possibility of Martian dynamo cessation due to localized CMB heating, but by a giant impact. The impact-induced thermal heterogeneity is modeled by shock wave heating emanating from the impact site (Pierazzo et al. 1997; Watters et al. 2009). The temperature rapidly decays from the impact center. In contrast to Sreenivasan and Jellinek (2012), the dynamo models of Kuang et al. (2014) are subcritical with moderate heterogeneity amplitudes of $\epsilon_l \leq 0.3$ (see Table 1). These subcritical dynamos were found to be hemispheric (Kuang et al. 2008), in contrast to other studies that argued that under subcritical conditions helicity generation is

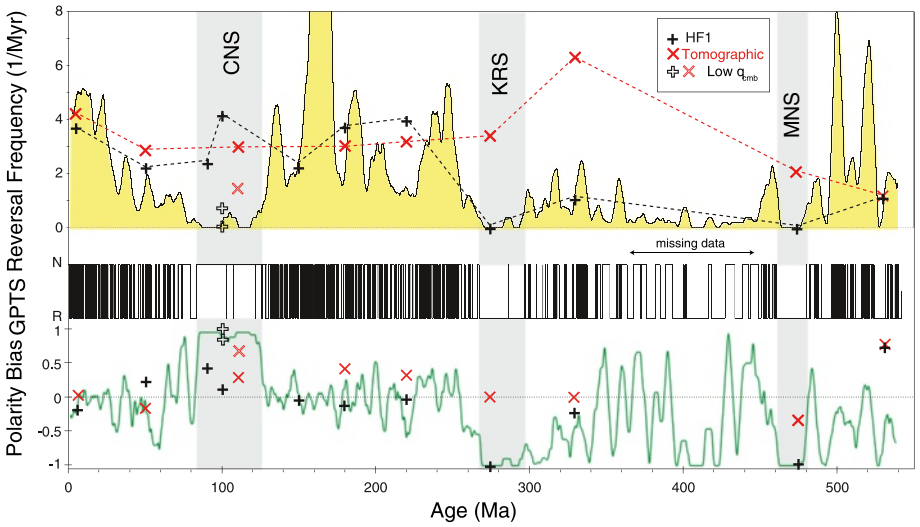

Fig. 10 *Top*: Geomagnetic reversal frequency (*yellow* and *barcode below*) based on the Geomagnetic Polarity Time Scale (GPTS) database of Gradstein et al. (2012) vs. reversal frequency in dynamo models with time-dependent CMB heat flux (*black pluses*) and fixed present-day tomographic pattern (*red crosses*). The Cretaceous Normal Superchron (CNS), Kiaman Reversed Superchron (KRS), and Moyero Normal Superchron (MNS) are *grey shaded*. *Bottom*: Polarity bias, i.e., the difference between time spent in normal and reversed polarities normalized by their sum. From Olson et al. (2013)

more efficient when the field is dipole-dominated (Hori and Wicht 2013; Sreenivasan and Jones 2011).

Kuang et al. (2014) also found that a giant impact at low-latitude and with a large heterogeneity amplitude is more likely to terminate the dynamo. Figure 15 shows that when the impacts where placed at latitude $60°N$ and higher the dynamos survived. The dynamos failed if the CMB heat flux heterogeneity amplitude was larger than a critical value. This critical value decreases with increasing latitude of the impact site. The dynamo failure occurs when the helicity is reduced in the hemisphere where most of the field is expected to be induced.

Localized mantle shock heating by a giant impact could have also altered the morphology of the Martian paleo dynamo. Monteux et al. (2015) uniquely determined the CMB heat flux lateral variations as well as the reduction in the mean CMB heat flux by the size and geographic location of the impactor. Figure 16 shows the CMB heat flux patterns resulting from an impactor of 800 km radius falling on the north pole (left) or the equator (right) of Mars' surface. Because it is thought that there is no inner core in Mars (Breuer et al. 2010; Schubert and Spohn 1990), purely thermal convection was modeled, with a volumetric homogeneous heat source ϵ that compensated for the loss of heat through the outer boundary (Amit et al. 2011a; Dietrich and Wicht 2013). A small inner core corresponding to $r_i/r_o = 0.2$ was retained to avoid numerical instabilities, but the inner boundary was set to be convectively passive (Table 1). Both non-reversing and reversing dynamos were examined.

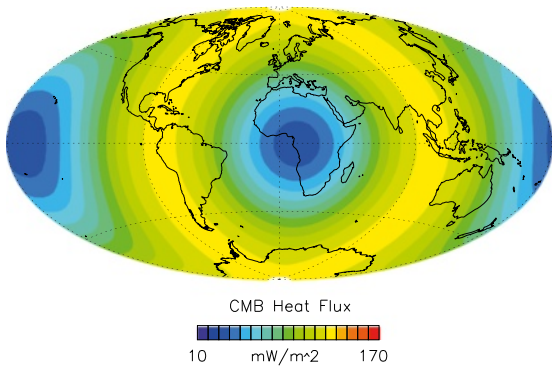

Fig. 11 CMB heat flux pattern in the dual superplume configuration. The mean heat flux is 100 mW/m^2 and the peak-to-peak variation is 60 mW/m^2. From Amit and Olson (2015)

Figure 17 shows the time-average RMS radial field at the CMB and the time-average field intensity at the surface of Mars for a dynamo model with an impactor of radius 800 km falling on the north geographic pole (Fig. 16 left). The impactor yields an hemispheric field similar to those obtained with synthetic Y_1^0 CMB heat flux patterns (Amit et al. 2011a; Dietrich and Wicht 2013; Stanley et al. 2008). Monteux et al. (2015) found that a polar impactor leads to a north-south hemispheric magnetic dichotomy that is stronger than an east-west dichotomy created by an equatorial impactor (in agreement with Amit et al. 2011a, Dietrich and Wicht 2013).

Monteux et al. (2015) found that an impactor radius of about 1000 km could have recovered the magnetic dichotomy observed in the Martian crustal field.

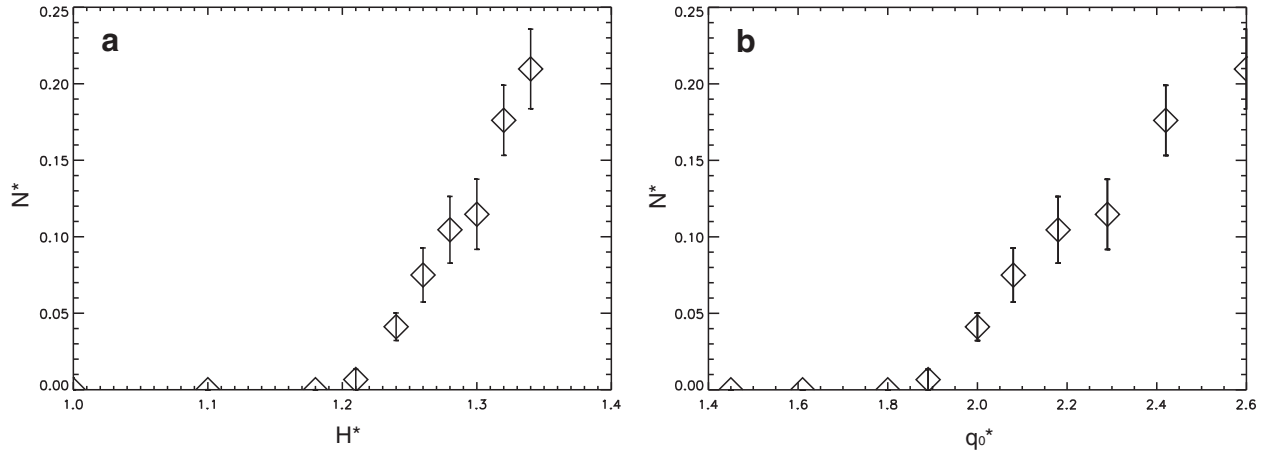

Fig. 12 Non-dimensional reversal frequency vs. non-dimensional pile height **a** and vs. non-dimensional mean CMB heat flux **b** in the set of dual pile (rotated Y_2^0) dynamo models. From Amit and Olson (2015)

However, strong enough magnetic dichotomies were obtained only for frequently reversing dynamos (as in Dietrich and Wicht 2013). Therefore, such dynamos may account for the observed field dichotomy only if very rapid post-impact magma cooling took place (Lebrun et al. 2013).

Conclusions

Discussion

The study of mantle control on planetary dynamos may be classified into three categories. In the first category, numerical dynamos with homogeneous boundary conditions have already reproduced successfully the most fundamental observed geodynamo properties, in particular the dipole dominance of the field (Glatzmaier and Roberts 1997) and its reversibility (Glatzmaier and Roberts 1995). Parametric studies of numerical dynamos show that increasing convection vigor (which is controlled by the mean CMB heat flux) causes a transition from dipole dominated non-reversing to multipolar reversing dynamos (Aubert et al. 2009; Christensen and Aubert 2006; Kutzner and Christensen 2002). The very different magnetic field geometries and amplitudes observed for the various planets and moons (Stevenson 1983) may represent different locations of their dynamos in parameter space with respect to this transition (Olson and Christensen 2006). In the second category, heterogeneous but simplified (i.e., not alternative) boundary conditions may help explain more refined dynamo properties, in particular for the Earth where detailed observations are available. In a third category, numerical dynamos with imposed alternative CMB heat flux can be considered as the next step to approach the recovery of more refined observations using more realistic CMB conditions.

Persistent morphological features of the present-day geodynamo were explained using alternative CMB heat flux models (Amit and Choblet 2009, 2012; Amit et al. in press). The modifications of the CMB heat flux patterns due to post-perovskite and thermal ridges are mild, and therefore their impact on the dynamo properties are also mild. Thus, in order to detect the differences between the reference dynamo models and those modified by the post-perovskite and thermal ridges effects (Table 2), long-term time-averaging is required (Amit and Choblet 2009, 2012). In contrast, the CMB heat flux pattern inferred from probabilistic tomography is dramatically distinctive from its reference (Amit et al. in press), and therefore provides a genuinely new insight into the possible control of the mantle heterogeneity on the geodynamo.

Dynamo models with imposed CMB heat flux inferred from both thermal ridges and probabilistic tomography were invoked to explain the presence of intense geomagnetic flux patches at low latitude (Amit and Choblet 2012; Amit et al. in press). In the latter models, enhanced low-latitude convective and magnetic activity is found, in particular during some occasional bursts during which the models exceed the observed relative low-latitude geomagnetic flux (Amit et al. in press). These robust low-latitude geomagnetic features (Jackson 2003) are more difficult to reproduce in dynamo models than high-latitude flux patches (Christensen et al. 1998), possibly due to flux dispersion by upwelling (Wicht et al. 2009) that reconnects with the downwellings near the tangent cylinder in the dynamo's meridional circulation (Aubert 2005). Intense low-latitude geomagnetic flux patches, which are indeed easier to recover with alternative CMB heat flux, have so far not been included explicitly as a morphological constraint for Earth-like dynamo models (Christensen et al. 2010).

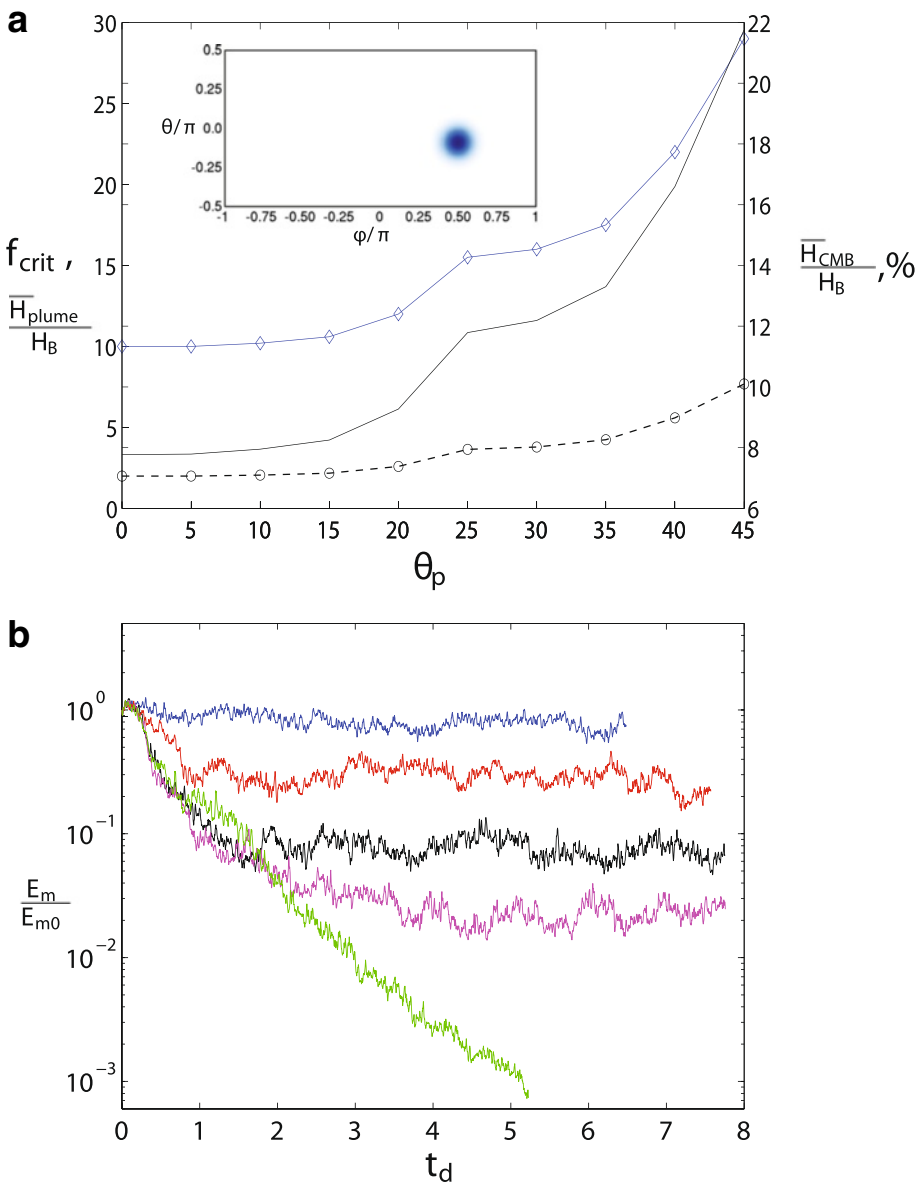

Fig. 13 a Critical heat flux heterogeneity amplitudes required for dynamo failure vs. plume latitude for a mantle plume centered at 15°S (see CMB heat flux pattern in inlet). The three curves are based on three definitions of the heterogeneity amplitude: f (*blue*, Eq. (12)), $\bar{H}_{CMB}/H_B$ (*solid black*), and $\bar{H}_{\text{plume}}/H_B$ (*dashed black*). **b** Timeseries of normalized magnetic energy for a mantle plume centered at 45°S with $f = 0$ (*blue*), $f = 4$ (*red*), $f = 10$ (*black*), $f = 25$ (*magenta*), and $f = 29$ (*green*). From Sreenivasan and Jellinek (2012)

Due to the very low viscosity and very large scale of planetary outer cores, dynamo models operate in a parametric regime very far from realistic conditions (e.g., Christensen and Wicht 2007; Glatzmaier 2002). The situation is more severe if long-term time-averaging is required to detect the impact of alternative or any heterogeneous mantle control, because long simulations are needed for adequate statistical convergence of the time-average dynamo properties. An especially extreme case concerns the study of reversal frequency which requires very long simulations to obtain significant statistics of rare events. Indeed the Ekman and magnetic Prandtl numbers in the studies by Olson et al. (2013) and Amit and Olson (2015) are very large (Table 1); the Ekman number is more than 10 orders of magnitude larger than its geophysical estimate (e.g., Olson 2007b). Amit and Olson (2015) explored some simulations with a lower Ekman number. They found qualitative agreement with their larger Ekman number results, but computational limitations prevented them from providing a confident quantitative analysis, in this case of the reversal frequency vs. pile height.

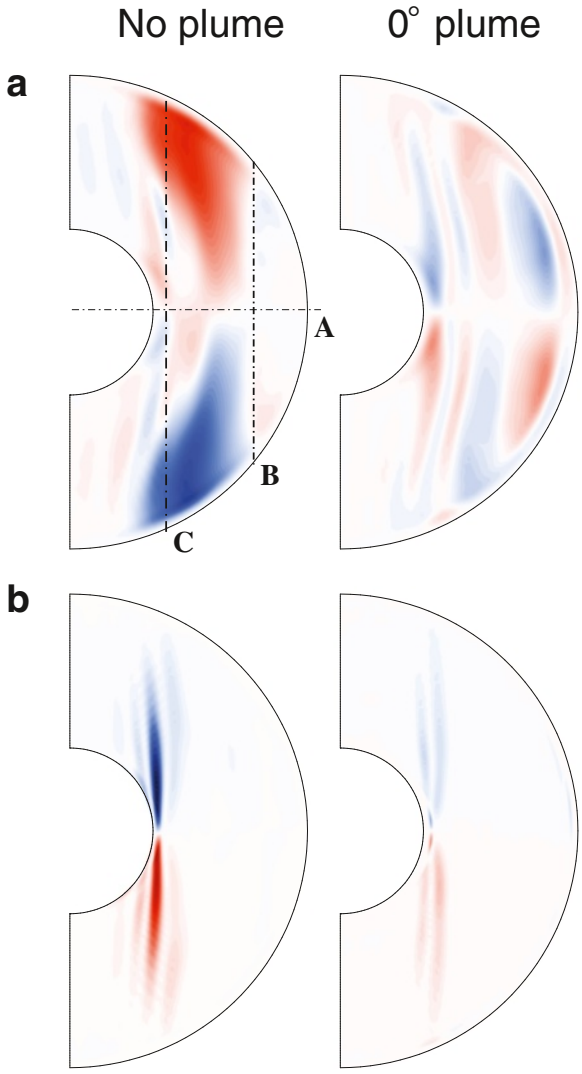

Fig. 14 Zonal profiles of non-dimensional axial velocity **a** and non-dimensional axial kinetic helicity **b** in dynamo models without (*left*) and with (*right*) a plume. The minimum and maximum axial velocity values are [−40.4, 34.4] (*left*) and [−19.3, 18.3] (*right*); the minimum and maximum axial kinetic helicity values are [−174.6, 137.8] (*left*) and [−23.6, 24.8] (*right*). From Sreenivasan and Jellinek (2012)

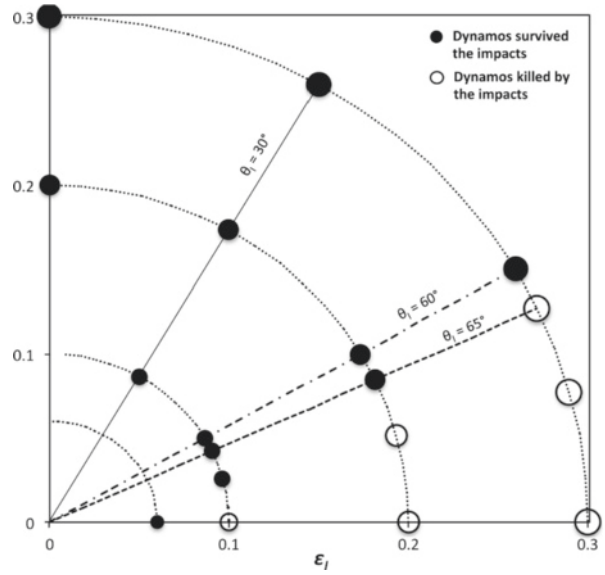

Fig. 15 Survivability of dynamos as a function of CMB heat flux heterogeneity amplitude ϵ_l (radial distance) and the co-latitude of the impact θ_l (angle from vertical axis). From Kuang et al. (2014)

The variability in the paleomagnetic reversal frequency was explained by alternative time-dependent CMB heat flux models (Amit and Olson 2015; Olson et al. 2013). The larger temporal variability in reversal frequency in the dynamo models with time-dependent CMB heat flux compared to those with a fixed tomographic pattern, in particular the presence of superchrons in the former, supports a time-dependent mantle convection structure over the past ∼500 Myr (Olson et al. 2013). It also shows that core evolution by its own cannot account for the large variability in the paleomagnetic reversal frequency. The HF1 model (Zhang and Zhong 2011) exhibits temporal variations in the mean CMB heat flux, its pattern and the amplitude of lateral heterogeneity (Fig. 9 and Table 1), all of which may affect reversal frequency (see Olson and Amit 2014, and references therein).

According to the HF1 model, the CMB heat flux pattern evolved from degree-1 dominance during Pangea to degree-2 at present. This transition is reflected in the time-average magnetic field of the dynamo models with prescribed heat flux pattern inferred from HF1. Olson et al. (2013) showed that at present, the dipole is very axial, whereas with increasing age the dipole axis substantially deviated from the geographic pole. The symmetry of the early time-average magnetic field highly correlates with the symmetry of the CMB heat flux heterogeneity, exhibiting magnetic field concentrations aligned with the axis of the large CMB heat flux.

Dziewonski et al. (2010) proposed that the CMB heat flux is quasi-stationary with two stable states that may each persist for hundreds of Myr. When the plates are organized in one supercontinent at Earth's surface, the CMB heat flux may be characterized by a rotated Y_1^0 pattern; when two continents are present, the CMB heat flux is expressed by a rotated Y_2^0 pattern. Amit and Olson (2015) showed that in both scenarios increasing pile height increases the mean CMB heat flux, the amplitude of its heterogeneity, and the resulting reversal frequency. For a given pile height, the rotated Y_1^0 pattern yields larger mean heat flux, heterogeneity amplitude and reversal frequency than the rotated Y_2^0 pattern (Amit and Olson

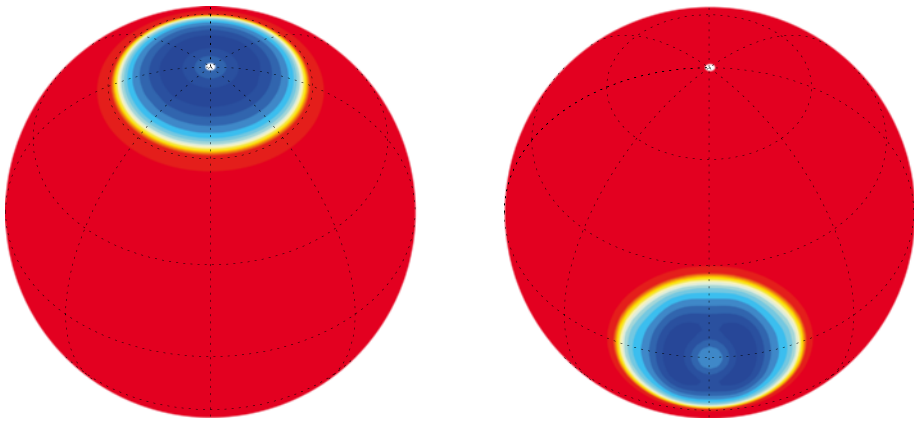

Fig. 16 Non-dimensional CMB heat flux resulting from an impactor of radius 800 km falling on the north pole (*left*) or the equator (*right*). The same pattern was used for different q^* values (see Table 1), hence the absence of a color bar. *Red/blue* denotes positive/negative heat flux anomalies, respectively. From Monteux et al. (2015)

2015), suggesting higher sensitivity of the paleomagnetic reversal frequency to changing mantle conditions prior to the KRS.

The dependence of the reversal frequency on the heterogeneity amplitude is not trivial. In particular, the rotated Y_2^0 case contains polar cooling that according to most studies may suppress reversals (Glatzmaier et al. 1999; Kutzner and Christensen 2004). Polar cooling results in axial-dipole dominance due to flux concentration at high-latitudes (Amit et al. 2010b) and therefore indeed suppresses reversals (a state termed geographic control by Olson and Amit 2014). However, when the dynamo is far from the onset of reversals, Olson and Amit (2014) found that the opposite occurs and polar cooling increases reversal frequency by producing more turbulent conditions (which they termed inertial control). In the piles model of Amit and Olson (2015), the effects of variable mean CMB heat flux and heterogeneity amplitude are non-separable. However, if indeed the rotated Y_2^0 pattern works in unison with the mean CMB heat flux to trigger reversals, it is suggestive of inertial rather than geographic control (Olson and Amit 2014).

The demise of the Martian dynamo was explained by a localized CMB heating (Kuang et al. 2014; Sreenivasan and Jellinek 2012). Sreenivasan and Jellinek (2012) imposed plume-induced thermal anomalies with large heterogeneity amplitudes on highly supercritical numerical dynamos, whereas Kuang et al. (2014) imposed impact-induced thermal anomalies with moderate heterogeneity amplitudes on subcritical dynamos. Under supercritical conditions, the CMB anomaly causes the dynamo to decay relatively slow—the field drops by one order of

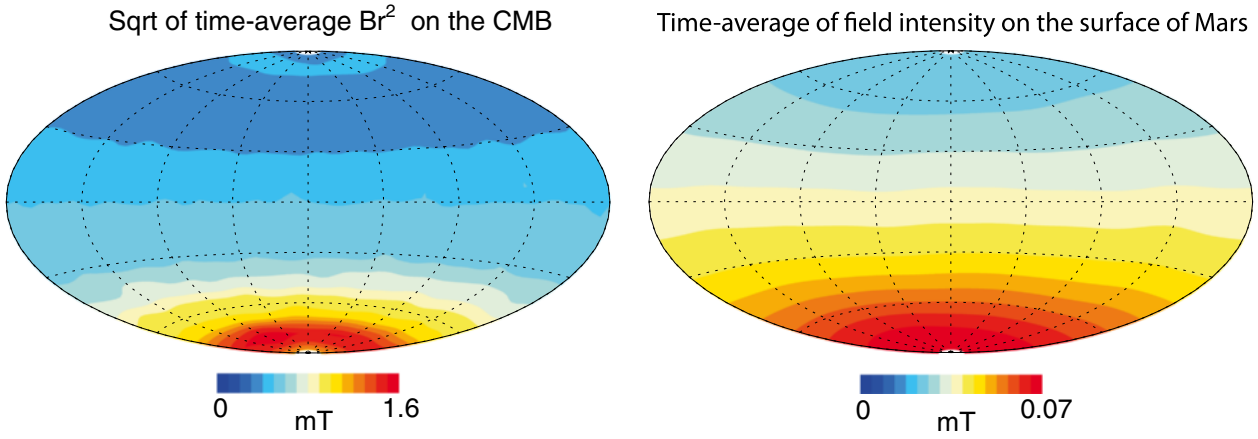

Fig. 17 Time-average magnetic field properties on the CMB (*left*) and on the surface of Mars (*right*) in a dynamo model with imposed outer boundary heat flux due to a polar impactor as in Fig. 16. From Monteux et al. (2015)

magnitude in ∼1.7 magnetic diffusion times (Sreenivasan and Jellinek 2012), whereas under subcritical conditions the termination is more sudden—the field decays ∼4 times faster (Kuang et al. 2014). The large heterogeneity amplitudes in the dynamo models of Sreenivasan and Jellinek (2012) imply that below the mantle plume the heat is flowing unrealistically into the core. Another problem is that under vigorous convection the dynamo is expected to restart once the mantle anomaly vanishes. Note that reducing dynamo efficiency by heterogeneous CMB heat flux is not trivial; another pattern may have the opposite effect, as was shown for Y_2^2 heterogeneity which enhances helical core flow and hence improves dynamo efficiency (Sreenivasan 2009).

In both cases (Kuang et al. 2014; Sreenivasan and Jellinek 2012) it was found that low-latitude localized heating is favorable for terminating the dynamo, despite the distinctive role of convection in these two types of dynamo models. Sreenivasan and Jellinek (2012) argued that the critical latitude for plume location in order to kill the dynamo depends on the lowest latitude where axial columns driven by rapid rotation (Busse 1970) impinge the CMB (see Fig. 14a). Overall, these results may pose upper bounds on the amount of possible planet reorientation in the history of the Martian paleodynamo (Kuang et al. 2014; Sreenivasan and Jellinek 2012). The possibility of a major true polar wander (TPW) event on Mars is under debate. Significant TPW has been advocated for Early Noachian from studies of the crustal geoid associated to dynamical models for the formation of the crustal dichotomy (Roberts and Zhong 2007). TPW was also proposed for the subsequent 4 Gyr from studies of paleomagnetic poles (Hood et al. 2005) and paleoshorelines (Perron et al. 2007) or from theoretical models (Matsuyama et al. 2006). However, to our best knowledge, observed geological evidence for such processes (e.g., Grimm and Solomon 1986) are still lacking. Furthermore, models of lithospheric shell rotation associated with the apparent migration of Tharsis (e.g., Srámek and Zhong 2012) could lead to tectonic observations identical to that caused by TPW, although the two underlying physical processes are very different.

Some of the results obtained by Kuang et al. (2014) seem somewhat counter-intuitive, in particular the field morphology (see their Fig. 3). Their homogeneous CMB heat flux subcritical dynamo model indeed produces a hemispheric magnetic field (as previously reported by Kuang et al. 2008), with a peak at a specific latitude (∼30°S). However, the field may reverse and this peak can migrate to different latitudes with time. It is therefore not clear why would the peak magnetic field of the heterogeneous dynamos almost coincide with that of the homogeneous case. It is also not intuitive that the field becomes spatially less heterogeneous with increasing heterogeneity amplitude. In addition, there is no suggestion for a depleted field at the location of the impact, as may be expected. Overall, it seems that the effects of mantle control on subcritical dynamos are distinctive from those in supercritical dynamos.

Finally, Monteux et al. (2015) imposed a localized impact-induced CMB heat flux pattern on numerical dynamos to explain the observed hemispheric dichotomy in the Martian crustal field (Acuña et al. 1998; Langlais et al. 2004). The amplitude of the hemispheric magnetic dichotomy is mostly controlled by the horizontal Rayleigh number which represents the vigor of the convection driven by the lateral variations of the CMB heat flux. Monteux et al. 2015 showed that, for a given horizontal Rayleigh number, an impact-induced CMB heat flux heterogeneity is more efficient than a synthetic degree-1 heterogeneity in generating strong hemispheric magnetic dichotomies. However, even with the more efficient impact-induced CMB heat flux pattern, several important conditions should be met in order to accept the impact-induced hemispheric dynamo scenario as the origin of the crustal field dichotomy, in particular the need for a very rapid crustal cooling rate (Dietrich and Wicht 2013). Dynamo models that recover the observed magnetic hemisphericity have a short average chron time of about 18 kyr (Monteux et al. 2015). However, in the case of molten material induced by a giant impact a major part of the atmosphere can be eroded and crustal formation may occur within only 1000 years (Lebrun et al. 2013; Solomatov 2007), possibly enabling the recording of the magnetic hemisphericity in the crust.

Future prospects

Because the CMB heat flux is an input to the dynamo models, understanding the dynamics of the lower mantle is a fundamental key to improve core dynamics models. In addition, progress in dynamo modeling is obviously relevant for all core-related problems, including the influence of heterogeneous (alternative or not) boundary conditions. Improved observations, in particular higher quality planetary magnetic field models, may provide tighter constraints on the dynamo models. Here we list some future prospects concerning alternative CMB heat flux and its influence on planetary dynamos. We also mention alternative scenarios that may also explain the non-trivial dynamo-related observations.

Knowledge of planetary magnetic fields will continue to grow in the coming years thanks to several new satellite missions that are currently flying or will soon be launched. Geomagnetic field and secular variation models will benefit from the successful Swarm ESA mission (Olsen et al. 2013). Three identical and magnetically dedicated satellites were launched simultaneously during the end of 2013 at two different altitudes to monitor with unprecedented

quality the Earth's magnetic field and its secular variation. Measurements of the NASA MESSENGER mission around Mercury revealed a weak, dipole-dominated, and hemispheric magnetic field (Anderson et al. 2012). However, these measurements have not yet been fully exploited, and it is anticipated that alternative modeling techniques (Oliveira et al. 2015) and/or the very low-altitude measurements at the end of the mission will bring new insights on the field morphology of Mercury. The ESA/JAXA BepiColombo mission that will be launched in 2017 will complete the geographical coverage of low altitudes of the planet and will lead to the first global view of the magnetic field of Mercury (Benkhoff et al. 2010). The description of the past Martian magnetic field and its interpretation in terms of past dynamo processes will be improved by the recently inserted-into-orbit MAVEN mission. These measurements will be completed by the upcoming InSight mission, which will study the internal structure of Mars and bring constraints on the size of the liquid core. The CASSINI mission to Saturn (Dougherty et al. 2004) is extended until 2016, and the forthcoming Juno (around Jupiter) and later JUICE (around Jupiter moons) missions (Grasset et al. 2013) will also bring new measurements around the giant gas planets and their moons. These new planetary magnetic field models will provide more reliable observational constraints on the processes generating the fields in the interior of the planets and moons.

The identification of the post-perovskite phase transition (Murakami et al. 2004) provided better constraints on the Earth's deepest mantle. Seismic observations with improved tomographic images as well as sophisticated analyses of seismic waves were obtained. A better description of lower mantle materials with laboratory experiments reaching the appropriate high pressure range as well as time-consuming ab initio quantum chemistry computations became possible. As can be expected, the emerging picture bears a much greater complexity which includes the probable role of compositional variations and possible contributions of mantle melting and spin transitions of iron. While the last decade opened new questions such as the complex effect of composition on the post-perovskite phase transition, the precise nature of the melting curve and the points of dissent that remain between laboratory experiments and computational mineralogy, the establishment over the coming decade of an integrative framework (Shim and Lay 2014) would offer a much clearer interpretation of seismic observations and allow to better extract the purely thermal contribution from tomographic models.

Progress in understanding the dynamics of the Earth mantle in the last hundreds of Myr ultimately requires a better description of plate motions in the framework of mantle convection. Promising research paths include conceptual developments such as the understanding of lithospheric damage (Bercovici and Ricard 2014) as well as an improved treatment of plate-like behavior in spherical simulations of mantle dynamics (Bello et al. 2014; Rolf et al. 2012, 2014). In the meantime, improved reconstructions of plate velocities (Seton et al. 2012) can be prescribed to mantle convection models to investigate the role of specific ingredients such as mantle rheology, phase transitions and the nature of a possible dense basal layer. A more thorough investigation of mantle convection models than the pioneering attempt of Zhang and Zhong (2011) may establish more robust CMB heat flux evolution models than HF1.

One direct consequence of the results of the reversal frequency studies is the possibility to invert the record of paleomagnetic reversal frequency (Gradstein et al. 2012) for time-dependent core energetics. If the relation between pile height and CMB heat flux (mean and heterogeneity amplitude) is indeed approximately linear (Amit and Olson 2015; Olson and Amit 2014), the observed reversal frequency may be transformed into a relative CMB heat flux. This may provide a glimpse into the history of core convection.

As for the distant past of the Earth, prospects for other planetary objects mostly rely on modeling progress. Specific planetary scenarios that involve large impacts will most probably remain attractive in the next decade, concerning the ancient Martian magnetic field as well as other planets. Better descriptions of such events than the simplified approaches mentioned above can be simulated (Marinova et al. 2008, 2011). In terms of CMB heat flux, the geometry of impact heating with both a mantle contribution and a possible core contribution (Roberts and Arkani-Hamed 2014) could be described by such numerical tools. As mentioned in Monteux et al. (2015), the presence of impact-induced molten material is key in recording the impact-influenced magnetic field, and the interplay between the cooling time of this material and the transient dynamo properties will ultimately dictate the nature of remnant magnetism. In this regard, impact simulations could also supply patterns and volumes of ejecta deposits on the planetary surface. Describing the dynamics of the bulk molten material could involve on longer timescale phenomena such as isostatic adjustment of the retained melt region and lateral spreading as a gravity current (Reese et al. 2011).

Applications to other planets (apart from the Earth and Mars) may also be considered by invoking alternative CMB heat flux models. A Y_2^0 CMB heat flux pattern combined with internal heating may trigger an unstable odd convective mode which may explain the hemispheric field of Mercury (Cao et al. 2014; Wicht and Heyner 2014) as observed by MESSENGER (Anderson et al. 2012). While their dynamical scenario is convincing, the justification

for a Y_2^0 thermal heterogeneity at the mantle of Mercury is somewhat vague. Examination of gravity and topographic heterogeneities in Mercury may provide a more realistic (alternative) model for the CMB heat flux which can be invoked to recover MESSENGER's magnetic observations.

Due to computational limitations, dynamo models operate in a parametric regime very far from that of planetary core conditions (Glatzmaier 2002). This is especially restrictive for long simulations, as is the case when the long-term impact of an heterogeneous mantle is investigated. One of the most challenging problems in terms of computer power is that of modeling strongly time-variable magnetic reversal frequency, because adequate statistics require extremely long simulations. For example, the Ekman numbers used by Olson et al. (2013) and Amit and Olson (2015) are about four orders of magnitudes off the lowest values that were reported for numerical dynamos (Sakuraba and Roberts 2009). Improved numerical techniques which will allow running simulations with more challenging parameters, in particular lower Ekman and magnetic Prandtl numbers, are therefore of great interest for studies of mantle control on planetary dynamos. More efficient, massively parallelized dynamo codes are currently under development (http://geodynamics.org/cig/working-groups/geodynamo/).

More accurate incorporation of physical phenomena in dynamo models will also improve their predictions. In particular, correct implementation of thermochemical convection is necessary. Currently, most studies use the co-density formulation (Braginsky and Roberts 1995). Apart from neglecting double-diffusive convection, this approach fails to accurately prescribe the inner boundary condition. Some models have already incorporated thermal and chemical convection with appropriate boundary conditions in numerical dynamos (Manglik et al. 2010; Takahashi 2014; Trümper et al. 2012). Tracer methods which are commonly used in mantle convection simulations (e.g., Tackley and King 2003) may be applied to chemical convection in dynamo codes for more accurate numerical schemes. Other physical complications such as stable stratification in some regions of the outer core (Gubbins and Davies 2013) and compressibility may also be incorporated into dynamo models.

Observed dynamo properties that require boundary heterogeneity may alternatively be explained by lateral anomalies at the inner core boundary. Olson and Deguen (2012) showed that the dipole eccentricity in archeomagnetic field models can be reproduced by dynamo simulations with heterogeneous Y_1^1 inner boundary bouyancy flux pattern, corresponding to the east-west seismic anomalies at the upper inner core (Tanaka and Hamaguchi 1997). Aubert et al. (2013) showed that the localization of the westward drift of the geomagnetic field at the Atlantic hemisphere is controlled by the same heterogeneous inner boundary buoyancy flux. In these studies, the inner boundary heterogeneity amplitude was set to be significantly larger than that of the outer boundary, therefore the role of the CMB heterogeneity becomes secondary. It would be interesting to explore dynamo models with comparable amplitude heterogeneities on both boundaries to investigate competing effects.

Progress in understanding mantle dynamics will lead to better description of boundary conditions for the dynamo and thus improved knowledge of core dynamics. On the other hand, magnetic observations may be used to constrain mantle convection scenarios. Overall, a multidisciplinary approach with interactive exchange of information among the different envelopes may advance the study of planetary deep interiors.

Abbreviations

CMB: core-mantle boundary; LLSVPs: large low shear-wave velocity provinces; ULVZs: ultra low velocity zones; KRS: Kiaman reversed superchron; CNS: cretaceous normal superchron; ESA: European Space Agency; NASA: National Aeronautics and Space Administration; MESSENGER: MErcury surface: Space ENvironment: GEochemistry: and ranging; JAXA: Japan Aerospace eXploration Agency; MAVEN: Mars atmosphere and volatile evolution; InSight: Interior exploration using seismic investigations: Geodesy and Heat Transport; JUICE: JUpiter lCy moon explorer.

Competing interests

The authors declare that they have no competing interests.

Authors' contributions

The idea to this paper was in fact conceived following an invitation of HA by Takashi Nakagawa to give a talk on the topic of this paper in SEDI 2014. HA and GC wrote the first draft. GC, FD, and JM designed the illustrative Fig. 1. All authors discussed and improved the draft. All authors read and approved the final manuscript.

Acknowledgements

We thank Takashi Nakagawa, Binod Sreenivasan, and Weijia Kuang for providing material from their papers and for helpful discussions. H. Amit, G. Choblet, J. Monteux, and B. Langlais were partly supported by ANR project MARMITE (ANR-13-BS05-0012). J. Monteux was partly funded by ANR project Oxydeep (ANR-13-BS06-0008). F. Deschamps was supported by Academia Sinica grant 102-CDA-M02. We are grateful to James Roberts and Johannes Wicht for detailed reviews that significantly improved this review paper.

Author details

[1]CNRS UMR 6112, Université de Nantes, Laboratoire de Planétologie et de Géodynamique, 2 rue de la Houssinière, Nantes, F-44000, France. [2]Department of Earth and Planetary Sciences, Johns Hopkins University, 21218 Baltimore, MD, USA. [3]Laboratoire Magmas et Volcans, Université Blaise Pascal - CNRS - IRD, OPGC, 5 rue Kessler, 63038 Clermont Ferrand, France. [4]Institute of Earth Sciences, Academia Sinica, 128 Academia Road Sec. 2, Nangang, Taipei 11529, Taiwan.

Received: 10 March 2015 Accepted: 18 August 2015
Published online: 09 September 2015

References

Acuña M, Connerney J, Wasilewski P, Lin R, Mitchell D, Anderson K, Carlson C, McFadden J, Remè H, Mazelle C, Vignes D, Bauer S, Cloutier P, Ness N (2001) Magnetic field of mars: Summary of results from the aerobraking and mapping orbits. J Gephys Res 106:23403–23417

Acuña MH, Connerney JEP, Wasilewski P, Lin RP, Anderson KA, Carlson CW, McFadden J, Curtis DW, Mitchell D, Reme H, Mazelle C, Sauvaud JA, d'Uston C, Cros A, Medale JL, Bauer SJ, Cloutier P, Mayhew M, Winterhalter

D, Ness NF (1998) Magnetic field and plasma observations at Mars: Initial results of the Mars global surveyor mission. Science 279:1676–1680
Alboussiére T, Deguen R, Melzani M (2010) Melting-induced stratification above the Earth's inner core due to convective translation. Nature 466:744–747
Amit H, Aubert J, Hulot G (2010a) Stationary, oscillating or drifting mantle-driven geomagnetic flux patches J Geophys Res B07108. doi:10.1029/2009JB006542
Amit H, Choblet G (2009) Mantle-driven geodynamo features - effects of post-perovskite phase transition. Earth Planets Space 61:1255–1268
Amit H, Choblet G (2012) Mantle-driven geodynamo features - effects of compositional and narrow d" anomalies. Phys Earth Planet Inter 190-191:34–43
Amit H, Christensen U (2008) Accounting for magnetic diffusion in core flow inversions from geomagnetic secular variation. Geophys J Int 175:913–924
Amit H, Christensen U, Langlais B (2011a) The influence of degree-1 mantle heterogeneity on the past dynamo of Mars. Phys Earth Planet Inter 189:63–79
Amit H, Deschamps F, Choblet G (in press) Numerical dynamos with outer boundary heat flux inferred from probabilistic tomography – consequences for latitudinal distribution of magnetic flux. Geophys J Int. doi:10.1093/gji/ggv332
Amit H, Korte M, Aubert J, Constable C, Hulot G (2011b) The time-dependence of intense archeomagnetic flux patches. J Geophys Res 116:B12106. doi:10.1029/2011JB008538
Amit H, Leonhardt R, Wicht J (2010b) Polarity reversals from paleomagnetic observations and numerical dynamo simulations. Space Sci Rev 155:293–335
Amit H, Olson P (2006) Time-average and time-dependent parts of core flow. Phys Earth Planet Inter 155:120–139
Amit, H, Olson P (2015) Lower mantle superplume growth excites geomagnetic reversals. Earth Planet Sci Lett 414:68–76
Anderson BJ, Johnson CL, Korth H, Purucker ME, Winslow RM, Slavin JA, Solomon SC, McNutt RL, Raines JM, Zurbuchen TH (2012) The global magnetic field of Mercury from MESSENGER orbital observations. Science 333:1859–1862
Arkani-Hamed J (2012) Life of the Martian dynamo. Phys Earth Planet Inter 196:83–96
Arkani-Hamed J, Olson P (2010) Giant impact stratification of the Martian core. Geophys Res Lett 37:L02201. doi:10.1029/2009GL041417
Aubert J (2005) Steady zonal flows in spherical shell fluid dynamos. J Fluid Mech 542:53–67
Aubert J, Amit H, Hulot G (2007) Detecting thermal boundary control in surface flows from numerical dynamos. Phys Earth Planet Inter 160:143–156
Aubert J, Amit H, Hulot G, Olson P (2008) Thermo-chemical wind flows couple Earth's inner core growth to mantle heterogeneity. Nature 454:758–761
Aubert J, Finlay CC, Fournier A (2013) Bottom-up control of geomagnetic secular variation by the Earth's inner core. Nature 502:219–223
Aubert J, Labrosse S, Poitou C (2009) Modelling the paleo-evolution of the geodynamo. Geophys J Int 179:1414–1428
Aurnou J, Andreadis S, Zhu L, Olson P (2003) Experiments on convection in Earth's core tangent cylinder. Earth Planet Sci Lett 212:119–134
Bello L, Coltice N, Rolf T, Tackley PJ (2014) On the predictability limit of convection models of the Earth's mantle. Geochem Geophys Geosys 15. doi:10.1002/2014GC005254
Benkhoff J, van Casteren J, Hayakawa H, Fujimoto M, Laakso H, Novara M, Ferri P, Middleton HR, Ziethe R (2010) BepiColombo - Comprehensive exploration of Mercury: Mission overview and science goals. Planet Space Sci58. doi:10.1016/j.pss.2009.09.020
Bercovici D, Ricard Y (2014) Plate tectonics, damage and inheritance. Nature 508:513–516
Biggin AJ, Steinberger B, Aubert J, Suttie N, Holme R, Torsvik TH, van der Meer DG, van Hinsbergen DJJ (2012) Possible links between long-term geomagnetic variations and whole-mantle convection processes. Nature Geosci 5:526–533
Bloxham J (2002) Time-independent and time-dependent behaviour of high-latitude flux bundles at the core-mantle boundary. Geophys Res Lett 29. doi:10.1029/2001gl014543
Braginsky SI, Roberts PH (1995) Equations governing convection in Earth's core and the geodynamo. Geophys Astrophys Fluid Dyn 79:1–97
Breuer D, Labrosse S, Spohn T (2010) Thermal evolution and magnetic field generation in terrestrial planets and satellites. Space Sci Rev 152:449–500
Bull AL, McNamara AK, Ritsema J (2009) Synthetic tomography of plume clusters and thermochemical piles. Earth Planet Sci Lett 278:152–162
Burke K (2011) Plate tectonics, the Wilson cycle, and mantle plumes: geodynamics from the top. Annu Rev Earth Planet Sci 39:1–29
Burke K, Steinberger B, Torsvik TH, Smethhurst MA (2008) Plume generation zones at the margins of large low shear velocity provinces on the core-mantle boundary. Earth Planet Sci Lett 265:49–60
Busse FH (1970) Thermal instabilities in rapidly rotating systems. J Fluid Mech 44:441–460
Cao H, Aurnou JM, Wicht J, Dietrich W, Soderlund KM, Russell CT (2014) A dynamo explanation for Mercury's anomalous magnetic field. Geophys Res Lett 41. doi:10.1002/2014GL060196
Christensen U, Aubert J (2006) Scaling properties of convection-driven dynamos in rotating spherical shells and application to planetary magnetic fields. Geophys J Int 166:97–114
Christensen U, Aubert J, Hulot G (2010) Conditions for Earth-like geodynamo models. Earth Planet Sci Lett 296:487–496
Christensen U, Olson P (2003) Secular variation in numerical geodynamo models with lateral variations of boundary heat flow. Phys Earth Planet Inter 138:39–54
Christensen U, Olson P, Glatzmaier G (1998) A dynamo model interpretation of geomagnetic field structures. Geophys Res Lett 25:1565–1568
Christensen U, Wicht J (2007) Numerical dynamo simulations. In: Olson P (ed). Treatise on Geophysics Vol 8. Elsevier Science, Amsterdam
Cizkova H, Cadek O, Matyska C, Yuen D (2010) Implications of post-perovskite properties for core-mantle dynamics. Phys Earth Planet Inter 180:235–243
Cobden L, Mosca I, Trampert JJR (2012) On the likelihood of post-perovskite near the core-mantle boundary: a statistical interpretation of seismic observations. Phys Earth Planet Inter 210-211:21–35
Cobden L, Thomas C (2013) The origin of d" reflections a systematic study of seismic array data sets. Geophys J Int 194:1091–1118
Coe RS, Hongre L, Glatzmaier GA (2000) An examination of simulated geomagnetic reversals from a palaeomagnetic perspective. Phil Trans R Soc Lond 358:1141–1170
Courtillot V, Besse J (1987) Magnetic field reversals, polar wander, and core-mantle coupling. Science 237:1140–1147
Davaille A (1999) Simultaneous generation of hotspots and superswells by convection in a heterogeneous planetary mantle. Nature 402:756–760
Davies CJ, Gubbins D, Willis AP, Jimack PK (2008) Time-averaged paleomagnetic field and secular variation: Predictions from dynamo solutions based on lower mantle seismic tomography. Phys Earth Planet Inter 169:194–203
Deschamps F, Cobden L, Tackley PJ (2012) The primitive nature of large low shear-wave velocity provinces. Earth Planet Sci Lett 349-350:198–208
Deuss A (2014) Heterogeneity and anisotropy of Earth's inner core. Ann Rev Earth Planet Sci 42:103–126
Dietrich W, Wicht J (2013) A hemispherical dynamo model: Implications for the Martian crustal magnetization. Phys Earth Planet Inter 217:10–21
Dougherty MK, Kellock S, Southwood DJ, Balogh A, Smith EJ, Tsurutani BT, Gerlach B, Glassmeier K-H, Gleim F, Russell CT, Erdos G, Neubauer FM, Cowley SWH (2004) The Cassini magnetic field investigation. Space Sc Rev 114. doi:10.1007/s11214–004–1432–2
Dziewonski AM, Lekic V, Romanowicz BA (2010) Mantle anchor structure: an argument for bottom up tectonics. Earth Planet Sci Lett 299:69–79
Elkins-Tanton LT, Zaranek SE, Parmentier EM, Hess PC (2005) Early magnetic field and magmatic activity on Mars from magma ocean cumulate overturn. Earth Planet Sci Lett 236:1–12
Gillet N, Pais MA, Jault D (2009) Ensemble inversion of time-dependent core flow models. Geochem Geophys Geosyst 10. doi:10.1029/2008GC002290
Glatzmaier GA (2002) Geodynamo simulations: how realistic are they Annu Rev Earth Planet Sci Lett 30:237–257
Glatzmaier GA, Coe R, Hongre L, Roberts PH (1999) The role of the earth's mantle in controlling the frequency of geomagnetic reversals. Nature 401:885–890
Glatzmaier GA, Roberts PH (1995) A three-dimensional self-consistent computer simulation of a geomagnetic field reversal. Nature 377:203–209
Glatzmaier, GA, Roberts PH (1997) Simulating the geodynamo. Contemp Phys 38:269–288

Glenn Sterenborg M, Crowley JW (2013) Thermal evolution of early solar system planetesimals and the possibility of sustained dynamos. Phys Earth Planet Inter 214:53–73
Gradstein F, Ogg J, Schmitz M, Ogg G (2012) The Geologic Time Scale 2012. Elsevier Science, Amsterdam
Grasset O, Dougherty MK, Coustenis A, Bunce EJ, Erd C, Titov D, Blanc M, Coates A, Drossart P, Fletcher LN, Hussmann H, Jaumann R, Krupp N, Lebreton J-P, Prieto-Ballesteros O, Tortora P, Tosi F, Van Hoolst T (2013) JUpiter ICy moons Explorer (JUICE): An ESA mission to orbit Ganymede and to characterise the Jupiter system. Planet Space Sci 78. doi:10.1016/j.pss.2012.12.002
Grimm RE, Solomon SC (1986) Tectonic tests of proposed polar wander paths for Mars and the Moon. Icarus 65:110–121
Gubbins D (2003) Thermal core-mantle interactions: theory and observations. In: Dehant V, Creager K, Karato S, Zatman S (eds). Earth's Core: dynamics, structure and rotation. AGU Geodynamics Series American Geophysical Union, Washington DC
Gubbins D, Davies CJ (2013) The stratified layer at the core-mantle boundary caused by barodiffusion of oxygen, sulphur and silicon. Phys Earth Planet Inter 215:21–28
Gubbins D, Sreenivasan B, Mound J, Rost S (2011) Melting of the Earth's inner core. Nature 473:361–363
Gubbins D, Willis PW, Sreenivasan B (2007) Correlation of Earth's magnetic field with lower mantle thermal and seismic structure. Phys Earth Planet Inter 162:256–260
Harder H, Christensen UR (1996) A one-plume model of Martian mantle convection. Nature 380:507–509
Heimpel MH, Evans ME (2013) Testing the geomagnetic dipole and reversing dynamo models over Earth's cooling history. Phys Earth Planet Inter 224:124–131
Hernlund J, Thomas C, Tackley PJ (2005) A doubling of the post-perovskite phase boundary and structure of the Earth's lowermost mantle. Nature 434:882–886
Hoffman KA (1996) Transitional paleomagnetic field behavior: Preferred paths or patches? Surv Geophys 17:207–211
Holme R (2007) Large-scale flow in the core. In: Olson P (ed). Treatise on Geophysics, Vol 8. Elsevier Science, Amsterdam
Holme R, Olsen N (2006) Core surface ow modelling from high-resolution secular variation. Geophys J Int 166:518–528
Hood LL, Young CN, Richmond NC, Harrison KP (2005) Modeling of major Martian magnetic anomalies: Further evidence for polar reorientations during the Noachian. Icarus 177. doi:10.1016/j.icarus.2005.02.008
Hori K, Wicht J (2013) Subcritical dynamos in the early Mars' core: Implications for cessation of the past Martian dynamo. Phys Earth Planet Inter 219:21–33
Hulot G, Eymin C, Langlais B, Mandea M, Olsen N (2002) Small-scale structure of the geodynamo inferred from Oersted and Magsat satellite data. Nature 416:620–623
Irving JCE, Deuss A (2011) Hemispherical structure in inner core velocity anisotropy. J Geophys Res 116. doi:10.1029/2010JB007942
Ishii M, Tromp J (1999) Normal-mode and free-air gravity constraints on lateral variations in velocity and density of Earth's mantle. Science 285:1231–1236
Jackson A (2003) Intense equatorial flux spots on the surface of the Earth's core. Nature 424:760–763
Jackson A, Jonkers ART, Walker MR (2000) Four centuries of geomagnetic secular variation from historical records. Phil Trans R Soc Lond A 358:957–990
Jellinek AM, Johnson CL, Schubert G (2008) Constraints on the elastic thickness, heat flow, and melt production at early Tharsis from topography and magnetic field observations. J Geophys Res 113:E09004
Johnson CL, Phillips RJ (2005) Evolution of the tharsis region of Mars: insights from magnetic field observations. Earth Planet Sci Lett 230:241–254
Jutzi M, Asphaug E (2011) Forming the lunar farside highlands by accretion of a companion moon. Nature 476:69–72
Ke Y, Solomatov VS (2006) Early transient superplumes and the origin of the Martian crustal dichotomy. J Geophys Res 111:10001
Ke Y, Solomatov VS (2009) Coupled core-mantle thermal evolution of early Mars. J Geophys Res 114:1–12
Kelly P, Gubbins D (1997) The geomagnetic field over the past 5 million years. Geophys J Int 128:315–330
Korte M, Donadini F, Constable C (2009) The geomagnetic field for 0-3ka: 2. a new series of time-varying global models. J Geophys Res 10:Q06008. doi:10.1029/2008GC002297
Korte M, Holme R (2010) On the persistence of geomagnetic flux lobes in global Holocene field models. Phys Earth Planet Inter 182:179–186
Kuang W, Jiang W, Roberts J, Frey HV (2014) Could giant basin-forming impacts have killed martian dynamo Geophys Res Lett 41:8006–8012
Kuang W, Jiang W, Wang T (2008) Sudden termination of Martian dynamo? implications from subcritical dynamo simulations. Geophys Res Lett 35:L14204
Kutzner C, Christensen UR (2002) From stable dipolar towards reversing numerical dynamos. Phys Earth Planet Inter 131:29–45
Kutzner C, Christensen UR (2004) Simulated geomagnetic reversals and preferred virtual geomagnetic pole paths. Geophys J Int 157: 1105–1118
Labrosse S (2003) Thermal and magnetic evolution of the earth's core. Phys Earth Planet Inter 140:127–143
Langlais B, Purucker M (2007) A polar magnetic paleopole associated with Apoolinaris Patera Mars. Planet Space Sci 55:270–279
Langlais B, Purucker M, Mandea M (2004) Crustal magnetic field of Mars. J Geophys Res 109:E02008
Lay T, Herlund J, Buffett B (2008) Core-mantle boundary heat flow. Nature Geosci 1:25–32
Lay T, Hernlund J, Garnero EJ, Thorne MS (2006) A post-perovskite lens and D" heat flux beneath the central Pacific. Science 314:1272–1276
Lebrun T, Massol H, Chassefiére E, Davaille A, Marcq E, Sarda P, Leblanc F, Branedeis G (2013) Thermal evolution of an early magma ocean in interaction with the atmosphere. J Geophys Res 118:1155–1176
Lekic V, Cottaar S, Dziewonski A, Romanowicz B (2012) Cluster analysis of global lower mantle tomography: A new class of structure and implications for chemical heterogeneity. Earth Planet Sci Lett 357-358:68–77
Lhuillier F, Hulot G, Gallet Y (2013) Statistical properties of reversals and chrons in numerical dynamos and implications for the geodynamo. Phys Earth Planet Inter 220:19–36
Lillis RJ, Frey HV, Manga M (2008) Rapid decrease in Martian crustal magnetisation in the Noachian era: implications for the dynamo and climate of early mars. Geophys Res Lett 35:L14203
Lithgow-Bertelloni C, Richards MA (1998) Dynamics of cenozoic and mesozoic plate motion. Rev Geophys 36:27–78
Love JJ (1998). Paleomagnetic volcanic data and geometric regularity of reversals and excursions 103:12435–12452
Manglik A, Wicht J, Christensen UR (2010) A dynamo model with double diffusive convection for Mercury's core. Earth Planet Sci Lett 289: 619–628
Marinova MM, Aharonson O, Asphaug E (2008) Mega-impact formation of the Mars hemispheric dichotomy. Nature 453:1216–219
Marinova MM, Aharonson O, Asphaug E (2011) Geophysical consequences of planetary-scale impacts into a Mars-like planet. Icarus 211:960–985
Masters G, Laske G, Bolton H, Dziewonski A (2000) The relative behavior of shear velocity, bulk sound velocity, and compressional velocity in the mantle: Implications for chemical and thermal structure. In: Karato S, Forte A, Liebermann R, Masters G, Stixrude L (eds). Earths deep interior, Vol 117. AGU Monograph, Washington D.C
Matsuyama I, Mitrovica JX, Manga M, Perron JT, Richards MA (2006) Rotational stability of dynamic planets with elastic lithospheres. J Geophys Res 111. doi:10.1029/2005JE002447
McNamara A, Garnero E, Rost S (2010) Tracking deep mantle reservoirs with ultra-low velocity zones. Earth Planet Sci Lett 299:1–9
McNamara A, Zhong S (2005) Thermochemical structures beneath Africa and the Pacific Ocean. Nature 437:1136–1139
Merrill RT, McElhinny MW, McFadden PL (1998) The Magnetic Field of the Earth: Paleomagnetism, the Core, and the Deep Mantle. Academic Press, San Diego, California, USA
Merrill RT, McFadden PL (1999) Geomagnetic polarity transitions 37:201–226
Milbury C, Schubert G, Raymond CA, Smrekar SE, Langlais B (2012) The history of Mars' dynamo as revealed by modeling magnetic anomalies near Tyrrhenus Mons and Syrtis Major. J Geophys Res 117. doi:10.1029/2012JE004099
Moffatt HK (1978) Magnetic Field Generation in Electrically Conducting Fluids. Cambridge University Press, Cambridge, UK
Monnereau M, Calvet M, Margerin L, Souriau A (2010) Lopsided growth of Earth's inner core. Science 238:1014–1017
Monteux J, Amit H, Choblet G, Langlais B, Tobie G (2015) Giant impacts, heterogeneous mantle heating and a past hemispheric dynamo on Mars. Phys Earth Planet Inter 240:114–124

Monteux J, Arkani-Hamed J (2014) Consequences of giant impacts in early Mars: Core merging and Martian dynamo evolution. J Geophys Res 119:480–505
Monteux J, Coltice N, Dubuffet F, Ricard Y (2007) Thermo-mechanical adjustment after impacts during planetary growth. Geophys Res Lett 34:24201–24205
Monteux J, Jellinek AM, Johnson CL (2011) Why might planets and moons have early dynamos Earth Planet Sci Lett 310:349–359
Monteux J, Jellinek AM, Johnson CL (2013) Dynamics of core merging after a mega-impact with applications to Mars' early dynamo. Icarus 226:20–32
Monteux J, Schaeffer N, Amit H, Cardin P (2012) Can a sinking metallic diapir generate a dynamo J Geophys Res 117:E10005. doi:10.1029/2012JE004075
Mosca I, Cobden L, Deuss A, Ritsema J, Trampert J (2012) Seismic and mineralogical structures of the lower mantle from probabilistic tomography. J Geophys Res 117. doi:10.1029/2011JB008851
Murakami M, Hirose K, Sata N, Ohishi Y, Kawamura K (2004) Post-perovskite phase transition in MgSio3. Science 304:855–858
Nakagawa T, Tackley PJ (2008) Lateral variations in cmb heat flux and deep mantle seismic velocity caused by a thermal-chemical-phase boundary layer in 3d spherical convection. Earth Planet Sci Lett 271:348–358
Nakagawa T, Tackley PJ (2011) Effects of low-viscosity post-perovskite on thermo-chemical mantle convection in a 3-D spherical shell. Geophys Res Lett 38:L04309
Ni S, Helmberger DV, Tromp J (2005) Three-dimensional structure of the African superplume from waveform modelling. Geophys J Int 161:283–294
Ni S, Tan E, Gurnis M, Helmberger D (2002) Sharp sides to the African superplume. Science 296:1850–1852
Nimmo F, Hart SD, Horycansky DG, Agnor CB (2008) Implications of an impact origin for the Martian hemispheric dichotomy. Nature 453:1220–1223
Oganov A, Ono S (2004) Theoretical and experimental evidence for a post-perovskite phase of MgSio3 in Earth's D" layer. Nature 430:445–448
Oliveira JS, Langlais B, Pais MA, Amit H (2015) A new method to model partially distributed magnetic field measurements, with application to Mercury. J Geophys Res. 120. doi:10.1002/2014JE004734
Olsen N, Luehr H, Finlay CC, Sabaka TJ, Michaelis I, Rauberg J, Tøffner-Clausen L (2014) The CHAOS-4 geomagnetic field model. Geophys J Int 197:815–827
Olson P (2007a) Gravitational dynamos and the low frequency geomagnetic secular variation. Proc Nat Acad Sci 104:20159–20166
Olson, P (2007b) Overview. In: Olson P (ed). Treatise on Geophysics, Vol 8. Elsevier Science, Amsterdam
Olsen N, Friis-Christensen E, Floberghagen R, Alken P, Beggan CD, Chulliat A, Doornbos E, da Encarnação JT, Hamilton B, Hulot G, van den IJssel J, Kuvshinov A, Lesur V, Lühr H, Macmillan S, Maus S, Noja M, Olsen PEH, Park J, Plank G, Püthe C, Rauberg J, Ritter P, Rother M, Sabaka TJ, Schachtschneider R, Sirol O, Stolle C, Thébault E, Thomson AWP, et al (2013) The Swarm Satellite Constellation Application and Research Facility (SCARF) and Swarm data products. Earth, Planets and Space 65(11):1189–1200. doi:10.5047/eps.2013.07.001
Olson P, Amit H (2014) Magnetic reversal frequency scaling in dynamos with thermochemical convection. Phys Earth Planet Inter 229:122–133
Olson P, Christensen U (2002) The time averaged magnetic field in numerical dynamos with nonuniform boundary heat flow. Geophys J Int 151:809–823
Olson P, Christensen U (2006) Dipole moment scaling for convection-driven planetary dynamos. Earth Planet Sci Lett 250:561–571
Olson P, Christensen UR, Glatzmaier GA (1999) Numerical modeling of the geodynamo: Mechanisms of field generation and equilibration. J Geophys Res 104:10383–110404
Olson P, Coe RS, Driscoll PE, Glatzmaier GA, Roberts PH (2010) Geodynamo reversal frequency and heterogeneous core-mantle boundary heat flow. Phys Earth Planet Inter 180:66–79
Olson P, Deguen R (2012) Lopsided inner core growth and eccentricity of the geomagnetic dipole. Nat Geosci 5(8):565–569
Olson P, Deguen R, Hinnov LA, Zhong S (2013) Controls on geomagnetic reversals and core evolution by mantle convection in the Phanerozoic. Phys Earth Planet Inter 214:87–103
Perron JT, Mitrovica JX, Manga M, Matsuyama I, Richards MA (2007) Evidence for an ancient Martian ocean in the topography of deformed shorelines. Nature 447:840–843
Pierazzo E, Vickery AM, Melosh HJ (1997) A reevaluation of impact melt production. Icarus 127:408–423
Pozzo M, Davies C, Gubbins D, Alfè D (2012) Thermal and electrical conductivity of iron at Earth's core conditions. Nature 485:355–358
Reese CC, Orth CP, Solomatov VS (2011) Impact megadomes and the origin of the martian crustal dichotomy. Icarus 213:433–442
Reese CC, Solomatov VS (2010) Early martian dynamo generation due to giant impacts. Icarus 207:82–97
Reese CC, Solomatov VS, Baumgardner JR (2002) Survival of impact-induced thermal anomalies in the Martian mantle. J Geophys Res 107:1–12
Ritsema J, McNamara A, Bull A (2007) Tomographic filtering of geodynamic models: Implications for model interpretation and large-scale mantle structure. J Geophys Res 112:B01303
Roberts JH, Arkani-Hamed J (2012) Impact-induced mantle dynamics on Mars. Icarus 218:278–289
Roberts JH, Arkani-Hamed J (2014) Impact heating and coupled core cooling and mantle dynamics on Mars. J Geophys Res 119:729–744
Roberts JH, Barnouin OS (2012) The effect of the Caloris impact on the mantle dynamics and volcanism of Mercury. J Geophys Res 117:E02007
Roberts JH, Lillis RJ, Manga M (2009) Giant impacts on early Mars and the cessation of the Martian dynamo. J Geophys Res 114:E04009. doi:10.1029/2008JE003287
Roberts JH, Zhong S (2006) Degree-1 convection in the Martian mantle and the origin of the hemispheric dichotomy. J Geophys Res 111:E06013
Roberts JH, Zhong S (2007) The cause for the north-south orientation of the crustal dichotomy and the equatorial location of Tharsis on Mars. Icarus 190(1):24–31
Rolf T, Coltice N, Tackley PJ (2012) Linking continental drift, plate tectonics and the thermal state of the Earth's mantle. Earth Planet Sci Lett. 351–352:134–146
Rolf T, Coltice N, Tackley PJ (2014) Statistical cyclicity of the supercontinent cycle. Geophys Res Lett 41. doi:10.1002/2014GL059595
Romanowicz B, Gung Y (2002) Superplumes from the core-mantle boundary to the lithosphere: Implications for heat flux. Science 296:513–516
Sakuraba A, Roberts PH (2009) Generation of a strong magnetic field using uniform heat flux at the surface of the core. Nat Geosci 2:802–805
Schubert G, Masters G, Olson P, Tackley P (2004) Superplumes or plume clusters Phys Earth Planet Inter 146:147–162
Schubert G, Spohn T (1990) Thermal history of Mars and the sulfur content of its core. J Geophys Res 95:14095–14104
Scotese CR (2001) Atlas of Earth history. In: PALEOMAP Progress Rep. 90-0497. Dep. of Geol, Univ. of Tex. at Arlington
Senshu H, Kuramoto K, Matsui T (2002) Thermal evolution of a growing mars. J Geophys Res 107:1–13
Seton M, Müller RD, Zahirovic S, Gaina C, Torsvik T, Shephard G, Talsma A, Gurnis M, Turner M, Maus S, Chandler M (2012) Global continental and ocean basin reconstructions since 200 Ma. Earth-Sci Rev 113: 212–270
Shim S-H, Lay T (2014) Post-perovskite at ten. Nat Geosci 7:621–623
Solomatov VS (2007) Magma oceans and primordial mantle differentiation. In: Schubert G (ed). Treatise on Geophysics, Vol 9. Elsevier Science, Amsterdam
Srámek O, Zhong S (2010) Long-wavelength stagnant lid convection with hemispheric variation in lithospheric thickness: link between Martian crustal dichotomy and Tharsis J Geophys Res 115:E09010
Srámek O, Zhong S (2012) Martian crustal dichotomy and Tharsis formation by partial melting coupled to early plume migration. J Geophys Res 117:E01005
Sreenivasan B (2009) On dynamo action produced by boundary thermal coupling. Phys Earth Planet Inter 177:130–138
Sreenivasan B, Gubbins D (2011) On mantle-induced heat flow variations at the inner core boundary. Phys Earth Planet Inter 187:336–341
Sreenivasan B, Jellinek AM (2012) Did the tharsis plume terminate the Martian dynamo? Earth Planet Sci Lett 209–217
Sreenivasan B, Jones CA (2011) Helicity generation and subcritical behaviour in rapidly rotating dynamos. J Fluid Mech 688:5–30
Stanley S (2010) A dynamo model for axisymmetrizing Saturn's magnetic field. Geophys Res Lett 37:5201
Stanley S, Elkins-Tanton L, Zuber MT, Parmentier EM (2008) Mars' paleomagnetic field as the result of a single-hemisphere dynamo. Science 321:1822–1825
Stevenson D (1983) Planetary magnetic fields. Rep Prog Phys 46:555–620
Tackley P (2002) The strong heterogeneity caused by deep mantle layering. Geophys Geochem Geosyst 3. doi:10.1029/2001GC000167

Tackley PJ (2011) Living dead slabs in 3-D: The dynamics of compositionally-stratified slabs entering a 'slab graveyard' above the core-mantle boundary. Phys Earth Planet Inter 188:150–162
Tackley PJ, King SD (2003) Testing the tracer ratio method for modeling active compositional fields in mantle convection simulations. Geochem Geophys Geosyst 4. doi:10.1029/2001GC000214
Takahashi F (2014) Double diffusive convection in the Earth's core and the morphology of the geomagnetic field. Phys Earth Planet Inter 226:83–87
Takahashi F, Tsunakawa H, Matsushima M, Mochizuki N, Honkura Y (2008) Effects of thermally heterogeneous structure in the lowermost mantle on the geomagnetic field strength. Earth Planet Sci Lett 272:738–746
Tan E, Gurnis M (2007) Compressible thermochemical convection and application to lower mantle structures. J Geophys Res 112. doi:10.1029/2006JB004505
Tanaka S, Hamaguchi H (1997) Degree one heterogeneity and hemispherical variation of anisotropy in the inner core from PKP(BC)-PKP(DF) times. J Geophys Res 102:2925–2938
To A, Romanowicz B, Capdeville Y, Takeuchi N (2005) 3D effects of sharp boundaries at the borders of the African and Pacific superplumes: Observation and modeling. Earth Planet Sci Lett 233:137–153
Tonks WB, Melosh HJ (1993) Magma ocean formation due to giant impacts. J Geophys Res 98:5319–5333
Torsvik TH, Burke K, Steinberger B, Webb SJ, Ashwel LD (2010) Diamonds sampled by plumes from the core-mantle boundary. Nature 466:352–355
Torsvik TH, Smethhurst MA, Burke K, Steinberger B (2006) Large igneous provinces generated from the margins of the large low-velocity provinces in the deep mantle. Geophys J Int 167:1447–1460
Trampert J, Deschamps F, Resovsky J, Yuen D (2004) Probabilistic tomography maps chemical heterogeneities throughout the lower mantle. Science 306:853–856
Trümper T, Breuer M, Hansen U (2012) Numerical study on double-diffusive convection in the Earth's core. Phys Earth Planet Inter 194–195:55–63
Wang Y, Wen L (2007) Geometry and P and S velocity structure of the "African Anomaly". J Geophys Res 112:B05313
Watters WA, Zuber MT, Hager BH (2009) Thermal perturbations caused by large impacts and consequences for mantle convection. J Geophys Res 114:E02001
Wicht J, Heyner D (2014) Mercury's magnetic field in the messenger era. In: Shuanggen J (ed). Planetray Geodesy and Remote Sensing. CRC Press, London
Wicht J, Stellmach S, Harder H (2009) Numerical models of the geodynamo: From fundamental Cartesian models to 3D simulations of field reversals. In: Glassmeier H, Soffel H, Negendank J (eds). Geomagnetic Field Variations - Space-time structure, processes, and effects on system Earth. Springer, Berlin
Wicht, J, Stellmach S, Harder H (2011) Numerical dynamo simulations: From basic concepts to realistic models. In: Freeden W, Nashed M, Sonar T (eds). Handbook of Geomathematics. Springer, Berlin - Heidelberg - New York
Williams GE (2000) Geological constraints on the Precambrian history of Earth's rotation and the Moon's orbit. Rev Geophys 38:37–59
Willis PW, Sreenivasan B, Gubbins D (2007) Thermal core-mantle interaction: Exploring regimes for 'locked' dynamo action. Phys Earth Planet Inter 165:83–92
Yoshida M, Santosh M (2011) Supercontinents, mantle dynamics and plate tectonics: A perspective based on conceptual vs. numerical models. Earth Sci Rev 105:1–24
Zhang N, Zhong S (2011) Heat fluxes at the Earth's surface and core-mantle boundary since Pangea formation and their implications for the geomagnetic superchrons. Earth Planet Sci Lett 306:205–2016
Zhang N, Zhong SJ, Leng W, Li ZX (2010) A model for the evolution of the Earth's mantle structure since the early Paleozoic. J Geophys Res 115:B06401
Zhang P, Cohen RE, Haule K (2015) Effects of electron correlations on transport properties of iron at Earth's core conditions. Nature 517:605–607
Zhong S, Zhang N, Li Z-X, Roberts JH (2007) Supercontinent cycles, true polar wander, and very long-wavelength mantle convection. Earth Planet Sci Lett 261:551–564

5 Couplage manteau-noyau et évolution long terme des dynamos planétaires

Une magnétisation rémanente et des champs magnétiques actifs ont été détectés pour plusieurs corps planétaires telluriques du Système Solaire (Terre, Mercure, Lune, Mars), ce qui suggère la présence de dynamos actives aux premiers stades de la formation de la planète et de durées de vie variables. Le champ magnétique de ces objets est la conséquence de mouvements convectifs vigoureux du fer dans la partie liquide de leur noyau (Jones, 2015). Cependant, la barrière chimique avec le manteau silicaté empêche la chaleur d'être transférée au manteau environnant par des mouvements advectifs. Les transferts de chaleur se font donc par conduction au travers des couches limites thermiques situées de part et d'autre de la frontière manteau-noyau. Le flux de chaleur conductif varie selon $k\Delta T/\delta$ avec k la conductivité du matériau, ΔT la différence de température de part et d'autre de la couche limite thermique et δ l'épaisseur de la couche limite thermique. Lorsque la convection est très vigoureuse comme c'est le cas dans le noyau métallique liquide et dans les manteaux primitifs, les couches limites sont très fines et le flux de chaleur conductif est très important. Par conséquent, les conductivités du noyau métallique et du manteau silicaté, la vigueur de la convection et la quantité d'énergie stockée dans le noyau exercent un contrôle primordial sur le flux de chaleur à la CMB. Ces paramètres contrôlent à la fois l'état thermique du noyau, le bilan thermique transféré dans le manteau au cours du temps et la possibilité de générer une dynamo.

5.1 Influence des conductivités thermiques : cas de Mercure

La mission MESSENGER a révélé que le champ magnétique de Mercure pourrait fonctionner depuis 3.7-3.9 Ga. La faible intensité du champ magnétique de Mercure a longtemps déconcerté la communauté scientifique planétaire. Diverses explications ont été proposées mais il n'y a pas de consensus sur la façon dont une dynamo intrinsèque avec une énergie aussi faible a pu exister sur Mercure pendant une période prolongée. Alors que le magnétisme intrinsèque suggère l'existence d'une dynamo active dans le noyau de Mercure, le mécanisme responsable du maintien de la dynamo pendant une période prolongée reste inconnu.

Parmi les facteurs qui contrôlent la possibilité de générer des dynamos internes, la dynamique du manteau silicaté entourant le noyau et ses propriétés thermiques associées sont cruciales. Le manteau régit l'évacuation de la chaleur du noyau et, par conséquent, la probabilité d'une dynamo thermique précoce. La capacité du manteau a évacuer de la chaleur est gouvernée par son nombre de Rayleigh :

$$Ra = \frac{\alpha \rho g \Delta T H^3}{\eta \kappa}, \tag{2}$$

avec ρ sa densité, α son coefficient de dilatation thermique, g la gravité, ΔT la différence

de temperature entre le haut et la bas du manteau, H l'épaisseur du manteau, η sa viscosité et κ sa conductivité. Dans le cas où l'épaisseur H du manteau d'une planète est importante (i.e. manteau associé à des nombres de Rayleigh potentiellement élevés), la chaleur du noyau est efficacement évacuée par la convection du manteau sus-jacent et des dynamos thermiques précoces sont favorisées. À l'inverse, les planètes dotées d'un manteau mince (associé à des nombres de Rayleigh potentiellement plus faibles) peuvent évacuer leur chaleur interne uniquement par diffusion, ce qui rend plus difficile la mise en place de dynamos thermiques précoces. Dans le Système Solaire, Mercure est un exemple potentiel d'un tel régime. Si la faible épaisseur de son manteau par rapport au rayon de la planète était inhérente à sa position proche du Soleil (Charlier and Namur, 2019), un tel contexte magnétique pourrait être omniprésent parmi les objets telluriques formés à proximité de leur étoile.

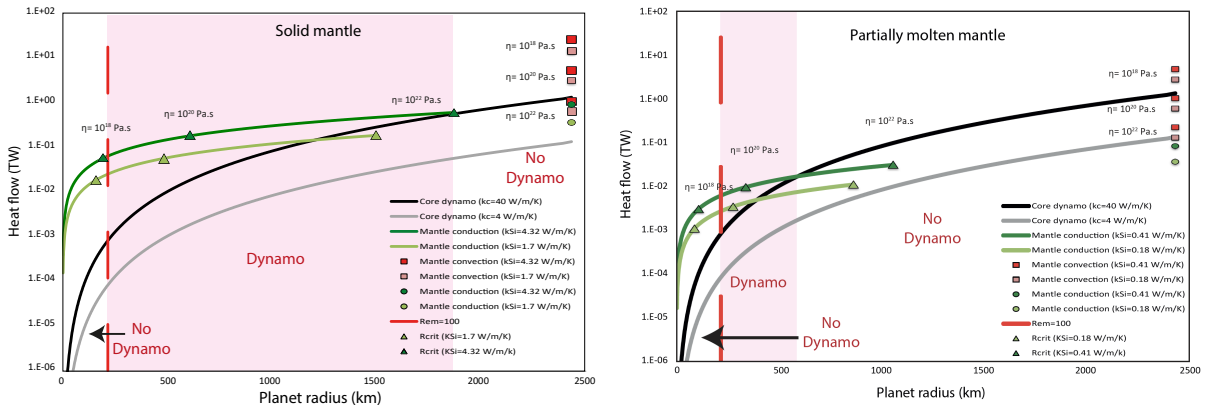

FIGURE 17 – *Flux de chaleur en fonction du rayon planétaire pour un manteau planétaire entièrement solide (gauche) ou partiellement fondu (droite). Les lignes noires et grises représentent le flux de chaleur critique nécessaire à une dynamo thermique pour une conductivité thermique du noyau de 40 et 4 W/m/K, respectivement. Les lignes vertes foncées et claires représentent le flux de chaleur du manteau dans un régime conductif pour la gamme de conductivité thermique des silicates obtenue expérimentalement. Les triangles verts représentent la taille critique de la planète pour laquelle $Ra = Ra_c$, ce qui correspond donc au flux de chaleur minimum à la CMB, pour une viscosité du manteau allant de 10^{18} à 10^{22} Pa.s. Les valeurs extrapolées à $R = R_{Mercure} = 2440$ km sont également représentées avec des cercles verts pour les transferts de chaleur conductifs et des carrés rouges et roses pour les cas convectifs avec les viscosités du manteau indiquées à proximité. La ligne pointillée rouge représente la valeur critique pour $Re_m = 100$. A gauche de cette ligne, une dynamo est peu probable. La zone probable pour un rayon de planète capable d'alimenter une dynamo est représentée par la zone ombrée en rose. À partir de Freitas et al. (2021).*

Pour savoir si une dynamo générée par de la convection thermique dans les planètes de type Mercure (avec un rapport rayon du noyau sur rayon de la planète élevé) est possible ou non, nous avons caractérisé la conductivité thermique de divers échantillons silicatés, solides,

vitreux et fondus (Freitas et al., 2021). Les conductivités thermiques ont été estimées pour des péridotites solides et partiellement fondues, avec différentes fractions de fusion, ainsi que pour des verres et des fondus basaltiques et rhyolitiques à des pressions de 2 GPa et à des températures allant jusqu'à 1700 K. Notre étude démontre que les matériels fondus ont des propriétés thermiques similaires malgré une large gamme de compositions étudiées. Les produits de fusion révèlent des conductivités thermiques beaucoup plus faibles que les solides, avec une diminution de près d'un ordre de grandeur : 1.70 (± 0.19) à 2.29 (± 0.26) W/m/K contre 0.18 (± 0.01) à 0.41 ($\pm 0,03$) W/m/K pour les péridotites à haute température et divers matériaux fondus respectivement. Les échantillons partiellement fondus se situent entre les deux et plusieurs lois prédictives sont proposées en fonction de la fraction fondue et de la texture solide/fondue. En utilisant nos résultats dans des calculs de flux de chaleur nécessaires pour la génération de dynamos pour les planètes de type Mercure, nous avons quantifié l'effet de la fusion du manteau sur la propension des noyaux planétaires à générer des dynamos par convection thermique (Figure 17). La présence d'un manteau "mushy" et ainsi de fusion partielle pourrait réduire de manière significative la capacité du manteau à évacuer la chaleur du noyau et peut empêcher ou affecter la présence d'un champ magnétique planétaire. La flottabilité et le devenir de la matière fondue dans ces corps peuvent donc influencer l'histoire magnétique de la planète. Les futures observations de planètes semblables à Mercure accrétées près de leur étoile et les détections de leurs signatures magnétiques pourraient fournir des contraintes sur leur état interne et leur histoire en terme de fusion partielle.

Avec G. Manthilake, nous avons aussi travaillé sur le rôle de la conductivité thermique des alliages Fe-S, la phase dominante dans le noyau externe de la planète Mercure, à une pression de 8 GPa et à des températures allant jusqu'à 1700 K (Manthilake et al., 2019). Nous avons montré que la conductivité électrique des alliages Fe-S à 1500 K est d'environ 10^3 S/m, soit deux ordres de grandeur de moins que la valeur précédemment supposée pour les calculs de la dynamo herméenne. La conductivité thermique a été ensuite estimée en utilisant la loi de Wiedemann-Franz. La conductivité thermique de l'alliage Fe-S est estimée à $\sim$4 Wm/K dans les conditions régnant à la limite noyau-manteau de Mercure. La faible conductivité thermique obtenue dans notre étude suggère que l'extraction de chaleur du noyau de Mercure à travers la couche solide de Fe-S est un processus relativement inefficace mais suggère qu'une dynamo thermique fonctionnant sur Mercure est plus probable que prévu. En effet, malgré cette faible conductivité, le flux de chaleur à la CMB reste supérieur au flux adiabatique dans le noyau ce qui est synonyme de convection et donc de dynamo pour un noyau de la taille de celui de Mercure (Figure 18). Si la flottabilité thermique est couplée à des sources de flottabilité chimique, il est possible de maintenir une dynamo intrinsèque pendant des échelles de temps compatibles avec les observations de MESSENGER. Nos estimations suggèrent que le flux de chaleur du noyau ne produit que moins de 1 TW d'énergie. Le faible flux de chaleur empêcherait le noyau herméen de se solidifier rapidement, ce qui pourrait favoriser le maintient d'une dynamo intrinsèque à Mercure depuis ~ 3.9 Ga.

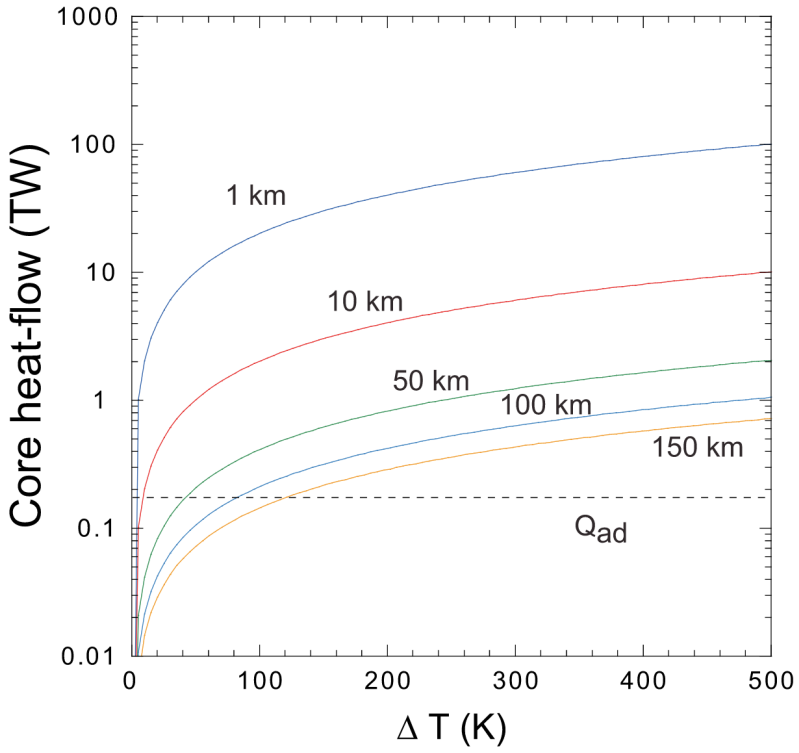

FIGURE 18 – *Flux de chaleur à la frontière entre le noyau et le manteau de Mercure. Les calculs sont basés sur une conductivité thermique totale moyenne (électrons + phonons) de 4 Wm/K pour le FeS pour diverses épaisseurs de couche limite thermique en fonction du contraste de température à travers cette couche. Le flux thermique adiabatique (Q_{ad}) est représenté par une ligne horizontale noire en pointillés (d'après Manthilake et al. (2019)).*

5.2 Une température à la CMB quasi constante au cours des temps géologiques

Les comparaisons entre les observations sismiques et les données de physique minérale sur les propriétés des réservoirs profonds fournissent des contraintes sur l'état thermique actuel de la Terre profonde. En particulier, le caractère non ubiquiste des zones à très faible vitesse (ULVZ) situées au-dessus du CMB fournit une température d'ancrage majeure de 4000 ($\pm$200) K à la CMB, soit quelques centaines de degrés en dessous de la température de fusion du manteau pyrolitique. L'existence d'une température à la CMB aussi élevée que $\sim$ 4000 K aujourd'hui soulève des questions sur la température à la CMB au début de l'histoire de la Terre. Le maintien de la géodynamo depuis les plus anciennes traces de champ paléomagnétique (il y a environ 4,2 Ga (Tarduno et al., 2010)) jusqu'à aujourd'hui par une combinaison de flottabilité thermique et de convection compositionnelle nécessite beaucoup d'énergie. Pour que cela soit possible, deux scénarios peuvent être envisagés : (a) une température initiale du

noyau très élevée diminuant lentement avec le temps ou (b) une forte concentration d'éléments radiogéniques dans le noyau, tels que le ^{40}K. Les deux hypothèses impliqueraient une fusion importante dans le manteau inférieur au début de la Terre.

Comme discuté précédemment, nous avons vu qu'un impact géant pourrait être à l'origine de la formation du système Terre-Lune (voir section 2). Cet impact a pu entraîner la fusion totale du manteau terrestre (Nakajima and Stevenson, 2015). Nous y reviendrons plus tard plus en détails mais le refroidissement d'un océan magmatique qui concernerait l'intégralité du manteau terrestre est un processus extrêmement efficace. En effet, nos modèles ont montré qu'en moins d'un millions d'années après l'impact, le manteau pourrait passer de complètement fondu à un taux de fusion de 40% (Monteux et al., 2016a). Durant ce laps de temps, une grande quantité de chaleur a pu être évacuée du noyau par un couplage efficace avec le manteau sus-jacent. À tel point qu'il est envisageable que le profil de température à l'intérieur de la Terre il y a 4.4 Ga ait pu atteindre son état actuel très rapidement. Le noyau solide aurait ainsi pu se former à la même époque soit quelques millions d'années après l'impact géant. Si une grande partie de l'énergie est évacuée rapidement du noyau, il est difficile de comprendre comment un champ magnétique peut être généré dans le noyau pendant plus de 4 Ga (Tarduno et al., 2010).

Dans ce contexte, la présence de la Lune a pu jouer un rôle essentiel pour maintenir le champ magnétique terrestre pendant aussi longtemps (Andrault et al., 2016) (Figure 19). En effet, la Terre adopte une forme aplatie, tourne autour d'un axe incliné qui oscille autour des pôles et son manteau se déforme élastiquement par effet de marée dû à la Lune. Nous avons ont montré que cet effet pourrait stimuler continuellement les mouvements de l'alliage de fer liquide qui constitue le noyau externe, et générer en retour le champ magnétique terrestre. Une puissance de 3 700 milliards de watts est constamment fournie à la Terre par transfert des énergies gravitationnelle et de rotation du système Terre-Lune-Soleil, et jusqu'à plus de mille milliards de watts seraient disponibles pour provoquer ce type de mouvements dans le noyau externe. Cette énergie est suffisante pour générer le champ magnétique terrestre ce qui, avec la Lune, résout le paradoxe majeur du modèle classique. Un tel effet des forces gravitationnelles sur le champ magnétique d'une planète est déjà amplement documenté pour Io, Europe, deux satellites naturels de Jupiter, et de nombreuses exoplanètes. De plus un tel scénario a été proposé par Le Bars et al. (2011) pour expliquer la dynamo lunaire.

Comme ni la rotation de la Terre autour de son axe, ni l'orientation de cet axe, ni l'orbite de la lune ne sont parfaitement régulières, leur influence cumulée sur les mouvements dans le noyau est instable et peut faire fluctuer la géodynamo. Ce phénomène permet d'expliquer certains pulses de chaleur dans le noyau externe et à sa frontière avec le manteau terrestre. Historiquement, cela a pu conduire à des pics de fusion dans le manteau profond et à d'éventuels évènements volcaniques majeurs à la surface de la Terre. Ce nouveau modèle souligne que l'influence de la Lune sur la Terre dépasse donc largement le simple cas des marées.

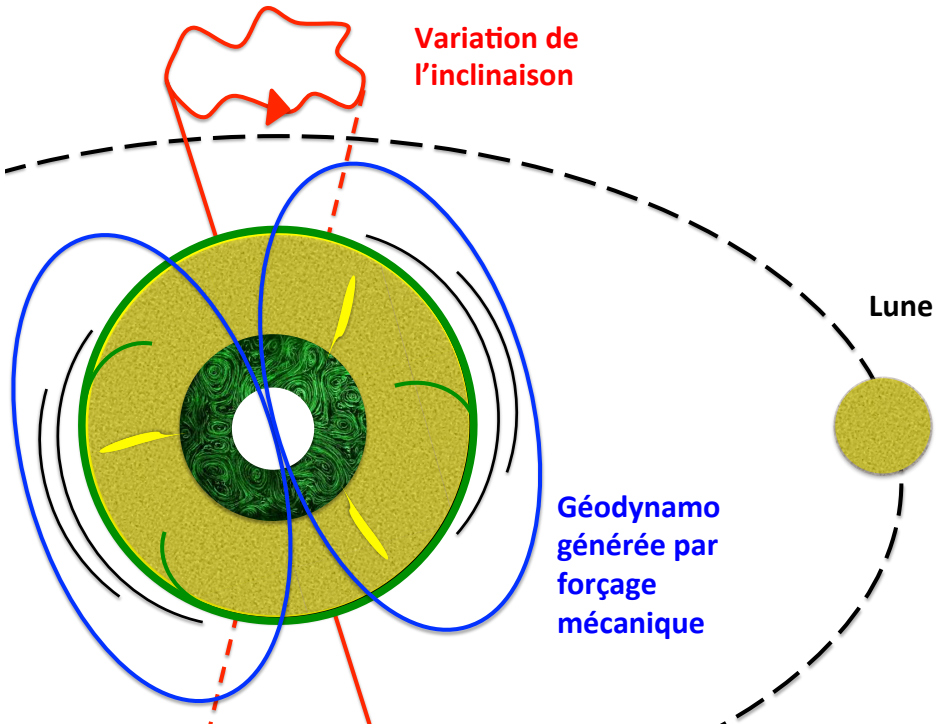

FIGURE 19 – *Les effets gravitationnels associés à la présence de la Lune et du Soleil induisent sur Terre la déformation cyclique du manteau et des oscillations de l'axe de rotation. Ce forçage mécanique appliqué à toute la planète induit de forts courants dans le noyau externe constitué d'un alliage de fer de très faible viscosité. Ces courants sont suffisants pour générer le champ magnétique terrestre.*

5.3 Perspectives : Conductivité thermique du fer et refroidissement séculaire de la frontière manteau-noyau

Les études théoriques et expérimentales proposent des valeurs de la conductivité thermique du fer (k_{Fe}) comprises entre ∼25 et ∼250 W/m/K dans les conditions P-T compatibles avec celles de la CMB soit 135 GPa et 4000 K. Les valeurs les plus basses (par exemple 28-29 W/mK dans les travaux de Stacey and Loper (2007)) permettraient de maintenir une géodynamo active pendant plusieurs Gy, et seraient également en accord avec l'état thermique actuel du noyau. En revanche, la conductivité thermique beaucoup plus élevée (80-100 W/m/K) signalée dans les calculs théoriques récents (Pozzo et al., 2012; Koker et al., 2012) et les expériences (Gomi et al., 2013; Ohta et al., 2016) donnent un flux thermique conducteur actuel de 10-15TW le long de l'adiabat du noyau, ce qui rend le bilan énergétique du noyau très difficile à établir. De manière surprenante, seuls les travaux expérimentaux de Konôpková et al. (2016) suggèrent une faible valeur de k_{Fe}, comprise entre 18 et 44 W/m/K. Le débat sur l'état thermique du noyau au cours de son histoire restera probablement intense jusqu'à ce que les

vraies valeurs de k_{Fe} soient confirmées par d'autres études.

La plupart des études précédentes ont déterminé la conductivité électrique du Fe ou des alliages de Fe, en utilisant soit des expériences dans la cellule à enclume de diamant chauffée au laser, soit des calculs théoriques ab initio. La conductivité électrique donne une valeur indirecte de k_{Fe} grâce à la loi de Wiedemann-Franz, dont le principe de base est que les électrons sont le principal vecteur des courants électriques et thermiques dans les métaux. La seule mesure directe disponible dans les conditions P-T relatives au noyau de la Terre utilise la méthode des impulsions laser (Konôpková et al., 2016). Cette méthode consiste à mesurer le temps nécessaire pour qu'une perturbation de température très courte ($\sim 10^{-7}$ s) produite d'un côté de l'échantillon traverse le volume de l'échantillon. Le défi expérimental consiste à détecter la perturbation de température des deux côtés de l'échantillon. Pour ce faire, cette étude a mis en place une expérience complexe avec une caméra à balayage couplée à un spectrographe à réseau. Elle fournit une mesure résolue dans le temps de la température sur l'une ou l'autre face de l'échantillon, mais pas sur les deux simultanément. Cela pourrait induire des artefacts dus aux difficultés de synchronisation de la caméra à bandes avec les impulsions de chaleur de chaque côté de l'échantillon.

Dans le projet que nous développons avec D. Andrault et L. Pison, nous effectuons des mesures directes de k_{Fe} en utilisant la méthode de l'impulsion laser, comme dans l'étude de Konôpková et al. (2016). Au lieu d'utiliser une caméra à bandes comme dans l'étude précédente, nous utilisons des mesures spectroscopiques beaucoup plus simples, qui ne fournissent pas la température réelle de l'impulsion. Cependant, les balayages temporels sont enregistrés simultanément sur les deux faces de l'échantillon, ce qui permet de déterminer avec une grande précision la propagation temporelle de l'impulsion thermique à travers l'échantillon. Nous effectuons ces mesures directes de la conductivité thermique du fer à l'aide du système LH-DAC disponible au Laboratoire Magmas et Volcans. La puissance de nos deux lasers à fibre continus est contrôlée pour stabiliser la température de $\sim$1200 K à plus de 3000 K, et la puissance d'un troisième laser à fibre pulsé est ajoutée pour produire l'impulsion de chaleur sur un côté de l'échantillon. Les mesures d'impulsion sont effectuées entre 20 et 130 GPa, et entre 1200 K et le point de fusion de l'échantillon de fer. Ces plages de P-T permettront de déterminer les effets croisés de la pression et de la température sur k_{Fe}. Grâce à notre nouveau dispositif, nous documenterons pour la première fois expérimentalement et à des pressions élevées la dépendance en température de k_{Fe}. Cependant, les mesures quantitatives nécessitent la détermination précise de l'épaisseur de l'échantillon (qui se situe entre 3 et 6 microns) dans toutes les expériences. Pour ce faire, nous devons découper la feuille de Fe récupérée lors des expériences, à l'aide d'un appareil à faisceau d'ions focalisé (FIB).

Pour obtenir la conductivité thermique de nos échantillons à partir des mesures expérimentales de la propagation de l'impulsion thermique à travers l'échantillon, nous avons développées des modèles numériques de propagation thermique à l'aide du logiciel COMSOL

Multiphysics (Figure 20). Grâce à cet outil de modélisation en éléments finis, nous modélisons l'évolution de la température dans un échantillon micrométrique soumis à un pulse thermique. Nous reproduisons pour cela les mêmes conditions que les conditions expérimentales que ce soit en terme de géométrie, de propriétés des matériaux ou de conditions aux limites. Nous considérons par exemple les propriétés du diamant, du milieu transmetteur de pression (couche de KCl) entre les diamants et l'échantillon et du joint au rhénium. Nous pouvons notamment implémenter les propriétés (densité, conductivité et capacité thermique) de ces divers matériaux. Nous considérons une géométrie axisymmétrique cylindrique et notre maillage est calculé directement par le mailleur de COMSOL. Cette comparaison permet de contraindre la conductivité thermique de l'échantillon comme cela a été fait dans l'étude de Konôpková et al. (2016). À terme, cette valeur affinée de k_{Fe} sera implémentée dans des modèles de refroidissement du noyau pour modéliser la variation séculaire de la température et le flux de chaleur à travers la CMB. Cela permettra d'affiner les conditions de température dans la couche D" depuis les premières étapes d'évolution de la Terre mais aussi des autres planètes telluriques mais aussi d'affiner la conductivité thermique k_{Fe} dans les conditions P-T du noyau externe de la Terre.

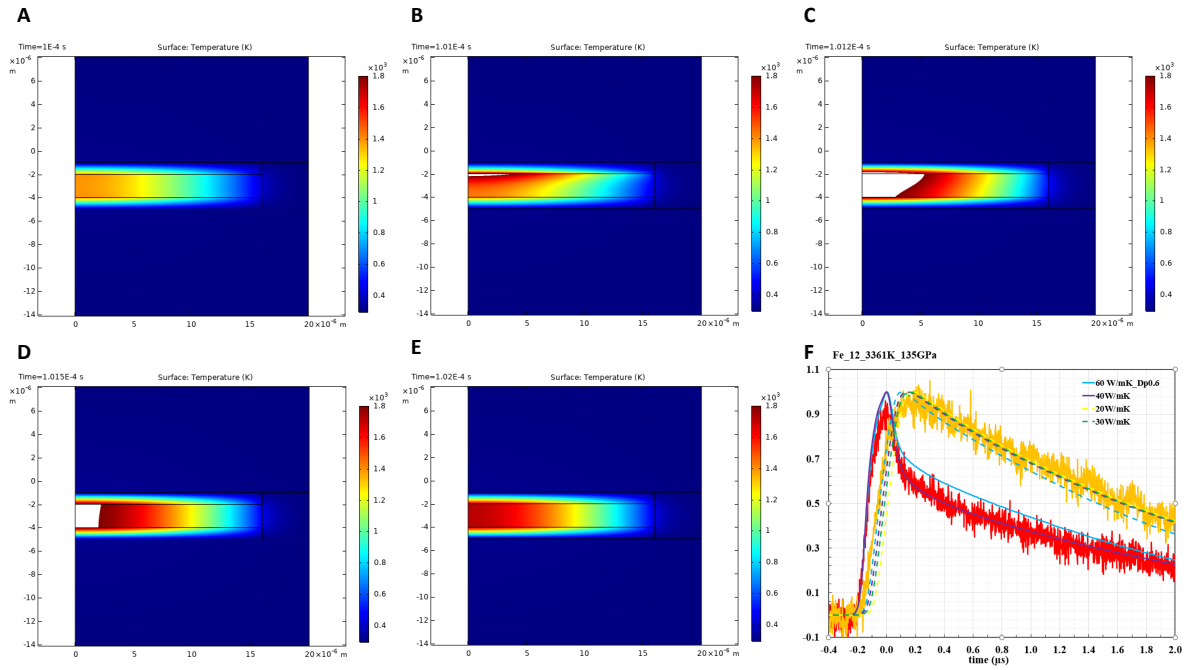

FIGURE 20 – *Panels A à E : Évolution temporelle de la temperature au sein d'un échantillon de Fer pris en sandwich entre deux couches de KCl et deux diamants et soumis à un pulse laser afin d'être chauffé. Panel F : Comparaison entre les évolutions temporelles de la température de part et d'autre de l'échantillon obtenues expérimentalement (courbes rouge et jaune) et les courbes obtenues par nos modèles numériques pour différentes values de* k_{Fe}.

Références personnelles

Andrault D., **Monteux, J.**, *Le Bars M., Samuel H., 2016, The deep Earth may not be cooling down. Earth and Planetary Science Letters vol.443, p.195-203.* **LIEN HAL**

Manthilake G., Chantel J., **Monteux, J.**, *Andrault D., Bouhifd A., Bolfan-Casanova N., Boulard E., Guignot N., King A., Itie J.P., 2019, Thermal Conductivity of FeS and Its Implications for Mercury's Long Sustaining Magnetic Field. Journal of Geophysical Research - Planets vol.124.* **LIEN HAL**

Freitas D., **Monteux, J.**, *Andrault D., Manthilake G., Mathieu A., Schiavi F., Cluzel N., 2021, Thermal conductivities of solid and molten silicates : Implications for dynamos in mercury-like proto-planets. Physics of the Earth and Planetary Interiors vol.312, p.106655.* **LIEN HAL**

Earth and Planetary Science Letters ••• (••••) •••–•••

Contents lists available at ScienceDirect

Earth and Planetary Science Letters

www.elsevier.com/locate/epsl

The deep Earth may not be cooling down

Denis Andrault [a,*], Julien Monteux [a], Michael Le Bars [b], Henri Samuel [c]

[a] Laboratoire Magmas et Volcans, CNRS-OPGC-IRD, Université Blaise Pascal, Clermont-Ferrand, France
[b] CNRS, Aix-Marseille Université, Ecole Centrale Marseille, IRPHE, UMR 7342, Marseille, France
[c] Institut de Recherche en Astrophysique et Planétologie, CNRS, Université Paul Sabatier, Toulouse, France

ARTICLE INFO

Article history:
Received 28 July 2015
Received in revised form 7 March 2016
Accepted 9 March 2016
Available online xxxx
Editor: C. Sotin

Keywords:
temperature profile in the deep Earth
secular cooling of the Earth
generation of the geomagnetic field

ABSTRACT

The Earth is a thermal engine generating the fundamental processes of geomagnetic field, plate tectonics and volcanism. Large amounts of heat are permanently lost at the surface yielding the classic view of the deep Earth continuously cooling down. Contrary to this conventional depiction, we propose that the temperature profile in the deep Earth has remained almost constant for the last ~4.3 billion years. The core–mantle boundary (CMB) has reached a temperature of ~4400 K in probably less than 1 million years after the Moon-forming impact, regardless the initial core temperature. This temperature corresponds to an abrupt increase in mantle viscosity atop the CMB, when ~60% of partial crystallization was achieved, accompanied with a major decrease in heat flow at the CMB. Then, the deep Earth underwent a very slow cooling until it reached ~4100 K today. This temperature at, or just below, the mantle solidus is suggested by seismological evidence of ultra-low velocity zones in the D"-layer. Such a steady thermal state of the CMB temperature excludes thermal buoyancy from being the predominant mechanism to power the geodynamo over geological time.

An alternative mechanism to sustain the geodynamo is mechanical forcing by tidal distortion and planetary precession. Motions in the outer core are generated by the conversion of gravitational and rotational energies of the Earth–Moon–Sun system. Mechanical forcing remains efficient to drive the geodynamo even for a sub-adiabatic temperature gradient in the outer core. Our thermal model of the deep Earth is compatible with an average CMB heat flow of 3.0 to 4.7 TW. Furthermore, the regime of core instabilities and/or secular changes in the astronomical forces could have supplied the lowermost mantle with a heat source of variable intensity through geological time. Episodic release of large amounts of heat could have remelted the lowermost mantle, thereby inducing the dramatic volcanic events that occurred during the Earth's history. In this scenario, because the Moon is a necessary ingredient to sustain the magnetic field, the habitability on Earth appears to require the existence of a large satellite.

1. Introduction

Our knowledge of the present-day thermal state of the deep Earth has largely improved based on comparisons between seismic observations and experimental and theoretical characterizations of the Earth's materials, including studies of phase transitions and melting curves. In addition, we now have a more precise idea of the early evolution of the deep Earth based on paleomagnetic and geochemistry data as well as numerical modeling. However, the path the deep Earth has followed from its early formation to its current state remains puzzling. In particular, the Earth's heat budget over the ~4.5 billion years (Gy) of its existence remains difficult to balance satisfactorily. In this article, we challenge the classical view that the Earth is continuously cooling. We propose an alternative model for the thermal and magnetic evolution of the deep Earth. First, we review the early and the present thermal states of the deep Earth (sections 2 and 3), then we highlight the major paradoxes implied by the classical scenario based on secular cooling (section 4). Finally, we propose a steady thermal state scenario (section 5) involving an alternative source of energy to power the geodynamo: precession and tides (section 6). Section 7 presents the energy budget of the deep Earth in the framework of our model. The implications of this scenario are presented in the final section.

2. The early temperature evolution of the deep Earth

2.1. The primordial core temperature

The initial core temperature is related to a variety of processes but primarily results from the mechanism of core–mantle segregation (Stevenson, 1990). Metal/silicate separation is a rapid event

* Corresponding author.
E-mail address: denis.andrault@univ-bpclermont.fr (D. Andrault).

http://dx.doi.org/10.1016/j.epsl.2016.03.020
0012-821X/

(<60 My) contemporaneous with the Earth's accretion from many planetary embryos (Kleine et al., 2002; Rudge et al., 2010). After a meteoritic impact, the Fe-droplets produced by fragmentation of the impactor's core descended and equilibrated thermally in a highly turbulent magma ocean (Deguen et al., 2011; Samuel, 2012; Wacheul et al., 2014). The resulting iron layer/pond that formed at the bottom of the magma ocean then descended through the underlying, more viscous mantle in the form of diapirs or, alternatively, through channels (Stevenson, 1990). In both cases, the corresponding gravitational potential energy released was dissipated into heat, but the heat partitioning between the iron and the silicate depends on the segregation mechanism (Rubie et al., 2015). The diapir mechanism tends to favor heat transfer to the viscous mantle (Monteux et al., 2009; Samuel et al., 2010), while channels favor a hotter core (Ke and Solomatov, 2009), yielding a wide range of plausible thermal states at the core–mantle boundary. If metal–silicate thermal equilibration had been efficient, the initial core temperature would be similar to that of the lowermost mantle. Taking into consideration the contributions of heating from large impacts and the decay of short-lived radionuclides, the early core was likely to be hotter than the mantle liquidus soon after its formation (Rubie et al., 2015).

2.2. Early cooling of the magma ocean

The giant Moon forming impact (MFI) that occurred ~60 million years (My) after the Earth's formation (Touboul et al., 2007), likely re-melted the entire mantle (Nakajima and Stevenson, 2015) and significantly heated up the Earth's core (Herzberg et al., 2010) (Fig. 1(a)). The MFI, through the release of energy induced by gravitational segregation of the impactor's core, could have potentially increased the core temperature further by 3500–4000 K (Rubie et al., 2015). This could have resulted in an initial CMB temperature on the order of 6000 K (Nakagawa and Tackley, 2010), which is well above the mantle solidus of ~4150 K (Andrault et al., 2011; Fiquet et al., 2010). Therefore, the MFI could have caused intensive melting in the lowermost mantle.

Upon cooling of this giant-impact induced magma ocean, a thin crust rapidly formed at the surface, within the cold upper thermal boundary layer (Solomatov, 2015) (Fig. 1(b)). Just below, the magma ocean is expected to have convected vigorously. Hence, its internal temperature would follow an adiabatic profile undergoing a progressive decrease in potential surface temperature with time (Abe, 1997; Solomatov, 2000). Due to the fact that the liquidus and solidus curves present P–T slopes steeper than the magma ocean adiabats for the chondritic-type composition (Andrault et al., 2011; Thomas and Asimow, 2013), the magma ocean should solidify from the bottom up (Fig. 1(b)). The heat flux at the surface could have been as high as $\sim 10^6$ W/m^2, which suggests crystallization of most of the magma ocean within $\sim 10^3$ yrs (Solomatov, 2015). However, the situation may have been complicated by physical and chemical processes such as suspension, turbulence, nucleation, and percolation or by the formation of an opaque atmosphere at the Earth's surface. These effects could have delayed the complete crystallization of the upper mantle up to 10^8 yrs after the magma ocean began cooling (e.g. after the MFI) (Fig. 1(c) and 1(d)) (Lebrun et al., 2013; Sleep et al., 2014).

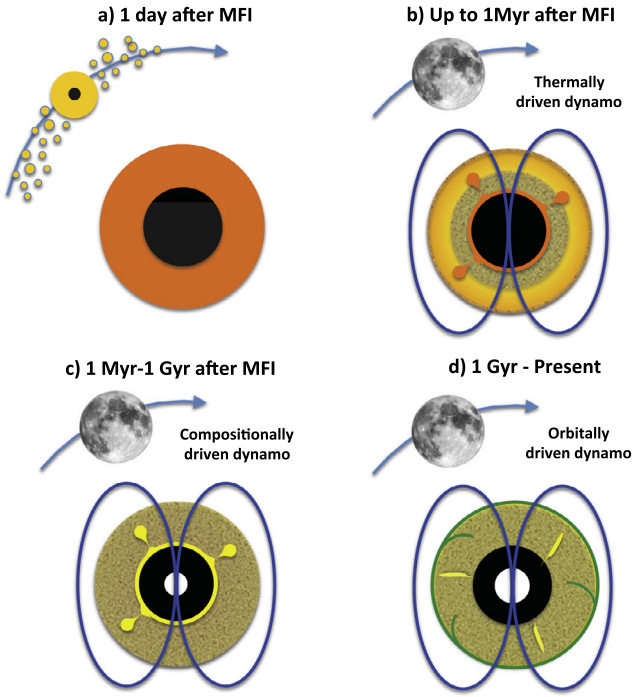

Fig. 1. Schematic representation of the Earth's interior evolution from the Moon forming impact (MFI) to the present. Full crystallization of the molten Earth was probably very complex due to suspension, turbulence, nucleation, and percolation processes (Solomatov, 2015). (a) The MFI occurred 50–100 Myr after the formation of the Ca–Al rich inclusions (CAI, the oldest objects in the solar system). It left the Earth mostly molten with a core temperature potentially above 6000 K (Rubie et al., 2015). (b) In the magma ocean, high temperatures and turbulent state should efficiently cool down the deep mantle and the liquid core. This could favor a thermally driven geodynamo. Progressive decrease of the potential temperature below the viscous threshold of 60% crystallization took within 10^3 to $\sim 10^6$ yrs, essentially depending on the magma ocean viscosity (Monteux et al., submitted for publication). During this time, a thin crust rapidly formed at the Earth's surface. Also, a basal magma ocean could have existed, however, its life time remains controversial (Labrosse et al., 2007; Monteux et al., submitted for publication). Large plumes of hot and/or partially-molten material could have migrated toward the Earth's surface. (c) The final step of mantle solidification could have taken longer, depending on the cooling efficiency at the Earth's surface (Lebrun et al., 2013; Sleep et al., 2014). This period would correspond to progressive decrease of the CMB temperature to the mantle solidus at ~4150 K (Fig. 2(a)), associated with the crystallization and the growth of the inner core (Fig. 2(b)). This would favor a compositionally driven geodynamo, an ingredient that could still today contribute to sustaining the geodynamo. (d) Later on, the long-term solid-state convection in the mantle, as we currently know it, started. At this period, the CMB temperature could have remained nearly constant for geological times. Because of moderate core cooling and growth of the inner core, a major ingredient to sustain the geodynamo could be mechanical forcing by astronomical forces. In fact, mechanical forcing could have started to induce core motions as soon as the moon was formed. Colors orange to gray (intermediate = yellow) correspond to the mantle encountering a degree of partial melting from 100% to 0% (intermediate = 40%), while black and white correspond to liquid (outer) and solid (inner) core, respectively. (For interpretation of the references to color in this figure legend, the reader is referred to the web version of this article.)

3. The present-day temperature profile in the deep Earth

3.1. Upper mantle, transition zone and the lower mantle

The temperature profile from the shallow mantle to a few hundred kilometers above the CMB is relatively well documented. The most robust constraints originate from the phase transformations at the 410, 520 and 660 km discontinuities; the depth of the phase transformations must be compatible with the phase diagram of the major upper mantle minerals, mainly olivine, which is well constrained experimentally. When including the effect of entropy variations between the different polymorphs, a temperature discontinuity of a few hundred degrees is induced at the seismic discontinuities (Katsura et al., 2010; Stacey and Davis, 2008). Complications in the temperature determination using the olivine phase diagram may arise from the uncertainties in mantle concentrations of FeO, water and ferric iron (e.g. Frost and Dolejs, 2007), because they modify the pressure of the phase transitions slightly. Lateral temperature variations are also expected from colder temperatures in subduction zones to hotter temperatures in regions of upwelling mantle (ocean ridges, for example). Altogether, the

Please cite this article in press as: Andrault, D., et al. The deep Earth may not be cooling down. Earth Planet. Sci. Lett. (2016), http://dx.doi.org/10.1016/j.epsl.2016.03.020

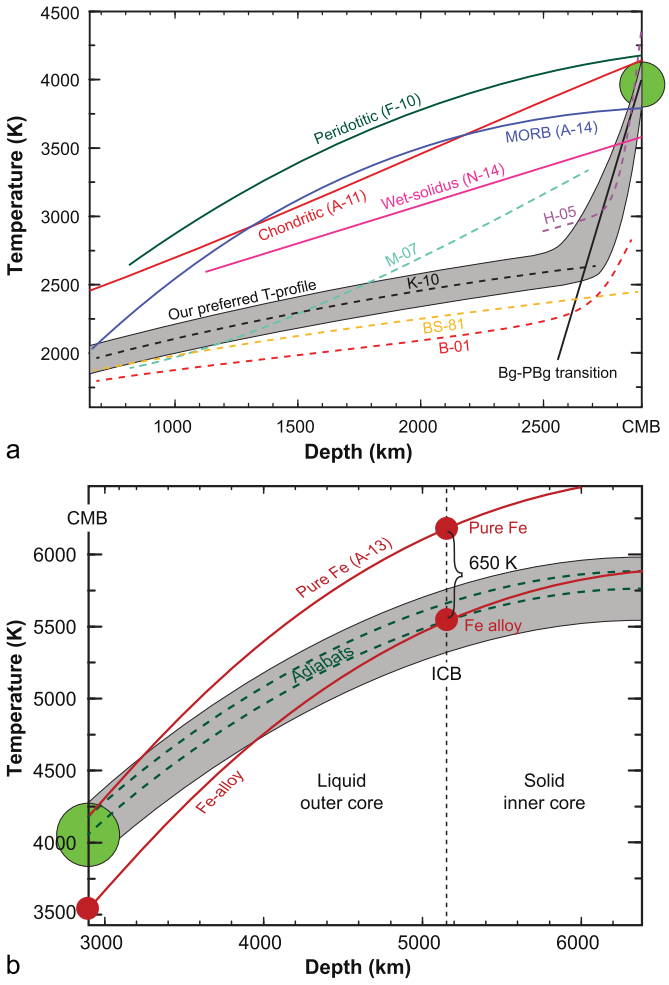

Fig. 2. Present-day temperature profile in the Earth's (a) mantle and (b) core inferred from several experimental arguments. Green circles correspond to the most likely temperature at the core–mantle boundary. (a) At the CMB pressure of 135 GPa, melting temperatures of 4180, 4150, 3800 and 3570 K were reported for peridotite (F-10, Fiquet et al., 2010), chondritic-type mantle (A-14, Andrault et al., 2014), mid-ocean ridge basalt (A-11, Andrault et al., 2011) and wet-pyrolite (N-14, Nomura et al., 2014), respectively. Dashed curves stand for adiabatic profiles (M-07, Matas et al., 2007, H-05, Hernlund et al., 2005, K-10, Katsura et al., 2010, BS-81, Brown and Shankland, 1981, B-01, Bunge et al., 2001). (b) Melting of pure Fe was reported at 4175 and 6230 K for pressure conditions of CMB (135 GPa) and ICB (330 GPa), respectively (A-13, Anzellini et al., 2013). A melting temperature depletion of ~650 K can account for the presence of light elements in the core (e.g. Morard et al., 2013). The CMB temperature is extrapolated from the ICB based on the adiabatic profile in the outer core. (For interpretation of the references to color in this figure legend, the reader is referred to the web version of this article.)

uncertainty is less than a couple of hundred degrees. Then, the temperature profile in the lower mantle is classically extrapolated from anchor points in the transition zone using an adiabatic gradient, which yields additional uncertainties. Slightly different temperature profiles can be obtained, depending on the equations of states used for the mantle (Brown and Shankland, 1981; Stacey and Davis, 2008). Other predictions give a significantly higher temperature profile when refining the seismic profiles (Vp, Vs, ρ) from the mineral equations of states (ρ, K, G) (Matas et al., 2007) (Fig. 2(a)).

3.2. The lowermost mantle

The thermal state of the lowermost mantle is not directly correlated to the surface potential temperature, but is rather tied to the temperature of the core and the heat flux at the CMB. The seismic observations of thermochemical heterogeneities and partial melting in the D"-region provide additional information to anchor the CMB temperature (Herzberg et al., 2013; Rost et al., 2005; Wen and Helmberger, 1998). It has been argued that the thermochemical piles present in this region could be interpreted as patches of post-bridgmanite (PBg) embedded in bridgmanite (Bg), which would require a double crossing of the Bg–PBg phase transition (Hernlund et al., 2005). Using the P–T Clapeyron slope of the polymorphic transition, this situation is possible if a sharp temperature change occurs when approaching the CMB, for a CMB temperature higher than 4000 K. This method based on the phase diagram of an *unrealistically* pure $MgSiO_3$ end-member has been subsequently challenged by experiments performed on the geophysically relevant Al-bearing $(Mg,Fe)SiO_3$ Bg (Andrault et al., 2010; Catalli et al., 2009). Still, the argument for a double crossing may stand for a partial and progressive transition in Bg (Hernlund, 2010).

The CMB temperature can also be constrained using the melting curve of the silicate mantle. The non-ubiquitous character of the seismic features in the D"-layer forces the CMB temperature to be lower than the mantle solidus. Otherwise, there would be a continuous melting line below which the mantle would be partially molten, due to higher temperatures in the thermal boundary layer when approaching the CMB. The solidus of chondritic-type material plots at 4150 (±150) K at a CMB pressure of 135 GPa (Andrault et al., 2011), very close to that of the peridotitic-type mantle (Fiquet et al., 2010). This solidus temperature should actually remain valid for any reasonable mineralogical system composed of Bg, $CaSiO_3$-perovskite and (Mg,Fe)O-ferropericlase, because of the pseudo-eutectic behavior. In contrast, the solidus temperature could be lowered in the presence of a high FeO-content (Mao et al., 2005), high volatile contents (Nomura et al., 2014) or when the excess mantle ferropericlase is replaced by an excess SiO_2, e.g., for a basaltic composition (Andrault et al., 2014). Water can have a dramatic effect, lowering the solidus temperature to ~3570 K, but it is unlikely that the lower mantle contains a very high water content (Bolfan-Casanova et al., 2003). In contrast, the descent of slabs toward the CMB is clearly imaged by seismic tomography (Grand et al., 1997), and slabs may very well reach the CMB. The solidus temperature of a mid-ocean ridge basalt at the CMB was reported to be 3800 (±150) K (Andrault et al., 2014), which suggests that a CMB temperature of 4000 (±200) K would produce discontinuous regions of partial melt, in agreement with seismic observations (Fig. 2(a)).

3.3. The core

The melting curve of pure iron was a long-running source of controversy until recent experimental measurements using laser-heated diamond anvil cells fell in perfect agreement with shock-wave data and ab-initio calculations (Anzellini et al., 2013) (Fig. 2(b)). The originality of this experiment relies on fast heating, to prevent the sample pollution from C diffusing out of the diamond anvils, together with the *in situ* detection of sample melting using X-ray diffraction. It suggests a melting temperature of pure Fe at the inner core boundary (ICB) of 6230 (±500) K. The light elements present in the outer core at a level of 10 wt% should lower this melting point. The melting-temperature depletions induced by the presence of S, O and Si are 100, 50 or 30 K/wt%, respectively. Unfortunately, the nature and combination of light elements in the outer core remain subject to debate. A reasonable composition could be 2.5, 5.0 and 5.0 wt% of S, O and Si, respectively, in agreement with the geochemical constraints (Dreibus and Palme, 1996), the density jump at the ICB (Alfè et al., 2002) and the seismic profiles (Vp, ρ) in the outer core (Morard et al., 2013). For this Fe-alloy composition, the melting-temperature depletion

can be estimated to 650 (±100) K. This yields an ICB temperature of 5580 (±600) K.

When this anchor point is extrapolated to the CMB using the equation of state of Fe, it yields a CMB temperature of 4100 K, if we assume a constant Grüneisen parameter of 1.51 (Vocadlo et al., 2003). The relative changes in the cocktail of light elements would not drastically change this extrapolated CMB temperature. We note that regardless of the thermal model considered for the core, the heat flux at the CMB remains moderate. Thermal boundary layers with a large temperature jump are unlikely to develop inside the liquid outer core. Therefore, the CMB temperature is a good proxy to discuss the core temperatures, using a relevant adiabatic profile. Based on the melting diagram of the Fe-alloy, the inner core should disappear for CMB temperatures above ∼4250 K. This temperature is only a couple hundred degrees above the current CMB temperature and is also just above the mantle solidus of ∼4150 K. This indicates that the onset of the inner core crystallization is expected to happen before the lowermost mantle completely solidified.

4. Secular cooling of the deep Earth? Major unresolved paradoxes

The different lines of reasoning mentioned above converge to the remarkable conclusion that today the CMB temperature is precisely at, or just below, the solidus of the silicate mantle, at 4100 K (±200) K. If the Earth has been cooling for the last ∼4.5 Gy, the early core would need to be significantly hotter in the past and, hence, overlaid by molten mantle, a primordial basal magma ocean (BMO) giving birth later to the D"-layer (Labrosse et al., 2007). In this article, we challenge this classic view of Earth's secular cooling based on three major paradoxes:

(i) Since when (and for how much additional time) the CMB temperature has (and will) remain *precisely* just below the solidus of the silicate mantle? It would be very unusual if this peculiar situation were a pure coincidence, since this temperature corresponds to a major change in the mantle state through a first-order phase transformation (the onset of melting at the solidus).

(ii) Producing the geodynamo by a combination of thermal buoyancy and compositional convection (Buffett, 2000) requires a heat flux through the CMB of possibly up to ∼10–15 terawatts (TW), depending on the controversial values of electrical and thermal conductivities of the outer core (Pozzo et al., 2012; Zhang et al., 2015). Three ingredients have been advanced to explain the persistence of a significant CMB heat flux from the oldest (4.2 Gy ago) evidences of paleo-magnetic field (Tarduno et al., 2015) to the present day: (a) The first is a tremendous initial core temperature of 5000–7000 K (Davies et al., 2015; Labrosse, 2015; Nakagawa and Tackley, 2010), well above the mantle solidus and even above the liquidus. Such high temperatures would delay the crystallization of the inner core, possibly to a period as late as 0.7 Gy ago (Labrosse, 2015), even if such a late start is still controversial (Biggin et al., 2015). (b) The second ingredient is a high concentration of radiogenic K in the core. Experimental determination of the K partitioning between metal and silicate suggests a maximum of 250 ppm K in the core (Bouhifd et al., 2007), while values below 50 ppm K appear more likely (Corgne et al., 2007; Watanabe et al., 2014). However, models of core cooling with values as high as 400–800 ppm K are not capable of sustaining the geodynamo until the present (Nakagawa and Tackley, 2010). (c) It was suggested that layered structures in the lowermost mantle (Nakagawa and Tackley, 2014) or at the top of the core (Buffett, 2014) may help to retain heat within the core, but the density contrast needs to be large to maintain a gravitationally stable liquid layer in the highly turbulent flows expected in a very hot Earth. Such a global density stratification in the mantle or in the core has not been undoubtedly demonstrated yet seismically.

(iii) The large initial temperature required for the primordial core implies large fractions of melt in the lowermost mantle. However, it seems very difficult to maintain a basal magma ocean (BMO) at a temperature significantly above the mantle solidus (or, more precisely, above the viscous transition in the mantle, which correspond to ∼40% of partial melting (Abe, 1997). This issue is detailed below) for a long period of time (see Monteux et al., submitted for publication). (a) The first reason for this is that the silicate melt viscosity is orders of magnitude lower than that of the solid mantle. To show its effect, let's assume a temperature jump of 1000 K in a super-adiabatic thermal boundary layer lying above the CMB. For a silicate melt, the boundary layer would be thinner than one meter (Solomatov, 2015), which would drive the heat flux to more than 10^6 TW. This implies a negligible temperature jump at the CMB when the silicate is liquid above the CMB. A detailed calculation of the cooling of a hot primitive core with or without a molten layer above the CMB suggests core cooling 10^6 times faster in the presence of a BMO (Monteux et al., 2011). (b) Another argument is based on the fact that the adiabatic profiles of solid, liquid and partially molten chondritic-type mantle present P–T slopes less steep than the mantle solidus (Andrault et al., 2011; Thomas and Asimow, 2013). This implies that the degree of mantle partial melting should increase with elevation from the CMB, not the contrary. For this reason, having a CMB temperature significantly above the mantle solidus would yield major mantle instabilities. If vertical chemical segregation would eventually produce a BMO with a composition different than the average mantle, the situation would not be drastically different. The temperature profile in the BMO would follow a quasi-adiabatic profile from the hot CMB to the interface between the BMO and the overlaying solid mantle. Then, all arguments raised above remain valid, but with a dominant interface for heat exchange being located between the BMO and the solid mantle, instead of exclusively at the CMB. (c) A last argument is that the hot melt could be unstable in the BMO because it is buoyant. It would travel through the mantle towards the Earth's surface. Unfortunately, this issue remains controversial (Andrault et al., 2012; Nomura et al., 2011).

5. A quasi-constant CMB temperature over geological time

The most likely thermal state after the mantle has achieved a stable character is that the BMO became significantly viscous, thus below the typical temperature threshold corresponding to 60% of crystallization. This happens at a CMB temperature of ∼4400 K for a chondritic-type mantle (Andrault et al., 2011). We note that a peridotitic mantle would become viscous at a slightly higher temperature (Fiquet et al., 2010), however, this composition is much less relevant to the primitive mantle at the CMB. As discussed above, this final temperature could be achieved in less than 10^8 yrs and it is weakly dependent on the initial CMB temperature (Lebrun et al., 2013; Sleep et al., 2014; Solomatov, 2015). This gives rise to a new paradox: while the CMB temperature reached ∼4400 K early in the Earth's history, it is only a few hundred degrees below today, at a temperature of ∼4100 K. We note that the uncertainty on the temperature difference of ∼300 K is independent of the uncertainty on the experimental determination of the solidus temperature. Indeed, the early and present-day CMB temperatures (slightly above, and just below, respectively) are determined relative to a same reference that is the solidus of the average mantle at the CMB. The uncertainty on the ∼300 K secular cooling of the CMB is estimated to ±100 K.

Such a stable CMB temperature is compatible with geological constraints on the time evolution of the mantle potential temperature (MPT, i.e. the extrapolation to the planetary surface of the mantle's adiabatic temperature profile). For example, petro-

Please cite this article in press as: Andrault, D., et al. The deep Earth may not be cooling down. Earth Planet. Sci. Lett. (2016), http://dx.doi.org/10.1016/j.epsl.2016.03.020

logical analyses of Archean and Proterozoic basalts (between 1.5 and 3.5 Gy old) preserved at the Earth's surface show primary magma compositions compatible with an MPT only ~200 K greater than today (Herzberg et al., 2010). A similar temperature change is reported between Archean tonalite–trondhjemite–granodiorite associations of 4.0 to 2.5 Gy old (Martin and Moyen, 2002). We note that the CMB temperature and the MPT are not formally linked to each other, due to an adjustable temperature jump in the thermal boundary layer above the CMB. Still, they both refer to the thermal state of the deep Earth.

Because the CMB temperature is intimately linked to the core thermal state, a steady CMB temperature over billions of years excludes core cooling as a major ingredient for driving the geodynamo during this period. There are two alternative sources that can induce the turbulent fluid motion in the outer core needed to produce the geomagnetic field: (i) Chemical buoyancy occurs when light elements (mainly O, Alfè et al., 2002) are released at the ICB due to inner core growth. This effect becomes significant when the temperature drops below ~4250 K, thus at only ~150 K above the present-day CMB temperature (Fig. 2(b)). Previous work dedicated to the analysis of the relative effects of compositional and thermal convection suggests that the same magnetic field can be generated with approximately half the heat throughput needed if the geodynamo was purely thermally driven (Gubbins et al., 2004). Still, none of the recent studies suggest that chemical buoyancy could drive alone the geomagnetic field for billions of years (Davies et al., 2015; Labrosse, 2015). Alternatively, (ii) mechanical forcing induced by precession and tidal distortions of the CMB (Dwyer et al., 2011; Le Bars et al., 2015; Tilgner, 2005) could have been a major ingredient to maintain the geomagnetic field, since the formation of the Moon. It could still operate today.

6. Precession and tides, an alternative mechanism to drive the geodynamo

Precession and tidal distortions of a planet's CMB induced by gravitational interactions with a companion (e.g. Earth and Moon) are both capable of generating core turbulence and of sustaining a dynamo with critical magnetic Reynolds numbers comparable to thermal and compositional dynamos (Cebron and Hollerbach, 2014; Tilgner, 2005). Indeed, planetary cores, as any rotating fluid, permit eigenmodes of oscillation called "inertial modes", whose restoring force is the Coriolis force. Precession and tides, seen from the mantle frame of reference as small periodic perturbations of the rotating fluid core, are capable of resonantly exciting those inertial modes, leading to fluid instabilities, turbulence and dynamo action. More specifically, two types of instabilities have been described in the literature, the same generic mechanisms working both for precession and tidal excitations (see details in Le Bars et al., 2015 and references therein): (1) the direct resonance of one given inertial mode, whose non-linear interactions produce a localized geostrophic shear layer, which can then destabilize and lead to turbulence (Malkus, 1968; Sauret et al., 2014); (2) the triadic resonance of two inertial modes with the harmonic forcing (Kerswell, 1993, 2002), which can either lead to sustained turbulence or to cycles of growth, saturation and collapse (Le Bars et al., 2010). In either case, it is important to recognize that a resonance is involved: even if the excitation amplitude is small, the resulting flows may be intense, draining their energy from the mechanism sustaining the excited waves, i.e. from the spin–orbit rotational energy of the considered system. Such mechanisms provide an appealing alternative explanation for planetary dynamos when the classical convective model does not apply. For instance, they have been proposed to explain the brief dynamos of the Moon and Mars (Stevenson, 2003), the size of these planets being insufficient to sustain long-lived thermally-driven dynamos. The disappearance of Mars' orbiting companion after it collided into the young planet (Arkani-Hamed, 2009) and the recession of the Moon (Dwyer et al., 2011) accompanied by a decrease in the precession intensity, could explain the end of their magnetic histories.

The question then remains to determine (1) whether or not mechanically forced instabilities are present in the Earth's core, and (2) whether or not the generated flows are sufficiently powerful to explain the geomagnetic field. Regarding the first point, the recent literature indeed shows that the present Earth, in the absence of a convectively imposed magnetic field (as would be the case in our non-conventional model), is subject to both tidal and precession instabilities generating turbulence (see e.g. Cebron et al., 2012). The second point has been the subject of a long debate between the seminal work of Malkus, (1968, 1963) and the subsequent studies of Rochester et al. (1975) and Loper (1975). This debate was resolved by Kerswell (1996): even if the laminar flows considered by Rochester et al. (1975) and Loper (1975) are insufficient to sustain a dynamo, the expected turbulent states in the Earth's core are largely sufficient, and the huge amount of energy stored in the Earth–Moon–Sun system (spin and orbit) provides very large source of energy to sustain the magnetic field over geological time (see e.g. Le Bars et al., 2015).

7. The energy budget to sustain the thermal steady state of the deep Earth

7.1. The core budget

Additional arguments to support this proposal are provided by considering the energy budget of the Earth's rotational dynamics as a whole. Models supported by precise measurements coming from lunar laser ranging indicate that 3.7 TW is continuously injected from the Earth–Moon–Sun orbital system into the Earth system (Munk and Wunsch, 1998; Wunsch and Ferrari, 2004). Models also indicate that 0.2 TW is dissipated into the Earth's atmosphere and its mantle; direct satellite estimates show that 1 TW is lost to the deep ocean; and the most accurate models indicate additional tidal dissipation in shallow seas of up to 2 TW (Ferrari, 2015). Hence, 0.5 to 1 TW of the dissipated rotational power is still missing in the current energy budget: it may very well be continuously injected into the outer core, where it can fulfill the energy thirst of the geodynamo, estimated to range between 0.1 to 2 TW (Buffett, 2002; Christensen and Tilgner, 2004). The situation was probably even more favorable in the past, when the Moon was closer to the Earth and when the Earth was rotating faster. Indeed, tidal distortion was previously larger and dissipation measured by the Ekman number was smaller, both ingredients being favorable to instability and turbulence (e.g. Cebron et al., 2012). One can thus imagine that throughout the history of the Earth–Moon system, turbulent flows and dynamos have been excited by mechanical forcing, the energy dissipated by both ohmic and viscous dissipations participating into the Moon's recession and deceleration (e.g. Le Bars et al., 2010).

In addition to the 0.5 to 1 TW rotational power injected into the core for dynamo action, part of which is ultimately transformed into heat by viscous and Joule dissipation, three sources could significantly contribute to the heat budget: (i) Radioactive disintegration of potassium (^{40}K) could provide between 0.2 to 1.4 TW today (Bouhifd et al., 2007; Buffett, 2002; Corgne et al., 2007; Watanabe et al., 2014), (ii) the latent heat of inner core crystallization contributes 0.3 TW, assuming that its crystallization occurs over a period of ~4.3 Gy. (iii) Finally, we note that despite a global steady state, the core temperature may have decreased from ~4400 K originally to ~4100 K today (Fig. 3). Core cooling by ~300 K over 4.3 Gy would provide an average CMB heat flux of

Please cite this article in press as: Andrault, D., et al. The deep Earth may not be cooling down. Earth Planet. Sci. Lett. (2016), http://dx.doi.org/10.1016/j.epsl.2016.03.020

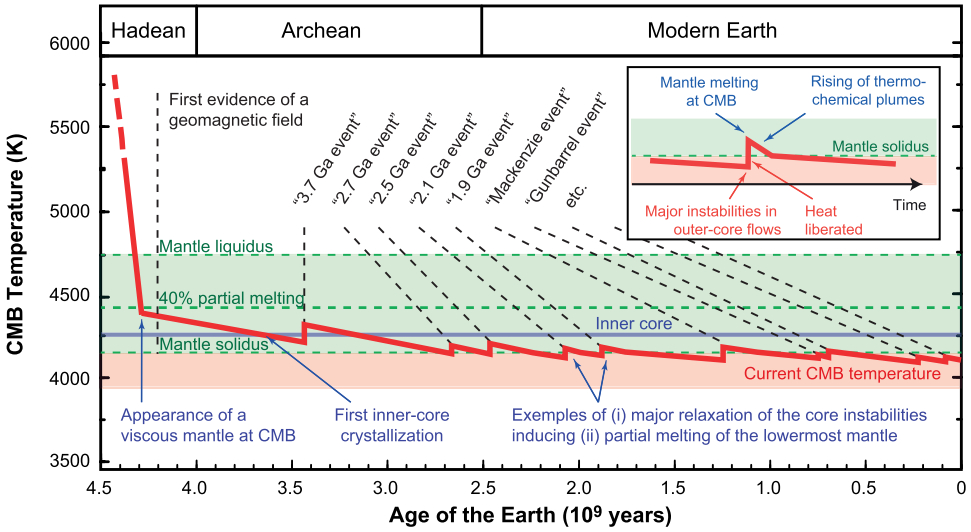

Fig. 3. Schematic evolution of the CMB temperature since the Earth's accretion. In the hypothesis of an initial CMB temperature above 6000 K (Rubie et al., 2015), rapid cooling is expected until the drastic increase in mantle viscosity at the CMB (see text and Monteux et al., submitted for publication). It corresponds to a degree of partial melting of ~40% (Abe, 1997), thus a temperature of ~4400 K for a primordial chondritic mantle (Andrault et al., 2011). Then, the complete mantle crystallization could have taken up to more than 1 Gy, as suggested by geodynamic modeling (e.g. Nakagawa and Tackley, 2010). After the mantle became significantly viscous, a purely thermally-driven dynamo becomes unlikely due to major slow-down of the CMB heat flux. As a result, the CMB temperature remained close to the mantle solidus, at ~4100 K, until today (see Fig. 2). At a period difficult to define precisely based on our model, the appearance of the inner core (indicating a CMB temperature below ~4250 K) provided buoyancy sources from the release of latent heat and light elements. Still, the sources of energy are insufficient to maintain the geodynamo from the first evidence of geomagnetic field, ~4.2 Gy ago (Tarduno et al., 2015) to present day. This strongly suggests that mechanical forcing induced by a combination of astronomical forces (see Le Bars et al., 2015) has been a major ingredient to maintain the geodynamo. Due to the intrinsically time-dependent character of the mechanical forcing, periods of growing instabilities and intense turbulent motions would alternate with cycles of relaxation associated with abrupt releases of large amounts of energy (e.g. Kerswell, 1993). Abrupt increases of the core temperature, triggering increases in partial mantle melting at the CMB (see inset), could be related to the geological evidence of periods of hot and intense volcanic eruptions (Arndt and Davaille, 2013; Martin et al., 2014).

~2 TW. Adding all contributions, the average heat flux coming out of the core could range between 3.0 and 4.7 TW.

On the other hand, the low range of values for the thermal conductivity of the outer core yields a heat flow along the outer-core adiabat between 1.7 to 3.6 TW (Buffett, 2002). For higher values of the conductivity, as suggested recently (Pozzo et al., 2012; Zhang et al., 2015), the adiabatic heat flow would be more than 10 TW (e.g. Labrosse, 2015). This range of values appears significantly higher than the 3.0 to 4.7 TW estimated using our model. We note, however, that the temperature profile in the outer core could very well be slightly sub-adiabatic. It would actually facilitate the vertical thermochemical stratification of the outer-core (Helffrich and Kaneshima, 2013). Dynamos excited by mechanical forcing do not require a super adiabatic temperature in the Earth's outer core: it has already been demonstrated that tidal and precession instabilities exist in a stratified environment, theoretically (Cebron et al., 2012), numerically (Cebron et al., 2010) and experimentally in a cylindrical geometry (Guimbard et al., 2010). Instability involves resonances of gravito-inertial waves rather than inertial waves, the main effect being to decrease the excited vertical wavelengths, with negligible or even positive effects on the instability threshold and growth. The same conclusion has been reached concerning other types of unstable flow, for instance Taylor–Couette flows (Le Bars and Le Gal, 2007): contrary to intuition, stratification is capable of increasing flow instability, and turbulence may develop while maintaining an overall global stratification. In addition to tides and precession, a dynamo driven by the solidification of the inner core could also lead to an overall subadiabiatic core, as studied for the case of Mercury (Manglik et al., 2010).

7.2. The thermal boundary layer in the lowermost mantle

The way the CMB heat flux, estimated above in the range of 3.0 to 4.7 TW from the core energy budget, is accommodated in the lowermost mantle depends on 3 major parameters: (i) the thickness of the thermal boundary layer (e_{TBL}) where conduction is the dominant mechanism of heat transfer. e_{TBL} is generally assumed to be the thickness of the D"-layer, thus 100 to 300 km, as reported by seismological studies (e.g. Lay et al., 2004). However, we note that the seismic anomalies used to define e_{TBL} are likely to be preferentially concentrated in the hottest (thus deepest) part of the TBL where the temperature approaches the mantle solidus. At larger distances from the CMB, the temperature profile could still be steeper than in the adiabatic profile (as expected within a TBL), which would however not produce detectable seismic anomalies because of the relatively lower temperatures. (ii) The thermal conductivity k of the lowermost mantle, which remains subject to controversial reports. A recent study based on *ab initio* calculations proposed $k = 3.5$ W/m/K for bridgmanite-$MgSiO_3$ (Tang et al., 2014), a value that could be even lowered, by up to 50%, if accounting for the presence of Fe and Al in the Bg-lattice (Manthilake et al., 2011). On the other hand, values up to 16 W/m/K have been proposed for $MgSiO_3$ Bg and post-Bg, with a relatively higher (but anisotropic) k value for post-Bg (Ohta et al., 2012). Also, intermediate values of 7–8 W/m/K were recently proposed, for the $MgSiO_3$ end-member again (Stackhouse et al., 2015). (iii) The difference (ΔT_{TBL}) between the CMB temperature (4100 ± 200 K) and the mantle temperature a few hundred kilometers above the CMB as extrapolated from the adiabatic profile (2600 ± 200 K). The temperature jump in the TBL could be ~1500 K (Fig. 2).

Using reasonable values of $e_{TBL} = 200$ km, $k = 5$ W/m/K, and $\Delta T_{TBL} = 1500$ K, we calculate a heat flux at the CMB of ~3.6 TW. This value falls well within the validity limit of our model that is 3 to 4.7 TW. We acknowledge that lower k values, or a thicker TLB, would induce a lower CMB heat flux. Considering all possible values of e_{TBL} from 100 to 300 km and k from 2 to 8 W/m/K results in plausible CMB heat fluxes ranging from 1.0 to 11.5 TW. Unfortunately, this broad range of uncertainties does not provide additional constraints to our model. We note that it has been sug-

gested that the possible presence of a dense viscous layer above the CMB could help reducing the CMB heat flux (Nakagawa and Tackley, 2014).

On the other hand, based on the heat carried by plumes ascending from the base of the mantle to the Earth's surface, the core heat loss has been estimated to be ~2.3 TW, or perhaps up to 3.5 TW if plumes loose significant amounts of heat during their ascent through the mantle (Davies, 2007). In such thermal budget, it is difficult to take into account the possible deep mantle complexities such as the cooling effect of plate tectonics, the insulating effect of a dense basal layer or also the importance of heat sources available in an enriched deep mantle, because the amplitude of these effects remain highly uncertain. One could argue that our estimated value of the CMB heat flux is much lower than that calculated in recent geodynamic models (e.g. Nakagawa and Tackley, 2014). However, such models generally assume a fully viscous mantle, even for an initial CMB temperature of 6000 K that is well above the mantle solidus and the viscous limit of 40% of partial melt. As acknowledged in Nakagawa and Tackley (2014), this artificially maintains a hot core for a long period of time, associated with a substantial CMB flux. In a recent study, it was instead shown that an extremely large CMB heat flux prevailed early in the Earth's history, until the viscous transition is reached in the lowermost mantle (Monteux et al., submitted for publication). It yields a CMB temperature of ~4400 K in less than ~1 My after the MFI, associated with a much lower CMB heat flux after the early fast cooling.

8. Implications for geodynamics and major geological events

In addition to generating the Earth's dynamo, turbulent motions excited by astronomical forcing can induce cycles of growth, saturation and abrupt relaxation of the hydrodynamic instabilities (Kerswell, 1993; Le Bars et al., 2010). The collapses could induce an abrupt release of energy, potentially up to 10^9 TW (Kerswell, 1996) over short periods of time, in addition to the resonances in the Earth–Moon–Sun spin–orbit system (Greff-Lefftz and Legros, 1999). The pulse duration could vary from a couple periods of rotation (a couple of days) to several hundred years. This corresponds to a broad range of thermal energy release, which could induce core heating by a few to a few hundred of degrees, depending on the integrated pulse amplitude. We note that the 0.5 to 1 TW currently dissipated into the Earth's outer core from the Earth–Moon–Sun orbital system cannot heat the core more than a couple hundred degrees. However, much larger heat pulses could have happened in the past when the Moon was closer to the Earth and when the Earth was rotating faster (Fig. 3).

Such fluctuations of the CMB temperature could have two major consequences. (a) Following the adiabatic temperature profile of the Fe-alloy from the CMB to the ICB, they should induce fluctuations in the size of the inner core (Fig. 2(b)): The abrupt release of hydrodynamic instabilities could reduce the size of the inner core and restore its capability to produce the geodynamo by chemical buoyancy, when the CMB temperature would eventually decrease again by cooling due to weaker dissipation by mechanical forcing. The possibility that an old inner core has undergone several changes in its size, with a rapid decrease and slow increase of its radius could be important for building the inner core anisotropy (Poupinet et al., 1983) as well as a mushy layer at the top of the inner core (Loper and Fearn, 1983). Indeed, both geophysical interpretation are closely related to the mechanism of inner core crystallization. (b) On the other hand, partial melting in the lowermost mantle could act as an efficient agent for transferring the excess heat of the core to the overlying mantle: Increasing the temperature above the mantle solidus at the CMB would result in an increase in the degree of partial melting in the lowermost mantle, which in turn would induce a larger CMB heat flux. This mechanism could damp the fluctuations in heat production in the turbulent outer core yielding a stable CMB temperature, precisely at, or just below, the mantle solidus. This thermal state corresponds well to the present-day view of the D"-layer, where piles of partially molten silicate material (the ultra-low velocity zones) interact with mantle convection. Adding heat to the current lowermost mantle would certainly enhance partial melting and the thermal instabilities (inset in Fig. 3). As a result, one should expect an increase of the volcanic activity at the Earth's surface shortly after the influx of heat at the CMB (Greff-Lefftz and Legros, 1999). If the brutal energy influx is important, this could explain dramatic eruptions such as the Deccan Trapps (Courtillot and Fluteau, 2010), as well as the periodic growth of continents at the Earth's surface (Arndt and Davaille, 2013; Martin et al., 2014).

Finally, because the Moon appears to be a necessary ingredient to sustain the magnetic field, and because a magnetic field is needed to shield the Earth's atmosphere from erosion by solar wind (e.g. Dehant et al., 2007), the habitability of Earth-like planet may be subordinated to the existence of a large satellite. While more than 1000 exoplanets have already been observed, the detection of an accompanying exo-moon is rare (Bennett et al., 2014). Hence, our model could have major implications in future planetary missions as exoplanets with orbiting moons would more likely host extraterrestrial life.

Acknowledgements

We thank D. Cébron, B. Favier, R. Ferrari, H. Martin and the anonymous reviewers for fruitful discussions and help. This work has gained value from previous collaborative works with N. Bolfan-Casanova, M.A. Bouhifd, M. Mezouar and G. Morard. This is an ANR-OxyDeep and ANR-Clervolc contribution No. 198.

References

Abe, Y., 1997. Thermal and chemical evolution of the terrestrial magma ocean. Phys. Earth Planet. Inter. 100, 27–39.

Alfè, D., Gillan, M.J., Price, G.D., 2002. Composition and temperature of the Earth's core constrained by combining ab initio and seismic data. Earth Planet. Sci. Lett. 195, 91–98.

Andrault, D., Bolfan-Casanova, N., Lo Nigro, G., Bouhifd, M.A., Garbarino, G., Mezouar, M., 2011. Melting curve of the deep mantle applied to properties of early magma ocean and actual core–mantle boundary. Earth Planet. Sci. Lett. 304, 251–259.

Andrault, D., Munoz, M., Bolfan-Casanova, N., Guignot, N., Perrillat, J.P., Aquilanti, G., Pascarelli, S., 2010. Experimental evidence for perovskite and post-perovskite coexistence throughout the whole D" region. Earth Planet. Sci. Lett. 293, 90–96.

Andrault, D., Pesce, G., Bouhifd, M.A., Bolfan-Casanova, N., Henot, J.M., Mezouar, M., 2014. Melting of subducted basalt at the core–mantle boundary. Science 344, 892–895.

Andrault, D., Petitgirard, S., Lo Nigro, G., Devidal, J.L., Veronesi, G., Garbarino, G., Mezouar, M., 2012. Solid–liquid iron partitioning in Earth's deep mantle. Nature 487, 354–357.

Anzellini, S., Dewaele, A., Mezouar, M., Loubeyre, P., Morard, G., 2013. Melting of iron at Earth's inner core boundary based on fast X-ray diffraction. Science 340, 464–466.

Arkani-Hamed, J., 2009. Did tidal deformation power the core dynamo of Mars? Icarus 201, 31–43.

Arndt, N., Davaille, A., 2013. Episodic Earth evolution. Tectonophysics 609, 661–674.

Bennett, D.P., Batista, V., Bond, I.A., Bennett, C.S., Suzuki, D., Beaulieu, J.P., Udalski, A., Donatowicz, J., Bozza, V., Abe, F., Botzler, C.S., Freeman, M., Fukunaga, D., Fukui, A., Itow, Y., Koshimoto, N., Ling, C.H., Masuda, K., Matsubara, Y., Muraki, Y., Namba, S., Ohnishi, K., Rattenbury, N.J., Saito, T., Sullivan, D.J., Sumi, T., Sweatman, W.L., Tristram, P.J., Tsurumi, N., Wada, K., Yock, P.C.M., Albrow, M.D., Bachelet, E., Brillant, S., Caldwell, J.A.R., Cassan, A., Cole, A.A., Corrales, E., Coutures, C., Dieters, S., Prester, D.D., Fouque, P., Greenhill, J., Horne, K., Koo, J.R., Kubas, D., Marquette, J.B., Martin, R., Menzies, J.W., Sahu, K.C., Wambsganss, J., Williams, A., Zub, M., Choi, J.Y., DePoy, D.L., Dong, S., Gaudi, B.S., Gould, A., Han, C., Henderson, C.B., McGregor, D., Lee, C.U., Pogge, R.W., Shin, I.G., Yee, J.C., Szymanski, M.K., Skowron, J., Poleski, R., Kozlowski, S., Wyrzykowski, L., Kubiak, M., Pietrukowicz, P., Pietrzynski, G., Soszynski, I., Ulaczyk, K., Tsapras, Y., Street, R.A., Dominik, M., Bramich, D.M., Browne, P., Hundertmark, M., Kains, N., Snodgrass,

C., Steele, I.A., Dekany, I., Gonzalez, O.A., Heyrovsky, D., Kandori, R., Kerins, E., Lucas, P.W., Minniti, D., Nagayama, T., Rejkuba, M., Robin, A.C., Saito, R., Collaboration M.O.A., Collaboration P., Collaboration F.U.N., Collaboration O., RoboNet C., 2014. MOA-2011-BLG-262Lb: a sub-Earth-mass moon orbiting a gas giant primary or a high velocity planetary system in the galactic bulge. Astrophys. J. 785.

Biggin, A.J., Piispa, E.J., Pesonen, L.J., Holme, R., Paterson, G.A., Veikkolainen, T., Tauxe, L., 2015. Palaeomagnetic field intensity variations suggest Mesoproterozoic inner-core nucleation. Nature 526, 245.

Bolfan-Casanova, N., Keppler, H., Rubie, D.C., 2003. Water partitioning at 660 km depth and evidence for very low water solubility in magnesium silicate perovskite. Geophys. Res. Lett. 30, L017182.

Bouhifd, M.A., Gautron, L., Bolfan-Casanova, N., Malavergne, V., Hammouda, T., Andrault, D., Jephcoat, A.P., 2007. Potassium partitioning into molten iron alloys at high-pressure: implications for Earth's core. Phys. Earth Planet. Inter. 160, 22–33.

Brown, J.M., Shankland, T.J., 1981. Thermodynamic parameters in the Earth as determined from seismic profiles. Geophys. J. R. Astron. Soc. 66, 579–596.

Buffett, B., 2014. Geomagnetic fluctuations reveal stable stratification at the top of the Earth's core. Nature 507, 484–487.

Buffett, B.A., 2000. Earth's core and the geodynamo. Science 288, 2007–2012.

Buffett, B.A., 2002. Estimates of heat flow in the deep mantle based on the power requirements for the geodynamo. Geophys. Res. Lett. 29.

Bunge, H.P., Ricard, Y., Matas, J., 2001. Non-adiabaticity in mantle convection. Geophys. Res. Lett. 28, 879–882.

Catalli, K., Shim, S.H., Prakapenka, V.B., 2009. Thickness and Clapeyron slope of the post-perovskite boundary. Nature 462, 782–785.

Cebron, D., Hollerbach, R., 2014. Tidally driven dynamos in a rotating sphere. Astrophys. J. Lett. 789.

Cebron, D., Le Bars, M., Moutou, C., Le Gal, P., 2012. Elliptical instability in terrestrial planets and moons. Astron. Astrophys. 539.

Cebron, D., Maubert, P., Le Bars, M., 2010. Tidal instability in a rotating and differentially heated ellipsoidal shell. Geophys. J. Int. 182, 1311–1318.

Christensen, U.R., Tilgner, A., 2004. Power requirement of the geodynamo from ohmic losses in numerical and laboratory dynamos. Nature 429, 169–171.

Corgne, A., Keshav, S., Fei, Y., McDonough, W.F., 2007. How much potassium is in the Earth's core? New insights from partitioning experiments. Earth Planet. Sci. Lett. 256, 567–576.

Courtillot, V., Fluteau, F., 2010. Cretaceous extinctions: the volcanic hypothesis. Science 328, 973–974.

Davies, C., Pozzo, M., Gubbins, D., Alfe, D., 2015. Constraints from material properties on the dynamics and evolution of Earth's core. Nat. Geosci. 8, 678.

Davies, G.F., 2007. Mantle regulation of core cooling: a geodynamo without core radioactivity? Phys. Earth Planet. Inter. 160, 215–229.

Deguen, R., Olson, P., Cardin, P., 2011. Experiments on turbulent metal–silicate mixing in a magma ocean. Earth Planet. Sci. Lett. 310, 303–313.

Dehant, V., Lammer, H., Kulikov, Y.N., Griessmeier, J.M., Breuer, D., Verhoeven, O., Karatekin, O., Van Hoolst, T., Korablev, O., Lognonne, P., 2007. Planetary magnetic dynamo effect on atmospheric protection of early Earth and Mars. Space Sci. Rev. 129, 279–300.

Dreibus, G., Palme, H., 1996. Cosmochemical constraints on the sulfur content in the Earth's core. Geochim. Cosmochim. Acta 60, 1125–1130.

Dwyer, C.A., Stevenson, D.J., Nimmo, F., 2011. A long-lived lunar dynamo driven by continuous mechanical stirring. Nature 479, 212–284.

Ferrari, R., 2015. Personal communication.

Fiquet, G., Auzende, A.L., Siebert, J., Corgne, A., Bureau, H., Ozawa, H., Garbarino, G., 2010. Melting of peridotite to 140 gigapascals. Science 329, 1516–1518.

Frost, D.J., Dolejs, D., 2007. Experimental determination of the effect of H_2O on the 410-km seismic discontinuity. Earth Planet. Sci. Lett. 256, 182–195.

Grand, S.P., Van der Hilst, R.D., Widiyantoro, S., 1997. High resolution global tomography: a snapshot of convection in the Earth. GSA Today 7, 1–7.

Greff-Lefftz, M., Legros, H., 1999. Core rotational dynamics and geological events. Science 286, 1707–1709.

Gubbins, D., Alfe, D., Masters, G., Price, G.D., Gillan, M., 2004. Gross thermodynamics of two-component core convection. Geophys. J. Int. 157, 1407–1414.

Guimbard, D., Le Dizes, S., Le Bars, M., Le Gal, P., Leblanc, S., 2010. Elliptic instability of a stratified fluid in a rotating cylinder. J. Fluid Mech. 660, 240–257.

Helffrich, G., Kaneshima, S., 2013. Causes and consequences of outer core stratification. Phys. Earth Planet. Inter. 223, 2–7.

Hernlund, J.W., 2010. On the interaction of the geotherm with a post-perovskite phase transition in the deep mantle. Phys. Earth Planet. Inter. 180, 222–234.

Hernlund, J.W., Thomas, C., Tackley, P.J., 2005. A doubling of the post-perovskite phase boundary and structure of the Earth's lowermost mantle. Nature 434, 882–886.

Herzberg, C., Asimow, P.D., Ionov, D.A., Vidito, C., Jackson, M.G., Geist, D., 2013. Nickel and helium evidence for melt above the core–mantle boundary. Nature 493. 393-U134.

Herzberg, C., Condie, K., Korenaga, J., 2010. Thermal history of the Earth and its petrological expression. Earth Planet. Sci. Lett. 292, 79–88.

Katsura, T., Yoneda, A., Yamazaki, D., Yoshino, T., Ito, E., 2010. Adiabatic temperature profile in the mantle. Phys. Earth Planet. Inter. 183, 212–218.

Ke, Y., Solomatov, V.S., 2009. Coupled core–mantle thermal evolution of early Mars. J. Geophys. Res., Planets 114.

Kerswell, R.R., 1993. The instability of precessing flow. Geophys. Astrophys. Fluid Dyn. 72, 107–144.

Kerswell, R.R., 1996. Upper bounds on the energy dissipation in turbulent precession. J. Fluid Mech. 321, 335–370.

Kerswell, R.R., 2002. Elliptical instability. Annu. Rev. Fluid Mech. 34, 83–113.

Kleine, T., Munker, C., Mezger, K., Palme, H., 2002. Rapid accretion and early core formation on asteroids and the terrestrial planets from Hf-W chronometry. Nature 418, 952–955.

Labrosse, S., 2015. Thermal evolution of the core with a high thermal conductivity. Phys. Earth Planet. Inter 247, 36–55.

Labrosse, S., Hernlund, J.W., Coltice, N., 2007. A crystallizing dense magma ocean at the base of the Earth's mantle. Nature 450, 866–869.

Lay, T., Garnero, E.J., Williams, Q., 2004. Partial melting in a thermo-chemical boundary layer at the base of the mantle. Phys. Earth Planet. Inter. 146, 441–467.

Le Bars, M., Cébron, D., Le Gal, P., 2015. Flows driven by libration, precession, and tides. Annu. Rev. Fluid Mech. 47, 163–193.

Le Bars, M., Lacaze, L., Le Dizes, S., Le Gal, P., Rieutord, M., 2010. Tidal instability in stellar and planetary binary systems. Phys. Earth Planet. Inter. 178, 48–55.

Le Bars, M., Le Gal, P., 2007. Experimental analysis of the stratorotational instability in a cylindrical Couette flow. Phys. Rev. Lett. 99.

Lebrun, T., Massol, H., Chassefiere, E., Davaille, A., Marcq, E., Sarda, P., Leblanc, F., Brandeis, G., 2013. Thermal evolution of an early magma ocean in interaction with the atmosphere. J. Geophys. Res., Planets 118, 1155–1176.

Loper, D.E., 1975. Torque balance and energy budget for precessional driven dynamo. Phys. Earth Planet. Inter. 11, 43–60.

Loper, D.E., Fearn, D.R., 1983. A seismic model of partially molten inner core. J. Geophys. Res. 88, 1235–1242.

Malkus, W.V.R., 1968. Precession of the Earth as the cause of geomagnetism. Science 160, 259–264.

Malkus, W.V.R., 1963. Precessional torques as cause of geomagnetism. J. Geophys. Res. 68, 2871.

Manglik, A., Wicht, J., Christensen, U.R., 2010. A dynamo model with double diffusive convection for Mercury's core. Earth Planet. Sci. Lett. 289, 619–628.

Manthilake, G.M., de Koker, N., Frost, D.J., McCammon, C.A., 2011. Lattice thermal conductivity of lower mantle minerals and heat flux from Earth's core. Proc. Natl. Acad. Sci. USA 108, 17901–17904.

Mao, W.L., Meng, Y., Shen, G., Prakapenka, V.B., Campbell, A.J., Heinz, D.L., Shu, J., Caracas, R., Cohen, R.E., Fei, Y., Hemley, R.J., Mao, H.K., 2005. Iron-rich silicate in the Earth's D" layer. Proc. Natl. Acad. Sci. USA 102, 9751–9753.

Martin, H., Moyen, J.F., 2002. Secular changes in tonalite–trondhjemite–granodiorite composition as markers of the progressive cooling of Earth. Geology 30, 319–322.

Martin, H., Moyen, J.F., Guitreau, M., Blichert-Toft, J., Le Pennec, J.L., 2014. Why Archaean TTG cannot be generated by MORB melting in subduction zones. Lithos 198, 1–13.

Matas, J., Bass, J.D., Ricard, Y., Mattern, E., Bukowinsky, M.S., 2007. On the bulk composition of the lower mantle: predictions and limitations from generalized inversion of radial seismic profiles. Geophys. J. Int. 170, 764–780.

Monteux, J., Andrault, D., Samuel, H., submitted for publication. On the cooling of a deep terrestrial magma ocean. Earth Planet. Sci. Lett.

Monteux, J., Jellinek, A.M., Johnson, C.L., 2011. Why might planets and moons have early dynamos? Earth Planet. Sci. Lett. 310, 349–359.

Monteux, J., Ricard, Y., Coltice, N., Dubuffet, F., Ulvrova, M., 2009. A model of metal–silicate separation on growing planets. Earth Planet. Sci. Lett. 287, 353–362.

Morard, G., Siebert, J., Andrault, D., Guignot, N., Garbarino, G., Guyot, F., Antonangeli, D., 2013. The Earth's core composition from high pressure density measurements of liquid iron alloys. Earth Planet. Sci. Lett. 373, 169–178.

Munk, W., Wunsch, C., 1998. Abyssal recipes II: energetics of tidal and wind mixing. Deep-Sea Res. Pt. I 45, 1977–2010.

Nakagawa, T., Tackley, P.J., 2010. Influence of initial CMB temperature and other parameters on the thermal evolution of Earth's core resulting from thermo-chemical spherical mantle convection. Geochem. Geophys. Geosyst. 11, Q06001.

Nakagawa, T., Tackley, P.J., 2014. Influence of combined primordial layering and recycled MORB on the coupled thermal evolution of Earth's mantle and core. Geochem. Geophys. Geosyst. 15, 619–633.

Nakajima, M., Stevenson, D.J., 2015. Melting and mixing states of the Earth's mantle after the Moon-forming impact. Earth Planet. Sci. Lett 427, 286–295.

Nomura, R., Hirose, K., Uesugi, K., Ohishi, Y., Tsuchiyama, A., Miyake, A., Ueno, Y., 2014. Low core–mantle boundary temperature inferred from the solidus of pyrolite. Science 343, 522–525.

Nomura, R., Ozawa, H., Tateno, S., Hirose, K., Hernlund, J.W., Muto, S., Ishii, H., Hiraoka, N., 2011. Spin crossover and iron-rich silicate melt in the Earth's deep mantle. Nature 473, 199–202.

Ohta, K., Yagi, T., Taketoshi, N., Hirose, K., Kornabayashi, T., Baba, T., Ohishi, Y., Hernlund, J., 2012. Lattice thermal conductivity of $MgSiO_3$ perovskite and post-perovskite at the core–mantle boundary. Earth Planet. Sci. Lett. 349, 109–115.

Poupinet, G., Pillet, R., Souriau, A., 1983. Possible heterogeneity of the Earth's core deduced from PKIKP travel times. Nature 305, 204–206.

Pozzo, M., Davies, C., Gubbins, D., Alfè, D., 2012. Thermal and electrical conductivity of iron at Earth's core conditions. Nature 485, 355–399.
Rochester, M.G., Jacobs, J.A., Smylie, D.E., Chong, K.F., 1975. Can precession power geomagnetic dynamo. Geophys. J. R. Astron. Soc. 43, 661–678.
Rost, S., Garnero, E.J., Williams, Q., Manga, M., 2005. Seismological constraints on a possible plume root at the core–mantle boundary. Nature 435, 666–669.
Rubie, D.C., Nimmo, H.J., Melosh, H.J., 2015. Formation of the Earth's core. In: Schubert, G. (Ed.), Treatise on Geophysics, 2nd ed. Elsevier, Amsterdam, pp. 43–79.
Rudge, J.F., Kleine, T., Bourdon, B., 2010. Broad bounds on Earth's accretion and core formation constrained by geochemical models. Nat. Geosci. 3, 439–443.
Samuel, H., 2012. A re-evaluation of metal diapir breakup and equilibration in terrestrial magma oceans. Earth Planet. Sci. Lett. 313, 105–114.
Samuel, H., Tackley, P.J., Evonuk, M., 2010. Heat partitioning in terrestrial planets during core formation by negative diapirism. Earth Planet. Sci. Lett. 290, 13–19.
Sauret, A., Le Bars, M., Le Gal, P., 2014. Tide-driven shear instability in planetary liquid cores. Geophys. Res. Lett. 41, 6078–6083.
Sleep, N.H., Zahnle, K.J., Lupu, R.E., 2014. Terrestrial aftermath of the Moon-forming impact. Philos. Trans. R. Soc. A 372.
Solomatov, V.S., 2000. Fluid dynamics of terrestrial magma ocean. In: Canup, R.M., Righter, K. (Eds.), Origin of the Earth and Moon. The University of Arizona Press, Tucson, Arizona, pp. 323–338.
Solomatov, V.S., 2015. Magma oceans and primordial mantle differentiation. In: Schubert, G. (Ed.), Treatise on Geophysics, 2nd ed. Elsevier, Amsterdam, pp. 81–104.
Stacey, F.D., Davis, P.M., 2008. Physics of the Earth, 4th ed. Cambridge University Press.
Stackhouse, S., Stixrude, L., Karki, B.B., 2015. First-principles calculations of the lattice thermal conductivity of the lower mantle. Earth Planet. Sci. Lett. 427, 11–17.
Stevenson, D.J., 1990. Fluid dynamics of core formation. In: Newsom, H., Jones, J.H. (Eds.), The Origin of the Earth. Oxford Press, London, pp. 231–249.
Stevenson, D.J., 2003. Planetary magnetic fields. Earth Planet. Sci. Lett. 208, 1–11.
Tang, X.L., Ntam, M.C., Dong, J.J., Rainey, E.S.G., Kavner, A., 2014. The thermal conductivity of Earth's lower mantle. Geophys. Res. Lett. 41, 2746–2752.
Tarduno, J.A., Cottrell, R.D., Davis, W.J., Nimmo, F., Bono, R.K., 2015. A Hadean to Paleoarchean geodynamo recorded by single zircon crystals. Science 349, 521–524.
Thomas, C.W., Asimow, P.D., 2013. Direct shock compression experiments on premolten forsterite and progress toward a consistent high-pressure equation of state for CaO–MgO–Al_2O_3–SiO_2–FeO liquids. J. Geophys. Res., Solid Earth 118, 5738–5752.
Tilgner, A., 2005. Precession driven dynamos. Phys. Fluids 17.
Touboul, M., Kleine, T., Bourdon, B., Palme, H., Wieler, R., 2007. Late formation and prolonged differentiation of the Moon inferred from W isotopes in lunar metals. Nature 450, 1206–1209.
Vocadlo, L., Alfe, D., Gillan, M.J., Wood, I.G., Brodholt, J.P., Price, G.D., 2003. Possible thermal and chemical stabilization of body-centred-cubic iron in the Earth's core. Nature 424, 536–539.
Wacheul, J.-B., Le Bars, M., Monteux, J., Aurnou, J.M., 2014. Laboratory experiments on the breakup of liquid metal diapirs. Earth Planet. Sci. Lett. 403, 236–245.
Watanabe, K., Ohtani, E., Kamada, S., Sakamaki, T., Miyahara, M., Ito, Y., 2014. The abundance of potassium in the Earth's core. Phys. Earth Planet. Inter. 237, 65–72.
Wen, L., Helmberger, D.V., 1998. Ultra-low velocity zones near the core–mantle boundary from broadband PKP precursors. Science 279, 1701–1703.
Wunsch, C., Ferrari, R., 2004. Vertical mixing, energy and the general circulation of the oceans. Annu. Rev. Fluid Mech. 36, 281–314.
Zhang, P., Cohen, R.E., Haule, K., 2015. Effects of electron correlations on transport properties of iron at Earth's core conditions. Nature 517, 605-NIL_376.

Please cite this article in press as: Andrault, D., et al. The deep Earth may not be cooling down. Earth Planet. Sci. Lett. (2016), http://dx.doi.org/10.1016/j.epsl.2016.03.020

JGR Planets

RESEARCH ARTICLE
10.1029/2019JE005979

Key Points:
- Incorporation of S significantly reduces both electrical and thermal conductivities of FeS
- The low thermal conductivity of FeS may have prevented the Mercurian core from rapid solidification
- Mercury dynamo can be driven by both thermal and chemical buoyancy forces

Correspondence to:
G. Manthilake,
geeth.manthilake@uca.fr

Citation:
Manthilake, G., Chantel, J., Monteux, J., Andrault, D., Bouhifd, M. A., Bolfan Casanova, N., et al. (2019). Thermal conductivity of FeS and its implications for Mercury's long-sustaining magnetic field. *Journal of Geophysical Research: Planets*, *124*. https://doi.org/10.1029/2019JE005979

Received 22 MAR 2019
Accepted 14 AUG 2019
Accepted article online 21 AUG 2019

Author Contributions:
Conceptualization: G. Manthilake
Data curation: G. Manthilake
Formal analysis: G. Manthilake, J. Chantel, D. Andrault, M. A. Bouhifd, N. Bolfan Casanova, E. Boulard
Funding acquisition: G. Manthilake
Investigation: G. Manthilake, J. Monteux, D. Andrault
Methodology: G. Manthilake, N. Guignot, A. King, J. P. Itie
Project administration: G. Manthilake
Resources: G. Manthilake, N. Guignot, A. King, J. P. Itie
Writing - original draft: G. Manthilake, J. Monteux
Writing – review & editing: G. Manthilake, J. Monteux

Thermal Conductivity of FeS and Its Implications for Mercury's Long-Sustaining Magnetic Field

G. Manthilake[1], J. Chantel[2], J. Monteux[1], D. Andrault[1], M. A. Bouhifd[1], N. Bolfan Casanova[1], E. Boulard[3], N. Guignot[3], A. King[3], and J. P. Itie[3]

[1]Laboratoire Magmas et Volcans, Université Clermont Auvergne, CNRS, IRD, OPGC, Clermont-Ferrand, France, [2]Unite Matériaux et Transformations, CNRS, Université de Lille, Villeneuve d'Ascq, France, [3]Sorbonne Universite, Museum National d'Histoire Naturelle, UMR CNRS 7590, IRD, Institut de Mineralogie, Physique des Materiaux et Cosmochimie - IMPMC, Paris, France

Abstract The MESSENGER mission revealed that Mercury's magnetic field might have operated since 3.7–3.9 Ga. While the intrinsic magnetism suggests an active dynamo within Mercury's core, the mechanism that is responsible for sustaining the dynamo for prolonged period of time remains unknown. Here we investigated the electrical conductivity of Fe-S alloys at pressure of 8 GPa and temperatures up to 1,700 K. We show that the electrical conductivity of Fe-S alloys at 1,500 K is about 10^3 S/m, 2 orders of magnitude lower than the previously assumed value for dynamo calculations. The thermal conductivity was estimated using the Wiedemann-Franz law. The total thermal conductivity of FeS is estimated to be ~4 Wm/K at the Mercurian core-mantle boundary conditions. The low thermal conductivity suggests that a thermally driven dynamo operating on Mercury is more likely than expected. If coupled with chemical buoyancy sources, it is possible to sustain an intrinsic dynamo during time scales compatible with the MESSENGER observations.

Plain Language Summary Mercury's weak magnetic field intensity that persisted over the last 3.9 billion years has long baffled the planetary science community. Various explanations have been proposed; nevertheless, there has been no consensus on how intrinsic dynamo with such weak energetics have existed in Mercury for prolonged period. In our submitted manuscript, we exclusively looked at the electrical and thermal conductivity in Fe-S alloys, the dominant phase in planet Mercury's outer core. Our results indicate that electrical conductivity of Fe-S alloys is 2 orders of magnitude lower than the previously assumed value for dynamo calculations. The low thermal conductivity obtained in this study suggests that the heat extraction from Mercury's core through the solid Fe-S layer is a highly inefficient process. Our estimations suggest the heat-flux from the core only produces less than 1 TW of energy. The low heat flux prevents the Mercurian core from rapid solidification, sustaining an intrinsic dynamo in Mercury since ~3.9 Ga.

1. Introduction

The planet Mercury currently exhibits a surface magnetic field with a *field* strength representing 1.1% that of the Earth's magnetic field (Anderson et al., 2011). The spin-aligned axisymmetric and offset dipole-dominated field is considered unique among planetary magnetic fields (Tian et al., 2015). The low-altitude magnetic field measurements by the MESSENGER mission have revealed a remnant magnetization in Mercury's crust with age of magnetization in the range of 3.7–3.9 Ga (Johnson et al., 2015). The presence of a magnetic field early in Mercury's history as early as 3.9 Ga and the extremely weak magnetic field strength in present-day Mercury suggest that Mercury's magnetic field may have been active for the last 3.7–3.9 Ga. While the observed intrinsic magnetism suggests an active dynamo generated in Mercury's liquid outer core, how Mercury's magnetic field sustained for a prolonged period of time remains puzzling even in the light of our current understanding of the Earth and planetary dynamos (Johnson et al., 2015).

It has been suggested that Mercury's dynamo is currently generated by chemical convection (Breuer et al., 2015; Cao et al., 2014; Chen et al., 2008; Dumberry & Rivoldini, 2015). The low magnetic field intensity of planet Mercury has been discussed using thermoelectric (Stevenson, 1987), thin shell (Stanley et al., 2005), thick shell (Heimpel et al., 2005), and feedback (Glassmeier et al., 2007) dynamo models. Recent dynamo studies linked the low intensity and the axisymmetry of the magnetic field to a stably stratified

layer with latitudinal heat-flux variations (Christensen & Wicht, 2008; Christensen, 2006; Schubert et al., 2004; Tian et al., 2015).

The chemical composition and the internal structure of Mercury remain poorly understood mainly due to the lack of observational constraints (Margot et al., 2018). Mercury's solid outer shell overlying the liquid core is estimated to be ~400 km thick and believed to consist mainly of silicate minerals (Hauck et al., 2013; Rivoldini & Van Hoolst, 2013). Recent gravity field analyses indicate that Mercury's internal structure consists of an Fe-S-Si liquid outer core (Chabot et al., 2014; Hauck et al., 2013; Knibbe & van Westrenen, 2015; Margot et al., 2018; Rivoldini & Van Hoolst, 2013; D. E. Smith et al., 2012). A substantial number of studies have considered S and Si as principal alloying elements in the liquid outer core (Chabot et al., 2014; Hauck et al., 2013; Malavergne et al., 2010; Namur et al., 2016; Rivoldini et al., 2009; Schubert et al., 1988; Stevenson et al., 1983). The presence of an inner core in Mercury has been debated (Margot et al., 2018). Different models for Mercury's interior suggest the presence of a solid inner core, which may have formed as a result of planetary cooling (Veasey & Dumberry, 2011). Recent estimations indicate that the diameter of the solid inner core would be 0.3–0.7 of the diameter of Mercury's core (Genova et al., 2019).

The elemental composition analyses during the MESSENGER mission indicate 1–4 wt % of Fe and S in Mercury's surface (Evans et al., 2012; Nittler et al., 2011). The high S abundance in the Mercury's mantle coupled with low surface abundance of Fe suggests that Mercury may have formed from highly reduced CB chondrites (Namur et al., 2016). The recent study based on S solubility in reduced mafic silicate melts suggest 7–11 wt % S in the mantle and <1.5 wt % S in the metallic inner core for a bulk S contents of 4 wt % in Mercury (Namur et al., 2016). Similarly, metal-silicate partitioning experiments indicate decrease of S contents in the core when Si contents increase (Chabot et al., 2014). These experimental results indicate that Mercury's core must contain Si if the S content in the core is <20 wt %. If Si contents in the core would be >10 wt %, the S contents in the core should be <2 wt % (Chabot et al., 2014).

The unusual feature in Mercury's internal structure models is the possibility of a solid FeS layer at the core-mantle boundary (D. E. Smith et al., 2012). The higher bulk density observed for Mercury's outer shell appears to be compatible with a silicate mantle coupled with an FeS layer with a thickness of ~90 km (Hauck et al., 2013; Namur et al., 2016). The immiscibility of Fe-S and Fe-Si liquids in the Fe-S-Si ternary system would result in segregation of Fe-S from Fe-S-Si liquids when the pressure is below 15 GPa (Morard & Katsura, 2010; Sanloup & Fei, 2004). The S contents up to 4 wt % in the silicate appear to fall within the liquid-liquid immiscibility field of Fe-S-Si system at the Mercury core-mantle boundary (CMB) pressure of about 8 GPa (Chabot et al., 2014; Namur et al., 2016). The origin of a FeS layer could also be explained by the crystallization of FeS in the binary Fe-FeS system from the segregated S-rich Fe liquids (Fei et al., 1997; Hauck et al., 2013). Due to the density contrast between solid FeS and Fe-S-Si liquid, the crystalized FeS is expected to float, forming a stable layer beneath the silicate mantle (Hauck et al., 2013). The possibility of a liquid FeS rich layer overlying an Fe-S-Si core has also been discussed in a recent study (Pommier et al., 2019). In this model, an insulating liquid FeS layer with the thickness >40 km is expected to control the heat flow from the core influencing the generation and the sustainability of Mercury's magnetic field (Pommier et al., 2019).

While a solid FeS layer at the CMB has been an important feature in Mercury's interior models, a number of recent studies have supported the low S contents or S absent conditions in Mercury's core, thereby questioning the stability of an FeS layer at the CMB (Chabot et al., 2014; Genova et al., 2019; Knibbe & van Westrenen, 2018; Margot et al., 2018). The silicate-metal partitioning experiments (Chabot et al., 2014) suggest S-free conditions, if the Si contents exceed 25 wt % in Mercury's core. However, such extreme partitioning of Si into the core would alter the major element ratios in the silicate mantle. Recent study investigating the density of FeS- and S-rich liquids (Knibbe & van Westrenen, 2015) reported higher density for FeS compared to the residual liquids, requiring a separate mechanism to stabilize a FeS layer at the base of Mercury's mantle. The recent geodetic constrains indicate a slightly higher value for gravitational potential Love number than previous estimations, supporting for a warm and weak mantle rather than rigid FeS layer at Mercury's CMB (Genova et al., 2019).

If the presence of a solidified FeS layer at the boundary between Mercury's liquid outer core and solid silicate mantle is assumed; this could have significant implications for the core dynamics. It has been suggested that the weak magnetic field strength observed for Mercury can be explained by the presence of conductive layer

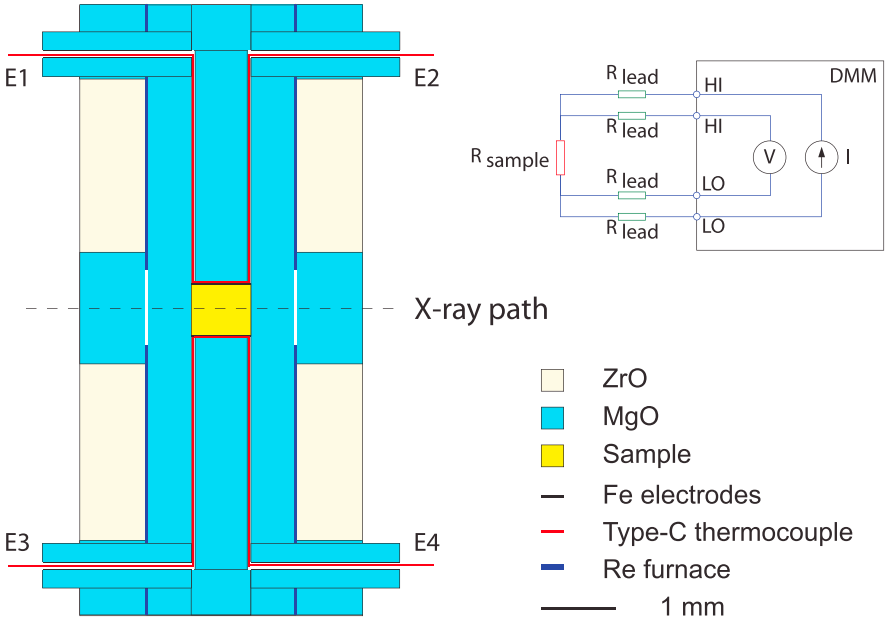

Figure 1. Schematic cross section of the multianvil assembly. The two sets of thermocouples placed top and bottom of the sample serve as electrodes for electrical conductivity measurements. Inset denotes a schematic diagram showing the electrode connections for the Kelvin (four-wire) resistance measurement technique.

overlying the convective liquid outer core (Ulrich R Christensen, 2006). Due to the stratification of the liquid core, the convection driven dynamo operates only in the deep part of the liquid core and the dynamo field may diffuse through the overlying conductive layers producing weak magnetic field strengths (Christensen, 2006). The heat flow across the CMB controls the solidification of the liquid core and the buoyancy sources available to generate a planetary dynamo (B. Buffett, 2003). The electrical and thermal conductivities of Fe-S compounds are therefore key physical properties to understand Mercury's core dynamics. In this study, we investigate the electrical and thermal conductivities of Fe-S alloys at high pressure and temperature, the principal constituent of Mercury's core-mantle boundary, with the aim of understanding the influence of Fe-S layer on the heat extraction from Mercury's core. We discuss how the outer core composition evolution influences the heat extraction from the core of Mercury and favor an intrinsic dynamo driven by thermal and chemical buoyancy forces and sustained for a prolonged period.

2. Methods

Three different FeS_x samples with varying sulfur contents (x, in mol) 0.01, 0.02, and 0.05 were prepared mixing reagent grade Fe and S powders. For the FeS (x = 0.5) composition we used commercially available reagent grade FeS power. The powder mixtures were compressed to desired pressure and kept at 1,000 K for more than 1 hr to obtain solid cylindrical samples for electrical conductivity measurements in multianvil apparatus. The high-pressure and high-temperature experiments were conducted at 8 GPa up to 1,700 K using the 1,200-t DIA-type multianvil module at the PSICHE beamline in SOLEIL Synchrotron (France). Additional off-line experiments were performed using 1,500-t multianvil press at the Laboratoire Magmas et Volcans, France. For high-pressure generation, we used an octahedral MgO + Cr_2O_3 pressure medium in a 10/4 multianvil configuration. In order to electrically insulate the sample from the Re furnace during the measurements of electrical conductivity, we placed the polycrystalline Fe-S samples within a MgO capsule. The two iron (Fe) disks placed on the top and at the bottom of the cylindrical Fe-S sample served as electrodes for electrical conductivity measurements. Sample temperature was monitored using a tungsten-rhenium ($W_{95}Re_5$-$W_{74}Re_{26}$) thermocouple junction located at one end of the sample (Figure 1).

Energy-dispersive X-ray diffraction using a CAESAR-type diffractometer (Wang et al., 2004) was used to determine the sample pressure and verify the sample state. We use the pressure–volume–temperature

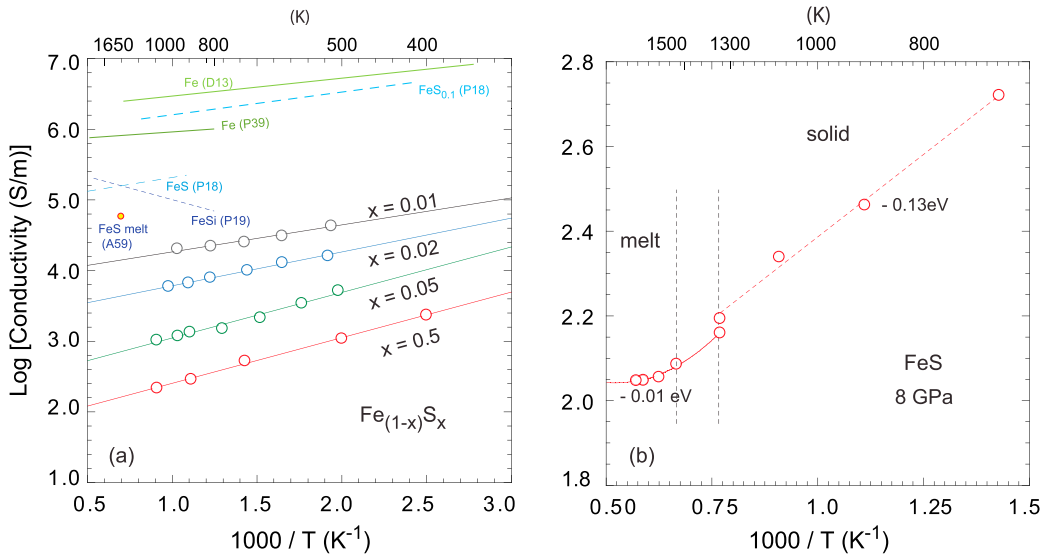

Figure 2. Electrical conductivity of Fe-S compounds. (a) As a function of reciprocal temperature for various sulfur contents. Note that the compositions are shown next to the fitting lines. Previous works on electrical conductivity of iron alloys are shown for comparison: A59 (Argyriades et al., 1959), D13 (Deng et al., 2013), P39 (Powell, 1939), P18 (Pommier, 2018), and P19 (Pommier et al., 2019) (b) Electrical conductivity before and after melting of FeS. The activation enthalpy changes with melting and the electrical conductivity of molten FeS depends weakly on temperature.

equation of state of MgO to determine the sample pressure and the accuracy of pressure determination is estimated to be ~0.5 GPa. Diffraction peaks corresponding to Fe-S alloys are clearly visible in solid samples and the melting of Fe-S is characterized by a broad band of diffuse scattering as described previously elsewhere (Andrault et al., 2018). We also acquired radiographic images of the sample to determine the sample lengths, which were crucial for the accurate determination of electrical conductivity at each temperature. The focused beam configuration used in these experiments has the advantage to produce almost flat field corrected images, a feature usually not available when using multianvil modules (Andrault et al., 2018).

The electrical conductivity measurements were performed using the Kelvin resistance measurement technique (e.g., Deng et al., 2013). In this method, the digital multimeter measured the current going through the subject and the voltage drop across it, eliminating the lead and contact resistance from the measurement (Figure 1). This is an advantage for precise measurement of sample with low-resistance values such as metals. The electrical conductivity at each temperature can be calculated using the sample dimensions obtained using the X-ray radiograph using, $\sigma = l/RA$ where σ is the electrical conductivity, l is the sample length, R is the measured sample resistance, and A is the area of the cylindrical cross section. The temperature dependence of the electrical conductivity σ can be described by the Arrhenius equation: $\sigma = \sigma_0 e^{-\Delta H/k_B T}$, where σ_0 is the preexponential factor, ΔH is the activation enthalpy in eV, k_B is the Boltzmann constant in eV/K, and T is the absolute temperature in K.

Thermal conductivity of Fe-S alloys was estimated using the *Wiedemann–Franz law* $\kappa = L_0 \sigma T$, an empirical law expressing the thermal conductivity (k) as a function of the electrical conductivity of a metal (σ) and the temperature (T) through a proportionality constant Lorenz ratio (L). The Lorenz ratio approaches the Sommerfeld derivation L_0, 2.44×10^{-8} WK^2, provided that the thermal conductivity is purely electronic, the electron gas is highly degenerate, and the relaxation time is the same for electrical and thermal conduction (Klemens, 1989). The deviation of the Lorenz ratio has been observed for Fe alloys (de Koker et al., 2012; Secco, 2017). In metallic alloys such as Fe-S, the thermal transport is a complex process due to the coexistence of electron and phonon conduction. The total thermal conductivity (κ_{tot}) is the sum of its electronic component (κ_e), and its phononic component (κ_{ph}). In high-purity metals, the electronic component dominates the thermal conduction; however, in metallic alloys the heat conduction through phonon vibration becomes significant (Klemens & Williams, 1986; Konôpková et al., 2016).

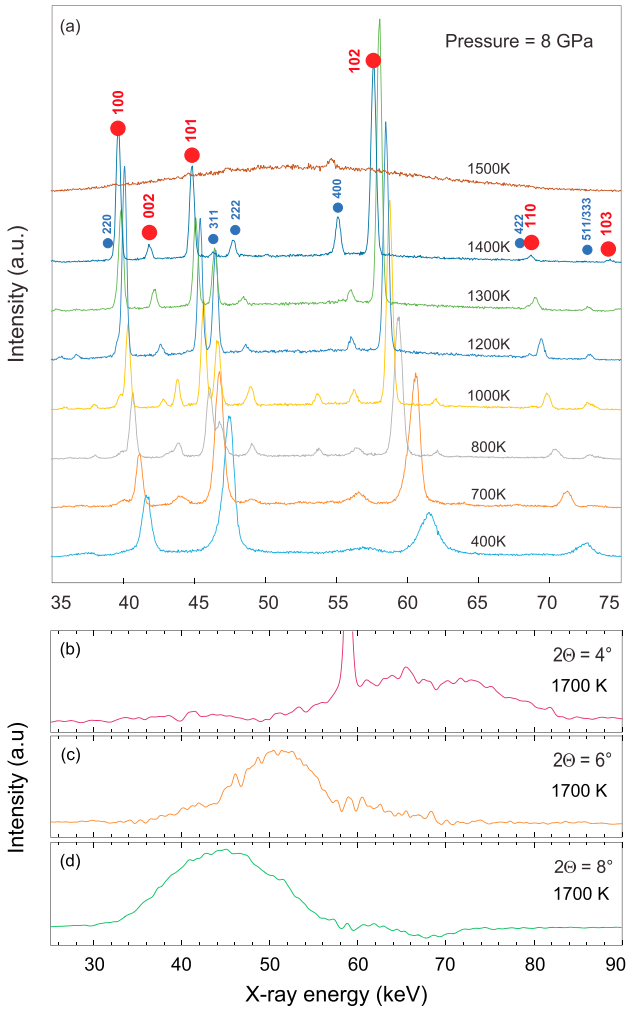

Figure 3. X-ray diffraction patterns of FeS recorded at high temperature. (a) Evolution with increasing temperature of the diffraction pattern for the run performed at ~8 GPa. Red and blue dots correspond to diffraction peaks indexed based on FeS-V and Fe_3O_4 magnetite, respectively. The ratio of diffraction peak intensities (following the Rietveld approach) suggests presence of magnetite in the sample, which Fe_3O_4 could come from the unavoidable oxidation of FeS starting material. The general drift of diffraction peaks toward low energies is due to thermal expansion. Diffraction peaks get thinner at high temperatures due to the release of deviatoric stresses built upon compression at 300 K. The melting of the sample occurs between 1,400 and 1,500 K. (b–d) At 1,700 K after melting of FeS at two-theta diffraction angles of 4, 6, and 8°, respectively.

3. Results

Our findings show that the electrical conductivity of Fe-S compounds decreases with increasing temperature characteristic of the electrical conduction in metals and metal alloys (Figure 2a). We observe that even a minor increase of sulfur contents reduces the electrical conductivity of Fe-S alloys (Figure 2a). At 1,000 K, the incorporation of 0.01 mol of S in Fe-S alloys decreases the electrical conductivity by 2 orders of magnitude to 10^4 S/m compared to pure Fe (10^6 S/m; Powell, 1939). The electrical conductivity of FeS, corresponding to the sulfur content expected at the solid layer at the Mercury's core-mantle boundary is thus expected to be about 10^2 S/m at 1,700 K. This value is about 3 orders of magnitude smaller than the value of 10^5 S/m used in previous dynamo models (D. J. Stevenson, 2003). A change in activation enthalpy on melting of FeS (Figure 2b) suggests a change of conduction mechanism from electronic conduction in a solid to electrolytic conduction in FeS melt.

The melting of FeS is confirmed by the disappearance of peaks above 1,500 K (Figure 3), consistent with experimentally derived Fe-S phase relations (Urakawa et al., 2004). The electrical conductivity of molten FeS is about 10^2 S/m at 1,700 K and remains relatively unchanged with increasing temperature.

Our measured electrical conductivities of Fe-S compositions at 8 GPa indicate significantly lower values compared to the previously reported values for Fe-S alloys (Pommier, 2018; Figure 4). While we could not determine the exact cause of the discrepancy among different laboratory measurements, it is possible that the high conductivity may originate from the presence of impurities in Fe-S alloys. For example, the experiments conducted on Al- and Sr-doped FeS_2 (Osuwa & Nwaokeorie, 2014) indicate that 0.02 M concentration of Al and Sr increases the electrical conductivity of FeS_2 by more than a factor of 10. However, calculations based on first-principle electronic band structure calculation of hcp Fe-based alloys at 40 GPa (Gomi & Yoshino, 2018) indicate that Si impurity concentrations up to 30 at. % is required to decrease the electrical conductivity by a factor of 100. Another possibility for high electrical conductivity could be the partial reaction of Fe and S to form Fe-S alloy with high Fe contents.

4. Discussion

In metallic alloys, the electrical conduction is controlled solely by the movements of electrons, while heat is carried by both electron vibrations and phonon collisions (Klemens & Williams, 1986). It is generally assumed that the phonon (lattice) thermal conductivity is negligible in metals and the electronic component is determined via the Sommerfeld value of the Lorentz ratio (L_0). The estimated electronic component of thermal conductivity varies from 0.5 Wm/K for $FeS_{0.01}$ to 0.006 Wm/K for FeS at 1,300 K (Figure 5). These values represent the lower bound of the thermal conductivity for Fe-S alloys (Pommier, 2018).

In metallic alloys however, scattering of electrons by solute atoms greatly reduces the electronic thermal conductivity, making heat transport via lattice vibrations a dominant factor (Klemens & Williams, 1986). Thus, for metallic alloys at high temperature, the thermal conductivity is described by the Smith-Palmer equation (C. S. Smith & Palmer, 1935), $\kappa = L_0\sigma T + D$, an empirical relation linking thermal conductivity to electrical conductivity via a constant D, which describes the temperature-dependent phonon thermal conductivity ($\kappa = L_0\sigma T + DT^{-a}$). Due to strong solute scattering, the phonon thermal conductivity of alloys are

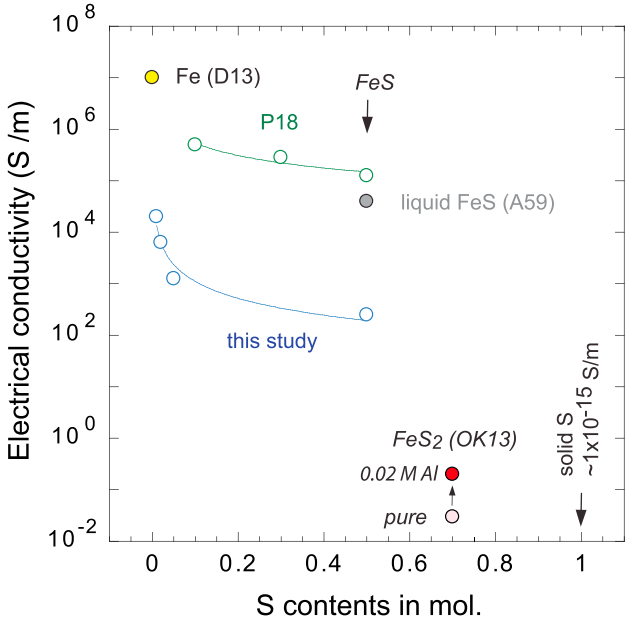

Figure 4. Electrical conductivity as a function of sulfur content in Fe-S alloys. Electrical conductivity decreases with increasing sulfur contents. Previous electrical conductivity data of Fe-S alloys and Fe are shown for comparison. P18 (Pommier, 2018), A59 (Argyriades et al., 1959), D13 (Deng et al., 2013), and OK13 (Osuwa & Nwaokeorie, 2014).

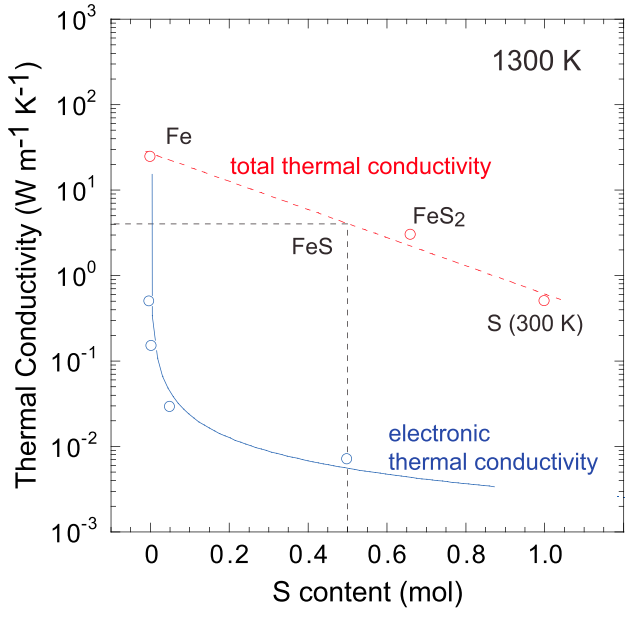

Figure 5. Thermal conductivity of Fe-S compounds. The electronic thermal conductivity estimated based on the Sommerfeld derivation of the *Wiedemann–Franz law* for our Fe-S compositions are shown in blue circles. The total thermal conductivity (electronic + phonon) of Fe, FeS_2, and S are shown in red circles. The thermal conductivity of FeS was estimated to be ~4 Wm/K at 1,000 K.

expected to approach a constant value at high temperature (Klemens & Williams, 1986). For example, the lattice thermal conductivity Fe-Cr-Ni alloy systems converge into a narrow range of 4.6–6.0 W/m K at 1,000 K (Klemens & Williams, 1986).

The lattice thermal conductivity measurements of Fe-S alloys were limited to FeS_2 composition, which was reported at supercooled conditions in the temperature range 50–300 K (Popov et al., 2013). The thermal conductivity of FeS_2 at 300 K is estimated to be 42 ± 1 Wm/K. Extrapolation of this value to high temperature based on the theoretically predicted temperature dependence of phonon thermal conductivity of T^{-a} (Klemens & Williams, 1986) indicates that the thermal conductivity of FeS_2 at 1,300 K would be about 3.6 W/m K. In order to estimate the total thermal conductivity of FeS (electronic + lattice), we have modeled the thermal conductivity of end-member Fe-S compositions together with data from the FeS_2 system (Figure 4). The thermal conductivity of Fe was calculated from electrical conductivity data of Powell (1939). Thermal conductivity of S at 300 K was obtained from Slack (1965). By fitting the total thermal conductivity of Fe, FeS_2, and S with powerlaw relation, we obtain a thermal conductivity ~4 Wm/K for the FeS at 1,300 K (Figure 5).

The temperature at Mercury's core mantle boundary has been investigated in numerous previous studies (Grott et al., 2011; Hauck et al., 2013; Tosi et al., 2013). The solidification of FeS below the CMB can be expected if the temperatures at the core mantle boundary decrease below 1,700 K (Breuer et al., 2015). We have obtained the thermal conductivity at 1,300 K, close to the eutectic temperature of Fe-FeS system at 10 GPa (Fei et al., 1997; Morard et al., 2007). Due to the weak temperature dependence of thermal conductivity at high temperature, a significant variation to the estimated phonon thermal conductivity could not be expected within 1,200–1,700-K temperature range.

Based on our estimation of the thermal conductivity of 4 Wm/K assumed for FeS at 1,300 K, we have computed the Mercurian core heat flow for a range of thermal boundary layer (TBL) thicknesses and possible temperature gradients across the TBL (Hauck et al., 2013; Rivoldini et al., 2009; Tosi et al., 2013; Figure 6). It is worth noting that our estimated value for the Fe-S thermal conductivity at the CMB conditions is close to the mantle thermal conductivity value usually assumed for Mercury's mantle convection models (Breuer et al., 2010; Tosi et al., 2013) meaning that the two reservoirs may be indistinct in terms of thermal conductivity. We have calculated the heat flow Q based on the Fourier's law of thermal conduction:

$$Q = 4\pi R_c^2 k_{tot}(\Delta T/\delta)$$

with R_c the core radius (=2,000 km for Mercury), ΔT the temperature difference across the thermal boundary layer, and δ the boundary layer thickness. The estimated heat flows computed from our thermal conductivity model indicate that the energy evacuated by core heat flow is ≈10 TW for a TBL with a thickness of 10 km and a temperature contrast of 500 K (Figure 4). The heat flow from the core is substantially reduced when increasing the TBL thickness, to ≈1 TW for a 100-km-thick TBL layer.

To drive a dynamo in a terrestrial planet, three conditions are necessary (e.g., Monteux et al., 2011): (1) the metallic core has to convect meaning

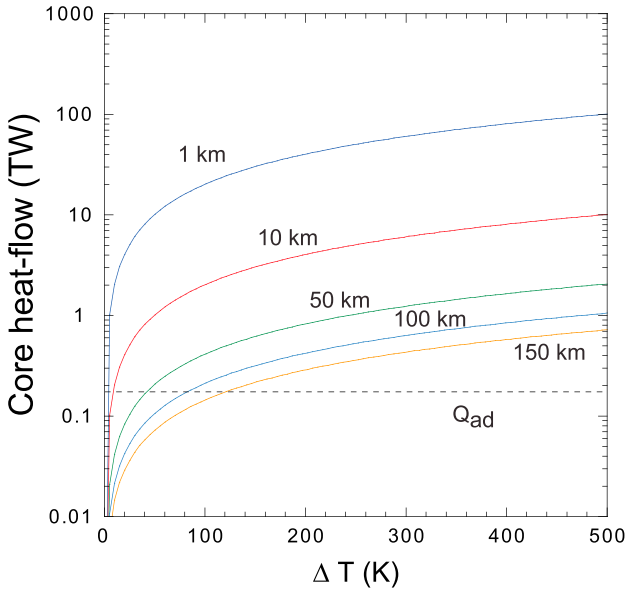

Figure 6. Mercury's core-mantle boundary heat flow. The calculations are based on an average total thermal conductivity (electron + phonon) of 4 Wm/K for FeS for diverse thermal boundary layer thicknesses as a function of the temperature contrast across the TBL. The adiabatic heat flow ($Q_{ad} = 4\pi R_c^2 k_{tot} \alpha_c g_c T_c / Cp$) is represented with a black horizontal dashed line (considering $R_c = 2{,}000$ km, $\alpha_c = 7E-5$ K, $g_c = 4$ m/s^2, $T_c = 1{,}800$ K, and $C_p = 850$ J·kg^{-1}·K^{-1}).

that the heat flow out of the core needs to overcome the adiabatic heat flow (David J. Stevenson et al., 1983), (2) the rate of gravitational potential energy released by convection has to be much larger than the rate of ohmic dissipation (B. A. Buffett, 2002), and (3) the convective motions have to exhibit a complex structure to carry the magnetic field lines (leading to a critical magnetic Reynolds number; U. R. Christensen & Aubert, 2006). Figure 6 shows that the heat flow inferred from our study is larger than the adiabatic heat flow for a wide range of temperature contrasts and thermal boundary thicknesses meaning that thermally driven dynamo is a likely process on Mercury. Low values for both thermal and electrical conductivities remain puzzling to explain Mercury's magnetic field. In the Earth's core, values of the thermal conductivity range between 90 and 150 Wm/K (de Koker et al., 2012; Pozzo et al., 2012). Recent laboratory measurements suggested that the thermal conductivity of polycrystalline iron at Mercury's core conditions is 113–125 Wm/K (Deng et al., 2013). Large thermal conductivities increase the heat flux along the core adiabat and reduce the lifetime of a thermally driven dynamo (Breuer et al., 2015). The electrical conductivity of Fe-S at P/T conditions compatible with Mercury's core is about 2 orders of magnitude lower than for pure iron. To overcome a critical magnetic Reynolds number of 50 (Wicht et al., 2007), 20mm/s typical flow speed is required to maintain an active dynamo for Mercury, which is about 200 times stronger than that of the Earth's outer core. Moreover, if sulfur is the major light element in Mercury's core and if its weak magnetic field is related to a low electrical conductivity, our results would also suggest a very weak magnetic field for Ganymede, which contradicts Galileo magnetometer measurements (Kivelson et al., 1996).

It is worth noting that the heat flux from the core is controlled by the thermal evolution of the mantle. In the early history of Mercury, its core was likely to be liquid with Fe alloys (Fe-S, Fe-Si; Figure 7a). Consequently, the thermal conductivity of the core was large; the primitive heat was efficiently evacuated possibly enhanced by a surrounding partially molten silicate magma ocean. In this early regime, the dynamo was only thermally driven. Numerical models (Tosi et al., 2013) assuming a core thermal conductivity of 40 Wm/K indicate that a thermally driven dynamo would be feasible during the first few hundred million years of the evolution of Mercury. The value of the thermal conductivity inferred from our study would reduce the adiabatic core heat flux threshold for thermally driven dynamo from ≈20 mW/m^2 (Tosi et al., 2013) to ≈3 mW/m^2. According to Tosi et al. (2013), such a low-threshold heat flux value could be overcome during the last ≈2 Gyr of Mercury's history. Our estimations (Figure 6) indicate that such heat-flux values can be achieved even with a presence of a thin (<1 km) FeS layer.

A low thermal conductivity within the core can enhance thermal convection by reducing the threshold for thermally driven dynamo. In the case of a vigorous and thermally driven convection, a stratified outer core would be difficult to envision as well as a strong skin-effect attenuation (Ulrich R. Christensen et al., 2009). However, a low thermal conductivity of the core combined with an overlying solid mantle would also limit the heat evacuation and favor the formation of a stable layer below the CMB. For a thick Fe-S layer to form and to possibly affect the magnetic field of Mercury, a complementary process can be invoked such as the formation of FeS layer during the solidification of Mercury's core. The growth of the inner core leads to an increase of the S concentration in the outer core (Figure 7b). However, for crystallization to progress, the energy barrier for the formation of the first nucleus needs to be overcome (Huguet et al., 2018). In the classical view, either a critical supercooling of the core on the order of 1,000 K or transportation of solid metallic seeds from the mantle to the core when core reached liquidus temperature are possible mechanisms that may surpass the nucleation energy barrier. It has been proposed recently that such nucleation substrates can be present in the core during the early in the planet's history, leading to a slower inner core growth with smaller buoyancy flux (Huguet et al., 2018).

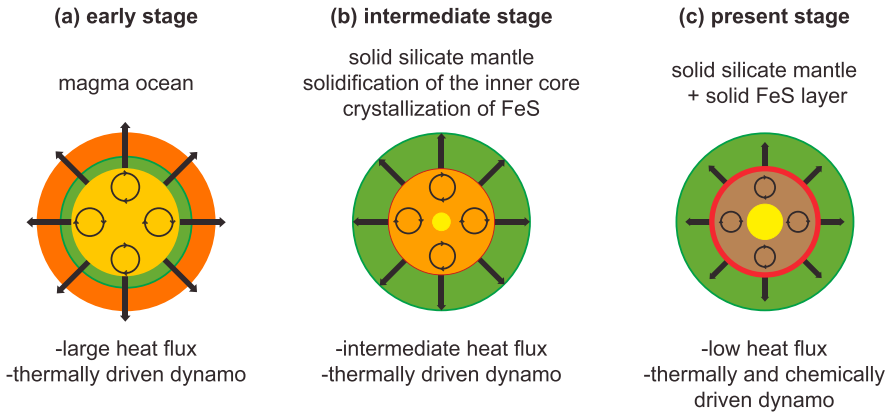

Figure 7. Schematic diagram illustrating the evolution of Mercury's dynamo. The thermochemical evolution of Mercury's interior coupled with core-mantle dynamics. (a and b) The early stages of Mercury core evolution indicate largely a thermally driven dynamo in Mercury due to high heat flux from the core. The present Mercury should have a low heat flux due to the presence of FeS layer at the core-mantle boundary and the dynamo may be powered by both chemical- and thermal-driven processes.

As the Fe-S concentration increases, the thermal conductivity of the outer core should decrease (Pommier, 2018). The low thermal conductivity (4 Wm/K) inferred from our experiments means that dynamo action in Fe-S liquid core can be driven by thermal convection. At present, the second source of buoyancy force is likely to be related to chemical processes driven by crystallization in the iron-rich core (Breuer et al., 2015; Dumberry & Rivoldini, 2015) but the low thermal conductivity of Fe-S means that the dynamo can be both thermally and chemically driven (Figure 7c). The sum of these two processes may explain the longevity of the dynamo of Mercury. Moreover, by limiting the amount of heat flowing from the core, the solidification of the Fe-S layer may have prevented the Mercurian core (and potentially the Ganymede's core) from rapid solidification, sustaining an intrinsic dynamo by buoyancy forces in Mercury for time scales larger than 1 Gyr compatible with the MESSENGER mission observations.

Acknowledgments
Discussions with David Stevenson and Ulrich R. Christensen help improved the manuscript. We thank the Editor Steven A. Hauck, II, A. Pommier, and the anonymous reviewer for their constructive comments. G.M. acknowledges funding from the French PNP program (INSU-CNRS). This research was financed by the French Government Laboratory of Excellence initiative ANR-10-LABX-0006, the Région Auvergne, and the European Regional Development Fund. This is ClerVolc contribution number 366. The authors confirm that the raw data supporting the findings of this study are available within the article (Figures 2–4).

References

Anderson, B. J., Johnson, C. L., Korth, H., Purucker, M. E., Winslow, R. M., Slavin, J. A., et al. (2011). The global magnetic field of Mercury from MESSENGER orbital observations. *Science*, *333*(6051), 1859–1862. https://doi.org/10.1126/science.1211001

Andrault, D., Pesce, G., Manthilake, G., Monteux, J., Bolfan-Casanova, N., Chantel, J., et al. (2018). Deep and persistent melt layer in the Archaean mantle. *Nature Geoscience*, *11*(2), 139–143. https://doi.org/10.1038/s41561-017-0053-9

Argyriades, D., Derge, G., & Pound, G. M. (1959). Electrical conductivity of molten FeS. *Transactions of the Metallurgical Society of Alme*, *215*(December), 909–912.

Breuer, D., Labrosse, S., & Spohn, T. (2010). Thermal evolution and magnetic field generation in terrestrial planets and satellites. *Space Science Reviews*, *152*(1–4), 449–500. https://doi.org/10.1007/s11214-009-9587-5

Breuer, D., Rueckriemen, T., & Spohn, T. (2015). Iron snow, crystal floats, and inner-core growth: modes of core solidification and implications for dynamos in terrestrial planets and moons. *Progress in Earth and Planetary Science*, *2*(1), 39. https://doi.org/10.1186/s40645-015-0069-y

Buffett, B. (2003). The thermal state of Earth's core. *Science*, *299*(5613), 1675–1677. https://doi.org/10.1126/science.1081518

Buffett, B. A. (2002). The thermal state of Earth's core. *Science*, *299*, 1675–1677.

Cao, H., Aurnou, J. M., Wicht, J., Dietrich, W., Soderlund, K. M., & Russell, C. T. (2014). A dynamo explanation for Mercury's anomalous magnetic field. *Geophysical Research Letters*, *41*, 4127–4134. https://doi.org/10.1002/2014GL060196

Chabot, N. L., Wollack, E. A., Klima, R. L., & Minitti, M. E. (2014). Experimental constraints on Mercury's core composition. *Earth and Planetary Science Letters*, *390*, 199–208. https://doi.org/10.1016/j.epsl.2014.01.004

Chen, B., Li, J., & Hauck, S. A. (2008). Non-ideal liquidus curve in the Fe-S system and Mercury's snowing core. *Geophysical Research Letters*, *35*, L07201. https://doi.org/10.1029/2008GL033311

Christensen, U. R., & Aubert, J. (2006). Scaling properties of convection-driven dynamos in rotating spherical shells and application to planetary magnetic fields. *Geophysical Journal International*, *166*(1), 97–114. https://doi.org/10.1111/j.1365-246X.2006.03009.x

Christensen, U. R., & Wicht, J. (2008). Models of magnetic field generation in partly stable planetary cores: Applications to Mercury and Saturn. *Icarus*, *196*(1), 16–34. https://doi.org/10.1016/j.icarus.2008.02.013

Christensen, U. R. (2006). A deep dynamo generating Mercury's magnetic field. *Nature*, *444*(7122), 1056–1058. https://doi.org/10.1038/nature05342

Christensen, U. R., Holzwarth, V., & Reiners, A. (2009). Energy flux determines magnetic field strength of planets and stars. *Nature*, *457*(7226), 167–169. https://doi.org/10.1038/nature07626

de Koker, N., Steinle-Neumann, G., & Vlcek, V. (2012). Electrical resistivity and thermal conductivity of liquid Fe alloys at high *P* and *T*, and heat flux in Earth's core. *Proceedings of the National Academy of Sciences*, *109*(11), 4070–4073. https://doi.org/10.1073/pnas.1111841109

Deng, L., Seagle, C., Fei, Y., & Shahar, A. (2013). High pressure and temperature electrical resistivity of iron and implications for planetary cores. *Geophysical Research Letters*, *40*, 33–37. https://doi.org/10.1029/2012GL054347

Dumberry, M., & Rivoldini, A. (2015). Mercury's inner core size and core-crystallization regime. *Icarus*, *248*, 254–268. https://doi.org/ https://doi.org/10.1016/j.icarus.2014.10.038

Evans, L. G., Peplowski, P. N., Rhodes, E. A., Lawrence, D. J., McCoy, T. J., Nittler, L. R., et al. (2012). Major-element abundances on the surface of mercury: Results from the messenger gamma-ray spectrometer. *Journal of Geophysical Research*, *117*, E00L07. https://doi.org/ 10.1029/2012JE004178

Fei, Y., Bertka, C. M., & Finger, L. W. (1997). High-pressure iron-sulfur compound Fe_3S_2, and melting relations in the system Fe–FeS. *Science*, *275*(5306), 1621–1623. https://doi.org/10.1126/science.275.5306.1621

Genova, A., Goossens, S., Mazarico, E., Lemoine, F. G., Neumann, G. A., Kuang, W., et al. (2019). Geodetic evidence that Mercury has a solid inner core. *Geophysical Research Letters*, *46*(7), 3625–3633. https://doi.org/10.1029/2018GL081135

Glassmeier, K. H., Auster, H. U., & Motschmann, U. (2007). A feedback dynamo generating Mercury's magnetic field. *Geophysical Research Letters*, *34*, L22201. https://doi.org/10.1029/2007GL031662

Gomi, H., & Yoshino, T. (2018). Impurity resistivity of fcc and hcp Fe-based alloys: Thermal stratification at the top of the core of super-Earths. *Frontiers in Earth Sciences*, *6*(217), 1–22. https://doi.org/10.3389/feart.2018.00217

Grott, M., Breuer, D., & Laneuville, M. (2011). Thermo-chemical evolution and global contraction of Mercury. *Earth and Planetary Science Letters*, *307*(1–2), 135–146. https://doi.org/10.1016/j.epsl.2011.04.040

Hauck, S. A. II, Margot, J. L., Solomon, S. C., Phillips, R. J., Johnson, C. L., Lemoine, F. G., et al. (2013). The curious case of Mercury's internal structure. *Journal of Geophysical Research: Planets*, *118*, 1204–1220. https://doi.org/10.1002/jgre.20091

Heimpel, M. H., Aurnou, J. M., Al-Shamali, F. M., & Gomez Perez, N. (2005). A numerical study of dynamo action as a function of spherical shell geometry. *Earth and Planetary Science Letters*, *236*(1–2), 542–557. https://doi.org/10.1016/j.epsl.2005.04.032

Huguet, L., Van Orman, J. A., Hauck, S. A., & Willard, M. A. (2018). Earth's inner core nucleation paradox. *Earth and Planetary Science Letters*, *487*, 9–20. https://doi.org/10.1016/j.epsl.2018.01.018

Johnson, C. L., Phillips, R. J., Purucker, M. E., Anderson, B. J., Byrne, P. K., Denevi, B. W., et al. (2015). Low-altitude magnetic field measurements by MESSENGER reveal Mercury's ancient crustal field. *Science*, *348*(6237), 892–895. https://doi.org/10.1126/science.aaa8720

Kivelson, M. G., Khurana, K. K., Russell, C. T., Walker, R. J., Warnecke, J., Coroniti, F. V., et al. (1996). Discovery of Ganymede's magnetic field by the Galileo spacecraft. *Nature*, *384*(6609), 537–541. https://doi.org/10.1038/384537a0

Klemens, P. G. (1989). Theory of Lorenz ratio of metals and alloys. In D. P. H. Hasselman, & J. R. Thomas (Eds.), *Thermal conductivity 20*, (pp. 63–69). Boston, MA: Springer US. https://doi.org/10.1007/978-1-4613-0761-7_6

Klemens, P. G., & Williams, R. K. (1986). Thermal conductivity of metals and alloys. *International Materials Reviews*, *31*(1), 197–215. https://doi.org/10.1179/095066086790324294

Knibbe, J., & van Westrenen, W. (2015). The interior configuration of planet Mercury constrained by moment of inertia and planetary contraction. *Journal of Geophysical Research: Planets*, *120*, 1904–1923. https://doi.org/10.1002/2015JD023618

Knibbe, J., & van Westrenen, W. (2018). The thermal evolution of Mercury's Fe–Si core. *Earth and Planetary Science Letters*, *482*, 147–159. https://doi.org/10.1016/j.epsl.2017.11.006

Konôpková, Z., McWilliams, R. S., Gómez-Pérez, N., & Goncharov, A. F. (2016). Direct measurement of thermal conductivity in solid iron at planetary core conditions. *Nature*, *534*(7605), 99–101. https://doi.org/10.1038/nature18009

Malavergne, V., Toplis, M. J., Berthet, S., & Jones, J. (2010). Highly reducing conditions during core formation on Mercury: Implications for internal structure and the origin of a magnetic field. *Icarus*, *206*(1), 199–209. https://doi.org/10.1016/j.icarus.2009.09.001

Margot, J.-L., Hauck, S. A., Mazarico, E., Padovan, S., & Peale, S. J. (2018). Mercury's internal structure. In S. C. Solomon, B. J. Anderson, & L. Nittler (Eds.), *Mercury—The view after MESSENGER* (pp. 85–113). Cambridge University Press. Retrieved from http://arxiv.org/abs/1806.02024

Monteux, J., Jellinek, A. M., & Johnson, C. L. (2011). Why might planets and moons have early dynamos? *Earth and Planetary Science Letters*, *310*(3–4), 349–359. https://doi.org/10.1016/j.epsl.2011.08.014

Morard, G., & Katsura, T. (2010). Pressure-temperature cartography of Fe-S-Si immiscible system. *Geochimica et Cosmochimica Acta*, *74*(12), 3659–3667. https://doi.org/10.1016/j.gca.2010.03.025

Morard, G., Sanloup, C., Fiquet, G., Mezouar, M., Rey, N., Poloni, R., & Beck, P. (2007). Structure of eutectic Fe-FeS melts to pressures up to 17 GPa: Implications for planetary cores. *Earth and Planetary Science Letters*, *263*(1–2), 128–139. https://doi.org/10.1016/j.epsl.2007.09.009

Namur, O., Charlier, B., Holtz, F., Cartier, C., & McCammon, C. (2016). Sulfur solubility in reduced mafic silicate melts: Implications for the speciation and distribution of sulfur on Mercury. *Earth and Planetary Science Letters*, *448*, 102–114. https://doi.org/10.1016/j.epsl.2016.05.024

Nittler, L. R., Starr, R. D., Weider, S. Z., McCoy, T. J., Boynton, W. V., Ebel, D. S., et al. (2011). The major-element composition of Mercury's surface from MESSENGER X-ray spectrometry. *Science*, *333*(6051), 1847–1850. https://doi.org/10.1126/science.1211567

Osuwa, J. C., & Nwaokeorie, S. E. (2014). Analysis of structural and electrical properties of iron sulfide (FeS_2) thin films doped with aluminum and strontium impurities. *IOSR Journal of Applied Physics*, *6*(6), 42–46. https://doi.org/10.9790/4861-06624246

Pommier, A. (2018). Influence of sulfur on the electrical resistivity of a crystallizing core in small terrestrial bodies. *Earth and Planetary Science Letters*, *496*, 37–46. https://doi.org/10.1016/j.epsl.2018.05.032

Pommier, A., Leinenweber, K., & Tran, T. (2019). Mercury's thermal evolution controlled by an insulating liquid outermost core? *Earth and Planetary Science Letters*, *517*, 125–134. https://doi.org/10.1016/j.epsl.2019.04.022

Popov, P. A., Fedorov, P. P., & Kuznetsov, S. V. (2013). Thermal conductivity of FeS_2 pyrite crystals in the temperature range 50–300 K. *Crystallography Reports*, *58*(2), 319–321. https://doi.org/10.1134/s1063774513020223

Powell, R. W. (1939). Further measurements of the thermal and electrical conductivity of iron at high temperature. *Proceedings of the Physical Society*, *51*(3), 407–418. https://doi.org/10.1088/0959-5309/51/3/304

Pozzo, M., Davies, C., Gubbins, D., & Alfè, D. (2012). Thermal and electrical conductivity of iron at Earth's core conditions. *Nature*, *393*, 159–164. https://doi.org/10.1016/j.epsl.2014.02.047

Rivoldini, A., & Van Hoolst, T. (2013). The interior structure of Mercury constrained by the low-degree gravity field and the rotation of Mercury. *Earth and Planetary Science Letters*, *377-378*, 62–72. https://doi.org/10.1016/j.epsl.2013.07.021

Rivoldini, A., Van Hoolst, T., & Verhoeven, O. (2009). The interior structure of Mercury and its core sulfur content. *Icarus*, *201*(1), 12–30. https://doi.org/10.1016/j.icarus.2008.12.020

Sanloup, C., & Fei, Y. (2004). Closure of the Fe-S-Si liquid miscibility gap at high pressure. *Physics of the Earth and Planetary Interiors*, *147*(1), 57–65. https://doi.org/10.1016/j.pepi.2004.06.008

Schubert, G., Chan, K. H., Liao, X., & Zhang, K. (2004). Planetary dynamos: Effects of electrically conducting flows overlying turbulent regions of magnetic field generation. *Icarus*, *172*(2), 305–315. https://doi.org/10.1016/j.icarus.2004.06.007

Schubert, G., Ross, M., Stevenson, D. J., & Spohn, T. (1988). Mercury's thermal history and the generation of its magnetic field. In F. Vilas, C. R. Chapman, & M. Matthews (Eds.), *Mercury*, (pp. 429–460). Tucson: The University of Arizona Press.

Secco, R. A. (2017). Thermal conductivity and Seebeck coefficient of Fe and Fe-Si alloys: Implications for variable Lorenz number. *Physics of the Earth and Planetary Interiors*, *265*, 23–34. https://doi.org/10.1016/j.pepi.2017.01.005

Slack, G. A. (1965). Thermal conductivity of elements with complex lattices: B, P, S. *Physical Review*, *139*(2A), A507–A515. https://doi.org/10.1103/PhysRev.139.A507

Smith, C. S., & Palmer, E. W. (1935). Thermal and electrical conductivities of copper alloys. *Transactions of the American Institute of Mining and Metallurgical Engineers*, *117*, 225–243.

Smith, D. E., Zuber, M. T., Phillips, R. J., Solomon, S. C., Hauck, S. A., Lemoine, F. G., et al. (2012). Gravity field and internal structure of Mercury from MESSENGER. *Science*, *336*(6078), 214–217. https://doi.org/10.1126/science.1218809

Stanley, S., Bloxham, J., Hutchison, W. E., & Zuber, M. T. (2005). Thin shell dynamo models consistent with Mercury's weak observed magnetic field. *Earth and Planetary Science Letters*, *234*(1–2), 27–38. https://doi.org/10.1016/j.epsl.2005.02.040

Stevenson, D. J. (1987). Mercury's magnetic field: A thermoelectric dynamo? *Earth and Planetary Science Letters*, *82*(1–2), 114–120. https://doi.org/10.1016/0012-821X(87)90111-7

Stevenson, D. J. (2003). Planetary magnetic fields. *Earth and Planetary Science Letters*, *6*(3), 213–214. https://doi.org/10.1029/GL006i003p00213

Stevenson, D. J., Spohn, T., & Schubert, G. (1983). Magnetism and thermal evolution of the terrestrial planets. *Icarus*, *54*(3), 466–489. https://doi.org/10.1016/0019-1035(83)90241-5

Tian, Z., Zuber, M. T., & Stanley, S. (2015). Magnetic field modeling for Mercury using dynamo models with a stable layer and laterally variable heat flux. *Icarus*, *260*, 263–268. https://doi.org/10.1016/j.icarus.2015.07.019

Tosi, N., Grott, M., Plesa, A. C., & Breuer, D. (2013). Thermochemical evolution of Mercury's interior. *Journal of Geophysical Research: Planets*, *118*, 2474–2487. https://doi.org/10.1002/jgre.20168

Urakawa, S., Someya, K., Terasaki, H., Katsura, T., Yokoshi, S., Funakoshi, K. I., et al. (2004). Phase relationships and equations of state for FeS at high pressures temperatures and implications for the internal structure of Mars. *Physics of the Earth and Planetary Interiors*, *143-144*(1–2), 469–479. https://doi.org/10.1016/j.pepi.2003.12.015

Veasey, M., & Dumberry, M. (2011). The influence of Mercury's inner core on its physical libration. *Icarus*, *214*(1), 265–274. https://doi.org/10.1016/j.icarus.2011.04.025

Wang, Y., Uchida, T., von Dreele, R., Rivers, M. L., Nishiyama, N., Funakoshi, K. I., et al. (2004). A new technique for angle-dispersive powder diffraction using an energy-dispersive setup and synchrotron radiation. *Journal of Applied Crystallography*, *37*(6), 947–956. https://doi.org/10.1107/S0021889804022502

Wicht, J., Mandea, M., Takahashi, F., Christensen, U. R., Matsushima, M., & Langlais, B. (2007). The origin of Mercury's internal magnetic field. *Space Science Reviews*, *132*(2–4), 261–290. https://doi.org/10.1007/s11214-007-9280-5

Physics of the Earth and Planetary Interiors 312 (2021) 106655

Contents lists available at ScienceDirect

Physics of the Earth and Planetary Interiors

journal homepage: www.elsevier.com/locate/pepi

Thermal conductivities of solid and molten silicates: Implications for dynamos in mercury-like proto-planets

D. Freitas [a,b,*], J. Monteux [a], D. Andrault [a], G. Manthilake [a], A. Mathieu [a], F. Schiavi [a], N. Cluzel [a]

[a] Université Clermont Auvergne, CNRS, IRD, OPGC, Laboratoire Magmas et Volcans, F-6300 Clermont-Ferrand, France
[b] School of Geosciences, Grant Institute, The King's Buildings, The University of Edinburgh, West Mains Road, Edinburgh EH9 3JW, United Kingdom

ARTICLE INFO

Keywords:
Thermal diffusivity
Thermal conductivity
Melts
Geodynamo
Mercury

ABSTRACT

Remanent magnetization and active magnetic fields have been detected for several telluric planetary bodies in the solar system (Earth, Mercury, Moon, Mars) suggesting the presence of core dynamos active at the early stages of the planet formation and variable lifetimes. Among the factors controlling the possibility of core dynamos generation, the dynamics of the surrounding silicate mantle and its associated thermal properties are crucial. The mantle governs the heat evacuation from the core and as a consequence the likeliness of an early thermally driven dynamo. In the case of planets with a thick mantle (associated with supercritical Rayleigh numbers), the core heat is efficiently removed by mantle convection and early thermally-driven dynamos are likely. At the opposite, planets with a thin mantle (associated with subcritical Rayleigh numbers) might evacuate their inner heat by diffusion only, making early thermally-driven dynamos difficult. Within the Solar System, Mercury is a potential example of such a regime. Its small mantle thickness over the planet radius ratio might be inherent to its small orbital semi-axis and hence, might be ubiquitous among the terrestrial objects formed close to their star.

To constrain the likeliness of a thermally driven dynamo on "Mercury-like" planets (i.e. with large Rc/R), we present new thermal diffusivity measurements of various solid, glassy and molten samples. We applied the Angstrom method on cylindrical samples during multi-anvil apparatus experiments at pressures of 2 GPa and temperatures up to 1700 K. Thermal diffusivities and conductivities were estimated for solid and partially molten peridotites, with various melt fractions, and for basaltic and rhyolitic glasses and melts. Our study demonstrates that melts have similar thermal properties despite a broad range of composition investigated. The melts reveal much lower thermal conductivities than the solids with almost an order of magnitude of decrease: 1.70 (±0.19) to 2.29 (±0.26) W/m/K against 0.18 (±0.01) to 0.41 (±0.03) W/m/K for peridotites at high temperatures and various melts respectively. Partially molten samples lie in between and several predictive laws are proposed as a function of the melt fraction and solid/melt texture.

Using our results into forward calculations of heat fluxes for dynamo generation for Mercury-like planets, we quantify the effect of mantle melting on the occurrence of thermally driven dynamos. The presence of a mushy mantle and partial melting could significantly reduce the ability of the mantle to evacuate the heat from the core and can prevent, shut or affect the presence of a planetary magnetic field. The buoyancy and fate of molten material in such bodies can thus influence the magnetic history of the planet. Future observations of Mercury-like planets accreted near their star and the detections of their magnetic signatures could provide constraints on their inner state and partial melting histories.

1. Introduction

The presence of internally generated magnetic fields is a variable feature among telluric bodies in the inner solar system. While few are currently active, such as for Mercury and Earth, several are now extinct, as observed for the Moon, Venus and Mars. On terrestrial planets currently exhibiting a dynamo, the generated magnetic fields characteristics are very different. Earth's magnetic field is very intense 25–65 μT, originating from the core and present for at least 3.5 *Ga* (Tarduno et al., 2010). Mercury's field strength is much weaker, representing

* Corresponding author at: School of Geosciences, Grant Institute, The King's Buildings, The University of Edinburgh, West Mains Road, Edinburgh EH9 3JW, United Kingdom.
E-mail address: damien.freitas@ed.ac.uk (D. Freitas).

https://doi.org/10.1016/j.pepi.2021.106655
Received 20 May 2020; Received in revised form 14 November 2020; Accepted 20 January 2021
Available online 28 January 2021

around a 1% of Earth's one (Kabin et al., 2008; Anderson et al., 2011) and its shape is also unique among the different detection in the solar system (Tian et al., 2015). According to the remnant magnetization measured in the crust, it was proposed that such weak magnetic activity occurred during the last 3.9 *Ga* (Johnson et al., 2015). The source of such a weak-and-prolonged dynamo is still largely debated (Manthilake et al., 2019). In the meantime, there are several evidences for an intrinsic dynamo during the early stages of both Mars and Moon (Acuna et al., 1999; Hood et al., 2010). Their dynamo seems to cease around 4.1–3.9 *Ga* ago for Mars (Johnson and Phillips, 2005; Lillis et al., 2008; Lillis et al., 2013) and exhibits a somewhat complicated history for the Moon with a strong dynamo between 4.25 and 3.5 *Ga*, followed by a weak persistence up to 2.5–2 *Ga* ago (Tikoo et al., 2014; Lawrence et al., 2008; Garrick-Bethell et al., 2009; Mighani et al., 2020). For Venus, the early presence of a dynamo remains yet unconstrained but may be detectable in future explorations (Nimmo, 2002; O'Rourke et al., 2019). More broadly, evidences of paleomagnetic anomalies indicate that the angrite parent bodies, originating from inner regions of the solar system, were subject to an early internally generated dynamo (Weiss et al., 2008). All these elements suggest that transient dynamos might be a somewhat common feature in telluric bodies (Monteux et al., 2011).

The presence of early dynamos is highly conditioned by the internal structure of the planet and its capacity to release the heat accumulated during the accretion processes (accretion, metal/silicate differentiation, core and mantle crystallization) as well as short-lived radiogenic heating. As heat conduction is an inefficient heat transport process in silicates at high temperatures (Hofmeister and Branlund, 2015), the onset of a mantle global convection is a crucial step in planet's thermal history. Convection starts when the Rayleigh number (*Ra*) of the terrestrial mantle is larger than the critical Rayleigh number (Ra_c). The higher is *Ra*, the stronger the convection, and the more efficient the heat transport. In contrast, heat is only transported by conduction for a terrestrial mantle with a $Ra < Ra_c$. As Ra scales with mantle thickness (h_{mantle}) as h^3_{mantle}, convection should take place easily in planets with a thick silicate mantle, even after the solidification of the early magma ocean stage. Consequences are efficient evacuation of the inner heat and the possible occurrence of a dynamo. At the opposite, bodies with a thinner mantle lead to smaller Ra values, making convection unlikely and dynamos more difficult to generate.

Mercury is the most interesting planet for our study. Indeed, its mantle is thin 420 ± 30 km (Hauck et al., 2013) and its core occupies almost 55% of planet's volume and 65% of the planet mass (Strom and Sprague, 2003; Charlier and Namur, 2019). Hence, the mantle of Mercury is controversially at the limit between conductive and convective regimes (Breuer et al., 2007). Different scenarios could explain the small h_{mantle}/planet radius (R) ratio on Mercury (Charlier and Namur, 2019): (1) primordial nebular processes, yielding to the enrichment of metal over silicate materials in the inner solar system (Ebel and Grossman, 2000; Wurm et al., 2013; Weidenschilling, 1978), (2) highly energetic accretional collisions inducing a major loss of the silicate fraction (Benz et al., 1988; Asphaug and Reufer, 2014), and (3) post–accretion scenarios, with major vaporization of the volatile and silicate elements from the planet during magma ocean stage (Fegley and Cameron, 1987; Boujibar et al., 2015). If scenarios (1) and (3) are dominant, then "Mercury-like" planets with small h_{mantle}/R ratio would be ubiquitous within all planetary systems. Moreover, such a small ratio would be prevailing during the whole accretionary processes. Mercury-like bodies could adopt a wide range of possible compositions depending on their history. For example, bodies accreted from reduced enstatite and/or carbonaceous bencubbinite chondrites (Malavergne et al., 2010) could present a mantle composition similar to terrestrial lherzolite, but with a sulfur content potentially as high as 11 wt% (Namur et al., 2016). Accordingly, the diversity of the silicate samples found on Earth in the forms of rocks, melts and glasses is a good proxy to decipher the properties of a range of mantle-relevant silicate compositions on Mercury-like bodies. Depending on the planet size and the h_{mantle}/R ratio, the internal pressure ranges from a few MPa to several GPa. We note that extensive mantle melting likely occurred at different stages of the history of such Mercury-like bodies. Major energy incomes are expected from the vicinity to the young Sun (2500 to 3500 K according Charlier and Namur, 2019), internal energy release (chemical and gravitational differentiation, core crystallization), and presence of short-period radioactive elements (Al^{26}, K^{40} etc.). The very high temperatures likely induce extensive melting of the thin mantle up to the core-mantle boundary (CMB).

As mentioned above, dynamo generation could be difficult for Mercury-like planets, due to the subcritical value of Ra possibly disabling mantle convection. In such case, heat transfer by conduction would dominate the planet history and the thermal conductivity of the silicate mantle is a key parameter governing the early core heat flow. Silicates thermal conduction properties are now well characterized at ambient conditions (Hofmeister and Branlund, 2015). Among them, the most common geological minerals were characterized in the forms of single crystal and polycrystalline aggregates: olivine (Osako et al., 2004; Xu et al., 2004; Pertermann and Hofmeister, 2006; Gibert et al., 2005), periclase (Hofmeister and Branlund, 2015), feldspar (Pertermann and Hofmeister, 2006; Hofmeister et al., 2009; Branlund and Hofmeister, 2012) and pyroxenes (Hofmeister et al., 2014, Hofmeister and Pertermann, 2008) as well as peridotite rocks (Gibert et al., 2005; Beck et al., 1978), which have been extensively studied due to their important geological implications. The thermal diffusivities of minerals are linked to the characteristics of their lattice structure and modes of phonon generation and propagation as a function of temperature. For silicates, lattice thermal diffusivities usually decrease with increasing temperature following a 1/T dependence. At the opposite, the diffusivities increase while increasing pressure, however, the temperature dependence is much greater than that of pressure over the considered ranges for small planets. The resulting implication is that mantle rocks and minerals are poor thermal conductors in planetary interiors. Recent measurements of thermal diffusivities of glasses and melts at ambient pressure suggested that the non-crystalline silicates are even more insulating than the minerals (Hofmeister et al., 2009, 2014; Romine et al., 2012).

Measurements of thermal diffusivities at relevant conditions of planetary mantles encompass important difficulties, which were overcome by the use of different techniques (see Hofmeister and Branlund, 2015 for a critical review). Measurements were reported over a wide P and T range for large volume samples of olivine, periclase, bridgmanite using Angström or Pulse method in solid pressure apparatus (Osako et al., 2004; Xu et al., 2004; Manthilake et al., 2011a and Manthilake et al., 2011b, Zhang et al., 2019). Up to now, accurate measurements of geologically relevant silicate glass, partially molten systems and melts at planetary interior conditions remain scarce, if not absent. The available results report a nearly flat evolution of thermal diffusivities with the temperature above 1000 K for silicates, glass and melts (Hofmeister et al., 2014; Hofmeister and Branlund, 2015), suggesting that the measurements above the melting temperature could be safely extrapolated to planetary P-T conditions.

In this study, we aim at better constraining the thermal properties of Mercury–like protoplanets where convection is unlikely and heat is mostly removed by diffusion. We perform HP-HT in situ thermal diffusivities measurements of solid, partially molten and fully molten silicate for various compositions in Multi-anvil apparatus and using Angström method. Then, we constrain the likeliness of a thermally driven dynamo during the early stages of the evolution of a Mercury-like planet. We consider a wide range of planet sizes ($1\ km < R < R_{Mercury}$) and thermal states (with solid and partially molten mantles) on the dynamo likeliness.

2. Experimental and analytical methods

2.1. High-pressure assemblies

High-pressure and high-temperature experiments were performed using a 1500-ton Kawai type Multi-anvil apparatus. All experiments were conducted at 2 GPa, based on a previous press-load vs sample pressure calibration (Boujibar et al., 2014), providing an uncertainty of ~0.1 GPa at pressures <5 GPa. We used octahedral pressure media with full length edges composed of MgO doped with Cr_2O_3 (5 wt%) in a 25/17 multi-anvil configuration (octahedron edge length / anvil truncation edge length) (Fig. 1). Our assembly was designed to accommodate the specific requirements for measurements of thermal conductivity of relatively large samples (4 mm long for 4–3.5 mm diameter). All ceramic parts of the cell assembly, including the pressure media, were fired at 1373 K prior assembling in order to remove the absorbed moisture. Oxygen fugacity of the sample was not controlled during the experiments but is expected to be quite reducing due to the presence of the graphite furnace. The use of a steeped graphite furnace helped reducing thermal gradients. Thermal loss from the sample zone was further reduced by the use of a thick zirconia (ZrO_2) sleeve around the furnace. Thermal gradients in our assembly were computed using the software developed by Hernlund et al., 2006. The models show temperature gradients within the sample volume limited to ~7.5 K/mm vertically and even less radially/horizontally (Fig. S1). On the other hand, uncertainties of our thermocouple reading (i.e. where the conductivity measurement is performed, see below) are less than 5 K on absolute and 0.1 K in relative temperatures.

Previous experimental studies described the difficulties to perform a good measurement of thermal diffusivity for a molten sample, due to a potential sample deformation (Hofmeister et al., 2009, 2014; Romine et al., 2012). However, deformation remained minor in our experiments, as evidenced by the good reproducibility of the measurements during the repeated cycles of heating and cooling (Figs. 1 and 2) as well as the shape of the recovered samples (Figs. S6, S7 and S8).

Two tungsten-rhenium ($W_{95}Re_5$-$W_{74}Re_{26}$) thermocouples of 75 μm of diameter were used to measure temperature oscillations at the center (in 300 and 600 μm drilled holes in solids and glasses, respectively) and at the edge of the cylindrical sample. Special care was given to ensure that the junction points of the two thermocouples were located in the same sample plane perpendicular to the cylinder axis. Measurements of

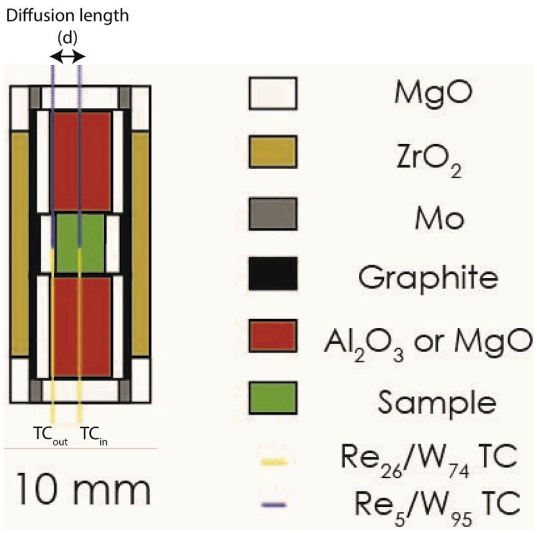

Fig. 1. Schematic cross-section of the high-pressure cell assembly used for Angstrom method with multi-anvil apparatus. For glass and melt experiments, thermocouples were inserted in alumina tubes of 0.6 mm diameter and 4.5 mm length in the sample zone.

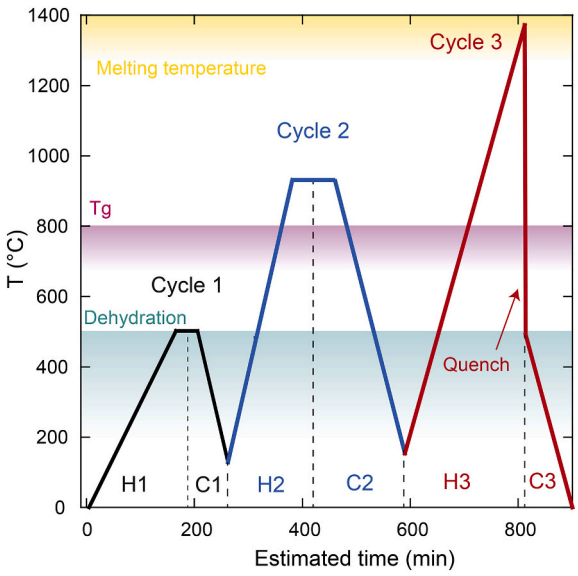

Fig. 2. Experimental procedure for the measurement of thermal diffusivity of peridotites, glasses and melts: black, blue and red for cycles 1, 2 and 3 respectively. Heating (H) and cooling (C) parts of the cycles are separated by black dashed lines (for example H1: 1st cycle heating). The expected temperatures for sample dehydration (up to ~500 °C), glass transition and melting are illustrated in shaded colors: green, pink and yellow respectively. (For interpretation of the references to colour in this figure legend, the reader is referred to the web version of this article.)

the thermal conductivity of melts and glasses have always been particularly challenging due to the risk of thermocouple short circuit, because melts, even dry, are good electrical conductors (Tyburczy and Waff, 1983; Ni et al., 2011). To prevent this effect, thermocouples were inserted in alumina tubes of 0.6 mm diameter and 170 μm wall thickness. While these tubes show good resistance to cold compression and almost no reaction with the samples, even at very high temperature, some leakages for low viscosity basaltic melts have been identified. Their occurrence was taken in account for thermal diffusivity estimations (see Supplementary Text S1 and Figs. S2 and S3).

2.2. Angström method for thermal diffusivity measurements

We aim at determining thermal diffusivities of geological samples such as peridotites, mafic and felsic glasses and their melts at high pressure and high temperature using a double contact method: the Angström method. Experimental configurations, assemblies and data treatment are similar to several previous studies (Fujisawa et al., 1968; Kanamori et al., 1969; Katsura, 1993; Xu et al., 2004; Manthilake et al., 2011a; Manthilake et al., 2011b). Briefly, a temperature wave is generated radially in a cylindrical sample by the surrounding heater sleeve of the multi-anvil assembly (Fig. 1). Oscillations are generated with controlled frequency and period by modulating the power supply. Periodic temperature signals are recorded by two thermocouples fixed in the center and on the edge of the sample cylinder. At frequencies higher than 1.5 Hz, the signal can get noisier due to a limited time resolution of the recording system.

The recorded signals, for each thermocouple channel, are fitted by a nonlinear least square solver (lsqcurvefit on Matlab© using Levenberg-Marquardt algorithm):

$$\Delta T = A_0 + A_1 t + A_2 sin\left(2\pi A_3 t + \frac{A_4 \pi}{180}\right) \quad (1)$$

Following this method, we obtained the amplitude of the temperature variation (A_2), frequency (A_3), and phase (A_4) of the recorded wave as a function of time (t), for the two thermocouples. Errors are quantified

based on the residue on the non-linear curve fitting (the *nlparci* function in Matlab©). To infer thermal diffusivity or conductivity from these parameters, the equation of conductive heat transport has to be solved. Here we consider the sample as an infinite uniform cylinder and assume that the heat flow is negligible in the vertical direction, thanks to a relatively long cylindrical heater. The following equation, expressed in cylindrical coordinates by Carlsaw and Jaegger (1959), has to be inverted in order to retrieve the diffusivity of the sample:

$$\frac{dT}{dt} = D\left(\frac{d^2T}{dr^2} + \frac{1}{r}\frac{dT}{dr}\right) \tag{2}$$

where r is the radial distance from the axis, T the temperature, t the time, and D the thermal diffusivity. The boundary condition of our setup is:

$$\frac{dT}{dr} = 0, at\ r = 0 \tag{3}$$

If we consider harmonic excitation at a distance $r = R$ from the axis in normal or complex form:

$$T_R = B_0 + B_1 coswt \leftrightarrow T_R = b_0 + b_1 Re\ (expiwt) \tag{4}$$

where B_0,B_1, b_0 and b_1 are constants and Re is the real part of the exponential. The solution of the radial flow equation with the boundary conditions developed above can be expressed as:

$$T_R = b_0 + b_1 \left[J_0\left(\sqrt{-i}*x\right)*\frac{exp(iwt)}{J_0\left(\sqrt{-i}*l\right)}\right] \tag{5}$$

where

$$l = \left(w/\kappa\right)^{1/2} R\ and\ x = \left(w/\kappa\right)^{1/2} r \tag{6}$$

for $0 \le r \le R$, where w is the angular frequency and J_0 is the Bessel function of the first kind (integer order $n = 0$). At $r = 0$ and $r = R$ we have:

$$T_0 = b_0 + b_1 \theta cos(wt - \varphi) \tag{7}$$

$$T_R = b_0 + b_1 coswt \tag{8}$$

where

$$\theta = \frac{1}{\sqrt{bei(u)^2 + ber(u)^2}} \tag{9}$$

$$\varphi = tan^{-1}\left(\frac{bei(u)}{ber(u)}\right) \tag{10}$$

where θ is the amplitude ratio and φ the phase shift between the two harmonic temperature measurements and *bei* and *ber* are imaginary and real parts of the Bessel function of the first kind, respectively. The solution to the Eq. (4) can be written using the dimensionless argument u, from which thermal diffusivity (D) can be directly estimated knowing angular frequency (w) and sample radius (d).

$$u = d(w/D)^{1/2} \tag{11}$$

Thanks to the Eqs. (9), (10), and (11), the diffusivity was then retrieved via forward Monte Carlo simulation and neighborhood algorithm (Sambridge and Mosegaard, 2002). In this step, different values of diffusivities are generated and theoretical phase shifts and amplitude ratios are calculated. These values are compared to the values measured in our experiments. When the differences between the computed solution and the experimental determination tend to 0 (minimization step), the correct diffusivity is then obtained if the sample radius (d) and angular frequency (w) are known. We note that mathematical solutions appear every 360° for the phase shift. Such erroneous solutions are checked manually and discarded.

For most of our experiments, we observe a significant variation of the refined raw-diffusivity value as a function of the heat-source frequency. This effect was already reported in the literature. Different equations were proposed to refine a real value of diffusivity, corresponding to the infinite frequency asymptote, based on non-linear equations. While Manthilake et al. (2011b) used:

$$D = D_\infty + A_0 exp(A_1 * f) \tag{12}$$

Xu et al. (2004) used:

$$D = D_\infty + A_0 exp\left(\frac{-f}{f_0}\right) \tag{13}$$

where D is diffusivity, f source frequency, f_0 asymptote frequency and A_0 and A_1 constants. In these equations, D_∞, A_n and f_0 are inverted parameters. For a better fit of our experimental data and to minimize the uncertainties on the parameters, we adopt Eq. (13). On the other hand, for experiments presenting no systematic dependence of the raw-diffusivity with frequency, we consider as real value the average value between the raw-diffusivity values measured at all frequencies (Xu et al., 2004; Manthilake et al., 2011b).

2.3. Experimental uncertainties

Experimental measurements of thermal diffusivities and their further transformation into thermal conductivities generate uncertainties originating from the estimations of pressure, temperature, sample dimensions and the data fitting itself. Experimental uncertainties on pressure and temperature are presented above (~0.1 GPa and ~ 5 K, respectively). Sample lengths prior to the sample loading (d_0) and after the melting experiments were determined with a high precision digital gauge (accuracy of ~1 μm) and using the Scanning Electron Microscope (FEG-SEM), respectively (see Table 1). Then, the sample radius during the experiment at high pressure and temperature was calculated using:

$$d(P,T) = d_0 * \left(1 - \alpha(T - 298) + \frac{P}{K}\right)^{-1/3} \tag{14}$$

where α is the thermal expansion and K the bulk modulus of the sample. For these calculations only samples radii before experiments were considered, as post mortem measurements are affected by decompression cracks (highlighted by the larger values measured after the experiments in Table 1). Moreover, the distance between the two thermocouples could not be measured precisely for a few samples. The values of all experimental parameters are provided in Supplementary Materials (Text S4 and Fig. S4). Altogether, final uncertainty on the sample length is between 5 and 10 μm.

There are other uncertainties associated with the procedure of data fitting for the determination of raw thermal diffusivities. Experimental phase shifts and amplitude ratios (Eqs. (9) and (10)) are determined with a precision generally better than 1% and majored by 3% in the worst cases. In the course of the Monte Carlo simulation, the differences between experimental and theoretical diffusivities are recorded and used a posteriori to refine uncertainties within 1σ errors.

Then, real thermal diffusivities are refined from the raw-diffusivities using either (i) the asymptotic non-linear fit for experiments presenting a dependence in frequency (Eq. (13), which yields important uncertainties on the refined parameters) or by averaging (see Methods). The error on average (σ_{AVG}) is:

$$\sigma_{AVG} = \sqrt{\left(\frac{1}{n}\right)^2 * \sum_{1:n} \sigma_D^2} \tag{15}$$

where n is the number of diffusivity measurements performed at different frequencies and σ_D is the error on each diffusivity. Raw diffusivities recovered from Monte Carlo processing have errors of ~1%, similar to those of phase shift and amplitude ratio. If the fitting step is

Table 1
Sum up of our Ansgtröm experiments with compositions, P-T ranges and associated parameters.

Run#	M662	M804	M807	M808	M836	M843	M844	M846	M847	M848	M850
Sample name	EPR-MORB	RP4-S2	DR07-S2	GD-S1	Haplo S1	ATHO-S1	DR11-S1	DR11-S2	RP4-S3	ATHO-S2	GD-S2
Composition	MORB	Peridotite	MORB	Rhyolite	haplobasalt	Rhyolite	MORB	MORB	Peridotite	Rhyolite	Rhyolite
Pressure (GPa)	2	2	2	2	2	2	2	2	2	2	2
length before (μm)	1400	1771.2	1061.9	1098.8	1124.6	1541. 9	1141.3	1048.2	1652.9	1045.1	1336.4
length after (μm)	1334.2	1780.0	–	1462.7	1213.2	1666.1	1287.6	1324.9	1643.6	1309.1	1287.4
expected Melting T° (K)	>1600	>1523	>1600	>1173	>1723	>1173	>1600	>1600	>1523	>1173	>1173
Max T (K)	1614	1681	1612	1146	1769	1219	1609	1284	1573	1325	1073
Run duration (min)	544	1089	953	480	832	800	834	439	767	761	610

realized with Eq. (13), errors of raw data are used as weights in the inversion. The standard deviations are usually between 1 and 10% of the real asymptotic diffusivity. If the averaging method is selected, the standard deviation, estimated via Eq. (15), is usually about 1% of the final value.

A final source of uncertainties come from other technical issues and apparatus reproducibility, which are inherent to such challenging experiments. We considered that final error must be majored by 5% of the value. The relative uncertainties become even higher after conversion into thermal conductivities due to uncertainties and simplifications on the sample density and heat capacity at high pressure and temperature (see Supplementary Text S4).

2.4. Experimental procedure

We performed a suite of three heating and cooling cycles to provide an important number of data and maximize the quality of recovered data. A first cycle was run up to 500 °C for moisture removal by 50 °C steps (Fig. 2). The second cycle was run up to glass transition temperature (Tg) by 100 °C steps. Tg varies according to rock composition and its water content (Giordano et al., 2005). For our dry samples, the temperature of 800 °C happened to be above Tg for all our compositions. The temperature was then decreased down to 150 °C by 100 °C steps. The quality of the measurement is usually better during the cooling cycle once (1) the sample has thermally equilibrated with the assembly, (2) moisture has been removed, and (3) a better contact was achieved between the sample and the thermocouples due to local flow in the solid-state. The redistribution of matter under high temperature cancels most of the potential artifacts associated with the presence of pores/voids between the sample and the thermocouples (Hofmeister et al., 2009). Hence, data recorded during the last cycles were considered for final values.

In the last cycle, we heated the sample up to its melting temperature by 100 °C steps or 50 °C near the melting point. The sample was maintained above its melting point for less than 1 h, to avoid sample leakage and chemical reaction with the surrounding parts. The sample was then quenched to 600–550 °C. This step produces a glassy sample from which measurements at low temperature are performed.

Temperature oscillations of the two thermocouples were measured at each temperature step for both heating and cooling cycles, at 12 different oscillating frequencies between 0.1 and 1.5 Hz. The measurements were performed after at least 2 min of thermal equilibration to reach a stable regime (the smaller is the frequency, the longer is the required equilibration time). Then, the recording duration was 1 to 2 min or at least 10 oscillating periods. The measurement at the 12 frequencies took between 20 and 30 min. Thus, the duration of each experiment was more than 12 h.

2.5. Chemical and textural analyses

Recovered samples were cut parallel and perpendicular to the cylindrical furnace and each section was polished with great care. We could observe the position of the two thermocouples junctions, measure the sample radius and perform the textural and chemical analyses (see Supplementary Figs. S6, S7, and S8).

Micro-textures were observed with a Scanning Electron Microscope (SEM) JEOL Jeol JSM-5910 LV using an accelerating voltage of 15 kV and a working distance of 11.4 mm. The 2D phase proportions of our partially molten peridotite samples were obtained from the analyses of qualitative chemical maps obtained by energy-dispersive X-ray spectroscopy (EDX) in the SEM. The images were binarized and phases were individually separated allowing textural analyses with the FOAMS software (Shea et al., 2010). A more detailed description is given in Freitas et al. (2019). On the other hand, quantitative chemical analyses were performed on both our starting materials and experiment products using the electron probe micro analyzer (EPMA). Chemical and textural analyses of starting materials are reported in the Supplementary Text S2, Figs. S6 to S13 and Tables S1, S2, S3 and S4. Analyses of recovered runs are detailed in Supplementary Text S3, supplementary Figs. S6 to S7 and Tables S1, S2, S3 and S4.

Water contents were estimated using the ICP-AES for the peridotite starting materials and via Raman spectroscopy for the recovered samples. Raman spectra were collected with a Renishaw InVia confocal Raman micro spectrometer, equipped with a 532 nm diode laser and a Leica DM 2500 M optical microscope. Measurements were carried out using a 2400 grooves/mm grating, a 100× microscope objective, a slit aperture set to either 20 μm or 65 μm and a laser power of 8 mW for glasses and 16 or 75 mW for olivine. The resulting lateral and axial resolutions were of ~1 and 3 μm, respectively, and the spectral resolution was better than 1 cm^{-1}. Daily calibration of the spectrometer was performed based on the 520.5 cm^{-1} peak of Si. Spectra were recorded from ~100 to 1300 cm^{-1} (alumino-silicate network domain) and from ~3000 to 3800 cm^{-1} (water domain), with variable acquisition times ranging between 5 and 120 s for silicate bands and 120 and 240 s for water domain depending on the water content (Figs. S11 to S17). For water quantification in olivine and glass, we followed the procedures reported by Bolfan-Casanova et al. (2014) and Schiavi et al. (2018). We used both (1) the external calibration procedure, which is based on a set of hydrous olivine standards from (Bolfan-Casanova et al., 2014) and different types of silicate glasses ranging from basaltic to rhyolitic compositions (Schiavi et al., 2018; Médard et al., 2008), and (2) the internal calibration procedure, based on the correlation between the water concentration in olivine or glass and the relative areas of the water and silicate Raman bands (OH/Si integrated intensity ratio). The discrepancy between the two methods is small. Water contents in the standard materials were previously determined using the FTIR technique.

3. Results

We performed a total of 11 thermal diffusivity experiments on various chemical compositions, using the Angström method (details in Table 1). In this section, we first describe phase shifts and amplitude ratios between the two thermocouples and their conversion into thermal diffusivities and conductivities. We detail the post-mortem chemical and textural analyses in the Supplementary Text S3, Tables S1 to S4 and Figs. S6 to S13.

3.1. Phase shift, amplitude ratio and the refined raw-thermal diffusivities

Signals recorded during the experiments are sinusoidal oscillations with varying frequencies. The thermocouple located at the sample center (labeled TC1 in Fig. 3) presents a phase delay and a smaller amplitude compared to the thermocouple located at the sample edge (labeled TC2 in Fig. 3). Typical raw signals and their fits are presented in Fig. 3, while the refined (absolute) phase shifts and amplitude ratio are reported in Fig. 4. Both the magnitude of phase shift and amplitude ratio change significantly with the type of sample and the experimental conditions, including the source frequency. At a constant frequency, the phase shift increases with increasing temperature. At a constant temperature, the phase shift increases with increasing the excitation frequency. The amplitude ratio is decreasing with increasing frequency and temperature.

Globally, the refined thermal diffusivities present a comparable

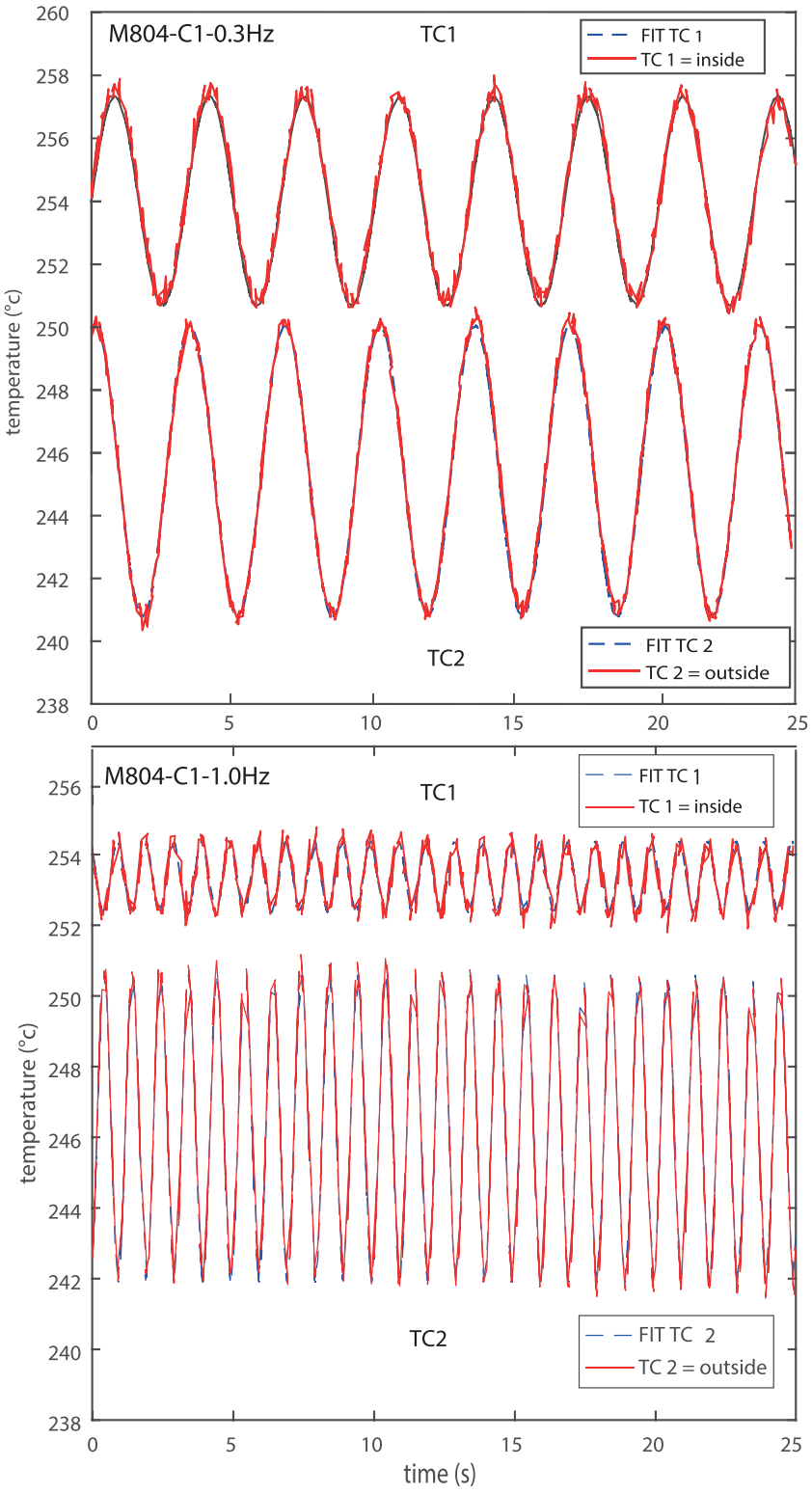

Fig. 3. Examples of temperature waves recorded at high temperature during M804 experiments. Such data set is acquired after the sample equilibration at target temperature conditions for a few minutes (here T = 250 °C). Acquisitions are performed at an interval ranging from 40 ms to 200 ms. At least 10 periods of the temperature oscillation are recorded to ensure a good extraction of phase shifts and amplitude ratio based on the fitting procedure described in Methods. Upper and lower frames correspond to temperature measurements performed at frequencies of 0.3 and 1 Hz, respectively. Red symbols are measured data and the dash thick lines represent the fitted sine waves. (For interpretation of the references to colour in this figure legend, the reader is referred to the web version of this article.)

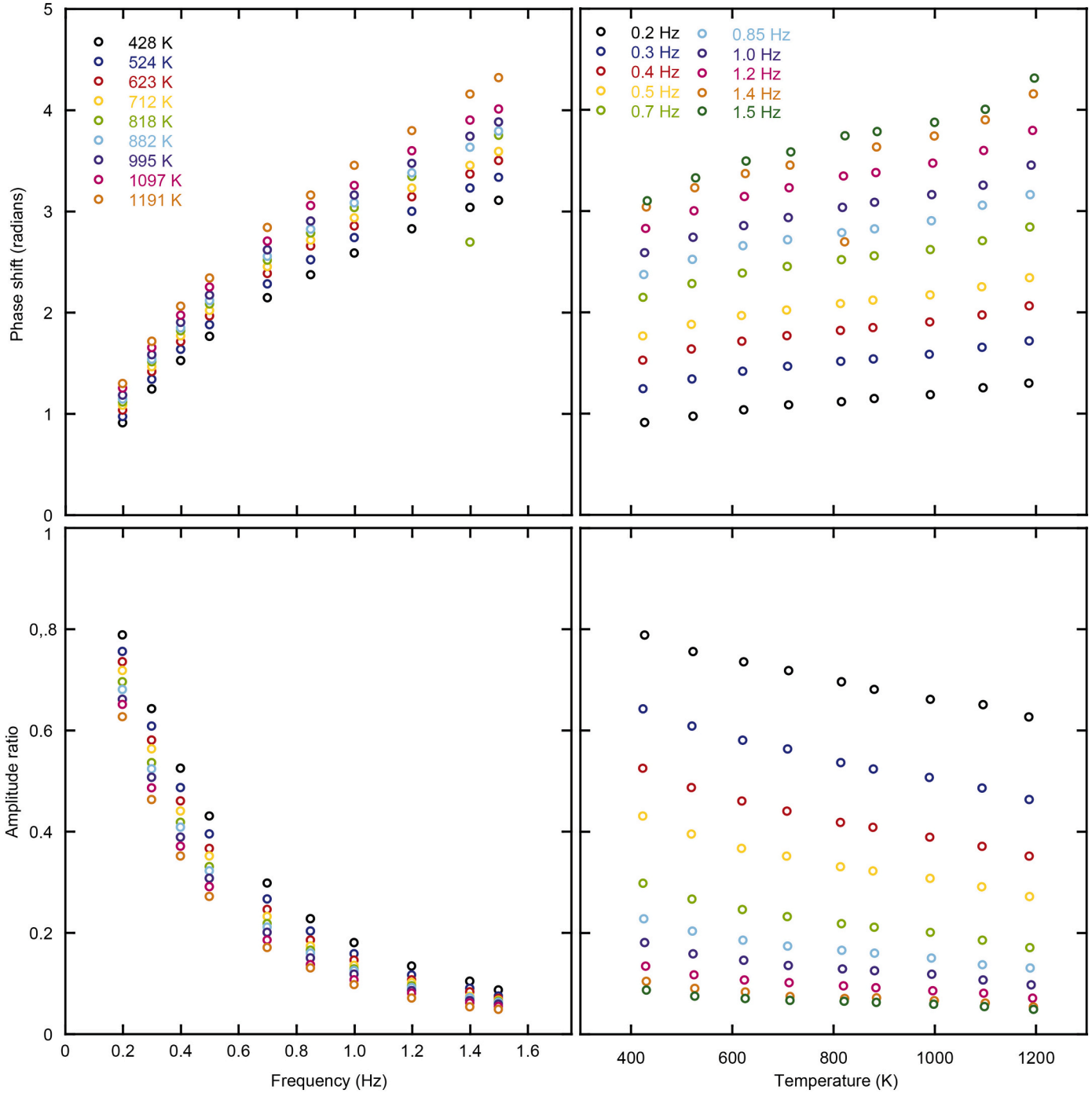

Fig. 4. Example of refined phase shifts (top panels) and amplitude ratio (bottom panels) as a function of frequency (from 0.2 to 1.5 Hz, left panels) and temperature (from 428 K to 1191 K, right panels) for sample M844.

evolution of temperature at all signal frequencies (see an example in Fig. 5). When the frequency dependence is larger than the experimental uncertainty (Fig. 6), we use Eq. (13) to refine the true asymptotic value of the thermal conductivity. Alternatively, when the temperature dependence is below the experimental uncertainty or when no clear frequency trends is visible, we average the different raw-diffusivity values (see Methods). In the wide majority of the cases, diffusivity values inferred from phase shifts appear to be more robust and with a lesser degree of uncertainty, compared to values inferred from difference of amplitude, in agreement with previous studies (Kanamori et al., 1969; Xu et al., 2004). Hence, despite similar values obtained with the two methods, values refined from phase shift were preferred.

3.1.1. *Results for peridotite*

For peridotite, our two successful experiments present a smooth evolution with temperature, yielding diffusivities values decreasing from 1.7(±0.1)e^{-6} to 7.5(±0.4)e^{-7} m^2/s for sample M804 and 1.5 (±0.8)e^{-6} to 5.5e^{-7} m^2/s for sample M847 (Fig. 6a), with an uncertainty of about 5 to 10% for each sample. We attribute the relative discrepancy to a difference of sample mineralogy between the two samples, due to the coarse grain size of the core drilled peridotite (see Supplementary Texts S2 and S3 and Figs. S8 and S9). Olivine has a higher intrinsic thermal diffusivity than the other phases present in peridotite such as pyroxenes and spinel (Hofmeister and Branlund, 2015). M804 may contain more olivine, inducing higher diffusivities than M847. In this

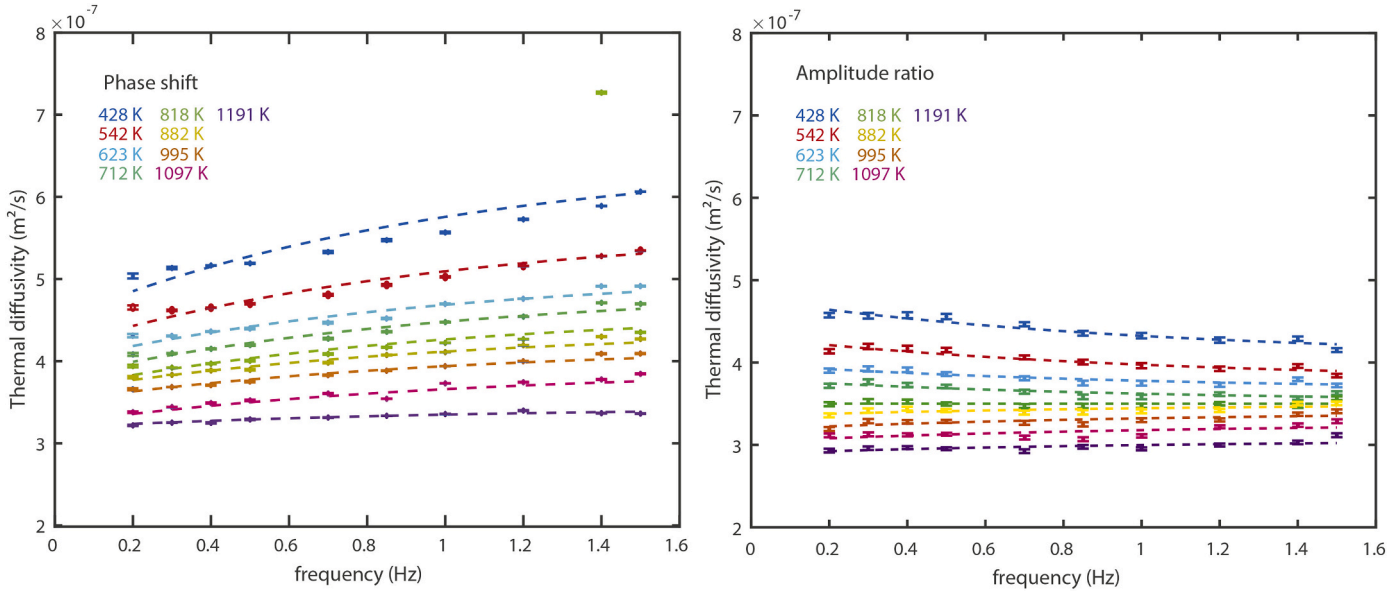

Fig. 5. Typical example of a set of raw values of the thermal diffusivity extracted from our measurements for a basaltic glass, presented as a function of the frequency of the heat source. Experimental temperatures range between ~430 and ~ 1200 K at a pressure of 2GPa (sample M844). Left and right panels correspond to thermal diffusivities calculated from phase shifts and amplitude ratios, respectively. The colour code is kept similar in both panels. The fit through the data is made following the equation $D = D_0 + A\ exp\ (-f/f_0)$ (Xu et al., 2004), were D_0 is the high-frequency asymptote of the diffusivity (see text). Error bars are generally within the size of the symbol.

respect, the results for two samples are thus compatible with each other and the differences are representative of the variability of thermal diffusivity that can be expected among the compositional variability of peridotites (from lherzolites to dunites).

Thermal diffusivities of our peridotite samples scale as a function of ~1/T, as expected from the standard equation provided by Hofmeister and Branlund, 2015:

$$D_{lat} = a^*T^{-b} + c^*T \quad (16)$$

where T is the temperature (K), and a, b and c are adjustable parameters (Table 2). The quality of the fit is excellent up to a temperature of ~1300 K corresponding to the onset of peridotite melting. We therefore exclude the data points above 1300 K to model the thermal properties of solid peridotite.

3.1.2. Results for basalts

For our basaltic samples, the measured thermal diffusivities plot over a broad range of values, from $1.0(\pm0.1)e^{-6}$ to $3.0(\pm0.2)e^{-7}$ m^2/s (Fig. 6b), with an uncertainty of ~5% for each experiment. The discrepancy is particularly important at low temperatures. Also, a same sample yields thermal diffusivity values significantly different along the different cycles of the experimental procedure (between C2, H3 and the final quench, see Fig. S5). Samples with the highest diffusivities at low temperatures present a rapid decrease of diffusivity with increasing temperature. On the other hand, samples with the lowest diffusivities show very small temperature dependence. It yields to a convergence of all diffusivity measurements at ~1000 K. Based on a study of rhyolitic glasses, Romine et al. (2012) reported a moderate temperature dependence, similar to our samples presenting a low diffusivity, and an increase of 0.0192 mm^2/s of the glass diffusivity per percent of crystallinity. For our starting materials with less than 5 vol% of crystals (see Supplementary Text S2 and S3, Fig. S7), the effect of microlites could account for ~0.1 mm^2/s of variation in our diffusivity values, which correspond to less than ~10% of observed differences. However, the presence of 35 vol% of crystals in the recovered sample M807 would explain not only its high thermal diffusivity at low temperature, but also its strong temperature dependence that is typical of crystals (see Beck et al., 1978; Romine et al., 2012; Hofmeister and Branlund, 2015 and our peridotite trends in Fig. 6a). The recrystallization of M807 is not surprising, since the second cycle of annealing was performed above its Tg (Figs. 2 and S5). The crystallinity of other samples depends on the applied cycles of annealing at a temperature eventually close to their Tg. Nonetheless, diffusivities of all samples converge at increasing temperatures, because the conductivity of crystals is not much greater than that of the glass at high temperature, especially if microlites are low thermal diffusivity silicates such as pyroxenes, plagioclase or spinels (see Hofmeister and Branlund, 2015 for mineral thermal diffusivity compilations). Over the 5 basaltic samples investigated in this study, the diffusivity trends indicate either significant recrystallization of M807 (DR07-MORB) and M662 (EPR-MORB), or negligible crystallization of M844 and M846 (DR11-MORB) and M836 (synthetic haplobasalt). The sample crystallization is likely to evolve during the thermal diffusivity measurements in step H3 (up to melting point) of the experiments performed at a temperature significantly above the Tg. For this reason, the crystallinity determined on the recovered samples is only a qualitative measurement of the sample properties at high temperatures.

3.1.3. Results for rhyolites

Measured thermal diffusivities of rhyolite samples also plot over a broad range of values from $1.4(\pm0.8)e^{-6}$ to $4.0(\pm0.2)e^{-7}$ m^2/s, with an uncertainty of about 5% for each experiment (Fig. 6c). The discrepancy appears similar than for the basalt samples, as the sample presenting higher diffusivities also show a major temperature dependence at low temperature. The presence of less than 2 vol% of crystals in the starting material could account for a diffusivity increase of 0.038 mm^2/s at maximum (Romine et al., 2012). Still, the diffusivity trends suggest a major recrystallization at high-temperature for M808 (Güney Dag) and M843 (ATHO), some crystallization for M843 (ATHO), and negligible crystallization for M850 (Güney Dag).

3.1.4. Properties of melts and partially molten samples

In addition to the evolutions described above, a strong decrease of the thermal diffusivity is observed for most of our samples at the highest temperatures (Fig. 6). The decrease occurs at temperatures around 1300 K for peridotites, 1200 K for basalts and > 1050 K for rhyolites. Such

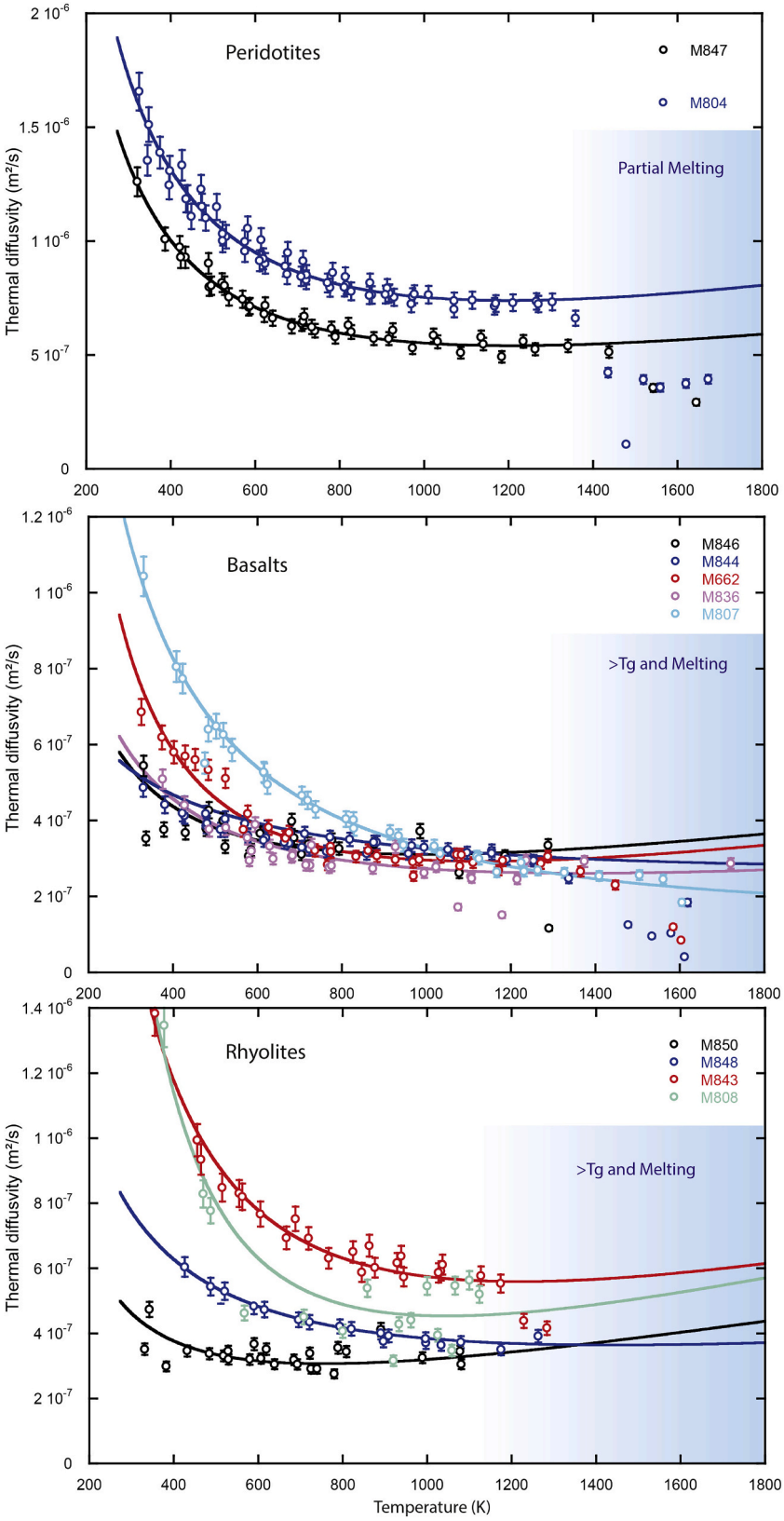

Fig. 6. Thermal diffusivities data refined for our peridotites, basalts and rhyolites samples (from top to bottom) as a function of temperature. Associated fits are represented with a solid line of the same colour than the symbols. Error bars are shown when larger than the symbol size. Several basaltic (M807, M662) and rhyolite (M848, M808) samples were partially recrystallized during the annealing and dehydration procedures prior to the conductivity measurement, as indicated by their high conductivity values at low temperatures. Thermal diffusivities values converge at high temperatures and melting.

temperatures are in agreement with the melting or glass transition temperatures, depending if the sample is a peridotite or a glass, recrystallized or not. Similar changes were already reported at temperatures above the glass transition (Hofmeister et al., 2009; Hofmeister et al., 2014; Romine et al., 2012).

The amplitude of the decrease is 45–50% in peridotites, which recovered samples present a degree of partial melting (F) up to 23%, 35–70% for basalts and $<$ 30% for rhyolites samples. The more pronounced decrease in molten peridotites is probably due to a more contrasted change of the local structure at the melting point, between the

Table 2
Fitting parameters obtained for the last cycle (C2-H3) of each experiment. Associated errors (1 STD) are given in parenthesis.

Run#	a	b	c	R^2	R^2 adj
Peridotites					
M804	7.0e-4 (2.2e-4)	1.06 (0.06)	2.97e-10 (2.8e-11)	0.9659	0.9647
M847	8.8e-4 (7e-4)	1.15 (0.05)	2.37e-10 (1.8e-11)	0.9763	0.9750
Basalts					
M846	8.6e-6 (1.5e-5)	0.5 (0.3)	9.7e-11 (8.4e-11)	0.3933	0.3294
M662	7.2e-4 (1.8e-4)	1.20 (0.04)	1.01e-10 (4.1e-12)	0.9964	0.9962
M836	5.6e-5 (7.6e-5)	0.84 (0.23)	1.03e-10 (3.5e-11)	0.5748	0.5421
M844	1.9e-5 (1.1e-5)	0.63 (0.10)	8.0e-11 (2.3e-11)	0.9608	0.9556
M807	8.1e-4 (1.9e-4)	2.15 (0.04)	4.1e-11 (9e-12)	0.9933	0.9929
Rhyolites					
M850	1.9e-5 (3.5e-5)	0.70 (0.32)	1.7e-10 (7e-11)	0.2788	0.2101
M808	1.8e-2 (7e-2)	1.7 (0.7)	2.3e-10 (1.4e-10)	0.8003	0.7696
M848	1.4e-4 (7e-5)	0.91 (0.09)	1.3e-10 (2.0e-11)	0.9851	0.9826
M843	5.1e-3 (3.3e-3)	1.42 (0.11)	3.18e-10 (3.6e-11)	0.9715	0.9684

minerals and the melt (see discussion). On the other hand, the minor change of diffusivity for rhyolites at Tg could be related to their high SiO_2-content, which preserves a polymerized structure in the melt above the glass transition.

3.2. Thermal conductivities

Thermal conductivities (κ) can then be computed from thermal diffusivities following:

$$\kappa\,(P,T) = D(P,T)^{*}\rho(P,T)^{*}C_P(P,T) \quad (17)$$

where $\rho(P,T)$ and $C_P(P,T)$ are the sample density and heat capacity, respectively. For our calculations, we considered ρ and Cp values in standard conditions when the P and/or T dependences were not available in the literature (see Supplementary Text S4 and Fig. S4).

Conductivities calculated for peridotites evolve from 4.32 (±0.48) to 1.70 (±0.19) W/m/K with increasing the temperature up to the melting point. Values for basalts range from 1.7 ($\pm 8.0e^{-2}$) to 0.5 ($\pm 4.0e^{-2}$) W/m/K, whereas those for rhyolite lie between 1.1 ($\pm 9.0e^{-2}$) and 0.3 ($\pm 3.0e^{-2}$) W/m/K for low to high temperatures, respectively. At the melting temperature, our partially molten peridotites display values of 1.19 (±0.16) to 0.93 (±0.10) W/m/K, whereas melts present relatively lower values of 0.34 (±0.2) to 0.18 (±0.1) W/m/K for basaltic and 0.41 (±0.3) to 0.31 (±0.3) for rhyolitic compositions (See Fig. 7 and Table 3). We note that the important difference in conductivity between basalts and rhyolites (Fig. 7) is predominantly due to differences between their heat capacities and densities, while their thermal diffusivities are found similar (Fig. 6).

4. Interpretation of results

4.1. General temperature dependence

For all compositions investigated in this study, thermal diffusivities decrease with increasing temperature until reaching a plateau at temperatures between 700 and 1000 K. Based on experiments performed at room pressure, it was observed that the plateau occurs at about the Debye temperature of the mantle minerals (Hofmeister et al., 2009, 2014). For this reason, it was proposed that thermal diffusivities vary largely with temperature until the complete activation of the vibration modes (phonons in minerals). The temperature range observed in our study for the occurrence of a plateau is fully compatible with this interpretation.

For basaltic glasses, a comparable but more moderate decrease of thermal diffusivity was reported up to a saturation temperature corresponding well to the glass Tg (Hofmeister et al., 2009, 2014; Romine et al., 2012). In our experiments, the decrease is of ~30% to 60% over the investigated temperature range, depending on the experiment. Such amplitude is compatible with the ~40% decrease observed during the heating of pyroxene glasses (Hofmeister et al., 2009).

For rhyolite samples, the thermal conductivity increases slightly with increasing the temperature (Fig. 7). This is due to the heat capacity that increases more with temperature than the density increases and diffusivity decreases (Eq. (17)). The increase is, however, smaller than reported in Romine et al. (2012), due to the use of a different Cp (Neuville et al., 1993) (see Supplementary Text S4) and a stronger temperature dependence of thermal diffusivities observed in our experiments because of different crystallizations states.

4.2. Effect of radiative conduction

Romine et al. (2012) reported an increase in thermal diffusivities of the melts at very high temperatures at ambient pressure. They attributed this feature to an increased role of the radiative component. Such a component can dominate the thermal diffusivity for a sample transparent to the infrared and visible photons at high temperatures. For thin samples, this effect can become problematic if the mean free path of photons is longer than the sample length (ballistic photons, see Hofmeister and Branlund, 2015). No significant increase in thermal diffusivity and conductivity is observed in our high-pressure experiments, except maybe for the rhyolitic samples (Figs. 6 and 7). The difference with the previous work is most probably related to the opacity of our basalts and peridotites samples, hence limiting the radiative transfers.

4.3. Effect of glass/melt composition

Overall, our conductivity values are compatible with the values available in the literature (see Fig. 8). Differences in absolute values are nonetheless present. Rhyolite melts (0.31–0.41 W/m/K) are found slightly more conductive than basaltic ones (0.18–0.34 W/m/K). Within the same family of glass, thermal conductivity varies by 0.10 to 0.15 W/m/K for rhyolitic and basaltic melts, respectively. This is slightly larger (of at least 10%) than the experimental uncertainty, an effect possibly due to larger uncertainties on the dimensions of the molten sample. No clear trend can be retrieved from the comparison between our different basaltic or rhyolitic compositions. Among the major elements, iron could be of major importance, due to its critical impact on glass/melt density. Indeed, the thermal diffusivity of glasses was reported to decrease with increasing density (Hofmeister et al., 2014). The comparison between our rhyolites and basalts is coherent with such a trend. However, our haplobasalt (M836) presents diffusivity values comparable with natural basalts (M662, M807, M844), as well as Fe-bearing (M843 and M848) and Fe-free (M808 and M850) rhyolites (Fig. 6), despite a variation of the Fe-content from 0 to 10 wt% in these different samples. Other elements could also impact the melt thermal diffusivity, in particular Si and Al, which favor polymerization of the liquid (and alkali elements for the opposite effect) (Ni et al., 2015). Still, within the experimental uncertainty, we observe no clear trend related to these elements, despite a variation of the SiO_2 content by more than 20%. Additionally, water, with a total content smaller than 1.10 wt%, should have a negligible effect on thermal conductivity (Romine et al., 2012; Ni et al., 2015). It could, however, impact the melt density at a low degree of partial melting (Hofmeister et al., 2014). As the water contents estimated in the recovered samples are similar to the ones obtained in starting materials (see Supplementary Text S2 and S3), water should not

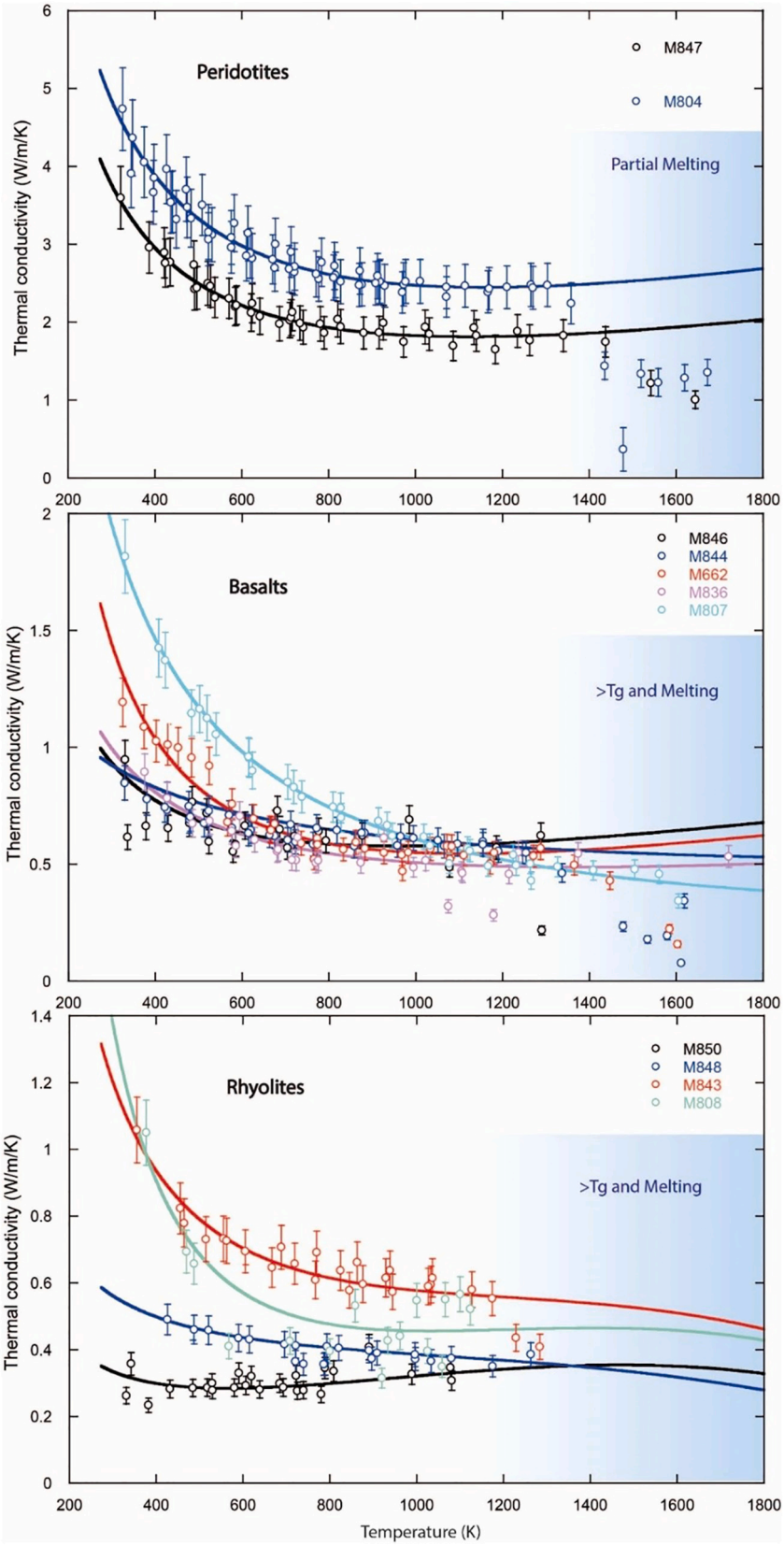

Fig. 7. Thermal conductivities inferred from diffusivities (Fig. 6), heat capacities and densities (see Fig. S4), based on Eq. (17) of the main text.

Table 3
Thermal diffusivities and conductivities retrieved for our samples at low and high temperatures for solids, above Tg and/or melting temperature (indicated for each group) for melts and partially molten samples.

Sample name	Temperature range (K)	Melt fraction (%)	STD (%)	K (W/m/K)	STD	D (m^2/s)	STD
SOLIDS							
M804	LT < 400 K	0	0	4.32	0.48	1.66E-06	2.05E-09
M847	LT < 400 K	0	0	3.28	0.37	1.26E-06	3.34E-09
M804	HT >1200 K	0	0	2.29	0.26	7.33E-07	1.80E-09
M847	HT >1200 K	0	0	1.70	0.19	5.39E-07	6.13E-10
Partially molten samples							
M804	>1300 K	6.44	2.98	1.19	0.16	3.74E-07	2.55E-08
M847	>1300 K	23.31	2	0.93	0.10	2.92E-07	1.22E-10
MELTS							
BASALTS	MELT >1200 K						
M807	>1224 K	100	0	0.34	0.02	1.84E-07	1.51E-09
M844	>1326 K	100	0	0.18	0.01	9.52E-08	2.96E-11
M662	>1450 K	100	0	0.22	0.16	1.20E-07	8.73E-08
M846	>1200 K	100	0	0.22	0.12	1.16E-07	6.47E-08
M836	1180 K	100	0	0.28	0.02	1.51E-07	6.94E-10
rhyolite	Melt >1000 K						
M850	> 1080 K	100	0	0.31	0.03	3.05E-07	2.42E-08
M808	>1060 K	100	0	0.35	0.03	3.47E-07	5.95E-10
M848	>1260 K	100	0	0.39	0.03	3.91E-07	6.21E-10
M843	> 1280 K	100	0	0.41	0.03	4.16E-07	2.36E-10
Literature							
SOLIDS							
Olivine Xu 0 GPa LT	294 K	0	0	4.15	0.42	4.10E-06	2.05E-07
Olivine Xu 0 GPa HT	1377 K	0	0	1.95	0.19	5.00E-07	2.50E-08
Olivine Hof 16 AVG	300 K	0	0	6.37	0.64	2.37E-06	4.75E-08
Olivine Hof 16 AVG	>1500 K	0	0	2.76	0.28	7.01E-07	1.40E-08
Dunite Per 06	300 K	0	0	4.22	0.42	1.57E-06	3.15E-08
Dunite 2 Per 06	300 K	0	0	5.35	0.53	1.99E-06	3.99E-08
Dunite Per 06	>1500 K	0	0	1.65	0.17	4.20E-07	8.40E-09
Dunite 2 Per 06	>1500 K	0	0	2.23	0.22	5.65E-07	1.13E-08
Dunite Beck 78 2Gpa	300 K	0	0	4.15	0.42		
Dunite Beck 78 2Gpa	300 K	0	0	5.49	0.55		
Dunite 2 GPa Dry Z19	300 K	0	0	5.21	0.26	1.71E-06	8.55E-08
Dunite 2 GPa 0.08% wt H_2O Z19	300 K	0	0	4.86	0.24	1.59E-06	7.95E-08
Melts							
Di Hof 09	>1140 K	100	0	1.25	0.13	2.89E-07	5.79E-09
An Hof 09	>1290 K	100	0	1.45	0.15	3.58E-07	7.16E-09
Fk Hof 09	>1245 K	100	0	1.45	0.15	4.75E-07	9.50E-09
Ab Hof 09	>1300 K	100	0	1.60	0.16	4.99E-07	9.99E-09
Rhyolite/obsidian							
Ncar Ro 12	1384 K	100	0	1.53	0.15	5.17E-07	1.03E-08
NCr Ro 12	1365 K	100	0	1.50	0.15	5.08E-07	1.02E-08
SCE Ro 12	1464 K	100	0	1.59	0.16	5.31E-07	1.06E-08

Literature estimates are also provided on the bottom part: "Xu" refers to polycrystalline olivine (dunite) measurements performed at ambient pressure (Xu et al., 2004). "Per06" refers to average values from 3 oriented (100,010,001) single crystal measurements at room pressure (Pertermann and Hofmeister, 2006) and some dunite values are also available in the same study. "Beck78" refers to Dunite measurements performed at 2 GPa (Beck et al., 1978). Regarding melts, literature data are taken from Hofmeister et al. (2009), Di: diopside, An: anorthite, Fk: orthose, Ab: albite. Finally, data from a few rhyolites Ncar, NCr and SCE are selected from Romine et al. (2012). When literature data are available in the form of thermal diffusivities, their conductivities are obtained using either the Cp and ρ provided in the source study or from our own parameters if not available (see Supplementary Materials).

induce any strong diffusivity variation in our data-set. We, therefore, conclude that chemical effects are secondary compared to the structural ones.

4.4. Mixing models for thermal conductivities of partially molten peridotite

Our results show that peridotites, and to a lower extent the glasses, present higher thermal diffusivities compared to the melts. This result is not surprising: thermal conductivity is strongly dependent on the local structure and its vibrational properties. The disorder in the atomic structure increases from solid, glasses to molten states (Hofmeister et al., 2014). The composition of the melt appears to be of secondary importance. The final set of thermal diffusivities and conductivities values selected for the applications are given in Tables 3, S5 and Figs. 9 and S14.

To propose a predictive law for thermal conductivity of partially molten rocks several mixing equations are now tested. Such equation generally describes the effect of a small amount of conductive phase into an insulating matrix. For thermal conduction, the problem is reversed because the melt is less conductive than the solid. In this section, we explore the different predictive models of thermal conductivity of binary mixtures:

1) Linear mixing model consider parallel thermal resistor:

$$\kappa_{bulk} = \kappa_s{}^*(1-F) + F\kappa_m \quad (18)$$

where *s* corresponds to the solid, *m* the melt and *F* the volume fraction of the melt.

2) Tube / Ashbie model consider 1/3 of tubes of melt aligned in the heat flow direction (Grant and West, 1965; Schmeling, 1986):

$$\kappa_{bulk} = \frac{1}{3}{}^*\kappa_s{}^*(1-F) + F\kappa_m \quad (19)$$

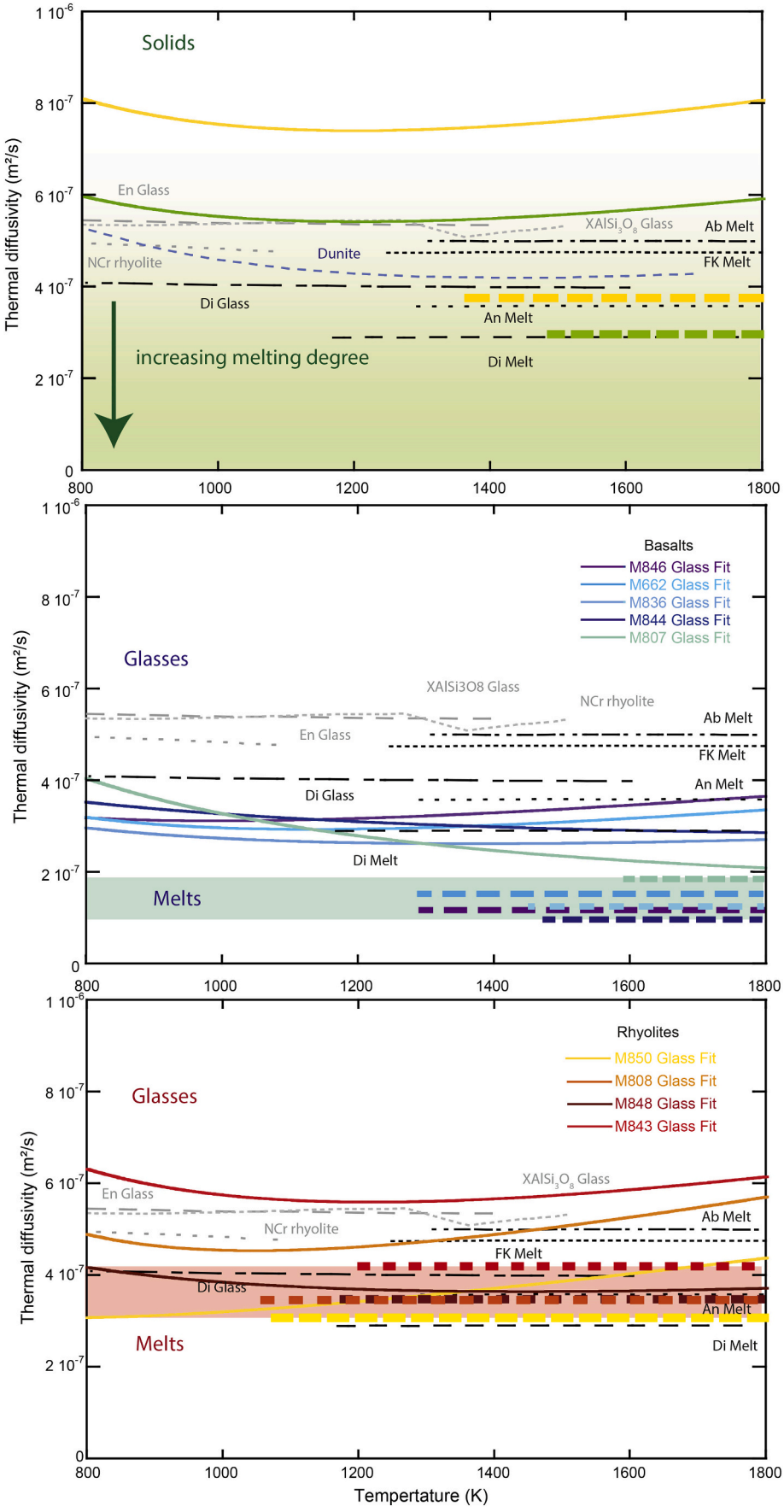

Fig. 8. Comparison with the literature of our thermal diffusivities obtained our peridotite (upper panel), basaltic (center panel) and rhyolitic (lower panel) starting materials. Solids (peridotite and glasses) and melts are represented in thick lines and thick dashed line, respectively. Literature data are reported with thinner dashed lines (grey to black). Diopside (Di) glass and melt, $XAlSi_3O_8$ glass, Anorthite melt (An), Albite melt (Ab) and orthose melt (FK) from Hofmeister et al., 2009, NCr Rhyolite from Romine et al., 2012 and Enstatite glass from Hofmeister et al., 2014.

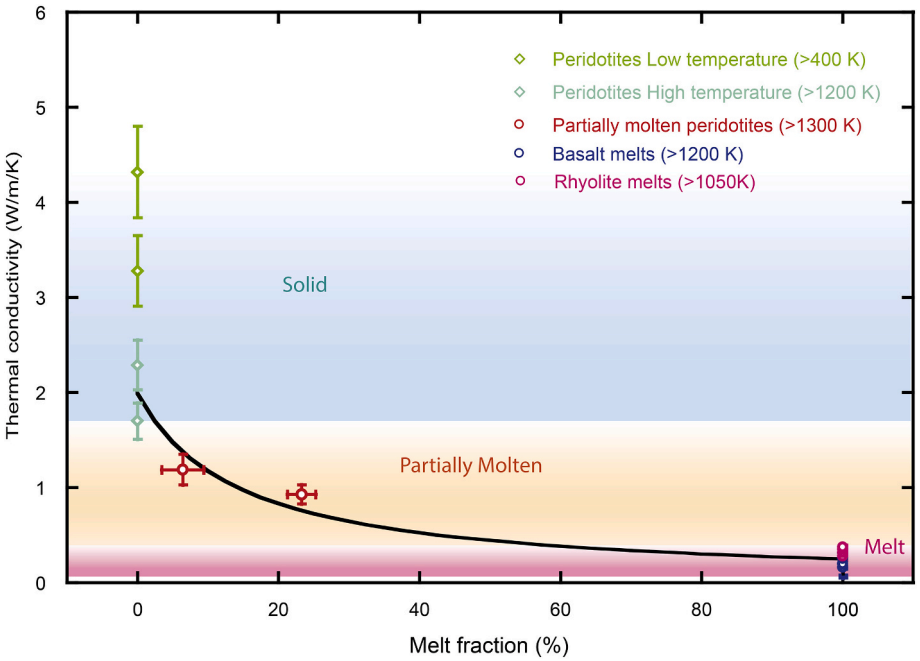

Fig. 9. Our best model of the evolution of thermal diffusivity as a function of the melt fraction at high temperature (>1200 K), based on all available data sets. Solid peridotites at low and high temperature are represented with green and blue diamonds, respectively. Partially molten peridotites with 6.4% and 23.3% of melt (see Supplementary Text S3) are represented with red circles and melts (basalts and rhyolites) are represented with blue and pink circles. All the errors represented are 1 standard deviation. The fit represented is using a model of thermal resistors in series (Eq. (22)), which fits our data set very well (see Fig. S14). (For interpretation of the references to colour in this figure legend, the reader is referred to the web version of this article.)

3) Cube model (Waff, 1974) representing cubes of solids into a melt matrix

$$\kappa_{bulk} = \left[1 - F^{2/3}\right] * \kappa_s \tag{20}$$

4) Archie's law, an empirical relation developed for electrical conductivity (Watanabe and Kurita, 1993)

$$\kappa_{bulk} = C * (1 - F)^n * \kappa_s \tag{21}$$

where C and n are constants.

5) Thermal resistors in series:

$$\kappa_{bulk} = \kappa_s * \frac{\kappa_m/\kappa_s}{\kappa_m/\kappa_s + F(1 - \kappa_m/\kappa_s)} \tag{22}$$

6) Hashin Shtrikman lower bound (HS^-), representing insulating melt spheres into a conductive solid matrix:

$$\kappa_{bulk} = \kappa_s * \frac{F}{1 \Big/ (\kappa_m/\kappa_s) + \frac{1-F}{3\kappa_s}} \tag{23}$$

7) Maxwell-Eucken relation:

$$\kappa_{bulk} = \kappa_s * \frac{\kappa_m + 2\kappa_s + 2F(\kappa_m - \kappa_s)}{\kappa_m + 2\kappa_s - F(\kappa_m - \kappa_s)} \tag{24}$$

8) Landauer relation, based on resistors in series:

$$\kappa_{bulk} = \frac{1}{4} * \left[\kappa_m(3F-1) + \kappa_s(2-3F) + \{(\kappa_m(3F-1) + \kappa_s(2-3F))2 + 8\kappa_s\kappa_m\}^{\frac{1}{2}}\right] \tag{25}$$

9) Russel-Rayleigh relation:

$$\kappa_{bulk} = \frac{\kappa_s\left[\kappa_s + F^{2/3}(\kappa_m - \kappa_s)\right]}{\kappa_s + (\kappa_m - \kappa_s)\left(\kappa_m^{\frac{2}{3}} - F\right)} \tag{26}$$

These equations provide a different evolution of the thermal conductivity with the fraction of melt (F). In Fig. S14, we present the results when either fixing κ_{solid} and κ_{melt} to the average value of our measurements, or adjusting their values to minimize the misfit between the mixing models and our results at varying F values (Table S5). Among the variety of fits obtained, it appears that the effect of partial melting is underestimated in most of the cases. Only the thermal resistors in series is capable to reproduce adequately the strong curvature observed experimentally at low F values, as well as the end-member values of solid and melt conductivities. For this reason, we use series model (Eq. (22)) for further discussions.

We note a lack of data points at high melt fractions, preventing to decipher more precisely the mixing trend. At very high temperatures, the experimental measurements become difficult on natural peridotite melting, in particular due to melt escape and chemical reactions with the experimental cell. Complementary data could be acquired working with analog system such as basalt/olivine mixture and could represent a further research direction.

4.5. Thermal conductivity of partially molten peridotite: influence of texture

The 3D solid/melt arrangement is known to influence significantly the geophysical properties of partially molten systems (Von Bargen and Waff, 1986; Laporte et al., 1997; Laporte and Provost, 2000; Minarik and Watson, 1995; Yoshino et al., 2005; Maumus et al., 2005; ten Grotenhuis et al., 2005; Freitas et al., 2019; Freitas and Manthilake, 2019). Their distribution is classically described using dihedral angle value, which translates the ability of a liquid to wet the grain boundaries as a consequence of interfacial energies. The dihedral angle decreases when increasing pressure, temperature, water content and decreasing silica/alumina content of the melt (Yoshino et al., 2007; Mibe et al., 1998, 1999; Laporte et al., 1997; Watson et al., 1991). Several studies with similar basaltic or peridotite melts (dry) have shown that basalt-like melts at mantle conditions have dihedral angles significantly lower than the interconnection threshold of 60°, with values between 30 and

40° at 2 GPa (Laporte et al., 1997; Yoshino et al., 2005, 2007). Our partially molten samples display a coherent texture and dihedral angles with these observations. Dihedral angles of 23.3° and 19.0° were measured from our samples containing 6.4% and 23.3% of melt, respectively (Fig. S15), in good agreement with previous data given that these mafic melts are moderately hydrous (Table S3). For each melt fraction, a thin layer of melt surround most of the grains, in particular olivines, which in 3D will result into the insulation of the solid gains from their surroundings (Fig. S9). This is very well visible on our low melt fraction sample (F = 6.4%) where the layers of melt are few microns thick (M804). Even if melt is more abundant near clinopyroxenes and spinel sites in M847 (F = 23.3%), the melt pockets are interconnected with similar thin melt layers (<10 μm) (Fig. S9). As a result, thermal conductivity is expected to drop brutally in the first degrees of melting. Still, some grain boundaries should remain un-wetted until the melt fraction rise significantly. For this reason, thermal conductivity should only stabilize at melt fraction corresponding to solid grains completely isolated from each other. This trend is visible in our data and parallel model (Figs. 9 and S14) with a strong decrease in the first 10% of melting highlighted by M804, the change of slope seems to occur around 15% and values decease more slowly in the 15–50% range as seen in M847, to stabilize and display near-melt values above 50%. The complete isolation of solids should occur at "packing" threshold, which is a function of the solid shapes and size distribution and is expected to occur between 40 and 60% of melting. Thus, the first degrees of melting are very crucial in the case of a wetting liquid and affecting importantly the thermal properties.

4.6. Thermal conductivity of peridotite: effect of the grain size

The modelling of thermal conductivity of peridotites and low F molten peridotites should also take in account the effect of grain boundaries thermal resistances as grain size may vary in the different geological contexts (from 100 μm to >1 cm), as seen in natural meteoritic examples, (Barrat et al., 1999; Busek, 1997; Keil, 2010; Floran et al., 1978). Indeed, grain boundary scattering could be important when the mean free paths of phonons approach the grain size. This effect, which only concerns solids and low fractions of melt, can be quantified with the following equation (Smith et al., 2003; Smith et al., 2013):

$$\frac{1}{\kappa_{poly}} = \frac{1}{\kappa_{single}} + nR_{boundary} \tag{27}$$

where κ_{poly} is the thermal conductivity of the polycrystalline sample, κ_{single} the thermal conductivity of a reference single crystal (average from olivine data of (Hofmeister et al., 2007, Table 3), n represents the surface of grain boundaries along the heat flow direction per unit length, and $R_{boundary}$ the thermal resistance of grain boundary plane. The n value should be almost constant with temperature (Smith et al., 2013) and is estimated between $4e^{-4}$ and $7e^{-3}$ m for our two peridotite samples via analyses of SEM images (grain size ranging from 25 to 140 μm, see Table S4 for textural parameters). We calculate $R_{boundary}$ values between $1.9e^{-6}$ and $5.9e^{-6}$ W/m^2/K for M804 and $9.3e^{-6}$ and $3.2e^{-5}$ W/m^2/K for M847. These values are compatible or slightly higher than hydrous polycrystalline olivine samples (Zhang et al., 2019).

As a result, the thermal conductivities quantified in our experiments are underestimations of natural ones as the grain size is <100 μm, in experiments compared to grain sizes of 100 μm up to >1 cm typical of mantle peridotites and reduced meteorites (which could be relic of bodies interiors, from cumulates (Floran et al., 1978), enstatite chondrite/achondrite (Keil, 2010), diogenite (Barrat et al., 1999) to pallasite (Busek, 1997)). Melts and high F partially molten systems are not affected by such effect, thus the observed decrease of thermal conductivity at the melting temperature is probably smaller in our experiments than in natural cases.

5. Implications for geodynamos on Mercury-like proto-planets

5.1. Suitable conditions for a dynamo

For a thermally driven dynamo to operate in a terrestrial planet, four conditions were found to be necessary (e.g., Monteux et al., 2011): the core heat flow must be at least adiabatic (1), the thermal convection within the core has to supply enough power to compensate the losses due to ohmic dissipation (2), the Reynolds magnetic number must be supercritical (complex turbulent convection) (3) and the mantle heat flow has to overcome the core heat flow needed to induce a dynamo (4). These conditions can be expressed in terms of heat flow balance (See Fig. 10 for a schematic representation) and are detailed here:

(1) The metallic core has to convect, meaning that the heat flow out of the core needs to overcome the adiabatic heat flow (Stevenson et al., 1983).

For this, the core thermal conductivity (κ_{core}) is a dominant parameter. A large κ_{core} value increases the heat flux along the core adiabat and reduces the lifetime of a thermally driven dynamo (Breuer et al., 2015). Several laboratory measurements suggested that the thermal conductivity of polycrystalline iron at Mercury's core conditions is 113–125 W/m/K (see Deng et al., 2013 and references therein). However, such values for Mercury are recently challenged with several recent studies proposing a much lower conductivity. In a first one, the conductivity of pure Fe and Fe-Si alloys is reported at 30–40 W/m/K and 35–40 W/m/K, respectively (Silber et al., 2019). Then, it is proposed that the thermal conductivity of Fe-S at the P-T conditions of Mercury's core is as low as ~4 W/m/K, thus 1–2 orders of magnitude lower than that of pure iron (Pommier et al., 2019; Manthilake et al., 2019).

This first condition can be expressed as:

$$Q_{CMB} > Q_{Ad} = \frac{\kappa_c \alpha_c g_c T_{CMB}}{C_{p,c}} 4\pi R_c^2 \tag{28}$$

To estimate this flux, we assume that T_{CMB} is the melting temperature of pure iron at P_{CMB}. This assumption gives a conservative value of the core heat flow in comparison with considering T_{ICB} since the core liquidus is steeper that the core adiabat. We estimate the relation between the melting temperature of pure iron and the pressure using the

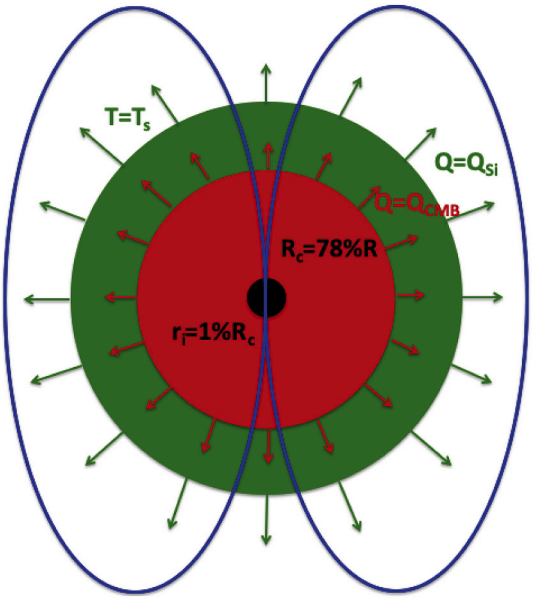

Fig. 10. Schematic representation of the geometry and of the heat flows computed in our model.

following expression obtained by fitting the experimental results from Anzellini et al., 2013 with a Simon and Glatzel equation:

$$T_{m,Fe} = 1800\left(\frac{P_{CMB}}{27.9}+1\right)^{1/2.08} \quad (29)$$

Such a melting temperature typically lies between the solidus and liquidus of a chondritic mantle for the same pressure conditions (Monteux et al., 2020 and references therein). We also assume that k_c, α_c and $C_{p,\,c}$ are constant (see values in Table 4) and P_{CMB} is calculated as follows (Monteux and Arkani-Hamed, 2014):

$$P_{CMB} = P(r=R_c) = \frac{2}{3}\pi G\rho_c^2\left(R_c^2-r^2\right)+\frac{2}{3}\pi G\rho_{Si}^2\left(R^2-R_c^2\right)+\frac{4}{3}\pi G\rho_{Si}R_c^3(\rho_c-\rho_{Si})\left(\frac{1}{R_c}-\frac{1}{R}\right) \quad (30)$$

(2) The energy supplied by thermal convection to the geodynamo has to compensate for the loss due to ohmic decay (Buffett, 2002).

This imposes a condition on the core heat flow at the CMB. In fact, core heat flow will need to overcome a critical value. Assuming that dynamo is generated only by thermal convection in the core, we can write:

$$Q_{CMB} > Q_{Ad} + \frac{4\upsilon_c\overline{B}^2C_{p,c}}{0.8\mu_c\alpha_cG\rho_cR_c} \quad (31)$$

This heat flux is estimated by considering that the characteristic magnetic length scale equals the radius of the core. The parameter $\overline{B}$ is the average strength of the magnetic field inside the core and was estimated using a scaling from Christensen and Aubert, 2006:

$$\overline{B} = 0.9\mu_c^{\frac{1}{2}}\rho_c^{\frac{1}{6}}\left(\frac{g_cQ_B(R_c-r_i)}{4\pi R_cr_i}\right)^{\frac{1}{3}} \quad (32)$$

With $Q_B = \alpha_cQ_{CMB}/C_{p,\,c}$ the buoyancy flux and r_i the radius of the inner core. In the scaling from Christensen and Aubert (2006), the inner core size cannot be set to 0. On Mercury the size of the inner core is currently not well constrained even if recent constraints via geodetic analysis (Genova et al., 2018) suggest its presence and a possible important size (r_i/R_c between 0.3 and 0.7). As we focus here on the effect of thermal cooling on dynamo generation (i.e. we do not consider the effect of compositional convection related to inner core growth), we consider a small inner core with $r_i/R_c = 0.01$. The scaling law used to calculate the average strength of the magnetic field inside the core (Eq. (32)) is valid for the Earth but overestimates $\overline{B}$ in the case of thin shell dynamos such as the one operating within Mercury (Christensen and Aubert (2006)). Mariner 10 spacecraft measurements showed that Mercury's magnetic field was 100 times weaker than the Earth's one. To account for this discrepancy, we consider that the average strength of the magnetic field is 1%$\overline{B}$ obtained from Eq. (32) when solving Eq. (31). We also consider that υ_c, μ_c and ρ_c are constants (see values in Table 4). We note that most of the power needed to overcome the criterion related to Eq. (31) can be supplied by thermal core convection (i.e. criterion related to Eq. (28)) especially for large metallic cores.

(3) The magnetic Reynolds number (Re_m) must be supercritical in order to have convective motions, inducing a complex structure needed to carry the magnetic field lines (U. R. Christensen and Aubert, 2006).

Reynolds magnetic number is calculated using Christensen and Aubert, 2006 formulation's and assuming that the characteristic magnetic length scale is the radius of the core:

$$Re_m = \left(\frac{Q_{CMB}G\alpha_c}{3C_{p,c}}\right)^{1/3}\frac{R_c}{\upsilon_c} > 10-100 \quad (33)$$

The value of the critical magnetic Reynolds number ($Re_{m,c}$) is usually constrained for models implying a large inner core. For Mercury-like planets, this value is less documented. Here we make the conservative assumption that this value ranges between 10 and 100.

(4) The mantle heat flow has to overcome the core heat flow needed to generate a dynamo.

The mantle's Rayleigh number (Ra) conditions the efficiency of heat evacuation from the mantle:

$$Ra = \frac{\alpha_{Si}\rho_{Si}g\Delta T{\delta_{Si}}^3}{\eta_{Si}\kappa_{Si}} \quad (34)$$

With α_{Si} the mantle thermal expansion coefficient, ρ_{Si} the mantle density, ΔT the temperature difference between the core and the surface of the planet, δ_{Si} the mantle thickness, η_{Si} the mantle viscosity,κ_{Si} the mantle heat diffusivity ($\kappa_{Si} = k_{Si}/(\rho_{Si}C_{p,\,Si})$), and $C_{p,\,Si}$ the mantle heat capacity. If Ra is lower than a critical value ($Ra_C \approx 1000$), the heat is evacuated from the mantle by conduction and the mantle heat flow Q_{Si} is:

$$Q_{Si} = \frac{k_{Si}\Delta T}{\delta_{Si}}4\pi R^2 \quad (35)$$

Alternatively, if the $Ra > Ra_C$, the heat is evacuated from the mantle by convection and Q_{Si} scales with $\mathrm{Ra}^{1/3}$(Solomatov, 2007):

$$Q_{Si} = 0.089\frac{k_{Si}\Delta T}{\delta_{Si}}4\pi R^2Ra^{1/3} \quad (36)$$

In any case, for a thermally-driven dynamo to operate, Q_{Si} has to be larger than the core heat flow Q_{Core}. For these calculations, we consider here that the surface gravity is dominated by the gravity at the CMB ($g = g_c$). On a planet with a core over planet radius ratio (R_c/R) of ~0.5, the mantle is thick enough so that $Ra > Ra_c$ and the heat is efficiently evacuated by convection. On such bodies, the dynamo is generated easily and should appear early in the planet history. If the heat evacuation is very efficient, the planet might cool down rapidly, which can potentially lead to a short-lived dynamo. On a Mercury-like body with a large R_c/R ratio, the mantle is thin compared to the core and its Rayleigh number, critical criterion for thermal convection, hardly overcomes Ra_c. Hence, conduction should be the main heat evacuation process within the mantle of Mercury-like planets, which can limit the occurrence of an early thermally-driven dynamo.

Table 4
Typical parameter values for heat fluxes calculations displayed in Figs. 11 and 12.

κ_c	Core thermal conductivity	4–40	W/m K^{-1}
α_c	Core thermal expansion	7.7×10^{-5}	K^{-1}
$C_{p,\,c}$	Core heat capacity	800	J kg^{-1} K^{-1}
υ_c	Core magnetic diffusivity	2	m^2 s^{-1}
μ_c	Core magnetic permeability	$4\pi\ 10^{-7}$	H m^{-1}
ρ_c	Core density	7500	kg m^{-3}
B	Average magnetic field strength	Eq. (3)	T
R	Planet radius		m
R_c	Core radius	77% R	m
r_i	Inner core radius	1% R_c	m
G	Gravitational constant	6.67×10^{-11}	m^3 kg^{-1} s^{-2}
κ_{Si}	Silicates thermal conductivity	4.32–1.70	W/m K^{-1}
κ_{Si}	Molten silicates thermal conductivity	0.18–0.41	W/m K^{-1}
α_{Si}	Silicates thermal expansion	1×10^{-5}	K^{-1}
$C_{p,\,Si}$	Silicates heat capacity	1000	J kg^{-1} K^{-1}
T_s	Surface temperature	500	K
δ_{Si}	Mantle thickness	33% R	m

5.2. Simulation results

We now compare the core heat flow needed to generate a dynamo within a Mercury-like body (with e.g. $R_c/R_{planets}$) (Figs. 11 and 12). To do this, we use a maximum possible range of solid conductivities between κ_{Si} = 4.32 and 1.70 W/m/K. We consider a maximum planet radius R = 2440 km with a thin mantle shell to stay in temperature and pressure conditions equivalent to the experimental conditions detailed above ($P \leq$ 2GPa and $T \leq$ 1700 K). We also report the critical size of the protoplanet (R = 215 km) above which Re_m is larger than 100 (Eq. (33)). The Fig. 11 shows that a solid conductive mantle is able to evacuate enough heat to induce a thermally driven dynamo if the planet radius is larger than ~215 km, regardless of the value of thermal conductivity in the outer core, at least up to more than 40 W/m/K. In contrast, the change of core conductivities from e.g. 40 W/m/K (Silber et al., 2019) to 4 W/m/K (Manthilake et al., 2019) has a major effect on the maximum size of a planet that can operate a thermally driven dynamo. For a core conductivity κ_{core} = 40 W/m/K, the maximum planet radius evolves from 1220 to 1880 km, for κ_{Si} = 1.70 and 4.32 W/m/K, respectively. When κ_{core} = 4 W/m/K, the maximum planet radius is more than 2500 km.

We now perform the same type of calculation for a mushy mantle using the silicate-melt conductivity refined in this study (Tables 3 and 4). We consider here neither a complete magma ocean that would evacuate the core heat very efficiently by turbulent convection (Monteux et al., 2016) nor a mushy mantle with a large melt fraction (larger than 40–60%) which would imply a strong decrease of the bulk viscosity of the mantle (Picard et al., 2013). We consider here a purely conductive mantle where the melt fraction is smaller than 20%. Hence, if this melt fraction is concentrated at the core mantle boundary, the molten layer is thin enough to avoid its convection, while if the liquid is equally distributed within the mantle, we can reasonably assume that the bulk viscosity is weakly affected by the liquid phase and close to the viscosity of subsolidus silicate material. Still, the presence of melt may affect mantle properties. An important parameter is the fate of melts, which is primarily controlled by the solid-melt density contrast. The molten material can either be evacuated at the surface during early volcanism or cumulate at the lowermost mantle. For peridotites, negative melt buoyancy is unlikely to happen at pressures lower than 7 GPa (Sakamaki et al., 2006; Matsukage et al., 2005; Freitas et al., 2017). However, the buoyancy of melts generated from the partial melting of a body with composition largely different from peridotite remains uncertain. Molten reservoirs may be trapped at shallow depths at the end of mushy mantle cooling (Monteux et al., 2020) or during the last stages of fractional crystallization within small bodies (e.g. Frossard et al., 2019). On a Moon-like body, a melt layer may be trapped below an anorthositic crust while on a Mercury-like body, anorthite is denser than the melt and then may not float allowing the melt to form a late shallow magma ocean. We consider here that the melt has neutral buoyancy and is equally distributed within the planetary mantle, with the consequence that the mantle viscosity is primarily controlled by the solid fraction of the mantle.

Due to the lower thermal conductivity of the melt compared to the solid mantle, the mushy mantle should limit the heat flow that can be

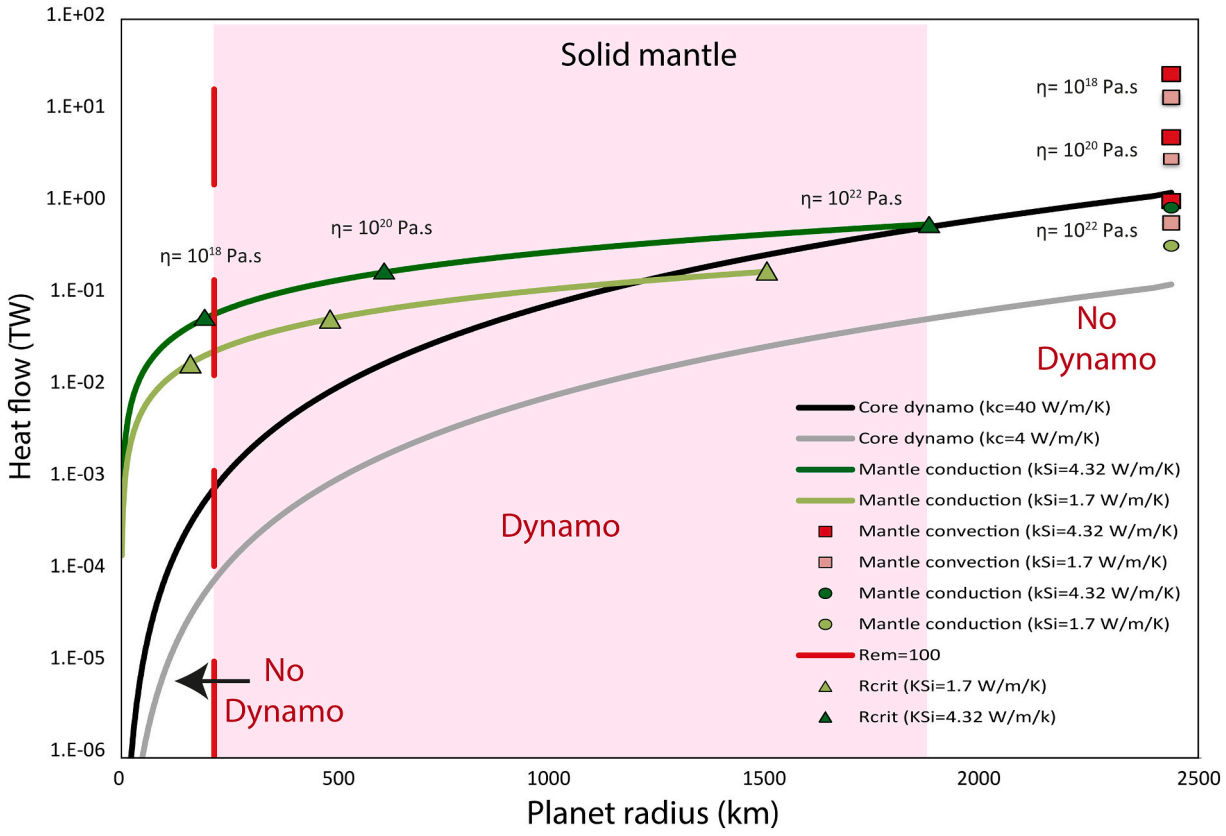

Fig. 11. Heat flows as a function of the planetary radius for a fully solid planetary mantle. The black and grey lines represent the critical heat flow needed for a thermally driven dynamo for k_c = 40 and 4 W/m/K, respectively (Conditions 1 and 2, Eq. (31)). The dark and light green lines represent the mantle heat flow in a conductive regime for κ_{Si} = 4.32 and 1.70 W/m/K, respectively (Eq. (35)). Green triangles represent the critical planet size at which Ra = Ra_c, therefore corresponding to the minimum heat flow at the CMB, for mantle viscosity ranging from 10^{18} to 10^{22} Pa.s. Extrapolated values at R = $R_{Mercury}$ = 2440 km are also represented with green circles for conductive heat transfers and red and pink squares for convective cases (Eq. (36)) with mantle viscosities indicated nearby. The red dashed line represents the critical value for Rem = 100 (Condition 3). At the left side of this line, a dynamo is unlikely. The likely zone for a planet radius capable of powering a dynamo is represented by the pink shaded area in case κ_{Si} = 4.32 W/m/K and κ_{core} = 40 W/m/K. (For interpretation of the references to colour in this figure legend, the reader is referred to the web version of this article.)

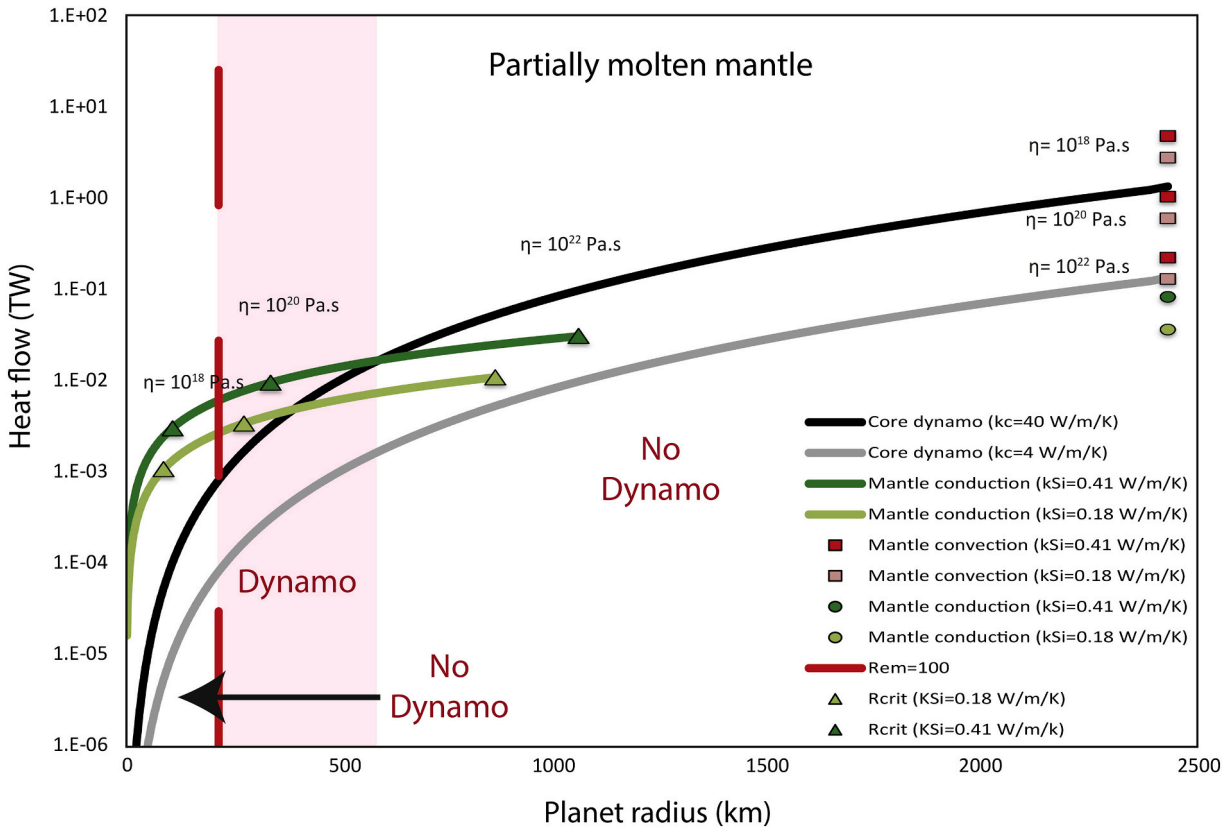

Fig. 12. Heat flows as a function of the planetary radius for a stagnant partially molten planetary mantle. The black and grey lines represent the critical heat flow for a thermally driven dynamo for $k_c = 40$ and 4 W/m/K, respectively (Conditions 1 and 2, Eq. (31)). The dark and light green lines represent the mantle heat flow for $\kappa_{Si} = 0.41$ and 0.18 W/m/K, respectively (Eq. (35)). Green triangles represent the critical planet size at which $Ra = Ra_c$, for mantle viscosity ranging from 10^{18} to 10^{22} Pa.s. Extrapolated values at $R = R_{Mercury} = 2440$ km are also represented with green circles for conductive heat transfers and red and pink squares for convective cases (Eq. (36)) with viscosities indicated nearby. The red dashed line represents the critical value for $Rem = 100$ (Condition 3). At the left side of this line, a dynamo is unlikely. The likely zone for a planet radius capable of powering a dynamo is represented by the pink shaded area in case $\kappa_{Si} = 0.41$ W/m/K and $\kappa_{core} = 40$ W/m/K. (For interpretation of the references to colour in this figure legend, the reader is referred to the web version of this article.)

extracted from the core. In our calculation, we consider for simplicity that the entire mantle has the same conductivity as the melt. As a result, the range of planetary radii for which a dynamo is plausible is much narrower than for a fully solid mantle (Fig. 12). For a core conductivity of 40 W/m/K, a thermally driven dynamo can only operate for planetary sizes ranging between 215 and 350–570 km, depending on the value of κ_{Si} and for $\kappa_{core} = 40$ W/m/K. The maximum planetary radius becomes 1000–1500 km for a core conductivity of 4 W/m/K. Therefore, the melting of a Mercury-like planetary mantle could limit the establishment of a magnetic field on the planet. This effect could last over different timescales, depending on the size of the planet and of the core, the initial core temperature, the fate of the melt material, etc.

The differences obtained for fully solid (Fig. 11) and molten (Fig. 12) models show that the presence of melt within a "Mercury-like" planet mantle could result into better thermal insulation of the core, which may prevent the occurrence of a thermally driven dynamo. Of course, planets presenting mantle with supercritical Rayleigh number would not be affected by this effect, because mantle convection could extract enough heat from the core at the CMB. As a consequence, the solid mantle viscosity plays a key role because (1) it controls the planet size above which mantle convection is likely, through the Ra value, and (2) it governs the efficiency of mantle heat evacuation once the critical Rayleigh number is overcome (see Eq. (36)). Decreasing the mantle viscosity from 10^{22} to 10^{18} Pa.s decreases the critical planet size for mantle convection by one order of magnitude (from 1600 to 1900 km to 160–200 km for a solid mantle and from 850 to 1050 km to 80–110 km for a mushy mantle, see Figs. 11 and 12). The figures also show that the lower is mantle viscosity, the easier the planet can meet the criteria for a thermally driven dynamo when the mantle of the planet is convecting. We note here that considering the influence of melt on the bulk mantle viscosity should lead to a decrease of the critical Rayleigh number and as a consequence of the critical planetary size where heat in only evacuated by thermal conduction (i.e. green triangles would move to the left). However, this effect should be negligible for the small melt fraction considered here.

The impact of mantle partial melting crucially depends on the melt quantity and its location within the mantle. Whether it is distributed in a mushy mantle or accumulated as a pond at a given mantle depth affects both, locally and globally, the mantle viscosity and the thermal diffusivity. As a consequence, the dynamic regime can evolve from conduction to convection, changing the thermal outputs at the CMB and making the heat flux enough, or insufficient, to power a thermally-driven dynamo. In this framework, transient phenomena such as mantle overturns (Elkins-Tanton et al., 2003; Ballmer et al., 2017) implying major melt migration will result in a brutal change in the planet magnetic signature. Similarly, the chemical stratification resulting in the production of a crust (anorthositic, basaltic etc.) may help insulating the planet interior in its early history suggesting weaker but longer sustained dynamos.

6. Conclusions

In this study, we constrain the thermal diffusivities of silicate melts with a wide range of composition at high pressure and temperature conditions using the multi-anvil apparatus and the Angström method. We observed that melting induces a significant decrease in both thermal diffusivities and conductivities. We measure melt thermal diffusivities ranging from 0.18 (±0.02) W/m/k to 0.41 (±0.04) W/m/K. The

composition of the melt does not have a significant impact on diffusivities. We then use our results to address the thermal properties of the molten silicate reservoirs, and the likeliness of a thermally driven dynamo within a Mercury-like planets presenting a large metallic core and a relatively thin silicate mantle (large Rc/Rplanet). The mantle of such bodies is not expected to be convecting easily ($Ra < Ra_c$) leading to an inefficient heat evacuation and difficulty generating a dynamo compared to planets with a thicker mantle (where easily $Ra > Ra_c$). Our results illustrate that the presence of a mushy mantle above the CMB in such a Mercury-like planet can significantly reduce the ability of the mantle to evacuate the heat from the core and limit the likeliness of a thermally-driven dynamo. As a consequence, the fate and the lifetime of such a mushy reservoir can have a profound impact on the thermal history of Mercury-like planets. Future observations of Mercury-like planets accreted in orbits close to their star and the eventual detection of their intrinsic magnetic field would in return constrain the state of the mantle surrounding their metallic core.

Author contributions

Conceptualization: DF and GM. **Data curation:** DF, FS, JM, DA and GM. **Resources & Software:** AM, NC, GM, DA and DF. **Writing - original draft:** DF, JM and DA. **Writing - review & editing:** DF, JM, DA, GM and FS. **Funding acquisition:** GM, DA and DF.

Declaration of Competing Interest

The authors declare that they have no known competing financial interests or personal relationships that could have appeared to influence the work reported in this paper.

Acknowledgments

We acknowledge D. Laporte, A. Gourgeau, O. Sigmarsson, J-L. Froger and S. Jouhannel for providing the natural samples used in this study, F. Pointud, C. Guillot and J.L. Fruquière for their technical assistance with high pressure apparatus and sample/assembly preparation, J-M Henot and E. Voyer for the SEM analyses, J-L Devidal for the electron microprobe analyses, C. Fonquernie for flash analyses and M. Benbakkar for ICP-AES measurements. This is Laboratory of Excellence ClerVolc contribution number 452.

Appendix A. Supplementary data

Supplementary data to this article can be found online at https://doi.org/10.1016/j.pepi.2021.106655.

References

Acuna, M.H., Connerney, J.E.P., Lin, R.P., Mitchell, D., Carlson, C.W., McFadden, J., et al., 1999. Global distribution of crustal magnetization discovered by the Mars global surveyor MAG/ER experiment. Science 284 (5415), 790–793.

Anderson, B.J., Johnson, C.L., Korth, H., Purucker, M.E., Winslow, R.M., Slavin, J.A., et al., 2011. The global magnetic field of mercury from MESSENGER orbital observations. Science 333 (6051), 1859–1862. https://doi.org/10.1126/science.1211001.

Anzellini, S., Dewaele, A., Mezouar, M., Loubeyre, P., Morard, G., 2013. Melting of iron at Earth's inner core boundary based on fast X-ray diffraction. Science 340, 464–466.

Asphaug, E., Reufer, A., 2014. Mercury and other iron-rich planetary bodies as relics of inefficient accretion. Nat. Geosci. 7 (8), 564–568. https://doi.org/10.1038/ngeo2189.

Ballmer, M.D., Lourenco, D.L., Hirose, K., Caracas, R., Nomura, R., 2017. Reconciling magma-ocean crystallization models with the present-day structure of the Earth's mantle. Geochem. Geophys. Geosyst. 18 (7), 2785–2806. https://doi.org/10.1002/2017gc006917.

Barrat, J.A., Gillet, P.H., Lesourd, M., Blicher-Toft, J., Poupeau, G.R., 1999. The Tatahouine diogenite: mineralogical and chemical effects of sixty-three years of terrestrial residence. Meteorit. Planet. Sci. 34, 91–97.

Beck, A.E., Darbha, D.M., Schloessin, H.H., 1978. Lattice conductivities of single-crystal and polycrystalline materials at mantle pressures and temperatures. Phys. Earth Planet. Inter. 17 (1), 35–53. https://doi.org/10.1016/0031-9201(78)90008-0.

Benz, W., Slattery, W.L., Cameron, A.G.W., 1988. Collisional stripping of Mercury's mantle. Icarus 74 (3), 516–528. https://doi.org/10.1016/0019-1035(88)90118-2.

Bolfan-Casanova, N., Montagnac, G., Reynard, B., 2014. Measurement of water contents in olivine using Raman spectroscopy. Am. Mineral. 99, 149–156. https://doi.org/10.2138/am.2014.4444.

Boujibar, A., Andrault, D., Ali, M., Bolfan-casanova, N., Devidal, J., Trcera, N., 2014. Metal – silicate partitioning of sulphur , new experimental and thermodynamic constraints on planetary accretion. Earth Planet. Sci. Lett. 391, 42–54. https://doi.org/10.1016/j.epsl.2014.01.021.

Boujibar, A., Andrault, D., Bolfan-Casanova, N., Bouhifd, M.A., Monteux, J., 2015. Cosmochemical fractionation by collisional erosion during the Earth's accretion. Nat. Commun. 6, 1–7. https://doi.org/10.1038/ncomms9295.

Branlund, J.M., Hofmeister, A.M., 2012. Heat transfer in plagioclase feldspars. Am. Mineral. 97, 1145–1154.

Breuer, D., Hauck, S.A., Buske, M., Pauer, M., Spohn, T., 2007. Interior evolution of mercury. Space Sci. Rev. 132, 229–260.

Breuer, D., Rueckriemen, T., Spohn, T., 2015. Iron snow, crystal floats, and inner-core growth: modes of core solidification and implications for dynamos in terrestrial planets and moons. Progr. Earth Planet. Sci. 2 (1), 39. https://doi.org/10.1186/s40645-015-0069-y.

Buffett, B.A., 2002. Estimates of heat flow in the deep mantle based on the power requirements for the geodynamo. Geophys. Res. Lett. 29 (12), 1–4.

Busek, P.R., 1997. Pallasite meteorites-mineralogy, petrology and geochemistry. Geochim. Cosmochim. Acta 41, 711–740.

Carslaw, H.S., Jaeger, J.C., 1959. Heat conduction in solids. Oxford Univ. Press.

Charlier, B., Namur, O., 2019. The origin and differentiation of planet mercury. Elements 15 (1), 9–14. https://doi.org/10.2138/gselements.15.1.9.

Christensen, U.R., Aubert, J., 2006. Scaling properties of convection-driven dynamos in rotating spherical shells and application to planetary magnetic fields. Geophys. J. Int. 166 (1), 97–114. https://doi.org/10.1111/j.1365-246X.2006.03009.x.

Deng, L., Seagle, C., Fei, Y., Shahar, A., 2013. High pressure and temperature electrical resistivity of iron and implications for planetary cores. Geophys. Res. Lett. 40, 33–37. https://doi.org/10.1029/2012GL054347.

Ebel, D.S., Grossman, L., 2000. Condens. Dust-Enrich. Syst. 64 (2), 339–366.

Elkins-Tanton, L.T., Parmentier, E.M., Hess, P.C., 2003. Magma Ocean fractional crystallization and cumulate overturn in terrestrial planets: implications for Mars. Meteorit. Planet. Sci. 38 (12), 1753–1771. https://doi.org/10.1111/j.1945-5100.2003.tb00013.x.

Fegley, B., Cameron, A.G.W., 1987. A vaporization model for iron/silicate fractionation in the mercury protoplanet. Earth Planet. Sci. Lett. 82 (3–4), 207–222. https://doi.org/10.1016/0012-821X(87)90196-8.

Floran, R.J., Prinz, M., Hlava, P.F., Keil, K., Nehru, C.E., Hinthorne, J.R., 1978. The Chassigny meteorite: a cumulate dunite with hydrous amphibole-bearing melt inclusions. Geochem. Comsochim. Acta 42 (8), 1213–1219. https://doi.org/10.1016/0016-7037(78)90115-1.

Freitas, D., Manthilake, G., 2019. Electrical Conductivity of Hydrous Silicate Melts : Implications for the Bottom-Up Hydration of Earth ' S Upper Mantle EPSL 523, 1–9. https://doi.org/10.1016/j.epsl.2019.115712.

Freitas, D., Manthilake, G., Schiavi, F., Chantel, J., Bolfan-Casanova, N., Bouhifd, M.A., Andrault, D., 2017. Experimental evidence supporting a global melt layer at the base of the Earth's upper mantle. Nat. Commun. 8, 2186. https://doi.org/10.1038/s41467-017-02275-9.

Freitas, D., Manthilake, G., Chantel, J., Bouhfid, M., Andrault, D., 2019. Simultaneous measurements of electrical conductivity and seismic velocity of partially molten geological materials: implications for melt fraction in the upper mantle. Phys. Chem. Miner. https://doi.org/10.1007/s00269-019-01021-5, 0, 0.

Frossard, P., Boyet, M., Bouvier, A., Hammouda, T., Monteux, J., 2019. Evidence for anorthositic crust formed on an inner solar system planetesimal. Geochem. Perspect. Lett. 11, 28–32. https://doi.org/10.7185/geochemlet.1921.

Fujisawa, H., Fujii, N., Mizutani, H., Kanmori, H., Akimoto, S., 1968. Thermal diffusivity of Mg2SiO4, Fe2SiO4, and NaCl at high pressures and temperatures. J. Geophys. Res. 73, 4727.

Garrick-Bethell, I., Weiss, B.P., Shuster, D.L., Buz, J., 2009. Early lunar magnetism. Science 323 (5912), 356–359. https://doi.org/10.1126/science.1166804.

Genova, A., Goossens, S., Mazarico, E., Lemoine, F.G., Neumann, G.A., Kuang, W., et al., 2018. Geodetic Evidence that Mercury Has a Solid Inner Core, 1–13. https://doi.org/10.1029/2018GL081135.

Gibert, B., Schilling, F.R., Gratz, K., Tommasi, A., 2005. Thermal diffusivity of olivine single crystals and a dunite at high temperature: Evidence for heat transfer by radiation in the upper mantle. Phys. Earth. Planet. Inter. 151, 129–141. https://doi.org/10.1016/j.pepi.2005.02.003.

Giordano, D., Nichols, A.R.L., Dingwell, D.B., 2005. Glass transition temperatures of natural hydrous melts: A relationship with shear viscosity and implications for the welding process. J. Volcanol. Geotherm. Res. 142 (1–2 SPEC ISS), 105–118. https://doi.org/10.1016/j.jvolgeores.2004.10.015.

Grant, F.S., West, G.F., 1965. Interpretation Theory in Applied Geophysics. McGraw-Hill Book Co., NY, p. 583.

Hauck, S.A., Margot, J.L., Solomon, S.C., Phillips, R.J., Johnson, C.L., Lemoine, F.G., et al., 2013. The curious case of Mercury's internal structure. J. Geophys. Res. E: Planets 118 (6), 1204–1220. https://doi.org/10.1002/jgre.20091.

Hernlund, J., Leinenweber, K., Locke, D., Tyburczy, J.A., 2006. A numerical model for steady-state temperature distributions in solid-medium high-pressure cell assemblies. Am. Mineral. 91 (2–3), 295–305. https://doi.org/10.2138/am.2006.1938.

Hofmeister, A.M., Branlund, J.M., 2015. Thermal conductivity of the earth. In: Treatise on Geophysics: Second Edition (Vol. 2). Elsevier B.V. https://doi.org/10.1016/B978-0-444-53802-4.00047-6.
Hofmeister, A.M., Pertermann, M., 2008. Thermal diffusivity of clinopyroxenes at elevated temperature. Eur. J. Mineral. 20, 537–549.
Hofmeister, Anne M., Whittington, A.G., Pertermann, M., 2009. Transport properties of high albite crystals, near-endmember feldspar and pyroxene glasses, and their melts to high temperature. Contrib. Mineral. Petrol. 158 (3), 381–400. https://doi.org/10.1007/s00410-009-0388-3.
Hofmeister, A.M., Branlund, J.M., Pertermann, M., 2007. Properties of rocks and minerals - thermal conductivity of the earth. Treatise Geophys. 2, 543–577. https://doi.org/10.1016/B978-044452748-6.00048-1.
Hofmeister, Anne M., Sehlke, A., Whittington, A.G., 2014. Thermal diffusivity of Fe-rich pyroxene glasses and their melts. Chem. Geol. 384, 1–9. https://doi.org/10.1016/j.chemgeo.2014.06.018.
Hood, L.L., Harrison, K.P., Langlais, B., Lillis, R.J., Poulet, F., Williams, D.A., 2010. Magnetic anomalies near Apollinaris Patera and the Medusae fossae formation in Lucus Planum, Mars. Icarus 208 (1), 118–131. https://doi.org/10.1016/j.icarus.2010.01.009.
Johnson, C.L., Phillips, R.J., Purucker, M.E., Anderson, B.J., Byrne, P.K., Denevi, B.W., et al., 2015. Low-altitude magnetic fieldmeasurements by MESSENGER reveal Mercury's ancient crustal field. Science 348 (6237), 892–895. https://doi.org/10.1126/science.aaa8720.
Johnson, Catherine L., Phillips, R.J., 2005. Evolution of the Tharsis region of Mars: insights from magnetic field observations. Earth Planet. Sci. Lett. 230 (3–4), 241–254. https://doi.org/10.1016/j.epsl.2004.10.038.
Kabin, K., Heimpel, M.H., Rankin, R., Aurnou, J.M., Gómez-Pérez, N., Paral, J., et al., 2008. Global MHD modeling of Mercury's magnetosphere with applications to the MESSENGER mission and dynamo theory. Icarus 195 (1), 1–15. https://doi.org/10.1016/j.icarus.2007.11.028.
Kanamori, H., Mizutani, H., Fujii, N., 1969. Method of thermal diffusivity measurement. J. Phys. Earth. 17, 43–53.
Katsura, T., 1993. Thermal diffusivity of silica glass at pressures up to 9 GPa. Phys. Chem. Miner. 20 (3), 201–208. https://doi.org/10.1007/BF00200122.
Keil, K., 2010. Enstatite achondrite meteorites (aubrites) and the histories of their asteroidal parent bodies. Chem. Erde 70 (4), 295–317. https://doi.org/10.1016/j.chemer.2010.02.002.
Laporte, D., Provost, A., 2000. Equilibrium geometry of a fluid phase in a polycrystalline aggregate with anisotropic surface energies: dry grain boundaries. J. Geophys. Res. Solid Earth 105, 25937–25953. https://doi.org/10.1029/2000jb900256.
Laporte, D., Rapaille, C., Provost, A., 1997. Wetting angles, equilibrium melt geometry, and the permeability threshold of partially molten crustal protoliths BT. In: Bouchez, J.L., Hutton, D.H.W., Stephens, W.E. (Eds.), Granite: From Segregation of Melt to Emplacement Fabrics. Springer Netherlands, Dordrecht, pp. 31–54.
Lawrence, K., Johnson, C., Tauxe, L., Gee, J., 2008. Lunar paleointensity measurements: implications for lunar magnetic evolution. Phys. Earth Planet. Inter. 168 (1–2), 71–87.
Lillis, R.J., Frey, H.V., Manga, M., Mitchell, D.L., Lin, R.P., Acuña, M.H., Bougher, S.W., 2008. An improved crustal magnetic field map of Mars from electron reflectometry: Highland volcano magmatic history and the end of the martian dynamo. Icarus 194 (2), 575–596. https://doi.org/10.1016/j.icarus.2007.09.032.
Lillis, R.J., Robbins, S., Manga, M., Halekas, J.S., Frey, H.V., 2013. Time history of the Martian dynamo from crater magnetic field analysis. J. Geophys. Res. E: Planets 118 (7), 1488–1511. https://doi.org/10.1002/jgre.20105.
Malavergne, V., Toplis, M.J., Berthet, S., Jones, J., 2010. Highly reducing conditions during core formation on mercury: implications for internal structure and the origin of a magnetic field. Icarus 206 (1), 199–209. https://doi.org/10.1016/j.icarus.2009.09.001.
Manthilake, G., Chantel, J., Monteux, J., Andrault, D., Bouhifd, M.A., Casanova, N.B., Boulard, E., Guignot, N., King, A., Itie, J.P., 2019. Thermal conductivity of FeS and its implications for Mercury's long sustaining magnetic field. J. Geophys. Res. E Planets. https://doi.org/10.1029/2019JE005979.
Manthilake, G.M., De Koker, N., Frost, D.J., McCammon, C.A., 2011b. Lattice thermal conductivity of lower mantle minerals and heat flux from Earth's core. Proc. Natl. Acad. Sci. U. S. A. 108 (44), 17901–17904. https://doi.org/10.1073/pnas.1110594108.
Manthilake, M.A.G.M., De Koker, N., Frost, D.J., 2011a. Thermal conductivity of CaGeO3 perovskite at high pressure. Geophys. Res. Lett. 38 (8), 3–6. https://doi.org/10.1029/2011GL046882.
Matsukage, K.N., Jing, Z., Karato, S., 2005. Density of hydrous silicate melt at the conditions of Earth's deep upper mantle. Nature 438, 488–491. https://doi.org/10.1038/nature04241.
Maumus, J., Bagdassarov, N., Schmeling, H., 2005. Electrical conductivity and partial melting of mafic rocks under pressure. Geochim. Cosmochim. Acta 69, 4703–4718. https://doi.org/10.1016/j.gca.2005.05.010.
Médard, E., McCammon, C.A., Barr, J.A., Grove, T.L., 2008. Oxygen fugacity, temperature reproducibility, and H2O contents of nominally anhydrous piston-cylinder experiments using graphite capsules. Am. Mineral. 93 (11−12), 1838–1844. https://doi.org/10.2138/am.2008.2842.
Mibe, K., Fujii, T., Yasuda, A., 1998. Connectivity of aqueous fluid in the Earth's upper mantle. Geophys. Res. Lett. 25, 1233–1236.
Mibe, K., Fujii, T., Yasuda, A., 1999. Control of the location of the volcanic front in island arcs by aqueous fluid connectivity in the mantle wedge. Nature 401, 259–262. https://doi.org/10.1038/45762.
Mighani, S., Wang, H., Shuster, D.L., Borlina, C.S., Nichols, C.I.O., Weiss, B.P., 2020. The end of the lunar dynamo. Science 1–8.
Minarik, W.G., Watson, E.B., 1995. Interconnectivity of carbonate melt at low melt fraction. Earth Planet. Sci. Lett. 133 (3–4), 423–437. https://doi.org/10.1016/0012-821X(95)00085.
Monteux, J., Arkani-Hamed, J., 2014. Consequences of giant impacts in early Mars: Core merging and Martian dynamo evolution. J. Geophys. Res. 119, 480–505.
Monteux, J., Jellinek, A.M., Johnson, C.L., 2011. Why might planets and moons have early dynamos? Earth Planet. Sci. Lett. 310 (3–4), 349–359. https://doi.org/10.1016/j.epsl.2011.08.014.
Monteux, J., Andrault, D., Samuel, H., 2016. On the cooling of a deep terrestrial magma ocean. Earth Planet. Sci. Lett. 448, 140–149. https://doi.org/10.1016/j.epsl.2016.05.010.
Monteux, J., Andrault, D., Guitreau, M., Samuel, H., Demouchy, S., 2020. A mushy Earth's mantle for more than 500 Myr after the magma ocean solidification. Geophys. J. Int. https://doi.org/10.1093/gji/ggaa064.
Namur, O., Collinet, M., Charlier, B., Grove, T.L., Holtz, F., McCammon, C., 2016. Melting processes and mantle sources of lavas on mercury. Earth Planet. Sci. Lett. 439, 117–128. https://doi.org/10.1016/j.epsl.2016.01.030.
Neuville, D.R., Courtial, P., Dingwell, D.B., Richet, P., 1993. Thermodynamic and rheological properties of silicate melts. Contrib. Mineral. Petrol. 113, 572–581.
Ni, H., Keppler, H., Behrens, H., 2011. Electrical conductivity of hydrous basaltic melts: implications for partial melting in the upper mantle. Contrib. Mineral. Petrol. 162 (3), 637–650. https://doi.org/10.1007/s00410-011-0617-4.
Ni, H., Hui, H., Steinle-Neumann, G., 2015. Transport properties of silicate melts. Rev. Geophys. 53, 715–744. https://doi.org/10.1002/2015RG000485.
Nimmo, F., 2002. Why does Venus lack a magnetic field? Geology 30 (11), 987–990. https://doi.org/10.1130/0091-7613(2002)030<0987:WDVLAM>2.0.CO;2.
O'Rourke, J.G., Buz, J., Fu, R.R., Lillis, R.J., 2019. Detectability of Remanent magnetism in the crust of Venus. Geophys. Res. Lett. 46 (11), 5768–5777. https://doi.org/10.1029/2019GL082725.
Osako, M., Ito, E., Yoneda, A., 2004. Simultaneous measurements of thermal conductivity and thermal diffusivity for garnet and olivine under high pressure. Phys. Earth Planet. Inter. 143, 311–320. https://doi.org/10.1016/j.pepi.2003.10.
Pertermann, M., Hofmeister, A.M., 2006. Thermal diffusivity of olivine-group minerals at high temperature. Am. Mineral. 91, 1747–1760.
Picard, D., Arbaret, L., Pichavant, M., Champallier, R., Launeau, P., 2013. The rheological transition in plagioclase-bearing magmas. J. Geophys. Res. Solid Earth 118 (4), 1363–1377.
Pommier, A., Leinenweber, K., Tran, T., 2019. Mercury ' s thermal evolution controlled by an insulating liquid outermost core ? Earth Planet. Sci. Lett. 517, 125–134. https://doi.org/10.1016/j.epsl.2019.04.022.
Romine, W.L., Whittington, A.G., Nabelek, P.I., Hofmeister, A.M., 2012. Thermal diffusivity of rhyolitic glasses and melts: effects of temperature, crystals and dissolved water. Bull. Volcanol. 74 (10), 2273–2287. https://doi.org/10.1007/s00445-012-0661-6.
Sakamaki, T., Suzuki, A., Ohtani, E., 2006. Stability of hydrous melt at the base of the Earth's upper mantle. Nature 439 (7073), 192–194. https://doi.org/10.1038/nature04352.
Sambridge, M., Mosegaard, K., 2002. Monte Carlo methods in geophysical inverse problems. Rev. Geophys. 40 (3), 1–3.
Schiavi, F., Bolfan-Casanova, N., Withers, A.C., Médard, E., Laumonier, M., Laporte, D., et al., 2018. Water quantification in silicate glasses by Raman spectroscopy: correcting for the effects of confocality, density and ferric iron. Chem. Geol. 483 (February), 312–331. https://doi.org/10.1016/j.chemgeo.2018.02.036.
Schmeling, H., 1986. Numerical models on the influence of partial Melton elastic, anelastic and electrical properties of rocks. Part II: electrical conductivity. Phys. Earth Planet. Inter. 43 (2), 123–136. https://doi.org/10.1016/0031-9201(86)90080-4.
Shea, T., Houghton, B.F., Gurioli, L., Cashman, K.V., Hammer, J.E., Hobden, B.J., 2010. Textural studies of vesicles in volcanic rocks: an integrated methodology. J. Volcanol. Geotherm. Res. 190 (3–4), 271–289. https://doi.org/10.1016/j.jvolgeores.2009.12.003.
Smith, D.S., Fayette, S., Grandjean, S., Martin, C., Telle, R., Tonnessen, T., 2003. Thermal resistance of grain boundaries in alumina ceramics and refractories. J. Am. Ceram. Soc. 86 (1), 105–111. https://doi.org/10.1111/j.1151-2916.2003.tb03285.x.
Silber, R.E., Secco, R.A., Yong, W.J., Littleton, J.A.H., 2019. Heat Flow in Earth's Core From Invariant Electrical Resistivity of Fe-Sion the Melting Boundary to 9 GPa: Do Light Elements Matter? J. Geophys. Res.: Solid Earth 124 (6), 5521–5543. https://doi.org/10.1029/2019jb017375.
Smith, D.S., Alzina, A., Bourret, J., Nait-Ali, B., Pennec, F., Tessier-Doyen, N., Otsu, K., Matsubara, H., Elser, P., Gonzenbach, U.T., 2013. Thermal conductivity of porous materials. J. Mater. Res. 28 (17).
Solomatov, V., 2007. Magma oceans and primordial mantle differentiation. In: Schubert, G. (Ed.), Treatise of Geophysics, 9. Elsevier.
Stevenson, D.J., Spohn, T., Schubert, G., 1983. Magnetism and thermal evolution of the terrestrial planets. Icarus 54 (3), 466–489. https://doi.org/10.1016/0019-1035(83)90241-5.
Strom, R.G., Sprague, A.L., 2003. Exploring Mercury: The Iron Planet. Springer Science & Business Media.
Tarduno, J.A., Cottrell, R.D., Watkeys, M.K., Hofmann, A., Doubrovine, P.V., Mamajek, E.E., Liu, D., Sibeck, D.G., Neukirch, L.P., Usui, Y., 2010. Geodynamo, solar wind, and magnetopause 3.4 to 3.45 billion years ago. Science 327 (5970), 1238–1240.
ten Grotenhuis, S.M., Drury, M.R., Spiers, C.J., Peach, C.J., 2005. Melt distribution in olivine rocks based on electrical conductivity measurements. J. Geophys. Res. Solid Earth 110, 1–11. https://doi.org/10.1029/2004JB003462.

Tian, Z., Zuber, M.T., Stanley, S., 2015. Magnetic field modeling for mercury using dynamo models with a stable layer and laterally variable heat flux. Icarus 260, 263–268. https://doi.org/10.1016/j.icarus.2015.07.019.

Tikoo, S.M., Weiss, B.P., Cassata, W.S., Shuster, D.L., Gattacceca, J.Ô., Lima, E.A., et al., 2014. Decline of the lunar core dynamo. Earth Planet. Sci. Lett. 404, 89–97. https://doi.org/10.1016/j.epsl.2014.07.010.

Tyburczy, J.A., Waff, H.S., 1983. Electrical conductivity of molten basalt and andesite to 25 kilobars pressures: geophysical significance and implications for charge transport and melt structure. J. Geophys. Res. 88 (2), 2413–2430.

Von Bargen, N., Waff, H.S., 1986. Permeabilities, interfacial areas and curvatures of partially molten systems: results of numerical computations of equilibrium microstructures. J. Geophys. Res. 91, 9261–9276.

Waff, H.S., 1974. Theoretical consideration of electrical conductivity in a partially molten mantle and implications for geothermometry. J. Geophys. Res. 79 (26), 4003–4010.

Watanabe, T., Kurita, K., 1993. The relationship between electrical conductivity and melt fraction in a partially molten simple system: Archie's law behavior. Phys. Earth Planet. Inter. 78 (1–2), 9–17.

Watson, E.B., Brenan, J.M., Baker, D.R., 1991. Continental Mantle. Oxford Univeristy Press.

Weidenschilling, S.J., 1978. Iron/silicate fractionation and the origin of mercury. Icarus 35 (1), 99–111. https://doi.org/10.1016/0019-1035(78)90064-7.

Weiss, B.P., Berdal, James S., Elkins-Tanton, L., Stanley, S., Lima, E.A., Carporzen, L., 2008. Magnetism on the Angrite differentiation of Planetesimals. Sci. Rep. 322 (October), 713–716.

Wurm, G., Trieloff, M., Rauer, H., 2013. Photophoretic separation of metals and silicates: the formation of mercury-like planets and metal depletion in chondrites. Astrophys. J. 769 (1) https://doi.org/10.1088/0004-637X/769/1/78.

Xu, Y., Shankland, T.J., Linhardt, S., Rubie, D.C., Langenhorst, F., Klasinski, K., 2004. Thermal diffusivity and conductivity of olivine, wadsleyite and ringwoodite to 20 GPa and 1373 K. Phys. Earth Planet. Inter. 143 (1–2), 321–336. https://doi.org/10.1016/j.pepi.2004.03.005.

Yoshino, T., Takei, Y., Wark, D.A., Watson, E.B., 2005. Grain boundary wetness of texturally equilibrated rocks, with implications for seismic properties of the upper mantle. J. Geophys. Res. B Solid Earth 110 (8), 1–16. https://doi.org/10.1029/2004JB003544.

Yoshino, T., Nishihara, Y., Karato, S.I., 2007. Complete wetting of olivine grain boundaries by a hydrous melt near the mantle transition zone. Earth Planet. Sci. Lett. 256, 466–472. https://doi.org/10.1016/j.epsl.2007.02.002.

Zhang, B., Ge, J., Xiong, Z., Zhai, S., 2019. Effect of water on the thermal properties of olivine with implications for lunar internal temperature. J. Geo. Res. Planets 124 (12), 3469–3481. https://doi.org/10.1029/2019JE006194.

6 Dynamique de refroidissement du manteau primitif terrestre

Le manteau silicaté constitue l'essentiel du volume de la Terre (83%) et de sa masse (66%). Actuellement, son immense inertie thermique contrôle le lent refroidissement de la planète et maintient la tectonique des plaques depuis au moins 2 milliards d'années et peut-être dès le refroidissement de la surface, quelques centaines de millions d'années après la formation de la Terre, il y a 4.54 milliards d'années. Mais ce refroidissement n'a pas toujours été aussi lent et des épisodes de fusion globale associés à des dynamiques turbulentes ont pu avoir lieu tôt dans l'histoire du manteau terrestre. Les causes de la tectonique des plaques qui n'a été observée sur aucune des planètes et satellites du système solaire, restent encore largement mystérieuses et pourraient bien être le résultat d'une dynamique complexe initiée depuis la formation du système Terre-Lune. Cette section est largement inspirée du chapitre le l'encyclopédie ISTE qui sera publiée prochainement (Monteux and Andrault, in press).

6.1 Le manteau au stade océan magmatique

Durant les dernières étapes d'accrétion, le manteau terrestre a probablement subi plusieurs épisodes de fusion plus ou moins complète appelés "stade océan magmatique". En effet, la formation du noyau terrestre s'est déroulée très tôt dans son évolution (entre 30 et 50 Ma) (Kleine et al., 2002) ce qui nécessite un important taux de fusion pour accommoder une séparation fer/silicates rapide. De plus, les données géochimiques montrent qu'une croûte a pu se former très tôt (entre 30 et 200 Ma) comme on peut l'attendre à la surface d'un océan magmatique (Boyet and Carlson, 2005). S'il existe un consensus sur l'existence de ces épisodes d'océans magmatiques, de nombreuses incertitudes demeurent sur leur durée de vie, l'évolution de la fraction de matériel fondu au cours du refroidissement, le degré de fractionnement chimique lors de leur solidification ainsi que sur les couplages avec le noyau métallique sous-jacent.

6.1.1 Un système en convection vigoureuse

La dynamique d'un océan magmatique avec une épaisseur supérieure à 1000 km est extrêmement turbulente (Solomatov, 2007). Afin de quantifier la vigueur de la convection dans un réservoir impliquant potentiellement toute l'épaisseur du manteau, il est possible de calculer le nombre de Rayleigh qui est le rapport entre le temps caractéristique de transfert de chaleur par conduction et le temps caractéristique de transfert de chaleur par advection (voir Eq.2) Pour entrer en convection, un reservoir de fluide doit avoir un Ra supérieur à une valeur critique Ra_c. Pour le manteau terrestre, $Ra_c \approx 1000$. En dessous de cette valeur critique, le refroidissement a lieu uniquement par conduction alors que pour des $Ra > Ra_c$, le transfert de chaleur se fait par advection et conduction : la convection. Le nombre de Rayleigh est

estimé dans le manteau terrestre actuel à $10^6 - 10^8$ ce qui indique qu'il doit convecter. En considérant que l'océan magmatique concerne tout le manteau et que la viscosité d'un magma liquide est comprise enter 10^{-2} et 10^2 Pa.s, les nombres de Rayleigh obtenus sont compris enter 10^{20} et 10^{30} (Solomatov, 2007) ce qui indique que la convection est très vigoureuse dans cet environnement. Les tailles caractéristiques des écoulements sont ainsi d'autant plus petites avec de petits tourbillons infra-métriques. Afin de caractériser une telle dynamique, plusieurs approches peuvent être envisagées.

6.1.2 Modélisation d'un océan magmatique

Pour comprendre la dynamique de systèmes à très hauts nombres de Rayleigh, on peut utiliser des modèles analogiques en laboratoire impliquant un reservoir rempli de gaz (He ou SF_6 par exemple) chauffé par le bas et refroidi par le haut (Roche, 2020). Couplées à des modèles analytiques théoriques (Siggia, 1994), ces expériences permettent de contraindre le refroidissement d'un fluide très turbulent et notamment de proposer des relations entre le flux de chaleur observé en surface du réservoir (caractérisé par le nombre de Nusselt, Nu) et la vigueur de la convection (caractérisé par le nombre de Rayleigh, Ra). Différents régimes de convection peuvent ainsi être mis en évidence allant de turbulent (avec $Nu \propto Ra^{1/3}$) jusqu'à des régimes ultra-turbulents (avec $Nu \propto Ra^{2/7}$) dans lesquels se trouvent probablement les océans magmatiques (Solomatov, 2007). D'autres modèles analogiques permettent aussi de quantifier la stabilité d'une couche de cristaux dans un réservoir en convection laminaire et turbulente (Solomatov et al., 1993).

Une autre approche de modélisation est cette fois-ci numérique. Elle consiste à résoudre les équations de conservation de la quantité de mouvement, de la masse et de la chaleur par un code numérique. De nombreux modèles d'évolution uni-dimensionnels d'océan magmatiques ont été développés (Solomatov and Stevenson, 1993; Abe, 1997; Monteux et al., 2016a) et présentent les avantages suivants : (1) ils peuvent caractériser des échelles de temps courtes et leur résolution spatiale peut atteindre celle des longueurs caractéristiques d'un milieu en convection turbulente (2) les modèles 1D peuvent modéliser des contrastes de viscosité extrêmes tel que ceux existants entre fraction solide et liquide dans un océan magmatique (3) il est assez facile d'implémenter dans ces modèles des contraintes issues des données récentes de la pétrologie expérimentale tels que les courbes de fusion (solidus et liquidus) ou des paramètres dont la valeur pourrait changer en fonction de la profondeur comme la densité ou la viscosité. Cependant, si les modèles 1D calculent des profils de température moyens sur toute la profondeur du réservoir, ils ne peuvent pas caractériser d'hétérogénéités latérales de température ou de densité. Il est donc impossible pour ces modèles de suivre l'initiation de la convection solide qui peut se mettre en place avant même la fin de la cristallisation de l'océan magmatique ou encore de mettre en évidence des phases d'overturn engendrées par des gradients de densité ou de température ce qu'il est possible de faire avec des outils de modélisation numérique (2D ou 3D (Maurice et al., 2017)). De plus, les modèles 1D ne permettant pas de calculer le champ de vitesse, ils doivent donc faire des hypothèses fortes sur le calcul des épaisseurs des couches

limites qui se mettent en place dans les zones où la vitesse d'écoulement diminue fortement (au fond ou à la surface de l'océan magmatique ou à proximité des zones cristallisées et stables).

6.1.3 Profils adiabatiques

Dans un système tel que le manteau terrestre, la pression est hydrostatique et augmente avec la profondeur. Si ce milieu est à l'équilibre, la température augmente avec la pression et donc avec la profondeur en suivant un profil adiabatique (ou adiabat). Des hétérogénéités thermiques, liées par exemple au fait que le noyau soit très chaud, provoquent des instabilités dans ce système qui peuvent rendre le gradient de température supérieur au gradient adiabatique et se traduire par de la convection thermique. Quand cette convection est vigoureuse, le gradient de température est légèrement supérieur au gradient adiabatique. Afin d'estimer le profil de température dans un océan magmatique, il est donc possible de se baser sur le calcul du profil de température adiabatique en suivant la relation :

$$\frac{dT}{dP} = \frac{\alpha T}{\rho C_p} \tag{3}$$

avec T la température, P la pression, α le coefficient de dilatation thermique, C_p la capacité thermique et ρ la masse volumique dans le manteau. Ainsi, en faisant un hypothèse sur la température potentielle T_p qui est la température de l'adiabat à la surface de la Terre à $P = 0$, il est possible de calculer au premier ordre des profils de température dans le manteau (Figure 21). Actuellement les données pétrologiques permettent d'estimer que le manteau profond terrestre suit un adiabat avec une température potentielle d'environ 1600 K. Or ce profil de température était probablement bien plus élevé juste après l'impact géant qui a donné naissance au système Terre-Lune. Si l'on fait l'hypothèse que tout le manteau était fondu, la température potentielle caractéristique du manteau post-impact était donc nécessairement supérieure à 3000 K (Figure 21).

6.1.4 Dynamique de refroidissement du manteau au stade "océan magmatique"

Suite à un impact géant, l'augmentation de température a probablement permis de faire fondre l'intégralité du manteau terrestre. Après l'impact, le noyau était potentiellement très chaud alors que la surface de la Terre était à une température d'équilibre pouvant dépasser les 3000 K selon les caractéristiques de l'atmosphère primitive (Lebrun et al., 2013). Rapidement après cet impact géant, l'océan magmatique s'est donc mis à convecter afin d'évacuer sa chaleur interne par la surface de la Terre où la température était beaucoup plus faible alors que le noyau était quant à lui toujours chaud. Après un refroidissement rapide à partir de la surface, la température décroit brutalement et passe en dessous de la température du liquidus au niveau du contact avec l'atmosphère où une croûte très fine et très instable se forme comme cela se produit à la surface d'un lac de lave. Deux couches limites thermiques extrêmement fines se sont

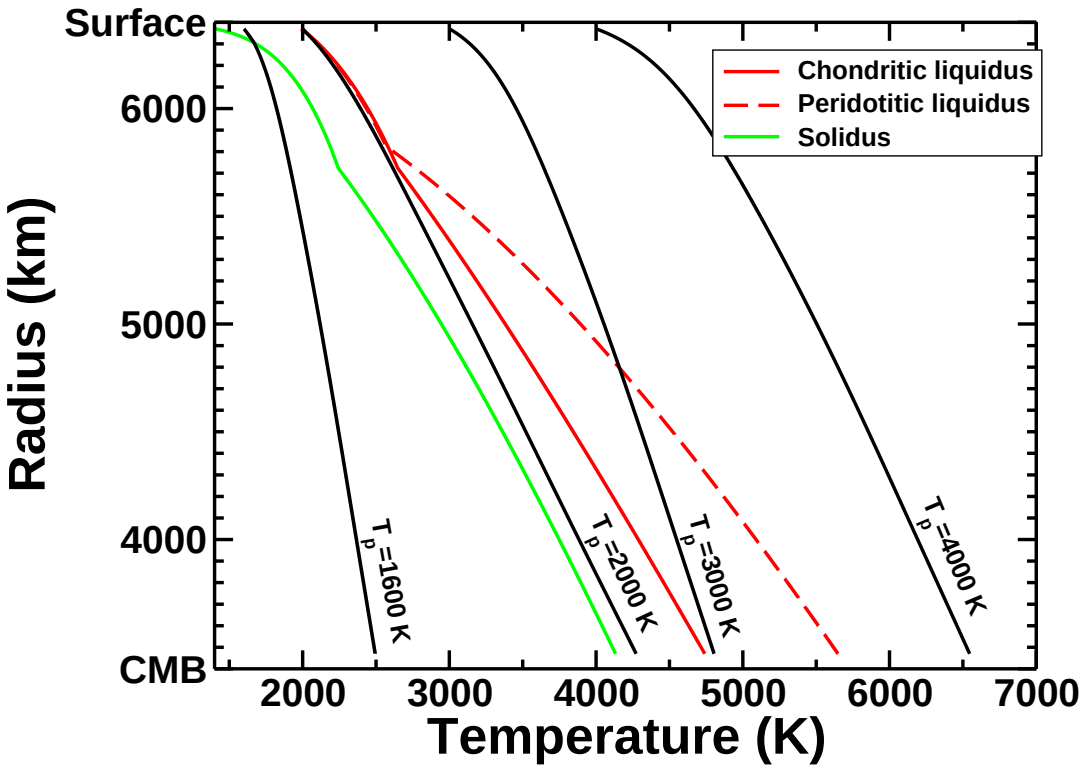

FIGURE 21 – *Profils de température adiabatiques à l'intérieur du manteau pour différentes température potentielles en surface. Le solidus et liquidus (chondritique et péridotitique) sont représentés respectivement en vert et rouge (à partir de Monteux et al. (2016a)).*

mises en place (1) à la base du manteau où s'opère une contraste entre du matériau silicaté et du matériau métallique (2) à la surface de l'océan magmatique à la frontière entre l'atmosphère et le manteau. Ces couches limites sont associées à une discontinuité du champ de vitesse et donc à un transfert de chaleur uniquement par conduction. Le profil de température à l'intérieur de l'océan magmatique s'est ajusté rapidement sur un profil adiabatique (Figure 22). Le refroidissement se traduit par un abaissement progressif de ce profil interne adiabatique avec une température potentielle de plus en plus faible.

Le manteau poursuit son refroidissement global jusqu'à que le profil de température croise le liquidus (Figure 22). Dans un modèle de manteau chondritique, ce croisement se produit au niveau de la frontière manteau noyau et la solidification de l'océan magmatique va donc s'établir du bas du manteau en direction de la surface (Monteux et al., 2016a). Cependant, si le croisement se fait au milieu du manteau, deux fronts de solidification peuvent se mettre en

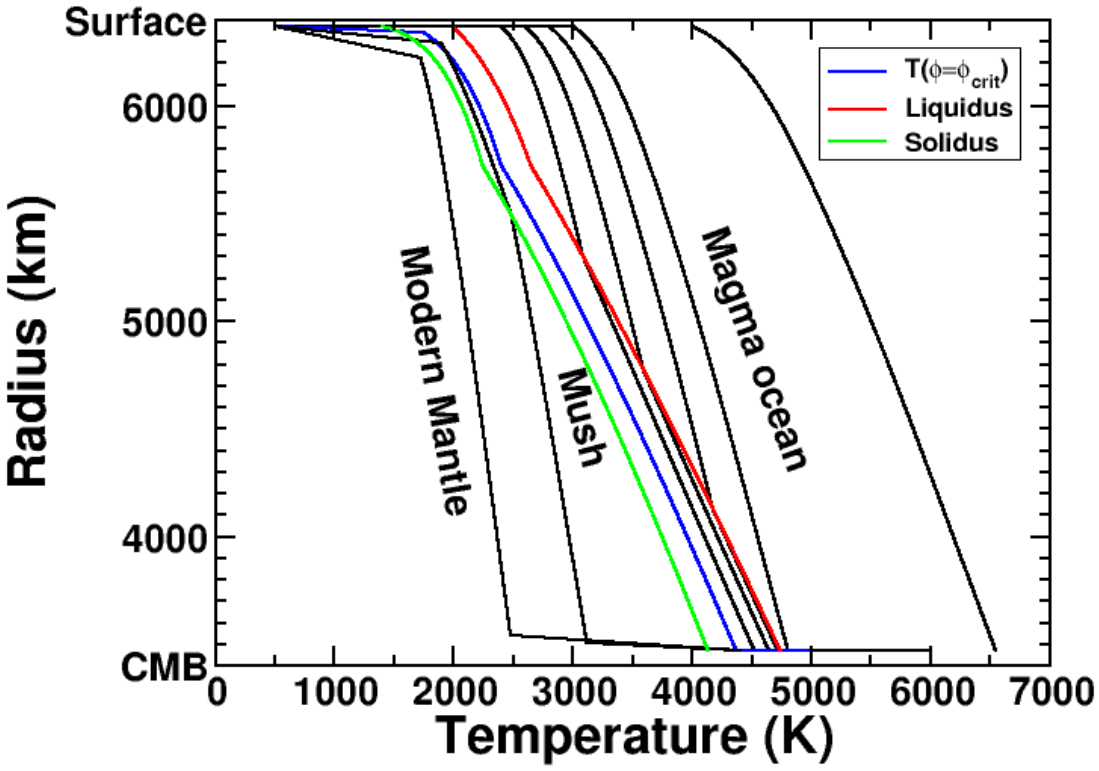

FIGURE 22 – *Évolution temporelle des profils de température à l'intérieur du manteau terrestre depuis une fusion globale (profil le plus à droite) jusqu'au profil actuel (le plus à gauche). Le solidus et liquidus chondritiques sont illustrés respectivement en vert et rouge . Le profil de température en bleu représente le profil à 40% de taux de fusion (i.e. 60% de cristaux). Arrivé à ce profil, le manteau passe du stade océan magmatique au stade mush qui est bien plus visqueux (à partir de Monteux et al. (2016a, 2020)).*

place : un front qui part du milieu du manteau vers la surface et un front qui part du milieu en direction de la frontière manteau-noyau. Dans ce cas-là, un océan magmatique peut se retrouver isolé à la base du manteau solide (Labrosse et al., 2007).

Le refroidissement de l'océan magmatique va subir un ralentissement brutal lorsque son profil de température va atteindre des valeurs correspondant à 40-50% de taux de fusion (i.e. un profil de température compris entre liquidus et solidus correspondant à 50-60% de cristallisation) (Figure 22). Ce ralentissement pourrait intervenir moins d'un million d'année après l'impact à l'origine du système Terre/Lune selon la viscosité du magma (Monteux et al., 2016a). À ce moment, la viscosité du matériel augmente fortement car les cristaux commencent à

interagir mécaniquement les uns avec les autres et à empêcher la déformation du fluide. Le mélange magma/minéraux appelé "mush" a un comportement rhéologique proche du comportement d'un solide. La fraction de matériel solide augmente jusqu'à ce qu'un seuil séparant le régime turbulent du régime visqueux à l'état solide soit atteint (Abe, 1997). Aussitôt que ce seuil est atteint, l'efficacité du refroidissement du manteau primitif devient limitée. Ceci a des conséquences importantes sur l'état thermique du manteau profond mais aussi sur la capacité de refroidissement du noyau et ainsi sur l'histoire magnétique de la Terre.

Une deuxième phase de refroidissement, beaucoup plus lente, va ainsi se mettre en place une fois que tout le manteau se trouve à environ 40% de taux de fusion. Durant cette phase, la viscosité de la phase solide devient critique car c'est elle qui va gouverner le taux de refroidissement mais aussi les profondeurs auxquelles vont se maintenir les dernières poches de fusion (Monteux et al., 2020).

6.2 Des océans magmatiques à la dynamique mantellique actuelle

Au cours du stade océan magmatique, le manteau terrestre primitif a subi un refroidissement global rapide jusqu'à ce que sa fraction fondue diminue jusqu'à une valeur critique ϕ_{crit} ($\sim 40\%$) associée à une augmentation importante de sa viscosité (Solomatov, 2000; Monteux and Arkani-Hamed, 2016). Cette étape a été suivie d'une étape de refroidissement lent qui a provoqué une cristallisation quasi complète du manteau silicaté (Solomatov, 2000). Cette deuxième étape de refroidissement aurait pu durer des centaines de Ma, voire quelques Ga car sa dynamique a été gouvernée par la rhéologie du manteau solide à déformation lente, contrairement à la première qui était gouvernée par la viscosité du magma (Solomatov, 2000; Ulvrová et al., 2012; Monteux et al., 2016a, 2020).

La profondeur à laquelle la cristallisation complète est atteinte est probablement régie par (1) la température de solidus qui contrôle la profondeur et la température de solidification, (2) l'épaisseur de la couche limite thermique supérieure où la chaleur convective du manteau profond est transférée à la surface par conduction, (3) le contraste de température des deux côtés de la couche limite thermiques qui contrôle l'efficacité de l'évacuation de la chaleur et (4) l'atmosphère primitive qui pourrait ralentir le refroidissement du manteau (Lebrun et al., 2013; Salvador et al., 2017). Dans le régime partiellement fondu, la viscosité du manteau solide est un paramètre clé, qui régit la dynamique du manteau et la formation des couches limites thermiques. Aujourd'hui, la viscosité du manteau terrestre est difficile à contraindre, en particulier dans le manteau inférieur (Cížková et al., 2012) et la valeur de la viscosité du manteau terrestre avant l'apparition d'événements majeurs de différenciation est encore plus hypothétique. Contraindre la valeur de cette grandeur physique est de première importance, car la viscosité du manteau solide profond régit probablement l'initiation de processus géologiques majeurs tels que la tectonique des plaques et la remontée de panaches mantelliques depuis la CMB (Sleep et al., 2014; Foley et al., 2014).

6.2.1 Taux de fusion et modèles de viscosité

La fraction de matériel fondu ϕ_{melt} joue un rôle fondamental dans la viscosité du manteau primitif (η) et donc sur sa dynamique de refroidissement. Au cours de son refroidissement, le manteau partiellement fondu cristallise et la fraction de matériel fondu diminue. Lorsque la fraction de matériel solide est suffisamment grande pour que les cristaux ne puissent plus entrer en suspension dans le fluide se produit une transition rhéologique majeure pour laquelle la viscosité augmente de plusieurs ordres de grandeur (Figure 23).

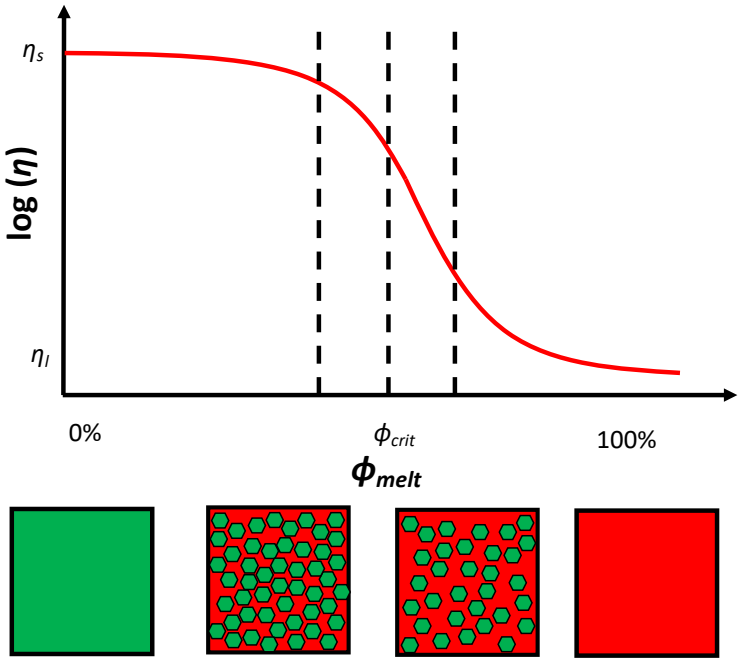

FIGURE 23 – *Représentation schématique de l'évolution de la viscosité d'un manteau partiellement fondu en fonction de la fraction solide.*

Ainsi, selon le taux de fusion ϕ_{melt}, plusieurs expressions pour le calcul de la viscosité du mélange magma/cristaux peuvent être considérées :

1. $\phi_{melt} = 1$: Au dessus du liquidus, le matériel mantellique se comporte comme un liquide. Dans ce cas, la viscosité de la phase liquide η_l dépend essentiellement de sa composition, de la température T et de la pression P. Karki and Stixrude (2010) ont développé une approche calculatoire et expérimentale afin de contraindre la viscosité de la phase liquide $MgSiO_3$ à des pressions et températures compatibles avec celles du manteau terrestre. Ils obtiennent ainsi la relation suivante :

$$\eta = \eta_l = \exp(-7.75 + 0.005P(\text{GPa}) - 0.00015P(\text{GPa})^2 + \frac{5000+135P(\text{GPa})+0.23P(\text{GPa})^2}{T-1000}) \quad (4)$$

Selon les estimations de Karki and Stixrude (2010), la viscosité de la phase silicatée liquide pourrait varier entre 0.001 et 1 Pa.s. Cette viscosité augmente en fonction de la pression et diminue avec la température.

2. $\phi_{melt} = 0$: La viscosité de la fraction solide dans le manteau profond est un paramètre difficile à contraindre que ce soit pour le manteau profond actuel (Cížková et al., 2012) ou pour le manteau primitif même si la viscosité d'un manteau profond « à bridgmanite » est de plus en plus documentée (Boioli et al., 2017; Reali et al., 2019). Les deux mécanismes principaux de déformation associés à de la convection mantellique sont le fluage par diffusion et le fluage par dislocation. Dans le cas du fluage par diffusion, la déformation est liée à de la diffusion atomique de défauts cristallins et cette diffusion est activée thermiquement. Dans le cas du fluage par dislocation, la déformation est accommodée par des glissements le long de dislocations qui sont des lignes d'imperfections dans la matrice cristalline. Les modèles expérimentaux et théoriques pour calculer la viscosité s'accordent sur l'expression suivante et commune aux deux mécanismes :

$$\eta = \eta_s = \frac{1}{A}\exp(\frac{E+PV}{RT}), \quad (5)$$

avec P la pression, R la constante des gaz (= 8.314 J K^{-1} mol^{-1}) et T la température absolue. A est le pré-facteur de viscosité, E est l'énergie d'activation, et V est le volume d'activation pour le mécanisme de fluage approprié (diffusion ou dislocation). Ces 3 paramètres (A, E et V) peuvent être contraints dans le manteau profond actuel par les vitesses de subduction de la lithosphère (Cížková et al., 2012). En raison de l'absence d'anisotropie sismique dans le manteau inférieur actuel, le fluage par diffusion est généralement considéré comme le mécanisme de déformation dominant dans le manteau profond (Boioli et al., 2017; Reali et al., 2019). Au début de l'histoire de la Terre, la température du manteau était plus élevée, et la diffusion ionique (donc le fluage de diffusion) devrait avoir été encore plus importante dans la fraction du manteau solide (Frost and Ashby, 1982) pour le manteau supérieur et inférieur. Par conséquent, nous pouvons supposer que la déformation de la phase solide interconnectée se produit uniquement par fluage par diffusion. De manière intéressante, la taille des grains intervient dans la valeur du pré-facteur de viscosité A (Monteux et al., 2020).

3. $0 < \phi_{melt} < 1$: Pour calculer la viscosité du manteau partiellement fondu, il convient de développer un formalisme tenant compte à la fois des propriétés de la phase solide et de la phase liquide. Nous détaillons ici le formalisme proposé par Lebrun et al. (2013). Lors des dernières étapes de solidification de l'océan magmatique, la fraction de matière solide augmente jusqu'à atteindre un seuil ($\phi_{melt} = \phi_{crit}$), qui sépare le régime "liquide" du régime "solide" (Solomatov, 2007). Cette fraction critique de matériel fondu peut être estimée par des expériences de migration de matériel fondu dans

des agrégats de matériel solide (Riley and Kohlstedt, 1991) ou par des experiences de compression tri-axiales à hautes températures (Scott and Kohlstedt, 2006). ϕ_{crit} dépend de nombreux paramètres (pression, température, composition chimique, taille des grains...). Scott and Kohlstedt (2006) ont estimé que ϕ_{crit} était compris entre 0.25 et 0.3 pour une péridotite à une pression de 300 MPa et une température d'environ 1500 K. Pour un océan magmatique profond, ϕ_{crit} pourrait atteindre 0.4 (Solomatov, 2000) (Figure 23).

Pour $\phi_{crit} < \phi_{melt} < 1$, la fraction en cristaux reste relativement faible et le mélange cristaux-magma se comporte comme un liquide. Ainsi la viscosité du matériau partiellement fondu est fonction de la viscosité du magma fondu η_l (Roscoe, 1952) :

$$\eta = \frac{\eta_l}{(1 - (\frac{1-\phi_{melt}}{1-\phi_{crit}}))^{2.5}} \tag{6}$$

Pour $0 < \phi_{melt} < \phi_{crit}$, le mélange cristaux-magma a plutôt tendance à se comporter comme un solide du fait de la forte interaction entre les cristaux. Dans ce cas, la viscosité du matériel dépend cette fois-ci de la viscosité de la phase solide η_s et peut s'exprimer de la façon suivante :

$$\eta = \eta_s \exp(-26\phi_{melt}) \tag{7}$$

Au cours du refroidissement, dès que le seuil de fraction fondue ($\phi_{melt} = \phi_{crit}$) est atteint dans la majeure partie du manteau, l'efficacité de refroidissement du manteau primitif diminue considérablement, même si le manteau peut rester partiellement fondu à certaines profondeurs (Monteux et al., 2016a, 2020).

6.2.2 Dynamique de refroidissement du manteau au stade "mushy"

Nous avons vu précédemment que le refroidissement d'un manteau complètement fondu était un processus rapide qui ralentissait brutalement lorsque qu'une partie significative du manteau passait en dessous de 40-50% de taux de fusion. Ce point critique est atteint dans des échelles de temps comprises entre 10^3 et 10^5 ans (Abe, 1997; Monteux et al., 2016a). Lorsque ce taux de fusion est atteint dans l'essentiel du manteau, celui-ci passe du stade "océan magmatique" au stade "mush" (mélange de solide et de liquide) (Figure 24).

Malgré une augmentation importante de la viscosité à la suite d'une solidification significative, les nombres de Rayleigh atteints dans le manteau restent très élevés et la convection reste vigoureuse. Les hauts nombres de Rayleigh mis en jeu lors du refroidissement rendent difficile la caractérisation de la dynamique du manteau dans son ensemble en 2 ou 3 dimensions. Ainsi les modèles 1D peuvent encore une fois être pertinents pour ce genre d'approche (Abe, 1997; Lebrun et al., 2013; Monteux et al., 2016a). Les profils de température vont avoir tendance à suivre des profils adiabatiques. Comme illustré dans la Figure 24, l'essentiel du manteau

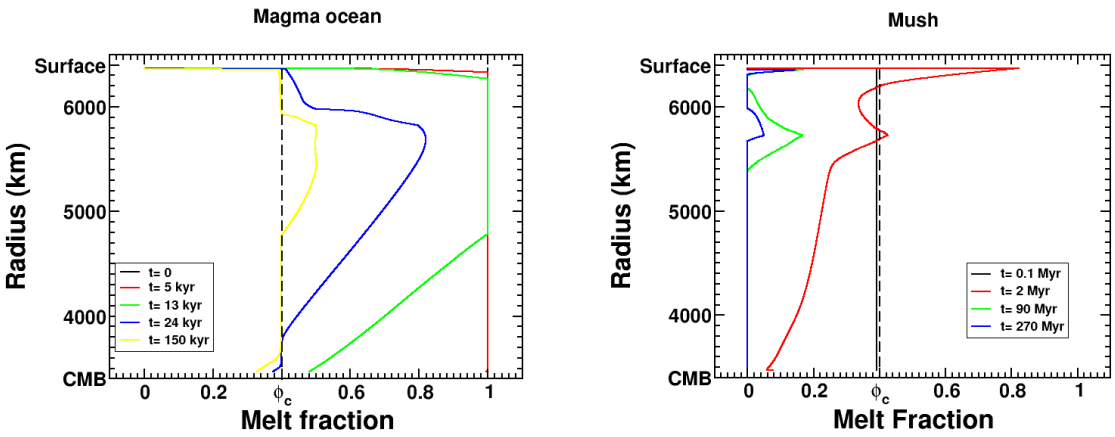

FIGURE 24 – *Évolution temporelle de la fraction de matériel dans le manteau fondu en fonction du rayon depuis le centre de la Terre au cours du stade océan magmatique (gauche) et du stade mush (à droite). À partir de Monteux et al. (2016a) et Monteux et al. (2020).*

et notamment du manteau inférieur va se solidifier en moins de 90 Ma même si la zone en contact avec la frontière manteau noyau (i.e. la couche limite thermique basale) peut atteindre une température supérieure au solidus du manteau ($\sim$ 4000 K). Dans le manteau supérieur, les adiabats peuvent être localement supérieurs au solidus et des zones partiellement fondues peuvent subsister.

Les modèles récents montrent que la durée de vie et les profondeurs des dernières zones fondues dans le manteau supérieur sont fortement dépendantes des paramètres considérés pour calculer la viscosité du manteau supérieur (voir Eq.5). Selon le profil de viscosité dans le manteau, il est ainsi possible de maintenir deux couches partiellement fondues en profondeur : (1) une couche située à des profondeurs comprises entre 800 et 1200 km pendant 40 à 400 Ma et (2) une couche plus superficielle (30-50 km de profondeur) pendant plus de 500 millions d'années (Monteux et al., 2020). En associant ces échelles de temps obtenues par des modèles numériques à des observations géologiques, il est ainsi possible d'apporter des contraintes sur la viscosité du manteau primitif profond, sur les paramètres utilisés pour calculer cette viscosité (voir Eq.5) et sur certains paramètres tels que la taille des grains (Monteux et al., 2020).

6.3 Stabilité d'une couche de cristaux dans un océan magmatique

La flottabilité de la phase fondue est de fait gouvernée par la propension qu'auront les éléments plutôt lourds tels que le fer à intégrer la phase solide ou liquide (Funamori and Sato, 2010). Cette capacité peut être estimée en laboratoire dans des conditions de P/T caractéristiques du manteau profond en calculant le coefficient de partage (D_i) d'un élément i entre

une phase solide silicatée (bridgmanite ou les polymorphes de l'olivine) et la phase liquide. Si les coefficients de partage sont aujourd'hui de mieux en mieux contraints pour une large gamme de pressions/températures, les implications géodynamiques et géochimiques de la différenciation du manteau primitif restent encore discutées. Ainsi, les travaux sur le partage du fer à hautes pressions peuvent conduire à des interprétations différentes : Nomura et al. (2011) suggèrent un liquide très riche en fer et plus dense que le manteau, alors que Andrault et al. (2012) suggèrent la remontée de la phase liquide vers la surface, tout en formant un résidu solide appauvri en éléments incompatibles en profondeur.

La différence de densité entre le solide et le liquide peut entrainer une séparation entre les 2 phases (Caracas et al., 2019) via des processus de sédimentation de cristaux dans l'océan magmatique. Cela peut produire une ségrégation chimique majeure entre les réservoirs géochimiques plus ou moins profonds que la différence de flottabilité soit positive ou négative. Les implications géodynamiques seront très différentes selon les cas. La vigueur de la convection s'opposera potentiellement à la sédimentation de la phase solide d'où la nécessité de modéliser la dynamique globale de cette ségrégation. L'ascension ou la descente de la phase liquide dans un manteau partiellement fondu pourra contribuer respectivement à du volcanisme en surface ou à la mise en place d'un océan magmatique en base de manteau.

Au début de la solidification de l'océan magmatique, les premiers cristaux formés ont pu se déposer en profondeur ou être efficacement mélangés par les mouvements de convection induits par le refroidissement de l'océan magmatique. Nous avons récemment développé des modèles numériques pour suivre l'évolution d'une fine couche de cristaux dans un océan magmatique (Monteux et al., 2023). Ces modèles ont caractérisé l'influence de la taille des cristaux, de la viscosité du magma et de la différence de densité entre les cristaux et le magma. Ces modèles ont mis en évidence l'importance du nombre de Shields (Sh) qui représente le rapport entre la contrainte tangentielle due à l'écoulement convectif et la contrainte de flottabilité liée à la différence de densité entre les cristaux et l'océan magmatique (Solomatov et al., 1993). Nous avons notamment contraint le nombre de Shields critique (Sh_c) séparant le régime où les cristaux sédimentent au fond du réservoir et le régime où les cristaux restent en suspension. Nos résultats montrent qu'au cours de la solidification d'un océan magmatique profond, les cristaux sont plus facilement mis en suspension que déposés au fond de l'océan magmatique car les mouvements de convection entrainent efficacement les cristaux malgré leur poids (Figure 25). Cette découverte tend à renforcer l'idée que la cristallisation de l'océan magmatique s'est faite à l'équilibre plutôt que de manière fractionnée.

La solidification de l'océan magmatique a ainsi joué un rôle déterminant dans la composition chimique du manteau primitif et contraint ainsi quels types de minéraux ont pu se former en fonction de la profondeur dans le manteau primitif. Pour mieux contraindre ce phénomène, nous avons comparé la différence de densité entre l'océan magmatique et les cristaux solides pour différentes compositions chimiques et la différence de densité critique à partir de laquelle la ségrégation des cristaux est susceptible de se produire. Nos résultats montrent que la ségrégation de la bridgmanite, première phase minérale à se former dans l'océan magmatique, est plus susceptible de se produire au fond d'un océan magmatique si celui-ci est enrichi en SiO_2.

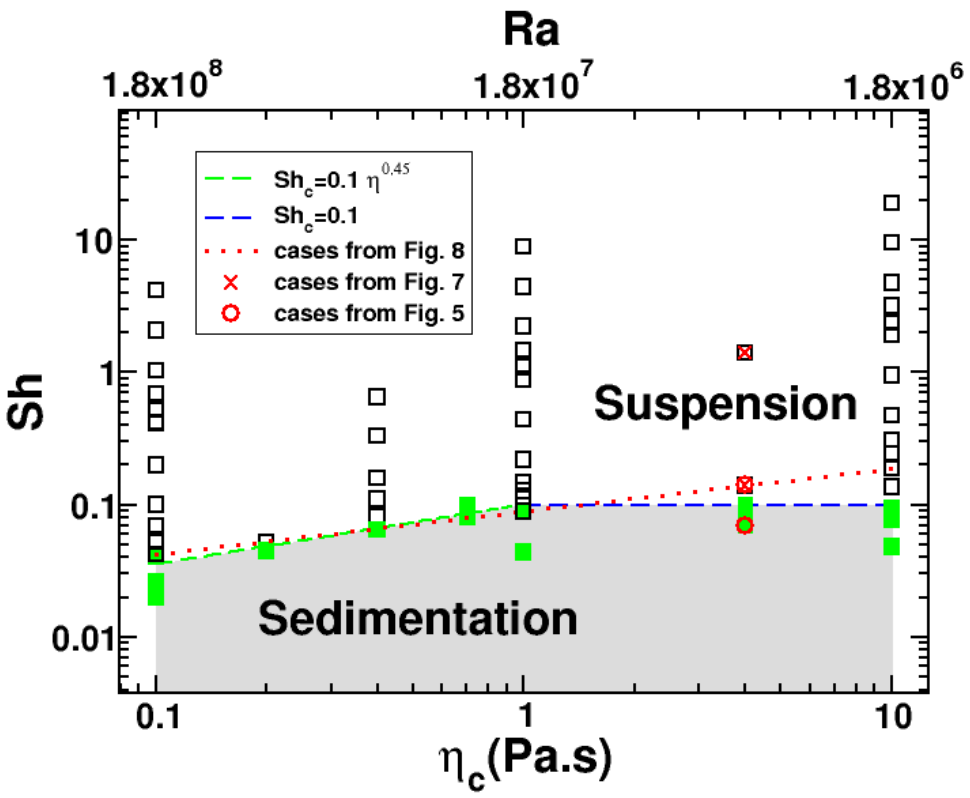

FIGURE 25 – *Valeur du nombre de Shields (Sh) en fonction de la viscosité de la phase continue fondue (η_c) (ou Ra pour l'axe x supérieur). Les symboles carrés correspondent aux modèles utilisés dans notre étude. Les symboles noirs vides représentent les cas où le régime de suspension est atteint. Les symboles verts remplis représentent les cas où le régime de sédimentation est atteint. Les deux régimes sont séparés par des lignes pointillées (vertes pour $\eta_c \leq 1$, bleues pour $\eta_c \geq 1$) illustrant le nombre de Shields critique (Sh_c). À partir de Monteux et al. (2023)*

6.4 Perspectives : Couplage entre le manteau primitif terrestre et la Lune

Plusieurs dizaines de millions d'années après le début de son accrétion, la Terre a subi un impact géant qui a conduit à la formation du système Terre-Lune (Hartmann and Davis, 1975) (voir Section 2.4). La modélisation numérique de cet impact géant a montré que cet événement a entraîné une forte augmentation de la température et la formation d'un océan de magma profond (Nakajima and Stevenson, 2015). À la suite de cet impact catastrophique, un énorme transfert de chaleur et une ségrégation chimique se sont produits pendant la cristallisation de ce manteau primitif (Monteux and Arkani-Hamed, 2016). Cependant, les hétérogénéités isotopiques identifiées dans plusieurs éléments radiogéniques formés par des systèmes à courte durée de vie suggèrent que le manteau terrestre n'a jamais été mélangé au point d'être homogénéisé (Boyet and Carlson, 2005). La préservation de telles hétérogénéités est en contradiction

avec les événements de fusion et de mélange de grande ampleur attendus d'un impact géant (Nakajima and Stevenson, 2015) et avec la capacité de la convection mantellique à préserver des réservoirs non traités à grande échelle pendant plusieurs années Gyr. S'il existe un consensus sur l'importance des épisodes d'océan magmatique sur l'évolution thermochimique précoce de la Terre, des questions majeures demeurent sur l'évolution de la fraction fondue lors du refroidissement et sur les modalités de différenciation chimique au sein d'un manteau partiellement fondu, qui se sont probablement poursuivies des centaines de millions d'années après l'impact géant.

Plusieurs années après l'impact, la Lune a été entièrement accrétée par les débris de la collision (Kokubo and Ida, 2000). À cette époque, la Lune était beaucoup plus proche de la Terre qu'aujourd'hui (Chen and Nimmo, 2016), ce qui a généré d'énormes forces de marée sur les deux corps. La Lune a potentiellement commencé à se recristalliser à une distance allant de 5 à 15 rayons terrestres. Le forçage de marée induit par la présence de la Lune génère un cisaillement oscillatoire caractérisé par un taux de cisaillement maximal et une fréquence de marée. Un tel cisaillement oscillatoire peut influencer le flux convectif avec l'océan magmatique et le processus de cristallisation (Ogilvie and Lesur, 2012).

Le but de ce projet est de répondre aux questions suivantes :

1. Quelle est l'influence de la jeune Lune sur la dynamique de refroidissement et de solidification du manteau terrestre en fusion ?
2. Le chauffage hétérogène du manteau terrestre dû aux fortes interactions de marée avec la jeune Lune pourrait-il influencer la différenciation chimique et expliquer la signature géochimique que nous mesurons aujourd'hui ?
3. Comment la dissipation dans les intérieurs partiellement fondus de la Terre et de la Lune primitives a-t-elle influencé leur évolution spin-orbite à long terme ?

Pour répondre à ces questions fondamentales, nous proposons de rassembler des expertises complémentaires en physique minérale, géochimie, modélisation numérique en mécanique des fluides, mécanique des milieux continus et mécanique céleste, à l'interface entre les sciences de la Terre et l'astrophysique, afin de développer une approche numérique innovante et collaborative qui contraindra l'influence de la jeune Lune sur l'évolution thermochimique précoce de la Terre.

La dynamique de refroidissement d'un océan de magma profond est actuellement un sujet très débattu (Ballmer et al., 2017; Maurice et al., 2017; Laneuville et al., 2018; Agrusta et al., 2020). Cependant, aucune des études récentes n'a considéré le couplage mécanique entre la ségrégation des cristaux, les effets de marées et la convection thermique turbulente en 2D/3D tout en considérant des contraintes expérimentales réalistes et récentes relatives aux courbes de fusion, au fractionnement chimique, aux diffusivités thermiques et aux paramètres thermo-dynamiques. Nous proposons pour la première fois de résoudre de manière cohérente le chauffage par les marées, l'évolution de la solidification et la différenciation chimique dans le manteau hadéen depuis le stade de cristallisation de l'océan magmatique jusqu'à la transition archéenne. Nous combinerons les principaux résultats des deux tâches suivantes pour

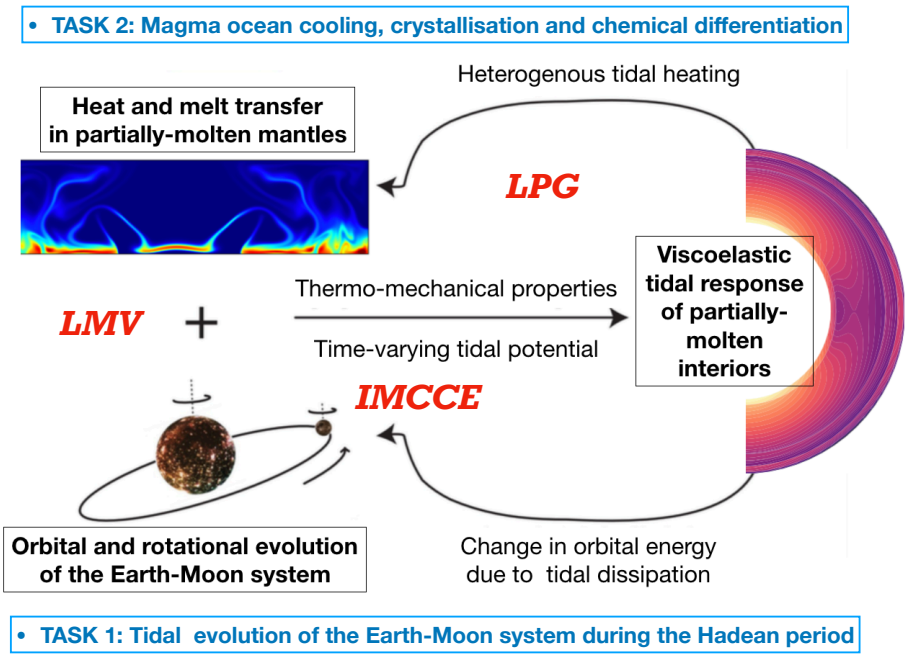

FIGURE 26 – *Principe général de l'approche numérique prévue pour la modélisation thermo-orbitale couplée du système Terre-Lune. La dissipation de marée pour un intérieur partiellement fondu sera calculée à l'aide du code LPG-Tide (TÂCHE 1) à partir des profils thermiques, de densité et de fusion moyens prédits par les modèles de transfert de chaleur et de matière fondue (TÂCHE 2). La puissance dissipée calculée affectera les bilans thermique et orbital. Le changement d'orbite et de rotation du système Terre-Lune sera calculé à l'aide des modèles d'évolution orbitale développés à l'IMCCE à partir de la puissance dissipée totale de la Terre et de la Lune, qui à son tour modifiera le potentiel de marée.*

proposer les premiers modèles d'évolution couplés complets du système Terre-Lune pendant l'ère Hadéenne.

Le projet DEMOTIC (Figure 26) vise à développer de nouveaux modèles numériques pour suivre l'évolution de la température et de la solidification de la Terre. En particulier l'objectif est de contraindre : (1) les effets réciproques des marées liés à la distance Lune-Terre et (2) l'influence des marées sur l'évolution thermochimique de la Terre hadéenne, y compris le fractionnement des éléments chimiques pendant la cristallisation de la MO. Pour la première fois, nous allons résoudre de manière cohérente le chauffage par les marées, l'évolution de la matière en fusion et la différenciation chimique dans le manteau Hadéen depuis le stade de cristallisation de la MO jusqu'à la transition archéenne. Ainsi, nous comprendrons si les marées et le chauffage hétérogène du manteau terrestre dû aux fortes interactions de marée avec la jeune Lune (1) peuvent influencer la différenciation chimique et expliquer la signature géochimique que nous mesurons aujourd'hui à partir des hétérogénéités isotopiques observées dans

la Terre profonde et (2) peuvent avoir une influence sur l'évolution orbitale e à long terme du système Terre-Lune. Dans ce but, le projet DEMOTIC rassemblera l'expertise multidisciplinaire complémentaire du LMV, du LPG Nantes et de l'IMCCE, à l'interface entre les sciences de la Terre et l'astrophysique, afin de développer une approche numérique innovante, collaborative et unique. Ce projet dont je suis le porteur principal vient d'obtenir un financement INSU (Origines) et fera l'objet d'une demande de financement ANR PRC en 2024.

Références personnelles

Monteux, J., *Andrault D., Samuel H., 2016, On the cooling of a deep terrestrial magma ocean. Earth and Planetary Science Letters vol.448, p.140-149.* **LIEN HAL**

Monteux, J., *Andrault D., Guitreau M., Samuel H., Demouchy S., 2020, A mushy Earth's mantle for more than 500 Myr after the magma ocean solidification, Geophysical Journal International vol.221, p.1165-1181, 2.* **LIEN HAL**

Monteux, J., *Qaddah B., Andrault D., 2023, Conditions for segregation of a crystal-rich layer within a convective magma ocean, Journal of Geophysical Research, Volume 128, Issue 5* **LIEN HAL**

Earth and Planetary Science Letters 448 (2016) 140–149

Contents lists available at ScienceDirect

Earth and Planetary Science Letters

www.elsevier.com/locate/epsl

On the cooling of a deep terrestrial magma ocean

J. Monteux [a,*], D. Andrault [a], H. Samuel [b]

[a] Laboratoire Magmas et Volcans, Université Blaise Pascal, CNRS, IRD, Clermont-Ferrand, France
[b] Institut de Recherche en Astrophysique et Planétologie, CNRS, Toulouse, France

ARTICLE INFO

Article history:
Received 18 November 2015
Received in revised form 21 April 2016
Accepted 7 May 2016
Available online 24 May 2016
Editor: C. Sotin

Keywords:
early Earth
thermal evolution
magma ocean
numerical modeling

ABSTRACT

Several episodes of complete melting have probably occurred during the first stages of the Earth's evolution. We have developed a numerical model to monitor the thermal and melt fraction evolutions of a cooling and crystallizing magma ocean from an initially fully molten mantle. For this purpose, we numerically solve the heat equation in 1D spherical geometry, accounting for turbulent heat transfer, and integrating recent and strong experimental constraints from mineral physics. We have explored different initial magma ocean viscosities, compositions, thermal boundary layer thicknesses and initial core temperatures.

We show that the cooling of a thick terrestrial magma ocean is a fast process, with the entire mantle becoming significantly more viscous within 20 kyr. Due to the slope difference between the adiabats and the melting curves, the solidification of the molten mantle occurs from the bottom up. In the meantime, a crust forms due to the high surface radiative heat flow, the last drop of fully molten silicate is restricted to the upper mantle. Among the studied parameters, the magma ocean lifetime is primarily governed by its viscosity. Depending on the thermal boundary layer thickness at the core–mantle boundary, the thermal coupling between the core and magma ocean can either insulate the core during the magma ocean solidification and favor a hot core or drain the heat out of the core simultaneously with the cooling of the magma ocean. Reasonable thickness for the thermal boundary layer, however, suggests rapid core cooling until the core–mantle boundary temperature results in a sluggish lowermost mantle. Once the crystallization of the lowermost mantle becomes significant, the efficiency of the core heat loss decreases. Since a hotter liquidus favors crystallization at hotter temperatures, a hotter deep mantle liquidus favors heat retention within the core. In the context of an initially fully molten mantle, it is difficult to envision the formation of a basal magma ocean or to prevent a major heat depletion of the core. As a consequence, an Earth's geodynamo sustained only by core cooling during 4 Gyr seems unlikely and other sources of motion need to be invoked.

1. Introduction

Geochemical evidence (Touboul et al., 2012; Rizo et al., 2013) suggests that the Earth's mantle has experienced several episodes of global melting during its early evolution, leading to the formation of the early continental crust and facilitating the core formation (Kleine et al., 2009). These episodes were probably enhanced by giant impacts occurring during the late stages of planetary formation (Agnor et al., 1999). Although not yet clearly established, it is likely that these giant impacts, such as the one that is thought to have formed the Earth–Moon system, could have melted 30 to 100% of the Earth's mantle depending on the impactor/target mass ratio and on the pre-impact thermal state of the target (Canup, 2012; Ćuk and Stewart, 2012; Nakajima and Stevenson, 2015). During the cooling and the subsequent crystallization of a magma ocean (MO), compatible elements (e.g. Mg, Cr) were preferentially collected in the solid phase while the incompatible elements (e.g. Al, Na, Fe) selectively partitioned into melts. In addition to temperature, the degree of solid–melt fractionation is highly sensitive to a variety of physical parameters, including pressure (Nomura et al., 2011; Andrault et al., 2012). Hence, characterizing the cooling of a deep terrestrial magma ocean and in particular the timescale and depth at which the last drop of melt solidifies are of first importance to understand the current chemical composition of the Earth's mantle and the dating of its major differentiation events (Boyet and Carlson, 2005).

The composition and the rheology of such a magma ocean directly affect its lifetime, but remain poorly constrained (Solomatov, 2007). The magma ocean is composed of low viscosity molten sili-

* Corresponding author.
E-mail address: j.monteux@opgc.univ-bpclermont.fr (J. Monteux).

http://dx.doi.org/10.1016/j.epsl.2016.05.010
0012-821X/

cate material but its chemical composition remains uncertain, with a MgO/SiO_2 ratio around those of chondritic or peridotitic compositions (Ringwood, 1966; Allègre et al., 1995; Javoy et al., 2010). Recent high-pressure laboratory measurements report the solidus and liquidus of both a chondritic and peridotitic mantle compositions up to pressures that are compatible with the Earth's lowermost mantle conditions (Fiquet et al., 2010; Andrault et al., 2011). Moreover, recent shock experiments now provide important constraints on the thermodynamic parameters used to determine the adiabatic profiles in the magma ocean up to 140 GPa (Mosenfelder et al., 2009; Thomas et al., 2012; Thomas and Asimow, 2013). Since the difference between their slopes governs the depth at which crystallization is initiated, both the liquidus and the adiabats play a key role in the cooling of the magma ocean. If the adiabat had a steeper slope than the liquidus in the mid-mantle (Mosenfelder et al., 2007; Stixrude et al., 2009), solidification would start at mid-mantle depth. In this case, a lowermost magma ocean would cool and solidify much more slowly because of the thermal blanketing of the overlying solid mantle (Labrosse et al., 2007). However, if the mantle liquidus had a steeper slope than the adiabat through the whole mantle (Thomas et al., 2012), solidification would start from the CMB thus reducing the likeliness of a basal magma ocean, unless invoking an enrichment in dense incompatible elements in the residual liquid. In any case, the important dynamical change does not occur when the adiabat crosses the liquidus, because the mantle keeps its liquid behavior, but rather when the degree of partial melting decreases below a critical value from which the mantle behaves as a solid. Therefore, the recent determination of melting curves and elastic parameters of silicate melts up to core–mantle boundary (CMB) conditions offers a great opportunity to improve our knowledge of the cooling dynamics of a deep terrestrial magma ocean.

The magma oceans such as the one generated by the Moon-forming impact participated to the core-formation process. The early thermal state of the core remains poorly constrained. It results from the contribution of the accretionary processes (Safronov, 1978; Kaula, 1979), including giant impact (Tonks and Melosh, 1992) and radiogenic heating (Yoshino et al., 2003) as well as the conversion of potential energy into heat via viscous dissipation during the metal/silicate separation (Ke and Solomatov, 2009; Monteux et al., 2009; Ricard et al., 2009; Samuel et al., 2010). The combined processes leading to core formation can yield a wide range of possible early thermal states, depending on the nature and timescale of core formation processes. The core could initially have had a temperature close to the deep mantle temperature if thermal equilibration was efficient. Alternatively, it could have been hotter than the mantle if the gravitational potential energy released during core formation was largely retained within the core itself, a situation which would be followed by a strong heating of the lowermost mantle from this superheated core (Samuel et al., 2010). In turn, the thermo-mechanical properties of the magma ocean can have a strong influence on the early evolution of the heat repartition between the core and the mantle. A key question is to determine how much a deep magma ocean can enhance core cooling. This can have important consequences on the duration and the generation of the Earth's dynamo (Monteux et al., 2011).

The low magma ocean viscosities resulting from the hot early temperatures imply that the cooling of such a deep molten mantle was highly turbulent (Solomatov, 2007). Studies of the early mantle have either characterized the cooling of a magma ocean restricted to the first 1000 km (Abe, 1997) or did not consider the presence of a molten layer just above the core–mantle boundary, and its effect of the CMB heat flow (Nakagawa and Tackley, 2014). However, the hypothesis of an early largely molten mantle combined with the determination of solidus/liquidus and thermodynamical properties of silicate melts up to 140 GPa now allow a more accurate characterization of the cooling of a deep terrestrial magma ocean and the thermal coupling with its underlying core. The aim of this work is to constrain the lifetime of a deep magma ocean and to determine the pressure at which the magma ocean crystallization finished. To achieve these goals, we have developed a numerical model to characterize the early evolution of (i) the temperature and melt fraction of an initially fully molten isochemical mantle and (ii) the temperature of the core. We incorporate in our models recent and strong experimental constraints on the solidus and liquidus profiles and on the thermodynamical properties of silicate melts up to ~140 GPa. We explore different core temperatures, magma ocean compositions and viscosities.

2. Convective cooling of the magma ocean

Miller et al. (1991) characterized the cooling and the subsequent crystallization of a magma ocean with a chondritic composition as a sequence of isentropes with decreasing potential temperature. Later on, Abe (1997) investigated the thermal evolution of magma ocean using a one-dimensional heat transfer model. However, these studies were restricted to the first 1000 km and did not integrate the mutual influence of the magma ocean and its underlying material on the cooling. Labrosse et al. (2007) studied the cooling of a stable dense molten layer above the CMB overlaid by a solid mantle. In their model they consider the crystallization of a single-component (forsterite) magma ocean assuming a solidification proceeding from the top to the bottom according to Mosenfelder et al. (2007). More recently, Nakagawa and Tackley (2014) characterized the coupled thermal evolution of Earth's early mantle and core considering a 2900 km thick viscous mantle but ignoring the potential presence of a molten layer just above the core–mantle boundary, and its effect of the CMB heat flow. Here, we model the secular cooling of an initially fully molten magma ocean by convective transport of heat in a 1-D spherically symmetric geometry. We assume a multicomponent chemically homogeneous magma ocean made of a combination of forsterite, enstatite, fayalite, anorthite and diopside. In the following sections, we describe the model setup and equations.

2.1. Physical model for planetary thermal evolution

We model the thermal evolution of a 2900 km thick isochemical silicate mantle overlying an iron core by solving the conservation of energy in a one-dimensional, spherically symmetric domain (with a radius ranging from 3500 to 6400 km):

$$\rho C_p \frac{\partial T}{\partial t} = \nabla.(k\nabla T), \tag{1}$$

with ρ the density, C_p the mantle heat capacity, T the temperature, t the time and k the thermal conductivity. Among the heat sources that have potentially delivered the energy required for significant melting in the early Earth, the decay of short-lived radioactive isotopes such as ^{26}Al and ^{60}Fe have probably played a major role especially for 10 to 100 km size objects (Yoshino et al., 2003). However, their half-life times (0.73 My and 1.5 My respectively) (Carlson and Lugmair, 2000) are much shorter than the time at which the Moon forming impact is supposed to have occurred (between 30 and 100 Myrs after the formation of the first solids of the Solar System) (Kleine and Rudge, 2011). Concerning the long-lived radioactive elements such as ^{40}K, Th or U, their concentrations were certainly significant at the time of the Moon-forming impact, but their heat production rates are much smaller. Hence the contribution form the long-lived radio-active elements during the magma ocean lifetime is negligible. Thus, we can reasonably neglect radiogenic heating in our models.

Thermal energy is transferred by convection in the region where the temperature gradient is steeper than the adiabatic temperature gradient, or by conduction elsewhere. To account for the heat transfer within a vigorously convecting magma ocean, in Eq. (1), the thermal conductivity k is the sum of the intrinsic thermal conductivity k_c and an effective conductivity due to thermal convection k_v. Following Neumann et al. (2014), the latter is estimated as follows:

$$k_v = F_{conv} L/\Delta T, \tag{2}$$

where L is the thickness of the magma ocean at time t, F_{conv} is the convective heat flux at radius r and time t and ΔT is the difference between the temperature profile and the adiabatic profile T_{ad} with a potential temperature corresponding to the temperature of the surface of the magma ocean.

At radius r, the convective heat flux F_{conv} depends on the local Rayleigh number Ra:

$$Ra = \frac{\alpha g C_p \rho^2 \Delta T L^3}{k_c \eta}, \tag{3}$$

where α is the thermal expansion coefficient of the magma ocean, g is the gravitational acceleration assumed to be constant through the whole mantle and η is the local dynamic viscosity.

In the context of an initially fully molten mantle, the convective velocities are estimated to $u_0 \sim 10$ m/s (Solomatov, 2007) leading to Reynolds number values ($Re = \rho u_0 L/\eta$) in the order of 10^9 (with $\eta = 100$ Pa s and $\rho = 4000$ kg m^{-3}) and, hence, to highly turbulent convective cooling. The low magma ocean viscosities induce Rayleigh numbers as large as 10^{30} (Solomatov, 2007). In such a context, two regimes arise depending on Ra (Solomatov, 2007; Neumann et al., 2014): the "soft-turbulent" regime (if $Ra < 10^{19}$) where

$$F_{conv} = 0.089 \frac{k_c \Delta T}{L} Ra^{1/3}, \tag{4}$$

and the "hard-turbulent" regime (if $Ra \geq 10^{19}$) where

$$F_{conv} = 0.22 \frac{k_c \Delta T}{L} Ra^{2/7} Pr^{-1/7} \lambda^{-3/7}, \tag{5}$$

where Pr is the local Prandtl number ($= C_p \eta / k_c$) and λ is the aspect ratio for the mean flow. We assume that $\lambda = 1$ and that rotation does not have any significant effect on the heat flow (Solomatov, 2007).

Depending on their ability to migrate either towards the solid phase (compatible) or towards the liquid phase (incompatible), the relative abundance of some chemical elements can potentially modify the buoyancy of both the liquid and solid phases during the crystallization of a magma ocean. This chemical fractionation process could be enhanced by the fractional crystallization of the magma ocean at least in the upper mantle (Solomatov, 2007) and would lead to a liquid residual phase that is more or less buoyant than the solid phase. A dense liquid phase could favor a basal magma ocean (Labrosse et al., 2007) or large scale cumulate overturns (Elkins-Tanton et al., 2003, 2005) while a dense solid phase would enhance volcanic activity (Moyen and Martin, 2012; Martin et al., 2014). However, the values of the partition coefficients at high pressures of the elements that have a key contribution in the density of each phase (e.g. Fe) are still debated (Andrault et al., 2012). In addition, crystals may also gravitationally separate with the dense cumulates sinking and the lighter ones floating toward the surface leading to a supplementary segregation process. In a highly turbulent environment such as a thick magma ocean, the vigor of the convection probably prevents from any chemical segregation especially during the early stages of the magma ocean solidification. Indeed, Tonks and Melosh (1990) have shown that the Rayleigh number for a planetary scale magma ocean was so high that crystals would remain entrained in the magma which would effectively preclude crystal separation. Therefore, we do not consider any spatial variation in the chemical composition and we currently consider neither the mass flux of melt owing to gravitational separation nor the mass flux of melt owing to convective mixing.

Viscosity is strongly dependent on the local melt fraction ϕ, which is calculated as follows:

$$\phi = \frac{T - T_{sol}}{T_{liq} - T_{sol}}, \tag{6}$$

where T_{liq} and T_{sol} are the liquidus and solidus temperatures, respectively. Following Abe (1997) the viscosity of partially molten silicates η varies between a fully molten end-member η_m (assumed to be constant) and a solid end-member η_s that is temperature dependent:

$$\eta = MIN \left[\frac{(1-\phi)\rho_m \eta_s + \phi \rho_s \eta_m}{(1-\phi)\rho_m + \phi \rho_s}, \eta_m \left\{ \frac{(1-\phi)\rho_m + \phi \rho_s}{(1-A)(1-\phi)\rho_m + \phi \rho_s} \right\}^{2.5}, 10^{21} \right], \tag{7}$$

where ρ_m is the density of the molten material, ρ_s is the density of the solid material and $A = 1.67$ (Abe, 1997). When the temperature, T, is lower than the solidus temperature of mantle, the viscosity of the solid mantle η_s is estimated as follows (Abe, 1997):

$$\eta_s = \eta_{s,0} \exp\left(B \frac{T_{liq}}{T} \right). \tag{8}$$

We used $\eta_{s,0} = 256$ Pa s, and $B = 25.17$ based on the olivine rheology (Karato and Wu, 1993; Abe, 1997). In the above equation, as for an Arrhenius relation, the viscosity of the solid mantle increases with the pressure. Assuming an adiabatic temperature profile with a potential temperature of 1600 K (Tackley, 2012) leads to a viscosity value of $\sim 10^{23}$ Pa s in the lowermost mantle compatible with estimates of the present-day mantle viscosity profiles (Čížková et al., 2012). Considering a relationship that involves the solidus rather than the liquidus in Eq. (8) would not affect our results since both the liquidus and the solidus used in our models have a similar trend. Since we consider here the evolution of a fully molten to partially molten magma ocean, the cooling timescale of the magma ocean is mainly governed by η_m and is weakly dependent on η_s as we shall see later.

A strong increase in viscosity occurs when the melt fraction equals 40% (Abe, 1997). Hence, when the melt fraction approaches this critical value, the presence of crystals drastically reduces the efficiency of the magma ocean cooling. In our models, the mantle is considered as part of the magma ocean as long as its melt fraction is larger than 50% (Neumann et al., 2014) and we stop our simulations when the thickness of the magma ocean drop below 100 km.

The pressure profile P is obtained fitting the PREM model (Dziewonski and Anderson, 1981) with a quadratic function of the radius r and is assumed to remain constant with time:

$$P = 4.0074 \times 10^{11} - 91862r + 0.0045483r^2. \tag{9}$$

2.2. Melting curves and adiabats

Due to the uncertainties related to the chemical composition of the magma ocean, we consider in our study two models for melting curves and elastic parameters: the F-peridotic model and the A-chondritic model. We describe these two models in the following sections.

2.2.1. Melting curves

The solidus and liquidus play a major role in the early thermal evolution of the magma ocean. Recent laboratory experiments now constrain the liquidus and solidus of mantle-like material up to pressures compatible with the CMB conditions (Fiquet et al., 2010; Andrault et al., 2011). However, the differences between these two studies, in particular the liquidus temperatures, appear too large to be solely due to the difference in chemical compositions between the two types of mantle materials. Regardless of the controversy, we performed calculations using the melting curves from both reports, leading to a F-peridotitic model (Fiquet et al., 2010) and a A-chondritic model (Andrault et al., 2011). The solidus and liquidus profiles are obtained fitting experimental results with a modified Simon and Glatzel equation (Simon and Glatzel, 1929). For pressures below $P = 20$ GPa, we use experimentally determined solidus and liquidus temperatures of chondritic mantle from Herzberg and Zhang (1996):

$$T_{sol} = 1661.2\left(\frac{P}{1.336\times10^9}+1\right)^{(1/7.437)}, \tag{10}$$

$$T_{liq} = 1982.1\left(\frac{P}{6.594\times10^9}+1\right)^{(1/5.374)}, \tag{11}$$

with T_{liq} is the liquidus temperature and T_{sol} the solidus temperature.

Since the difference between the F-peridotitic and A-chondritic solidus for pressures larger than $P = 20$ GPa is not large, we use the experimentally determined A-chondritic solidus from Andrault et al. (2011):

$$T_{sol} = 2081.8\left(\frac{P}{101.69\times10^9}+1\right)^{(1/1.226)}. \tag{12}$$

For pressures above 20 GPa, the difference between the F-peridotitic and the A-chondritic liquidus is more important. We use the following expression

$$T_{liq} = c_1\left(\frac{P}{c_2}+1\right)^{(1/c_3)}, \tag{13}$$

with ($c_1 = 78.74$, $c_2 = 4.054\times10^6$, $c_3 = 2.44$) for F-peridotitic liquidus (Fiquet et al., 2010) and ($c_1 = 2006.8$, $c_2 = 34.65\times10^9$, $c_3 = 1.844$) for A-chondritic liquidus (Andrault et al., 2011).

2.2.2. Thermodynamical parameters

The thermodynamical parameters for the molten magma ocean are closely related to its chemical composition. Volume and elastic parameters of silicate liquids has been recently characterized up to 140 GPa using shock compression experiments (Mosenfelder et al., 2007, 2009; Thomas et al., 2012; Thomas and Asimow, 2013). We assume here two multicomponent systems for (i) a A-chondritic composition (62% enstatite + 24% forsterite + 8% fayalite + 4% anorthite + 2% diopside) and (ii) a F-peridotitic composition (33% enstatite + 56% forsterite + 7% fayalite + 3% anorthite + 0.7% diopside). Using fourth-order Birch–Murnaghan/Mie–Grüneisen equation of state fits for molten silicate liquids from Thomas and Asimow (2013), we obtain the melt density ρ_m, the volumetric thermal expansion α as a function of pressure as well as the specific heat C_p of the molten material for these two multicomponent assemblages. The density of the solid phase is then calculated as:

$$\rho_s = \rho_m + \Delta\rho, \tag{14}$$

with $\Delta\rho$ the density difference between solid and liquid (see Tables 1 and 2 for values).

Table 1
Constant and fixed parameter values for numerical models.

Earth radius	R	6370 km
Core radius	R_{core}	3470 km
Mantle thickness	$R - R_{core}$	2900 km
Mantle properties		
Solid density	ρ_s	$= \rho_m + \Delta\rho$
Density contrast	$\Delta\rho/\rho$	1.5% (Tosi et al., 2013)
Specific enthalpy change	ΔH	4×10^5 J/kg (Ghosh and McSween, 1998)
Viscosity of melt phase	η_m	1–10^4 Pa s
Bottom TBL thickness	e_{TBL}	10^{-3}–10^3 m
Core properties		
Density	ρ_{Fe}	10 000 kg m^{-3}
Heat capacity	$C_{p,Fe}$	800 J kg^{-1} K^{-1}

For a zone of partial melting, the density ρ', the coefficient of volumetric thermal expansion α' and the specific heat C'_p are given as follows (Solomatov, 2007):

$$\frac{1}{\rho'} = \frac{1-\phi}{\rho_s} + \frac{\phi}{\rho_m}, \tag{15}$$

$$\alpha' = \alpha + \frac{\Delta\rho}{\rho(T_{liq}-T_{sol})}, \tag{16}$$

$$C'_p = C_p + \frac{\Delta H}{T_{liq}-T_{sol}}, \tag{17}$$

where ΔH is the latent heat released during solidification.

2.2.3. Adiabats

In vigorously convecting systems such as magma oceans, the temperature distribution is nearly adiabatic and isentropic (Solomatov, 2007). In one-phase systems, such as a completely molten or a completely solid layer, the equation for an adiabat is

$$\left(\frac{\partial T}{\partial r}\right)_S = -\frac{\alpha g}{C_p}T. \tag{18}$$

In two-phase systems, the effects of phase changes need to be considered (Solomatov, 2007). The equation for such adiabat is given by:

$$\left(\frac{\partial T}{\partial r}\right)_S = -\frac{\alpha' g}{C'_p}T. \tag{19}$$

This leads to a two-phase adiabat that is steeper than the purely liquid or solid one-phase adiabats (Solomatov, 2007). The adiabatic temperature profiles are calculated by numerical integration of Eq. (18) and Eq. (19) using a fourth-order Runge–Kutta method (Press et al., 1993). These adiabatic temperature profiles are used to calculate at each depth and, when super-adiabatic, the temperature difference ΔT from Eq. (3). The liquidus and solidus profiles as well as the adiabatic profiles obtained from Eq. (18) for temperatures ranging between 1400 and 4000 K are shown in Fig. 1. We start our models assuming an adiabatic temperature profile with a potential surface temperature $T_p = 3200$ K.

2.3. Boundary conditions

Large impacts can generate a rock vapor atmosphere that can last for some years until its energy is radiated to space (Svetsov, 2005). The presence of an atmosphere is expected to slow down the radiation of heat to space (Hamano et al., 2013; Lebrun et al., 2013). However, most of the pre-impact atmosphere is likely to be eroded after a giant impact (Shuvalov, 2009). Thus, in our models,

Table 2
Variable and non-dimensional parameter values for numerical models.

Melt density	ρ_m	A-model: 2684–5274 kg m^{-3} F-model: 2679 – 5378 kg m^{-3}	Computed from Thomas and Asimow (2013)
Heat capacity	C_p	A-model: 1742 J kg^{-1} K^{-1} F-model: 1800 J kg^{-1} K^{-1}	Computed from Thomas and Asimow (2013)
Thermal expansion coefficient	α	A-model: 1.3×10^{-5}–7.9×10^{-5} K^{-1} F-model: 2×10^{-5}–9.6×10^{-5} K^{-1}	Computed from Thomas and Asimow (2013)
Viscosity of solid phase	η_s		From Eq. (8) with $\eta_{s,0}=256$ Pa s and B = 25.17
Viscosity of the magma ocean	η	1–10^{21} Pa s	From Eq. (7)
Total conductivity	k	5–10^{7} W m^{-1} K^{-1}	$=k_c+k_v$
Rayleigh number	Ra	at $t=0$: 1×10^{27}–3×10^{27}	Computed from Eq. (3)
Prandtl number	Pr	350–3.6×10^{24}	$=C_p\eta/k_c$
Reynolds number	Re	at $t=0$: $Re\sim10^{9}$	From Solomatov (2007)

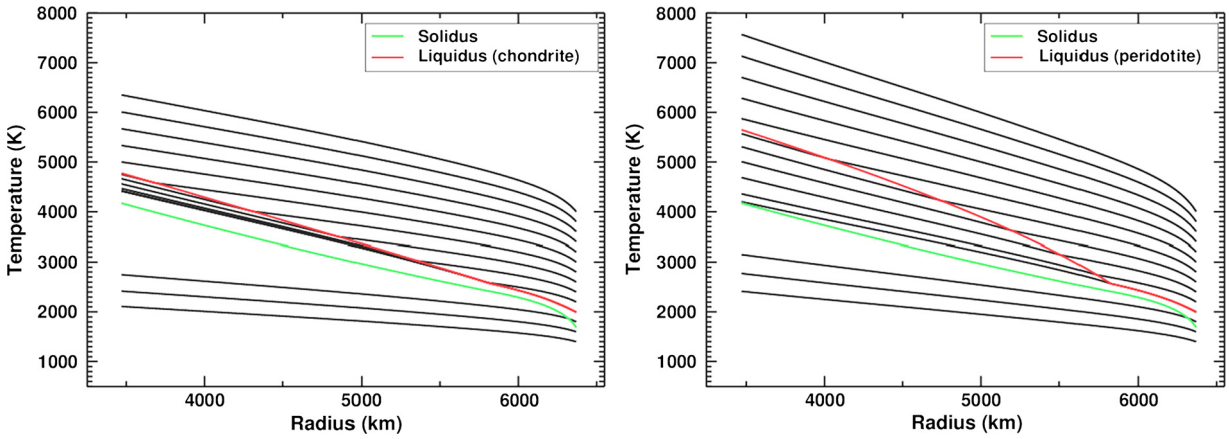

Fig. 1. Adiabats (with T_p ranging between 1400 and 4000 K) computed for the A-chondritic model (left) and the F-peridotitic model (right). The corresponding solidus and liquidus are represented in green and red respectively. (For interpretation of the references to color in this figure legend, the reader is referred to the web version of this article.)

we neglect the effect of thermal blanketing, and impose a radiative heat flux boundary condition at the surface:

$$F_{surf}=\sigma\left(T_{surf}^4-T_{eq}^4\right), \tag{20}$$

with T_{surf} the temperature at the surface of the MO, σ the Stefan–Boltzman constant and $T_{eq}=273$ K the expected equilibrium surface temperature.

At the base of the silicate mantle, core–mantle thermal coupling is accounted for via a conductive heat flux imposed at the core–mantle boundary (CMB):

$$F_{core}=\frac{k_c(T^{core}-T_{CMB}^{mantle})}{e_{TBL}}, \tag{21}$$

where T^{core} is the average core temperature at the CMB (i.e. we neglect the thermal boundary layer within the core) and T_{CMB}^{mantle} is the mantle temperature right above the CMB. e_{TBL} is the thickness of the thermal boundary layer at the bottom of the mantle where the heat is extracted from the core by conduction. T_{CMB}^{mantle} is obtained solving Eq. (1) while T^{core} is obtained from:

$$V_{core}\rho_{Fe}C_{p,Fe}\frac{dT^{core}}{dt}=S_{core}F_{core}, \tag{22}$$

where V_{core} is the core volume, S_{core} is the core surface, ρ_{Fe} is the core density, $C_{p,Fe}$ is the core heat capacity and F_{core} is the heat flux through the CMB. This formulation allows to follow the evolution of core temperature as a function of time, based on the CMB heat flux.

2.4. Numerical model

Eq. (1) is discretized using a semi-implicit predictor–corrector Finite Difference scheme, of second-order in both space and time (Press et al., 1993). Our scheme was successfully benchmarked against steady and unsteady analytical solutions for diffusion problems (Crank, 1975). The mantle is discretized using $n=2900$ equally spaced grid points resulting in a constant spatial resolution $\Delta r=1$ km. Non-linear effects are handled via a fixed-point/picard iteration procedure. The variable time step is determined as $\Delta t=\min(\Delta r^2/\kappa)$, where $\kappa(r)=k/(\rho Cp)$ is the effective diffusivity.

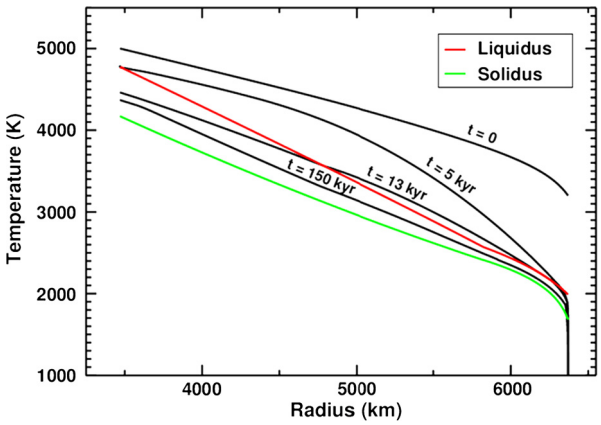

Fig. 2. Temperature evolution from an initially adiabatic temperature profile with $T_p=3200$ K and $T_0^{core}=5000$ K. The liquidus and solidus used in our models are those obtained for the A-chondritic model and are represented respectively with red and green curves. In this model $e_{TBL}=1$ m and $\eta_m=100$ Pa s. (For interpretation of the references to color in this figure legend, the reader is referred to the web version of this article.)

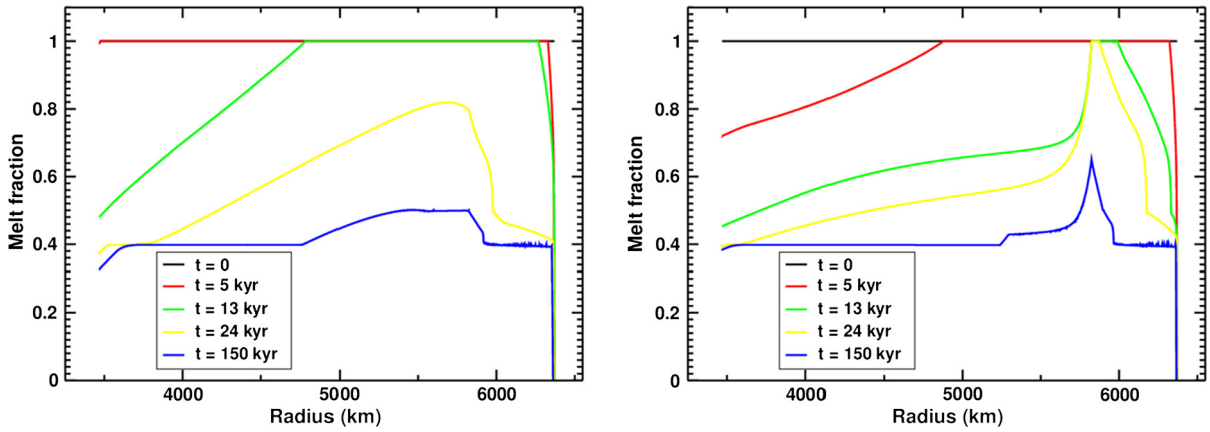

Fig. 3. Left panel: Melt fraction evolution from an initially completely molten magma ocean and corresponding to the case illustrated in Fig. 2. A melt fraction of 0.4 is a major discontinuity for the magma ocean viscosity (see text). **Right panel**: same with a F-peridotitic model ant $T_0^{core} = 7000$ K.

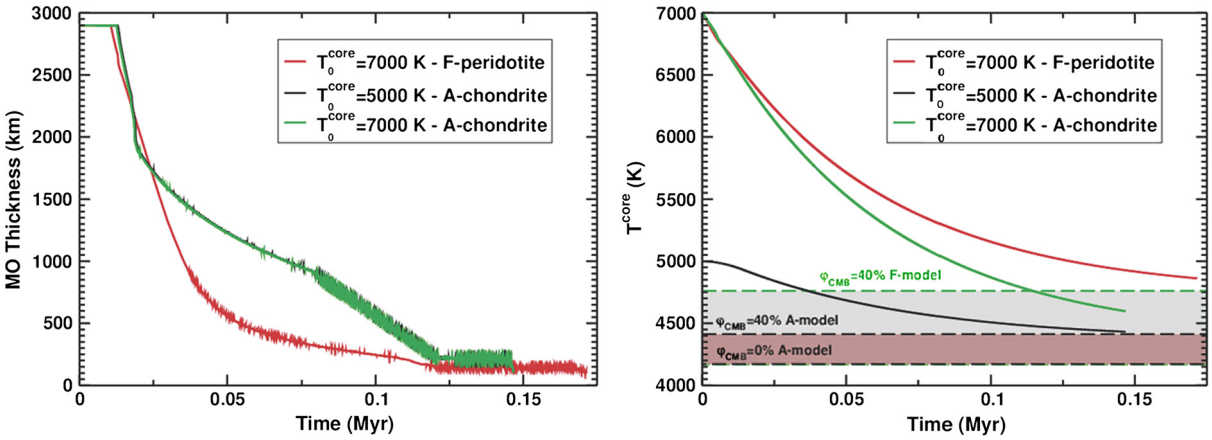

Fig. 4. Left panel: Time evolution of the magma ocean thickness (where the melt fraction is larger than 50%) for different initial core temperatures T_0^{core} and different initial compositions (with $e_{TBL} = 1$ m and $\eta_m = 100$ Pa s). **Right panel**: Time evolution of the core temperature for different initial core temperatures and different initial compositions (with $e_{TBL} = 1$ m, $\eta_m = 100$ Pa s). (For interpretation of the references to color in this figure legend, the reader is referred to the web version of this article.)

3. Results

3.1. Thermal evolution of a deep magma ocean

We follow the thermal evolution of a deep magma ocean with an initially adiabatic temperature profile with $T_p = 3200$ K. Before we study the effect of each magma ocean parameter, we consider the following model as a reference case: a A-chondritic model, a 1 m thick bottom thermal boundary layer (e_{TBL}), a melt viscosity value of $\eta_m = 100$ Pa s and an initial core temperature $T_0^{core} = 5000$ K. Fig. 2 shows that the temperature rapidly decreases from the surface where heat is efficiently removed by radiative cooling even if a thin solid crust is formed within this upper thermal boundary layer. In the deepest part of the mantle, the temperature profile remains adiabatic but the cooling is slower. After 5000 yr, solidification occurs from the CMB where the liquidus is steeper than the adiabatic profile. As cooling proceeds, the melt fraction decreases and the last parcel with 100% melt starts to solidify in the upper mantle (see Fig. 3, left). Finally, the whole magma ocean drops below a 50% melt value in $t_{MO} \sim 150$ kyr with t_{MO} being the magma ocean lifetime. This time ranges between the two characteristic timescales mentioned in Solomatov (2000): 10^3 yr when crystallization starts from the bottom and 10^8 yr when crystallization of the last drop of melt occurs in the shallow magma ocean. Clearly, our magma ocean lifetime is much shorter than the cooling timescale of ~4 Gyr proposed by Labrosse et al. (2007). This is due to the fact that, in our model, the solidification occurs from the bottom-up which prevents our magma ocean from being overlaid by a thick insulating solid mantle. In Abe (1997), the magma ocean was restricted to a 1000 km-deep domain and the melting curves were steeper than the one used in our model. Hence, within 150 kyr, most of the mantle temperature profile computed from Abe (1997) is well below the solidus.

We monitored the thickness of the magma ocean (i.e. the thickness of the material having a melt fraction larger than 50%) as a function of time. Fig. 4 (left, black line) shows that after a short period (~20 kyr) where the mantle remains mostly molten, the thickness of the magma ocean rapidly decreases from 2900 km to 200 km, with a change of slope for a thickness of ~ 2000 km for the A-chondritic model. At the change of slope, the melt fraction reaches the critical value of 40% in the lowermost mantle, which induces an abrupt increase of its viscosity. Then the melt fraction progressively decreases at all mantle depths until we stop our simulations when the magma ocean thickness drops below 100 km. Fig. 4 (right, black line) shows the core temperature as a function of time for our reference case. In this model, the core temperature decreases monotonically from its initial value of 5000 K to a value of 4430 K, which corresponds to a melt fraction $\phi \sim 40\%$ at $P = 140$ GPa (i.e. when the abrupt change in viscosity occurs).

We monitored the time evolution of the heat flow coming at the CMB from the core F_{core} and the heat loss at the surface F_{surf} (Fig. 5, a). During the first 20 kyr, the heat flow at the CMB rapidly increases from ~10^{16} to a nearly constant value of ~10^{17} W. In the meantime the surface heat flow decreases from

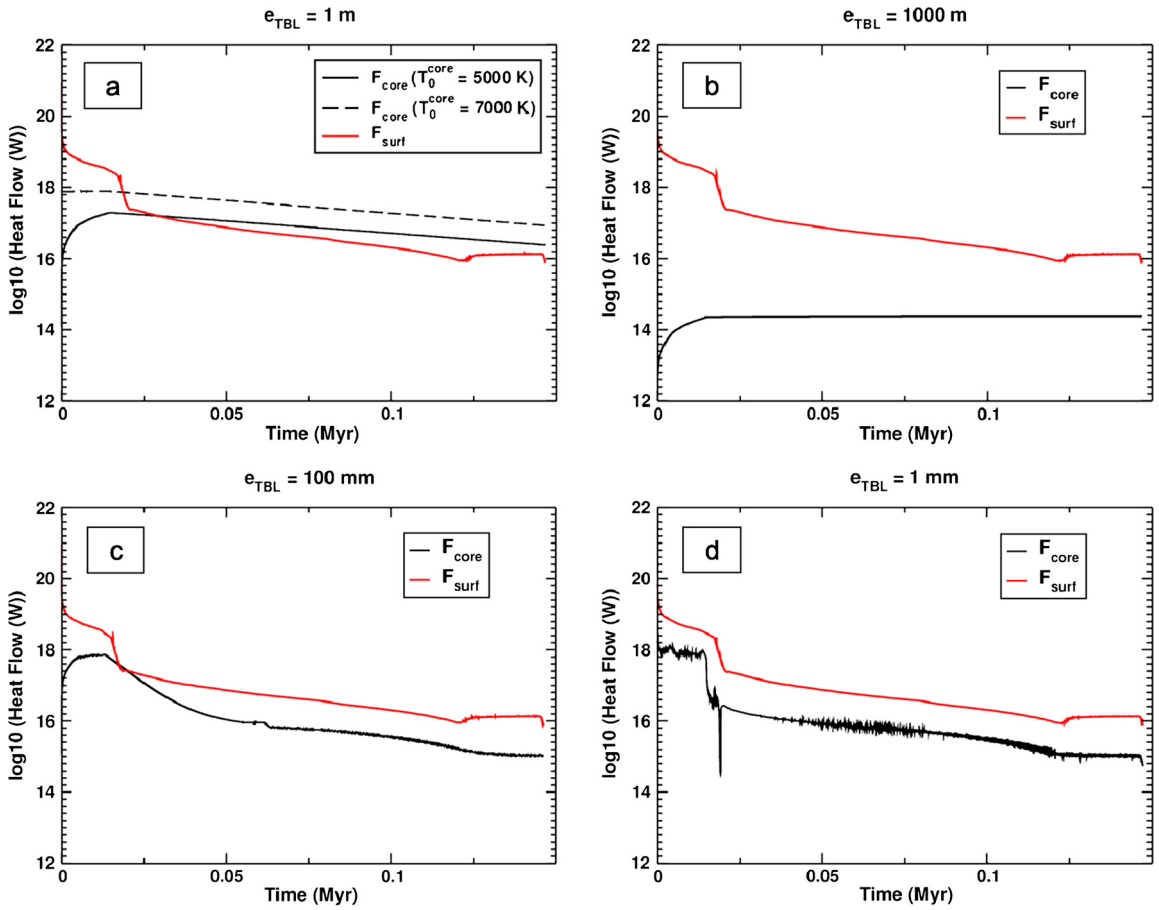

Fig. 5. (a): Time evolution of the CMB (black) and surface (red) heat flows for a A-chondritic model (assuming $e_{TBL} = 1$ m, $\eta_m = 100$ Pa s and $T_0^{core} = 5000$ K except for the black dashed line where $T_0^{core} = 7000$ K). **(b)**: Same with $e_{TBL} = 1000$ m. **(c)**: Same with $e_{TBL} = 100$ mm. **(d)**: Same with $e_{TBL} = 1$ mm. In all these models, the magma ocean lifetimes (time at which the plots ends up) are very close. (For interpretation of the references to color in this figure legend, the reader is referred to the web version of this article.)

$\sim 10^{19}$ (in agreement with the value proposed by Solomatov, 2000) to $\sim 10^{17}$ W. Then, both the surface and the core heat flows decrease down to a value of $\sim 10^{16}$ W until the end of the magma ocean stage (within $t_{MO} = 150$ kyr).

3.2. Influence initial of core temperature

We monitored the influence of the initial core temperature on the cooling of the deep magma ocean considering two values: (1) $T_0^{core} = 5000$ K, which is equal to the temperature at the bottom of the magma ocean for $T_p = 3200$ K in the A-chondritic model and (2) $T_0^{core} = 7000$ K, which corresponds to a core significantly hotter than the mantle. The comparison of the black and green curves in Fig. 4 (left) shows that the initial temperature has a negligible influence on the evolution of the magma ocean thickness as well as on its cooling timescale. When $T_0^{core} = 7000$ K, the initial core heat flow is large ($\sim 10^{18}$ W) (Fig. 5, a) because of the initial temperature contrast ($= 2000$ K) with the lowermost mantle. Then the heat flow decreases as a consequence of both the progressive solidification of the overlying mantle and the core heat depletion. When $T_0^{core} = 5000$ K, the initial CMB heat flow is much smaller than when $T_0^{core} = 7000$ K, but it increases rapidly due to rapid cooling of the lowermost mantle. In both cases, the heat flow decreases when the lowermost mantle has cooled sufficiently to reach the critical melt fraction of 40%. A significantly hotter initial core leads to an increase of the core heat flow, by a factor of 3 between 5000 K and 7000 K (Fig. 5, a). However, this increase of the initial core temperature, which should lead to an increase of the surface heat flow, is not visible on the surface heat flow evolution because of the stronger efficiency of the surface cooling.

Also, a core initially 2000 K hotter than the lowermost mantle ends up 170 K hotter at the end of the MO stage (Fig. 4, right). When $T_0^{core} = 7000$ K the final core temperature is $T^{core} = 4600$ K which is slightly larger than the temperature at which the melt fraction of the lowermost mantle reaches the 40% critical value in the A-chondritic model.

3.3. A-chondritic vs. F-peridotitic model

Here we compare the evolutions of temperature and melt fraction between the A-chondritic and F-peridotitic models (using the corresponding liquidus and thermodynamical parameters). We focus on cases where $T_0^{core} = 7000$ K (with $T_0^{core} = 5000$ K, the core temperature would be lower than the liquidus for the F-peridotitic model at the CMB pressure). Fig. 4 (left) shows that for an initial core temperature $T_0^{core} = 7000$ K, the magma ocean thickness decreases more rapidly in the F-peridotitic model (red curve) than in the A-chondritic model (green curve). This is the direct consequence of a liquidus being significantly higher for a F-peridotitic model than for a A-chondritic model (Fig. 1). Hence, during the cooling of an initial fully molten magma ocean, the onset of mantle crystallization occurs earlier and the melt fraction decreases more rapidly in the F-peridotitic case (Fig. 3, right). The comparison of the A-chondritic and the F-peridotitic models shows a peak of the melt faction in the latter case occurring at a depth of ~600 km. This corresponds to the important slope change in the F-peridotitic liquidus that occurs at 20 GPa (see Fig. 1, right). Since the melt

fraction is a strong function of the liquidus, this discontinuity happens to affect the precise depth at which the last drop of melt should solidify. However, the last part to solidify should still be located in the shallow mantle, regardless the shape of the liquidus in this region. In addition, the magma ocean lifetime t_{MO} appears to be weakly affected by the choice of the model and ranges between 147 kyr (in the A-chondritic case) to 171 kyr (in the F-peridotitic case).

Still, the F-peridotitic and A-chondritic models show a significant difference on the evolution of the core temperature (Fig. 4, right). For both cases, the core temperature decreases asymptotically from its initial value to a value that ranges between 4600 K (A-chondritic case) and 4860 K (F-peridotitic) in about 0.15 Myr. Since the lowermost mantle solidifies more rapidly when considering a hotter liquidus, a F-peridotitic model for the magma ocean helps to retain some heat in the core. For both cases, the final core temperature is 100 to 150 K larger than the temperature at which the melt fraction of the lowermost mantle reaches the 40% critical value.

3.4. Influence of the bottom thermal boundary layer

The thickness of the bottom thermal boundary layer e_{TBL} governs both the cooling rate of the core and the energy supplied to the magma ocean (Eq. (21)). In a hard-turbulent context, this thickness is difficult to determine from laboratory experiments and only theoretical models can constrain this parameter (Spiegel, 1971). Therefore, a rough estimation of e_{TBL} can be obtained for $Ra \sim 10^{20}$ based on the Nusselt number calculation: $Nu \sim (RaPr)^{1/2}$ (Spiegel, 1971). Considering that $Nu \sim L/e_{TBL}$, we obtain $e_{TBL} \sim L(RaPr)^{-1/2}$. In our magma ocean context and assuming that the scaling law is still valid at Rayleigh numbers up to 10^{30}, this corresponds to a value $e_{TBL} \sim 10^{-6}$ m. This thickness is extremely thin, however, it is compatible with previous reports (Solomatov, 2007; Lebrun et al., 2013). As a first attempt to understand the influence of bottom thermal boundary layer in the magma ocean cooling dynamics, we performed various calculations with e_{TBL} fixed and ranging from 1 mm to 1 km. The lower range values can be seen as unrealistic in comparison with, for example, the core topography. However, the wide range of values considered for e_{TBL} allows a better illustration of its influence on the magma ocean cooling timescales.

We find that the magma ocean lifetime does not depend largely on e_{TBL} and its value remains close to 150 kyr for the whole range of e_{TBL} values assumed here. Fig. 5 shows the CMB and the surface heat flows for four different values of e_{TBL}. For $e_{TBL} = 1000$ m (Fig. 5, b), the surface heat flow is several orders of magnitude larger than the core heat flow and the thermal coupling between these two reservoirs is inefficient. For values of thermal boundary layer thicknesses below 1 m (Fig. 5, c and d), the heat flows become comparable and the thermal coupling between the core and the molten overlying mantle becomes efficient. Ideally, e_{TBL} should be an adjustable parameter in our calculation, related to the effective value of the Rayleigh number. However, this would result in extremely small e_{TBL} values of the order of 10^{-6} m. We show in Fig. 5 that decreasing the value of e_{TBL} from 100 mm to a value of 1 mm does influence neither the shape of the surface heat flow nor the magma ocean lifetime (Fig. 5, c and d). In that cases, the core heat flow rapidly reaches a maximal value and decreases within the first 20 kyr, which corresponds to the time needed by the melt fraction of the bottom of the magma ocean to reach the critical value of 40% (Fig. 6). During this brief period of time, although heat is efficiently removed from the core (Fig. 6), the CMB heat flow remains considerably smaller that the surface heat loss. This is the reason why e_{TBL} does not significantly influence the magma ocean lifetime. Hence, decreasing e_{TBL} to a smaller value

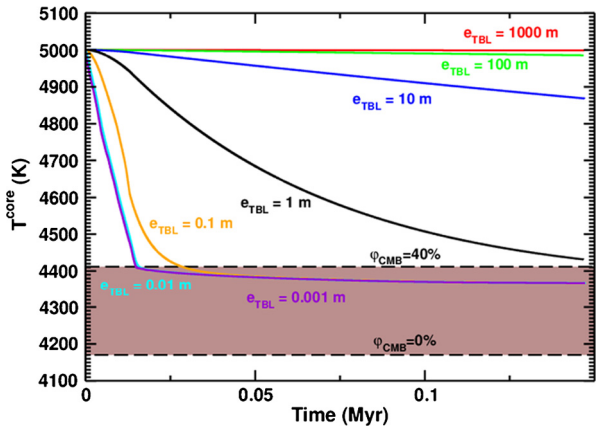

Fig. 6. Time evolution of the core temperature for different thicknesses of the bottom thermal boundary layer (assuming a A-chondritic model, $\eta_m = 100$ Pa s and $T_0^{core} = 5000$ K).

(i.e. $e_{TBL} << 10^{-6}$ m) as suggested by our theoretical estimation of the TBL thickness or to relate e_{TBL} to the Rayleigh number that is initially extremely high should not influence the results of our study.

Such a behavior is confirmed by the time evolution of T^{core}, which is a strong function of e_{TBL} (Fig. 6). As long as e_{TBL} is larger than 100 m, the initial core heat is efficiently retained and the core cooling is not influenced by the cooling of the overlying magma ocean. However, for $e_{TBL} \leq 100$ m the thermal coupling between the core and the MO becomes important. For $e_{TBL} < 1$ m, the core rapidly cools down to ~4400 K, which corresponds to the temperature where the lowermost mantle reaches the critical melt fraction value of 40%. Then the core cooling efficiency strongly decreases as the lowermost mantle is becoming much more viscous. Finally, the core temperature ends up at a temperature of ~4370 K for e_{TBL} values ranging between 1 mm to 10 cm.

3.5. Influence of the magma ocean viscosity

Measurements (Liebske et al., 2005) and ab initio calculations (Karki and Stixrude, 2010) estimate that the dynamic viscosity η_m of peridotitic melt is in the range 10^{-2}–10^{-1} Pa s. At low degrees of partial melting of a peridotite, the viscosity of the generated liquid can eventually increase up to 100 Pa s (Kushiro, 1986). The viscosity of molten mafic silicate should range between 10^{-2}–10^{2} Pa s (Rubie et al., 2003). To take into account the effect of this uncertainty on the magma ocean lifetime, we perform numerical simulations considering that the fully molten magma ocean viscosity η_m ranges between 10^{-2}–10^{2} Pa s.

Dimensional analysis of Eq. (1) indicates that t_{MO} is inversely proportional to F_{conv}. In the hard turbulent regime relevant to a thick MO context this term scales as $\eta_m^{-3/7}$. Consequently, the lifetime of a magma ocean should scale as $\eta_m^{3/7}$. This is confirmed by our numerical results (Fig. 7), and consistent with previous work (Solomatov, 2007):

$$t_{MO}(\text{Myr}) = 0.018\, \eta_m^{3/7}. \tag{23}$$

Most importantly, for realistic viscosities of the fully molten early mantle, the melt fraction drops below 50% at all mantle depths in less than 1 Myr. For the lower range of η_m, this characteristic time scale can decrease down to several kyrs, rather than 1 Myr.

4. Conclusion

The cooling of a thick terrestrial magma ocean is a fast process. The magma ocean lifetime is principally governed by its viscosity

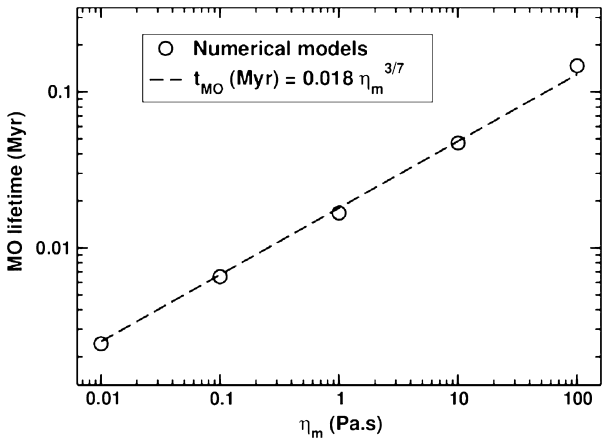

Fig. 7. Magma ocean lifetime as a function of the magma ocean viscosity η_m (assuming a A-chondritic model, $e_{TBL} = 1$ m and $T_0^{core} = 5000$ K).

and, for the mid range of realistic viscosities, the magma ocean reaches a 50% melt fraction at all mantle depths within 20 kyr. Depending on the thermal boundary layer at the CMB, the thermal coupling between the core and MO can either insulate the core during the MO solidification and favor a hot core (for thick TBL), or drain the heat out of the core. However, as suggested by theoretical calculations, an extremely thin thermal boundary layer in an ultra-turbulent environment implies that much of the heat is removed from the core during the cooling of the overlying mantle. In this context, our F-peridotitic model (with a higher liquidus) is more willing to retain the core heat than our A-chondritic model, yielding a difference of temperature of ~170 K after the magma ocean has crystallized. In addition, the final core temperature increases by a couple hundred degrees as its early temperature increases. However, for all cases, the average core temperature at the CMB (T^{core}) ends up close to the 40% melt fraction temperature of the silicate magma ocean: ±100 K depending on the initial core temperature and on the thickness of the bottom thermal boundary layer.

In contrast with previous reports (Labrosse et al., 2007), our model shows that the crystallization occurs relatively rapidly at the CMB and, after some crystallization has proceeded, the highest amount of partial melting is found at intermediate depth between the surface and the CMB (see Fig. 3). One could argue that this result is dictated by the fact that our calculation neglects the possible effects of chemical segregation during mantle cooling. On the contrary, we believe that the segregation of a melt above the core mantle boundary would not help to retain heat in the core (Labrosse, 2015; Davies et al., 2015). A melt that would accumulate just above the CMB by gravitational segregation would be depleted in refractory elements, thus with a liquidus lower than the rest of the mantle. The temperature at which this part of the mantle becomes viscous (at 40% of partial melting) would be lowered and thus the core heat would escape more easily in the presence of a basal magma ocean (Ulvrová et al., 2012; Nakagawa and Tackley, 2014), in agreement with our results displayed in Fig. 4.

These results have important consequences for the magnetic history of the Earth. Indeed, if at some point, a full magma ocean has existed on the Earth, it is likely that most of the core heat has been removed rapidly. In less than 1 Myr, a tremendous heat flow may have lead to a significant decrease of the core temperature until it reached a value that is close or slightly above the temperature at which the melt fraction of the lowermost mantle reaches the 40% critical value (i.e. ~4400 K). Assuming that the Earth–Moon system was formed by a giant impact 100 Myrs after the first solids of the Solar System (Kleine and Rudge, 2011), and that this giant impact has completely molten the Earth's mantle (Nakajima and Stevenson, 2015), it is difficult to envision that a large amount of heat could be retained in the core to sustain the geomagnetic field by thermal convection for several Gyr (Andrault et al., 2016), in contrast with the proposition of the most recent reports (Labrosse, 2015; Davies et al., 2015).

Finally, we acknowledge that our current model neglects the effect of vertical chemical segregation. While this effect is unlikely to dominate the dynamics in a highly turbulent magma ocean (Tonks and Melosh, 1990), it could become more important when the degree of partial melting becomes close or lower than ~40% (i.e. when viscosity increases). At this point, the knowledge of the density contrast between the solid at the liquidus (the first crystal to form) and the ambient liquid becomes of major importance. Whether the melt sinks, or floats has important ramifications for understanding the first steps in the dynamic modeling of the Earth's differentiation. In the near future, a modeling effort to integrate the compositional contribution in the buoyancy calculation between liquid and solid will constitute an important step forward towards the understanding of the earliest stages of Earth's evolution.

Acknowledgements

The authors thank J. Roberts and anonymous reviewer for thoughtful and constructive comments. The authors also thank G. Tobie and B. Cecconi for their useful help in the development of the numerical model as well as M. Le Bars and J. Lunine for fruitful discussions and help. J. Monteux and D. Andrault are funded by Agence Nationale de la Recherche (Oxydeep decision no. ANR-13-BS06-0008). J. Monteux is also funded by the Auvergne Fellowship program. H. Samuel acknowledges the support from the Deutsche Forschungsgemeinschaft (project SA 2042/3). This is Laboratory of Excellence ClerVolc contribution no. 205.

References

Abe, Y., 1997. Thermal and chemical evolution of the terrestrial magma ocean. Phys. Earth Planet. Inter. 100, 27–39. http://dx.doi.org/10.1016/S0031-9201(96)03229-3.

Agnor, C.B., Canup, R.M., Levison, H.F., 1999. On the character and consequences of large impacts in the late stage of terrestrial planet formation. Icarus 142, 219–237. http://dx.doi.org/10.1006/icar.1999.6201.

Allègre, C.J., Poirier, J.-P., Humler, E., Hofmann, A.W., 1995. The chemical composition of the Earth. Earth Planet. Sci. Lett. 134, 515–526. http://dx.doi.org/10.1016/0012-821X(95)00123-T.

Andrault, D., Bolfan-Casanova, N., Nigro, G.L., Bouhifd, M.A., Garbarino, G., Mezouar, M., 2011. Solidus and liquidus profiles of chondritic mantle: implication for melting of the Earth across its history. Earth Planet. Sci. Lett. 304, 251–259. http://dx.doi.org/10.1016/j.epsl.2011.02.006.

Andrault, D., Petitgirard, S., Lo Nigro, G., Devidal, J.-L., Veronesi, G., Garbarino, G., Mezouar, M., 2012. Solid-liquid iron partitioning in Earth's deep mantle. Nature 487, 354–357. http://dx.doi.org/10.1038/nature11294.

Andrault, D., Monteux, J., Le Bars, M., Samuel, H., 2016. The deep Earth may not be cooling down. Earth Planet. Sci. Lett. 443, 195–203. http://dx.doi.org/10.1016/j.epsl.2016.03.020.

Boyet, M., Carlson, R.W., 2005. ^{142}Nd evidence for early (>4.53 Ga) global differentiation of the silicate Earth. Science 309, 576–581. http://dx.doi.org/10.1126/science.1113634.

Canup, R.M., 2012. Forming a Moon with an Earth-like composition via a giant impact. Science 338, 1052. http://dx.doi.org/10.1126/science.1226073.

Carlson, R.W., Lugmair, G.W., 2000. Timescales of Planetesimal Formation and Differentiation Based on Extinct and Extant Radioisotopes. Ariz. Univ. Press, Tucson, pp. 25–44.

Crank, J., 1975. The Mathematics of Diffusion, 2nd ed. Clarendon Press, Oxford. viii, 414 p.

Ćuk, M., Stewart, S.T., 2012. Making the Moon from a fast-spinning Earth: a giant impact followed by resonant despinning. Science 338, 1047. http://dx.doi.org/10.1126/science.1225542.

Davies, C., Pozzo, M., Gubbins, D., Alfè, D., 2015. Constraints from material properties on the dynamics and evolution of Earth's core. Nat. Geosci. 8, 678–685. http://dx.doi.org/10.1038/ngeo2492.

Dziewonski, A.M., Anderson, D.L., 1981. Preliminary reference Earth model. Phys. Earth Planet. Inter. 25, 297–356. http://dx.doi.org/10.1016/0031-9201(81)90046-7.

Elkins-Tanton, L.T., Parmentier, E.M., Hess, P.C., 2003. Magma ocean fractional crystallization and cumulate overturn in terrestrial planets: implications for Mars. Meteorit. Planet. Sci. 38, 1753–1771.

Elkins-Tanton, L.T., Zaranek, S.E., Parmentier, E.M., Hess, P.C., 2005. Early magnetic field and magmatic activity on Mars from magma ocean cumulate overturn. Earth Planet. Sci. Lett. 236, 1–12.

Fiquet, G., Auzende, A.L., Siebert, J., Corgne, A., Bureau, H., Ozawa, H., Garbarino, G., 2010. Melting of peridotite to 140 gigapascals. Science 329, 1516. http://dx.doi.org/10.1126/science.1192448.

Ghosh, A., McSween, H.Y., 1998. A thermal model for the differentiation of asteroid 4 Vesta, based on radiogenic heating. Icarus 134, 187–206. http://dx.doi.org/10.1006/icar.1998.5956.

Hamano, K., Abe, Y., Genda, H., 2013. Emergence of two types of terrestrial planet on solidification of magma ocean. Nature 497, 607–610. http://dx.doi.org/10.1038/nature12163.

Herzberg, C., Zhang, J., 1996. Melting experiments on anhydrous peridotite klb-1: compositions of magmas in the upper mantle and transition zone. J. Geophys. Res., Solid Earth 101 (B4), 8271–8295. http://dx.doi.org/10.1029/96JB00170.

Javoy, M., Kaminski, E., Guyot, F., Andrault, D., Sanloup, C., Moreira, M., Labrosse, S., Jambon, A., Agrinier, P., Davaille, A., Jaupart, C., 2010. The chemical composition of the Earth: enstatite chondrite models. Earth Planet. Sci. Lett. 293, 259–268. http://dx.doi.org/10.1016/j.epsl.2010.02.033.

Karato, S.-I., Wu, P., 1993. Rheology of the upper mantle – a synthesis. Science 260, 771–778. http://dx.doi.org/10.1126/science.260.5109.771.

Karki, B.B., Stixrude, L.P., 2010. Viscosity of $MgSiO_3$ liquid at Earth's mantle conditions: implications for an Early magma ocean. Science 328, 740. http://dx.doi.org/10.1126/science.1188327.

Kaula, W.M., 1979. Thermal evolution of Earth and Moon growing by planetesimal impacts. J. Geophys. Res. 84, 999–1008.

Ke, Y., Solomatov, V.S., 2009. Coupled core–mantle thermal evolution of early Mars. J. Geophys. Res., Planets 114 (13), 1–12.

Kleine, T., Rudge, J.F., 2011. Chronometry of meteorites and the formation of the Earth and Moon. Elements 7, 41–46. http://dx.doi.org/10.1016/j.gca.2006.06.004.

Kleine, T., Touboul, M., Bourdon, B., Nimmo, F., Mezger, K., Palme, H., Jacobsen, S.B., Yin, Q.-Z., Halliday, A.N., 2009. Hf–W chronology of the accretion and early evolution of asteroids and terrestrial planets. Geochim. Cosmochim. Acta 73, 5150–5188. http://dx.doi.org/10.1016/j.gca.2008.11.047.

Kushiro, I., 1986. Viscosity of partial melts in the upper mantle. J. Geophys. Res. 91, 9343–9350. http://dx.doi.org/10.1029/JB091iB09p09343.

Labrosse, S., 2015. Thermal evolution of the core with a high thermal conductivity. Phys. Earth Planet. Inter. 247, 36–55. http://dx.doi.org/10.1016/j.pepi.2015.02.002.

Labrosse, S., Hernlund, J.W., Coltice, N., 2007. A crystallizing dense magma ocean at the base of the Earth's mantle. Nature 450, 866–869. http://dx.doi.org/10.1038/nature06355.

Lebrun, T., Massol, H., Chassefière, E., Davaille, A., Marcq, E., Sarda, P., Leblanc, F., Brandeis, G., 2013. Thermal evolution of an early magma ocean in interaction with the atmosphere. J. Geophys. Res., Planets 118, 1155–1176. http://dx.doi.org/10.1002/jgre.20068.

Liebske, C., Schmickler, B., Terasaki, H., Poe, B.T., Suzuki, A., Funakoshi, K.-i., Ando, R., Rubie, D.C., 2005. Viscosity of peridotite liquid up to 13 GPa: implications for magma ocean viscosities [rapid communication]. Earth Planet. Sci. Lett. 240, 589–604. http://dx.doi.org/10.1016/j.epsl.2005.10.004.

Martin, H., Moyen, J.-F., Guitreau, M., Blichert-Toft, J., Le Pennec, J.-L., 2014. Why Archaean TTG cannot be generated by MORB melting in subduction zones. Lithos 198, 1–13. http://dx.doi.org/10.1016/j.lithos.2014.02.017.

Miller, G.H., Stolper, E.M., Ahrens, T.J., 1991. The equation of state of a molten komatiite: 2. Application to komatiite petrogenesis and the Hadean Mantle. J. Geophys. Res. 96, 11,849. http://dx.doi.org/10.1029/91JB01203.

Monteux, J., Ricard, Y., Coltice, N., Dubuffet, F., Ulvrova, M., 2009. A model of metal–silicate separation on growing planets. Earth Planet. Sci. Lett. 287, 353–362.

Monteux, J., Jellinek, A.M., Johnson, C.L., 2011. Why might planets and moons have early dynamos? Earth Planet. Sci. Lett. 310, 349–359. http://dx.doi.org/10.1016/j.epsl.2011.08.014.

Mosenfelder, J.L., Asimow, P.D., Ahrens, T.J., 2007. Thermodynamic properties of Mg_2SiO_4 liquid at ultra-high pressures from shock measurements to 200 GPa on forsterite and wadsleyite. J. Geophys. Res., Solid Earth 112, B06208. http://dx.doi.org/10.1029/2006JB004364.

Mosenfelder, J.L., Asimow, P.D., Frost, D.J., Rubie, D.C., Ahrens, T.J., 2009. The $MgSiO_3$ system at high pressure: thermodynamic properties of perovskite, postperovskite, and melt from global inversion of shock and static compression data. J. Geophys. Res., Solid Earth 114, B01203. http://dx.doi.org/10.1029/2008JB005900.

Moyen, J.-F., Martin, H., 2012. Forty years of TTG research. Lithos 148, 312–336. http://dx.doi.org/10.1016/j.lithos.2012.06.010.

Nakagawa, T., Tackley, P.J., 2014. Influence of combined primordial layering and recycled MORB on the coupled thermal evolution of Earth's mantle and core. Geochem. Geophys. Geosyst. 15, 619–633. http://dx.doi.org/10.1002/2013GC005128.

Nakajima, M., Stevenson, D.J., 2015. Melting and mixing states of the Earth's mantle after the Moon-forming impact. Earth Planet. Sci. Lett. 427, 286–295. http://dx.doi.org/10.1016/j.epsl.2015.06.023.

Neumann, W., Breuer, D., Spohn, T., 2014. Differentiation of Vesta: implications for a shallow magma ocean. Earth Planet. Sci. Lett. 395, 267–280. http://dx.doi.org/10.1016/j.epsl.2014.03.033.

Nomura, R., Ozawa, H., Tateno, S., Hirose, K., Hernlund, J., Muto, S., Ishii, H., Hiraoka, N., 2011. Spin crossover and iron-rich silicate melt in the Earth's deep mantle. Nature 473, 199–202. http://dx.doi.org/10.1038/nature09940.

Press, W.H., Teukolsky, S.A., Vetterling, W.T., Flannery, B.P., 1993. Numerical Recipes in FORTRAN the Art of Scientific Computing, 2nd ed. Cambridge University Press, New York, NY, USA.

Ricard, Y., Šrámek, O., Dubuffet, F., 2009. A multi-phase model of runaway core–mantle segregation in planetary embryos. Earth Planet. Sci. Lett. 284, 144–150.

Ringwood, A.E., 1966. Chemical evolution of the terrestrial planets. Geochim. Cosmochim. Acta 30, 41–104. http://dx.doi.org/10.1016/0016-7037(66)90090-1.

Rizo, H., Boyet, M., Blichert-Toft, J., Rosing, M.T., 2013. Early mantle dynamics inferred from ^{142}Nd variations in Archean rocks from southwest Greenland. Earth Planet. Sci. Lett. 377, 324–335. http://dx.doi.org/10.1016/j.epsl.2013.07.012.

Rubie, D.C., Melosh, H.J., Reid, J.E., Liebske, C., Righter, K., 2003. Mechanisms of metal–silicate equilibration in the terrestrial magma ocean. Earth Planet. Sci. Lett. 205, 239–255.

Safronov, V.S., 1978. The heating of the earth during its formation. Icarus 33, 3–12. http://dx.doi.org/10.1016/0019-1035(78)90019-2.

Samuel, H., Tackley, P.J., Evonuk, M., 2010. Heat partitioning in terrestrial planets during core formation by negative diapirism. Earth Planet. Sci. Lett. 290, 13–19.

Shuvalov, V., 2009. Atmospheric erosion induced by oblique impacts. Meteorit. Planet. Sci. 44, 1095–1105. http://dx.doi.org/10.1111/j.1945-5100.2009.tb01209.x.

Simon, F., Glatzel, 1929. Fusion–pressure curve. Z. Anorg. Allg. Chem. 178, 309.

Solomatov, V., 2007. Magma Oceans and Primordial Mantle Differentiation. Schubert, G. (Ed.), Treatise of Geophysics, vol. 9. Elsevier.

Solomatov, V.S., 2000. Fluid dynamics of a terrestrial magma ocean. In: Canup, R.M., Righter, K., 69 collaborating authors (Eds.), Origin of the Earth and Moon. University of Arizona Press, Tucson, pp. 323–338.

Spiegel, E.A., 1971. Convection in stars: I. Basic Boussinesq convection. Annu. Rev. Astron. Astrophys. 9, 323. http://dx.doi.org/10.1146/annurev.aa.09.090171.001543.

Stixrude, L., de Koker, N., Sun, N., Mookherjee, M., Karki, B.B., 2009. Thermodynamics of silicate liquids in the deep Earth. Earth Planet. Sci. Lett. 278, 226–232. http://dx.doi.org/10.1016/j.epsl.2008.12.006.

Svetsov, V.V., 2005. Numerical simulations of very large impacts on the Earth. Planet. Space Sci. 53, 1205–1220. http://dx.doi.org/10.1016/j.pss.2005.04.011.

Tackley, P.J., 2012. Dynamics and evolution of the deep mantle resulting from thermal, chemical, phase and melting effects. Earth-Sci. Rev. 110, 1–25. http://dx.doi.org/10.1016/j.earscirev.2011.10.001.

Thomas, C.W., Asimow, P.D., 2013. Direct shock compression experiments on premolten forsterite and progress toward a consistent high-pressure equation of state for $CaO–MgO–Al_2O_3–SiO_2–FeO$ liquids. J. Geophys. Res., Solid Earth 118, 5738–5752. http://dx.doi.org/10.1002/jgrb.50374.

Thomas, C.W., Liu, Q., Agee, C.B., Asimow, P.D., Lange, R.A., 2012. Multi-technique equation of state for Fe_2SiO_4 melt and the density of Fe-bearing silicate melts from 0 to 161 GPa. J. Geophys. Res., Solid Earth 117, B10206. http://dx.doi.org/10.1029/2012JB009403.

Tonks, W.B., Melosh, H.J., 1990. The Physics of Crystal Settling and Suspension in a Turbulent Magma Ocean. Oxford University Press, pp. 151–174.

Tonks, W.B., Melosh, H.J., 1992. Core formation by giant impacts. Icarus 100, 326–346.

Tosi, N., Plesa, A.-C., Breuer, D., 2013. Overturn and evolution of a crystallized magma ocean: a numerical parameter study for Mars. J. Geophys. Res., Planets 118, 1512–1528. http://dx.doi.org/10.1002/jgre.20109.

Touboul, M., Puchtel, I.S., Walker, R.J., 2012. W-182 evidence for long-term preservation of early mantle differentiation products. Science 335 (6072), 1065–1069. http://dx.doi.org/10.1126/science.1216351.

Ulvrová, M., Labrosse, S., Coltice, N., Råback, P., Tackley, P.J., 2012. Numerical modelling of convection interacting with a melting and solidification front: application to the thermal evolution of the basal magma ocean. Phys. Earth Planet. Inter. 206, 51–66. http://dx.doi.org/10.1016/j.pepi.2012.06.008.

Čížková, H., van den Berg, A.P., Spakman, W., Matyska, C., 2012. The viscosity of Earth's lower mantle inferred from sinking speed of subducted lithosphere. Phys. Earth Planet. Inter. 200, 56–62. http://dx.doi.org/10.1016/j.pepi.2012.02.010.

Yoshino, T., Walter, M.J., Katsura, T., 2003. Core formation in planetesimals triggered by permeable flow. Nature 422, 154–157.

Geophysical Journal International

Geophys. J. Int. (2020) **221,** 1165–1181
Advance Access publication 2020 February 03
GJI Geodynamics and tectonics

doi: 10.1093/gji/ggaa064

A mushy Earth's mantle for more than 500 Myr after the magma ocean solidification

J. Monteux,[1] D. Andrault,[1] M. Guitreau,[1] H. Samuel[2] and S. Demouchy[1,3]

[1] *Université Clermont Auvergne, CNRS, IRD, OPGC, Laboratoire Magmas et Volcans, F*-63000 *Clermont-Ferrand, France. E-mail: julien.monteux@uca.fr*
[2] *Institut de Physique du Globe de Paris, Université Sorbonne Paris Cité,* 75005 *Paris, France*
[3] *Géosciences Montpellier – Université Montpellier & CNRS, F*-34095 *Montpellier, France*

Accepted 2020 January 24. Received 2020 January 22; in original form 2019 July 17

SUMMARY

In its early evolution, the Earth mantle likely experienced several episodes of complete melting enhanced by giant impact heating, short-lived radionuclides heating and viscous dissipation during the metal/silicate separation. After a first stage of rapid and significant crystallization (Magma Ocean stage), the mantle cooling is slowed down due to the rheological transition, which occurs at a critical melt fraction of 40–50%. This transition first occurs in the lowermost mantle, before the mushy zone migrates toward the Earth's surface with further mantle cooling. Thick thermal boundary layers form above and below this reservoir. We have developed numerical models to monitor the thermal evolution of a cooling and crystallizing deep mushy mantle. For this purpose, we use a 1-D approach in spherical geometry accounting for turbulent convective heat transfer and integrating recent and solid experimental constraints from mineral physics. Our results show that the last stages of the mushy mantle solidification occur in two separate mantle layers. The lifetime and depth of each layer are strongly dependent on the considered viscosity model and in particular on the viscosity contrast between the solid upper and lower mantle. In any case, the full solidification should occur at the Hadean–Eoarchean boundary 500–800 Myr after Earth's formation. The persistence of molten reservoirs during the Hadean may favor the absence of early reliefs at that time and maintain isolation of the early crust from the underlying mantle dynamics.

Key words: Numerical modelling; Heat flow; Rheology: Mantle; Dynamics: convection currents, and mantle plumes; Heat generation and transport.

1. INTRODUCTION

After the giant impact which led to the formation of the Earth–Moon system, the Earth's mantle was likely completely molten (e.g. Nakajima & Stevenson 2015). During the subsequent Magma Ocean (MO) stage, the Earth's early mantle undergone a rapid global cooling until its melt fraction decrease to a critical value φ_c ($\approx$40%) associated with a major increase of its viscosity (Solomatov 2007; Monteux *et al.* 2016). This step was followed by a slow cooling stage that triggered a complete crystallization of the silicate mantle (Solomatov 2007). This second cooling stage could have lasted hundreds of Ma, or even a couple of Ga as its dynamics was governed by the rheology of the slowly deforming solid-like mantle, in contrast to the first one which was driven by the magma viscosity (Solomatov 2007; Ulvrová *et al.* 2012; Monteux *et al.* 2016).

Recent experimental results have shown that the upper mantle solidus is at lower temperature than previously expected for a chondritic composition (Andrault *et al.* 2018). According to this study, such a solidus associated with a hotter earlier mantle would enable the presence of a deep and persistent molten layer in the Archean mantle. The progressive solidification of this melt layer could have enhanced the mechanical coupling between the lithosphere and the asthenosphere. Such a change might explain the transition from surface dynamics dominated by a stagnant lid to modern plate tectonics with deep-slab subductions. Assuming that the intersect between the mantle solidus and an adiabat temperature profile with a potential surface temperature corresponding to a surface melt fraction of $\varphi_c \approx 40\%$ could constrain the depth of the bottom of the remaining partially molten layer, Solomatov (2007) obtained a depth $\approx$300 km. In the case of bottom-up solidification of a mushy mantle, the depth of the last remaining partially molten layer should, hence, be smaller than 300 km and the full mantle crystallization should occur within $\approx$1 Ga (Sleep *et al.* 2014).

The depth at which the full crystallization is reached is likely governed by (1) the solidus temperature which controls the depth and temperature of solidification, (2) the thickness of the top thermal boundary layer (TBL), where heat convecting from the deep mantle is transferred to the surface by conduction and (3) the temperature contrast on both sides of the TBL which controls the efficiency of heat evacuation. In the mushy regime, the mantle viscosity is a

key parameter, which governs mantle dynamics and the formation of TBLs. This day viscosity of the Earth's mantle is difficult to constrain, particularly in the lower mantle (Čížková *et al.* 2012), and the value of the viscosity of the Earth's early mantle prior to the occurrence of major differentiation events is even more hypothetical. Constraining the value of this physical quantity is of first importance, since deep mantle viscosity likely governs the initiation of major geological features, such as plate tectonics and mantle plumes (Sleep 2014; Foley *et al.* 2014).

We have developed a numerical model to monitor the cooling, and crystallization of an isochemical mantle, starting from a partially molten stage. We aim to characterize the influence of the viscosity of the solid early mantle on its cooling dynamics. In particular, we tested the impact of variation in activation energy and the viscosity prefactor, as well as monitored the cooling and crystallization processes to determine the solidification timescales and the depths at which the last melt fraction solidifies.

2. MODEL

We considered the cooling of a partially molten magma ocean with an initial depth of 2900 km, which we modelled using a thermal evolution described below.

2.1 Thermal evolution model

2.1.1 Heat transfer model

We used a 1-D spherical approach (e.g. Abe 1997; Laneuville *et al.* 2018) accounting for turbulent convective heat transfer (e.g. Abe 1997; Monteux *et al.* 2016; Bower *et al.* 2018). This approach is relevant for the ranges of low viscosities and high Rayleigh numbers expected within a partially molten planetary mantle which are difficult to numerically resolve in 2-D and 3-D spatial domains. Indeed, even if *Ra* numbers are lower during the mushy stage than during the magma ocean stage, *Ra* numbers are still too high (up to 10^{30}) to correctly solve the TBLs in such a dynamic reservoir. Moreover, molten reservoirs may survive during the early thermal evolution of the mushy mantle. In these regions, the melt fraction can reach values larger than 40% with very low associated viscosity of the mushy material, making the local Rayleigh number too high for 2-D or 3-D computational domains.

Our numerical model solves the following heat equation:

$$\rho C_p \frac{\partial T}{\partial t} = \nabla.(k\nabla T) + \rho H, \tag{1}$$

where ρ is the density, C_p is the heat capacity, T is the temperature and H is the heat production from radiogenic sources. k is an 'effective' conductivity defined as:

$$k = k_c + k_v, \tag{2}$$

with k_v the effective conductivity relative to thermal convection of the mushy material is:

$$k_v = \frac{F_{\text{conv}} L}{\Delta T}, \tag{3}$$

F_{conv} is the convective heat flux accounting for thermal buoyancy, L is the thickness of the Earth's mantle and k_c the intrinsic thermal conductivity of the material ($k_c = 5$ W.m^{-1}.K^{-1}).

For mantle convection to occur, the temperature gradient must be larger than the adiabatic gradient:

$$\left(\frac{\mathrm{d}T}{\mathrm{d}r}\right)_S = \frac{-\alpha g T}{C_p}. \tag{4}$$

When the temperature gradient is subadiabatic, the mantle heat is transported only by conduction, and $k = k_c$. When the temperature gradient is superadiabatic, the mantle is convecting. The convective heat flux F_{conv} depends on the local Rayleigh number *Ra*:

$$Ra = \frac{\alpha g C_p \rho^2 \Delta T L^3}{k_c \eta}, \tag{5}$$

where α is the thermal expansion coefficient of the mushy material, g is the gravitational acceleration assumed to be constant through the whole mantle and η is the local dynamic viscosity. In eq. (5), k_c is constant, C_p is a function of the melt fraction, α and ρ vary with depth and melt fraction. η varies with depth, temperature and melt fraction. ΔT is the thermal driving force for the convection, therefore the temperature difference between the surface and the core–mantle boundary (CMB) minored by the increase of temperature along the mantle adiabat. Mantle dynamics and cooling is also governed by the Prandtl number, *Pr*:

$$Pr = \frac{\eta C_p}{k_c}, \tag{6}$$

which is the ratio of the momentum diffusivity over the thermal diffusivity. *Pr* is calculated at each depth using the local viscosity value η. Depending on the values of *Pr* and *Ra*, two flow regimes arise and as a consequence two convective heat fluxes:

(1) a soft turbulent regime where the corresponding convective heat flux is (Solomatov 2007; Monteux *et al.* 2016):

$$F_{\text{conv}} = \frac{0.089 k_c \Delta T Ra^{1/3}}{L} \text{ if } Ra < 10^8 Pr^{5/3}; \tag{7a}$$

(2) and a hard turbulent regime (following Solomatov 2007; Monteux *et al.* 2016) where:

$$F_{\text{conv}} = \frac{0.22 k_c \Delta T Ra^{2/7} Pr^{-1/7}}{L} \text{ if } Ra > 10^8 Pr^{5/3}. \tag{7b}$$

In our numerical model, we compare the temperature gradient to the adiabatic gradient. If the temperature gradient is larger, k_v is calculated according to eq. (3). If the temperature gradient is lower, $k = k_c$.

2.1.2 Boundary and initial conditions

The large impacts, radiogenic heating and the energy dissipated during metal-silicate separation control the early thermal state of the core. The core temperature at the end of the magma ocean stage is governed by the heat accumulated in this reservoir during its formation but also by the efficiency of the magma ocean to retain heat within the core by forming thick TBLs (Monteux *et al.* 2016). The core heat flow at the CMB can be expressed as:

$$F_{\text{core}} = \frac{k_c \left(T^{\text{core}} - T_{\text{CMB}}^{mantle}\right)}{\delta_{\text{TBL,bot}}}, \tag{8}$$

where T^{core} is the average core temperature just below the CMB (i.e. here, a TBL within the core is not considered) and $T_{\text{CMB}}^{\text{mantle}}$ is the mantle temperature above the CMB. $\delta_{\text{TBL,bot}}$ is the thickness of the TBL at the bottom of the mantle where the heat is extracted from the core by conduction. $T_{\text{CMB}}^{\text{mantle}}$ is calculated form eq. (1) whereas T^{core}

is obtained by the integration of the following differential equation:

$$V_{\rm core}\rho_{\rm Fe}C_{p,{\rm Fe}}\frac{{\rm d}T^{\rm core}}{{\rm d}t} = S_{\rm core}\ F_{\rm core}, \tag{9}$$

where $V_{\rm core}$ is the core volume, $S_{\rm core}$ is the core surface, $\rho_{\rm Fe}$ is the core density, $C_{p,{\rm Fe}}$ is the core heat capacity. This formulation does not consider the increase in adiabatic temperature within the core but allows following the evolution of core temperature right below the CMB as a function of time, based on the CMB heat flux. The error associated with this simplification (which in the case of an Earth-like body would amount to less than 10%) is small compared to uncertainties in other model parameters.

The efficiency of mantle cooling also depends on the heat transfer at the surface. During the magma ocean cooling, heat is efficiently radiated toward space, but the formation of a primitive atmosphere may significantly slow down the cooling. With a primitive atmosphere composed of 300 bars H_2O and 100 bars CO_2 overlaying the magma ocean, Lebrun *et al.* (2013) estimated that the surface temperature remains constant throughout the entire duration of the mushy stage at $T_{\rm surf} \approx 500$ K. Sleep *et al.* (2014) also showed that the surface temperature during the mushy stage was maintained at ≈500 K for 1000 bars and 100 bars atmospheres in equilibrium with bulk silicated magmas.

2.1.3 TBLs parametrization

Monteux *et al.* (2016) showed that the initial core heat can only be efficiently retained within the core when the bottom TBL thickness ($\delta_{\rm TBL,bot}$) is larger than ≈100 m. For $\delta_{\rm TBL,bot} < 100$ m the thermal coupling between the core and the MO is important and the core's heat is efficiently transferred to the mantle during the short timescales of the MO cooling. For $\delta_{\rm TBL,bot} < 1$ m, the core rapidly cools down to ≈4400 K, which corresponds to the core-mantle boundary temperature at a critical melt fraction $\varphi = \varphi_{\rm crit}$. Actually, the thicknesses of both the bottom and top TBL are governed by the cooling dynamics of the mantle (Solomatov 1995). The formation of a TBL is induced by the velocity field decrease close to the boundary. In 1-D models, the TBL cannot form numerically by themselves because the velocity field is not calculated and, hence, it has to be parametrized. Moreover, as we consider a compressible fluid with properties changing with depth, the top and bottom TBL do not have the same thicknesses. In our models, we consider that the thermal boundary thickness scale as (Grott & Breuer 2008):

$$\delta_{\rm TBL} = L\left(\frac{Ra_{\rm crit}}{\overline{Ra}}\right)^{1/3}, \tag{10}$$

with $Ra_{\rm crit} = 450$ (Choblet & Sotin 2000) and $\overline{Ra}$ is the Rayleigh number value calculated using eq. (5) and the characteristic parameters corresponding to either the top or the bottom of the magma ocean, for upper and lower TBL, respectively. It results in a TBL thicker at the top of the mantle, than at the bottom of the mantle. Strictly, the value of $Ra_{\rm crit}$ should be different when considering the upper or lower TBL (Thiriet *et al.* 2019). The value of 450 is adapted for the upper mantle. For the lower mantle, it should be expressed as a function of the internal Rayleigh number (Deschamps & Sotin 2000). We have implemented such a parametrization in our models. Our numerical tests (not shown here) show that the bottom TBL thickness derived from Deschamps & Sotin (2000) leads to a decrease of the bottom TBL thickness, but does not change significantly the solidification depth and time scales. Hence, we used $Ra_{\rm crit} = 450$ for both top and bottom TBL calculations. Within the TBLs, the heat is transferred by conduction and, again, $k = k_c$. In all the models presented here, the TBL thickness has a thickness larger than 10 km, therefore given our 1-km grid spacing, at least 10 gridpoints are used to identify and characterize the heat transfer in the TBL.

2.2 Geochemical model and derived parameters

Despite the difficulty to characterize the chemical composition of the Earth's early mantle, a consensus has emerged that Earth's mantle should be of chondritic composition (e.g. Mc Donough & Sun 1995; Javoy *et al.* 2010; Palme & O'Neill 2014). Still, chondrites present a large diversity in major, minor and trace element compositions. According to several isotopic tracers, Earth has accreted from a large majority of building blocks typical of high-enstatite chondrites (EH, Javoy *et al.* 2010). Then, late-accretion processes and core–mantle differentiation (Rubie *et al.* 2011) have induced a drift of the bulk mantle composition to an MgO-enriched composition, compared to EH (e.g. Mc Donough & Sun 1995; Palme & O'Neill 2014). In the following section, we detail our chemical model for the mushy mantle following the magma ocean stage.

2.2.1 Radiogenic heating

Short timescales inferred for the duration of the magma ocean stage appear comparable to the timescales for the decay of short-lived radionuclides such as ^{26}Al. However, large bodies such as the proto-Earth, or the Theia Earth's impactor, appeared only much later, from the accretion of pre-differentiated planetesimals. Therefore, only the long-lived radiogenic elements, such as ^{238}U, ^{235}U, ^{232}Th and ^{40}K can provide heat at the long time scale corresponding to the cooling of the mushy mantle. In our models, we consider the radiogenic heating from these radionuclides in eq. (1) assuming that the abundance of these elements in the primitive mantle is similar to the concentration in EH-chondrites (Javoy 1999). The radiogenic heat production rate is computed as:

$$H = \Sigma A_i\,[{\rm i}]\,H_i \exp\left(-\lambda_i\,(t - t_0)\right), \tag{11}$$

where the meaning of A_i, E_i, H_i, λ_i is detailed in Table 1.

2.2.2 Solidus and liquidus temperatures

The chemical composition of the mantle governs its melting properties, based on its solidus and liquidus profiles. The latter plays a major role in the early thermal evolution of the magma ocean, because it defines the temperature and the depth at which crystallization starts. Laboratory experiments have constrained the liquidus and solidus of mantle-like material up to pressures compatible with the CMB conditions (Fiquet *et al.* 2010; Andrault *et al.* 2011). We performed calculations using the melting curves derived from chondritic-type mantle composition from Andrault *et al.* (2011, Fig. 1). The experimental solidus and liquidus profiles are fitted with a modified Simon and Glatzel equation (Simon & Glatzel 1929). For pressures P below 24 GPa, we use solidus and liquidus temperatures of chondritic mantle reported from Andrault *et al.* (2018):

$$T_{\rm sol} = 1373.\left(\frac{P}{0.82\ \times 10^9} + 1\right)^{(1/6.94)}, \tag{12a}$$

$$T_{\rm liq} = 1983.4\left(\frac{P}{6.48\ \times 10^9} + 1\right)^{(1/5.35)}. \tag{12b}$$

Table 1. Radiogenic heat sources and characteristics (from Javoy 1999).

Isotope/element	Half-life (λ_i) (yr)	Heat production per unit mass of isotope (H_i) (W kg^{-1})	Natural Abundance (A_i) (%)	Present-day concentrations ([i]) (ppm wt.)
^{238}U	4.46×10^9	9.17×10^{-5}	99.28	
^{235}U	7.04×10^8	5.75×10^{-4}	0.72	
U				0.20
^{232}Th	1.4×10^{11}	2.56×10^{-5}	100	
Th				0.069
^{40}K	1.26×10^9	2.97×10^{-5}	0.0117	
K				270

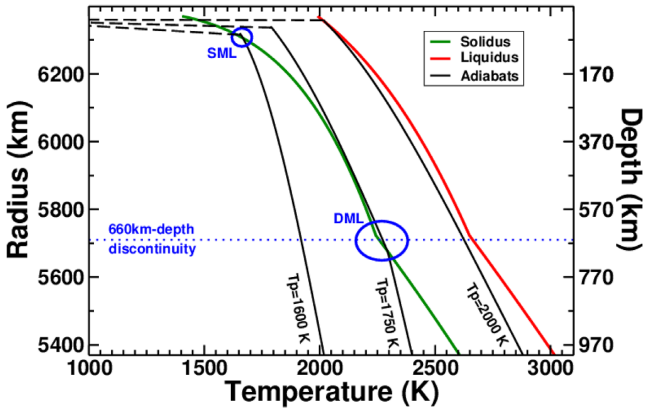

Figure 1. Solidus (green) and liquidus (red) (computed from eq. 12) as a function of the Earth's radius. Black solid lines show adiabatic temperature profiles (computed from eqs 4 and 18) with three different potential temperatures (1600, 1750 and 2000 K). Note that these three temperature profiles are arbitrary and do not result from our numerical model. The blue dashed line separates the upper and lower mantle. The dashed lines correspond to the hypothetic conductive temperature profiles in the top thermal boundary layer (i.e. recalculated at each step of our modelling procedure). The two ellipsoids illustrate critical points where deep and shallow last molten layers should solidify (SML, shallow mantle layer and DML, deep mantle layer).

For pressures larger than $P = 24$ GPa, we use results from Andrault *et al.* (2011):

$$T_{\rm sol} = 1334.5\left(\frac{P}{9.63 \times 10^9} + 1\right)^{(1/2.41)}, \tag{12c}$$

$$T_{\rm liq} = 1862.\left(\frac{P}{21.15 \times 10^9} + 1\right)^{(1/2.15)}. \tag{12d}$$

Mantle solidification may induce some chemical fractionation. In such case, the melting curves may evolve (Andrault *et al.* 2017). Major changes concern the liquidus temperature, which increases with the $MgSiO_3$-content in the mantle. On the other hand, the mantle's solidus is almost independent of composition. These effects are not accounted in our study, because there is an insufficient knowledge on melting properties as a function of pressure, temperature and mantle composition.

2.2.3 *Thermodynamic parameters*

Thermodynamic parameters of the magma ocean depend of its chemical composition. Volumetric and elastic parameters of silicate liquids have been characterized up to a pressure of 140 GPa using shock compression experiments (Mosenfelder *et al.* 2007, 2009; Thomas *et al.* 2012; Thomas & Asimow 2013). Here we assume a multicomponent system with a chondritic-type composition (62% enstatite + 24% forsterite + 8% fayalite + 4% anorthite + 2% diopside). Using fourth-order Birch-Murnaghan/Mie-Grüneisen equation of state fits for molten silicate liquids from Thomas & Asimow (2013), we obtain the melt density $\rho_{\rm m}$, the volumetric thermal expansion α as a function of pressure as well as the specific heat C_p of the molten material for a chondritic multicomponent assemblage. The density of the solid phase is then calculated as:

$$\rho_s = \rho_m + \Delta\rho, \tag{13}$$

with $\Delta\rho$ being the density difference between solid and liquid phases which is fixed to 64 kg m^{-3} (Monteux *et al.* 2016).

For a partially molten material, the density ρ', the coefficient of volumetric thermal expansion α' and the specific heat C'_p are given as follows (Solomatov 2007):

$$\frac{1}{\rho'} = \frac{1-\varphi}{\rho_s} + \frac{\varphi}{\rho_m}, \tag{14}$$

$$\alpha' = \alpha + \frac{\Delta\rho}{\rho\left(T_{\rm liq} - T_{\rm sol}\right)}, \tag{15}$$

$$C'_p = C_p + \frac{\Delta H}{T_{\rm liq} - T_{\rm sol}}, \tag{16}$$

where ΔH is the latent heat released during solidification, and φ is the melt fraction:

$$\varphi = \frac{T - T_{\rm sol}}{T_{\rm liq} - T_{\rm sol}}. \tag{17}$$

2.2.4 *Adiabats*

In vigorously convecting systems such as magma oceans, the temperature distribution is nearly adiabatic (Solomatov 2007). For one-phase systems, such as a completely molten or a completely solid layer, eq. (4) gives the equation for an adiabat. In two-phase systems (liquid + solid), the effects of phase changes need to be considered (Solomatov 2007). The equation for such adiabat follows:

$$\left(\frac{{\rm d}T}{{\rm d}r}\right)_S = \frac{-\alpha' g T}{C'_p}. \tag{18}$$

This results in an increase of the adiabat gradient at depth where the two phases coexist, compared to the purely liquid or solid one-phase adiabats (Solomatov 2007). Fig. 1 compares three adiabatic temperature profiles and the melting curves used in our study. The adiabatic temperature profiles are calculated by numerical integration of eqs (4) and (18) using a fourth-order Runge–Kutta method

(Press *et al.* 1993*)*. These adiabatic temperature profiles are used to calculate at each depth, and when it is super-adiabatic, the temperature difference ΔT from eq. (5).

2.2.5 Assumptions

During the solidification of the early mantle (i.e. the magma ocean and mushy mantle stages) chemical fractionation may occur between compatible and incompatible elements that partition preferentially into solid and liquid phases, respectively. Initially, the bridgmanite grains are denser than the liquid and they could fall toward the core–mantle boundary. Then, after a significant fraction of the MO is crystallized, the liquid could become denser as iron is a relatively incompatible element in mantle minerals. This could produce late mantle overturns (e.g. Boukaré *et al.* 2015). Such chemical differentiations could also induce heterogeneous distribution of radiogenic elements due to their incompatible behaviour. Still, the early chemical fractionation of the Earth's mantle history remains debated, based on contradictory geodynamical (Solomatov 2000) and geochemical (Mc Donough & Sun 1995*;* Boyet & Carlson 2005*;* Palme & O'Neill 2014) arguments. Therefore, we do not consider chemical differentiation in the solidifying mushy mantle in this study. Hence, melting curves, density and concentration of radiogenic elements are considered unchanged along the cooling process.

2.3 Viscosity model

Viscosity governs mantle cooling dynamics, which is strongly dependent on the melt fraction φ. In our study we consider that φ is a linear function of the temperature difference between the liquidus and the solidus (eq. 17). In the following section, we detail the parametrization used to compute the viscosity in our numerical models.

2.3.1 Liquid fraction viscosity ($\varphi = 1$)

During the cooling of a mushy mantle, the melt fraction globally decreases; however, locally, mantle layers may remain largely molten for a long period of time. Therefore, a mushy mantle may locally be extremely turbulent because of the low viscosity of the molten mantle material (Cochain *et al.* 2017). For the fully molten mantle (i.e. when $\varphi = 1$), we consider that its viscosity is equal to the viscosity reported for liquid $MgSiO_3$ (Karki & Stixrude 2010):

$$\eta = \eta_l = \exp\left(-7.75 + 0.005P(\text{GPa}) - 0.00015P(\text{GPa})^2 + \frac{5000 + 135P(\text{GPa}) + 0.23P(\text{GPa})^2}{T - 1000}\right). \quad (19a)$$

2.3.2 Solid fraction viscosity ($\varphi = 0$)

The viscosity of the solid fraction within the early Earth's deep mantle is a key parameter, which governs its cooling efficiency during the mushy stage. However, such a quantity is poorly constrained for a chondritic mantle. Instead, the viscosity of a deep 'bridgmanite-bearing' mantle has become increasingly documented (e.g. Boioli *et al.* 2017; Reali *et al*. 2019). Due to the absence of seismic anisotropy in the current lower mantle, diffusion creep was generally considered to be the dominant deformation mechanism at these depths (e.g. Karato & Li 1992), however, recent results advocate for diffusion-driven pure dislocation climb creep as a main deformation mechanism for bridgmanite (e.g. Boioli *et al.* 2017; Reali *et al*. 2019). During the early Earth's history, the mantle temperatures were hotter, and ionic diffusion (thus diffusion creep) is expected to have been even more important in the solid mantle fraction (e.g. Frost & Ashby 1982) for both upper and lower mantle. Therefore, we assume here that the deformation of the interconnected solid phase occurs via diffusion creep only. We neglect the possible effect of polymineralic aggregates as one phase is expected to be volumetrically abundant (olivine or bridgmanite in the upper or lower mantle, respectively, see Ji *et al.* 2001*;* Huet *et al.* 2014). Hence for $\varphi = 0$:

$$\eta = \eta_s = \frac{1}{A_{\text{diff}}} \exp\left(\frac{E_{\text{diff}} + PV_{\text{diff}}}{RT}\right), \quad (19b)$$

with P the pressure, R the gas constant ($= 8.314$ J K^{-1} mol^{-1}) and T the absolute temperature. A_{diff} is the viscosity pre-factor, which includes grain-size sensitivity. Here the grain size is kept constant, as well as the grain size exponent (i.e. equals to 3). E_{diff} is the activation energy, and V_{diff} is the activation volume for diffusion creep.

In addition, we considered E_{diff}, V_{diff} and A_{diff} values based on two requirements: (1) the values of the rheological parameters must be compatible with those derived from experiments (e.g. Hirth & Kohlstedt 2003 for dry olivine/upper mantle, and Xu *et al.* 2011 for the bridgmanite/lower mantle), (2) the calculated viscosity profile corresponding to a realistic present-day Earth mantle geotherm [for an adiabatic temperature profile with $T_p = 1600$ K (Tackley 2012) and references therein] and a PREM pressure profile in eq. (19b), must be compatible with viscosity profiles constrained by geoid and postglacial rebound [see Čížková *et al.* (2012) and references therein, Fig. 2 and Table 2].

In our calculations, we also investigate the potential role of the upper mantle, which presents a different mineralogy and, therefore, distinct rheological properties. For the sake of simplicity, we did not implement a transition zone (composed of wadsleyite (410–520 km) and ringwoodite (520–660 km). The mineralogical transition from olivine to bridgmanite significantly increases the viscosity of the mantle, which in turn could affect the ability of the mantle to lose its primordial heat. The rheological parameters for the upper mantle (whenever considered) are listed in Table 2.

2.3.2 Viscosity of the partially molten mantle ($0 \leq \varphi \leq 1$)

During the solidification of the mushy mantle, the fraction of solid material increases until reaching a threshold ($\varphi = \varphi_{\text{crit}}$), which separates the turbulent regime from viscous regime (Solomatov 2015). For $\varphi_{\text{crit}} < \varphi < 1$, the viscosity of the highly molten material scales with the viscosity of the molten mantle η_l (Roscoe 1952):

$$\eta = \frac{\eta_l}{\left(1 - \left(\frac{1-\varphi}{1-\varphi_{\text{crit}}}\right)\right)^{2.5}}. \quad (19c)$$

As soon as the melt fraction threshold is reached at any mantle depth, the cooling efficiency of the primitive mantle significantly reduces, even if the mantle remains partially molten at other depths (Monteux *et al.* 2016). In a mushy mantle context where most of the material is solid, the viscosity is still strongly influenced by the fraction of the molten material φ. For $0 < \varphi < \varphi_{\text{crit}}$ the partially molten viscosity scales with the solid mantle viscosity η_s:

$$\eta = \eta_s \exp\left(-\alpha_n \varphi\right), \quad (19d)$$

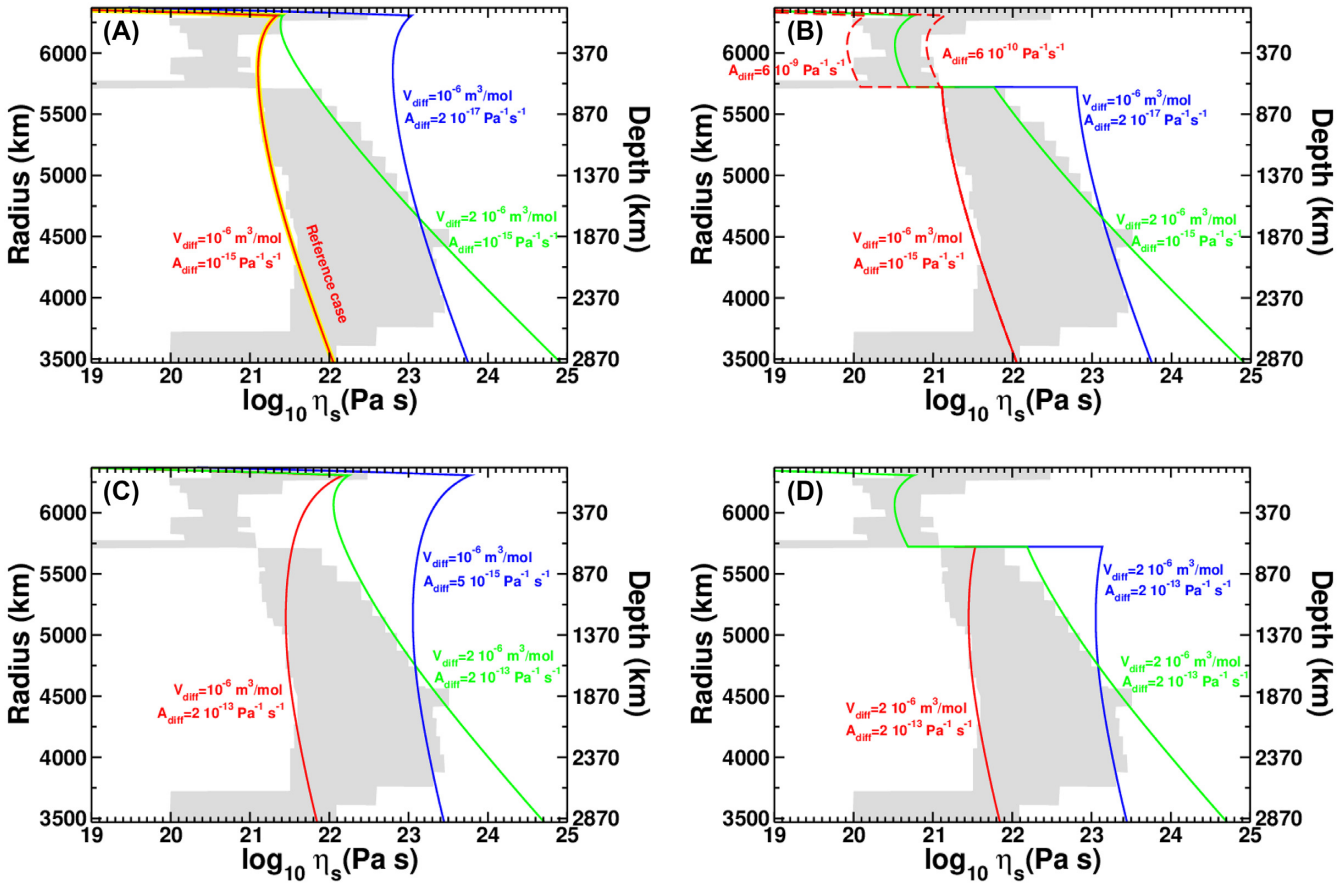

Figure 2. The different mantle viscosity profiles considered in our models for the solid phase, computed using eq. (19b). Upper panels, $E_{\rm diff} = 200$ kJ mol^{-1} (with reference case highlighted in yellow) and lower panels $E_{\rm diff} = 300$ kJ mol^{-1}. Grey domain viscosity models from geoid inversion and post-glacial rebound [Čížková *et al.* (2012) and references therein]. Left-hand frame: no viscous dichotomy between the upper and lower mantle is considered. Right-hand frame: when a different upper mantle is considered. We performed calculations for $A_{\rm diff}$ and $V_{\rm diff}$ ranging from 2×10^{-17} to 2×10^{-13} Pa^{-1}s^{-1} and 10^{-6} to 2×10^{-6} Pa^{-1}s^{-1}, respectively (Table 2). In the B-frame, we have also studied the influence of the upper mantle viscosity with $A_{\rm diff}$ ranging from 6×10^{-10} to 6×10^{-9} Pa^{-1}s^{-1}. The viscosity profiles (red, green and blue lines) are calculated considering an adiabatic temperature profile with $T_p = 1600$ K from the surface of the Earth to the CMB, thus neglecting the presence of top and bottom boundary layers for the figure readability.

Table 2. Values used in eq. (19b) to calculate the solid mantle viscosity.

Lower 'bridgmanite-like' mantle rheology:			
$A_{\rm diff}$	Pre-exponential parameter for diffusion creep	2×10^{-17} to 2×10^{-13}	Pa^{-1}s^{-1}
$E_{\rm diff}$	Activation energy for diffusion creep	200 (Čížková *et al.* 2012) 300 (Xu *et al.* 2011)	kJ mol^{-1}
$V_{\rm diff}$	Activation volume for diffusion creep	1×10^{-6} to 2×10^{-6}	m^3 mol^{-1}
Upper mantle rheology (dry olivine, grain size = 15 μm):			
$A_{\rm diff}$	Pre-exponential parameter for diffusion creep	6×10^{-9} to 6×10^{-10}	Pa^{-1}s^{-1}
$E_{\rm diff}$	Activation energy for diffusion creep	375 (Hirth & Kohlstedt 2003)	kJ mol^{-1}
$V_{\rm diff}$	Activation volume for diffusion creep	2.5×10^{-6} (Hirth & Kohlstedt 2003)	m^3 mol^{-1}

with α_n the coefficient in melt fraction-dependent viscosity. The latter equals 26 for deformation via olivine diffusion creep mechanism under anhydrous conditions (Mei *et al.* 2002).

2.4 Numerical model

We model the thermal evolution of a 2900-km-thick isochemical silicate mantle overlying an iron core by solving for the conservation of energy (eq. 1) in a 1-D, spherically symmetric domain (with a radius ranging from 3500 to 6400 km). To this end, we used a modified version of the numerical model developed in Monteux *et al.* (2016). Eq. (1) is discretized using a semi-implicit predictor–corrector Finite Difference scheme, of second-order in both space and time (Press *et al.* 1993). Our numerical scheme was successfully benchmarked against steady and unsteady analytical solutions for diffusion problems (Crank 1975). We have also successfully benchmarked our physical model with 3-D spherical calculations at both steady and transient states from the models developed by Wagner *et al.* (2019)

Table 3. Parameter values used to calculate the viscosity of the lower mantle. Viscosity layering means that we consider an upper mantle in our model.

Series #	Viscosity layering	E_{diff} (kJ mol^{-1})	V_{diff} (m^3 mol^{-1})	A_{diff} (Pa^{-1} s^{-1})
1	No	200	1×10^{-6}–2×10^{-6}	2×10^{-17}–1×10^{-15}
2	Yes	200	1×10^{-6}–2×10^{-6}	2×10^{-17}–1×10^{-15}
3	No	300	1×10^{-6}–2×10^{-6}	5×10^{-15}–2×10^{-13}
4	Yes	300	1×10^{-6}–2×10^{-6}	5×10^{-15}–2×10^{-13}

considering a relatively lower *Ra* number and a smaller viscosity contrast (see the Appendix). The mantle is discretized using 2900 equally spaced gridpoints resulting in a constant spatial resolution $\delta r = 1$ km. The variable time step is set as $\delta t = \min(\delta r^2/\kappa(r))$, where $\kappa(r) = k/(\rho Cp)$ is the effective diffusivity. The boundary conditions in our models are those described in Section 2.1.2: isothermal at the surface with $T_{surf} = 500$ K and variable heat flux accounting for heat transfer between the core and the mantle at the CMB. In all our models, the core temperature below and just above the CMB are initialized to the same value ($T_{0,core} = 4370$ K).

3. RESULTS: COOLING AND SOLIDIFICATION DYNAMICS

3.1 A reference case

We followed the thermal evolution of a deep mushy ocean with an initial temperature profile corresponding to a melt fraction of 40% throughout the whole mantle. As a reference case, we considered the chondritic-type mantle from Series 1 with $A_{diff} = 10^{-15}$ Pa^{-1}s^{-1} and $V_{diff} = 10^{-6}$ m^3 mol^{-1} through the whole mantle (see Table 3). This reference case represents a lower bound in terms of viscosity (Fig. 2). The temperature initially decreases rapidly from the surface where heat is efficiently extracted by conductive cooling, and where a thin TBL initially forms (Fig. 3). In the deepest part of the mantle, the temperature profile bends towards an adiabatic temperature profile, which is more vertical than the solidus profile. As a consequence, the solidification front starts from the lowermost mantle. After 100 Myr, most of the lower mantle temperatures lie below the solidus, nevertheless two molten reservoirs remain (named hereafter SML and DML). Fig. 3 (bottom panels) shows that 270 Myr after the beginning of our simulation, the deeper one (DML) is located at a depth centred at 650 km, and the depth of shallower one (SML) ranges between 20 and 60 km. Full solidification of DML occurs prior to that of SML. Finally, after 900 Myr of cooling, the entire temperature profile is below the solidus, but remains super adiabatic,

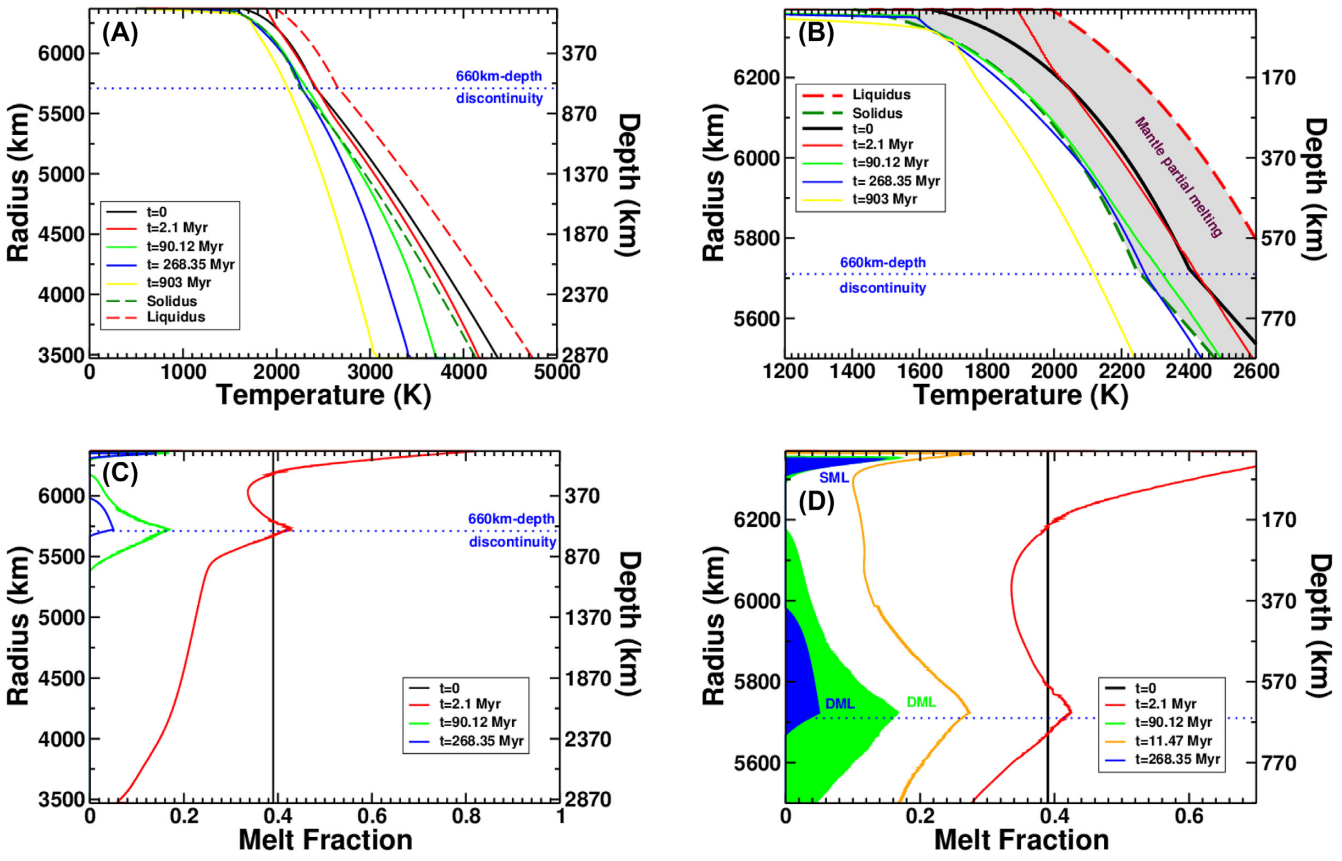

Figure 3. Upper panels: temperature time evolution as a function of depth. Lower panels: melt fraction time evolution as a function of depth. In this reference case (Series 1, $A_{diff} = 10^{-15}$ Pa^{-1} s^{-1} and $V_{diff} = 10^{-6}$ m^3 mol^{-1}), no dichotomy in the viscosity model is considered between the upper and lower mantle. The blue dashed line separates the upper and lower mantle. The right-hand panels represent close-up views of the left-hand panels. When $t > 90$ Myr, the partially molten layer is separated in 2 layers: SML and DML.

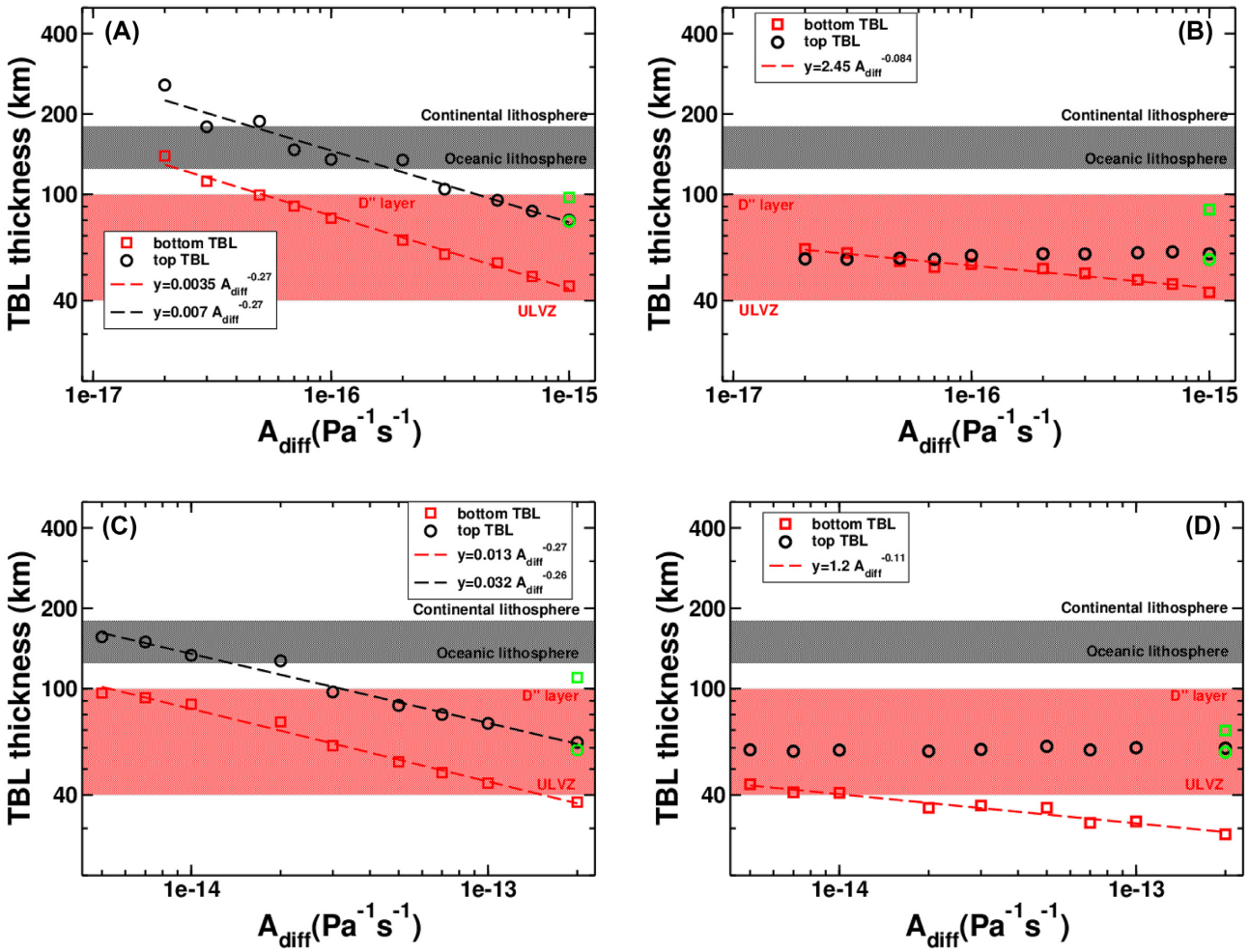

Figure 4. Thickness of the top (circles) and bottom (squares) thermal boundary layer when the mushy mantle is fully solidified as a function of $A_{\rm diff}$ and $E_{\rm diff}$ (i.e. $E_{\rm diff} = 200$ kJ mol^{-1} for top figures or $E_{\rm diff} = 300$ kJ mol^{-1} for bottom figures). The A, B, C, D panels correspond to Series 1, 2, 3, 4, respectively (see Tables 2 and 3 for complete set of parameter values). The cases with $V_{\rm diff} = 10^{-6}$ m^3 mol^{-1} are illustrated with red (bottom TBL) and black (top TBL) symbols and cases with $V_{\rm diff} = 2 \times 10^{-6}$ m^3 mol^{-1} are illustrated with green symbols. Dashed lines represent power law fits to the thermal evolution data points.

especially in the mid-top mantle. This solidification timescale is in good agreement with the timescale proposed by Solomatov (2000), where the complete crystallization of the shallow early mantle could last more than 10^8 yr.

3.2 Influence of the viscosity parameters on the mushy mantle solidification

3.2.1 TBL thicknesses

From the initial thermal state, two TBLs rapidly form above and below the convecting portion of the mantle. Upon cooling, the Rayleigh number within the convecting mantle decreases and the two boundary layers thicken following the scaling used in eq. (10). Therefore, the thickness of the boundary layers scales with $Ra^{-1/3}$ and as a consequence scales with $\eta^{1/3}$ and $A_{\rm diff}^{-1/3}$. In Fig. 4, we plotted both the bottom (red) and top (black) boundary layer thicknesses at the end of the mushy stage (i.e. as soon as the mantle reaches complete solidification) as a function of the viscosity exponential pre-factor ($A_{\rm diff}$) and for two different values of the activation energy ($E_{\rm diff}$) and activation volume ($V_{\rm diff}$). Our results show that the evolution of the TBL thickness is strongly dependent on the value of the activation energy ($E_{\rm diff} = 200$ or 300 kJ mol^{-1}) and on $A_{\rm diff}$ as illustrated in Fig. 4. For Series 1 (Fig. 4a), both the top and bottom boundary layer thicknesses scale with $A_{\rm diff}^{-0.27}$, which is close to the theoretical scaling of $A_{\rm diff}^{-1/3}$ for an entirely solid mantle. This indicates that the viscosity of the solid mantle governs the thickness of the two TBL. At the end of the mushy stage, the top boundary layer thickness ranges between 80 and 250 km, whereas the bottom boundary layer thickness ranges between 45 and 140 km. For Series 3 (Fig. 4c), the behaviour of the bottom TBL thickness is similar to the Series 1 cases. The bottom TBL thickness decreases as $A_{\rm diff}^{-0.26}$ with corresponding values ranging from ≈40 to ≈100 km, and the top TBL thickness decreases as $A_{\rm diff}^{-0.27}$, with corresponding values ranging from ≈60 to ≈160 km.

When an upper mantle is considered (Figs 4b and d), the influence of the lower mantle viscosity on both the top and bottom TBL thicknesses vanishes. The bottom TBL thickness decreases as $A_{\rm diff}^{-0.084}$ for Series 2 and as $A_{\rm diff}^{-0.11}$ for Series 4. For both values of $E_{\rm diff}$ we used for the lower mantle viscosity, the top TBL thickness decreases to a value of ≈60 km at the end of the mushy stage, independently of the value of $E_{\rm diff}$.

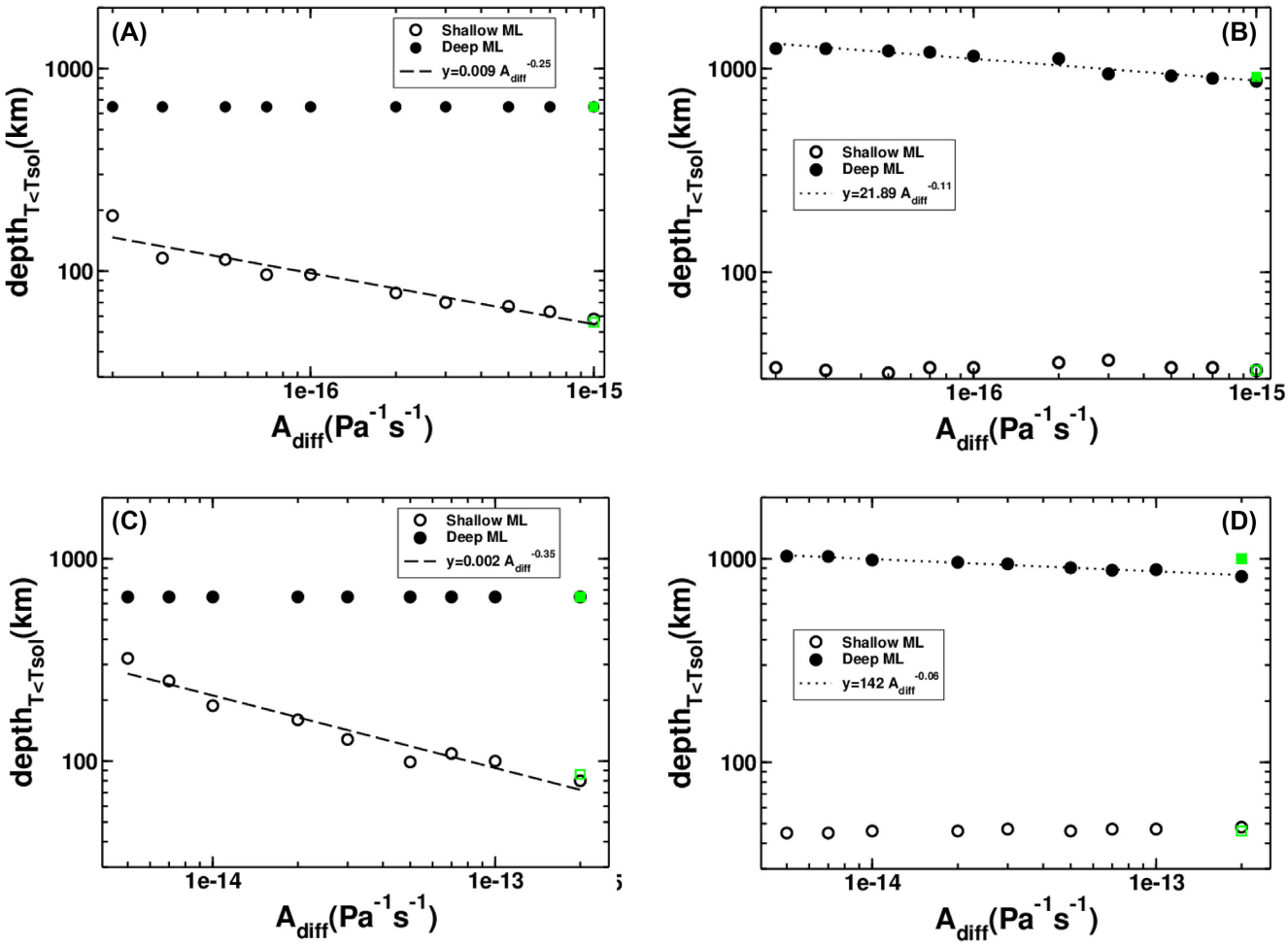

Figure 5. Depth at which the last layers of partially molten material solidify as a function of A_{diff}. Open symbols represent the solidification depth of the upper molten layer (SML) whereas solid symbols illustrate the solidification depth of the lower molten layer (DML) (See also Figs 3c and d). The a, b, c, d panels correspond to Series 1, 2, 3, 4, respectively (see Tables 2 and 3 for parameter values). The cases with $V_{\text{diff}} = 10^{-6}$ m^3 mol^{-1} are in black symbols and cases with $V_{\text{diff}} = 2 \times 10^{-6}$ m^3 mol^{-1} are in green symbols. Dashed and dotted lines represent power law fits of the numerical data for SML and DML, respectively.

Also, the top TBL thickness is weakly dependent on the value of V_{diff}, as shown in Fig. 4. However, this parameter strongly influences the bottom TBL thickness. Indeed, increasing V_{diff} from 1×10^{-6} to 2×10^{-6} m^3 mol^{-1} results into a viscosity increase by at least a factor 2 to 3 for both $E_{\text{diff}} = 200$ kJ mol^{-1} and $E_{\text{diff}} = 300$ kJ mol^{-1} cases, and for cases considering an upper mantle and its influence in rheology or not. This result illustrates the influence of V_{diff} on the viscosity, and can be understood when comparing the red and green viscosity profiles from Fig. 2. As the value of V_{diff} governs how the viscosity increases with depth from a reference value, increasing V_{diff} does not change significantly the viscosity close to the Earth's surface. However, increasing V_{diff} increases significantly the viscosity in the lowermost mantle, leading to a significant thickening of the TBL above the core mantle-boundary. In our models, right after the solidification of the molten layers (SML and DML), the viscosity above the bottom TBL for cases with $V_{\text{diff}} = 2 \times 10^{-6}$ m^3 mol^{-1} is larger than the viscosity above the bottom TBL for $V_{\text{diff}} = 1 \times 10^{-6}$ m^3 mol^{-1} by a factor 10–30. This important increase in the lower mantle viscosity explains the increase in TBL thickness illustrated in Fig. 4 for our range of V_{diff} values as the TBL scales with $\eta^{1/3}$.

3.2.2 *Depth of final melt layer*

During the cooling and the solidification of the mushy mantle, the melt fraction decreases from a global value of 0.4 to 0 (Figs 3c and d). Depending on the solid viscosity parameters used for the early mushy mantle, two layers can remain molten before full solidification: a deep one (DML) and a shallower one (SML, see also Fig. 3). The depths at which the two last layers of melt solidify as a function of A_{diff} for two different values of E_{diff} and V_{diff} is reported in Fig. 5. This figure shows that the crystallization mechanism strongly depends on the presence of a viscosity dichotomy between the upper and lower mantle. When no dichotomy is considered (Figs 5a and c), the behaviour is similar for $E_{\text{diff}} = 200$ kJ mol^{-1} and $E_{\text{diff}} = 300$ kJ mol^{-1}. For both E_{diff} values, the solidification depth of the upper molten layer (SML) decreases as the viscosity decreases (scaling with $A_{\text{diff}}^{-0.25}$ and $A_{\text{diff}}^{-0.35}$, respectively) whereas the solidification depth of the deep molten layer (DML) is constant and equals 660 km (i.e. the depth of the transition between the upper and lower mantle). In the later case, the transition is not the consequence of rheological properties but is related to the change of the solidus slope (eqs (12a) and (12c) and Fig. 3), which is steeper in the lower mantle than in the upper mantle. These

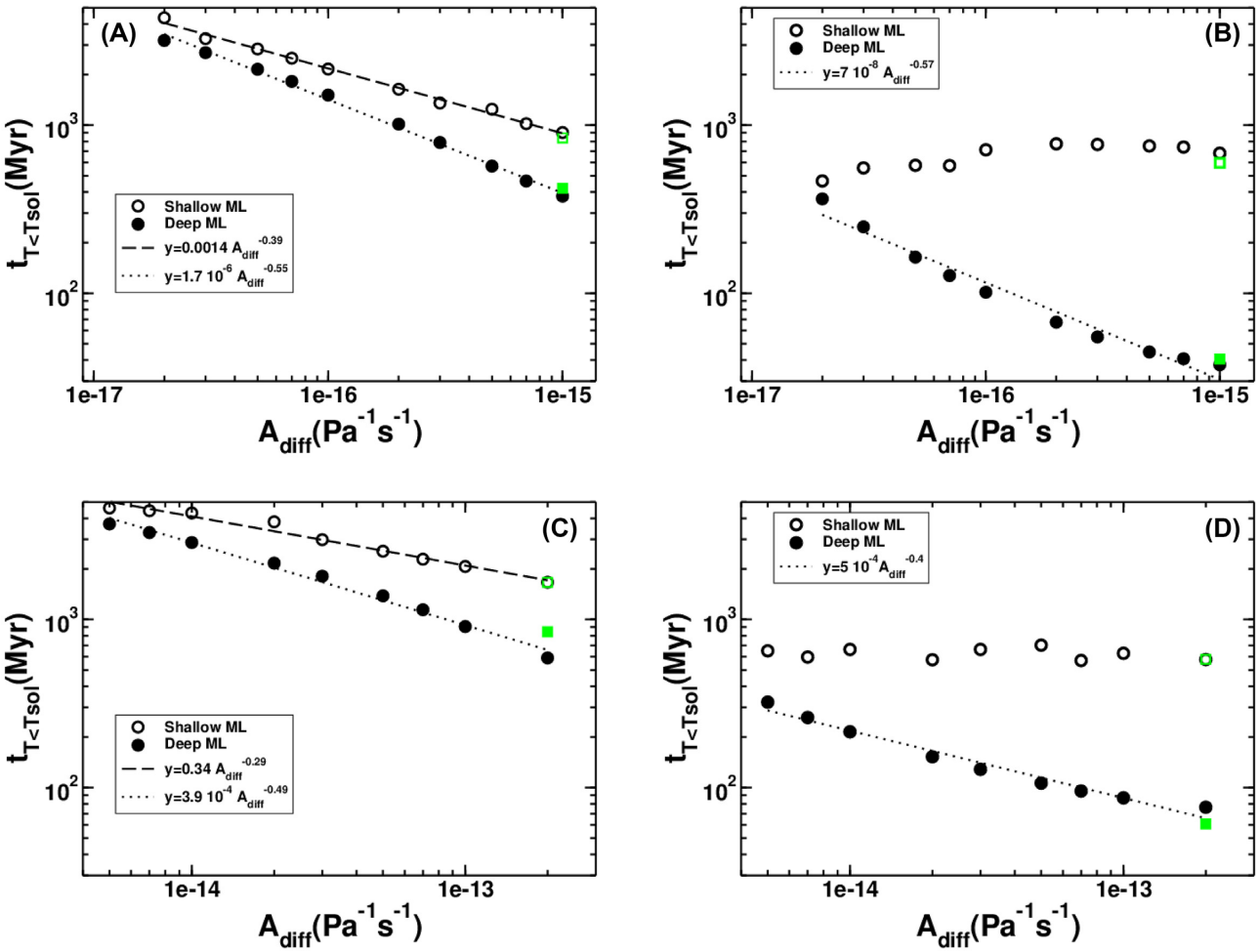

Figure 6. Duration for full solidification of the mushy mantle (initially with $\varphi = 0.4$). Open symbols represent the solidification time of the upper molten layer (SML) whereas solid symbols illustrate the solidification time of the lower molten layer (DML). The a, b, c, d panels correspond to Series 1, 2, 3, 4, respectively (see Tables 2 and 3 for parameter values). The cases with $V_{\rm diff} = 10^{-6}$ m^3 mol^{-1} are illustrated with black symbols and cases with $V_{\rm diff} = 2 \times 10^{-6}$ m^3 mol^{-1} are illustrated with green symbols. Dashed and dotted lines represent power law fits of the numerical data for SML and DML, respectively.

changes in the melting properties with depth coupled with the slope of the temperature profile computed from our models explain this particular behaviour. In these cases, the depth of the deep molten layer is insensitive to the value of the viscosity parameters.

However, a mineralogical dichotomy between the upper and lower mantle is likely to appear rapidly during the solidification of the mushy mantle, due to the high-pressure polymorphism. When considering rheologically distinct upper and lower mantles (Figs 5b and d), the solidification depth of the deep molten layer is no longer tied to a depth of 660 km, but now depends on the viscosity of the lower mantle. The depth at which DML solidifies decreases when $A_{\rm diff}$ increases (i.e. when the lower mantle viscosity decreases) and scales with $A_{\rm diff}^{-(0.06-0.1)}$ (Figs 5b and d). This results in a deep solidification stage occurring at depth decreasing from 1250 to 800 km when $A_{\rm diff}$ increases within the range envisioned in our study (i.e. when the deep mantle viscosity decreases). In contrast, the depth of final upper molten layer SML remains nearly constant (≈30–50 km) for the whole range of lower mantle viscosities considered in Fig. 5. This illustrates the fact that the depth at which the last upper layer of melt solidifies is not governed by the viscosity of the lower mantle but rather by the rheological properties of the upper mantle (we tested this hypothesis in Section 3.2.4).

3.2.3 *Mushy stage timescale*

The influence of $A_{\rm diff}$ on the time required to fully solidify a partially molten mantle and for two different values of $E_{\rm diff}$ and $V_{\rm diff}$ is reported in Fig. 6. A quick inspection of eq. (1) indicates that this solidification timescale should be inversely proportional to the convective heat flux $F_{\rm conv}$. In the hard-turbulent regime, this term scales as $\eta^{-3/7}$ whereas in the soft-turbulent regime, this term scales as $\eta^{-1/3}$. The eq. (19b) implies that an increase of either $E_{\rm diff}$ or $V_{\rm diff}$ yields an increase of the viscosity. On the contrary, an increase of $A_{\rm diff}$ yields a decrease of the solid viscosity at given P and T conditions scaling with $A_{\rm diff}^{-1}$. Consequently, if the viscosity of its solid fraction governs the characteristic solidification timescale, this time should scale as $A_{\rm diff}^{-n}$ with n ranging between 1/3 and 3/7. This is confirmed by our numerical results (Figs 6a and c). The time required for the upper molten layer (SML) to fully solidify scales with $A_{\rm diff}^{-0.39}$ for Series 1 (Fig. 6a) and with $A_{\rm diff}^{-0.29}$ for Series 3 (Fig. 6c). For the lower molten layer (DML), the influence of mantle viscosity is even stronger and the time required for DML to fully solidify scales with $A_{\rm diff}^{-0.55}$ for Series 1 (Fig. 6A) and with $A_{\rm diff}^{-0.49}$ for Series 3 (Fig. 6c).

When no upper/lower mantle dichotomy is considered, the duration of the complete mushy mantle solidification ranges between

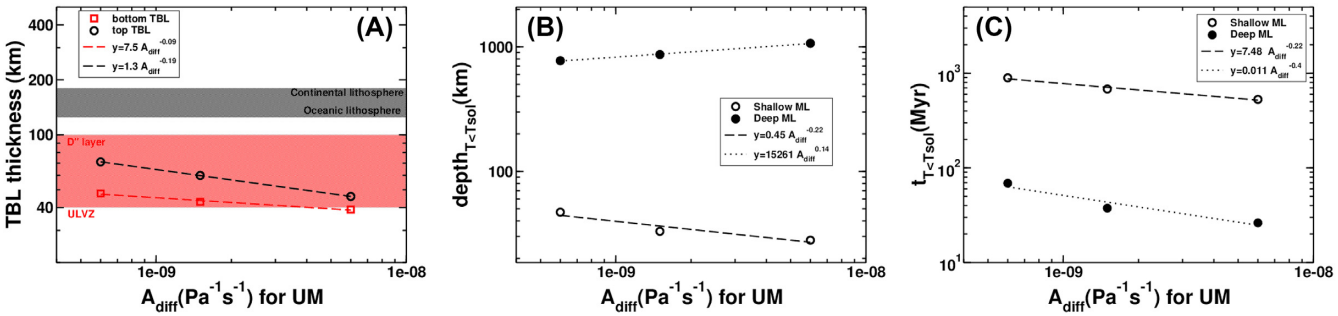

Figure 7. TBL thickness (a), depth at which the last layers (upper and lower) of partially molten material solidify (b) and time to fully solidify the last layers (upper and lower) of partially molten (c) as a function of the value of $A_{\rm diff}$ in the upper mantle. In these figures, $A_{\rm diff} = 10^{-15}$ Pa^{-1}s^{-1}, $E_{\rm diff} = 200$ kJ mol^{-1} and $V_{\rm diff} = 10^{-6}$ m^3 mol^{-1} in the lower mantle whereas $E_{\rm diff} = 375$ kJ mol^{-1} and $V_{\rm diff} = 2.5 \times 10^{-6}$ m^3 mol^{-1} in the upper mantle. Open symbols represent the solidification time of the upper molten layer (SML) whereas solid symbols illustrate the solidification time of the lower molten layer (DML). Dashed and dotted lines represent power law fits of the numerical data for SML and DML, respectively.

900 Myr and 4.4 Gyr for Series 1 (Fig. 6a). For Series 3 (Fig. 6c), the solidification duration ranges between 1.6 and 4.6 Gyr. Our results also show that the solidification of the deeper DML occurs prior to that of the shallower SML, with times ranging between 375 Myr and 3.2 Gyr for $E_{\rm diff} = 200$ kJ mol^{-1} or between 590 Myr and 3.7 Gyr for $E_{\rm diff} = 300$ kJ mol^{-1}. Fig. 6 also shows that our solidification timescale is nearly insensitive to the value of $V_{\rm diff}$.

When considering an upper mantle rheologically different from the lower mantle (Figs 6b and d), several changes occur, compared to models without viscous dichotomy. The solidification timescale for the upper molten layer (SML) is less affected by changes in the value of $A_{\rm diff}$ than DML. Thus, the time required to fully solidify the whole mantle (SML and DML) exhibits a narrower range of values (between 460 and 770 Myr for Series 2 and between 570 and 700 Myr for Series 4). On the contrary, the solidification time of the deeper molten layer DML strongly depends on the viscosity of the lower mantle and scales with $A_{\rm diff}^{-0.57}$ for Series 2 and with $A_{\rm diff}^{-0.4}$ for Series 4. Again, the solidification time of DML is faster than SML (between 37 and 365 Myr for Series 2 or between 76 and 322 Myr for Series 4). Our results suggest that the solidification of the SML (i.e. the final episode of solidification of the early mantle in our models) is weakly sensitive to the viscosity of the lower mantle but is mostly governed by the viscosity of the upper mantle. On the other hand, the solidification time of the DML is in comparison faster, and the viscosity of the lower mantle governs the time delay. This is certainly related to the relatively low upper mantle viscosity used in this calculation (see Fig. 2).

3.2.4 *Influence of the upper mantle viscosity*

We then investigated the influence of the upper mantle viscosity on the characteristic time and length scales of mushy terrestrial mantle crystallization. Thus we considered the reference case detailed in Fig. 3 with a dichotomy in the viscosity between the upper and lower mantle. In this section, we consider constant values for $A_{\rm diff}$, $E_{\rm diff}$ and $V_{\rm diff}$ for the lower mantle, and we used three different values for $A_{\rm diff}$ for the upper mantle ranging between 6×10^{-10} and 6×10^{-9} Pa^{-1}s^{-1}.

The results given in Fig. 7 show that the viscosity of the upper mantle influences both the shallow characteristic time and length scales. We recall here that increasing the value of $A_{\rm diff}$ results in a viscosity decrease. Fig. 7(a) shows that both the top and the bottom TBL thicknesses now decrease when $A_{\rm diff}$ in the upper mantle increases. The top TBL is more sensitive to variations in the $A_{\rm diff}$ values in the upper mantle than the bottom TBL (power exponent –0.19 compared to –0.9 in top and bottom TBL, respectively). In Fig. 7(b), the results show that the depth at which the shallow molten layer SML solidifies decreases with $A_{\rm diff}^{-0.22}$, whereas the depth at which the deep molten layer DML solidifies increases with $A_{\rm diff}^{0.14}$. This means that decreasing the upper mantle viscosity (i.e. increasing $A_{\rm diff}$ in the upper mantle) favors a deeper solidification of DML, while favoring the solidification of SML closer to the surface. Finally, results from Fig. 7(c) shows that both the time at which SML and DML solidify decrease when increasing $A_{\rm diff}$ in the upper mantle. Interestingly, the viscosity of the upper mantle has a stronger influence on the solidification time for the DML than on the shallow SML (power exponent –0.4 compared to –0.22). Hence, by controlling the heat loss in the shallower part of the early Earth, the upper mantle viscosity strongly influences the characteristic solidification time and length scales.

Figs 5(b), (d) and 6(b), (d) show that, when a dichotomy in viscosity is considered, the depth and solidification time of the shallow molten layer are weakly dependent on the viscosity of the deep mantle. However, Fig. 7 illustrates that the viscosity of the upper mantle plays a key role on the time and depth of solidification of the shallow molten layer and is more important than the influence of the lower mantle on this time. Concerning the DML, a decrease of either upper or lower mantle viscosity leads to a decrease of the solidification time of this layer. Nevertheless, this time is more influenced by the viscosity of the deep mantle than by the viscosity of the upper mantle (power exponent –0.57 compared to –0.4). An interesting behaviour arises from the depth at which the deep molten layer DML solidifies. Indeed, Figs 5(b)–(d) shows that this depth decreases when $A_{\rm diff}$ in the lower mantle increases (i.e. when the viscosity decreases) for a fixed value of $A_{\rm diff}$ in the upper mantle. On the contrary, the depth at which DML solidifies increases when $A_{\rm diff}$ in the upper mantle increases for a fixed value of $A_{\rm diff}$ in the lower mantle. Our results show that the rheological parameters of both the upper and lower mantle govern the deep processes of solidification in the lower mantle, whereas the shallower solidification processes are governed only by the properties of the upper mantle.

3.2.5 *Summary*

We have developed a numerical approach to constrain the characteristic depth and time of solidification of a mushy mantle. We have identified two persistent molten layers (SML) and (DML). We show that the cooling and solidification dynamics are very sensitive to the

Rayleigh number that increases with decreasing viscosity. Hence, an increase of the pre-exponential factor A_{diff} (i.e. a decrease of the viscosity) systematically leads to a decrease of the TBL thicknesses (in agreement with eq. 10) and as a consequence to the depth of solidification of the last layer of molten material. As higher *Ra* values lead to a more efficient cooling of the early mantle, the timescale of complete solidification of the mantle also decreases with decreasing A_{diff}. Within a moderately convecting viscous mantle, the TBL thickness and the cooling timescale are expected to scale with $Ra^{-1/3}$ while within a turbulent reservoir they are expected to scale with $Ra^{-2/7}$. In our models were important changes in the parameters occur with temperature, pressure and melt fraction, the value of the exponent in the power law is slightly different (from –0.25 to –0.55 when no viscous dichotomy is considered) but the behaviour is similar.

We have characterized the influence of the solid mantle viscosity with or without a rheological contrast between the upper and lower mantle. Our parametrical study shows that the viscosity of the deep mantle influences the solidification of the DML. This result is not surprising since the bottom TBL thickness is related to the viscosity of the deep material. Hence, one can expect that the solidification characteristics (depth and time scales) of the DML to be strongly influenced by the values of A_{diff} in the lower mantle. Our results show that the same reasoning can be applied to the solidification characteristics of the SML that is governed by the values of A_{diff} in the upper mantle.

Our results show that the viscosity of the upper mantle affects the DML solidification characteristics. This feature illustrates that the upper mantle governs the global mantle dynamics by acting as a thermal blanket that reduces the efficiency of heat loss. Hence, a decrease in the upper mantle viscosity leads to an increase of the surface heat flux, to a more vigorous internal convection associated with a thinner bottom TBL (Fig. 7a), and to a more rapid solidification (Fig. 7c). Conversely, the viscosity of the lower mantle does not influence significantly the SML solidification characteristics (Figs 4–6, right-hand panels). Again, this illustrates that the viscosity of the upper mantle mostly controls the cooling and solidification dynamics. A low viscosity lower mantle enhances the heat transfer from the core toward the mantle but the mantle heat loss is limited by the viscous properties of the upper mantle.

4. DISCUSSION

4.1 Geological constraints

A mineralogical dichotomy and a subsequent transition of the viscous behaviour between the upper and lower mantle are likely to appear rapidly during the solidification of the mushy mantle. In the following discussion we only consider the results from the models that account for a viscous dichotomy between the upper and lower mantle (i.e. left-hand column, b and d graphics in Figs 4–6). Our model results show that the top melt layer (SML) crystallizes at the Hadean-Eoarchean boundary (500–800 Myr after Earth's formation; Fig. 6), regardless of the model, and the crystallization proceeds at relatively shallow depths of 35–45 km (Fig. 5). On the contrary, the bottom melt layer (DML) crystallizes at deeper levels (800–1000 km; Fig. 5) and earlier (40–400 Myr after Earth's formation; Fig. 6). If the upper mantle viscosity is considered separately, these time and depth estimates are only slightly decreased or increased (Fig. 7).

The presence of molten material and the resulting rheological weakening may have profound effect on the evolution of the early crust, on its ability to deform and on how orogens develop (Sawyer *et al.* 2011). The persistence of a melt layer at shallow depth during the Hadean and its final crystallization around the Hadean–Eoarchean boundary could prevent the formation of elevated orogenic formations due to fast isostatic compensation of any created reliefs and development of large-scale tectonic fault and shear-zones. The absence of reliefs would, in turn, result in a water-world with most of the Earth being covered by shallow water. Major faults and shear-zones could represent pathways for liquid water to penetrate to lower crustal levels and, in turn, induce intense hydrothermal activity. In addition, this weak layer at the depth of the lower crust could possibly isolate the crust from the underlying mantle. Doglioni *et al.* (2011) proposed that a stable partial melt layer between the asthenosphere and the lithosphere could induce an effective viscous decoupling between the two layers and explain the lifetime of cratonic roots. At the Hadean–Eoarchean, the viscous coupling between the mantle and the crust could have induced the beginning of large-scale Hadean crust reworking and the formation of stable Archean crustal blocks. The persistence of SML could, hence, account for the absence of Hadean crustal fragments in geological record and at the beginning of the Archean geological record. They are solid outputs from our geodynamic models and, therefore, they should have affected the dynamics of our planet early in its history. Hence, linking the timing of major differentiation events in the geological record with SML and DML crystallization could help understanding early shallow processes.

Little is known about the Hadean period since we do not have the rock record at the Hadean–Eoarchean boundary (e.g. Goodwin 1996; Guitreau *et al.* 2012). Yet, some detrital zircon crystals, formed during the Hadean, survived until today. They offer a window into the Earth's infancy (e.g. Froude *et al.* 1983; Cavosie *et al.* 2019). In addition, relics of global chemical fractionation that occurred during the Hadean are recorded by extinct radionuclides, such as ^{142}Nd and ^{182}W (e.g. Boyet *et al.* 2003; Touboul *et al.* 2012). The ^{182}Hf-^{182}W system operated during the first 50 Myr after Solar System formation, and it is, hence, unlikely to have recorded processes depicted in our model. In contrast, the lifetime of ^{146}Sm-^{142}Nd system matches very well the timescale for DML crystallization and is, hence, very appropriate to help constrain the physical parameters of our models. Interestingly, most ^{142}Nd signatures point to major differentiation event(s) of the Earth around 4.3–4.4 Ga (i.e. 150–250 Ma after the Earth's formation, e.g. Saji *et al.* 2018, and references therein, Guitreau *et al.* 2019), also consistent with detrital zircon ages (e.g. Cavosie *et al.* 2019). On the other hand, the disappearance of SML would correspond to the start of the rock record (i.e. preservation of stable crustal blocks) between 4.0 and 3.8 Ga.

Considering that the SML crystallization is correlated with the end of major resurfacing on Earth, the comparison with Venus is quite appealing. Based on the crater population, it was suggested that the surface of Venus seems uniformly young. With absence of plate tectonics, this observation suggested that catastrophic resurfacing occurs episodically on Venus (Phillips & Hansen 1998; Harris & Bédard 2014; Smrekar *et al.* 2018). The available geodynamic models point out the importance of radioactive heating in the Venusian mantle which, correlated to the presence of a rigid stagnant lid, could have resulted in an increase of the mantle potential temperature with geological time, especially in the first 1–2 Ga (O'Rourke & Korenaga 2012; Tosi *et al.* 2017). The mantle potential temperature could still be today above 1800 K on Venus, thus at a similar

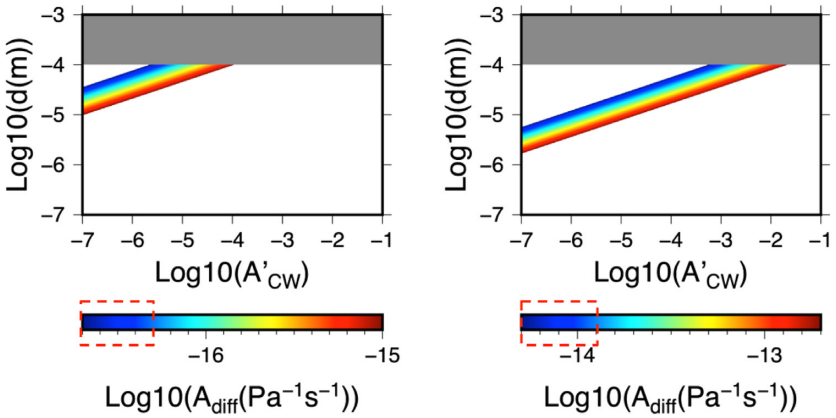

Figure 8. For the lower mantle, range of A_{diff} values considered in our study for (left-hand panel) $E_{diff} = 200$ kJ mol^{-1} and (right-hand panel) $E_{diff} = 300$ kJ mol^{-1}. The grey domain marks dislocation creep regime, below is diffusion creep regime. The white domains represent A_{diff} values not considered in our study. The red dashed domains on the colour bar represent the values derived from the geological constraints.

level than it was early in the Earth's history (e.g. Herzberg *et al.* 2010). A logical conclusion is that partial melting still takes place today at shallow depths in the Venusian mantle.

4.2 Refinement of mantle's rheological parameters

Following the idea that SML and DML final crystallization correspond to identified Hadean geological events on Earth, the exact timing of these events can help refine most realistic values of A_{diff}, E_{diff} and V_{diff}. In our models, the upper mantle viscosity does not significantly influence the solidification time of the last global molten layers, and should not strongly affect the timing of the geological events discussed above. We cannot estimate the best pair of E_{diff} and V_{diff}, since V_{diff} has very little influence on the timing of crystallization of SML and DML. Nevertheless, we can propose a couple of solutions for fixed values of E_{diff}. SML crystallization is essentially insensitive to A_{diff} values and we, hence, cannot use it to estimate A_{diff} values. On the other hand, the crystallization of DML is sensitive to A_{diff} values. In order to explain the ages of 4.3–4.4 Ga inferred form ^{142}Nd signatures, the lower mantle A_{diff} values should range between 3×10^{-17} and 7×10^{-17} Pa^{-1}s^{-1} for Series 2, and 7×10^{-15} Pa^{-1}s^{-1} to 2×10^{-14} for Series 4. Assuming that SML accounts for the start of the geological record (i.e. preservation of stable crustal blocks) between 4.0 and 3.8 Ga, the upper-mantle A_{diff} values should range between 1×10^{-9} and 4×10^{-9} Pa^{-1}s^{-1}. These ranges of values obtained for A_{diff} in the lower and upper mantle are pretty narrow given that reference viscosities are generally unknown to multiple orders of magnitude. Moreover, the values inferred for both the lower and the upper mantle are within the range of those proposed for the mantle (Čížková *et al.* 2012).

4.3 Chemical weakening and grain size

Among the parameters used to compute the solid-state mantle viscosity the pre-exponential factor exhibits a large range of plausible values (typically two orders of magnitude). While A_{diff} is called the material constant, its variability expresses the grain size sensitivity and the potential influence of chemical weakening. For olivine, this influence has been experimentally characterized for hydrogen at crustal and upper mantle pressures (e.g. Mackwell *et al.* 1985; Mei & Kohlstedt 2000a, b, Demouchy *et al.* 2012; Girard *et al.* 2013; Tielke *et al.* 2017), for iron (Zhao *et al.* 2009; Hansen *et al.* 2012), and for titanium, (Faul *et al.* 2016). It can be expressed as:

$$\frac{1}{A_{diff}} = 2\left(\frac{A\, A'^{\,\prime}_{CW}}{\mu}\right)^{-1}\left(\frac{b}{d}\right)^{-3}, \tag{20}$$

where A is thus a material constant ($A = 8.17 \times 10^{15}$ s^{-1}), μ is the shear modulus ($\mu = 80$ GPa), b is the magnitude of the Burgers vector ($b = 0.55 \times 10^{-9}$ m) and d is the grain size (Karato & Wu 1993). A'_{CW} is a dimensionless parameter characterizing the influence of the potential chemical weakening due to the incorporation of, for example Al^{3+}, $Fe^{2+/3+}$, Ti^{4+} in mantle minerals. A'_{CW} can be envisioned as a stress factor in the sense that an increase of its value leads to an increase of A_{diff} and, as a consequence, to a viscosity decrease. Note that hydrogen is expected to have only very minor to negligible effect on lower mantle properties, since hydrogen can barely be embedded in bridgmanite as a point defects (Bolfan-Cavanova, Keppler & Rubie 2003) and since the hydrogen solubility in periclase remains very limited (Bolfan-Casanova *et al.* 2002, see Bolfan-Casanova 2005, for a review). Therefore, 'water' weakening in the lower mantle is discarded in this study.

In our models, we have considered different values for A_{diff} ranging between 2×10^{-17} Pa^{-1}s^{-1} and 10^{-15} Pa^{-1}s^{-1} for $E_{diff} = 200$ kJ mol^{-1} and between 5×10^{-15} Pa^{-1}s^{-1} and 2×10^{-13} Pa^{-1}s^{-1} for $E_{diff} = 300$ kJ mol^{-1}. According to eq. (20), each value of A_{diff} corresponds to a set of values for the pair d and A'_{CW}. In Fig. 8, we plotted A_{diff} as a function of d and A'_{CW}. From Fig. 8, we can estimate the range of plausible values for d and A'_{CW} corresponding to the values of A_{diff} considered in our models. The transition from diffusion to dislocation creep is expected to occur for d larger than 100 μm in the lower mantle (Boioli *et al.* 2017). Considering only a domain where the diffusion creep scaling applies, Fig. 8 illustrates that d ranges between 10 and 100 μm for $E_{diff} = 200$ kJ mol^{-1} and between 1 and 100 μm for $E_{diff} = 300$ kJ mol^{-1}. In the mean time, A'_{CW} ranges between 10^{-7} and 10^{-4} for $E_{diff} = 200$ kJ mol^{-1} and between 10^{-7} and 10^{-2} for $E_{diff} = 300$ kJ mol^{-1}. Fig. 8 shows that when increasing the grain size by a factor 10, the stress factor associated to chemical weakening has to be increased by a factor 1000 to maintain a constant pre-exponential factor A_{diff}.

Our arguments developed in previous sections suggest the following range for A_{diff} values within the lower mantle: between 3×10^{-17} and 7×10^{-17} Pa^{-1}s^{-1} for $E_{diff} = 200$ kJ mol^{-1}, and between 7×10^{-15} Pa^{-1}s^{-1} and 2×10^{-14} Pa^{-1}s^{-1} for $E_{diff} = 300$ kJ mol^{-1},

based on the comparison between our models and geological features. When reporting these two ranges of values in Fig. 8, we illustrate that these values correspond to the material colored within the red dashed box. Using eq. (20), we can relate our preferred values for A_{diff} and the grain size that prevailed in the deep mantle during this period. Hence we can constrain d between 30 and 100 μm when $E_{\text{diff}} = 200$ kJ mol^{-1} and between 3 and 100 μm when $E_{\text{diff}} = 300$ kJ mol^{-1}. In the meantime, from our models, the dimensionless parameter characterizing the influence of the chemical weakening A'_{CW} would range between 10^{-7} and 10^{-5} when $E_{\text{diff}} = 200$ kJ mol^{-1} and between 10^{-7} and 10^{-3} when $E_{\text{diff}} = 300$ kJ mol^{-1}. Therefore, constraining the E_{diff} values in the deep mantle from geological features could help to reduce the range of potential stress factor related to chemical weakening and grain size within the deep mantle.

4.4 Model limitations

1-D models are appropriate to characterize the first order cooling and solidification dynamics of a compressible mushy mantle where viscosity contrasts between solid mantle and magmas can reach up to 20 orders of magnitude. However, we acknowledge that the timescales for SML and DML crystallization may be affected by 3-D lateral variations. The early geotherms obtained from our models can be implemented in geometrically more realistic models developed to characterize the global geodynamic regime that operated prior to the onset of modern plate tectonics (Rozel *et al.* 2017; Agrusta *et al.* 2018).

The surface temperature and the ability of the top boundary layer to facilitate the heat loss are key parameters that also control the cooling dynamics of the mushy mantle. In our study we have assumed that the surface temperature was constant (=500 K) according to Lebrun *et al.* (2013) and Sleep *et al.* (2014). However, this surface temperature may be overestimated, as the dissolution of CO_2 in the condensed water is not accounted. In addition, depending on the buoyancy of the residual melt, partial melting in the shallow melt layer is likely to rise towards the surface through magma conduits and cool the interior efficiently by volcanic heat transport (Ricard *et al.* 2014; Kankanamge & Moore 2019). Both these shallow processes may enhance the heat evacuation and affect the timescales and depths obtained in our study.

The chemical differentiation that is not accounted in our models could affect the results obtained from our models by different ways.

(1) The vertical chemical segregation due to compatible/incompatible elements separation could be an important feature during this early cooling event (Ballmer *et al.* 2017) and could delay the solidification. Such a vertical segregation depends on the possible occurrence of gravitational fractionation of the Fe-enriched melt and the solid in a turbulent magma ocean.

(2) Considering a chemical differentiation between compatible/incompatible elements would also affect the partitioning of radiogenic heat producing elements. Indeed, K, Th and U are incompatible elements which will accumulate preferentially in the molten reservoirs. Hence the chemical segregation is likely to affect the heat partitioning within the mantle and as a consequence its cooling dynamics.

(3) During the chemical segregation, the composition of the molten phase will evolve towards an enrichment in incompatible elements. This chemical evolution will affect the melting curves (Andrault *et al.* 2017)

5. CONCLUSION

We have performed 1-D numerical simulations to monitor the temperature and melt fraction evolutions of an initially 40% molten early mantle. In our models, we have implemented recent and solid experimental constraints from mineral physics. We have considered a range of solid fraction viscosity compatible with the knowledge of the current lowermost mantle viscosity. Our models illustrate the influence of the solid mantle fraction viscosity on the cooling of a deep mushy mantle, and in particular on the characteristic time and depth at which complete solidification is achieved. Considering that deformation occurs via diffusion creep, the cooling dynamics is mainly governed by the pre-exponential factor A_{diff}. Our models highlight two molten layers (SML and DML) whose complete crystallization are separated both in time and space: DML solidifying earlier (between 40 and 400 Ma) and deeper (between 800 and 1200 km) than SML, whose solidification occurs during the first 400–800 Ma, and at depth ranging between 30 and 50 km. The viscosity of the upper mantle plays a key role on the time and depth of solidification of the shallow SML, whereas the viscosity of the deep mantle governs the duration of DML solidification.

The solidification timescales derived from our models suggest a full crystallization of the early mantle at the Hadean-Eoarchean boundary. A shallow molten layer stable during 150–250 Ma after the Earth's formation could favor the absence of early reliefs and isolate the early crust from the underlying mantle dynamics. We associate the crystallization of SML and DML to major events in the geological record. Then, we use the timing of these records to refine a preferred set of parameters defining the mantle viscosity. Our models favor the highest values of the range of deep mantle viscosities derived from geoid inversion and post-glacial rebound (Čížková *et al.* 2012, and references therein). From our preferred viscosity models, our study suggests a 3–100 μm range for grain size and a chemical weakening parameter ranging between 10^{-7} and 10^{-3}. Our 1-D approach is relevant when characterizing a fully mushy early mantle where large viscosity contrasts associated to large Rayleigh numbers can persist during the whole solidification of the reservoir. The temperature profiles and the TBLs characteristics inferred from our study can easily be incorporated in thermochemical evolution models of a solid terrestrial mantle.

ACKNOWLEDGEMENTS

The authors thank Maud Boyet, Craig Storey and Hugo Moreira for fruitful discussions. The authors also thank J. Roberts and anonymous reviewer for thoughtful and constructive comments. The authors also thank G. Tobie and B. Cecconi for their useful help in the development of the numerical model. This is ClerVolc contribution number 400. H. S. acknowledges the support from the "Deutsche Forschungsgemeinschaft" (grant number SA 2042/3-1).

References

Abe, Y., 1997. Thermal and chemical evolution of the terrestrial magma ocean, *Phys. Earth planet. Inter.,* **100,** 27–39.

Agrusta, R., van Hunen, J. & Goes, S., 2018. Strong plates enhance mantle mixing in early Earth, *Nature Communications,* **9,** 2708.

Andrault, D., Bolfan-Casanova, N., Lo Nigro, G., Bouhifd, M.A., Garbarino, G. & Mezouar, M., 2011. Melting curve of the deep mantle applied to properties of early magma ocean and actual core-mantle boundary, *Earth planet. Sci. Lett.,* **304,** 251–259.

Andrault, D., *et al.*, 2018. Deep and persistent melt layer in the Archaean mantle, *Nat. Geosci.,* **11,** 139–143, doi:10.1038/s41561-017-0053-9.

Andrault, D. *et al.*, 2017. Toward a coherent model for the melting behaviour of the deep Earth's mantle, *Phys. Earth planet. Inter.,* **265,** 67–81.

Ballmer, M.D., Lourenço, D.L., Hirose, K., Caracas, R. & Nomura, R., 2017. Reconciling magma-ocean crystallization models with the present-day structure of the Earth's mantle, *Geochem. Geophys. Geosyst.,* **18,** 2785–2806.

Boioli, F., Carrez, P., Cordier, P., Devincre, B., Gouriet, K., Hirel, P., Kraych, A. & Ritterbex, S., 2017. Pure climb creep mechanism drives flow in the Earth's lower mantle, *Sci. Adv.,* **3,** e1601958, doi: 10.1126/sciadv.1601958.

Bolfan-Casanova, N., 2005. Water in the Earth's mantle, *Mineral. Mag.,* **69,** 3, 229–257.

Bolfan-Casanova, N., Keppler, H. & Rubie, D., 2003. Water partitioning at 660 km depth and evidence for very low water solubility in magnesium silicate perovskite. *Geophys. Res. Lett.,* **30,** doi: 10.1029/2003GL017182.

Bolfan-Casanova, N., Mackwell, S., Keppler, H., McCammon, C. & Rubie, D., 2002. Pressure dependence of h solubility in magnesiowustite up to 25 GPa: Implications for the storage of water in the Earth's lower mantle, *Geophys. Res. Lett.,* **29,** 1449, 1–4.

Boukare, C.E., Ricard, Y. & Fiquet, G., 2015. Thermodynamics of the MgO-FeO-SiO_2 system up to 140 GPa: application to the crystallization of Earth's magma ocean, *J. geophys. Res.,* **120,** 6085–6101.

Bower, D.J., Sanan, P. & Wolf, A.S., 2018. Numerical solution of a non-linear conservation law applicable to the interior dynamics of partially molten planets, *Phys. Earth planet. Inter.,* **274,** 49–62.

Boyet, M., Blichert-Toft, J., Rosing, M., Storey, M., Télouk, P. & Albarède, F., 2003. 142Nd evidence for early Earth differentiation, *Earth planet. Sci. Lett.* **214,** 427–442.

Boyet, M. & Carlson, R.W., 2005. 142Nd evidence for early (>4.53 Ga) global differentiation of the silicate Earth, *Science* **309,** 576–581.

Cavosie, A.J., Valley, J.W. & Wilde, S.A., 2019. The oldest terrestrial mineral record: Thirty years of research on Hadean zircon from Jack Hills, Western Australia, in: *Earth's Oldest Rocks,* 2nd edn, Chapter 12, pp. 255–278, eds Van Kranendonk, M.J. Bennett, V.C. & Hoffmann, J.E., Elsevier.

Choblet, G. & Sotin, C., 2000. 3D thermal convection with variable viscosity: can transient cooling be described by a quasi-static scaling law?, *Phys. Earth planet. Inter.* **119,** 321–336.

Cochain, B., Sanloup, C., Leroy, C. & Kono, Y., 2017. Viscosity of mafic magmas at high pressures, *Geophys. Res. Lett.,* **44**(2), 818–826.

Crank, J., 1975. *The Mathematics of Diffusion,* 2nd edn, Clarendon Press. viii, 414 p.

Čížková, H., van den Berg, A.P., Spakman, W. & Matyska, C., 2012. The viscosity of Earth's lower mantle inferred from sinking speed of subducted lithosphere, *Phys. Earth Planet. Inter.,* **200–201,** 56–62.

Demouchy, S., Tommasi, A., Barou, F., Mainprice, D. & Cordier, P., 2012. Deformation of olivine in torsion under hydrous conditions, *Phys. Earth planet. Inter.,* **202-203,** 56–70.

Deschamps, F. & Sotin, C., 2000. Inversion of two-dimensional numerical convection experiments for a fluid with a strongly temperature-dependent viscosity, *Geophys. J. Int.,* **143,** 204–218.

Doglioni, C., Ismail-Zadeh, A., Panza, G. & Riguzzi, F., 2011. Lithosphere–asthenosphere viscosity contrast and decoupling, *Phys. Earth planet. Inter.,* **189,** 1–8.

Faul, U.H., Cline, C.J., David, E.C. & Jackson, I., 2016. Titanium-hydroxyl defect-controlled rheology of the Earth's upper mantle, *Earth planet. Sci. Lett.,* **452,** 227–237.

Fiquet, G., Auzende, A.L., Siebert, J., Corgne, A., Bureau, H., Ozawa, H. & Garbarino, G., 2010. Melting of Peridotite to 140 Gigapascals, *Science,* **329,** 1516–1518.

Foley, B.J., Bercovici, D. & Elkins-Tanton, L.T., 2014. Initiation of plate tectonics from post-magma ocean thermochemical convection, *J. geophys. Res.,* **119,** 8538–8561.

Frost, H.J. & Ashby, M.F., 1982, *Deformation-Mechanism Maps: The Plasticity and Creep of Metals and Ceramics,* Pergamon, Oxford.

Froude, D.O., Ireland, T.R., Kinny, P.D., Williams, I.S. & Compston, W., 1983. Ion microprobe identification of 4,100-4,200 Myr-old terrestrial zircons, *Nature,* **304,** 616–618.

Girard, J., Chen, J., Raterron, P. & Holyoke, C.W., 2013. Hydrolytic weakening of olivine at mantle pressure: Evidence of [100](010) slip system softening from single-crystal deformation experiments. 1–9.

Goodwin, A.M., 1996. *Principles of Precambrian Geology,* pp. 327, Academic Press.

Grott, M. & Breuer, D., 2008, The evolution of the martian elastic lithosphere and implications for crustal and mantle rheology, *Icarus,* **193,** 503–515.

Guitreau, M., Blichert-Toft, J., Martin, H., Mojzsis, S.J. & Albarède, F., 2012. Hafnium isotope evidence from Archean granitic rocks for deep mantle origin of continental crust, *Earth planet. Sci. Lett.,* **337–338,** 211–223.

Guitreau, M., Boyet, M., Paquette, J.-L., Gannoun, A., Konc, Z., Benbakkar, M., Suchorski, K. & Hénot, J.-M., 2019, Hadean protocrust reworking at the origin of the Archean Napier Complex (Antarctica), *Geochem. Perspect. Lett.,* **12,** 7–11.

Hansen., L.N., Zimmerman, M.E. & Kohlstedt, D.L., 2012. The influence of microstructure on deformation of olivine in the grain-boundary sliding regime., *J. geophys.Res.,* **117,** B09201, doi: 10.1029/2012JB009305.

Harris, L. & Bédard, J., 2014. Modern approaches in solid earth sciences, in *Evolution of Archean Crust and Early Life,* Vol. **7,** Chapter 9, pp. 215–288, eds Dilek, Y. & Furnes, H., Springer.

Herzberg, C., Condie, K. & Korenaga, J., 2010. Thermal history of the Earth and its petrological expression, *Earth planet. Sci. Lett.,* **292,** 79–88.

Hirth, G. & Kohlstedt, D.L., 2003. Rheology of the upper mantle and the mantle wedge: a review from the experimentalists, in *Inside the Subduction Factory,* Geophys. Monogr. Ser., Vol. **138,** pp. 83–105, ed. Eiler, J., AGU.

Huet, B., Yamato, P. & Grasemann, B., 2014. The minimized power geometric model: an analytical mixing model for calculating polyphase rock viscosities consistent with experimental data, *J. geophys. Res.,* **119,** 3897–3924.

Javoy, M., 1999. Chemical earth models, *C. R. Acad. Sci. Paris,* **329,** 537–555.

Javoy, M. *et al.*, 2010. The chemical composition of the Earth: Enstatite chondrite models, *Earth planet. Sci. Lett.,* **293,** 259–268.

Ji, S., Wang, Z. & Wirth, R., 2001. Bulk flow strength of Forsterite-Enstatite composites as a function of forsterite content, *Tectonophysics,* **341,** 69–93.

Kankanamge, D.G.J. & Moore, W.B., 2019. A parameterization for volcanic heat flux in heat pipe planets, *J. geophys. Res.,* **124,** 114–127.

Karato, S., & Li, P., 1992. Diffusion creep in perovskite: Implications for the rheology of the lower mantle, *Science,* **255,** 1238–1240, doi:10.1126/science.255.5049.1238.

Karato, S.I. & Wu, P., 1993. Rheology of the upper mantle: a synthesis, *Science,* **260,** 771–778.

Karki, B.B. & Stixrude, L.P., 2010. Viscosity of $MgSiO_3$ liquid at Earth's mantle conditions: implications for an early magma ocean, *Science,* **328,** 740–742.

Laneuville, M., Hernlund, J., Labrosse, S. & Guttenberg, N., 2018. Crystallization of a compositionally stratified basal magma ocean, *Phys. Earth planet. Inter.,* **276,** 86–92.

Lebrun, T., Massol, H., Chassefiere, E., Davaille, A., Marcq, E., Sarda, P., Leblanc, F. & Brandeis, G., 2013. Thermal evolution of an early magma ocean in interaction with the atmosphere, *J. geophys. Res.,* **118,** 1155–1176.

Mackwell, S.J., Kohlstedt, D.L. & Paterson, M.S., 1985. The role of water in the deformation of olivine single crystals, *J. Geophys. Res.,* **90,** 11319–11333.

McDonough, W. & Sun, S.-s., 1995. The composition of the Earth, *Chem. Geol.,* **120**(3-4), 223–253.

Mei, S., Bai, W., Hiraga, T. & Kohlstedt, D.L., 2002. Influence of melt on the creep behavior of olivine-basalt aggregates under hydrous conditions, *Earth planet. Sci. Lett.,* **201,** 491–507.

Mei, S. & Kohlstedt, D.L., 2000a. Influence of water on plastic deformation of olivine aggregates 2. Dislocation creep regime, *J. geophys. Res.,* **105,** 21 471–21 481.

Mei, S. & Kohlstedt, D.L., 2000b. Influence of water on the plastic deformation of olivine aggregates: 1. Diffusion creep regime, *J. geophys. Res.,* **105,** 21 457–21 469.

Monteux, J., Andrault, D. & Samuel, H., 2016. On the cooling of a deep terrestrial magma ocean, *Earth planet. Sci. Lett.,* **448,** 140–149.
Mosenfelder, J.L., Asimow, P.D. & Ahrens, T.J., 2007. Thermodynamic properties of Mg_2SiO_4 liquid at ultra-high pressures from shock measurements to 200 GPa on forsterite and wadsleyite, *J. geophys. Res.,* **112,** B06208, doi:10.1029/2006JB004364.
Mosenfelder, J.L., Asimow, P.D., Frost, D.J., Rubie, D.C. & Ahrens, T.J., 2009. The $MgSiO_3$ system at high pressure: thermodynamic properties of perovskite, post-perovskite, and melt from global inversion of shock and static compression data, *J. geophys. Res.,* **114,** B01203.
Nakajima, M. & Stevenson, D.J., 2015. Melting and mixing states of the Earth's mantle after the Moon-forming impact, *Earth planet. Sci. Lett.,* **427,** 286–295.
O'Rourke, J.G. & Korenaga, J., 2012. Terrestrial planet evolution in the stagnant-lid regime: size effects and the formation of self-destabilizing crust, *Icarus,* **221,** 1043–1060.
Palme, H. & O'Neill, H., 2014. Cosmochemical estimates of mantle composition, in ed. *Treatise on Geochemistry,* 2nd edn, Vol. **3**. pp. 1–39, ed. Carlson, R.W., Elsevier.
Phillips, R.J. & Hansen, V.L., 1998, Geological evolution of Venus: rises, plains, plumes and plateaus, *Science,* **279,** 1492–1497.
Press, W.H., Teukolsky, S.A., Vetterling, W.T. & Flannery, B.P., 1993. *Numerical Recipes in FORTRAN the Art of Scientific Computing,* 2nd edn. Cambridge Univ. Press.
Reali, R., van Orman, J., Pigott, J., Jackson, J.M., Boioli, F., Carrez, P. & Cordier, P., 2019. The role of diffusion-driven pure climb creep on the rheology of bridgmanite under lower mantle conditions, *Sci. Rep.,* **9,** 2053.
Ricard, Y., Labrosse, S. & Dubuffet, F., 2014. Lifting the cover of the cauldron: convection in hot planets, *Geochem. Geophys. Geosyst.,* **15,** 4617–4630.
Roscoe, R., 1952. The viscosity of suspensions of rigid spheres, *Br. J. Appl. Phys.,* **3,** 267–269.
Rozel, A.B., Golabek, G.J., Jain, C., Tackley, P.J. & Gerya, T., 2017. Continental crust formation on early Earth controlled by intrusive magmatism, *Nature,* **545,** 332–335.
Rubie, D.C. *et al.*, 2011. Heterogeneous accretion, composition and core-mantle differentiation of the Earth, *Earth planet. Sci. Lett.,* **301,** 31–42.
Saji, N.S., Larsen, K., Wielandt, D., Schiller, M., Costa, M.M., Whitehouse, M.J., Rosing, M.T. & Bizzarro, M., 2018. Hadean geodynamics inferred from time-varying 142Nd/144Nd in the early Earth rock record, *Geochem.. Perspect. Lett.,* **7,** 43–48, doi:10.7185/geochemlet.1818.
Sawyer, E.W., Cesare, B. & Brown, M., 2011. When the continental crust melts, *Elements,* **7,** 229–234.
Simon, F. & Glatzel, G., 1929. Fusion–pressure curve, *Z. Anorg. Allg. Chem.,* **178,** 309.
Sleep, N.H., Zahnle, K.J. & Lupu, R.E., 2014. Terrestrial aftermath of the Moon-forming impact, *Philos. Trans. R. Soc. A,* **372,** doi:10.1098/rsta.2013.0172.
Smrekar, S., Davaille, A. & Sotin, C., 2018. Venus interior structure and dynamics, *Space Sci. Rev.,* **214**(5), 88, 34 pp.
Solomatov, V., 1995. Scaling of temperature-and stress-dependent viscosity convection, *Phys. Fluids,* **7,** 266.
Solomatov, V., 2007. Magma Oceans and Primordial Mantle Differentiation, in *Treatise of Geophysics,* Vol. **9,** ed. Schubert, G., Elsevier.
Solomatov, V.S., 2000. Fluid dynamics of terrestrial magma ocean, in *Origin of the Earth and Moon,* pp. 323–338, eds Canup, R.M. & Righter, K., The University of Arizona Press.
Solomatov, V.S., 2015, Magma oceans and primordial mantle differentiation, *in Treatise on Geophysics,* 2nd edn., pp. 81–104, ed. Schubert, G., Elsevier, Amsterdam.
Tackley, P.J., 2012. Dynamics and evolution of the deep mantle resulting from thermal, chemical, phase and melting effects, *Earth Sci. Rev.,* **110,** 1–25.
Thiriet, M., Breuer, D., Michaut, C. & Plesa, A.-C., 2019. Scaling laws of convection for cooling planets in a stagnant lid regime, *Phys. Earth planet. Inter.,* **286,** 138–153.
Thomas, C.W. & Asimow, P.D., 2013. Direct shock compression experiments on premolten forsterite and progress toward a consistent high-pressure equation of state for CaO-MgO-Al_2O_3-SiO_2-FeO liquids, *J. geophys. Res.,* **118,** 5738–5752.
Thomas, C.W., Liu, Q., Agee, C.B., Asimow, P.D. & Lange, R.A., 2012. Multi-technique equation of state for Fe2SiO4 melt and the density of Fe-bearing silicate melts from 0 to 161 GPa, *J. Geophys. Res., Solid Earth,* **117,** B10206, doi:10.1029/2012JB009403.
Tielke, J.A., Zimmerman, M.E. & Kohlstedt, D.L. 2017. Hydrolytic weakening in olivine single crystals, *J. geophys. Res.,* **122,** 3465–3479.
Tosi, N. *et al.*, 2017. The habitability of a stagnant-lid Earth, *Astron. Astrophys.,* **605,** A71.
Touboul, M., Puchtel, I.S. & Walker, R.J., 2012. 182W evidence for long-term preservation of early mantle differentiation products, *Science,* **335,** 1065–1069.
Ulvrová, M., Labrosse, S., Coltice, N., Råback, P. & Tackley, P.J., 2012. Numerical modelling of convection interacting with a melting and solidification front: application to the thermal evolution of the basal magma ocean, *Phys. Earth Planet. Inter.,* **206,** 51–66, http://dx.doi.org/10.1016/j.pepi.2012.06.008.
Wagner, F.W., Plesa, A.C. & Rozel, A.B., 2019. Calibrating mixing-length theory for thermal convection in rocky planets, *Geophys. J. Int.,* **217,** 75–89.
Xu, J., Yamazaki, D., Katsura, T., Wu, X., Remmert, P., Yurimoto, H. & Chakraborty, S., 2011. Silicon and magnesium diffusion in a single crystal of $MgSiO_3$ perovskite, *J. geophys. Res.,* **116,** B12205, doi: 10.1029/2011JB008444.
Zhao, Y.H, Zimmerman, M.E. & Kohlstedt, D.L. 2009. Effect of iron content on the creep behavior of olivine, 1: anhydrous conditions, *Earth planet. Sci. Lett.,* **287** (1), 229–240.

APPENDIX: NUMERICAL BENCHMARK OF THE ENERGY BALANCE EQUATION

We validated our numerical approach by benchmarking our model with the analytical non-steady state diffusion problem (eq 6.18 in the section 6. Diffusion in a sphere from Crank 1975) and obtained a relative error below 10^{-7}. We also benchmarked our physical approach by comparing our model with those developed for modeling convection in rocky planets from Wagner *et al.* (2019). In particular, we considered the same setting used to obtain their Fig. 8(a) where they $Ra = 10^7$ and they impose a viscosity contrast of 100 between the top and the bottom of the mantle. This comparison is illustrated in Fig. A1.

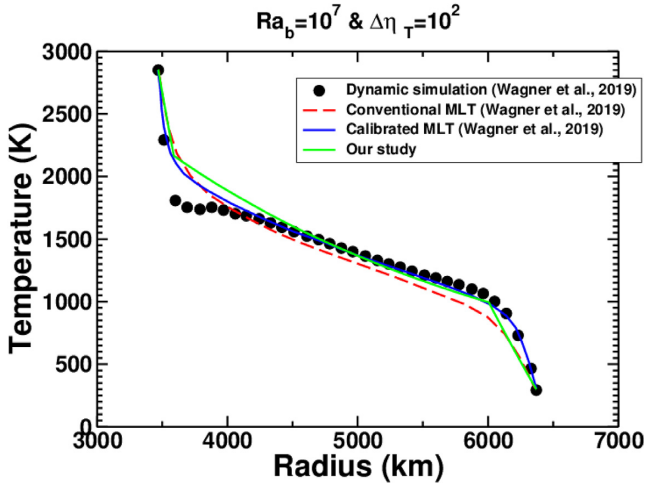

Figure A1. Comparison of the temperature profiles obtained by Wagner *et al.* 2019 (Fig. 8a from their study) (black dots, red dashed line and solid blue line) and the temperature profile obtained from our 1-D model with the same parametrization ($Ra = 10^7$ and a viscosity contrast of 100).

Fig. A1 shows that our results reasonably agree with spherical calculations displayed in the study quoted above, which confirms that our approach can reproduce the thermal evolution in non-symmetric spherical geometry. Moreover, Fig. A1 shows that our results are in agreement with the 1-D (Mixing Length Theory) approach and the evolutions computed in spherical geometry by Wagner *et al.* (2019). Differences between our approach and the MLT approach by Wagner *et al.* (2019) are due to different parametrization details. Moreover, as we impose a conductive heat flux within the two TBLs, it leads to a change in the temperature profile between the convective mantle, and the conductive TBL that is less smooth than in the models from Wagner *et al.* (2019). In the two TBL, the error between our models and the models from Wagner *et al.* (2019) can reach $\approx$20% while in the central parts of the mushy mantle, the error is less than 5%. However, for larger values of Ra numbers that are more relevant to our study, the TBL are considerably thinner, therefore these differences are expected to vanish.

JGR Planets

RESEARCH ARTICLE
10.1029/2023JE007805

Conditions for Segregation of a Crystal-Rich Layer Within a Convective Magma Ocean

J. Monteux[1], B. Qaddah[1,2], and D. Andrault[1]

[1]Laboratoire Magmas et Volcans, Université Clermont-Auvergne, CNRS, IRD, Clermont-Ferrand, France, [2]Institut Jean Lamour, Campus Artem, Université de Lorraine, Nancy, France

Key Points:

- We develop numerical models to monitor the crystal fraction evolution within a convecting magma ocean
- We illustrate that during the early crystallization of a magma ocean, suspension should be the dominant process compared to sedimentation
- We observe that bridgmanite segregation is more likely to occur at the bottom of a MO enriched in SiO_2 compared to pyrolite

Correspondence to:
J. Monteux,
julien.monteux@uca.fr

Citation:
Monteux, J., Qaddah, B., & Andrault, D. (2023). Conditions for segregation of a crystal-rich layer within a convective magma ocean. *Journal of Geophysical Research: Planets*, *128*, e2023JE007805. https://doi.org/10.1029/2023JE007805

Received 28 FEB 2023
Accepted 11 APR 2023

Abstract The vigor of the thermal convection in a terrestrial magma ocean tends to prevent the sedimentation of the solid grains. Understanding of the overall dynamical behavior of this solid phase segregation is required to anticipate the solidification mechanisms in the early Earth mantle. We develop numerical models to monitor the crystal fraction evolution of a convecting magmatic reservoir. Our models show that the ability of the crystal fraction to disperse or sediment within the domain strongly depends on the crystal size, the density difference and the magma viscosity. Our models show that the critical value of the convection/buoyancy stress ratio separating sedimentation/suspension regimes can be smaller than 0.1. Hence, during the early crystallization of a magma ocean, suspension should be the dominant process. We then investigate the possibility of bridgmanite segregation by comparing the density difference between the MO and the solid crystals for different compositions and the critical density contrast above which crystal segregation is likely to occur. We define the relevant set of parameters; including the P-V-T equations of state of coexisting melt and bridgmanite in the mushy MO. We observe that bridgmanite grains are unlikely to segregate in a mantle of pyrolite composition. However, bridgmanite segregation is more likely to occur at the bottom of a MO enriched in SiO_2, compared to pyrolite. When a solidifying layer contains 60% of bridgmanite and 40% of melt, we observe a significant SiO_2 enrichment with increasing mantle depth in a primitive mantle compatible with seismic and geochemical observations.

Plain Language Summary Following the giant impact that formed the Earth-Moon system, the Earth's mantle probably underwent a major melting episode forming a magma ocean several hundred kilometers thick. During the solidification of this magma ocean, the first crystals either settled at depth or were efficiently mixed with the magma. This process played a determining role in the chemical composition of the early mantle. We have developed numerical models to monitor the evolution of a thin layer of crystals in a magma ocean. Our models characterize the influence of crystal size, magma viscosity and density difference between crystals and magma. Our models support efficient mixing of crystals in the magma ocean. However, in some settings such as a SiO_2-rich magma ocean, bridgmanite grains may separate from the magma and form a solid layer at the base of the Earth's mantle early during cooling. This process may generate SiO_2 enrichment with depth in agreement with seismic and geochemical observations.

1. Introduction

During its early history, the Earth experienced several episodes during which a significant volume fraction of its mantle was molten. These melting events were enhanced by radiogenic heating (Yoshino et al., 2003), viscous dissipation during core formation (Monteux et al., 2009; Samuel et al., 2010) and kinetic energy converted into heat during large impacts (Tonks & Melosh, 1993). The giant impact leading to the Earth/Moon system could even have resulted in complete melting of the Earth mantle (Nakajima & Stevenson, 2015) and the subsequent formation of a nearly 3,000 km-thick magma ocean.

Extremely vigorous convection is likely to occur within such a molten reservoir (Monteux et al., 2016; V. Solomatov, 2015). The variations in temperature are strong enough to generate significant natural convective flows. Moreover the potentially large thickness of a molten-silicate reservoir coupled with low viscosity material (Karki & Stixrude, 2010; Xie et al., 2021) leads to Rayleigh numbers (comparing advective and diffusive timescales) ranging from 10^{20} to 10^{30} (Patočka et al., 2020) compared to the current Rayleigh number of the Earth's mantle of 10^6–10^8 (Ricard, 2007). The cooling and solidification dynamics are difficult to monitor within such

an environment. However, recent numerical models agree on the characteristic cooling timescales that can be constrained to several thousands of years (Lebrun et al., 2013; Monteux et al., 2016).

The study of particle sedimentation in vigorously convecting fluids and, by extension, the study of crystal behavior in convecting magmas is a highly debated subject in both fluid dynamics (Lavorel & Le Bars, 2009) and Earth Sciences (Jaupart & Tait, 1995). A large number of studies have investigated crystal settling in magma chambers using laboratory experiments (Martin & Nokes, 1988; Sturtz et al., 2021), numerical modeling (Höink et al., 2005; Verhoeven & Schmalzl, 2009) or both (Weinstein et al., 1988). All these studies point out the importance of particle deposition and the subsequent differentiation mechanisms that might occur within large plutonic reservoirs. In magma oceans, the physical context is quite different, with potentially more vigorous convection involving much thicker reservoirs. Recent numerical models from Patočka et al. (2020) constrained the settling of inertial particles in turbulent Rayleigh-Bénard convection without taking into consideration the re-entrainment process. In particular, Patočka et al. (2020) identified different settling regimes and derived characteristic residence timescales. For their range of particle sizes and densities, their results show that the settling should be rapid, much shorter than the typical timescales for the solidification of a whole-mantle terrestrial magma ocean, thus supporting the idea of fully fractional crystallization. However, using analog models, V. S. Solomatov et al. (1993) introduced the conditions for particle re-entrainment after sedimentation at the bottom of a convecting reservoir. At sufficiently high Rayleigh numbers, their models illustrate that the particles might be re-entrained by the viscous stress produced by thermal plumes, emphasizing that entrainment of crystals cumulated in dunes was likely at the bottom of magma oceans. Such a re-entrainment process could therefore favor equilibrium crystallization. More recent laboratory experiments from Lavorel & Le Bars (2009) confirmed the findings of V. S. Solomatov et al. (1993) and characterized the influence of the density ratio between fluid and crystals and the temperature difference driving thermal convection.

Several parameters likely influence the settling dynamics: (a) the density difference between the settling crystal and the surrounding convecting magma ocean, (b) the crystal size, which is strongly dependent on the magma ocean cooling rate, and (c) the viscosity of the magma ocean whose value may span several orders of magnitude depending on the pressure/temperature conditions within the early magma ocean. Recently, Caracas et al. (2019) proposed that the accumulation of crystals might occur near the depth of neutral buoyancy between crystals and the coexisting melt. They determined this neutral buoyancy depth for different values of iron partition coefficients between melt and solid fractions. They showed that the crystals can cumulate and form a mushy layer within the magma ocean, thus separating a shallow MO from a basal MO. Here, we monitor the stability of a thin mushy layer cumulated within a magma ocean. We evaluate the effects of grain size, density difference between crystals and the surrounding magma ocean, and viscosity values for the magma ocean derived from petrological experiments. The main purpose of our models is to determine if the crystal layer is sedimented at the bottom of the reservoir or is efficiently mixed into the convective reservoir.

The hypothesis of a fully molten mantle is difficult to reconcile with geochemical data and the need for hidden reservoirs (Boyet & Carlson, 2005). However, the cooling and solidification processes occurring within large partially molten silicate reservoirs may lead to significant chemical differentiation events and thus to chemical segregation. The depth at which solidification initiates is governed by the intersection between the early geotherm and the melting curves (Caracas et al., 2019) proposed that crystal settling would occur toward neutral buoyancy depths where crystals are paradoxically more easily entrained by the convective flow. Both chemical composition and temperature contribute to the buoyancy of a crystal layer within a convecting reservoir. The chemical differentiation that happens following a large melting event is strongly related to the ability of the crystal fraction to sink or float within the convective reservoir. This ability is itself governed by the ability of the crystallized minerals to integrate heavy elements such as Fe into their structure (Andrault et al., 2012; Nomura et al., 2011). Depending on the crystal buoyancy relative to the molten magma, different scenarios may involve either a bottom up solidification (Monteux et al., 2016) or a mid-mantle solidification, in which case a basal magma ocean would be possible (Labrosse et al., 2007). In our study, we discuss the implications of our model on the mechanism of magma ocean solidification after a major Moon-forming impact on an Earth-like planet.

In this study, we have developed a numerical model to monitor the cooling, segregation and chemical evolution of the early Earth mantle. Our study is laid out as follows. In Section 2, we present our physical and numerical models. In Section 3, we present the main numerical results from our systematic parametric study emphasizing the influence of melt viscosity, crystal size and density difference between crystals and melt. Section 4 details a

Table 1
Symbol Definitions and Values of the Physical Parameters Used in This Study

	Symbol	Value or range
Magma ocean density	$\rho_{c,0}$	3,000 kg/m^3
Crystals density	$\rho_{d,0}$	$\rho_{c,0} + \Delta\rho$
Density difference	$\Delta\rho$	5–100 kg/m^3
Magma ocean viscosity	η_c	0.1–10 Pa.s
Crystal diameter	D_d	10^{-4}–10^{-3} m
Heat capacity	C_p	1,000 J.kg^{-1}.K^{-1}
Thermal conductivity	k	5 W.m^{-1}.K^{-1}
Thermal diffusivity	$\kappa = k/(\rho_{c,0}C_p)$	1.7×10^{-6} m^2.s^{-1}
Thermal expansion coefficient	α	10^{-5} K^{-1}
Reference temperature	T_0	4,000 K
Temperature difference	ΔT	100 K

criterion for the stability of a crystallizing layer. Finally, Section 5 describes the evolution of mushy material in the context of progressive magma ocean crystallization. The results and conclusion are presented in Section 6.

2. Physical and Numerical Models

2.1. Governing Equations

We monitored the stability of a horizontal mushy layer composed of solid crystals within an initially convecting fully molten magma reservoir. For this purpose, we used the Euler-Euler model which is an accurate dispersed multiphase flow model describing both the crystal and liquid phases. We defined two non-miscible phases in our models: the continuous phase (subscript c) to represent the liquid magma ocean and the dispersed phase (subscript d) that represents the crystal phase. Both phases behaved as Newtonian and incompressible fluids. The local volume fraction of the fluid continuous phase ϕ_c and the dispersed solid phase ϕ_d were the local average volume of melt and crystals respectively ($\phi_c = 1 - \phi_d$).

The dynamic and thermal evolution of the mushy layer and ambient liquid are governed by the Navier-Stokes and heat transfer equations. We initially solved the equations for the continuous phase heat in 2D rectangular geometry using the Rayleigh-Bénard system. Once it reached a steady state, we solved the dynamic evolution of the mushy layer within the convective reservoir. The Euler-Euler flow model defines one set of Navier-Stokes equations for each phase:

- Mass conservation is represented by the continuity equations (Crowe et al., 1998):

$$\frac{\partial \phi_d}{\partial t} + \nabla.(\phi_d \boldsymbol{u_d}) = 0 \tag{1}$$

$$\nabla.((1-\phi_d)\boldsymbol{u_c} + \phi_d \boldsymbol{u_d}) = 0, \tag{2}$$

  with $\boldsymbol{u_d}$ and $\boldsymbol{u_c}$ representing the dispersed phase and the continuous phase fluid velocity vector respectively (m.s^{-1}). We assumed that the mass transfer between the two phases was zero. In our study, we did not consider either solidification or melting processes but choose to develop a parametric study (see Section 3) in which the parameters such as particle volume fraction, density contrast and particle radii vary within a range of values compatible with particle sedimentation for magma ocean conditions.

- Conservation of momentum is represented by the Navier-Stokes equations. These equations represent a balance between the inertial, pressure, viscous, gravitational and drag forces. In the case of an incompressible Newtonian fluid, this yields

$$\rho_{c,0}\left(\frac{\partial \boldsymbol{u_c}}{\partial t} + \boldsymbol{u_c}.\nabla \boldsymbol{u_c}\right) = \boldsymbol{\nabla}.\left[-P\boldsymbol{I} + \eta_c\left(\nabla \boldsymbol{u_c} + (\nabla \boldsymbol{u_c})^T\right)\right] + \rho_c \boldsymbol{g} + \frac{\boldsymbol{F_{m,c}}}{\phi_c} \tag{3}$$

$$\rho_{d,0}\left(\frac{\partial \boldsymbol{u_d}}{\partial t} + \boldsymbol{u_d}.\nabla \boldsymbol{u_d}\right) = \boldsymbol{\nabla}.\left[-P\boldsymbol{I} + \eta_d\left(\nabla \boldsymbol{u_d} + (\nabla \boldsymbol{u_d})^T\right)\right] + \rho_d \boldsymbol{g} + \frac{\boldsymbol{F_{m,d}}}{\phi_d} \tag{4}$$

  with $\rho_{c,0}$ the reference melt density, $\rho_{d,0}$ the reference solid phase density (see Table 1 for values), ρ_c the melt density (kg.m^{-3}), ρ_d the solid phase density, η_c the melt viscosity (Pa.s), η_d the solid phase viscosity (Pa.s), t the time (s), P the fluid pressure (Pa), $\boldsymbol{g}$ the gravitational acceleration (m.s^{-2}) and $\boldsymbol{I}$ the identity matrix. $F_{m,c}$ and $F_{m,d}$ are the drag forces (N/m^3).

- Heat conservation: Assuming an incompressible fluid with no viscous dissipation and no internal heat sources, the internal energy balance can be written as

$$\rho_{c,0} C_p\left[\frac{\partial T}{\partial t} + \boldsymbol{u}.\nabla T\right] + \boldsymbol{\nabla}.[-k\boldsymbol{\nabla} T] = 0 \tag{5}$$

  with C_p the heat capacity at constant pressure (J.kg^{-1}.K^{-1}), T the fluid temperature (K), $\boldsymbol{u}$ the fluid velocity vector (m.s^{-1}), k the thermal conductivity (W.m^{-1}.K^{-1}). No heat source was considered in our models (e.g.,

radiogenic, tidal or latent heat). For simplicity, we assigned the same heat capacities and thermal conductivities for both the continuous and dispersed phases.

For each fluid parcel, the viscosity ranges between the viscosity of the fully molten phase η_c, which is imposed for each simulation (see Table 1 for values), and the mixture viscosity η, which depends on the dispersed solid phase volume fraction ϕ_d. In our magma ocean context, it is the liquid phase viscosity that governs the flow (Monteux et al., 2016), and the solid phase viscosity is not used in our calculations. For the mixture, we applied a Krieger-type dynamic viscosity which is appropriate for monitoring dispersed phases:

$$\eta = \eta_c \left(1 - MIN\left(\frac{\phi_d}{\phi_{d,\max}}, 0.999\right)\right)^{-2.5\phi_{d,\max}} \tag{6}$$

where $\phi_{d,\max}$ is the maximum packing concentration. $\phi_{d,\max}$ depends on the geometry of the crystals within the system and on the shear rate. For mono-dispersed systems with spheres and low shear rates, $\phi_{d,\max}$ ranges between 0.5 and 0.7 (Dörr et al., 2013). In our models $\phi_{d,\max}$ was set to 0.6 which is the critical packing crystal fraction at which it becomes rheologically impossible for a magma to erupt (Marsh, 1981). In our calculations, there is no requirement for ϕ_d to remain between 0 and $\phi_{d,\max}$. The maximum value $\phi_{d,\max}$ was only used in the expression of the viscosity (Equation 6), which controls the behavior of the flow. When $\phi_d \geq \phi_{d,\max}$, the solid viscosity should govern the flow (e.g., Monteux et al., 2020) instead of the liquid viscosity. Hence the viscosity calculation in Equation 6 should account for this discrepancy. Since the cases of our study fall mainly around the suspension/sedimentation criteria, the crystal fraction never overcome maximum packing concentration.

The drag force acts in opposition to the relative motion of the crystals in the surrounding magma. It is governed by the particle shape and the relative Reynolds number (comparing inertial and viscous forces). In reality the crystal shapes are various and complex. To compute the drag force $\boldsymbol{F}_m$, we considered the Schiller-Naumann drag model, a widely used model in the multiphase flow literature that is particularly relevant for dispersed rigid spheres and for the range of Reynolds number values in our study (lower than 10^4) (Ibrahim & Meguid, 2020; Schiller & Naumann, 1935). $\boldsymbol{F}_m$ is defined as:

$$\boldsymbol{F}_{m,c} = -\boldsymbol{F}_{m,d} = \beta(\boldsymbol{u}_d - \boldsymbol{u}_c) \tag{7}$$

with β the momentum transfer coefficient (in kg m^{-3} s^{-1}) between fluid and solid particles (Ibrahim & Meguid, 2020)

$$\beta = \frac{3}{4}\frac{\rho_{c,0}\phi_d C_D(\boldsymbol{u}_d - \boldsymbol{u}_c)}{D_d} \tag{8}$$

D_d is the particle diameter (m) and C_D is the drag coefficient for a single particle. For Re < 1,000 (Schiller & Naumann, 1935):

$$C_D = \frac{24\left(1 + 0.15Re^{0.687}\right)}{Re} \tag{9}$$

For Re > 1,000, $C_D = 0.44$ (Wen & Yu, 1966).

The density of the magma ocean varies linearly with temperature in the buoyancy term of the momentum equation following the Boussinesq approximation. The density calculation accounts for the contrast relating to the thermal effects and the phase influence. It was calculated as follows:

$$\rho_c = \rho_{c,0}(1 - \alpha(T - T_0)) \tag{10}$$

where T_0 is the reference temperature (in K) and α is the thermal expansion coefficient (K^{-1}). The initial reference temperature for the reservoir is highly influenced by the full thermal history of the early Earth as well as its depth within the Earth mantle. Here we fixed $T_0 = 4000$ K. The particle density was calculated as:

$$\rho_d = \rho_c + \Delta\rho \tag{11}$$

with $\Delta\rho$ the intrinsic density difference between the molten silicates and the solid crystals.

For the dynamics, we used free-slip boundary conditions at all the system boundaries for both the dispersed and continuous phases. Considering free-slip boundary conditions at the bottom of the reservoir favors re-suspension compared to cases with no-slip boundary conditions. We fixed the temperature to 4100 K at the bottom boundary

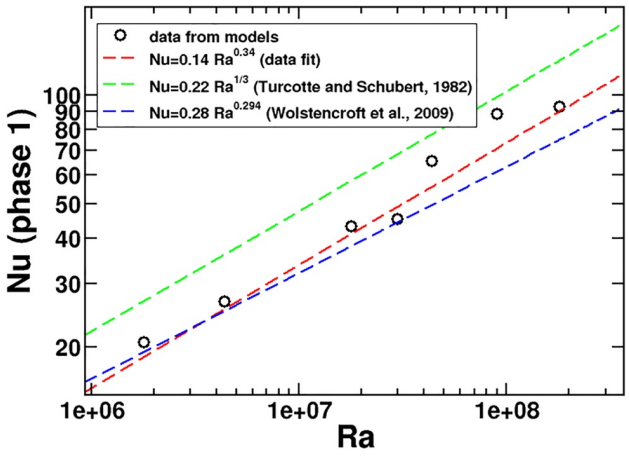

Figure 1. Nusselt number as a function of the Rayleigh number during the first phase where only thermal convection is considered (no settling of particles). Results from our models are shown by black circles. For comparison, we plot the scaling laws proposed by Wolstencroft et al. (2009) and Turcotte and Schubert (1982) with blue and green dashed lines respectively. The red dashed line represents the result from a power-law fit of our numerical results. Corresponding scaling laws are detailed in the legend of the figure.

and to 4000 K at the top boundary (i.e., $\Delta T = 100$ K), with no flux conditions at lateral boundaries.

2.2. Non Dimensional Parameters

Before considering the stability of a crystal layer within the molten reservoir, we first solved only the equations relating to thermal convection within the reservoir. In our geophysical investigation, the least constrained parameter was the magma ocean viscosity, which ranges widely in value. Here we used viscosities for the continuous phase ($\eta_{c,0}$) ranging between 0.1 and 10 Pa.s (Karki & Stixrude, 2010; Xie et al., 2021). The convection flow induced within the magma ocean was characterized by the thermal Rayleigh number (Ra) describing the vigor of convection as a consequence of basal heating:

$$Ra = \frac{\alpha \rho_{c,0} g \Delta T H^3}{\eta_c \kappa} \tag{12}$$

with κ the heat diffusivity of the convective fluid (see Table 1 for value) and H the thickness of the reservoir in our models. We used a reservoir thickness $H = 1$ m which led to Ra values ranging between 1.8×10^6 and 1.8×10^8. In reality, the magma ocean is likely to involve the full thickness of the Earth's early mantle (i.e., a thickness of 2,900 km). In these conditions the Rayleigh number could reach values as high as 10^{30} and the associated dynamics would be extremely turbulent, playing a role on all scales down that of the crystals (V. S. Solomatov, 2000). However, crystal settling is likely to occur close to mechanical boundaries (CMB or solidified wall) where the velocity is lower than in the middle of the magma ocean. Hence our choice of parameters is relevant for monitoring the crystal settling at the bottom of a cooling magma ocean.

From our purely thermally convective models, we monitored the surface heat flux F which is proportional to the average value of the temperature gradient at the surface of the reservoir. We obtained F as a function of time for the range of Ra values considered in our study. We stopped our thermally convective simulations once the surface heat flux had converged to a constant value and used this value to calculate the corresponding Nusselt number Nu:

$$Nu = \frac{HF}{k\Delta T} \tag{13}$$

Figure 1 shows the Nu-Ra relation obtained from our models and compares our numerical results with the scalings obtained from Turcotte and Schubert (1982) and Wolstencroft et al. (2009). Our results show an agreement with these two scalings and we obtain $Nu = 0.14Ra^{0.34}$. For each Ra value used in our models, we obtained a velocity field for the continuous phase and a temperature field that were used as the initial temperature and velocity fields for the Euler-Euler model when we investigated the stability of a thin mushy layer with different characteristics (D_d and $\Delta\rho$). The initial velocity field for the dispersed phase used in the Euler-Euler model is null.

2.3. Numerical Model

We used the commercial software COMSOL Multiphysics (version 5.4) that has been previously validated for two phase flow applications (Qaddah et al. (2019, 2020)). Equations 1–5 were solved using the multiphase-flow tool-suite of COMSOL Multiphysics 5.4 (*Computational Fluid Dynamics* and *Heat transfer* modules) (For more informations see the *Code Availability* section). We used a 2D domain with a thickness H and a width of $4H$ (see Figure 2). Applying the model to a 2D geometry involves making assumptions, which may lead to discrepancies when compared with 3D models (e.g., V. S. Solomatov et al., 1993). The difference between 2D and 3D Rayleigh-Bénard simulations varies with the Prandtl number (Pr) which is the ratio between the momentum and the thermal diffusivities. For the range of Ra values used in our study, the $Nu - Ra$ and the $Nu - Pr$ scalings are similar for Pr values larger than 1 but differ when Pr values are close to 1 (van der Poel et al., 2013). In our simulations, the Prandtl numbers were much greater than 1 which makes our 2D models a reliable means of characterizing the

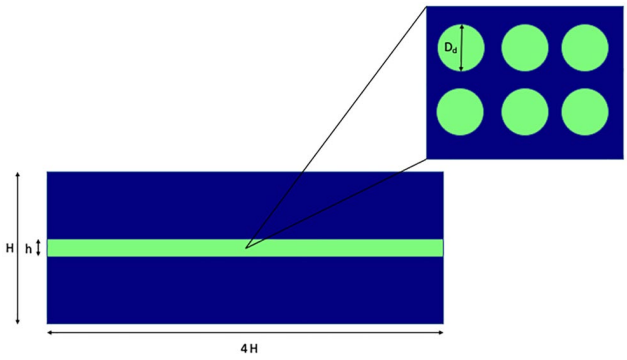

Figure 2. Schematic representation of the computational domain of our study. The blue material represents the continuous phase (molten silicates) and the green material represents the initially mixed continuous and dispersed phases. A zoomed view is illustrated in the top-right panel.

particle sinking dynamics in a thermally convecting reservoir. The computational cost of 2D models being significantly lower than for 3D models, we considered a 2D Cartesian geometry in our models as a first step toward more realistic models (Patočka et al., 2020). 3D models can be developed with COMSOL Multiphysics and will be the subject of a future study.

As a first attempt to characterize the stability of a thin newly formed mushy layer within a convective magma ocean, we arbitrarily considered that the thickness of this mushy layer was $h = H/10$. The mush thickness was set as a constant in all our models. Within the mushy layer, the crystals were considered as spheres with a fixed diameter D_d. In our models, this diameter ranges between 10^{-4} and 10^{-3} m. The initial volume fraction of crystal $\phi_{d,0}$ was also set to a constant value ($\phi_{d,0} = 0.1$).

The COMSOL Multiphysics software applies a finite-element method to a grid mesh to solve the set of equations (Equations 1–5). In order to study the sensitivity analysis of mesh size on the main results of this paper, we ran several models varying the size of the mesh (between 1.6 and 50 mm). In these resolution tests we looked at the overturn of a mushy layer with $h = H/10$, $\phi_{d,0} = 0.5$, $\eta_c = 10$ Pa.s (i.e., Ra $= 1.8 \times 10^6$) and $\Delta\rho = 30$ kg.m^{-3}. Figure 3 shows the average value $\phi_{d,average}$ along a horizontal profile located at the bottom of the reservoir at $t = 600$ s when the mushy layer is fully sedimented. $\phi_{d,average}$ increases with decrease in the mesh size from 0.05 to 0.01 m. However, below a mesh size value of 0.01 m, $\phi_{d,average}$ converges to a constant value of 0.45. In order to save computational time, we used a mesh size of 0.008 which gave an error of 7.7% relative to the converged value obtained for the smallest mesh size. In addition, for the most vigorously convective contexts, we decreased the size of the mesh by a factor of two either in the lowermost part of the reservoir where crystal-rich patches are likely to settle or within the whole reservoir. Therefore, the calculation domain was composed of 100,000–180,000 mesh elements. We list the details of our models in Table 2. Each run presented in this study represents (for the Euler-Euler flow model only) 12–72 hr computation time on a bi-processor, 8-cores, 3.2-GHz workstation.

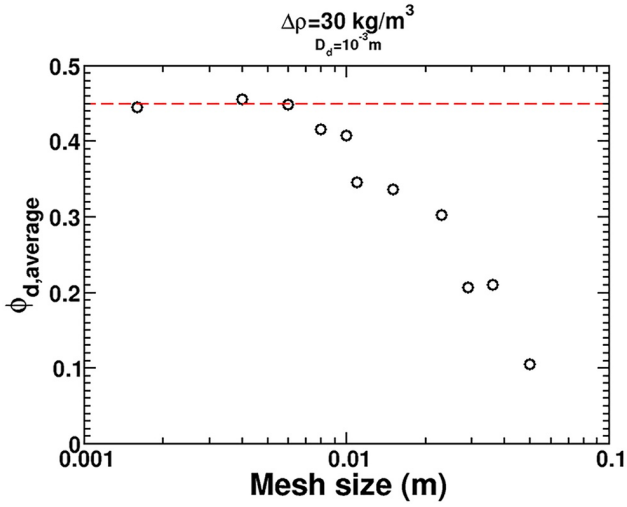

Figure 3. Dispersed fraction averaged along an horizontal profile at the bottom of the computational domain as a function of the mesh size. In these models, $h = H/10$, $\phi_{d,0} = 0.5$, $\eta_c = 10$ Pa.s, and $\Delta\rho = 30$ kg.m^{-3}. The red dashed line represents the asymptotic value at which $\phi_{d,average}$ converges for high-resolution (i.e., small mesh size) models.

2.4. Reference Case

In this subsection, we detail the case corresponding to simulation no. 47 in Table 2. For this reference case, we used Ra $= 4.4 \times 10^6$ (corresponding to $\eta_c = 4$ Pa.s), $\Delta\rho = 50$ kg.m^{-3} ($\Delta\rho/\rho_{c,0} = 1.7\%$) and $D_d = 10^{-3}$ m. Figure 4 illustrates the thermal and dynamic time evolutions of the convective magma ocean and the mushy crystal layer. Because of negative buoyancy, the crystal layer sinks rapidly. Figure 4 shows that a rapid overturn occurs concentrating the crystals in the lower part of the reservoir during the first hundreds of seconds after the formation of the layer. First, the crystal fraction is diluted in the lower reservoir. Then it starts to separate out into patches in which the concentration is much higher than the initial concentration. This early stage limits the heat transfer from the bottom surface to the reservoir, leading to a transient cooling of the magma.

To monitor the evolution of the average concentration C (particles/m^3) of crystals in the upper mid reservoir for the reference case, we defined:

$$e = \frac{\int_{H/2}^{H}\int_{0}^{4H} C\,dx\,dz}{\int_{0}^{H}\int_{0}^{4H} C\,dx\,dz} \tag{14}$$

Höink et al. (2005) refers to this parameter as the relative entrainment. Figure 5 illustrates the time evolution of e for our reference case and shows that for a period of 2,000 s, the upper reservoir is depleted in crystals. After nearly 10,000 s, large hot plumes form at the bottom of the reservoir (see Figure 4) and transport the crystals up to the upper reservoir. Hence the crystal concentration in the upper reservoir increases. This second phase lead to

Table 2
Parameters for All Simulations Used in This Study

	η_c(Pa.s)	Ra	D_d (m)	$\Delta\rho$ (kg/m^3)	Sh
#1	0.1	1.8×10^8	10^{-4}	5	4.16
#2	0.1	1.8×10^8	10^{-4}	10	2.08
#3	0.1	1.8×10^8	10^{-4}	20	1.04
#4	0.1	1.8×10^8	10^{-4}	30	0.69
#5	0.1	1.8×10^8	10^{-4}	40	0.52
#6	0.1	1.8×10^8	10^{-4}	50	0.42
#7	0.1	1.8×10^8	10^{-3}	5	0.41
#8	0.1	1.8×10^8	10^{-3}	10	0.2
#9	0.1	1.8×10^8	10^{-3}	20	0.1
#10	0.1	1.8×10^8	10^{-3}	30	0.07
#11	0.1	1.8×10^8	10^{-3}	40	0.052
#12	0.1	1.8×10^8	10^{-3}	50	0.042
#13	0.1	1.8×10^8	10^{-3}	80	0.026
#14	0.1	1.8×10^8	10^{-3}	100	0.02
#15	0.2	$9. \times 10^7$	10^{-3}	50	0.052
#16	0.2	$9. \times 10^7$	10^{-3}	60	0.044
#17	0.4	4.4×10^7	10^{-3}	5	0.65
#18	0.4	4.4×10^7	10^{-3}	10	0.33
#19	0.4	4.4×10^7	10^{-3}	20	0.16
#20	0.4	4.4×10^7	10^{-3}	30	0.11
#21	0.4	4.4×10^7	10^{-3}	40	0.082
#22	0.4	4.4×10^7	10^{-3}	50	0.065
#23	0.7	$3. \times 10^7$	10^{-3}	40	0.1
#24	0.7	$3. \times 10^7$	10^{-3}	50	0.081
#25	1.	1.8×10^7	10^{-4}	5	8.9
#26	1.	1.8×10^7	10^{-4}	10	4.45
#27	1.	1.8×10^7	10^{-4}	20	2.22
#28	1.	1.8×10^7	10^{-4}	30	1.48
#29	1.	1.8×10^7	10^{-4}	40	1.1
#30	1.	1.8×10^7	10^{-4}	50	0.089
#31	1.	1.8×10^7	10^{-3}	10	0.44
#32	1.	1.8×10^7	10^{-3}	20	0.22
#33	1.	1.8×10^7	10^{-3}	30	0.148
#34	1.	1.8×10^7	10^{-3}	35	0.127
#35	1.	1.8×10^7	10^{-3}	40	0.111
#36	1.	1.8×10^7	10^{-3}	50	0.09
#37	1.	1.8×10^7	10^{-3}	100	0.044
#38	4.	4.4×10^6	10^{-4}	50	1.4
#39	4.	4.4×10^6	3×10^{-4}	50	0.47
#40	4.	4.4×10^6	6×10^{-4}	50	0.23
#41	4.	4.4×10^6	10^{-3}	50	0.14
#42	4.	4.4×10^6	10^{-3}	70	0.1
#43	4.	4.4×10^6	10^{-3}	80	0.0875

efficient mixing of the whole reservoir and the crystal concentration returns to its initial value, with slight oscillations. Figure 5 shows that the initial concentration in the upper reservoir is slightly higher than its theoretical value of 0.01. This is due to the mesh properties that encompass a larger volume of crystal leading to an initial value of $e = 0.0105$.

3. Parametric Study

In the following section, we look at the influence of the density difference between the crystals and the magma, the crystal size, and the magma viscosity on the settling dynamics within a convecting magma ocean.

3.1. Influence of the Density Difference $\Delta\rho$

During the solidification of the magma ocean, the density of the crystal phase varies relative to the molten phase based on its ability to integrate dense chemical elements into its structure. Within the fully molten mantle, the first crystal to form is bridgmanite. This first crystal is Fe-poor, and achieves neutral chemical buoyancy close to the core mantle boundary (Caracas et al., 2019). The relative Fe content then increases in the melt, potentially leading to the formation of a basal magma ocean overlain by a thick layer of bridgmanite. The level of neutral buoyancy moves toward the shallow mantle as solidification proceeds (Boukaré et al., 2015; Caracas et al., 2019; V. S. Solomatov, 2000). This scenario could lead to fractional crystallization of the early mantle (Patočka et al., 2020). However, if re-entrainment enhanced by vigorous convection is taken into account, crystal dispersion might be an efficient process that would favor batch (or equilibrium) crystallization of the early mantle (V. S. Solomatov et al., 1993). The melt-crystal density crossover in both these scenarios is discussed by Caracas et al. (2019). Here, we monitor the influence of the chemical density difference on the settling dynamics considering relatively small chemical density differences ($10 - 100$ kg.m^{-3}), such as are relevant during the early stages of mantle solidification. The chemical density difference is fixed in each simulation and is superimposed onto the thermal density difference which can evolve during cooling. We note that in our models, the density difference related to temperature differences ($\alpha\rho\Delta T = 3$ kg.m^{-3}) is smaller than the density difference between the magma and the crystals.

In Figure 6, we illustrate the reference case presented in Figure 4, but in which the density difference has been increased from $\Delta\rho = 50$ kg.m^{-3} to $\Delta\rho = 100$ kg.m^{-3}. As already illustrated in Figures 4 and 6 show that because of negative buoyancy, the crystal layer sinks rapidly. After this fast settling at the bottom of the reservoir, particle entrainment occurs from the dunes (10,000 s after initiation of the settling). However, because of a larger density difference between the dispersed phase and the continuous phase, efficient mixing does not occur in this case. Particle entrainment dwindles until the layer is fully sedimented at the bottom of the reservoir (28,000 s after initiation of the settling). Again, the sedimented layer acts as an insulating layer by limiting heat transfer from the bottom of the reservoir. As a consequence, the mean temperature is significantly lower due to this insulating layer at the bottom when full sedimentation is achieved.

Figure 5 compares the time evolution of the concentration of particles in the upper part of the reservoir for the two density differences illustrated in Figures 4 and 6. Throughout the simulation, the particle concentration for $\Delta\rho = 50$ kg.m^{-3} remains higher than the concentration for $\Delta\rho = 100$ kg.m^{-3}. This feature is in agreement with Lavorel and Le Bars (2009) who monitored the relative number of particles in suspension as a function of the fluid/

Table 2
Continued

	η_c(Pa.s)	Ra	D_d (m)	$\Delta\rho$ (kg/m^3)	Sh
#44	4.	4.4×10^6	10^{-3}	100	0.07
#45	10	1.8×10^6	10^{-4}	5	19
#46	10	1.8×10^6	10^{-4}	10	9.51
#47	10	1.8×10^6	10^{-4}	20	4.76
#48	10	1.8×10^6	10^{-4}	30	3.17
#49	10	1.8×10^6	10^{-4}	40	2.37
#50	10	1.8×10^6	10^{-4}	50	1.9
#51	10	1.8×10^6	10^{-4}	100	0.95
#52	10	1.8×10^6	10^{-3}	5	1.9
#53	10	1.8×10^6	10^{-3}	10	0.95
#54	10	1.8×10^6	10^{-3}	20	0.47
#55	10	1.8×10^6	10^{-3}	30	0.31
#56	10	1.8×10^6	10^{-3}	40	0.24
#57	10	1.8×10^6	10^{-3}	50	0.19
#58	10	1.8×10^6	10^{-3}	70	0.136
#59	10	1.8×10^6	10^{-3}	100	0.095
#60	10	1.8×10^6	10^{-3}	125	0.076
#61	10	1.8×10^6	10^{-3}	200	0.048

Note. We calculate the Sh value from Equation 15 by combining Equations 12 and 13 and the expression $\mathrm{Nu} = 0.14\mathrm{Ra}^{0.34}$ obtained from Figure 1 to compute the heat flow F.

particle density difference during the first 1,000 s from a starting scenario of uniform distribution within the reservoir. Figure 5 also shows that increasing the density difference decreases both the minimum value of the particle concentration in the upper reservoir and the time taken to reach this minimum.

3.2. Influence of the Crystal Size

Upon solidifying, crystals form following the nucleation and growth mechanisms (V. Solomatov, 2015). The crystal size reached at equilibrium depends on the nature of the mineral and on the cooling rate within the convecting reservoir. The grain size ranges between 10^{-4} and 10^{-3} m in typical magma ocean conditions (V. Solomatov, 2015). Here, we monitor the influence of the crystal size in our models. It was not possible for us to consider grain sizes larger than our grid mesh size (8×10^{-3} m). Indeed, when the mesh size and crystal size are similar, the Euler-Euler description is no longer relevant because (a) the solid fraction ϕ_d as a smooth local average of the volume fraction of the solid phase becomes ill-defined at the scale of the crystal size, and (b) given that the crystals are of comparable size to the flow features, taking their shape into consideration becomes important for solving the flow itself. Hence, we compare the reference case (with $D_d = 10^{-3}$ m) to cases with smaller sizes (down to $D_d = 10^{-4}$ m).

Figure 7 shows the time evolution of the crystal fraction in the upper part of the reservoir for the four particle diameters D_d considered. It shows that for the range of crystal sizes considered ($10^{-4} \leq D_d \leq 10^{-3}$ m), the time needed for the relative entrainment e to reach its minimum value is very little affected the particle diameter D_d and typically ranges between 305 and 315 s. Moreover the final behavior of the reservoir in terms of sedimentation/suspension is not dependent on the crystal size for the range of sizes considered here. For our range of particle diameters and in the range of controlling parameters corresponding to the suspension regime, the overturn process is rapidly followed by a suspension regime in which the particles are efficiently mixed within the convecting reservoir.

3.3. Influence of the Viscosity

The viscosity of the molten phase (η_c) is a key parameter governing the cooling dynamics of the magma ocean and in particular the solidification timescale (Monteux et al., 2016). According to Karki and Stixrude (2010), η_c for anhydrous $MgSiO_3$ melt may decrease down to 0.048 Pa.s at mid-mantle conditions ($P = 70$ GPa and $T = 4000$ K along the magma ocean adiabat). For molten peridotite, Xie et al. (2021) obtained a viscosity ranging between 0.017 and 0.038 Pa.s. It should be noted that vertical velocities are low and the flow is much less turbulent adjacent to horizontal solid boundaries rather than in the center of a deep convecting magma ocean (Elkins-Tanton, 2012). In the context of this study (i.e., close to solid boundaries), the flow is laminar. Hence the characteristic Reynolds number has to be maintained below a value of $\sim 10^3$ and the range of viscosity values in our models must be chosen accordingly. To maintain laminar flow, we consider $0.1 \leq \eta_c \leq 10$ Pa.s.

The initial conditions for the continuous phase velocity and temperature fields change as a function of the viscosity. To ensure that the differences we observe between the various viscosity values are not due to differences in the initial conditions, we ran each model for a fixed viscosity value with different time values corresponding to different initial conditions. Figure 8 shows that the continuous phase viscosity governs the ability of the solid phase to mix or settle at the bottom of the reservoir. What is interesting is non linearity of this process. In Figure 8 we can see that for the lowest viscosity, the crystal layer rapidly mixes with the convecting reservoir. However, for $0.4 \leq \eta_c \leq 1$, the rapid overturn process is not followed by a mixing process, and the final concentration within the upper part of the reservoir does not reach the value typical of efficient mixing. Finally, for $\eta_c > 1$ Pa.s, the overturn process is followed by a vigorous mixing process similarly to the case with $\eta_c = 0.1$ Pa.s. Figure 8 shows that the molten phase viscosity also governs the timing of the early overturn (i.e., the time needed for the particle concentration in the upper part of the reservoir to reach the minimal value). This overturn time increases from nearly 40 s (for $\eta_c = 0.1$ Pa.s) up to 2,000 s (for $\eta_c = 10$ Pa.s).

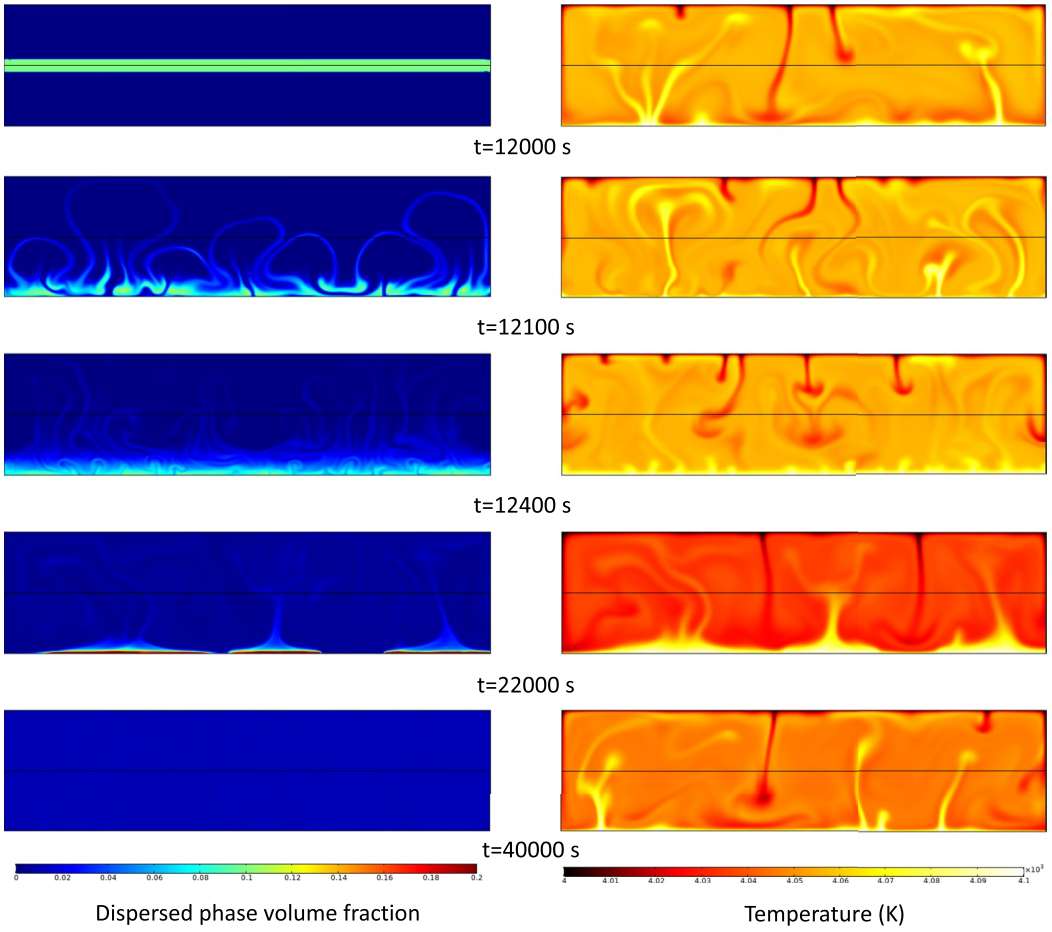

Figure 4. Time evolution (from top to bottom) of the dispersed volume concentration (left) and the temperature (right) for the reference case (with Ra = 4.4×10^6 (corresponding to $\eta_c = 4$ Pa.s), $\Delta\rho = 50$ kg.m^{-3}, and $D_d = 10^{-3}$m).

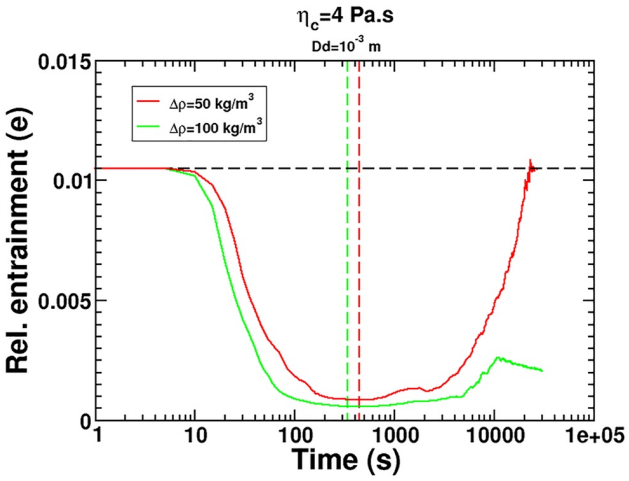

Figure 5. Time evolution of the particles concentration in the upper part of the reservoir with Ra = 4.4×10^6 (corresponding to $\eta_c = 4$ Pa.s) and $D_d = 10^{-3}$ m. The red line illustrates the case where $\Delta\rho = 50$ kg.m^{-3} and the green line the case where $\Delta\rho = 100$ kg.m^{-3}. Vertical dashed lines illustrate the time when the minimum value of e is obtained.

4. A Criterion for the Stability of a Crystallizing Layer

We have illustrated the separate influences of the density difference between crystals and melt, grain size and melt viscosity on the behavior of a crystallizing layer within a magma ocean. We now look at the ability of the flow generated by convection within the magma ocean to initiate movement and suspension of sedimented crystals and to lead to efficient mixing within the magma ocean. We introduce the Shields number Sh which is the ratio of the tangential stress from convective flow over the buoyancy stress relative to the density difference between the crystals and the melt (V. S. Solomatov et al., 1993):

$$Sh = \left(\frac{\eta_c \alpha g F}{C_p}\right)^{1/2} \frac{1}{\Delta\rho g D_d} \tag{15}$$

Large Sh values favor a suspension regime while small Sh values favor a sedimentation regime. The two regimes are separated by a critical Shields number value Sh_c. From their analog experiments, V. S. Solomatov et al. (1993) estimated a critical value $Sh_c = 0.1 - 0.2$. We have run a total of 61 numerical models (see Table 2 for values) with different sets of D_d, $\Delta\rho$, and η_c whose value ranges are given in Table 1. Each model corresponds to an Sh value

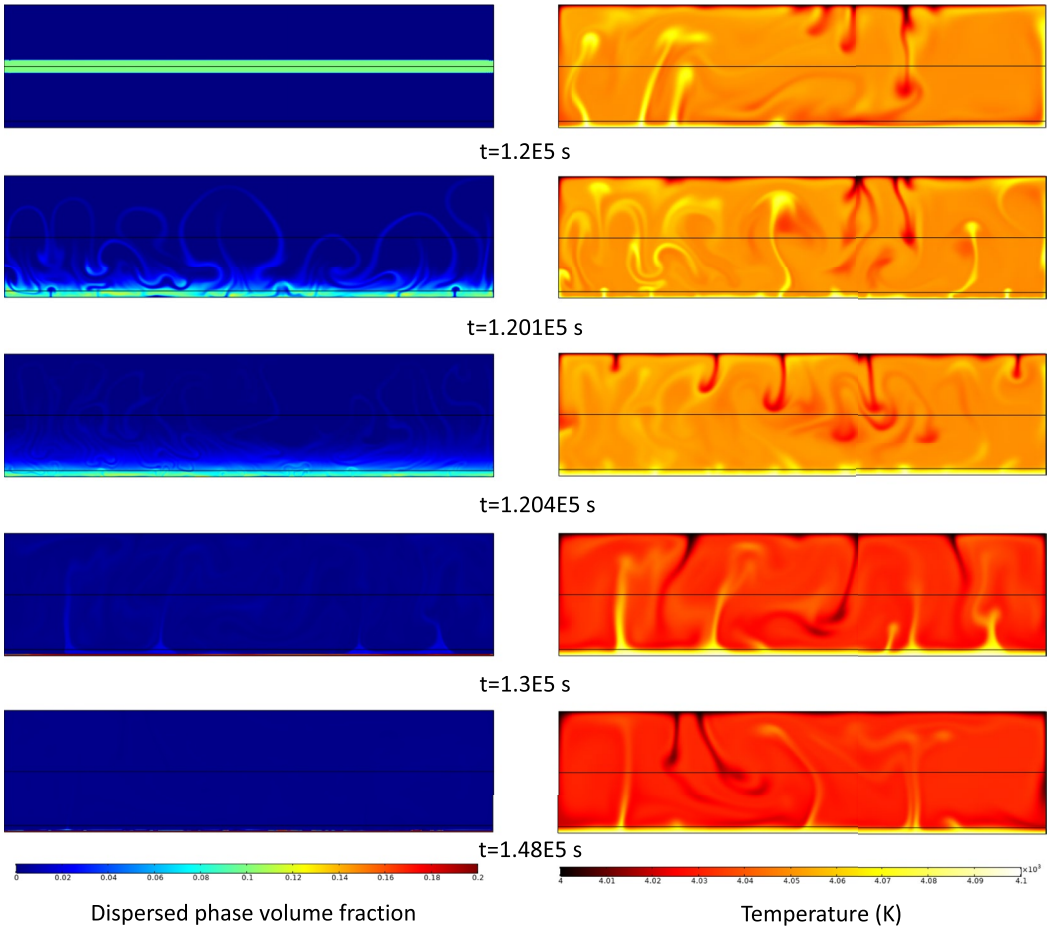

Figure 6. Time evolution (from top to bottom) of the dispersed volume concentration (left) and the temperature (right) for the case with Ra = 4.4×10^6 (corresponding to $\eta_c = 4$ Pa.s), $\Delta\rho = 100$ kg.m^{-3}, and $D_d = 10^{-3}$ m.

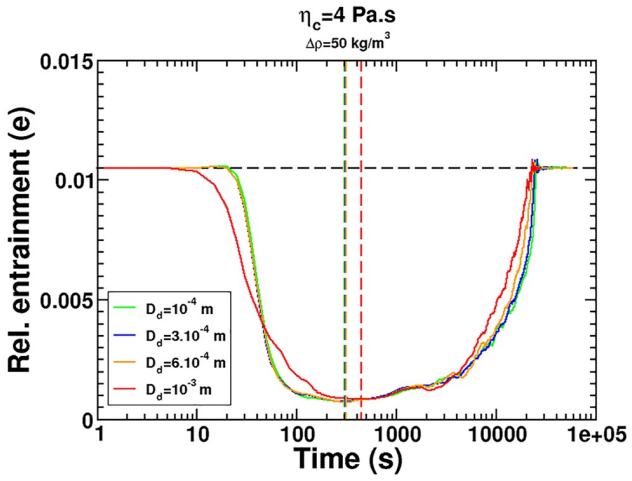

Figure 7. Time evolution of the particle concentration in the upper part of the reservoir with Ra = 4.4×10^6 (corresponding to $\eta_c = 4$ Pa.s) and $\Delta\rho = 50$ kg.m^{-3}. The red line illustrates the case with $D_d = 10^{-3}$ m, the green line the case with $D_d = 10^{-4}$ m, the blue line the case with $D_d = 3 \times 10^{-4}$ m and the orange line the case with $D_d = 6 \times 10^{-4}$ m. Vertical dashed lines illustrate the time when the minimum value of e is obtained.

calculated using a combination of Equations 12 and 13 and the expression $\mathrm{Nu} = 0.14\mathrm{Ra}^{0.34}$ obtained from Figure 1 to compute the heat flow F (see Table 2 for values). Monitoring the concentration of grains in the upper reservoir ($e(t)$) in each model makes it possible to determine whether the models end up in the suspension or sedimentation regime.

In Figure 9, we illustrate the Sh values as a function of the molten phase viscosity η_c. Two regimes are considered: one in which the grain concentration in the upper part of the reservoir (e) does not return to its initial value, known as the sedimentation regime; another one in which the grain concentration in the upper part of the reservoir does return to its initial value, known as the suspension regime. As shown in Figure 8, some cases may end up in an intermediate zone where the final concentration is $0.005 < e < 0.01$. We consider that these intermediate cases fall into the sedimentation regime. Sedimentation and suspension regimes are separated by the critical Shields number value (Sh_c).

According to Figure 9, the Sh_c value is a non-linear function of the continuous molten phase viscosity. For $\eta_c > 1$, Sh_c seems to be constant and independent of the η_c value. However, when $\eta_c < 1$, the Sh_c value decreases with decreasing viscosity values following $\mathrm{Sh}_c = 0.1\eta_c^{0.45}$. As a consequence Sh_c is not influenced by the increase in Rayleigh number up to Ra = 1.8×10^7. For Ra values higher than 1.8×10^7 the increase in kinetic energy induced by the vigorous convection in the system results in the following decrease in Sh_c:

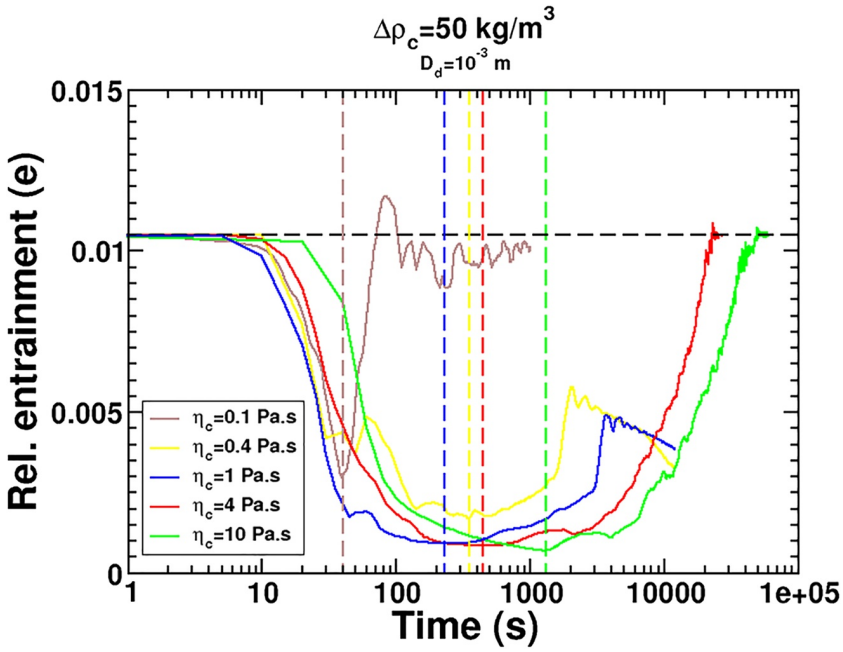

Figure 8. Time evolution of the particles concentration in the upper part of the reservoir with $\Delta\rho = 50$ kg.m^{-3} and $D_d = 10^{-3}$ m. The different color lines illustrate cases with different viscosities for the continuous phase ranging from 0.1 to 10 Pa.s. Vertical dashed lines illustrate the time when the minimum value of e is obtained. Note that we tested the case with $\eta_c = 0.1$ Pa.s with two different meshes (6 and 8 mm mesh) and the difference between the two curves is not significant.

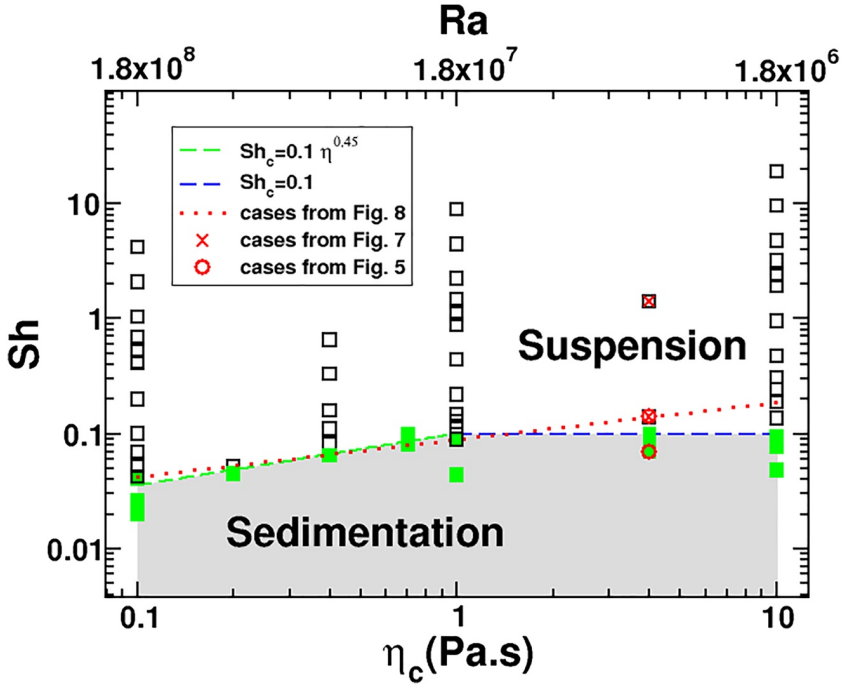

Figure 9. Shields number value (Sh) as a function of the molten continuous phase viscosity (η_c) (or Ra for the top x-axis). Square symbols correspond to the models run in this study (see Table 2 for values). Empty black symbols represent cases where the suspension regime is reached. Filled green symbols represent cases where the sedimentation regime is reached. The two regimes are separated by dashed lines (green for $\eta_c \leq 1$, blue for $\eta_c \geq 1$) illustrating the critical Shields number (Sh_c). Red symbols and the red dotted line illustrate the values for the cases represented in Figures 5, 7, and 8 respectively. We calculate the Sh values by combining Equations 12 and 13 and the expression $Nu = 0.14Ra^{0.34}$ obtained from Figure 1 to compute the heat flow F within Equation 15.

$$Sh_c = 184.Ra^{-0.45} \quad (16)$$

The non-linear dependence of Sh_c on viscosity explains why the crystal settling behavior can vary back and forth between sedimentation and suspension regimes when the viscosity increases, as shown with a dotted red line in Figure 9, which shows the path followed by the models detailed in Figure 8. Moreover, Figure 9 shows that Sh_c is smaller than the range of values proposed by V. S. Solomatov et al. (1993) (0.1 − 0.2). This feature is particularly visible for the lowest range of viscosities used in our models. For a magma ocean viscosity value of 0.1 Pa.s, the Sh_c value may decrease down to 0.04 which makes it difficult to envision crystal settling in such a convecting environment, especially given the typical viscosity values for a magma ocean (Karki & Stixrude, 2010; Xie et al., 2021). Decreasing the viscosity down to the lowest values proposed by Xie et al. (2021) may enhance this feature. Finally, we have tested the cases with $Ra = 1.8 \times 10^6$ (i.e., $\eta_c = 10$ Pa.s) (cases referred as #52–#61 in Table 2) considering no-slip boundary conditions. From these models (not shown here), we obtain $0.19 < Sh_c < 0.31$ while, when considering free-slip boundary conditions, we obtain $0.095 < Sh_c < 0.136$. This result illustrates that free-slip boundary conditions favor suspension regimes compared to no-slip boundary conditions.

5. Fate of Mushy Material in the Context of a Progressive Magma Ocean Crystallization

In the previous sections, we showed the influence of the viscosity, crystal size and density difference between melt and crystals on the crystals settling dynamics within a convecting magma ocean. We proposed a criterion (Sh_c) to determine the stability of a crystallizing layer based on the convection/buoyancy stress ratio. We showed that the transition between suspension and sedimentation could occur for Sh_c values lower than 0.1. In the Sh_c expression (see Equation 15), the buoyancy relation between newly formed crystals and the magma ocean itself is a major parameter for determining how the crystal settling and the early mantle differentiation is likely to have occurred. Caracas et al. (2019) have constrained the evolution of the neutral buoyancy depth during magma ocean solidification and the progressive enrichment in Fe content of the residual melt. In particular, they showed that the neutral buoyancy depth moved toward shallower depths during magma ocean solidification, thus favoring the formation of a basal magma ocean. In the following sections, we aim to constrain the magma ocean crystallization dynamics by comparing (a) the critical density difference separating the suspension and sedimentation regimes derived from our detailed numerical approach described above and (b) the density difference between crystals and melt calculated from a plausible range of chemical compositions.

5.1. Parameters Controlling the Solidification of a Magma Ocean on an Earth-Like Planet

We investigated the implications of our model on the mechanism of magma ocean (MO) solidification on Earth. More precisely, we investigated the possibility of bridgmanite (Bg) segregation based on its buoyancy (positive or negative). For this, we compared the density difference between the MO and the solid crystal $\Delta\rho_{MO}$ calculated for different compositions and the critical density contrast $\Delta\rho_{crit}$ above which crystal segregation is likely to occur. $\Delta\rho_{crit}$ is derived from Equation 15 by calculating:

$$\Delta\rho_{crit} = \left(\frac{\eta_c \alpha g F}{C_p}\right)^{1/2} \frac{1}{Sh_c g D_d} \quad (17)$$

and considering $Sh_c = 0.1$ which is a conservative value for a magma ocean viscosity of 0.1 Pa.s or less (Xie et al., 2021). At a given depth (z), a $\Delta\rho_{MO}$ higher than the critical value $\Delta\rho_{crit}$ would lead to efficient Bg sedimentation at the bottom of the MO. By extension, we also considered that Bg would efficiently segregate into a solid layer above a basal magma ocean for $\Delta\rho_{MO}/\Delta\rho_{crit}$ of less than −1. Calculating $\Delta\rho_{MO}$ requires a number of assumptions:

1. We used pyrolite as a reference model for the mantle composition. Pyrolite is obtained by adding a crustal component to the present-day depleted (peridotitic) upper mantle (Ringwood, 1975). To retain some flexibility in terms of possible mantle composition, we subtracted or added bridgmanite (Bg) to pyrolite, producing a more or less mafic mantle material, respectively. Below, we argue that the composition of the primitive upper mantle (PUM) should be close to that of pyrolite, as is widely accepted.
2. The composition of the bulk silicate Earth (BSE) is still not well established, because a number of deep mantle reservoirs could have a different composition to pyrolite: The large low seismic velocity provinces (LLSVP)

seem to present a different mineralogy (e.g., Vilella et al., 2021), with the deep lower mantle possibly being more like bridgmanitic than pyrolitic (Murakami et al., 2012) and there could be relics of a basal magma ocean above the core-mantle boundary (CMB) (Labrosse et al., 2007) or of early mantle overturns (e.g., Boukaré et al., 2015). In our models, we allowed a lot of variation in terms of the size of the possible Bg-rich or mafic reservoirs that might have segregated in the deep mantle during the solidification of the MO. Variance of the BSE composition was achieved by adding or subtracting up to 40% of Bg to the pyrolite mantle reference. This is a much broader range of chemical variation than the current uncertainty on the major element concentration in the BSE.

3. The Bg composition was calculated by equilibrating it with the melt in the mushy MO, using partitioning coefficients $K(\mathrm{Al})^{Bg/Melt} = 0.5$ and $K(\mathrm{Fe})^{Bg/Melt} = 0.1$ or 0.25. The value of $K(\mathrm{Al})^{Bg/Melt}$ does not significantly impact our calculations. $K(\mathrm{Fe})^{Bg/Melt}$ remains controversial as values in the literature range from ∼0.07 to ∼0.5 (Andrault et al., 2012; Nomura et al., 2011). The former value might be an underestimate as it was measured in a sample showing extreme chemical segregation along a temperature gradient, which artificially heightens Fe-depletion in Bg at the highest temperatures. In the latter study, the experimental conditions corresponded to solidus-like temperatures, at which Fe is more compatible in Bg. Relevant temperatures for MO solidification cover the range from liquidus-like to intermediate between liquidus and solidus. Therefore, we chose values for $K(\mathrm{Fe})^{Bg/Melt}$ of 0.1 or 0.25 for our calculations.
4. As a reference model for the mushy MO, we used a Bg grain diameter (D_{Bg}) of 0.1–10 mm, viscosity (η) of 0.1 Pa.s (Xie et al., 2020), intrinsic conductivity (k) of 5 W/m/K (Hofmeister, 1999) and heat capacity (Cp) of 1,800 J/kg/K (Asimow, 2018). We considered that the melt had the same composition at all depths because of efficient mixing in a turbulent MO.
5. We considered that the term ΔT used in F calculation from Equations 13 and 17 was the temperature difference between the Earth's surface and the bottom of the MO, after correcting for the adiabatic increase in temperature with mantle depth. We initially fixed the surface temperature (T_{surf}) to 500 K (Lebrun et al., 2013; Monteux et al., 2020), but later investigated T_{surf} of 1000 and 1500 K. We considered that the bottom of the MO (z_{MO}) was the depth where mantle solidification was achieved for a mixture of 60% Bg and 40% melt. During mantle solidification, z_{MO} evolves from the CMB depth toward the surface. We assumed that the temperature at a depth z_{MO} followed the solidus temperature profile of pyrolite ($T_{sol}(z_{MO})$) (Pierru et al., 2022). We note that using the solidus profile yields a conservative ΔT compared to the true temperature which should lie between the solidus and the liquidus. Then, we calculated $\Delta T(z_{MO})$ of a MO extending from a depth z_{MO} to the Earth's surface using the following equation:

$$\Delta T(z_{MO}) = T_{sol}(z_{MO}) - T_{surf} - \Delta T_{ad}(z_{MO}) \quad (18)$$

where $\Delta T_{ad}(z_{MO})$ is the temperature difference between $T_{sol}(z_{MO})$ and the corresponding potential surface temperature extrapolated from $T_{sol}(z_{MO})$ to the surface along the MO adiabatic temperature profile. The adiabatic gradient in the MO was calculated using the equations of state available for different silicate melt compositions (Asimow, 2018). $\Delta T(z_{MO})$ is found to range between ∼1300 K and ∼2000 K for MO extending from 660 km (24 GPa) to 2,800 km (135 GPa), respectively (see Figure 10).

6. We calculated the density of Bg (ρ_{Bg}) along the mantle solidus, using the equations of state (EoS) for $MgSiO_3$, $FeSiO_3$, and Al_2O_3 end-members (Matas et al., 2007). The breakdown into end-members assumes Bg of $(Mg_{1-x-y}Fe_xAl_y)(Si_{1-y}Al_y)O_3$ stoichiometry with a dominant fraction of Fe^{2+} over Fe^{3+} at lower mantle conditions, in agreement with previous works (e.g., Andrault et al., 2018). This assumption has little impact on the Bg density; the dominant parameter is the global Fe content in Bg, itself controlled by $K(\mathrm{Fe})^{Bg/Melt}$ (discussed above). At the same P-T conditions, we calculated the MO density (ρ_{Melt}) and thermal expansion (α_{Melt}) using the EoS of the molten end-member $MgSiO_3$ enstatite, Mg_2SiO_4 forsterite, Fe_2SiO_4 fayalite, $CaMgSi_2O_6$ diopside, and $CaAl_2Si_2O_8$ anorthite (Asimow, 2018). These calculations yield the Bg-to-melt density contrast ($\Delta\rho_{MO} = \rho_{Bg} - \rho_{Melt}$, Figure 11) along the mantle solidus: $\Delta\rho$ decreases with increasing pressure regardless of the composition of the mushy mantle, because the melt is more compressible than Bg.
7. We did not attempt to model the final stages of MO crystallization, when the bottom of the MO would be shallower than 660 km depth, because the phase relations rely on the melting diagrams at upper mantle P-T conditions.

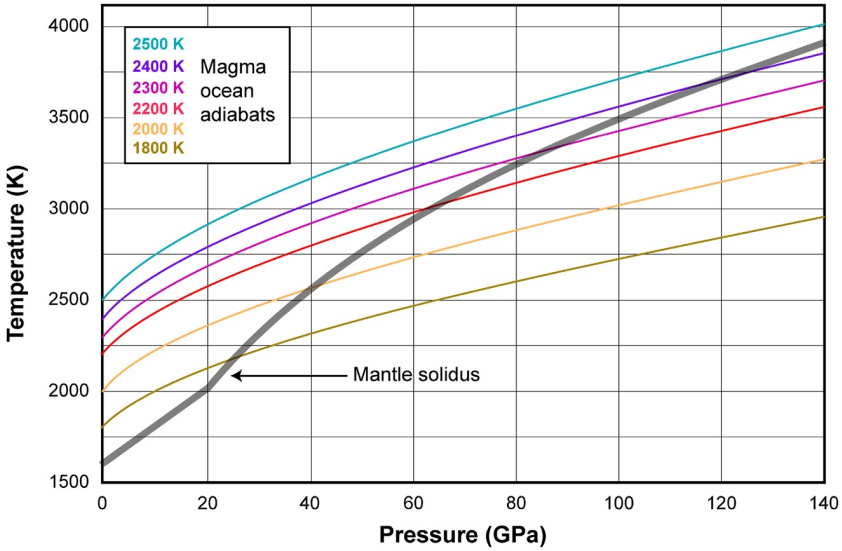

Figure 10. Temperature profiles corresponding to (gray thick line) the solidus of the pyrolite mantle (Pierru et al., 2022) and (colored lines) adiabatic gradients of MO for potential surface temperatures from 1800 to 2500 K.

5.2. Conditions for Segregation of Bg in the Mushy Magma Ocean

5.2.1. Effect of Melt Composition

We then calculated the ratio of density differences $\chi_\rho = \Delta\rho_{MO}/\Delta\rho_{crit}$ at all lower mantle depths using the parameters defined above. First, we fixed the grain size of Bg to 1 mm, $K(Fe)^{Bg/Melt}$ to 0.1 or 0.25, and varied the MO composition from pyrolite −40% Bg to pyrolite +40% Bg (i.e., 70% pyrolite and 30% Bg). χ_ρ was either positive or negative (Figure 12), depending on the solid-melt density difference (Figure 11). A $\Delta\rho_{MO}$ value greater than $\Delta\rho_{crit}$ (i.e., $\chi_\rho > 1$) indicates efficient Bg segregation to the bottom of the MO. Our calculations show that Bg

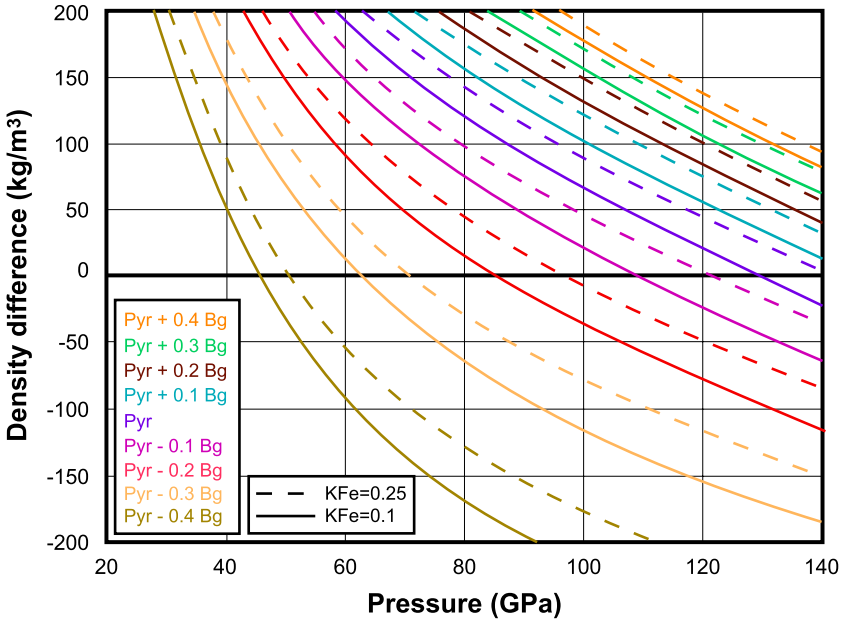

Figure 11. Solid-melt density difference ($\Delta\rho_{MO} = \rho_{Bg} - \rho_{melt}$) calculated using the P-V-T equation of state for Bg (Matas et al., 2007) and MO (Asimow, 2018), after decomposition into end-members. Calculations are performed for several MO compositions by adding or subtracting a fraction of Bg to a pyrolite-based mantle reference, and for Fe partition coefficients between Bg and MO ($K(\mathrm{Fe})^{Bg/Melt}$) of 0.1 or 0.25. Positive values indicate lighter melt.

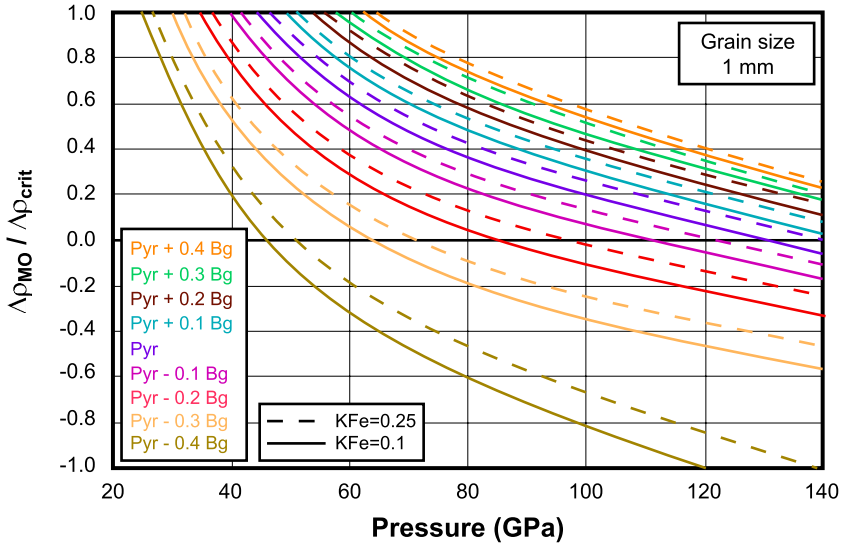

Figure 12. Density contrast ratio $\Delta\rho_{MO}/\Delta\rho_{crit}$ in the MO. Values greater than 1, or less than −1, indicate efficient Bg segregation below, or above, a mushy MO, respectively.

segregation happens in shallow MOs for all chemical compositions investigated. For pyrolite, this is in agreement with previous work to determine the MO viscosity (Xie et al., 2020). The higher the Bg content in the MO, the earlier (and deeper) Bg segregation occurs during the MO solidification; this is because $\Delta\rho_{MO}$ is higher when the bulk Fe-content is lower. As expected, lower $K(\mathrm{Fe})^{Bg/Melt}$ favors a denser melt, and thus lower $\Delta\rho_{MO}$. Still, our calculations show a moderate impact on the $K(\mathrm{Fe})^{Bg/Melt}$ variations, from 0.1 to 0.25. Finally, efficient Bg segregation could occur above a dense MO for an MO composition highly depleted in Bg; this is suggested by $\chi_\rho < -1$ for pyrolite −40%Bg at pressures greater than ∼120 GPa, for a Bg grain size of 1 mm (Figure 12) or more (see below).

5.2.2. Effect of Grain Size

We also investigated the role of the Bg grain size, for five different mantle compositions (Figure 13). First we focused on a melt of pyrolite composition. χ_ρ is found to be positive at most mantle depths, because $\Delta\rho_{MO}$ is also positive (Figure 11), except in the lowermost mantle for $K(\mathrm{Fe})^{Bg/Melt} = 0.1$. Still, χ_ρ can only be greater than 1 for D_{Bg} of more than 0.5 mm; Bg-grains of for example, 2 mm segregate when pressure (depth) is lower than 70 GPa (1,650 km). Grain size in a crystallizing MO remains a complicated issue (V. Solomatov, 2015): (a) as long as the MO is fully liquid close to the planetary surface, grains are often remelted within the large scale convection movements, meaning that grain size is controlled by nucleation processes; (b) When the crystallization zone reaches the surface, it enables some grains to grow indefinitely. Depending on the curves of the mantle solidus and liquidus, this change in mechanism could happen when the bottom of the MO reaches a depth of 1,000 km (40 GPa) (see Xie et al., 2020). In this article, we are aiming to model the chemical segregation in the initial stages of the MO solidification, when grain size is controlled by nucleation processes. D_{Bg} in these conditions depends largely on the cooling rate of the MO, with estimated values of 0.1–1 mm (V. Solomatov, 2015). For a grain size of 1 mm, χ_ρ is higher than unity at pressures (depths) lower than 45 GPa (1,100 km) (Figure 12). As a result, it appears unlikely that Bg grains could segregate in a crystallizing MO of pyrolite composition at depths greater than ∼1,100 km.

A BSE composition enriched in Bg yields a lighter melt during the early stages of MO solidification, and thus a higher $\Delta\rho_{MO}$. It facilitates the segregation of Bg at the bottom of the mushy MO. For a melt composition enriched by 20% or 40% of Bg, Bg grains of 1 mm could efficiently segregate at pressures (depths) lower than 55 GPa (1,350 km) or 65 GPa (1,550 km), respectively (Figures 13a and 13b). From a geochemical point of view, early segregation of Bg to the CMB requires a BSE composition enriched in Bg if the late shallow MO is of pyrolite composition; we will discuss this matter later in the article.

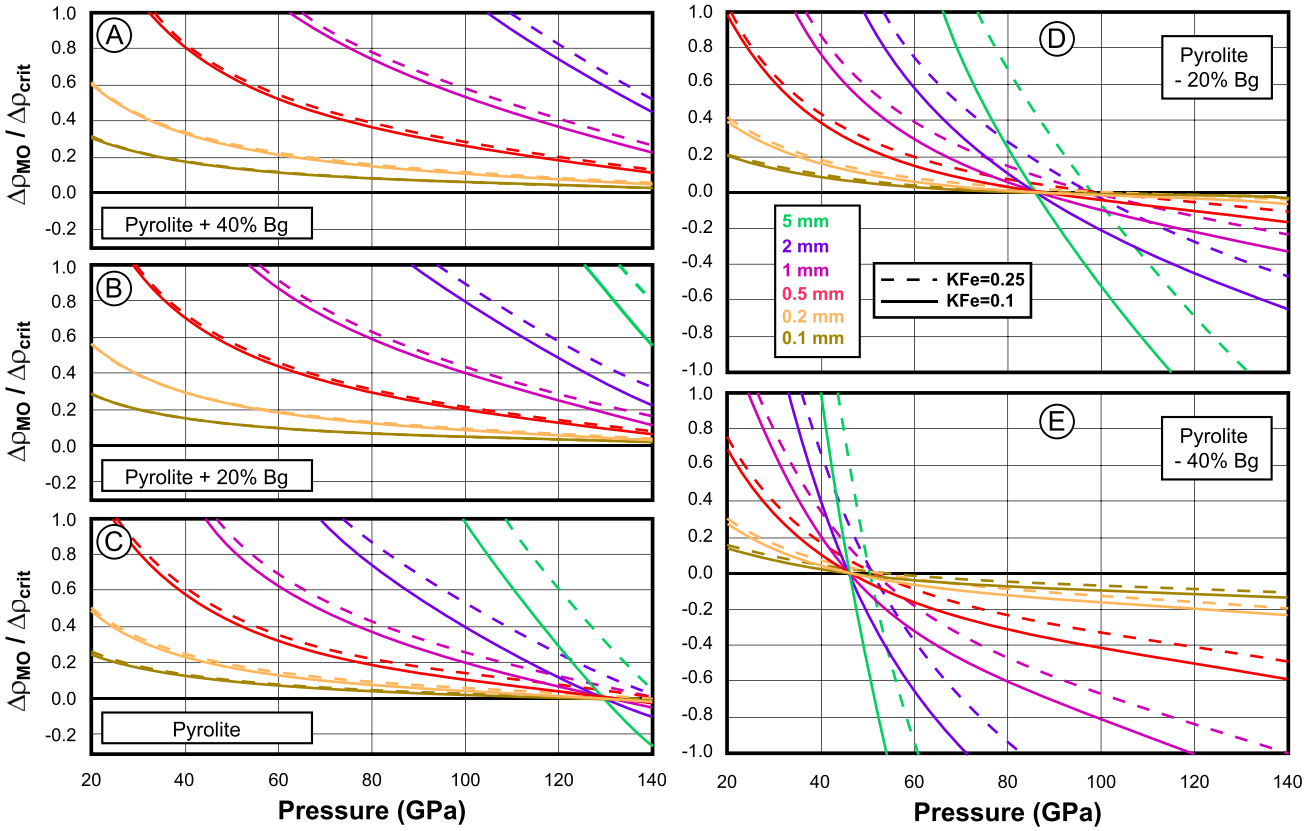

Figure 13. Density contrast ratio $\Delta\rho_{MO}/\Delta\rho_{crit}$ in the MO calculated as a function of the Bg grain size, from 0.1 to 5 mm, for 5 different melt compositions, from pyrolite −40%Bg to pyrolite +40%Bg. Values greater than 1 or less than −1 indicate efficient Bg segregation below, or above, the mushy MO, respectively. $\chi_\rho = 0$ is found for $\Delta\rho_{MO} = 0$ (Figure 11). It indicates an infinite value for Sh and perfect crystal suspension (Figure 9). Continuous and dashed lines indicate $K(\mathrm{Fe})^{Bg/Melt}$ of 0.1 and 0.25, respectively.

Alternatively, a BSE composition depleted in Bg yields a denser melt in the mushy MO, as discussed in several works (Ballmer, Lourenço, et al., 2017; Boukaré et al., 2015; Caracas et al., 2019). Our calculations of χ_ρ for melt compositions of pyrolite −20% and −40% Bg show that Bg is indeed less dense than the melts over a large fraction of the lower mantle (Figure 11). Bg remains denser at low pressures, due to its very high bulk modulus. For a Bg grain size of 1 mm, values of χ_ρ are found to be lower than −1 at pressures (depths) greater than 120 GPa (2,600 km) for a melt composition of pyrolite −40% of Bg (Figure 13e). The pressure (depth) at which Bg could segregate upwards decreases with increasing Bg grain size. From a geochemical point of view, early segregation close to the CMB of a Bg-depleted melt requires a BSE composition depleted in Bg, if the shallow MO were to be pyrolitic.

5.2.3. Effect of Temperature

Another important parameter in $\Delta\rho_{crit}$ is ΔT (Equation 18), which is intrinsically related to the rate of MO cooling. During the mushy stage of MO solidification, the surface temperature is ≈500 K, which leads to final MO solidification 100–200 thousands years after the Moon-forming impact (Lebrun et al., 2013; Monteux et al., 2020). Presence of a blanketing atmosphere above the MO would induce a higher surface temperature and a lower rate of cooling (Salvador et al., 2017; Sleep et al., 2014). We note that the formation of a blanketing atmosphere is unlikely to affect the early stages of MO solidification for a number of reasons: (a) H_2O (a highly efficient blanketing compound) is only efficiently vaporised into the atmosphere after a high degree of MO solidification (Elkins-Tanton, 2008; Salvador et al., 2017). (b) A surface temperature higher than 1500 K yields an atmosphere dominated by rock-vapor, which is not efficient at stopping the surface cooling by thermal radiation (Sleep et al., 2014). For these reasons, we also performed calculations of $\Delta\rho_{MO}$ for surface temperatures of 500, 1000, and 1500 K (Figure 14).

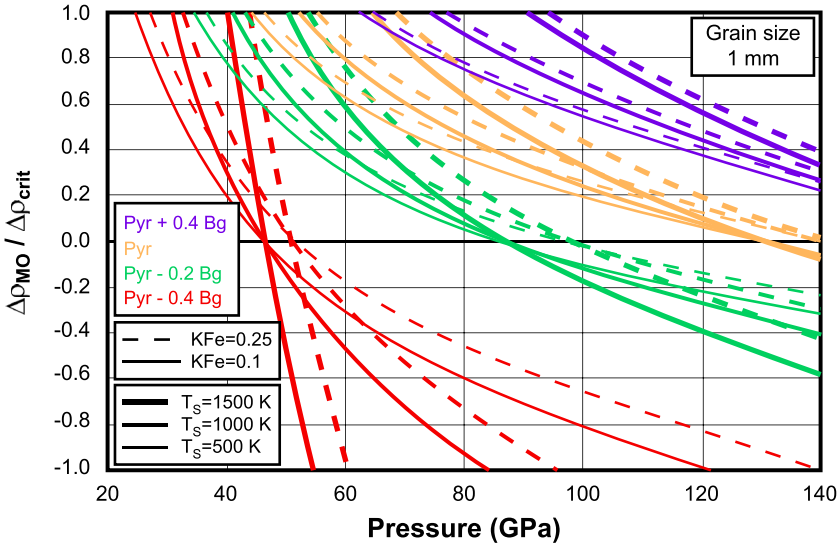

Figure 14. Density contrast ratio $\Delta\rho_{MO}/\Delta\rho_{crit}$ calculated for various surface temperatures (Equation 18). Thick, intermediate and thin lines correspond to 500, 1000, and 1500 K, respectively. The calculations are also performed for various mantle compositions and $K(\mathrm{Fe})^{Bg/Melt}$ values.

Calculations show that higher surface temperatures yield more extreme positive and negative values of χ_ρ and therefore easier Bg segregation. This is because higher T_{surf} corresponds to a smaller temperature difference ΔT (Equation 18) and thus a less turbulent MO. Still, the impact remains modest; for a pyrolite mantle, a variation in T_{surf} from 500 to 1500 K yields Bg segregation at pressures (depths) lower than 45 GPa (1,100 km) and 67 GPa (1,600 km), respectively.

5.3. Possible Scenarios for MO Solidification

5.3.1. Conditions for Bg Segregation at the Bottom of the MO

Geochemical scenarios of the Earth's formation involve building blocks of chondritic composition. Uncertainties remain about the composition of the primitive "chondritic-type" mantle after the core-mantle segregation. Still, it is very likely that it would have been enriched in SiO_2, compared to pyrolite (Allègre et al., 1995; Javoy, 1995; McDonough & Sun, 1995). Such enrichment has raised long-running discussions about how much Si the core might contain and how much the deep mantle might be enriched in SiO_2, compared to the present day upper mantle. A high $MgSiO_3$/MgO ratio in the lower mantle is compatible with results from inversions of seismic profiles based on elastic parameters of minerals (Matas et al., 2007; Murakami et al., 2012; Samuel et al., 2005).

Our model shows that increasing the Bg content in BSE favors the segregation of Bg in a deep MO (Figures 13a and 13b). Bg grains of 1 mm diameter segregate efficiently (i.e., $\chi_\rho > 1$) at pressures (depths) lower than 45 GPa (1,100 km), 55 GPa (1,350 km), and 65 GPa (1,550 km) for pyrolite, pyrolite with addition of +20%Bg and +40%Bg, respectively. Still, Bg grains would segregate during the early stages of the solidification if the grain size were 5 mm or more. Such large grains are not expected in a very thick MO (V. Solomatov, 2015). Bg segregation becomes possible when the MO is shallower, and the greater the Bg enrichment, the earlier (and deeper) the Bg-segregation occurs. For a grain size of 1 mm, a Bg layer could form at MO depths of 1,100–1,550 km, depending on the BSE composition. Such a thin MO could also favor grain growth, because the MO would be partially crystallized up to the Earth's surface (V. Solomatov, 2015; Xie et al., 2020). This Bg-layer could yield silica-enriched domains (Ballmer, Houser, et al., 2017). Unfortunately, our models are not able to asses the effects of changes in the thickness of this layer, because there are too many adjustable parameters. For a BSE enriched in Bg, segregation of Bg in the lower mantle would drive the MO toward a pyrolite mantle composition. Decreasing the Bg-content would then make the segregation of Bg grains less efficient (Figure 12).

5.3.2. Solidification of a Pyrolite-Type Bulk Silicate Earth

A pyrolite-like BSE would solidify with no Bg segregation from the melt, as long as the Bg grain size remained lower than 0.5 mm (Figure 13c). Bg segregation could still happen in the uppermost lower mantle if the Bg grain size were to increase. We note, however, that the grain growth of olivine and other minerals of the upper mantle may have a moderate impact on the grain size of Bg in the lower mantle. Modeling the mechanism of MO solidification in the upper mantle is beyond the scope of this article.

Interestingly, the absence of Bg segregation does not imply a chemically homogeneous mantle once it is entirely solidified. The origin of this effect is that the solidified mantle contains ~60% Bg and ~40% melt, while the overlying mushy MO contains a different fraction of the two phases. Here we assume a rate of mushy-mantle compaction (with extraction of the melt) that is significantly slower than the rate of MO solidification, following previous work (V. Solomatov, 2015). We modeled the chemical stratification resulting from homogeneous solidification as follows: (a) we chose a BSE composition close to pyrolite, albeit with an ajustable Bg content, to allow the final shallow MO (thickness of ~660 km) composition to be as close as possible to that of pyrolite. (b) At each time step of the progressive MO solidification, we estimated the fraction of Bg grains in the MO above the bottom of the MO (ϕ_{MO}) based on our previous model of progressive MO solidification (Figure 3 of Monteux et al. (2016)). (c) We calculated the composition of the coexisting melt and Bg grains, fixing $K(\mathrm{Fe})^{Bg/Melt} = 0.25$. (The value of $K(\mathrm{Fe})^{Bg/Melt}$ has no significant impact on this calculation in any case). (d) Starting from the CMB, we cooled the mantle and calculated the composition of a mixture of 60% Bg grains and 40% melt that solidified at the bottom of the MO. The chemical content of this basal layer was then subtracted from the composition of the overlying mushy MO, before a next step of the solidification was performed within a thinner MO.

This calculation shows significant changes in the SiO_2, FeO, and CaO contents with depth in the solidified mantle (Figure 15). They occur due to Bg having higher SiO_2 and lower FeO and CaO contents compared to the melt. The shallow MO has a chemical composition close to that of pyrolite, when the BSE composition is adjusted to 80% pyrolite and 20% Bg. The SiO_2 content in the deep mantle is found to decrease from ~46% to 39%, which translates into a decrease from ~90% to 70% in Bg-content, with decreasing depth from 2,900 to 660 km, respectively. The Fe-content also increases with decreasing depth, because of its incompatible character; this effect is found even greater when using $K(\mathrm{Fe})^{Bg/Melt} = 0.1$, instead of $K(\mathrm{Fe})^{Bg/Melt} = 0.25$. However, the overlying mushy MO does not become denser than the solidified layers, because Bg is denser than the melt at all mantle depths for Bg-enriched BSE compositions (Figure 11).

Such chemical layering would only survive in a mantle that became stagnant after solidification. Instead, one could expect significant vertical mixing in a mushy mantle with a relatively low viscosity and with a major heat flux from the core to the surface (Monteux et al., 2016). Another effect that might moderate the chemical stratification is simultaneous mantle solidification over a large range of mantle depths. Upon cooling, the temperature profile becomes almost parallel to the solidus (Miller et al., 1991; Monteux et al., 2016; Stixrude et al., 2009), which could result in bulk solidification. However, these effects may not entirely suppress the chemical gradients, in particular between a shallow MO and the lower mantle. The progressive enrichment of Bg with mantle depth is in good agreement with the mineralogical models of for example, Samuel et al. (2005); Matas et al. (2007); Murakami et al. (2012), as well as with the difference between the shallow mantle composition today (pyrolite) and a "chondritic-type" BSE (see above).

We note that the scenario of Bg-segregation in the lowermost mantle does not help explain the LLSVPs above the CMB. Several origins have been proposed for the LLSVP, in particular primitive mantle that did not melt following the Moon forming impact. Primitive mantle compositions imply a relatively low proportion of ferropericlase, which is compatible with the comparison between the LLSVP seismic signature and the elastic parameters of the minerals (Vilella et al., 2021). Still, LLSVPs represent a quite small fraction of the mantle volume, typically 1.5%–2.5% (Burke et al., 2008). Therefore, our models would not be much different if some primitive mantle were to have survived melting during the Moon-Forming impact.

5.3.3. Conditions for the Formation of a Primary Basal Magma Ocean

The segregation of large Bg grains at the bottom of a pyrolite mantle would yield a mafic Fe-enriched MO on top of this Bg solid layer. Following this scenario, it has been proposed that the melt could become denser than the underlying mantle and induce early mantle overturns (Ballmer, Lourenço, et al., 2017; Boukaré et al., 2015; Caracas et al., 2019). Such a reversal could result in a secondary basal MO in the lowermost mantle with a

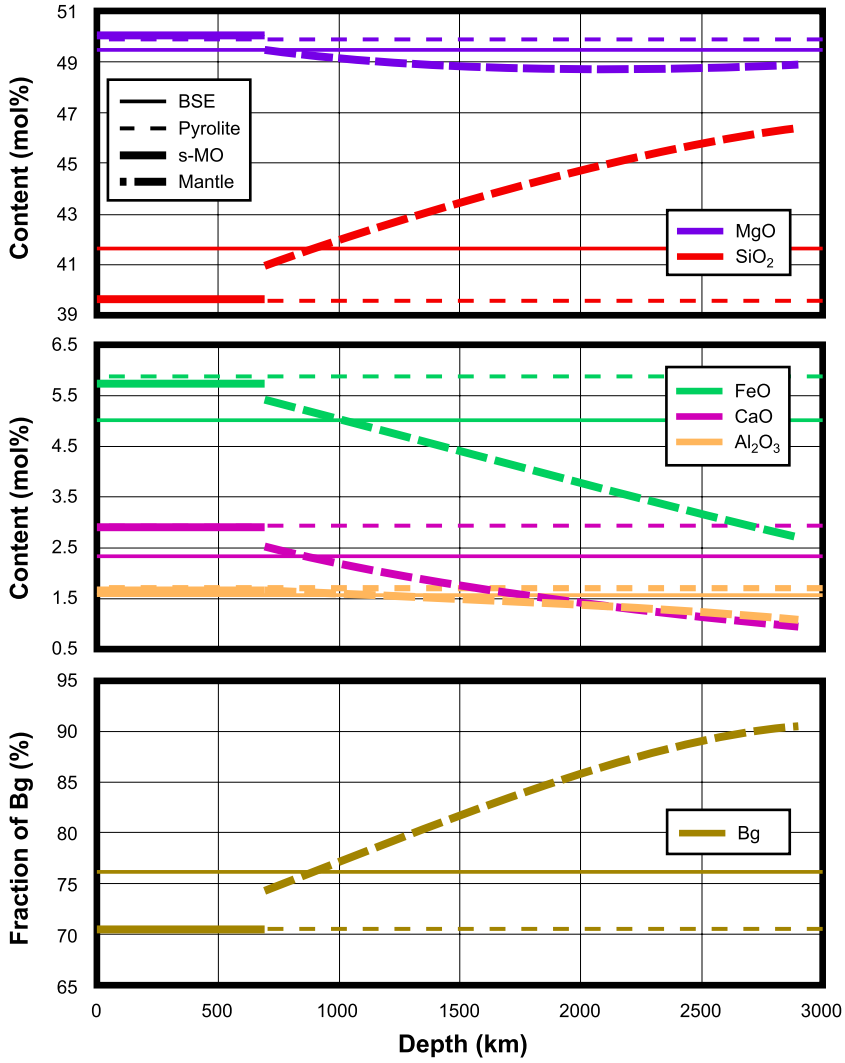

Figure 15. Chemical profiles obtained for the case in which there is no Bg segregation from the melt. The chemical gradient comes from the solidification of ~60% Bg and 40% of the melt at the bottom of the MO. These profiles assume no mantle mixing once the mantle layers are eventually solidified. "BSE" and "s-MO" are bulk silicate Earth and a shallow MO extending up to 660 km depth, respectively. Here, the BSE composition is adjusted to 80% pyrolite and 20% Bg.

composition typical of the shallow MO. Our results do not strongly support this scenario, because the lower the Bg-content in the mushy MO, the less efficient the Bg segregation (Figure 13). Therefore, bulk solidification is more likely, after a certain amount of Bg-segregation in a thick MO. Mantle overturns may still occur due to the crystallization processes in the upper mantle; this should be investigated in future work based on analysis of the melting diagrams in the upper mantle.

Formation of a basal MO during the solidification process (i.e., a primary basal MO) would require efficient segregation of Bg into an overlying solid layer (Labrosse et al., 2007). These conditions translate into $\chi_\rho < -1$ in our model. Such conditions are reached for a mafic BSE composition, which has a lower Bg content compared to pyrolite (Figures 13c and 13d). However, our calculations show that upward Bg segregation is only expected (a) in the lowermost part of the MO, (b) for a BSE composition depleted in more than −20% Bg compared to pyrolite, and (c) for Bg grain sizes larger than 0.5 mm. We note that low $K(\mathrm{Fe})^{Bg/Melt}$ values at these conditions help make the melt denser than Bg (Figure 12, Nomura et al. (2011)). For an MO composed of pyrolite −40% Bg, Bg grains of 1 mm diameter would aggregate efficiently into a Bg-rich layer at a pressure (depth) of 120 GPa (2,600 km). For an MO composed of pyrolite −20% Bg, only Bg grains of 5 mm diameter could efficiently segregate upwards (Figure 13d). The simultaneous formation of a basal MO and a solid Bg layer may ensure that the

composition of the overlying MO remains mafic. No further Bg segregation would be expected above ~2,500 km (i.e., 100–110 GPa) in a mafic MO, for a reasonable Bg grain size. If the MO were to be further depleted in Bg due to the "at equilibrium fractionation" mechanism described above (Figure 15), it would become even more mafic. At this point, it is difficult to imagine how such major mafic MO could have disappeared through dynamical processes, since seismic tomography does not provide evidence of such mantle reservoir today. Thus a pyrolite-type upper mantle seems difficult to form following this scenario. It makes the formation of a primary basal MO simultaneously with MO solidification quite unlikely.

6. Conclusion

Solidification within a deep convecting magma ocean (MO) was a key process in the formation of the Earth's interior (Ballmer, Lourenço, et al., 2017) and likely in the early mantle evolution for other planets: Mars (Elkins-Tanton et al., 2005), Mercury (Mouser et al., 2021) and the Moon (Dygert et al., 2017; Elkins-Tanton et al., 2011). This process is responsible for the separation of compatible elements that prefer the solid phase (e.g., Mg, Si) from incompatible elements which prefer the liquid phase (e.g., Al, Na, Fe). The solidification depth is governed by the geotherm and the melting curves. With density profiles of the melt and bridgmanite crystals crossing in the lower mantle, Caracas et al. (2019) suggested that crystal settling may occur toward neutral buoyancy depths. However, Both chemical composition and temperature contribute to the buoyancy of a crystal layer within a convecting reservoir. A low density contrast between crystals and melt would then paradoxically favor entrainment of crystals by the convective flow. Hence different scenarios may emerge: bottom-up solidification, or mid-mantle solidification making it possible to form a basal magma ocean.

In our study we have shown that the ability of the crystal fraction to sediment or to disperse within the domain is the result of a combination of the influence of the crystal size, the density difference between the crystals and the magma and the magma viscosity. We have shown that this ability is a function of the ratio of the convection over the buoyancy stress (expressed as the Sh dimensionless number). For a relevant range of parameters, we observe that the critical Sh_c values separating the suspension and sedimentation regimes can be lower than those values previously obtained from analog models (V. S. Solomatov et al., 1993). As a consequence, our results strengthen the idea that a suspension mechanism would be dominant over sedimentation during magma ocean solidification and, as a consequence, equilibrium crystallization would be favored compared to fractional crystallization.

In our models, we consider a particle size range ($10^{-4} - 10^{-3}$ m) and a density difference range between the magma and the particles ($10 - 100$ kg.m^{-3}), which are probably closer to the relevant MO conditions (see e.g., $\Delta\rho = -200$ to 200 kg/m^3 in Figure 11) than the range of parameters proposed by Patočka et al. (2020) ($0.5 \times 10^{-3} - 10^{-2}$ m and $10 - 3{,}000$ kg.m^{-3}). Moreover, their models neglect a re-entrainment process by eliminating the particles that reach the bottom of the reservoir. Hence, it is not surprising that their models favor rapid crystal settling and fractional crystallization. Patočka et al. (2020) identified three settling regimes: "stone-like," bi-linear and "dust-like" regimes depending on the ratio between the crystal's terminal velocity and the average vertical velocity of the flow. It appears that our models mostly fall into the "dust-like regime" where the terminal velocity of a particle is smaller than the average velocity within the convective reservoir. In the "dust-like" regime the particles from the models developed by Patočka et al. (2020) appear to be uniformly distributed in the reservoir in agreement with our models.

We also considered the density contrasts calculated from different end-members for the chemical composition of the early mantle by adding or subtracting up to 40% of bridgmanite (Bg) to a pyrolite mantle reference. Exploring the early mantle composition within such a range leads to a wide range of density differences between the molten and the solid phases. Hence the chemical composition also influences the ability of the crystals to cumulate at the bottom or in the middle of the magma ocean. Our models emphasize that (a) Bg grains are unlikely to segregate in a mantle of pyrolite composition, except in a shallow MO when the grain size may increase to 1 mm or more, (b) Bg grains are likely to segregate at the bottom of a MO enriched in SiO_2, compared to pyrolite, and (c) the formation of a basal MO simultaneously with mantle solidification is a possibility for mafic BSE compositions (although difficult to reconcile with the geochemical models of the Earth). We also note that a homogeneous bottom-up solidification of the MO is expected to produce a significant SiO_2 enrichment with increasing mantle depth in a primitive mantle (compatible with seismic observations) and a higher SiO_2 content in the BSE compared to pyrolite (compatible with geochemical models of the Earth).

While our study is a step toward a more realistic approach, several other processes not accounted here could be worth implementing in future models:

1. In our models we did not consider the time evolutions of the (a) crystal size, (b) the crystal fraction or (c) the density contrast during the chemical differentiation of the magma ocean. The kinetics of crystal nucleation and growth is difficult to constrain within a magma ocean environment. The crystal fraction evolves during the cooling of the magma ocean and will likely naturally increase as the temperature decreases. However, crystals may also reach higher temperature zones of the reservoir when entrained by convection which will lead to a decrease in the crystal fraction. Even if this complexity is not accounted for in our models, our parametric approach enable to anticipate between suspension or sedimentation regime for a given set of parameter values.
2. We have restricted our study to the crystal settling that may occur close to mechanical boundaries (CMB or solidified walls) where the velocity is lower than in the middle of the magma ocean (in "calm" conditions). Future models should explore parameters compatible with the center of the magma ocean (i.e., larger Rayleigh numbers). This would imply using much higher Reynolds numbers to correctly characterize the turbulent motion occurring from the scale of the crystal up to that of the whole magma ocean. In such a context, models would need to consider the inertial forces and turbulence equations.
3. Early in the Earth's evolution, the Moon was much closer to the Earth than today (Chen & Nimmo, 2016), which has generated huge tidal forces on both bodies. The Moon potentially started to re-accrete at a distance ranging from 5 to 15 Earth radii (today the distance is nearly 60 Earth radii). The tidal forcing induced by the presence of the Moon generates an oscillatory shear characterized by a maximum shear rate and a tidal frequency. Such an oscillatory shear may influence the convective flow within the magma ocean and the crystallization process (Ogilvie & Lesur, 2012). This effect would have varied in time during both the magma ocean solidification and as the Moon moved away from the Earth.
4. After the giant impact that probably induced the thickest magma ocean episode (Nakajima & Stevenson, 2015), the orbit parameters of the Earth were strongly affected and the Earth's spinning rate was probably much higher than today (Ćuk & Stewart, 2012). While strong turbulence may favor suspension over sedimentation regimes, Julien et al. (1996) showed that accounting for Coriolis forces may lead to a reduction in the convective velocity and, as a consequence, favor sedimentation over suspension regimes. Strong turbulence in the presence of rotation is a complex process that is difficult to constrain in a solidifying magma ocean context in which solid and liquid phases co-exist (Fernando et al., 1991).
5. When crystallization of the magma ocean occurs close to a rigid layer, the relevant boundary conditions for crystal settling are closer to no-slip boundary conditions (Patočka et al., 2020) than to free-slip boundary conditions since the newly formed solid is much more viscous than the liquid. When considering non-interacting particles as in laboratory experiments (V. S. Solomatov et al., 1993) or free-slip boundary conditions as in our models, crystals cannot form solid bonds as observed in experiments on magmas (Lejeune & Richet, 1995). Because of the sintering effect, the bonds between crystals and the underlying bed can easily prevent re-entrainment and lead to a decrease in the efficiency of particle re-suspension.

These factors may affect the physics of convection and, hence, sedimentation and entrainment. If none of the current numerical models can simultaneously handle all of these complexities, the effects listed above should be accounted for in future developments of numerical models dedicated to crystal settling within a convective magma ocean. In any case, our study emphasizes the need to implement state of the art petrological and geochemical models within fluid dynamics models to better describe the early evolution of the Earth's mantle.

Data Availability Statement

The data that support the findings of this study were obtained using the commercial software COMSOL Multiphysics (version 5.4). COMSOL Multiphysics is a simulation platform that provides fully coupled multiphysics and single-physics modeling capabilities. COMSOL Multiphysics (version 5.4) has been previously validated for two phase flow applications (Qaddah et al. (2019, 2020)). To compute our simulations we used the Heat Transfer (www.comsol.com/heat-transfer-module) and Computational Flow Dynamics (www.comsol.com/cfd-module) modules in addition to the main Multiphysics platform (www.comsol.com/comsol-multiphysics). All the parameters used in our simulation are listed and described in the manuscript. The open source software used for data visualization was Xmgrace (https://plasma-gate.weizmann.ac.il/Grace/). Data obtained can be downloaded from the following link: https://zenodo.org/record/7858690#.ZEZwxy0itAY.

Code Availability: The software used for this study is the commercial software COMSOL Multiphysics (version 5.4) previously validated for two phase flow applications (Qaddah et al. (2019, 2020)). User manual can be downloaded here: https://doc.comsol.com/5.4/doc/com.comsol.help.cfd/CFDModuleUsersGuide.pdf. A trial version of COMSOL Multiphysics may be requested (see www.comsol.com).
More details can be found on the following COMSOL webpages:

1. On the Foundations of the General Heat Transfer Equation: https://doc.comsol.com/6.1/docserver/#!/com.comsol.help.heat/heat_ug_theory.07.002.html.
2. Theory for Heat Transfer in Fluids: https://doc.comsol.com/6.1/docserver/#!/com.comsol.help.heat/heat_ug_theory.07.008.html.
3. The Euler Model Equations and in particular how incompressibility is handled: https://doc.comsol.com/6.1/docserver/#!/com.comsol.help.cfd/cfd_ug_fluidflow_multi.09.153.html.
4. The Boussinesq Approximation: https://doc.comsol.com/6.1/docserver/#!/com.comsol.help.cfd/cfd_ug_fluidflow_noniso.07.20.html.

Acknowledgments
The authors thank Pierre Bonnand and Maylis Landeau for fruitful discussions. We thank Frances van Wyk de Vries for deep English proofread. We also thank the two anonymous reviewers for their constructive comments. This research received funding from French PNP program (INSU-CNRS) and the French Government Laboratory of Excellence initiative No. ANR-10-LABX-0006. This is contribution No. 598 of the ClerVolc program of the International Research Center for Disaster Sciences and Sustainable Development of the University of Clermont Auvergne.

References

Allègre, C. J., Poirier, J.-P., Humler, E., & Hofmann, A. W. (1995). The chemical composition of the Earth. *Earth and Planetary Science Letters*, *134*(3–4), 515–526. https://doi.org/10.1016/0012-821X(95)00123-T

Andrault, D., Muñoz, M., Pesce, G., Cerantola, V., Chumakov, A. I., Kantor, I., et al. (2018). Large oxygen excess in the primitive mantle could be the source of the Great Oxygenation Event. *Geochemical Perspectives Letters*, *6*, 5–10. https://doi.org/10.7185/geochemlet.1801

Andrault, D., Petitgirard, S., Lo Nigro, G., Devidal, J.-L., Veronesi, G., Garbarino, G., & Mezouar, M. (2012). Solid-liquid iron partitioning in Earth's deep mantle. *Nature*, *487*(7407), 354–357. https://doi.org/10.1038/nature11294

Asimow, P. (2018). Melts under extreme conditions from shock experiments. In Y. Kono, & C. Sanloup (Eds.), *Magmas under pressure* (pp. 387–418). Elsevier.

Ballmer, M. D., Houser, C., Hernlund, J. W., Wentzcovitch, R. M., & Hirose, K. (2017). Persistence of strong silica-enriched domains in the Earth's lower mantle. *Nature Geoscience*, *10*(3), 236–240. https://doi.org/10.1038/ngeo2898

Ballmer, M. D., Lourenço, D. L., Hirose, K., Caracas, R., & Nomura, R. (2017). Reconciling magma-ocean crystallization models with the present-day structure of the Earth's mantle. *Geochemistry, Geophysics, Geosystems*, *18*(7), 2785–2806. https://doi.org/10.1002/2017GC006917

Boukaré, C. E., Ricard, Y., & Fiquet, G. (2015). Thermodynamics of the MgO-FeO-SiO_2 system up to 140 GPa: Application to the crystallization of Earth's magma ocean. *Journal of Geophysical Research: Solid Earth*, *120*(9), 6085–6101. https://doi.org/10.1002/2015jb011929

Boyet, M., & Carlson, R. W. (2005). ^{142}Nd evidence for early (>4.53 Ga) global differentiation of the silicate Earth. *Science*, *309*(5734), 576–581. https://doi.org/10.1126/science.1113634

Burke, K., Steinberger, B., Torsvik, T. H., & Smethurst, M. A. (2008). Plume generation zones at the margins of large low shear velocity provinces on the core mantle boundary. *Earth and Planetary Science Letters*, *265*(1–2), 49–60. https://doi.org/10.1016/j.epsl.2007.09.042

Caracas, R., Hirose, K., Nomura, R., & Ballmer, M. D. (2019). Melt-crystal density crossover in a deep magma ocean. *Earth and Planetary Science Letters*, *516*, 202–211. https://doi.org/10.1016/j.epsl.2019.03.031

Chen, E. M. A., & Nimmo, F. (2016). Tidal dissipation in the lunar magma ocean and its effect on the early evolution of the Earth-Moon system. *Icarus*, *275*, 132–142. https://doi.org/10.1016/j.icarus.2016.04.012

Crowe, C., Sommerfeld, M., & Tsuji, Y. (1998). *Multiphase flows with droplets and particles*. CRC Press.

Ćuk, M., & Stewart, S. T. (2012). Making the Moon from a fast-spinning Earth: A giant impact followed by resonant despinning. *Science*, *338*(6110), 1047–1052. https://doi.org/10.1126/science.1225542

Dörr, A., Sadiki, A., & Mehdizadeh, A. (2013). A discrete model for the apparent viscosity of polydisperse suspensions including maximum packing fraction. *Journal of Rheology*, *57*(3), 743–765. https://doi.org/10.1122/1.4795746

Dygert, N., Lin, J.-F., Marshall, E. W., Kono, Y., & Gardner, J. E. (2017). A low viscosity lunar magma ocean forms a stratified anorthitic flotation crust with mafic poor and rich units. *Geophysical Research Letters*, *44*(22), 11282–11291. https://doi.org/10.1002/2017GL075703

Elkins-Tanton, L. T. (2008). Linked magma ocean solidification and atmospheric growth for Earth and Mars. *Earth and Planetary Science Letters*, *271*(1–4), 181–191. https://doi.org/10.1016/j.epsl.2008.03.062

Elkins-Tanton, L. T. (2012). Magma oceans in the inner solar system. *Annual Review of Earth and Planetary Sciences*, *40*(1), 113–139. https://doi.org/10.1146/annurev-earth-042711-105503

Elkins-Tanton, L. T., Burgess, S., & Yin, Q.-Z. (2011). The lunar magma ocean: Reconciling the solidification process with lunar petrology and geochronology. *Earth and Planetary Science Letters*, *304*(3–4), 326–336. https://doi.org/10.1016/j.epsl.2011.02.004

Elkins-Tanton, L. T., Zaranek, S. E., Parmentier, E. M., & Hess, P. C. (2005). Early magnetic field and magmatic activity on Mars from magma ocean cumulate overturn. *Earth and Planetary Science Letters*, *236*(1–2), 1–12. https://doi.org/10.1016/j.epsl.2005.04.044

Fernando, H. J. S., Chen, R.-R., & Boyer, D. L. (1991). Effects of rotation on convective turbulence. *Journal of Fluid Mechanics*, *228*, 513–547. https://doi.org/10.1017/s002211209100280x

Hofmeister, A. M. (1999). Mantle values of thermal conductivity and the geotherm from phonon lifetimes. *Science*, *283*(5408), 1699–1706. https://doi.org/10.1126/science.283.5408.1699

Höink, T., Schmalzl, J., & Hansen, U. (2005). Formation of compositional structures by sedimentation in vigorous convection. *Physics of the Earth and Planetary Interiors*, *153*(1–3), 11–20. https://doi.org/10.1016/j.pepi.2005.03.014

Ibrahim, A., & Meguid, M. (2020). Coupled flow modelling in geotechnical and ground engineering: An overview. *International Journal of Geosynthetics and Ground Engineering*, *39*(3), 1–25. https://doi.org/10.1007/s40891-020-00223-0

Jaupart, C., & Tait, S. (1995). Dynamics of differentiation in magma reservoirs. *Journal of Geophysical Research*, *100*(B9), 17615–17636. https://doi.org/10.1029/95JB01239

Javoy, M. (1995). The integral enstatite chondrite model of the Earth. *Geophysical Research Letters*, *22*(16), 2219–2222. https://doi.org/10.1029/95gl02015

Julien, K., Legg, S., McWilliams, J., & Werne, J. (1996). Hard turbulence in rotating Rayleigh-Bénard convection. *Physical Review E*, *53*(6), R5557–R5560. https://doi.org/10.1103/PhysRevE.53.R5557

Karki, B. B., & Stixrude, L. P. (2010). Viscosity of $MgSiO_3$ liquid at Earthś mantle conditions: Implications for an early magma ocean. *Science*, *328*(5979), 740–742. https://doi.org/10.1126/science.1188327

Labrosse, S., Hernlund, J. W., & Coltice, N. (2007). A crystallizing dense magma ocean at the base of the Earth's mantle. *Nature*, *450*(7171), 866–869. https://doi.org/10.1038/nature06355

Lavorel, G., & Le Bars, M. (2009). Sedimentation of particles in a vigorously convecting fluid. *Physical Review Fluids*, *80*(4), 046324. https://doi.org/10.1103/PhysRevE.80.046324

Lebrun, T., Massol, H., ChassefièRe, E., Davaille, A., Marcq, E., Sarda, P., et al. (2013). Thermal evolution of an early magma ocean in interaction with the atmosphere. *Journal of Geophysical Research: Planets*, *118*(6), 1155–1176. https://doi.org/10.1002/jgre.20068

Lejeune, A., & Richet, P. (1995). Rheology of crystal-bearing silicate melts: An experimental study at high viscosities. *Journal of Geophysical Research*, *100*(B3), 4215–4229. https://doi.org/10.1029/94jb02985

Marsh, B. D. (1981). On the crystallinity, probability of occurrence, and rheology of lava and magma. *Contributions to Mineralogy and Petrology*, *78*(1), 85–98. https://doi.org/10.1007/BF00371146

Martin, D., & Nokes, R. (1988). Crystal settling in a vigorously converting magma chamber. *Nature*, *332*(6164), 534–536. https://doi.org/10.1038/332534a0

Matas, J., Bass, J., Ricard, Y., Mattern, E., & Bukowinski, M. S. T. (2007). On the bulk composition of the lower mantle: Predictions and limitations from generalized inversion of radial seismic profiles. *Geophysical Journal International*, *170*(2), 764–780. https://doi.org/10.1111/j.1365-246x.2007.03454.x

McDonough, W., & Sun, S. (1995). The composition of the Earth. *Chemical Geology*, *120*(3–4), 223–253. https://doi.org/10.1016/0009-2541(94)00140-4

Miller, G. H., Stolper, E. M., & Ahrens, T. J. (1991). The equation of state of a molten komatiite: 2. Application to komatiite petrogenesis and the Hadean mantle. *Journal of Geophysical Research*, *96*(B7), 11849. https://doi.org/10.1029/91JB01203

Monteux, J., Andrault, D., Guitreau, M., Samuel, H., & Demouchy, S. (2020). A mushy Earth's mantle for more than 500 Myr after the magma ocean solidification. *Geophysical Journal International*, *221*(2), 1165–1181. https://doi.org/10.1093/gji/ggaa064

Monteux, J., Andrault, D., & Samuel, H. (2016). On the cooling of a deep terrestrial magma ocean. *Earth and Planetary Science Letters*, *448*, 140–149. https://doi.org/10.1016/j.epsl.2016.05.010

Monteux, J., Ricard, Y., Coltice, N., Dubuffet, F., & Ulvrova, M. (2009). A model of metal-silicate separation on growing planets. *Earth and Planetary Science Letters*, *287*(3–4), 353–362. https://doi.org/10.1016/j.epsl.2009.08.020

Mouser, M. D., Dygert, N., Anzures, B. A., Grambling, N. L., Hrubiak, R., Kono, Y., et al. (2021). Experimental investigation of Mercury's magma ocean viscosity: Implications for the formation of Mercury's cumulate mantle, its subsequent dynamic evolution, and crustal petrogenesis. *Journal of Geophysical Research: Planets*, *126*(11), e06946. https://doi.org/10.1029/2021JE006946

Murakami, M., Ohishi, Y., Hirao, N., & Hirose, K. (2012). A perovskitic lower mantle inferred from high-pressure, high-temperature sound velocity data. *Nature*, *485*(7396), 90–94. https://doi.org/10.1007/s12594-012-0111-2

Nakajima, M., & Stevenson, D. J. (2015). Melting and mixing states of the Earth's mantle after the Moon-forming impact. *Earth and Planetary Science Letters*, *427*, 286–295. https://doi.org/10.1016/j.epsl.2015.06.023

Nomura, R., Ozawa, H., Tateno, S., Hirose, K., Hernlund, J., Muto, S., et al. (2011). Spin crossover and iron-rich silicate melt in the Earth's deep mantle. *Nature*, *473*(7346), 199–202. https://doi.org/10.1038/nature09940

Ogilvie, G. I., & Lesur, G. (2012). On the interaction between tides and convection. *Monthly Notices of the Royal Astronomical Society*, *422*(3), 1975–1987. https://doi.org/10.1111/j.1365-2966.2012.20630.x

Patočka, V., Calzavarini, E., & Tosi, N. (2020). Settling of inertial particles in turbulent Rayleigh-Bénard convection. *Physical Review Fluids*, *5*(11), 114304. https://doi.org/10.1103/PhysRevFluids.5.114304

Pierru, R., Pison, L., Mathieu, A., Gardès, E., Garbarino, G., Mezouar, M., et al. (2022). Melting curve of pyrolite and bridgmanite: Implication for the thermochemical state of the Earth's interior. *Earth and Planetary Science Letters*, *595*, 117770. https://doi.org/10.1016/j.epsl.2022.117770

Qaddah, B., Monteux, J., Clesi, V., Bouhifd, M. A., & Le Bars, M. (2019). Dynamics and stability of an iron drop falling in a magma ocean. *Physics of the Earth and Planetary Interiors*, *289*, 75–89. https://doi.org/10.1016/j.pepi.2019.02.006

Qaddah, B., Monteux, J., & Le Bars, M. (2020). Thermal evolution of a metal drop falling in a less dense, more viscous fluid. *Physical Review Fluids*, *5*(5), 053801. https://doi.org/10.1103/PhysRevFluids.5.053801

Ricard, Y. (2007). Physics of mantle convection. In G. Schubert (Ed.), editor in Chief, *Treatise of geophysics* (Vol. 7). Elsevier.

Ringwood, A. (1975). Pyrolite and the chondritic Earth model. In M. GrawHill (Ed.), *International series in the Earth's and planetary Sciences* (pp. 189–194).

Salvador, A., Massol, H., Davaille, A., Marcq, E., Sarda, P., & Chassefière, E. (2017). The relative influence of H_2O and CO_2 on the primitive surface conditions and evolution of rocky planets. *Journal of Geophysical Research: Planets*, *122*(7), 1458–1486. https://doi.org/10.1002/2017je005286

Samuel, H., Farnetani, C. G., & Andrault, D. (2005). In R. D. Van DerHilst, J. D. Bass, J. Matas, & J. Trampert (Eds.), *Heterogeneous lowermost mantle: Compositional constraints and seismological observables* (pp. 1001–1116).

Samuel, H., Tackley, P. J., & Evonuk, M. (2010). Heat partitioning in terrestrial planets during core formation by negative diapirism. *Earth and Planetary Science Letters*, *290*(1–2), 13–19. https://doi.org/10.1016/j.epsl.2009.11.050

Schiller, L., & Naumann, A. (1935). A drag coefficient correlation. *Zeitschrift des Vereins Deutscher Ingenieure*, *77*, 318–320.

Sleep, N. H., Zahnle, K. J., & Lupu, R. E. (2014). Terrestrial aftermath of the Moon-forming impact. *Philosophical Transactions of the Royal Society of London, Series A*, *372*(2024), 20130172. https://doi.org/10.1098/rsta.2013.0172

Solomatov, V. (2015). Magma oceans and primordial mantle differentiation. In G. Schubert (Ed.), editor in Chief, *Treatise of geophysics* (Vol. 9) Elsevier.

Solomatov, V. S. (2000). Fluid dynamics of a terrestrial magma ocean. In R. M. Canup & K. Righter (Eds.), *Origin of the earth and moon* (pp. 323–338). University of Arizona Press.

Solomatov, V. S., Olson, P., & Stevenson, D. J. (1993). Entrainment from a bed of particles by thermal convection. *Earth and Planetary Science Letters*, *120*(3–4), 387–393. https://doi.org/10.1016/0012-821x(93)90252-5

Stixrude, L., de Koker, N., Sun, N., Mookherjee, M., & Karki, B. B. (2009). Thermodynamics of silicate liquids in the deep Earth. *Earth and Planetary Science Letters*, *278*(3–4), 226–232. https://doi.org/10.1016/j.epsl.2008.12.006

Sturtz, C., Kaminski, É., Limare, A., & Tait, S. (2021). The fate of particles in a volumetrically heated convective fluid at high Prandtl number. *Journal of Fluid Mechanics*, *929*, A28. https://doi.org/10.1017/jfm.2021.862

Tonks, W. B., & Melosh, H. J. (1993). Magma ocean formation due to giant impacts. *Journal of Geophysical Research*, *98*(E3), 5319–5333. https://doi.org/10.1029/92je02726

Turcotte, D., & Schubert, G. (1982). *Geodynamics, applications of continuum physics to geological problems*. John Wiley and Sons.

van der Poel, E. P., Stevens, R. J. A. M., & Lohse, D. (2013). Comparison between two- and three-dimensional Rayleigh-Benard convection. *Journal of Fluid Mechanics*, *736*, 177–194. https://doi.org/10.1017/jfm.2013.488

Verhoeven, J., & Schmalzl, J. (2009). A numerical method for investigating crystal settling in convecting magma chambers. *Geochemistry, Geophysics, Geosystems*, *10*(12), Q12007. https://doi.org/10.1029/2009GC002509

Vilella, K., Bodin, T., Boukaré, C.-E., Deschamps, F., Badro, J., Ballmer, M. D., & Li, Y. (2021). Constraints on the composition and temperature of LLSVPs from seismic properties of lower mantle minerals. *Earth and Planetary Science Letters*, *554*(116), 685. https://doi.org/10.1016/j.epsl.2020.116685

Weinstein, S. A., Yuen, D. A., & Olson, P. L. (1988). Evolution of crystal-settling in magma-chamber convection. *Earth and Planetary Science Letters*, *87*(1–2), 237–248. https://doi.org/10.1016/0012-821X(88)90078-7

Wen, C., & Yu, Y. (1966). Mechanics of fluidization. *Chemical Engineering Progress Symposium Series*, *162*, 100–111.

Wolstencroft, M., Davies, J. H., & Davies, D. R. (2009). Nusselt-Rayleigh number scaling for spherical shell Earth mantle simulation up to a Rayleigh number of 10^9. *Physics of the Earth and Planetary Interiors*, *176*(1–2), 132–141. https://doi.org/10.1016/j.pepi.2009.05.002

Xie, L., Yoneda, A., Katsura, T., Andrault, D., Tange, Y., & Higo, Y. (2021). Direct viscosity measurement of peridotite melt to lower-mantle conditions: A further support for a fractional magma-ocean solidification at the top of the lower mantle. *Geophysical Research Letters*, *48*(19), e94507. https://doi.org/10.1029/2021GL094507

Xie, L., Yoneda, A., Yamazaki, D., Manthilake, G., Higo, Y., Tange, Y., et al. (2020). Formation of bridgmanite-enriched layer at the top lower-mantle during magma ocean solidification. *Nature Communications*, *11*(1), 548. https://doi.org/10.1038/s41467-019-14071-8

Yoshino, T., Walter, M. J., & Katsura, T. (2003). Core formation in planetesimals triggered by permeable flow. *Nature*, *422*(6928), 154–157. https://doi.org/10.1038/nature01459

7 Évolution primitive du manteau : conséquences géologiques, pétrologiques et géochimiques

Les dernières étapes de solidification du manteau terrestre ont eu des conséquences majeures sur son évolution et sur sa structure interne telle que nous l'envisageons aujourd'hui. Les étapes qui ont suivi la solidification du manteau ont ainsi gouverné la structuration chimique de l'intérieur de la Terre, la mise en place de la tectonique des plaques et les phénomènes de volcanisme à grande échelle qui se sont déroulés à l'Archéen.

Dans cette section, je présente des travaux résultant de collaborations avec des collègues pétrologues et/ou géochimistes auxquelles j'ai participé depuis mon arrivé au LMV. Je présente notamment l'influence qu'ont pu avoir les dernières étapes d'accrétion sur la composition chimique finale de la Terre, l'analyse d'une météorite qui pourrait être un reste de croute de planétésimal, les conséquences d'un solidus plus bas pour le matériel représentatif du manteau supérieur à l'Archéen ou encore l'origine des larges provinces volcaniques archéennes.

7.1 Érosion collisionnelle et rapport Mg/Si

Tôt dans l'histoire du Système Solaire, les collisions entre corps différenciés ont aussi affecté la composition finale des planètes telluriques par destructions partielles des parties les plus superficielles (Asphaug, 2010). Les chondrites à Enstatite sont considérées comme des reliques du matériel primordial ayant formé la Terre (Javoy et al., 2010). Cependant, il existe des différences significatives de composition chimique entre notre planète et cette classe de météorites qui restent à expliquer et notamment leur rapport Mg/Si. En nous appuyant sur des expériences en laboratoire (expériences de fusion jusqu'à 25 GPa) et sur des modélisations, nous avons proposé pour la première fois un scénario complet qui rend compte de ces différences : les collisions à répétition qui ont construit la Terre l'ont aussi amputée d'une fraction de sa masse, faisant ainsi évoluer sa composition chimique (Boujibar et al., 2015). Une érosion collisionnelle >15% de la masse de la Terre primitive permet de réconcilier les différences de composition entre les chondrites à Enstatite et la Terre. À faibles pressions les premiers silicates fondus sont enrichis en éléments incompatibles (Si, Al, Na) et appauvris en Mg. La perte significative de la proto-croûte lors d'impacts répétés a permis une augmentation du rapport Mg/Si jusqu'à sa valeur actuelle. Pour reproduire toutes les compositions en éléments majeurs ainsi que certains mineurs, notre modèle implique une perte préférentielle en éléments volatils lithophiles et une re-condensation des éléments réfractaires lithophiles après les impacts. Ce travail a donné lieu à une publication dans la revue *Nature Communications* (Boujibar et al., 2015).

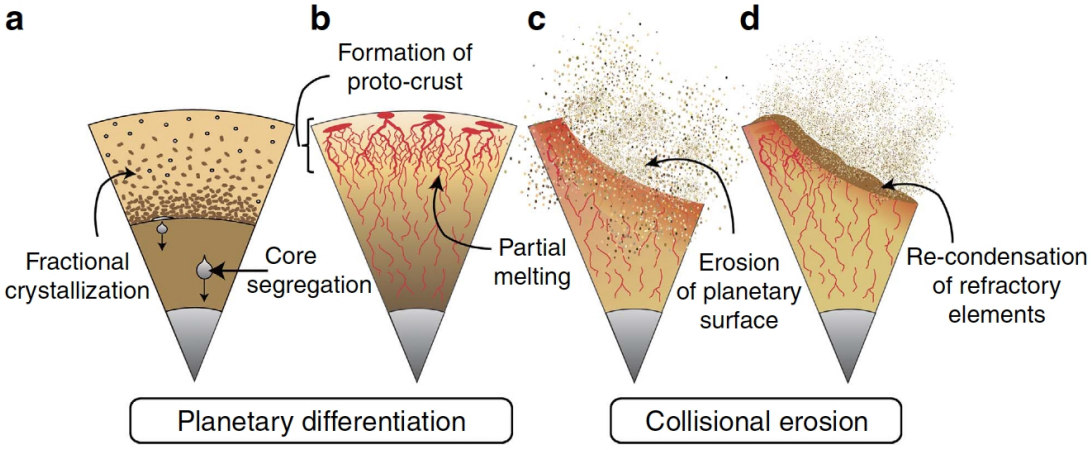

FIGURE 27 – *Représentation schématique du fractionnement chimique par érosion collisionnelle. (a,b) Le chauffage primitif favorise une séparation rapide manteau-noyau suivie par le fractionnement chimique induit par cristallisation d'un océan magmatique profond (a) et/ou de zones partiellement fondues (b) qui permettent le transfert rapide de matériel fondu à la surface. Les 2 scénarios peuvent entraîner une stratification de la composition chimique et la formation d'une proto-croûte riche en SiO_2. Les collisions répétées permettent une érosion de la proto-croûte enrichie en éléments incompatibles et d'une partie du manteau (c). Parmi la fraction de matériel volatilisée par impacts, la re-condensation des éléments réfractaires (d) est favorisée par rapport aux éléments volatils (D'après Boujibar et al. (2015)).*

7.2 Fusion et formation d'une croûte sur un planétésimal

Les météorites sont les seules rescapées de l'histoire chaotique du Système Solaire et nous renseignent sur sa composition et son évolution. Des planétésimaux les plus anciens, seuls les noyaux métalliques formant leur centre nous sont parvenus sous la forme des météorites de fer. Il est beaucoup plus rare de trouver des échantillons provenant de leur surface. Ainsi, nous disposons de peu d'informations concernant la nature des planétésimaux qui ont formé les planètes actuelles. L'étude de la météorite NWA 8486, trouvée dans le désert du Sahara en 2014, met en évidence la composition d'un planétésimal formé durant les deux premiers millions d'années de l'histoire du Système Solaire. Ainsi, ce planétésimal présenterait à sa surface une croûte anorthositique, similaire à la croûte lunaire. La météorite Northwest Africa (NWA) 8486 représente donc un échantillon unique.

L'étude des minéraux de cette roche unique dans le cadre de la thèse de Paul Frossard a permis de préciser l'histoire du planétésimal sur lequel elle s'est formée (Frossard et al., 2019). Chose surprenante, les minéraux qui la composent ont de très fortes teneurs en europium et strontium. Ces deux éléments sont généralement concentrés dans des roches très particulières

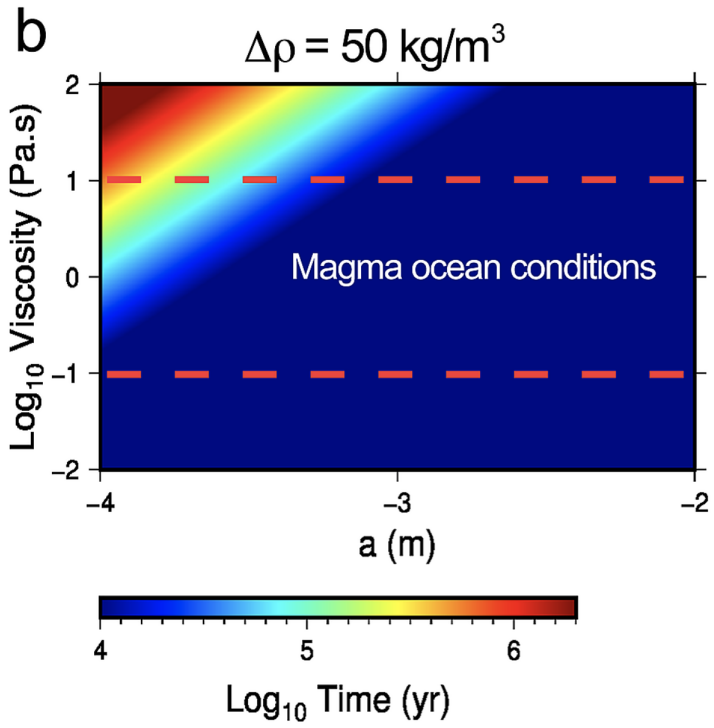

FIGURE 28 – *Temps d'ascension des cristaux de plagioclase durant la phase tardive d'un océan magmatique. Ce temps est calculé pour une gamme de viscosités (0.1 à 10 Pa.s), de diamètres de cristaux (de 100 μm à 1 cm) et pour un contraste de densité $\Delta\rho = 50$ kg/m^3 entre le cristal et la phase liquide. Le temps nécessaire à un cristal pour atteindre la surface de l'océan magmatique est représenté par une échelle de couleurs allant de 10 kyr (bleu) à 2 Myr (rouge). Cette figure montre que le temps de remontée du cristal est de quelques dizaines de milliers d'années dans les conditions de l'océan magmatique, sauf pour les petits cristaux d'environ 100 μm et les viscosités élevées de >10 Pa.s pour lesquels le temps de remontée est plus long (D'après Frossard et al. (2019)).*

appelées anorthosites. Les anorthosites composent la majorité de la surface de la Lune. Depuis le retour des premiers échantillons lunaires associés aux missions Apollo, leur contexte de formation a été compris. Les anorthosites se seraient formées pendant le refroidissement de l'océan magmatique lunaire. La faible densité de ce minéral leur permet de flotter pour former une croûte en surface. Les échelles de temps nécessaire à la flottaison de ces minéraux sont essentiellement fonction de la viscosité du magma et de la taille des minéraux (Figure 28). Il est possible de produire les teneurs en europium et strontium dans cette météorite avec la fusion d'anorthosites lors d'un impact. Grâce à la forte production de chaleur par radioactivité dans les premiers millions d'années du Système Solaire, une grande partie des planétésimaux ont été partiellement fondus produisant un stade d'océan magmatique. Cette découverte montre que

les océans magmatiques sur les planétésimaux du Système Solaire interne ont pu former des roches similaires à celles présentes sur la Lune. La présence de telles croûtes sur des planétésimaux a pu influencer de manière significative la composition des planètes. Cette découverte a fait l'objet d'un article publié dans Geochemical Perspectives Letters (Frossard et al., 2019).

7.3 Fin de solidification et mise en place de la tectonique des plaques

Nous avons montré précédemment que les dernières étapes de solidification du manteau primitif se déroulaient au sein de fines couches plus ou moins profondes (voir section 6.2.2). La présence d'une couche fondue à faible profondeur pendant l'Hadéen et sa cristallisation finale autour de la limite Hadéen-Éoarchéen pourraient empêcher l'apparition de formations orogéniques élevées en raison de la compensation isostatique rapide de tout relief créé et du développement de failles tectoniques à grande échelle et zones de cisaillement (Monteux et al., 2020). L'absence de reliefs favoriserait à son tour une Terre où la majeure partie de sa surface serait recouverte d'eau peu profonde. Les failles majeures et les zones de cisaillement pourraient représenter des voies pour que l'eau liquide pénètre jusqu'aux niveaux inférieurs de la croûte provoquant ainsi une activité hydrothermale intense. En outre, cette couche très déformable à la profondeur de la croûte inférieure pourrait éventuellement isoler la croûte du manteau sous-jacent. Doglioni et al. (2011) ont proposé qu'une couche de fusion partielle stable entre l'asthénosphère et la lithosphère pourrait induire un découplage visqueux efficace entre les deux couches et expliquer la durée de vie des racines cratoniques. A l'Hadéen-Eoarchéen, le couplage visqueux entre le manteau et la croûte pourrait avoir induit le début du remaniement à grande échelle de la croûte hadéenne et la formation de blocs crustaux archéens stables. La persistance d'une couche partiellement fondue pourrait donc expliquer l'absence de fragments de croûte de l'Hadéen dans les archives géologiques et au début des archives géologiques de l'Archéen. Par conséquent, l'établissement d'un lien entre la chronologie des principaux événements de différenciation dans les archives géologiques et la cristallisation des dernières couches partiellement fondues pourrait aider à comprendre certains processus superficiels précoces.

Le passage de l'archéen au protérozoïque a mis fin à une période de grande instabilité à la surface de la Terre. Cette transition pourrait être liée à un changement de dynamique de l'intérieur de la Terre. Des expériences menées au LMV ont montré que le solidus du manteau supérieur était à une température plus basse que prévue pour une composition chondritique (Andrault et al., 2018). Selon cette étude, un tel solidus associé à un manteau plus chaud permettrait la présence d'une couche fondue profonde et persistante dans le manteau archéen. La solidification progressive de cette couche fondue aurait pu renforcer le couplage mécanique entre la lithosphère et l'asthénosphère. Un tel changement pourrait expliquer la transition d'une dynamique de surface dominée par un couvercle stagnant à une tectonique des plaques moderne avec des subductions profondes. L'intersection entre le solidus du manteau et un profil de température adiabatique avec une température potentielle correspondant à une fraction de $\phi_c \sim 40\%$ pourrait contraindre la profondeur du fond de la couche partiellement

fondue restante. Dans le cas de la solidification d'un manteau partiellement fondu depuis la frontière manteau-noyau vers la surface, la profondeur de la dernière couche partiellement fondue restante devrait donc être inférieure à 300 km comme proposé par Solomatov (2007). La cristallisation complète du manteau devrait se produire moins d'$\sim$1 Ga (Sleep et al., 2014) après la formation de l'océan magmatique lié à l'impact à l'origine du système Terre-Lune.

7.4 Origine des larges provinces volcaniques archéennes

Par le passé, des événements volcaniques majeurs ont induit des extinctions massives de la vie, la dislocation de continents et de grands soulèvements régionaux. Leur formation reste énigmatique car elle nécessite la fusion du manteau à des taux élevés et à grande profondeur. Pour sonder les propriétés du manteau partiellement fondu, des chercheurs ont réalisé des expériences à l'aide d'une presse à multi-enclumes couplée à des méthodes avancées de mesures in situ. Ils mettent en évidence l'importance d'une grande quantité de chaleur concentrée dans les profondeurs du manteau après la solidification d'un océan magmatique global. L'ascension de panaches mantelliques de régions profondes induit des anomalies thermiques de plusieurs centaines de degrés et la fusion du manteau dans les premiers 1000 km de profondeur. Ce mécanisme explique non seulement la composition chimique des laves anciennes, mais aussi l'évolution du volcanisme de point chaud au cours de l'histoire de la Terre. La composition des laves anciennes suggère la fusion du manteau à des profondeurs d'au moins 600-700 km et des taux de fusion entre 10 et 50%. Mais les conditions précises pour produire les différentes laves, par exemple les komatiites, restent mal contraintes. L'interprétation des compositions est d'autant plus difficile que les laves sont plus anciennes. Des études antérieures mettent en exergue la complexité des mécanismes de fusion à cause de la présence probable d'eau et de CO_2, et aussi à cause de l'évolution thermochimique des magmas lors de leur remonté vers la surface.

Dans le cadre de la thèse de Remy Pierru, nous avons fait une étude détaillée des conditions de pression et température nécessaires à la production des laves anciennes par la fusion du manteau de composition pyrolitique (Pierru et al., 2022). Grace à des méthodes originales de détection in situ de la fusion, nous avons pu synthétiser des échantillons avec des taux de fusion variés, pour une grande gamme de profondeurs dans le manteau, et de façon reproductible. Il apparait que la nature des laves anciennes trouvées en surface est compatible avec la longue persistance d'un fort gradient de température dans le manteau profond. Ce type de gradient dit super-adiabatique est attendu après la solidification d'un océan magmatique profond. Avec l'établissement progressif des grands mouvements de convection dans le manteau qui caractérise la dynamique moderne de la Terre interne, de gros panaches mantelliques remontent vers la surface (Figure 29). Leur température élevée induit leur fusion progressive à de grandes profondeurs. Sur la base d'une modélisation géodynamique, nous montrons l'aplatissement progressif du profil super-adiabatique avec le refroidissement séculaire de la Terre. Cet effet est compatible avec la disparition progressive des laves anciennes générées à plus grandes profondeurs, sans pour autant empêcher les remontés de panaches profonds issus de

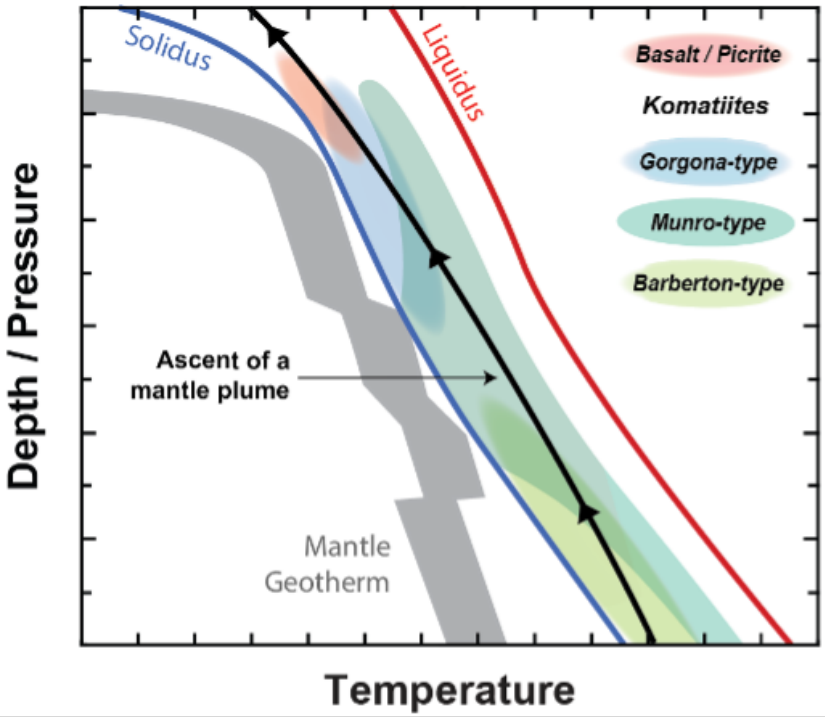

FIGURE 29 – *Diagramme de fusion du manteau : La chaleur accumulée dans le manteau profond après les épisodes d'océan magmatique induit la persistance d'un fort gradient de température. Dans ce cadre, un panache mantellique ascendant (ligne noire) est plusieurs centaines de degrés plus chaud que le manteau environnant. Ce type de panache fond partiellement lorsque sa température s'établie entre le solidus (bleu) et le liquidus (rouge) du manteau. Cela génère des magmas de compositions Komatiites, picrites et basaltes à plus de 700 km de profondeur et pour des taux de fusion atteignant jusqu'à 50%. À partir de Pierru et al. (2022).*

la frontière noyau-manteau à l'origine de certaines îles océaniques.

Références personnelles

Boujibar, A., Andrault, D., Bolfan-Casanova, N., Bouhifd, M.A., **Monteux, J.**, *2015, Cosmochemical fractionation by collisional erosion during the Earth's accretion, Nature Communications, 6 :8295.* **LIEN HAL**

Andrault D., Bolfan-Casanova N., Bouhifd A., Boujibar A., Garbarino G., Manthilake G., Mezouar M., **Monteux, J.**, *Parisiades P., Pesce G., 2017, Toward a coherent model for the melting behavior of the deep Earth's mantle, Physics of the Earth and Planetary Interiors vol.265, p.67-81.* **LIEN HAL**

Andrault D., Pesce G., Manthilake G., **Monteux, J.**, *Bolfan-Casanova N., Chantel J.,*

Novella D., Guignot N., King A., Itié J.P., Hennet L., 2018, Deep and persistent melt layer in the Archaean mantle, Nature Geoscience. **LIEN HAL**

Frossard P., Boyet M., Bouvier A., Hammouda T., **Monteux, J.***, 2019, Evidence for anorthositic crust formed on an inner solar system planetesimal, Geochemical Perspectives Letters vol.11, p.28-32.* **LIEN HAL**

Pierru R., Andrault D., Manthilake G., **Monteux, J.***, Devidal J.L., Guignot N., King A., Henry L. 2022, Deep mantle origin of large igneous provinces and komatiites, Sci. Adv. 8, eabo1036.* **LIEN HAL**

nature COMMUNICATIONS

ARTICLE

Received 13 Jun 2015 | Accepted 7 Aug 2015 | Published 23 Sep 2015

DOI: 10.1038/ncomms9295 OPEN

Cosmochemical fractionation by collisional erosion during the Earth's accretion

Asmaa Boujibar[1,†], Denis Andrault[1], Nathalie Bolfan-Casanova[1], Mohamed Ali Bouhifd[1] & Julien Monteux[1]

Early in the Solar System's history, energetic collisions of differentiated bodies affected the final composition of the terrestrial planets through partial destruction. Enstatite chondrites (EC) are the best candidates to represent the primordial terrestrial precursors as they present the most similar isotopic compositions to Earth. Here we report that collisional erosion of >15% of the early Earth's mass can reconcile the remaining compositional differences between EC and the Earth. We base our demonstration on experimental melting of an EC composition at pressures between 1 bar and 25 GPa. At low pressures, the first silicate melts are highly enriched in incompatible elements Si, Al and Na, and depleted in Mg. Loss of proto-crusts through impacts raises the Earth's Mg/Si ratio to its present value. To match all major element compositions, our model implies preferential loss of volatile lithophile elements and re-condensation of refractory lithophile elements after the impacts.

[1] Laboratoire Magmas et Volcans, Université Blaise Pascal, CNRS UMR-6524, 5 rue Kessler, 63000 Clermont-Ferrand, France. † Present address: Astromaterials Research and Exploration Science, NASA Johnson Space Center, 2101 Nasa Parkway, Houston, Texas 77058, USA. Correspondence and requests for materials should be addressed to A.B. (email: asmaa.boujibar@nasa.gov).

Large-scale melting occurred broadly in the first stages of planetary accretion[1]. The impressive homogeneity of stable isotopic compositions of large bodies suggests extensive melting and formation of magma oceans[1]. However, while large-scale melting can efficiently erase isotopic heterogeneities, low degrees of partial melting are a primary cause of chemical segregation. The possibility to form proto-crusts by low degrees of melting of chondritic material is evidenced by the discovery of felsic achondrites (GRA-06128/9; ref. 2). Early differentiation of planetary embryos was also recently suggested by a study that determined the initial content of the short-lived radionuclide ^{26}Al in angrites[3]. Therefore, early crusts could form by different processes, such as fractional crystallization of a magma ocean or the migration of silicate melts over networks of veins and dikes[4]. Despite the formation mechanism of these proto-crusts, their occurrence on accreting bodies should have played a major role in the final planetary composition, because energetic episodes of accretion have eroded the planetary surfaces[5–8].

The chemical composition of the building blocks that accreted to form the Earth remains controversial. Our planet shows remarkable isotopic similarities with enstatite chondrites (EC), especially with those of the EH type[9], for the elements whose isotopes do not fractionate during core segregation (O, Ca, N, Mo, Ru, Os, Cr, Ni, Ti and Sr). However, EC and the Earth present important chemical differences. First, EC are so reduced that their silicate phases are free of FeO, which differs from the present-day silicate mantle with 8 wt% FeO. This issue may eventually be solved by internal oxidation processes for some of the Fe metal[9,10]. A second issue is that EC show a Mg/Si weight ratio lower than 1 (~0.63; ref. 11), differing substantially from that of the Earth's upper mantle (~1.1; ref. 12). The Mg/Si ratio of bulk Earth (BE) could be slightly overestimated if the lowermost mantle is bridgmanitic (that is, perovskitic) rather than pyrolitic[13]. Furthermore, the Earth shows higher abundances of refractory lithophile elements (RLE) and lower concentrations of moderately volatile elements (as the alkali elements Li, Na, K and Rb) compared with EC and all other chondrites (Fig. 1).

In this study, we test whether collisional erosion of early crusts can explain the chemical divergence between the BE and EC. Based on experiments on the melting properties of synthetic EC at pressures between 1 bar and 25 GPa, we show that early differentiated planetary bodies can develop silica- and alkali-enriched crusts. Loss of these crusts through impact erosion can ultimately increase the Mg/Si ratio of the planetary bodies to match the current Earth ratio. In addition, to further increase the budget in RLE and accurately reproduce the terrestrial concentrations of the major and minor elements, impact erosion must be accompanied with preferential loss of volatile lithophile elements and re-condensation of RLE.

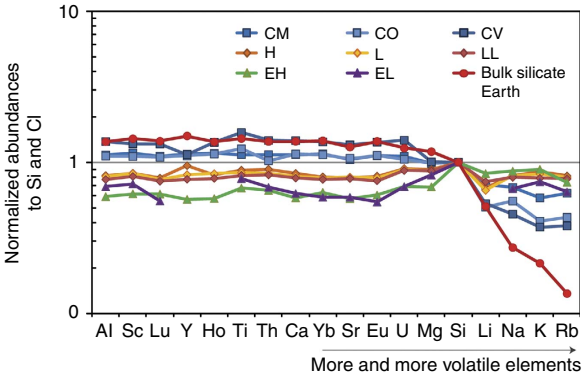

Figure 1 | Major chemical differences between the chondrites and the bulk silicate Earth (BSE). The abundances are normalized to Si and CI chondrites[11,12]. From left to right, the lithophile elements are reported with decreasing their 50% condensation temperature. The depletion of volatile elements in the BSE results from the erosion of crusts enriched with incompatible elements and the subsequent loss of the most volatile elements.

Results

Partial melting of enstatite chondrites. We experimentally investigated the composition of melts produced by low degrees of melting of synthetic EC powders, at low oxygen fugacity (3.6 to 1.8 log units below the iron/wustite buffer), at different pressure conditions expected for melt segregation in partially molten planetary embryos (see Methods section and Supplementary Fig. 1). Our pseudo-eutectic melts are all characterized by high concentrations of SiO_2, Al_2O_3 and Na_2O, and low MgO contents (Fig. 2). The change with pressure of the low-degree melt composition agrees with that previously reported at 1 bar (ref. 14). The most striking features are the increase of MgO (Fig. 2b) and decrease of SiO_2 (Fig. 2a) and Al_2O_3 (Fig. 2c) with pressure. The disappearance of clinopyroxene at 16 GPa and garnet at 24 GPa

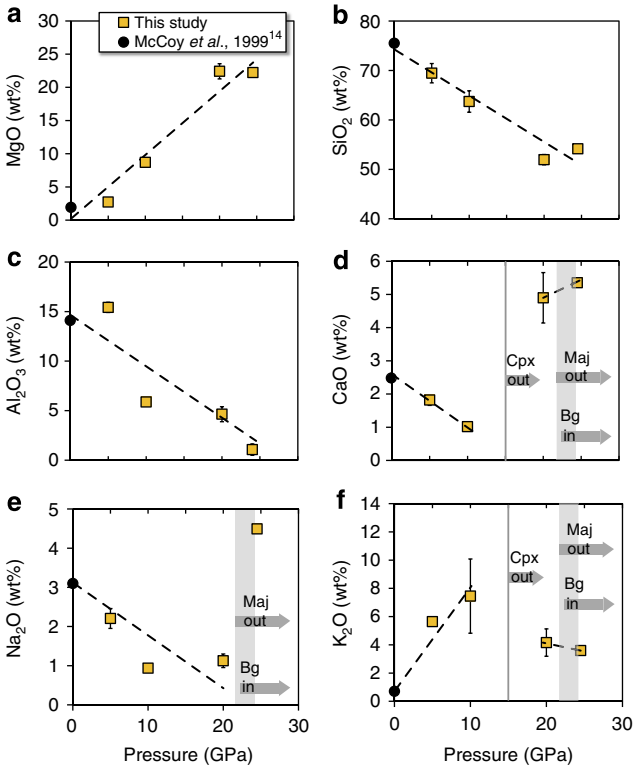

Figure 2 | Chemical composition of pseudo-eutectic melts synthesized at high pressures. We report the compositions of melts generated by partial melting of an EC-like mantle at pressures between 5 and 25 GPa (yellow squares). Our data set plots are in agreement with previous results performed at 1 bar (ref. 14) (dark circles). Whereas MgO content (**a**) increases with pressure in the silicate melts, the concentrations of SiO_2 (**b**) and Al_2O_3 (**c**) decrease. Sharp changes of the liquid compositions occur when the sample encounters phase transformations (shown with the grey arrows), in particular, with the disappearance of clinopyroxene (Cpx) at 15 GPa (vertical lines in **d** and **f**) and simultaneous disappearance of majorite (Maj) and appearance of bridgmanite (Bg, the $MgSiO_3$ perovskite; vertical grey areas in **d**–**f**) at 24 GPa.

(ref. 15) induces major CaO (Fig. 2d), Na_2O (Fig. 2e) and K_2O (Fig. 2f) enrichment of the liquid, respectively. Altogether, pseudo-eutectic liquids show compositions between rhyolitic and trachy-andesitic in the range of pressures investigated. In partially molten planetesimals, such melts should ascend relatively easily towards the planetary surface due to their low melt densities, even for low degrees of partial melting[4]. As the melts can re-equilibrate during their ascent to the surface, those produced at shallower depths are more likely to stay unaltered and produce proto-crusts enriched in incompatible elements. The most appropriate melts for the formation of proto-crusts should then be those produced at relatively low pressures and degrees of partial melting.

Change of proto-Earth composition with collisional erosion. We now evaluate how collisional erosion of proto-crusts made of these pseudo-eutectic liquids would affect the chemical composition of an EH-type planetary embryo[11]. First, we calculate the Mg/Si ratio of a planetary body after removal of pseudo-eutectic melts generated at average pressures of 1 bar to 25 GPa and compare it with the BE[12], with the hypothesis that ~7 wt% Si is present in the Earth's core[9,16]. By increasing the amount of crustal erosion, the Mg/Si ratio of the depleted EH planetoid increases towards the present-day BE ratio of ~0.9, owing to the high SiO_2 content of the melts (Fig. 3a). The lower the pressure of melt-solid equilibration, the higher the SiO_2 content in the melt, and therefore the crustal erosion should be the less extensive. The BE Mg/Si ratio can be achieved by accretion of EH chondrites and erosion of a crust of 15–18% of the planetary mass for solid-melt equilibrium at pressures below 10 GPa. This amount of crustal erosion is comparable to the loss of highly incompatible elements required to explain the mantle budget in volatile elements[17], and is comparable to the amount of mass lost during hit and run simulations[18]. As the formation of such SiO_2-rich crust necessitates a low degree of partial melting (at a level of 5–7%), removing proto-crust to a level of 15–18 wt% of the planetary mass requires repeated processes of proto-crust formation and collisional erosion. Repeated partial melting of the EH-type mantle would constantly produce an SiO_2-rich proto-crust, owing to the fixed pseudo-eutectic composition. The nature of planetary accretion itself provides the necessary energy to melt planetesimals and erode them or even disrupt them (see below). Simulations indicate that an accreting proto-planet should experience ~10^5 collisions[18].

Removal of proto-crust also affects the Al/Si, Ca/Si and Na/Si ratios (Fig. 3b and Supplementary Fig. 2). Interestingly, the misfits between Mg/Si, Al/Si, Ca/Si and Na/Si ratios in BE and in our model of EH-type planetoid depleted by crustal erosion show a clear correlation with the condensation temperatures of the elements of interest[19] (Fig. 3b). Rather than being fortuitous, this trend can be understood in terms of differential re-condensation of the elements after collisional erosion. Our model implies that early differentiation of a planetary embryo forms a silica-rich crust (Fig. 4a,b) that is subsequently eroded and vaporized by energetic impacts (Fig. 4c). The eroded material is then chemically fractionated with a preferential condensation of the refractory elements relative to the volatiles (Fig. 4d). This explains the previously reported marked consequences on

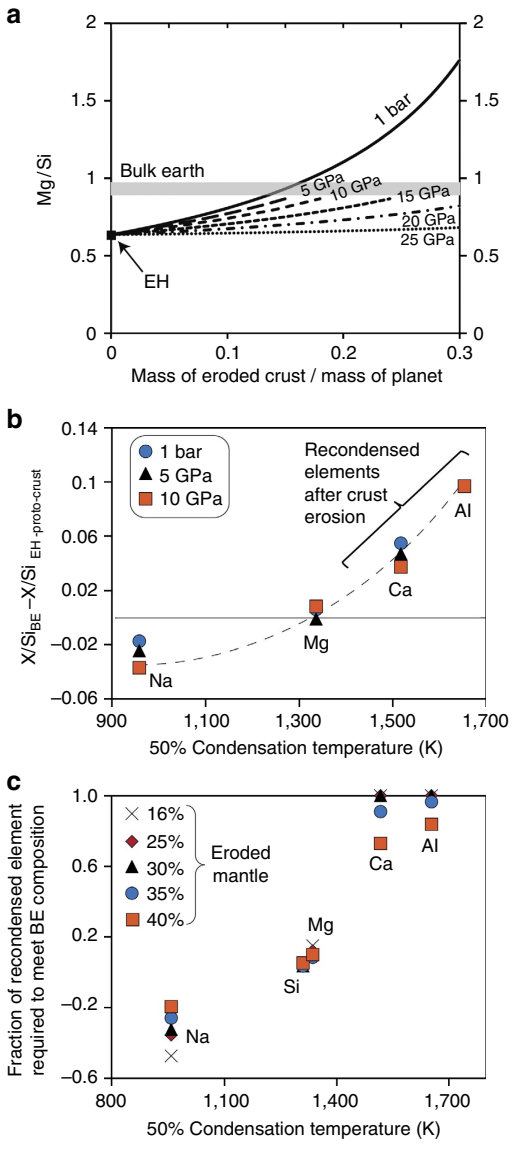

Figure 3 | Change by collisional erosion of the proto-planetary chemical composition. (**a**) Change by collisional erosion of the planetary Mg/Si ratio by removal of a differentiated crust with a composition equivalent to that of pseudo-eutectic melts produced at pressures of 1 bar and 5, 10, 15, 20 and 25 GPa. Removal by collisional erosion from the model EH composition results in an increase of the Mg/Si ratio of the planetesimal. The grey area represents the Mg/Si ratio of the BE with 7 wt% Si dissolved into the core[9,16]. Erosion of a crust of >15% of the planet mass is required to reconcile the Mg/Si ratio of an EH-type planet with the present-day BE[12]. (**b**) Correlation between residual misfits between BE and the EH proto-planet X/Si for X = Na, Ca and Al as a function of the 50% condensation temperature of the elements[19]. After the mass of eroded crust is adjusted to meet the Mg/Si ratios of BSE, there is a residual misfit for the abundances of other major elements (Supplementary Fig. 2). The correlation between BE enrichments and the condensation temperatures of the different elements suggests chemical fractionation during the processes of vaporization of the planetary surface, with re-condensation of the eroded material on the planetary surface (Fig. 4). (**c**) Degree of chemical fractionation required by our model, for different amounts of collisional erosion. Here we consider that the 15% of the crust (produced in the 0–5-GPa range) required to match the Mg/Si ratio of the BE and 16–40% of the planetary mantle are eroded by the impacts. For a total erosion of 31–45% of the planetary mass, for example, the actual Na/Si, Mg/Si, Ca/Si and Al/Si ratios of BE are reproduced when 100% of Al and Ca, 10% of Mg and 5% of Si are re-condensed on the planetary surface, which is in agreement with their condensation temperature. A negative value for Na denotes the fact that the residual mantle of our EH-type model (after collisional erosion) would still contain high Na contents compared with BE. In this case, additional Na volatilization from the residual mantle is required.

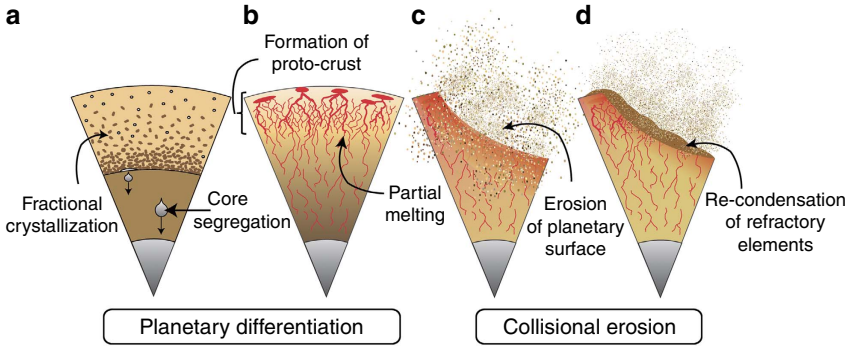

Figure 4 | Schematic model of chemical fractionation by collisional erosion. (**a**,**b**) Early heating leads to the rapid segregation of Fe-rich metal into the core. It is accompanied with the formation of a deep magma ocean[1] (**a**) and/or small-scale partial melting and formation of complex networks of veins and dikes[4] (**b**) which allows fast transfer of melts to the surface[4]. Both can yield compositional stratification of the mantle and the formation of an SiO_2-rich proto-crust. (**c**) The repeated collisions induce erosion of the proto-crust enriched in incompatible elements, as well as part of the planetary mantle. (**d**) Within the fraction of material volatilized by meteoritic impacts, re-condensation of refractory elements is favoured compared with the volatile elements.

the thermal history of Earth that could result from the loss of incompatible and refractory heat-producing elements, such as U and Th[5,20,21].

In fact, the Earth's budget in RLE can be reached by a number of different erosion and re-condensation models. The lowest amount of erosion (15–18 wt% of proto-crust to meet the right Mg/Si ratio) requires re-condensation of 100% of the refractory elements (Ca and Al) on the planetary surface (Fig. 3c). For higher amounts of planetary surface erosion (15–18 wt% proto-crust plus a mantle fraction), the models require less chemical fractionation during vaporization or re-condensation. For 40% mantle erosion, re-condensation of 84% of Al, 73% of Ca, 10% of Mg and 5% of Si is necessary (Fig. 3c and Table 1) to produce a planetary composition similar to Earth. Comparable fractionation of major elements with Ca- and Al-rich condensates depleted in Mg and Si was reported in the most primitive unequilibrated Semarkona ordinary chondrites (LL3.0; ref. 22). Also, such a degree of chemical fractionation during re-condensation may not be necessary if the composition of the parent body deviates from the EH chondrites (see below). Then, non-equilibrium processes, such as solar wind, could have favoured the loss of volatile elements from the gravitational field of the proto-planet. In addition, the volatile elements could have been partially atmophile due to hot planetary surfaces, which could have contributed to the volatile and refractory fractionation.

The major sources of energy provided by planetary accretion. During planetesimal growth, the thermal state of a proto-planet depends on its initial heating caused by the decay of short-lived radionuclides such as ^{26}Al and ^{60}Fe (ref. 23), on its accretionary history and on how potential energy is dissipated during the iron/silicates segregation. Temperatures in excess of 2,000 K could have been reached within the first 2–3 million years after the formation of the first solids of the Solar System (calcium–aluminium-rich inclusions, CAI)[24]. The early radioactive heating can therefore cause both segregation of a metal-rich core and silicate melting on planetary embryos that have quickly accreted (to attain a radius of 30 km within the first 3 million years; see Fig. 2 in Yoshino *et al.*[24]). Kleine *et al.*[25] showed that high temperatures of early asteroids are in agreement with the young ages of iron meteorites, OC, CO and CR chondrites and the peak temperatures recorded by the same meteorites (see in ref. 25).

In addition to this radioactive heating, in the shallow parts of the impacted planet, impact heating (ΔT), superimposed to a sufficiently hot proto-planetary interior (with an initial

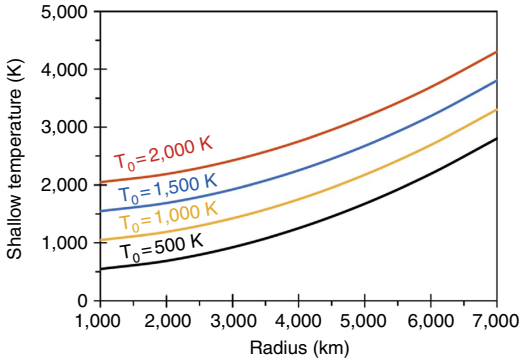

Figure 5 | Shallow post-impact temperature as a function of the target radius R. Different pre-impact temperatures are illustrated (from $T_0 = 500$ to 2,000 K). We consider that (i) surface gravity is equal to $g = 4/3\ \pi\ G\ \rho\ R$ (G is the gravitational constant and ρ is the density of the target), (ii) kinetic energy of the impactor is controlled by the escape velocity of the impacted body (that is, $v_{impactor} = \sqrt{(2gR)}$), (iii) the impactor and impacted body have the same densities, and (iv) only 30% of the incoming kinetic energy is converted into heat.

temperature of T_0) can lead to temperatures ($T = T_0 + \Delta T$) much larger than the vaporization temperature of silicates ($\sim$1,300 °C at 0.001 bar; see Fig. 5 above). This heating is localized in a spherical region called the isobaric core, just beneath the impact site (for example, ref. 26). By making the conservative assumptions that (i) kinetic energy of the impactor is controlled by the escape velocity of the impacted body, (ii) impactor and target body have the same densities and (iii) only 30% of the incoming kinetic energy is converted into heat, a simple energy balance indicates that $\Delta T\ (\mathrm{K}) = 4.7 \times 10^{-5} \times R^2$ (km) (refs 26,27).

Assuming that the impact occurs with the escape velocity of the impacted body is a conservative assumption in the sense that it is the minimum impact velocity; larger impact velocities can substantially increase the post-impact temperature below the surface. For instance, some episodes of hypervelocity impacts have probably played a major role during the accretion of the terrestrial planets. For example, a recent model suggests that Jupiter and Saturn have likely migrated inwards and then outwards early in the Solar System history[28], leading to strong resonance and high eccentricities of the planetesimals. As the resonance with Jupiter can significantly increase the impact

Table 1 | Resulting compositions with dual processes of collisional erosion and fractional re-condensation.

	Bulk Earth	Assumed core composition[44]	EH-like planet			EH-like planet with adjusted core size		
			0% eroded mantle	25% eroded mantle	40% eroded mantle	0% eroded mantle	25% eroded mantle	40% eroded mantle
Mg	15.6		13.8	12.8	10.8	15.9	15.8	15.6
Al	1.6		1.0	1.1	1.1	1.2	1.4	1.6
Si	16.6	7	15.0	13.7	11.5	17.2	16.9	16.6
Ca	1.7		1.1	1.2	1.2	1.3	1.5	1.7
Na	0.2		0.2	0.2	0.1	0.2	0.2	0.2
K	0.0		0.0	0.0	0.0	0.0	0.0	0.0
O	30.5	4	27.9	25.8	21.9	30.5	30.5	30.5
Fe	31.4	82	38.0	41.9	49.6	31.4	31.4	31.4
Co	0.1	0.1	0.1	0.1	0.1	0.1	0.1	0.1
Ni	1.6	5	2.3	2.5	3.0	1.6	1.6	1.6
S	0.6	2	0.6	0.6	0.7	0.6	0.6	0.6

We compare the actual bulk Earth composition (first column) (calculated based on bulk silicate Earth[12] composition and cosmochemical estimates of core composition[44] (second column)) with the EH-like Earth (third column) after erosion of (i) 15% of a crust composed of pseudo-eutectic melts produced at 0–5 GPa and (ii) 0–40% of its mantle. The erosion yields a significant depletion in the lithophile elements (Mg, Si, O, Na, Al and Ca) compared with the siderophile elements (Fe, Ni, Co and S). By adjusting the core size to the actual terrestrial core size (by fixing the concentrations of the siderophile elements to that of the Bulk Earth), the composition of our EH-like planetary model can reach values very close to that observed in the present-day Earth.

velocities[29], the kinetic energy, available during the impact processes on growing bodies, may have enhanced the vaporization and the excavation of their shallow material. This model, with marked migration of Jupiter and Saturn, is one suggested model of the dynamical evolution of the Solar System. Other models may not produce such high velocity collisions, but they would have a longer period during which frequent collisions could occur.

Vaporization following collisional erosion from large impacts is widely accepted[30]. The abundance of impacts is supported by observations of the iron meteorites, which represent fragments of cores of differentiated bodies, which are now destroyed. These iron meteorite parent bodies are as old as the CAI, which are the oldest objects of the Solar System, that formed during the first million year after T_0 (ref. 31). Thus, collisional stripping operated in the very early stages of the formation of the Solar System.

Discussion

Our experimental results show that surface erosion modifies more efficiently the planetary composition of smaller planetary bodies owing to lower internal pressures (Fig. 3a). This suggests a more efficient chemical fractionation early in the accretion history. As a matter of fact, silica- and alkali-rich compositions (andesitic to rhyolitic and trachyitic) have been observed in various asteroidal materials: bulk achondrites (GRA-06128/09), silicate enclaves in iron meteorites, glass inclusions or igneous clasts in aubrites, glass inclusions in the howardite, eucrite and diogenite meteorites, clasts in the ureilites. The oldest sampled materials of the Solar System with a granitic composition are only 5–30 Myr younger than the formation of the Solar System (see ref. 32 for a review). This indicates the formation of silicic crust nuclei very early in the inner Solar System.

A widespread Si isotopic dichotomy is observed between planetary/asteroidal bodies and the chondrites. There is a correlation between the enrichment in heavy Si (^{30}Si) with both (i) the depletion of the moderately volatile elements (K) and (ii) the depletion of Si relative to Mg for the Earth, the Moon, Vesta, Mars, the angrites (basaltic meteorites) parent body and the chondrites[33]. As suggested by Pringle *et al.*[33], this correlation could be caused by early impact-induced evaporative loss, occurring as early as the formation of angrites, 2 Myr later than the formation of the oldest currently known objects of the Solar System[34,35] (Supplementary Note 1). Thus, the Si isotopic measurements fully support our model of early collisional erosion. It has also been proposed that energetic episodes of impacts can induce significant chemical fractionation of RLE in EL chondrites[36].

In contrast to the other planetary differentiation processes, such as core segregation or magma ocean crystallization, an early impact erosion affects the composition of both planetary bodies and the remaining unaccreted material, in a complementary way. Owing to a higher surface/volume ratio compared with the planetesimals, the chondritic material that was left over from the accretion may have preferentially reacted with gases produced by vaporization of the eroded crusts, which are enriched in SiO_2 and volatile lithophile elements. This can explain the enrichments in Na, S and Si observed at the edges of chondrules contained in carbonaceous and ordinary chondrites[37–39]. EC are the most alkali- and silica-rich chondrites[11,40] (Fig. 1), but in contrast to the carbonaceous chondrites, this enrichment is global and not limited to chondrules (Supplementary Note 2). This is likely owing to the fact that EC have experienced important thermal metamorphism that usually erases the chemical gradients. Several studies have analysed the behaviour of alkali elements in chondrules in order to retrieve the conditions under which the chondrules form. The majority of these studies concluded that very high dust densities with high solid/gas ratios are required in the nebula to enrich the edges of chondrules in Na[37]. This was previously attributed to aqueous alteration[41]. In light of our results, we propose that the destruction and vaporization of eroded proto-crusts can also contribute to this elevation of the dust/gas ratio of the nebula in the formation regions of chondrules.

The EH meteorites that are sampled today could have suffered an SiO_2 enrichment compared with their parent bodies, owing to interaction with crusts eroded from primordial planetesimals. This would have drifted their composition away from that of the Earth, compared with the original building blocks (Fig. 1). This common original material could have had a higher Mg/Si ratio and lower content in alkali elements than the EH chondrites. Consequently, our quantitative model of collisional erosion developed in this study (for example, Fig. 3) can be considered as the most extreme one, as less proto-crust erosion would be required to meet the actual BE chemical composition. Altogether, we show that collisional erosion could readily explain the major chemical divergences between the EH chondrites and Earth. It reinforces the model of the EH-like Earth[9], nevertheless adding to

this model the idea that the common starting material could have been slightly depleted in SiO_2 and volatile lithophile elements in comparison with the EH chondrites.

Methods

Preparation of starting materials. The starting material was composed of 68 wt% silicate and 32 wt% metal with a chemical composition equivalent to the average composition of EC[9] (Supplementary Table 1). While we are exclusively interested in the silicate properties, the presence of metals helps reproduce the EH-Earth conditions more precisely and buffer the oxygen fugacity. The silicate fraction was composed of ultra-pure oxides and carbonates (SiO_2, MgO, Al_2O_3, TiO_2, Cr_2O_3, MnO, Na_2CO_3, $CaCO_3$ and K_2CO_3) that were finely ground together, decarbonized and then dried overnight at 1,000 °C. The metal powders were composed of a fine mixture of ultra-pure Fe, Ni, Si, Mn, Co and/or FeS. All samples were S free, except for 5 wt% S in the metal of sample no. 104. Silicate and metal fractions were intimately mixed to obtain a homogeneous chondritic powder, that was kept constantly in a vacuum oven to avoid hydration.

Details of the experimental conditions. We conducted experiments at 5, 10, 20 and 25 GPa, with temperatures ranging from 1,380 to 1,900 °C using Kawai-type 1,000-t and 1,500-t multi-anvil presses. We heated the experiments to temperatures at or slightly above the solidus, that is, between 1,380 and 1,900 °C, for oxygen fugacities between −2.1 and −3.6 log units below the IW buffer (Supplementary Table 2). Assemblies were composed of Cr-doped MgO octahedra pressure media with edges of 18, 14 and 10 mm, coupled with tungsten carbide cubes with 11, 6 and 4 mm truncations, respectively. Pressure calibrations of both 1,000-t and 1,500-t presses were previously described[42]. The sample powder was loaded into a graphite capsule that was surrounded by MgO sleeves to prevent the sample pollution. High temperatures were achieved using an $LaCrO_3$ furnace and a ZrO_2 sleeve thermal insulator. Temperature was measured using a $W_5Re/W_{26}Re$ thermocouple in experiment nos. 1,223 and 174, and estimated using the relation between temperature and electrical power for experiment nos. 1,216 and 104. Pressure and temperature uncertainties are estimated to be ~0.5 GPa and 100 °C, respectively.

To achieve homogeneous samples without relict of the starting powders, we first heated the samples above the liquidus temperature[43] for a couple of minutes. Temperature was then rapidly reduced (with a rate of 100 K in <20 s) to a temperature just above the reported solidus. The sample was then equilibrated between 30 min and 3 h. This procedure helps grain growth and allows segregation of relatively large pools of melt, which are usually difficult to collect with low degrees of partial melting[43].

Chemical compositions of the coexisting phases. The microstructure of recovered samples was observed using a scanning electron microscope (Supplementary Fig. 1). Phase relations and chemical compositions were determined using a CAMECA SX100 electron probe micro-analyser (Supplementary Table 1). We used an accelerating voltage of 15 kV, an electron beam defocused to 2–20 μm and a current of 15 nA, except for the chemical analyses of bridgmanites that were analysed with 2 nA. As standards, we used pure metals and silicates.

References

1. Greenwood, R. C., Franchi, I. A., Jambon, A. & Buchanan, P. C. Widespread magma oceans on asteroidal bodies in the early Solar System. *Nature* **435,** 916–918 (2005).
2. Day, J. M. D. *et al.* Early formation of evolved asteroidal crust. *Nature* **457,** 179–182 (2009).
3. Schiller, M., Connely, J. N., Glad, A. C., Mikouchi, T. & Bizzarro, M. Early accretion of protoplanets inferred from a reduced inner solar system ^{26}Al inventory. *Earth Planet. Sci. Lett.* **420,** 45–54 (2015).
4. Wilson, L. & Keil, K. Volcanic activity on differentiated asteroids: a review and analysis. *Chemie der Erde - Geochemistry* **72,** 289–321 (2012).
5. O'Neill, H. S. C. & Palme, H. Collisional erosion and the non-chondritic composition of the terrestrial planets. *Phil. Trans. R. Soc. A* **366,** 4205–4238 (2008).
6. Asphaug, E., Agnor, C. B. & Williams, Q. Hit-and-run planetary collisions. *Nature* **439,** 155–160 (2006).
7. Leinhardt, Z. M. & Stewart, S. T. Collisions between gravity-dominated bodies. I. Outcome regimes and scaling laws. *Astrophys. J.* **745,** 79 (2012).
8. Davison, T. M., O'Brien, D. P., Ciesla, F. J. & Collins, G. S. The early impact histories of meteorite parent bodies. *Meteor. Planet. Sci.* **48,** 1894–1918 (2013).
9. Javoy, M. *et al.* The chemical composition of the Earth: enstatite chondrite models. *Earth Planet. Sci. Lett.* **293,** 259–268 (2010).
10. Wade, J. & Wood, B. J. Core formation and the oxidation state of the Earth. *Earth Planet. Sci. Lett.* **236,** 78–95 (2005).
11. Wasson, J. T. & Kallemeyn, G. W. Composition of chondrites. *Phil. Trans. R. Soc. Lond.* **A325,** 535–544 (1988).
12. McDonough, W. F. & Sun, S. S. The composition of the Earth. *Chem. Geol.* **120,** 223–253 (1995).
13. Murakami, M., Ohishi, Y., Hirao, N. & Hirose, K. A perovskitic lower mantle inferred from high-pressure, high-temperature sound velocity data. *Nature* **485,** 90–94 (2012).
14. McCoy, T., Dickinson, T. L. & Lofgren, G. Partial melting of the Indarch (EH4) meteorite: a textural, chemical, and phase relations view of melting and melt migration. *Meteor. Planet. Sci.* **34,** 735–746 (1999).
15. Liebske, C. & Frost, D. J. Melting phase relations in the MgO–$MgSiO_3$ system between 16 and 26 GPa: implications for melting in Earth's deep interior. *Earth Planet. Sci. Lett.* **345-348,** 159–170 (2012).
16. Gessmann, C. K., Wood, B. J., Rubie, D. C. & Kilburn, M. R. Solubility of silicon in liquid metal at high pressure: implications for the composition of the Earth's core. *Earth Planet. Sci. Lett.* **184,** 367–376 (2001).
17. Halliday, A. N. The origins of volatiles in the terrestrial planets. *Geochim. Cosmochim. Acta* **105,** 146–171 (2013).
18. Bonsor, A. *et al.* A collisional origin to Earth's non chondritic composition? *Icarus* **247,** 291–300 (2015).
19. Lodders, K. Solar System abundances and condensation temperatures of the elements. *Astrophys. J.* **591,** 1220–1247 (2003).
20. Warren, P. H. A depleted, not ideally chondritic bulk Earth: The explosive-volcanic basalt loss hypothesis. *Geochim. Cosmochim. Acta* **72,** 2217–2235 (2008).
21. Jackson, M. G. & Jellinek, A. M. Major and trace element composition of the high $^3He/^4He$ mantle: Implications for the composition of a nonchonditic Earth. *Geochem. Geophys. Geosyst.* **14,** 2954–2976 (2013).
22. Nagahara, H., Kita, N. T., Ozawa, K. & Morishita, Y. Condensation of major elements during chondrule formation and its implication to the origin of chondrules. *Geochim. Cosmochim. Acta* **72,** 1442–1465 (2008).
23. Urey, H. C. The cosmic abundances of potassium, uranium and thorium and the heat balances of the Earth, the Moon and Mars. *Proc. Natl Acad. Sci. USA* **41,** 127–144 (1955).
24. Yoshino, T., Walter, M. J. & Katsura, T. Core formation in planetesimals triggered by permeable flow. *Nature* **422,** 154–157 (2003).
25. Kleine, T. *et al.* Hf-W chronology of the accretion and early evolution of asteroids and terrestrial planets. *Geochim. Cosmochim. Acta* **73,** 5150–5188 (2009).
26. Pierazzo, E., Vickery, A. M. & Melosh, H. J. A reevaluation of impact melt production. *Icarus* **127,** 408–423 (1997).
27. Monteux, J., Coltice, N., Dubuffet, F. & Ricard, Y. Themo-mecahnical adjustment after impacts during planetary growth. *Geophys. Res. Lett.* **34,** L24201 (2007).
28. Walsh, K. J., Morbidelli, A., Raymond, S. N., O'Brien, D. P. & Mandell, A. M. A low mass for Mars from Jupiter's early gas-driven migration. *Nature* **475,** 206–209 (2011).
29. Weidenschilling, S. J., Davis, D. R. & Marzari, F. Very early collisonal evolution in the asteroid belt. *Earth Planets Space* **53,** 1093–1097 (2001).
30. Canup, R. M. & Asphaug, E. Origin of the Moon in a giant impact near the end of the Earth's formation. *Nature* **412,** 708–712 (2001).
31. Amelin, Y., Krot, A. N., Hutcheon, I. D. & Ulyanov, A. A. Lead isotopic ages of chondrules and calcium-aluminum-rich inclusions. *Science* **297,** 1678–1683 (2002).
32. Bonin, B. Extra-terrestrial igneous granites and related rocks: a review of their occurrence and petrogenesis. *Lithos* **153,** 3–24 (2012).
33. Pringle, E. A., Moynier, F., Savage, P. S., Badro, J. & Barrat, J.-A. Silicon isotopes in angrites and volatile loss in planetesimals. *Proc. Natl Acad. Sci. USA* **111,** 17027–17032 (2014).
34. Baker, J. A., Bizzarro, M., Witting, N., Connelly, J. & Haak, H. Early planetesimal melting from an age of 4.5662 Gyr for differentiated meteorites. *Nature* **436,** 1127–1131 (2005).
35. Bouvier, A. & Wadhwa, M. The age of the solar system redefined by the oldest Pb-Pb age of a meteoritic inclusion. *Nat. Geosci.* **3,** 637–641 (2010).
36. Rubin, A. E., Huber, H. & Wasson, J. T. Possible impact-induced refractory-lithophile fractionations in EL chondrites. *Geochim. Cosmochim. Acta* **73,** 1523–1537 (2009).
37. Libourel, G., Krot, A. N. & Tissandier, L. Role of gas-melt interaction during chondrule formation. *Earth Planet. Sci. Lett.* **251,** 232–240 (2006).
38. Alexander, C. M. O. & Grossman, J. N. Alkali elemental and potassium isotopic compositions of Semarkona chondrules. *Meteor. Planet. Sci.* **40,** 541–556 (2005).
39. Marrocchi, Y. & Libourel, G. Sulfur and sulfides in chondrules. *Geochim. Cosmochim. Acta* **119,** 117–136 (2013).
40. Krot, A. N., Keil, K., Goodrich, C. A., Scott, E. R. D. & Weisberg, M. K. in *Treatise on Geochemistry.* (ed. Davis, A. M.) Vol. 1 (Elsevier, 2003).
41. Alexander, C. M. O., Grossman, J. N., Ebel, D. S. & Ciesla, F. J. The formation conditions of chondrules and chondrites. *Science* **320,** 1617–1619 (2008).
42. Boujibar, A. *et al.* Metal–silicate partitioning of sulphur, new experimental and thermodynamic constraints on planetary accretion. *Earth Planet. Sci. Lett.* **391,** 42–54 (2014).

43. Tsuruta, K. & Takahashi, E. Melting study of an alkali basalt JB-1 up to 12.5 GPa: behavior of potassium in the deep mantle. *Physi. Earth Planet. Inter.* **107,** 119–130 (1998).
44. Allègre, J. A., Poirier, J. P., Humler, E. & Hofmann, A. W. The chemical composition of the Earth. *Earth Planet. Sci. Lett.* **134,** 515–526 (1995).

Acknowledgements

We thank B. Bourdon, M. Boyet, S. Charnoz, M. Javoy, E. Kaminski, R. Mishra, S. Keshav, D. Laporte, G. Libourel, H. Martin, Y. Marrocchi, M. Toplis, K. Righter and M. Zolensky for their fruitful discussions and various members of the Laboratoire Magmas et Volcans staff for essential help. This project received funds from INSU-CNRS, Université Blaise Pascal, Région Auvergne and the ANR 'Oxydeep' project. It is a LabEx Clervolc 170 contribution.

Author contributions

A.B. conceived the study, conducted the experiments and acquired the data. A.B., D.A., N.B.-C. and J.M. modelled, interpreted and discussed the results. The manuscript was prepared by A.B., D.A., N.B.-C., M.A.B. and J.M.

Additional information

Supplementary Information accompanies this paper at http://www.nature.com/naturecommunications

Competing financial interests: The authors declare no competing financial interests.

Reprints and permission information is available online at http://npg.nature.com/reprintsandpermissions/

How to cite this article: Boujibar, A. *et al.* Cosmochemical fractionation by collisional erosion during the Earth's accretion. *Nat. Commun.* 6:8295 doi: 10.1038/ncomms9295 (2015).

Physics of the Earth and Planetary Interiors 265 (2017) 67–81

Contents lists available at ScienceDirect

Physics of the Earth and Planetary Interiors

journal homepage: www.elsevier.com/locate/pepi

Invited Review

Toward a coherent model for the melting behavior of the deep Earth's mantle

D. Andrault [a,*], N. Bolfan-Casanova [a], M.A. Bouhifd [a], A. Boujibar [a], G. Garbarino [b], G. Manthilake [a], M. Mezouar [b], J. Monteux [a], P. Parisiades [b], G. Pesce [a]

[a] Laboratoire Magmas et Volcans, CNRS-OPGC-IRD, Université Clermont Auvergne, Clermont-Ferrand, France
[b] European Synchrotron Radiation Facility, Grenoble, France

ARTICLE INFO

Article history:
Received 13 May 2016
Received in revised form 20 January 2017
Accepted 13 February 2017
Available online 16 February 2017

ABSTRACT

Knowledge of melting properties is critical to predict the nature and the fate of melts produced in the deep mantle. Early in the Earth's history, melting properties controlled the magma ocean crystallization, which potentially induced chemical segregation in distinct reservoirs. Today, partial melting most probably occurs in the lowermost mantle as well as at mid upper-mantle depths, which control important aspects of mantle dynamics, including some types of volcanism. Unfortunately, despite major experimental and theoretical efforts, major controversies remain about several aspects of mantle melting. For example, the liquidus of the mantle was reported (for peridotitic or chondritic-type composition) with a temperature difference of ~1000 K at high mantle depths. Also, the Fe partitioning coefficient ($D_{Fe}^{Bg/melt}$) between bridgmanite (Bg, the major lower mantle mineral) and a melt was reported between ~0.1 and ~0.5, for a mantle depth of ~2000 km. Until now, these uncertainties had prevented the construction of a coherent picture of the melting behavior of the deep mantle.

In this article, we perform a critical review of previous works and develop a coherent, semi-quantitative, model. We first address the melting curve of Bg with the help of original experimental measurements, which yields a constraint on the volume change upon melting (ΔV_m). Secondly, we apply a basic thermodynamical approach to discuss the melting behavior of mineralogical assemblages made of fractions of Bg, $CaSiO_3$-perovskite and (Mg,Fe)O-ferropericlase. Our analysis yields quantitative constraints on the SiO_2-content in the pseudo-eutectic melt and the degree of partial melting (F) as a function of pressure, temperature and mantle composition; For examples, we find that F could be more than 40% at the solidus temperature, except if the presence of volatile elements induces incipient melting. We then discuss the melt buoyancy in a partial molten lower mantle as a function of pressure, F and $D_{Fe}^{Bg/melt}$. In the lower mantle, density inversions (i.e. sinking melts) appear to be restricted to low F values and highest mantle pressures.

The coherent melting model has direct geophysical implications: (i) in the early Earth, the magma ocean crystallization could not occur for a core temperature higher than ~5400 K at the core-mantle boundary (CMB). This temperature corresponds to the melting of pure Bg at 135 GPa. For a mantle composition more realistic than pure Bg, the right CMB temperature for magma ocean crystallization could have been as low as ~4400 K. (ii) There are converging arguments for the formation of a relatively homogeneous mantle after magma ocean crystallization. In particular, we predict the bulk crystallization of a relatively large mantle fraction, when the temperature becomes lower than the pseudo-eutectic temperature. Some chemical segregation could still be possible as a result of some Bg segregation in the lowermost mantle during the first stage of the magma ocean crystallization, and due to a much later descent of very low F, Fe-enriched, melts toward the CMB. (iii) The descent of such melts could still take place today. There formation should to be related to incipient mantle melting due to the presence of volatile elements. Even though, these melts can only be denser than the mantle (at high mantle depths) if the controversial value of $D_{Fe}^{Bg/melt}$ is indeed as low as suggested by some experimental studies. This type of melts could contribute to produce ultra-low seismic velocity anomalies in the lowermost mantle.

* Corresponding author.
E-mail address: denis.andrault@univ-bpclermont.fr (D. Andrault).

http://dx.doi.org/10.1016/j.pepi.2017.02.009
0031-9201/

Contents

1. Introduction

1.1. Melting in the early Earth's mantle

Within the first 100 million years of the Earth's history, the giant Moon forming impact (MFI) melted the Earth almost entirely (Nakajima and Stevenson, 2015). The release of energy induced by the gravitational segregation of the impactor's core could have potentially heated the Earth's core by 3500–4000 degrees above the temperature reached prior to the giant impact (Herzberg et al., 2010; Rubie et al., 2015). It could have led to a core-mantle boundary (CMB) temperature of the order of 6000 K (Davies et al., 2015; Labrosse, 2015; Nakagawa and Tackley, 2010), well above the mantle solidus of ~4150 K (Andrault et al., 2011; Fiquet et al., 2010). Therefore, the MFI could have caused intensive melting of the mantle at all depths. However, geochemical evidences point out to large scale isotopic heterogeneities that seem to have survived the episode of MFI. For example, the excess in ^{182}W (produced by the decay of ^{182}Hf) measured in 2.7 Ga-old komatiites requires a large-scale magmatic differentiation during the first 30 Ma of the Solar system's history (Touboul et al., 2012). The difference in Xenon isotopic composition between MORBs and the Icelandic plume (Mukhopadhyay, 2012), also indicates two sources with distinct isotopic composition. Finally, geodynamical arguments suggest the presence of an unmixed and primordial material in the deep mantle (Davaille, 1999; Kellogg et al., 1999). Therefore, it is unlikely that primordial mantle temperatures exceeded the liquidus throughout the mantle.

A low viscosity of the magma-ocean is expected to induce vigorous and turbulent convective flow, favoring a homogeneous mixing. Heat flux at the magma ocean surface could have been as high as $\sim 10^6$ W/m^2, which suggests a very fast crystallization, within $\sim 10^3$ years after the MFI (Solomatov, 2007). Longer time scales for cooling are also possible, due to the possible formation of an opaque atmosphere at the Earth's surface preventing heat loss, or other geodynamical complications, such as physical or chemical mantle layering, etc. (Lebrun et al., 2013; Sleep et al., 2014). On the other hand, petrological analyses of Archean and Proterozoic basalts preserved on the Earth's surface show primary magma compositions compatible with mantle potential temperatures of only 200–300 degrees higher than today (Herzberg et al., 2010). A similar temperature change is reported for Archean tonalite-tro ndhjemite-granodiorite associations of 4.0–2.5 Ga old (Martin and Moyen, 2002). Such a modest difference of mantle temperature compared to the present situation suggests a relatively rapid mantle cooling just after the MFI.

Finally, it has been suggested that a basal magma ocean (BMO) could have lasted in the lowermost mantle for very long times, billions of years, in correlation with an outer-core temperature significantly higher than the mantle solidus (e.g. Labrosse (2015)). This issue remains largely debated, however, because geodynamical models do not explain what could prevent such a hot core from rapid cooling (Monteux et al., 2016; Nakagawa and Tackley, 2010)).

1.2. Evidences for mantle melting today

In the upper mantle, seismic and magneto-telluric profiles present prominent anomalies, in particular at depths between 80 and 200 km (e.g. Romanowicz (1995)). Low velocity anomalies have also been reported atop the 410-km mantle discontinuity (Song et al., 2004; Tauzin et al., 2010). Low degree partial melting has often been advocated to explain these anomalies (Revenaugh and Sipkin, 1994), as thermochemical effects alone cannot explain the magnitude of geophysical anomalies. Possible mechanisms for mantle melting, however, are many. As for the temperature profile, anchor points of the geotherm are provided by phase transformations in major mantle minerals, typically olivine, the constituent responsible for the seismic discontinuities between 410 and 660 km depths. It yields a potential temperature (Tp) of ~1600 K, which corresponds to the extrapolation to the Earth's surface of the adiabatic temperature profile passing through these anchor points (Katsura et al., 2010). Such a mantle geotherm plots at

significantly lower temperatures compared to the melting curve of the peridotitic mantle determined experimentally (Zhang and Herzberg, 1994). Noticeable exceptions exist, for example at mantle ridges, where the adiabatic decompression leads to mantle melting in the asthenosphere. Mantle melting at higher depths implies either higher temperatures (such as for Oceanic Island Basalts (OIB)) or the presence of volatiles that depress the solidus (e.g. Hirschmann et al. (1999)).

Temperatures in the lowermost mantle depart from the upper mantle geotherm as they are influenced by the hot core. A large decrease (>10%) of shear wave velocities is reported in the D''-layer sitting just above the CMB. Even if alternative interpretations are possible, such as a solid-state origin (e.g. Fe-enriched (Mg,Fe)O (Wicks et al., 2010)), it strongly suggests occurrence of partial melting (e.g. Herzberg et al. (2013), Rost et al. (2005))). Furthermore, the non-ubiquitous character of the seismic features in the D″-layer implies a CMB temperature lower than the mantle solidus. Otherwise, there would be a continuous melting line above the CMB. At the CMB pressure of 135 GPa, the solidus temperature of chondritic and peridotitic mantle was reported to be ~4150 K (Andrault et al., 2011; Fiquet et al., 2010). There, where seismic anomalies appear, mantle partial melting could occur for different reasons: (i) presence of volatile elements, such as in the study of (Nomura et al., 2014) where their pyrolitic composition included ~400 ppm H_2O, which lowered the solidus temperature to ~3570 K. However, we note that a high water content is unlikely in the lower mantle, due to the limited capability of lower mantle minerals to store water below the 660 km discontinuity (Bolfan-Casanova et al., 2003; Panero et al., 2015); (ii) presence of an excess of silica; The solidus temperature at the CMB of a mid-ocean ridge basalt, was reported to be 3800 (±150) K, thus significantly lower than for the melting of the average mantle (Andrault et al., 2014). Presence of basalt in the lowermost mantle is supported by seismic tomography imaging deep descent of slabs toward the CMB (e.g. (van der Hilst and Karason, 1999)); (iii) a very large amount of FeO could also lower the melting point of the mantle (Mao et al., 2005). Altogether, the non-ubiquitous seismic features in the D″-layer could very well be correlated to the presence of volatiles, basalt and/or high FeO concentration, together with a CMB temperature of 4100 (±200) K (e.g. Andrault et al. (2016)).,l

2. Melting of pure bridgmanite

2.1. Important bridgmanite properties

MgO becomes extremely refractory with increasing pressure, with a melting point estimated at ~8000 K for a pressure of 135 GPa (Du and Lee, 2014). This contributes in making ferropericlase (Fp) the liquidus phase above 25 GPa, but only up to ~33 GPa, where Bg becomes the liquidus phase for mantle compositions (Ito et al., 2004). The melting curve of Bg dominates the topology of melting diagrams at high mantle depths. The role of Bg is further emphasized by a possible increase of Bg-content with increasing mantle depth, as the comparison between geophysical observations and experiments (e.g. Murakami et al. (2012), Samuel et al. (2005)) suggest a mantle (Mg+Fe)/Si ratio closer to unity.

Mantle Bg can adopt chemical compositions ranging from (Mg, Fe)SiO_3, produced after decomposition of olivine, to Al-bearing (Mg,Fe)SiO_3, after the high pressure transformation of majoritic garnet below the 660 km discontinuity. A higher compositional variability could also come from the intrinsic high compliance of the Bg crystal structure, which composition can be decomposed in a number of (theoretical) end-members ($MgSiO_3$, $FeSiO_3$, $FeAlO_3$, Al_2O_3, $MgAlO_{2.5}$). It can adopt variable Mg/Si, $Fe^{3+}/\Sigma Fe$, Al/Fe ratios and Fe-content as a function of pressure, temperature, oxygen fugacity, and exchange with ferropericlase. (e.g. Boujibar et al. (2016), Lauterbach et al. (2000)). The Bg crystal chemistry can thus vary with mantle depth (Andrault et al., 2007) and also laterally if the mantle presents significant heterogeneities. We also remind that the transition pressure from majoritic garnet to Bg increases significantly with the Al-content: compared to pure $MgSiO_3$, an additional 3–4 GPa is required to produce Bg with ~10 wt% Al_2O_3 (Akaogi and Ito, 1999; Irifune et al., 1996).

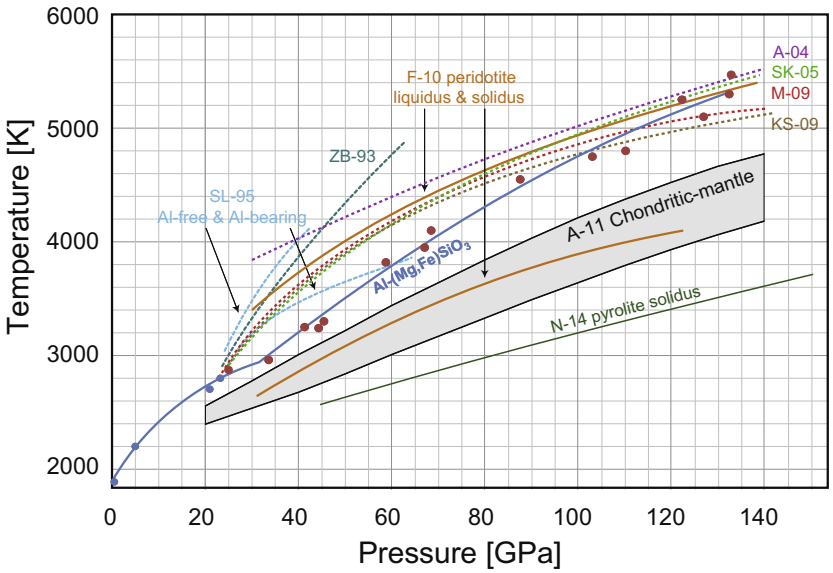

Fig. 1. Melting curve of Bg inferred from different experimental and theoretical studies determined using LH-DAC for ($Mg_{0.88}Fe_{0.12}SiO_3$) (Zerr and Boehler, 1993), $MgSiO_3$ and $Mg_3Al_2Si_3O_{12}$ (Shen and Lazor, 1995), shock measurements for $MgSiO_3$ (Akins et al., 2004; Mosenfelder et al., 2009) and *ab initio* calculations for $MgSiO_3$ (e.g. de Koker and Stixrude (2009), Stixrude and Karki (2005)). We also include experimental reports of solidus and liquidus of peridotite (Fiquet et al., 2010), chondritic-type mantle (Andrault et al., 2011) and pyrolite with ~400 ppm H_2O (Nomura et al., 2014). Our new LH-DAC measurements performed from ~24 to ~135 GPa on a (Fe,Al)-rich Bg (red dots and blue guide for the eyes) plot in continuity with previous determinations of mantle melting performed at lower pressures using the large volume press (Blue dots, (Katsura and Ito, 1990; Presnall and Gasparik, 1990)).

2.2. Previous studies of bridgmanite melting

In early experiments using laser-heating in the diamond anvil cell (LH-DAC), visual observations of the sample behavior were used as a major criterion to address the melting of Bg (Fig. 1). Two studies performed on $MgSiO_3$ and $(Mg,Fe)SiO_3$ compositions agree for a steep melting curve above the transition zone pressure, at ~24 GPa (Shen and Lazor, 1995; Zerr and Boehler, 1993). Comparison between the melting curves of $MgSiO_3$ and $Mg_3Al_2Si_3O_{12}$ evidences a significant melting temperature depletion, by ~300 K at 40 GPa, due to the presence of Al (Shen and Lazor, 1995). Early works were limited to 60–70 GPa, compared to the 135 GPa prevailing at the CMB. Concerning melting of $MgSiO_3$ in the upper mantle, we note an important curvature of the melting line typical of the lower-density polymorphs (Katsura and Ito, 1990; Presnall and Gasparik, 1990). It can be related to a rapid decrease of the volume of melting (ΔV_m) with increasing pressure and, thus, a relatively high melt compressibility.

Several theoretical works address the equation of state and the melting curve of Bg up to more than 135 GPa, using *ab initio* calculations (Fig. 1). The $MgSiO_3$ end-member is generally studied, because such calculations encounter difficulties in addressing the role of transition elements and point defects (such as Al^{3+}, Fe^{3+}, etc.). In all calculations, the initial slope of the melting curve (above ~24 GPa) is relatively steep. This points out to a relatively large volume of $MgSiO_3$-Bg melting, which is dominated by the ~10% volume change at the transition from majoritic garnet to Bg at 660 km-depth (Yu et al., 2011).

Based on the propagation of shock waves, $MgSiO_3$ melting was identified at 5000–5500 K for a pressure above 100 GPa (Akins et al., 2004; Mosenfelder et al., 2009). It was suggested that the volume of Bg melting becomes very small at pressures typical of the lowermost mantle (Mosenfelder et al., 2009; Petitgirard et al., 2015). From 1 bar to ~24 GPa, there is also a clear decrease of the melting slope of $MgSiO_3$ with increasing pressure (Katsura and Ito, 1990; Presnall and Gasparik, 1990). It can be related to a rapid decrease of the volume of melting (ΔV_m) with increasing pressure associated to a relatively high melt compressibility.

2.3. Updated melting curve of bridgmanite

In this article, we report original measurements of the melting curve of a (Fe,Al)-bearing Bg phase with Fe/(Mg + Fe) = 0.12 and Al/Fe = 0.9. We acknowledge that this composition corresponds to relatively high Al and Fe contents compared to the expected composition for natural Bg. Experiments were performed using LH-DAC coupled with *in situ* X-ray diffraction on the ID-27 beamline (ESRF, France). All experimental methods are detailed in Supplementary Materials. At relatively low pressures, the melting curve of this Bg appears significantly more flat than those reported for pure $MgSiO_3$ (Fig. 1). This observation tends to confirm a significant effect of Al on the melting slope, as reported previously between Al-free and Al-bearing starting materials (Shen and Lazor, 1995). We also find that the discontinuous increase of the melting curve slope, related to the majorite to Bg phase transition, is not observed at ~24 GPa, but instead at ~30–35 GPa for this (Fe,Al)-bearing composition. This behavior can be logically related to extension to higher pressures of the garnet stability field in the presence of Al, as described in previous works for Fe-free starting materials (Akaogi and Ito, 1999; Irifune et al., 1996). The relatively lower melting temperature of (Fe,Al)-bearing Bg in the 25–35 GPa pressure range, compared to pure-$MgSiO_3$ and, most importantly, to other lower mantle minerals such as MgO, explains why Bg is not the liquidus phase in this pressure range for typical mantle compositions (Ito et al., 2004).

At higher pressures, the slope of the (Fe,Al)-bearing Bg melting curve remains fairly constant up to the CMB pressure of 135 GPa, which contrasts with the flattening reported for $MgSiO_3$. This makes the different available results to converge to a temperature of 5100–5500 K for the melting of Bg at the CMB. We remind that the melting curve of $MgSiO_3$-Bg should always plot at higher temperature than that of the (Fe,Al)-bearing composition, due to the incompatible character of Fe and Al. Thus, our experimental determination of the (Fe,Al)-bearing Bg melting curve implies that the melting temperature of $MgSiO_3$-Bg at very high mantle pressures was underestimated by a couple hundred degrees in some previous studies (de Koker and Stixrude, 2009; Mosenfelder et al., 2009). Thus, for further discussions, we will choose as a reference the higher melting curve of $MgSiO_3$ Bg as determined from *ab initio* calculations (Stixrude and Karki, 2005). It can be modeled using a modified Simon and Glatzel equation $[T = T_0\ (P/a\ +\ 1)^{1/c}]$ with parameters $T_0 = 91$ K, $a = 0.00125$ GPa and $c = 2.83$ (Simon and Glatzel, 1929).

We note that the liquidus temperature profile reported previously for peridotite (Fiquet et al., 2010) appears superimposed with the melting curve of $MgSiO_3$-Bg derived from *ab initio* calculations and shock experiments (Fig. 1). This is unexpected because (i) the more complex chemical composition of the peridotitic Bg phase, compared to $MgSiO_3$, and (ii) additional Fp and $CaSiO_3$-perovskite (CaPv) phases should both lower the peridotite liquidus below the melting temperature of pure $MgSiO_3$. In their study, (Fiquet et al., 2010) observed large crystals of Bg at the center of the heated spot, where the melting behavior was monitored using *in situ* X-ray diffraction. Chemical composition of Bg grains measured at different locations on a sample synthesized at ~61 GPa show Fe/(Mg + Fe) and Al/Si ratios of ~2.5% and ~8%, respectively. It is possible that their reported measurements of the peridotite liquidus correspond in fact to the melting curve of these large Bg grains.

2.4. Volume of bridgmanite melting

The dT/dP slope of the Bg melting curve is directly related to the volume (ΔV_m) and entropy (ΔS_m) of Bg melting through the classical Clapeyron relation $dT/dP = \Delta V_m/\Delta S_m$. ΔS_m was reported to be 42.2 J/mol K for $MgSiO_3$ at room pressure, based on calorimetric measurements (Stebbins et al., 1984). For melting of $MgSiO_3$ in the stability field of Bg, *ab initio* simulations suggest a ΔS_m value 1.5 times higher (Stixrude et al., 2009). Assuming then a constant ΔS_m value of 63.3 J/mol K for melting of (Fe,Al)-bearing Bg at all lower mantle conditions, we now calculate ΔV_m values from the Clapeyron slopes of the different melting curves available for Bg (Fig. 2a). For the (Fe,Al)-bearing composition, we observe a progressive decrease of $\Delta V_m/V_{Bg}$ (V_{Bg} being the Bg volume) from ~9% to ~5%, when pressure increases from 30 to 140 GPa, respectively. For comparison, earlier studies of the melting behavior of pure $MgSiO_3$ suggest a significantly larger effect of pressure, with $\Delta V_m/V_{Bg}$ varying from 13% at low pressures for some *ab initio* calculations (Stixrude et al., 2009) or even 19% for a shock-wave study (Mosenfelder et al., 2009), to 3–4% at pressures of 135 GPa. The flatter ΔV_m found for the (Fe,Al)-bearing implied by our results is due to a more linear melting curve measured from 30 to 35 GPa to 135 GPa, compared to pure $MgSiO_3$ (Fig. 1). We also show recent measurements of the $MgSiO_3$-glass density performed in the DAC at 300 K up to the CMB pressure (Petitgirard et al., 2015). The $\Delta V_m/V_{Bg}$ recalculated from the later study is significantly lower than all other calculations at high pressures, which should translate into a very flat melting curve. Based on the shadowed region in Fig. 2a, we define a most probable range of $\Delta V_m/V_{Bg}$ values decreasing from 11(±2)% to 4(±1)% when pressure is increased from 24 to 140 GPa, respectively.

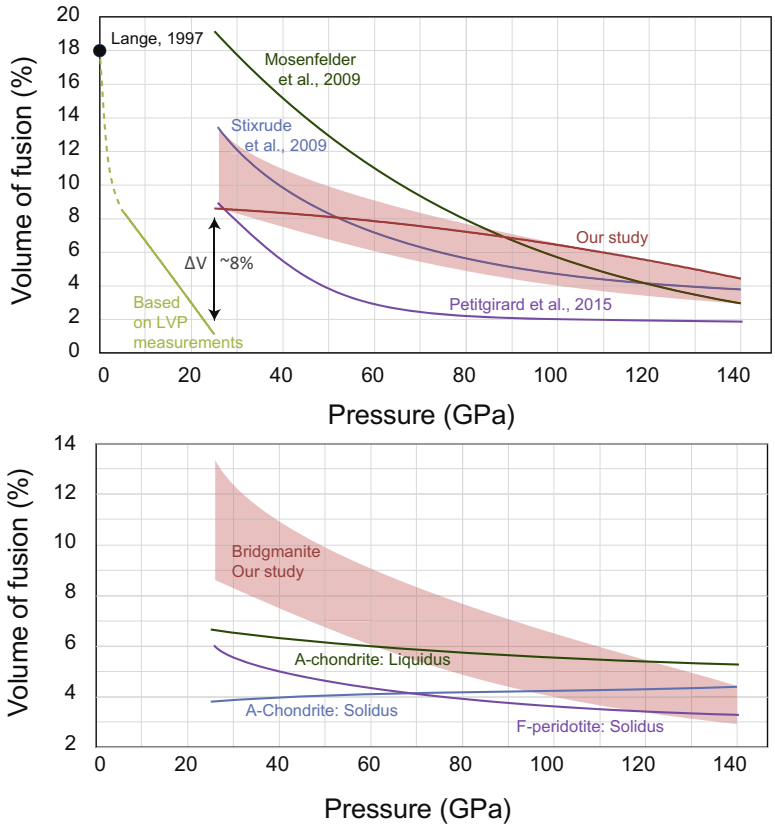

Fig. 2. (a) Normalized volume of melting ($\Delta V_m/V_{Bg}$, where $\Delta V_m = V_{melt} - V_{Solid}$ and V_{Bg} is volume of Bridgmanite) derived from the melting curve of Bg (Fig. 1) with various (Mg,Fe)(Si,Al)O_3 compositions We also report the value of 18% measured for pure $MgSiO_3$ at 1 bar (Lange, 1997) and $\Delta V_m/V_{Bg}$ recalculated from density measurements of $MgSiO_3$-glass in a DAC (Petitgirard et al., 2015). Shadowed pink region is the most probable range of mantle $\Delta V_m/V_{Bg}$ values. (b) ΔV_m derived from the solidus and/or liquidus profiles of the A-chondritic (Andrault et al., 2011) and F-peridotitic (Fiquet et al., 2010) models of mantle melting. Calculation of $\Delta V_m/V_{Bg}$ along solidus and liquidus profiles using the Clapeyron relation assume an ideal mixing model to estimate the melt entropy (see paragraph 4.2).

We also calculated ΔV_m at pressures below 24 GPa using $\Delta S_m = 42.2$ J/mol K (Stebbins et al., 1984) and using the Clapeyron of melting curves measured in large volume press (LVP) experiments. We note that the final interpretation of ΔV_m can be complicated by the occurrence of four different $MgSiO_3$ polymorphs between 1 bar and 24 GPa (Presnall, 1995). In particular, the Clapeyron slope of majorite melting remains largely uncertain, due to a limited pressure range available. For this reason, we modeled the $MgSiO_3$ melting line using a 2nd degree polynomial regression across the whole pressure range from 0 to 24 GPa. The calculated $\Delta V_m/V_{Bg}$ decreases strongly with increasing pressure converging to 1% at ~24 GPa (Fig. 2a). It makes a volume change of ~8% at the majorite to Bg transition for the (Fe,Al)-bearing composition of our study, or ~10% in average for the most probable range of $\Delta V_m/V_{Bg}$ that we have defined above, both values agreeing well with the ~10% suggested previously for $MgSiO_3$ (Yu et al., 2011).

3. Melting diagrams for typical lower mantle materials

3.1. Experimental determination of the melting behavior

Studying experimentally phase relations in a partially molten geological material under P-T conditions of the Earth's interior remains a challenging task. The use of LVP facilitates largely the chemical analysis of coexisting phases in recovered samples, compared to LH-DAC. For example, melting behavior of fertile peridotite and CI chondritic mantle were documented up to ~35 GPa (Ito et al., 2004). It was demonstrated that the liquidus phase changes from Fp to Bg at about 33 GPa, a situation that was confirmed later by LH-DAC experiments (Andrault et al., 2011; Fiquet et al., 2010). However, LVP samples (and *a fortiori* LH-DAC samples) synthesized at lower mantle conditions always encounter relatively large temperature gradients, which yields heterogeneous microstructure and chemical zoning. In such cases, the sequence of phase disappearance from solidus to liquidus temperatures is usually retrieved from the position of phases relative to the temperature gradient. Still, this procedure prevents the precise determination of the equilibrium solid-liquid partition coefficients.

When coupled with *in situ* X-ray diffraction, LH-DAC is well suited to determine melting curves of various geological materials, because the available temperature range extends up to more than 6000 K (Suppl. Fig. 1). Melting criteria are generally based on the disappearance of diffraction peaks and phase(s), which corresponds in fact to the determination of a pseudo-eutectic temperature (PET). Recently, pseudo-eutectic melting of peridotite (Fiquet et al., 2010), chondritic-mantle (Andrault et al., 2011) and pyrolite (Nomura et al., 2014) was reported at substantially different temperatures. Disagreements cannot be reconciled based on the moderate compositional variations between starting materials, among which the major difference lies in the Bg/(Bg + CaPv + Fp) ratio from 0.59, 0.63 and 0.75 for peridotite, pyrolite and chondritic mantle, respectively. Studies using peridotitic (F-peridotitic model) and chondritic (A-chondritic model) starting materials show similar solidus evolution as a function of pressure, pointing out to a PET of 4150 ± 150 K at the CMB. The lower value reported in the study using pyrolite could be due to a more precise determination of the solidus, thanks to the use of 3D X-ray tomography, but more likely

because of the presence in their sample of 400 ppm H_2O that triggers melting (Nomura et al., 2014).

3.2. Pseudo-eutectic type melting in the deep mantle?

The melting diagram between the three lower mantle phases (Bg, CaPv and Fp) presents an eutectic behavior (e.g. de Koker et al. (2013), Liebske et al. (2005), Liebske and Frost (2012)), which implies (i) a PET and (ii) a melt composition at the PET located within the ternary diagram. The PET and the melt composition should be independent of the Bg, CaPv and Fp molar fractions in the bulk material, as long as the chemical compositions of these three phases do not vary significantly. A major issue for geological materials is that the onset of melting (the solidus) can possibly occur at a temperature lower than the PET. In such a case, a melt appears without disappearance of a phase from the mineral assemblage. This can happen when the solubility limit of an incompatible element is overpassed at a given condition of pressure and temperature. This behavior has not been reported yet for any mantle compositions under the P-T conditions typical of the lower mantle. In contrast, available LH-DAC experiments report disappearance of one phase at the onset of melting. Also, chemical analyses of melts obtained after partial melting of peridotite at ~24 GPa show compositions close to the starting material (e.g. with a relatively lower MgO/SiO_2 ratio (Tronnes and Frost, 2002)), which is incompatible with incipient mantle melting.

Above the solidus temperature, partition coefficients between Bg or CaPv and the melt ($D_i^{Solid/melt}$) were investigated experimentally for many elements. Except for a very few of them (such as Li and Ba), $D_i^{Solid/melt}$ values are found to lie above 3×10^{-1}, which corresponds to a moderately incompatible behavior (Corgne et al., 2005). These results suggests that the minor elements may not reach their solubility limit and, therefore, melting would not occur below the PET.

Of course, volatiles such as H_2O (but also CO_2) are well known to depress the solidus and potentially favor incipient mantle melting. We note, however, that (i) carbonate phases may be relatively refractory in the lower mantle (Thomson et al., 2014) and (ii) a high water content in the lower mantle is unlikely, due to limited capability of the lower mantle minerals to store water below the 660 km discontinuity (Bolfan-Casanova et al., 2003). Thus, even if water has an effect on the solidus, water may not be actually present. In summary, experimental evidences strongly suggest a moderate temperature difference between solidus and PET, if any.

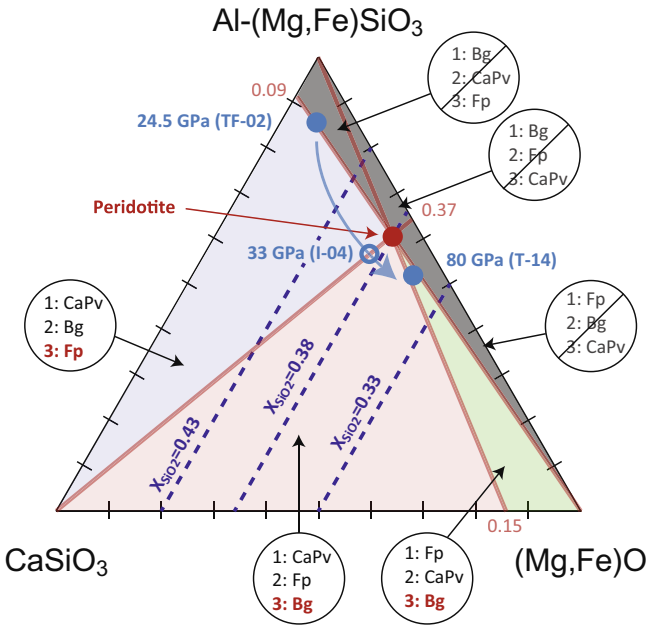

Fig. 3. Ternary diagram between Bg, Fp and CaPv, the three major phases in the lower mantle. Due to its eutectic shape, melt compositions should always plot within this diagram. The Red dot and lines correspond to the peridotitic composition and its associated Fp/Bg, CaPv/Bg and CaPv/Fp ratios. Blue dots are melt compositions determined experimentally (Ito et al., 2004; Tateno et al., 2014; Tronnes and Frost, 2002). The blue arrow shows the change in melt composition with pressure. In each colored region of the ternary diagram, the expected sequence of phase disappearance upon melting are reported inside circles: 1, 2 and 3 are solidus, intermediate and liquidus phases, respectively.

3.3. Sequence of phase disappearance upon melting

In the ternary diagram between Bg, CaPv and Fp, the difference in composition between the bulk mantle composition and the melt defines the sequence of phase disappearance upon melting. For example, melting of peridotite would likely induce a melting sequence from CaPv (at solidus), Bg to Fp (at liquidus), if the PE-melt would present significantly higher $CaSiO_3$-content and lower (Mg,Fe)O-content, compared to peridotite. Thus, the ternary diagram can be divided into six different regions where the melting sequence should be different, depending on the PE-melt composition (Fig. 3).

Composition of melts relevant to deep mantle partial melting were reported after experiments performed at 24.5 GPa using LVP (Tronnes and Frost, 2002) and 80 GPa using LH-DAC (Tateno et al., 2014). Despite the fact that these melts may differ from PE-melts, if experimental temperatures have been higher than PET, they provide precious anchors for melt compositions in the ternary diagram. Composition of these two melts (corresponding to 24.5 and 80 GPa) plot on each side of the Fp/Bg ratio of 0.37, which corresponds to the peridotite composition. This observation is compatible with a third experimental anchor point where the liquidus phase has changed from Fp to Bg at about ~33 GPa for a fertile peridotite (Ito et al., 2004). Thus, the melt composition evolves toward higher (Mg,Fe)O-contents with increasing pressure.

Another important observation is the melt composition at 80 GPa, which presents a CaPv/Fp ratio very close to the peridotitic value of 0.15. It suggests that both phases, CaPv and Fp, disappear almost simultaneously at the PET upon partial melting of peridotite in the deep lower mantle. In this work, we make the assumption that CaPv and Fp disappear simultaneously at the PET at lower mantle pressures. This assumption is not severe. If Fp would disappear first, negligible amount of CaPv would remain. Indeed, the total amount of CaPv is below ~6 mol% for compositions relevant to the deep mantle. In the case CaPv would disappear first, higher Fp content could theoretically remain after melting at the PET. Indeed, Fp is found at a level of 19, 32 or 35 mol%, for chondritic, pyrolitic or peridotitic compositions, respectively. However, the molar volume of Fp is twice less than those of Bg and CaPv. Also, it is likely that the melt dissolves a significant part of Fp at the PET (Tateno et al., 2014; Tronnes and Frost, 2002), which should yield to a relatively low Fp-content in the residual solid.

3.4. Liquidus temperatures and Bg-content in melts

The melting behavior can be modeled at various mantle pressures (for example 40 GPa, 80 GPa and 135 GPa) using (pseudo) binary phase diagrams, where one end-member is Bg, the liquidus phase, and the other is the sum of all the other chemical components (Fig. 4). We prefer to use Fe-free Bg as an end-member, instead of (Fe,Al)-bearing Bg, due to the preferential partition of Fe to the melt (this matter is discussed later in the article). Still,

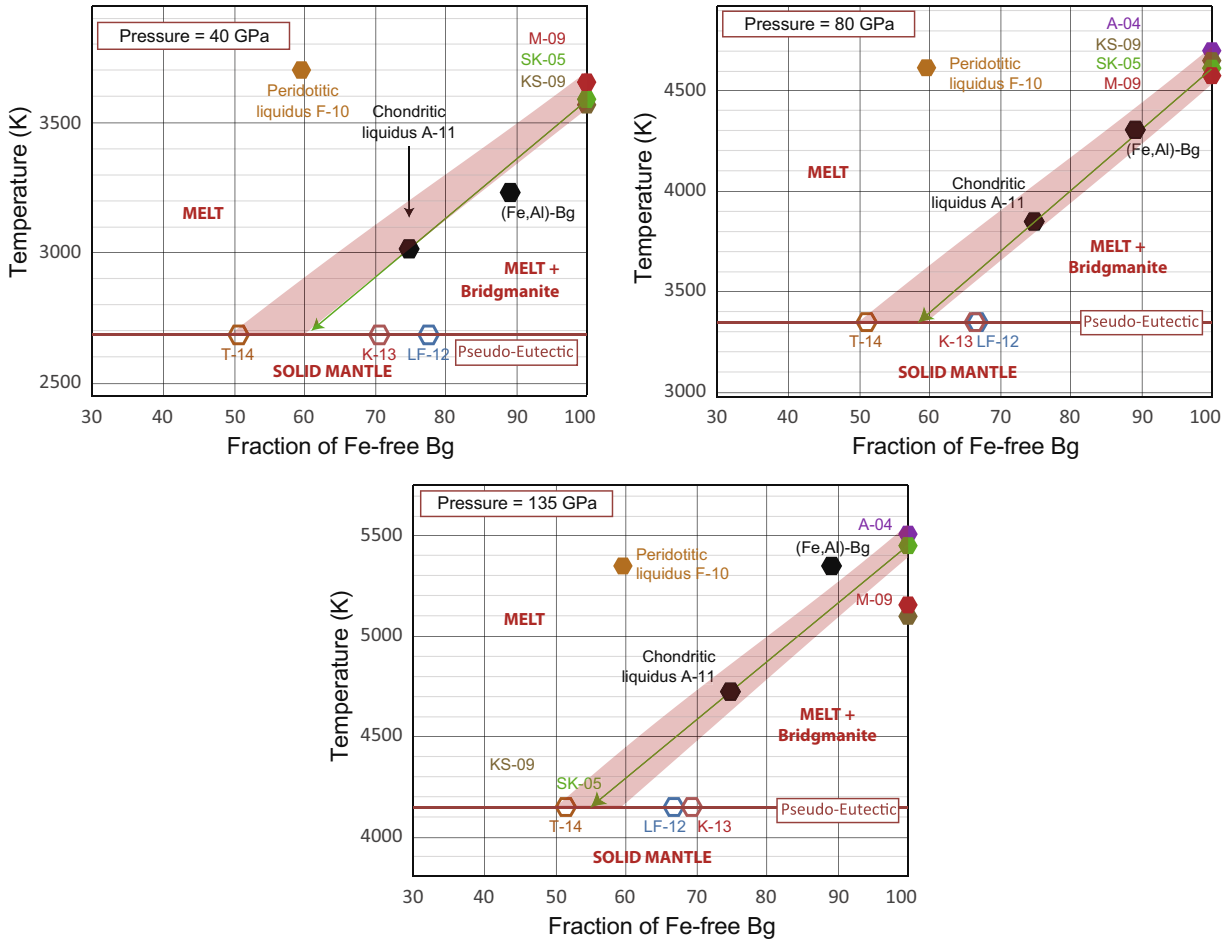

Fig. 4. Binary melting diagram at 40, 80 and 135 GPa between Fe-free Bg and the sum of all other chemical components. Anchor points for the binary melting diagram are the melting temperature of the mantle relevant Bg ((Stixrude and Karki, 2005), see Fig. 1) and the A-chondritic solidus and liquidus temperatures (Andrault et al., 2011). We also report previous estimates of $MgSiO_3$-content in PE-melt (de Koker et al., 2013; Liebske and Frost, 2012; Tateno et al., 2014).

we consider an Al-bearing Bg end-member, because the Al-behavior upon partial melting remains poorly constrained. Compositional axis of such binary diagram is thus the molar fraction of Fe-free Bg. Melts include Fp, CaPv, (virtual) $FeSiO_3$-Bg and a fraction of Fe-free Bg end-members. Peridotitic and chondritic mantle, as well as our (Fe,Al)-bearing Bg composition plot at 59, 75 and 88 mol% of Fe-free Bg, respectively. For the PET, the A-chondritic model indicate "solidus" temperatures of 2690, 3340 and 4130 K at pressures of 40, 80 and 135 GPa, respectively (Andrault et al., 2011). For the Fe-free Bg end-member, we use *ab initio* calculations for $MgSiO_3$-Bg (Stixrude and Karki, 2005), as discussed above. Two LH-DAC studies report liquidus temperatures of A-chondritic and F-peridotitic models (Andrault et al., 2011; Fiquet et al., 2010). Finally, the independent reports of the Bg-content in melts (i) measured after partial melting of pyrolite (Tateno et al., 2014) and (ii) calculated in the $MgSiO_3$-MgO system (de Koker et al., 2013; Liebske and Frost, 2012) are also shown. We note that the two later studies did not included the CaPv component, which could numerically yield an overestimation of the Bg-content in the melt.

At each selected mantle pressure, we draw lines from the melting temperature of the Bg end-member, through the liquidus temperature of the A-chondritic model, toward the PET (Fig. 4). These lines provide estimates of liquidus temperatures as a function of the bulk mantle composition. In addition, intersections between these lines and PET provide estimates of the Bg-content in PE-melts, as a function of pressure. Uncertainties arise from (i) controversial reports of the Bg melting temperature as a function of pressure (Fig. 1) and (ii) unknown curvature of the liquidus profile in these diagrams. Consequently, we colored in pink regions where the presence of liquidus is the most probable. We excluded from colored regions PE-melts with a fraction of Fe-free Bg higher than peridotite, because it would be contradictory with Bg becoming the liquidus phase above ~33 GPa (Ito et al., 2004). We note that our method is not appropriate to pressures lower than ~33 GPa, when Bg is not the liquidus phase.

Based on the width of the regions of confidence, liquidus temperatures appears to be constrained within ±150 K at all mantle pressure, temperature and compositions. An uncertainty to which we should add a similar value associated to the experimental error in the determination of PET and Bg melting temperature. On the other hand, uncertainty in Bg-content in PE-melt and along liquidus lines is about ±5%. The Bg-content in the PE-melt appears almost independent of lower mantle pressure at a value of 55 (±5) mol%. With increasing temperature above PET, the Bg-content in melt should logically increase until it reaches the bulk mantle composition. Altogether, these binary melting diagrams can be numerically constrained by three parameters: (i) a constant Bg-content of 55(±5) mol% in PE-melt, and two modified Simon and Glatzel (SG) equations $[T(P) = T_0\ (P/a+1)^{1/c}]$ with parameters (ii) T_0 = 2045 K, a = 92 GPa and c = 1.3 for the PET (Andrault et al., 2011) and (iii) T_0 = 91 K, a = 0.00125 GPa and c = 2.83 for the Bg end-member (Stixrude and Karki, 2005). Then, liquidus temperatures between PE-melt and Bg can be defined as a function of pressure and mantle composition using:

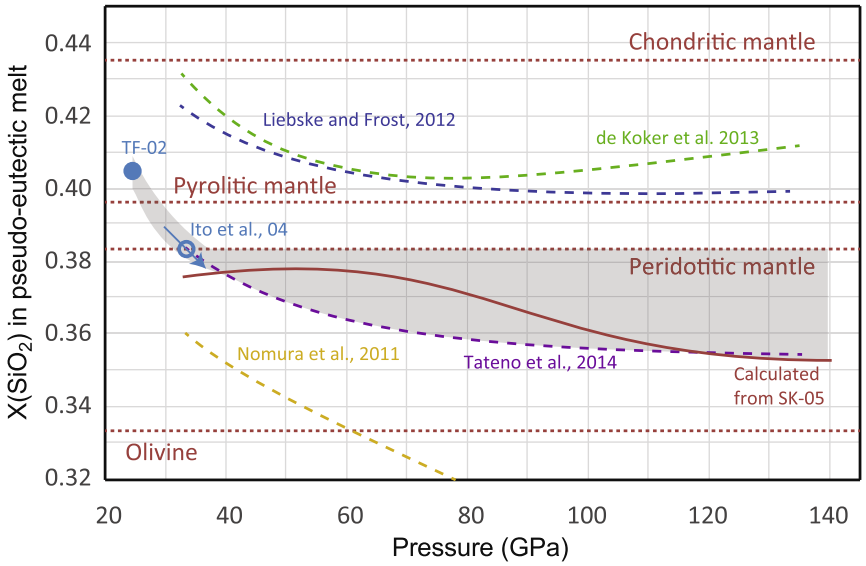

Fig. 5. Pressure change of the SiO_2-content in pseudo-eutectic melt. Horizontal dotted lines are $X(SiO_2)$ typical of olivine, peridotite, pyrolite and chondritic-mantle. The red line is derived from the Bg melting curve (Stixrude and Karki, 2005) associated with the thermodynamical treatment elaborated for the discussion of Fig. 4. Dashed lines represent previous calculations (de Koker et al., 2013; Liebske and Frost, 2012) or the experimental determination (Tateno et al., 2014) of $X(SiO_2)$ in melts. The shaded gray area corresponds to the most likely $X(SiO_2)$ of lower mantle melts.

$$T^{Liq}_{Mantle}(P,X^{Mantle}_{Bg}) = SG(Bg) - [(SG(Bg) - SG(PEM)) * (1 - X^{Mantle}_{Bg})/(1 - X^{PEM}_{Bg})]$$

where SG(PEM) and SG(Bg) are PE-melt and Bg melting temperatures, respectively, calculated at a target mantle pressure (P) using SG equations. X^{PEM}_{Bg} and X^{Mantle}_{Bg} are Bg mole fractions in the PE-melt (fixed at 55 mol%) and the bulk mantle, respectively.

For a peridotitic mantle composition, binary phase diagrams suggest a difference of less than 300 K between PET and liquidus at all lower mantle pressures. This is in very good agreement with the value of 250 K proposed based on a thermodynamic melting model (Liebske and Frost, 2012). The difference between the PET and the liquidus increases for larger fractions of Bg in the bulk material, and in a primitive chondritic mantle it can reach up to 500 degrees. This confirms the wide range of mantle depths where partial melting should have occurred in the framework of an early magma ocean (e.g. Kojitani and Akaogi (1997), Miller et al. (1991)).

3.5. SiO_2 content in pseudo-eutectic melts

Another parameter controlling the melt properties is its SiO_2-content ($X(SiO_2)$). It can be derived directly from Fig. 4, by converting the amount of Fe-free Bg in the melt into its SiO_2 contribution. Based on our primary assumption that Fp and CaPv dissolve concomitantly in the melt at the PET, the SiO_2-content of the CaPv component is also added to the melt composition. This calculation can be performed for all types of melt along liquidii, as long as pressure is above ~33 GPa. Still, we only discuss here the composition of PE-melts. We actually translate into $X(SiO_2)$ the regions of confidence defined above for Bg-contents in PE-melts (Fig. 5). Independent values of $X(SiO_2)$ in lower mantle melts were reported previously based on *ab initio* calculations (de Koker et al., 2013), thermodynamic modeling of LVP experiments (Liebske and Frost, 2012) and chemical analyses of LH-DAC samples (Nomura et al., 2011; Tateno et al., 2014). At about ~33 GPa, the change of liquidus phase from Fp to Bg reported upon peridotite melting suggests that $X(SiO_2)$ in the melt crosses the peridotitic value of 38.3% (Ito et al., 2004).

The melt $X(SiO_2)$ likely remains significantly lower than 0.40 at higher pressures in the lower mantle, because Bg was broadly reported to be at the liquidus for pyrolite (Nomura et al., 2014) and peridotite (Fiquet et al., 2010). The fact that two models (de Koker et al., 2013; Liebske and Frost, 2012) propose higher $X(SiO_2)$ could be related to calculations restricted to the $MgSiO_3$-MgO system. The difference between the simple MgO-SiO_2 system and the mantle-relevant compositions suggests that Ca and Fe should enter the melt preferentially as CaO and FeO, rather than $CaSiO_3$ and $FeSiO_3$, thus lowering $X(SiO_2)$. Such behavior translates into a significantly stronger incompatible character of Ca and Fe, compared to Mg and Si (Liebske et al., 2005), which is already well known for low-pressure melting. The range of possible melt $X(SiO_2)$ appears to extend between the peridotite and a previous work performed on LH-DAC samples (Tateno et al., 2014). It corresponds to an almost fixed $X(SiO_2)$ value of 37.0% (±1.5%). This most probable range of $X(SiO_2)$ plots in good continuity with data reported at lower pressure based on LVP experiments (Ito et al., 2004; Tronnes and Frost, 2002). In summary, deep PE-melts appear to adopt a composition only slightly enriched in Fp compared to peridotite, if any.

3.6. Degree of partial melting at pseudo-eutectic temperatures

We can now calculate the expected degree of partial melting (F) at the PET for peridotitic, pyrolitic and chondritic mantle compositions, based on our estimation of deep-mantle melt compositions (Figs. 4 and 5). F (in vol%) at PET can be estimated using the molar volumes for Bg, Fp and CaPv (The equations of state defining the effect of pressure and temperature on volumes are described below). Logically, the calculated F value at PET varies with the difference in composition between the PE-melt and the bulk material. The closest the mantle composition is from the melt, the highest F value is expected at the PET. Calculated ranges of possible F values at PET appear to be more than 83, 74 and 46 vol%, for peridotitic, pyrolitic and chondritic mantle compositions, respectively (Fig. 6).

We note that a similar conclusion was reached previously (e.g. Herzberg and Zhang (1998)) based on the residual harzburgite signature of most komatiites with Cretaceous and late-Archaean

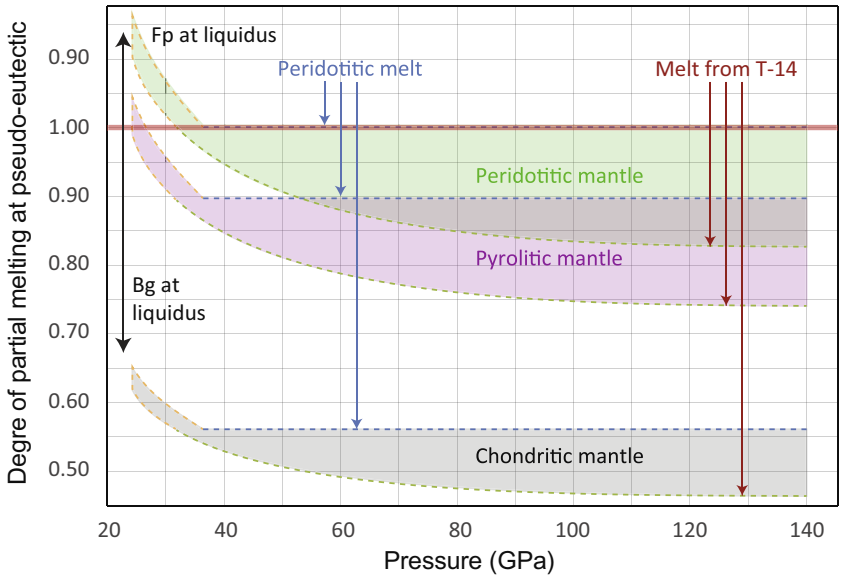

Fig. 6. Degrees of mantle partial melting (vol%) expected at pseudo-eutectic temperature (PET) in the lower mantle under the assumptions that CaPv and Fp phases disappear jointly upon melting. Degrees of partial melting are calculated for typical chondritic, pyrolitic and peridotitic mantle compositions, based on the possible range of PE-melt composition refined in Fig. 5. T-14 stands for Tateno et al. (2014).

ages, which can be interpreted to have formed by about 25–60% anhydrous melting of mantle peridotite in hot plumes.

The melting relations discussed above have implications for our understanding of the melting in the deep mantle today. For example, in the ultra-low velocity zones (ULVZ) just above the CMB, the high F values determined for PET in this study imply that the ULVZ cannot correspond to partial melting of the average mantle, because the degree of partial melting in the ULVZ as inferred by seismology is much lower than the minimum value of 46% calculated for a chondritic-type mantle. A lower F-value could be achieved (i) for a locally high concentration in volatile elements, which would favor incipient mantle melting below the PET or (ii) for another type of geological material, such as subducted basalts (Andrault et al., 2014).

4. Melt buoyancy in the deep mantle

4.1. Major parameters controlling the melt buoyancy

Dynamical behavior of a partially molten mantle is largely affected by the density contrast between the melt and the solid fractions ($\Delta\rho_{m\text{-}s} = (\rho_m - \rho_s)/\rho_s$). While melt buoyancy plays a major role in chemical segregation and planetary differentiation, the fact that its sign is positive or negative produces two different geodynamical situations. Melt buoyancy can also vary with mantle depth, due to (i) a possible change of the melt composition and (ii) different PVT equations of state for the melt and the mantle residue. In the present-day mantle, ascent, or descent, of some melts could contribute to surface volcanism, or accumulation of melts in the lowermost mantle, respectively. In a crystallizing magma ocean, it is classically accepted that crystals would settle, compact and reject the melt toward the Earth's surface (Boukare et al., 2015; Solomatov, 2007). However, this question became much debated after it was proposed that an early basal magma ocean could be produced by dense melts stored above the CMB (Labrosse et al., 2007; Nomura et al., 2011). Solid-liquid density inversions are not unusual. Many years ago, it was already proposed that basaltic and komatiitic magmas would become denser than olivine and garnet at depths of 245–500 km (Agee, 1998).

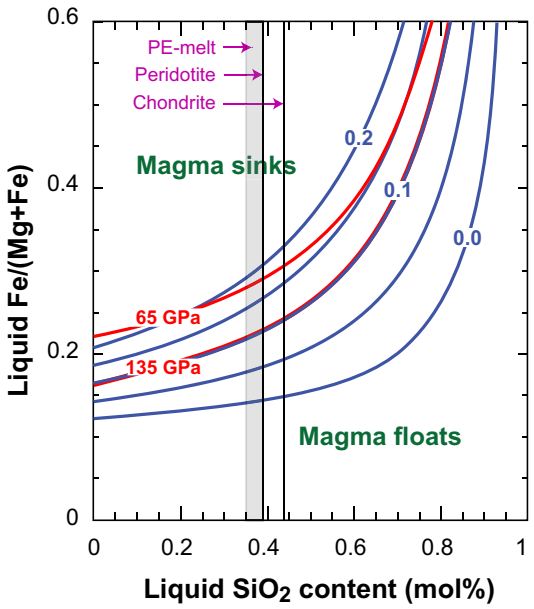

Fig. 7. Relative buoyancy between mantle melts of various compositions and (i) the (Mg,Fe)SiO_3 Bg with Fe-contents of 0, 10, or 20% (blue lines) and (ii) the lower mantle at pressures of 65 and 135 GPa (red lines). Along each blue or red lines, the melt and the given solid phase (Bg or lower mantle) have the same density. Higher SiO_2-content or lower Fe/(Mg + Fe) ratio, compared to a given line, yield melts buoyant compared to the solid phase considered. The gray region corresponds to the likely SiO_2-content in PET-melts in the mantle (see Fig. 5). SiO_2-content values for chondritic and peridotitic mantle are also reported. This Figure is modified from (Funamori and Sato, 2010).

Major parameters controlling the buoyancy of deep-mantle melts are (i) changes in atomic packing between solid and liquid phases, which most generally produces a positive volume of melting (ΔV_m), (ii) Fe partition coefficient between the solid residue and the melt ($D_{Fe}^{Bg/melt}$), because Fe is the heaviest major element, and (iii) MgO/SiO_2 ratio in the melt, because SiO_2-based atomic packing presents a relatively high bulk modulus. We chose to use $D_{Fe}^{Bg/melt}$ ($D = X_{Fe}^{Bg}/X_{Fe}^{melt}$, with X being the molar fraction), rather than

the distribution coefficient $K_{Fe}^{Bg/melt}$ ($K = (X_{Fe}/X_{Mg})^{Bg}/(X_{Fe}/X_{Mg})^{melt}$), because X_{Mg}^{melt} can vary with pressure, temperature and bulk composition independently from X_{Fe}^{melt}. Nothing prevents X_{Mg}^{melt} and X_{Fe}^{melt} to vary in a correlated way, which would contradict the proper definition of K.

Concerning the volume difference between solids and melts, both phases undergo (i) volume changes upon P and T according to their respective equation of state and (ii) a number of structural transformations with increasing mantle depth. In the solid state, equation of states of major mantle minerals are relatively well constrained (e.g. (Matas et al., 2007)). Structural transformations in the melt are much more progressive than in the solid, but can still contribute to a net increase of the melt density with increasing mantle depths. Due to the disordered and time-dependent nature of the melt structure, each structural entity has a finite lifetime. And when pressure is applied, structural entities can progressively evolve. In polymerized liquids, polyhedral chains can bend, eventually break and recompose differently (Stolper and Ahrens, 1987; Wang et al., 2014). All major cations progressively change their coordination shell (Bajgain et al., 2015) to allow compaction of the oxygen sub-lattice (Zeidler et al., 2014). The major change is probably Si, which progressively changes coordination number from fourfold to sixfold between ~20 and ~40 GPa (Benmore et al., 2010; Guillot and Sator, 2007; Sanloup et al., 2013; Sato and Funamori, 2010). These progressive transformations yield a room pressure bulk modulus significantly lower for the melt than for the crystalline counterpart. However, the pressure derivative of the bulk modulus is generally much higher, due to the progressive loss of some compaction mechanisms, after major voids have disappeared from the melt structure at moderate pressures.

At shallow mantle depths, while the melt structure has already undergone significant compaction, major mantle minerals, in particular olivine, have not yet transformed to a denser polymorph. For this reason, there could be a neutral melt buoyancy, or even a positive $\Delta\rho_{m-s}$ (i.e. a sinking melt), at mantle depths just above the 410 km discontinuity (Matsukage et al., 2005; Sakamaki et al., 2006). It could produce a kind of density trap, where melts produced above and below would accumulate and remain gravitationally stable in this mantle region (e.g. Lee et al. (2010)). At lower mantle pressures, a previous study tentatively addresses $\Delta\rho_{m-s}$ for a number of melt and solid compositions (Fig. 7; (Funamori and Sato, 2010), see also (Thomas et al., 2012)). Reporting in this diagram our estimates of $X(SiO_2)$ in PE-melt retrieved from Fig. 5 narrows down the range of possible silica contents between ~35.2 and ~38.3 mol%. We note that the SiO_2-content in the melt should increase with increasing temperature above the PET, because the PE-melt is relatively depleted in SiO_2 compared to the mantle composition. Ultimately, the melt and the bulk mantle become similar at the liquidus temperature, when the solid residue disappears completely. Altogether, the rather limited range of possible SiO_2-content in mantle melts points out to the fact that the less constrained parameters needed to address melt buoyancy at mantle depths are ΔV_m, the volume of melting, and $D_{Fe}^{Bg/melt}$, the Fe solid-liquid partitioning.

4.2. Volume of mantle melting

While the ΔV_m corresponding to the melting of a pure phase, such as Bg, can be estimated based on its melting curve (Fig. 2a), the volume of melting becomes more difficult to address in the case of the partial melting of the mantle between its solidus and liquidus. In addition, the equation of state of the melt changes significantly with its composition (de Koker et al., 2013; Thomas and Asimow, 2013). For example, Mg_2SiO_4-liquid becomes denser than lower mantle phases at pressures above ~40 GPa, while $MgSiO_3$-liquid remains buoyant at all mantle pressures (Thomas and Asimow, 2013). Thus, assuming a simplified melt composition, such as $MgSiO_3$, may not be much relevant for discussing the buoyancy of natural melts in the deep mantle. A more realistic exercise is to estimate the real density difference between the solid residue and a melt of relevant composition in the Bg-CaPv-Fp system. The solid residue can be a simple phase (Bg, or Fp below ~33 GPa), or a typical mantle composition (e.g. pyrolite), which would be relevant to model melt buoyancy in the context of an early crystallizing magma ocean (high F), or partial melting in the present-day lower mantle (low F), respectively. The melt composition at various P and T can be derived from the melting diagrams (Fig. 4).

In Fig. 2b, we intend to use the slopes of solidus and liquidus reported for mantle melting from LH-DAC experiments (Andrault et al., 2011; Fiquet et al., 2010) to retrieve thermodynamical information relevant to melts. We compare the solidus, or liquidus, profile to a Clapeyron slope which would record melting of the first fraction of solid mantle, or the last fraction of Bg, respectively. At the solidus temperature, the entropy of melting (ΔS_m) can be estimated from the sum of melting entropies of each phase present in the melt, plus a mixing entropy. We used ΔS_m^i values of 63.3, 63.3 and 13.0 J/mol K for the melting entropy of Bg (Stixrude et al., 2009), CaPv (similar to Bg) and Fp, respectively. We note that the room pressure value of ΔS_m^{MgO} was reported to be significantly larger than that of Fp, at ~35 J/mol K, however, it decreases rapidly with increasing pressure to 25 GPa (Vocadlo and Price, 1996). Composition of the PE-melt is considered to be 60% Bg, 30% Fp and 10% CaPv, in agreement with Figs. 3 and 4. However, changing the phase contents does not affect greatly the calculated ΔS_m value of ~55 J/mol K. At the liquidus temperature, we assume that the ΔS_m of the bulk rock is similar to that of Bg, neglecting the fact that the melt in which last grains of Bg get dissolved has a composition slightly different from Bg. Based on these assumptions, we calculate volumes of melting at solidus and liquidus, using the Clapeyron equation (Fig. 2b).

For the A-chondritic model, the values of $\Delta V_m/V_{Bg}$ at the solidus and at the liquidus appear almost independent of mantle pressure, at values of 4(±1)% and 6(±1)%, respectively. The $\Delta V_m/V_{Bg}$ at the solidus of the F-peridotitic model plots at similar values, however, due to a larger curvature in the melting curve, its associated $\Delta V_m/V_{Bg}$ varies more with pressure. We note that if we would have included a supplementary non-ideal mixing contribution to ΔS_m (de Koker et al., 2013), the $\Delta V_m/V_{Bg}$ values would have been ~0.5% higher. Altogether, the different trends available suggest

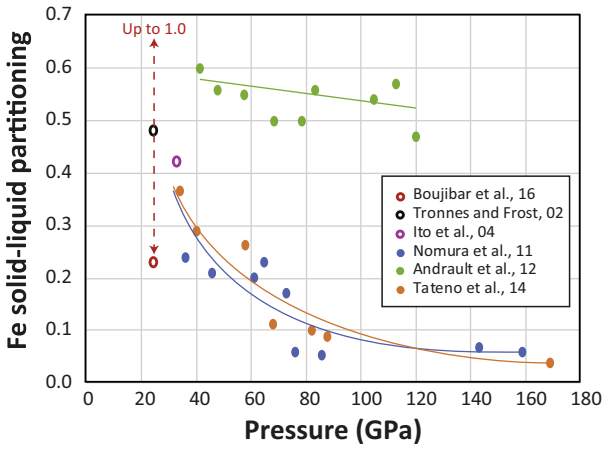

Fig. 8. Change in Fe partitioning ($D_{Fe}^{Bg/melt}$) between the Bg and a coexisting melt. Starting materials for LH-DAC experiments were olivine (blue, (Nomura et al., 2011)), chondritic-type mantle (green, (Andrault et al., 2012)) and peridotite (red, (Tateno et al., 2014)). Open circles correspond to previous multi-anvil experiments (Boujibar et al., 2016; Ito et al., 2004; Tronnes and Frost, 2002). The red arrow corresponds to the range of $D_{Fe}^{Bg/melt}$ measured in a same study at varying F values.

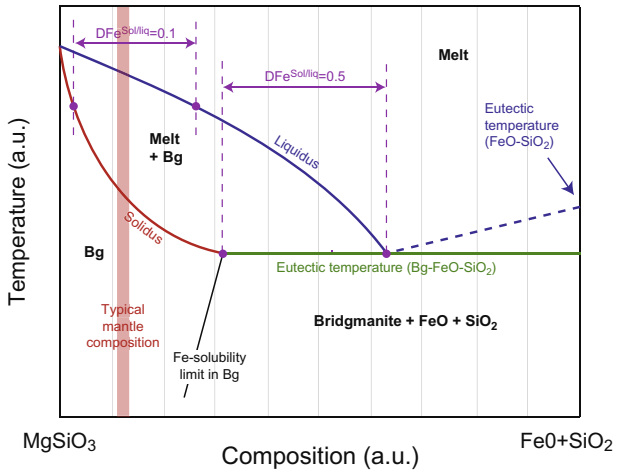

Fig. 9. A possible, schematic, melting diagram between $MgSiO_3$ and $FeSiO_3$ in the lower mantle. We plot FeO + SiO_2 as the Fe-bearing end-member because $FeSiO_3$-Bg is unstable, except maybe at very high pressures. Vertical purple dashed lines are compositions of coexisting Bg and melt. Strong curvatures of solidus and liquidus lines can yield a decrease of $D_{Fe}^{Bg/melt}$ with increasing temperature between the eutectic and the liquidus temperature, in agreement with a previous study (Boujibar et al., 2016).

(i) a small variation of the volume of melting with temperature increasing from the solidus to the liquidus and (ii) a small decrease with pressure from ~6% to ~4% from 30 to 130 GPa, respectively. This significantly positive value of $\Delta V_m/V_{Bg}$ should contribute to a positive melt buoyancy for all types of melts.

4.3. Liquid-solid Fe partitioning

Based on LVP experiments performed up to ~35 GPa, Fe is recognized as an incompatible element, with a concentration ~1.5 to ~3 times higher in the melt compared to the solid mantle (e.g. Ito et al. (2004), Liebske et al. (2005)). For samples recovered from LH-DAC experiments, Fe was reported to become extremely incompatible with the Bg structure at pressures above ~70 GPa, with a Fe concentration more than 10 times higher in the melt, compared to Bg (Nomura et al., 2011) (Fig. 8). Such an enrichment of iron in melts (associated to a very low Fe-concentration in the residual Bg) favors their higher density relative to the solid residue, facilitating their sinking towards the CMB. In this previous study, olivine was used as a starting material and the absence of Al could have favored a relatively low $D_{Fe}^{Bg/melt}$ value (Wood and Rubie, 1996). Still, another study performed on an Al-bearing peridotitic composition using the same experimental methodology confirms the very low Fe-content in the residual Bg (Tateno et al., 2014). We note that the Al partition coefficient between Bg and melt ($D_{Al}^{Bg/melt}$) was also reported to decrease significantly from 1.8 to 0.64 with increasing pressure from 34 to 88 GPa in the same study. On the other hand, much higher $D_{Fe}^{Bg/melt}$ values of 0.5–0.6 were reported for a chondritic-mantle starting material using *in situ* X-ray fluorescence spectroscopy (Andrault et al., 2012). These last results favor denser Bg grains and buoyant melts. The controversy cannot arise from slight compositional differences between starting materials, especially between peridotitic and chondritic mantle compositions used in Tateno et al. (2014) and Andrault et al. (2012), respectively. It should be related to differences in experimental and/or analytical techniques.

A recent study addresses the value of $D_{Fe}^{Bg/melt}$ as a function of F, the degree of partial melting, based on LVP experiments performed at ~25 GPa (Boujibar et al., 2016). $D_{Fe}^{Bg/melt}$ was found to vary from ~1 to a constant value of ~0.3, for F values below ~5 wt% or above 10 wt%, respectively. It suggests a $D_{Fe}^{Bg/melt}$ negatively correlated with temperature between the solidus and the liquidus, in agreement with a typical binary melting diagram (Fig. 9). Thus, controversial results between previous LH-DAC experiments could arise from different heating conditions. Experiments reporting very low $D_{Fe}^{Bg/melt}$ values were performed using a very thin insulating material (hardly detectable using X-ray diffraction). A clear advantage is to facilitate the recovery of relatively thick samples, which can be cut after the experiment in order to obtain relatively large and homogeneous sample regions for chemical analyses using the electron microprobe. However, such experimental procedure implies strong axial temperature gradient between the two diamonds. The center part of the recovered samples is likely experience relatively high temperatures, potentially close to the liquidus (high F possibly inducing low $D_{Fe}^{Bg/melt}$, Fig. 9). Alternatively, experiments reporting higher $D_{Fe}^{Bg/melt}$ values used very thin samples well embedded in the insulating material (producing major diffraction peaks). While this type of loading minimizes axial temperature gradients in the sample, it makes the sample recovery much more difficult. In a previous study, X-ray diffraction was used to monitor carefully the onset of melting at the solidus temperature (Andrault et al., 2011) (low F possibly inducing high $D_{Fe}^{Bg/melt}$). Differences in heating procedure and thus in melting temperature between previous works could have induce significantly different values of $D_{Fe}^{Bg/melt}$. We note that the Fe behavior could be complicated by other factors: (i) the role of Al, which is not well constrained at high pressures; Due to the strong Al-Fe coupling in the Bg structure, an Al-depletion from the Bg structure would contribute to lower $D_{Fe}^{Bg/melt}$; (ii) the variable Fe^{2+} and Fe^{3+} fractions, because each one could partition differently between Bg and the melt, etc. A full quantitative model of $D_{Fe}^{Bg/melt}$ at lower mantle conditions requires additional experimental and theoretical studies.

4.4. Solid–liquid density contrast

The $\Delta\rho_{m-s}$ can be evaluated based on the density of both phases. In the following calculations, we consider a bulk mantle of pyrolitic composition with a bulk Fe/(Mg + Fe) ratio (Fe#) of 0.1. We adjust the Fe-contents in the solid and the melt in order to reproduce the bulk mantle Fe-content, for various values of $D_{Fe}^{Bg/melt}$, which remains an adjustable parameter in the calculation. For coexisting solid and melt compositions, we first calculate the densities in the solid state, before we apply a correction to the melt density of 6% to 4% for pressures between 30 and 130 GPa, respectively, to take into account the volume of melting (Fig. 2). Composition of the solid can correspond either to (i) pure Bg, as expected for the residual solid from solidus to liquidus temperatures in our pseudo-binary melting diagrams (Fig. 4), or to (ii) the mineral assemblage typical of pyrolite, which would correspond to the mantle composition in case of incipient melting. On the other hand, composition of the melt is approximated by a mixture of 55% Bg, 6.2% CaPv and 38.8% Fp, which represents well the PE-melt at all lower mantle pressures (Fig. 4). We neglect the P-T dependence of melt composition, because the $X(SiO_2)$ value of the PET (i) does not vary significantly with pressure and (ii) is not very different from the bulk pyrolitic mantle. Densities at high P and T of the solid and the melt are calculated based on their respective molar fractions of the following five different end-members: Al-bearing $MgSiO_3$, $FeSiO_3$, MgO, FeO, CaPv, using the PVT equation of state of each of them. We used the Mie-Grüneisen formalism with an auto-coherent set of elastic parameters (Matas et al., 2007).

For the solid-liquid density contrast, two end-member situations arise:

(A) During the first stages of magma ocean crystallization, F values are expected to be large (Fig. 10). They could range between ~0.6 and 1, which corresponds to temperatures

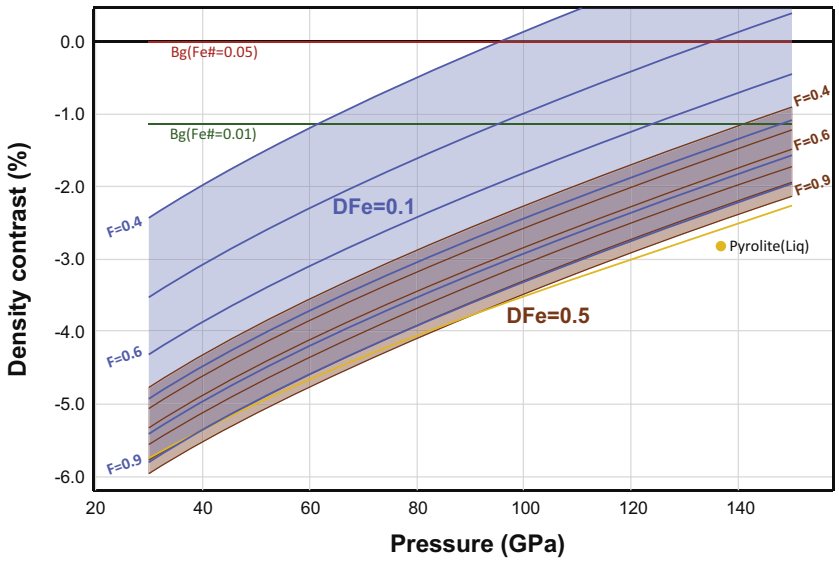

Fig. 10. Density contrast for various couples of coexisting melt and Bg, in the context of a crystallizing magma ocean (F higher than 0.4). All values are normalized to the density of a same Bg having an Fe# of 5% (red). Negative values correspond to buoyant melt. We report relative densities of Bg with Fe# of 1% (green), fully molten pyrolite (yellow) and partial melts calculated for F values from 0.9 to 0.4. We perform the calculation for $D_{Fe}^{Bg/melt}$ values of 0.1 (blue area, corresponding to Nomura et al. (2011), Tateno et al. (2014)) and 0.5 (brown area, corresponding to Andrault et al. (2012)).

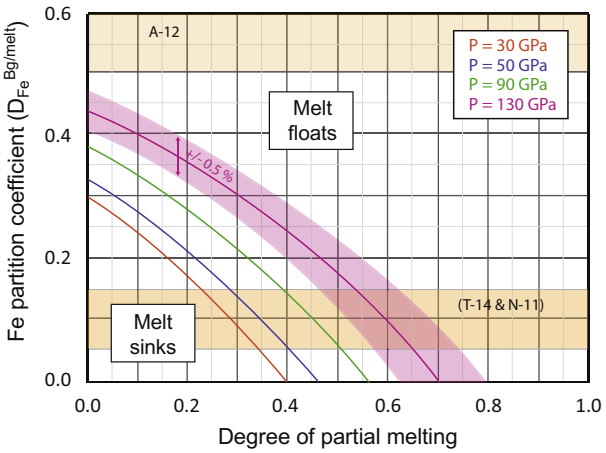

Fig. 11. Domains of positive or negative melt buoyancy for varying degrees of mantle partial melting and various possible values of the solid-liquid Fe partition coefficient. We report boundaries between "sink" and "float" domains at pressures of 30, 50, 90 and 130 GPa. The pink shaded region corresponds to a density contrast within 0.5%. Horizontal orange shaded regions correspond to ranges of $D_{Fe}^{Bg/melt}$ reported around 0.1 (T-14 & N-11; (Nomura et al., 2011; Tateno et al., 2014)) and 0.5 (A-12; (Andrault et al., 2012)) at high mantle depths (Fig. 8).

between the PET and the liquidus (Fig. 6). The situation corresponds to a variable fraction of Bg grains entrained in a major amount of melt. Close to the liquidus (F ~ 1), Fe# in Bg could vary from ~0.05 to ~0.01, depending on the controversial values of $D_{Fe}^{Bg/Melt}$ from 0.5 to 0.1, respectively, because the Fe# in the melt is ~0.1, similar to the bulk mantle. Using the procedure described above, we calculate $\Delta\rho_{m\text{-}s}$ between coexisting Bg and pyrolitic melt along melting curves and obtain mostly negative values, meaning relatively denser Bg grains (Fig. 10). The value of $\Delta\rho_{m\text{-}s}$ increases with pressure, due to a smaller volume of fusion at higher pressures but remains negative at all pressures from 30 to 135 GPa. $\Delta\rho_{m\text{-}s}$ also increases with decreasing the melt fraction, because the melt Fe# increases faster than the solid Fe#. We find no solid-melt density crossover for $D_{Fe}^{Bg/Melt} = 0.5$, at least for F values higher than 0.4. For $D_{Fe}^{Bg/Melt} = 0.1$, Bg can become less dense than the melt for F values below ~0.7 in the lower mantle.

(B) At the latest stages of magma ocean crystallization, as well as in the context of partial melting in the present-day lower mantle, the situation corresponds to a minor amount of melt trapped in the solid mantle. This situation corresponds to incipient mantle melting below the PET (low F) made possible due to the presence of volatile elements. The solid phase can be Bg or pyrolite, depending on the melting degree, F. Here, we report $\Delta\rho_{m\text{-}s}$ values corresponding to a solid phase made of pure Bg, however, results are not very different for pyrolite. Due to the lack of constraints, we assume a melt with $X(SiO_2)$ equal to that of the PE-melt. Under these assumptions, the major change in melt composition with decreasing F is a higher Fe#. Calculations show that a denser melt, compared to a bridgmanitic mantle, is favored for (i) lower $D_{Fe}^{Bg/Melt}$, (ii) lower F and (iii) higher pressures (Fig. 11). There is a significant range of parameters, for values of F below 0.7 and $D_{Fe}^{Bg/Melt}$ below 0.45, where melts could sink in the solid mantle toward the CMB. Still, we remind here that the possible increase of $D_{Fe}^{Bg/Melt}$ at low F values (Boujibar et al., 2016) would favor buoyant melts.

5. Implications for crystallization of the magma ocean

5.1. Dynamics of the magma ocean crystallization

The crystallization of the early magma ocean is the primary mechanism invoked to produce a chemical stratification of the mantle (Boyet and Carlson, 2005; Caro et al., 2005). Concerning the mantle depth at which the crystallization began, our model suggests a mantle liquidus increasing smoothly with pressure up to the CMB pressure of 135 GPa (i.e. the A-chondritic model in Fig. 1). Thus, the adiabatic temperature profile of the cooling magma ocean, which also presents a relatively constant slope, would likely cross the liquidus starting from the CMB upwards (e.g. Fig. 7a in (Thomas and Asimow, 2013)). Magma ocean solidification should therefore occur from bottom up. Talking about the magma ocean *solidification*, we note that major changes in

the dynamics of the magma ocean should occur at F values lower than ~40%, the critical melt fraction when the mantle becomes more viscous (Abe, 1997), rather than when the adiabatic profile crosses the liquidus or the solidus (Monteux et al., 2016).

It has been proposed that Bg grains could settle in the magma ocean, inducing rejection of melts toward the Earth's surface (Boukare et al., 2015; Solomatov, 2007). Our calculations confirm a Bg denser than the coexisting melt at F values higher than 0.7 (Fig. 11). Still, the effective gravitational segregation of Bg grains in a crystallizing magma ocean is not obvious. Highly turbulent flows have certainly dominated in the molten mantle. $\Delta\rho_{m\text{-}s}$ may not have been be sufficiently high to counterbalance mixing forces, especially in the lowermost mantle where $\Delta\rho_{m\text{-}s}$ decreases. This could have prevented major chemical segregation until late stages of the magma ocean crystallization. On the other hand, while an abrupt change in rheological behavior at $F \sim 40\%$ should disable turbulent mixing flows, it should also slow down chemical segregation by inhibiting the atomic diffusion. Thus, the two side-effects of crystallization, turbulent flow followed by high mantle viscosity, are not in favor of large scale chemical heterogeneities early in the crystallizing Earth's mantle.

Following the assumption that Bg grains have efficiently segregated from the crystallizing magma ocean, the melt composition should drift toward higher Fe#, because Fe enters preferentially into the melt (e.g. Boukare et al. (2015)) and also to a slightly higher SiO_2-content (due to the composition of the PET melt, Fig. 5). Increasing the Fe# in melt favors higher $\Delta\rho_{m\text{-}s}$ and sinking melts. This effect could have contributed to produce an early BMO (Labrosse et al., 2007) and/or overturns (Elkins-Tanton, 2008). However, our melting model suggests that the Fe-enrichment of the melt could remain moderate. If we consider the most extreme case of (i) full gravitational segregation of the crystallizing Bg grains, (ii) a $D_{Fe}^{Sol/liq}$ value close to 0 and (iii) a bulk fractional crystallization of 60% (thus F = 0.4), we find that the melt would reach Fe# of ~0.25 (for a bulk pyrolitic mantle with Fe# of ~0.1). For a more reasonable sets of parameters, a high degree of Fe-enrichment can only occur at the very final stages of the magma ocean crystallization.

5.2. Chemical similarities between the pseudo Eutectic-melt and peridotite

Major consequences arise from the very high F values found at the PET (Fig. 6). Brutal solidification of the magma ocean could occur when the degree of partial melting becomes lower than 83% (for peridotite), 74% (for pyrolite) or 56% (for chondritic mantle) at a given mantle depth. Such F values are significantly higher than the threshold value of 40% necessary to produce a relatively viscous mantle (Abe, 1997). Therefore, final mantle crystallization could be achieved at the same time as the mantle became viscous. It would disable chemical segregation by melt gravitation in a mushy mantle and favor instead a homogeneous mantle after bulk magma ocean crystallization. Mantle overturn would also be unlikely, because the magma ocean would crystallize before a too significant Fe-enrichment of the melt.

Our model shows that the peridotite composition is close to the PE-melt at high pressure (Figs. 3–6). This compositional similarity was already discussed a long time ago (e.g. Zhang and Herzberg (1994)). This situation could result from a large scale chemical differentiation during magma ocean crystallization, where the upper part of the mantle would correspond to the last melt that solidified, and the residual solid, Bg, would be concentrated in the deep mantle. A floating layer of peridotitic melt of several hundred kilometers thickness (possibly even more than 1000 km) would have crystallized as a bulk, in agreement with our high F values at the PET. A highly bridgmanitic deep lower mantle would agree with previous studies (Matas et al., 2007; Murakami et al., 2012; Samuel et al., 2005).

Today, presence of volatile elements could induce incipient partial melting in the deep mantle. The melt could be denser than the mantle and sink, in the case the value of $D_{Fe}^{Bg/melt}$ would indeed be as low as 0.4, as suggested by some previous studies (Nomura et al., 2011; Tateno et al., 2014). Sinking melts could produce the ULVZ in the lowermost mantle, independently from the temperature prevailing in the lowermost mantle early in Earth's history. This scenario contrasts with another one suggesting that the ULVZ are the relic of an ancient BMO (Labrosse et al., 2007).

5.3. Maximum core temperature after magma ocean crystallization

After the Moon forming giant impact, the Earth has been largely molten. Subsequent cooling of the magma ocean could have been relatively fast, within 100 ky (Abe, 1997; Monteux et al., 2016; Solomatov, 2007). It was proposed that a BMO could have persisted in the lowermost mantle for a much longer time, due to a large amount of heat stored in the core (Labrosse et al., 2007). Still, the early temperature of the CMB (a good proxy for the core temperature), as well as the lifetime of the BMO remain highly debated. To keep a hot BMO thermally stable, there must be a layer of solid material just above it producing an efficient thermal blanketing between the molten BMO in contact with the hot core and the solid mantle. This solid shell would hamper escape of the core heat. This solid material could only be Bg, the liquidus phase in the deep mantle. Consequently, the Bg melting point of ~5400 K at a pressure of 135 GPa (Fig. 1) corresponds formally to the highest possible CMB temperature after crystallization of the magma ocean. It is ~1300 K above the current CMB temperature.

However, a temperature of ~5400 K represents an improbable upper limit for the early CMB temperature. The reason is that the physical contact between the BMO and the overlaying Bg layer can react chemically. The further away from Bg is the chemical composition of the BMO, the lower should be the equilibrium temperature, in agreement with binary phase diagrams (Fig. 4). Therefore, the more likely the CMB temperature after magma ocean crystallization could correspond to the first occurrence of a more viscous mantle at the CMB (Monteux et al., 2016). This temperature is estimated to ~4400 K, only ~300 K higher than the CMB temperature today (Andrault et al., 2016).

Acknowledgments

This work has been supported by the ANR contract "OxyDeep". This research was financed by the French Government Laboratory of Excellence initiative no. ANR-10-LABX-0006, the Région Auvergne and the European Regional Development Fund. This is Laboratory of Excellence ClerVolc contribution number 242.

Appendix A. Supplementary data

Supplementary data associated with this article can be found, in the online version, at http://dx.doi.org/10.1016/j.pepi.2017.02.009.

References

Abe, Y., 1997. Thermal and chemical evolution of the terrestrial magma ocean. Phys. Earth Planet. Inter. 100, 27–39.
Agee, C.B., 1998. Crystal-liquid density inversions in terrestrial and lunar magmas. Phys. Earth Planet. Inter. 107, 63–74.
Akaogi, M., Ito, E., 1999. Calorimetric study on majorite-perovskite transition in the system $Mg_4Si_4O_{12}$-$Mg_3Al_2Si_3O_{12}$: transition boundaries with positive pressure-temperature slopes. Phys. Earth Planet. Inter. 114, 129–140.
Akins, J.A., Luo, S.N., Asimow, P.D., Ahrens, T.J., 2004. Shock-induced melting of $MgSiO_3$ perovskite and implications for melts in Earth's lowermost mantle. Geophys. Res. Lett. 31, L14612.

Andrault, D., Bolfan-Casanova, N., Bouhifd, M.A., Guignot, N., Kawamoto, T., 2007. The role of Al-defects on the equation of state of Al-(Mg, Fe)SiO_3 perovskite. Earth Planet. Sci. Lett. 263, 167–179.
Andrault, D., Bolfan-Casanova, N., Lo Nigro, G., Bouhifd, M.A., Garbarino, G., Mezouar, M., 2011. Melting curve of the deep mantle applied to properties of early magma ocean and actual core-mantle boundary. Earth Planet. Sci. Lett. 304, 251–259.
Andrault, D., Petitgirard, S., Lo Nigro, G., Devidal, J.L., Veronesi, G., Garbarino, G., Mezouar, M., 2012. Solid-liquid iron partitioning in Earth's deep mantle. Nature 487, 354–357.
Andrault, D., Pesce, G., Bouhifd, M.A., Bolfan-Casanova, N., Henot, J.M., Mezouar, M., 2014. Melting of subducted basalt at the core-mantle boundary. Science 344, 892–895.
Andrault, D., Monteux, J., Le Bars, M., Samuel, H., 2016. The deep Earth may not be cooling down. Earth Planet. Sci. Lett. 443, 195–203.
Bajgain, S., Ghosh, D.B., Karki, B.B., 2015. Structure and density of basaltic melts at mantle conditions from first-principles simulations. Nat. Commun. 6.
Benmore, C.J., Soignard, E., Amin, S.A., Guthrie, M., Shastri, S.D., Lee, P.L., Yarger, J.L., 2010. Structural and topological changes in silica glass at pressure. Phys. Rev. B 81.
Bolfan-Casanova, N., Keppler, H., Rubie, D.C., 2003. Water partitioning at 660 km depth and evidence for very low water solubility in magnesium silicate perovskite. Geophys. Res. Lett. 30, L017182.
Boujibar, A., Bolfan-Casanova, N., Andrault, D., Bouhifd, M.A., Trcera, N., 2016. Incorporation of Fe^{2+} and Fe^{3+} in bridgmanite during magma ocean crystallization. Am. Miner. 101, 1560–1570.
Boukare, C.E., Ricard, Y., Fiquet, G., 2015. Thermodynamics of the MgO-FeO-SiO_2 system up to 140 GPa: application to the crystallization of Earth's magma ocean. J. Geophys. Res.: Solid Earth 120, 6085–6101.
Boyet, M., Carlson, R.W., 2005. Nd-142 evidence for early (>4.53 Ga) global differentiation of the silicate Earth. Science 309, 576–581.
Caro, G., Bourdon, B., Wood, B.J., Corgne, A., 2005. Trace-element fractionation in Hadean mantle generated by melt segregation from a magma ocean. Nature 436, 246–249.
Corgne, A., Liebske, C., Wood, B.J., Rubie, D.C., Frost, D.J., 2005. Silicate perovskite-melt partitioning of trace elements and geochemical signature of a deep perovskitic reservoir. Geochim. Cosmochim. Acta 69, 485–496.
Davaille, A., 1999. A simultaneous generation of hotpots and superswells by convection in a heterogeneous planetary mantle. Nature 402, 756–760.
Davies, C., Pozzo, M., Gubbins, D., Alfe, D., 2015. Constraints from material properties on the dynamics and evolution of Earth's core. Nat. Geosci. 8, 678.
de Koker, N., Stixrude, L., 2009. Self-consistent thermodynamic description of silicate liquids, with application to shock melting of MgO periclase and $MgSiO_3$ perovskite. Geophys. J. Int. 178, 162–179.
de Koker, N., Karki, B.B., Stixrude, L., 2013. Thermodynamics of the MgO-SiO_2 liquid system in Earth's lowermost mantle from first principles. Earth Planet. Sci. Lett. 361, 58–63.
Du, Z., Lee, K.K.M., 2014. High-pressure melting of MgO from (Mg, Fe)O solid solutions. Geophys. Res. Lett. 41, 8061–8066.
Elkins-Tanton, L.T., 2008. Linked magma ocean solidification and atmospheric growth for Earth and Mars. Earth Planet. Sci. Lett. 271, 181–191.
Fiquet, G., Auzende, A.L., Siebert, J., Corgne, A., Bureau, H., Ozawa, H., Garbarino, G., 2010. Melting of Peridotite to 140 Gigapascals. Science 329, 1516–1518.
Funamori, N., Sato, T., 2010. Density contrast between silicate melts and crystals in the deep mantle: an integrated view based on static-compression data. Earth Planet. Sci. Lett. 295, 435–440.
Guillot, B., Sator, N., 2007. A computer simulation study of natural silicate melts. Part II: high pressure properties. Geochim. Cosmochim. Acta 71, 4538–4556.
Herzberg, C., Zhang, J.Z., 1998. Melting experiments in the systems CaO-MgO-Al_2O_3-SiO_2 and MgO-SiO_2 at 3 to 15 GPa. Am. Miner. 83, 491–500.
Herzberg, C., Condie, K., Korenaga, J., 2010. Thermal history of the Earth and its petrological expression. Earth Planet. Sci. Lett. 292, 79–88.
Herzberg, C., Asimow, P.D., Ionov, D.A., Vidito, C., Jackson, M.G., Geist, D., 2013. Nickel and helium evidence for melt above the core-mantle boundary. Nature 493, U134–U393.
Hirschmann, M.M., Asimow, P.D., Ghiorso, M.S., Stolper, E.M., 1999. Calculation of peridotite partial melting from thermodynamic models of minerals and melts. III. Controls on isobaric melt production and the effect of water on melt production. J. Petrol. 40, 831–851.
Irifune, T., Koizumi, T., Ando, J., 1996. An experimental study of the garnet-perovskite transformation in the system $MgSiO_3$-$Mg_3Al_2Si_3O_{12}$. Phys. Earth Planet. Inter. 96, 147–157.
Ito, E., Kubo, A., Katsura, T., Walter, M.J., 2004. Melting experiments of mantle materials under lower mantle conditions with implications for magma ocean differentiation. Phys. Earth Planet. Inter. 143–144, 397–406.
Katsura, T., Ito, E., 1990. Melting and subsolidus phase-relations in the $MgSiO_3$-$MgCO_3$-system at high-pressures – implications to the evolution of the Earth's atmosphere. Earth Planet. Sci. Lett. 99, 110–117.
Katsura, T., Yoneda, A., Yamazaki, D., Yoshino, T., Ito, E., 2010. Adiabatic temperature profile in the mantle. Phys. Earth Planet. Inter. 183, 212–218.
Kellogg, L.H., Hager, B.H., van der Hilst, R.D., 1999. Compositional stratification in the deep mantle. Science 283, 1881–1884.
Kojitani, H., Akaogi, M., 1997. Melting enthalpies of mantle peridotite: calorimetric determinations in the system CaO-MgO-Al_2O_3-SiO_2 and application to magma generation. Earth Planet. Sci. Lett. 153, 209–222.
Labrosse, S., 2015. Thermal evolution of the core with a high thermal conductivity. Phys. Earth Planet. Inter. 247, 36–55.
Labrosse, S., Hernlund, J.W., Coltice, N., 2007. A crystallizing dense magma ocean at the base of the Earth's mantle. Nature 450, 866–869.
Lange, R.A., 1997. A revised model for the density and thermal expansivity of K_2O-Na_2O-CaO-MgO-Al_2O_3-SiO_2 liquids from 700 to 1900 K: extension to crustal magmatic temperatures. Contrib. Mineral. Petrol. 130, 1–11.
Lauterbach, S., McCammon, C.A., van Aken, P., Langenhorst, F., Seifert, F., 2000. Mössbauer and ELNES spectroscopy of (Mg, Fe)(Si, Al)O_3 perovskite: a highly oxidized component of the lower mantle. Contrib. Mineral. Petrol. 138, 17–26.
Lebrun, T., Massol, H., Chassefiere, E., Davaille, A., Marcq, E., Sarda, P., Leblanc, F., Brandeis, G., 2013. Thermal evolution of an early magma ocean in interaction with the atmosphere. J. Geophys. Res.: Planets 118, 1155–1176.
Lee, C.-T.A., Luffi, P., Hoink, T., Li, J., Dasgupta, R., Hernlund, J.W., 2010. Upside-down differentiation and generation of a "primordial" lower mantle. Nature 463, 930–933.
Liebske, C., Frost, D.J., 2012. Melting phase relations in the MgO-$MgSiO_3$ system between 16 and 26 GPa: Implications for melting in Earth's deep interior. Earth Planet. Sci. Lett. 345, 159–170.
Liebske, C., Corgne, A., Frost, D.J., Rubie, D.C., Wood, B.J., 2005. Compositional effects on element partitioning between Mg-silicate perovskite and silicate melts. Contrib. Mineral. Petrol. 149.
Mao, W.L., Meng, Y., Shen, G., Prakapenka, V.B., Campbell, A.J., Heinz, D.L., Shu, J., Caracas, R., Cohen, R.E., Fei, Y., Hemley, R.J., Mao, H.K., 2005. Iron-rich silicate in the Earth's D'' layer. Proc. Natl. Acad. Sci. USA 102, 9751–9753.
Martin, H., Moyen, J.F., 2002. Secular changes in tonalite-trondhjemite-granodiorite composition as markers of the progressive cooling of Earth. Geology 30, 319–322.
Matas, J., Bass, J.D., Ricard, Y., Mattern, E., Bukowinsky, M.S., 2007. On the bulk composition of the lower mantle: predictions and limitations from generalized inversion of radial seismic profiles. Geophys. J. Int. 170, 764–780.
Matsukage, K.N., Jing, Z.C., Karato, S., 2005. Density of hydrous silicate melt at the conditions of Earth's deep upper mantle. Nature 438, 488–491.
Miller, G.H., Stolper, E.M., Ahrens, T.J., 1991. The equation of state of a Molten Komatiite 2. Application to Komatiite Petrogenesis and the Hadean Mantle. J. Geophys. Res. 96. 11,849–811,864.
Monteux, J., Andrault, D., Samuel, H., 2016. On the cooling of a deep terrestrial magma ocean. Earth Planet. Sci. Lett. 448, 140–149.
Mosenfelder, J.L., Asimow, P.D., Frost, D.J., Rubie, D.C., Ahrens, T.J., 2009. The $MgSiO_3$ system at high pressure: thermodynamic properties of perovskite, postperovskite, and melt from global inversion of shock and static compression data. J. Geophys. Res.: Solid Earth 114, B01203.
Mukhopadhyay, S., 2012. Early differentiation and volatile accretion recorded in deep-mantle neon and xenon. Nature 486, 101–U124.
Murakami, M., Ohishi, Y., Hirao, N., Hirose, K., 2012. A perovskitic lower mantle inferred from high-pressure, high-temperature sound velocity data. Nature 485, 90–U118.
Nakagawa, T., Tackley, P.J., 2010. Influence of initial CMB temperature and other parameters on the thermal evolution of Earth's core resulting from thermochemical spherical mantle convection. Geochem. Geophys. Geosyst. 11, Q06001.
Nakajima, M., Stevenson, D.J., 2015. Melting and mixing states of the Earth's Mantle after the moon-forming impact. Earth Planet. Sci. Lett. 427, 286–295.
Nomura, R., Ozawa, H., Tateno, S., Hirose, K., Hernlund, J.W., Muto, S., Ishii, H., Hiraoka, N., 2011. Spin crossover and iron-rich silicate melt in the Earth's deep mantle. Nature 473, 199–202.
Nomura, R., Hirose, K., Uesugi, K., Ohishi, Y., Tsuchiyama, A., Miyake, A., Ueno, Y., 2014. Low core-mantle boundary temperature inferred from the solidus of pyrolite. Science 343, 522–525.
Panero, W.R., Pigott, J.S., Reaman, D.M., Kabbes, J.E., Liu, Z.X., 2015. Dry (Mg, Fe)SiO_3 perovskite in the Earth's lower mantle. J. Geophys. Res.: Solid Earth 120, 894–908.
Petitgirard, S., Malfait, W.J., Sinmyo, R., Kupenko, I., Hennet, L., Harries, D., Dane, T., Burghammer, M., Rubie, D.C., 2015. Fate of $MgSiO_3$ melts at core–mantle boundary conditions. Proc Natl Acad Sci 112, 14186–14190.
Presnall, D.C., 1995. Phase diagrams of Earth-forming minerals. In: Ahrens, T. (Ed.), Mineral Physics and Crystallography. AGU, Washington, D.C., pp. 248–268.
Presnall, D.C., Gasparik, T., 1990. Melting of enstatite ($MgSiO_3$) from 10 to 16.5 GPa and the forsterite (Mg_2SiO_4) – majorite ($MgSiO_3$) eutectic at 16.5 GPa – implications for the origin of the mantle. J. Geophys. Res. 95, 15771–15777.
Revenaugh, J., Sipkin, S.A., 1994. Seismic evidence for silicate melt atop the 410 km mantle discontinuity. Nature 369, 474–476.
Romanowicz, B., 1995. A global tomographic model of the shear attenuation in the upper mantle. J. Geophys. Res.: Solid Earth 100, 12375–12394.
Rost, S., Garnero, E.J., Williams, Q., Manga, M., 2005. Seismological constraints on a possible plume root at the core-mantle boundary. Nature 435, 666–669.
Rubie, D.C., Nimmo, H.J., Melosh, H.J., 2015. Formation of the Earth's core. In: Schubert, G. (Ed.), Treatise on Geophysics. 2nd ed. Elsevier, Amsterdam, pp. 43–79.
Sakamaki, T., Suzuki, A., Ohtani, E., 2006. Stability of hydrous melt at the base of the Earth's upper mantle. Nature 439, 192–194.
Samuel, H., Farnetani, C.G., Andrault, D., 2005. Heterogeneous lowermost mantle: Compositional constraints and seismological observables. In: VanDerHilst, R.D., Bass, J.D., Matas, J., Trampert, J. (Eds.), Earth's Deep Mantle: Structure, Composition, and Evolution, pp. 101–116.

Sanloup, C., Drewitt, J.W.E., Konopkova, Z., Dalladay-Simpson, P., Morton, D.M., Rai, N., van Westrenen, W., Morgenroth, W., 2013. Structural change in molten basalt at deep mantle conditions. Nature 503, 104.
Sato, T., Funamori, N., 2010. High-pressure structural transformation of SiO_2 glass up to 100 GPa. Phys. Rev. B 82.
Shen, G., Lazor, P., 1995. Measurement of melting temperatures of some minerals under lower mantle conditions. J. Geophys. Res. 100, 17699–17713.
Simon, F., Glatzel, G., 1929. Fusion-pressure curve. Zeitschrift für anorganische und allgemeine Chemie 178, 309–316.
Sleep, N.H., Zahnle, K.J., Lupu, R.E., 2014. Terrestrial aftermath of the Moon-forming impact. Philos. Trans. R. Soc. A 372.
Solomatov, V.S., 2007. Magma oceans and primordial mantle differentiation. In: Schubert, G. (Ed.), Treatise on Geophysics. Elsevier, Amsterdam, pp. 91–119.
Song, T.R.A., Helmberger, D.V., Grand, S.P., 2004. Low-velocity zone atop the 410-km seismic discontinuity in the northwestern United States. Nature 427, 530–533.
Stebbins, J.F., Carmichael, I.S.E., Moret, L.K., 1984. Heat-capacities and entropies of silicate liquids and glasses. Contrib. Mineral. Petrol. 86, 131–148.
Stixrude, L., Karki, B.B., 2005. Structure and freezing of $MgSiO_3$ liquid in the Earth's lower mantle. Science 310, 297–299.
Stixrude, L., de Koker, N., Sun, N., Mookherjee, M., Karki, B.B., 2009. Thermodynamics of silicate liquids in the deep Earth. Earth Planet. Sci. Lett. 278, 226–232.
Stolper, E.M., Ahrens, T.J., 1987. On the nature of pressure induced coordination changes in silicate melts or glasses. Geophys. Res. Lett. 14, 1231–1233.
Tateno, S., Hirose, K., Ohishi, Y., 2014. Melting experiments on peridotite to lowermost mantle conditions. J. Geophys. Res.: Solid Earth 119, 4684–4694.
Tauzin, B., Debayle, E., Wittlinger, G., 2010. Seismic evidence for a global low-velocity layer within the Earth's upper mantle. Nat. Geosci. 3, 718–721.
Thomas, C.W., Asimow, P.D., 2013. Direct shock compression experiments on premolten forsterite and progress toward a consistent high-pressure equation of state for CaO-MgO-Al_2O_3-SiO_2-FeO liquids. J. Geophys. Res.: Solid Earth 118, 5738–5752.
Thomas, C.W., Liu, Q., Agee, C.B., Asimow, P.D., Lange, R.A., 2012. Multi-technique equation of state for Fe_2SiO_4 melt and the density of Fe-bearing silicate melts from 0 to 161 GPa. J. Geophys. Res.: Solid Earth 117, 2.
Thomson, A.R., Walter, M.J., Lord, O.T., Kohn, S.C., 2014. Experimental determination of melting in the systems enstatite-magnesite and magnesite-calcite from 15 to 80 GPa. Am. Miner. 99, 1544–1554.
Touboul, M., Puchtel, I.S., Walker, R.J., 2012. W-182 evidence for long-term preservation of early mantle differentiation products. Science 335, 1065–1069.
Tronnes, R.G., Frost, D.J., 2002. Peridotite melting and mineral–melt partitioning of major and minor elements at 22–24.5 GPa. Earth Planet. Sci. Lett. 197, 117–131.
van der Hilst, R.D., Karason, H., 1999. Compositional heterogeneity in the bottom 1000 kilometers of Earth's mantle: toward a hybrid convection model. Science 283, 1885–1888.
Vocadlo, L., Price, G.D., 1996. The melting of MgO – computer calculations via molecular dynamics. Phys. Chem. Miner. 23, 42–49.
Wang, Y.B., Sakamaki, T., Skinner, L.B., Jing, Z.C., Yu, T., Kono, Y., Park, C., Shen, G.Y., Rivers, M.L., Sutton, S.R., 2014. Atomistic insight into viscosity and density of silicate melts under pressure. Nat. Commun. 5.
Wicks, J.K., Jackson, J.M., Sturhahn, W., 2010. Very low sound velocities in iron-rich (Mg, Fe)O: Implications for the core-mantle boundary region. Geophys. Res. Lett. 37.
Wood, B.J., Rubie, D.C., 1996. The effect of alumina on phase transformations at the 660-kilometer discontinuity from Fe-Mg partitioning experiments. Science 273, 1522–1524.
Yu, Y.G., Wentzcovitch, R.M., Vinograd, V.L., Angel, R.J., 2011. Thermodynamic properties of $MgSiO_3$ majorite and phase transitions near 660 km depth in $MgSiO_3$ and Mg_2SiO_4: a first principles study. J. Geophys. Res. Solid Earth 116.
Zeidler, A., Salmon, P.S., Skinner, L.B., 2014. Packing and the structural transformations in liquid and amorphous oxides from ambient to extreme conditions. Proc. Natl. Acad. Sci. USA 111, 10045–10048.
Zerr, A., Boehler, R., 1993. Melting of (Mg, Fe)SiO_3-perovskite to 625 kbar: Indication of a high melting temperature in the lower mantle. Science 262, 553–555.
Zhang, J., Herzberg, C., 1994. Melting experiments on anhydrous peridotite KLB-1 from 5.0 to 22.5 GPa. J. Geophys. Res. 99, 17729–17742.

nature geoscience

ARTICLES

https://doi.org/10.1038/s41561-017-0053-9

Deep and persistent melt layer in the Archaean mantle

Denis Andrault[1*], Giacomo Pesce[1,4], Geeth Manthilake[1], Julien Monteux[1], Nathalie Bolfan-Casanova[1], Julien Chantel[1], Davide Novella[1], Nicolas Guignot[2], Andrew King[2], Jean-Paul Itié[2] and Louis Hennet[3]

The transition from the Archaean to the Proterozoic eon ended a period of great instability at the Earth's surface. The origin of this transition could be a change in the dynamic regime of the Earth's interior. Here we use laboratory experiments to investigate the solidus of samples representative of the Archaean upper mantle. Our two complementary in situ measurements of the melting curve reveal a solidus that is 200–250 K lower than previously reported at depths higher than about 100 km. Such a lower solidus temperature makes partial melting today easier than previously thought, particularly in the presence of volatiles (H_2O and CO_2). A lower solidus could also account for the early high production of melts such as komatiites. For an Archaean mantle that was 200–300 K hotter than today, significant melting is expected at depths from 100–150 km to more than 400 km. Thus, a persistent layer of melt may have existed in the Archaean upper mantle. This shell of molten material may have progressively disappeared because of secular cooling of the mantle. Crystallization would have increased the upper mantle viscosity and could have enhanced mechanical coupling between the lithosphere and the asthenosphere. Such a change might explain the transition from surface dynamics dominated by a stagnant lid on the early Earth to modern-like plate tectonics with deep slab subduction.

Melting is a first-order phase transformation that has drastic consequences for various geophysically observable material properties, such as seismic-wave velocities and electrical conductivity (EC). As geological materials are chemically complex, they generally melt partially over a wide range of temperatures between their solidus and liquidus. In the early stages of the Earth's formation, extensive melting occurred down to great mantle depths, with the formation of a magma ocean, through the combination of radiogenic heating, impact-induced heating during accretionary events and gravitational energy release during core–mantle separation[1]. Partial melting can still occur today in the mantle, but at limited degrees of partial melting (F) and in specific regions. It occurs close to the Earth's surface when hot mantle materials undergo decompression, as at mid-ocean ridges. Also, seismic, magnetotelluric and electrical anomalies suggest the presence of melts at mantle depths between 80 and 200 km (ref. [2]), just atop the 410 km mantle discontinuity[3] and above the core–mantle boundary[4]. In these regions, thermochemical heterogeneities alone cannot explain the magnitude of anomalies.

Careful experiments are needed to address properly the evolution of the mantle solidus with pressure. Ideally, one should determine the onset of melting in the presence of the right amount of volatiles, such as CO_2 and H_2O, which unfortunately remains uncertain[5] and could vary from one geological setting to another. Generally, the dry solidus is used as a reference to which is added the role of volatiles[6]. The dry-solidus profile currently accepted for the upper mantle is derived from a few studies performed on KLB-1 peridotite[7–9], garnet peridotite[10], Allende meteorite[11] and the CMAS (CaO, MgO, Al_2O_3 and SiO_2) composition[12]. All these studies report melting temperatures significantly higher than the present-day temperature profile[13] (Supplementary Fig. 1). All previous studies used the so-called 'quench method' based on the analyses of recovered samples. This method is not well adapted to detect the onset of melting, which can correspond to F values smaller than 1 wt% in natural samples[14].

In this study, we determined the mantle solidus temperature using two independent in situ techniques, EC and X-ray diffraction, at pressures and temperatures up to 28 GPa and 2,300 K, in a multi-anvil apparatus.

Determination of the mantle solidus

Using EC, we first observed dehydration of the cell assembly, followed by crystallization of the glass starting material at a temperature below 1,573 K (Supplementary Fig. 5a). A complete sample dehydration and crystallization is evidenced by a perfect reproducibility of the sample conductivity when performing various cycles of cooling and heating. Full crystallization in this temperature range is also evidenced by analyses of the microstructure of quenched samples. On further heating, we observed a sudden increase of the slope in the EC profile, above a threshold temperature of 1,815–1,865 K (Fig. 1, Supplementary Fig. 5b and Supplementary Table 2). This can be interpreted as that just above the solidus temperature, F is very low in the sample and the melt wets only some specific grain surfaces, and not others, because the surface energy depends on its crystallographic orientation. With increasing temperature, the melt interconnection between the two electrodes improves. The melt progressively becomes the dominant conductive phase, with an ionic conduction mechanism[15]. Previous studies on partial melting report precisely the same behaviour in the evolution of sample conductivity with temperature[16–18].

Using X-ray diffraction, we first monitored the sample crystallization at temperatures from 1,200 K to 1,600 K (Supplementary Fig. 6), until the diffraction pattern remained independent of time. At this point, the set of diffractions peaks corresponded well with the expected mineralogy (Supplementary Fig. 7). We observed

[1]Université Clermont Auvergne, CNRS, IRD, OPGC, Laboratorie Magmas et Volcans, Clermont-Ferrand, France. [2]Synchrotron SOLEIL, Gif-sur-Yvette, France. [3]Conditions Extrêmes et Matériaux: Haute Température et Irradiation, CNRS, Orléans, France. Present address: [4]School of Geosciences, The University of Edinburgh, Edinburgh, UK. *e-mail: denis.andrault@uca.fr

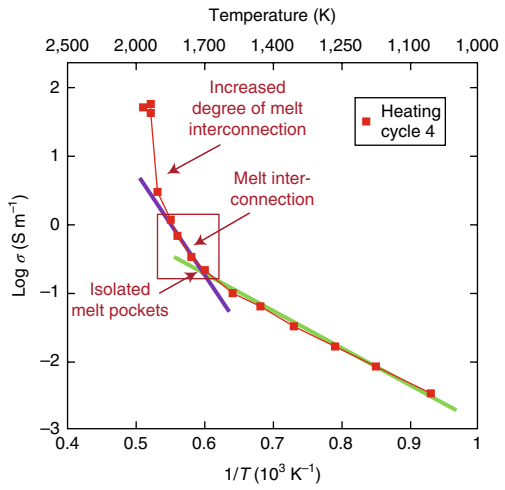

Fig. 1 | EC results. The sample EC was measured at increasing temperatures for a nominal pressure of 5 GPa after various pre-heating cycles. The clear change in slope at 1,700 K indicates a change in the conductivity mechanism at the onset of sample melting. A further increase of temperature induces a better interconnection of the melt between the electrodes, before ionic conduction in the interconnected melt becomes largely dominant (additional details are reported in Supplementary Fig. 5).

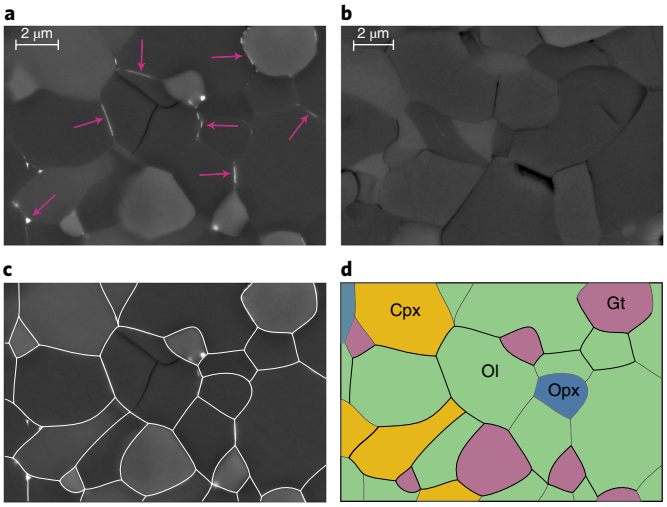

Fig. 2 | Images of recovered samples. a,**b**, Using the field-emission gun electron microscope, microphotographs were acquired on samples recovered after heating just above (**a**) and just below (**b**) the solidus temperature. In both cases, the pressure was 5 GPa. For a temperature above the solidus, very thin films and nanometre-size pockets of melt are clearly visible (pink arrows). **c**, The polygonal shape of grains is typical of good textural equilibrium. **d**, The sample mineralogy was refined from chemical map. Ol, olivine; Cpx, clinopyroxene; Gt, garnet; Opx, orthopyroxene.

olivine and its high-pressure polymorphs, and majoritic garnet and pyroxenes were also visible for pressures below ~14 GPa. At subsolidus conditions, the relative peak intensities were very compatible with those theoretically expected based on atomic topologies, which hence revealed an equilibrated microstructure. No significant changes were observed on further heating until the sample behaviour changed abruptly: all the diffraction peaks from the sample suddenly underwent major changes of their intensities with time. Large intensity variations could be seen in real time on diffraction profiles recorded by the Ge detector (Supplementary Fig. 8). Such instability denotes a fast grain rotation in the X-ray beam. We estimate that a grain rotation of less than 1° is enough to stop the diffraction signal of a grain previously oriented in ideal Bragg conditions. Decreasing the sample temperature by 10–20 K stopped entirely the rapid variation in peak intensities. Thus, this sudden change above a critical temperature is not compatible with a continuous increase with temperature of grain-growth rate. Instead, the observed fast grain rotation can be related to the presence of a thin film of melt at the grain boundary. The melt induces a discontinuous increase in the rate of atomic diffusion, which possibly favours growth of some surfaces of the grains at the expense of others. A similar technique was used previously to determine the solidus of basalt in a laser-heated diamond anvil cell[19].

Some experimental charges were quenched at temperatures just below or just above the onset of melting to probe the textural evolution using a scanning electron microscope (SEM). Under subsolidus conditions, the starting material appears well recrystallized into grains of several microns with polygonal shape (Fig. 2). A good textural equilibrium is evidenced by sharp grain-boundary angles, often close to 120°, and linear grain boundaries in between junctions[20]. Based on chemical maps, the mineralogical content at 5 GPa, for example, is an intimate mixture of olivine, clinopyroxene, orthopyroxene and garnet. No remaining traces of the glass starting material were observed. Above the solidus, we could observe some melt after an extensive search using the SEM. The melt occurs in the shape of very thin films along grain boundaries and nanometre-size pockets at triple junctions, as typically observed in partially molten systems[21,22]. Due to the short duration of the experiments, the microstructure may not correspond to full equilibrium. However, one can estimate the degree of partial melting to less than 1%, based on the fraction of sample surface covered by the melt (the most-shiny regions). The melt composition could not be determined accurately because of chemical interferences with the composition of surrounding minerals.

Based on the new mantle solidus and using $T_0 = 1{,}373$ K at room pressure[23], we calculated an equation of melting using the Simon and Glatzel (SG)[24] equation $[T_m(P) = T_0(P/a+1)^{1/c}]$. In this equation, a and c are adjustable parameters and P is pressure (Supplementary Table 3). A similar SG equation can model the dry liquidus reported in previous studies performed on KLB-1 peridotite[8,25]. The change in chemical composition, for example, between KLB peridotite and the chondritic-type mantle used in this study could induce significant differences in the solidus and liquidus temperatures[23]. However, the data set on the melting properties of the mantle-relevant compositions at mantle depths higher than 100–150 km remains insufficient to discuss these potential differences, which are therefore included in the uncertainties.

Comparison with previous melting studies

Although our data set is consistent with previous studies below 3–4 GPa (our study is not more precise than previous works at low pressures), it shows a mantle solidus lower than those previously reported for higher pressures (Fig. 3). The difference is, on average, 250 K for mantle depths greater than 200 km. The only study in close agreement with ours is that performed on an Allende-meteorite type composition, which included sulfur in the starting material[11]. The reason for the discrepancy with other studies can be manifold:

(1) Some previous studies used compositions that were too simplistic to represent properly the mantle state, for example, the CMAS composition used in Litasov and Ohtani[12]. For such a composition, the onset of melting may only occur when the pseudo-eutectic temperature is reached. In our study, the starting material contains Fe, Ti, Cr and Na in addition to the

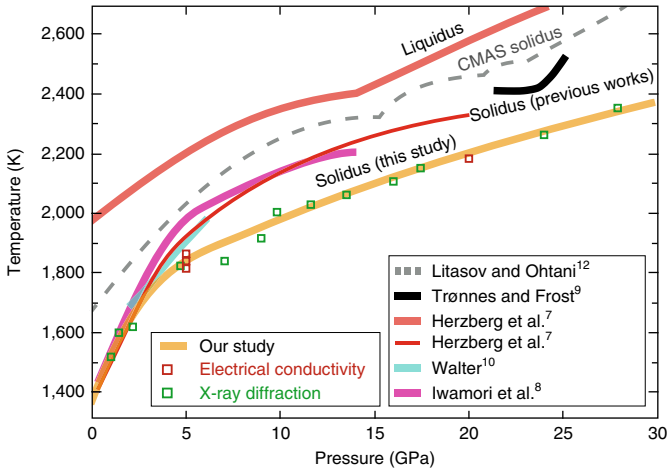

Fig. 3 | The new solidus temperature profile. The onset of the melting of a chondritic-type mantle composition was determined up to 28 GPa using EC (red squares) and X-ray diffraction (green squares). The new solidus is compared with previous studies performed using the quench method on the peridotitic mantle[7–10] or the simplified CMAS[12] composition. The new solidus plots significantly lower at pressures above 4–5 GPa.

CMAS basis. It was shown that such compositional changes can yield a difference of solidus temperature of a couple 100 K (refs [7,23]).

(2) The major melting criterion used in previous studies is the observation of molten regions in recovered samples. The formation of melt pockets can be difficult to detect at the lowest F values. Previous studies dedicated to this matter have established special techniques to detect the onset of melting[14,26]. However, the SEM images published in previous works correspond to an extremely high F, with a large fraction of the sample fully molten[9,12,25]. In contrast, our two in situ techniques are very sensitive to detect the onset of melting (Methods). In a previous study, the transmission electron microscope was used to differentiate grains that were solid at high temperature from secondary grains that rapidly recrystallized at the grain interfaces on quenching[7]. Some of the reported experiments show the absence of melt at temperatures higher than our new solidus temperatures, which we can only try to explain by the next point.

(3) Previous studies used mixtures of oxide powders with typical grain sizes on the order of micrometres. The heterogeneous grain composition does not favour the occurrence of nanoscale regions with the chemical composition of the solidus melt. Significant atomic diffusion is needed, over a distance typical of the grain size, to induce melting at the solidus temperature. The mean atomic path is estimated to be less than 10 nm per minute in the solid state at 2,000 K (ref. [27]). Therefore, kinetic effects, which were not taken into account in previous studies, can largely inhibit the melting of a mixture of oxides at the solidus temperature. In contrast, we used a glass with an ideal chemical homogeneity at the atomic scale. Chemical interactions are much facilitated, even though the glass eventually recrystallized in nanograins above the glass–liquid transition temperature, as observed in our study.

Only a few studies report the value of F at temperatures between the solidus and the liquidus at upper mantle conditions and these studies do not agree well with each other (Supplementary Fig. 9). The disagreement could come from differences in the chemical composition between the starting materials (peridotite[8], garnet–peridotite[10] or CMAS[12]) or to a difficult control of P–T conditions during the melting experiments. A theoretical study dedicated to the melting behaviour at relatively low pressure shows that the melt productivity can be highly variable with pressure, temperature and chemical composition[28]. In particular, the nature and the concentration of incompatible elements (Na and K) and *a fortiori* of volatile elements (H, C and S) can help to maintain relatively low F values over a significant temperature range above the solidus. Therefore, although the two in situ techniques used in this study are well suited to determine the solidus (because they can detect a small amount of melt), the variation of F with temperature between the solidus and the liquidus remains uncertain. This matter requires additional experimental studies.

Partial melting in the mantle today

We now compare our solidus profile with geotherms reported for the first 700 km mantle depths (Supplementary Fig. 1). First, we remember that the shallow temperature profile depends on the type of geological setting: the younger is the crust, the steeper is the thermal gradient close to the Earth's surface. Nevertheless, all the geotherms meet a mean adiabatic temperature gradient at mantle depths greater than ~250 km (ref. [13]). At the present-day, the surface potential temperature (T_p) is reported from ~1,600 K to a maximum of 1,750 K (ref. [29]). Both oceanic and continental lithosphere geotherms[30] currently plot at lower temperatures than the solidus, in agreement with a mantle state that is essentially solid. In that sense, our new measurements confirm that the possible occurrence of partial melting in specific regions of the upper mantle, suggested by geophysical measurements[3,22], should be dominated by the role of volatiles (H_2O and CO_2). Still, the lower solidus temperature makes upper-mantle partial melting easier than previously thought.

Partial melting in the Archaean mantle

Studies of non-arc basalts of Archaean and Proterozoic ages have revealed that the mantle T_p was significantly higher, by 50–100 K or more, compared with the present-day maximum T_p of ~1,750 K (refs [31–33]). Komatiitic lavas, which are generated from hotter mantle plumes, also point to a significantly hotter mantle temperature in the past. The shallow temperature profile was also different during the Archaean. The internal heat production was twice to four times that of today[34], which favours a steeper temperature profile in the lithosphere. Other effects instead favour a thicker lithosphere: (1) the early Earth initially operated in a regime dominated by a stagnant lid, with only episodic subduction of ageing plates[35] and (2) the transport of heat to the surface could have been dominated by intense volcanism, which plays a heat-pipe role[36]. Altogether, it was modelled that the early temperature profile in the shallow mantle could have lain in between the steeper oceanic and milder continental profiles[37] (Fig. 4 and Supplementary Fig. 1).

According to our results, an increase in the T_p of the ambient mantle above 1,800–1,850 K should generate a partially molten layer within the upper mantle (Fig. 4). Comparable slopes between the mantle solidus and the adiabatic gradient at depths greater than 200–250 km make $T_p \approx 1{,}900$ K a maximum value before intensive melting occurs in the entire upper mantle. It is actually possible that the value of $T_p = 1{,}900$ K was reached just after crystallization of the early magma ocean; a higher T_p would be associated with high F values, which implies a low viscosity that favours a rapid mantle cooling[38]. Our discussion does not include the role of volatile elements (H_2O and CO_2), because their concentrations in the early mantle remain poorly constrained. Their presence is expected to decrease the mantle solidus and favour mantle melting, possibly at T_p values significantly lower than 1,900 K. A partially molten layer could remain stable for long geological ages, because melts can be neutrally buoyant at mantle depths within a couple of hundred kilometres above the 410 km mantle discontinuity[39,40].

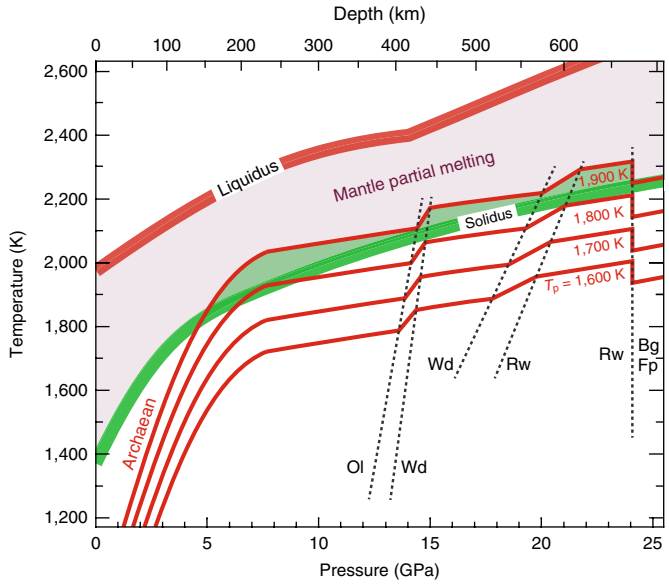

Fig. 4 | Partial melting in the early mantle. The current adiabatic profile of the mantle corresponds to a surface T_p between 1,600 K and up to 1,750 K (Supplementary Fig. 1). At the Archaean-to-Proterozoic transition, T_p was significantly higher, at 1,800–1,850 K (ref. [31]). For a T_p even higher than 1,800–1,850 K, a large part of the upper mantle should be partially molten. The transition between the younger, relatively hot and largely molten mantle and the older, colder and less molten mantle could have played a major role in the change of mantle dynamics at the transition. Ol, olivine; Wd, wadsleyite; Rw, ringwoodite; Bg, bridgmanite; Fp, ferropericlase.

Mantle changes at the Archaean-to-Proterozoic transition

The Archaean-to-Proterozoic transition is associated with major changes in the mantle dynamics with a progressive establishment of modern plate tectonics[32,35]. An increasing number of arc signatures in greenstone belts younger than 3.5 Ga suggests that slab subduction became a more-common process after this transition. This global change could be correlated to a transition in the upper-mantle mechanical properties. Indeed, it was shown that the coupling strength between tectonic plates and the underlying mantle is inversely proportional to the viscosity at the lithosphere–asthenosphere interface[41–43]. A hotter mantle during the Archaean would favour the formation of a partially molten layer and the mechanical weakening at a mid-upper-mantle depth. In addition, shear deformation can produce laminated lithologies and aligned melt accumulations, with further weakening[44]. Therefore, the presence of a partially molten layer could have favoured the early geodynamic regime dominated by a stagnant lid.

With secular mantle cooling, the degree of partial melting in the upper mantle eventually decreased. At one point, the state of the upper mantle became comparable to the present-day situation, in which partial melting still takes place, but at relatively low F values[22]. The decrease of F below a certain threshold value should be associated with a mechanical hardening, which favours mechanical coupling at the lithosphere–asthenosphere interface. This transition could have induced the change of geodynamic regime at the Archaean-to-Proterozoic transition.

Methods

Methods, including statements of data availability and any associated accession codes and references, are available at https://doi.org/10.1038/s41561-017-0053-9.

Received: 26 June 2017; Accepted: 13 December 2017;
Published online: 22 January 2018

References

1. Solomatov, V. S. in *Treatise on Geophysics* Vol. 9 (ed. G. Schubert) 81–104 (Elsevier, Amsterdam, 2015).
2. Romanowicz, B. A global tomographic model of the shear attenuation in the upper mantle. *J. Geophys. Res. Solid Earth* **100**, 12375–12394 (1995).
3. Tauzin, B., Debayle, E. & Wittlinger, G. Seismic evidence for a global low-velocity layer within the Earth's upper mantle. *Nat. Geosci.* **3**, 718–721 (2010).
4. Lay, T., Garnero, E. J. & Williams, Q. Partial melting in a thermo-chemical boundary layer at the base of the mantle. *Phys. Earth Planet. Inter.* **146**, 441–467 (2004).
5. Ferot, A. & Bolfan-Casanova, N. Water storage capacity in olivine and pyroxene to 14 GPa: implications for the water content of the Earth's upper mantle and nature of seismic discontinuities. *Earth Planet. Sci. Lett.* **349**, 218–230 (2012).
6. Aubaud, C., Hauri, E. H. & Hirschmann, M. M. Hydrogen partition coefficients between nominally anhydrous minerals and basaltic melts. *Geophys. Res. Lett.* **31**, L20611 (2004).
7. Herzberg, C., Raterron, P. & Zhang, J. New experimental observations on the anhydrous solidus for peridotite KLB-1. *Geochem. Geophys. Geosyst.* **1**, 1051 (2000).
8. Iwamori, H., McKenzie, D. & Takahashi, E. Melt generation by isentropic mantle upwelling. *Earth Planet. Sci. Lett.* **134**, 253–266 (1995).
9. Trønnes, R. G. & Frost, D. J. Peridotite melting and mineral–melt partitioning of major and minor elements at 22–24.5 GPa. *Earth Planet. Sci. Lett.* **197**, 117–131 (2002).
10. Walter, M. J. Melting of garnet peridotite and the origin of komatiite and depleted lithosphere. *J. Petrol.* **39**, 29–60 (1998).
11. Agee, C. B., Li, J., Shannon, M. C. & Circone, S. Pressure–temperature phase-diagram for the Allende meteorite. *J. Geophys. Res. Solid Earth* **100**, 17725–17740 (1995).
12. Litasov, K. & Ohtani, E. Phase relations and melt compositions in CMAS–pyrolite–H_2O system up to 25 GPa. *Phys. Earth Planet. Inter.* **134**, 105–127 (2002).
13. Katsura, T., Yoneda, A., Yamazaki, D., Yoshino, T. & Ito, E. Adiabatic temperature profile in the mantle. *Phys. Earth Planet. Inter.* **183**, 212–218 (2010).
14. Laporte, D., Toplis, M. J., Seyler, M. & Devidal, J. L. A new experimental technique for extracting liquids from peridotite at very low degrees of melting: application to partial melting of depleted peridotite. *Contrib. Mineral. Petrol.* **146**, 463–484 (2004).
15. Sifre, D. et al. Electrical conductivity during incipient melting in the oceanic low-velocity zone. *Nature* **509**, 81–85 (2014).
16. Sato, H. & Ida, Y. Low frequency electrical impedance of partially molten gabbro: the effect of melt geometry on electrical properties. *Tectonophysics* **107**, 105–134 (1984).
17. Partzsch, G. M., Schilling, F. R. & Arndt, J. The influence of partial melting on the electrical behavior of crustal rocks: laboratory examinations, model calculations and geological interpretations. *Tectonophysics* **317**, 189–203 (2000).
18. Maumus, J., Bagdassarov, N. & Schmeling, H. Electrical conductivity and partial melting of mafic rocks under pressure. *Geochim. Cosmochim. Acta* **69**, 4703–4718 (2005).
19. Andrault, D. et al. Melting of subducted basalt at the core–mantle boundary. *Science* **344**, 892–895 (2014).
20. Davis, F. A., Hirschmann, M. M. & Humayun, M. The composition of the incipient partial melt of garnet peridotite at 3 GPa and the origin of OIB. *Earth Planet. Sci. Lett.* **308**, 380–390 (2011).
21. Yoshino, T., Laumonier, M., McIsaac, E. & Katsura, T. Electrical conductivity of basaltic and carbonatite melt-bearing peridotites at high pressures: implications for melt distribution and melt fraction in the upper mantle. *Earth Planet. Sci. Lett.* **295**, 593–602 (2010).
22. Chantel, J. et al. Experimental evidence supports mantle partial melting in the asthenosphere. *Sci. Adv.* **2**, e1600246 (2016).
23. Hirschmann, M. M. Mantle solidus: experimental constraints and the effects of peridotite composition. *Geochem. Geophys. Geosyst.* **1**, C000070 (2000).
24. Simon, F. & Glatzel, G. Fusion–pressure curve. *Z. Anorg. Allg. Chem.* **178**, 309–316 (1929).
25. Zhang, J. & Herzberg, C. Melting experiments on anhydrous peridotite KLB-1 from 5.0 to 22.5 GPa. *J. Geophys. Res.* **99**, 17729–17742 (1994).
26. Hirose, K. & Kushiro, I. Partial melting of dry peridotite at high-pressures—determination of compositions of melts segregated from peridotite using aggregates of diamonds. *Earth Planet. Sci. Lett.* **114**, 477–489 (1993).

27. Béjina, F., Jaoul, O. & Liebermann, R. C. Diffusion in minerals at high pressure: a review. *Phys. Earth Planet. Inter.* **139**, 3–20 (2003).
28. Hirschmann, M. M., Asimow, P. D., Ghiorso, M. S. & Stolper, E. M. Calculation of peridotite partial melting from thermodynamic models of minerals and melts. III. Controls on isobaric melt production and the effect of water on melt production. *J. Petrol.* **40**, 831–851 (1999).
29. Dalton, C. A., Langmuir, C. H. & Gale, A. Geophysical and geochemical evidence for deep temperature variations beneath mid-ocean ridges. *Science* **344**, 80–83 (2014).
30. Litasov, K. D., Shatskiy, A. & Ohtani, E. Melting and subsolidus phase relations in peridotite and eclogite systems with reduced C–O–H fluid at 3–16 GPa. *Earth Planet. Sci. Lett.* **391**, 87–99 (2014).
31. Herzberg, C., Condie, K. & Korenaga, J. Thermal history of the Earth and its petrological expression. *Earth Planet. Sci. Lett.* **292**, 79–88 (2010).
32. Kamber, B. S. The evolving nature of terrestrial crust from the Hadean, through the Archaean, into the Proterozoic. *Precambrian Res.* **258**, 48–82 (2015).
33. Arndt, J., Barnes, S. J. & Lesher, C. M. *Komatiite* (Cambridge Univ. Press, Cambridge, 2008).
34. Korenaga, J. Initiation and evolution of plate tectonics on Earth: theories and observations. *Annu. Rev. Earth Planet. Sci.* **41**, 117–151 (2013).
35. van Hunen, J. & Moyen, J.-F. in *Annual Review of Earth and Planetary Sciences* Vol. 40 (ed. R. Jeanloz) 195–219 (Annual Reviews, Palo Alto, CA, 2012).
36. Moore, W. B. & Webb, A. A. G. Heat-pipe Earth. *Nature* **501**, 501–505 (2013).
37. Michaut, C. & Jaupart, C. Secular cooling and thermal structure of continental lithosphere. *Earth Planet. Sci. Lett.* **257**, 83–96 (2007).
38. Monteux, J., Andrault, D. & Samuel, H. On the cooling of a deep terrestrial magma ocean. *Earth Planet. Sci. Lett.* **448**, 140–149 (2016).
39. Matsukage, K. N., Jing, Z. C. & Karato, S. Density of hydrous silicate melt at the conditions of Earth's deep upper mantle. *Nature* **438**, 488–491 (2005).
40. Sakamaki, T., Suzuki, A. & Ohtani, E. Stability of hydrous melt at the base of the Earth's upper mantle. *Nature* **439**, 192–194 (2006).
41. Sizova, E., Gerya, T., Brown, M. & Perchuk, L. L. Subduction styles in the Precambrian: insight from numerical experiments. *Lithos* **116**, 209–229 (2010).
42. Foley, B. J., Bercovici, D. & Elkins-Tanton, L. T. Initiation of plate tectonics from post-magma ocean thermochemical convection. *J. Geophys. Res. Solid Earth* **119**, 8538–8561 (2014).
43. Doglioni, C., Ismail-Zadeh, A., Panza, G. & Riguzzi, F. Lithosphere–asthenosphere viscosity contrast and decoupling. *Phys. Earth Planet. Inter.* **189**, 1–8 (2011).
44. Jin, Z. M., Green, H. W. & Zhou, Y. Melt topology in partially molten mantle peridotite during ductile deformation. *Nature* **372**, 164–167 (1994).

Acknowledgements

We thank A. Bouhifd, N. Cayzer, M. Guitreau, T. Kawamoto, T. Komabayashi, D. Laporte, M. Laumonier, H. Martin, S. Parman, B. Reynard and F. Schiavi for help and fruitful discussions. This work was supported by the French National Research Agency (ANR) contract 'OxyDeep'. This research was financed by the French Government Laboratory of Excellence initiative no. ANR-10-LABX-0006, the Région Auvergne and the European Regional Development Fund. This is Laboratory of Excellence ClerVolc contribution number 279.

Author Contributions

L.H. and G.P. synthesized the glass starting material. G.P. and G.M. performed the EC measurements. G.P., D.A., G.M., N.B.C., D.N., N.G. and A.K. performed the X-ray diffraction measurements, which were subsequently treated by D.A. G.P. and N.B.C. determined the water content in samples using infrared spectroscopy. D.A. wrote the manuscript with help from G.P., G.M. and J.M. All of the authors discussed and commented on various versions of the manuscript.

Additional information

Supplementary information is available for this paper at https://doi.org/10.1038/s41561-017-0053-9.

Reprints and permissions information is available at www.nature.com/reprints.

Correspondence and requests for materials should be addressed to D.A.

Methods

Preparation of starting material. Our sample consisted of a mixture of oxides with the composition of the chondritic mantle after core segregation (Supplementary Table 1). We selected this composition because it could represent well both the early Earth's mantle and the deep mantle today. Our composition includes the minor elements Ti, Cr and Na, in addition to the major Si, Mg, Al, Fe and Ca elements. This is an important difference with some previous works based on simplified composition (for example, the CMAS composition[12]). No trace elements were added, as their effect on the solidus is negligible as long as their solubility limit in solid phases is not exceeded[45].

Under upper-mantle *P*–*T* conditions, we expect the sample mineralogy dominated, on the one hand, by olivine and its high-pressure polymorphs (wadsleyite (Wd) and ringwoodite (Rw)) and, on the other hand, a variable amount of pyroxenes and majoritic garnet. In our experiments, these lithologies were confirmed by in situ X-ray diffraction (see below). Final-phase fractions may be slightly different than those present in the mantle, first because the true mantle composition remains relatively open and second because of potential chemical heterogeneities. The chemical activities of the major and minor elements should not be largely different if the model composition changes between peridotite, pyrolite or chondritic-type materials. Therefore, these compositions should present similar solidus temperatures.

The mixture of oxides was ground in an agate mortar for approximately 1 h to ensure a homogeneous powder. Then, glass spheres of ~2.5 mm in diameter were prepared using the high-temperature aerodynamic levitation technique associated with CO_2 laser heating at CNRS[46]. This containerless method uses a conical nozzle that enables the diffusion of a regulated gas flow below the sample, which eliminates completely any contact between the sample and the container. In this process, the powder is first cold-pressed under a load of 6 tons. Weighted pieces of the recovered agglomerate are then melted at a temperature above 2,273 K, which gives a spherical shape to the sample. After a couple of minutes, samples were quenched to room temperature with a typical cooling rate of 500 K s^{-1}. The gas used for the sample levitation was pure Ar, with less than 0.05 ppm of oxygen; however, the vessel remained open to air during the synthesis at high temperature. This prevents the formation of metallic Fe at very high temperatures when using a reduced atmosphere.

For each experiment, an initial sphere of glass 2–3 mm in diameter was reshaped in the form of a cylinder and directly inserted into the capsule of the high-pressure assembly. Such a starting material provides consistent advantages when performing studies of the melting behaviour. First, the amount of moisture adsorbed at the sample surface is drastically reduced compared with that adsorbed by a powder (Supplementary Fig. 2). Second, the glass presents an ideal chemical homogeneity (as confirmed by electron microprobe analyses) compared with the intrinsic heterogeneities typical of mixtures of oxide powders.

Determination of the water content in our samples. Infrared spectroscopy was performed to determine the H_2O content in our samples before and after the melting experiment. Infrared spectra were measured in air on double-polished sections with thicknesses of 600 µm (for the glass starting material) or 900 µm (for the recovered samples). Spectra were collected between 700 and 7,000 cm^{-1} with 2 cm^{-1} steps and 300 scans for the sample and 100 scans for the background. In the starting glass, we measured less than 1 ppm wt H_2O, which indicates a starting material nominally dry. For samples recovered from high-pressure–high-temperature conditions, the grain size was significantly smaller (Fig. 2) than the infrared beam. We performed several measurements within the same sample, which appeared to be consistent with each other. From the broad asymmetric band centred at 3,500 cm^{-1} and the OH peaks related to point defects in olivine[5] at 3,572, 3,527 and 3,357 cm^{-1}, we calculate a H_2O content of ~90 ppm (Supplementary Fig. 2). These observations confirm that the H_2O contamination remained very limited during the melting experiments. The sample H_2O content on melting is critical because the presence of volatile elements can induce a significant decrease in the melting temperature. Still, due to the presence of 90 ppm water in our samples, we corrected all experimental solidus temperatures by +35 to +55 K, based on the previously reported cryoscopic relation[47] (Supplementary Table 2).

EC measurements. We measured the EC of our samples up to their melting point in a 1,500-ton 6-8 split cylinder Kawai-type multi-anvil apparatus at the Laboratory of Magmas and Volcanoes in Clermont-Ferrand. Quasi-hydrostatic pressures of 5 or 20 GPa were obtained using eight tungsten–carbide cubic anvils with edges truncated to 11 or 4 mm, respectively (Supplementary Figs. 3 and 4). We used an octahedral pressure medium with an edge length of 18 or 10 mm made of semisintered MgO with 5% Cr_2O_3. The pressure calibration for these assemblages has an uncertainty of ~0.5 GPa (ref. [48]). The heater was made of a 50 µm thick Re foil folded into a cylindrical shape and inserted in the ZrO_2 sleeve, which served as a thermal insulator. We applied an alternating current with a frequency of 100 Hz to generate temperatures up to more than 2,500 K. A cylindrical sleeve of MgO was inserted between the heater and the sample to prevent chemical reactions with the Re heater, ensure electrical insulation of the sample and maintain the sample shape on melting.

Temperatures were measured using type C thermocouple ($WRe_{5\%}$–$WRe_{26\%}$). We added a third $WRe_{5\%}$ wire to the opposite side of the cylindrical sample to allow measurements of the sample impedance. Two Re discs were placed on the top and bottom of the cylindrical sample. The discs served as electrodes for EC measurements. As the determination of temperature gradients is essential in this work, we modelled thermal gradients in the cell assembly based on a finite-element method[49] for thermocouple temperatures between 1,473 and 2,273 K (Supplementary Fig. 3b). As expected, the hottest part is found at the centre of the sample (extreme top-left position in Supplementary Fig. 3b). Each temperature contour (thin black lines) represents a temperature interval of 50 K in Supplementary Fig. 3b. In all the simulations, the temperature difference (ΔT_{Simul}) between the sample centre and the thermocouple does not exceed 100 K. We therefore apply a temperature correction of ΔT_{Simul} to all our temperature measurements (Supplementary Table 2).

The sample EC was determined using the impedance spectroscopy method in the frequency range of 10^6 to 10^1 Hz (ref. [50]) (Supplementary Fig. 4). The insulation resistance (detection limit) of the assembly was determined at similar pressure–temperature conditions prior to the actual experiments. Polycrystalline samples are characterized by a combination of resister and constant-phase element (R-C/CPE) circuits and the resistance can be obtained by fitting the impedance spectra to appropriate equivalent circuits. Once the sample resistance has been determined, conductivity can be calculated using the sample diameter and length measured after each experiment, assuming the sample geometry remains unchanged during the experiment. The activation enthalpy (ΔH) of each conduction mechanism can be obtained by fitting data to the Arrhenius equation, where σ is the EC (S m^{-1}), T is the absolute temperature, σ_0 is the pre-exponential factor (S m^{-1}) and k is the Boltzmann constant (J K^{-1}):

$$\sigma = \sigma_0 \, e^{(-\Delta H/kT)}$$

For each experiment, we performed a series of heating and cooling cycles, similar to those in previous works[51] (Supplementary Fig. 5a). In a first heating cycle, below 573 K, a low activation enthalpy is likely to result from an extrinsic mechanism associated with the presence of free protons (adsorbed moisture, mostly around the sample). At the desired pressure, a sample was kept at 573 K for more than 12 h. While maintaining 573 K, the electrical resistance of the sample was measured along regular intervals and the next heating cycle started once the sample resistance reached a steady value, which is often 1–2 orders of magnitude higher than the resistance measured at the beginning of the heating cycle. This crucial step ensures the removal of the absorbed moisture from the sample and the surrounding assembly materials. The absorbed moisture could otherwise interfere with measurements at higher temperatures.

The crystallization of our samples was observed between 1,370 and 1,570 K, thus at temperatures at least 300 K below the solidus temperature (Supplementary Table 2). The temperature was kept constant above the crystallization temperature for 2–3 h to allow full crystallization of the initial glass samples. The EC of the crystalline samples was measured in several heating and cooling cycles until the heating and cooling paths were reproducible.

The crystallized samples show an activation energy of 1.02 eV (Fig. 1, green line). This is typical of a conduction mechanism with electron hole hopping between Fe^{2+} and Fe^{3+} (small polaron conduction)[50]. At a temperature of ~1,700 K for a nominal pressure of 5 GPa, we observe a first-order change of slope in the conductivity profile (Fig. 1, blue line). The change of slope can be interpreted as the first occurrence of an interconnected partial melt. The experimental uncertainty for the determination of the solidus temperature is about ±25 degree. The errors associated with EC measurements were less than 5%, and were mainly associated with temperature estimations, data-fitting errors and the estimation of sample dimensions. A good reproducibility is observed for EC profiles obtained for our different samples (Supplementary Fig. 5b). Our EC results compare well with ECs of both solid minerals and melts reported in previous studies.

X-ray diffraction measurements. In situ X-ray diffraction experiments were performed using the 1,200-ton DIA-type multi-anvil apparatus installed at the PSICHE beamline of the SOLEIL synchrotron in Gif-sur-Yvette. Pressures up to 28 GPa (Supplementary Table 2) were generated using a 7/3 multi-anvil assembly configuration. We used 14 mm WC cubes as secondary anvils (Supplementary Fig. 6). Similar to EC measurements, we used semisintered MgO with a 5% Cr_2O_3 octahedron pressure media and a cylindrical ZrO_2 sleeve in which a 50 µm thick Re-foil heater was inserted. The cylindrical sample of chondritic glass was inserted into an MgO capsule. The Re furnace was oriented horizontally to allow an X-ray beam path parallel to the Re tube. To apply electrical power, two Re electrodes were placed in contact with the furnace. Temperature was measured using a W/Re thermocouple that touched the Re furnace. The thermocouple signal was filtered to remove the common electrical mode at 100 Hz. We used alternatively gaskets made of pyrophilite or a mixture of boron and epoxy. The sample pressure was determined based on the pressure–volume–temperature equation of state of MgO of its capsule, with an accuracy of ~0.5 GPa.

At PSICHE, an under-vacuum wiggler produces a white X-ray beam with energy range from 20 to more than 80 keV. The X-ray beam is focused vertically

between the anvil gap of the multi-anvil apparatus using a horizontal mirror located at 18.5 m from the source and 4 m from the sample. The resulting vertical full-width at half-maximum of the beam at the sample position is approximately 20 µm, which corresponds to almost a one order of magnitude flux gain compared with the unfocused beam. The beam is then collimated horizontally to a typical width of 50 µm. Two different modes were used: (1) samples were first aligned in the beam using X-ray radiography, for which the press was scanned vertically in the X-ray beam and the image was then reconstructed numerically (Supplementary Fig. 6c), and (2) diffraction was performed in an energy-dispersive mode using a Caesar-type diffractometer[52]. A best resolution in interplanar distance d_{hkl} is achieved when the diffracted X-ray beam is collimated horizontally to ~50 µm by two slit systems located after the sample. A typical diffraction 2θ angle of 8.0° is convenient to register the major diffraction lines of our silicate samples. The resolution in diffraction angle is about 10^{-3} degrees.

On heating, the sample temperature was kept at 700 K for several minutes to remove the adsorbed moisture in the transmitting media. This procedure also mimics the experimental procedure followed for EC measurements. We then increased the temperature until sample crystallization was observed, based on a clear evolution of X-ray diffraction (Supplementary Table 2). At this point, we wait several minutes to finalize the grain growth until no significant change with time was observed on the diffraction pattern. At temperatures below the solidus, the absence of melt prevents the atomic diffusion required for additional grain growth in such a multiphasic system (that is, the Ostwald ripening effect[53] (Fig. 3)).

For each phase, relative intensities between different diffraction peaks follow quite well those theoretically expected based on the atomic packing in the unit-cell lattice (Supplementary Fig. 6). Such an achievement is typical of very small grains in a sample free of stresses. Still, the use of the energy-dispersive X-ray diffraction technique (compared with the angle-dispersive one) prevents the refinement of phase fractions for the coexisting olivine (or its high-pressure polymorphs), garnet and pyroxenes phases present in our samples. In addition, the limited energy resolution of the Ge detector produces peaks that overlap and the identification of minor phases sometimes becomes difficult. In contrast, this method enables the acquisition of a decent X-ray-diffraction pattern every few seconds, which offers new criteria for the determination of the solidus temperature.

Analysis of recovered samples. Recovered samples were cut in two using a diamond-wire saw. A sample half was embedded in epoxy, polished to a mirror-like surface and coated with a thin layer of carbon using a low-vacuum sputter-coater machine. Textural and semiquantitative chemical analyses were performed using a JEOL JSM-5910 LV SEM equipped with a PGT microanalysis system at Laboratory of Magmas and Volcanoes and a Carl Zeiss SIGMA HD VP Field Emission SEM with an Oxford AZtec ED X-ray analysis operated at the University of Edinburgh. Textural analyses with a field-emission gun SEM were performed at a high accelerating voltage (15 kV) and a small working distance (6–10 mm). These conditions are ideal to detect small features in samples with a low degree of partial melting. For the semiquantitative analysis based on X-ray fluorescence, we instead used a working distance of 20 mm. Energy was also lowered to 5 kV to minimize the penetration of electrons in samples and, consequently, to optimize the spatial resolution.

Data availability. The data that support the findings of this study are available from the corresponding author on request.

References

45. Corgne, A., Liebske, C., Wood, B. J., Rubie, D. C. & Frost, D. J. Silicate perovskite-melt partitioning of trace elements and geochemical signature of a deep perovskitic reservoir. *Geochim. Cosmochim. Acta* **69**, 485–496 (2005).
46. Hennet, L. et al. Aerodynamic levitation and laser heating: applications at synchrotron and neutron sources. *Eur. Phys. J. Spec. Top.* **196**, 151–165 (2011).
47. Tenner, T. J. & Hirschmann, M. M. & Humayun, M. The effect of H_2O on partial melting of garnet peridotite at 3.5 GPa.*Geochem. Geophys. Geosyst.* **13**, Q03016 (2012).
48. Boujibar, A. et al. Metal–silicate partitioning of sulphur, new experimental and thermodynamic constraints on planetary accretion. *Earth Planet. Sci. Lett.* **391**, 42–54 (2014).
49. Hernlund, J., Leinenweber, K., Locke, D. & Tyburczy, J. A. A numerical model for steady-state temperature distributions in solid-medium high-pressure cell assemblies. *Am. Miner.* **91**, 295–305 (2006).
50. Yoshino, T. Laboratory electrical conductivity measurement of mantle minerals. *Surv. Geophys.* **31**, 163–206 (2010).
51. Manthilake, M. et al. Electrical conductivity of wadsleyite as a function of temperature and water content. *Phys. Earth Planet. Inter* **174**, 10–18 (2009).
52. Wang, Y. B. et al. A new technique for angle-dispersive powder diffraction using an energy-dispersive setup and synchrotron radiation. *J. Appl. Crystallogr.* **37**, 947–956 (2004).
53. Yamazaki, D., Kato, T., Ohtani, E. & Toriumi, M. Grain growth rates of $MgSiO_3$ perovskite and periclase under lower mantle conditions. *Science* **274**, 2052–2054 (1996).

Geochemical Perspectives Letters

Evidence for anorthositic crust formed on an inner solar system planetesimal

P. Frossard[1*], M. Boyet[1], A. Bouvier[2,3], T. Hammouda[1], J. Monteux[1]

OPEN ACCESS
doi: 10.7185/geochemlet.1921

Abstract

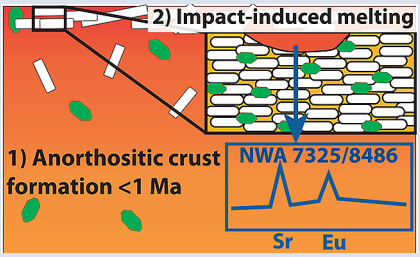

During the first million years of solar system history, planetesimals experienced extensive melting powered by the radioactive decay of ^{26}Al (Lee *et al.*, 1977). To date, the only known anorthositic crust on a solar system body is that of the Moon, formed by plagioclase flotation on top of the magma ocean (Wood *et al.*, 1970). Here we show evidence from the ungrouped achondrite meteorite Northwest Africa (NWA) 8486 that an anorthositic crust formed on a planetesimal very early in solar system history (<1.7 Ma). NWA 8486 displays the highest anomalies in Eu and Sr found in achondrites so far and, for the first time, this characteristic is also identified in clinopyroxene. Elemental modelling, together with calculated timescales for crystal settling, show that only the melting of an anorthosite can produce NWA 8486 within the first 5 million years of solar system history. Our results indicate that such a differentiation scenario was achievable over short timescales within the inner solar system, and must have contributed to the making and elemental budget of the terrestrial planets.

Received 18 March 2019 | Accepted 14 August 2019 | Published 7 October 2019

Introduction

Over 80 ungrouped achondrites have been found in the past 20 years, enriching our collections with new types of meteoritic samples. Northwest Africa (NWA) 8486 is one of several paired stones, along with the ungrouped achondrites NWA 7325 and 8014, that have been found in the Sahara desert (Ruzicka *et al.*, 2017). They are plagioclase-rich cumulative gabbros that experienced remelting and fast cooling (Yang *et al.*, 2019), with a very peculiar calcic and magnesian mineralogy. NWA 8486 formed under reduced conditions, with an oxygen fugacity (fO_2) of 3.2 log units below the iron-wüstite (IW) buffer (Sutton *et al.*, 2017), and therefore likely originates from the inner solar system. Based on Cr, Ti and O isotopic compositions, NWA 7325/8486 have affinities with both acapulcoite-lodranite and ureilite groups (Barrat *et al.*, 2015; Weber *et al.*, 2016; Goodrich *et al.*, 2017). The Pb-Pb isochron age of 4563.4 ± 2.6 Ma, Al–Mg age of 4563.09 ± 0.26 Ma and initial Mg isotopic composition for NWA 7325 indicate that the parent material of this meteorite had to be formed within 1-2 Myr after Solar System formation (Koefoed *et al.*, 2016).

Eu and Sr Anomalies in NWA 7325/8486

We investigated major and trace element composition of NWA 8486 through *in situ* and in solution analyses. The mineral compositions of NWA 8486 are consistent with those of NWA 7325 (Barrat *et al.*, 2015; Weber *et al.*, 2016; Goodrich *et al.*, 2017), with $An_{88.7\pm3.0}Ab_{11.2\pm3.0}$ plagioclase, $Wo_{45.4\pm0.5}En_{53.4\pm0.5}Fs_{1.2\pm0.1}$ clinopyroxene and $Fo_{97.1\pm0.3}$ olivine. The modal compositions reported for different fragments of NWA 7325 vary (Barrat *et al.*, 2015; Weber *et al.*, 2016; Goodrich *et al.*, 2017), illustrating the heterogeneous distribution of the minerals at the centimetre scale. The fragment of NWA 8486 studied here contains the highest pyroxene modal content at 52 %, the lowest plagioclase content at 44 %, with the remaining 4 % consisting of olivine, sulphides and metal. The range reported for NWA 7325 is 30-44 % for pyroxene, 54-60 % for plagioclase and 2-15 % for olivine (Barrat *et al.*, 2015; Weber *et al.*, 2016; Goodrich *et al.*, 2017).

We report trace element abundances in mineral (plagioclase, pyroxene and olivine) and a whole rock powder of NWA 8486. Minerals were analysed either *in situ* or in solution after mechanical separation (Supplementary Information). The whole rock composition slightly differs from that of NWA 7325 from Barrat *et al.* (2015) as a consequence of different modal compositions (Fig. 1). Incompatible and moderately volatile elements are depleted in this meteorite, below 0.5 × CI chondrites for the whole rock with the exceptions of Eu and Sr. Positive Eu and Sr anomalies (Eu/Eu* and Sr/Sr*) are present in each mineral phase with different magnitudes, from 1.8 to 6.5 in pyroxene and 450 to 1039 in plagioclase (Supplementary Information). Their amplitude in the whole rock is much higher than that measured in lunar anorthosites (Fig. 1).

1. Université Clermont Auvergne, CNRS, IRD, OPGC, Laboratoire Magmas et Volcans, F-63000 Clermont-Ferrand, France
2. Department of Earth Sciences, Centre for Planetary Science and Exploration, University of Western Ontario, Ontario, Canada
3. Bayerisches Geoinstitut, Universität Bayreuth, Germany
* Corresponding author (email: paul.frossard@uca.fr)

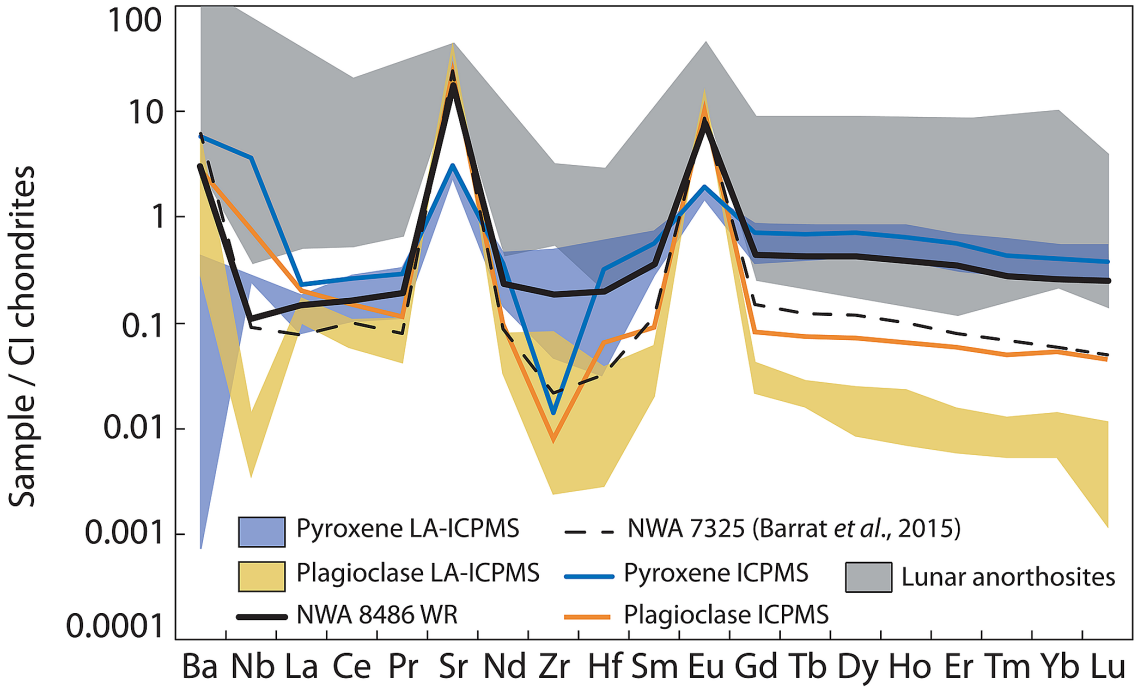

Figure 1 Trace element composition of NWA 8486 normalised to CI chondrites (Anders and Grevesse, 1989). All fractions exhibit Eu and Sr positive anomalies. NWA 7325 has a lower content for most incompatible elements compared to NWA 8486 owing to its modal enrichment in plagioclase. Lunar anorthosites are reported for comparison (data from Haskin *et al.*, 1973 and Norman *et al.*, 2003).

Europium changes valence in a continuum from a 3+ state to a 2+ state around the IW buffer (where $Eu^{3+}/\Sigma Eu = 0.5$) and in these conditions plagioclase preferentially incorporates Eu^{2+} in its lattice, resulting in an enrichment in Eu over the other trivalent rare earth elements (REE^{3+}). The similar plagioclase/melt partition coefficients of Sr^{2+} and Eu^{2+} arise from very close ionic radii. NWA 7325/8486 formed within an fO_2 of IW-3.2 ± 0.2, which is more reduced than for lunar rocks that formed in a range of IW-2 to IW (Wadhwa, 2008; Sutton *et al.*, 2017). Despite their higher fO_2, lunar anorthosite plagioclases show similar Eu anomalies to reduced meteorites (Fig. S-4). Thus, even considering variations due to parental melt composition, there should be little difference between NWA 8486 and lunar anorthosite plagioclase compositions if they were formed under similar conditions. Although positive Eu and Sr anomalies are common in plagioclase, the present data are the first report of positive Eu and Sr anomalies in clinopyroxene in an achondritic meteorite. Europium partitioning in clinopyroxene changes depending on the composition of the system with Eu^{2+} being either similarly or less compatible than Eu^{3+} (Karner *et al.*, 2010). Therefore, the peculiar trace element inventory of NWA 8486 cannot be solely attributed to redox conditions.

Anorthosites as Source Rocks of NWA 7325/8486

NWA 8486 stands out as a unique meteorite when compared to the composition of other achondrites and lunar anorthosites. Pyroxene, plagioclase and whole rock data from all known types of achondrites define separate fields in an Eu_N/Sm_N *versus* Sr_N/Nd_N diagram (with $_N$ indicating concentrations normalised to corresponding CI chondrite abundances) (Fig. 2). The composition for NWA 8486 is shifted towards both higher Eu_N/Sm_N and Sr_N/Nd_N ratios compared to other planetary compositions. The rare felsic (Si-rich, evolved) achondrites GRA 06128/9 and Almahata Sitta (ALM-A clast) do not appear any different from other achondrites in terms of Eu and Sr enrichments. Early occurrences of such felsic rocks have been related to partial melting of chondritic material instead of the multi-stage processes involved to form felsic crust on Earth (Day *et al.*, 2009; Bischoff *et al.*, 2014). Therefore, the particular composition of NWA 7325/8486 must be related to the melting of a specific source which was already enriched in Eu (relative to other REEs) and Sr. Barrat *et al.* (2015) suggested that impact melting of a gabbroic crust might produce such anomalies. In view of a homogeneous distribution of ^{26}Al in the solar system, Barrat *et al.* (2015) and Koefoed *et al.* (2016) calculated that the differentiation event for NWA 7325's parent body was ~1-2 Myr after formation of the solar system, while its crystallisation (from Pb-Pb chronometry) occurred within about 3 Myr after that. Considering the diopside-anorthite binary system at 1 atm (Osborn, 1942), the source of NWA 7325/8486 parent melt needs to be already enriched in plagioclase to reach the high plagioclase modal compositions for the meteorite, at least 48 % plagioclase to match NWA 8486. The modal composition of NWA 8486 lies on the eutectic point of the diagram. Thus, basaltic sources with low plagioclase content can produce eutectic compositions, but higher anorthite modes cannot be reached. We performed melting models of varied compositions and compared the compositions of these liquids with those in equilibrium with NWA 8486 minerals (Supplementary Information). The enrichment in Eu and the general depletion of incompatible elements are not reproduced with cumulate eucrite (Moore County) compositions (Fig. 3). The only possibility found to produce a parental magma enriched in both Eu and Sr is melting of a plagioclase-, Mg- and Ca-rich rock. Low degree melting (below 5 %) of an anorthosite (98 % anorthite) produces liquids corresponding to NWA 7325/8486 modes, but does not yield both high enough Eu anomalies and REE depletion. However, a higher pyroxene content can produce a larger amount of melt of eutectic composition. NWA 8486 features can be reproduced by 20-50 % melting of a pyroxene-rich anorthosite (Apollo noritic anorthosite 62236 with 20 % pyroxene) (Fig. 3). Anorthosites are therefore the most likely source for the parental magma of the NWA 7325/8486 suite.

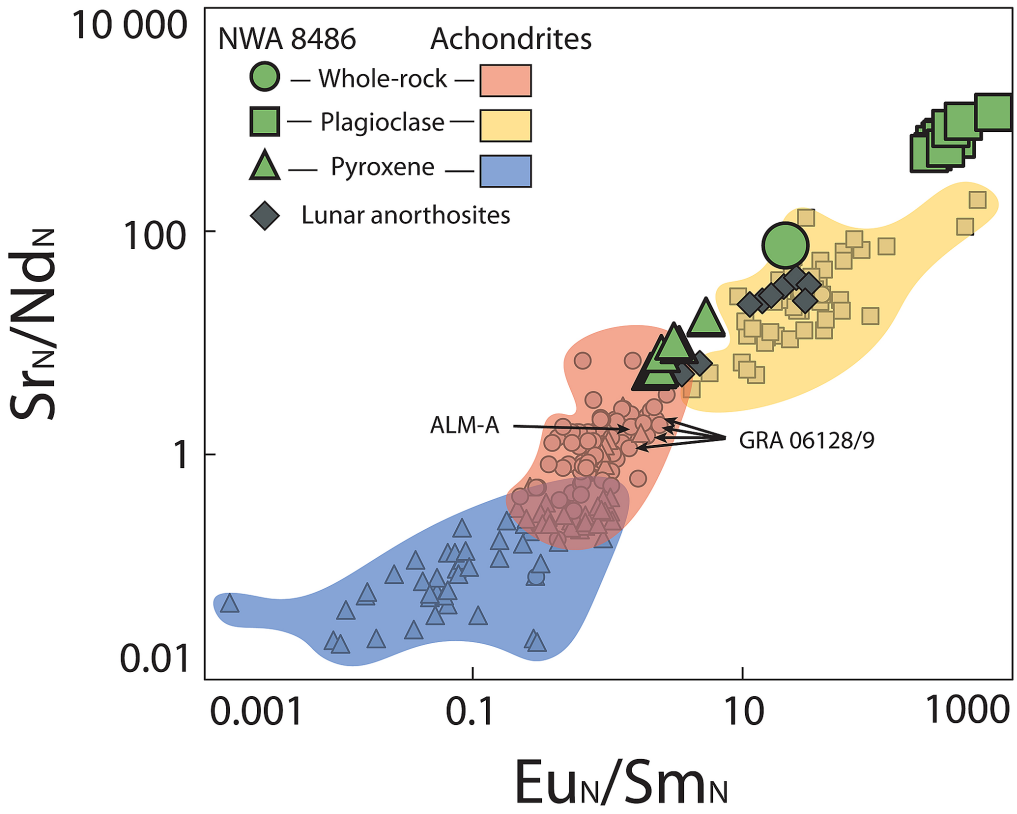

Figure 2 Eu/Sm and Sr/Nd ratios of achondrites and NWA 8486 normalised to CI chondrites (Anders and Grevesse, 1989). Overlap between the different fields is due to whole rocks mainly composed of pyroxene or plagioclase (*e.g.*, aubrites, ureilites, lunar anorthosites). For each field group, NWA 8486 exhibits higher Eu_N/Sm_N and Sr_N/Nd_N. Only lunar anorthosites are similar to NWA 8486 whole rock, but they contain much more plagioclase than NWA 8486. See Supplementary Information for data sources.

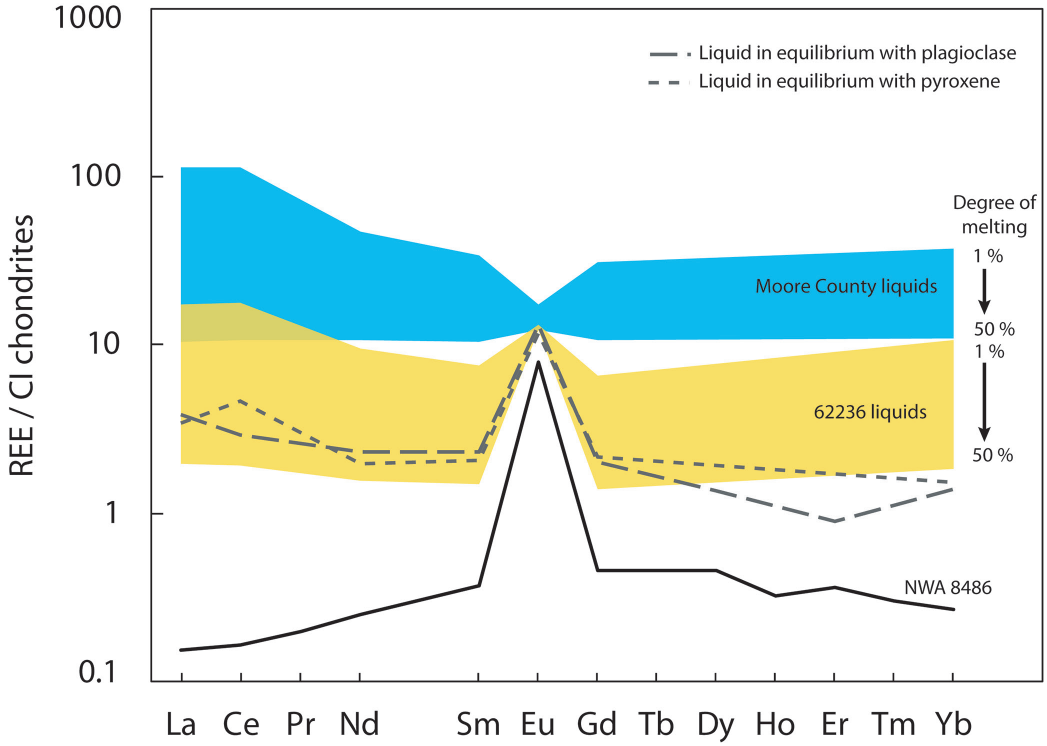

Figure 3 REE composition of liquids in equilibrium with NWA 8486 minerals (in grey dashed lines) compared to liquids modelled with compositions of the cumulate eucrite Moore County and the pyroxene-rich lunar anorthosite Apollo 62236, normalised to CI chondrites (Anders and Grevesse, 1989). A non-modal melting is considered, in agreement with petrological constraints, of eutectic proportions of 42 % plagioclase and 58 % pyroxene (Osborn, 1942). The range of composition of the liquids from 1 % to 50 % degree of melting is represented for each source composition. NWA 8486 whole rock composition is shown (black line) for comparison. See Supplementary Information for details on the model.

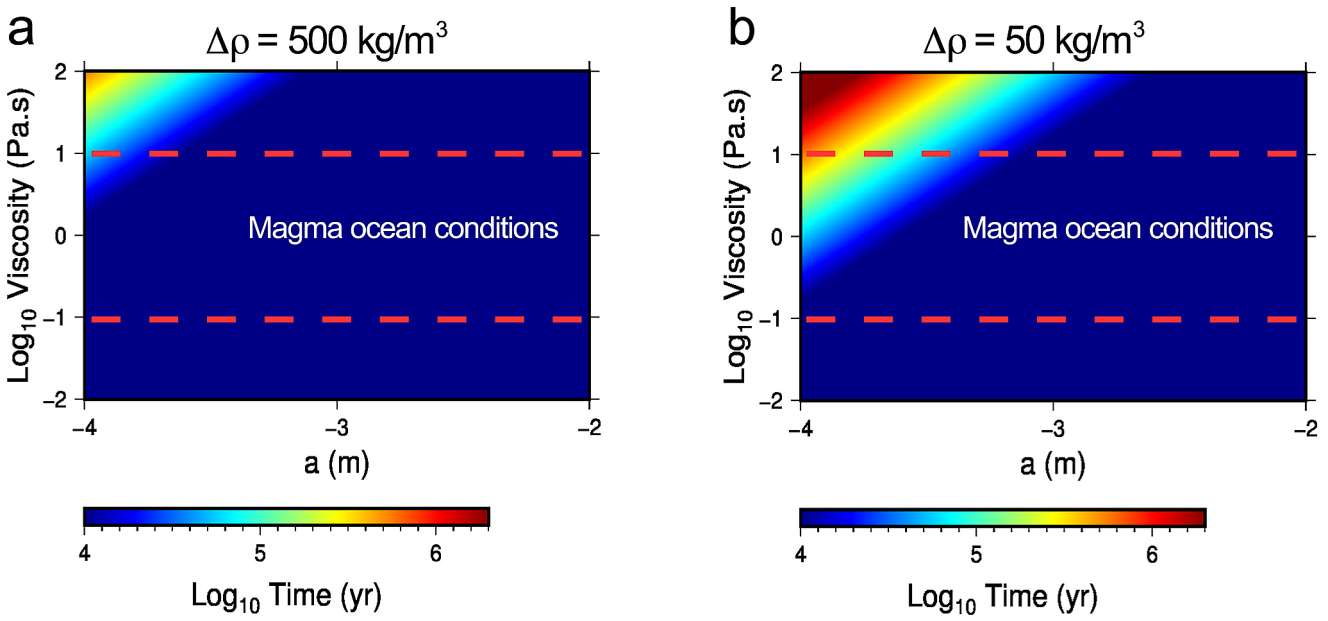

Figure 4 Time for plagioclase crystal ascent during the late stage of a magma ocean. This time is calculated for a range of viscosities (0.1 to 10 Pa.*s*), crystal diameters (a; 100 µm to 1 cm) and density contrasts (Δρ; 50 to 500 kg/m^3) between the crystal and the liquid phase. The time for a crystal to reach the surface of the magma ocean is represented with a colour scale ranging between 10 kyr (blue) and 2 Myr (red). Both panels show that the time of ascent of the crystal is a few tens of thousands of years in magma ocean conditions, except for small crystals around 100 µm and high viscosities of >10 Pa.s for which time of ascent is longer.

Timescales of Anorthosite Formation on Early Solar System Planetesimals

Anorthosites are associated with large magma systems that experience fractional crystallisation, in which plagioclase floats at the surface. Lunar anorthosites are derived from a magma ocean (MO) that formed subsequently to the Moon-forming impact event, but their petrogenesis model is still debated. Specific conditions are required for anorthositic crust formation (Albarède and Blichert-Toft, 2007). The body needs to be rather dry, as plagioclase formation is delayed in presence of water and would appear late in the crystallisation sequence (Elkins-Tanton, 2008). The size of the planetary body is also important as plagioclase is stable up to 1 GPa, which corresponds to a depth of 75 km for a Mars-like body or 200 km for a Moon-like body (Albarède and Blichert-Toft, 2007). Studies on Mercury's MO have shown that in very reduced conditions anorthite is denser than the melt and then may not float (Brown and Elkins-Tanton, 2009; Vander Kaaden and McCubbin, 2015). Crystal settling that enables anorthositic crust formation may be hindered by highly turbulent convection on small parent bodies with low gravity. Nonetheless, some authors have suggested that crystal settling can occur in such environments (Taylor *et al.*, 1993; Elkins-Tanton, 2012).

Geochemical modelling indicates that the NWA 7325/8486 source was most likely an anorthosite. Although Mercury may not be an analogue to NWA 7325/8486 parent body, it may represent an end member in terms of density and composition of the MO. Calculations have been carried out to constrain the timescales of formation of an anorthositic crust in a MO. The plagioclase formation occurs generally when the MO is crystallised by 70-80 vol. % (Supplementary Information). Assuming that the remaining molten material (≈20 vol. %) forms a buoyant layer over the solidified mantle and that 15 vol. % of the inner body is made of a metallic core, we can estimate the depth of the molten layer relative to the radius of the body (Supplementary Information). Considering that the rising velocity for plagioclase crystals in a MO scales with a Stokes' Law settling velocity (Martin and Nokes, 1989), the time for a plagioclase crystal to reach the surface in a shallow MO can be assessed. The calculation yields that for the MO viscosity range (10^{-1}-10^{1} Pa.s, Dygert *et al.*, 2017) and density contrasts between crystal and magma (50-500 kg/m^3, Brown and Elkins-Tanton, 2009; Dygert *et al.*, 2017), a crystal of at least 100 µm in diameter will reach the surface of the MO in a few tens of thousands of years (Fig. 4). The time of ascent of plagioclase is much smaller than the age of the first differentiation on NWA 7325/8486 estimated at 1.7 Ma using the ^{26}Al-^{26}Mg systematics (Koefoed *et al.*, 2016). Therefore, we believe that NWA 7325/8486 is the first evidence of the formation and re-processing of an anorthositic crust on a planetesimal very early in the solar system.

If anorthosite could form quickly on planetesimals and magma oceans were common in the first few million years of the solar system, where are the anorthosites in the meteorite record? The reason for the absence of anorthositic crusts on achondrite parent bodies probably lies in their thermal and chemical evolution. The conditions necessary for magma oceans to form with anorthositic crusts may have been limited by the time and place of accretion (Greenwood *et al.*, 2012). Inner solar system planetesimals that accreted early were enriched in ^{26}Al and were thus more likely to have experienced magma ocean conditions (Grimm and McSween Jr, 1993). Iron meteorites are evidence of these processes. Their parent bodies were rather small (20 to 200 km; Chabot and Haack, 2006) and possibly formed within the terrestrial accretion zone below 1 AU before being scattered into the main asteroid belt. Silicate layers from these bodies have a low probability of survival in the chaotic early inner solar system (Bottke *et al.*, 2006, O'Neill and Palme, 2008). It is likely, then, that anorthositic crusts were formed in the inner solar system but rarely preserved. Material from these planetesimal silicate layers could have been subsequently added to the accreting terrestrial planets, providing a non-chondritic source for refractory lithophile elements.

Acknowledgements

We thank Dr. L. Garvie (Center for Meteorite Studies, Arizona State University) for the loan of NWA 8486, J.-L. Devidal for assistance with electron microprobe and LA-ICP-MS analyses, and J.-M. Hénot for assistance with SEM analyses. We also thank T. Withers for comments and J.-A. Barrat for enriching discussions on geochemical modelling. Helen Williams is acknowledged for editorial handling and Addi Bischoff and Stephen Elardo for constructive and thorough reviews that greatly improved the manuscript. This project has received funding from the European Research Council (ERC) under the European Union's Horizon 2020 research and innovation program (Grant Agreement No 682778 – ISOREE to MB), and NSERC Discovery Grant, Canada Research Chair, and the Canada Foundation for Innovation JELF programs (to AB). This is Laboratory of Excellence ClerVolc contribution number 369.

Editor: Helen Williams

Additional Information

Supplementary Information accompanies this letter at http://www.geochemicalperspectivesletters.org/article1921.

Cite this letter as: Frossard, P., Boyet, M., Bouvier, A., Hammouda, T., Monteux, J. (2019) Evidence for anorthositic crust formed on an inner solar system planetesimal. *Geochem. Persp. Let.* 11, 28–32.

References

Albarède, F., Blichert-Toft, J. (2007) The split fate of the early Earth, Mars, Venus, and Moon. *Comptes Rendus Geosciences* 339, 917-927.

Anders, E., Grevesse, N. (1989) Abundances of the elements: Meteoritic and solar. *Geochimica et Cosmochimica Acta* 53, 197-214.

Barrat, J.-A., Greenwood, R.C., Verchovsky, A.B., Gillet, P., Bollinger, C., Langlade, J.A., Liorzou, C., Franchi, I.A. (2015) Crustal differentiation in the early solar system: Clues from the unique achondrite Northwest Africa 7325 (NWA 7325). *Geochimica et Cosmochimica Acta* 168, 280-292.

Bischoff, A., Horstmann, M., Barrat, J.-A., Chaussidon, M., Pack, A., Herwartz, D., Ward, D., Vollmer, C., Decker, S. (2014) Trachyandesitic volcanism in the early solar system. *Proceedings of the National Academy of Sciences* 111, 12689-12692.

Bottke, W.F., Nesvorný, D., Grimm, R.E., Morbidelli, A., O'Brien, D.P. (2006) Iron meteorites as remnants of planetesimals formed in the terrestrial planet region. *Nature* 439, 821-824.

Brown, S.M., Elkins-Tanton, L.T. (2009) Compositions of Mercury's earliest crust from magma ocean models. *Earth and Planetary Science Letters* 286, 446-455.

Chabot, N., Haack, H. (2006) Evolution of Asteroidal Cores. In: Lauretta, D.S., McSween Jr., H.Y. (Eds.) *Meteoritics and the Early Solar System II*. The University of Arizona Press, Tucson, 747-771.

Day, J.M., Ash, R.D., Liu, Y., Bellucci, J.J., Rumble III, D., McDonough, W.F., Walker, R.J., Taylor, L.A. (2009) Early formation of evolved asteroidal crust. *Nature* 457, 179-182.

Dygert, N., Lin, J., Marshall, E.W., Kono, Y., Gardner, J.E. (2017) A low viscosity lunar magma ocean forms a stratified anorthitic flotation crust with mafic poor and rich units. *Geophysical Research Letters* 44, 11,282-11,291.

Elkins-Tanton, L.T. (2008) Linked magma ocean solidification and atmospheric growth for Earth and Mars. *Earth and Planetary Science Letters* 271, 181-191.

Elkins-Tanton, L.T. (2012) Magma oceans in the inner solar system. *Annual Review of Earth and Planetary Science* 40, 113-139.

Goodrich, C.A., Kita, N.T., Yin, Q.-Z., Sanborn, M.E., Williams, C.D., Nakashima, D., Lane, M.D., Boyle, S. (2017) Petrogenesis and Provenance of Ungrouped Achondrite Northwest Africa 7325 from Petrology, Trace Elements, Oxygen, Chromium and Titanium Isotopes, and Mid-IR Spectroscopy. *Geochimica et Cosmochimica Acta* 203, 381-403.

Greenwood, R., Franchi, I., Gibson, J., Benedix, G. (2012) Oxygen isotope variation in primitive achondrites: The influence of primordial, asteroidal and terrestrial processes. *Geochimica et Cosmochimica Acta* 94, 146-163.

Grimm, R.E., McSween Jr, H.Y. (1993) Heliocentric zoning of the asteroid belt by aluminum-26 heating. *Science* 653-655.

Haskin. L. A., Helmke P. A., Blanchard D. P., Jacobs J. W., Telander K. (1973) Major and trace elements abundances in samples from lunar highlands. *Proceedings of the Lunar Science Conference* 4, 1275-1296.

Karner, J.M., Papike, J.J., Sutton, S.R., Burger, P.V., Shearer, C.K., Le, L., Newville, M., Choi, Y. (2010) Partitioning of Eu between augite and a highly spiked martian basalt composition as a function of oxygen fugacity (IW-1 to QFM): Determination of Eu^{2+}/Eu^{3+} ratios by XANES. *American Mineralogist* 95, 410-413.

Koefoed, P., Amelin, Y., Yin, Q.-Z., Wimpenny, J., Sanborn, M.E., Iizuka, T., Irving, A.J. (2016) U–Pb and Al–Mg systematics of the ungrouped achondrite Northwest Africa 7325. *Geochimica et Cosmochimica Acta* 183, 31-45.

Lee, T., Papanastassiou, D., Wasserburg, G. (1977) Aluminum-26 in the early solar system-Fossil or fuel. *Astrophysical Journal* 211, L107-L110.

Martin, D., Nokes, R. (1989) A fluid-dynamical study of crystal settling in convecting magmas. *Journal of Petrology* 30, 1471-1500.

Norman, M.D., Borg, L.E., Nyquist, L.E., Bogard, D.D (2003) Chronology, geochemistry, and petrology of a ferroan noritic anorthosite clast from Descartes breccia 67215: Clues to the age, origin, structure, and impact history of the lunar crust. *Meteoritics and Planetary Science* 38, 645-661.

O'Neill, H.S.C., Palme, H. (2008) Collisional erosion and the non-chondritic composition of the terrestrial planets. *Philosophical Transactions of the Royal Society A: Mathematical, Physical and Engineering Sciences* 366, 4205-4238.

Osborn, E.F. (1942) The system $CaSiO_3$-diopside-anorthite. *American Journal of Science* 240, 751-788.

Ruzicka, A., Grossman, J., Bouvier, A., Agee, C.B. (2017) The Meteoritical Bulletin, No. 103. *Meteoritics and Planetary Science* 52, 1014.

Sutton, S.R., Goodrich, C.A., Wirick, S. (2017) Titanium, Vanadium and Chromium Valences in Silicates of Ungrouped Achondrite (NWA) 7325 and Ureilite Y-791538 Record Highly-Reduced Origins. *Geochimica et Cosmochimica Acta* 204, 313-330.

Taylor, G.J., Keil, K., McCoy, T., Haack, H., Scott, E.R. (1993) Asteroid differentiation: Pyroclastic volcanism to magma oceans. *Meteoritics* 28, 34-52.

Vander Kaaden, K.E., McCubbin, F.M. (2015) Exotic crust formation on Mercury: Consequences of a shallow, FeO-poor mantle. *Journal of Geophysical Research: Planets* 120, 195-209.

Wadhwa, M. (2008) Redox conditions on small bodies, the Moon and Mars. *Reviews in Mineralogy and Geochemistry* 68, 493-510.

Weber, I., Morlok, A., Bischoff, A., Hiesinger, H., Ward, D., Joy, K., Crowther, S., Jastrzebski, N., Gilmour, J., Clay, P. (2016) Cosmochemical and spectroscopic properties of Northwest Africa 7325—A consortium study. *Meteoritics and Planetary Science* 51, 3-30.

Wood, J.A., Dickey Jr, J., Marvin, U.B., Powell, B. (1970) Lunar anorthosites and a geophysical model of the moon. *Geochimica et Cosmochimica Acta Supplements* 1, 965-988.

Yang, J., Zhang, C., Miyahara, M., Tang, X., Gu, L., Lin, Y. (2019) Evidence for early impact on hot differentiated plantesimal from Al-rich micro-inclusions in ungrouped achondrite Northwest Africa 7325. *Geochimica et Cosmochimica Acta* 258, 310-335.

PLANETARY SCIENCE

Deep mantle origin of large igneous provinces and komatiites

Rémy Pierru[1]*, Denis Andrault[1], Geeth Manthilake[1], Julien Monteux[1], Jean Luc Devidal[1], Nicolas Guignot[2], Andrew King[2], Laura Henry[2]

Large igneous provinces (LIPs) resulted from intraplate magmatic events mobilizing volumes of magma up to several million cubic kilometers. LIPs and lavas with deep mantle sources have compositions ranging from komatiites found in Archean greenstone belts to basalts and picrites in Phanerozoic flood basalt and recent oceanic islands. In this study, we identify the mantle conditions appropriate to each type of lava based on an experimental study of the melting of pyrolite. The depth of the mantle source decreases from 600 to 700 km for the oldest komatiites to 100 to 300 km for picrites and basalts, and the extent of mantle melting ranges from 10 to 50%. We develop a geodynamical model that explains the origin of the hot mantle plumes capable of generating these melting *P-T* conditions. Within a superadiabatic temperature gradient persisting in the deep mantle, the ascent of hot mantle plumes creates excess temperatures up to 250 to 300 K by adiabatic decompression.

INTRODUCTION

The mantle potential temperature

The mantle temperature (T) is generally defined by the potential surface temperature (T_p), which corresponds to the extrapolation to the surface of the adiabatic T gradient. The mantle T_p can be refined from the analysis of primary magmas formed along accretionary ridges (*1*) and is calculated after a calibration of, e.g., the melt MgO content against several parameters including T and pressure (P) (*2*, *3*). Currently, T_p of 1350° ± 50°C is suggested by primary basalts with MgO and FeO contents at 10 to 13 weight % (wt%) and 6.5 to 8.0 wt%, respectively (*4*). Still, there are "hot" primary magmas (basaltic-picritic) requiring T_p as high as ~1600°C (*5*). These are "hot spots," such as Hawaii, and they could be related to instabilities in the thermal boundary layer in the lowermost mantle (*6*).

The Archean mantle T_p has important implications for understanding the geodynamics of the early Earth and the onset of plate tectonics. Recent geodynamic models have recognized the importance of the reevaluation of Archean mantle T_p for crustal formation mechanisms in stagnant lava environments (*7*). Average T_p estimates for large igneous provinces (LIPs) and Hawaii is ΔT = +200 K or higher than the average mantle T_p. In Tortugal, where komatiites occur, ΔT can exceed +300 K (*8*).

Regarding the accuracy of the T_p determination, note that the agreement between the compositions of experimental melts and primary magmas on the field are in very good agreement only if the source is not very deep (P lower than 6 to 7 GPa). At higher P, the accuracy of T_p is more questionable, especially for Archean sources of ultramafic rocks. This is, in part, because experimental conditions are less well controlled at high P and the composition of the melt at equilibrium is also more difficult to measure. For example, estimates of the T_p required to produce a primary magma with MgO >20 wt% diverge by ~100 K with the PRIMELT calculation (*3*). In a more general manner, any uncertainty on the melting diagram is directly transferred into uncertainties on the knowledge of the melting condition in the mantle.

In addition to this, anomalously high water contents in the mantle could produce comparable effects as high T, as water lowers the solidus. Where T_p estimates from dry material show rather consistent results, melts produced from a wet mantle do not seem to provide usable computational solutions (*9*). More generally, the likely presence of chemical heterogeneities increases the uncertainty on the T_p determination locally (*10*).

A broad range of primitive lavas

Mafic-ultramafic tholeiitic lavas such as basalts, picrites, and komatiites (*11*) represent the deepest and hottest magmas that erupted on Earth. Three main families of komatiites are distinguished depending on their chemical composition; nicknames have been given to them according to locality of the main outcrops (*12*): Al-depleted komatiites (ADK; Barberton type), Al-undepleted komatiites (AUK; Munro type), and Al-enriched komatiites/picrites (AEK; Gorgona type). These rocks show a large diversity of chemical composition resulting from different geological contexts including (i) mantle source, composition, depth, extent of melting (Φ), and possible presence of fluids and (ii) fractional crystallization, contamination, or assimilation possibly occurring during the ascent of melts to the lithosphere (*13*). There is a clear evolution of the composition of LIPs and komatiites through time over the past ~4 billion years (Ga; Fig. 1 and fig. S1). Unlike basalts and picrites that can be found at all ages, ADK seems to be only formed during the Archean from −4 to −2.8 Ga, while AUK erupted until about −1.9 Ga in Paleo-Proterozoic. Association of basalts and picrites with komatiites can be found, for example, in the form of dykes into Archean greenstone belts (*14*). Last, AEK formed from the Archean to the Phanerozoic. The most recent komatiites have been dated at ~90 Ma (*15*).

Picrites are rare intrusive igneous lavas enriched in magnesium (>12% MgO) (*16*) compared to the basalts erupting today on Earth. These lavas seem to be products of mantle melting at P above ~3 GPa and extent of melting (Φ) close to 20 to 30% (*17*). However, several other possible origins were proposed such as high rate of melting of lherzolitic mantle, partial melting of mantle with high Mg content, or olivine enrichment through processes of magmatic differentiation.

[1]Université Clermont Auvergne, CNRS, IRD, OPGC, LMV, F-63000 Clermont-Ferrand, France. [2]Synchrotron SOLEIL, Gif-sur-Yvette, France.
*Corresponding author. Email: r.pierru30@gmail.com

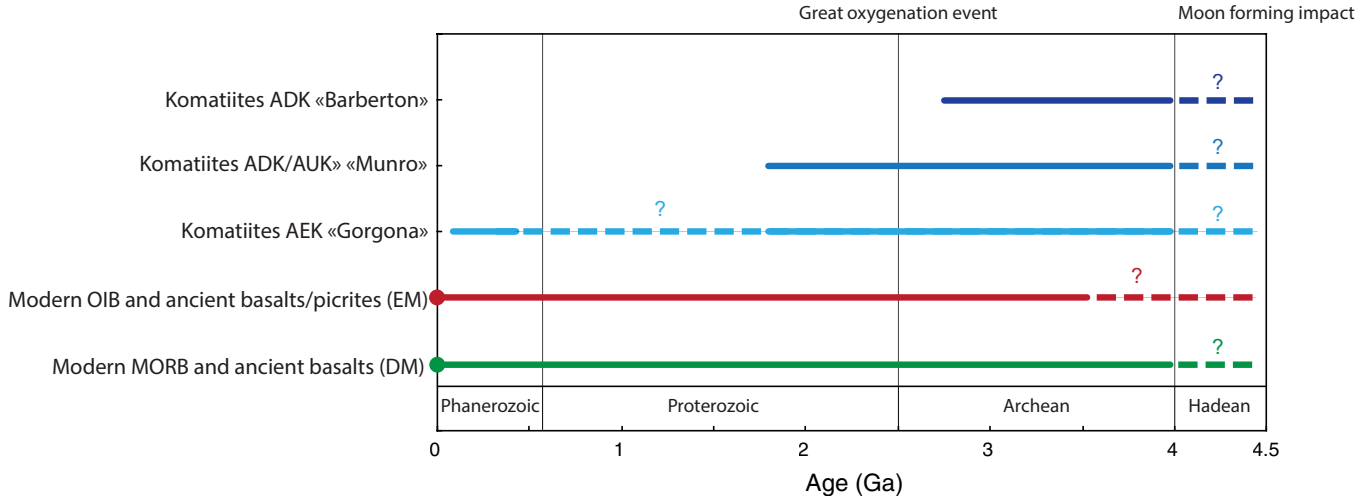

Fig. 1. Age of the different lavas found in LIPs: References are the same as those used for fig. S1.

Komatiites contain up to 34 wt% MgO, present very high liquidus *T* at atmospheric *P* (*18*) and have a close chemical relationship with mantle peridotites. For these reasons, komatiites must have formed at relatively high extents of melting in a mantle warmer than today (+200 to 300 K) (*1*). Alternatively, komatiites could be hydrated magmas formed at *T* not much higher than the surrounding mantle (*5*); the source of volatiles would be non-degassed primordial mantle or subducted oceanic crust.

1) ADKs present the very high MgO contents (≥30 wt%) and CaO/Al_2O_3 ratios (>~1.5), low $A1_20_3/TiO_2$ ratios (<10 to 15), and high Gd/Yb ratios, compared to chondrites. They are also enriched in trace elements and light rare earth elements (REEs) but depleted in heavy REE (HREE). However, their composition could not be reproduced experimentally from melting of typical mantle materials. Still, we note that CaO/Al_2O_3 ratios greater than 1.5 in melts were successfully reproduced by melting either KLB-1 peridotite at extent lower than 1% (*19*), peridotite with addition of up to 10% water (*20*), or ad hoc dry or hydrated $CaO\text{-}MgO\text{-}Al_2O_3\text{-}SiO_2$ (CMAS) compositions (*21*). The composition of ADK suggests melting with a residual Al-bearing phase (majoritic garnet and bridgmanite), which requires *P* over 15 to 17 GPa (*22*–*25*). Zirconium and hafnium, which are high in ADK, act as incompatible elements for melting processes at moderate Φ only (*26*), suggesting ADK magmas produced at lower Φ (~30%) than the other Archean komatiites.

2) AUKs present low $CaO/A1_2O_3$ ratios (~1 or less), high Al_20_3/TiO_2 ratios (~15 to 20), low MgO content (<30 wt%) compared to ADK, and an REE pattern close to chondrites. A robust characteristic is moderate to strong depletion of HREE and other immobile incompatible trace elements. The degree of depletion approaches, but rarely meets or exceeds, that of modern mid-ocean ridge N-type basalts (MORB). AUKs are less rich in zirconium than ADKs (*12*). According to batch melting models based on the available partition coefficients [e.g., (*18*)], AUK could result from high extent of melting (~50%). The composition of AUKs from the late Archean are difficult to explain by a single melting event, as they present conflicting nonchondritic Al_2O_3/TiO_2 and CaO/Al_2O_3 ratios implying the presence of residual garnet and quasi-chondritic Gd/Yb ratio implying no residual garnet (*23*). Alternatively, a deep mantle source undergoing high extent of melting could produce a melt with high MgO content, however depleted in Al_2O_3, before the slow uplift of such melt would induce progressive enrichment in Al_2O_3 and depletion in MgO [e.g., (*2*, *12*)]. All arguments suggest AUK mantle sources considerably shallower than for ADKs. This difference, together with a lower MgO content (<30 wt%), indicates lower formation *T* for AUKs than ADKs.

3) AEKs have similar $CaO/A1_2O_3$ ratios and REE patterns to AUKs (*12*). However, they present high Al_2O_3/TiO_2 ratios ranging from the chondritic value of ~20 to as high as 50. AEKs are richer in Al_2O_3 than other komatiites and contain less MgO (>20 wt%). Accordingly, they formed by mantle melting at relatively low *P* (3 to 4 GPa), under conditions where garnet is absent from the residue. If the source were to be a mantle fertile peridotite, then the average Φ should be 30 to 40% (*26*). In terms of chemistry, AEK makes a transition from komatiites to picrites, as both compositions are similar.

Possible origin of the primitive lavas

The correlation between komatiite compositions, timing of the eruptions, and the depth of the primary sources indicates that over time, there is less magma originating from the deeper mantle regions (*19*, *23*, *27*). This evolution could be explained by the secular mantle cooling; however, this hypothesis remains partially speculative. The debate is still vivid about the magmatic processes capable of generating LIPs with large volume of mafic to ultramafic magmas in short pulses (typically less than a million years). In addition, komatiitic ultramafic lavas require large extent of melting at high *T* (*28*, *29*). The greenstone belts, for example, may represent a small fragment only of a much larger LIP (*11*). LIPs and komatiites could be associated with the rise of hot mantle plumes from the deep mantle (*30*), potentially induced by the formation of a subducted-slab graveyard (*31*). This plume could generate a positive anomaly in *T* and/or volatile element (H_2O, CO_2) concentration and favor major mantle melting. Other models propose shallower mechanisms such as mantle warming beneath supercontinents (*32*), plate-related processes (*29*), or lithospheric delamination (*33*).

The isotopic signature of LIPs and komatiites inform on the nature of their source. Similar to modern hotspots [e.g., Galapagos, Iceland, Hawaii, and Samoa (*34*)], the LIP signature overlaps with many mantle components such as depleted MORB mantle (DMM),

ocean island basalts (OIB), Focal zone (Fozo), etc. (*35*). FOZO is interpreted as being located in the lower mantle (*36*). Together with high $^3He/^4He$ anomalies measured in some LIPs, it provides evidence for a source originating from deep mantle regions containing primordial ^3He (*28*). In contrast, the DMM component represents the upper mantle depleted by ~3 Ga of MORB extraction. In addition, reservoirs enriched mantle 1 (EM1), enriched mantle 2 (EM2), and hight-μ (HIMU) are likely located in the sublithospheric mantle. The overlaps found in LIPs suggest the involvement of deep sublithospheric or asthenospheric mantle components, as well as crustal or lithospheric contamination. Concerning komatiites, isotopic studies of Hf, Sr, and Nd show the overlap with the OIB component [e.g., (*37*)]. Together with high levels of He isotopes (*38*), it indicates the presence in the komatiite source of material from the deep mantle. With the high *T* required to form komatiitic magmas, this information strongly supports that komatiites formed by melting of mantle plumes coming from the very deep mantle.

Up to now, the variation of magma chemistry with *P*, *T*, and Φ is only well constrained experimentally for the first 100- to 200-km mantle depths (*23*, *39*–*44*). Higher *P* have also been investigated, however, for compositions different from those expected for the sources of LIPs and komatiites [e.g., CaO-MgO-Al_2O_3-SiO_2 system (*21*)] and limited ranges of Φ [e.g., around 1% (*19*)]. Previous experiments proposed global tendencies for the change of melt composition with *P* and *T*; however, the ranges of *P*-*T*-Φ covered by experimental studies remain insufficient to accurately model mantle melting at depths greater than 200 km.

RESULTS

Melting diagram of pyrolite

Solidus temperatures

To bring new constraints on the origin of LIPs and komatiites, we undertook an experimental determination of the melting diagram and of the melt composition for the first 700-km depth (i.e., ~26 GPa) for a pyrolitic mantle composition (table S1). Our experimental strategy was to synthesize samples at controlled Φ values using in situ techniques: electrical conductivity and x-ray diffraction (figs. S2 to S5 and table S2). Pyrolite solidus is found similar, within ~100 K, to the chondritic-type mantle measured with similar methods (*45*). This is substantially lower than previous reports on peridotite solidus (fig. S6) (*19*, *23*, *27*, *42*, *46*). As developed in (*45*), reasons for this discrepancy with previous works cannot be a difference in composition alone. It could result from several factors: (i) Use of simplified sample compositions, for example, CMAS (*21*). It is well accepted that additional elements induce lower solidus *T* for a typical mantle mineralogy. (ii) Use of coarse grain powders, instead of a glass sample in our study. Slow atomic diffusion may impede the formation of a solidus melt composition at grain interfaces. (iii) Lack of in situ

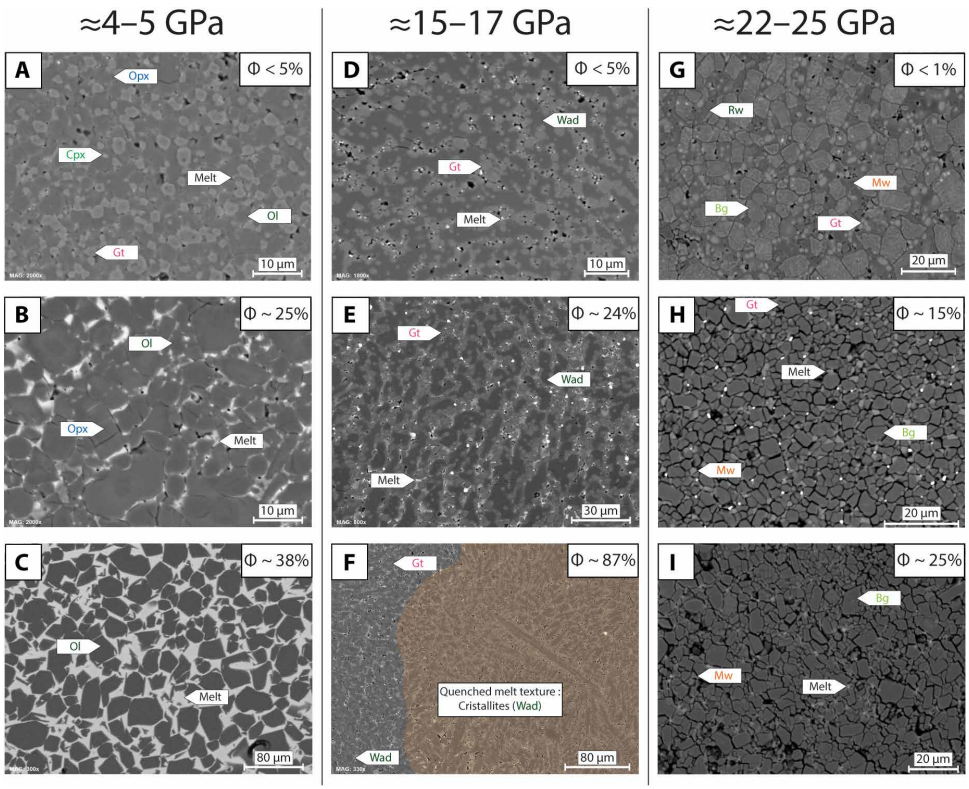

Fig. 2. Progressive increase of the extent of melting associated with disappearance of residual minerals. Left frames show experiments realised at 4 to 5 GPa, central frames 15 to 17 GPa, and right frames 22 to 25 GPa. (**A** and **B**) *MA105*, (**C**) *T2*, (**D**) *MA119*, (**E** and **F**) *MA116*, (**G**) *MA149*, (**H**) *MA143*, and (**I**) *MA144*. At *P* around 4 to 5 GPa, several mineral phases [clinopyroxene (Cpx) and garnet (Gt)] disappear at small extent of melting. With increasing *T*, orthopyroxene (Opx) is enriched in compatible elements (i.e., MgO) and presents grain size exceeding that of olivine. At higher *T*, melting of Opx is associated with a major growth of olivine grain, which is the liquidus phase. At *P* around 15 to 17 GPa, wadsleyite (Wad) and garnet continue to coexist up to very high melting extent. Garnet appears to be the liquidus phase of pyrolite at *P* > 15 GPa. For *P* > 22 GPa, ringwoodite (Rw) and garnet disappear at a relatively low concentration (<25%). After that, bridgmanite (Bg) starts to melt and ferropericlase (Mw) becomes the liquidus phase.

melting criterion and characterization method insufficiently sensitive to detect thin melt films in the recovered samples. Small pockets of melt can be destroyed during the polishing steps. In addition, melt films can be difficult to identify using the scanning electron microscope (SEM) (*47*). (iv) Last, important thermal gradient within the sample charge can lead to T and Φ errors.

Apart from (*45*) that is in good agreement with our melting curves, none of the studies cited above used in situ techniques to detect the onset of melting (such as electrical conductivity and x-rays), and none probes the evolution of Φ at higher T (such as a falling sphere). In previous works, melting was generally detected on the basis of "trials and errors" and the solidus and liquidus T were sometimes identified using the T gradient in a single sample. However, major thermal gradients induce melt migration; the presence of chemical gradients within the capsule disables the determination of the melting behavior of the starting material. For example, a solid residue identified in an unmelted zone of the sample can result from the compaction of refractory minerals, which melting T can be far above the solidus and liquidus of the bulk composition.

Extent of melting

To probe the melting properties at higher Φ, we developed an original falling sphere technique to detect in situ the occurrence of the rheological transition upon heating (fig. S5). When Φ becomes 30 to 40%, a Re sphere falls at an irregular speed in the melt located between the solid grains. It indicates the change of rheological behavior from solid type to liquid type (*48*). The samples were quenched at the rheological transition or at a slightly higher T on the basis of thermocouple reading. The extent of melting was determined for each sample by numerical analyses (Fig. 2 and fig. S7). To achieve a maximum precision, we correlated backscattering electron images and chemical maps obtained by SEM; melt regions present a maximum concentration of incompatible elements. A rapid increase of Φ up to 30 to 40% melt within the first 100 K above the solidus was observed (Figs. 3 and 4). Then, Φ increases less steeply at higher T. At high extent of melting, the grain size of the residual solid phases becomes 10 to 30 μm or more, with well-developed polygonal textures, especially for olivine, orthopyroxene, and bridgmanite.

Liquidus temperatures

Liquidus T can primarily be constrained on the basis of the extrapolation to 100% of the relationship between Φ and T (Fig. 3). Additional constraints come from T measured for (i) very fast and linear trajectory of the falling sphere indicating the absence of solid grains [such as in (*49*)] and (ii) complete disappearance of x-ray diffraction peaks from the sample. (iii) We also monitored the reappearance of crystallites upon cooling and (iv) microstructure of a number of "trial and error" syntheses at variable T, indicating whether the sample has been fully molten or not. All evidences converge on a pyrolitic-mantle liquidus 275 ± 50 K higher than the solidus at all upper mantle depths. Our experiments are compatible with previous works showing that for the pyrolitic/peridotitic composition, majorite replaces olivine at the liquidus between 13 and 16 GPa, and ferropericlase replaces majorite at ~22 GPa (table S3) (*19*, *23*, *46*).

Comparison between experimental melts and natural lavas

Chemical compositions of the melts were determined using the electron microprobe (Supplementary Materials, Figs. 5 and 6, fig. S8, and table S4). From the correlation between Al_2O_3 content and CaO/Al_2O_3 ratio in experimental melts (*19*, *23*), three major trends arise: (i) High extent of melting yields low CaO/Al_2O_3 ratio and low Al_2O_3 content. The pyrolitic melt (i.e., Φ =100%) presents CaO/Al_2O_3 ~ 0.45 and Al_2O_3 ~ 4.5 wt%. (ii) Low P favors high Al_2O_3 content and (iii) high P favors high CaO/Al_2O_3 ratio. In this figure, we superimpose a compilation of the composition of numerous basalts, picrites, and komatiites of different ages and locations. The domains where the different LIPs and komatiites overlap with experimental melts provide strong constraints on their mantle origin (see the Supplementary Information for a discussion of the role of alteration on the CaO/Al_2O_3 ratio in LIPs and komatiites).

The comparison suggests a minimum depth of 550 to 600 km (20 to 23 GPa) to produce the old ADK (Fig. 6). Their compositions

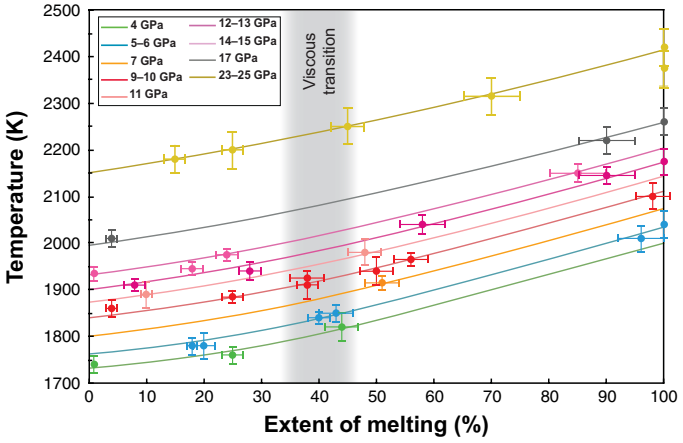

Fig. 3. Temperature dependence of extent of melting. The volumetric extent of melting (Φ) is determined at various P and T on the basis of the joint analyses of electron microphotographs and chemical maps of the recovered samples. High melting extents are also constrained from mass balance calculations. Extrapolation to Φ = 100% of the quasi-linear relation found at high Φ yields a good estimate of the liquidus T as a function of P (distinguished by colors).

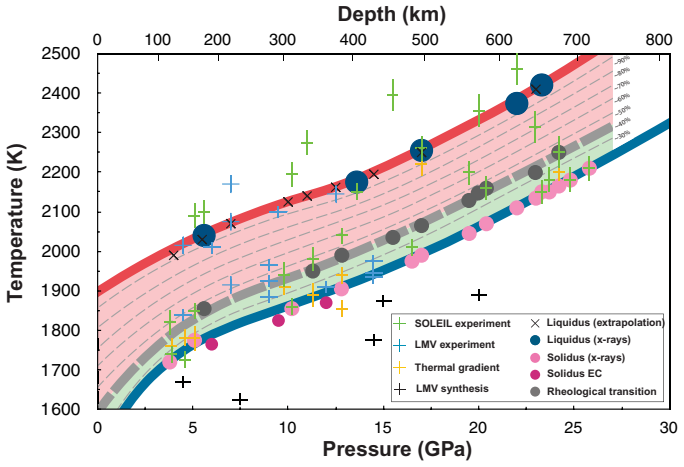

Fig. 4. Melting diagram of the pyrolitic mantle. The solidus is determined up to 25 GPa using in situ electrical conductivity (red circles) and x-ray diffraction (pink circle). The rheological transition at 30 to 40% of melt (gray dashed line) and the liquidus are determined using various methods, including a new falling sphere technique (Supplementary Materials). Both solidus and liquidus present a change of slope at ~15 GPa, when the high-P polymorphs of olivine become stable.

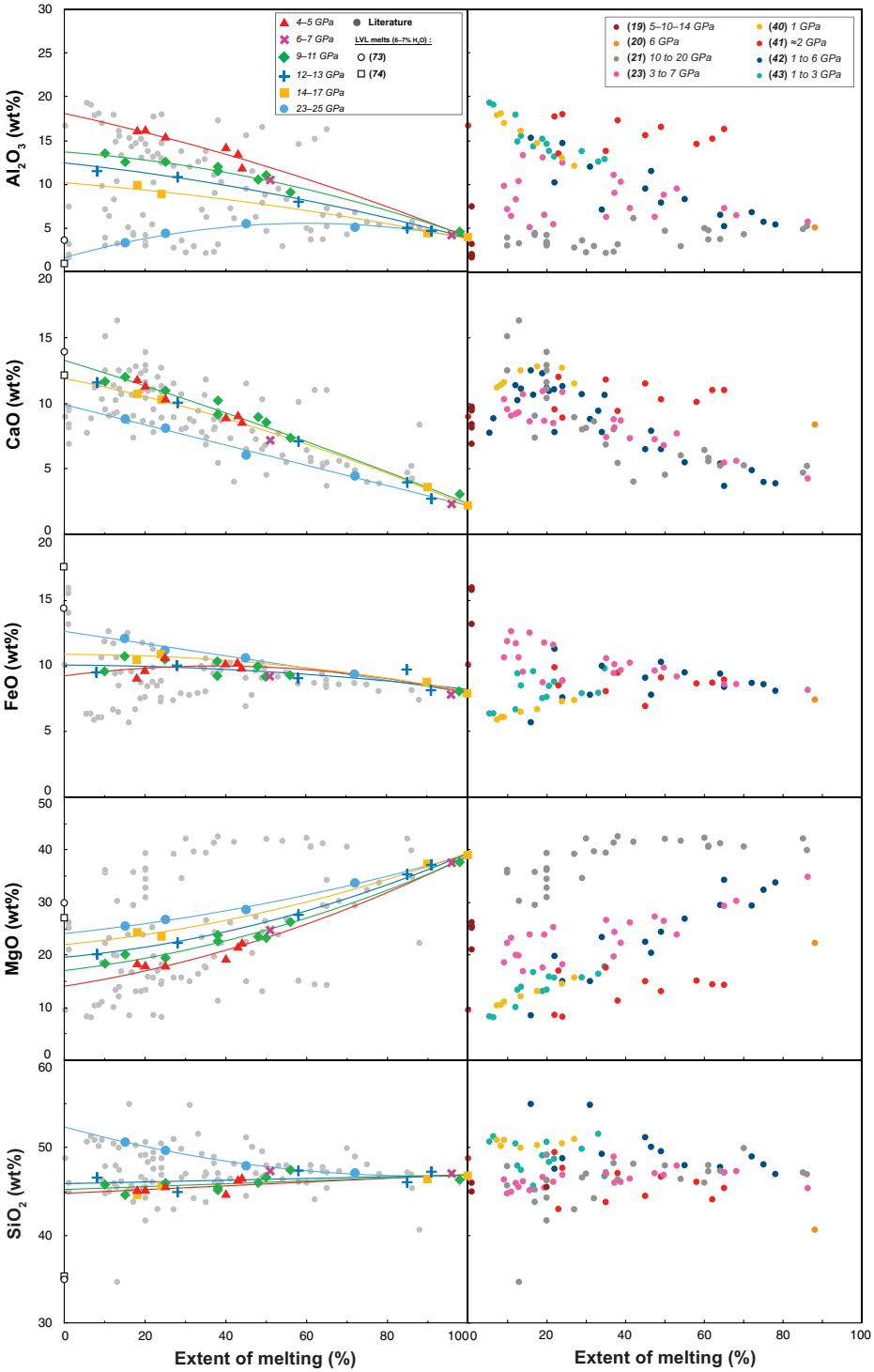

Fig. 5. Variation diagrams showing oxide abundances of melt versus extent of melting (wt%). (**Left**) Chemistry of our melts at various pressures and degrees of mantle melting. Averages of several electron microprobe analyses in the melt regions of our samples are plotted as colored symbols, for *P* between 4 and 25 GPa. One SD is <5% for each melt composition. (**Right**) Chemistry of melt's literature at various pressures and degrees of mantle melting. Each color represents a different study for the pyrolitic/peridotitic upper mantle: (*19*, *21*, *23*, *39*–*44*).

overlap with melts at Φ values ranging between 10 and 25% and 20 and 50% for highest and lowest *P* (thus with decreasing CaO/Al_2O_3 ratio), respectively. The presence of residual Al-bearing garnet at moderate *P* can induce low Al content in the melt. However, the CaO/Al_2O_3 ratio cannot be very high in this case because garnet also incorporates CaO easily. At lower mantle pressures, bridgmanite and davemaoite (Dvm; $CaSiO_3$-perovskite) are rich in Al and Ca, respectively. Melting of Dvm above solidus yields primary melts enriched

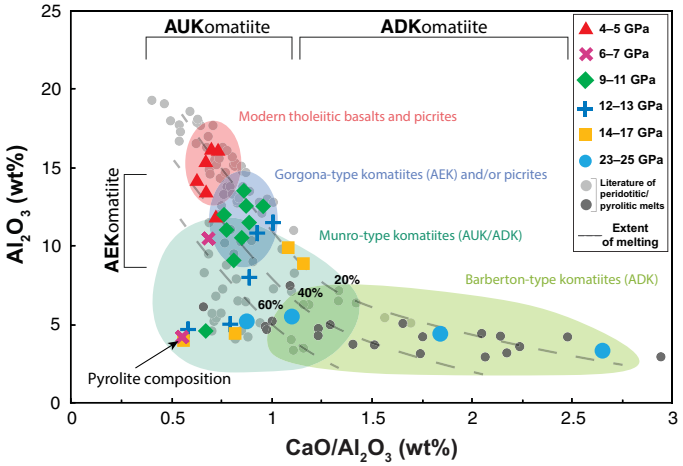

Fig. 6. Correlation between Al_2O_3 contents and CaO/Al_2O_3 ratio of experimental melts and natural lavas. Melt compositions are regrouped by experimental *P* ranges (colored symbols). We also report melt composition from previous experimental reports: Light or dark gray circles indicate studies reproducing the CaO/Al_2O_3 ratio from melting of peridotite/pyrolite under mantle relevant (*23*, *27*, *39*–*43*, *46*, *79*) or more specific (*19*–*21*) experimental conditions, respectively. Colored areas correspond to natural lavas of Barberton-type (ADK, light green), Munro-type (AUK, dark green), Gorgona-type (AEK), and ancient (blue) and recent (red) picrites and basalts [see (*54*)]. On the basis of the degree of partial melting (Φ) measured in our samples (Fig. 3), we draw contour lines corresponding to Φ ~ 20, 40, and 60% (dashed gray lines). Comparing the composition of LIPs/komatiites of different ages (fig. S1) and experimental melts at varying *P* and Φ indicates the mantle source for each type of lava.

in CaO and poor in Al_2O_3. In these mantle conditions, melts with high MgO and SiO_2 contents and high CaO/Al_2O_3 ratios can be produced at relatively low extent of melting. These results are in relatively good agreement with previous works (*22*–*25*), including (*50*) that suggests that komatiite genesis involves a high extent of melting (>30%) at low $P < 5$ to 6 GPa, after adiabatic decompression of mantle diapirs that begin to melt in the transition zone ($P > 15$ GPa) or at even higher depth ($P > 20$ GPa). In all cases, T_p at the time of ADK formation should be appreciably higher than that prevailing today (*1*).

The intermediate position of AUK suggests mantle sources of 300- to 550-km depth (i.e., 10 to 20 GPa), as proposed previously [e.g., (*19*, *23*, *27*)]. To produce Al-undepleted melts, the presence of a residual garnet is not mandatory. There is a smooth transition between the ADK and AUK between 20 and 25 GPa, which explains the coexistence of AUK and ADK in some Munro-type outcrops. Because of similar sources, the two melts present similar major element contents, but the *P* difference can still induce substantial differences in minor and trace elements. Formation of the AUK occurred primarily during the Late Archean and could therefore correspond to lower *T* than the Barberton komatiites (*11*, *12*). On the basis of our experiments at AUK, lavas are compatible with Φ from 15% to more than 60%, which makes AUK compositions quite close to bulk pyrolite. AUK can be produced in a wide range of *P* from ~5 to 10 GPa to ~25 to 30 GPa, when Φ is very high (>50%).

AEK, picrites, and basalts align along near-vertical trends at CaO/Al_2O_3 ratio between 0.5 and 1 and with Al_2O_3 contents varying from ~8 to ~17 wt%. AEK can be produced by melting at 200- to 400-km depth [i.e., 7 to 13 GPa, in agreement with (*2*, *19*, *23*)] and picrites and basalts at 100 to 200 km (i.e., 4 to 5 GPa). Our results suggest moderate extent of melting (Φ < 50%) for recent Gorgona-type komatiites and picrites; melts enriched in Al_2O_3 suggest mantle melting without garnet in the solid residue. Last, picritic and basaltic lavas, which represent LIPS and recent hotspots such as Hawaii or Reunion Island, correspond to melting extents lower than 30% (*2*, *17*).

The melt contents in other major elements confirm the trends presented above. We draw correlation diagrams between them, which show the effect of *P* on the melt composition (Fig. 5). The bulk sample composition, pyrolite, is a singular point in these diagrams because the melt composition evolves toward it with increasing Φ, irrespective of the experimental *P*. On these diagrams, we superimpose the compositions previously reported for basalts, picrites, and komatiites (fig. S8): (i) CaO versus SiO_2 diagram. The high SiO_2 content obtained at the highest experimental *P* and moderate Φ explains well the composition of ADKs. (ii) Al_2O_3 versus CaO and Al_2O_3 versus MgO diagrams. At relatively low Φ (i.e., at high CaO or low MgO content), the sequence of natural lavas (ADK, AUK, AEK, and picrites/basalts) is well compatible with the *P*-induced decrease of Al_2O_3 content in melts (Fig. 5). (iii) CaO versus FeO diagram. The increasing FeO content with increasing *P* at relatively low Φ is also well compatible with the sequence of natural lavas.

DISCUSSION

Mantle conditions for the origin of LIPs and komatiites

We now combine the evolution of Φ between the solidus and liquidus of pyrolite at various mantle depths (from Fig. 3) with the chemical overlap between experimental melts and natural lavas (from Fig. 6). The result (Fig. 7) highlights the likely source region for primary magmas at the origin of LIPs and komatiites. In addition, we plot, the current mantle geotherm (*51*) and its range of uncertainties (gray area), as well as mantle geotherms with T_p 100, 200, and 300 K higher than today (gray lines) (*1*). We acknowledge that these *T* profiles do not formally correspond to mantle *T* profiles; as they go through regions between the solidus and liquidus, the effect of latent heat of mantle fusion should be included. Still, the mantle depth at which an adiabatic profile crosses the solidus informs truthfully on the onset of mantle melting along a decompression path. It appears clear that $T_p > 200$ to 300 K higher than today induces melting in the *P* domain corresponding to ADK. Secular mantle cooling can explain the progressive disappearance of ADK, with preservation of AUK lavas when T_p was >150 to 200 K above that prevailing today (Fig. 1). Last, a mantle plume >50 to 150 K hotter than the average mantle would yield the production of picrites and deep basalts, which are currently found at oceanic islands (e.g., La Reunion) and mid-oceanic ridges, as well as AEK. These hot mantle plumes could still be uprising today (*52*), producing supervolcanoes like Toba (Indonesia) or Yellowstone (the United States).

Previous works were based on the modeling of mantle cooling using the Urey ratio (*53*) or thermodynamical modeling using the PRIMELT method (*1*, *3*). Other less extreme scenarios exist on the basis of similar calculation from the Urey ratio or petrological modeling technique to derive primary magma compositions using large datasets of non-arc basaltic lavas (*9*, *54*, *55*). Our estimates of Archean temperatures are in better agreement with the most recent studies. These discrepancies can be explained by several critical points in the thermodynamical calculations. Different petrological models give different parameterizations for the MgO content in the melt

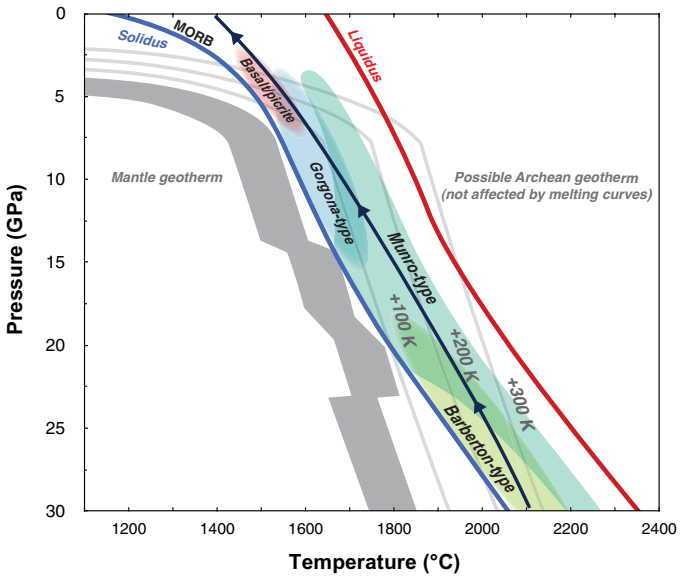

Fig. 7. Mantle *P-T* regions are sources of the different LIPs and komatiites. Solidus (blue line) and liquidus (red line) of pyrolite are reported together with the current mantle geotherm (gray zone), and *T* profiles that are 100, 200, and 300 K higher than the geotherm (light gray lines; these *T* profiles are not corrected for the effect of latent heat of fusion between the solidus and liquidus). Φ values between solidus and liquidus are constrained from our experiments (Fig. 3). The likely source region of the different types of lavas is determined on the basis of their composition (Figs. 5 and 6). The low-*P* basalts and picrites plotted in the figure correspond to flood basalts and OIBs found in the Phanerozoic. MgO-rich picrites (i.e., corresponding to higher *P* and melting extents) found on the islands of Gorgona and Curaçao present a chemistry close to komatiites and are therefore classified in the Gorgona-type group. The thicker blue line serves as a guide to the eyes for the ascent of a hot mantle plume that could be the origin of the oldest komatiites (see Fig. 8).

produced by decompression melting, as a function of *P* and *T* [e.g., (*56*)]. The thermodynamical models rely heavily on the available experimental data, and before our work, these data were limited to *P* below 7 to 8 GPa concerning the formation of high MgO magmas (*2*, *23*). We show that Archean komatiites can be produced at higher *P* than previously thought. A major reason of this discrepancy is our lower solidus profile; it yields differences of 100 to 200 K lower than previous works for the T_p value of the primitive mantle. In addition, we provide an accurate determination of the rate of melting as a function of *P* and *T* for the anhydrous mantle. This yields a more accurate dataset on the melt chemistry over a wide range of mantle *P-T*. Still, we observe relatively good agreement with the literature, indicating that the key point is the accuracy of the *T* measurement within the sample, and the relationship between melting rate and *T* between solidus and liquidus.

Which mantle thermal state produces primitive ultramafic magmas?

The production of a large volume of mafic to ultramafic magma is generally explained by the rising of a hot mantle plume (*29*, *30*). However, if the mantle *T* profile follows an adiabatic gradient [corresponding to T_p of 1600 K or higher (*57*)], then substantial thermal anomalies can only be generated if the ascending material comes from the hot thermal boundary layer in contact with the core. Such mechanism can explain the present-day OIB (*28*, *58*); the hot material can eventually form a dome and rise toward the surface. Still, the thickness of the hot-layer atop the core-mantle boundary (CMB) could only be several hundred kilometers, yielding mantle plume with a reduced volume. These smaller plumes are unlikely to generate great LIPs.

T_p higher in the past than that prevailing today would yield ubiquitous and persistent mantle melting in a wide range of mantle depths (Fig. 7). This thermal state is not consistent with the sporadic character of the LIPs. In addition, if the extent of melting should become larger than ~40%, as required to explain the composition of some komatiites, then this would indicate a layer of very low viscosity within the upper mantle for a very long time, which is a new concept with implications to be investigated. Last, warmer adiabatic *T* profiles with a mushy upper mantle are not found in line with the cooling history of Earth, when the starting point is the MO solidification after the Moon-forming impact [see e.g., (*59*)]. Alternatively, major thermal anomalies within the deep mantle could more simply explain the properties of LIPs and komatiites.

The simplest mechanism to produce large mantle plumes with positive *T* anomalies is a superadiabatic *T* profile in the deep solid mantle (Fig. 8). This favors mantle instabilities and overturns; large volumes of deep mantle can rise to the surface and become hotter than the surrounding mantle because they cool less during the adiabatic decompression than the superadiabatic gradient prevailing in the mantle. We recently demonstrated that super adiabatic gradients should prevail in the deep mantle for 1 Ga or more after the major Moon-forming impact (*59*). This thermal state is a necessary step between (i) the solidification of the global magma ocean, which yields a *T* profile close to the mantle solidus and (ii) the adiabatic profile of the present-day mantle with T_p of 1600 to 1650 K (if an adiabatic *T* gradient is really achieved today). Along this cooling stage, *T* should decrease by 500 to 1000 K in the lowermost mantle. It implies the extraction of a huge amount of heat, especially because of other sources of energy available, such as radioactive disintegration.

Superadiabatic mantle gradients could be at the origin of LIPs

Following previous work (*59*), we recalculate the evolution of the mantle *T* profile over time after the crystallization of a pyrolitic magma ocean. A most appreciable difference in the parameters is the solidus of pyrolite, which presents a progressive increase with increasing depths in the upper mantle (fig. S6). Because of this curvature, the last mantle region to solidify upon cooling is at mid-upper mantle depths (fig. S9), instead of just below the surface for the chondritic-type mantle composition used in the previous work. It results that the cooling rate of the pyrolitic mantle is significantly slower, with a *T* profile remaining largely superadiabatic in the deep mantle for 2 to 3 Ga or more (Fig. 8 and fig. S9). Together with the fact that melting happens solely in the first 1000 km of the mantle (fig. S12), such long time scale provides a primary justification for using the properties of the pyrolite mantle for our discussions; while the bulk primitive mantle could very well be of chondritic-type composition after the core segregation, the mean mantle involved in the convection processes 2 to 3 Ga later in the shallow mantle is believed to be similar to pyrolite composition.

We also calculate the *P-T* path that uprising material would follow along adiabatic decompression paths, taking into account the latent heat of fusion [e.g., (*50*)] when the plume enters the *P-T* domain between the solidus and the liquidus. The adiabatic uprising

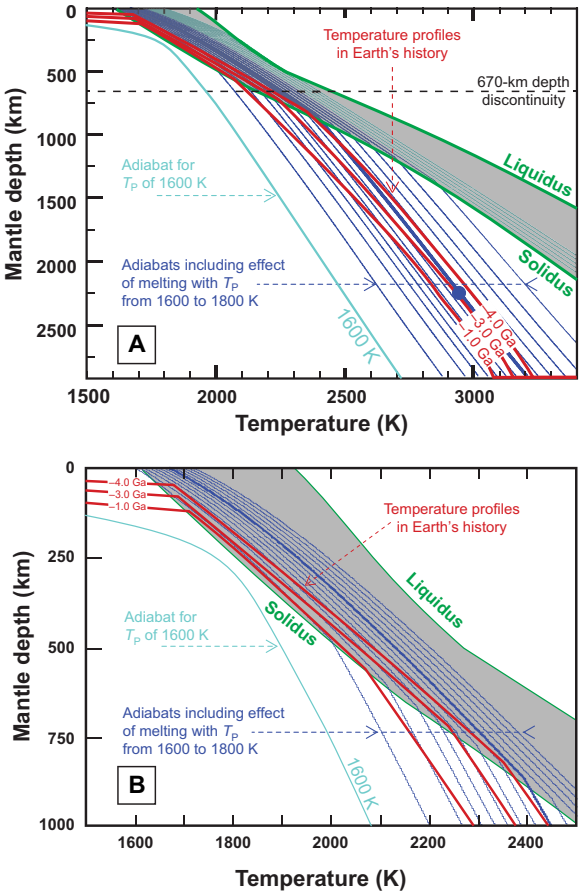

Fig. 8. Thermal state in the ancient mantle. Panel (**A**) reports the solidus and liquidus of the pyrolitic mantle (green lines), the present-day reference adiabatic T gradient for Tp = 1600 K (light blue), ancient adiabatic T gradients going through a mushy zone in the upper mantle (blue lines), and ancient T profiles with ages from 4.0 to 1.0 Ga before present (red lines). Panel (**B**) is a zoom of the figure A between 0 and 1000 km and 1500 to 2500 K. The T profiles result from modeling the cooling of a pyrolitic mantle composition from a global magma ocean, following previous work (*59*). The thicker blue line is a guide for eyes for the ascent of a hot mantle plume. With an initial temperature typical of an ancient T profile, for example, 2850 K at 2300-km depth in a ~3-Ga-old mantle [blue dot in (A)], a rapid decompression path along its corresponding adiabatic T gradient (bold blue line) yields a mantle plume with a major T excess in the shallow mantle, compared to the average T profile. This plume would cross the solidus at ~800-km depth and melt partially at levels of 25 to 30%, ~50%, and 30 to 40%, at mantle depths of 660 km, 300 to 500 km, and 100 to 200 km, respectively. This information is given by the position of the thick blue line between the solidus and liquidus in (B), following the expected extent of melting as a function of P and T (Fig. 3). These conditions are compatible with the formation of Barberton-type komatiites (Fig. 7). Our model of liquid komatiite petrogenesis by adiabatic decompression is similar to that of picrite or MORB petrogenesis, except that it involves a superadiabatic T gradient to generate hot mantle plume coming from great mantle depths.

of a mantle blob from 2300-km depth and 2850 K (which corresponds to mantle conditions about 3 Ga ago; blue dot in Fig. 8) would cross the solidus at ~800-km depth and melt partially at levels of 25 to 30%, ~50%, and 30 to 40% at depths of 660 km, 300 to 500 km, and 100 to 200 km, respectively (fig. S8). These melting conditions are very compatible with those needed to produce ADK, AUK, and early AEK-picrite lavas, respectively (Fig. 6). Therefore, the prevalence of superadiabatic gradients in Archean and early Proterozoic mantle offers new explanations for the sources of LIPs and komatiites. Within the first ~1000-km depth, the magnitude of the *T* excess of the mantle plume, compared to the average mantle, depends on the level of mantle superadiabaticity of the *T* profile in the deep mantle and the depth from which the mantle plume originates. With secular cooling, the level of superadiabaticity decreases, inducing smaller *T* anomalies in the shallow mantle.

Another major aspect that still needs to be addressed is the volume of uprising material, which needs to be several million cubic kilometers to produce major LIPs. While the presence of superadiabatic mantle gradients could provide an explanation for the presence of hot plumes in the upper mantle, the dynamics of such hot mantle could be different from today. A steep *T* profile in the past implies high Rayleigh number value and turbulent mantle convection. Unsteady convection cells could have developed with characteristic length scales much smaller than the mantle thickness (*60*). At early time, uprising of hot material from the deep Earth may have occurred sporadically along heat pipes (*61*). Mantle cooling over the Hadean and the Archean should have progressively increased the length scale of mantle convection, due to the decrease of the Rayleigh number, before global mantle convection is progressively established (*62*). Under these circumstances, the production of LIPs and komatiites and slab subduction would be precursors of the establishment of global mantle convection prevailing in modern Earth.

MATERIALS AND METHODS

Sample preparation

As starting material, we used a typical composition of pyrolitic mantle. This model is constructed by adding some MORB to mantle peridotite. It is dedicated to represent a primitive undepleted upper mantle (*63*). Our pyrolitic composition (table S1) is not far from KLB-1 (*27*) and fertile oceanic peridotites (*64*). A mixture of synthetic powders was homogenized in an agate mortar, before glass spheres of diameter ~2.5 mm were produced using an aerodynamic levitation system (*65*). The use of a regulated flow of pure Ar yields a convenient $Fe^{3+}/(Fe^{2+}+Fe^{3+})$ ratio of 7 to 8% for such type of sample composition (*66*).

We determine the water content in the pyrolitic glass using infrared spectroscopy, based on the Beer-Lambert law and absorption coefficients given for basaltic (*67*) and basanitic (*68*) glasses. These coefficients are valid when using the height of a water band located at, e.g., 3450 cm^{-1}. With water contents ranging between 18 and 22 parts per million, we consider the glass starting material nominally dry.

Glass spheres are reshaped by polishing in the form of a cylinder to be directly inserted in the high-*P* assembly of the multi-anvil press (MAP). The cylinder of glass offers several advantages including a rigid shape during compression and a very small surface/volume ratio for moisture absorption, compared to powders. We keep the sample length less than 1 mm to reduce *T* gradients during high *P* and *T* experiments.

Electrical conductivity measurements

Electrical conductivity measurements are performed up to 20 GPa at the Laboratoire Magmas et Volcans using the same experimental procedure as in our previous work (*45*). We use tungsten carbide cubes with edge truncation of 11, 6, or 4 mm, octahedron *P* medium made of Cr_2O_3-doped MgO with edge length of 18, 14, or 10 mm,

respectively, and cylindrical furnace made of a Re foil of 25-μm thickness. The heater is surrounded by a zirconia sleeve, which serves as thermal insulator. The sample is inserted in an MgO capsule; MgO is softer than alumina parts, which minimizes the deformation of the molten sample. Before preparation of the assembly, all ceramic parts are fired at 1000°C for 1 hour and stored in a vacuum furnace at 150°C together with the glass sample. The sample length is determined before and after the experiment using a high-precision digital gauge and the SEM. We apply a correction based on elastic parameters to account for the change of sample length due to compression and thermal expansion. *P* is determined on the basis of a press-load versus sample-*P* calibration using the well-known phase transition in mantle minerals. The uncertainty evolves from 0.5 to 1 GPa with increasing *P* (*69*).

Rhenium disks electrodes with diameter of 1 mm are positioned at the top and bottom of the sample. They maintain the electrical connection between the sample and the electrodes and favor the spreading of the current at the sample surface. On one sample side, we insert the two wires of a C-type thermocouple ($W_{0.95}Re_{0.05}$-$W_{0.74}Re_{0.26}$) through the MgO cylinder and in contact with the Re disk. A third $W_{0.95}Re_{0.05}$ wire is positioned at the other sample side. On the basis of this configuration, the sample *T* can be measured on one sample side and impedance spectra are collected between the two $W_{0.95}Re_{0.05}$ wires. Because of the proximity with the Re furnace, we estimate our sample fO_2 close to the Re-Re_{Ox} buffer.

Absence of a metallic capsule around the silicate sample can induce the escape of some melt from the sample core, especially when achieving high extent of melting. This melt could react with the MgO sleeve. Fortunately, this effect is reduced when a stronger cohesion of the cell assembly is achieved at high *P* (*70*). In addition, we perform fast heating after the solidus *T* is detected (see below). Using the trial-and-error method, we optimized the experimental duration to obtain a good textural and chemical equilibrium together with minimum melt migration.

Electrical impedance of samples was recorded using the ModuLab MTS Impedance/Gain-Phase Analyzer in a range of frequencies between 1 MHz and 1 Hz [see details in (*45*)]. After compression to the target *P*, we performed different cycles of heating and cooling to remove adsorbed moisture from the assembly components, until a reproducible sample conductivity is achieved. Then, *T* is raised up to ~1300 K, which is above the glass transition of our pyrolite glass. The sample resistivity increases again as a sign of final dehydration and crystallization. The grain size is up to 2 to 10 μm, based on the microstructure of quenched samples. After this step, the sample is cooled to 600 to 800 K before the final heating up to the melting *T*. Our major criterion for the detection of solidus is the change of slope in the *T* dependence of sample conductivity (fig. S4).

X-ray measurements

We performed x-ray diffraction and contrast imaging in situ in the MAP operating at the PSICHE beamline of the SOLEIL synchrotron using the same experimental procedure as in our previous work [see details in (*45*)]. *P* up to 27 GPa is generated using WC cubes with 3- or 4-mm truncation edges mounted with 7- or 10-mm-length Cr-doped MgO octahedra. High *T* is provided by a Re tubular furnace surrounded by a ZrO_2 sleeve for thermal insulation. Re electrodes with a donut shape are used to connect each furnace extremity to one cube truncation. Heating is obtained by applying an alternating current at 100 Hz.

T is monitored by a C-type thermocouple (W/Re) in contact with the furnace at the center of the assembly. All pieces are positioned horizontally in parallel with the x-ray beam.

The beamline configuration is similar to that for a previous study dedicated to measuring the silicate melt viscosity (*49*). At the sample position, we use either (i) a relatively large beam of about 2 mm by 2 mm to record the sample image as a function of time using a fast charge-coupled device camera (>100 frames per second) located behind the MAP or (ii) a beam collimated to 50 μm by 200 μm to characterize the sample mineralogy and monitor *P*. X-ray diffraction patterns are recorded in energy-dispersive mode using a Ge solid-state detector coupled to the Caesar-type diffractometer. A 2θ diffraction angle of 8.0° ($\pm 10^{-3}$) is convenient to register the major diffraction lines of our silicate samples. On the basis of uncertainties of the determination of the MgO cell parameter and on the MgO equation of state itself, the uncertainty in the *P* determination is ~0.3 GPa (*71*).

The new falling sphere technique

We investigate the rheological transition occurring in the sample at an extent of melting (Φ) of 30 to 40% using x-ray imaging and an original "falling sphere" method (fig. S5). For this, using laser ablation, we drill a small hole on the lateral surface of the cylindrical sample at equal distance from the two ends. One or two rhenium spheres with diameters of 50 to 80 μm are inserted in the hole. We verify that Re spheres are located on the upper side of sample when inserting the assembly in the MAP. The sample *P* is determined on the basis of the x-ray diffraction signal of the MgO disks located on each side of the sample.

Upon heating above the solidus, we first observe some instabilities in the position of the sphere likely produced by an increasing Φ in the sample. With further *T* increase, the sphere starts to fall within the sample. Its movement appear to be chaotic, indicating the sphere bouncing on the surrounding mineral grains. The sphere does not fall at a constant speed and takes several seconds to go across the sample. Its complete fall takes orders of magnitude longer than a sphere fall through a fully molten sample at similar *P* (*49*). The slow falling of the sphere evidences a rheological transition between solid-like to liquid-like behavior. This transition occurs when the amount of melt is sufficient to disrupt the rigid cohesion between grains forming the solid matrix. Still, the high fraction of solid grains prevents a rapid fall of the sphere. We have heated some of our samples to even higher *T*, and in this case, the sphere falls through the entire sample in milliseconds (~200 ms). Using this technique, we have monitored the rheological transition at eight different *P* from 5 to 24 GPa and at *T* ranging from ~1855 to ~2250 K (table S2) The extent of melting is determined a posteriori on the recovered samples.

Temperature gradients and uncertainties

Estimation of thermal gradients is crucial for an accurate determination of the pyrolite melting *T*. They can yield to heterogeneities in partially molten samples, although the sample volume is less than 1 mm^3. Our recovered samples do not present significant zoning when using the 18/11 cell assembly, neither in Φ nor in the chemical composition of the different phases. The situation is not as ideal when using the smaller 14/6, 10/4, or 7/3 assemblies. We limit artifacts possibly generated by chemical segregations by duplicating experiments several times and crosschecking the petrological and chemical analyses of different samples. For a few samples, the texture and

sample mineralogy were slightly different at the two capsule ends because of non-negligible *T* gradients. If the overall chemical homogeneity is well preserved, then these samples can still be used to determine the melt composition, based on chemical analyses of the different sample areas.

We model the *T* field for our different cell assemblies for thermocouple readings between 1773 and 2273 K (fig. S10) (*72*). We obtain a *T* difference of less than 100 K between the sample and the thermocouple located in contact with (i) an electrode at the top of the sample for electrical conductivity experiments and (ii) the tubular furnace around the sample for x-ray experiments. The difference can only be higher if the sample is significantly off the center of the assembly (and especially for 10/4 and 7/3 assemblies), which can be checked on the recovered samples. The coldest zones are the top and bottom of the cylindrical sample, while the central plane of the sample records the highest temperatures. We applied a correction to all *T* measurements based on the modeled *T* gradients.

For conductivity measurements, the sample volume is ~0.8 mm^3 and maximum *T* difference of 60 or 70 to 80 K is calculated using 18/11 or 14/6 and 10/4 assemblies, respectively. For x-ray measurements, maximum *T* difference is 80, or 90 K, for 10/4 assembly with a sample volume of 0.4 to 0.5 mm^3, or 7/3 assembly with a sample of 0.2 to 0.3 mm^3, respectively.

Microstructure of recovered samples

Texture and mineralogy of recovered samples is characterized using the SEM. Samples are mounted in an epoxy resin and polished to mirror-like surface. Longitudinal section (along the furnace axis) is the most convenient to check the sample homogeneity and estimate the extent of melting and abundance of the different minerals. Observations are carried out using both JEOL (JSM-5910 LV at LMV) and field-emission gun ZEISS (supra 55VP at 2MAtech, Aubière, France) SEMs with accelerating voltage of 15 kV and working distance (WD) from 6 to 11.6 mm. The use of small WD enables the detection of small veins of melts typical of low Φ.

Observations confirm that the initial shape of the samples is well preserved, even at high melting extents. Images show a good textural equilibrium for all our samples, based on well-crystallized polygonal grains with diameters of several micrometers and grain boundary angles close to 120° (Fig. 2 and figs. S3 and S7). The particles size does not change significantly with *P* but rather with increasing *T*. The presence of cracks in some samples could result from tensile stresses during quench and decompression.

Several chemical maps (Si, Fe, Mg, Ca, Al, and K) have been recorded using energy-dispersive spectroscopy to image the elemental distribution between the melt and the solid residue. Mg, Al, and Si provide a rapid identification of major minerals; olivine and its high-*P* polymorphs, pyroxenes, and garnet. Fe, Ca, and K provide clues for the identification of the network of melt pockets.

Determination of the extent of melting

We use high-resolution electron microphotographs to determine Φ in our samples. At the solidus *T*, samples show nanometric traces of melts at the grain triple junctions and along grain boundaries. In this case, the size of melt pockets or films is generally too small to enable a precise measurement of the melt composition, due to chemical interferences with the adjacent minerals. At *T* of 20 to 50 K or more above the solidus, the interconnected melt presents a very low dihedral angle (fig. S3). To prevent artifacts in the determination of Φ, we used the MATLAB software to correlate the backscattered electron images with chemical maps of the incompatible elements, which present a maximum concentration in the melt regions. We perform several calculations with adaptable pixel sizes to check the robustness of our method; uncertainties on calculated Φ are <2 and <5% for low and high extents of melting, respectively (Fig. 2 and table S3). These Φ values are in very good agreement with other Φ values calculated on the basis of the chemical composition of all the phases coexisting in a same sample. Still, the mass balance technique provides larger uncertainties compared to image analyses. When a thermal gradient is detectable inside a sample, the extent of melting is studied in the different regions and the *T* in each zone is estimated from modeled *T* gradients (fig. S10).

Chemical analyses

Chemical compositions of melts are determined by electron probe microanalyses. We used alternatively Cameca SX100 and SXFiveTactis electron probes with a same accelerating voltage of 15 kV and a beam current of 20 nA. Quantitative analyses are obtained for eight elements (Si, K, Fe, Na, Ti, Al, Ca, and Mg) with counting times of 20 s on peak maxima and 2 × 10 s on the background. As standards, we use natural minerals and synthetic oxides (Si and Ca, wollastonite; Mg, forsterite; Al, Al_2O_3; Fe, fayalite; Na, albite; K, orthoclase; Ti and Mn, $MnTiO_3$; Cr, Cr_2O_3; and Ni, NiO) and pure metal (Fe, Mn, Mg, Ni, and Cr) for metal alloys. Mineral phases and vein of melts are analyzed with a focused beam (2 to 5 μm), while large melt pools (with texture of quench) are analyzed with a beam defocused to diameter of ~10 μm. In this case, standards are also analyzed with the defocused beam.

Regions of melt could be adequately localized on the basis of chemical maps obtained using SEM. In this work, we do not attempt to analyze the incipient melt composition (the smallest Φ). Instead, we cover the most extensive *P*-*T*-Φ domain typical of current and primitive upper mantle. As logically expected, the melt composition evolves toward pyrolite, the sample bulk composition, with increasing Φ (Fig. 5). Chemical trends, however, vary significantly with experimental *P*. Noticeable trends are the following:

1) CaO and Al_2O_3 contents in melt decrease significantly with increasing *T* because of their known incompatible character. CaO presents a major decrease from 10 to 15 to ~3 wt% at all *P*, except at 23 to 25 GPa where it becomes slightly less incompatible. Al_2O_3 content also decreases largely with *T* from ~17 to ~5% at 4 to 5 GPa.

2) The incompatible character of Al disappears with increasing *P*, as expected from the presence of residual garnet above the solidus for *P* higher than ~7 GPa. At low Φ, the Al content in the melt increases from ~2 to ~18 wt% with *P* from 4 to 5 GPa to 23 to 25 GPa, respectively.

3) Our melt FeO contents are low, indicating a moderately incompatible behavior. They present a relative stagnation up to Φ ~ 60%, independently of the *P*, except at 23 to 25 GPa. It suggests solid-melt partition coefficients close to unity with the solid phases that disappear before Φ ~ 60% and an incompatible behavior only relative to the mineral phase that remain stable up the liquidus. We note that our FeO results diverge from previous works performed at very low melting extents, as significantly higher Fe content is reported in the incipient melt [e.g., (*73*, *74*)].

4) MgO presents a major increase of its content from 15 to 25 wt% to ~40 wt% with increasing Φ. Still, its compatible character decreases with increasing *P*; its content in the melt at low Φ evolves

from ~15 to ~25 wt% with increasing P. At high Φ, melts produced at P higher than ~7 GPa contain 25 to 30% MgO, similar to komatiitic liquids.

5) SiO_2 contents in the melt stagnate at 43 to 48 wt% at all Φ and below 23 to 25 GPa. Therefore, upper mantle melts should not be particularly depleted or enriched in SiO_2 compared to pyrolite. The highest melt SiO_2 content is 50 to 52% at 23 to 25 GPa and Φ lower than 20%. This effect can be related to ferropericlase being the liquidus phase in this P range [as reported in (*75*) for peridotite].

6) Simultaneous low MgO and stagnant or high SiO_2 contents yield high SiO_2/MgO ratio in the first melts to form [e.g., (*76*)].

7) High Ti, Na, and K concentrations are measured in the first drops of melts (table S4), and these contents decrease fast with increasing Φ, as expected for strongly incompatible elements.

Geodynamical modeling

Following our previous work (*59*), we calculate the time evolution of the pyrolitic-mantle geotherm during the first ~3 Ga of Earth's history. First, we set the primordial mantle T gradient parallel and slightly above the mantle solidus. It corresponds to the thermal state of the mushy mantle when the magma ocean has solidified to Φ of ~40% at all depths, several thousand years after the major Moon-forming impact (*77*). We note that this model could rise discussions; still, such highly superadiabatic T gradient is very likely to happen after the global magma ocean solidification. Then, we use a one-dimensional numerical model in spherical geometry accounting for turbulent convective heat transfer to calculate the extent of cooling at all mantle depths. This is the same calculations as recently reported for a chondritic-type mantle [see details in (*59*)].

We adopt the physical parameters typical of the pyrolitic mantle model. The composition establishes a number of thermodynamical parameters; e.g., equation of state, heat capacity, and latent heat of fusion, which are all calculated using a mixing model based on the molar fractions of enstatite (37.63%), forsterite (51.64%), fayalite (5.39%), anorthite (3.13%), and diopside (2.22%). Concerning the pyrolite solidus and liquidus, we used (i) the solidus and liquidus measured below ~27 GPa in this study (Fig. 4), (ii) the solidus measured recently in LMV using the laser-heated diamond anvil cell, which is very similar to the solidus of the chondritic-type mantle (*78*), and (iii) the same liquidus as reported for the chondritic-type mantle (*78*) but shifted by −200 K to match the liquidus T of pyrolite found at ~25 GPa and ~2500 K in this study.

We observe that the liquidus T profile in the lower mantle does not have a substantial impact on the results of our calculations. When fitted using Simon-Glatzel equations $T_m(P) = T_0(P/a + 1)^{1/c}$, where $T_m(P)$ and P are melting T(K) and P(GPa), respectively, it yields (i) (T_0 = 1622.7; a = 237.79; c = 0.33615) and (T_0 = 349.82; a = 0.10937; c = 2.9646) for the pyrolite solidus at P below and above 24 GPa, respectively, and (ii) (T_0 = 1931.2; a = 222.27; c = 0.48148) and (T_0 = 1498.9; a = 10.760; c = 2.3668) for the pyrolite liquidus at P below and above 18 GPa, respectively (Fig. 8).

For mantle viscosity, we consider equation 19B of (*59*) with $A_{diff} = 10^{-15}$ Pa^{-1} s^{-1}, $V_{diff} = 10^{-6}$ m^3 mol^{-1}, E_{diff} = 200 kJ mol^{-1}, and no dichotomy between upper and lower mantle viscosity. We also considered radiogenic heating as in our previous work.

In addition to the calculated pyrolitic-mantle geotherm as a function of time, we also calculate several mantle adiabatic T profiles for the deep mantle. They are primarily constrained by the pyrolite equation of state; however, complications arise at T between the solidus and the liquidus, where the degree of mantle partial melting can change with depth. This is taken into account by considering the latent heat of fusion for the variation of Φ with depth, as already described in previous works [e.g., (*50*)]. It yields adiabatic T profiles steeper for the mushy mantle between the solidus and liquidus compared to subsolidus mantle conditions (Fig. 8).

SUPPLEMENTARY MATERIALS

Supplementary material for this article is available at https://science.org/doi/10.1126/sciadv.abo1036

REFERENCES AND NOTES

1. C. Herzberg, K. Condie, J. Korenaga, Thermal history of the Earth and its petrological expression. *Earth Planet. Sci. Lett.* **292**, 79–88 (2010).
2. C. Herzberg, M. J. O'Hara, Plume-associated ultramafic magmas of phanerozoic age. *J. Petrol.* **43**, 1857–1883 (2002).
3. C. Herzberg, P. D. Asimow, Petrology of some oceanic island basalts: PRIMELT2.XLS software for primary magma calculation. *Geochem. Geophys. Geosystems* **9**, Q09001 (2008).
4. C.-T. Lee, P. Luffi, T. Plank, H. Dalton, W. Leeman, Constraints on the depths and temperatures of basaltic magma generation on Earth and other terrestrial planets using new thermobarometers for mafic magmas. *Earth Planet. Sci. Lett.* **279**, 20–33 (2009).
5. T. Grove, S. Parman, Thermal evolution of the Earth as recorded by komatiites. *Earth Planet. Sci. Lett.* **219**, 173–187 (2004).
6. I. H. Campbell, R. W. Griffiths, The changing nature of mantle hotspots through time: Implications for the chemical evolution of the mantle. *J. Geol.* **100**, 497–523 (1992).
7. A. Piccolo, B. Kaus, R. White, R. Palin, Generation of earth's early continents from a relatively cool archean mantle. *Geochem. Geophys. Geosystems* **20**, 1679–1697 (2019).
8. S. Matthews, K. Wong, O. Shorttle, M. Edmonds, J. Maclennan, Do olivine crystallization temperatures faithfully record mantle temperature variability? *Geochem. Geophys. Geosystems* **22**, e2020GC009157 (2021).
9. J. Ganne, X. Feng, Primary magmas and mantle temperatures through time. *Geochem. Geophys. Geosystems* **18**, 872–888 (2017).
10. M. Yoshida, A new conceptual model for whole mantle convection and the origin of hotspot plumes. *J. Geodyn.* **78**, 32–41 (2014).
11. R. E. Ernst, *Large Igneous Provinces* (Cambridge University Press, 2014).
12. J. Arndt, S. J. Barnes, C. M. Lesher, *Komatiite* (Cambridge University Press, 2008).
13. J. M. D. Day, Hotspot volcanism and highly siderophile elements. *Chem. Geol.* **341**, 50–74 (2013).
14. S. A. Gibson, Major element heterogeneity in archean to recent mantle plume starting-heads. *Earth Planet. Sci. Lett.* **195**, 59–74 (2002).
15. B. Jahn, G. Gruau, A. Glikson, Komatiites of the Onverwacht Group, S. Africa: REE geochemistry, Sm/Nd age and mantle evolution. *Contrib. to Mineral. Petrol.* **80**, 25–40 (1982).
16. M. le Bas, IUGS reclassification of the high-mg and picritic volcanic rocks. *J. Petrol.* **41**, 1467–1470 (2000).
17. C. Herzberg, M. J. O'Hara, Phase equilibrium constraints on the origin of basalts, picrites, and komatiites. *Earth Sci. Rev.* **44**, 39–79 (1998).
18. D. Green, Genesis of archean peridotitic magmas and constraints on archean geothermal gradients and tectonics. *Geology* **3**, 15–18 (1975).
19. C. Herzberg, J. Zhang, Melting experiments on anhydrous peridotite KLB-1: Compositions of magmas in the upper mantle and transition zone. *J. Geophys. Res.* **101**, 8271–8295 (1996).
20. R. Nomura, K. Hirose, K. Uesugi, Y. Ohishi, A. Tsuchiyama, A. Miyake, Y. Ueno, Low core-mantle boundary temperature inferred from the solidus of pyrolite. *Science* **343**, 522–525 (2014).
21. K. Litasov, E. Ohtani, Phase relations and melt compositions in CMAS–pyrolite–H_2O system up to 25 GPa. *Phys. Earth Planet. Inter.* **134**, 105–127 (2002).
22. T. Inoue, R. P. Rapp, J. Z. Zhang, T. Gasparik, D. J. Weidner, T. Irifune, Garnet fractionation in a hydrous magma ocean and the origin of Al-depleted komatiites: Melting experiments of hydrous pyrolite with REEs at high pressure. *Earth Planet. Sci. Lett.* **177**, 81–87 (2000).
23. M. J. Walter, Melting of garnet peridotite and the origin of komatiite and depleted lithosphere. *J. Petrol.* **39**, 29–60 (1998).
24. M. Boyet, M. Garçon, N. Arndt, R. W. Carlson, Z. Konc, Residual liquid from deep magma ocean crystallization in the source of komatiites from the ICDP drill core in the Barberton Greenstone Belt. *Geochim. Cosmochim. Acta* **304**, 141–159 (2021).
25. C. Herzberg, Generation of plume magmas through time: An experimental perspective. *Chem. Geol.* **126**, 1–16 (1995).

26. A. C. Kerr, G. F. Marriner, N. T. Arndt, J. Tarney, A. Nivia, A. D. Saunders, R. A. Duncan, The petrogenesis of Gorgona komatiites, picrites and basalts: New field, petrographic and geochemical constraints. *Lithos.* **37**, 245–260 (1996).
27. E. Takahashi, Melting of a dry peridotite KLB-1 up to 14 GPa—Implications on the origin of the peridotitic upper mantle. *J. Geophys. Res. Solid Earth Planets* **91**, 9367–9382 (1986).
28. V. Courtillot, A. Davaille, J. Besse, J. Stock, Three distinct types of hotspots in the Earth's mantle. *Earth Planet. Sci. Lett.* **205**, 295–308 (2003).
29. G. Foulger, J. Natland, D. Presnall, D. Anderson, *Plates, Plumes, and Paradigms* (Geological Society of America, 2005).
30. C. A. Dalton, C. H. Langmuir, A. Gale, Geophysical and geochemical evidence for deep temperature variations beneath mid-ocean ridges. *Science* **344**, 80–83 (2014).
31. S. Maruyama, M. Santosh, D. Zhao, Superplume, supercontinent, and post-perovskite: Mantle dynamics and anti-plate tectonics on the core–mantle boundary. *Gondw. Res.* **11**, 7–37 (2007).
32. N. Coltice, H. Bertrand, P. Rey, F. Jourdan, B. R. Phillips, Y. Ricard, Global warming of the mantle beneath continents back to the Archaean. *Gondw. Res.* **15**, 254–266 (2009).
33. L. T. Elkins-Tanton, Continental magmatism, volatile recycling, and a heterogeneous mantle caused by lithospheric gravitational instabilities. *J. Geophys. Res. Solid Earth* **112**, B03405 (2007).
34. C. Hemond, N. T. Arndt, U. Lichtenstein, A. W. Hofmann, N. Oskarsson, S. Steinthorsson, The heterogeneous Iceland plume: Nd-Sr-O isotopes and trace element constraints. *J. Geophys. Res.* **98**, 15833–15850 (1993).
35. F. Jourdan, A. Marzoli, H. Bertrand, S. Cirilli, L. Tanner, D. Kontak, G. McHone, P. Renne, G. Bellieni, $^{40}Ar/^{39}Ar$ ages of CAMP in North America: Implications for the Triassic–Jurassic boundary and the ^{40}K decay constant bias. *Lithos* **110**, 167–180 (2009).
36. M. G. Jackson, M. D. Kurz, S. R. Hart, R. K. Workman, New Samoan lavas from Ofu Island reveal a hemispherically heterogeneous high 3He/4He mantle. *Earth Planet. Sci. Lett.* **264**, 360–374 (2007).
37. J. Blichert-Toft, N. T. Arndt, Hf isotope compositions of komatiites. *Earth Planet. Sci. Lett.* **171**, 439–451 (1999).
38. T. Matsumoto, A. Seta, J. Matsuda, M. Takebe, Y. Chen, S. Arai, Helium in the Archean komatiites revisited: Significantly high 3He/4He ratios revealed by fractional crushing gas extraction. *Earth Planet. Sci. Lett.* **196**, 213–225 (2002).
39. F. A. Davis, M. M. Hirschmann, M. Humayun, The composition of the incipient partial melt of garnet peridotite at 3 GPa and the origin of OIB. *Earth Planet. Sci. Lett.* **308**, 380–390 (2011).
40. M. B. Baker, E. M. Stolper, Determining the composition of high-pressure mantle melts using diamond aggregates. *Geochim. Cosmochim. Acta* **58**, 2811–2827 (1994).
41. R. J. Kinzler, Melting of mantle peridotite at pressures approaching the spinel to garnet transition: Application to mid-ocean ridge basalt petrogenesis. *J. Geophys. Res. B Solid Earth* **102**, 853–874 (1997).
42. E. Takahashi, T. Shimazaki, Y. Tsuzaki, H. Yoshida, Melting study of a peridotite KLB-1 to 6.5 GPa, and the origin of basaltic magmas. *Philos. Trans. Royal Soc. Phys. Sci. Eng.* **342**, 105–120 (1993).
43. K. Hirose, I. Kushiro, Partial melting of dry peridotite at high-pressures—Determination of compositions of melts segregated from peridotite using aggregates of diamonds. *Earth Planet. Sci. Lett.* **114**, 477–489 (1993).
44. D. Novella, D. J. Frost, The composition of hydrous partial melts of garnet peridotite at 6 GPa: Implications for the origin of group II kimberlites. *J. Petrol.* **55**, 2097–2123 (2014).
45. D. Andrault, G. Pesce, G. Manthilake, J. Monteux, N. Bolfan-Casanova, J. Chantel, D. Novella, N. Guignot, A. King, J.-P. Itie, L. Hennet, Deep and persistent melt layer in the Archaean mantle. *Nat. Geosci.* **11**, 139–143 (2018).
46. R. G. Trønnes, D. J. Frost, Peridotite melting and mineral–Melt partitioning of major and minor elements at 22–24.5 GPa. *Earth Planet. Sci. Lett.* **197**, 117–131 (2002).
47. C. Herzberg, P. Raterron, J. Zhang, New experimental observations on the anhydrous solidus for peridotite KLB-1. *Geochim. Cosmochim. Acta* **1**, 1051-14 (2000).
48. T. Scott, D. L. Kohlstedt, The effect of large melt fraction on the deformation behavior of peridotite. *Geochim. Cosmochim. Acta* **246**, 177–187 (2006).
49. L. Xie, A. Yoneda, D. Yamazaki, G. Manthilake, Y. Higo, Y. Tange, N. Guignot, A. King, M. Scheel, D. Andrault, Formation of bridgmanite-enriched layer at the top lower-mantle during magma ocean solidification. *Nat. Commun.* **11**, 548 (2020).
50. G. H. Miller, E. M. Stolper, T. J. Ahrens, The equation of state of a molten komatiite 2, Application to komatiite petrogenesis and the Hadean mantle. *J. Geophys. Res.* **96**, 11849–11864 (1991).
51. T. Katsura, A. Yoneda, D. Yamazaki, T. Yoshino, E. Ito, Adiabatic temperature profile in the mantle. *Phys. Earth Planet. Inter.* **183**, 212–218 (2010).
52. A. Davaille, A simultaneous generation of hotpots and superswells by convection in a heterogeneous planetary mantle. *Nature* **402**, 756–760 (1999).
53. J. Korenaga, Urey ratio and the structure and evolution of Earth's mantle. *Rev. Geophys.* **46**, RG2007 (2008).
54. K. C. Condie, R. C. Aster, J. van Hunen, A great thermal divergence in the mantle beginning 2.5 Ga: Geochemical constraints from greenstone basalts and komatiites. *Geosci. Front.* **7**, 543–553 (2016).
55. G. F. Davies, Effect of plate bending on the Urey ratio and the thermal evolution of the mantle. *Earth Planet. Sci. Lett.* **287**, 513–518 (2009).
56. H. Iwamori, D. McKenzie, E. Takahashi, Melt generation by isentropic mantle upwelling. *Earth Planet. Sci. Lett.* **134**, 253–266 (1995).
57. C. Herzberg, P. D. Asimow, N. Arndt, Y. Niu, C. M. Lesher, J. G. Fitton, M. J. Cheadle, A. D. Saunders, Temperatures in ambient mantle and plumes: Constraints from basalts, picrites, and komatiites. *Geochem. Geophys. Geosystems* **8**, 2006GC001390 (2007).
58. C. G. Farnetani, A. W. Hofmann, Dynamics and internal structure of the Hawaiian plume. *Earth Planet. Sci. Lett.* **295**, 231–240 (2010).
59. J. Monteux, D. Andrault, M. Guitreau, H. Samuel, S. Demouchy, A mushy Earth's mantle for more than 500 Myr after the magma ocean solidification. *Geophys. J. Int.* **221**, 1165–1181 (2020).
60. N. Arndt, A. Davaille, Episodic earth evolution. *Tectonophysics* **609**, 661–674 (2013).
61. W. B. Moore, A. A. G. Webb, Heat-pipe earth. *Nature* **501**, 501–505 (2013).
62. M. Maurice, N. Tosi, H. Samuel, A. C. Plesa, C. Huttig, D. Breuer, Onset of solid-state mantle convection and mixing during magma ocean solidification. *J. Geophys. Res. Planets* **122**, 577–598 (2017).
63. A. E. Ringwood, in *International Series in the Earth's and Planetary Sciences*, (McGraw-Hill, 1975), pp. 189–194.
64. W. F. McDonough, S. S. Sun, The composition of the earth. *Chem. Geol.* **120**, 223–253 (1995).
65. L. Hennet, V. Cristiglio, J. Kozaily, I. Pozdnyakova, H. E. Fischer, A. Bytchkov, J. W. E. Drewitt, M. Leydier, D. Thiaudiere, S. Gruner, S. Brassamin, D. Zanghi, G. J. Cuello, M. Koza, S. Magazu, G. N. Greaves, D. L. Price, Aerodynamic levitation and laser heating: Applications at synchrotron and neutron sources. *Eur. Phys. J. Spec. Top.* **196**, 151–165 (2011).
66. D. Andrault, M. Muñoz, G. Pesce, V. Cerantola, A. Chumakov, I. Kantor, S. Pascarelli, R. Rüffer, L. Hennet, Large oxygen excess in the primitive mantle could be the source of the great oxygenation event. *Geochem. Perspect. Lett.* **6**, 5–10 (2018).
67. M. Mercier, A. Di Muro, N. Métrich, D. Giordano, O. Belhadj, C. W. Mandeville, Spectroscopic analysis (FTIR, Raman) of water in mafic and intermediate glasses and glass inclusions. *Geochim. Cosmochim. Acta* **74**, 5641–5656 (2010).
68. T. A. Shishkina, R. E. Botcharnikov, F. Holtz, R. R. Almeev, A. M. Jazwa, A. A. Jakubiak, Compositional and pressure effects on the solubility of H_2O and CO_2 in mafic melts. *Chem. Geol.* **388**, 112–129 (2014).
69. A. Boujibar, D. Andrault, M. A. Bouhifd, N. Bolfan-Casanova, J.-L. Devidal, N. Trcera, Metal-silicate partitioning of sulphur, new experimental and thermodynamic constraints on planetary accretion. *Earth Planet. Sci. Lett.* **391**, 42–54 (2014).
70. A. Pommier, K. Leinenweber, D. L. Kohlstedt, C. Qi, E. J. Garnero, S. J. MacKwell, J. A. Tyburczy, Experimental constraints on the electrical anisotropy of the lithosphere-asthenosphere system. *Nature* **522**, 202–206 (2015).
71. Y. Tange, E. Takahashi, Y. Nishihara, K. I. Funakoshi, N. Sata, Phase relations in the system MgO-FeO-SiO_2 to 50 GPa and 2000 degrees C: An application of experimental techniques using multianvil apparatus with sintered diamond anvils. *J. Geophys. Res. Solid Earth.* **114**, B02214 (2009).
72. J. Hernlund, K. Leinenweber, D. Locke, J. A. Tyburczy, A numerical model for steady-state temperature distributions in solid-medium high-pressure cell assemblies. *Am. Mineral.* **91**, 295–305 (2006).
73. K. N. Matsukage, Z. Jing, S. I. Karato, Density of hydrous silicate melt at the conditions of Earth's deep upper mantle. *Nature* **438**, 488–491 (2005).
74. P. Condamine, D. J. Frost, in *Annual Report* (Bayerisches Geoinstitute, 2018).
75. E. Ito, A. Kubo, T. Katsura, M. J. Walter, Melting experiments of mantle materials under lower mantle conditions with implications for magma ocean differentiation. *Phys. Earth Planet. Inter.* **143–144**, 397–406 (2004).
76. C. Liebske, D. J. Frost, Melting phase relations in the MgO-$MgSiO_3$ system between 16 and 26 GPa: Implications for melting in Earth's deep interior. *Earth Planet. Sci. Lett.* **345**, 159–170 (2012).
77. J. Monteux, D. Andrault, H. Samuel, On the cooling of a deep terrestrial magma ocean. *Earth Planet. Sci. Lett.* **448**, 140–149 (2016).
78. D. Andrault, N. Bolfan-Casanova, G. Lo Nigro, M. A. Bouhifd, G. Garbarino, M. Mezouar, Melting curve of the deep mantle applied to properties of early magma ocean and actual core-mantle boundary. *Earth Planet. Sci. Lett.* **304**, 251–259 (2011).
79. W. Wang, E. Takahashi, Subsolidus and melting experiments of K-doped peridotite KLB-1 to 27 GPa: Its geophysical and geochemical implications. *Most* **105**, 2855–2868 (2000).
80. H. S. Smith, A. J. Erlank, Geochemistry and petrogenesis of komatiites from the Barberton greenstone belt, South Africa. *Komatiites* , 347–397 (1982).
81. C. Herzberg, Depth and degree of melting of komatiites. *J. Geophys. Res.* **97**, 4521–4540 (1992).
82. Y. Lahaye, N. Arndt, Alteration of a komatiite flow from Alexo, Ontario, Canada. *J. Petrol.* **37**, 1261–1284 (1996).
83. M. J. de Wit, R. A. Hart, R. J. Hart, The Jamestown Ophiolite Complex, Barberton mountain belt: A section through 3.5 Ga oceanic crust. *J. African Earth Sci (1983)* **6**, 681–730 (1987).

84. D. R. Pyke, A. J. Naldrett, O. R. Eckstrand, Archean ultramafic flows in Munro Township, Ontario. *GSA Bull.* **84**, 955–978 (1973).
85. B. Aitken, L. Echeverría, Petrology and geochemistry of komatiites and tholeiites from Gorgona Island, Colombia. *Contrib. to Mineral. Petrol.* **86**, 94–105 (1984).
86. E. Nisbet, N. Arndt, M. Bickle, W. Cameron, C. Chauvel, M. Cheadle, E. Hegner, A. Martin, R. Renner, E. Roedder, Uniquely fresh 2.7 Ga Komatiites from the Belingwe Greenstone-Belt, Zimbabwe. *Geology* **15**, 1147–1150 (1987).
87. M. Bickle, A. Martin, E. G. Nisbet, Basaltic and peridotitic komatiites and stromatolites above a basal unconformity in the Belingwe greenstone belt, Rhodesia. *Earth Planet. Sci. Lett.* **27**, 155–162 (1975).
88. Q. Xie, R. Kerrich, J. Fan, HFSE/REE fractionations recorded in three komatiite-basalt sequences, Archean Abitibi greenstone belt: Implications for multiple plume sources and depths. *Geochim. Cosmochim. Acta* **57**, 4111–4118 (1993).
89. E. Nisbet, M. Bickle, A. Martin, The mafic and ultramafic lavas of the belingwe greenstone belt, Rhodesia. *J. Petrol.* **18**, 521–566 (1977).
90. J. G. Arth, N. T. Arndt, A. J. Naldrett, Genesis of archean komatiites from Munro Township, Ontario: Trace-element evidence. *Geology* **5**, 590–594 (1977).
91. J. A. Hallberg, D. A. C. Williams, Archaean mafic and ultramafic rock associations in the Eastern Goldfields region, Western Australia. *Earth Planet. Sci. Lett.* **15**, 191–200 (1972).
92. S. S. Sun, R. W. Nesbitt, Petrogenesis of Archaean ultrabasic and basic volcanics: Evidence from rare earth elements. *Contrib. to Mineral. Petrol.* **65**, 301–325 (1978).
93. R. Nesbitt, S. S. Sun, A. C. Purvis, Komatiites: Geochemistry and genesis. *Can. Mineral.* **17**, 165–186 (1979).
94. B.-M. Jahn, B. Auvray, S. Blais, R. Capdevila, J. Cornichet, F. Vidal, J. Hameurt, Trace element geochemistry and petrogenesis of finnish greenstone belts. *J. Petrol.* **21**, 201–244 (1980).
95. R. Nesbitt, S.-S. Sun, Geochemistry of Archaean spinifex-textured peridotites and magnesian and low-magnesian tholeiites. *Earth Planet. Sci. Lett.* **31**, 433–453 (1976).
96. D. A. C. Williams, R. G. Furnell, Reassessment of part of the Barberton type area, South Africa. *Precambrian Res.* **9**, 325–347 (1979).
97. G. Gruau, C. Chauvel, N. T. Arndt, J. Cornichet, Aluminum depletion in komatiites and garnet fractionation in the early Archean mantle: Hafnium isotopic constraints. *Geochim. Cosmochim. Acta* **54**, 3095–3101 (1990).
98. T. Chaudhuri, M. Satish-Kumar, R. Mazumder, S. Biswas, Geochemistry and Sm-Nd isotopic characteristics of the Paleoarchean Komatiites from Singhbhum Craton, Eastern India and their implications. *Precambrian Res.* **298**, 385–402 (2017).
99. N. Arndt, Komatiites, kimberlites, and boninites. *J. Geophys. Res.* **108**, 2293 (2003).
100. N. Arndt, A. Fowler, Textures in komatiites and variolitic basalts, in *The Precambrian Earth: Tempos and Events* (Elsevier, 2004).
101. P. A. Sossi, S. M. Eggins, R. W. Nesbitt, O. Nebel, J. M. Hergt, I. H. Campbell, H. S. C. O'Neill, M. Van Kranendonk, D. R. Davies, Petrogenesis and geochemistry of archean komatiites. *J. Petrol.* **57**, 147–184 (2016).
102. Y. Lahaye, N. Arndt, G. Byerly, C. Chauvel, S. Fourcade, G. Gruau, The influence of alteration on the trace-element and Nd isotopic compositions of komatiites. *Chem. Geol.* **126**, 43–64 (1995).
103. S. Sun, (1984).
104. F. F. Guo, S. Svetov, W. D. Maier, E. Hanski, S. H. Yang, Z. Rybnikova, Geochemistry of komatiites and basalts in Archean greenstone belts of Russian Karelia with emphasis on platinum-group elements. *Miner. Depos.* **55**, 971–990 (2020).
105. M. J. Bickle, N. T. Arndt, E. G. Nisbet, J. L. Orpen, A. Martin, R. R. Keays, R. Renner, Geochemistry of the igneous rocks of the Belingwe greenstone belt: Alteration, contamination and petrogenesis, in *The Geology of the Belingwe Greenstone Belt, Zimbabwe* (CRC Press, 2020) pp. 175–213.
106. I. Vlastélic, T. Staudacher, M. Semet, Rapid change of lava composition from 1998 to 2002 at Piton de la Fournaise (Réunion) inferred from Pb isotopes and trace elements: Evidence for variable crustal contamination. *J. Petrol.* **46**, 79–107 (2005).
107. P. M. Holm, R. C. O. Gill, A. K. Pedersen, J. G. Larsen, N. Hald, T. F. D. Nielsen, M. F. Thirlwall, The tertiary picrites of West Greenland: Contributions from 'Icelandic' and other sources. *Earth Planet. Sci. Lett.* **115**, 227–244 (1993).
108. J. F. G. Wilkinson, H. D. Hensel, The petrology of some picrites from Mauna Loa and Kilauea volcanoes, Hawaii. *Contrib. to Mineral. Petrol.* **98**, 326–345 (1988).
109. S. Révillon, N. T. Arndt, E. Hallot, A. C. Kerr, J. Tarney, Petrogenesis of picrites from the Caribbean Plateau and the North Atlantic magmatic province. *Lithos* **49**, 1–21 (1999).
110. A. Kerr, J. Mahoney, Oceanic plateaus: Problematic plumes, potential paradigms. *Chem. Geol.* **241**, 332–353 (2007).
111. A. C. Kerr, *Oceanic Plateaus* (Elsevier, ed. 2, 2014), vol. 4.
112. Z. Zhang, J. J. Mahoney, J. Mao, F. Wang, Geochemistry of picritic and associated basalt flows of the western emeishan flood basalt province, China. *J. Petrol.* **47**, 1997–2019 (2006).
113. D. Wang, S. Karato, Electrical conductivity of talc aggregates at 0.5 GPa: Influence of dehydration. *Phys. Chem. Miner.* **40**, 11–17 (2013).
114. H. Brandstätter, I. Hanzu, M. Wilkening, Myth and reality about the origin of inductive loops in impedance spectra of lithium-ion electrodes—A critical experimental approach. *Electrochim. Acta* **207**, 218–223 (2016).
115. D. Klotz, Negative capacitance or inductive loop?—A general assessment of a common low frequency impedance feature. *Electrochem. Commun.* **98**, 58–62 (2019).
116. T. Yoshino, A. Shimojuku, S. Shan, X. Guo, D. Yamazaki, E. Ito, Y. Higo, K. I. Funakoshi, Effect of temperature, pressure and iron content on the electrical conductivity of olivine and its high-pressure polymorphs. *J. Geophys. Res. Solid Earth* **117**, 1–15 (2012).
117. T. Yoshino, Laboratory electrical conductivity measurement of mantle minerals. *Surv. Geophys.* **31**, 163–206 (2010).
118. J. Zhang, C. Herzberg, Melting experiments on anhydrous peridotite KLB-1 from 5.0 to 22.5 GPa. *J. Geophys. Res.* **99**, 17729–17742 (1994).

Acknowledgments: We thank two anonymous reviewers for their thoughtful comments. We thank L. Hennet for the preparation of the pyrolitic glasses and L. Xie, Q. Dumont, and M. Garçon for help and fruitful discussions. **Funding:** This research was financed by the French Government Laboratory of Excellence initiative no. ANR-10-LABX-0006 and the Université Clermont Auvergne. This is the laboratory of excellence Clervolc contribution no. 561.
Author contributions: R.P. prepared all experiments. R.P. and G.M. performed the conductivity measurements. R.P., D.A., G.M., N.G., A.K., and L.H. performed the experiments at SOLEIL. R.P. and J.L.D. performed the sample characterization and chemical analyses of melts. J.M. and D.A. elaborated the geodynamic modeling. R.P. and D.A. wrote the manuscript, which was revised by G.M. and J.M. and validated by all coauthors. **Competing interests:** The authors declare that they have no competing interests. **Data and materials availability:** All data needed to evaluate the conclusions in the paper are present in the paper and/or the Supplementary Materials.

Submitted 13 January 2022
Accepted 17 August 2022
Published 2 November 2022
10.1126/sciadv.abo1036

ScienceAdvances

Deep mantle origin of large igneous provinces and komatiites

Rmy Pierru, Denis Andrault, Geeth Manthilake, Julien Monteux, Jean Luc Devidal, Nicolas Guignot, Andrew King, and Laura Henry

Sci. Adv., **8** (44), eabo1036.
DOI: 10.1126/sciadv.abo1036

8 Cas des satellites de glace

La plupart des processus physiques évoqués lors des premières étapes de la formation des planètes se produisent également dans la partie extérieure du Système Solaire, lors de la formation des satellites de glace. Dans la majorité de ces corps, le manteau est principalement composé de glace d'eau, tandis que le noyau est essentiellement constitué de matériaux rocheux. Cependant, des différences de composition et de structure interne existent entre les principaux satellites glacés de Jupiter et de Saturne, suggérant des histoires d'accrétion et de différenciation distinctes (par exemple Tobie et al. (2013) et Monteux et al. (2018)). Ces satellites se seraient formés dans des disques circum-planétaires à partir d'agrégats de glace et de roche (Canup and Ward, 2002; Estrada et al., 2008). Bien que la variété des structures internes des lunes glacées soit encore débattue, le rôle essentiel de l'accrétion est largement accepté pour comprendre les différences entre les lunes glacées.

8.1 Impact géant et déformation du noyau d'Encelade

Malgré sa petite taille (R=252 km), Encelade, une des lunes de Saturne, est l'un des corps géologiquement les plus actifs du système solaire. Son activité endogène surprenante est caractérisée par une province très active au pôle sud, d'où des éruptions de vapeur d'eau et de grains de glace émanant de crêtes tectoniques chaudes ont été observées par la sonde Cassini (Porco et al., 2006; Hansen et al., 2006; Waite et al., 2006; Spencer et al., 2006). Cette activité est associée à une énorme puissance thermique estimée entre 5 et 15 GW (Spencer and Nimmo, 2013), ce qui implique un intérieur chaud, compatible avec une couche d'eau liquide sous une couche de glace et un intérieur différencié (Nimmo and Kleine, 2007; Schubert et al., 2007). Les modèles de dissipation des marées peuvent expliquer pourquoi l'activité est concentrée aux pôles, où la dissipation devrait être maximale (Tobie et al., 2008; Běhounková et al., 2010). Cependant, il n'y a toujours pas d'explication satisfaisante sur la raison pour laquelle cette activité est localisée uniquement au sud, et non au nord.

Il a été proposé que la dichotomie entre les hémisphères nord et sud soit le résultat d'une asymétrie dans la forme du noyau rocheux McKinnon (2013). En raison de la faible pression et de la température modérée attendues dans le noyau d'Encelade, de grandes anomalies de topographie peuvent en effet être conservées sur de très longues périodes et peuvent expliquer pourquoi les activités de convection dans la couche de glace sont confinées uniquement au pôle sud (Showman et al., 2013). Outre la dépression polaire sud, les anomalies de topographie du noyau pourraient expliquer, au moins en partie, l'existence d'autres grandes dépressions observées à des latitudes modérées et non corrélées à des limites géologiques (Schenk and McKinnon, 2009). McKinnon (2013) a proposé trois hypothèses pour expliquer l'irrégularité possible du noyau rocheux d'Encelade : la fusion lors de l'accrétion de la région externe d'Encelade associée à une instabilité de degré un, l'accrétion de proto-lunes glacées autour de morceaux de roche irréguliers et l'assemblage par collision de deux proto-lunes précédemment différenciées.

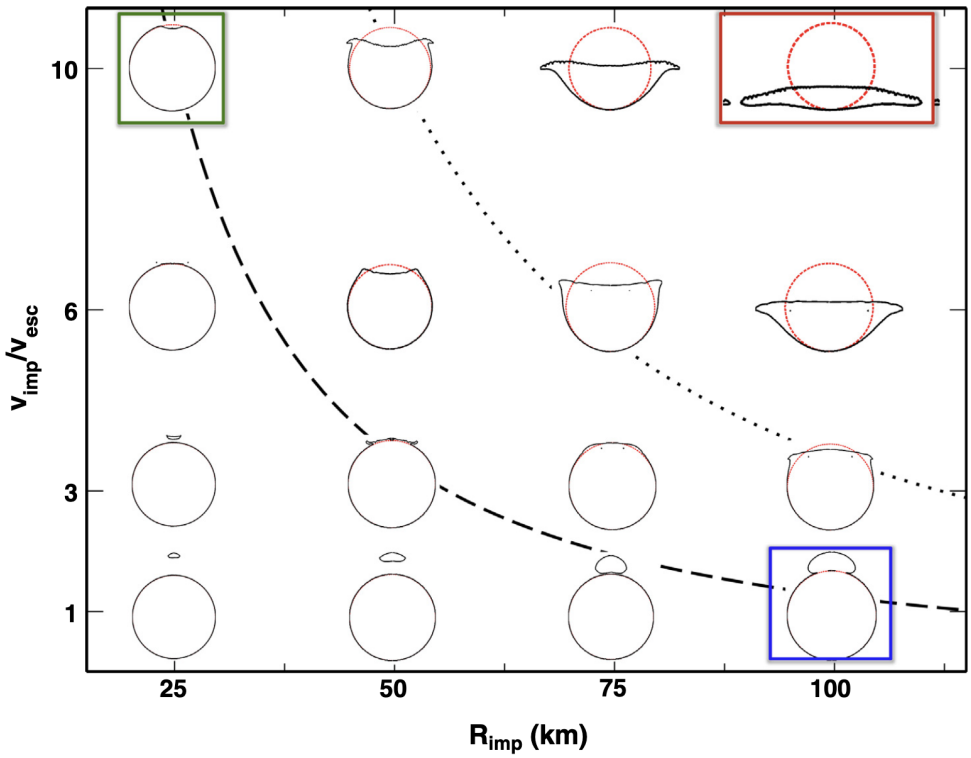

FIGURE 30 – Morphologie du noyau rocheux en fonction de la taille de l'impacteur et de la vitesse d'impact ($v_{esc} = 240$ m/s). Pour chaque morphologie, le cercle rouge représente la forme sphérique avant impact du noyau impacté. Au-dessus de la courbe noire en tirets, la topographie induite par l'impact est négative. En dessous de cette ligne théorique critique, la topographie induite par l'impact est positive. Au-dessus de la courbe noire en pointillés, des noyaux très fortement déformés se forment et la fluidisation acoustique peut contribuer à leur forme finale. Cependant la déformation est trop importante et probablement non compatible avec la morphologie d'Encelade. Nous limitons le temps de simulation post-impact à une heure, ce qui signifie que pour les grandes vitesses d'impact (≥ 6 km/s) et les grands rayons d'impact (≥ 75 km), le matériau rocheux excavé du noyau d'Encelade et en orbite autour de la lune se déplace toujours avec une vitesse significative à la fin de la simulation.(D'après Monteux et al. (2016b)).

Dans une étude développée au LPG Nantes, nous avons étudié les conséquences des collisions avec de grands impacteurs sur la forme du noyau. Nous avons effectué des simulations d'impact à l'aide du code iSALE2D (Wünnemann et al., 2006) en considérant de grands impacteurs différenciés ayant un rayon compris entre 25 et 100 km et des vitesses d'impact comprises entre 0.24 et 2.4 km/s. Nos simulations ont montré que les principaux paramètres contrôlant la forme du noyau rocheux d'Encelade après l'impact sont le rayon et la vitesse de l'impacteur et, dans une moindre mesure, la présence d'un océan d'eau interne ainsi que la porosité

et la résistance du noyau rocheux. Pour les impacts de faible énergie, les impacteurs ne traversent pas complètement le manteau glacé. L'enfoncement et l'étalement ultérieurs du noyau rocheux de l'impacteur entraînent une anomalie topographique positive du noyau. Dans le cas d'impacts modérément énergétiques, les impacteurs pénètrent complètement dans le manteau glacé, ce qui induit une topographie négative du noyau entourée d'une anomalie positive de moindre amplitude. La profondeur et l'étendue latérale de la zone excavée sont principalement déterminées par le rayon et la vitesse de l'impacteur. Dans le cas d'impacts très énergétiques, le noyau rocheux est fortement déformé et le corps entier est susceptible d'être perturbé. L'explication de la forme irrégulière du noyau d'Encelade sur de grandes longueurs d'onde par des impacts impliquerait de multiples collisions à faible vitesse (< 2.4 km/s) avec des impacteurs différenciés déca-kilométriques, ce qui n'est possible qu'après la période LHB.

8.2 Accrétion et évolution thermique des satellites de glace

Des différences de composition et de structure interne existent entre les principaux satellites glacés de Jupiter et de Saturne, suggérant des histoires d'accrétion et de différenciation distinctes (Kirk and Stevenson, 1987; Mueller and McKinnon, 1988; Mosqueira and Estrada, 2003; Barr and Canup, 2008). Le facteur de moment d'inertie élevé déduit des mesures gravimétriques de Galileo ($C/MR^2 = 0.346$) (Anderson et al., 2001) suggère que la séparation glace-roche pourrait être incomplète à l'intérieur de Callisto, une des lunes de Jupiter. En revanche, Ganymède a un moment d'inertie beaucoup plus faible ($C/MR^2 = 0.31$) (Anderson et al., 2001) et montre des signes d'activité endogène passée (Pappalardo et al., 2004). Une séparation complète de la glace et de la roche est suggérée pour Ganymède, ainsi que la formation d'un noyau métallique, à l'origine d'un champ magnétique intrinsèque relativement intense (Kivelson et al., 1998).

Avec une taille et une masse similaires, Titan, lune de Saturne, pourrait être un cas intermédiaire entre Callisto et Ganymède. Son moment d'inertie estimé à partir des mesures de gravité de Cassini (Iess et al., 2010, 2012) suggère que l'intérieur de Titan est plus différencié que Callisto mais probablement beaucoup moins que Ganymède. Comme Callisto, Titan pourrait encore posséder une couche de mélange glace-roche entre un noyau rocheux et un manteau extérieur riche en glace, à moins que le noyau rocheux ne soit principalement composé de minéraux fortement hydratés (Sohl et al., 2010; Castillo-Rogez and Lunine, 2010). Le fait que l'intérieur de Callisto et peut-être de Titan puissent encore contenir une couche de mélange glace-roche suggère que le satellite a pu éviter une fusion importante lors de l'accrétion et de l'évolution ultérieure.

Il est possible d'éviter la fusion si l'accumulation de l'énergie d'accrétion est inefficace, c'est-à-dire si l'énergie est rayonnée à un taux comparable au taux d'accrétion (Schubert et al., 1981; Squyres et al., 1988; Kossacki and Leliwa-Kopystyński, 1993; Coradini et al., 1995; Grasset and Sotin, 1996; Barr and Canup, 2008, 2010). L'échelle de temps d'accrétion devrait être supérieure à 1 Myr pour éviter une fusion importante et donc une différenciation de Cal-

listo, tandis qu'une échelle de temps d'accrétion aussi courte que 1000-10 0000 ans pourrait être possible pour Ganymède. Cependant, ces échelles de temps dépendent de la façon dont le dépôt de chaleur et le refroidissement sont traités.

En utilisant une approche unidimensionnelle comme initialement développée pour l'accrétion des planètes terrestres (Safronov, 1978; Kaula, 1979), la croissance d'un corps peut être modélisée comme un dépôt de couches successives de matière. Dans ce cas, l'effet thermique d'un impact n'est pas considéré individuellement, mais est moyenné sur toute la surface et intégré. Cette approche est valable tant que les impacteurs restent petits (> 1 km) et sont distribués de manière aléatoire à la surface. Cela pourrait être le cas au tout début du processus d'accrétion, mais les impacteurs de plus de 1 km sont probablement devenus de plus en plus abondants à la fin de la phase d'accrétion (Estrada et al., 2009). On peut également s'attendre à des impacteurs de plus de 100 km (Sekine and Genda, 2012; Dwyer et al., 2013). Pour des impacts aussi volumineux, il est nécessaire de disposer d'une description détaillée de chaque impact, y compris du dépôt et du transfert d'énergie.

Afin de mieux comprendre l'évolution thermique des satellites de glace en croissance, nous avons développé un modèle numérique tri-dimensionel à partir du code numérique Oedipus développé par Choblet et al. (2007). Ce modèle numérique retrace, à partir d'une population réaliste d'impacteurs, l'évolution thermique d'un satellite de glace pendant son accrétion. Mes résultats montrent que la durée de l'accrétion ou les tailles caractéristiques des impacteurs influent peu sur l'état thermique du corps pendant son accrétion (Monteux et al., 2014). Cependant, l'efficacité avec laquelle l'énergie cinétique de l'impacteur est transmise au corps impacté sous forme de chaleur est un paramètre clé qui gouverne le taux de fusion final du satellite et ainsi sa structure interne. Par ailleurs, mes modèles montrent qu'il est probable que Callisto soit actuellement différenciée.

8.3 Le rôle de l'accrétion dans évolution de l'atmosphère de Titan

Titan, le plus gros satellite de Saturne, est aussi le seul satellite du système solaire à posséder une atmosphère massive. La masse et la composition de l'atmosphère massive de Titan, qui est actuellement dominée par N_2 et CH_4, ont probablement varié tout au long de son histoire en raison d'une combinaison de processus exogènes et endogènes. Les processus de formation de cette atmosphère riche en azote et méthane sont encore assez mal contraints (Tobie et al., 2013). Des études en laboratoire ont permis de quantifier la quantité de N_2 dégazé lors d'un impact sur un objet riche en NH_3 et de mettre en évidence l'importance des paramètres d'accrétion sur l'évolution de l'épaisseur de cette atmosphère (Sekine et al., 2011).

J'ai développé avec N. Marounina un modèle numérique pour déterminer la quantité de gaz qui peut être dégagée lors d'impacts géants se produisant au cours de l'accrétion de Titan et pendant le premier milliard d'années d'évolution (Marounina et al., 2015). Dans cette étude, nous étudions l'évolution de l'atmosphère de Titan pendant le late heavy bombardment (LHB) en modélisant la perte et l'apport compétitifs de volatils par les impacts cométaires

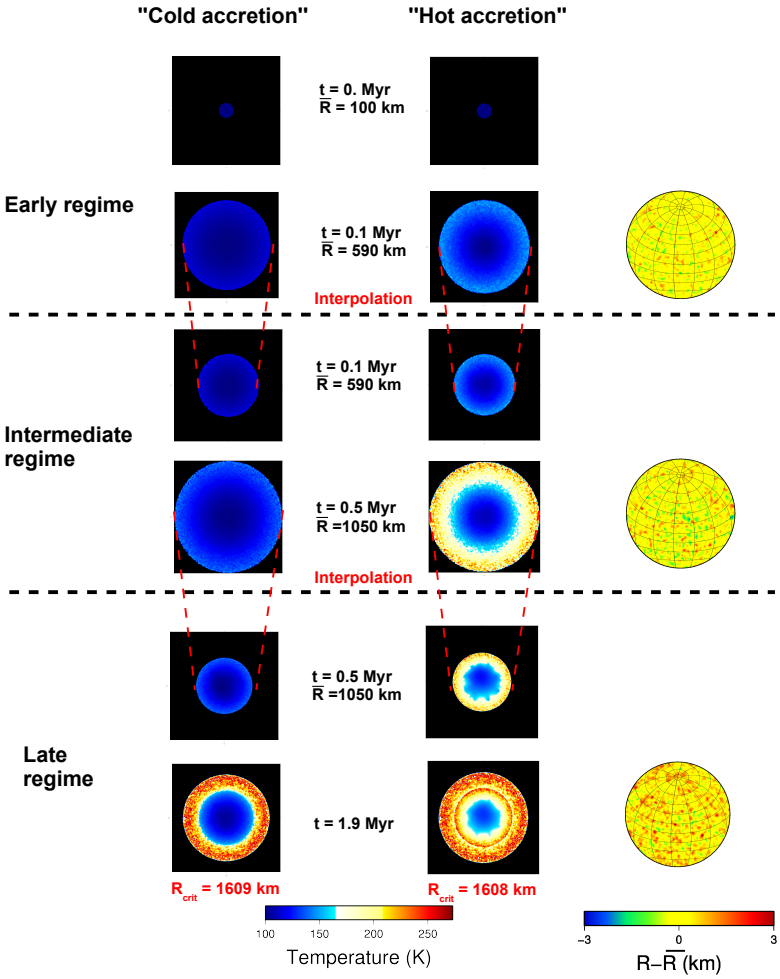

FIGURE 31 – Coupes équatoriales du champ de température (colonnes de gauche et du milieu) et représentations topographiques 3D (à droite) du satellite de glace en croissance en fonction du temps (de haut en bas). La colonne de gauche représente l'évolution d'un cas avec "accrétion froide" où, jusqu'à la fin du régime intermédiaire, $\gamma_{li} = \gamma_{lay} = 0.1$, $x_{m,li} = 10\%$ tandis que la colonne du milieu représente d'un cas avec "accrétion chaude" où $\gamma_{li} = \gamma_{lay} = 0.3$ et $x_{m,li} = 33\%$. L'échelle de couleur de la température est saturée en blanc pour la température au point de fusion de la glace (> 273 K). Entre chaque régime (précoce, intermédiaire, tardif), le champ de température est interpolé sur une grille plus large. Dans le régime tardif, $\gamma_{li} = 0.1$, $\gamma_{lay} = 0.3$; $x_{m,li} = 33\%$, $r_{min} = 10$ km et $r_{max} = 100$ km pour les colonnes de gauche et du milieu (D'après Monteux et al. (2014)).

et leurs conséquences sur l'équilibre atmosphérique. Nous modélisons le dégazage et le re-

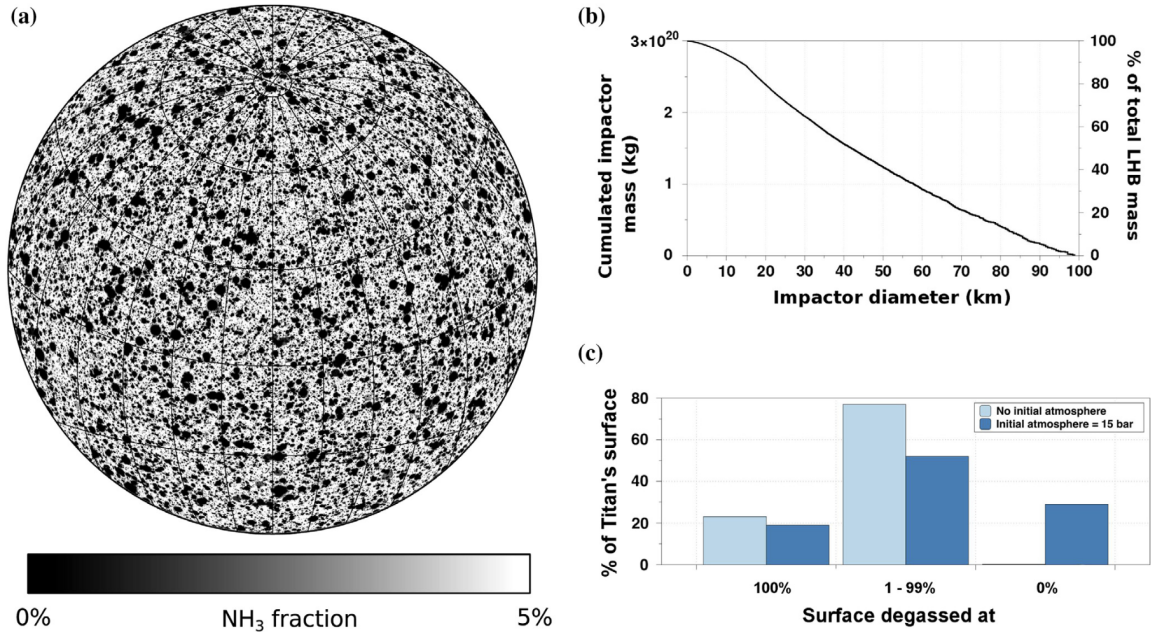

FIGURE 32 – (a) Distribution du NH_3 à la surface de Titan après un épisode de LHB (b) distribution des tailles d'impact cumulées pendant ce LHB et (c) taux de dégazage à la surface de Titan après le LHB pour la distribution illustrée dans le panel (a) (D'après Marounina et al. (2015).

froidissement de la croûte suite à des impacts géants et tout en tenant compte de l'érosion de l'atmosphère lors des impacts (Svetsov, 2007; Shuvalov, 2009). Pour des albédos de surface compris entre 0.1 et 0.7, nous avons examiné l'émergence d'une atmosphère pendant le LHB ainsi que l'évolution d'une atmosphère primitive de différentes masses et compositions avant cet événement, en tenant compte de la conversion NH3-N2 de la croûte induite par l'impact et du dégazage subséquent ainsi que de l'érosion atmosphérique induite par l'impact. En considérant une population d'impacteurs caractéristique du LHB, nous avons montré que la génération d'une atmosphère riche en N2 avec une masse équivalente à celle d'aujourd'hui nécessite une fraction de masse d'ammoniac de 2-5%, dépendant des albédos de surface, dans une couche glacée d'au moins 50 km sous la surface, impliquant un intérieur indifférencié au moment du LHB. A l'exception des albédos de surface élevés ($\geq$ 0.7) où la plupart du N2 libéré reste gelé à la surface, nos calculs indiquent que les impacts à grande vitesse ont conduit à une forte érosion atmosphérique. Pour un Titan différencié avec une fine croûte enrichie en ammoniac (65 km) et un albédo inférieur à 0.6, toute atmosphère préexistante au LHB devrait être plus de 5 fois plus massive qu'actuellement, afin de maintenir une atmosphère équivalente à celle d'aujourd'hui. Ceci implique qu'une atmosphère massive s'est formée sur Titan lors de son accrétion ou que l'atmosphère riche en azote a été générée après le LHB.

Référence personnelle

Tobie, G., Lunine, J., **Monteux, J.**, *Mouzis, O., Nimmo, F., 2013, The origin and evolution of Titan. In : Mueller-Wodarg, I., Griffith, C., Cravens, T., Lellouch, E. (Eds.), Titan : Surface, Atmosphere and Magnetosphere.* **LIEN HAL**.

Monteux, J., *G., Tobie, G., Choblet, M., Le Feuvre, 2014b, Can large icy Moons accrete undifferentiated, Icarus, Volume 237, Pages 377-387.* **LIEN HAL**.

Marounina, N., Tobie, G., Carpy, S., **Monteux, J.**, *Charnay, B., Grasset, O., 2015, Evolution of Titan's Atmosphere during the Late Heavy Bombardment, Icarus, 257, 324-335.* **LIEN HAL**.

Monteux, J., *Collins G.S., Tobie G., Choblet G., 2016b, Consequences of large impacts on Enceladus' core shape. Icarus vol.264, p.300-310.* **LIEN HAL**.

Monteux, J., *Golabek G.J., Rubie D.C., Tobie G., Young E.D., 2018, Water and the interior structure of terrestrial planets and icy bodies. Space Science Reviews.* **LIEN HAL**.

2

The Origin and Evolution of Titan

G. TOBIE, J.I. LUNINE, J. MONTEUX, O. MOUSIS AND F. NIMMO

Abstract

Saturn's moon Titan is the second largest natural satellite in the solar system, and the only one that possesses a substantial atmosphere. The origin of the massive nitrogen atmosphere and the source of the present-day methane, which is continuously destroyed by UV-driven photochemistry, has long been debated. Data collected by the *Cassini-Huygens* mission since its arrival to Saturn in 2004 now provide key constraints on Titan's atmosphere composition, surface morphology and interior structure, which restrict the possible scenarios of formation and evolution. In the present chapter, after reviewing our present knowledge about the interior structure and composition based on the *Cassini-Huygens* data, we present the different physical and chemical processes that have potentially affected the origin and evolution of Titan. In particular, we argue that all along Titan's evolution, from accretion to present, interactions between the icy shell, the internal water ocean and the deep rock-dominated interior may have affected the evolution of the atmosphere. In spite of considerable progresses in our understanding of Titan thanks to *Cassini-Huygens*, many questions still remain, and we conclude on how they may be addressed by future exploration missions.

2.1 INTRODUCTION

Although Titan is similar in terms of mass and size to Jupiter's moons, Ganymede and Callisto, it is the only one harboring a massive atmosphere. Moreover, unlike the Jovian system populated with four large moons, Titan is the only large moon around Saturn. The other Saturnian moons are much smaller and have an average density at least 25% less that Titan's uncompressed density and much below the density expected for a Solar composition (Johnson and Lunine, 2005), although with a large variation from satellite to satellite. Both Jupiter's and Saturn's moon systems are thought to have formed in a disk around the growing giant planet. However, the difference in architecture between the two systems probably reflects different disk characteristics and evolution (e.g. Sasaki et al., 2010), and in the case of Saturn, possibly the catastrophic loss of one or more Titan-sized moons (Canup, 2010). Moreover, the presence of a massive atmosphere on Titan as well as the emission of gases from Enceladus' active south polar region (Waite et al., 2009) suggest that the primordial building blocks that comprise the Saturnian system were probably more volatile-rich than Jupiter's.

The composition of the present-day atmosphere, dominated by nitrogen, with a few percent methane and lesser amounts of other species, probably does not directly reflect the composition of the primordial building blocks and is rather the result of complex evolutionary processes involving internal chemistry and outgassing, impact cratering, photochemistry, escape, crustal storage and recycling, and other processes. The low $^{36}Ar/N_2$ ratio measured by the GCMS on *Huygens* (Niemann et al., 2005, 2010) suggest that nitrogen was not brought to Titan in the form of N_2, but rather in the form of NH_3 (Owen, 1982). The argument goes as follows: Ar and N_2 have similar volatility and affinity with water ice. Thus, if the primary carrier of Titan's N_2 were molecular nitrogen itself, the Ar/N_2 ratio on Titan should be within an order of magnitude of the solar composition ratio of about 0.1 (Lunine and Stevenson, 1985), which is about 500,000 times larger than the observed ratio. This indicates that nitrogen has been brought in the form of easily condensable compounds, most likely ammonia, which then has been converted *in situ* by impact-driven chemistry (McKay et al., 1988; Sekine et al., 2011; Ishimaru et al., 2011) or by photochemistry (Atreya et al., 1978). As will be further discussed in the chapter, both conversion processes required restrictive conditions to occur, and therefore specific evolutionary scenarios for Titan.

Photochemical processes are also known to lead to an irreversible destruction of methane, implying that a source of replenishment must exist to explain its few percent abundance (vertically averaged) in the atmosphere. In the absence of such a replenishment, the atmospheric methane should disappear over a timescale of several tens of millions of years. Before the *Cassini-Huygens* mission, the atmospheric methane was proposed to be in equilibrium with a global surface liquid reservoir (e.g. Lunine et al., 1983). Even though liquid reservoirs have been identified on Titan's surface by *Cassini* in the form of lakes and seas at high latitudes (Stofan et al., 2007), their estimated total volume is too small to sustain methane in the atmosphere on geologic timescales (Lorenz et al., 2008a). This suggests that a subsurface reservoir of methane exists and replenishes the atmospheric reservoir episodically or continuously. Different sources have been proposed, but despite a number

of new constraints from the *Cassini-Huygens* mission, we lack a strong discriminant among them. The $^{12}C/\ ^{13}C$ ratio measured in methane by the GCMS on *Huygens* (Niemann et al., 2010) is similar to the $^{12}C/\ ^{13}C$ ratio measured in several solar system objects, and close to the solar value, possibly reflecting an atmospheric methane inventory that has not been affected by atmospheric escape. The analysis of Mandt et al. (2009) indicates that if the current atmospheric methane is the remnant of methane injected into the atmosphere more than about two hundred million years ago the $^{12}C/\ ^{13}C$ should be decreased by at least 10% compared to the initial value. The current atmospheric methane may then have been recently delivered to the surface, from whatever reservoir. The detection of a significant amount of ^{40}Ar (the decay product of ^{40}K initially contained in silicate phases) further indicates that exchanges with the rocky interior have occurred (Niemann et al., 2010).

In this chapter we argue that exchange between the interior and atmosphere of Titan is likely to have occurred throughout Titan's evolution, at least during accretion and in the following billion years, and possibly until the present. A better understanding of these exchange processes requires good knowledge of the interior structure. Based on its mean density of 1881 $kg.m^{-3}$, Titan has long been known to be composed of a roughly 60%-40% mixture of rock and ice by mass. Gravimetric and altimetric data collected by the *Cassini* spacecraft permit us to constrain the distribution of these components in the interior. However, as is further discussed in Section 2, the solution remains non-unique and the different possible structures of the interior imply a range of formation and evolution scenarios. Other data from the *Cassini-Huygens* mission suggest the presence of a water ocean, possibly doped with ammonia or other agents depressing the ocean crystallization point, beneath the solid icy shell. The existence of such an internal water ocean at present has important consequences for the evolution of Titan as well as for its astrobiological potential.

In Section 2.2, we review the present-day constraints on the structure and dynamics of Titan's interior and present different possible interior models. The present-day composition and structure of the atmosphere and surface are already discussed in other chapters and will not be repeated here. A good knowledge of the present-day state of Titan is a necessary preliminary to understanding its origin and evolution. Section 2.3 presents some theoretical constraints on the formation of the Saturnian system and describes the accretion process(es) of Titan. Coupled evolution of the interior, surface and atmosphere, including internal differentiation and generation and recycling of the atmosphere, are then discussed in Section 2.4. Finally, we conclude in Section 2.5 by listing a series of remaining questions and how they may be addressed by future exploration missions.

2.2 PRESENT-DAY INTERIOR STRUCTURE AND DYNAMICS

Models of Titan's formation (Section 2.3) and subsequent evolution (Section 2.4) are constrained by its present-day interior structure and dynamics. In this Section, we focus on three questions which are of particular relevance to Titan's history.

1. *To what extent is Titan differentiated?* The degree of differentiation depends mainly on the thermal conditions during and just after accretion. Thus, Titan's degree of differentiation constrains the conditions under which it formed and evolved during the first billion years.

2. *Is the ice shell convecting?* The long-term thermal evolution of Titan's interior is determined by the rate at which heat can be transferred across its icy outer layer(s). Thus, whether or not convection is taking place controls how rapidly Titan cools. If an ocean is present, the lifetime of the ocean (and thus its habitability) is controlled by the behaviour of the overlying ice shell. The ice shell also controls transport between the interior and the atmosphere, as well as potential tectonic and cryovolcanic activities.

3. *Does Titan possess a sub-surface ocean?* If an ocean is present, Titan's astrobiological potential is increased. Moreover, an ocean can have profound geophysical consequences; for instance, it will likely increase the rate of tidal dissipation in the overlying ice shell.

Prior to the *Cassini-Huygens* mission, there were essentially no observational constraints on any of these questions. Below we discuss the data sets relevant to the internal structure and dynamics of Titan.

2.2.1 Interior structure inferred from the gravity field data

Measurements of Titan's gravity field are made by precise radio tracking of the *Cassini* spacecraft as it passes close to Titan. Unfortunately, because of the lack of a scan platform, gravity tracking precludes the acquisition of most other observations, therefore the number of flybys dedicated to these measurements is limited. Furthermore, Titan's extended atmosphere can result in non-gravitational forces on the spacecraft, which complicates the analysis and requires that the closest approach distance is farther from Titan than what is desirable for an optimal resolution of the gravity field. Despite these obstacles, Titan's degree-two gravity coefficients have been determined with relatively high confidence, as well as the degree-three coefficients but with much less confidence (Iess et al., 2010). The degree-two spherical harmonic coefficients, which are the dominant coefficients for a body subjected to tidal and rotational forces, $J_2 = (-C_{20})$ and C_{22} are tabulated in Table 2.1. Because of the number of flybys, the coefficients were determined in-

dependently, without requiring a value of 10/3 for the ratio of J_2 to C_{22}. This situation differs from bodies where fewer flybys have been carried out, such as Callisto (Anderson et al., 2001) and Rhea (Mackenzie et al., 2008).

The degree-two coefficients provide very important constraints on the radial mass distribution within the body. It can be shown mathematically that they are directly related to the principal moments of inertia (MoI), A, B and C:

$$C_{20}^{obs} = \frac{(A+B)/2 - C}{M_T \bar{a}^2} \quad ; \quad C_{22}^{obs} = \frac{B-A}{4M_T\bar{a}^2} \qquad (2.1)$$

with M_T Titan's mass and $\bar{a}$ the mean equatorial radius. Thus, measuring the C_{20} and C_{22} coefficients only gives the difference between the principal moments of inertia. In order to determine their absolute value, a third condition is needed. For Mars and the Earth, measurement of the precession rate (which gives $(C-\overline{A})/C$, where C and $\overline{A}$ are the polar and averaged equatorial moments of inertia) allows retrieval of the exact values of the three principal moments of inertia. In the case of Titan, such a measurement is not available. To infer the moment of inertia, one approach is to use the Radau-Darwin approximation, which assumes that the body responds to tidal and rotational forces as a fluid body (i.e. it has no long-term strength, and therefore it is in hydrostatic equilibrium). This approximation assumes that the body surface as well as each interface between internal layers correspond to an iso-potential surface. The potential at each interface is the sum of the tidal potential, centrifugal potential and gravitational potential. If the body is in hydrostatic equilibrium, the degree-two gravitational potential is proportional to the tidal and centrifugal potential. The response of the body to the tidal and centrifugal degree-two potential is classically described with the fluid Love number k_2^f. In hydrostatic equilibrium,

$$C_{20}^{th} = -\left(\frac{\alpha}{2} + \frac{q}{3}\right) k_2^f \quad ; \quad C_{22}^{th} = \frac{\alpha}{4} k_2^f \qquad (2.2)$$

where $\alpha = M_S/M_T \times (R_T/D_{ST})^3$, is the tidal parameter, and $q = \omega^2 R_T^3/GM_T$ is the rotational parameter (with M_S Saturn's mass, R_T Titan's mean radius, D_{ST} Saturn-Titan mean distance, ω Titan's spin rate). In the case of a synchronously rotating body in a circular orbit, $\alpha = q$ and therefore $C_{20}/C_{22} = -10/3$ if the body is hydrostatic. For Titan, $\alpha = q = 3.9555 \times 10^{-5}$.

In the Radau-Darwin approximation, the normalized moment of inertia about the spin axis, $C/M_T R_T^2$ can then be calculated from the fluid Love number, inferred from the gravity coefficients assuming that they result from a fluid response of the body and in the limit of small density variations:

$$\frac{C}{M_T R_T^2} = \frac{2}{3}\left[1 - \frac{2}{5}\left(\frac{5}{k_2^f + 1} - 1\right)^{1/2}\right] \qquad (2.3)$$

In the case of Titan, the ratio between the observed C_{20}^{obs} and C_{22}^{obs} is close to -10/3, suggesting that Titan is relatively close to hydrostatic equilibrium. We can therefore use the degree two gravity coefficients to first order to estimate the fluid Love number and the corresponding moment of inertia. Depending on whether we use the C_{20} or C_{22} coefficients as a reference to determine the fluid Love number, the normalized moment of inertia varies between 0.335 and 0.342. This may be compared with the value of 0.4 for a uniform sphere, 0.394 for the Moon, 0.33 for the Earth, 0.31 for Ganymede and 0.355 for Callisto (assuming hydrostatic equilibrium (Anderson et al., 1996, 2001)). The moment of inertia factor of Titan is therefore intermediate between Ganymede and Callisto, suggesting a modest increase of density toward the center.

Table 2.1. *Observed (C_{lm}) un-normalized degree-two gravity coefficients. Observed values are from Iess et al. (2010), where SOL1 and SOL2 refer to the multi-arc and global solutions, respectively, and errors are given as $\pm 2\sigma$. Un-normalized surface topography coefficients C_{lm}^h are derived from data detailed in Zebker et al. (2009b) and quoted from Nimmo and Bills (2010). Normalized moment of inertia $C/M_T R_T^2$ was calculated assuming hydrostatic equilibrium using equation 2.3.*

	$C_{lm} \times 10^{-6}$ SOL1	$C_{lm} \times 10^{-6}$ SOL2	C_{lm}^h m
$l=2, m=0$	-31.80±0.80	-33.46±1.26	-358
$l=2, m=2$	9.98±0.08	10.02±0.14	63
ratio	-3.19±0.08	-3.34±0.13	-5.68
$k_2^f(C_{20})$	0.965	1.015	-
$k_2^f(C_{22})$	1.010	1.013	-
$C/M_T R_T^2(C_{20})$	0.335	0.342	-
$C/M_T R_T^2(C_{22})$	0.341	0.342	-

As already mentioned, this interpretation however assumes that the C_{20}^{obs} or C_{22}^{obs} coefficient is entirely determined by the dynamical distortion of the satellite under the action of tidal and rotational forces. In reality, part of the gravity signal may be attributed to non-hydrostatic contributions such as uncompensated relief, ice shell thickness variations or lateral density variations. The fact that the $C_{20}^{obs}/C_{22}^{obs}$ ratio is not exactly -10/3 and that the degree three gravity coefficients are not zero clearly indicates that there are some non-hydrostatic contributions to the observed signals and that the gravity field of Titan is not only attributed to the dynamical distortion of a radially-distributed mass interior. The degree-three coefficients indicate that non negligible lateral variations in the mass distribution exist on Titan. These should affect the estimation of the moment of inertia. If we assume that the non-hydrostatic contributions to degree two are comparable to the inferred degree 3 terms, a few to 10% of the observed degree two signals may be attributed to the non-hydrostatic (Iess et al., 2010, Supplementary Information). According to the Radau-Darwin equation, a 5%-10% overestimate of the hydrostatic parts would shift $C/M_R R_T^2$ from 0.341 to 0.334-0.327.

In summary, the interpretation of the gravity data indicates that the normalized moment of inertia of Titan is of the order of 0.33-0.34. This MoI value combined with the mean density of Titan indicates that the density of the core is low, which may be explained by incomplete separation of rock from ice (Iess et al., 2010) or the presence of highly hydrated silicate minerals (Castillo-Rogez and Lunine, 2010; Fortes, 2011). Based on the present data, the presence of a small iron core (< 500 km) cannot be ruled out (Castillo-Rogez and Lunine, 2010; Fortes, 2011), but the low internal temperatures ($< 900 - 1000$K) required to maintain either an ice-rock mixture or highly hydrated silicate minerals are incompatible with the segregation of iron and the formation of a iron core. The most likely present-day structures is either a pure rock core, mostly anhydrous, surrounded by a mixture of ice and rock, surrounded by pure water ice (Fig. 2.5, top and middle), or a low density rock core consisting mainly, but not entirely, of hydrated silicate minerals surrounded by H_2O (Fig. 2.5, bottom). In both cases, a liquid water layer may be present between a high-pressure ice mantle and an outer ice shell. We will discuss the possible evolution scenarios leading to these interior structures in more details in Section 2.4.

2.2.2 Global shape: Constraints on the structure and thermal state of the ice shell

Just as with gravity, the degree-two shape of a synchronous body can be used to determine its moment of inertia - as long as the body is in hydrostatic equilibrium. As with gravity, the degree-two shape coefficients of such a body, C^h_{20} and C^h_{22}, will be in the ratio -1/2. Thus, with sufficiently good topography we can check whether or not the hydrostatic condition is satisfied.

Titan's shape has been measured (Zebker et al., 2009b) by a combination of traditional radar altimetry (Zebker et al., 2009a), and a new technique which uses overlaps in the SAR-imaging swaths to determine topography (Stiles et al., 2009). In contrast to the results obtained from gravity, C^h_{20} and C^h_{22} were not in the expected -1/2 ratio (see Table 2.1).

This result is apparently paradoxical: how can Titan have nearly hydrostatic gravity but non-hydrostatic topography? The hydrostatic gravity rules out scenarios in which Titan's shape is derived from an earlier epoch (a "fossil bulge" similar to that of the Moon). One possibility is that Titan's outer ice shell - presuming the existence of an ocean - is of varying thickness or density and is (Airy or Pratt) isostatically compensated. An isostatic shell would give rise to only very small gravity anomalies (see below), while the shell thickness variations would result in a long-wavelength non-hydrostatic shape.

Nimmo and Bills (2010) explored a version of the Airy scenario, in which shell thickness variations were caused by spatial variations in tidal heating in the ice shell (cf. Ojakangas and Stevenson, 1989). They found that the observed topography could be fitted with a mean ice shell of thickness $D \approx 100$ km, heated from below at a rate of 4-5 mW m^{-2} (appropriate to a chondritic Titan) and from within at a rate about one-tenth as large (due to tidal dissipation). The tidal Love number h_2, which describes the response of the body to the eccentricity tides, was found to be ≈ 1.2, consistent with theoretical predictions (Sohl et al., 2003). Given the relatively modest rate of tidal dissipation, the e-folding timescale to damp Titan's eccentricity is quite long (2-3 Gyr). Alternatively, Choukroun and Sotin (2012) proposed that the flattened shape of Titan may result from the accumulation of dense hydrocarbon clathrates at high latitudes owing to enhanced ethane precipitation. Their Pratt isostatic compensation model may explain the ~ 300 m difference between expected and measured polar radii if the ethane-rich clathrate crust is about 3-km thick.

Although the variable-thickness or variable-density shell is assumed isostatic, it will still have a small effect on the degree-2 gravity coefficients. Correcting for this effect before using equation (2.3) changes the resulting moment of inertia by about 2% (the MoI factor is still between 0.33 and 0.34). An isostatic shell is probably a good assumption: a shell with an elastic thickness of 50 km would still be about 95% compensated at degree-2 (Turcotte et al., 1981), assuming a Young's modulus of 9 GPa.

Perhaps the most surprising result of these studies is that, if it is correct, Titan's ice shell must be conductive, or at most weakly convecting, in order to support thickness or density variations on the long term. In the thickness-variation model, surface topography generates pressure gradients at depth; if the ice shell were convecting, the ice viscosity would be low enough to flow in response to these pressure gradients and progressively remove the surface topography (Stevenson, 2000). Whether or not an ice shell convects depends on whether its Rayleigh number Ra of the whole ice layer exceeds some critical value Ra_{cr} (e.g. Mitri and Showman, 2008):

$$Ra = \frac{\rho g \alpha \Delta T D^3}{\kappa \eta_b} \approx 3{\times}10^8 \left(\frac{D}{100\mathrm{km}}\right)^3 \left(\frac{10^{14}\ \mathrm{Pa\ s}}{\eta_b}\right) \geq Ra_{cr} \quad (2.4)$$

Here ρ,α,κ,η_b are the density, thermal expansivity, thermal diffusivity and basal viscosity of the ice shell, respectively, ΔT is the temperature contrast across the shell ($\Delta T \simeq 170 - 180$ K between the surface and the ocean) and numerical values assumed are from Nimmo and Bills (2010). The value of Ra_{cr} depends on how sensitive viscosity is to temperature changes, and the geometry of the shell (Solomatov, 1995; Barr and McKinnon, 2007), and for Titan is $\approx 4 \times 10^7$ in the stagnant lid regime. Equation (2.4) shows that whether or not the shell convects is a sensitive function of the viscosity of the base of the ice shell. For pure ice, the viscosity in turn depends mainly on the temperature of the ocean beneath, and secondarily on the ice grain size. The ocean temperature is controlled by how much ammonia is present; a sufficiently ammonia-rich ocean and/or large ice grain sizes would prevent convection because the ice would

be too viscous (e.g. Tobie et al., 2005b).

Nevertheless, it is possible that the ice shell was convective in the past and that convection ceased as the ocean crystallized and the ammonia concentration increased owing to reduced ocean volume (Tobie et al., 2005b; Mitri and Showman, 2008). The elevated orbital eccentricity of Titan indicates however that this convective period should have lasted less than about 0.5-1 billion of years (Tobie et al., 2005b). In contrast to the Galilean moons where the Laplace resonance excites the eccentricity of Europa and Io, there is no major resonance in the Saturnian system to force Titan's eccentricity. Unless some unknown process has recently forced the eccentricity, the latter should have monotonically decayed as a function of time since the formation of the system owing to tidal dissipation at the surface and in the interior (Sears, 1995; Sohl et al., 1995; Tobie et al., 2005b). The dissipation rate is reduced either if the interior is totally rigid (with no internal ocean) (Sohl et al., 1995) or if the outer ice shell above the ocean is thin and/or cold (i.e. conductive) (Tobie et al., 2005b). Indeed, the volume wherein tidal energy is dissipated is much bigger in a convective ice shell (where about half of the shell has a temperature larger than 240 K) than in a conductive ice shell where the warm temperature is confined at the bottom of the ice shell.

If Titan has an internal ocean at present, it implies that the ice shell remained conductive and relatively thin ($< 30 - 40$ km) during most of Titan's evolution, in order to reduce the eccentricity damping (Tobie et al., 2005b). This is possible if the viscosity of the icy shell is large enough due to large grain sizes or to low oceanic temperatures (owing to ammonia Tobie et al. (2005b) or methanol Deschamps et al. (2010)) and/or if the icy shell contains large fraction of low conductivity materials such as methane clathrate (Tobie et al., 2006). Following this requirement, the icy shell has never been convecting or has been convecting only during a limited period of time. A possible scenario may be that the ice shell started convecting during the last roughly billion years and then stopped later because of ocean crystallization as the concentration in ammonia or methanol in the ocean became too high and the temperature too low to allow convection in the overlying viscous ice shell (e.g. Mitri and Showman, 2008). Indeed, even for initially moderate ammonia fraction (about 2-3% relative to the total mass of H_2O), the concentration significantly increases as the ocean crystallizes and the ocean temperature gets below 250 K when the ammonia concentration in the crystallizing ocean reaches 10 wt% (Tobie et al., 2005b). At such a temperature, the viscosity at the base of the ice shell exceeds $5.10^{15} - 10^{16}$ Pa.s, which is too large to promote convection even for a 100 km-thick ice shell.

2.2.3 Geophysical evidence for an internal water ocean

For the Galilean moons, the most convincing evidence for subsurface oceans came from analysis of the magnetic data acquired by the Galileo mission during close flybys. The tilt of Jupiter's magnetic field relative to its spin pole means that the Galilean satellites experience a time-varying field and resulting induction currents. This effect has been used to probe the conductivity structure of the satellites, and deduce the presence of oceans for the three outer satellites (Khurana et al., 1998; Kivelson et al., 2002), and a partially-molten mantle for Io (Khurana et al., 2011). Unfortunately, Saturn's spin and magnetic poles are almost exactly coplanar, so the induction technique is very difficult to use at Titan (Saur et al., 2010). A recent study of Titan's magnetic field did not see any induction effects, and did not detect any permanent internal magnetic field (Wei et al. 2010). Although it is possible to have a molten core without generating a magnetic field (e.g. Venus, Io), this result is perhaps consistent with Titan's interior being cold and not fully differentiated.

On Titan, another technique based on the measurements of the electric field during the *Huygens* descent by the Permittivity, Wave and Altimetry (PWA) instrument (Béghin et al., 2007) provides however some information on the subsurface electrical conductivity. The measurements of low frequency waves and atmospheric conductivity by the PWA instrument revealed the existence of a Schumann-like resonance trapped within Titan's atmospheric cavity. The observed signal may be triggered and sustained by strong electric currents induced in the ionosphere by Saturn's magnetospheric plasma flow (Simões et al., 2007; Béghin et al., 2009, 2010). The characterisitics of this trapped-resonant mode imply the presence of a conductive layer at about 30-60 km below the surface (Béghin et al., 2010), which may correspond to the ice/ocean interface provided that the ocean is sufficiently conductive, possibly doped with small amounts of ammonia and/or salts (Béghin et al., 2010).

As explained in Section 2.2.2, the observed topography may be explained by variations in ice shell thickness, resulting from inhomogeneous crystallization of an underlying ocean. If this analysis is correct, it implies that an internal ocean is still present in Titan's interior and that it is currently slowly crystallizing. This constitutes additional indirect evidence for an internal ocean inside Titan.

Another piece of evidence is provided by Titan's spin state. A non-spherical body, such as a synchronous satellite, precesses about its rotation axis at a rate determined by the ratio, $(C - \overline{A})/C$. Since the gravity coefficient $J_2 = (C - \overline{A})/M_T R_T^2$, if J_2 and the precession rate can be measured, the moment of inertia C may be determined directly without assuming hydrostatic equilibrium. Although measuring a satellite's precession rate directly is difficult, measuring the obliquity (the angle between spin pole and

orbit pole) is relatively easy. If a satellite is dissipative, tidal torques drive the obliquity to a state in which the spin pole and orbit pole remain coplanar as the latter precesses around a fixed (invariable) pole (e.g. Peale, 1969). If this state, known as a damped Cassini state, exists, then measuring the obliquity is sufficient to determine the satellite moment of inertia (e.g. Bills and Nimmo, 2011). In practice, other small effects (such as Saturn's spin pole precession) have to be taken into account, but they do not alter the underlying physical picture.

Titan's spin pole location has been established through analysis of SAR images. It is very nearly coplanar with the invariable and orbit poles (suggesting occupation of a Cassini state), and corresponds to an obliquity of 0.32° (Stiles et al., 2008, 2010). If Titan occupies a damped Cassini state, the implied value of $C/(M_T R_T^2)$ is 0.45 ± 0.02 (Bills and Nimmo, 2011). This result is clearly unreasonable, in that it suggests a body which is under-dense in the interior, and also disagrees with the results derived from gravity. The solution is probably a combination of two factors. First, the fact that Titan's spin pole is not quite coplanar with the orbit and invariable poles suggests some degree of present-day excitation of the obliquity. Two possible candidate sources of excitation are the atmosphere (Tokano et al., 2011) or fluid motion in a subsurface ocean, both of which can transfer angular momentum to the ice shell. The second factor is that Titan is probably not acting as a rigid body (which the Cassini state analysis assumes), and that instead the ice shell is partially decoupled from the interior by an ocean. If the shell were totally decoupled, its normalized moment of inertia would be 0.67. The derived value of 0.45 suggests some degree of coupling, perhaps due to pressure or gravitational torques (Baland et al., 2011). Fortunately, continued monitoring of the position of Titan's spin pole should be able to disentangle these two effects, but the current results are strongly indicative of a subsurface ocean.

Another potential source of evidence for a subsurface ocean would be the existence of non-synchronous rotation (NSR) of the ice shell (Ojakangas and Stevenson, 1989). It was initially thought that Titan's shell was exhibiting such behaviour (Lorenz et al., 2008b), but this observation turned out to be erroneous and there is currently no evidence for NSR (Stiles et al., 2010).

Probably, the most promising technique to confirm the existence of a subsurface ocean would be to measure the tidal fluctuation from accurate gravity or topography measurements. The Radio Science Experiment on *Cassini* has in theory the capability to measure the tide-generated gravity signals (Rappaport et al., 1997, 2008). However, the atmospheric drag due to the extended atmosphere as well as the existence of relatively large signals in harmonics of degree three (Iess et al., 2010), suggesting significant signal at degrees 4 and 5 (Sotin et al., 2010), make the analysis more difficult than initially anticipated. In spite of these difficulties, a recent analysis of the *Cassini* gravity data obtained during six close flybys indicates that Titan responds to the variable tidal field exerted by Saturn at a detectable level, providing further evidence for a global ocean at depth on Titan (Iess et al., 2012). A future mission with dedicated multiple flybys or even better in orbit around Titan will be required to confirm this detection and to get more precise informations on the ocean and ice shell thicknesses.

2.2.4 Summary

At the start of this Section we posed three questions; we will conclude by providing some provisional answers.

1. *To what extent is Titan differentiated?* Based on the gravity results (Section 2.2.1), the normalized moment of inertia of Titan is estimated between 0.33 and 0.34. This clearly indicates that Titan is not fully differentiated and does not have an iron core like Ganymede. Earlier we suggested two possible internal structures – one in which rock and ice are incompletely separated, the other involving a rocky core that is partially hydrated – that satisfy the rather high moment of inertia. We discuss this further in Sections 2.3.4 and 2.4.1.1.

2. *Is the ice shell convecting?*
   A conductive ice shell is favoured by the model for Titan's long-wavelength shape (Section 2.2.2) and is consistent with the requirement that its eccentricity not damp too rapidly. To avoid convection, the ice shell must have a high viscosity, which can be achieved if the ocean beneath is ammonia-rich and therefore cold. Convection may have occurred in the past before the ammonia concentration increased, but this convective period must have lasted less than 0.5-1 billion years in order to explain Titan's present-day elevated orbital eccentricity.

3. *Does Titan possess a sub-surface ocean?* Electric signals measured in Titan's atmosphere by *Huygens* suggest the presence of a conductive layer at depth, possibly a water ocean doped with small amounts of salts or ammonia to increase the electrical conductivity. Titan's spin state and tidal gravity response are also suggestive of a decoupled shell (Section 2.2.3) while its long-wavelength shape can be explained if a subsurface ocean is assumed (Section 2.2.2). Given the existence of subsurface oceans on the comparably-sized Galilean satellites, Callisto and Ganymede, it would be surprising if Titan did not possess an ocean. However, one important difference is that Titan's ocean may be colder and more ammonia-rich (see below).

2.3 ORIGIN OF THE SATURNIAN SYSTEM AND ACCRETION OF TITAN

Titan was formed as a regular satellite in a disk that was the outgrowth of the formation of Saturn itself. The conditions under which Saturn formed therefore had a direct impact on the formation of Titan. They determined its composition, the architecture of the whole system as well as the final assemblage that led to the formation of Titan and of the other regular moons. The present section is structured around three main questions which are of particular relevance to Titan's formation.

1. *What was the composition of the primordial building blocks that formed Titan and the Saturnian system?* Titan and the other Saturnian moons formed from a mixture of rock and ice initially present in the vicinity of Saturn. We will present in this section different theoretical and observational constraints that can be used to estimate the composition of these ice-rock blocks, notably their volatile content.

2. *What makes the Jupiter and Saturn systems so different?* Contrary to the Jovian system, there is no gradual variation of density and hence rock/ice ratio in the Saturnian moons as a function of planet distance. Titan is the unique big moon, the second largest moon Rhea having a mass less than 2% of Titan's mass. Another particular characteristic of Saturn is its extended ring system. In this Section, we will describe the main phases of satellite formation in a disk around giant planets and try to identify which processes differed between Jupiter and Saturn.

3. *Can Titan accrete undifferentiated?* The *Cassini* gravity data suggests that Titan is moderately differentiated at present (section 2.2.1), suggesting that the differentiation process has been limited. One possibility is that Titan accreted relatively cold, which would have delayed the differentiation. To address that question, we will review the physics of accretion and determine under which conditions Titan might have remained cold during accretion.

2.3.1 Formation of ices in Saturn's environment

The primitive building blocks that formed Titan and the rest of the satellite system were presumably composed of a complex assemblage of various ices, hydrates, silicate minerals and organics. An important issue associated with the formation of giant planets and their satellite systems concerns the condensation of water ice and other ice compounds as the solar nebula cools down. The condensation sequence depends on the initial gas phase, the cooling rate of the disk and the stability of the gas molecules in solid phases.

The composition of the initial gas phase of the disk can be defined by assuming that the abundances of all elements, including oxygen, are protosolar (Asplund et al., 2009) and that O, C, and N exist only in the form of H_2O, CO, CO_2, CH_3OH, CH_4, N_2, and NH_3. The abundances of CO, CO_2, CH_3OH, CH_4, N_2 and NH_3 are then determined from the adopted $CO/CO_2/CH_3OH/CH_4$ and N_2/NH_3 gas phase molecular ratios. Once the abundances of these molecules are fixed, the remaining O gives the abundance of H_2O. Concerning the distribution of elements in the main volatile molecules, the ratio of $CO/CO_2/CH_3OH/CH_4$ can be set to 70/10/2/1 in the gas phase of the disk, values that are consistent with the ISM measurements considering the contributions of both gas and solid phases in the lines of sight (Mousis et al., 2009c). In addition, S is assumed to exist in the form of H_2S, with $H_2S/H_2 = 0.5 \times (S/H_2)_\odot$, and other refractory sulfide components (Pasek et al., 2005). N_2/NH_3 is assumed equal to 10/1 in the nebula gas-phase, a value compatible with thermochemical models of the solar nebula (Lewis and Prinn, 1980) and with observations of cometary comae (e.g. Hersant et al., 2008).

To first order, the process by which volatiles are trapped in icy planetesimals can be calculated assuming thermodynamic equilibrium. The sequence of clathration[1] and condensation can be determined by using the equilibrium curves of stochiometric hydrates, clathrates and pure condensates, and the thermodynamic path (hereafter cooling curve) detailing the evolution of temperature and pressure between roughly 5 and 20 AU, a distance range largely encompassing the migration path followed by proto-Jupiter and proto-Saturn during their formation in the solar nebula (Alibert et al., 2005b). We refer the reader to the works of Papaloizou and Terquem (1999) and Alibert et al. (2005a) for a full description of the turbulent model of accretion disk used here. For the pressure range expected in the solar nebula, most of the gas compounds, except CO_2, are enclathrated at temperatures higher than the temperatures they condense in the form of pure condensates. This has fundamental consequences for the trapping of volatiles in primordial building blocks.

As illustrated in Figure 2.1, the cooling curve intercepts the equilibrium curves of the different ices at particular temperatures and pressures. For each ice considered, the domain of stability is the region located below its corresponding equilibrium curve. The clathration process stops when no more crystalline water ice is available to trap the volatile species. As CO_2 is the only species that crystallizes at a higher temperature than its associated clathrate, solid CO_2 is assumed to be the only existing condensed form of CO_2 in this environment. In addition, CH_3OH is assumed to be in the form of pure ice, since, to the best of our knowledge, no experimental data concerning the equilibrium curve of its associated clathrate have been reported in the literature.

[1] Clathrate hydrates are crystalline water-based structures that form cages in which gas molecules can be trapped (Lunine and Stevenson, 1985; Choukroun et al., 2011), and for this reason they play a crucial role in the volatile trapping. They also play a key role in the evolution of the volatile inventory on Titan as it will be further discussed in Sections 2.4.1.3 and 2.4.1.4.

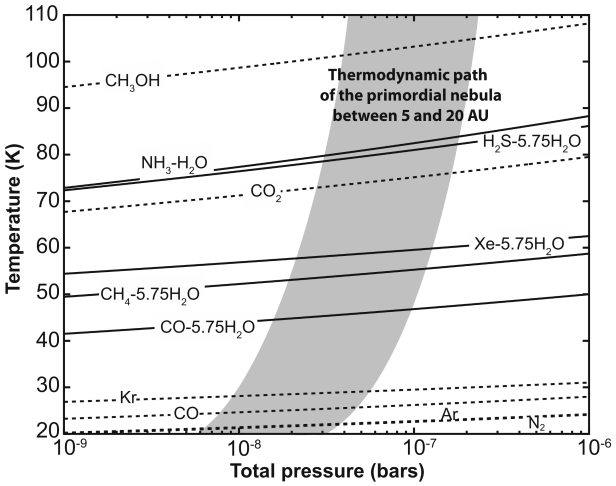

Figure 2.1 Equilibrium curves of NH_3-H_2O hydrate, H_2S, Xe, CH_4 and CO clathrates (solid lines), CH_3OH, CO_2, Kr, CO, Ar and N_2 pure condensates (dotted lines), and thermodynamic path followed by the primordial nebula between 5 and 20 AU as a function of time, respectively, assuming a full efficiency of clathration. Species remain in the gas phase above the equilibrium curves. Below, they are trapped as clathrates or simply condense. The equilibrium curves of hydrates and clathrates derive from Lunine and Stevenson (1985)'s compilation of published experimental work, in which data are available at relatively low temperatures and pressures. The equilibrium curves of pure condensates used here derive from the compilation of laboratory data provided by Lide (2004).

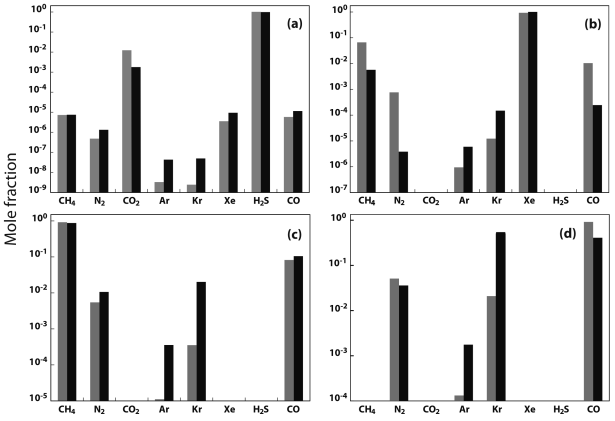

Figure 2.2 Mole fraction of volatiles encaged in H_2S (a), Xe (b), CH_4 (c) and CO (d) clathrates. Grey and dark bars correspond to structure I and structure II clathrates, respectively, which are two possible clathrate structures with slightly different cage sizes (e.g. Sloan, 1998).

For simplicity, the clathration efficiency is assumed to be total, implying that guest molecules had the time to diffuse through porous water-ice solids before their growth into planetesimals and their accretion by proto-planets or proto-satellites. This statement remains plausible only if collisions between planetesimals have exposed essentially all the ice to the gas over time scales shorter or equal to planetesimal lifetimes in the nebula (Lunine and Stevenson, 1985). In the present case, which is based on the protosolar abundances of Asplund et al. (2009), NH_3, H_2S, Xe, CH_4 and $\sim 31.5\%$ of CO form NH_3-H_2O hydrate and H_2S, Xe, CH_4 and CO clathrates with the available water in the outer nebula. The remaining CO, as well as N_2, Kr, Ar and Ne (not shown on the figure), whose clathration normally occurs at lower temperatures, remain in the gas phase until the nebula cools enough to allow the formation of pure condensates. As the gas phase composition of the disk is assumed not to vary with heliocentric distance, the calculated clathration conditions remain the same in the 5–20 AU range of the nebula (see Marboeuf et al. (2008) for details). Once crystallized, these ices will agglomerate and form planetesimals large enough to decouple from the nebular gas and will be accreted by the forming giant planets and satellites.

Many works published in the last decade and detailing the formation conditions of ices in the solar nebula (Gautier et al., 2001; Hersant et al., 2008; Mousis and Alibert, 2006; Alibert and Mousis, 2007, e.g.) have used the equilibrium curves established experimentally for single guest molecules (similar to the curves shown on Fig. 2.2). This simplified approach permits an understanding to first order of the condensation sequence in the nebula, but in reality, clathrates forming in a gas mixture always simultaneously trap several guest molecules (e.g. Lunine and Stevenson, 1985; Sloan, 1998). Here we consider the effect of simultaneous trapping of guest species on the predicted composition of volatiles trapped in the water ice.

The composition of the clathrate phases can be constrained by using a statistical thermodynamic model derived from the approach of van der Waals and Platteeuw (1959) (see Lunine and Stevenson, 1985; Mousis et al., 2010, for details). This thermodynamic approach is based on the use of intermolecular potentials, which themselves depend on parameters describing the interaction between the guest molecule and the cage made of water molecules, called "Kihara parameters". The afore-mentioned formation sequence of the different ices occurring during the cooling of the solar nebula is considered (see Fig. 2.1). As a consequence, any volatile already trapped or condensed at a higher temperature than the formation temperature of the clathrate under consideration is excluded from the coexisting gas phase composition. This implies that CO_2, Xe, CH_4, CO, Kr, Ar and N_2 are considered as possible guests in the case of H_2S clathrate. On the other hand, only N_2, Ar, Kr can become guests in CO clathrate. Figure 2.2 represents the mole fraction f of volatiles encaged in structure I and structure II clathrates *a priori* dominated by H_2S, Xe, CH_4 and CO and formed in the primordial nebula. This figure shows that H_2S, Xe, CH_4 and CO are the dominating guest species if structure I clathrates form in the nebula. However, in the case of structure II clathrate formation, CO becomes a minor compound in the clathrate that is expected to be dominated by this molecule. Indeed, Kr becomes more abundant than CO in this clathrate, irrespective of their initial abundances in the gas phase

of the nebula. On the other hand, structure I should be the most likely form of clathrate produced in the nebula since H_2S, Xe, CH_4 and CO clathrates are all of structure I (Lunine and Stevenson, 1985). Figure 2.2 also shows that, depending on the considered structure, the Kr/CH_4 ratio in CH_4–dominated clathrate is order of or greater than the value derived from the nebula gas phase composition used in our model. This implies that Kr can be enclathrated at a temperature of ∼55 K instead of condensing in the 20–30 K range in the solar nebula (see Fig. 2.1).

2.3.2 Formation of Saturn and the circumplanetary disk: Consequences for the delivery of volatiles

2.3.2.1 Saturn's formation and envelope enrichment

Favored theories of giant planet formation center around two main paradigms, namely the core accretion model (Safronov, V. S., 1969; Goldreich and Ward, 1973; Pollack et al., 1996) and the gravitational instability model (Cameron, 1978; Boss, 1997). In the frame of the core accretion model, a solid core forms from the accretion of planetesimals and becomes massive enough (∼5–10 $M_\oplus$) to initiate runaway gravitational infall of a large gaseous envelope in which gas-coupled solids continue their accretion (Alibert et al., 2005b; Hubickyj et al., 2005; Mordasini et al., 2009). This model provides the large amount of heavy elements necessary to explain the supersolar metallicities observed in Jupiter and Saturn via the accretion of planetesimals in their envelopes (Gautier et al., 2001; Saumon and Guillot, 2004; Alibert et al., 2005b; Mousis et al., 2006, 2009c). In the frame of the gravitational instability model, gas giant protoplanets form rapidly through a gravitational instability of the gaseous portion of the disk and then more slowly contract to planetary densities (Boss, 1997, 2005). In this scenario, due to the limited efficiency of planetesimals accretion during the planet formation, its metallicity should be almost equal to that of the parent star (Helled and Bodenheimer, 2010).

By using the sequences of ice formation described in Section 2.3.1, it is possible to predict the abundances of major species (C,N, O, S, P) and noble gases (Ar, Kr, Xe) in Saturn's atmosphere in the context of the core-accretion model (Hersant et al., 2008; Mousis et al., 2009c), and to compare to the observed abundances when available. For instance, adjusting the model to the observed carbon abundance provides constraints on the minimum mass range of ices required in the envelope (estimated between 14.3 and 15.6 $M_\oplus$, Mousis et al. (2009c). Such an approach also provides information on the typical composition of the planetesimals in the feeding zone of Saturn, which in turn can be used to constrain the composition of the building blocks of Titan. The analysis of Hersant et al. (2008), based on a simplified description of volatile trapping by clathration and condensation, suggests that the planetesimals that reached Saturn's envelope contained significant amounts of CO_2, NH_3, CH_4 and H_2S, and were depleted in CO and N_2. This also seems consistent with the composition of Enceladus' plumes, where CO_2, NH_3, CH_4 and H_2S have been detected by the Cassini Ion and Neutral Mass Spectrometer (INMS) (Waite et al., 2009). If this is correct, it would imply that the solids that enrich Saturn's envelope in heavy elements have a composition close to the ones that formed the regular satellites.

2.3.2.2 Structure and evolution of Saturn's subnebula

At the beginning of Saturn's formation process, the total radius of the planet equals its Hill's radius, and no subnebula can exist. At the end of the formation process, the cooling rate of the planet's envelope is such that its radius shrinks faster than the disk can supply additional gas. Accretion of gas now proceeds through streamers which eventually collide and form a circumplanetary disk (Lubow et al. 1999). When the radius of proto-Saturn becomes small enough, a subnebula emerges from the contracting atmosphere. This subnebula is fed by gas and solids accreted from Saturn's feeding zone. The accretion rate of gas from the solar nebula to the subnebula is therefore directly driven by the planet's accretion rate of gas, which is derived from giant planet formation models (e.g. Alibert et al., 2005a).

Different models of subdisks have been proposed in the literature (e.g. Canup and Ward, 2002; Mosqueira and Estrada, 2003a; Estrada and Mosqueira, 2006; Sasaki et al., 2010). Here we describe in more details the so-called gas-starved disk model initially introduced by Canup and Ward (2002) and then used by Alibert et al. (2005a) and Alibert and Mousis (2007). Alibert and Mousis (2007) described a model of Saturn's subnebula whose evolution proceeds in two phases. During the first phase, when the solar nebula is still present, the subnebula is hot and dense, and fed through its outer edge (fixed to 1/5 Hill's radius – see Alibert and Mousis (2007) for details), at a rate controlled by Saturn's formation. This justifies a posteriori the use of an equilibrium model as an initial model of the subnebula. This phase lasts until the solar nebula has disappeared and the temporal evolution of the subnebula is therefore directly governed by the last phase of Saturn's formation. The accretion rate as a function of the distance to Saturn is no longer constant and the temperature and pressure conditions of the subnebula decrease rapidly.

Figure 2.3 represents the temporal evolution of the temperature profile within the Saturn's subnebula depicted by Alibert and Mousis (2007). The solid lines are plotted, from top to bottom, at $t = 0$ Myr (corresponding to the time when Saturn has accreted 70% of its final mass), 0.1 Myr, 0.2 Myr, 0.3 Myr, 0.35 Myr, 0.4 Myr, 0.5 Myr, 0.6 Myr and 0.7 Myr. The switch from phase 1 to phase 2 of the subnebula evolution occurs at 0.36 Myr. The dotted line gives the temperature 2000 years after the beginning of phase 2, and illustrates the fast evolution of the subnebula during this stage.

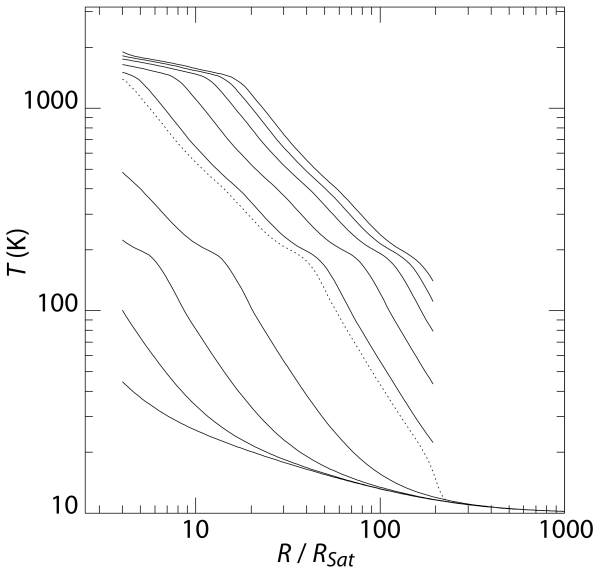

Figure 2.3 Temperature inside the subnebula, as a function of the distance from Saturn (expressed in Saturn's radii R_{Sat}) and represented at different epochs of its evolution (figure adapted from Alibert and Mousis (2007) – see text).

2.3.3 Delivery of solids and conditions of Titan's formation

Regardless the considered formation mechanism of Saturn's satellites within the subnebula (accretion at their present orbit or migration and growth starting from the edge of the subnebula), the delivery of solids to the disk is an essential step, because it determines the amount of volatiles that can be retained and ultimately incorporated in the interiors of these bodies. Different processes have been advocated (see for instance Estrada et al. (2009) and Canup and Ward (2009) for a detailed discussion): (1) direct transport of small particles into the disk with the inflowing gas, (2) ablation and gas drag capture of planetesimals orbiting the Sun through the gas-rich circumplanetary disk, (3) break-up, dissolution and recondensation of planetesimals in the extended envelope of the forming planet, (4) collisional capture of planetesimals .

Mechanism (1) is valid for micron- to millimeter-sized particles that remain coupled to the subdisk's gas while mechanism (2) requires larger size particles ($\sim$ 1 m) to allow their capture and inward drift due to gas drag. Mechanism (3) is probably not valid for Saturn's subnebula because the D/H measurement performed at Enceladus by the Cassini spacecraft (Waite et al., 2009), which is close to the cometary value, suggests that the building blocks of this satellite were formed in the solar nebula. In contrast, planetesimals formed via this mechanism would have a protosolar D/H ratio. Mechanism (4) applies for gas-poor or no gas environments and may have taken place at epochs subsequent to the subnebula phase. In any case, the relative contribution of each of these mechanisms to the delivery of solids to the disk is still under debate (see for instance Estrada et al. (2009) and Canup and Ward (2009)). In term of volatile delivery, each of these processes has very different consequences. In mechanism (1), and to a lower extent in mechanism (2), the particles may preserve the volatile content they acquired in the solar nebula during the condensation sequence, while in mechanism (3) a large fraction of volatile would be likely released when incorporated into the disk. Even in mechanism (4), a significant fraction may be lost during collisions at high velocity.

As a consequence, the volatile content in the building blocks of Titan may be significantly smaller than their content in the planetesimals initially formed in the solar nebula in the vicinity of Saturn. Even for small particles entrained by the gas inflow, they could have been altered once embedded in the subdisk, if they encountered gas temperature and pressure conditions high enough to generate a loss of volatiles during their migration, and if they remained relatively porous, which seems a reasonable assumption. Mousis et al. (2009b), for instance, favored this mechanism to explain the carbon monoxide and argon deficiencies in the atmosphere of Titan. This scenario is based on the fact that CO-dominated clathrate, CO, N_2 and Ar pure condensates are not stable at temperatures greater than $\sim$50 K in the gas phase conditions of the nebula or the subnebula (see Fig. 2.1). This implies that if porous planetesimals ultimately accreted by Titan experienced intrinsic temperatures of $\sim$50 K during their migration and accretion in Saturn's subnebula, they are expected to release most of their CO, Ar, Ne and N_2 while CH_4 and NH_3 are expected to remain trapped, or at least to partly re-condense if released. Similarly, if planetesimals are captured by gas drag or collisional capture, the most volatile species, CO, N_2, Ne, Ar should be released while the most stable one should be preferentially retained.

Such a volatile loss scenario cannot however account for the deficiency of Titan's atmosphere in Kr and Xe because Kr is significantly trapped in CH_4-dominated clathrate (see Fig. 2.2) and Xe is also enclathrated at temperatures higher than $\sim$50 K. However, as is further discussed in Section 2.4.2.2, both Xe and Kr may be sequestred in Titan's icy shell and interior owing to clathration process, partly dissolved in the hydrocarbon seas of Titan (Cordier et al., 2010) or trapped in aerosols (Jacovi and Bar-Nun, 2008), thus potentially explaining their deficiency while predicted to be present in significant amounts in the building blocks.

This scenario seems also problematic regarding the tentative detection of ^{22}Ne by the *Huygens* GCMS (Niemann et al., 2010). According to this scenario, the building blocks should be strongly depleted in Ne with $^{22}Ne/^{36}Ar << 1$, while the ratio estimated in the atmosphere from the *Huygens* GCMS measurements is close to 1 (Niemann et al., 2010). Note, however, that the GCMS detection of ^{22}Ne is only tentative, and the errors are still very large. In situ measurements of Ne, Ar, Kr and Xe abundances in Saturn's atmosphere by a future probe as well as in surface

sampling on Titan could constrain the origin of their unexpected abundances in Titan's atmosphere. This would help in understanding the process of noble gas trapping in the Saturnian system, thus providing key information on the composition of Titan's building blocks.

Another issue concerns the satellite growth from the solids present in the disk. In a gas-rich disk, the growing solid objects should migrate inward as a result of gas drag for small objects and then of type I and/or II migration for largest objects ($\sim$ 1000 km) (e.g. Estrada et al., 2009; Canup and Ward, 2009). A growing satellite may survive if it grows large enough to open a gap in the disk, limiting the migration (Mosqueira and Estrada, 2003b), or if the gas disk dissipates on a timescale comparable to the satellite formation timescale (Canup and Ward, 2002; Alibert et al., 2005a). In the case of Saturn, only one big moon has survived this migration process.

Nevertheless, several large moons may have existed originally and been lost before the disk dissipates (Canup and Ward, 2006; Sasaki et al., 2010). The difference of satellite architecture between Jupiter and Saturn may thus result from differences in disk evolution and satellite migration (e.g. Sasaki et al., 2010). By considering two different disk evolution/structure models for Jupiter and Saturn, Sasaki et al. (2010) proposed that in the case of Jupiter, the satellite migration may have stopped due to quick truncation of gas infall caused by Jupiter opening a gap in the solar nebula, while the subdisk was still relatively hot. In contrast, in the case of Saturn, the gas infall would have never stopped abruptly, and rather slowly decayed. Most of the moons that formed collided with the planet, and only one last big moon would have survived. This surviving satellite would have formed on long timescales ($\sim$Myrs), owing to reduced mass infall. This is obviously only one scenario among others, and several alternative scenarios may be envisioned.

The accretion by Saturn of early formed satellites with sizes analogous to that of Titan may also provide an explanation for the formation of the ring and the inner regular moons. Numerical simulations performed by Canup (2010) suggest that the tidal removal of mass from a differentiated, Titan-sized satellite as it migrates inward towards Saturn may be the origin of the giant planet's ring and inner moons. These simulations show that planetary tidal forces preferentially strip material from the satellite's outer icy layers, while its rocky core remains intact and is lost by collision with the planet. The result of these computations is a pure ice ring much more massive than Saturn's current rings. As the ring evolves, its mass decreases and icy moons are spawned from its outer edge with estimated masses consistent with Saturn's ice-rich moons interior to and including Tethys.

The latter scenario has been further investigated by Charnoz et al. (2011), who confirmed that all the moons interior to Titan's orbit may have been formed by these accretion processes, if Saturn has a sufficiently low dissipation factor Q (< 2000). This latter condition is required to provide sufficient tidal expansion in order for the satellites to move from the edge of a massive ring system to their present orbital position. They also show that the accretion of the satellites from the outer edge of such a ring system may explain the diversity of rock/ice ratios among the mid-sized moons. Alternatively, the variation in rock/ice fraction among the mid-sized satellites may be attributed to the stochastic nature of late-stage accretion, characterized by giant impacts, as suggested by Sekine and Genda (2011). Unfortunately, the different proposed models lack strong observational discriminants. Estimation of Saturn's Q factor from astrometric measurements is probably one of the most constraining observables. Preliminary analysis by Lainey et al. (2011) indicates that the Q factor may be lower than 2000. Future observations will be needed to confirm this unexpectedly low dissipation factor, which still remains puzzling.

2.3.4 Accretion of Titan

There is some analogy between the formation of the terrestrial planets and that of the icy moons. As described above, icy moons probably accreted within the first million years of the Solar System history in circumplanetary disks from aggregates of ice and rock (e.g. Canup and Ward, 2002; Estrada et al., 2009). Among the major icy satellites, Ganymede and Callisto seem to exhibit a strong dichotomy in their degree of differentiation. This has often been attributed to differences in the accretion processes. Titan may represent an intermediate case. However, the presence of its massive atmosphere suggests that Titan formed from different materials than did its Galilean cousins, which may have significant consequences for the final assemblage.

2.3.4.1 Assemblage sequence: Role of impactor distribution

A number of models have been developed for accretional heating of icy moons (e.g. Schubert et al., 1981; Squyres et al., 1988; Coradini et al., 1989; Barr et al., 2010)). Although some ingredients change from one model to another, all these models follow the same approach which was initially proposed by Safronov (1978) and Kaula (1979) for the accretion of the Earth. The main differences between the different models concern the assumption for the impact energy partitioning as well as for impactor size and velocity distributions. The most recent study based on this approach was developed by Barr et al. (2010). In their approach, they assumed that during the satellite growth the impactors are small enough that the impact energy is deposited at shallow depth and is efficiently radiated away. In this condition, they showed that if Titan accreted slowly from numerous cold and small embryos more than 5 Myrs after CAI formation, the melting of the outer layer may have been avoided and the undifferentiated proto-core may extend up to the surface.

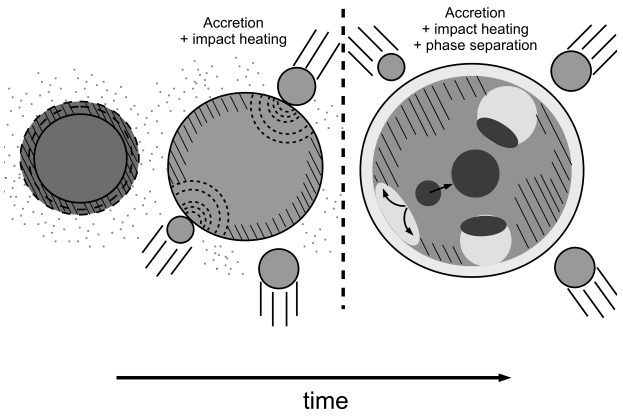

Figure 2.4 Assemblage sequence and consequences for thermal evolution of the growing planet

In reality, the size and velocity distribution of the impactors have probably varied during the accretion phase. Two reservoirs of bodies may have contributed to the satellite growth: bodies in orbit around the planet, formed or captured within the circumplanetary disk, and bodies in orbit around the Sun, colliding directly with the growing satellite (e.g. Squyres et al., 1988). The contribution of each of these two reservoirs probably varied as the circumplanetary disk evolved. When the accretion sequence started, centimeter-sized planetocentric particles were probably predominant, while kilometer-sized and larger bodies became more and more frequent during the late-stage of accretion (see Figure 2.4).

The temporal evolution of the size of impactors played an important role in the differentiation of icy satellites since it determined the accretion rate and the volume of the heated region after an impact. The increase of temperature upon impact in the outer region of the satellite is mainly controlled by the efficiency of post-impact cooling. The cooling is determined by radiation at the surface, subsurface thermal conduction as well as local heat advection associated with melting, excavation and impact-induced convection (e.g. Senshu et al., 2002). If the impact rate is too high or if the impact energy is buried at depths larger than a few kilometers, radiation and conduction are not efficient enough to cool the subsurface and the temperature increases.

As noted above, the averaged size of impactors is expected to increase as a function of time during the accretion, and large impactors will be more and more frequent, possibly leading to giant impacts during the late-stage of accretion (Sekine and Genda, 2011). This has major consequences for the efficiency of cooling of the satellite and the possible occurrence of melting during accretion. Heliocentric impactors with high velocities may also become more and more frequent (Agnor et al., 1999) resulting in larger increases of temperature. High velocity impacts may locally induce significant melting and vaporization (Artemieva and Lunine, 2003, 2005). As the volume of melted material scales with the impact velocity and the impactor volume (Tonks and Melosh, 1992), giant impact events occurring at the end of planetary accretion may generate oceans of melt (e.g. Sekine et al., 2011). Even for impact with moderate velocities, their cumulative effect (especially for large impactors) may lead to progressive increase of temperature up to the melting point of water ice.

2.3.4.2 Energy budget during the early stage of Titan's evolution

During the early stages of Titan's history, in addition to impact heating, three main sources of energy may have contributed to the internal thermal budget: radiogenic heating by short-lived radioactive isotopes (mainly ^{26}Al), tidal heating associated with despinning and viscous heating due to ice-rock separation. In this section, we provide some simple estimates of these sources of energy in order to evaluate their potential impact on the thermal budget of early Titan.

Impact heating results from the deposition of impactor kinetic energy during satellite accretion. It therefore depends on the velocity and the mass of the impactor as well as the way kinetic energy is converted into heat. The impact creates a shock wave that compresses the satellite beneath the impact site. Below the impact site, the peak pressure is almost uniform in a quasi-spherical region, called the isobaric core (e.g. Croft, 1982; Senshu et al., 2002). As shock compression is an irreversible process, the entropy below the impact site increases, leading to a temperature increase. Most of existing shock simulations have been performed at high impact velocity ($>$ 10 km.s^{-1}, Pierazzo et al. (1997); Barr and Canup (2010)), so that they cannot be used directly to constrain the shock heating in the low velocity regime expected during the satellite growth. The heating and associated temperature increase can however be estimated from energy balance considerations. The temperature increase is determined from the peak pressure within the isobaric core, which is directly related to the impactor velocity, and from the intrinsic properties of the target materials (density, specific heat, thermal expansion, etc.) (e.g. Senshu et al., 2002).

The impact velocity v_{imp} is a contribution of the infinite velocity $v_\infty \propto \sqrt{e^2 + i^2}$ with e the eccentricity and i the inclination of the planetary embryos and of the escape velocity $v_{esc} = \sqrt{8/3\pi G\rho R^2}$ of the growing icy satellite with R its radius, ρ its density and G the gravitational constant.

$$v_{imp}^2 = v_{esc}^2 + v_\infty^2 \tag{2.5}$$

The contribution of infinite and escape velocities to the impact velocity can be expressed under the form of the gravitational focusing F_g (Kaula, 1979; Schubert et al., 1981; Barr et al., 2010):

$$F_g = 1 + \left(\frac{v_{esc}}{v_\infty}\right)^2 \tag{2.6}$$

During the early stages of planetary formation, dynamical friction reduces eccentricities and inclinations of growing bodies. Hence, early impacts on Titan probably occurred near the two-body escape velocity (i.e. v_∞ was negligible) (Kokubo and Ida, 1996; Agnor et al., 1999).

In this case and assuming that no significant melting occurs when the icy satellite is small, energy balance between kinetic energy and impact heating leads to a local temperature increase ΔT_0 that is proportional to the square of the radius of the growing icy moon (Monteux et al., 2007):

$$\Delta T_0 = \frac{4\pi}{9}\frac{\gamma}{f(m)}\frac{\rho G R^2}{C_p} \tag{2.7}$$

where γ is the percentage of kinetic energy retained as heat deep below the surface, $f(m)$ is the volume effectively heated over the volume of the isobaric core (typically equal to 2.5-3, Pierazzo et al. (1997); Monteux et al. (2007)) and C_p is the averaged heat capacity (typically varying between 1000-1500 J.kg^{-1}.K^{-1} for ice-rock mixtures). As long as the radius of the growing satellite is below 1000 km, the local temperature increase is less than 10-15 K after each impact. Above 2000 km, the increase of temperature is larger than 50 K.

Radiogenic heating by short-lived radioisotopes (^{26}Al, ^{60}Fe, ^{53}Mn) may also significantly contribute during the accretion period. For simplicity, we consider here only ^{26}Al, which is the principal contributor (e.g. Robuchon et al., 2010; Barr et al., 2010). The increase of temperature due to the decay of ^{26}Al at a radius r depends on the time, t_f, at which the layer at radius r has been formed and it is given by (e.g. Barr et al., 2010):

$$\Delta T_{26}(r) = \frac{m_r q_{26}(0)}{C_p}\frac{\tau_{26}}{\ln 2}\exp\left(-\ln 2\frac{t_f(r)}{\tau_{26}}\right), \tag{2.8}$$

where m_r is the rock mass fraction in the accreting material (around 0.5 in the case of Titan), τ_{26} is the half-life time of ^{26}Al (τ_{26} = 0.716 Myr) and $q_{26}(0)$ is the initial ^{26}Al heating rate at the time of the calcium-aluminium-rich inclusions (CAI's). t_f denotes the time after the formation of CAIs. The initial heating rate is determined by the specific heat production of ^{26}Al $H_{26}(0)$=0.341 W.kg^{-1} (Robuchon et al., 2010), the Al content in rocks, [Al] and the initial ^{26}Al/^{27}Al. Assuming a rock composition similar to CI chondrites, [Al] = 0.865 wt% and initial ^{26}Al/^{27}Al of 5.85×10^{-5} (Thrane et al., 2006; Barr et al., 2010) leads to $q_{26}(0) = 1.725 \times 10^{-7}$ W.kg^{-1}. This is about 20 million times larger than the radiogenic heating rate due to the decay of long-lived isotopes expected at present within Titan. However, this huge heat production rapidly decays. For an accretion time of 2 Myr after CAI formation, the temperature increase due to ^{26}Al decay would be of the order of 100 K, but it becomes less than 10 K for accretion times above 5 Myrs. Radiogenic heating by short-lived radioisotopes may have been of importance for the first materials to accrete, i.e. for the materials that formed the inner part of the satellite. By contrast, impact heating becomes significant for layers above a radius of about 1000 km.

An additional source of heating corresponds to dissipation due to enhanced tidal friction before the satellite reaches synchronous rotation. It is indeed likely that Titan has an initial spin period much shorter that its present-day period of 15.95 days. Initial spin periods as low as 6-10 hours are possible (Lissauer and Safronov, 1991; Robuchon et al., 2010). In this condition, the tidal bulge raised by Saturn rotates relative to the satellite body frame. Owing to the anelastic properties of the interior, the fast-rotating satellite does not respond perfectly to the tidal forcing, resulting in a misalignment of the tidal bulge with respect to Saturn's direction. This acts as a torque that tends to slowdown the satellite spin, until the satellite is locked in spin-orbit resonance. The gradual decrease of the spin rate ω as a function of time t is determined from the tidal torque acting on the satellite and is given by:

$$\frac{d\omega}{dt} = \frac{3}{2}\frac{k_2 G M_S^2 R^5}{D_{ST}^6 Q C}, \tag{2.9}$$

with k_2 tidal Love number, M_S Saturn's mass, D_{ST} mean distance between Titan and Saturn, Q dissipation factor of Titan and C its polar moment of inertia ($C \simeq 0.4 \times M_T R^2$ at the time of accretion). As the despinning rate scales with R^5, it rapidly increases when the satellite reaches its final size. For $k_2 \simeq 0.07$, the expected value for an homogeneous rigid interior (Sohl et al., 1995) and Q=100-500 and initial rotation period of 10 hours, the time needed to reach the 16-days period range between 2 and 10 Myrs, suggesting that despinning is achieved shortly after the accretion. Note that once large-scale melting occurs, a global liquid layer may form, thus increasing the Love number and the despinning rate, so that the current period is reached even faster. The total amount of energy dissipated during the despinning stage is given by the difference of body rotation energy between the initial and final periods and leads to the following temperature increase:

$$\Delta T_{desp} = \frac{1}{2}\frac{C(\omega_0^2 - \omega_c^2)}{C_p M_T}, \tag{2.10}$$

with ω_0 and ω_c the initial and current angular rotation rates, respectively, and M_T Titan's mass. For initial periods varying between 10 and 6 hours, the averaged temperature increase would range between 25 and 75 K, respectively. The localization of the dissipation is very sensitive to the internal structure (Tobie et al., 2005a). For a homogeneous interior, the dissipation will rather uniform, with a maximum of dissipation at about mid-radius. For a differentiated structure, the dissipation will be mainly located in the outer regions (liquid water and ice I) and would be more efficiently transported to the surface.

Ice-rock separation, which may be triggered already during the accretion phase, may also significantly contribute to the energy budget. The total increase of internal temperature due to ice-rock differentiation, ΔT_{diff}, can be estimated from the change of gravitational energy, ΔE_g, between a homogeneous interior and a differentiated interior

consisting of a rock core and a thick H_2O mantle (e.g. Friedson and Stevenson, 1983):

$$\Delta E_g \simeq \frac{3}{5}\frac{GM_T^2}{R_T}\left[1-\left(\frac{\rho_r}{\bar{\rho}}\right)^2 X_c^5+\left(\frac{\rho_i}{\bar{\rho}}\right)^2\left(1-X_c^5\right)\right. \tag{2.11}$$

$$\left.+\frac{5}{2}\frac{\rho_i}{\bar{\rho}}\left(\frac{\rho_r}{\bar{\rho}}-\frac{\rho_i}{\bar{\rho}}\right)X_c^3\left(1-X_c^2\right)\right]$$

with ρ_r the density of rock, ρ_i the averaged density of ices and liquid water, X_c the ratio between the rock core radius, R_c and Titan's radius, R_T. For $\rho_r = 2700$ kg.m^{-3} and $\rho_i = 1250$ kg.m^{-3}, $X_c = 0.75$ and $\Delta T_{diff} = \Delta E_g/c_p M \simeq 100-150$ K (for $c_p = 1000-1500$ kg.m^{-3}). If the differentiation process is slow (> 1 Gyr), the convective heat transfer should be able to transport this additional energy. If the ice-rock separation is fast enough (< 0.5 Gyr), the dissipation of potential energy may induce runaway melting and thus may create a catastrophic differentiation (Friedson and Stevenson, 1983; Kirk and Stevenson, 1987). In particular, giant impact events occurring at the end of planetary accretion (e.g. Sekine et al., 2011) may generate locally large volume of melts, leading to the formation of rock diapir migrating toward the center (Figure 2.4). The viscous heating associated to the migration of large rock diapirs may generate significant melting in the surrounding ice, potentially triggering differentiation runaway in a way similar to what is expected in terrestrial planets (e.g Monteux et al., 2009; Ricard et al., 2009).

2.3.4.3 Possible post-accretional interior structure

Depending on the conditions under which Titan accreted, different post-accretional interior structures are possible just after accretion as illustrated in Figure 2.5. If the accretion is very slow (> 1 Myr) and the impactors remain small all along the accretion period (< 100 m), the surface should able to cool down between successive impacts, and differentiation may be avoided. A fully undifferentiated structure also requires that the accretion starts about 3-4 Myr after the CAI formation, in order to limit the increase of internal temperature due to short-lived radiogenic elements, and that the initial spin period of Titan was larger than 8-10 hours. In such a cold accretion case, no significant atmosphere would be generated, and the formation of a significant atmosphere should occur later during the satellite evolution (for instance during the LHB event).

If the growing satellite is hit by larger impactors at the end of accretion, a surface water ocean may be generated ($R > 2300-2400$ km) (Figure 2.5, middle). Even if only 10-20% of the total volume of ice melts, release of gases (mainly CO_2 and CH_4, Tobie et al. (2011)) trapped in the ice phase may generate an atmosphere up to 5-10 bars. Even if a global ocean is generated, most of the mass of Titan would still be undifferentiated. Finally, if the accretion is faster and/or if the impactors are large even during the earliest stage of accretion, ice melting rapidly occur during the satellite growth. In this case, a very massive ocean in equilibrium with a very massive atmosphere ($P > 50$ bars) would be generated. Rock blocks resulting from the melting of icy impactors would sediment at the base of the ocean forming a thick layer of unconsolidated rock (Kirk and Stevenson, 1987; Lunine and Stevenson, 1987). The subsequent evolution of these different possible initial structure is discussed in Section 2.4.1.

2.3.5 Summary

At the start of this Section we posed three questions; we will conclude by providing some provisional answers.

1. *What was the composition of the primordial building blocks that built Titan and the Saturnian system ?* Most of the solids that formed the Saturnian system probably originate from the surrounding solar nebula. They are predicted to be composed of rock and ice and to contain significant amounts of volatiles (NH_3, CH_4, CO_2, H_2S) trapped in the form of hydrate and pure condensate. The apparent deficit in primordial CO, N_2, Ar in Titan relative to proto-solar composition may be explained by partial devolatilization of building blocks during their migration in Saturn's subnebula.

2. *What make the Jupiter and Saturn systems so different ?* The difference in satellite architectures may be explained by different evolutions of the circumplanetary disk. In the case of Jupiter, the feeding of the disk may have stopped abruptly, while in the case of Saturn, the satellite accretion in the disk may have lasted longer owing to reduced mass infall. During the accretion process, several Titan-size moons may have been formed and lost by migration into proto-Saturn. Titan would be the only surviving big moon of Saturn, while Jupiter was able to retain four big ones.

3. *Can Titan accrete undifferentiated ?*
It seems extremely difficult to avoid ice melting during the accretion phase, owing to combined effects of impact heating, radiogenic heating by short-lived isotopes and tidal despinning. Melting may be prevented only if Titan accreted slowly (> 1 Myr) from a swarm of small building blocks (< 100 m). Even for faster accretion with larger impactors, large-scale melting is only reached toward the end of the accretional growth, so that the inner part of the interior structure (< 1500 km) remains undifferentiated. In any case, a totally undifferentiated structure after accretion is not needed to explain the present-day moderately differentiated structure.

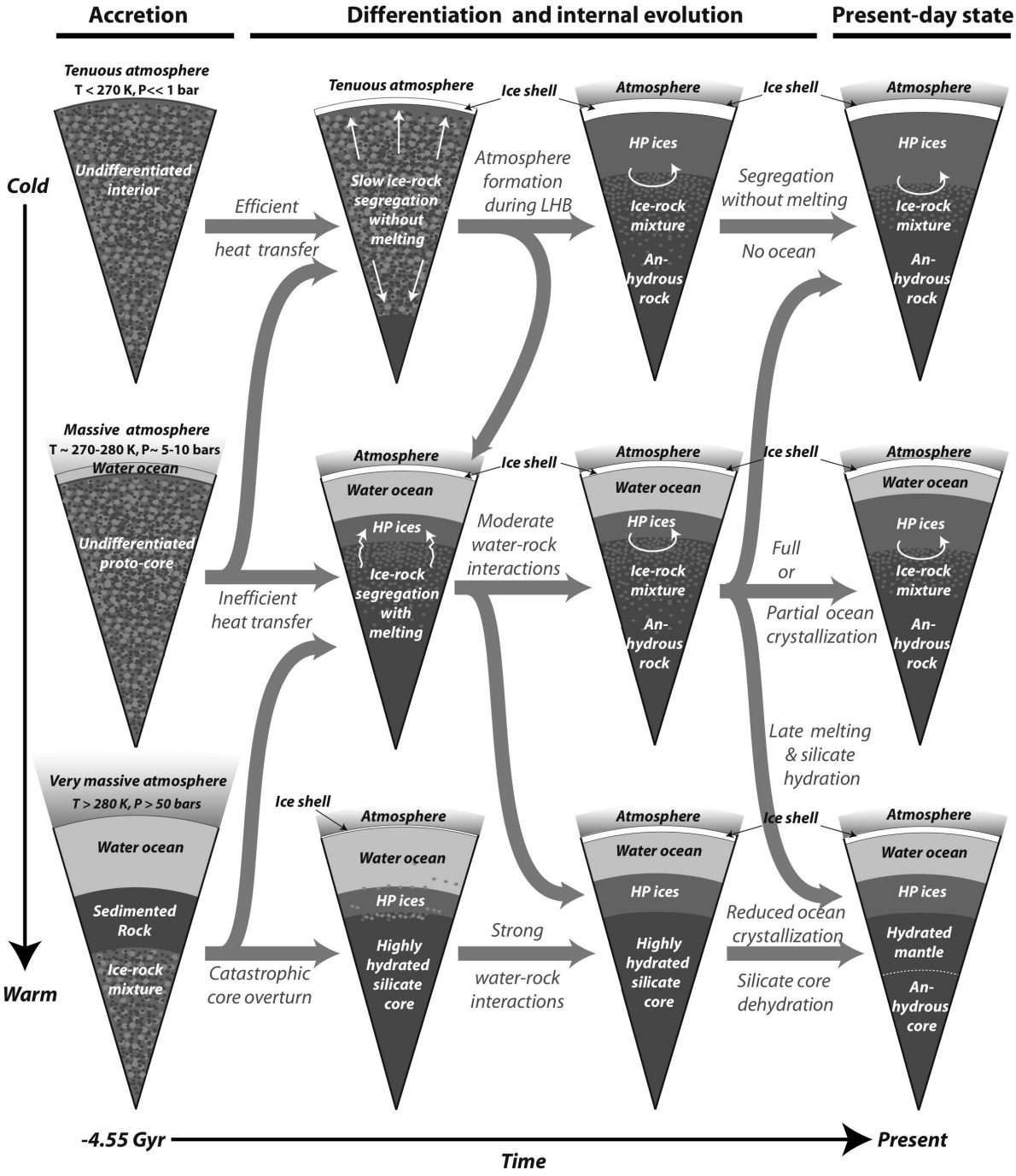

Figure 2.5 Possible evolution scenarios for the interior of Titan for different initial states. Depending mostly on the efficiency of heat transfer in the interior, different bifurcations in the evolutionnary path may have occurred.

2.4 COUPLED EVOLUTION OF THE ATMOSPHERE, SURFACE AND INTERIOR OF TITAN

During and after the accretion, exchanges between the interior, surface and atmosphere are likely to have occurred. The icy shell has probably played a crucial role all along Titan's evolution by storing and transferring volatile compounds from the internal ocean to the surface. These exchanges have probably influenced the composition of the atmosphere during most of Titan's evolution, and they are maybe still operating at present. In this section, we discuss the coupled evolution between the different envelops of Titan, and try to address the three questions listed below.

1. *To what extent did the interior of Titan influence the evolution of its atmosphere ?* Evidence for exchange with the interior is provided by the detection of a significant amount of ^{40}Ar in the atmosphere. However, the degree and timing of internal outgassing still remain unconstrained. In this section, we review the different internal processes that may have occurred all along Titan's evolution and discuss their implications for the evolution of the atmosphere.

2. *Did Titan always possess a massive N_2-CH_4 atmosphere ?* The composition and the mass of Titan's atmosphere have probably varied since the satellite accretion. Depending on the initial state acquired during the accretion and on the efficiency of internal outgassing, we will discuss the different evolution scenarios that can be envisioned.

3. *Where is the missing hydrocarbon inventory ?* Hydrocarbon lakes has been identified at the surface of Titan (Stofan et al., 2007). However, the estimated volume is much smaller than what is expected from continuous photolysis of methane since the formation of Titan (Lorenz et al., 2008a). This suggests that either a large fraction of hydrocarbon products has been removed from the surface or that the photochemical production has not been constant through time. We will discuss the implications of these two different hypotheses for the long-term evolution of Titan.

2.4.1 Differentiation and long-term evolution of the interior

2.4.1.1 Ice-rock segregation and formation of a rocky core

As already discussed in Section 2, the moment of inertia ($C/M_T R_T^2 = 0.33 - 0.34$) inferred from *Cassini* gravity measurements suggest that Titan's differentiation was not complete. Titan probably does not have an iron core, and a layer consisting of a rock-ice mixture may still exist between a rocky core and a high-pressure ice layer. This possible uncompleted ice-rock separation has been proposed to be the result of cold accretion process (Barr et al., 2010). However, limited differentiation requires not only slow accretion but also implies that the convective heat transfer was efficient enough to remove heat from the interior (Friedson and Stevenson, 1983; Mueller and McKinnon, 1988; Nagel et al., 2004). This is possible if the viscosity of the ice-rock mixtures is sufficiently low. Nagel et al. (2004) showed that, in the case of Callisto, if the average size of rocks was of the order of meters to tens of meters, the interior may have experienced a gradual, but still incomplete unmixing of the two components. Significant lateral heterogeneities among the ice/rock mixtures existing after accretion could also have enhanced the differentiation processes (O'Rourke and Stevenson, 2011). In these conditions, convective motions associated with ice-rock unmixing processes may be efficient enough to avoid melting. Following this scenario, the interior of Titan would be relatively similar to Callisto, but with a thinner layer of ice-rock mixed materials, as suggested by its smaller MoI factor.

Nevertheless, uncompleted ice-rock separation is not necessarily needed, as the MoI factor may also be consistent with a highly hydrated silicate interior, possibly dominated by antigorite serpentine (Castillo-Rogez and Lunine, 2010; Fortes, 2011). The formation of a highly hydrated core may result from a rapid differentiation process, implying large-scale melting and efficient water-rock interactions (e.g. Fortes et al., 2007; Castillo-Rogez and Lunine, 2010; Fortes, 2011). The combined effect of accretional heating, radiogenic decay by short-lived isotopes, tidal heating associated to despinning, and viscous heating associated with negative rock diapirs may increase the internal temperature above the melting point of ice. The presence of freezing point depressing agents such as ammonia or methanol (Lunine and Stevenson, 1987; Grasset and Sotin, 1996; Grasset and Pargamin, 2005; Deschamps et al., 2010) would further favor the generation of melts as they strongly decrease the melting point of ice. The aqueous melt, which is less dense than ice-rock mixtures, at least at pressure above 100 MPa, will percolate upward, thus interacting with surrounding rock particles. During their ascent, aqueous solutions in proto-Titan may have been able to interact chemically with silicate minerals (Engel and Lunine, 1994) and with other substances in solution, such as sulfates (Fortes et al., 2007). Interactions of aqueous fluids with initially anhydrous silicate minerals at low temperature may result in the formation of hydrated silicate minerals, called serpentine (Fortes et al., 2007; Castillo-Rogez and Lunine, 2010; Fortes, 2011). The hydrated minerals may remain stable as long as the rocky core temperature remains below approximately 900 K (Grindrod et al., 2008; Castillo-Rogez and Lunine, 2010). Above this temperature, dehydration would be expected, releasing warm supercritical water fluids which may interact again with overlying rocks during their ascent (Castillo-Rogez and Lunine, 2010).

As pointed out by Iess et al. (2010), the main challenge with this hypothesis is to keep most of the core hydrated (i.e. < 900 K until present). Thermal convection is unlikely to start in a cold core dominated by hydrated silicates

(Castillo-Rogez and Lunine, 2010). As thermal diffusion is not efficient enough to extract heat, the core temperature should rise up to the dehydration temperature. The temperature increase can however be limited if the core is depleted in radiogenic elements. Castillo-Rogez and Lunine (2010) showed that if at least 30% of potassium are leached into the ocean from the silicate minerals during the earlier hydration event, the internal temperature would slowly increase and the outer part of the core would remain hydrated. As shown by Castillo-Rogez and Lunine (2010), a rock core consisting of only antigorite serpentine is not required to explain the present-day moment of inertia. An inner anhydrous core with radius up to 1300 km overlaid by a hydrated mantle is compatible with the MoI factor of 0.33-0.34 (see Figure 2.5 bottom right). The scenario of a fully hydrated core initially investigated by (Fortes et al., 2007) must be considered as a very extreme case, maybe not fully realistic. Nevertheless, the idea that a large fraction of the core remain hydrated during most of Titan's evolution should be considered as a possible scenario. More complete chemical and thermal evolution models are probably needed in the future to test in more detail this hypothesis.

As illustrated on Figure 2.5, different evolutionnary paths are possible, some of them combining both solid-state unmixing and ice melting processes. For instance, for an initially warm and gravitationally unstable interior (Fig. 2.5, bottom), the rock core may form rapidly owing to runaway melting of the undifferentiated proto-core, resulting in a catastrophic core overturn (Kirk and Stevenson, 1987), or more slowly with progressive ice-rock separation and limited ice melting (e.g. Estrada and Mosqueira, 2011). By contrast, an initially cold undifferentiated interior may slowly differentiate with no melting and no formation of ocean during the entire evolution. Any intermediate evolution is also possible.

2.4.1.2 Water-rock interactions in Titan's conditions

On Titan, the crystallization of the internal liquid water results in the formation of a low-pressure ice layer at its top and of a high-pressure ice layer at its base. On smaller icy moons, such a high-pressure ice layer does not exist due to reduced pressure (high-pressure phases only exist above about 200 MPa). On Europa and Enceladus for instance, the internal water ocean is permanently in contact with the rocky core, thus favoring water-rock interactions all along the satellite evolution. By contrast, on Titan, a thick layer of high-pressure ice rapidly forms during the interior evolution (Figure 2.5). The water ocean is expected to be in direct contact with underlying rocks only during a brief period of time (< 100 Myr) just after accretion, and only in the case of relatively warm accretion (Figure 2.5).

However, even if there is no direct contact between the water ocean and the rocky core, water-rock interactions may have occurred at different periods during Titan's evolution, especially during the differentiation. As discussed in Section 2.3.1, non-water ice components such as CH_3OH, NH_3, CO_2, H_2S are likely to have been incorporated inside Titan. In this condition, eutectic solutions at temperatures well below 273 K would have formed (e.g. Sohl et al., 2010). These highly concentrated eutectic solutions should facilitate dissolution of mineral phases and chemical reactions. In the case of ammonia-rich fluids, Engel and Lunine (1994) indicated that NH_4^+-ions contained in the aqueous solution may efficiently replace ions such as K^+, Na^+, Rb^+ and Ca^{2+} contained in the mineral phase. Ammonia-rich liquids are also expected to react with magnesium sulfate, contained in the chondritic phase and with carbon dioxide brought in the ice phase to form ammonium sulfate and ammonium carbonate, respectively (Kargel, 1992; Fortes et al., 2007).

During the migration of the enriched fluids toward the surface, their composition should vary as new elements are extracted from primary minerals and other precipitate in secondary phases (e.g. Zolotov, 2010). In turn, the circulation of aqueous solutions leads to oxydation and hydration reactions, analogous to aqueous processes on chondrite parent bodies (e.g. Sohl et al., 2010). These reactions are well documented at low pressure conditions and have been used for instance to constrain the possible composition of Europa and Enceladus' ocean (e.g. Zolotov, 2007; Zolotov and Kargel, 2009), but they are still poorly known at the high pressure range of Titan's proto-core (> 1 GPa). Only one study by Scott et al. (2002) tried to investigate the aqueous alteration of chondritic materials at high pressure. However, Scott et al. (2002) did not take into account the probable presence of ammonia, methanol or other compounds, which may significantly affect the chemical equilibrium. Future experimental and thermodynamical investigations will be needed to better understand the complex chemistry that probably occurred during the differentiation.

After the complete separation of rock and ice, water-rock interactions are limited to the ice-rock interface at the base of the high-pressure layer. Even though water is mostly in the form of high-pressure ice phase at this interface owing to the elevated pressure ($> 0.8 - 1$ GPa), liquid water may locally exist and potentially circulate in the upper part of the rock core. In order to efficiently transfer the heat coming from the rocky core through the high-pressure ice layer, the temperature profile in the high-pressure ice is probably close to the melting curve of water ice (e.g. Sotin and Tobie, 2004). In this context, the formation of a transient liquid reservoir at the rock-ice interface is likely. These liquids may potentially interact with the underlying rocks before percolating upward to the ocean. Warm liquid water may also be released from the core when the dehydration temperature is reached (Castillo-Rogez and Lunine, 2010). This hydration event may occur relatively late during Titan's evolution ($> 3 - 3.5$ Gyr after formation), provided sufficient amounts of radiogenic potassium were leached from the core and that thermal diffusivity in the core is not too low (Castillo-Rogez and Lunine, 2010) (see Section 2.4.1.1). In summary, in warm evolution scenarios, intensive water-rock interactions

were likely during two main sequences of Titan's evolution: before 1 Gyr during the differentiation and after 3-3.5 Gyr during core dehydration. Moreover, reduced water-rock interactions may also exist all along Titan's evolution owing to circulation of high-pressure ice melts at the rock-ice interface.

It has been proposed that water-rock interactions may lead to efficient production of methane from carbon dioxide, carbon grains or organic matters by serpentinization (Atreya et al., 2006). However, this mode of production seems incompatible with the D/H ratio observed at present in the atmospheric methane, which is about three times greater than the value expected in hydrothermally produced methane (Mousis et al., 2009a). It has also been suggested that the oxidation of primordial NH_3 to N_2 may also occur in hydrothermal systems on early Titan (Glein et al., 2009), as well as on early Enceladus (Matson et al., 2007; Glein et al., 2008). The endogenic production of N_2 from NH_3 is possible only if the hydrothermal systems were sufficiently oxidized with C existing predominately in the form of CO_2, not CH_4. It also implies that primordial NH_3 was enriched in ^{15}N in order to explain the elevated $^{15}N/^{14}N$ observed in atmospheric N_2. Although water-rock interactions and associated chemical reactions are thermally plausible, there are essentially no constraints available to assess their likelihood. For instance, constraints on the possible primordial value of $^{15}N/^{14}N$ in NH_3 or D/H in water are still missing. Future measurements in comets by Rosetta for instance will bring new bear on these ideas.

Circumstantial evidence for water-rock interactions is, however, provided by the detection of ^{40}Ar in the atmosphere (Niemann et al., 2005; Waite et al., 2005; Niemann et al., 2010). ^{40}Ar is one of the decay products of ^{40}K initially contained in silicate minerals (e.g. Engel and Lunine, 1994). The mass of ^{40}Ar in the atmosphere is estimated between 4.0 and 4.6×10^{14} kg (Niemann et al., 2010), which corresponds to about 7.5-9% of the total mass that may be contained in the rocky core, assuming a CI chondritic composition (Tobie et al., 2011). As a comparison, on Earth, Mars and Venus, the fraction of ^{40}Ar outgassed from the silicate mantle is estimated to about 50% on the Earth (Allègre et al., 1996) and about 25% on Mars and Venus (Hutchins and Jakosky, 1996; Kaula, 1999). The outgassing process is probably very different on Titan. On Earth and terrestrial planets, ^{40}Ar is progressively outgassed from the silicate mantle through volcanism (e.g. Xie and Tackley, 2004). ^{40}K decays into ^{40}Ar in the silicate minerals and the latter is released when the minerals are brought near the surface by convective motions and melt. On Titan, as suggested by the gravity data, Titan's rocky core is probably relatively cold during most of its evolution (< 1000 K, Castillo-Rogez and Lunine (2010)), therefore it has probably never reached magmatic temperatures (at least on a global scale). Moreover, even if silicate melting has occurred, outgassing of erupting silicate magmas should be limited due to the high pressure conditions expected at the surface of the rocky core (1 ? 1.5 GPa) (McKinnon, 2010).

On Titan, the extraction of ^{40}Ar is more likely the result of a three step mechanism. ^{40}K may have been extracted first from the silicate minerals by water interactions (e.g. Engel and Lunine, 1994). Then dissolved $^{40}K^+$ ions in the ocean would have decayed into ^{40}Ar. Finally, the ^{40}Ar contained in the ocean would be extracted through direct outgassing of the ocean or progressive incorporation in the outer shell in the form of clathrate hydrate and then destabilization near the surface by cryovolcanism (e.g. Tobie et al., 2006) or impact (e.g. Barr et al., 2010). Assuming that 30% of potassium has been leached into the ocean implies that about 25-30% of the produced ^{40}Ar has been outgassed through the outer icy shell, which seems a reasonable outgassing efficiency.

The presence of significant amount of ^{22}Ne in the atmosphere, if confirmed, may also be indicative of water-rock interactions and efficient outgassing processes (Tobie et al., 2011). Indeed, a chondritic core may contain ^{22}Ne in sufficient amounts to explain the tentatively observed abundance in the atmosphere (Niemann et al., 2010). As further discussed in Section 2.4.1.4, neon is the least stable gas compound in the form of clathrate and the less soluble in liquid water, and therefore it is expected to be very efficiently extracted during methane-driven outgassing events. The accurate determination of the abundance of the different isotopes of Ne (^{20}Ne, ^{21}Ne and ^{22}Ne) by a future mission will permit confirmation of the tentative detection of neon by *Huygens*, and it will provide pertinent tests on the origin of neon and on its extraction mechanism from the interior.

2.4.1.3 Volatile storage in the H_2O mantle

A major issue on Titan concerns the storage and transport of gas compounds in the H_2O mantle, which constitute about 60-70% of the satellite volume. The amount of gas compounds that can be stored in the ocean and in the ice layers is determined by their solubility in water and their stability relative to the clathrate phase. NH_3 and CH_3OH, for instance, are highly soluble in liquid water and do not form clathrate structures. At low temperature ($T < 177$ K), ammonia combines with water molecules to form ammonia hydrate (not clathrate) and methanol solidifies at relatively similar temperatures. Such low temperature conditions can be reached only near the cold surface, and both ammonia hydrates and methanol ice become unstable below a depth of 5-10 km (depending on the subsurface thermal gradient). As a consequence, ammonia and methanol should be nearly exclusively stored dissolved in the internal ocean.

Although the solubility of most of the other gases, for instance methane, in liquid water is low, large quantities of gas can be stored dissolved in the liquid water as the ocean is very massive on Titan and it is confined at relatively elevated pressures (> 25 MPa). For example, more than

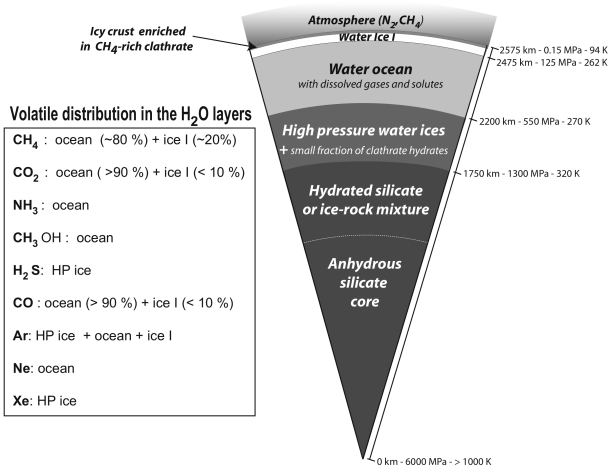

Figure 2.6 Possible present-day structure of Titan's interior and estimated volatile distribution within the thick H_2O mantle. The radius, temperature and pressure of each interface are only indicative.

2000 times the present-day mass of atmospheric methane may be stored dissolved in the ocean (Tobie et al., 2011).

Depending on their stability relative to the clathrate phase, a fraction of the gases dissolved in liquid water can however be incorporated in the form of clathrate hydrate (Choukroun et al., 2010; Tobie et al., 2011; Choukroun et al., 2011). The most stable species expected in the ocean, such as H_2S and Xe, should be preferentially incorporated in the form of clathrate hydrate, whereas the least stable species such as CO and Ne remain mainly in the liquid phase (Tobie et al., 2011). The fraction incorporated in the clathrate phase should also increase as the ocean cools down and crystallizes. Clathrate hydrates which have a composition dominated by H_2S have a density larger that liquid water, so that they are expected to sink to the base of the ocean. As an example, clathrate structures containing 75% of H_2S, 20% of CO_2 and 5 % of CH_4 have a density of about 1050 kg.m^{-3}. These H_2S-rich sinking clathrates will also preferentially incorporate Xe owing to its very high stability in clathrate phase. As a consequence, H_2S and Xe are expected to be mostly stored in the form of clathrate hydrate within the high-pressure ice layer.

During the clathration process, the dissolved fraction of H_2S progressively reduces, and CH_4 and CO_2 eventually become the dominant clathrate former. When CH_4 becomes the dominant clathrate former gas, the clathrate density gets lower than the density of liquid water, and clathrate hydrates accumulate at the top of the ocean. Differentiation of Titan's interior during the early stage of its evolution may also lead to massive release of methane-rich clathrate hydrates, and hence accumulation in the outer shell above the ocean (Tobie et al., 2006). Both early differentiation and late ocean crystallization may result in the accumulation of methane-rich clathrate hydrates in the outer shell. However, even in these conditions, the total thickness of methane-rich clathrates incorporated in the outer ice shell should not exceed 5-10 km, corresponding to about 20% of the total mass of methane that is potentially contained in the interior (Fig. 2.6, Tobie et al. (2011)). A fraction of CO_2, CO and Ar should also be incorporated in the outer shell in the form of clathrate, but to a lesser extent than methane due to differences in solubility and clathrate stability.

2.4.1.4 Volatile release from the H_2O mantle

Even though the interior may potentially contain large quantities of volatiles, their release into the atmosphere is limited owing to their solubility in the internal ocean and owing to clathration processes within the H_2O mantle. Outgassing from the interior may occur through two different mechanisms: (1) destabilization of clathrates stored in the outer ice shell by thermal convective plumes or by impacts, (2) mobilization of dissolved gas molecules contained in the water ocean and subsequent bubble formation if the ocean gets saturated (Tobie et al., 2006, 2009). Both processes are controlled by methane, since it is the dominant gas in the form of clathrate hydrate in the outer shell and since it is the only gas compound that may reach the saturation point in the ocean during periods of reduced ice shell thicknesses. The other dominant compounds, CO_2, NH_3 or H_2S, are more soluble in liquid water, so that they will never reach saturation. For noble gases such Ne or Ar, although they have a low solubility, their concentration is very low and always remain below the saturation point. However, when methane reaches the saturation point, Ne and Ar owing to their low solubility in water may be preferentially incorporated in CH_4-rich bubbles formed at the ocean-ice interface and transported upward with the percolating fluids. Following this extraction mechanism, the detection of ^{40}Ar (and potentially ^{22}Ne) suggests that the atmospheric mass of methane has been renewed at least 20-30 times during Titan's evolution (Tobie et al., 2011).

2.4.2 Formation and evolution of the atmosphere

2.4.2.1 Origin of the massive N_2-CH_4 atmosphere

The formation of Titan's atmosphere is certainly an event which occurred relatively early in its history, otherwise we should see a number of impact craters too small to have been formed under the dense atmosphere of today. However, whether it is an accretionally generated atmosphere (e.g. Lunine and Stevenson, 1987; Kuramoto and Matsui, 1994) or a late veneer generated during a subsequent late heavy bombardment (Zahnle et al., 1992; Sekine et al., 2011) is an issue that cuts to the heart of the question of whether Titan's formation environment was chemically and thermally distinct from that of Jupiter (see above). If the disk around Saturn was colder than that at Jupiter, rich in volatiles like

methane and ammonia, then the atmosphere most likely was primordial. The likely presence of an interior water ocean, outgassing through time of methane needed to replace that destroyed by photolysis, and the elevated nitrogen isotopic ratio in Titan's atmosphere (Niemann et al., 2010) all hint at the likelihood that Titan acquired its volatile inventory throughout accretion, the present atmosphere being an outgassed remnant of a volatile-rich Titan.

A volatile rich Titan formed under all but the coldest accretional scenarios would have had an initially warm ammonia-rich atmosphere, if indeed the dominant carrier of nitrogen was ammonia. This seems to be required by the measurement of ^{36}Ar to nitrogen (Niemann et al., 2010), which can be interpreted as requiring that molecular nitrogen was initially in the form of ammonia (Owen, 1982). Arguments to the contrary–that somehow the argon is being sequestered by a condensed or crustal reservoir–don't seem to make sense in light of the presence of radiogenic argon at two orders of magnitude larger mixing ratio. Thus we can assume that ammonia was in abundance on early Titan, initially in the form of an atmosphere and surface ammonia-water ocean supported by accretional heating and a strong greenhouse effect (Lunine et al., 2010a). Conversion of ammonia to molecular nitrogen by photolysis (Atreya et al., 1978) and shock heating (Jones and Lewis, 1987; McKay et al., 1988) all provide a plausible story in which the ammonia is rapidly consumed, the atmosphere cools and condenses out, and nitrogen takes its place. Ishimaru et al. (2011), however, demonstrated that efficient conversion of NH_3 into N_2 by impact shock requires on oxidizing CO_2-rich proto-atmosphere on Titan. This is consistent with CO_2 as the dominant gas compound in the building blocks that formed Titan as predicted by Hersant et al. (2008); Mousis et al. (2009c); Tobie et al. (2011).

Sekine et al. (2011) also proposed, based on laser-gun experiments, that ammonia ice contained in the outer icy shell may have been efficiently converted to N_2 by high-velocity impacts during the LHB. The generation of the N_2-rich atmosphere by this process requires the presence of several percents of ammonia in the outer shell, which implies that Titan's outer layer has remained undifferentiated and unmelted until the LHB era. As already discussed, it is very difficult to avoid melting and partial differentiation during the accretion, so that it is unlikely that Titan's icy shell contained ammonia in sufficient amounts at the time of the LHB. While the LHB event has probably affected the evolution of the atmosphere, notably by inducing a significant atmospheric erosion (Korycansky and Zahnle, 2011; Ishimaru et al., 2011), it seems unlikely that it has been the main contributor for the atmosphere generation, a massive atmosphere probably already existed prior to that event.

Outgassing of methane during the accretion and possibly during the LHB would have been vigorous. However, the present-day methane in the atmosphere is unlikely to be the remnant of this primordial outgassing. If it was the case, the C^{13}/C^{12} in CH_4 should be much larger than the observed value, which is close to the solar value (Mandt et al., 2009; Niemann et al., 2010). This nearly unmodified ratio suggests that methane released during the early stage of evolution should have been totally lost or rapidly re-trapped in the subsurface without being affected by atmospheric fractionation processes. Today's methane has probably been injected much later during the evolution, possibly due to the destabilization of crustal reservoir of CH_4-rich clathrate (Tobie et al., 2006). The only record of the accretional time lies in the nitrogen isotopic ratio, modestly heavier than the terrestrial value (Mandt et al., 2009) , suggesting a source distinct form the Earth, or loss of nitrogen to space, or both. However, a single isotope ratio is a poor constraint on the rate and volume of the loss because isotopic enrichment is a function of the rate and mechanism of escape. Further extensive discussion of the early Titan atmosphere may be found elsewhere (Lunine et al., 2010a).

2.4.2.2 Interactions with the icy shell

All along Titan's evolution, interactions with the solid icy shell has likely influenced the composition of the atmosphere. During the post-accretional cooling leading to the crystallization of the primordial water ocean, part of the atmospheric gases, notably CO_2 and CH_4, may be re-trapped first by clathration and then by condensation (Choukroun et al., 2010; Lunine et al., 2010a). Large quantities of CO_2 and CH_4 were probably incorporated in the primitive icy shell. Additional CH_4-rich clathrates released during the differentiation of the deep interior may have also accumulated at the base of this primitive outer shell, leading to the formation of a thick ($>$ 10 km) CH_4-rich clathrate layer (Tobie et al., 2006). This shell would then thin in response to the release of heat associated to the core evolution (Tobie et al., 2006), resulting in the release of large amounts of methane which would be mainly stored dissolved in the ocean, only the gas in excess may have been outgassed (Tobie et al., 2009).

According to this scenario, several kilometers of CH_4-rich clathrates may still be present in the outer icy shell at present, and recent thermal destabilizations of this reservoir may explain the present-day atmospheric methane (Tobie et al., 2006). CH_4-rich clathrates are probably not the only crustal reservoir. Large volumes of liquid hydrocarbons may also be potentially stored in a porous crust (Kossacki and Lorenz, 1996; Voss et al., 2007). The morphology and distribution of the hydrocarbon lakes on Titan suggest that they are connected to a subsurface reservoir (Hayes et al., 2008) (see also Aharonson et al. this book). However, no constraints exist on the extension of this subsurface reservoir as well as on the methane content. The lakes seems dominated by ethane (Mitri et al., 2007; Brown et al., 2008; Cordier et al., 2009), which suggests that the methane fraction in a subsurface liquid reservoir is limited at present. Based on the available observations, it is impossible to constrain the contribution of this potential reservoir to

the methane inventory. Additional observations, such as subsurface sounding by a future exploration mission, will be needed to better constrain the nature of the subsurface reservoir.

The mysterious absence or rarity of the primordial noble gases in Titan's atmosphere may also be indicative of interactions of the atmosphere with the solid icy shell. It has been shown recently that the apparent deficit in noble gases could be essentially due to the formation of multiple guest clathrates at the surface-atmosphere interface of the satellite (Mousis et al., 2011). These clathrates would preferentially store some species, including all heavy noble gases, over others. These results have been obtained from the use of a statistical-thermodynamic model based on recent determinations of intermolecular potentials and supersede the previous ones that suggested a limited trapping of argon (Osegovic and Max, 2005; Thomas et al., 2008). In fact, the clean water ice needed for the formation of these clathrates may be delivered by successive episodes of cryovolcanic deposits. In this scenario, the formation of clathrates in the porous lavas and their propensity for trapping Ar, Kr, and Xe would progressively remove these species from the atmosphere of Titan over its history. A global clathrate shell with an average thickness not exceeding a few meters may be sufficient on Titan for a complete removal of the heavy noble gases from the atmosphere. Note, however, that there has been no convincing and unambiguous evidence for cryovolcanic activities on Titan so far (see for instance Moore and Pappalardo, 2011), so that the proposed trapping mechanism still remains hypothetic.

If clathrate formation is an efficient process as hypothesized for the noble gases, then it is possible that clathrates are also a sink for the prodigious amounts of ethane, and lesser amounts of propane, expected to have been produced over the history of Titan by photochemical processing of methane. Episodes of crustal volcanism could encourage formation of ethane clathrate (Mousis and Schmitt, 2008), as could impacts (Lunine et al., 2010b), or simple percolation through a heavily fractured crust might progressively allow the substitution of ethane for methane in crustal clathrate hydrate, and reconversion of water ice that once was clathrate prior to losing methane by outgassing. Regardless of the process, while methane clathrate hydrate is slightly less dense than the underlying water-ammonia ocean, ethane clathrate is not. Hence any ethane clathrate will have a tendency to move downward in a predominantly methane clathrate shell, and once at the bottom will sink in the ocean–to exist stably at the bottom. Timescales might be an issue here, leaving most of the ethane in the outer shell, but sequestered away from the surface-atmosphere system. If this view is correct, Titan's outer shell is laden with ethane clathrate from billions of years of methane photolysis–the lakes and seas being only the most recently produced ethane.

2.4.2.3 Long-term climate stability of Titan's atmosphere.

Titan's atmosphere has been unstable on timescales of between tens and hundreds of millions of years unless large areas of methane seas and oceans, an order of magnitude or more larger than the present-day lakes and seas, have existed on the surface throughout geologic time. In the absence of such sustaining bodies of liquid methane, or an implausibly finely tuned outgassing rate that keeps the atmospheric methane content within a factor of several of the current abundance for billions of years, the methane in Titan's atmosphere must have been periodically depleted. For the first half of Titan's history, when the Sun's luminosity was less than 80-85% of its current value, loss of methane may have caused the nitrogen to rain out onto Titan's surface (McKay et al., 1993; Lorenz et al., 1997a), producing a global sea of liquid nitrogen under a thinner clear atmosphere.

This scenario, bizarre in its contrast with the present-day state, raises all sorts of issues: (1) Is there geologic evidence for a long-standing ancient global sea of either liquid nitrogen or (to avoid this catastrophe) a standing ancient global sea of methane and ethane? (2) How could a thicker atmosphere be restored, even with massive outgassing of methane (why wouldn't the methane simply freeze out at the lower global temperatures for which liquid nitrogen is stable)? (3) What would prevent under a thin atmosphere the formation of massive ice caps of nitrogen at cold poles, possibly rendering as in point (2) a permanently frozen Titan? It is possible that freeze out did not occur even under a fainter young Sun, and indeed for values of the solar luminosity within 15-20% of the present-day, it seems that a nitrogen atmosphere not much different from that at present could have been sustained in the absence of methane (Lorenz et al., 1997a).

As crustal and deeper sources of methane continue to be depleted by photolysis, it seems inevitable that a state will be reached in which Titan will lose its surface methane and revert to a nearly pure nitrogen atmosphere, largely clear of aerosols, but with a surface temperature not much different from today or even larger as the Sun continues to grow in luminosity. Eventually, when the Sun becomes a red giant, Titan will have lost much of its atmosphere thanks to a strongly enhanced solar wind, but will for a time support a surface water ocean until the red giant's luminosity begins to fade (Lorenz et al., 1997b) . Perhaps any life extant in the deep water interior might then adapt to the surface, develop a form of photosynthesis, etc., if time is not too brief. Such speculations would be in the realm of science fiction were it not for the likelihood that Titan is representative of a class of planets that would stably exist within 1 AU of M to K dwarfs, with a spectrum of environments from the present-day state to an ancient nitrogen sea state, to the ultimate warmer version discussed here, simply by virtue of adjusting the stellar spectral type from late M to K (Lunine, 2010).

2.4.3 Summary

At the start of this Section we posed three questions; we will conclude by providing some provisional answers.

1. *To what extent did the interior of Titan influence the evolution of its atmosphere ?* The probable existence of an internal ocean at present suggests that the differentiation of Titan's interior has been accompanied by significant water-rock interactions and massive releases of gas compounds initially incorporated in clathrate structure. Although most of gas species should be stored dissolved in the massive internal ocean and in the form of clathrate in both the outer ice layer and the high-pressure ice layer, a significant fraction of CH_4 was likely outgassed through time.

2. *Did Titan always possess a massive N_2-CH_4 atmosphere ?* Titan likely acquired its atmosphere during its first hundred millions of years, at the latest during the LHB. The atmospheric composition and mass have probably varied along Titan's evolution. The early atmosphere may have been more massive and dominated by CO_2. Following the post-accretional cooling phase, nitrogen probably rapidly became the dominant gas. It is still unclear how nitrogen has been produced from ammonia and how atmospheric escape has influenced the nitrogen inventory. The methane abundance has probably significantly varied through time depending on the balance between replenishing and destruction. Long periods without atmospheric methane may even be envisioned.

3. *Where is the missing hydrocarbon inventory ?* Large volumes of hydrocarbon may be stored in the form of liquid or clathrate hydrate in the solid icy shell. However, there are still no direct constraints on the volume of these putative reservoirs. Alternatively, the lack of extensive hydrocarbon reservoirs may indicate that the production of hydrocarbons from methane photolysis has been less efficient than previously anticipated. This may suggest that methane has been present in the atmosphere during limited periods of time.

2.5 CONCLUSION AND QUESTIONS FOR FUTURE MISSIONS

Since the arrival of the *Cassini-Huygens* mission to the Saturn system, a large amount of data has been collected on Titan and various models have been developed to interpret them in an evolution context. In spite of considerable progresses in our understanding of Titan's origin and evolution, many questions remain, and they will probably not be answered by the end of the *Cassini-Huygens* mission. A series of investigations *in situ* and from the orbit will be needed in the future to address all the mysteries of Titan that *Cassini-Huygens* just started to unveil. Specifically, some of the remaining problems include:

1. *What was the composition of the building blocks that formed Titan ?* Theorotical models of planetary formation suggest that the building blocks that formed Titan contained a few percents of various gas compounds, mainly CO_2, NH_3, CH_4, as well as sulfur compounds, methanol and traces of noble gases. Most of the gas compounds initially expected have not been detected so far. Xe and Kr, for instance, appear to be depleted relative to the predicted abundance. By contrast, Ne, which was not expected, has been tentatively detected. CO_2, which is predicted to be the dominant carbon-bearing species, has only been identified at *Huygens*' landing site (Niemann et al., 2010) and tentatively in some other specific areas (McCord et al., 2008). Constraining the CO_2 fraction on Titan as well as the noble gas content will provide key constraints on the conditions under which the building blocks formed. Atmospheric sampling by a future exploration mission will permit us to determine more accurately the noble gas content of Titan's atmosphere, in particular to confirm the detection of neon. Determination of noble gas abundance in Saturn's atmosphere by an entry probe will also be extremely useful to determine the efficiency of noble gas trapping in planetesimals embedded in the feeding zone of Saturn. Moreover, *in situ* analysis in different materials collected at the surface will also provide pertinent information on the possible CO_2 content in the outer shell as well as on the possible sequestration of noble gases in the subsurface.

2. *How did Titan's N_2-dominating atmosphere form and evolve ?* It is likely that Titan's atmosphere has been acquired relatively early during the satellite evolution. However, it is still unclear how the N_2-dominating atmosphere has been produced and how its composition has evolved through time. The elevated $^{15}N/^{14}N$ ratio observed in Titan's nitrogen is commonly attributed to enhancement due to massive atmospheric escape. However, we are still missing constraints on the initial value in Titan. Determination of $^{15}N/^{14}N$ ratio in NH_3 in comets, in particular by the *Rosetta* mission on Comet 67P/Churyumov-Gerasimenko, will provide the first direct constraint. Such measurements together with determination of isotopic ratios in non-radiogenic isotopes of argon ($^{38}Ar/^{36}Ar$) and neon ($^{22}Ne/^{20}Ne$) by *in situ* sampling will allow us to determine how much mass Titan's atmosphere have lost since its formation, thus providing constraints on the early state of Titan's atmosphere.

3. *How efficient was the interaction between rock and H_2O in the interior ?* The moment of inertia inferred from *Cassini* gravity data as well as the detection of ^{40}Ar in the atmosphere is indicative of prolonged interactions between silicate minerals and H_2O (liquid water or water ice). Such an interaction has key implications for the chemical evolution of Titan's interior, in particular

for the astrobiological potential of its internal ocean. Its efficiency may be constrained by future exploration missions (i) by constraining the degree of differentiation and ocean characteristics (size and composition) from tidal and magnetic monitoring as well as from seismic detection using a fixed lander network at the surface; (ii) by detecting salts and ammonia hydrates at the surface from spectroscopy and surface samplings and (iii) by measuring the ratio between radiogenic and non-radiogenic isotopes in noble gases other than Ar from *in situ* mass spectrometry in the atmosphere and/or in hydrocarbon lakes.

4. *Are Titan's ice shell and interior currently active ?* In spite of the Earth-like landscape of Titan, there is still some doubt regarding the internal activity of Titan. Although there is some evidence of interactions with the interior in the past, it is uncertain if Titan's interior has still an influence on the evolution of the atmosphere and surface. Precise determination of the topography and gravity field by a future mission may provide key information on the structure of the icy shell, thus on its internal dynamics. Identification of recent (unambiguous) cryovolcanic flows using high-resolution images and IR spectra would hint at the likelihood of recent activities. The detection of helium, which has a very short residence time in the atmosphere, would be indicative of contemporaneous internal outgassing. Finally, direct observations of eruption would be the most convincing evidence.

5. *How long has the methane cycle been active on Titan ?* At present, Titan has a very active methane cycle, characterized by photochemical production of more complex hydrocarbon species, formation of a haze layer, cloud formation and rain fall, accumulation of hydrocarbon liquids in near-polar lakes and seas. However, it is still unclear if this cycle has existed during most of Titan's evolution or if it was triggered only relatively recently. Determining the possible volume of hydrocarbon stored under the surface by subsurface sounding with ground penetrating radar by a future mission will provide pertinent constraints on the duration of CH_4-driven chemistry on Titan. Identification of clathrates of methane, ethane and others at the surface by *in situ* sampling at the surface will also permit us to evaluate the role of clathration in the storage of hydrocarbon in the subsurface. Determination of $^{13}C/^{12}C$ in various carbon-bearing materials collected at the surface will also provide key information on the atmospheric fractionation process, and potentially on the duration of active methane cycle. High-resolution mapping of the surface may also provide information on different climatic conditions in the past, such as evidences for more extended methane seas associated with wetter climate or for N_2 ice caps associated to dryer and colder climate.

References

Agnor, C. B., Canup, R. M., and Levison, H. F. 1999. On the Character and Consequences of Large Impacts in the Late Stage of Terrestrial Planet Formation. *Icarus*, **142**, 219–237.

Alibert, Y., and Mousis, O. 2007. Formation of Titan in Saturn's subnebula: constraints from Huygens probe measurements. *Astron. Astrophys.*, **465**, 1051–1060.

Alibert, Y., Mousis, O., and Benz, W. 2005a. Modeling the Jovian subnebula. I. Thermodynamic conditions and migration of proto-satellites. *Astron. Astrophys.*, **439**, 1205–1213.

Alibert, Y., Mousis, O., Mordasini, C., and Benz, W. 2005b. New Jupiter and Saturn Formation Models Meet Observations. *Astroph. J.*, **626**, L57–L60.

Allègre, C. J., Hofmann, A., and O'Nions, K. 1996. The Argon constraints on mantle structure. *Geophys. Res. Lett.*, **23**, 3555–3558.

Anderson, J. D., Lau, E. L., Sjogren, W. L., Schubert, G., and Moore, W. B. 1996. Gravitational constraints on the internal structure of Ganymede. *Nature*, **384**, 541–543.

Anderson, J. D., Jacobson, R. A., McElrath, T. P., Moore, W. B., Schubert, G., and Thomas, P. C. 2001. Shape, Mean Radius, Gravity Field, and Interior Structure of Callisto. *Icarus*, **153**, 157–161.

Artemieva, N., and Lunine, J. 2003. Cratering on Titan: impact melt, ejecta, and the fate of surface organics. *Icarus*, **164**, 471–480.

Artemieva, N., and Lunine, J. I. 2005. Impact cratering on Titan II. Global melt, escaping ejecta, and aqueous alteration of surface organics. *Icarus*, **175**, 522–533.

Asplund, M., Grevesse, N., Sauval, A. J., and Scott, P. 2009. The Chemical Composition of the Sun. *Ann. Rev. Astron. Astroph.*, **47**, 481–522.

Atreya, S. K., Donahue, T. M., and Kuhn, W. R. 1978. Evolution of a nitrogen atmosphere on Titan. *Science*, **201**, 611–613.

Atreya, S. K., Adams, E. Y., Niemann, H. B., Demick-Montelara, J. E., Owen, T. C., Fulchignoni, M., Ferri, F., and Wilson, E. H. 2006. Titan's methane cycle. *Planet. Space Sci.*, **54**, 1177–1187.

Baland, R.-M., van Hoolst, T., Yseboodt, M., and Karatekin, Ö. 2011. Titan's obliquity as evidence of a subsurface ocean? *Astron. Astrophys.*, **530**, A141.

Barr, A. C., and Canup, R. M. 2010. Origin of the Ganymede-Callisto dichotomy by impacts during the late heavy bombardment. *Nature Geoscience*, **3**, 164–167.

Barr, A. C., and McKinnon, W. B. 2007. Convection in Enceladus' ice shell: Conditions for initiation. *Geophys. Res. Lett.*, **340**, L09202.

Barr, A. C., Citron, R. I., and Canup, R. M. 2010. Origin of a partially differentiated Titan. *Icarus*, **209**, 858–862.

Béghin, C., Simões, F., Krasnoselskikh, V., Schwingenschuh, K., Berthelier, J. J., Besser, B. P., Bettanini, C., Grard, R., Hamelin, M., López-Moreno, J. J., Molina-Cuberos, G. J., and Tokano, T. 2007. A Schumann-like resonance on Titan driven by Saturn's magnetosphere possibly revealed by the Huygens Probe. *Icarus*, **191**, 251–266.

Béghin, C., Canu, P., Karkoschka, E., Sotin, C., Bertucci, C., Kurth, W. S., Berthelier, J. J., Grard, R., Hamelin, M., Schwingenschuh, K., and Simões, F. 2009. New insights on Titan's plasma-driven Schumann resonance inferred from Huygens and Cassini data. *Planet. Space. Sci.*, **57**, 1872–1888.

Béghin, C., Sotin, C., and Hamelin, M. 2010. Titan's native ocean revealed beneath some 45km of ice by a Schumann-like resonance. *Comptes Rendus Geoscience*, **342**, 425–433.

Bills, B. G., and Nimmo, F. 2011. Rotational dynamics and internal structure of Titan. *Icarus*, **214**, 351–355.

Boss, A. P. 1997. Giant planet formation by gravitational instability. *Science*, **276**, 1836–1839.

Boss, A. P. 2005. Collapse and Fragmentation of Molecular Cloud Cores. VIII. Magnetically Supported Infinite Sheets. *Astroph. J.*, **622**, 393–403.

Brown, R. H., Soderblom, L. A., Soderblom, J. M., Clark, R. N., Jaumann, R., Barnes, J. W., Sotin, C., Buratti, B., Baines, K. H., and Nicholson, P. D. 2008. The identification of liquid ethane in Titan's Ontario Lacus. *Nature*, **454**, 607–610.

Cameron, A. G. W. 1978. Physics of the primitive solar accretion disk. *Moon and Planets*, **18**, 5–40.

Canup, R. M. 2010. Origin of Saturn's rings and inner moons by mass removal from a lost Titan-sized satellite. *Nature*, **468**, 943–926.

Canup, R. M., and Ward, W. R. 2002. Formation of the Galilean Satellites: Conditions of Accretion. *Astron. J.*, **124**, 3404–3423.

Canup, R. M., and Ward, W. R. 2006. A common mass scaling for satellite systems of gaseous planets. *Nature*, **441**, 834–839.

Canup, R. M., and Ward, W. R. 2009. Origin of Europa and the Galilean Satellites. *In:* Pappalardo et al. (2009).

Castillo-Rogez, J. C., and Lunine, J. I. 2010. Evolution of Titan's rocky core constrained by Cassini observations. *Geophys. Res. Lett.*, **37**, L20205.

Charnoz, S., Crida, A., Castillo-Rogez, J. C., Lainey, V., Dones, L., Karatekin, Ö., Tobie, G., Mathis, S., Le Poncin-Lafitte, C., and Salmon, J. 2011. Accretion of Saturn's mid-sized moons during the viscous spreading of young massive rings: solving the paradox of silicate-poor rings versus silicate-rich moons. *Icarus*, in press.

Choukroun, M., and Sotin, C. 2012. Is Titan's Shape Caused by its Meteorological and Carbon Cycle? *Geophys. Res. Lett.*, **39**, in press.

Choukroun, M., Grasset, O., Tobie, G., and Sotin, C. 2010. Stability of methane clathrate hydrates under pressure: Influence on outgassing processes of methane on Titan. *Icarus*, **205**, 581–593.

Choukroun, M., Kieffer, S. W., Lu, X., and Tobie, G. 2011. Formation of the satellites of the outer solar system - Sources of their atmospheres. Pages – (in press) of: Gudipati, M., and Castillo-Rogez, J.C. (eds), *The Science of Solar System Ices*, 3rd edn. Springer.

Coradini, A., Cerroni, P., Magni, G., and Federico, C. 1989. Formation of the satellites of the outer solar system - Sources of their atmospheres. Pages 723–762 of: Atreya, S. K., Pollack, J. B., and Matthews, M. S. (eds), *Origin and Evolution of Planetary and Satellite Atmospheres*. Tucson, AZ, University of Arizona Press.

Cordier, D., Mousis, O., Lunine, J. I., Lavvas, P., and Vuitton, V. 2009. An Estimate of the Chemical Composition of Titan's Lakes. *Astroph. J.*, **707**, L128–L131.

Cordier, D., Mousis, O., Lunine, J. I., Lebonnois, S., Lavvas, P., Lobo, L. Q., and Ferreira, A. G. M. 2010. About the Possible Role of Hydrocarbon Lakes in the Origin of Titan's Noble Gas Atmospheric Depletion. *Astroph. J.*, **721**, L117–L120.

Croft, S. K. 1982. A first-order estimate of shock heating and vaporization in oceanic impacts. In: Silver, T. L., and Schultz, P. H. (eds), *Geological Implications of Impacts of Large Asteroids and Comets on Earth*, vol. 190. Spec. Pap. Geol. Soc. Am.

Deschamps, F., Mousis, O., Sanchez-Valle, C., and Lunine, J. I. 2010. The Role of Methanol in the Crystallization of Titan's Primordial Ocean. *Astroph. J.*, **724**, 887–894.

Engel, S., and Lunine, J. I. 1994. Silicate interactions with ammonia-water fluids on early Titan. *J. Geophys. Res.*, **99**, 3745–3752.

Estrada, P. R., and Mosqueira, I. 2006. A gas-poor planetesimal capture model for the formation of giant planet satellite systems. *Icarus*, **181**, 486–509.

Estrada, P. R., and Mosqueira, I. 2011. Titan's Accretion and Long Term Thermal History. Page 1679 of: *Lunar and Planetary Institute Science Conference Abstracts*. Lunar and Planetary Inst. Technical Report, vol. 42.

Estrada, P. R., Mosqueira, I., Lissauer, J. J., D'Angelo, G., and Cruikshank, D. P. 2009. Formation of Jupiter and Conditions for Accretion of the Galilean Satellites. *In:* Pappalardo et al. (2009).

Fortes, A. D. 2011. Titan's internal structure and the evolutionary consequences. *Planet. Space Sci.*, in press.

Fortes, A. D., Grindrod, P. M., Trickett, S. K., and Vočadlo, L. 2007. Ammonium sulfate on Titan: Possible origin and role in cryovolcanism. *Icarus*, **188**, 139–153.

Friedson, A. J., and Stevenson, D. J. 1983. Viscosity of rock-ice mixtures and applications to the evolution of icy satellites. *Icarus*, **56**, 1–14.

Gautier, D., Hersant, F., Mousis, O., and Lunine, J. I. 2001. Enrichments in Volatiles in Jupiter: A New Interpretation of the Galileo Measurements. *Astrophys. J.*, **550**, L227–L230.

Glein, C. R., Zolotov, M. Y., and Shock, E. L. 2008. The oxidation state of hydrothermal systems on early Enceladus. *Icarus*, **197**, 157–163.

Glein, C. R., Desch, S. J., and Shock, E. L. 2009. The absence of endogenic methane on Titan and its implications for the origin of atmospheric nitrogen. *Icarus*, **204**, 637–644.

Goldreich, P., and Ward, W. R. 1973. The Formation of Planetesimals. *Astroph. J.*, **183**, 1051–1062.

Grasset, O., and Pargamin, J. 2005. The ammonia-water system at high pressures: Implications for the methane of Titan. *Planet. Space Sci.*, **53**, 371–384.

Grasset, O., and Sotin, C. 1996. The cooling rate of a liquid shell in Titan's interior. *Icarus*, **123**, 101–112.

Grindrod, P. M., Fortes, A. D., Nimmo, F., Feltham, D. L., Brodholt, J. P., and Vočadlo, L. 2008. The long-term stability of a possible aqueous ammonium sulfate ocean inside Titan. *Icarus*, **197**, 137–151.

Hayes, A., Aharonson, O., Callahan, P., Elachi, C., Gim, Y., Kirk, R., Lewis, K., Lopes, R., Lorenz, R., Lunine, J., Mitchell, K., Mitri, G., Stofan, E., and Wall, S. 2008. Hydrocarbon lakes on Titan: Distribution and interaction with a porous regolith. *Geophys. Res. Lett.*, **35**, L09204.

Helled, R., and Bodenheimer, P. 2010. Metallicity of the massive protoplanets around HR 8799 If formed by gravitational instability. *Icarus*, **207**, 503–508.

Hersant, F., Gautier, D., Tobie, G., and Lunine, J. I. 2008. Interpretation of the carbon abundance in Saturn measured by Cassini. *Planet. Space Sci.*, **56**, 1103–1111.

Hubickyj, O., Bodenheimer, P., and Lissauer, J. J. 2005. Accretion of the gaseous envelope of Jupiter around a 5 10 Earth-mass core. *Icarus*, **179**, 415–431.

Hutchins, K. S., and Jakosky, B. M. 1996. Evolution of Martian atmospheric argon: Implications for sources of volatiles. *J. Geophys. Res.*, **101**, 14933–14950.

Iess, L., Rappaport, N. J., Jacobson, R. A., Racioppa, P., Stevenson, D. J., Tortora, P., Armstrong, J. W., and Asmar, S. W. 2010. Gravity Field, Shape, and Moment of Inertia of Titan. *Science*, **327**, 1367–1369.

Iess, L., Jacobson, R. A., Ducci, M., Stevenson, D. J., Lunine, J. I., Armstrong, J. W., Asmar, S. W., Racioppa, P., Rappaport, N. J., and Tortora, P. 2012. The Tides of Titan. *Science*, submitted.

Ishimaru, R., Sekine, Y., Matsui, T., and Mousis, O. 2011. Oxidizing Proto-atmosphere on Titan: Constraint from N_2 Formation by Impact Shock. *Astroph. J. Lett.*, **741**, L10.

Jacovi, R., and Bar-Nun, A. 2008. Removal of Titan's noble gases by their trapping in its haze. *Icarus*, **196**, 302–304.

Johnson, T. V., and Lunine, J. I. 2005. Saturn's moon Phoebe as a captured body from the outer Solar System. *Nature*, **435**, 69–71.

Jones, T. D., and Lewis, J. S. 1987. Estimated impact shock production of N_2 and organic compounds on early Titan. *Icarus*, **72**(Nov.), 381–393.

Kargel, J. S. 1992. Ammonia-water volcanism on icy satellites - Phase relations at 1 atmosphere. *Icarus*, **100**, 556–574.

Kaula, W. M. 1979. Thermal evolution of earth and moon growing by planetesimal impacts. *J. Geophys. Res.*, **84**, 999–1008.

Kaula, W. M. 1999. Constraints on Venus Evolution from Radiogenic Argon. *Icarus*, **139**, 32–39.

Khurana, K. K., Kivelson, M. G., Stevenson, D. J., Schubert, G., Russell, C. T., Walker, R. J., and Polanskey, C. 1998. Induced magnetic fields as evidence for subsurface oceans in Europa and Callisto. *Nature*, **395**, 777–780.

Khurana, K. K., Jia, X., Kivelson, M. G., Nimmo, F., Schubert, G., and Russell, C. T. 2011. Evidence of a Global Magma Ocean in Io's Interior. *Science*, **332**, 1186–1189.

Kirk, R. L., and Stevenson, D. J. 1987. Thermal evolution of a differentiated Ganymede and implications for surface features. *Icarus*, **69**, 91–134.

Kivelson, M. G., Khurana, K. K., and Volwerk, M. 2002. The Permanent and Inductive Magnetic Moments of Ganymede. *Icarus*, **157**, 507–522.

Kokubo, E., and Ida, S. 1996. On Runaway Growth of Planetesimals. *Icarus*, **123**, 180–191.

Korycansky, D. G., and Zahnle, K. J. 2011. Titan impacts and escape. *Icarus*, **211**, 707–721.

Kossacki, K. J., and Lorenz, R. D. 1996. Hiding Titan's ocean: densification and hydrocarbon storage in an icy regolith. *Planet. Space Sci.*, **44**, 1029–1037.

Kuramoto, K., and Matsui, T. 1994. Formation of a hot proto-atmosphere on the accreting giant icy satellite: Implications for the origin and evolution of Titan, Ganymede, and Callisto. *J. Geophys. Res.*, **99**, 21,183–21,200.

Lainey, V., Karatekin, Ö, Desmars, J., Charnoz, S., Arlot, J. E., Emelyanov, N., , Le Poncin-Lafitte, C., Mathis, S., Remus, F., Tobie, G., and Zahn, J. P. 2011. Strong tidal dissipation in Saturn and constraints on Enceladus thermal state from astrometry. *Astroph. J.*, in revision.

Lewis, J. S., and Prinn, R. G. 1980. Kinetic inhibition of CO and N2 reduction in the solar nebula. *Astroph. J.*, **238**, 357–364.

Lide, D. R. (ed). 2004. *CRC Handbook of chemistry and physics : a ready-reference book of chemical and physical data*. 85th edn. CRC Press, Boca Raton London New York Washington, D.C.

Lissauer, J. J., and Safronov, V. S. 1991. The random component of planetary rotation. *Icarus*, **93**, 288–297.

Lorenz, R. D., McKay, C. P., and Lunine, J. I. 1997a. Photochemically-induced collapse of Titan's atmosphere. *Science*, **275**, 642–644.

Lorenz, R. D., Lunine, J. I., and McKay, C. P. 1997b. Titan under a red giant sun: A new kind of 'habitable' moon. *Geophys. Res. Lett.*, **24**, 2905.

Lorenz, R. D., Mitchell, K. L., Kirk, R. L., and the Cassini RADAR team. 2008a. Titan's inventory of organic surface materials. *Geophys. Res. Lett.*, **35**, L02206.

Lorenz, R. D., Stiles, B. W., Kirk, R. L., Allison, M. D., Persi del Marmo, P., Iess, L., Lunine, J. I., Ostro, S. J., and Hensley, S. 2008b. Titan's Rotation Reveals an Internal Ocean and Changing Zonal Winds. *Science*, **319**, 1649–1652.

Lunine, J., Choukroun, M., Stevenson, D., and Tobie, G. 2010a. The Origin and Evolution of Titan. Pages 35–59 of: Brown, R. H., Lebreton, J.-P., and Waite, J. H. (eds), *Titan from Cassini-Huygens*. Springer Science+Business Media B.V.

Lunine, J. I. 2010. Titan and habitable planets around M-dwarfs. *Faraday Discussions*, **147**, 405.

Lunine, J. I., and Stevenson, D. J. 1985. Thermodynamics of clathrate hydrate at low and high pressures with application to the outer solar system. *Astrophys. J. Suppl.*, **58**, 493–531.

Lunine, J. I., and Stevenson, D. J. 1987. Clathrate and ammonia hydrates at high pressure - Application to the origin of methane on Titan. *Icarus*, **70**, 61–77.

Lunine, J. I., Stevenson, D. J., and Yung, Y. L. 1983. Ethane ocean on Titan. *Science*, **222**, 1229–1231.

Lunine, J. I., Artemieva, N., and Tobie, G. 2010b. Impact cratering on Titan : Hydrocarbons versus water. Page 1533 of: *Lunar and Planetary Institute Science Conference Abstracts*. Lunar and Planetary Institute Science Conference Abstracts.

Mackenzie, R. A., Iess, L., Tortora, P., and Rappaport, N. J. 2008. A non-hydrostatic Rhea. *Geophys. Res. Lett.*, **350**, L05204.

Mandt, K. E., Waite, J. H., Lewis, W., Magee, B., Bell, J., Lunine, J., Mousis, O., and Cordier, D. 2009. Isotopic evolution of the major constituents of Titan's atmosphere based on Cassini data. *Planet. Space Sci.*, **57**, 1917–1930.

Marboeuf, U., Mousis, O., Ehrenreich, D., Alibert, Y., Cassan, A., Wakelam, V., and Beaulieu, J.-P. 2008. Composition of Ices in Low-Mass Extrasolar Planets. *Astroph. J.*, **681**, 1624–1630.

Matson, D. L., Castillo, J. C., Lunine, J., and Johnson, T. V. 2007. Enceladus' plume: Compositional evidence for a hot interior. *Icarus*, **187**, 569–573.

McCord, T. B., Hayne, P., Combe, J.-P., Hansen, G. B., Barnes, J. W., Rodriguez, S., Le Mouélic, S., Baines, E. K. H., Buratti, B. J., Sotin, C., Nicholson, P., Jaumann, R., Nelson, R., and The Cassini Vims Team. 2008. Titan's surface: Search for spectral diversity and composition using the Cassini VIMS investigation. *Icarus*, **194**, 212–242.

McKay, C. P., Scattergood, T. W., Pollack, J. B., Borucki, W. J., and van Ghyseghem, H. T. 1988. High-temperature shock formation of N2 and organics on primordial Titan. *Nature*, **332**, 520–522.

McKay, C. P., Pollack, J. B., Lunine, J. I., and Courtin, R. 1993. Coupled atmosphere-ocean models of Titan's past. *Icarus*, **102**, 88–98.

McKinnon, W. B. 2010. Radiogenic Argon Release from Titan: Sources, Efficiency, and Role of the Ocean (Invited). *AGU Fall Meeting Abstracts*, P22A–01.

Mitri, G., and Showman, A. P. 2008. Thermal convection in ice-I shells of Titan and Enceladus. *Icarus*, **193**, 387–396.

Mitri, G., Showman, A. P., Lunine, J. I., and Lorenz, R. D. 2007. Hydrocarbon lakes on Titan. *Icarus*, **186**, 385–394.

Monteux, J., Coltice, N., Dubuffet, F., and Ricard, Y. 2007. Thermo-mechanical adjustment after impacts during planetary growth. *Geophys. Res. Lett.*, **342**, L24201.

Monteux, J., Ricard, Y., Coltice, N., Dubuffet, F., and Ulvrova, M. 2009. A model of metal-silicate separation on growing planets. *Earth Planet. Sci. Lett.*, **287**, 353–362.

Moore, J. M., and Pappalardo, R. T. 2011. Titan: An exogenic world? *Icarus*, **212**, 790–806.

Mordasini, C., Alibert, Y., and Benz, W. 2009. Extrasolar planet population synthesis. I. Method, formation tracks, and mass-distance distribution. *Astron. Astroph.*, **501**, 1139–1160.

Mosqueira, I., and Estrada, P. R. 2003a. Formation of the regular satellites of giant planets in an extended gaseous nebula I: subnebula model and accretion of satellites. *Icarus*, **163**, 198–231.

Mosqueira, I., and Estrada, P. R. 2003b. Formation of the regular satellites of giant planets in an extended gaseous nebula II: satellite migration and survival. *Icarus*, **163**, 232–255.

Mousis, O., and Alibert, Y. 2006. Modeling the Jovian subnebula. II. Composition of regular satellite ices. *Astron. Astrophys.*, **448**, 771–778.

Mousis, O., and Schmitt, B. 2008. Sequestration of ethane in the cryovolcanic subsurface of Titan. *Astrophys. J.*, **677**, L67–L70.

Mousis, O., Alibert, Y., and Benz, W. 2006. Saturn's internal structure and carbon enrichment. *Astron. Astroph.*, **449**, 411–415.

Mousis, O., Lunine, J. I., Pasek, M., Cordier, D., Hunter Waite, J., Mandt, K. E., Lewis, W. S., and Nguyen, M.-J. 2009a. A primordial origin for the atmospheric methane of Saturn's moon Titan. *Icarus*, **204**, 749–751.

Mousis, O., Lunine, J. I., Thomas, C., Pasek, M., Marbœuf, U., Alibert, Y., Ballenegger, V., Cordier, D., Ellinger, Y., Pauzat, F., and Picaud, S. 2009b. Clathration of Volatiles in the Solar Nebula and Implications for the Origin of Titan's Atmosphere. *Astrophys. J.*, **691**, 1780–1786.

Mousis, O., Marboeuf, U., Lunine, J. I., Alibert, Y., Fletcher, L. N., Orton, G. S., Pauzat, F., and Ellinger, Y. 2009c. Determination of the Minimum Masses of Heavy Elements in the Envelopes of Jupiter and Saturn. *Astroph. J.*, **696**, 1348–1354.

Mousis, O., Lunine, J. I., Picaud, S., and Cordier, D. 2010. Volatile inventories in clathrate hydrates formed in the primordial nebula. *Faraday Discussions*, **147**, 509.

Mousis, O., Lunine, J. I., Picaud, S., Cordier, D., Waite, Jr., J. H., and Mandt, K. E. 2011. Removal of Titan's Atmospheric Noble Gases by Their Sequestration in Surface Clathrates. *Astroph. J.*, **740**, L9.

Mueller, S., and McKinnon, W. B. 1988. Three-layered models of Ganymede and Callisto - Compositions, structures, and aspects of evolution. *Icarus*, **76**, 437–464.

Nagel, K., Breuer, D., and Spohn, T. 2004. A model for the interior structure, evolution, and differentiation of Callisto. *Icarus*, **169**, 402–412.

Niemann, H. B., Atreya, S. K., and the Huygens GCMS team. 2005. The abundances of constituents of Titan's atmosphere from the GCMS instrument on the Huygens probe. *Nature*, **438**, 779–784.

Niemann, H. B., Atreya, S. K., Demick, J. E., Gautier, D., Haberman, J. A., Harpold, D. N., Kasprzak, W. T., Lunine, J. I., Owen, T. C., and Raulin, F. 2010. Composition of Titan's lower atmosphere and simple surface volatiles as measured by the Cassini-Huygens probe gas chromatograph mass spectrometer experiment. *J. Geophys. Res.*, **115**(E14), E12006.

Nimmo, F., and Bills, B. G. 2010. Shell thickness variations and the long-wavelength topography of Titan. *Icarus*, **208**, 896–904.

Ojakangas, G. W., and Stevenson, D. J. 1989. Thermal state of an ice shell on Europa. *Icarus*, **81**, 220–241.

O'Rourke, J. G., and Stevenson, D. J. 2011. Stability of Ice/Rock Mixtures with Application to Titan. Page 1629 of: *Lunar and Planetary Institute Science Conference Abstracts*. Lunar and Planetary Inst. Technical Report, vol. 42.

Osegovic, J. P., and Max, M. D. 2005. Compound clathrate hydrate on Titan's surface. *J. Geophys. Res.*, **110(E9)**, 8004.

Owen, T. 1982. The composition and origin of Titan's atmosphere. *Planet. Space Sci.*, **30**, 833–838.

Papaloizou, J. C. B., and Terquem, C. 1999. Critical Protoplanetary Core Masses in Protoplanetary Disks and the Formation of Short-Period Giant Planets. *Astroph. J.*, **521**, 823–838.

Pappalardo, R. T., McKinnon, W. B., and Khurana, K. (eds). 2009. *Europa*. The University of Arizona Press, Tucson.

Pasek, M. A., Milsom, J. A., Ciesla, F. J., Lauretta, D. S., Sharp, C. M., and Lunine, J. I. 2005. Sulfur chemistry with time-varying oxygen abundance during Solar System formation. *Icarus*, **175**, 1–14.

Peale, S. J. 1969. Generalized Cassini's Laws. *Astron. J.*, **74**, 483–+.

Pierazzo, E., Vickery, A. M., and Melosh, H. J. 1997. A Reevaluation of Impact Melt Production. *Icarus*, **127**, 408–423.

Pollack, J. B., Hubickyj, O., Bodenheimer, P., Lissauer, J. J., Podolak, M., and Greenzweig, Y. 1996. Formation of the Giant Planets by Concurrent Accretion of Solids and Gas. *Icarus*, **124**, 62–85.

Rappaport, N., Bertotti, B., Giampieri, G., and Anderson, J. D. 1997. Doppler Measurements of the Quadrupole Moments of Titan. *Icarus*, **126**, 313–323.

Rappaport, N. J., Iess, L., Wahr, J., Lunine, J. I., Armstrong, J. W., Asmar, S. W., Tortora, P., di Benedetto, M., and Racioppa, P. 2008. Can Cassini detect a subsurface ocean in Titan from gravity measurements? *Icarus*, **194**, 711–720.

Ricard, Y., Šrámek, O., and Dubuffet, F. 2009. A multi-phase model of runaway core-mantle segregation in planetary embryos. *Earth Planet. Sci. Lett.*, **284**, 144–150.

Robuchon, G., Choblet, G., Tobie, G., Čadek, O., Sotin, C., and Grasset, O. 2010. Coupling of thermal evolution and despinning of early Iapetus. *Icarus*, **207**, 959–971.

Safronov, V. S. 1978. The heating of the earth during its formation. *Icarus*, **33**, 3–12.

Safronov, V. S. (ed). 1969. Evoliutsiia doplanetnogo oblaka, (English transl.: Evolution of the Protoplanetary Cloud and Formation of Earth and the Planets, NASA Tech. Transl. F-677, Jerusalem: Israel Sci. Transl. 1972).

Sasaki, T., Stewart, G. R., and Ida, S. 2010. Origin of the Different Architectures of the Jovian and Saturnian Satellite Systems. *Astrophys. J.*, **714**, 1052–1064.

Saumon, D., and Guillot, T. 2004. Shock Compression of Deuterium and the Interiors of Jupiter and Saturn. *Astroph. J.*, **609**, 1170–1180.

Saur, J., Neubauer, F. M., and Glassmeier, K.-H. 2010. Induced Magnetic Fields in Solar System Bodies. *Space Sci. Rev.*, **152**, 391–421.

Schubert, G., Stevenson, D. J., and Ellsworth, K. 1981. Internal structures of the Galilean satellites. *Icarus*, **47**, 46–59.

Scott, H. P., Williams, Q., and Ryerson, F. J. 2002. Experimental constraints on the chemical evolution of large icy satellites. *Earth Planet. Sci. Lett.*, **203**, 399–412.

Sears, W. D. 1995. Tidal dissipation in oceans on Titan. *Icarus*, **113**, 39–56.

Sekine, Y., and Genda, H. 2011. Giant impacts in the Saturnian System: a possible origin of diversity in the inner mid-sized satellites. *Planet. Space Sci.*, in press.

Sekine, Y., Genda, H., Sugita, S., Kadono, T., and Matsui, T. 2011. Replacement and late formation of atmospheric N2 on undifferentiated Titan by impacts. *Nature Geos.*, **4**, 359–362.

Senshu, H., Kuramoto, K., and Matsui, T. 2002. Thermal evolution of a growing Mars. *J. Geophys. Res. (Planets)*, **107**, 5118.

Simões, F., Grard, R., Hamelin, M., López-Moreno, J. J., Schwingenschuh, K., Béghin, C., Berthelier, J.-J., Besser, B., Brown, V. J. G., Chabassière, M., Falkner, P., Ferri, F., Fulchignoni, M., Hofe, R., Jernej, I., Jeronimo, J. M., Molina-Cuberos, G. J., Rodrigo, R., Svedhem, H., Tokano, T., and Trautner, R. 2007. A new numerical model for the simulation of ELF wave propagation and the computation of eigenmodes in the atmosphere of Titan: Did Huygens observe any Schumann resonance? *Planet. Space Sci.*, **55**, 1978–1989.

Sloan, E. D. Jr. 1998. *Clathrate hydrates of natural gases*. Second edn. Marcel Dekker Inc.:New York.

Sohl, F., Sears, W. D., and Lorenz, R. D. 1995. Tidal dissipation on Titan. *Icarus*, **115**, 278–294.

Sohl, F., Hussmann, H., Schwenker, B., and Spohn, T. 2003. Interior structure models and tidal Love numbers of Titan. *J. Geophys. Res.*, **108(E12)**, 5130.

Sohl, F., Choukroun, M., Kargel, J., Kimura, J., Pappalardo, R., Vance, S., and Zolotov, M. 2010. Subsurface Water Oceans on Icy Satellites: Chemical Composition and Exchange Processes. *Space Sci. Rev.*, **153**, 485–510.

Solomatov, V. S. 1995. Scaling of temperature- and stress-dependent viscosity convection. *Physics of Fluids*, **7**, 266–274.

Sotin, C., and Tobie, G. 2004. Internal structure and dynamics of the large icy satellites. *Comptes Rendus Physique*, **5**, 769–780.

Sotin, C., Mitri, G., Rappaport, N., Schubert, G., and Stevenson, D. 2010. Titan's Interior Structure. Pages 61–73 of: Brown, R. H., Lebreton, J.-P., and Waite, J. H. (eds), *Titan from Cassini-Huygens*. Springer Science+Business Media B.V.

Squyres, S. W., Reynolds, R. T., Summers, A. L., and Shung, F. 1988. Accretional heating of the satellites of Saturn and Uranus. *J. Geophys. Res.*, **93**, 8779–8794.

Stevenson, D. J. 2000. Limits on the Variation of Thickness of Europa's Ice Shell. Page 1506 of: *Lunar and Planetary Institute Science Conference Abstracts*. Lunar and Planetary Inst. Technical Report, vol. 31.

Stiles, B. W., Kirk, R. L., Lorenz, R. D., Hensley, S., Lee, E., Ostro, S. J., Allison, M. D., Callahan, P. S., Gim, Y., Iess, L., Perci del Marmo, P., Hamilton, G., Johnson, W. T. K., West, R. D., and The Cassini RADAR Team. 2008. Determining Titan's Spin State from Cassini RADAR Images. *Astron. J.*, **135**, 1669–1680.

Stiles, B. W., Hensley, S., Gim, Y., Bates, D. M., Kirk, R. L., Hayes, A., Radebaugh, J., Lorenz, R. D., Mitchell, K. L., Callahan, P. S., Zebker, H., Johnson, W. T. K., Wall, S. D., Lunine, J. I., Wood, C. A., Janssen, M., Pelletier, F., West, R. D., Veeramacheneni, C., and Cassini RADAR Team. 2009. Determining Titan surface topography from Cassini SAR data. *Icarus*, **202**, 584–598.

Stiles, B. W., Kirk, R. L., Lorenz, R. D., Hensley, S., Lee, E., Ostro, S. J., Allison, M. D., Callahan, P. S., Gim, Y., Iess, L., Perci del Marmo, P., Hamilton, G., Johnson, W. T. K., West, R. D., and The Cassini RADAR Team. 2010. ERRATUM: "Determining Titan's Spin State from Cassini Radar Images" (2008, AJ, 135, 1669). *Astron. J.*, **139**, 311.

Stofan, E. R., Elachi, C., Lunine, J. I., and the Cassini RADAR team. 2007. The lakes of Titan. *Nature*, **445**, 61–64.

Thomas, C., Picaud, S., Mousis, O., and Ballenegger, V. 2008. A theoretical investigation into the trapping of noble gases by clathrates on Titan. *Planet. Space Sci.*, **56**, 1607–1617.

Thrane, K., Bizzarro, M., and Baker, J. A. 2006. Extremely Brief Formation Interval for Refractory Inclusions and Uniform Distribution of ^{26}Al in the Early Solar System. *Astroph. J.*, **646**, L159–L162.

Tobie, G., Mocquet, A., and Sotin, C. 2005a. Tidal dissipation within large icy satellites: Applications to Europa and Titan. *Icarus*, **177**, 534–549.

Tobie, G., Grasset, O., Lunine, J. I., Mocquet, A., and Sotin, C. 2005b. Titan's internal structure inferred from a coupled thermal-orbital model. *Icarus*, **175**, 496–502.

Tobie, G., Lunine, J. I., and Sotin, C. 2006. Episodic outgassing as the origin of atmospheric methane on Titan. *Nature*, **440**, 61–64.

Tobie, G., Choukroun, M., Grasset, O., Le Mouélic, S., Lunine, J. I., Sotin, C., Bourgeois, O., Gautier, D., Hirtzig, M., Lebonnois, S., and Le Corre, L. 2009. Evolution of Titan and implications for its hydrocarbon cycle. *Phil. Trans. R. Soc. A*, **367**, 617–631.

Tobie, G., Gautier, D., and Hersant, F. 2011. Titan's bulk composition constrained by Cassini-Huygens: Implications for internal outgassing. *Astroph. J.*, in revision.

Tokano, T., Van Hoolst, T., and Karatekin, Ö. 2011. Polar motion of Titan forced by the atmosphere. *J. Geophys. Res.*, **116**(E15), E05002.

Tonks, W. B., and Melosh, H. J. 1992. Core formation by giant impacts. *Icarus*, **100**, 326–346.

Turcotte, D. L., Willemann, R. J., Haxby, W. F., and Norberry, J. 1981. Role of membrane stresses in the support of planetary topography. *J. Geophys. Res.*, **86**, 3951–3959.

van der Waals, J. H., and Platteeuw, J. C. 1959. *Clathrate Solutions*. Advances in chemical physics edn. Vol. 2. New York: Interscience.

Voss, L. F., Henson, B. F., and Robinson, J. M. 2007. Methane thermodynamics in nanoporous ice: A new methane reservoir on Titan. *J. Geophys. Res. (Planets)*, **112**(E11), E05002.

Waite, J. H., Niemann, H., Yelle, R. V., Kasprzak, W. T., Cravens, T. E., Luhmann, J. G., McNutt, R. L., Ip, W.-H., Gell, D., De La Haye, V., Müller-Wordag, I., Magee, B., Borggren, N., Ledvina, S., Fletcher, G., Walter, E., Miller, R., Scherer, S., Thorpe, R., Xu, J., Block, B., and Arnett, K. 2005. Ion Neutral Mass Spectrometer Results from the First Flyby of Titan. *Science*, **308**, 982–986.

Waite, Jr., J. H., Lewis, W. S., Magee, B. A., Lunine, J. I., McKinnon, W. B., Glein, C. R., Mousis, O., Young, D. T., Brockwell, T., Westlake, J., Nguyen, M.-J., Teolis, B. D., Niemann, H. B., McNutt, R. L., Perry, M., and Ip, W.-H. 2009. Liquid water on Enceladus from observations of ammonia and ^{40}Ar in the plume. *Nature*, **460**, 487–490.

Xie, S., and Tackley, P. J. 2004. Evolution of helium and argon isotopes in a convecting mantle. *Phys. Earth Planet. Int.*, **146**, 417–439.

Zahnle, K., Pollack, J. B., Grinspoon, D., and Dones, L. 1992. Impact-generated atmospheres over Titan, Ganymede, and Callisto. *Icarus*, **95**, 1–23.

Zebker, H. A., Gim, Y., Callahan, P., Hensley, S., Lorenz, R., and Cassini Radar Team. 2009a. Analysis and interpretation of Cassini Titan radar altimeter echoes. *Icarus*, **200**, 240–255.

Zebker, H. A., Stiles, B., Hensley, S., Lorenz, R., Kirk, R. L., and Lunine, J. 2009b. Size and Shape of Saturn's Moon Titan. *Science*, **324**, 921–923.

Zolotov, M. Y. 2007. An oceanic composition on early and today's Enceladus. *Geophys. Res. Lett.*, **34**, L23203.

Zolotov, M. Y. 2010. Oceanic Chemical Evolution on Icy Moons. *LPI Contributions*, **1538**, 5304.

Zolotov, M. Y., and Kargel, J. S. 2009. *On the Chemical Composition of Europa's Icy Shell, Ocean, and Underlying Rocks*. in Europa, edited by R. T. Pappalardo, W. B. McKinnon, K. K. Khurana edn. University of Arizona Press, Tucson. Page 431.

Icarus 237 (2014) 377–387

Contents lists available at ScienceDirect

Icarus

journal homepage: www.elsevier.com/locate/icarus

Can large icy moons accrete undifferentiated?

J. Monteux [a,*], G. Tobie [a], G. Choblet [a], M. Le Feuvre [b]

[a] Laboratoire de Planétologie et de Géodynamique, LPG Nantes, CNRS UMR6112, Université de Nantes, France
[b] Laboratoire Auscultation et Imagerie, IFSTTAR, Nantes, France

ARTICLE INFO

Article history:
Received 14 November 2013
Revised 22 April 2014
Accepted 23 April 2014
Available online 6 May 2014

Keywords:
Thermal histories
Accretion
Satellites, formation
Impact processes

ABSTRACT

The apparent moments of inertia of Callisto and Titan inferred from gravity data suggest incomplete differentiation of their interior, commonly attributed to slow and cold accretion. To understand whether such large icy moons can really avoid global melting and subsequent differentiation during their accretion, we have developed a 3D numerical model that characterizes the thermal evolution of a satellite growing by multi-impacts, simulating the satellite growth and thermal evolution for a body radius ranging from 100 to 2000 km. The effects of individual impacts (energy deposition, excavation) are simulated and integrated for impactor sizes ranging from a few kilometers to one hundred kilometers, while for smaller impactors, a simplified approach with successive thin uniform layers spreading all over the satellite is considered. Our simulations show that the accretion rate plays only a minor role and that extending the duration of accretion does not significantly limit the increase of the internal temperature. The mass fraction brought by large impactors plays a more crucial role. Our results indicate that a satellite exceeding 2000 km in radius may accrete without experiencing significant melting only if its accretion is dominated by small impactors (<a few kilometers) and that the conversion of impact energy into heat is unrealistically inefficient (<10–15%). Based on our simulations, if more than 10% of satellite mass was brought by satellitesimals larger than 1 km, global melting for large bodies like Titan or Callisto cannot be avoided.

1. Introduction

Differences in composition and internal structure exist between the major icy satellites of Jupiter and Saturn, suggesting distinct accretion and differentiation histories (e.g., Kirk and Stevenson, 1987; Mueller and McKinnon, 1988; Mosqueira and Estrada, 2003a; Barr and Canup, 2008). The high moment of inertia factor inferred from *Galileo* gravity measurements ($C/MR^2 = 0.346$) (Anderson et al., 2001) suggests that ice-rock separation may be incomplete in the interior of Jupiter's moon Callisto. By contrast, Ganymede has a much smaller moment of inertia ($C/MR^2 = 0.31$) (Anderson et al., 2001) and shows signs of past endogenic activity (Pappalardo et al., 2004). A full separation of ice and rock is suggested for Ganymede together with the formation of a metallic core, which is at the origin of a relatively intense intrinsic magnetic field (Kivelson et al., 1998).

With similar size and mass, Saturn's moon Titan may be an intermediate case between Callisto and Ganymede. Its moment of inertia factor, C/MR^2 estimated to ~0.33–0.34 from Cassini gravity measurements (Iess et al., 2010, 2012) suggests that Titan's interior is more differentiated than Callisto but probably much less than Ganymede. Like Callisto, Titan might still possess a layer of ice–rock mixture between a rocky core and an outer ice-rich mantle, unless the rocky core is mostly composed of highly hydrated minerals (Sohl et al., 2010; Castillo-Rogez and Lunine, 2010). The fact that the interior of Callisto and possibly Titan may still contain a layer of ice–rock mixture suggests that the satellite may have avoided significant melting during accretion and subsequent evolution.

The accretion of giant planet's moons is intimately linked with the evolution of the circumplanetary disk that formed during the transition stage of the planet's accretion, when the planet became massive enough to contract and accrete gas and dust from the circumsolar disk (e.g., Estrada et al., 2009). The timescale of the satellite accretion is therefore mostly controlled by the disk structure, the mass inflow rate, and the lifetime of the circumplanetary disk. Two main categories of circumplanetary disk models have been proposed: the solids-enhanced minimum mass (SEMM) model (Mosqueira and Estrada, 2003a,b; Estrada et al., 2009) and the gas-starved disk model (Canup and Ward, 2002, 2006; Ward and Canup, 2010). In the gas-starved disk model, the disk is assumed to be continuously supplied by ongoing inflow of gas

* Corresponding author.
E-mail address: julien.monteux@univ-nantes.fr (J. Monteux).

http://dx.doi.org/10.1016/j.icarus.2014.04.041
0019-1035/

and dust particles from the surrounding proto-planetary disk while in the SEMM model, solid components of the disk are supplied by ablation and capture of planetesimal fragments passing through the disk. These two approaches result in different characteristic impactor sizes, ranging typically from a few meters to a few kilometers in the gas-starved approach (Barr and Canup, 2008), while a significant fraction of impactors with radii above 1 km size and up to 100–200 km is envisioned in the SEMM model (Estrada and Mosqueira, 2011). The impactor size is crucial to determine whether the impact energy is buried deep beneath the surface or efficiently released to the space. Hence these two formation models can potentially lead to different early thermal evolutions of growing icy moons.

Previous studies showed that it was possible to avoid melting if the accumulation of accretion energy was inefficient, i.e. if the energy was radiated away at a rate comparable to the accretion rate (e.g., Schubert et al., 1981; Squyres et al., 1988; Kossacki and Leliwa-Kopystyński, 1993; Coradini et al., 1995; Grasset and Sotin, 1996; Barr and Canup, 2008; Barr et al., 2010). Based on these models, the accretion timescales t_{acc} should be longer than 1 Myr to avoid significant melting and hence differentiation of Callisto while an accretion timescale as short as 10^{3-4} yr may be possible for Ganymede. However, these timescales are dependent on the way heat deposition and cooling are treated. These studies used a one-dimensional approach initially developed for the accretion of terrestrial planets (Safronov, 1978; Kaula, 1979). In this approach, the evolution is parameterized by deposition of successive material layers. The thermal effect of an impact is not considered individually, but is averaged over the entire surface and integrated. This approach is valid as long as the impactors remain small ($\leqslant$1 km) and are randomly distributed at the surface. This might be the case during the very early stage of the accretion process, but impactors larger than 1 km probably became more and more abundant at the end of the accretion stage (e.g., Estrada et al., 2009). Impactors larger than 100 km might also be expected (e.g., Sekine and Genda, 2012; Dwyer et al., 2013). For such large impacts, a detailed description of each impact including energy deposition and transfer is required.

For this purpose, we have developed a three-dimensional model that characterizes the thermal evolution of a satellite growing by multi-impacts. The satellite growth and thermal evolution are simulated for a radius ranging from 100 km to 2000 km from different populations of undifferentiated icy impactors, by assuming different accretion rates and conversion rates of impact energy into heat. The effects of individual impacts are simulated and integrated for impactor sizes ranging from a few kilometers to one hundred kilometers. For each impact event, we consider the thermal effects due to the dissipation of the impactor's kinetic energy as heat as well as the topographical effect associated to excavation process. For impactor sizes smaller than a few kilometers, we do not treat the impact individually because the number of impacts to simulate will be extremely time consuming. The small and numerous impactors are modeled by successive thin uniform layers spreading all over the moon. As the icy moon grows, gravitational forces increase and impacts become more and more violent. Due to this, as well as the accumulation of warmed icy material, melting events may occur once the icy moon reaches a critical size. As the main objective of our work is to determine the maximum radius reached by a growing satellite before significant melting occurs (>5%), we make some simple assumptions corresponding to the least efficient scenario for initiating ice melting. The impacts are assumed to occur with the smallest possible velocity corresponding to the escape velocity determined by the mass of the growing satellite. Hence, the accretion efficiency is assumed to be 100% and all impacted mass remains on the growing satellite (Asphaug, 2010). With these assumptions, we minimize the energy accumulated in the satellite during the growth, and therefore we provide an upper limit for the radius that the satellite can reach without experiencing significant melting. In Sections 2 and 3, we present the details of our model. We first describe the process associated to a single impact event and then we present our multi-impact approach. The results of our simulations for different accretion parameters are provided in Section 4. Finally, in Section 5, we briefly discuss the implications of our results for the post-accretional structure of large icy moons and the subsequent differentiation processes.

2. Single impact model

Following an impact and the formation of a crater, a significant amount of heat is buried deep below the impact site. In the following section we describe the scaling laws used to model the thermal and topographical consequences of a large single impact on a growing icy moon.

2.1. Impact heating

During an impact event, the initial kinetic energy of the impactor is converted into internal energy produced by shock heating of the satellite and of the impactor, internal energy produced by plastic work, and kinetic energy of ejected material (e.g. O'Keefe et al., 1977; Squyres et al., 1988). O'Keefe et al. (1977) estimated that the fraction, γ_{li}, of the impactor kinetic energy going into shock heating of the satellite ranged from 0.2 for low-velocity impacts to about 0.6 for very high velocities. As this parameter is difficult to constrain, especially for large impacts, we consider here that it is a free parameter.

During the impact, a shock wave propagates from the impact site. Following the adiabatic pressure release, the peak pressure being almost independent of impactor size, a thermal anomaly remains below the impact site. The heat deposition is nearly uniform in a hemispherical (for $v_{imp} < 1$ km/s) to spherical region next to the impact (the isobaric core), and strongly decays away from it (Croft, 1982; Squyres et al., 1988; Senshu et al., 2002) (see Fig. 1). For simplicity, we consider in our models that the shape of the isobaric core is spherical and that it does not depend on the impact velocity. Energy balance calculations and shock simulations suggest that, for impact velocities lower than 10 km s^{-1}, the radius of the isobaric core r_{ic} is comparable or slightly larger than that of the impactor r_{imp} (Pierazzo et al., 1997; Senshu et al., 2002; Kraus et al., 2011). Considering the extreme case in which all of the impact energy is perfectly transferred to the internal energy within the isobaric core and impactor itself gives an estimation of the maximum value for $r_{ic}/r_{imp} = 3^{1/3}$ (Senshu et al., 2002). Hence, after a large impact, a large amount of heat can be buried deep below the impact site at a depth $\sim 2r_{imp}$ and contribute to the early thermal evolution of the growing moon (Kraus et al., 2011).

As already explained in the introduction, we neglect here the velocity at infinity of the impactor ($v_\infty = 0$) as we want to determine the maximal size a moon can reach without significant melting. For simulations presented here, we do not consider any transplanetary impactor with $v_{imp} \gg v_{esc}$ (Squyres et al., 1988). The impactor velocity is only determined by the gravitational acceleration of the growing target: $v_{imp} = v_{esc} = \sqrt{2gR}$ with g the gravity at the surface of a moon with radius R. The impactor velocity is therefore proportional to the satellite size. For isobaric core volume $V_{ic} = 3V_{imp}$, a balance between the kinetic energy delivered to the growing moon and the energy used to heat up the growing

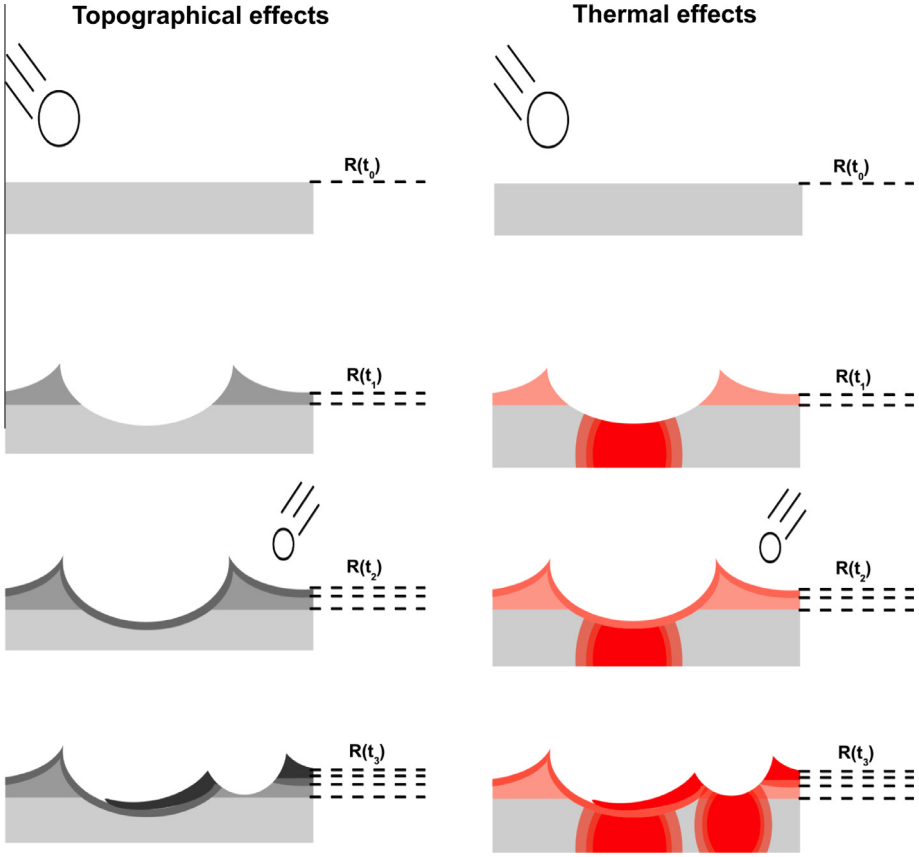

Fig. 1. Schematic illustration of the topographical (left) and thermal (right) evolutions after large impacts. When the first large impact occurs (first line), a crater with diameter D_f, depth z_f and rim height δ_0 is formed (second line, left). Before the next large impact, the layer deposition occurs (third line, left). When a second impact occurs close enough to the first one (fourth line), the pre-existing topography is modified according to Eq. (11). When a large impact occurs (first and second line, right), heat is buried deep below the impact site following Eq. (1) while the ejecta rim temperature is the average temperature below the impact site over a volume that is D_f large and z_f thick. The temperature of the layer deposited before the next large impact (third line, right) obeys Eq. (13).

moon (isobaric core and the material surrounding it) without melting leads to (Monteux et al., 2007):

$$\Delta T_0 = \frac{4\pi}{9}\frac{\gamma_{li}\rho G\overline{R_t}^2}{h_m C_p} \tag{1}$$

where $\overline{R_t}$ is the mean radius of the growing moon, ρ is the mean density of the moon, h_m represents the volume effectively heated normalized by the volume of the isobaric core and scales with the power m (see values in Table 1). γ_{li} is the fraction of the impactor kinetic energy that is used to heat up the deep material of the impacted body. Hence, the post-impact temperature increase scales with the square of the moon radius at the time of impact (see (1)).

Table 1
Typical parameter values for numerical models.

Moon radius	R	100–2000 km
Impactor radius	r_{imp}	4–100 km
Isobaric core radius	r_{ic}	
Average moon density	ρ	1500–2000 kg m^{-3}
Mean heat capacity	C_p	1200 J K^{-1} kg^{-1}
Environment temperature	T_e	100 K
Mean heat diffusivity	κ	10^{-6} m^2 s^{-1}
Large impact energy fraction retained	γ_{li}	0.1–0.6
Temperature power decrease from the isobaric core	m	3.4
Volume effectively heated by impact	h_m	5.8
Layer deposit energy fraction retained	$\gamma_{lay} \leqslant \gamma_{li}$	0.1–0.3
Gravitational constant	G	6.67×10^{-11} m^3 kg^{-1} s^{-2}

Using parameter values from Table 1 and $\gamma_{li} = 30\%$, for an impacted body with a radius ranging from 1000 km to 2500 km, $v_{imp} < 3$ km/s and ΔT_0 ranges from ~10 K to 100 K. Obviously, if the velocity at infinity is non-negligible, the delivered energy and hence temperature increase would be higher. However, as we want to determine the maximum radius that a growing satellite can reach without significant melting, we consider the most favorable case where the velocity at infinity is zero.

Away from the isobaric core the peak pressure decays with the distance from the surface of the isobaric core (Pierazzo et al., 1997; Kraus et al., 2011) (see Fig. 1). This pressure decay can be faster for an ice/rock mixture than for terrestrial material because of the ice properties (Kraus et al., 2011). Just after the adiabatic pressure release, the thermal perturbation corresponds to an isothermal sphere of radius r_{ic} and temperature $T_0 + \Delta T_0$ that decays when $\bar{r} > r_{ic}$ as (see Fig. 1)

$$T(r) = T_0 + \Delta T_0 \left(\frac{r_{ic}}{\bar{r}}\right)^m \tag{2}$$

where $\bar{r}$ is the distance from the center of the isobaric core, T_0 is the pre-impact temperature and m is the power characterizing the temperature decrease from the isobaric core (Pierazzo et al., 1997; Senshu et al., 2002). The post-impact temperature increase is a function of the pressure increase below the impact site. For small impact velocities (i.e. <3 km s^{-1}), the pressure P may increase to peak values of 8 GPa and the post-impact temperature increase scales with $P^{0.7-1}$ (Stewart and Ahrens, 2005). As the pressure typically decays from the isobaric core with $\sim(r_{ic}/r)^4$ (Kraus et al.,

2011), the post impact temperature increase decays from the isobaric core following $(r_{ic}/r)^m$ with m ranging from 2.8 to 4. In this study we choose a medium value of $m = 3.4$.

2.2. Topographical effect

An impact leads to the formation of a transient cavity of diameter D_s, reaching its final size D_f after some modifications. The diameter of the transient crater D_s can be related to the impactor diameter d_{imp} (in km) through (Zahnle et al., 2003):

$$D_s = a_0 \left(\frac{v_{imp}^2}{v_{esc}^2}\right)^{a_1} \left(\frac{\rho_{imp}}{\rho}\right)^{a_2} R^{a_3} d_{imp}^{a_4} \cos(\theta)^{a_5} \quad (3)$$

where v_{imp} is the impactor velocity, v_{esc} is the escape velocity of the impacted moon, ρ_{imp} is the impactor density, R is the radius of the moon (in km) and θ is the impact angle. For simplicity, we assume $\rho_{imp} = \rho$ and we set $\theta = 45^\circ$ (the most likely angle of impact and the average value for a uniform bombardment (Shoemaker, 1962)). a_0, a_1, a_2, a_3, a_4 and a_5 are constant values listed in Table 2. These are derived from laboratory experiments as well as numerical modeling, and are consistent with planetary surface observations.

If the transient crater diameter is smaller than a critical value D_c, no later significant modifications occur and its final diameter is $D_f = D_c$. Among the parameters listed in Table 2, D_c is the one that exhibits the largest range of values as this parameter depends on the mechanical properties and gravity of each icy moon (McKinnon et al., 1991; Zahnle et al., 2003). D_c typically ranges between 2 and 3 km for Ganymede and Callisto and up to 15 km for most of the medium-sized satellites (Schenk et al., 2004). Hence, D_c is expected to vary during the growth of the icy moon. Here for simplicity we consider a single value, $D_c = 15$ km (see Table 2). In our models, the majority of the impacts leads to the formation of craters that are larger than D_c. Above D_c, the post-impact strength of the target material is insufficient to prevent collapse under gravity, crater modifications occur, resulting in a complex crater with a flat floor, a central peak or peak ring, and a terraced rim. Its final diameter thus becomes:

$$D_f = D_s \left(\frac{D_s}{D_c}\right)^{b_0} \quad (4)$$

We express the maximal depth at the center of the crater z_f as a function of the transient simple crater diameter (Pike, 1977; Schenk, 1991):

$$z_f = \begin{cases} K_1 D_s^{b_1} & \text{if} \quad D_s < D_c \\ K_2 D_s^{b_2} & \text{if} \quad D_s > D_c \end{cases} \quad (5)$$

Table 2
Crater geometrical parameters used in our models.

Parameter	Value	References
a_0	1.1	Zahnle et al. (1998, 2003)
a_1	0.217	Zahnle et al. (1998, 2003)
a_2	0.333	Zahnle et al. (1998, 2003)
a_3	0.217	Zahnle et al. (1998, 2003)
a_4	0.783	Zahnle et al. (1998, 2003)
a_5	0.44	Zahnle et al. (1998, 2003)
D_c	15 km	McKinnon et al. (1991)
b_0	0.13	McKinnon et al. (1991)
K_1	0.15	McKinnon et al. (1991) and Zahnle et al. (2003)
b_1	0.88	McKinnon et al. (1991) and Zahnle et al. (2003)
K_2	0.75	McKinnon et al. (1991) and Zahnle et al. (2003)
b_2	0.3	McKinnon et al. (1991) and Zahnle et al. (2003)
K_3	0.017	Schenk (1991)
b_3	0.976	Schenk (1991)
p	2–3	Howard (2007)
n	2–3.5	Howard (2007)

We consider that the maximum ejecta thickness δ_0 at the crater rim is (Schenk, 1991):

$$\delta_0 = K_3 D_f^{b_3} \quad (6)$$

b_0, b_1, b_2 and b_3 are constant values listed in Table 2. The elevation variation depends on whether we consider a position inside or outside the crater. Within the crater, the depth increases from center to the top of the ejecta rim with a power p. Outside the crater, elevation decreases from the top of the ejecta rim to a reference elevation with a power $-n$. We define $\Delta H(\eta, \xi)$ as the elevation variation between the post-impact topography and a reference elevation (equal to 0 far form the impact site):

$$\Delta H(\eta, \xi) = \begin{cases} z_f + (z_f + \delta_0)\left(\frac{2r}{D_f}\right)^p & \text{if} \quad r < D_f/2 \\ \delta_0 \left(\frac{2r}{D_f}\right)^{-n} & \text{if} \quad r > D_f/2 \end{cases} \quad (7)$$

where η is the longitude and ξ the latitude. r is the distance from the crater center:

$$r = \overline{R_t} \arccos[\cos(\eta)\cos(\eta_{imp})\cos(\xi - \xi_{imp}) + \sin(\eta)\sin(\eta_{imp})] \quad (8)$$

with η_{imp} the impact longitude and ξ_{imp} the impact latitude.

2.3. Ejected material and ejecta temperature

The fraction of material from the impactor and from the impacted body escaping the growing moon decreases with decreasing impact velocities (Asphaug, 2010; Korycansky and Zahnle, 2011). For impact velocities considered in our models ($v_{imp} = v_{esc} < 3$ km s^{-1}) and for 45° impact angle, the accretion is supposed to be efficient and this fraction should remain small (less than 10% of the impactor's mass) (Asphaug, 2010; Korycansky and Zahnle, 2011). After a large impact, part of the material beneath the impact site is excavated and redeposited within the ejecta rim (see Fig. 1). We thus set n from Eq. (7) to a value typically ranging between 2 and 3 in order for the efficiency of mass accretion to be close to 100% during the whole accretion period and we consider that the whole impactor is deposited in the ejecta rim.

The temperature of this material depends on the pre-impact temperature, the temperature increase from the impact and the temperature of the impactor. The volume fraction of excavated material that is shock-heated increases with final crater size and this hot material is redeposited in the most external part of the ejecta rim (Maxwell, 1977; Barnhart and Nimmo, 2011). Hence, the thermal repartition within the ejecta rim should also depend on the interactions between the ejected material and the atmosphere during the excavation and the fallback processes (Kieffer and Simonds, 1980). For simplicity, we will consider in our models that the temperature of the ejecta rim is the average temperature below the impact site over a cylindrical volume with a diameter D_f and a thickness z_f.

3. Multi-impact approach

The accretion of an icy moon is the result of material deposited from a wide range of impactor sizes (i.e. from dusts to 100 km size objects). In the following sections we describe our model of accretion from multi-impacts.

3.1. Impactor population

For the mass distribution of the impactor, we consider a power law distribution with an exponent equal to −2.5: $dN_c/dm \propto m^{-2.5}$, consistent with N-body simulations (Kokubo and Ida, 2000). We use Monte Carlo sampling to generate the impactor population

(Zahnle et al., 2001; Lognonné et al., 2009). By random drawing, we determine the impactor mass (or equivalently, radius) according to the above power law distribution. The time of impact is taken from a uniform probability distribution, while the latitude and longitude of the crater center are randomly drawn so that an isotropic impact flux is obtained. To limit the computation time, a lower size limit, r_{min}, is imposed on the impactor distribution (see Fig. 2). Below this lower limit, individual impact events are not simulated and a parameterized approach using successive deposit layers is used (see Section 3.3 for further details). We assumed a lower limit, r_{min}, typically between 1 and 10 km. We also prescribed an upper limit, r_{max}, typically 100–200 km. Above these values, the validity of the scaling laws used here becomes questionable. Accretion from such large bodies would require more complex impact simulations, which is beyond the scope of the present paper. Nevertheless, 200 km is probably a reasonable upper limit since the growing moon is likely to perturb large objects that were migrating in from the outer disk possibly leading to their breakup. Hyperion, for instance, may be considered as an example of such large satellitesimals (Mosqueira and Estrada, 2003a,b; Estrada et al., 2009). The probability of impacts with objects exceeding 200 km is thus likely low, except maybe during the very late stage of accretion (e.g., Sekine and Genda, 2012).

For simplicity, the impactor population is assumed to be infinite (meaning that the number of impactors of a given size does not decrease as a function of time) and the accretion rates of large impactors $\tau_{acc,li}$ and layer deposit $\tau_{acc,lay}$ are assumed constant during one simulation. To measure the influence of large impactors ($r_{min} < r < r_{max}$) relative to small impactors ($r < r_{min}$), we define the ratio:

$$x_{m,li} = m_{li}/m_{acc} \tag{9}$$

where m_{li} is the mass accreted from large impactors and m_{acc} is the total mass accreted. We define the total accretion rate τ_{acc} as

$$\tau_{acc} = \tau_{acc,li} + \tau_{acc,lay} \tag{10}$$

where $\tau_{acc,li}$ is the accretion rate from large impacts and $\tau_{acc,lay}$ is the accretion rate from small impactors modeled as thin layer deposits (see Section 3.3). We assume that the composition of the icy moon (and of the impactor) is a mixture of ice and rocks and that its density ρ is uniform with depth.

3.2. Multi-impact-induced topography

To account for the pre-impact topography, we use the multi-cratering approach developed by Howard (2007). At the i_{th} impact, the new elevation variation $\Delta E_i(\eta,\xi)$ is

$$\Delta E_i(\eta,\xi) = \begin{cases} \Delta H(\eta,\xi) + (R_{i-1}(\eta,\xi) - \overline{R_{i-1}})(1-(2r/D_f)^2) & \text{when } r < D_f/2 \\ \Delta H(\eta,\xi) + (R_{i-1}(\eta,\xi) - \overline{R_{i-1}}) & \text{when } r > D_f/2 \end{cases} \tag{11}$$

$\Delta E_i(\eta,\xi)$ depends on the local pre-impact topography variation $(R_{i-1}(\eta,\xi)) - \overline{R_{i-1}})$. We consider here no late deformation of the topography before the impact (the degree of inheritance is 1 inside and outside the crater (Howard, 2007)). After the i_{th} impact, the local radius becomes $R_i(\eta,\xi) = R_{i-1}(\eta,\xi) + \Delta E_i(\eta,\xi)$ and the mean radius of the growing moon increases from $\overline{R_{i-1}}$ to $\overline{R_i}$.

The growth of the satellite requires that at least part of the impactor material remains on the growing satellite. Since we consider that the volume of the impactor is retained within the ejecta rim in our models, this growth requirement provides constraints on the scaling law describing the ejecta blanket distribution. For large n values, the topography decreases rapidly from the crater rim and the volume of material accumulated in the ejecta rim decreases. On the contrary, for small n values and for the same crater rim height, the topography decreases more linearly from the crater rim and the volume of material accumulated in the ejecta rim is large. The falloff in ejecta thickness is steep. Depending on the target properties, n ranges between 2.5 and 3 (Housen et al., 1983; Moore et al., 2004). In Fig. 3, we monitor the average radius of the growing moon as a function of time for different values of n and compare it with the theoretical mean radius resulting from the 100% accretion of 1.4×10^6 impactors ranging from 10 to 100 km radii. From this figure, we see that increasing n decreases the mass accumulated and leads to a growth that is less than 100% accretive. For $n = 3$, the accretion is not fully efficient and about 30% of the impacted mass remains on the impacted body while for $n = 2.5$, 95% is accreted (see Fig. 3). For n values smaller than 2.5, the growth is unrealistic since it is more than 100% accretive. We choose a value of 2.5 which maximizes the fraction of accreted material.

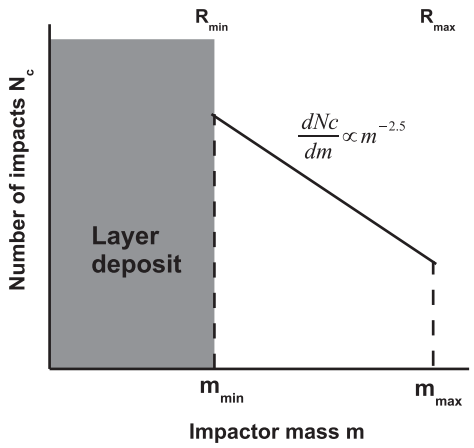

Fig. 2. Schematic representation of the cumulated number of impacts as a function of the impactor mass. All the material with a mass smaller than m_{min} (i.e. with $r < r_{min}$) is deposited as a thin global layer over the moon surface. The impactors with a mass ranging from m_{min} to m_{max} are considered here as successive impact events (selected randomly) and their effects (impact cratering and heating) are treated individually.

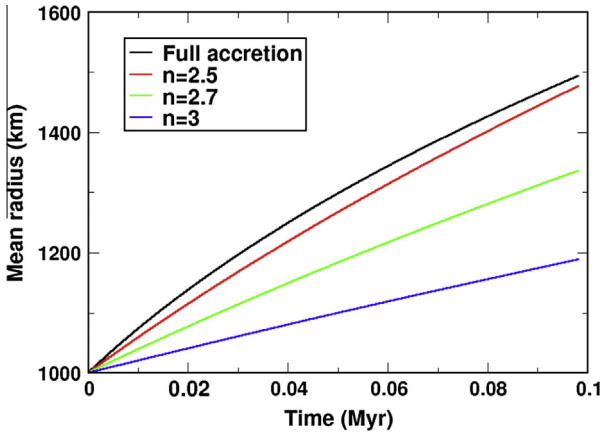

Fig. 3. Time evolution of the average radius of the growing icy moon after the accretion of 1.4×10^6 impactors ranging from 10 to 100 km radii with $n = 2.5$ (red solid line), $n = 2.7$ (green solid line) and $n = 3$ (blue solid line). For comparison, we also represent the time evolution of the average radius consisting in the 100% accretive accumulation of the impactor bodies (black solid line). (For interpretation of the references to color in this figure legend, the reader is referred to the web version of this article.)

3.3. Layer deposits from small impactors

As explained previously, for numerical reasons, individual impact events for $r < r_{min}$ are not simulated. We consider that the accreted mass from small impactors is averaged and uniformly added on the surface. For a prescribed accretion rate, $\tau_{acc,lay} = \tau_{acc} \times (1 - x_{m,li})$, the thickness δ_{lay} of the uniform layer deposit between two individual large impacts is then:

$$\delta_{lay} = \left(\frac{3\tau_{acc,lay}\Delta t}{4\pi\rho} + R_i^3\right)^{1/3} - R_i \quad (12)$$

At any point at the surface, this additional layer is added uniformly. We assume that the temperature of this deposit layer is homogeneous over the entire thickness δ_{lay}. The layer temperature depends on the radius of the growing moon $\overline{R_t}$ and is calculated following an approach that is similar to the "classic" one from Schubert et al. (1981). In their 1D thermal evolution models, Schubert et al. (1981) considered that a fraction h of the kinetic energy accumulated during accretion progressively heats up the near surface of the growing satellite (Kaula, 1979; Schubert et al., 1981; Lunine and Stevenson, 1987; Grasset and Sotin, 1996). Hence the corresponding temperature profile is:

$$T(\overline{R_t}) = \frac{hGM(\overline{R_t})}{C_p\overline{R_t}}\left(1 + \frac{\overline{R_t}v_\infty^2}{2GM(\overline{R_t})}\right) + T_e \quad (13)$$

Considering that $v_\infty^2 = 0$ (i.e. $v_{imp} = v_{esc}$), Eq. (13) becomes

$$T(\overline{R_t}) = \frac{\gamma_{lay}}{2C_p}v_{imp}^2 + T_e \quad (14)$$

where C_p is the heat capacity of the icy satellite material/mixture and T_e is the temperature of the surrounding environment. The coefficient γ_{lay} represents the fraction of energy that is retained in the layer as heat. Note that the coefficients γ_{li} and γ_{lay} defined here differ from the coefficient h used in Eq. (13). h implicitly includes the post-impact surface cooling, while γ_{li} and γ_{lay} only represent the fraction of kinetic energy converted as heat from the small impacts deposited as an uniform layer (γ_{lay}) or from large impacts (γ_{li}). γ_{lay} is considered as a free parameter. It accounts for the effect of mechanical mixing in the shallow layers which has been described in Squyres et al. (1988) by a larger thermal diffusivity. Due to the heat removal by this "gardening" effect of numerous small impacts (Davies, 2009), it is reasonable to assume that $\gamma_{lay} \leqslant \gamma_{li}$.

3.4. Numerical method

As the satellite grows, impactors bring material and thermal energy used to build-up and heat-up the moon. We monitor the thermal evolution of a growing icy satellite using the 3D-tool OEDIPUS (Choblet et al., 2007) to obtain a three-dimensional solution of the energy equation in a spherical shell. We use a finite-volume formulation and a mesh based on the "cubed sphere" transformation, the resulting grid consisting in six identical blocks. The computational grid in one block consists typically of $128 \times 64 \times 64$ discrete cells. Initially, the growing satellite in our models consists of a core surrounded by a shell with a thickness leading to a R_0 radius body. In the numerical domain, the overlaying shell (between R_0 and the final moon radius) is initially empty and gradually filled by impacted material during the accretion history. As the accretion time is relatively short compared to the onset time of solid-state convection (e.g., Robuchon et al., 2010), we consider only the diffusion of heat with no advective term. Melt transport and water/rock separation are not considered here and simulations are stopped when a few percent of material exceeding the melting point of water ice is reached. The accreted material is assumed to be an undifferentiated mixture of ice and rocks with a thermal diffusivity that does not depend on temperature, $\kappa = 10^{-6}$ m^2 s^{-1} (Squyres et al., 1988; Barr et al., 2010).

To maintain an accurate spatial resolution in our models during the entire accretion, we subdivide the accretion in successive stages between which the mesh grid is modified. Between two stages, the temperature field from the previous regime is interpolated on the mesh grid that we use in the next regime (see Fig. 4). The free accretionary parameters of our models are the ratio of material accreted from a large impacts $x_{m,li}$ and the accretion rate τ_{acc}. The free energy conversion factors are γ_{lay} (layer heating) and γ_{li} (large impact heating). γ_{lay} and γ_{li} are independent parameters.

3.5. Post-impact surface cooling

After an impact, the efficient radiative heat transfer at the surface leads to a rapid cooling of the uppermost part of the heated zone (including the impact site and the surrounding ejecta blanket). As such a rapid post-impact cooling cannot be properly described in the framework of the relatively coarse grid mesh used by the 3D OEDIPUS tool, we have implemented a more precise description of heat transfer in this region. In the uppermost grid mesh of OEDIPUS, the conduction of heat for uniform heat conductivity is solved in the radial direction using refined sublayers with a Crank–Nicholson method (similarly to Tobie et al. (2003)). The number of sub-layers varies between 50 and 150, depending on the distance between the local surface radius $R_i(\eta, \xi)$ and the first underlying OEDIPUS grid mesh. A radiative heat flux boundary condition is imposed at the surface:

$$F = \sigma\left(T(R_i)^4 - T_{eq}^4\right) \quad (15)$$

with σ the Stefan–Boltzman constant and T_{eq} the expected equilibrium surface temperature. In the calculations presented below, $T_{eq} = 100$ K. The temperature at the base of the refined column correspond to the temperature value provided in OEDIPUS. The conductive heat flux predicted in the refined column at the base of the first underlying OEDIPUS mesh interface is then imposed as heat flux boundary conditions at the top of the coarse grid domain.

4. Numerical results

4.1. Early and intermediate regimes: from 100 km to 1000 km

We first consider the accretion of a 1000 km size ice-rock body from a 100 km satellite embryo. For simplicity, the initial temperature from $R = 30$ km to $R = R_0 = 100$ km is set to a uniform value, here $T = T_e = 100$ K. To maintain a good spatial resolution, we subdivide the accretion history of the icy satellite in two stages: an early stage where the moon is growing from 100 km to 500 km, an intermediate stage where the moon is growing from 500 km to 1000 km.

Fig. 4 illustrates the temperature evolution during these two accretionary regimes. In order to test the influence of the early and intermediate regimes on the late accretive stage, we consider two accretionary different scenarios for both the early and intermediate stages: a "cold accretion" where $\gamma_{li} = \gamma_{lay} = 0.1$, $x_{m,li} = 10\%$ (Fig. 4, left column) and a "hot accretion" where $\gamma_{li} = \gamma_{lay} = 0.3, x_{m,li} = 33\%$ (Fig. 4, middle column). The accretion parameters used for the "Early regime" simulation are $r_{min} = 4$ km and $r_{max} = 10$ km, while for the "Intermediate regime", we used $r_{min} = 8$ km and $r_{max} = 20$ km. At the end of the intermediate regime, $t_{acc} = 0.5$ Myr and the impactor velocities remain small (<1 km s^{-1}) which corresponds to small temperature increases deep below the impact site (<10 K).

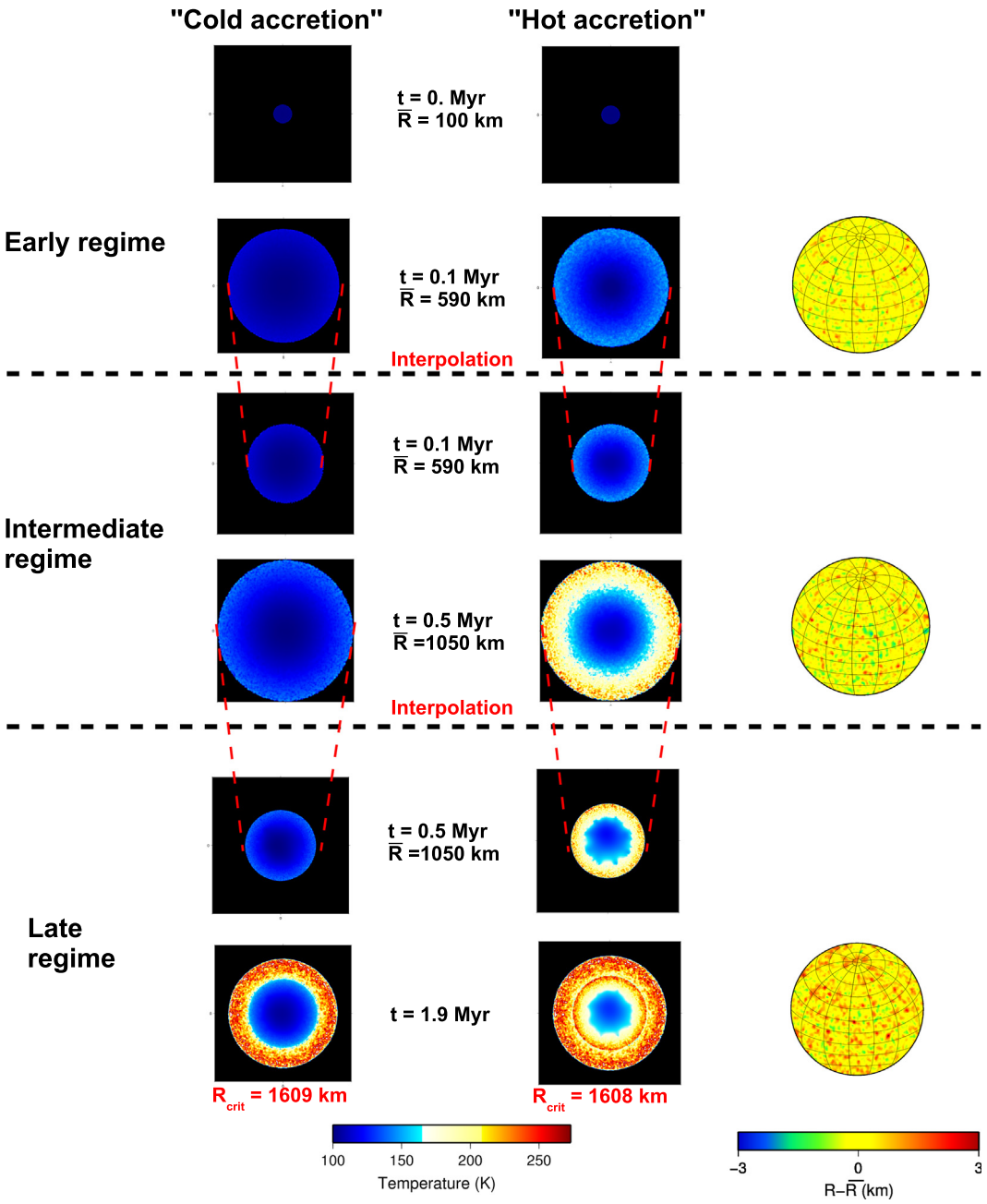

Fig. 4. Equatorial cross sections of the temperature field (left and middle columns) and 3D topographical representations (right) of the growing icy moon as a function of time (from top to bottom). The left column represents the "cold accretion" evolution where, up to the end of the intermediate regime, $\gamma_{li} = \gamma_{lay} = 0.1, x_{m,li} = 10\%$ while the middle column represents the "hot accretion" evolution where $\gamma_{li} = \gamma_{lay} = 0.3$, $x_{m,li} = 33\%$ (Fig. 4, middle column). Temperature color scale is saturated in white for temperature at the melting point (>273 K). Between each regime (early, intermediate, late), the temperature field is interpolated to a larger mesh grid. In the "Late regime", $\gamma_{li} = 0.1$, $\gamma_{lay} = 0.3$, $x_{m,li} = 33\%$, $r_{min} = 10$ km and $r_{max} = 100$ km for both the left and middle columns. (For interpretation of the references to color in this figure legend, the reader is referred to the web version of this article.)

When the moons reach a radius of 1050 km, the temperature barely exceeds 120 K in the cold accretive case, while it can reach values up to 250 K (near the melting point of water ice) for the hot accretive scenario. As we will show later in Section 4.2, although the obtained temperature fields are very different in these two cases, this has no major influence on the evolution of the temperature field in the outer part above 1000 km. Fig. 4 (third column) also represents the 3D topography at the surface of the icy moon at the end of the two stages. As we increase the r_{min} and r_{max} values between the two simulations, the impact craters become larger and the contrast in topography (the difference between the $R(\eta, \xi)$ and the mean radius $\bar{R}$) also increases.

4.2. Late accretive regime: >1000 km

To simulate the evolution for $R > 1000$ km (late accretion regime), we use the thermal state reached at the end of the intermediate regime as the initial thermal state. In Fig. 4 we show results obtained for the same accretionary parameters in the late regime ($\gamma_{li} = 0.1, \gamma_{lay} = 0.3, x_{m,li} = 33\%$, $r_{min} = 10$ km and $r_{max} = 100$ km) but for different initial temperature fields: "cold accretion" scenario (left column) and "hot accretion" scenario (middle column) obtained at the end of the corresponding intermediate regime. Fig. 4 illustrates that the temperature field obtained from the intermediate regime (hot or cold accretion

scenario) only plays a minor role on the critical radius above which melting becomes significant during the late regime. Using the intermediate thermal state obtained form the cold accretion regime leads to $R_{crit} = 1609$ km while using the intermediate thermal state obtained form the hot accretion regime leads to $R_{crit} = 1608$ km (Fig. 4, last line). For this reason, in the following, the temperature field and topography from the "hot accretion scenario" are considered as initial conditions for all simulations of the accretion of bodies larger than 1000 km.

As explained previously, we assume that the impactor velocity is only determined by the gravitational acceleration, and we specifically test the influence of (1) accretion rate τ_{acc}, (2) mass fraction provided by large impactors $x_{m,li}$ and (3) energy conversion factors (i.e. γ_{li} and γ_{lay}) on the thermal state of the growing moon. We monitor the temperature field evolution as well as the volume fraction of satellite material that reaches the melting temperature of pure water ice (i.e. with $T > 273$ K) as a function of satellite growth (see Fig. 4). As complex physical processes associated with melting and water–rock separation are beyond the scope of the present study, we interrupt the simulations when the volume fraction of the growing moon where $T > T_{melt}$ exceeds a threshold value fixed to 5% here. We define R_{crit} as the satellite radius at which this threshold is reached. In this "late regime", the accretionary parameters can be different from the values used in the previous regimes which may lead to temperature "discontinuities" within the growing moon as emphasized in Fig. 4). As indicated above, such artefacts do not influence the value of R_{crit}. As illustrated in Fig. 4, the regions where melting occurs (the regions where the temperature scale is saturated in white) are mainly confined in the most external parts of the growing moon.

4.3. Influence of the accretion rate, τ_{acc} and of the fraction of large impactors, $x_{m,li}$

For this simulation, we assume that the conversion rate of impact energy is similar for small and large impactors: $\gamma_{li} = \gamma_{lay} = 30\%$ or 10%. and we focus only on the late accretive regime. From our models, we can measure the influence of large impacts relative to layer deposition of small impactors by varying the value of $x_{m,li}$. Fig. 5 shows the evolution of R_{crit} as a function of $x_{m,li}$ and for three different accretion rates. For a better comparison with other studies, we express the accretion rate, τ_{acc}, in terms of M_{Titan}/Myr, where M_{Titan} is the mass of Titan (=1.345×10^{23} kg) and we consider values ranging between 0.015 M_{Titan}/Myr (=2×10^{15} kg yr^{-1}) and 1.5 M_{Titan}/Myr (=2×10^{17} kg yr^{-1}). $\tau_{acc} \leqslant 1.5$ M_{Titan}/Myr corresponds to a relatively slow accretion, which is commonly assumed for the accretion of Callisto (Mosqueira and Estrada, 2003a; Barr and Canup, 2008).

Fig. 5 shows that, even for the least efficient conversion rate of impact energy ($\gamma_{li} = \gamma_{lay} = 10\%$), the satellite cannot grow above 1500 km without significant melting, if the accretion is dominated by large impactors ($x_{m,li} \sim 1$). For $\gamma_{li} = \gamma_{lay} = 30\%$, the critical radius is even below 1200 km. The critical radius can be increased only if a significant fraction of small impactors (<10 km) is considered. However, even if small impactors dominate, the critical radius does not exceed 1400 km if $\gamma_{li} = \gamma_{lay} = 30\%$. The critical radius can exceed 2000 km only if $\gamma_{lay} = 10\%$ and if at least 50% of the accreted mass is brought by small impactors ($x_{m,li} < 0.5$).

The accretion rate has some influence on the results only if the accretion is dominated by small impactors, as the rate at which new layers are added limits the cooling of the previously accreted layers. For simulations dominated by large impactors, as most of the energy is buried a few kilometers below the surface, the cooling is very inefficient and the progressive temperature increase only weakly depends on the accretion rate. Therefore, the size distribution of impactors is more crucial than the accretion rate in controlling the thermal evolution of growing satellites. However, as illustrated by the comparison between $\gamma_{li} = \gamma_{lay} = 10\%$ and $\gamma_{li} = \gamma_{lay} = 30\%$ in Fig. 5, the energy conversion rate remains the most crucial parameters, and we explore in more details the sensitivity of our results to γ_{lay} and γ_{li} in the next subsection.

4.4. Influence of the energy conversion parameters, γ_{lay} and γ_{li}

As shown in Fig. 6, for $x_{m,li} = 33\%$ and $\tau_{acc} = 0.15$ M_{Titan}/Myr, γ_{lay} and γ_{li} must be smaller than 0.12 to allow the accretion of a body larger than 2000 km without significant melting. Conversion parameters as low as 0.1 correspond to the lowest value usually considered in previous studies (e.g., Squyres et al., 1988; Coradini et al., 1995). Such low values could be obtained for small impactors, but are probably a strong underestimation for large impactors. Fig. 6 also illustrates the relatively weak

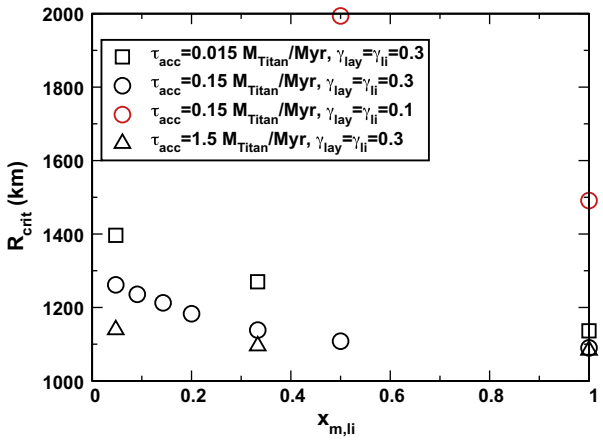

Fig. 5. Critical radius R_{crit} (above which more than 5% of the volume of the icy moon has a temperature larger than the melting temperature) as a function of the fraction of material accreted from large impacts $x_{m,li}$ for different accretion rates ranging from 0.015 M_{Titan}/Myr to 1.55 M_{Titan}/Myr. Black symbols represent R_{crit} for $\gamma_{lay} = \gamma_{li} = 0.3$ while red circles represent R_{crit} for $\gamma_{lay} = \gamma_{li} = 0.1$. (For interpretation of the references to color in this figure legend, the reader is referred to the web version of this article.)

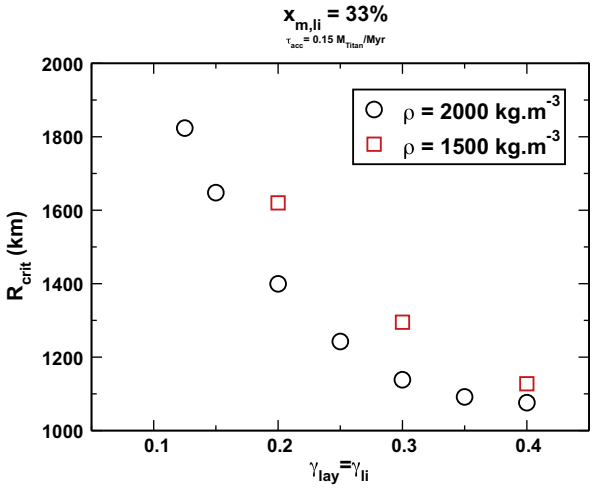

Fig. 6. Critical radius R_{crit} (above which more than 5% of the volume of the icy moon has a temperature larger than the melting temperature) as a function of the energy conversion coefficients (γ_{lay} and γ_{li}) for two density values ($\rho = 1500$ kg m^{-3} and $\rho = 2000$ kg m^{-3}). In these models, the energy conversion coefficients are set to be equal $\gamma_{lay} = \gamma_{li}$, the accretion rate is set to 0.15 M_{Titan}/Myr and the mass fraction of material accreted from large impacts is $x_{m,li} = 33\%$.

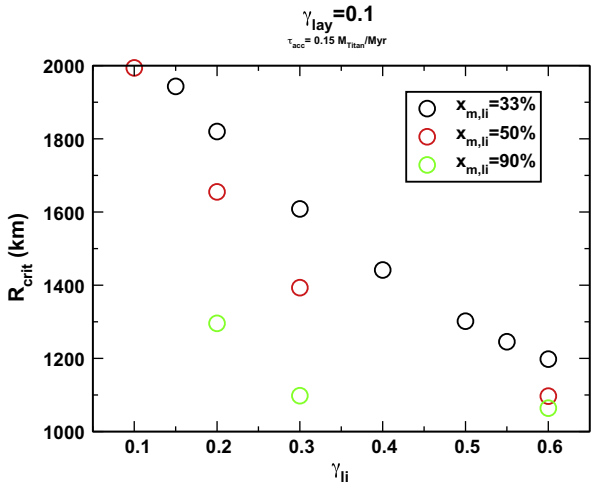

Fig. 7. Critical radius R_{crit} (above which more than 5% of the volume of the icy moon has a temperature larger than the melting temperature) as a function of the energy conversion coefficient γ_{li}, for three values of $x_{m,li}$ (33%, 50% and 90%). In these simulations, the energy conversion coefficient γ_{lay} is set to $\gamma_{lay} = 0.1$ and the accretion rate is set to 0.15 M_{Titan}/Myr.

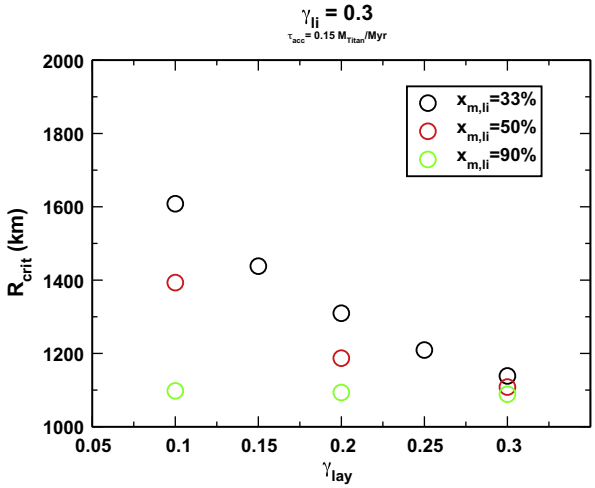

Fig. 8. Critical radius R_{crit} (above which more than 5% of the volume of the icy moon has a temperature larger than the melting temperature) as a function of the energy conversion coefficient γ_{lay} for three values of $x_{m,li}$ (33%, 50% and 90%). In these simulations, the energy conversion coefficient γ_{li} is set to $\gamma_{li} = 0.3$. We only represent the results with $\gamma_{lay} \leqslant \gamma_{li}$. The accretion rate is set to 0.15 M_{Titan}/Myr.

influence of the mean density on the thermal evolution of the growing moon. A decrease in the average density leads to a decay of the impact-induced temperature increase (see Eq. (1)). As a consequence, decreasing ρ by 25% increases R_{crit} by ~15%.

Fig. 7 shows the influence of increasing the energy conversion rate associated to large impactors, γ_{li} for a fixed value of γ_{lay} (= 0.1) for small impactors and for three different values of $x_{m,li}$. As expected, the critical radius strongly decreases when the conversion rate and the mass fraction associated to large impactors are increased. For $\gamma_{li} = 0.3$ (Fig. 8), the critical radius never exceeds 1600 km. Fig. 9 represents the stability domain of a growing icy moon with $x_{m,li} = 33\%$ and $\tau_{acc} = 0.15$ M_{Titan}/Myr for different values of γ_{lay} and γ_{li}. From Fig. 9, we see that, for $\gamma_{li} \sim 0.3$ (O'Keefe et al., 1977; Squyres et al., 1988; Monteux et al., 2007) melting is more likely to occur as soon as the growing moon reaches a radius of 1200–1500 km which is in good agreement with Estrada and Mosqueira (2011). According to Fig. 9, it is

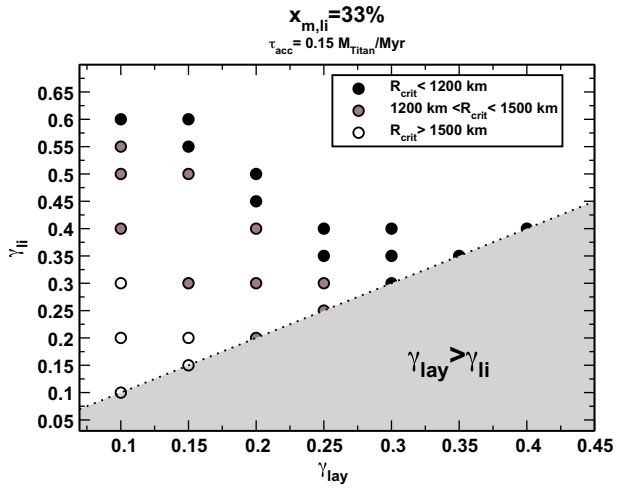

Fig. 9. Melting behavior of a growing icy moon as a function of the energy conversion coefficients γ_{lay} and γ_{li}. For black-filled symbols, $R_{crit} < 1200$ km. For brown-filled symbols, $1200 < R_{crit} < 1500$ km. For white-filled symbols, $R_{crit} > 1500$ km. In these simulations, the accretion rate is set to 0.15 M_{Titan}/Myr and the mass fraction of material accreted from large impacts is $x_{m,li} = 33\%$. In the gray domain, $\gamma_{lay} > \gamma_{li}$ and the corresponding cases are not considered here.

difficult to envision a cold accretion as soon as γ_{lay} is larger than 0.3 even with small γ_{li}. However, we may envision that the icy moon grows unmelted up to a radius of 1200 km even with $\gamma_{li} > 0.5$ only if γ_{lay} is smaller than 0.15.

5. Conclusion

We have developed a 3D numerical model that accounts for the influence of large impacts on the thermal evolution of growing icy satellites and have considered the least efficient scenarios and parameters to initiate melting. Our results show that the size distribution of impactors (i.e. ratio between large and small impactors) is a key factor in determining the temperature increase during the accretion stage. We show that the accretion rate as well as the thermal state of the satellite embryo only play a minor role, therefore the apparent degree of differentiation of a satellite's interior cannot be used to constrain the duration of its accretion.

Our simulations confirm that the most crucial parameter is the coefficient of impact energy conversion into heat (γ_{lay} and γ_{li}). Our results show that it is impossible to avoid significant melting during accretion, unless the fraction of impact energy retained as heat is very low, in the order of 10%. Such an inefficient conversion rate is difficult to explain and does not seem realistic with respect to available estimates from impact experiments (e.g., Ahrens and O'keefe, 1985). Much lower initial temperature of the impactors as well as more efficient subsurface cooling associated with impact gardening (not modeled explicitly here but included in the γ_{lay} conversion efficiency) may reduce the effective conversion rates (Anderson, 1989). Lower environment temperature (<100 K) may also increase the cooling rate of the shallow layers. Therefore, the absence of extensive melting during accretion may reflect a very cold ambient subnebula rather than a long accretionary timescale.

Several additional heat sources such as radiogenic heating, tidal/despinning heating or heating associated with high-velocity impact, have not been considered in the heat budget in our model. Including these would require an even less efficient energy conversion and storage to avoid melting and subsequent differentiation. We also made the conservative assumption that the impacts are 100% accretive. If some fraction of impact is not fully accretive, more impacts are needed to accrete the same mass resulting in

more impact energy. Hence, the temperature increase would be higher and melting even more likely. Therefore, the maximal radii of the accreted satellite reached without significant melting in our simulations can be considered as upper limits.

Based on our simulations, when more than 10% of the accreted mass is brought by impactors larger than 1 km, it seems unlikely that a satellite larger than 2000 km may accrete without significant melting unless the environment is extremely cold and the conversion rate of impact energy unrealistically low (<10–15%). If the accretion is dominated by km-size impactors, impact-induced melting may occur for radii as small as 1100–1500 km. Above this critical radius, separation between liquid water and rock should initiate, thus leading to the accumulation of dense rock blocks above the undifferentiated core consisting of a mixture of rock and ice (e.g., Kirk and Stevenson, 1987). The dense layer of accumulated rock is gravitationally unstable, and in such conditions it is difficult to avoid subsequent full separation of rock and ice phases. Depending on the size of the core and thickness of the rocky layer, the differentiation may be catastrophic (Kirk and Stevenson, 1987) or more gradual (Nagel et al., 2004). Recently, O'Rourke and Stevenson (2014) showed that although rock–ice separation may be delayed by double-diffusive convection in the ice–rock interior, ice melting due to progressive radiogenic heating and subsequent differentiation cannot be prevented. Further modeling efforts are needed to better understand the processes controlling rock–ice segregation and how the internal structure inherited from the accretion process has evolved to the present-day state.

A series of arguments now questions the apparent partially differentiated state of Callisto and Titan, suggested by their elevated moment of inertia as estimated using the Radau-Darwin Approximation (e.g., Anderson et al., 2001; Iess et al., 2010; Gao and Stevenson, 2013). On Titan, the existence of a non-negligible degree-three in the gravity field as well as significant topography suggest that non-hydrostatic effects may significantly affect the estimation of the Moment-of-Inertia factor (Iess et al., 2010; Gao and Stevenson, 2013; Baland et al., in press) and that the MoI factor may be significantly smaller than the value estimated from the Radau-Darwin Approximation. On Callisto, similar non hydrostatic contributions originating in the lithosphere may also affect the estimation of its moment of inertia (McKinnon, 1997; Gao and Stevenson, 2013). On these two moons, the hydrostatic dynamical flattening is relatively small as they orbit relatively far from their planet, and therefore the non-hydrostatic contributions need to be correctly estimated in order to accurately infer the moment of inertia and the density profile of their interior. On Callisto, future measurements performed by the ESA JUICE mission that will be launched in 2022 (Grasset, 2013) will provide constraints on the non-hydrostatic contribution by measuring independently the different quadrupole coefficients, as well as by estimating the degree three and four coefficients of the gravity field. On Titan, future measurements during Cassini flybys will also permit a better determination of the degree-four (Iess, 2012), which will provide pertinent tests on the topography compensation process in the outer ice shell (Hemingway et al., 2013; Lefevre et al., 2014), and consequently on the non-hydrostatic corrections required to infer more precisely the moment of inertia.

Acknowledgments

The authors thank the anonymous reviewers for constructive comments. J. Monteux is funded by Agence Nationale de la Recherche (Accretis decision No. ANR-10-PDOC-001-01). The research leading to these results has received funding from the European Research Council under the European Community's Seventh Framework Programme (FP7/2007-2013 Grant Agreement No. 259285).

References

Ahrens, T.J., O'keefe, J.D., 1985. Shock vaporization and the accretion of the icy satellites of Jupiter and Saturn. In: Klinger, J., Benest, D., Dollfus, A., Smoluchowski, R. (Eds.), NATO ASIC Proc. 156: Ices in the Solar System, pp. 631–654.

Anderson, D., 1989. The terrestrial planets. In: Theory of the Earth. Blackwell Scientific Publications, Boston, Chapter 1.

Anderson, J.D., Jacobson, R.A., McElrath, T.P., Moore, W.B., Schubert, G., Thomas, P.C., 2001. Shape, mean radius, gravity field, and interior structure of Callisto. Icarus 153, 157–161. http://dx.doi.org/10.1006/icar.2001.6664.

Asphaug, E., 2010. Similar-sized collisions and the diversity of planets. Chemie der Erde/Geochemistry 70, 199–219. http://dx.doi.org/10.1016/j.chemer.2010.01.004.

Baland, R., Tobie, G., Lefevre, A., Van Hoolst, T., in press. Titan's internal structure inferred from its gravity field, shape, and rotation state. Icarus.

Barnhart, C.J., Nimmo, F., 2011. Role of impact excavation in distributing clays over Noachian surfaces. J. Geophys. Res. (Planets) 116, E01009. http://dx.doi.org/10.1029/2010JE003629.

Barr, A.C., Canup, R.M., 2008. Constraints on gas giant satellite formation from the interior states of partially differentiated satellites. Icarus 198, 163–177. http://dx.doi.org/10.1016/j.icarus.2008.07.004.

Barr, A.C., Citron, R.I., Canup, R.M., 2010. Origin of a partially differentiated Titan. Icarus 209, 858–862. http://dx.doi.org/10.1016/j.icarus.2010.05.028.

Canup, R.M., Ward, W.R., 2002. Formation of the Galilean satellites: Conditions of accretion. Astron. J. 124, 3404–3423. http://dx.doi.org/10.1086/344684.

Canup, R.M., Ward, W.R., 2006. A common mass scaling for satellite systems of gaseous planets. Nature 441, 834–839. http://dx.doi.org/10.1038/nature04860.

Castillo-Rogez, J.C., Lunine, J.I., 2010. Evolution of Titan's rocky core constrained by Cassini observations. Geophys. Res. Lett. 37, L20205. http://dx.doi.org/10.1029/2010GL044398.

Choblet, G., Čadek, O., Couturier, F., Dumoulin, C., 2007. ŒDIPUS: A new tool to study the dynamics of planetary interiors. Geophys. J. Int. 170, 9–30. http://dx.doi.org/10.1111/j.1365-246X.2007.03419.x.

Coradini, A., Federico, C., Forni, O., Magni, G., 1995. Origin and thermal evolution of icy satellites. Surveys Geophys. 16, 533–591. http://dx.doi.org/10.1007/BF00665684.

Croft, S.K., 1982. A first-order estimate of shock heating and vaporization in oceanic impacts. In: Silver, T.L., Schultz, P.H. (Eds.), Geological Implications of Impacts of Large Asteroids and Comets on Earth. In: Spec. Pap. Geol. Soc. Am. 190, 143–152.

Davies, G., 2009. Thermal evolution of the mantle. In: Schubert, G. (Editor-in-Chief), Treatise of Geophysics, vol. 9. Elsevier, pp. 197–216.

Dwyer, C., Nimmo, F., Ogihara, M., Ida, S., 2013. The influence of imperfect accretion and radial mixing on ice:rock ratios in the Galilean satellites. Icarus 225 (1), 390–402, http://dx.doi.org/10.1016/j.icarus.2013.03.025.

Estrada, P.R., Mosqueira, I., 2011. Titan's accretion and long term thermal history. In: Lunar and Planetary Institute Science Conference Abstracts, Lunar and Planetary Institute Science Conference Abstracts, vol. 42, p. 1679.

Estrada, P.R., Mosqueira, I., Lissauer, J.J., D'Angelo, G., Cruikshank, D.P., 2009. Formation of Jupiter and Conditions for Accretion of the Galilean Satellites. University of Arizona Press, pp. 27–58.

Gao, P., Stevenson, D.J., 2013. Nonhydrostatic effects and the determination of icy satellites' moment of inertia. Icarus 226, 1185–1191. http://dx.doi.org/10.1016/j.icarus.2013.07.034.

Grasset, O. et al., 2013. JUpiter ICy moons Explorer (JUICE): An ESA mission to orbit Ganymede and to characterise the Jupiter system. Planet. Space Sci. 78, 1–21. http://dx.doi.org/10.1016/j.pss.2012.12.002.

Grasset, O., Sotin, C., 1996. The cooling rate of a liquid shell in Titan's interior. Icarus 123, 101–112. http://dx.doi.org/10.1006/icar.1996.0144.

Hemingway, D., Nimmo, F., Zebker, H., Iess, L., 2013. A rigid and weathered ice shell on Titan. Nature 500, 550–552. http://dx.doi.org/10.1038/nature12400.

Housen, K.R., Schmidt, R.M., Holsapple, K.A., 1983. Crater ejecta scaling laws – Fundamental forms based on dimensional analysis. J. Geophys. Res. 88, 2485–2499. http://dx.doi.org/10.1029/JB088iB03p02485.

Howard, A.D., 2007. Simulating the development of martian highland landscapes through the interaction of impact cratering, fluvial erosion, and variable hydrologic forcing. Geomorphology 91, 332–363. http://dx.doi.org/10.1016/j.geomorph.2007.04.017.

Iess, L. et al., 2010. Gravity field, shape, and moment of inertia of Titan. Science 327, 1367–1369. http://dx.doi.org/10.1126/science.1182583.

Iess, L. et al., 2012. The tides of Titan. Science 337, 457. http://dx.doi.org/10.1126/science.1219631.

Kaula, W.M., 1979. Thermal evolution of Earth and moon growing by planetesimal impacts. J. Geophys. Res. 84, 999–1008.

Kieffer, S.W., Simonds, C.H., 1980. The role of volatiles and lithology in the impact cratering process. Rev. Geophys. Space Phys. 18, 143–181. http://dx.doi.org/10.1029/RG018i001p00143.

Kirk, R.L., Stevenson, D.J., 1987. Thermal evolution of a differentiated Ganymede and implications for surface features. Icarus 69, 91–134. http://dx.doi.org/10.1016/0019-1035(87)90009-1.

Kivelson, M.G. et al., 1998. Ganymede's magnetosphere: Magnetometer overview. J. Geophys. Res. 103, 19,963–19,972. http://dx.doi.org/10.1029/98JE00227.

Kokubo, E., Ida, S., 2000. Formation of protoplanets from planetesimals in the solar nebula. Icarus 143, 15–27. http://dx.doi.org/10.1006/icar.1999.6237.

Korycansky, D.G., Zahnle, K.J., 2011. Titan impacts and escape. Icarus 211, 707–721. http://dx.doi.org/10.1016/j.icarus.2010.09.013.
Kossacki, K.J., Leliwa-Kopystyński, J., 1993. Medium-sized icy satellites: Thermal and structural evolution during accretion. Planet. Space Sci. 41, 729–741. http://dx.doi.org/10.1016/0032-0633(93)90115-I.
Kraus, R., Senft, L., Stewart, S., 2011. Impacts onto h2o ice: Scaling laws for melting, vaporization, excavation, and final crater size. Icarus.
Lefevre, A., Tobie, G., Choblet, G., Čadek, O., 2014. Structure and dynamics of Titan's outer icy shell constrained from Cassini data. Icarus, in press.
Lognonné, P., Le Feuvre, M., Johnson, C.L., Weber, R.C., 2009. Moon meteoritic seismic hum: Steady state prediction. J. Geophys. Res. (Planets) 114, E12003. http://dx.doi.org/10.1029/2008JE003294.
Lunine, J.I., Stevenson, D.J., 1987. Clathrate and ammonia hydrates at high pressure – Application to the origin of methane on Titan. Icarus 70, 61–77. http://dx.doi.org/10.1016/0019-1035(87)90075-3.
Maxwell, D.E., 1977. Simple Z model for cratering, ejection, and the overturned flap. In: Roddy, D.J., Pepin, R.O., Merrill, R.B. (Eds.), Impact and Explosion Cratering: Planetary and Terrestrial Implications, pp. 1003–1008.
McKinnon, W.B., 1997. Note: Mystery of Callisto: Is it undifferentiated? Icarus 130, 540–543. http://dx.doi.org/10.1006/icar.1997.5826.
McKinnon, W.B., Chapman, C.R., Housen, K.R., 1991. Cratering of the Uranian Satellites. University of Arizona Press, pp. 629–692.
Monteux, J., Coltice, N., Dubuffet, F., Ricard, Y., 2007. Thermo-mechanical adjustment after impacts during planetary growth. Geophys. Res. Lett. 34, 24,201–24,205.
Moore, J.M., Schenk, P.M., Bruesch, L.S., Asphaug, E., McKinnon, W.B., 2004. Large impact features on middle-sized icy satellites. Icarus 171, 421–443. http://dx.doi.org/10.1016/j.icarus.2004.05.009.
Mosqueira, I., Estrada, P.R., 2003a. Formation of the regular satellites of giant planets in an extended gaseous nebula. I: Subnebula model and accretion of satellites. Icarus 163, 198–231. http://dx.doi.org/10.1016/S0019-1035(03)00076-9.
Mosqueira, I., Estrada, P.R., 2003b. Formation of the regular satellites of giant planets in an extended gaseous nebula. II: Satellite migration and survival. Icarus 163, 232–255. http://dx.doi.org/10.1016/S0019-1035(03)00077-0.
Mueller, S., McKinnon, W.B., 1988. Three-layered models of Ganymede and Callisto – Compositions, structures, and aspects of evolution. Icarus 76, 437–464. http://dx.doi.org/10.1016/0019-1035(88)90014-0.
Nagel, K., Breuer, D., Spohn, T., 2004. A model for the interior structure, evolution, and differentiation of Callisto. Icarus 169, 402–412. http://dx.doi.org/10.1016/j.icarus.2003.12.019.
O'Keefe, J.D., Ahrens, T.J., 1977. Impact-induced energy partitioning, melting, and vaporization on terrestrial planets. In: Merril, R.B. (Ed.), Lun. Planet. Sci., vol. 8, pp. 3357–3374.
O'Rourke, P., Stevenson, D.J., 2014. Stability of ice/rock mixtures with application to a partially differentiated Titan. Icarus 227, 67–77. http://dx.doi.org/10.1016/j.icarus.2013.07.034, in press.
Pappalardo, R.T., Collins, G.C., Head III, J.W., Helfenstein, P., McCord, T.B., Moore, J.M., Prockter, L.M., Schenk, P.M., Spencer, J.R., 2004. Geology of Ganymede. In: Bagenal, F., Dowling, T.E., McKinnon, W.B. (Eds.), Jupiter: The Planet, Satellites and Magnetosphere. Cambridge Planetary Science, pp. 363–396.
Pierazzo, E., Vickery, A.M., Melosh, H.J., 1997. A reevaluation of impact melt production. Icarus 127, 408–423.
Pike, R.J., 1977. Apparent depth/apparent diameter relation for lunar craters. In: Merril, R.B. (Ed.), Lunar and Planetary Science Conference Proceedings, vol. 8, pp. 3427–3436.
Robuchon, G., Choblet, G., Tobie, G., Čadek, O., Sotin, C., Grasset, O., 2010. Coupling of thermal evolution and despinning of early Iapetus. Icarus 207, 959–971. http://dx.doi.org/10.1016/j.icarus.2009.12.002.
Safronov, V.S., 1978. The heating of the Earth during its formation. Icarus 33, 3–12. http://dx.doi.org/10.1016/0019-1035(78)90019-2.
Schenk, P.M., 1991. Ganymede and Callisto – Complex crater formation and planetary crusts. J. Geophys. Res. 96, 15,63. http://dx.doi.org/10.1029/91JE00932.
Schenk, P.M., Chapman, C.R., Zahnle, K., Moore, J.M., 2004. Ages and interiors: The cratering record of the Galilean satellites, In: Bagenal, F., Dowling, T.E., McKinnon, W.B. (Eds.), Jupiter: The Planet, Satellites and Magnetosphere. Cambridge Planetary Science, pp. 427–456.
Schubert, G., Stevenson, D.J., Ellsworth, K., 1981. Internal structures of the Galilean satellites. Icarus 47, 46–59. http://dx.doi.org/10.1016/0019-1035(81)90090-7.
Sekine, Y., Genda, H., 2012. Giant impacts in the Saturnian system: A possible origin of diversity in the inner mid-sized satellites. Planet. Space Sci. 63, 133–138. http://dx.doi.org/10.1016/j.pss.2011.05.015.
Senshu, H., Kuramoto, K., Matsui, T., 2002. Thermal evolution of a growing Mars. J. Geophys. Res. 107, 1–13.
Shoemaker, E.M., 1962. Interpretation of Lunar Craters. Academic Press, San Diego, pp. 283–359.
Sohl, F. et al., 2010. Subsurface water oceans on icy satellites: Chemical composition and exchange processes. Space Sci. Rev. 153, 485–510. http://dx.doi.org/10.1007/s11214-010-9646-y.
Squyres, S.W., Reynolds, R.T., Summers, A.L., Shung, F., 1988. Accretional heating of the satellites of Saturn and Uranus. J. Geophys. Res. 93, 8779–8794. http://dx.doi.org/10.1029/JB093iB08p08779.
Stewart, S.T., Ahrens, T.J., 2005. Shock properties of H_2O ice. J. Geophys. Res. (Planets) 110, E03005. http://dx.doi.org/10.1029/2004JE002305.
Tobie, G., Choblet, G., Sotin, C., 2003. Tidally heated convection: Constraints on Europa's ice shell thickness. J. Geophys. Res. (Planets) 108, 5124. http://dx.doi.org/10.1029/2003JE002099.
Ward, W.R., Canup, R.M., 2010. Circumplanetary disk formation. Astron. J. 140, 1168–1193. http://dx.doi.org/10.1088/0004-6256/140/5/1168.
Zahnle, K., Dones, L., Levison, H.F., 1998. Cratering rates on the Galilean satellites. Icarus 136, 202–222. http://dx.doi.org/10.1006/icar.1998.6015.
Zahnle, K., Schenk, P., Sobieszczyk, S., Dones, L., Levison, H.F., 2001. Differential cratering of synchronously rotating satellites by ecliptic comets. Icarus 153, 111–129. http://dx.doi.org/10.1006/icar.2001.6668.
Zahnle, K., Schenk, P., Levison, H., Dones, L., 2003. Cratering rates in the outer Solar System. Icarus 163, 263–289. http://dx.doi.org/10.1016/S0019-1035(03)00048-4.

Icarus 257 (2015) 324–335

Contents lists available at ScienceDirect

Icarus

journal homepage: www.elsevier.com/locate/icarus

Evolution of Titan's atmosphere during the Late Heavy Bombardment

Nadejda Marounina [a,*], Gabriel Tobie [a], Sabrina Carpy [a], Julien Monteux [a,b], Benjamin Charnay [c], Olivier Grasset [a]

[a] Laboratoire de Planétologie et Géodynamique, Université de Nantes, CNRS, UMR-6112, 2, rue de la Houssinière, 44322 Nantes cedex 03, France
[b] Laboratoire Magmas et Volcans, Université Blaise Pascal – CNRS – IRD, OPGC, 5 rue Kessler, 63038 Clermont-Ferrand, France
[c] Virtual Planetary Laboratory, University of Washington, Seattle, WA 98195, USA

ARTICLE INFO

Article history:
Received 4 November 2014
Revised 20 April 2015
Accepted 11 May 2015
Available online 19 May 2015

Keywords:
Titan, atmosphere
Impact processes
Atmosphere, evolution

ABSTRACT

The mass and composition of Titan's massive atmosphere, which is dominated by N_2 and CH_4 at present, have probably varied all along its history owing to a combination of exogenous and endogenous processes. In the present study, we investigate its fate during the Late Heavy Bombardment (LHB) by modeling the competitive loss and supply of volatiles by cometary impacts and their consequences on the atmospheric balance. For surface albedos ranging between 0.1 and 0.7, we examine the emergence of an atmosphere during the LHB as well as the evolution of a primitive atmosphere with various masses and compositions prior to this event, accounting for impact-induced crustal NH_3–N_2 conversion and subsequent outgassing as well as impact-induced atmospheric erosion. By considering an impactor population characteristic of the LHB, we show that the generation of a N_2-rich atmosphere with a mass equivalent to the present-day one requires ammonia mass fraction of 2–5%, depending on surface albedos, in an icy layer of at least 50 km below the surface, implying an undifferentiated interior at the time of LHB. Except for high surface albedos ($A_S \geqslant 0.7$) where most of the released N_2 remain frozen at the surface, our calculations indicate that the high-velocity impacts led to a strong atmospheric erosion. For a differentiated Titan with a thin ammonia-enriched crust ($\leqslant$5 km) and $A_S < 0.6$, any atmosphere pre-existing before the LHB should be more than 5 times more massive than at present, in order to sustain an atmosphere equivalent to the present-day one. This implies that either a massive atmosphere was formed on Titan during its accretion or that the nitrogen-rich atmosphere was generated after the LHB.

1. Introduction

Saturn's largest satellite Titan is the only satellite in the Solar System possessing a dense atmosphere. Presently, it is composed predominantly of N_2 (~98%) and CH_4 (~2%) (e.g. Griffith et al., 2013). However, this atmospheric composition has probably varied through time since the accretion of the satellite due to various external and internal processes. Owing to continuous photochemical destruction and atmospheric escape, the lifetime of atmospheric methane is currently of the order of ~20 Ma (e.g. Griffith et al., 2013). Moreover, the isotopic $^{13}C/^{12}C$ ratio in CH_4, measured by the mass spectrometer of the Huygens probe (GCMS) (Niemann et al., 2010), indicates that the present-day methane is not fractionated relative to Solar System standards, implying that it has been recently injected in the atmosphere (less than 1 Gyr ago (Mandt et al., 2012)).

The origin of N_2 is probably more ancient. The main constraint on its origin is provided by the $^{36}Ar/N_2$ ratio measured by the Huygens GCMS ($\sim 2.7 \times 10^{-7}$, Niemann et al. (2010)), which is $\sim 3 \times 10^5$ times smaller than the solar value (Owen, 1982). As N_2 and ^{36}Ar should be trapped in similar rates either by direct condensation or clathration in the solar nebula (Owen, 1982; Mousis et al., 2002), this low value indicates that the nitrogen was not originally captured as N_2 but as easily condensible nitrogen compounds such as NH_3 (Atreya et al., 2009). Moreover, Mandt et al. (2014) showed that the $^{14}N/^{15}N$ ratio measured in Titan's N_2 (Niemann et al., 2010) is consistent with isotopic ratio recently inferred from NH_2 radicals produced by the photodissociation of NH_3 in comets (Rousselot et al., 2014; Shinnaka et al., 2014), providing additional evidence for ammonia as the main source of nitrogen on Titan. Several mechanisms have been proposed to explain the conversion of NH_3 into N_2 at Titan's conditions: photochemical conversion (Atreya et al., 1978), impact-induced conversion in the atmosphere (McKay et al., 1988; Ishimaru et al., 2011) or in a NH_3-enriched icy crust (Sekine et al., 2011), as well as endogenic processes (Glein

* Corresponding author.

http://dx.doi.org/10.1016/j.icarus.2015.05.011
0019-1035/

et al., 2009; Tobie et al., 2012). Here we focus on the conversion proposed by Sekine et al. (2011).

Delivery of volatiles by impact has likely occurred all along Titan's history (Griffith and Zahnle, 1995), with more intense flux during the accretion period and the Late Heavy Bombardment (LHB). Following the Nice model (Gomes et al., 2005; Morbidelli et al., 2005; Tsiganis et al., 2005), this intense bombardment would have affected the entire Solar System, due to the destabilization of the planetesimal disk beyond Neptune's orbit. Because of the gravitational focusing of Saturn (Zahnle et al., 2003), the cumulative mass delivered on Titan during the LHB is estimated to 3×10^{20} kg (Barr et al., 2010). This intense bombardment, characterized by high impact velocities ($\gg v_{esc}$, the escape velocity of the planet or the satellite), may have supplied a huge amount of volatiles (e.g. CH_4 and NH_3) either by direct contribution from impactor volatilization or by impact-induced degassing of Titan's crust, as suggested by Sekine et al. (2011). High-velocity impactors are also expected to erode the atmosphere during the impact. Studies of impact-induced atmospheric erosion based either on analytic approaches or numerical simulations have been mostly focused on Mars and the Earth (Melosh and Vickery, 1989; Svetsov, 2000, 2007; Genda and Abe, 2005; Shuvalov, 2009). Parameterizations of impact-induced erosion were used by Pham et al. (2011) and de Niem et al. (2012) to investigate the atmospheric balance between erosion and volatile supply during the LHB on Mars, Earth and Venus. Here we follow a similar approach for Titan, combining a pressure-induced ammonia conversion from Sekine et al. (2011) and a parameterization of atmospheric erosion by impact from Shuvalov (2010).

To investigate the predominant mechanism that governs the fate of Titan's atmosphere during the LHB, we combine a stochastic approach for the impactor sampling and we monitor the atmospheric mass balance between the supply of N_2 and CH_4 by both impactor and crustal degassing and atmospheric erosion induced by impact. At pressures and temperatures expected on Titan, part of the supplied volatiles may condense at the surface. To estimate the partitioning between the volatiles in the atmosphere and those condensed at the surface, we implemented the atmospheric model developed by Lorenz et al. (1999) including radiative and gas–liquid equilibrium. In the particular case of a pure N_2 atmosphere, we use the atmospheric equilibrium constrained from 3D GCM simulations.

A detailed description of the model is provided in the following section. Simulations of the evolution of Titan's atmosphere during the LHB, considering a wide range of initial conditions, are presented in Section 3. Implications for the origin and evolution of Titan's atmosphere are discussed in Section 4 and our conclusions are summarized in Section 5.

2. Model description

2.1. Model of the atmospheric equilibrium

The composition of Titan's atmosphere may have varied throughout Titan's history. As the mass and composition of Titan's atmosphere before the LHB is uncertain, we consider various initial conditions prior to the LHB. The presence of methane in Titan's atmosphere might only be recent and/or episodic (Tobie et al., 2006; Mandt et al., 2012). It is therefore possible that the atmosphere was composed solely of nitrogen at the time of the LHB. Then we consider either pure N_2 or N_2–CH_4 atmospheres up to 10 times Titan's present-day atmospheric mass. To model the radiative balance as well as the thermodynamic equilibrium between atmospheric and surface volatile reservoirs, we adopt two different modeling approaches for pure N_2 and mixed N_2–CH_4 atmosphere model as detailed hereafter.

2.1.1. Pure N_2 atmosphere

In the case of a pure N_2 atmosphere, the greenhouse effect is limited to collision-induced absorptions of N_2–N_2, as N_2 has no absorption band in the infrared and visible (Lorenz et al., 1997; Charnay et al., 2014). Equilibrium temperatures and pressures have been evaluated for surface albedos varying between 0.2 and 0.7 (see Table 1), from full 3D GCM simulations, using the Generic LMDZ code employed and described in Charnay et al. (2014), accounting for Rayleigh scattering by N_2 and N_2 condensation and precipitation at the surface. These simulations showed that the greenhouse effect is counterbalanced by the increase of atmospheric albedo due to Rayleigh diffusion, so that the surface temperature is mostly determined by the surface albedo. Moreover, although the condensation of N_2 and the atmospheric pressure are mostly controlled by the pole temperature, the GCM simulations showed that the average surface temperature remains a good parameter to predict the average atmospheric pressure and hence the average amount of condensed N_2 at the surface. For a surface albedo A_s lower than 0.68, the surface temperature is above the freezing point and atmospheric N_2 is in equilibrium with liquid N_2 at the surface. For $A_s > 0.68$, the atmospheric N_2 is in equilibrium with solid N_2. Atmospheric pressures displayed in Table 1 correspond to saturation pressures of N_2. Any excess of N_2 is condensed at the surface. Although latitudinal variations of nitrogen condensation are expected based on GCM simulations (Charnay et al., 2014), we assume a uniform distribution of solids or liquids at the surface, and we consider the average temperature and pressure as representative of the surface conditions. When the atmospheric pressure drops below the saturation pressure, the surface temperature is maintained at the same value i.e. the value predicted and displayed in Table 1, for a given surface albedo. As the greenhouse effect is very small (~1–2 K), assuming a constant temperature once the pressure is below the saturation pressure remains a very good approximation.

2.1.2. N_2–CH_4 atmosphere

Once CH_4 is incorporated, the radiative equilibrium and the thermal structure of the atmosphere is significantly affected. In addition to the N_2–N_2 collision-induced absorption, those of CH_4–N_2 and N_2–H_2 (resulting from CH_4 dissociation) as well as absorption of sunlight by CH_4 and photochemical haze in the upper atmosphere contribute to the radiative balance (McKay et al., 1999; Lorenz et al., 1999). To determine the atmospheric radiative equilibrium, we use the parameterized model of Lorenz et al. (1999), based on a semi-empirical gray radiative formulation. It requires the presence of a small amount of methane in the atmosphere and therefore cannot be applied to the pure N_2 case. For the thermodynamical equilibrium, the vapor phase is described by an ideal gas. The liquid phase is described following the regular solution theory (Thompson, 1985; McKay et al., 1999) using the saturation

Table 1
Average surface pressure, P_s, and temperature, T_s, as a function of surface albedo, A_s, evaluated using GCM simulations for a pure N_2 atmosphere.

A_s	P_s (bar)	T_s (K)	Nitrogen condensed state
0.2	1.14	79.9	Liquid
0.3	0.89	77.5	Liquid
0.4	0.63	75.1	Liquid
0.5	0.41	72.0	Liquid
0.6	0.21	67.2	Liquid
0.7	0.09	61.7	Solid

vapor pressures from NIST Chemistry WebBook (Linstrom and Mallard, 2015).

2.2. Volatile supply by impact

During an impact, volatile compounds can be released in the atmosphere by degassing of both impactor and target materials. The amount of released volatiles depends on their compositions as well as on the impact-induced pressure increase. In the present study, we consider only the release of N_2 and CH_4. We consider an impact-induced conversion scenario of NH_3 into N_2 following Sekine et al. (2011). NH_3 is assumed to be the only source of nitrogen, as it is the main N-bearing molecule detected in comets (e.g. Bockelée-Morvan and Crovisier, 2004). In the following, we discuss the abundances and the localization of the chemical species of interest and the parametrization of the conversion of the NH_3 into N_2 in the impactor and in the Titan's icy crust.

2.2.1. Volatile content of the impactor and the target

Assuming a cometary composition for the LHB impactors, NH_3 and CH_4 concentrations vary typically between 0.5% and 1%, 0.1% and 1% relative to bulk water (Bockelée-Morvan and Crovisier, 2004), respectively. In our model, the mass fractions are fixed to 1% for NH_3 and to 0% or 1% for CH_4. Other volatiles such as CO, CO_2, HCN, and H_2S, which are also present in significant abundances in comets and might be converted upon impacts are, for simplicity, not considered in our model.

The composition of the target (i.e. Titan's crust) is determined by the composition of the primordial bricks that formed Titan as well as by chemical differentiation processes subsequent to the accretion of the satellite. Abundance of ammonia in Enceladus' plume (Waite et al., 2009), volatile enrichments in Saturn's atmosphere (Hersant et al., 2008) and models of Saturn's subnebula (e.g. Alibert and Mousis, 2007) suggest that Titan's building blocks contained typically between ~1% and 5% of NH_3. If Titan was undifferentiated at the time of the LHB, NH_3 would be rather uniformly distributed in the interior and the concentration of the outer layer would be equivalent to the primordial value. If Titan was differentiated, NH_3 would be mostly contained in the subsurface ocean owing to the high solubility of ammonia into liquid water (Grasset et al., 2000; Tobie et al., 2012). However, even in this condition, some NH_3 might have been incorporated into the crust by intrusion of ammonia-enriched liquids (Kargel, 1991; Fortes et al., 2007; Choukroun and Grasset, 2010). To encompass various differentiation states for Titan's interior at the time of the LHB, either homogeneous distribution of NH_3 or NH_3-enriched icy crust of 1-to-5-km thickness must be considered, with ammonia mass fractions ranging between 1% and 5%.

2.2.2. Degassing by impact

For a fixed ammonia content, the amount of N_2 that is degassed upon an impact depends on the pressure increase and the volume affected by the impact (see Fig. 1). During an impact, the kinetic energy of the impactor is transferred to the satellite as a shock wave that propagates downward in the target and upward in the projectile. Two domains can be considered (Croft, 1982). The first domain is a truncated spherical zone called an isobaric core. It is a zone below the target surface where the pressure is constant. The burial depth of the isobaric core depends on the impactor velocity. Beyond the isobaric core limit, the shock wave attenuates and pressure decays following a power law, where the exponent also depends on the impactor velocity. The distribution of the impact pressure also depends on the impact angle (e.g. Pierazzo, 2000; Kraus et al., 2011). Here, we consider only vertical impacts, which maximize impact-induced degassing.

The impact-induced pressure increase in the isobaric core can be expressed as (Senshu, 2002):

$$P_{ic} = \frac{\rho_t}{2} v_i \left[C_t + \frac{1}{2} S_t v_i \right], \quad \text{for } r < R_{ic}, \tag{1}$$

where ρ_t is the density of the icy crust, C_t its bulk sound wave velocity, S_t a dimensionless constant, v_i the velocity of the impactor immediately above the impact site in m s^{-1}, r the distance from the center of the isobaric core and R_{ic} is the radius of the isobaric core. Material constants for pure water ice are summarized in Table 2. To account for the deceleration of the impactor owing to the atmospheric drag, the impactor velocity is computed following Svetsov (2000):

$$v_i = v_0 \exp\left(-\frac{\rho_{atm}}{\rho_i} \left(\frac{H}{2r_i} + \frac{4H^2 \rho_{atm}^{1/2}}{3 r_i^2 \rho_i^{1/2}} + \frac{2H^3 \rho_{atm}}{r_i^3 \rho_i} \right) \right), \tag{2}$$

where v_0 is the initial impactor velocity before entering Titan's atmosphere, ρ_{atm} the atmospheric density, ρ_i is the density of the impactor, hereafter considered equal to the density of pure water ice (see Table 2), and H is the atmospheric scale height $H = RT_s/(Mg_T)$ where R is the ideal gas constant, T_s is the surface temperature, M is the mean molar molecular mass of the atmosphere and g_T is Titan's surface gravity (see Table 2). When the velocity computed with Eq. (2) is equal to zero, the impactor is considered to be disintegrated into the atmosphere. Otherwise, the impactor hits the surface with the velocity v_i.

The size of the isobaric core depends on the size of the impactor, the impactor velocity and the physical properties of the compressed material, e.g. porosity or composition (Davison et al., 2010; Barr and Citron, 2011). To characterize the isobaric core radius R_{ic} and burial z_{ic}, we use scaling laws from Kraus et al. (2011), for pure water ice:

$$\log_{10}\left(\frac{R_{ic}}{r_i}\right) = 0.22 - 0.18 \log_{10}(v_i/1000), \tag{3}$$

where r_i is the radius of the impactor. The depth of the burial of the isobaric core z_{ic} is described by:

$$\log_{10}\left(\frac{z_{ic}}{r_i}\right) = -0.17 - 0.09 \log_{10}(v_i/1000). \tag{4}$$

Outside the isobaric core, the pressure decreases with distance (Croft, 1982; Pierazzo and Melosh, 2000):

$$P(r) = P_{ic}\left(\frac{r}{R_{ic}}\right)^{-n}, \quad \text{for } r > R_{ic}, \tag{5}$$

with n being defined as (Kraus et al., 2011):

$$n = 2.9 + 0.47 \log_{10}(v_i/1000). \tag{6}$$

Finally, the total amount of N_2 produced from NH_3 dissociation is determined using the N_2 production efficiency f, taken from Sekine et al. (2011):

$$f = \begin{cases} 0\%, & \text{for } 0 < P < 8 \text{ GPa}, \\ 100 \times \frac{P-8}{23-8}\%, & \text{for } 8 < P < 23 \text{ GPa}, \\ 100\%, & \text{for } P > 23 \text{ GPa}. \end{cases} \tag{7}$$

For the impactor, we assume a uniform pressure equal to the isobaric core pressure. CH_4 contained in the impactor – if any – is assumed to be entirely released into the atmosphere.

2.3. Atmospheric erosion by impact

When entering the atmosphere, the impactor induces an atmospheric escape following two major processes: (i) Along its trajectory through the atmosphere, the impactor forms a rarefied hot

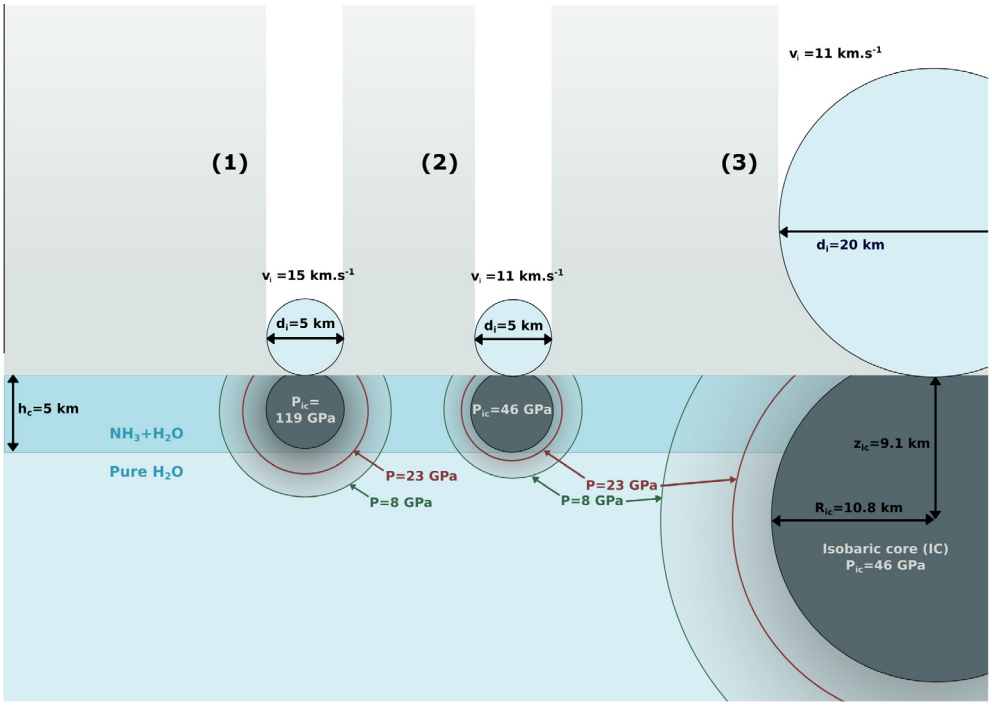

Fig. 1. Schematic representation at scale of the impact pressure field, as considered in this study, for two impactor sizes: $d_i = 5$ km and 20 km and two impactor velocities: $v_i = 11$ km s^{-1} and 15 km s^{-1}, hitting a NH_3-enriched icy layer of thickness h_c. The impact-induced pressure field remains nearly constant in a region beneath the impact site, called isobaric core, characterized by its radius R_{ic} and the depth of its center below the surface, z_{ic}. The comparison between case (1) and case (2) shows the influence of the impact velocity on the impact-induced pressure field: owing to higher impact velocity in case (1), the pressure inside the isobaric core is higher and the decay pressure zone is larger. As shown by comparing case (2) and case (3), a greater impactor increases the size of the isobaric core but does not affect the peak pressure.

Table 2
Physical constants for the numerical modelisation.

Parameter	Name	Value	Reference
R_T	Titan's radius	2575 km	
g_T	Titan's gravity	1.35 m s^{-2}	
v_{esc}	Escape velocity	2639 m s^{-2}	
M_{TA}	Titan's present day atmospheric mass	$9.2 \cdot 10^{18}$ kg	Niemann et al. (2010)
ρ_t	Density of the icy crust (target)	917 kg m^{-3}	Stewart (2005)
ρ_i	Density of the impactor	917 kg m^{-3}	Stewart (2005)
C_t	Bulk sound wave velocity in water ice	3610 m s^{-1}	Stewart (2005)
S_t	Non dimensional constant	0.92	Stewart (2005)

channel with a density that is 1–2 orders of magnitude lower than the ambient air density. The heated gas flow expands outward through this channel and is possibly ejected into space. (ii) When hitting the surface, an expanding plume develops above the impact site, where the gas molecules are also heated and can be accelerated upward to escape the gravity of Titan (see Shuvalov (2009) for more details). We describe these atmospheric erosion processes using the parameterization of Shuvalov (2009), initially built up for the Earth. This parameterization is valid for a broad range of atmospheric densities and impactor sizes compatible with LHB population and it has been adapted here to Titan.

According to hydrodynamic simulations of Shuvalov (2009), the normalized eroded mass χ_a is related to the impact erosion efficiency ξ defined respectively as:

$$\chi_a = \frac{m_a}{m_i}\frac{v_{esc}^2}{v_i^2 - v_{esc}^2}, \tag{8}$$

$$\xi = \frac{d_i^3 \rho_i}{H^3 \rho_{atm}}\frac{(v_i^2 - v_{esc}^2)}{v_{esc}^2}\frac{\rho_t}{(\rho_t + \rho_i)}, \tag{9}$$

with m_a the atmospheric mass escaped during the impact, m_i the impactor mass, d_i the impactor diameter and v_{esc} the escape velocity. By fitting simulation results obtained on a broad range of χ_a and ξ, Shuvalov (2010) proposed the following polynomial relationship:

$$\begin{aligned}\log_{10}(\chi_a) = &-6.375 + 5.239(\log_{10}(\xi)) - 2.121(\log_{10}(\xi))^2 \\ &+ 0.397(\log_{10}(\xi))^3 - 0.037(\log_{10}(\xi))^4 \\ &+ 0.0013(\log_{10}(\xi))^5.\end{aligned} \tag{10}$$

To adapt this parameterization to Titan, we compute ξ, then using Eq. (10) we find χ_a and finally m_a by replacing the parameters appropriate for Titan in each expression. The range of ξ values we encounter during the simulations is comparable to the range explored in Shuvalov (2009). In Fig. 2 we compare the atmospheric erosion obtained with the parametrization of Shuvalov (2009) to the hydrocode simulations of impact-induced erosion of Korycansky and Zahnle (2011), a study devoted to Titan. Fig. 2 presents the total amount of atmosphere that is eroded on Titan following the parameterization of Shuvalov (2009), as a function of the impactor diameter and for three different atmospheric pressures (15 bar, 1.5 bar, 0.01 bar) and an impact velocity of 10 km s^{-1}. For the case with 1.5 bar, we compare our calculations to the values obtained by Korycansky and Zahnle (2011) from hydrocode simulations. The parameterization of Shuvalov (2009) consider an eroded mass averaged over the impact angle. When compared to the simulations of Korycansky and Zahnle (2011) for fixed impact angle of 45° and 75°, and impactor diameters of 10 km, the atmospheric mass loss is comparable for the two studies. For larger impactors, there are some discrepancies between the two models, but the magnitudes remain comparable. Fig. 2 also illustrates that the erosion decreases rapidly with decreasing impactor sizes. This results in a more efficient deceleration of the smallest impactors by atmospheric drag, leading to a smaller

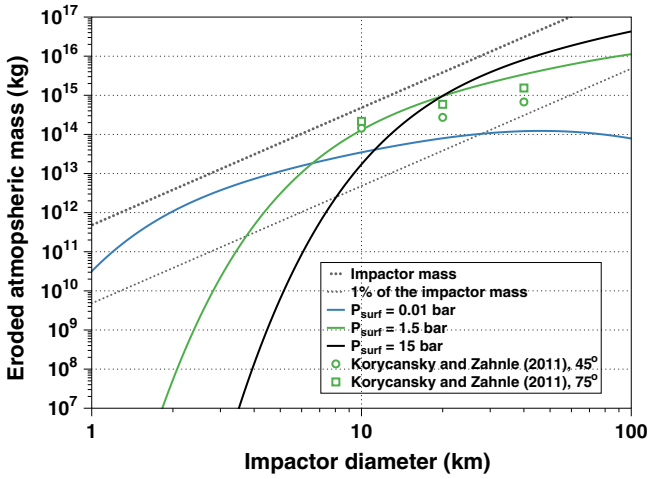

Fig. 2. Eroded atmospheric mass as a function of the impactor diameter for the model of Shuvalov (2009, 2010), for a v_0 = 10 km s^{-1}. Korycansky and Zahnle (2011) values are given for a present-day Titan's atmosphere, for a 2D plane-polar geometry calculations on a 800 × 1280 grid and v_0 = 10 km s^{-1}.

impact-induced plume. For impactors larger than ~50 km, the eroded atmospheric mass is limited by an asymptotic value corresponding to the atmospheric mass above the plane tangent to the satellite's surface.

2.4. Evolution by multi-impact

We implement the parametrizations described above into a multi-impact approach, using an impactor flux characteristic of the LHB event. Then, we integrate the evolution of the volatile reservoir throughout the LHB-era.

2.4.1. Multi-impact approach

To generate our LHB impactor population, we carried out a Monte-Carlo calculation. Sampling procedures for the impactor diameter, velocity and coordinates of the impact sites are adapted from Zahnle (2001) and Zahnle et al. (2003). Impactor diameters are chosen from a size distribution characteristic of the LHB and scaled to match the crater record on Iapetus (Charnoz et al., 2009). The velocity distribution follows a Gaussian distribution (Korycansky and Zahnle, 2011). Assuming an isotropic impact flux, the latitude and longitude of the impact site are randomly drawn. Parameters used to define the distributions are summarized in Table 3.

To limit the computation time, we assume a lower limit of 1 m for impactor diameters. We also prescribe an upper limit of 100 km. Above this value, the validity of the scaling laws used here becomes questionable because they do not include physical parameters that may influence the impact processes at large scales, such as the curvature of the satellite and its internal structure (Louzada and Stewart, 2009; Bruesch and Asphaug, 2004).

Table 3
Impactor sampling parameters. The Gaussian distribution of the impactor velocity v_0 is taken from Korycansky and Zahnle (2005).

Parameter	Distribution	Interval of sampling
d_i – impactor diameter	From Charnoz et al. (2009)	1 m to 100 km
v_0 – initial velocity of the impactor	Gaussian	11.3 km s^{-1} ± 4 km s^{-1} (1σ)
λ – longitude	Linear	0–360°
ϕ – latitude	cos(ϕ)	−90° to 90°

For each impact, we compute the velocity decrease due to atmospheric drag using Eq. (2), we determine the impact pressure field and corresponding degassing using Eqs. (1), (5) and (7) and the atmospheric mass loss using Eqs. (8)–(10). The new atmospheric equilibrium as well as the crustal NH_3 distribution are re-evaluated after each impact. The simulations are stopped when the total mass of impactors delivered to Titan reaches a value of ~3 × 10^{20} kg (Barr et al., 2010).

2.4.2. Subsurface distribution and numerical evolution of NH_3 reservoirs

The distribution of NH_3 at the time of the LHB is mostly governed by Titan's degree of differentiation, which is strongly related to its accretional history (e.g. Monteux et al., 2014). NH_3 could be either homogeneously distributed within an undifferentiated interior or mostly located in a chemically differentiated crust. To explore different possibilities, we consider different initial NH_3 distributions and simplified evolutions of NH_3 reservoirs summarized in the three following cases:

- Case A: we consider a uniform and constant distribution of NH_3 all along the simulation. This simplified case considers an infinite reservoir of NH_3.
- Case B: the reservoir is assumed initially uniform throughout a given thickness (up to 100 km), and the remaining fraction of ammonia is reevaluated after each impact as a function of depth. This one-dimensional approach allows us to take into account the averaged progressive depletion in ammonia as a function of depth during the simulation.
- Case C: a reservoir of limited depth (less than 5 km) is modeled as a spherical shell with a 0.1° spatial resolution in latitude and longitude. The spatial distribution of NH_3 is re-evaluated in each cell after an impact, assuming that the lost fraction of NH_3 is uniform over the cell volume. This two-dimensional approach allows us to record the local depletion in NH_3, but do not take into account the variations with depth. Fig. 3 shows an example of such distribution in the end of the simulation (no. 14, see Table 5). A full 3D evolution of the reservoir, including lateral and depth variation would be too much CPU time and therefore has not been considered here.

Case A considering an infinite NH_3 reservoir is used only to compare our results to those of Sekine et al. (2011). Case B can be used either for undifferentiated or differentiated interior, depending on the assumed thickness of NH_3 reservoir. Case C is valid only for relatively thin NH_3 reservoir ($\leq$5 km), and therefore represents a differentiated interior case with a crust enriched in NH_3. For these three cases, the volume affected by impact is computed from Eqs. (1), (3), (4) and (5). The only difference between these three cases concerns the evolution of NH_3 distribution for each reservoir after an impact: no NH_3 depletion in Titan's interior for the case A, NH_3 depletion with depth for the case B and NH_3 depletion at Titan's surface, as displayed for case C in Fig. 3(a).

As the surface and atmospheric conditions on early Titan are unconstrained, we performed numerous simulations (49 in total) to cover a wide range of possible parameter values, such as the surface albedo, the size and concentration of crustal NH_3 reservoir, and the mass and composition of the pre-LHB atmosphere (see Table 4). For the surface albedo, we considered values ranging between 0.1 and 0.7. Except Enceladus and Triton, most of the icy moons has albedos comprised between 0.1 and 0.6. The present-day surface albedo on Titan is estimated between 0.1 and 0.2, its dark surface being mostly the consequences of deposition of photochemically-produced organics. In absence of methane in the past, no photochemical byproducts would accumulate, and

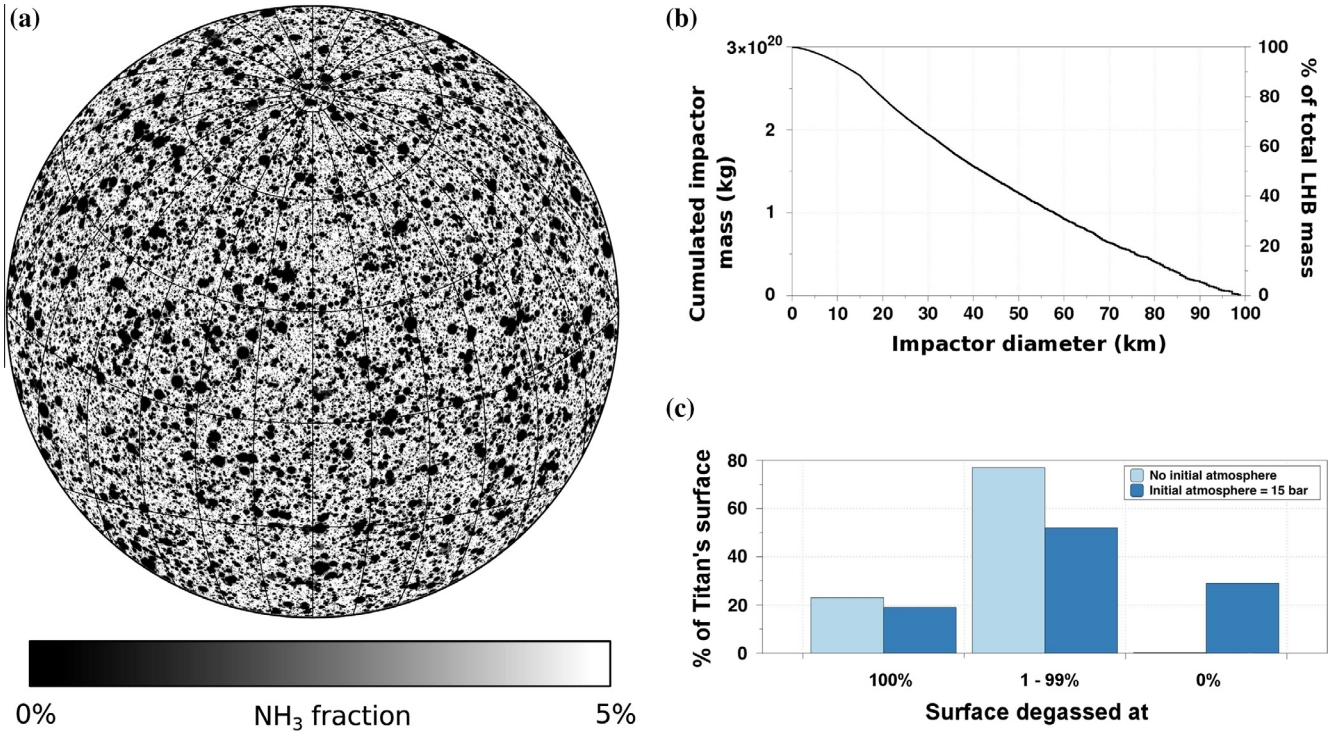

Fig. 3. (a) Distribution of the NH_3 at Titan's surface after the simulation no. 14 in Table 5: no initial atmosphere was considered here; (b) distribution of cumulated impact sizes during the LHB for the same simulation; and (c) distribution of affected terrains after the LHB for the map (a) and the simulation no. 26 in Table 5.

Table 4
List of parameters explored in this study and the corresponding range of values.

Parameter	Symbol	Range of values explored in this study
Surface albedo	A_s	0.1–0.7
Initial atmospheric mass	M^A_{ini}	0–10 M_{TA}
CH_4 fraction in the impactor	$X^i_{CH_4}$	0% or 1%
Initial CH_4 fraction in the atmosphere	$X^A_{CH_4}$	0–10%
Mass concentration of NH_3 in the icy crust	X_{NH_3}	1–5%
Mass concentration of NH_3 in the impactor	$X^i_{NH_3}$	1%
Thickness of the NH_3-enriched icy layer	h_c	∞ for case A 5–50 km for case B 1–5 km for case C

therefore its surface may have been much brighter, that's why we considered values as high as 0.7. We also investigated different scenarios for NH_3 enrichment in the outer layers corresponding to different differentiation state at the time of LHB, with ammonia mass fraction varying between 1% and 5%. As initial conditions, we considered either no atmosphere or the presence of an pre-LHB atmosphere with a mass up to 10 times present-day Titan's atmospheric mass and with methane mass fraction up to 10%. The corresponding results are presented in Table 5 for simulations with no preexisting atmosphere and in Table 6 for the simulations with pre-LHB atmospheres.

3. Results

In the following, we first present the atmospheric mass balances between atmospheric loss and supply for individual impacts. Then we investigate the possible emergence of an atmosphere from an initially air-less body and after the evolution of initially massive atmosphere for multiple impacts characteristic of the LHB.

3.1. Balance between atmospheric loss and supply

Fig. 4 presents the balance between N_2 crustal degassing and atmospheric erosion for individual impacts as a function of the impactor diameter for three different atmospheric pressures (Fig. 4a), impactor velocities (Fig. 4b) and crustal reservoirs (Fig. 4c). Our calculations show that the maximal erosion rate is obtained for impactor diameters of 2.5, 12 and 30 km for atmospheric pressures of 0.015, 1.5 and 15 bars, respectively, explaining the minima in the N_2 balance (Fig. 4a).

For impact diameters smaller than these optimal values, the efficiency of erosion rapidly decays, as the balance is mostly controlled by the degassing efficiency. Owing to both decrease in atmospheric erosion and increase in N_2 degassing relatively to the impactor mass, the balance becomes positive for diameters lower than 1.3, 6, and 13 km for atmospheric pressures of 0.015, 1.5 and 15 bars, respectively (see Fig. 4 a). However, as impactors smaller than 13 km represent only 11% of the total mass of the LHB impact flux, erosion should prevail.

For even smaller impactor diameters, the atmospheric drag significantly decelerates the impactors leading to reduced impactor velocities and hence to lower shock pressures and degassing rates. Below diameters of 1.2 and 6 km for surface pressures of 1.5 and 15 bars respectively (Fig. 4a), the atmospheric balance is zero because both degassing and impact-induced erosion become negligible. As decreasing impactor velocity leads to a lower degassing efficiency and lower atmospheric erosion, the atmospheric balance curves in Fig. 4b are more and more flattened with decreasing velocity and the minima and maxima shift toward larger impactors. Naturally, as shown in Fig. 4c the balance is positive for a wider range of diameters if larger reservoirs of NH_3 are considered.

Table 5
List of parameters and results for an initially air-less Titan simulations. M_A is the final atmospheric mass, M_C is the final mass of condensed volatiles at Titan's surface, M_{TA} is the present-day Titan's atmospheric mass.

No.	A_s	CH_4	NH_3 reservoir	X_{NH_3} (%)	h_c (km)	M_A/M_{TA} (% of CH_4)	M_C/M_{TA} (% of CH_4)
1	0.2	no CH_4	Case A	1	–	0.06	0
2	0.2	no CH_4	Case A	1.5	–	0.14	0
3	0.2	no CH_4	Case A	2	–	0.24	0
4	0.3	no CH_4	Case A	2	–	0.31	0
5	0.4	no CH_4	Case A	2	–	0.30	0
6	0.5	no CH_4	Case A	2	–	0.27	0.1 (liquid)
7	0.6	no CH_4	Case A	2	–	0.14	0.95 (liquid)
8	0.7	no CH_4	Case A	2	–	0.06	1.65 (solid)
9	0.2	1% in the impactor	Case B	5	5	0.03 (26%)	0
10	0.2	no CH_4	Case B	1	50	0.03	0
11	0.2	no CH_4	Case B	1.5	50	0.06	0
12	0.2	no CH_4	Case B	2	50	0.10	0
13	0.5	no CH_4	Case B	2	50	0.14	0
14	0.7	no CH_4	Case B	2	50	0.06	0.91 (solid)
15	0.2	1% in the impactor	Case B	5	50	0.93 (6%)	0
16	0.2	no CH_4	Case B	1	100	0.04	0
17	0.2	no CH_4	Case B	1.5	100	0.08	0
18	0.2	no CH_4	Case B	2	100	0.17	0
19	0.2	1% in the impactor	Case B	5	100	1.43 (5%)	0
20	0.2	no CH_4	Case C	5	5	0.02	0
21	0.2	no CH_4	Case C	2	5	0.006	0
22	0.2	1% in the impactor	Case C	5	5	0.03 (24%)	0
23	0.3	1% in the impactor	Case C	5	5	0.04 (27%)	0
24	0.5	1% in the impactor	Case C	5	5	0.03 (16%)	0.15 (94%, liquid)
25	0.5	no CH_4	Case C	5	5	0.02	0
26	0.7	no CH_4	Case C	5	5	0.03	0
27	0.7	no CH_4	Case C	2	5	0.01	0

Table 6
List of parameters and results for simulations with an initial atmosphere. $X^i_{CH_4}$ and $X^A_{CH_4}$ represent the bulk fraction of CH_4 in the impactor and in the initial atmosphere, respectively. In all simulations the NH_3 reservoir is the one described by the case C, with X_{NH_3} = 5% and h_c = 5 km.

No.	A_s	M_{ini}/M_{TA}	$X^i_{CH_4}$ (%)	$X^A_{CH_4}$ (%)	M_A/M_{TA} (% of CH_4)	M_C/M_{TA} (% of CH_4)
28	0.2	1	1	5	0.03 (24%)	0
29	0.2	1	0	0	0.02	0
30	0.2	2	1	5	0.04 (39%)	0.05 (97%)
31	0.2	2	0	0	0.02	0
32	0.2	5	1	5	0.18 (9%)	0.17 (81%)
33	0.2	5	0	0	0.77	1.27
34	0.2	7	1	5	0.76 (5%)	0.15 (59%)
35	0.2	8	1	5	1.42 (11%)	0
36	0.2	10	1	5	2.91 (9%)	0
37	0.2	10	0	0	0.8	6.25
38	0.1	1	1	5	0.03 (25%)	0
39	0.3	1	1	5	0.04 (32%)	0.8 (97%)
40	0.3	5	1	5	0.19 (5%)	0.22 (74%)
41	0.3	1	0	0	0.02	0
42	0.5	1	1	5	0.03 (17%)	0.25 (94%)
43	0.5	5	1	5	0.17 (0.05%)	0.31 (67%)
44	0.5	1	0	0	0.03	0
45	0.7	1	0	0	0.06	0.8
46	0.2	1	1	10	0.04 (62%)	0
47	0.2	2	1	10	0.04 (35%)	0.09 (97%)
48	0.2	5	1	10	0.15 (10%)	0.23 (85%)
49	0.2	10	1	10	2.75 (13%)	0

Nevertheless even in the most optimistic case (Case A, X_{NH_3} = 5%), a negative balance is obtained for diameters from 6.5 to 27 km.

3.2. Simulations with no initial atmosphere

In the following set of simulations, we assume an initially air-less Titan with various NH_3 reservoirs and impactors containing 1% of NH_3 and either 0% or 1% of CH_4. All of the simulations with no initial atmosphere are presented in Table 5. Fig. 5 shows the influence of the albedo and NH_3 reservoir on the accumulation of volatiles on Titan's surface. For Case A with X_{NH_3} = 2% (Fig. 5a and b), the total mass of N_2 at the end of the simulations never exceed 0.4 M_{TA} as long as the albedos remains below 0.5. For A_s = 0.5, even if the saturation pressure is reached and N_2 starts condensing at half of the simulation (Fig. 5a), the accumulation of volatiles at Titan's surface remains limited. The effect of N_2 accumulation at the surface becomes important only for $A_s \geqslant 0.6$, as N_2 condensation starts directly at the beginning of the simulations. For this

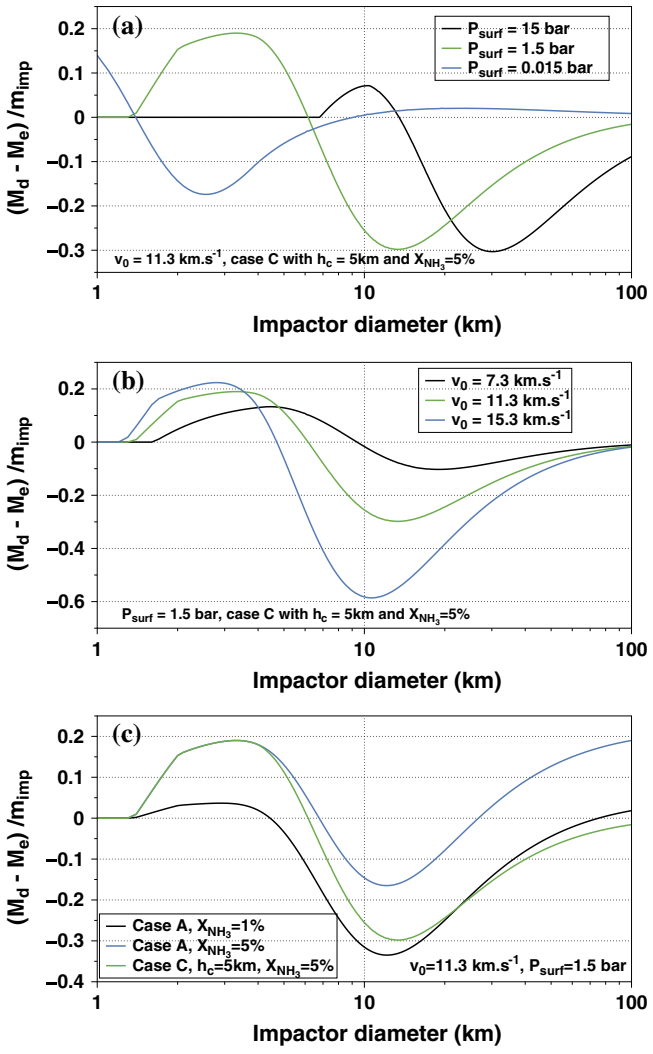

Fig. 4. Balance between the mass of N_2 degassed from NH_3 crustal reservoir by impact (M_d) and the atmospheric mass lost by impact-induced erosion (M_e), normalized by the impactor mass (m_{imp}), as a function of impactor diameters for three different values of (a) surface pressures, (b) impact velocities before entering the atmosphere, (c) initial reservoirs of NH_3. X_{NH_3} is the mass fraction of the NH_3 contained in the NH_3-enriched surface layer and h_c is the thickness of this layer. For comparison, in all three figures, the green curve has the same parameters. (For interpretation of the references to color in this figure legend, the reader is referred to the web version of this article.)

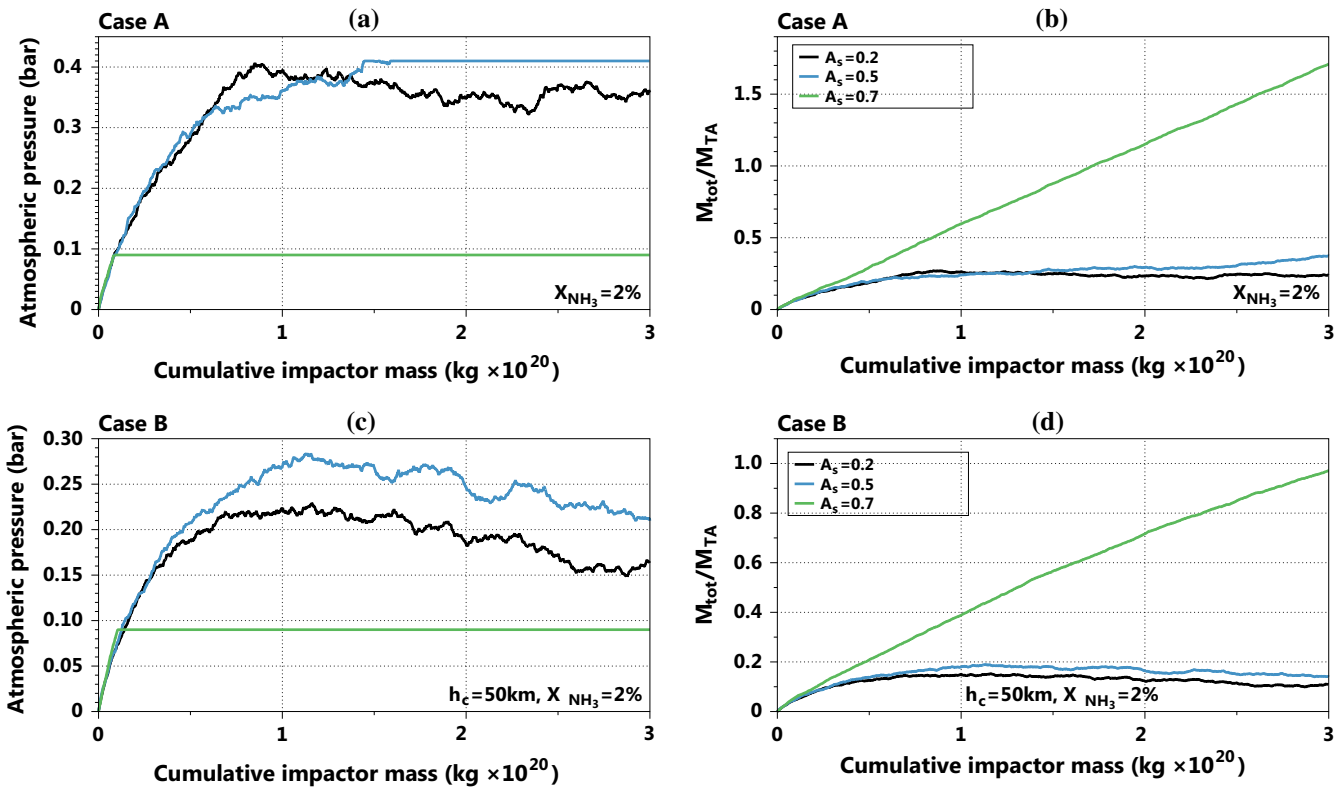

Fig. 5. Evolution of atmospheric pressure (a, c) and M_{tot}, the total mass of N_2 in the atmosphere and condensed at the surface (b, d) during the LHB for an initially air-less Titan for cases A (infinite reservoir; a–b) and B (h_c = 50 km, c–d) with ammonia fraction X_{NH_3} of 2%, and three different values of surface albedos (A_S = 0.2, 0.5 and 0.7). Simulations displayed on panels a and b correspond to simulations nos. 3, 6 and 8 in Table 5, on panels c and d to simulations nos. 12, 13 and 14, respectively.

most favorable case where no depletion of the crustal NH_3 reservoir is considered, the mass of N_2 accumulated at the end of the simulation, mostly in the form of N_2 ices, can exceed 1.5 M_{TA}. This result is comparable to the result obtained by Sekine et al. (2011) for a cold Titan, an infinite reservoir of crustal NH_3 (2%), and impactor radius of 20 km.

For simulations including a progressive depletion of NH_3 in the outer layer owing to successive impacts (Case B), an atmospheric mass comparable to the present one is obtained only if the enriched layer is at least 50 km thick. For A_S = 0.7, ~2% of ammonia in this layer is sufficient to generate nearly 1 M_{TA} (simulation no. 14), while for A_S = 0.2, 5% of ammonia is needed (simulations nos. 15 and 19).

For more realistic thicknesses of ammonia-enriched crust (h_c = 5 km and X_{NH_3} = 5%), the final atmospheric pressures are considerably lower (see Figs. 5 and 6), and the accumulated volatile mass barely exceeds 0.04 M_{TA} (see Table 5, simulation nos. 20, 21, 25, 26 and 27). Adding the contribution of methane brought by the impactors has only a moderate effect on the atmosphere evolution (simulations nos. 22, 23 and 24 in Table 5).

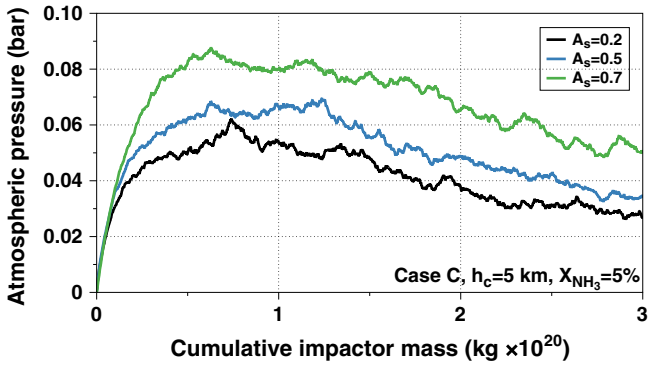

Fig. 6. Evolution of the atmospheric pressure at Titan's surface during the LHB, for an initially air-less Titan, the case C and 0.7, 0.5 and 0.2 albedos of surface (simulations nos. 20, 25, 26 from Table 5).

3.3. Simulations with an initial atmosphere

In the following set of simulations, we consider preexisting N_2–CH_4 atmospheres with composition between 0% and 10% of CH_4 and masses ranging from 1 to 10 present-day Titan's atmospheric mass (M_{TA}), at the beginning of the LHB. Fig. 7 shows that an atmosphere with an initial mass of 1 M_{TA} is severely eroded by impacts: after half of the LHB mass has accumulated, about 85% of the initial atmosphere is lost. For a surface albedo of 0.2, and initial temperature of 90 K, all volatiles are in the gaseous phase. The surface liquid condensates when the surface pressure and temperature reach values of 1.08 bar and 87 K, respectively. At its maximum, 24% of the remaining volatiles are condensed at the surface. Most of the condensed liquids is composed of CH_4 (67%), while the atmosphere is dominated by N_2 (95%). After this maximum, the liquid reservoir progressively evaporates as the atmosphere is continuously eroded by impacts.

For albedos of 0.1, 0.2, 0.3 and 0.5, and similar atmospheric parameters, comparable atmospheric evolutions are obtained (see Fig. 8). The difference between these simulations (nos. 38, 39 and 42 in Table 6) is the mass of volatiles condensed at the surface. For increasing albedos, the condensed volatile reservoir tends to remain longer at the surface of the satellite. For a 0.1 surface albedo, 1.8 × 10^{20} kg of impactors are sufficient to erode the atmosphere and evaporate the surface liquids. For surface albedo of 0.3,

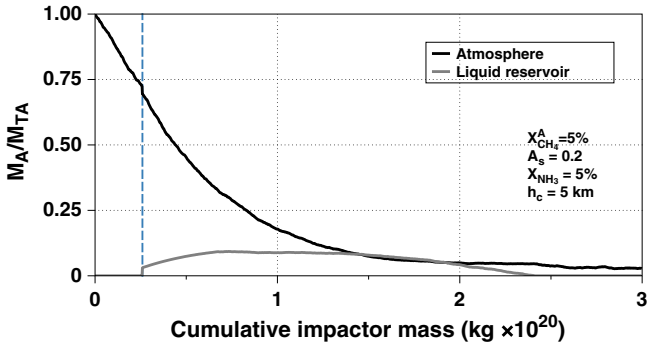

Fig. 7. Evolution of the atmospheric and condensed volatile mass during the LHB for an initial atmospheric mass equivalent to the present-day Titan's atmospheric mass (simulation no. 28 in Table 6). The vertical line marks the beginning of the condensation of volatiles at the surface.

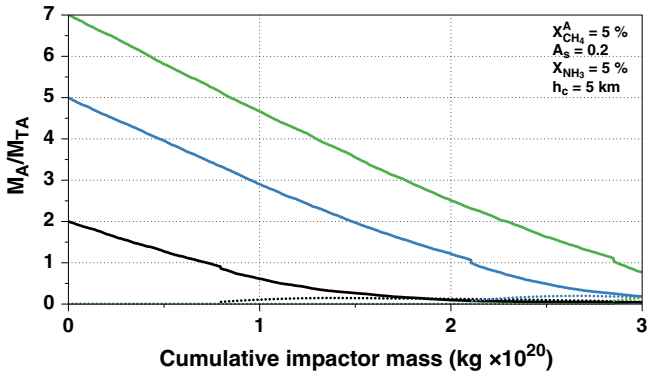

Fig. 9. Evolution of reservoirs of volatile (atmospheric + condensed masses) during the LHB for several initial atmospheric masses. Solid lines represent the evolution of atmospheric reservoirs, while dotted lines represent the evolution of the liquid surface reservoir.

the surface liquids are maintained during the LHB, while for the simulation with an albedo of 0.5 the surface condensed reservoir keeps increasing all along the simulation.

A strong erosion of the atmosphere during the LHB is observed for all initial atmospheric masses tested in this study. Whatever the initial atmospheric mass, when surface pressure reaches ~1.1 bar, volatiles condense at the surface in the form of a liquid layer (Fig. 9). Liquid reservoirs are mostly composed of CH_4, while the atmospheric compositions are dominated by N_2. For the set of simulations shown in Fig. 9, an atmosphere mass comparable to the present-day mass is preserved only if the initial atmospheric mass is about 7 times the present-day one.

In Fig. 10 we compare the evolution of volatile reservoirs for different initial atmospheric CH_4 fractions. Evolutions of the volatile reservoirs for initial 5% and 10% of CH_4 atmosphere are similar. They only differ in the initiation times of the volatiles condensation. Pure N_2 reservoir experiences less severe erosion. Unlike the previous cases, the liquids at the surface in the N_2 pure case are conserved and the atmospheric surface pressure remains constant all along the simulation. As the atmospheric surface pressure is lower than the atmospheric surface pressure of N_2–CH_4 cases, the erosion is less efficient (see Fig. 4(a)). As a result, a less massive initial volatile reservoir is required to lead to a volatile mass comparable to a present-day one.

Fig. 11 presents an extreme case with a very high albedo (A_s = 0.7) and without CH_4, where N_2 remains frozen during the entire LHB. In these conditions, Titan's surface remains in the frozen state during the entire simulation. Due to the low surface pressure, the impact-induced atmospheric erosion is much lower and the atmosphere is globally maintained trough the LHB.

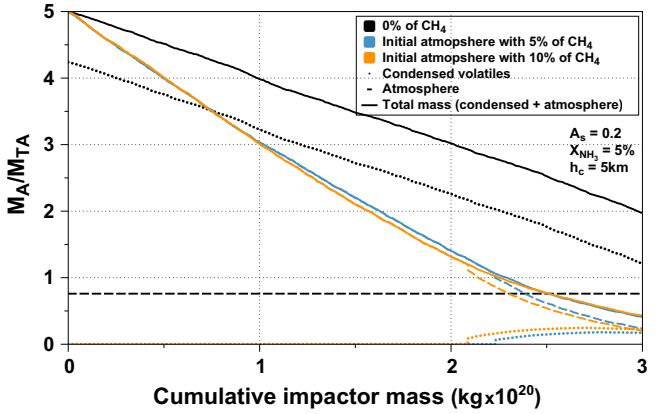

Fig. 10. Evolution of the volatile reservoirs for an initial atmosphere ×5 M_{TA}, for three different CH_4 abundances, for a surface albedo of 0.2, and a case C reservoir with X_{NH_3} = 5% and h_c = 5 km.

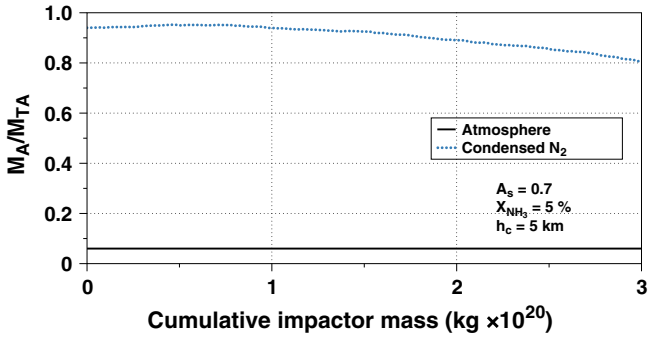

Fig. 11. Evolution of the atmospheric and condensed N_2 during the LHB for a surface albedo of 0.7, for an initial N_2 mass equivalent to a present-day Titan's atmospheric mass.

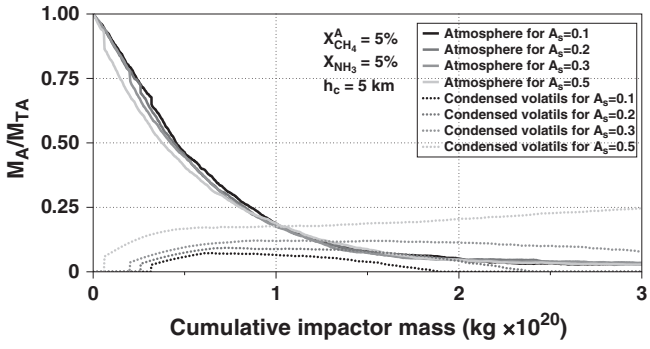

Fig. 8. Evolution of volatiles masses for 0.1, 0.2, 0.3 and 0.5 surface albedos.

4. Discussion

Following the scenario proposed by Sekine et al. (2011), we tested the possible formation of a N_2-rich atmosphere during the LHB by impact-induced conversion and outgassing of a NH_3 crustal reservoir. To expand the study of Sekine et al. (2011) that considered constant impactor sizes equal to either 20 or 30 km, we considered in our study a distribution of impactor sizes and velocities representative of LHB. To estimate the degassed mass in the impacted crust, we used the scaling laws of Kraus et al. (2011)

derived from hydrocode simulations using a new 5-phase model equation of state for H_2O (Stewart, 2005). Using these scaling laws, we found that an impactor of 20 or 30 km in radius hitting the surface at a velocity of 11 km s^{-1} degases a crustal volume equal to about five times the impactor mass, while Sekine et al. (2011) predicted a factor of eight for similar conditions. Despite these differences, we obtained results relatively similar to those of Sekine et al. (2011) for initially airless Titan with a high surface albedo ($A_S \geqslant 0.7$) and a constant ammonia fraction (~2%) in the interior (Case A). By taking into account the progressive ammonia depletion in the outer layer owing to successive impacts (Case B), which was not considered in Sekine et al. (2011), we confirmed that, for high surface albedo ($A_S \geqslant 0.7$), a N_2 mass equivalent to the present-day mass may be generated if the outer layer contained about 2% of ammonia over a thickness of at least 50 km. For lower albedos, equivalent generated masses require higher ammonia content: for example, for $A_S = 0.2$, an ammonia content of 5% is needed. Having a few percents of ammonia over a thickness of 50–100 km might be possible only if Titan was undifferentiated at the time of LHB, which requires a cold accretion. If the outer layer melts during accretion, which is suggested by thermo-accretional modeling (Monteux et al., 2014), most of the ammonia initially incorporated in Titan would migrate in the internal ocean, leaving the outer ice shell depleted in ammonia. Ammonia might be reinjected in a secondary crust formed by cryovolcanic activity (Choukroun and Grasset, 2010), however it seems unlikely that this enriched crust exceeds 5–10 km. In case of a crust enriched in ammonia (Case C), we showed that no atmosphere can be generated and that preexisting atmospheres are severely eroded by impacts during the LHB, independently of the initial atmospheric masses or methane fractions. Our simulations showed that the impact-induced erosion appears to be a controlling process in the evolution of Titan's atmosphere. Our results rely on the parameterization of Shuvalov (2009), dedicated to Earth conditions and where the impactor diameters range between 1 and 30 km. As suggested by the comparison with the simulations of Korycansky and Zahnle (2011) dedicated to Titan's atmosphere (see Fig. 2), it is possible that the erosion efficiency predicted by Shuvalov's scaling laws is overestimated for larger impactors. To test the sensitivity of our model to the erosion parameterization, we arbitrarily divided the erosion efficiency by 2, 3 and 5, independently of impactor diameters. These tests showed that the erosion can be counterbalanced if the erosion efficiency is divided by three and if the most favorable degassing scenario (case C, $X_{NH_3} = 5\%$, $h_c = 5$ km) is considered. These tests indicate that our results may change only if there is a significant overestimation of the erosion efficiency by Shuvalov (2009). A lower impactor flux may also limit the atmospheric erosion. It was suggested by Nimmo and Korycansky (2012) that the total impactor mass delivered during the LHB could be ~10 times smaller than the value used here, estimated from the Nice model (Charnoz et al., 2009). Obviously in these conditions, the erosion will be strongly reduced for preexisting massive atmosphere, reducing the requirement on the mass for the primitive atmosphere. However, it would still be impossible to generate a massive atmosphere.

Impact-induced erosion of volatiles condensed at the surface may be another source of uncertainties. Indeed, in our approach we do not consider this process. For the simulation where the initial atmosphere is seven times more massive than the present day atmosphere, the fraction of volatiles in the liquid phase never exceeds 16%. Therefore, its influence on the surface erosion remains negligible. Surface liquid fractions may play a non negligible role in simulations with moderate initial atmospheric masses (1–5 times the present-day Titan's atmospheric mass, see Figs. 7 and 9). In these cases, we do not preserve a massive atmosphere at the end of the simulations. Including the surface erosion will only enhance the volatile loss, therefore it should not change our conclusions. In cases of a high surface albedo (>0.7), most of the atmospheric mass condenses at the surface and is preserved through the LHB, because low atmospheric pressure leads to a lower impact-induced atmospheric erosion. These are the only cases where the surface erosion could have a non-negligible influence on the volatile mass at Titan's surface and this result has to be examined with caution. Indeed, the study of Nimmo and Korycansky (2012) showed that the surface erosion by impact may eject a non negligible mass of surface material during the LHB. Therefore, even in the favorable case with a high surface albedo, a significant fraction of condensed N_2 may be still lost by successive impacts.

Another critical aspect in the evolution of the atmospheric balance is the volatile mass supplied to the atmosphere during the impact. In our study we consider only the methane supplied by the impactor, no crustal CH_4 degassing is estimated. Nevertheless, methane could be present in a significant amount in the form of clathrates hydrates (Osegovic and Max, 2005; Tobie et al., 2006, 2012). The pressures and temperatures reached during the high-velocity impacts are high enough to destabilize the methane clathrate and, hence, to release CH_4 to Titan's atmosphere. Our simulations show that Titan's surface layers are significantly affected by the impacts at the end of the LHB. An important fraction of methane that might be stored in the crust should be released during the LHB. The non-degassed terrains represent 30% of Titan's surface in the case of an initial atmosphere ten times more massive than the present-day Titan's atmosphere and only 0.02% for an initially air-less body (see Fig. 3c). Even though the destabilization of CH_4 clathrate reservoir is different from crustal degassing implemented here, we expect that a large part of CH_4 should be degassed by impact during the LHB. If a clathrate-rich crust was already formed at the time of the LHB, most of this crustal reservoir would be destabilized leading to accumulation of several hundred of meters of liquid methane at the surface. Other gas compounds present in comets or in the crust in similar or higher proportions than NH_3 and CH_4, in particular CO or CO_2, could also affect the atmospheric balance. The low CO abundance in today's atmosphere (Baines et al., 2006; de Kok et al., 2007) suggests that either a small amount of CO was brought to Titan, which seems in contradiction with cometary composition, or that a very efficient process (still to be determined) destroyed most of the primordial CO. CO_2 brought by the LHB impactors, degassed from the crust or possibly converted from CO during impacts (Ishimaru et al., 2011), will remain in the condensed phase and should therefore not affect significantly the radiative balance. However, further studies are needed to evaluate the influence of these chemical species and their fate during the LHB era.

As shown in Section 3.1, the atmospheric mass balance is also sensitive to the impactor diameter, and therefore our results depend on the assumed size distribution. Here, we have used the size distribution of Charnoz et al. (2009) relying on the Nice model and scaled to Iapetus' crater distribution. Considering the 1.5 bar atmosphere case from Fig. 4 a. and using this size distribution, only 0.03% of the total mass is brought by impactors smaller than 6 km, that is the critical impactor diameter above which the atmospheric mass balance become negative. However, this fraction should be at least 50% in order to limit erosion and generate an atmosphere. Increasing this tendency would imply a significant change in the assumed size distribution. Secondary debris resulting from a giant impact in the system of Saturn (e.g. Levison et al., 2011; Asphaug and Reufer, 2013) could possibly provide a source of small impactors (Nakamura and Fujiwara, 1991). As suggested by Farinella et al. (1997) and Dobrovolskis and Lissauer (2004), Hyperion may have resulted from such giant impacts. The total mass of debris

resulting from proto-Hyperion disruption and possibly re-accreted by Titan is evaluated ranging between $\sim 10^{19}$ and several times 10^{20} kg, which is comparable to the estimated LHB cumulative mass. These debris have a significantly lower velocity (<4 km s^{-1}) (Farinella et al., 1997) resulting in less atmospheric erosion but also limited degassing as the impact pressure barely exceeds 8 GPa (obtained for a velocity of 3.4 km s^{-1}). Large impactors might also be more numerous than assumed here, and have more complex effects than what we considered in the present model. As shown by Zahnle et al. (2014), impactors larger than $d_i > 13$ km with an impact velocity of 11 km s^{-1} may completely break the ice crust, resulting in a major water flooding event and strong degassing from volatiles contained in the ocean (Tobie et al., 2012). Such catastrophic events would strongly affect the atmospheric balance, possibly leading to the formation of the atmosphere. This suggests that a few large impact events may be more favorable to the generation of an atmosphere than a continuous flux of kilometric-size impactors. A full approach, solving consistently the impact dynamics and the coupling between the subsurface ocean, ice shell and atmosphere, is required to investigate the consequences of such large impacts on Titan's atmospheric balance.

5. Conclusion

We investigate the supply and loss of N_2 and CH_4 by impacts on Titan. We show that an atmosphere with a mass equivalent to the present-day is unlikely to form during the LHB era. We investigate the sensitivity of the emergence of Titan's atmosphere on the NH_3 crustal reservoir and on the surface conditions. We show that a N_2-rich atmosphere can be generated during the LHB only if Titan contained a few percents of ammonia over at least 50 km beneath its surface, implying an undifferentiated interior. We also show that preexisting N_2 atmospheric mass equivalent to the present-day atmosphere mass could survive to the LHB only for very high surface albedos resulting in very low atmospheric pressures and if the impact-induced loss of N_2 condensed at the surface is limited. Further modeling efforts are needed to understand the coupled evolution of crustal, surface and atmospheric reservoir of N-bearing species and the consequence for the emergence of atmosphere on early Titan.

Except for high surface albedos ($A_S \geqslant 0.7$) where most of the released volatiles are frozen at the surface, the high-velocity impacts during the LHB led to a strong atmospheric erosion. The atmospheric loss by impact is controlled by the equilibrium atmospheric pressure, which depends mostly on the surface albedo and the fraction of methane. For albedo of 0.2 and initial methane fraction between 0% and 5% in the atmosphere the pre-LHB atmosphere should be between ~5 and 7 times more massive than at present to sustain an atmosphere equivalent to the present-day one.

If Titan was differentiated at the time of the LHB and had a surface albedo lower than 0.6, our results imply that either a massive atmosphere was formed on Titan during its accretion or that the nitrogen-rich atmosphere was generated after the LHB. The first hypothesis involves a warm accretion with an efficient conversion of NH_3 into N_2, due to either photochemistry (Atreya et al., 1978) or impact-induced chemistry (McKay et al., 1988; Ishimaru et al., 2011). This is likely that a massive atmosphere interacting with a water ocean formed at the end of accretion due to cumulative impact heating (Monteux et al., 2014). However it is still unclear if the conditions to produce several bars of N_2 from NH_3 or other N-bearing molecules was met. The second hypothesis implies an efficient outgassing process and an internal conversion of N-bearing compounds into N_2, as suggested by (Glein et al., 2009; Tobie et al., 2012). Here again, though outgassing is possible, the internal production of N_2 remains unconstrained. Further studies will be needed to constrain these two possible scenarios.

Acknowledgments

We thank two anonymous reviewers, whose comments improved the manuscript. The research leading to these results has received funding from the European Research Council under the European Community's Seventh Framework Programme (FP7/2007-2013 Grant Agreement no. 259285). J. Monteux was funded by Agence Nationale de Recherche (Accretis decision ANR-10-PDOC-001-01). B. Charnay acknowledges support from an appointment to the NASA Postdoctoral Program at NAI Virtual Planetary Laboratory, administered by Oak Ridge Affiliated Universities.

References

Alibert, Y., Mousis, O., 2007. Formation of Titan in Saturn's subnebula: Constraints from Huygens probe measurements. Astron. Astrophys. 1060, 1051–1060.
Asphaug, E., Reufer, A., 2013. Late origin of the Saturn system. Icarus 223, 544–565.
Atreya, S.K., Donahue, T., Kuhn, W., 1978. Evolution of a nitrogen atmosphere on Titan. Science 201, 611–613.
Atreya, S.K., Lorenz, R.D., Waite, J.H., 2009. Volatile origin and cycles: Nitrogen and methane. In: Titan from Cassini-Huygens, pp. 177–199.
Baines, K. et al., 2006. On the discovery of CO nighttime emissions on Titan by Cassini/VIMS: Derived stratospheric abundances and geological implications. Planet. Space Sci. 109, 1552–1562.
Barr, A.C., Citron, R.I., 2011. Scaling of melt production in hypervelocity impacts from high-resolution numerical simulations. Icarus 211, 913–916.
Barr, A.C., Citron, R.I., Canup, R.M., 2010. Origin of a partially differentiated Titan. Icarus 209, 858–862.
Bockelée-Morvan, D., Crovisier, J., 2004. The composition of cometary volatiles. In: Comets II, pp. 391–424.
Bruesch, L.S., Asphaug, E.I., 2004. Modeling global impact effects on middle-sized icy bodies: Applications to Saturn's moons. Icarus 168, 457–466.
Charnay, B. et al., 2014. Titans past and future: 3D modeling of a pure nitrogen atmosphere and geological implications. Icarus 241, 269–279.
Charnoz, S. et al., 2009. Did Saturn's rings form during the Late Heavy Bombardment? Icarus 199, 413–428.
Choukroun, M., Grasset, O., 2010. Thermodynamic data and modeling of the water and ammonia–water phase diagrams up to 2.2 GPa for planetary geophysics. J. Chem. Phys. 133, 144502.
Croft, S., 1982. A first-order estimate of shock heating and vaporization in oceanic impacts. Geol. Soc. Am. 190, 143–152.
Davison, T., Collins, G., Ciesla, F., 2010. Numerical modelling of heating in porous planetesimal collisions. Icarus 208, 468–481.
de Kok, R. et al., 2007. Oxygen compounds in Titan's stratosphere as observed by Cassini CIRS. Icarus 186, 354–363.
de Niem, D. et al., 2012. Atmospheric erosion and replenishment induced by impacts upon the Earth and Mars during a heavy bombardment. Icarus 221, 495–507.
Dobrovolskis, A.R., Lissauer, J.J., 2004. The fate of ejecta from Hyperion. Icarus 169, 462–473.
Farinella, P., Marzari, F., Matteoli, S., 1997. The disruption of Hyperion and the origin of Titan's atmosphere. Astron. J. 113, 2312–2316.
Fortes, A. et al., 2007. Ammonium sulfate on Titan: Possible origin and role in cryovolcanism. Icarus 188, 139–153.
Genda, H., Abe, Y., 2005. Enhanced atmospheric loss on protoplanets at the giant impact phase in the presence of oceans. Nature 433, 842–844.
Glein, C.R., Desch, S.J., Shock, E.L., 2009. The absence of endogenic methane on Titan and its implications for the origin of atmospheric nitrogen. Icarus 204, 637–644.
Gomes, R. et al., 2005. Origin of the cataclysmic Late Heavy Bombardment period of the terrestrial planets. Nature 435, 466–469.
Grasset, O., Sotin, C., Deschamps, F., 2000. On the internal structure and dynamics of Titan. Planet. Space Sci. 48, 617–636.
Griffith, A., Zahnle, K.J., 1995. Influx of cometary volatiles to planetary moons: The atmospheres of 1000 possible Titans. J. Geophys. Res. 100, 16907–16922.
Griffith, C. et al., 2013. Titan's evolving climate. In: Comparative Climatology of Terrestrial Planets, pp. 1–27.
Hersant, F. et al., 2008. Interpretation of the carbon abundance in Saturn measured by Cassini. Planet. Space Sci. 56, 1103–1111.
Ishimaru, R. et al., 2011. Oxidizing proto-atmosphere on Titan: Constraint from N_2 formation by impact shock. Astrophys. J. 741, L10.
Kargel, J.S., 1991. Brine volcanism and the interior structures of asteroids and icy satellites. Icarus 94, 368–390.
Korycansky, D.G., Zahnle, K.J., 2005. Modeling crater populations on Venus and Titan. Planet. Space Sci. 53, 695–710.
Korycansky, D.G., Zahnle, K.J., 2011. Titan impacts and escape. Icarus 211, 707–721.

Kraus, R.G., Senft, L.E., Stewart, S.T., 2011. Impacts onto H2O ice: Scaling laws for melting, vaporization, excavation, and final crater size. Icarus 214, 724–738.
Levison, H. et al., 2011. Ridge formation and de-spinning of Iapetus via an impact-generated satellite. Icarus 214, 773–778.
Linstrom, P.J., Mallard, W.G. (Eds.), 2015. NIST Chemistry WebBook, NIST Standard Reference Database Number 69. National Institute of Standards and Technology, Gaithersburg MD, p. 20899, http://webbook.nist.gov.
Lorenz, R.D., Lunine, J.I., McKay, C.P., 1997. Titan under a red giant Sun: A new kind of habitable Moon. Geophys. Res. Lett. 24, 2905–2908.
Lorenz, R.D., McKay, C.P., Lunine, J.I., 1999. Analytic investigation of climate stability on Titan: Sensitivity to volatile inventory. Planet. Space Sci. 47, 1503–1515.
Louzada, K.L., Stewart, S.T., 2009. Effects of planet curvature and crust on the shock pressure field around impact basins. Geophys. Res. Lett. 36, L15203.
Mandt, K.E. et al., 2012. The 12C/ 13C Ratio on Titan from Cassini INMS measurements and implications for the evolution of methane. Astrophys. J., 749
Mandt, K.E. et al., 2014. Protosolar ammonia as the unique source of Titan's nitrogen. Astrophys. J. 788, L24.
McKay, C.P., Scattergood, T., Pollack, J.B., 1988. High-temperature shock formation of N_2 and organics on primordial Titan. Nature 332, 520–522.
McKay, C.P., Lorenz, R., Lunine, J., 1999. Analytic solutions for the antigreenhouse effect: Titan and the early Earth. Icarus 61, 56–61.
Melosh, H., Vickery, A., 1989. Impact erosion of the primordial atmosphere of Mars. Nature 338, 487–489.
Monteux, J. et al., 2014. Can large icy moons accrete undifferentiated? Icarus 237, 377–387.
Morbidelli, A. et al., 2005. Chaotic capture of Jupiter's Trojan asteroids in the early Solar System. Nature 435, 462–465.
Mousis, O., Gautier, D., Bockelée-Morvan, D., 2002. An evolutionary turbulent model of Saturn's subnebula: Implications for the origin of the atmosphere of Titan. Icarus 156, 162–175.
Nakamura, A., Fujiwara, A., 1991. Velocity distribution of fragments formed in a simulated collisional disruption. Icarus 92, 132–146.
Niemann, H.B. et al., 2010. Composition of Titan's lower atmosphere and simple surface volatiles as measured by the Cassini–Huygens probe gas chromatograph mass spectrometer experiment. J. Geophys. Res. 115, E12006.
Nimmo, F., Korycansky, D.G., 2012. Impact-driven ice loss in outer Solar System satellites: Consequences for the Late Heavy Bombardment. Icarus 219, 508–510.
Osegovic, J.P., Max, M.D., 2005. Compound clathrate hydrate on Titan's surface. J. Geophys. Res. 110, E08004.
Owen, T.C., 1982. The composition and origin of Titan's atmosphere. Planet. Space Sci. 30, 833–838.
Pham, L., Karatekin, O., Dehant, V., 2011. Effects of impacts on the atmospheric evolution: Comparison between Mars, Earth, and Venus. Planet. Space Sci. 59, 1087–1092.
Pierazzo, E., 2000. Melt production in oblique impacts. Icarus 145, 252–261.
Pierazzo, E., Melosh, H., 2000. Understanding oblique impacts from experiments, observations, and modeling. Annu. Rev. Earth Planet. Sci. 28, 141–167.
Rousselot, P. et al., 2014. Toward a unique nitrogen isotopic ratio in cometary ices. Astrophys. J. 780, L17.
Sekine, Y. et al., 2011. Replacement and late formation of atmospheric N_2 on undifferentiated Titan by impacts. Nat. Geosci. 4, 359–362.
Senshu, H., 2002. Thermal evolution of a growing Mars. J. Geophys. Res. 107, 5118.
Shinnaka, Y. et al., 2014. $^{14}NH_2/^{15}NH_2$ ratio in comet C/2012 S1 (ISON) observed during its Outburst in 2013 November. Astrophys. J. 782, L16.
Shuvalov, V., 2009. Atmospheric erosion induced by oblique impacts. Meteorit. Planet. Sci. 44, 1095–1105.
Shuvalov, V., 2010. Atmospheric erosion induced by oblique impacts. In: Lunar and Planetary Science Conference.
Stewart, S.T., 2005. Shock properties of H2O ice. J. Geophys. Res. 110, E03005.
Svetsov, V.V., 2000. On the efficiency of the impact mechanism of atmospheric erosion. Sol. Syst. Res. 34, 441–453.
Svetsov, V.V., 2007. Atmospheric erosion and replenishment induced by impacts of cosmic bodies upon the Earth and Mars. Sol. Syst. Res. 41, 28–41.
Thompson, W.R., 1985. In: Rolfe, E., Battrick, B. (Eds.), Phase Equilibria in N_2-Hydrocarbon Systems: Applications to Titan. ESA Special Publication, pp. 109–119.
Tobie, G., Lunine, J.I., Sotin, C., 2006. Episodic outgassing as the origin of atmospheric methane on Titan. Nature 440, 61–64.
Tobie, G., Gautier, D., Hersant, F., 2012. Titan's bulk composition constrained by Cassini–Huygens: Implication for internal outgassing. Astrophys. J. 752, 125.
Tsiganis, K. et al., 2005. Origin of the orbital architecture of the giant planets of the Solar System. Nature 435, 459–461.
Waite, J.H. et al., 2009. Liquid water on Enceladus from observations of ammonia and 40Ar in the plume. Nature 460, 487–490.
Zahnle, K.J., 2001. Differential cratering of synchronously rotating satellites by ecliptic comets. Icarus 153, 111–129.
Zahnle, K.J. et al., 2003. Cratering rates in the outer Solar System. Icarus 163, 263–289.
Zahnle, K.J., Korycansky, D.G., Nixon, C.A., 2014. Transient climate effects of large impacts on Titan. Icarus 229, 378–391.

Icarus 264 (2016) 300–310

Contents lists available at ScienceDirect

Icarus

journal homepage: www.journals.elsevier.com/icarus

Consequences of large impacts on Enceladus' core shape

J. Monteux [a,b,*], G.S. Collins [c], G. Tobie [b], G. Choblet [b]

[a] Laboratoire Magmas et Volcans, Université Blaise Pascal, CNRS, IRD, Clermont-Ferrand, France
[b] Laboratoire de Planétologie et de Géodynamique, LPG Nantes, CNRS UMR6112, Université de Nantes, France
[c] Impacts and Astromaterials Research Centre, Department of Earth Science and Engineering, Imperial College London, United Kingdom

ARTICLE INFO

Article history:
Received 13 May 2015
Revised 31 August 2015
Accepted 22 September 2015
Available online 8 October 2015

Keywords:
Enceladus
Impact processes
Cratering
Interiors
Accretion

ABSTRACT

The intense activity on Enceladus suggests a differentiated interior consisting of a rocky core, an internal ocean and an icy mantle. However, topography and gravity data suggests large heterogeneity in the interior, possibly including significant core topography. In the present study, we investigated the consequences of collisions with large impactors on the core shape. We performed impact simulations using the code iSALE2D considering large differentiated impactors with radius ranging between 25 and 100 km and impact velocities ranging between 0.24 and 2.4 km/s. Our simulations showed that the main controlling parameters for the post-impact shape of Enceladus' rock core are the impactor radius and velocity and to a lesser extent the presence of an internal water ocean and the porosity and strength of the rock core. For low energy impacts, the impactors do not pass completely through the icy mantle. Subsequent sinking and spreading of the impactor rock core lead to a positive core topographic anomaly. For moderately energetic impacts, the impactors completely penetrate through the icy mantle, inducing a negative core topography surrounded by a positive anomaly of smaller amplitude. The depth and lateral extent of the excavated area is mostly determined by the impactor radius and velocity. For highly energetic impacts, the rocky core is strongly deformed, and the full body is likely to be disrupted. Explaining the long-wavelength irregular shape of Enceladus' core by impacts would imply multiple low velocity (<2.4 km/s) collisions with deca-kilometric differentiated impactors, which is possible only after the LHB period.

1. Introduction

Despite its small size ($R = 252$ km), Saturn's moon Enceladus is one of the most geologically active body of the Solar System. Its surprising endogenic activity is characterized by a very active province at the South Pole, from which eruptions of water vapor and ice grains emanating from warm tectonic ridges have been observed by the Cassini spacecraft (Porco et al., 2006; Hansen et al., 2006; Waite et al., 2006; Spencer et al., 2006). This activity is associated with a huge heat power estimated between 5 and 15 GW from thermal emission (Spencer and Nimmo, 2013), which implies a warm interior, consistent with a liquid water layer underneath the ice shell and a differentiated interior (Nimmo et al., 2007; Schubert et al., 2007). Models of tidal dissipation may explain why the activity is concentrated at the poles, where dissipation is predicted to be maximal (Tobie et al., 2008; Běhounková et al., 2010). However, there is still no satisfactory explanation for why this activity is located only in the south, and not in the north.

Based on the global shape data which show a depression at the south pole (Thomas et al., 2007), it has been proposed that the ocean may be located only in the southern hemisphere (Collins and Goodman, 2007), thus explaining why the activity would be concentrated at the south (Tobie et al., 2008). Gravity and shape data indicate that such an ocean would be at depths of about 30–40 km and extend up to south latitudes of about 50° (Iess et al., 2014). It has been proposed that the dichotomy between the north and south hemispheres may be the result of asymmetry in core shape (McKinnon, 2013). Due to the low pressure and moderate temperature expected in Enceladus' core, large topography anomalies may indeed be retained on very long periods of time (McKinnon, 2013) and may explain why convection-driven activities in the ice shell is confined only to the south polar terrain (Showman et al., 2013). Besides the south polar depression, core topography anomalies could explain, at least partly, the existence of other big depressions observed at moderate latitudes (between 15°S and 50°N) and uncorrelated with any geological boundaries (Schenk and McKinnon, 2009).

* Corresponding author at: Laboratoire Magmas et Volcans, Université Blaise Pascal, CNRS, IRD, Clermont-Ferrand, France.

http://dx.doi.org/10.1016/j.icarus.2015.09.034
0019-1035/

McKinnon (2013) proposed three hypotheses to explain the possible irregularity of Enceladus' rocky core: accretional melting of the outer region of the icy moon associated with a degree-one instability; accretion of icy protomoons around irregular rock chunks; and collisional merger of two previously differentiated protomoons. Here we test the latter hypothesis by investigating the consequences of the collision of a large differentiated impactor on the shape of Enceladus' core. Collisions with large differentiated bodies were likely at the end of satellite accretion, during the final assemblage phase (e.g. Asphaug and Reufer, 2013). Large impact basins on other saturnian moons (e.g. Iapetus (Giese et al., 2008), Mimas (Schenk, 2011), Titan (Neish and Lorenz, 2012)) and other Solar System bodies (e.g. Vesta (Schenk et al., 2012)) could represent remnant evidences of such collisions. Large impacts occurring at the end of the accretion and after, during the rest of the satellite's evolution, likely influenced the internal structure and especially the shape of its rocky core. It is also important to determine the conditions under which Enceladus would have survived disruption by collisions with deca-kilometric objects, which would place constraints on its accretion and the subsequent impact history.

To constrain the consequences of large-scale impacts on Enceladus, we simulated head-on collisions of differentiated impactors with diameter ranging between 50 and 200 km using the iSALE2D shock physics code (Wünnemann et al., 2006; Collins et al., 2004; Davison et al., 2010). From these simulations, we tracked the evolution of rock fragments coming from the impactor and the impact-induced modification of Enceladus's core shape. In particular, we quantified the sensitivity in these outcomes to key model parameters, such as impactor velocity and radius, as well as structure and mechanical properties of Enceladus' interior (porosity, strength, temperature profile, core size, presence of an internal ocean). In Section 2, we describe our numerical modelling approach; in Section 3 we present our results. We discuss our results in the context of the presence of a water ocean in Section 3.3. Conclusions are highlighted in Section 4.

2. Impact modeling

To model the thermo-mechanical evolution of material during an impact between two differentiated icy bodies, we use iSALE2D (Wünnemann et al., 2006; Collins et al., 2004). This numerical model is a multi-rheology, multi-material shock physics code based on the SALE hydrocode (Amsden et al., 1980) that has been extended and modified specifically to model planetary-scale impact crater formation (e.g., Amsden et al., 1980; Melosh et al., 1992; Ivanov et al., 1997; Collins et al., 2004; Wünnemann et al., 2006; Davison et al., 2010). In our simulations, the target structure and the impactor were simplified to two- or three-layer spherical bodies consisting of a rocky core, an icy mantle and for the three-layer case an internal ocean. Interpretation of gravity data collected by the Cassini spacecraft indicates that the core density could be as low as 2400 kg m^{-3}, corresponding to a core radius of about 200 km (Iess et al., 2014). However, as Enceladus appears to be relatively far from hydrostatic equilibrium (Iess et al., 2014), there are still significant uncertainties on the core radius and density. The low core density inferred from gravity data suggests that the rocky core might be significantly porous, with pores filled by water ice and/or liquid water, and that a significant fraction of the core may consist of hydrated silicate minerals. Currently, iSALE2D does not have provision to describe the behavior of an ice–rock or water–rock mixture. In our simulations, for simplicity, we assume complete segregation of the rock and ice-water phase into discrete layers and we consider dunite as representative of the rock phase (with density $\rho_s = 3330$ kg m^{-3}). We reduce the density of the core by including some initial porosity ϕ (defined as the ratio of pore volume to total volume) within it, varying from 0% to 50%, corresponding to radius varying between typically 160 km and 200 km. Assuming a core made of pure dunite, a radius as large as 200 km is consistent with a core porosity of about 50%, which is at the upper end of the estimated porosity in large asteroids (Lindsay et al., 2015). A significant fraction of the core may also consist of hydrated minerals such as serpentine. In this case a 200 km core radius would imply a lower porosity. For simplicity, we consider only dunite as core materials and vary the porosity up to values of 50%. We also test the possible effect of porosity in the ice shell by considering values up to 20% as suggested by Besserer et al. (2013).

In our models, we consider the extreme case where the pores of both ice and rocks consist of voids, and are not filled with secondary materials (i.e. water or ice in rock pores). The difference between saturated porosity (with ice or liquid water) and voids may lead to differences in terms of mechanical and thermal properties. This aspect will be discussed in the last section. The effect of both rock and ice porosity is treated using the ϵ–α porosity compaction model (Wünnemann et al., 2006; Collins et al., 2013), which accounts for the collapse of pore space by assuming that the compaction function depends upon volumetric strain. For sake of simplicity, we assume that the impactor material has an identical composition and porosity to those of the target.

The impact velocity v_{imp} can be decomposed into two contributions:

$$v_{imp} = \sqrt{v_{esc}^2 + v_\infty^2} \quad (1)$$

where v_{esc} is the escape velocity of the impacted planet and v_∞ is the velocity of the impactor at a distance much greater than that over which the gravitational attraction of the impacted planet is important. The escape velocity of Enceladus is $v_{esc} = 240$ m/s. As we consider collisions with relatively large objects (R_{imp} = 25–100 km), we limit our analysis to moderate relative velocities, varying between v_{esc} and $10 \times v_{esc}$, in order to limit the impact-induced deformation of the satellite and avoid full disruption (Benz and Asphaug, 1999; Asphaug, 2010). Moreover, this low-velocity impact regime is representative of the collisional environment at the end of the accretion. Indeed, N-body simulations from Dwyer et al. (2013) show that random impact velocity of proto-satellites mostly ranges between v_{esc} and $5v_{esc}$.

We approximated the thermodynamic response of the icy material using the Tillotson EoS for Ice as in Bray et al. (2008) and of the rocky material using the ANEOS EoS for dunite material as in Benz et al. (1989) and Davison et al. (2010) (see Table 1 for parameter values). Standard strength parameters for dunite were used to form the static strength model for the rocky core (Collins et al., 2004; Davison et al., 2010). The static strength model for ice used in iSALE was derived from low temperature, high pressure laboratory data and accounts for the material strength dependence on pressure, damage and thermal softening (Bray et al., 2008). We also explored the effect on our results of the cohesion of the damaged material (referred to here as Y_i for ice and Y_s rocks), which represents the minimum zero-pressure shear strength of cold material (strength is reduced to zero at the melt temperature). The minimum strength values considered in our models range between 10–500 kPa for ice and 100–10^4 kPa for silicate material. The Tillotson EoS for ice is severely limited in its applicability for hypervelocity impact; it includes no solid state or liquid phase changes. However, as we limit here our analysis to low velocity encounters ($240 < v_{imp} < 2400$ m s^{-1}), thought to be dominant at the end of the accretion, as shown in our simulations, no significant ice melting occurs and the use of Tillotson EoS is a reasonable approximation. We also used the Tillotson EoS for the liquid water.

Table 1
Typical parameter values for numerical models.

Enceladus radius	R	250 km
Rocky core radius	R_{core}	160–200 km
Icy mantle thickness	δ_m	50–90 km
Surface gravity field	g_0	0.113 m s^{-2}
Escape velocity	v_{esc}	240 m/s
Impactor radius	R_{imp}	25–100 km
Impact velocity	v_{imp}	240–2400 m/s
Mantle properties (Ice)		
Initial density	ρ_i	820 kg m^{-3}
Equation of state type		Tillotson
Poisson		0.33
Porosity		0–20%
Minimum strength	Y_i	10–500 kPa
Core properties (Dunite)		
Rocky core density	ρ_s	3330 kg m^{-3}
Equation of state type		ANEOS
Poisson		0.25
Porosity		0–50%
Minimum strength	Y_s	100 kPa–10 MPa

Material weakening during impact may also be achieved by acoustic fluidization and/or thermal softening (Melosh and Ivanov, 1999), the latter of which is especially efficient for large-scale events (Potter et al., 2012). Our simulations including acoustic fluidization that assumed typical block-model parameters favored in other works showed no significant effect on simulation results (see also discussion section). Hence, for simplicity and to reduce the number of free parameters, we chose to neglect acoustic fluidization. We do, however, include the effect of temperature on shear strength using the temperature–strength relationship proposed by Ohnaka (1995) and described by Collins et al. (2004) and we set the thermal softening coefficient in this expression to 1.2 as suggested by Bray et al. (2008). Since we consider the thermal softening during the impact, the thermal structure of Enceladus before the impact is probably a key parameter governing the post-impact state. However, the early temperature profile for such a small body is poorly constrained. Accretionary models seem to favor a cold accretion with inner temperatures close to the equilibrium temperature (Schubert et al., 1981; Monteux et al., 2014). To test the influence of the initial thermal conditions, we consider three different pre-impact temperature profiles for the impacted moon: constant temperature, conductive profile, two-layered advective profile. The impactor is assumed to have a constant temperature with $T = 100$ K.

Owing to the axisymmetric geometry of iSALE2D, we consider only head-on collisions (impact angle of 90° to the target tangent plane). The role of impact angle is left to future studies. To limit computation time, a 1-to-2 km spatial resolution is used, which is sufficient to describe the deflection of the rock core surface. The gravity is calculated from the density structure. For the largest and fastest impacts, we use iSALE2D's self-gravity gravity model (Collins et al., 2011) to correctly assess the gravity field as the body is strongly deformed and the center of mass of the target moves upon the collision. As this self-gravity model is expensive in terms of computational time, we limit our post impact monitoring to the time needed to deform the rocky core (i.e. we consider that the fall-back of icy material and the icy-mantle slumping has only a very minor effect on the morphology of the rocky core). For all the impacts characterized here, this corresponds to the first hour after the impact.

3. Numerical results

3.1. Non-porous models

Fig. 1 shows three characteristic simulations: ($v_{imp} = 10 v_{esc}$, $R_{imp} = 25$ km), ($v_{imp} = 10 v_{esc}, R_{imp} = 75$ km) and ($v_{imp} = v_{esc}$, $R_{imp} = 75$ km). After such events, a large volume of Enceladus' mantle is displaced or escapes the orbit of the icy moon. To get a quantitative measure of deformation induced by the impact event, we monitor the plastic strain experienced by the impacted material. In particular, we calculate the total plastic strain which is the accumulated sum of plastic shear deformation, regardless of the sense of shear (Collins et al., 2004). As represented in Fig. 1, the icy material is highly disturbed by the impact and most of the plastic deformation occurs in this layer. For the largest impact velocities (Fig. 1, left and middle), deformation also occurs at the top of the rocky core and leads to the formation of a depression. The material removed from the depression is displaced in a very small uplift of the core, surrounding the depression.

For small impact velocities (Fig. 1, right), the icy mantle is also highly deformed but the impactor's rocky core is trapped within the ice layer. In this low-velocity case, the deformation of the target's core and the impact melt production are minor but the surrounding ice is warmed up. Hence, over a longer time scale governed by a Stokes' flow, the impactor's core gently spreads over the surface of the pre-existing rocky core favoring the formation of successive fragmented silicate layers (Roberts, 2015). Depending on the impactor size and impact velocities, our simulations show that core merging occurs into three distinct regimes (Fig. 2):

(1) For small impactors and impact velocities close to $\sim v_{esc}$, the impactor's core is simply buried within Enceladus' icy mantle at a depth that scales with the penetration depth p (Orphal et al., 1980; Murr et al., 1998):

$$p/R_{imp} = A v_{imp}^{2/3} \quad (2)$$

where A is a function of the bulk sound velocity, the geometry and density difference between the impactor and the target.

(2) For higher impact velocities or larger impactors, the kinetic energy increases and hence penetration of the impactor's core through the target ice mantle is facilitated. When the impactor penetration depth, p (2), exceeds the ice-mantle thickness, δ_m, the impactor induces a deflection of the core boundary (Fig. 2), the amplitude of which depends on the impactor energy remaining after crossing the ice mantle. For $p \sim \delta_m$ or slightly larger, the impactor core spreads above the target's core (leading to a positive core-topography anomaly defined as the difference of post- and pre-impact core radii below the impact site). (3) However, if more energy is available, $p > \delta_m$ and the core is strongly deformed, possibly leading to severe deformation of the satellite, as illustrated in Fig. 2 for impactors larger than 75 km and/or impact velocities $\geqslant 10 v_{esc}$. It has to be noted that, as we limit our post impact monitoring to one hour, for the most energetic impact cases with large impact velocities ($\geqslant$6 km/s) and large impactor radii ($\geqslant$75 km) the rocky material excavated from Enceladus' core and orbiting around the moon is still moving with significant velocity at the end of the simulation.

The thermal softening is an efficient process for large-scale events (Potter et al., 2012). This process is strongly dependent on the pre-impact temperature field that is unfortunately poorly constrained. To test the influence of the pre-impact thermal state, we consider three different pre-impact temperature profiles for the impacted moon (Fig. 3): constant temperature (with $T \sim 100$ K), conductive profile (with a temperature gradient value of 1 K/km), two-layered convective profile (with a core temperature of 450 K and a mantle temperature of 250 K). As illustrated in Fig. 3, a hotter temperature profile in the icy shell strongly enhances the ice flow back and the refill of the core depression. One hour after the impact, a large cavity remains open in the icy mantle for the constant and cold temperature case. For the two-layered convective case where the mantle temperature is close to the melting temperature of ice, the icy mantle rapidly flows back leading to a huge jet

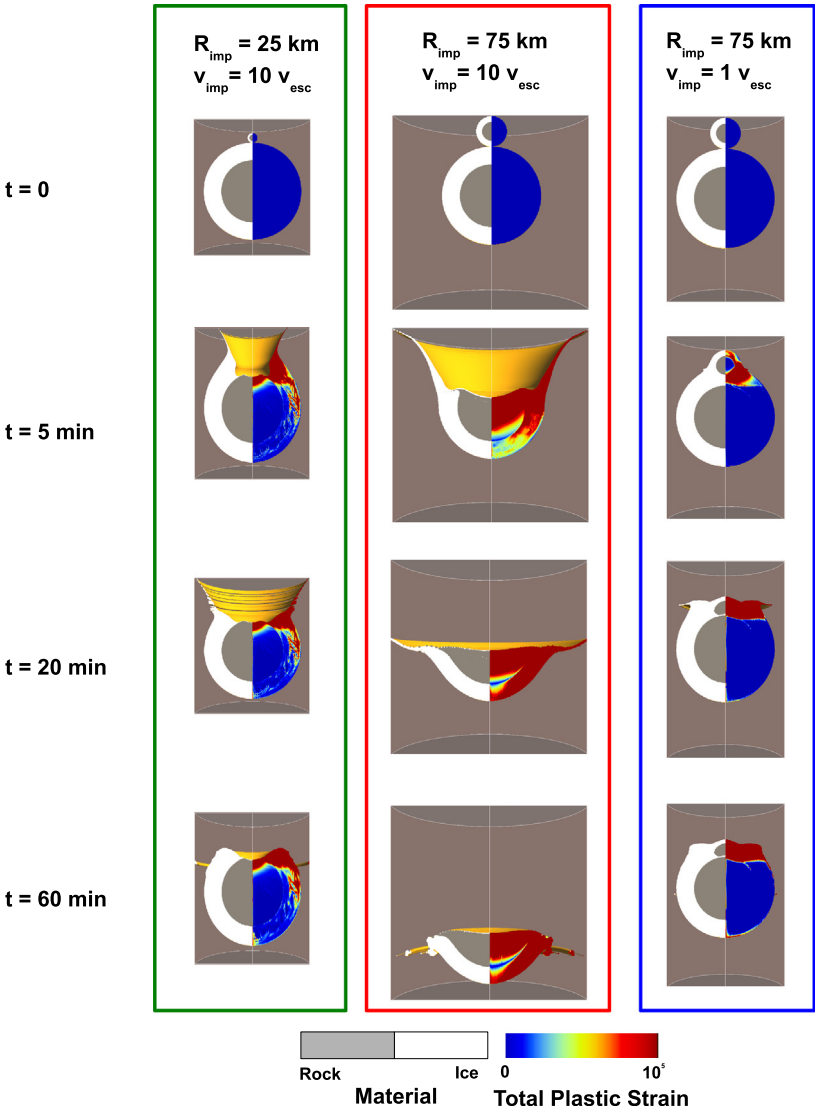

Fig. 1. Material repartition (left column) and total plastic deformation (right column) as a function of time (from top to bottom) on Enceladus for 3 impact cases: ($v_{imp} = 10 v_{esc}, R_{imp} = 25$ km) (left), ($v_{imp} = 10 v_{esc}, R_{imp} = 75$ km) (center) and ($v_{imp} = v_{esc}, R_{imp} = 75$ km) (right). In these models, the grid resolution is 1 km in all directions. Here both the rocky core and the icy material are considered as nonporous materials.

of ice at the impact site. However, even if considering three pre-impact thermal states significantly modifies the post-impact dynamics of the icy mantle, this only weakly affects the depth of the depression within the rocky core that ranges between 12 and 15 km (Fig. 3). Hence, in the following, we consider models with a constant pre-impact temperature field.

3.2. Influence of ice and rock porosity

The porosity of the material involved during the impact is known to be a key factor in both the fragmentation and disruption of the impactor and the target (Jutzi et al., 2008, 2009), and therefore it may play a role in our results. Enceladus is believed to contain a high degree of porosity, as are many other small bodies in the different populations of asteroids and comets (e.g. Lindsay et al., 2015). To explain the long-wavelength topography of Enceladus, recent models also invoke porosity values ranging between 20% and 30% within the icy mantle of Enceladus (Besserer et al., 2013). We monitored the rocky core deformation as a function of the icy mantle porosity with porosities ranging between 0% and 20%. Similar to the simulations with different initial thermal conditions (Fig. 3), the dynamics of post-impact ice flow in the deep cavity depends significantly on the porosity, as it affects the ice mechanical properties (Fig. 4). When the ice porosity equals 20% and because the compacted ice is thermally softened, the icy material (which is heated by impact to temperatures up to 250 K) re-fills the impact induced cavity in less than one hour.

Nevertheless, as illustrated in Fig. 5, the effect of the icy mantle porosity on the post-impact core morphology is rather small, at least for initial porosities ranging from 0% to 20% and for impact parameters leading to moderate core deformation ($v_{imp} = 10 v_{esc}$ and $R_{imp} = 25$ km). Fig. 6 shows the depth of the impact-induced core depression as a function of the mantle porosity. According to this figure, the depth of the depression ranges between 8 and 13 km. As mentioned earlier (see Fig. 4), the major influence of the mantle porosity is its ability to flow back and refill the core depression. As the impacted ice is severely deformed and compacted during the shockwave propagation, the impact will increase locally the porosity and the temperature of the icy mantle below the impact site.

Figs. 6 and 7 show that the influence of core porosity on core deformation is larger than the corresponding influence of mantle

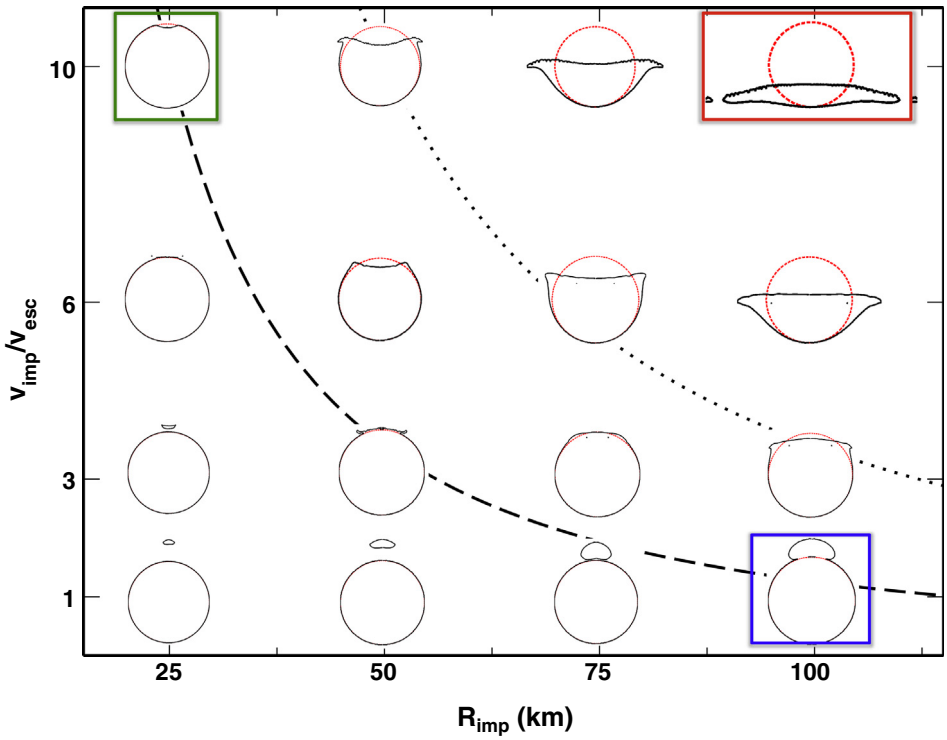

Fig. 2. Rocky core morphology as a function of the impactor size and the impact velocity ($v_{esc} = 240$ m/s). In these models the porosity of the icy material is zero. For each morphology, the red circle represents the pre-impact spherical shape of the impacted core. The dashed black line represents Eq. (2) with $A = 2$. Above this critical theoretical line, the impact induced topography is negative. Below this critical theoretical line, the impact induced topography is positive. The dotted black line represents Eq. (2) with $A = 1$. Above this critical theoretical line, very highly deformed cores are formed and acoustic fluidization may contribute to their final shape. However the deformation is too large and probably not compatible with the Enceladus morphology. We limit our post impact monitoring to one hour which means that for large impact velocities ($\geqslant 6$ km/s) and large impactor radii ($\geqslant 75$ km) the rocky material excavated from Enceladus' core and orbiting around the moon is still moving with significant velocity at the end of the simulation. (For interpretation of the references to color in this figure legend, the reader is referred to the web version of this article.)

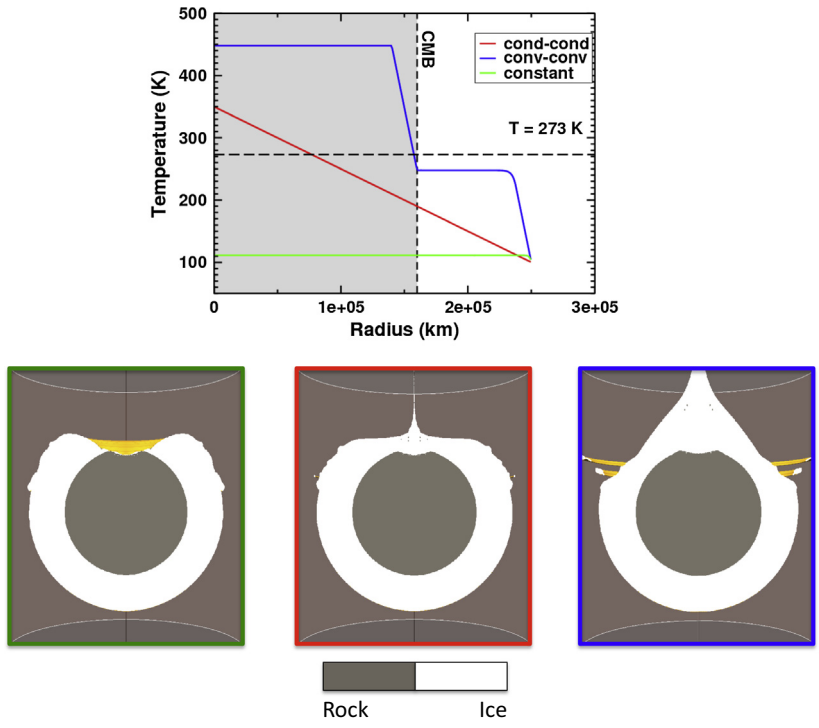

Fig. 3. Material repartition one hour after the impact (bottom) for three different pre-impact temperature profiles (top) (with $v_{imp} = 10 v_{esc}$, $R_{core} = 160$ km and $R_{imp} = 25$ km). The color of the temperature profile corresponds to the color of the rectangle surrounding the material repartition snapshot. (For interpretation of the references to color in this figure legend, the reader is referred to the web version of this article.)

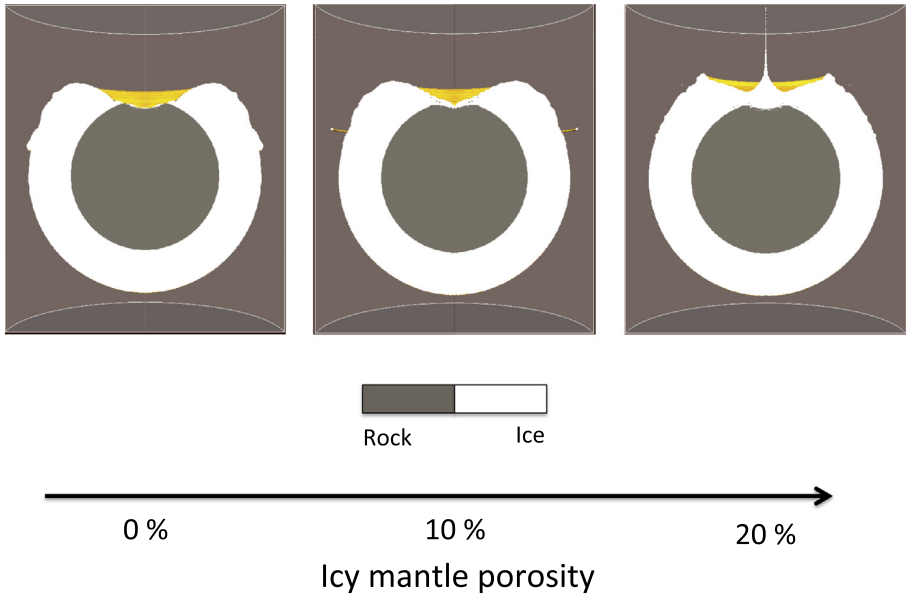

Fig. 4. Material repartition as a function of the icy mantle porosity one hour after the impact ($v_{imp} = 10 v_{esc}$, $R_{imp} = 25$ km). The rocky core is represented in gray while the icy material is represented in white. In these models, the grid resolution is 1 km in all directions.

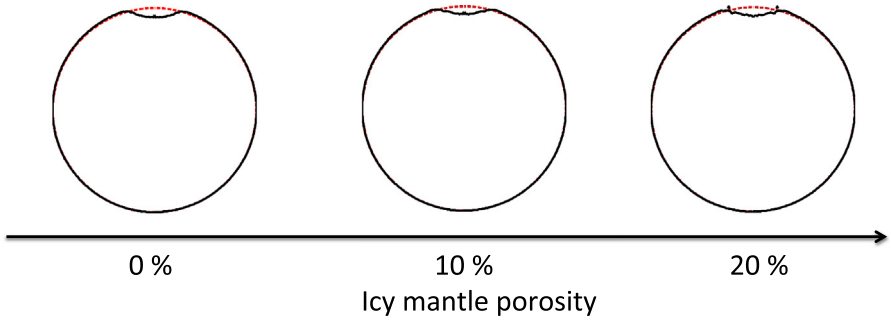

Fig. 5. Rocky core morphology as a function of the icy mantle porosity (with $R_{core} = 160$ km). For each morphology, the red circle represents the pre-impact spherical shape of the impacted core. (For interpretation of the references to colour in this figure legend, the reader is referred to the web version of this article.)

porosity. Indeed, increasing the porosity of the core from 0% to 50% (and thus increasing its radius from 160 to 200) increases the maximum depth of the depression caused by the impact from ~13 km to ~31.5 km. To explain this feature, two effects shall be invoked. The first one is that increasing the rocky core porosity increases its size to maintain its mass. Hence, the top of the rocky core is closer to the surface and the impactor penetration depth needed to deform the rocky core is reduced accordingly. The second one is that porosity can enhance the rocky core deformation because the core material is less dense and easier to compact. To decipher between these two effects we ran a non-consistent model with a non-porous 200 km rocky core radius surrounded by a 50 km thick icy mantle (Fig. 8, first column). At the end of this model, the depression depth is 18.5 km (compared to 31.5 km when the rocky core porosity is 50% and to 13 km when the rocky core has a radius of 160 km) meaning that both increasing the core size and the porosity favor deeper impact-induced depressions. This also suggests that density/compaction has a greater influence than core radius on the depth of the impact-induced core depression. We also ran a model with a 50% porosity 160 km rocky core radius (Fig. 6) where the obtained depression depth is 15 km (close to value obtained in the non-porous case). In this non-consistent case, a 8 km-thick ice block is trapped between the impactor and the target's core that prevents the formation of a deeper cavity. We should, however, keep in mind that in our simulations, we consider void porosity, while in reality pores should be filled by liquid water or water ice, which would affect compaction. The results presented here should be considered as an estimation of the maximal effect associated to impact-induced porosity compaction.

3.3. Influence of minimum strength values and water ocean

In all the models described above, the minimum strength values were set to $Y_i = 500$ kPa for ice and $Y_s = 10$ MPa for silicate material. These values represent the upper range of the plausible values since recent estimates of the strength of the surface of Comet Tempel-1 obtained minima strength values in the order of 1–10 kPa (Richardson and Melosh, 2013). For the minimum strength of the rocky mantle, this value is also likely to range between the strength of the lunar soil (1 kPa) to the strength of the terrestrial soil (<100 kPa) (Mitchell et al., 1972; Lambe and Whitman, 1979). We have tested the influence of these two parameters using lower values, $Y_i = 10$ kPa and $Y_s = 100$ kPa. As illustrated in Fig. 9 (second column) (called "highly deformable"), decreasing the minimum strength of both the ice and the rocky materials tends to increase the deformability of the rock core leading to both a deeper and wider depression. Ultimately, for a 200 km radius rocky core with 50% porosity (Fig. 9, second columns), the depth of the depression can reach 54.5 km. Here again, the conditions in term of porosity and strength are rather extreme, and the objectives of

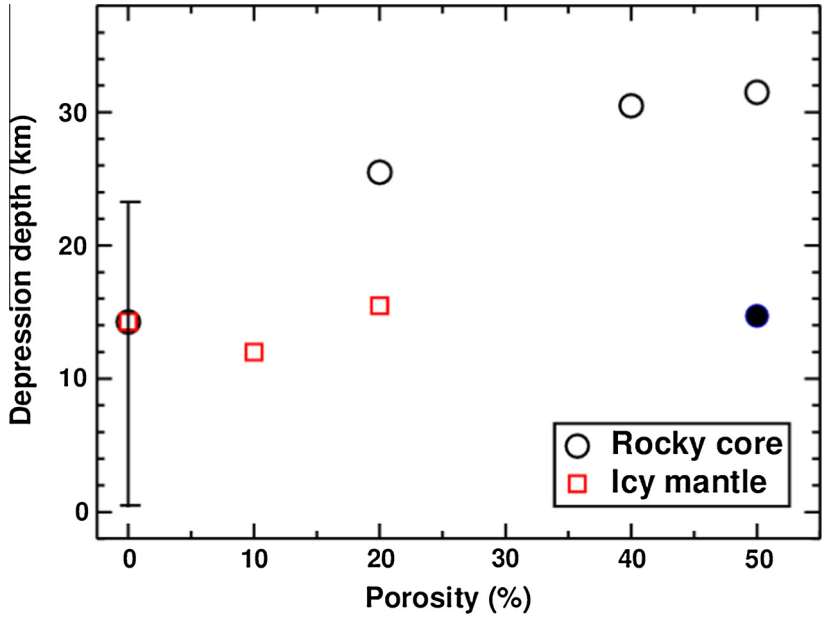

Fig. 6. Depth of the impact induced depression as a function of the rocky core porosity (black circles) and as a function of the icy mantle porosity (red squares) ($v_{imp} = 10 v_{esc}$ and $R_{imp} = 25$ km). The vertical line for 0% porosity represents the range of depression depths obtained when considering a 100% icy (lower value) and a 100% rocky (upper value) impactor. The black filled circle at 50% porosity represents the unrealistic case with a core radius of 160 km (while in the other cases the core radius increases with porosity). (For interpretation of the references to color in this figure legend, the reader is referred to the web version of this article.)

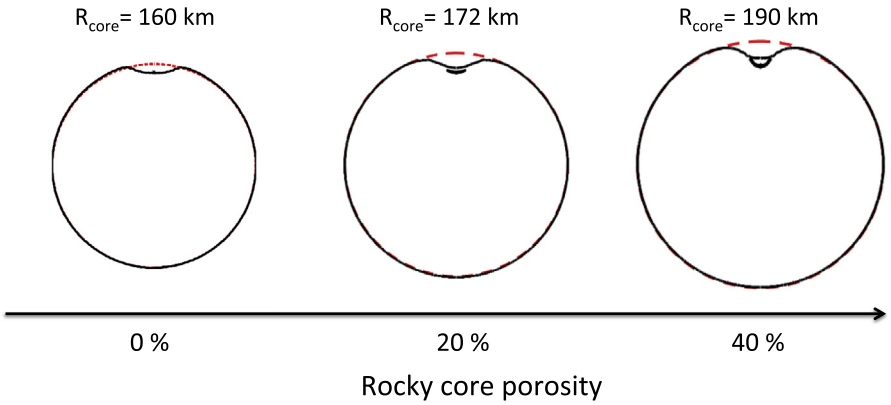

Fig. 7. Rocky core morphology as a function of the rocky core porosity. For each morphology, the red circle represents the pre-impact spherical shape of the impacted core. (For interpretation of the references to color in this figure legend, the reader is referred to the web version of this article.)

this simulation are to illustrate the maximal depression depth that could be generated by a large impact on Enceladus.

Figs. 8 (third and fourth columns) and 9 (third column) show that the presence of a deep water ocean (considered as an inviscid fluid with a density of 910 kg/m^3) above the rocky core tends to reduce the impact-induced deflection of the core surface. Liquid water and water ice have comparable compressibility, water being slightly more compressible. The main difference concerns their resistance to shear. Liquid water has no strength (and is considered a completely inviscid material in the simulation), while ice has some strength. In the presence of liquid water, there is complete mechanical decoupling of shear deformation between the water and the core, whereas in the latter case shear stresses exist at the ice-core boundary. In the presence of the water ocean, the lateral extent of the morphology anomaly as well as its depth are smaller than without an ocean. Indeed, for $R_{core} = 160$ km, the depth of the impact induced cavity decreases from 13 km without an ocean to 3.5 km with an ocean. For $R_{core} = 200$ km and $\phi = 50\%$, the depth of the impact induced cavity decreases from 31.5 km without an ocean to 22.5 km with an ocean. This tends to illustrate that it is easier to enhance post-impact negative topography anomalies in the absence of a water ocean. Including a thick subsurface water ocean has the opposite effect of increasing the impact velocity or the impactor size, because it concentrates deformation in the ice mantle above, decoupling it from the rocky core below. On the other hand, the presence of the ocean seems to enhance the plastic strain in the deepest part of the core (Fig. 8, third and fourth columns). In parallel to compaction, impact-induced fracturing is likely to generate a porosity increase (via the dilatancy process) (Collins, 2014) that could in return favor fluid circulation within the deformed rocky core.

4. Discussion and conclusion

In order to investigate the morphological consequences of collisions between differentiated impactors and Enceladus, we performed numerical impact simulations for impactor radii and

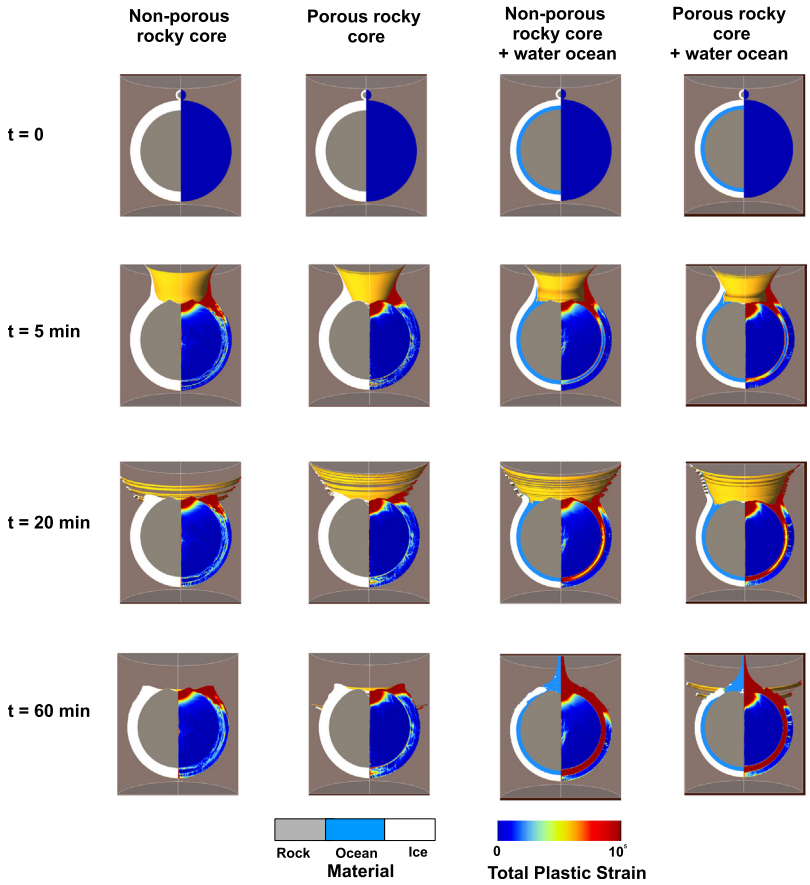

Fig. 8. Material repartition (left column) and total plastic deformation (right column) as a function of time (from top to bottom) on Enceladus for $R_{core} = 200$ km, ($v_{imp} = 10 v_{esc}$ and $R_{imp} = 25$ km). We consider 4 models: a non-consistent non-porous rocky core (first column), a porous rocky core with a porosity of 50% (second column), a non-consistent non-porous rocky core overlaid by a 20 km thick water ocean (third column) and a porous rocky core with a porosity of 50% overlaid by a 20 km thick water ocean (fourth column). In these models, the grid resolution is 1 km in all directions.

velocities ranging between 10% and 40% Enceladus' radius and 1–10 times Enceladus' escape velocity (0.24–2.4 km/s), and for various assumptions for the structure and mechanical properties of Enceladus' interior. Our results showed that the dynamical response of the icy mantle to the impact is strongly dependent on the assumed thermo-mechanical properties for the ice. However, the icy mantle response has minor effects on the impact-induced deformation of the rock core. Only the presence of an internal ocean between the icy mantle and the rock core can significantly limit the rock core deformation.

Our simulations showed that the main controlling parameters for the post-impact shape of Enceladus' rock core are the impactor radius and velocity. We have identified three regimes: (1) For low energy impacts ($\leqslant 1.5$–2×10^{23} J), the impactors do not pass completely through the icy mantle and the core surface remains unmodified. The rock core of the impactors are deformed by the impact events, but remains trapped within the icy mantle. The impactor core embedded in the icy mantle would then progressively sink and spread, leading to a positive core topographic anomaly. (2) For more energetic impacts, the impactors completely penetrate though the icy mantle and hit the core surface. The impact leads to a negative core topography surrounded by a positive anomaly of smaller amplitude. The depth and lateral extent of the excavated area is mostly determined by the impactor radius and velocity. The shape of the excavated area can be significantly enhanced for high core porosity and very low material strengths, but its amplitude and extent remain primarily determined by the impactor parameters. In this regime, accounting for the acoustic fluidization does not change the final core morphology (not shown here). (3) For even more energetic impacts, the core is very strongly deformed, which does not appear to be compatible with Enceladus' core morphology (see Fig. 2). Our simulations of these events do not follow the full evolution of the impact scenario so we cannot predict the final core structure; however, it is likely that some of these events lead to full body disruption and that, in non-disruptive impacts, acoustic fluidization may contribute to the final shape of the rocky core and would therefore need to be included to analyze possible outcomes.

For impact velocities higher than 2.4 km s^{-1}($10 \times v_{esc}$), moderate deformation of the core is possible only for impactors smaller than 25 km. During the Late Heavy Bombardment, high-velocity collisions with impactors exceeding 20 km is likely and therefore, as recently highlighted by Movshovitz et al. (2015), full disruption and re-accretion of the satellite may have occurred possibly several times during this period. This implies that any large impact leaving a long-wavelength signature on the core shape should have taken place after the Late Heavy Bombardement. This also requires relatively low velocity impacts, and therefore encounter with planetocentric bodies rather than with heliocentric bodies. Alternatively, as proposed by Charnoz et al. (2011), Enceladus may have formed late during the history of the Saturn system, thus limiting the risk of full disruption. Following the model of Charnoz et al. (2011), Enceladus may have accreted from a swarm of differentiated embryos emerging from the outer edge of a massive ring system. In such a model, multiple low velocity collisions between decametric differentiated impactors and a growing Enceladus are expected.

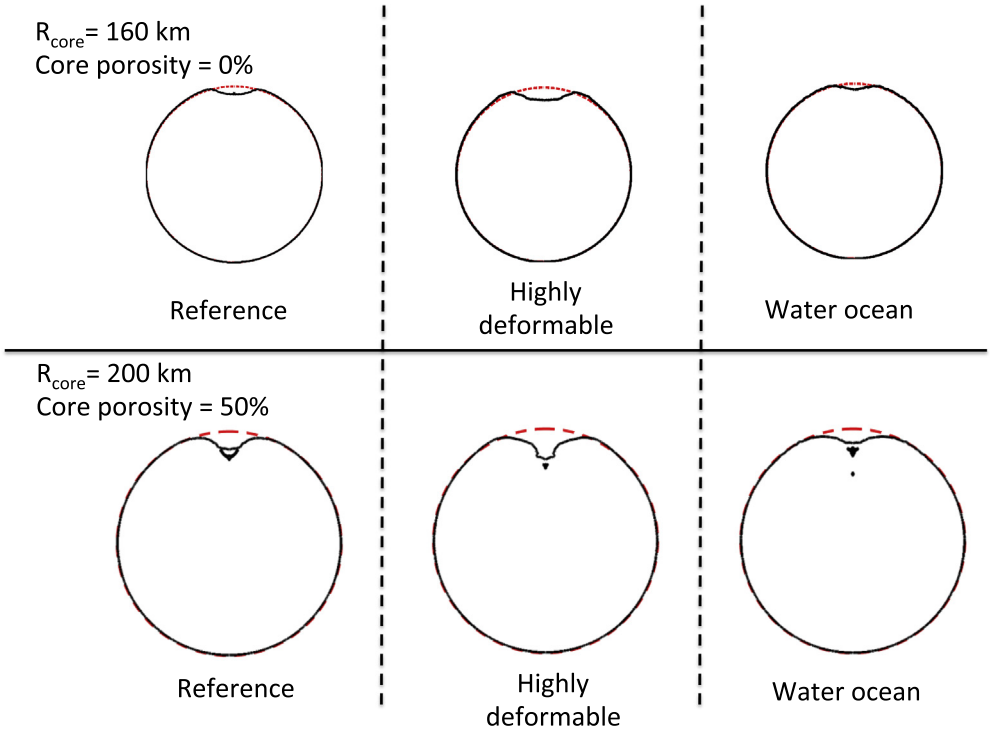

Fig. 9. Rocky core morphology for different pre-impact core radii (R_{core} = 160 km (top) and 200 km (bottom)). First and third columns: Y_i = 500 kPa and Y_s = 10 MPa, second column ("highly deformable") Y_i = 10 kPa and Y_s = 100 kPa. In the third column we consider a water ocean (with a thickness of 20 km) above the rocky core. For each morphology, the red circle represents the pre-impact spherical shape of the impacted core. (For interpretation of the references to color in this figure legend, the reader is referred to the web version of this article.)

The irregular core shape of Enceladus, as constrained from Cassini gravity and topography data (McKinnon, 2013; Lefèvre et al., 2015), may constitute a record of this accretional process.

Various processes will probably alter the core topography after an impact event, so that the amplitude of core deflection predicted in our simulations should be considered as an upper limit. Rock fragments would be likely transported by the ice flow back to the impact cavity, filling partly the impact-induced depression. Even if the core is relatively cold, topography relaxation may occur to some extent, especially for low-strength rock material. Prolonged water interactions may also partly erode the topography and again reduce the topography anomaly. Detailed modelling of the subsequent topography evolution is beyond the scope of the present study, and will require future modeling effort. The 2D nature of our simulations also optimizes the amplitude of impact-induced core deflection as only head-on collisions can be considered. It is known that impact angle affects the strength and distribution of the shock wave generated in the impact and therefore the perturbed region (e.g. Pierazzo and Melosh, 2000). For more oblique impacts, the impactor kinetic energy will be more efficiently transferred to the icy mantle, leading to a more efficient deformation of the icy mantle and a larger amount of escaping materials (e.g. Korycansky and Zahnle, 2011). The volume of icy mantle affected by the impact, which is already large for head-on collisions as shown with our 2D simulations, will be further increased. Another limitation of our modelling approach is the assumption regarding the mechanical properties of the rock core. We considered dunite with various degree of void porosity as representative of the rock core composition, since a relatively well-defined equation of state exists for this material (Davison et al., 2010). Based on the interpretation of the Cassini gravity data, which suggest a low density core (2400 kg m^{-3}, Iess et al. (2014)), the rock core may contain a significant fraction of highly hydrated minerals, as well as free water or/and ice in rock pores. Currently, we are not able to consider a mixture of ice and rocks for both the impactor's core and the target's core. However, to estimate an upper limit of the deformation, we have performed a run corresponding to our classical impact model ($v_{imp} = 10 v_{esc}$ and R_{imp} = 25 km) with 100% ice-filled pores (i.e. a core made of pure ice). In this unrealistic case (not shown here), the impactor's core is eventually buried at a depth of ~170 km (i.e. 80 km below the core-mantle boundary) which is far larger than the depth of the depression (~30 km) obtained with a 50% porous rocky core. This limitation also stands for the structure of the impactor's core that is likely to have remained undifferentiated in the context of an early formation. To estimate the influence of the impactor's degree of differentiation, we have also considered the $v_{imp} = 10 v_{esc}$ case with a 25 km radius impactor made of pure ice and an impactor made of pure dunite. In the first case, the impact induces a flattening of ~0.4 km at the core's surface below the impact site (see Fig. 6). In the second case, the impact induces a flattening of ~23.2 km. This result, even if performed for an unrealistic water ice content, suggests the ice/rock ratio in the core may play a strong influence on the response of the core to large impacts. This suggests that the results presented here should be considered valid only for differentiated interior models with rock-dominated core and a relatively small porosity content (<10–20%). Future works are required constrain more precisely the effect of hydrated minerals and mixture with high ice-water/rock ratio in the interior.

Large impacts are likely to modify the ice/rock ratio by eroding significantly the shallower part of the impacted moon. Our results show that vertical impacts with $v_{imp} > 6 v_{esc}$ and $R_{imp} > 75$ km, can erode up to half the ice volume from the impacted body (Fig. 1, second column). Several factors such as a hot, porous pre-impact mantle and the presence of a deep water ocean increase the ability of the icy mantle to deform. Hence, these parameters are also likely

to influence the post-impact ice/rock ratio by decreasing the fraction of ice in the post-impact moon. The impact angle is another key parameter that governs the fraction of escaped material (e.g. Korycansky and Zahnle, 2011). However, to limit the computational time and as we have restricted our study to vertical impacts, monitoring the long-term evolution of the ice/rock ratio is beyond the scope of our study.

Despite the limitations, the simulations we performed highlight the crucial role played by impacts on the evolution of Enceladus. Besides explaining the irregular shape of the core, impacts also provide efficient mechanisms to enhance thermo-chemical exchanges between the deep interior and the surface. For models with an internal water ocean, we can see that a large volume of the ocean is temporarily exposed to the surface, thus potentially releasing a large fraction of volatile initially stored dissolved in the ocean. Large impacts cause a strong damage of the ice on a very large portion of the icy mantle, which will likely have consequences on the subsequent convective mantle dynamics and interaction with the fractured surface. These also lead to a large plastic strain in the rock core underneath the impact site, which may enhance macroporosity. This would promote fluid circulation throughout a large fraction of the core, favoring serpentinization processes (Malamud and Prialnik, 2013) and hydrothermal activities (e.g. Hsu et al., 2015). Further modeling efforts will be needed to understand the consequences of such impact events on the long-term evolution of Enceladus. Lastly, the effects of large impacts are not confined to Enceladus. Similar effects are very likely on the other moons of Saturn as well as on other planetary objects, such as Ceres (e.g. Davison et al., 2015; Ivanov, 2015) and Pluto (e.g. Bray and Schenk, 2015) for which impact bombardment has probably played a key role in their evolution.

Acknowledgments

J. Monteux was funded by Agence Nationale de la Recherche (Accretis decision No. ANR-10-PDOC-001-01). The research leading to these results has received funding from the European Research Council under the European Community's Seventh Framework Programme (FP7/2007-2013 Grant Agreement No. 259285). We thank James Roberts and the anonymous reviewer for constructive comments. We gratefully acknowledge the developers of iSALE, including Kai Wünnemann, Boris Ivanov, Jay Melosh, and Dirk Elbeshausen. We also thank Katarina Miljkovich and Tom Davison for useful discussions.

References

Amsden, A.A., Ruppel, H.M., Hirt, C.W., 1980. SALE: Simplified ALE Computer Program for Fluid Flow at All Speeds, Tech. Rep. LA-8095. Los Alamos Natl. Lab., Los Alamos, NM.

Asphaug, E., 2010. Similar-sized collisions and the diversity of planets. Chemie der Erde/Geochem. 70, 199–219. http://dx.doi.org/10.1016/j.chemer.2010.01.004.

Asphaug, E., Reufer, A., 2013. Late origin of the Saturn system. Icarus 223, 544–565. http://dx.doi.org/10.1016/j.icarus.2012.12.009.

Benz, W., Asphaug, E., 1999. Catastrophic disruptions revisited. Icarus 142, 5–20. http://dx.doi.org/10.1006/icar.1999.6204.

Benz, W., Cameron, A.G.W., Melosh, H.J., 1989. The origin of the moon and the single impact hypothesis. III. Icarus 81, 113–131. http://dx.doi.org/10.1016/0019-1035(89)90129-2.

Besserer, J. et al., 2013. Convection-driven compaction as a possible origin of Enceladus's long wavelength topography. J. Geophys. Res. (Planets) 118, 908–915. http://dx.doi.org/10.1002/jgre.20079.

Bray, V.J., Schenk, P.M., 2015. Pristine impact crater morphology on Pluto – Expectations for new horizons. Icarus 246, 156–164. http://dx.doi.org/10.1016/j.icarus.2014.05.005.

Bray, V.J. et al., 2008. The effect of target properties on crater morphology: Comparison of central peak craters on the moon and Ganymede. Meteoritics Planet. Sci. 43, 1979–1992. http://dx.doi.org/10.1111/j.1945-5100.2008.tb00656.x.

Běhounková, M. et al., 2010. Coupling mantle convection and tidal dissipation: Applications to Enceladus and Earth-like planets. J. Geophys. Res. (Planets) 115, E09011. http://dx.doi.org/10.1029/2009JE003564.

Charnoz, S. et al., 2011. Accretion of Saturn's mid-sized moons during the viscous spreading of young massive rings: Solving the paradox of silicate-poor rings versus silicate-rich moons. Icarus 216, 535–550. http://dx.doi.org/10.1016/j.icarus.2011.09.017.

Collins, G.S., 2014. Numerical simulations of impact crater formation with dilatancy. J. Geophys. Res. Planets 119, 1–20. http://dx.doi.org/10.1002/2014JE004708.

Collins, G.C., Goodman, J.C., 2007. Enceladus' south polar sea. Icarus 189, 72–82. http://dx.doi.org/10.1016/j.icarus.2007.01.010.

Collins, G.S., Davison, T.M., Ciesla, F.J., 2011. Numerical simulations of sub-catastrophic porous planetesimal collisions. Proc. Lunar Sci. Conf. 42, 1933.

Collins, G.S., Melosh, H.J., Wünnemann, K., 2013. Improvements to the ϵ–α porous compaction model for simulating impacts into high-porosity Solar System objects. Int. J. Impact Eng. 38, 434–439.

Collins, G.S., Melosh, H.J., Ivanov, B.A., 2004. Modeling damage and deformation in impact simulations. Meteoritics Planet. Sci. 39, 217–231. http://dx.doi.org/10.1111/j.1945-5100.2004.tb00337.x.

Davison, T.M., Collins, G.S., Ciesla, F.J., 2010. Numerical modelling of heating in porous planetesimal collisions. Icarus 208, 468–481. http://dx.doi.org/10.1016/j.icarus.2010.01.034.

Davison, T.M. et al., 2015. Impact bombardment of ceres. Proc. Lunar Sci. Conf. 46, 2116.

Dwyer, C.A. et al., 2013. The influence of imperfect accretion and radial mixing on ice:rock ratios in the Galilean satellites. Icarus 225, 390–402. http://dx.doi.org/10.1016/j.icarus.2013.03.025.

Giese, B. et al., 2008. Enceladus: An estimate of heat flux and lithospheric thickness from flexurally supported topography. Geophys. Res. Lett. 35, L24204. http://dx.doi.org/10.1029/2008GL036149.

Hansen, C.J. et al., 2006. Enceladus' water vapor plume. Science 311, 1422–1425. http://dx.doi.org/10.1126/science.1121254.

Hsu, H.-W. et al., 2015. Ongoing hydrothermal activities within Enceladus. Nature 519, 207–210. http://dx.doi.org/10.1038/nature14262.

Iess, L. et al., 2014. The gravity field and interior structure of Enceladus. Science 344, 78–80. http://dx.doi.org/10.1126/science.1250551.

Ivanov, B.A., 2015. Ceres: possible records of giant impacts. Proc. Lunar Sci. Conf. 46, 1077.

Ivanov, B.A., Deniem, D., Neukum, G., 1997. Implementation of dynamic strength models into 2D hydrocodes: Applications for atmospheric breakup and impact cratering. Int. J. Impact Eng. 20, 411–430.

Jutzi, M., Benz, W., Michel, P., 2008. Numerical simulations of impacts involving porous bodies. I. Implementing sub-resolution porosity in a 3D SPH hydrocode. Icarus 198, 242–255. http://dx.doi.org/10.1016/j.icarus.2008.06.013.

Jutzi, M. et al., 2009. Numerical simulations of impacts involving porous bodies. II. Comparison with laboratory experiments. Icarus 201, 802–813. http://dx.doi.org/10.1016/j.icarus.2009.01.018.

Korycansky, D.G., Zahnle, K.J., 2011. Titan impacts and escape. Icarus 211, 707–721. http://dx.doi.org/10.1016/j.icarus.2010.09.013.

Lambe, T., Whitman, R., 1979. Soil mechanics, SI version. In: Series in Soil Engineering. Wiley.

Lefèvre, A. et al., 2015. Enceladus' internal ocean constrained from Cassini gravity and topography data. In: European Planetary Science Conference.

Lindsay, S.S. et al., 2015. Composition, mineralogy, and porosity of multiple asteroid systems from visible and near-infrared spectral data. Icarus 247, 53–70. http://dx.doi.org/10.1016/j.icarus.2014.08.040.

Malamud, U., Prialnik, D., 2013. Modeling serpentinization: Applied to the early evolution of Enceladus and Mimas. Icarus 225, 763–774. http://dx.doi.org/10.1016/j.icarus.2013.04.024.

McKinnon, W.B., 2013. The shape of Enceladus as explained by an irregular core: Implications for gravity, libration, and survival of its subsurface ocean. J. Geophys. Res. (Planets) 118, 1775–1788. http://dx.doi.org/10.1002/jgre.20122.

Melosh, H.J., Ivanov, B.A., 1999. Impact crater collapse. Annu. Rev. Earth Planet. Sci. 27, 385–415. http://dx.doi.org/10.1146/annurev.earth.27.1.385.

Melosh, H.J., Ryan, E.V., Asphaug, E., 1992. Dynamic fragmentation in impacts – Hydrocode simulation of laboratory impacts. J. Geophys. Res. 97, 14,73. http://dx.doi.org/10.1029/92JE01632.

Mitchell, J.K. et al., 1972. Mechanical properties of lunar soil: Density, porosity, cohesion and angle of internal friction. In: Metzger, A.E. et al. (Eds.), Proc. Lunar Sci. Conf., vol. 3, p. 3235.

Monteux, J. et al., 2014. Can large icy moons accrete undifferentiated? Icarus 237, 377–387. http://dx.doi.org/10.1016/j.icarus.2014.04.041.

Movshovitz, N. et al., 2015. Disruption and reaccretion of midsized moons during an outer Solar System Late Heavy Bombardment. Geophys. Res. Lett. 42, 256–263. http://dx.doi.org/10.1002/2014GL062133.

Murr, L. et al., 1998. The low-velocity-to-hypervelocity penetration transition for impact craters in metal targets. Mater. Sci. Eng. 256, 166–182.

Neish, C.D., Lorenz, R.D., 2012. Titan's global crater population: A new assessment. Planet. Space Sci. 60, 26–33. http://dx.doi.org/10.1016/j.pss.2011.02.016.

Nimmo, F. et al., 2007. Shear heating as the origin of the plumes and heat flux on Enceladus. Nature 447, 289–291. http://dx.doi.org/10.1038/nature05783.

Ohnaka, M., 1995. A shear failure strength law of rock in the brittle-plastic transition regime. Geophys. Res. Lett. 22, 25–28. http://dx.doi.org/10.1029/94GL02791.

Orphal, D.L. et al., 1980. Impact melt generation and transport. In: Bedini, S.A. (Ed.), Proc. Lunar Sci. Conf. vol. 11, pp. 2309–2323.

Pierazzo, E., Melosh, H.J., 2000. Melt production in oblique impacts. Icarus 145, 252–261. http://dx.doi.org/10.1006/icar.1999.6332.
Porco, C.C. et al., 2006. Cassini observes the active south pole of Enceladus. Science 311, 1393–1401. http://dx.doi.org/10.1126/science.1123013.
Potter, R.W.K. et al., 2012. Constraining the size of the South Pole-Aitken basin impact. Icarus 220, 730–743. http://dx.doi.org/10.1016/j.icarus.2012.05.032.
Richardson, J.E., Melosh, J.H., 2013. An examination of the Deep Impact collision site on Comet Tempel 1 via Stardust-NExT: Placing further constraints on cometary surface properties. Icarus 222, 492–501. http://dx.doi.org/10.1016/j.icarus.2012.04.019.
Roberts, J.H., 2015. The fluffy core of Enceladus. Icarus 258, 54–66. http://dx.doi.org/10.1016/j.icarus.2015.05.033.
Schenk, P., 2011. Geology of Mimas? In: Lunar and Planetary Science Conference, Lunar and Planetary Inst. Technical Report, vol. 42, p. 2729.
Schenk, P.M., McKinnon, W.B., 2009. One-hundred-km-scale basins on Enceladus: Evidence for an active ice shell. Geophys. Res. Lett. 36, L16202. http://dx.doi.org/10.1029/2009GL039916.
Schenk, P. et al., 2012. The geologically recent giant impact basins at Vesta south pole. Science 336, 694. http://dx.doi.org/10.1126/science.1223272.
Schubert, G., Stevenson, D.J., Ellsworth, K., 1981. Internal structures of the Galilean satellites. Icarus 47, 46–59. http://dx.doi.org/10.1016/0019-1035(81)90090-7.
Schubert, G. et al., 2007. Enceladus: Present internal structure and differentiation by early and long-term radiogenic heating. Icarus 188, 345–355. http://dx.doi.org/10.1016/j.icarus.2006.12.012.
Showman, A.P., Han, L., Hubbard, W.B., 2013. The effect of an asymmetric core on convection in Enceladus' ice shell: Implications for south polar tectonics and heat flux. Geophys. Res. Lett. 40, 5610–5614. http://dx.doi.org/10.1002/2013GL057149.
Spencer, J.R., Nimmo, F., 2013. Enceladus: An active ice world in the Saturn system. Annu. Rev. Earth Planet. Sci. 41, 693–717. http://dx.doi.org/10.1146/annurev-earth-050212-124025.
Spencer, J.R. et al., 2006. Cassini encounters Enceladus: Background and the discovery of a south polar hot spot. Science 311, 1401–1405. http://dx.doi.org/10.1126/science.1121661.
Thomas, P.C. et al., 2007. Shapes of the saturnian icy satellites and their significance. Icarus 190, 573–584. http://dx.doi.org/10.1016/j.icarus.2007.03.012.
Tobie, G., Čadek, O., Sotin, C., 2008. Solid tidal friction above a liquid water reservoir as the origin of the south pole hotspot on Enceladus. Icarus 196, 642–652. http://dx.doi.org/10.1016/j.icarus.2008.03.008.
Waite, J.H. et al., 2006. Cassini ion and neutral mass spectrometer: Enceladus plume composition and structure. Science 311, 1419–1422. http://dx.doi.org/10.1126/science.1121290.
Wünnemann, K., Collins, G.S., Melosh, H.J., 2006. A strain-based porosity model for use in hydrocode simulations of impacts and implications for transient crater growth in porous targets. Icarus 180, 514–527. http://dx.doi.org/10.1016/j.icarus.2005.10.013.

Space Sci Rev (2018) 214:39
https://doi.org/10.1007/s11214-018-0473-x

Water and the Interior Structure of Terrestrial Planets and Icy Bodies

J. Monteux[1] · G.J. Golabek[2] · D.C. Rubie[2] · G. Tobie[3] · E.D. Young[4]

Received: 30 July 2016 / Accepted: 11 January 2018

Abstract Water content and the internal evolution of terrestrial planets and icy bodies are closely linked. The distribution of water in planetary systems is controlled by the temperature structure in the protoplanetary disk and dynamics and migration of planetesimals and planetary embryos. This results in the formation of planetesimals and planetary embryos with a great variety of compositions, water contents and degrees of oxidation. The internal evolution and especially the formation time of planetesimals relative to the timescale of radiogenic heating by short-lived ^{26}Al decay may govern the amount of hydrous silicates and leftover rock–ice mixtures available in the late stages of their evolution. In turn, water content may affect the early internal evolution of the planetesimals and in particular metal-silicate separation processes. Moreover, water content may contribute to an increase of oxygen fugacity and thus affect the concentrations of siderophile elements within the silicate reservoirs of Solar System objects. Finally, the water content strongly influences the differentiation rate of the icy moons, controls their internal evolution and governs the alteration processes occurring in their deep interiors.

Keywords Water · Differentiation · Internal evolution · Terrestrial planets · Icy moons

The Delivery of Water to Protoplanets, Planets and Satellites
Edited by Michel Blanc, Allessandro Morbidelli, Yann Alibert, Lindy Elkins-Tanton, Paul Estrada, Keiko Hamano, Helmut Lammer, Sean Raymond and Maria Schönbächler

J. Monteux
julien.monteux@uca.fr

1 CNRS, IRD, OPGC, Laboratoire Magmas et Volcans, Université Clermont Auvergne, 63000 Clermont-Ferrand, France

2 Bayerisches Geoinstitut, Universität Bayreuth, Universitätsstrasse 30, 95440 Bayreuth, Germany

3 Laboratoire de Planétologie et Géodynamique, UMR-CNRS 6112, Université de Nantes, 44322 Nantes Cedex, France

4 Department of Earth, Planetary, and Space Sciences, University of California Los Angeles, Los Angeles, CA 90095, USA

Published online: 24 January 2018

1 Introduction

The Solar System displays a strong dichotomy between the inner region that is characterized by relatively dry planetary objects having a very small water fraction (<0.1%), and the outer solar system where water ice constitutes a large fraction of solid material (>20%), which is inherited from accretion processes. When compared with other planetary systems, the Solar System seems however rather unusual. Exoplanet surveys have revealed that planets intermediate in mass between Earth and Neptune are surprisingly common, but are notably absent in the Solar System (Mayor et al. 2014; Howard et al. 2012; Marcy 2014). Model mass-radius relationships indicate a great diversity of interior compositions and atmospheric extents for the Super-Earth/Mini-Neptune-planet class (e.g. Howard et al. 2012), suggesting a wide range of volatile contents (including water) and compositions.

The distribution of water in the planetary system is controlled by the temperature structure in the protoplanetary disk and dynamics and migration of planetesimals and planetary embryos (Raymond et al. 2004; Cowan and Abbot 2014; O'Brien et al. 2014; Rubie et al. 2015a). This results in the formation of planetesimals and planetary embryos with a great variety of compositions and water contents. Subsequent accretionary processes can lead to the formation of planets that range from completely dry planets to "water worlds" with more than 100 Earth-oceans of water (1 ocean $= 1.5 \times 10^{21}$ kg H_2O) (Raymond et al. 2004; Cowan and Abbot 2014; O'Brien et al. 2014; Rubie et al. 2015a). As the evolution of water content inside a growing proto-planet is a strong function of pressure-temperature conditions, the early stages of planetary formation that govern their accretion rates and their early heat budget may have played a major role in the water distribution in the solar system. Indeed, depending on the accretion rate and on the formation time of the building blocks of the terrestrial planets relative to the timescale of radiogenic heating by the decay of short-lived ^{26}Al, water can either be incorporated as an ice–rock mixture or in the form of hydrated silicates or be absent. Aqueous alteration appears to be common in carbonaceous chondrites (Kerridge and Bunch 1979; Zolensky et al. 1989; Krot et al. 1998). The proportion of planetesimal water incorporated into rock depends critically on whether water was mobile or stagnant (e.g., Young 2001; Young et al. 1999, 2003; Bland et al. 2009; Fu et al. 2017; Castillo-Rogez and Young 2017). In turn, the water content of Solar System objects likely played a key role in the internal evolution of the solar system bodies. For example, water dissolved in silicate minerals is known to significantly reduce mantle viscosity and melting temperature (e.g. Hirth and Kohlstedt 1996; Katz et al. 2003; Hirschmann 2006). It has therefore a potential influence on the early differentiation processes and a strong feedback on the thermal state of the mantle and the vigor of convection (e.g. Korenaga 2010).

Water is also the major constituent of the moons orbiting Jupiter (except for Io), Saturn, Uranus and Neptune, and all planetary objects beyond Neptune (e.g. Hussmann et al. 2015). In these icy objects, water is likely present either as thick ice shells or deep water oceans (e.g. Hussmann et al. 2006) and in some cases is being ejected from venting plumes composed mainly of water vapor and ice particles (e.g. Porco et al. 2006 for Enceladus, Roth et al. 2014 for Europa). The combined effect of accretional heating, radiogenic decay by short-lived isotopes, tidal heating associated with despinning, and viscous heating associated with sinking negative rock diapirs may increase the internal temperature above the melting point of ice (e.g. Tobie et al. 2013). This may result in a partial to full ice–rock separation. During this differentiation as well as at the present-day, interactions between solid rock and liquid water might have promoted chemical reactions facilitated by the presence of ammonia (Schubert et al. 2010; Sohl et al. 2010). It is also possible that aqueous alteration

might have led to serpentinization of olivine-rich rocks and to the formation of a highly hydrated rocky core that may result from a rapid differentiation process that implies large-scale melting events, as proposed for Saturn's moon Titan (e.g. Castillo-Rogez and Lunine 2010).

Finally, comets and comet-like objects are another class of objects in which ice has been detected as a major component (80%) (Encrenaz 2008). These bodies, with radii usually smaller than 10 km, were formed in the outer Solar System. Comets are undifferentiated and, hence, represent weakly altered remnants of the early stages of solar-system formation. Because of radiogenic heating from ^{26}Al and ^{60}Fe, the interior of comets may reach temperatures above the melting point of water and ultravolatile species may be lost (Prialnik et al. 2008; Mousis et al. 2017). In the following study, we do not consider the comets and we will only focus on objects with radii larger than 25 km (see review of Prialnik et al. 2008 for more details).

The structure of this article is as follows: We first detail the distribution of water in the protoplanetary disc and its effect on oxidation. Second, we present a discussion of the effect of internal evolution of planetesimals on water content based on numerical models. In particular we investigate the influence of planetesimal radius and formation time. We then discuss the role of water on the internal evolution of proto-planets and terrestrial bodies focusing particularly on metal/silicate separation and oxygen fugacity evolution. Finally we briefly describe the internal evolution of icy satellites from their accretion to their present-day activity and emphasize the role of water in differentiation and alteration processes.

2 Distribution of Water in the Protoplanetary Disc and Its Effect on Oxidation

Protoplanetary disks of gas and dust are by necessity characterized by radial increases in temperature and pressure towards the nascent star at their center. The inner portions of the disk are heated by two mechanisms. So-called "passive" disks are heated at their surfaces by illumination from the central star. Viscous heating in "active" accretion disks can warm up the inner portions of the disk to temperatures well above those imposed by passive illumination alone. The degree of viscous heating depends on the mechanism for angular transport (accretion onto the star) (e.g., Bai and Stone 2013). The greater the effective viscosity of the disk, the greater the heating related to accretion. In all cases, there will be specific radii corresponding to the condensation fronts for various volatile components (referred to as "snowlines"). From the perspective of volatiles and planet formation, the most important of these may be that for water. The water snowline separating the inner regions of the disk where water vapor is stable from the more distal regions of the disk where water ice is stable is thought to exert a first-order control on the chemistry of planetesimals. The snowline in an accretion disk is closest to the star at the midplane where the intervening mass of gas and dust shields the disk from light from the central star. Higher in the disk, the snowline curves to greater radial distances due to heating of the surfaces of the disk by the central star. We are most concerned with the position of the water snowline at the midplane when contemplating planetesimal formation. However it must be kept in mind that the time-dependent position of the snowline in the midplane and its effects on planetesimal formation over time are still debated (e.g., Morbidelli et al. 2016).

The bulk compositions of planetesimals and planetary embryos in the protoplanetary disc, including water and some volatile element abundances, have been constrained by core formation modelling (Rubie et al. 2015a, 2016). Mantle abundances of siderophile elements

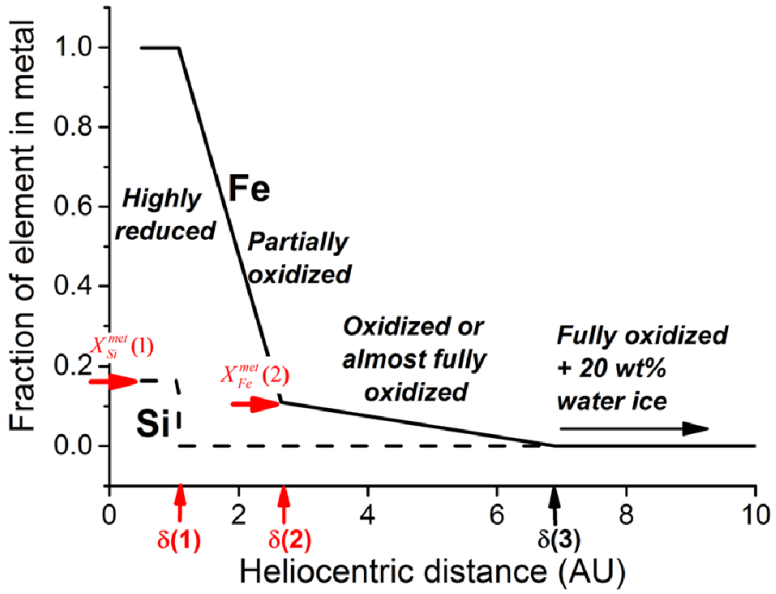

Fig. 1 The composition of initial bodies (embryos and planetesimals) as a function of heliocentric distance determined in the accretion/core formation model of Rubie et al. (2015a). At heliocentric distances less than ~1 au, 99% of all Fe is present as metal and ~18% of total Si is dissolved in the metal—which makes the bulk composition very reduced. Beyond ~1 au, compositions become increasingly oxidized with increasing heliocentric distance because the fraction of Fe present as metal decreases and the fraction of Fe present as FeO in the silicate increases. Beyond 6–7 au, compositions are fully oxidized (no metal) and contain 20 wt% water—these are bodies that originally accreted beyond the snowline. The *red arrows* indicate values of parameters that were refined by least squares

(Ni, Co, W etc.) can be reproduced in multistage core formation models when the initial 60–70% of Earth accretes from highly reduced material and the final 30–40% from relatively-oxidized material, in combination with the effects of Si partitioning into the core (Rubie et al. 2011). The late accretion of oxidized material is also consistent with the relatively late accretion of volatile elements to the Earth (e.g. Schönbächler et al. 2010; Dauphas 2017). This scenario was developed further by Rubie et al. (2015a, 2016) by formulating a combined accretion/core formation model. This was based on "Grand Tack" N-body accretion models (Walsh et al. 2011; O'Brien et al. 2014) that started with up to ~200 embryos (distributed from 0.7 to 3.0 au) embedded in a protoplanetary disc consisting of up to 4400 planetesimals (distributed from 0.7 to 9.5 au). Each accretional collision between embryos and other embryos and planetesimals was considered to result in an episode of core formation, provided the impactor was metal-bearing. The bulk composition of each of the starting bodies was defined in terms of CI ratios of non-volatile elements, with oxygen and water contents varying as a function of heliocentric distance. Based on these bulk compositions, the compositions of equilibrated metal and silicate in each core-formation event were determined by a combined mass balance/element partitioning approach, thus enabling the evolving compositions of the mantles and cores of all growing planets to be modeled. The composition of the model Earth in each simulation was fit to Earth's mantle composition by a least squares refinement of the metal-silicate equilibration pressure and several parameters that describe the compositions of initial bodies (Fig. 1). Best fits to Earth's mantle composition were obtained when compositions of bodies close to the Sun are highly reduced and those further out are relatively oxidized (Fig. 1).

The gradient in Fig. 1 requires explanation in the context of the young solar protoplanetary disk. Dynamical models have shown that radial mixing within the protoplanetary disk was likely to occur especially during the late stages of planetary formation (e.g. Chambers

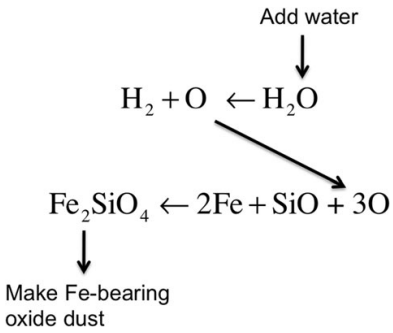

Fig. 2 Schematic illustrating the enhancement of the fayalite component in olivine due to an increase in water. This scheme could have operated at moderately high temperatures in the protoplanetary disk where dust was processed

2013; Raymond et al. 2004). Variation in oxygen fugacity across the protoplanetary gaseous disk is a longstanding question. At temperatures greater than about 500 to 600 K or so, Fe_2SiO_4, representing oxidized iron, is unstable at solar oxygen fugacities. This temperature is lower than the ca. 1400 K required for diffusion and annealing of silicate grains (Figs. 2 and 3). The solution is to pump up the oxidation state of the vapor phase by infusing it with water inside of the snowline. As the protoplanetary disk evolved, small icy bodies will have drifted inwards of the snowline, resulting in addition of H_2O vapor by subsequent sublimation of water ice. The longevity of this vapor depended critically on the competing rates of inward migration across the snowline and the outward diffusive flux of water driven by freezing of water at the snowline (e.g., Cuzzi and Zahnle 2004). The result of the competing fluxes may have been a pulse of elevated H_2O/H_2 just inside the snowline (Fig. 4). Such a localized pulse of water vapor has been observed in the TW Hydra transition disk at a distance of about 4 au from the central star (Zhang et al. 2013). The significant amount of oxidized iron in grains comprising chondrite matrix, even in rocks with limited evidence for water–rock reactions, is testament to the fact that such a process must have occurred where planetesimals were forming (Grossman et al. 2012). The amount of water required can be estimated from the equilibrium relationship

$$H_2 + 1/2O_2 \Leftrightarrow H_2O$$

for which we obtain the equation for f_{O_2} (e.g., Krot et al. 2000)

$$\log(f_{O_2}) \simeq 2\log\left(\frac{H_2O}{H_2}\right) + 5.67 - \frac{256664}{T\,(\mathrm{K})}. \quad (1)$$

Inspection of this equation shows that in order to change oxygen fugacity by ~5 log units as required to shift from solar to "planetary" oxidation states, H_2O/H_2 must have increased by a factor of ~375 at inner disk temperatures of ~1400 K (Fig. 5). Geometric considerations suggest that focusing solar abundances of water into the inner 5 au of the disk by inward transport can only raise the H_2O/H_2 ratio by about a factor of 10 (where, for example, surface density varies as $1/R$ where R is the radial distance from the Sun).

The picture that emerges is one in which ice accreted within planetesimals outside of the snowline may have reacted with the host rock as the planetesimals evolved in response to heating by ^{26}Al (see also Sect. 3). Liquid water reactions with rock will have oxidized the rock. Inside of the snowline there was likely a region where inward migration of ice enhanced the H_2O/H_2 ratio in the vapor phase just inside of the snowline, but further into the disk in the region of terrestrial planet formation, the ambient conditions favored reduced iron over oxidized iron as a result of higher temperatures and a decrease in gaseous H_2O toward the star. The snowline must have migrated inward with time in response to a decrease

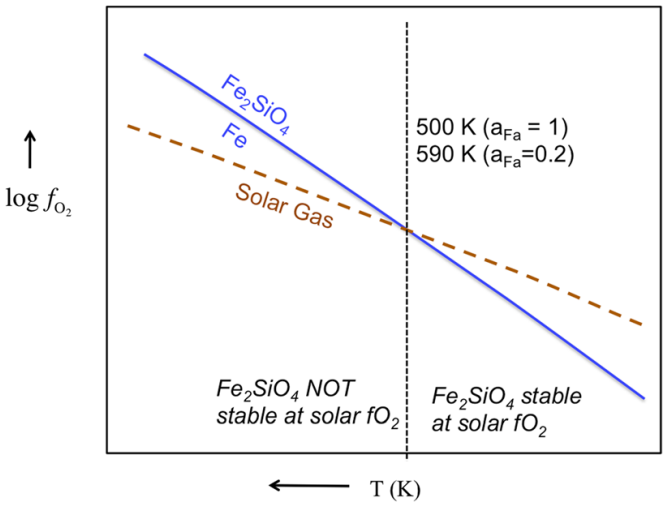

Fig. 3 Schematic diagram showing the relationship between oxygen fugacity and temperature for a solar gas and for the oxidation state of iron. At higher temperatures, reduced iron is favored over the fayalite component for a solar-like gas. At lower temperatures, Fe_2SiO_4 can be stabilized, but whether this reaction can actually occur at lower temperatures is in question. Typical activities for fayalite in olivine at two different temperatures are shown for illustration

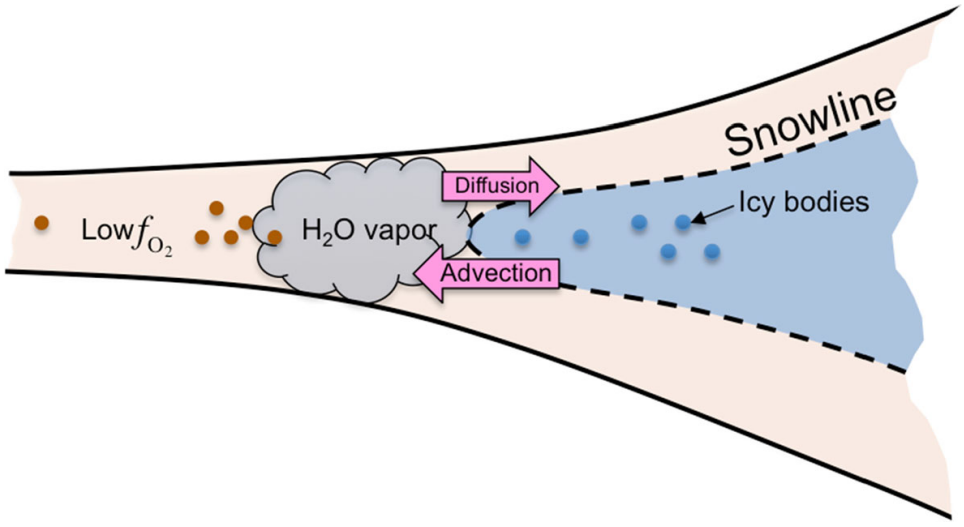

Fig. 4 Schematic diagram illustrating the competition between advection of icy material through the snowline of the protoplanetary disk and backwards net transfer of water via diffusion driven by a buildup of water vapor inside of the snowline. The process is described by Cuzzi and Zahnle (2004) and is consistent with Spitzer and Herschel observations of TW Hydra (Zhang et al. 2013)

in the stellar accretion rate, and the best fit shown in Fig. 1 suggests that its time-integrated "fossilized" location (see below) was somewhere between 6 and 2 au.

The position of the midplane water snowline as a function of time can be obtained from the temperature and pressure structure of a generic protoplanetary accretion disk. The T and P structure of the disk can be modeled using basic principles of dissipative radiative losses resulting from orbital torques. The torques are sustained by the viscosity of the disk that results in the inward spiral of gas towards the growing star. For dimensionless viscosity parameter α (e.g., Shakura and Sunyaev 1973), sound speed c_s, and scale height $H(R)$, the effective viscosity of the disk is $\upsilon = \alpha c_s H(R)$. The temperature at the midplane of the disk can be written in terms of the accretion rate of the system, $\dot{m}$, as follows

$$T_{\text{midplane}} = \left[\frac{\frac{3}{2}\Sigma(R)\kappa_R}{4} + 1\right]^{1/4}\left[\frac{3}{8\pi\sigma}\frac{GM_*\dot{m}}{R^3}\right]^{1/4} \quad (2)$$

where κ_R is the Rosseland mean opacity, $\Sigma(R)$ is the surface density of the disk that is a function of R from the central star, G is the gravitational constant, M_* is the mass of the

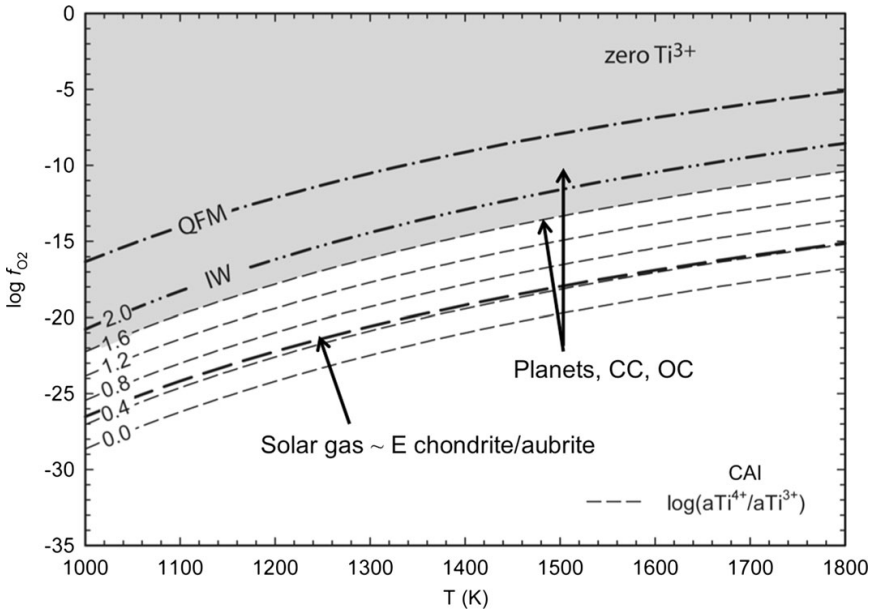

Fig. 5 The logarithm of oxygen fugacity versus temperature for various oxygen buffers relevant for the early solar system. The heavy *dashed line* shows the relationship for a solar gas. For comparison, planetary materials (Earth's mantle, basalts from various bodies) exhibit oxygen fugacities closer to the iron-wüstite (IW) and quartz–fayalite–magnetite (QFM) oxygen buffers. Note that the difference between a solar gas and those planetary materials implies an increase of more than 5 orders of magnitude in oxygen fugacity. The region shaded in *grey* represents oxidation states that favor Ti^{3+} over Ti^{4+} in calcium–aluminum-rich inclusions (CAIs) in carbonaceous chondrites. *Contours* for the activity ratio of the two forms of Ti in CAIs are also shown

central star, $\dot{m}$ is the accretion rate and σ is the Stefan–Boltzmann constant. The first term on the right-hand-side of (2) accounts for the optical depth perpendicular to the midplane and is equivalent to $T_{\text{midplane}}/T_{\text{surface}}$. The surface temperature is given by the second term. Equation (2) shows that the temperature of the disk at any radial distance R from the star depends on the rate of mass accretion through the disk. The latter has been measured in young stellar objects today and varies from about $10^{-6}\ M_{\odot}\ \text{yr}^{-1}$ early in the history of stellar accretion to $10^{-8}\ M_{\odot}\ \text{yr}^{-1}$ (Hartmann 2000) later on.

Evaluation of (2) requires evaluating the surface density with distance from the star, $\Sigma(R)$. The surface density can be written in terms of the viscosity as (Armitage 2010)

$$\Sigma(R) = \frac{\dot{m}}{3\pi\alpha c_s H(R)}, \tag{3}$$

where scale height H of the disk as a function of radial distance from the star is

$$H(R) = \frac{c_s}{\Omega} = \sqrt{\frac{k_{\text{b}} T R^3}{G M_* \mu}}, \tag{4}$$

and where Ω is orbital angular velocity, k_{b} is Boltzmann's constant, T is the temperature and μ is the average molecular mass for the gas comprising the disk. Equation (2) can be evaluated analytically with reasonable precision by assuming a constant value of $1\ \text{m}^2/\text{kg}$ for κ_R and replacing (3) with a parameterization for $\Sigma(R)$ suggested by the mass distribution of planets in the solar system: $\Sigma(R) \sim 1200\ \text{kg/m}^2\ (R/5\ \text{au})^{-3/4}$ (compare with Chiang and Youdin 2010). The result for $10^{-7}\ M_{\odot}\ \text{yr}^{-1}$ is shown in Fig. 6.

The competing rates of temperature and pressure-dependent adsorption and desorption of water onto grain surfaces in the disk define the position of the water snow line. Pressure

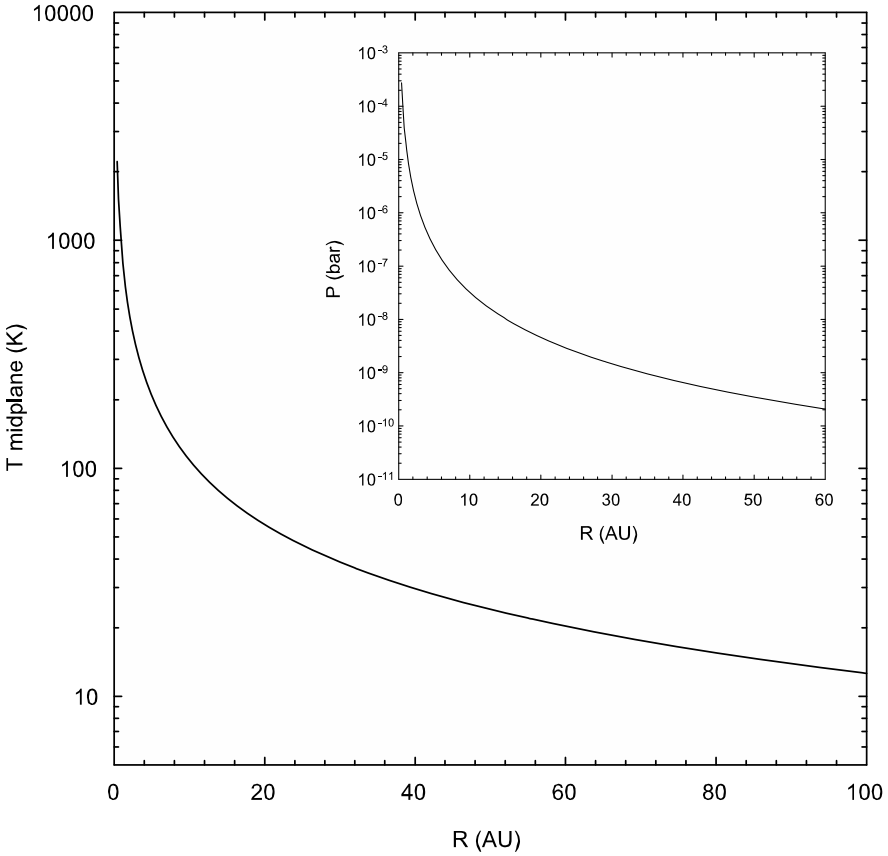

Fig. 6 Calculated temperature and pressure vs. distance from the central star for a solar-like protoplanetary accretion disk with a mass accretion rate of 10^{-7} solar masses per year

defines the total number density n_{total} of molecules since $P = n_{\text{total}} k_{\text{b}} T$. Midplane pressures as a function of radial distance from the star are

$$P(R) = \frac{\Sigma}{\sqrt{\pi} H(R)} \frac{k_{\text{b}} T}{\mu}. \tag{5}$$

The kinetic theory of gases yields the rate constant for adsorption of molecules onto grain surfaces:

$$k_{\text{ads}} = \left\langle \pi r_{\text{grains}}^2 \right\rangle \hat{V}_{\text{gas}} n_{\text{grains}} \tag{6}$$

where k_{ads} is the rate constant (s^{-1}), r_{grains} is the average radius of the dust grains, n_{grains} is the number density of the dust grains (cm^{-3}), and $\hat{V}_{\text{gas}} = \sqrt{8 k_{\text{b}} T / (\pi \mu)}$ is the average gas velocity. Hasegawa et al. (1992) suggest a parameterization for the number density of grains based on total hydrogen such that $n_{\text{grains}} \sim 1.33 \times 10^{-12} n_{\text{H}}$ and $n_{\text{H}} = 2 \times n_{\text{H2}} \sim n_{\text{total}}$. Substitution of this expression into (6), together with the mass of water molecules, yields in SI units

$$k_{\text{ads}} = \left\langle \pi r_{\text{grains}}^2 \right\rangle \sqrt{1.18 \times 10^4 T(\text{K})} 1.33 \times 10^{-6} (P_{\text{H}_2} / (k_{\text{b}} T)). \tag{7}$$

Equation (7) can be evaluated using midplane temperatures and pressures ((2), (4), and (5)) and the fact that typical radii for dust grains relevant to the protoplanetary disk environment are 0.1 μm, or 1×10^{-7} m. The competing rate constant for desorption of water from grains in SI units is (Willacy et al. 1998):

$$k_{\text{des}} = 1 \times 10^{12} \exp(-4815 / T(\text{K})). \tag{8}$$

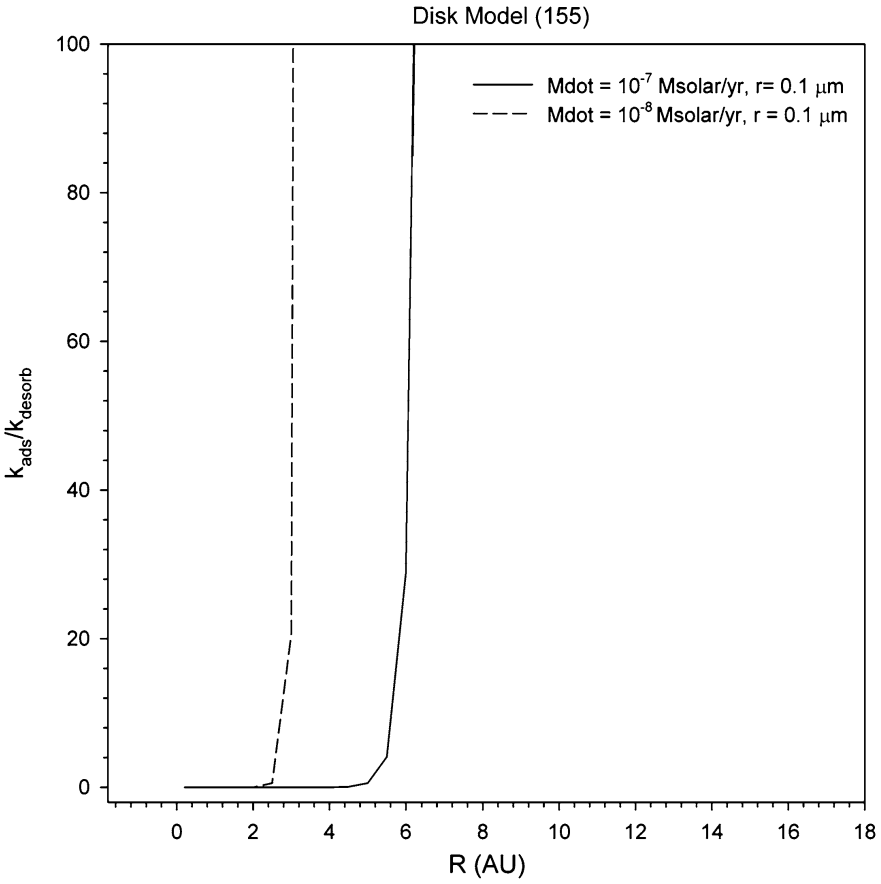

Fig. 7 Position of the water snow line as a function of mass accretion rate as defined by the ratio of the adsorption and desorption rate constants

At equilibrium rates of adsorption and desorption of water onto dust grains are equal so we have $k_{\rm ads} n_{\rm H_2O,gas} = k_{\rm des} n_{\rm H_2O,grains}$. Therefore, $k_{\rm ads}/k_{\rm des} \gg 1$ represents water frozen to grains and $k_{\rm ads}/k_{\rm des} \ll 1$ represents where most water molecules exist in the gas phase. A unit value for $k_{\rm ads}/k_{\rm des}$ defines conditions corresponding to the effective position of the snow line in the midplane of the disk. Substitution of (2) and (5) into (7) and (8) yields the plot in Fig. 7 showing the calculated position of the snowline in the disk as a function of accretion rate. The effective freeze out temperature for $\dot{m} = 10^{-8}\ M_\odot$/yr is ~190 K. The effective temperature for freeze out of water is 170 K for $\dot{m} = 10^{-7}\ M_\odot$/yr. Most importantly, we note that basic physics of accretion disks indicates that the calculated position of the snow line varies from ~5 au to 2 au when accretion rate varies from $10^{-7}\ M_\odot$/yr to $10^{-8}\ M_\odot$/yr, respectively. This is the basis for the assertion that in a solar-like protoplanetary disk, we have a good idea of where the snowline should have been as a function of time.

Of course, radial drift complicates the simple picture described above. Morbidelli et al. (2016) point out that decoupling of radial drift velocities between dust and gas can result in a decoupling of "wet" and "dry" gas from the position of the snowline. The rates of icy particle drift inwards towards the star compared with the rates of planetesimal formation then become critical for understanding the compliments of water in protoplanetary materials, as described above in connection with Fig. 1. Morbidelli et al. (2016) suggested that the apparent position of the water snowline recorded by planetesimal formation may be a "fossilized" snowline imprinted on the disk by the gap opened up by a growing Jupiter. Therefore, the rough correspondence between the position of the shift in oxygen fugacity in Fig. 1 and the

natural position of the water snowline for disk mass accretion rates of between 10^{-7} $M_{\odot}$/yr and 10^{-8} $M_{\odot}$/yr could be a manifestation of a locking in of the position of the snowline at these accretion rates by opening of a gap in the vicinity of the snowline by proto-Jupiter.

3 Effect of Internal Evolution on Water

During the early evolution of the terrestrial planets and icy bodies, four main sources of energy may have contributed to their internal thermal budget (e.g. Tobie et al. 2013): (i) Tidal heating associated with despinning, (ii) radiogenic heating by the decay of short-lived radioactive isotopes, (iii) impact heating and (iv) conversion of potential energy into heat via viscous dissipation during core-mantle separation. These four sources of energy likely concern different growth stages or reservoirs and hence will be separated in time and space. For planetesimals, only short-lived radiogenic (mainly ^{26}Al) heating is relevant (Yoshino et al. 2003; Rubie et al. 2015b). This source of energy was for several million times larger than the radiogenic heating rate due to the decay of long-lived isotopes currently expected on planets and moons. However, this huge heat production decayed rapidly. On the other hand on planetary embryos and fully accreted terrestrial planets, the release of potential energy and impact heating have to be taken into account in addition to radiogenic heating. The impact heating strongly depends on the impact velocity, on the masses of the target and the impactor as well as the way kinetic energy is converted into heat (Monteux et al. 2007). Hence the size of the growing body that governs the minimum impact velocity (i.e. the escape velocity) is a key factor. For large growing bodies, large impact events may generate significant melting within the target and trigger metal–rock or ice–rock separation potentially leading to runaway differentiation processes (Golabek et al. 2009; Ricard et al. 2009). Finally on icy moons long-lived radiogenic heating and tidal dissipation are the most important energy sources, while only the largest impact heating events can play a role (Monteux et al. 2014).

The composition of the building blocks from which planetary objects form as well as the early thermal budget should control the amount of water that can be stored in planetary embryos. To get a first order estimation of the amount of hydrous silicates and leftover rock–ice mixture available at the end of the thermo-mechanical evolution of planetesimals, we perform numerical models in 2D infinite cylinder geometry using the finite-difference marker-in-cell code I2ELVIS (Gerya and Yuen 2007; Golabek et al. 2014; Lichtenberg et al. 2016). The physical parameters and the setup employed are identical to those used in our previous studies (see Golabek et al. 2014; Lichtenberg et al. 2016).

Based on current planetesimal formation models (e.g. Johansen et al. 2015; Simon et al. 2016), we model planetesimals with radii R_{P} ranging between 25 and 230 km and consider instantaneous formation times t_{form} ranging from 0 to 3.5 Myr after formation of Ca–Al-rich inclusions (CAIs). We study here the evolution of planetesimals that formed across the snowline and were scattered later into the inner solar system (Raymond and Izidoro 2017). Thus we assume for each planetesimal a starting temperature equal to the temperature of surrounding space $T_{\mathrm{space}} = 150$ K. Since for small objects the release of potential energy related to accretion is small (Schubert et al. 1986), the resulting temperature increase is negligible and is not considered here. Thus only short-lived radiogenic heating is relevant. For simplicity we assume that the planetesimals do not contain metal because both formation of hydrated silicates and their dehydration occur at lower temperatures than the melting temperature of the eutectic Fe–FeS mixture (1243 K) at low pressures (Brett and Bell 1969),

so core formation due to percolation is expected to start only after the breakdown of hydrated silicates. Therefore we assume that at the start of the model each planetesimal is composed only of a rock–ice mixture. Here we assume that at $T = 273$ K the ice melts and hydrated silicates can form. Under the low-pressure conditions inside a planetesimal the most temperature-resistant hydrated silicates (amphibolites) break down at $T \approx 1223$ K and dehydrate (Fu and Elkins-Tanton 2014). However it should be taken into account that by considering the breakdown of amphibolites the current models give only an upper limit for the amount of hydrated silicates present, since for example more abundant hydrated silicates like serpentine-phyllosilicates break down at significantly lower temperatures (573–673 K) (Nakamura 2006; Nakato et al. 2008).

The following additional assumptions and simplifications are used in the numerical model: We ignore here reaction kinetics and assume that both the formation of hydrated silicates and their breakdown occur instantaneously at the given temperatures. Also we ignore possible water delivery or loss processes related to impact events. Additionally we do not consider pore water convection (Young et al. 2003) suggested for smaller planetesimals ($R_P < 40$–60 km) and assume that after silicate dehydration the water previously incorporated into hydrated silicates is completely lost to space. Also it should be kept in mind that even dry silicates still contain small amounts of water (see e.g. Fu and Elkins-Tanton 2014), thus even planetesimals loosing all hydrated silicates still contain some water, which is not considered in our numerical model.

The time-dependent amount of hydrated silicate material in each modeled planetesimal is tracked on the markers of the numerical model. The final 2D area covered by (a) rock–ice mixture and (b) hydrated silicates is converted for representation purposes analytically into a 3D volume (see Fig. 8a, b).

The general results show that the amount of both remaining rock–ice mixture and hydrated silicates is strongly dependent on the formation time t_{start} since this parameter controls the abundance of short-lived ^{26}Al ($t_{1/2} = 0.716$ Myr), while the radius has only a modest effect (see Fig. 8a, b). As expected late formed objects contain orders of magnitude more rock–ice mixture and hydrated silicates than early-formed planetesimals. Since formation of hydrated silicates requires some heating, more of the interior contains hydrated silicates in late-formed, but large planetesimals, while a primordial rock–ice mixture is best preserved in the smallest objects experiencing fast cooling. However the results also show that less hydrated silicates form in planetesimals that accreted very late because the reduced amount of ^{26}Al radiogenic heating is insufficient to allow for the formation of hydrated silicates throughout the bulk of the planetesimal interior. This leads to a "sweet spot" for the formation of hydrated silicates, which is narrower for small planetesimals with $R_P < 80$ km since these objects cool more efficiently than large planetesimals (see Fig. 8a).

All models start with a rock–ice mixture. Because the temperature at the center of the planetesimal reaches the maximum value, formation of hydrated silicates starts there and over time the formation front propagates outwards. For large objects ($R_P \geq 100$ km) that formed early enough ($t_{form} < 0.75$ Myr) the center is also the location where dehydration starts during later evolution and a dehydration front propagates from there towards the surface. For planetesimals with sufficient ^{26}Al heating both the formation and later the dehydration front are able to propagate throughout the entire planetesimal interior and within $\sim 10^6$ years the entire planetesimal will loose all hydrated silicates (see Fig. 9). On smaller objects full dehydration occurs only on objects that formed earlier than $t_{form} < 0.75$ Myr, while in the smallest planetesimals considered ($R_P \leq 50$ km) complete loss of hydrated silicates is not achieved even inside planetesimals formed at the same time as CAIs (see Fig. 8a).

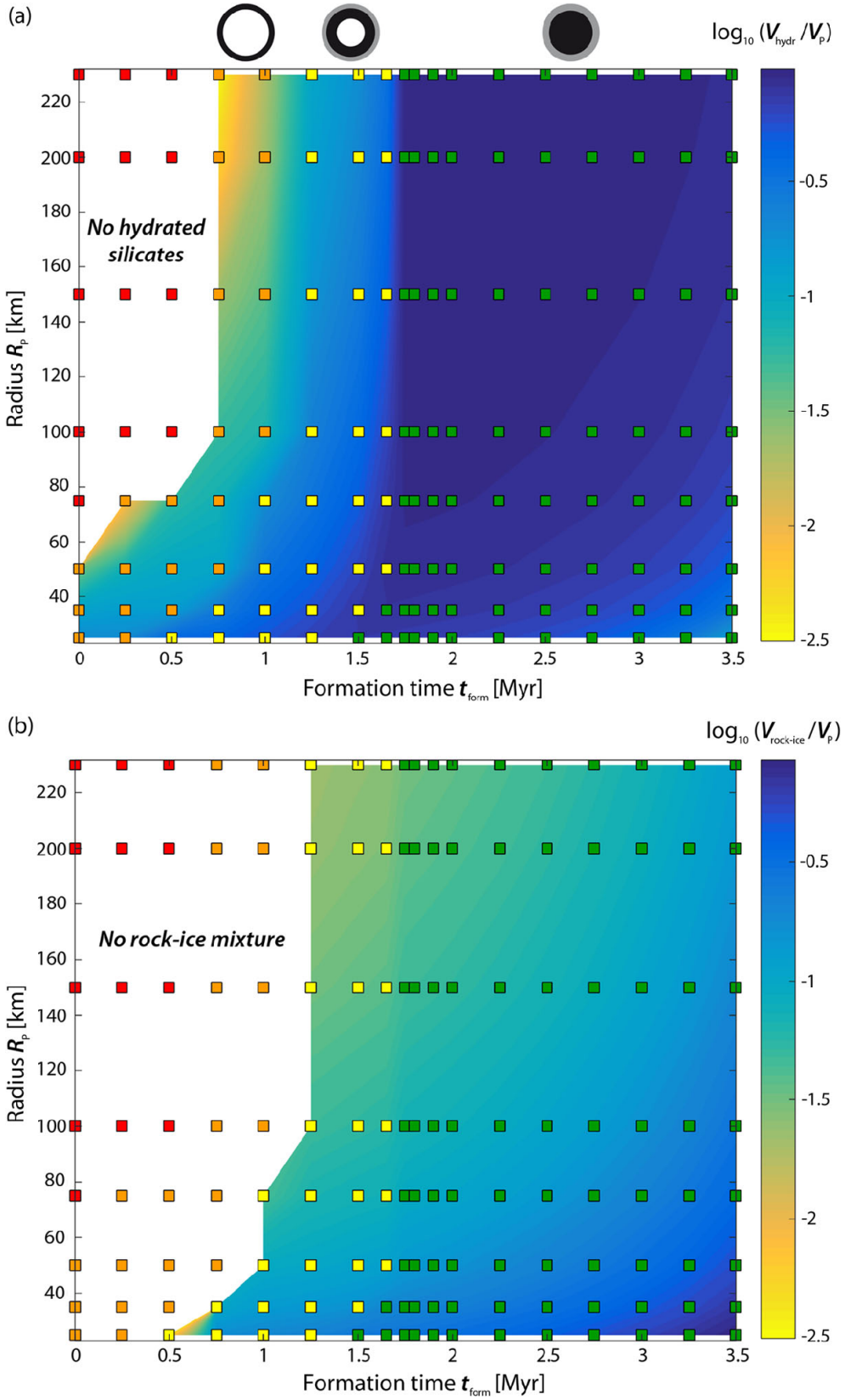

Fig. 8 (**a**) Final volume of hydrated silicates V_{hydr} and (**b**) final volume of rock–ice mixture $V_{\mathrm{rock\text{-}ice}}$. Both volumes are scaled by the total volume of the specific planetesimal V_{P} for models with different planetesimal radii R_{P} and formation times t_{form} assuming an initial temperature $T_{\mathrm{space}} = 150$ K. *Squares* represent the numerical model results. *Colours* of the squares stand for various final internal states: No hydrous silicates left (*red*), outer hydrated shell (*orange*), inner hydrated shell (*yellow*) and hydrated interior (*green*). For clarity three of the possible final outcomes are sketched on top of subfigure (a) with dehydrated silicates (*white*), hydrated silicates (*black*) and rock–ice mixture (*grey*)

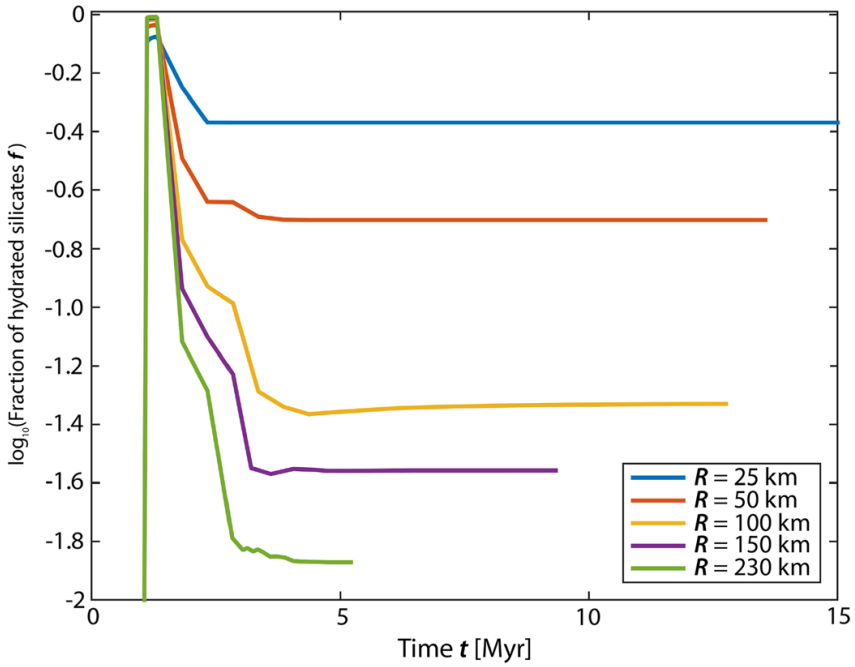

Fig. 9 Time-dependent fraction of hydrated silicates inside planetesimals with $t_{\rm form} = 1$ Myr and $R_{\rm P} = 25$–230 km.

Large, but later-formed planetesimals (0.75 Ma $\leq t_{\rm form} < 1.25$ Myr) or early-formed, but small objects exhibit a different final outcome, namely an outer hydrated shell, where the formation front reached the object's surface, while the propagation of the dehydration front ceased at depth due to insufficient ^{26}Al radiogenic heating. Inside large planetesimals that formed even later (1.25 Ma $\leq t_{\rm form} < 1.75$ Myr) neither the formation nor the dehydration front reach the surface. Under these circumstances the surface is still composed of a rock–ice mixture while the deep interior is dehydrated and an annulus at intermediate depth contains hydrated silicates. For late-formed objects (large objects with $t_{\rm form} \geq 1.75$ Myr or for smaller planetesimals with $t_{\rm form} \sim 1.5$ Myr after CAI formation) temperatures are never sufficiently high as to start dehydration and these objects display a hydrated interior and a rock–ice mixture closer to the surface (see Fig. 8a, b). This is in agreement with observations indicating that some asteroids contain even at present-day significant amounts of volatiles (Hsieh and Jewitt 2006; Jewitt et al. 2009; Küppers et al. 2014).

Based on these simple models, we can speculate that large ($R_{\rm P} > 80$ km), late-formed planetesimals ($t_{\rm form} > 1.7$ Myr), initially formed across the snowline and implanted into the main asteroid belt or scattered into the inner solar system during the accretion of the gas giants (Raymond and Izidoro 2017), can contribute significant amounts of water in the form of hydrated silicates to growing planetary embryos. This is in general agreement with both the classical model (e.g. Chambers 2013; Raymond et al. 2009) and the Grand Tack scenario (Walsh et al. 2011; Rubie et al. 2015a) suggesting that during the later stages of accretion planetary embryos will accrete material that formed at larger distances from the Sun.

In conclusion, we have shown that the internal evolution and especially the formation time of planetesimals relative to the timescale of radiogenic heating by short-lived ^{26}Al decay may govern the amount of hydrous silicates and leftover rock–ice mixture available during the late stages of their evolution. In turn, water content may affect the early internal evolution of the planetesimals and in particular the metal-silicate separation processes to be discussed in the next section.

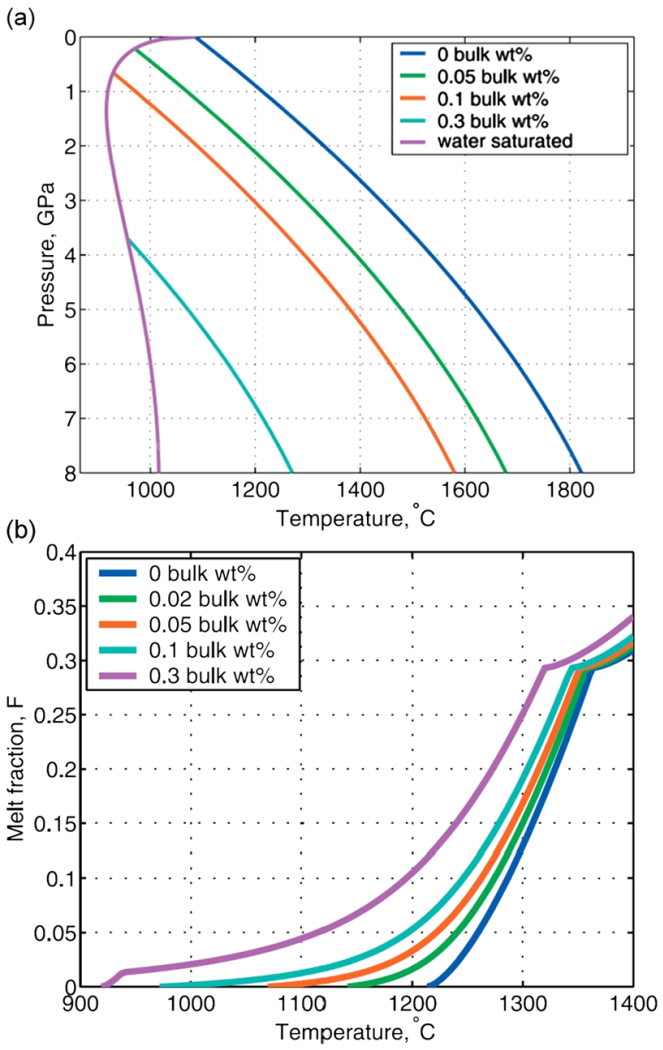

Fig. 10 Effects of water on the melting of peridotite. (**a**) Depression of the peridotite solidus temperature as a function of pressure for bulk water contents of 0, 0.05, 0.1 and 0.3 wt%. (**b**) Effect of water on melt fraction F during partial melting of peridotite shown as isobaric melting curves at 1 GPa for bulk water contents ranging from 0 to 0.3 wt%. Note that the kink at a melt fraction of ∼0.3 is caused by the disappearance of clinopyroxene from the mineral assemblage (from Katz et al. 2003). Note that equivalent temperatures for a bulk chondritic composition are lower by ∼200 °C (Fig. 7 in Asahara et al. 2004). Also the addition of any incompatible elements (e.g. the C and S that are present in chondritic meteorites) will reduce melting temperatures

4 Effects of Water on Internal Evolution

The most important process occurring during the early internal evolution of a rocky planetary body is differentiation that results in a silicate mantle and a metallic iron-rich core. The terrestrial planets, Mercury, Venus, Earth and Mars, as well some asteroids, such as Vesta, all underwent core-mantle differentiation. In addition, based on the existence of iron meteorites, many early-formed planetesimals also experienced core-mantle differentiation. Undifferentiated material, as represented by chondritic meteorites, consists of intimate mixtures of metal, sulfide, silicate and oxide grains. The formation of metallic cores in differentiated bodies therefore requires metal and silicate to separate over significant length scales (up to 3000 km in the case of Earth but on the order of 100–500 km in the case of planetesimals). Such segregation was only physically possible at high temperatures at which at least the metal and probably also the silicates were in a molten state (Stevenson 1990; Rubie et al. 2015b). High temperatures were the result of the decay of the short-lived ^{26}Al isotope in planetesimals during the first ∼3 Myr of Solar System history and were later the result of high-energy collisions that took place during planetary accretion (e.g. Rubie et al. 2015b; de Vries et al. 2016). Thus planetesimals could only differentiate early, while ^{26}Al was extant, and were largely unaffected by impact-induced heating because of their low masses (see Rubie et al. 2015b, Fig. 10). In general, core-mantle differentiation that occurred as a consequence of impact-induced melting could only happen later after bodies had grown sufficiently in mass. Physical and chemical conditions differed significantly during these respec-

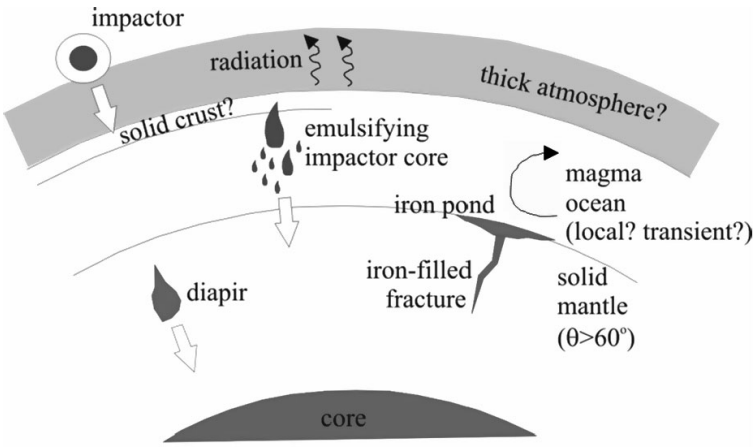

Fig. 11 Schematic section through a terrestrial planet during core formation. A global magma ocean is shown overlying solid crystalline mantle below which lies the metallic proto-core. Metal is delivered by impactors, many of which are likely to have been differentiated into core and mantle. The molten impactor cores partially or completely emulsify in the magma ocean to form small droplets that sink to the base of the magma ocean and collect there to form liquid "iron ponds". These sink through the crystalline mantle as diapirs or possibly are transported through fractures (see Rubie et al. 2015b for a review). Although a possible solid crust is shown, this may not form when an atmosphere is present because its insulating effect keeps the temperature at the surface of a magma ocean above the solidus (e.g., Matsui and Abe 1986)

tive episodes. For example, gravitational forces were much smaller during early planetesimal differentiation and such bodies likely differentiated in the presence of nebular gases, which dispersed before the formation of the terrestrial planets.

The presence of water in planetary bodies could have had a significant effect on both the physical processes of core formation and their chemical consequences. For example, the presence of even small amounts of water strongly reduces the solidus temperature of silicates (Fig. 10a). It also increases the melt fraction at a given temperature, although this effect is largest close to the solidus and becomes much smaller as the degree of melting increases (Fig. 10b).

4.1 Effects of Water on Mechanisms of Core Formation

There are several different mechanisms by which metal and silicate could have segregated (Fig. 11) and the presence of water would have affected each of these differently. Potentially the mechanisms shown in Fig. 11 could all operate during the differentiation of an Earth-mass planet. However, as discussed towards the end of this section, core-mantle differentiation on small bodies (planetesimals) likely required significant melting (with a melt fraction of at least 30–50%) as the result of heat produced by the decay of ^{26}Al (see also Scheinberg et al. 2015).

We first review the possible metal-silicate segregation mechanisms and how these would be affected by the presence of water and then discuss chemical consequences of water during core-mantle differentiation.

Percolation of Liquid Metal Through a Polycrystalline or Partially-molten Silicate Matrix Liquid iron-rich metal or sulfide, (Fe, Ni)S, can percolate through a solid polycrystalline silicate matrix by porous flow provided the liquid phase forms an interconnected network along grain boundaries or grain edges rather than isolated melt pockets. Interconnection depends upon the dihedral angle, θ, which is the angle between two solid–liquid boundaries that are intersected by a solid–solid boundary at a triple junction (Fig. 12; von

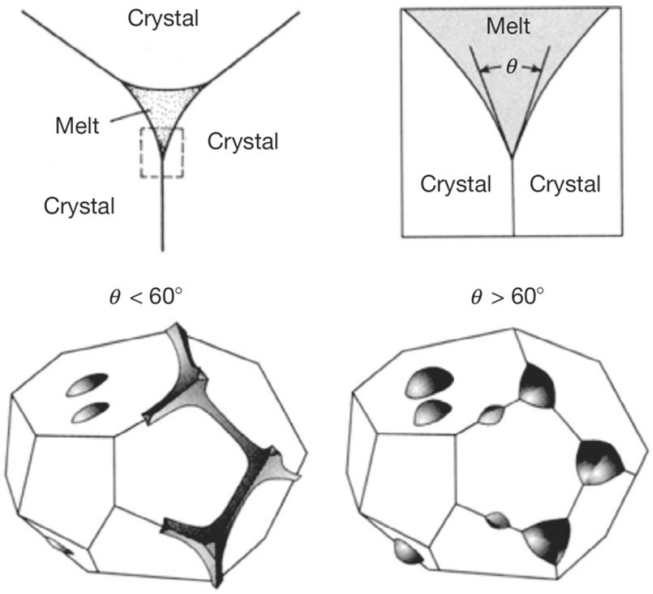

Fig. 12 The dihedral angle θ is the angle between two melt–crystal interfaces where they are intersected by a crystal–crystal grain boundary at a triple junction. When $\theta < 60°$, the melt forms an interconnected network along grain edges (*bottom left*), whereas when $\theta > 60°$ there is no interconnectivity (unless the melt fraction is high) (from Stevenson 1990)

Bargen and Waff 1986; Stevenson 1990; Rubie et al. 2015b). When θ is less than 60°, the liquid metal phase is interconnected at any melt fraction and can percolate efficiently through the crystalline matrix. When θ exceeds 60°, interconnection only occurs when a critical melt fraction (e.g. a few volume % or more) is exceeded, which means that metal-silicate segregation cannot occur efficiently. Experimental studies of both natural and synthetic systems relevant to core formation have shown that, in general, θ lies in the range 80–120°, at least up to pressures of ~25 GPa (Rubie et al. 2015b and references therein). Therefore percolation is unlikely to be a major mechanism of metal-silicate segregation in the terrestrial planets. However, at pressures <2–3 GPa, the dihedral angle is less than 60° if the liquid Fe contains significant concentrations of oxygen and sulfur (Terasaki et al. 2005, 2008). It is therefore possible that under oxidizing conditions percolation was an important core formation mechanism in planetesimals during heating by ^{26}Al decay, especially when the metal contains sulfur (which reduces the melting temperature of the metal relative to that of the silicate).

As discussed in the previous section, dehydration of silicates is likely to leave only a few hundred ppm of water in planetesimals that have been heated by the decay of ^{26}Al. However, such H_2O concentrations would be sufficient to lower the silicate solidus temperature by 100–150 K (Fig. 10a), which means that the percolation of liquid metal or sulfide through partially molten silicates, rather than crystalline silicates, needs to be considered. Intuitively, it might be expected that a few percent silicate liquid in the system would enhance the ability of liquid metal to percolate. However, the opposite is the case and the presence of silicate melt actually reduces the interconnectivity of metallic liquids (Holzheid et al. 2000; Rushmer and Petford 2011; Holzheid 2013; Cerantola et al. 2015; Todd et al. 2016). This is the result of the high liquid metal-liquid silicate interfacial energy that causes metallic blobs to adopt a spherical geometry so that they become isolated in silicate melt. Consequently the metallic blobs become trapped in interstices in the partial molten aggregate. Thus, once silicate liquid forms by partial melting, as temperature increases, any interconnectivity of liquid metal or sulfide is destroyed. As the temperature rises further, the silicate melt fraction will eventually become large enough to enable the metallic droplets to become mobile and to segregate gravitationally. The value of the silicate melt fraction at which this happens is poorly known but is likely to be in the range 30–50% (Stevenson 1990; Minarik et al. 1996; Holzheid et al. 2000; Costa et al. 2009; Solomatov 2015). At this degree of partial

melting a magma ocean forms and the segregation mechanism changes to that described below. Thus the presence of water is likely to significantly delay metal-silicate segregation in planetesimals by requiring a higher temperature to start than under anhydrous conditions.

Segregation of Liquid Metal in a Silicate Magma Ocean As described above, when the fraction of silicate melt exceeds a certain value (probably 30–50%), a magma ocean state is achieved. When the metallic cores of impacting bodies sink through a magma ocean by gravitational settling, they tend to break up into smaller masses, eventually forming small droplets through emulsification. The extent to which emulsification occurs is important because it determines the fraction of accreted metal that equilibrates chemically with silicate liquid of the magma ocean (e.g., Nimmo et al. 2010; Rudge et al. 2010; Rubie et al. 2015a). When emulsification and equilibration fail to occur, the impactor's core merges directly with the core of the target body by "core merging". The efficiency of emulsification is uncertain, especially for the cores of giant impactors (Rubie et al. 2003; Dahl and Stevenson 2010; Samuel 2012; Deguen et al. 2014; Wacheul et al. 2014; Kendall and Melosh 2016; Landeau et al. 2016). The process is extremely difficult to study numerically because the length scales involved range from 100's km (or more) to a few mm. In the case of the Earth, it has been estimated that emulsified droplets of liquid Fe have a stable diameter of $\sim$1 cm and sink with a velocity of $\sim$0.5 m/s (Stevenson 1990; Rubie et al. 2003). Such parameters are a result of molten peridotite having a very low viscosity (Liebske et al. 2005)—which also results in magma oceans convecting vigorously in a turbulent regime. Because peridotite liquid is already highly depolymerized, the addition of water is unlikely to have a significant effect on its viscosity. In addition, as shown in Fig. 10b, the presence of water will have only a small effect on the temperature of magma ocean formation when the latter is defined to have a silicate melt fraction $\geq$0.3.

Descent of Diapirs of Liquid Metal Through Crystalline Mantle It has been proposed that segregated liquid metal accumulates as a pool at the bottom of a magma ocean during the differentiation of terrestrial planets. If the base of the magma ocean is separated from the proto-core by a crystalline mantle, it is likely that the iron melt pool sinks through the latter as diapirs, perhaps 1–10 km in diameter or larger (Fig. 11; e.g. Stevenson 1990; Karato and Murthy 1997; Samuel et al. 2010). Water dissolved in crystalline upper mantle rocks has a strong weakening effect on rheology and reduces the viscosity of solid-state flow by up to 2–3 orders of magnitude. For example, Hirth and Kohlstedt (1996) show that 810 ± 490 H/10^6 Si dissolved in olivine reduces the viscosity by a factor of 500 ± 300 compared with that of dry olivine. The descent velocity of metal diapirs can be described by Stokes' Law. Since the Stokes' sinking velocity is inversely proportional to mantle viscosity, the effect of water is large and could enhance the descent velocity by up to 2–3 orders of magnitude, at least in upper mantle peridotite.

Numerical models of diapirs sinking through the solid mantle of Earth-sized bodies indicate that a wet rheology favors diapir sinking, while a dry rheology leads to preferential formation of iron-filled dikes (Golabek et al. 2009). It was shown both analytically and numerically that this changes the heat partitioning between iron and silicates (Ke and Solomatov 2009; Golabek et al. 2009). Whereas the sinking of diapirs results in heat preferentially partitioning into the silicate mantle, the propagation of iron dikes results in the preferential heating of the iron. Thus the presence of water in the crystalline mantle could affect the thermal state of a terrestrial planet after core formation.

In summary, the effect of water on the temperature and timing of magma ocean formation in accreting planetary bodies, as required for metal-silicate segregation, is very small.

In relatively oxidized planetesimals, the presence of water may eliminate the possibility of metal-silicate segregation by percolation, as proposed by Terasaki et al. (2008), so that segregation only starts at a magma ocean stage after mantle material is at least 30–50% molten. If the descent of diapirs of liquid metal through crystalline mantle occurs, water dissolved in the mantle material would greatly enhance the rate of this process. On the other hand, an absence of water could change the descent mode from sinking diapirs to diking, thus affecting the heat partitioning between iron and silicates and modifying the thermal state of the early terrestrial planet.

4.2 Effects of Water on the Chemistry of Core Formation

The main geochemical effect of metal-silicate segregation to form the core and mantle of a planetary body is that siderophile (metal-loving) elements, such as Ni, Co, V, Cr, W, Mo, etc., partition into liquid metal and are thus transported from the mantle into the core. Consequently, all siderophile elements are variably depleted in Earth's mantle, relative to solar relative abundances, by factors of up to almost 1000. The degree of depletion depends on the extent to which an element partitions into metal. This is described by the metal-silicate partition coefficient, $D_{\mathrm{M}}^{\mathrm{met\text{-}sil}}$, which for element M is defined simply as:

$$D_{\mathrm{M}}^{\mathrm{met\text{-}sil}} = \frac{C_{\mathrm{M}}^{\mathrm{met}}}{C_{\mathrm{M}}^{\mathrm{sil}}}$$

where $C_{\mathrm{M}}^{\mathrm{met}}$ and $C_{\mathrm{M}}^{\mathrm{sil}}$ are the molar (or wt%) concentrations of M in the metal and silicate, respectively. Most metal-silicate partition coefficients for siderophile elements depend on pressure (P) and/or temperature (T). In addition, and of great importance for the present discussion, they depend strongly on oxygen fugacity f_{O_2}, as shown by the redox reaction:

$$\underset{\text{metal}}{\mathrm{M} + (n/4)\mathrm{O}_2} = \underset{\text{silicate liquid}}{\mathrm{MO}_{n/2}}$$

where n is the valence of element M when incorporated in silicate liquid as an oxide component. When f_{O_2} is low, this reaction shifts to the left thus increasing $D_{\mathrm{M}}^{\mathrm{met\text{-}sil}}$, whereas when f_{O_2} is high the reaction shifts to the right thus decreasing $D_{\mathrm{M}}^{\mathrm{met\text{-}sil}}$.

When modeling core formation, the extent to which Earth's mantle has been depleted in siderophile elements enables estimates to be made of the conditions (P, T, f_{O_2}) of metal-silicate equilibration during core formation (e.g. Wade and Wood 2005; Walter and Cottrell 2013; Rubie et al. 2011, 2015a, 2016). Traditionally, it has been assumed that core formation was a single-stage event, thus enabling unique values for P, T and f_{O_2} to be determined (Walter and Cottrell 2013; see Table 3 in Rubie et al. 2015b). However, "single-stage" core formation is clearly unrealistic because metal is delivered to a growing planet during the entire accretion process, which in the case of Earth likely lasted for up to 100 Myr (e.g. Jacobson et al. 2014). Thus, in recent years more realistic core formation models have been formulated. Firstly, in models of "continuous" core formation (Wade and Wood 2005; Wood et al. 2006), material is accreted to Earth in small (1%) increments with the metal component being equilibrated with the silicate mantle at the base of a magma ocean. In a second class of models, core formation is multi-stage and the accretion of mostly-differentiated embryos and planetesimals to growing planets is linked to episodes of metal-silicate equilibration and core formation (Rubie et al. 2011, 2015a, 2016). In both types of models, magma ocean depth increases as planets grow

so that the pressure and temperature of metal-silicate equilibration both increase as accretion proceeds. In addition, the oxygen fugacity at which metal and silicate equilibrate has to increase by 2–3 orders of magnitude during accretion in order to reproduce the concentrations of siderophile elements in Earth's mantle (Wade and Wood 2005; Wood et al. 2006; Rubie et al. 2011). There are at least three mechanisms that can result in, or contribute to, this increase of f_{O_2}, two of which are intimately related to water. Note that oxygen fugacity is determined from the compositions of co-existing metal and silicate relative to that of the iron-wüstite (IW) buffer, as follows:

$$\Delta\mathrm{IW} = 2\log\left[\frac{a_{\mathrm{FeO}}}{a_{\mathrm{Fe}}}\right].$$

Here ΔIW is the deviation of f_{O_2} from the IW buffer in log units, and a_{FeO} and a_{Fe} are the activities of FeO and Fe in the silicate and metal, respectively. Under low oxygen fugacities (e.g. $\Delta\mathrm{IW} = -4$) the FeO content of the silicate is low (e.g. <1 wt%), whereas at higher oxygen fugacities (e.g. $\Delta\mathrm{IW} = -2$) the FeO content becomes similar to that of Earth's mantle ($\sim$8 wt%).

Partitioning of Silicon into the Core Under reducing conditions and especially at high temperature, Si becomes siderophile (e.g. Mann et al. 2009) and this element partitions into liquid core-forming metal by the reaction

$$\underset{\text{mantle}}{\mathrm{SiO_2}} + \underset{\text{core}}{2\mathrm{Fe}} \rightarrow \underset{\text{core}}{\mathrm{Si}} + \underset{\text{mantle}}{2\mathrm{FeO}}.$$

According to this reaction, for every mole of Si that partitions into the core, two moles of FeO are added to the mantle. This reaction is therefore very efficient at increasing the oxygen fugacity, as required by the core formation models of Wade and Wood (2005) and Rubie et al. (2011, 2015b).

Oxidation of Metal by Accreted Water At the end of core formation, the oxygen fugacity of Earth's mantle was low ($\sim$IW $-$ 2) whereas it is currently several orders of magnitude higher (close to the FMQ buffer). In the upper mantle, the currently high oxygen fugacity is the result of a high Fe^{3+} concentration in some of the constituent minerals (O'Neill et al. 1993). The increase in f_{O_2} after core formation may have been caused by the disproportionation reaction

$$\mathrm{Fe^{2+}} \rightarrow \mathrm{Fe^{3+}} + \mathrm{Fe\ metal}$$

which occurs as a result of the crystallization of the lower-mantle mineral bridgmanite (silicate perovskite) (Frost et al. 2004). Water can also potentially cause oxidization in planetary interiors, for example by the reaction:

$$\mathrm{H_2O} + \underset{\text{metal}}{\mathrm{Fe}} \rightarrow \mathrm{H_2} + \underset{\text{silicate}}{\mathrm{FeO}},$$

for which the loss of hydrogen is required, or, in the absence of metal, by the dissociation of H_2O into oxygen and hydrogen, with the latter being lost. Sharp et al. (2013) proposed that such reactions were the cause of the increase in f_{O_2} of Earth's mantle following core formation.

All oxidation reactions that are caused by water require that hydrogen is lost from the system. In the absence of metal, this may be problematic because hydrogen is a strong reducing agent. Therefore, if oxidation is taking place deep in the Earth's interior, the released hydrogen has to migrate to the Earth's surface without causing any reduction of the material that it comes into contact with, which seems very unlikely. If metal is present, the hydrogen may be removed by dissolving in the metal, so that, during core formation, it would be transported to the core of the planet. It is uncertain how efficient this process would be because the partitioning of hydrogen between metal and silicate under core formation conditions is poorly known (Okuchi 1997). The oxidation of metal by water during core formation has been included in the accretion/core formation model of Rubie et al. (2015b) assuming that all released hydrogen dissolves in the metal. It was thus shown that the role of accreted water in oxidizing the mantle during core formation is insignificant and that all oxidation (up to the end of core formation) can be explained by the dissolution of Si into the core (as discussed above) combined with the effects of the accretion of oxidized bodies due to an oxidation gradient in the solar nebula (Fig. 1).

5 Differentiation and Evolution of Water-Rich Objects: From Icy Moons to Ocean-Planets

Most of the physical processes that are discussed to occur during the early stages of planetary formation also occur in the outer part of the Solar System during the formation of icy moons. In these bodies the mantle is composed mainly of water ice while their core is essentially made of rocky material. While the variety of internal structures among the icy moons is still debated, the essential role of the water is widely accepted. These objects are discussed in this section.

5.1 Variety of Internal Structures of Icy Moons

Differences in composition and internal structure exist among the major icy satellites of Jupiter and Saturn, suggesting distinct accretion and differentiation histories (e.g., Kirk and Stevenson 1987; Mueller and McKinnon 1988; Mosqueira and Estrada 2003; Barr and Canup 2008; Monteux et al. 2014). In this section we will focus particularly on the largest icy moons having a planetary scale, namely Jupiter's moons Ganymede and Callisto, and Saturn's moon Titan. The internal structure of these bodies has been constrained from the measurements of the gravity coefficients from spacecraft radio tracking during close flybys (e.g. Galileo, Cassini) (Anderson et al. 1996, 2001; Iess et al. 2010, 2012). The degree-2 gravity coefficients can then be used to infer the moment of inertia of the satellite, thus providing constraints on the density structure. The normalized moment of inertia about the spin axis, $C/(M_T R_T^2)$, is commonly calculated from the fluid Love number using the Radau–Darwin approximation. This formulation implies that the body's equipotential corresponds to the equilibrium shape due to fluid dynamic flattening. In this approximation, the degree-two gravity coefficients, C_{20} and C_{22}, should be equal to $-10/3$ and are proportional to the fluid Love number.

In the case of Titan, the ratio between the observed C_{20}^{obs} and C_{22}^{obs} is close to $-10/3$ (Iess et al. 2010), suggesting that Titan is relatively close to hydrostatic equilibrium. We can therefore use the degree-two gravity coefficients to first order to estimate the fluid Love number and the corresponding moment of inertia factor. Depending on whether we use the C_{20} or C_{22}

coefficients as a reference to determine the fluid Love number, the normalized moment of inertia varies between 0.335 and 0.342. For Ganymede and Callisto, the two coefficients have not been determined independently, and the $-10/3$ relationship has been prescribed when inverting the degree-two gravity coefficients. Using the degree-two coefficients, and applying the Radau–Darwin relationship, the moment of inertia factors of Ganymede and Callisto are estimated to be 0.31 and 0.355 (assuming hydrostatic equilibrium), respectively (Anderson et al. 1996, 2001). Titan's value is therefore intermediate between those of Ganymede and Callisto, suggesting a modest increase of density toward the center. The high moment of inertia factor obtained by Galileo gravity measurements ($C/(MR^2) = 0.355$) (Anderson et al. 2001) suggests an incomplete ice–rock separation within Callisto. In contrast, Ganymede has a much smaller moment of inertia ($C/(MR^2) = 0.31$) (Anderson et al. 2001) and shows signs of past endogenic activity (Pappalardo et al. 2004). Hence, Ganymede is potentially fully differentiated with an icy upper mantle, a rocky lower mantle and a metallic core, which is the origin of a relatively intense intrinsic magnetic field (Kivelson et al. 1998). With similar size and mass, Titan may be an intermediate case between Callisto and Ganymede. Based on the estimation of its moment of inertia factor, Titan's interior is more differentiated than Callisto's but probably much less than Ganymede's interior. Like Callisto, Titan might still possess a layer of ice–rock mixture between a rocky core and an outer ice-rich mantle, unless the rocky core is composed mostly of hydrated minerals (Sohl et al. 2010; Castillo-Rogez and Lunine 2010). A dense atmosphere is currently present at its surface but no intrinsic magnetic field has yet been detected on Titan. However the presence of a metallic core is plausible within Titan if enough iron was delivered during its accretion (Grasset et al. 2000). The fact that the interior of Callisto and possibly Titan may still contain a layer of ice–rock mixture suggests that the satellites have avoided significant melting during accretion and subsequent evolution.

We now discuss the apparently partially-differentiated state of Callisto and Titan, as suggested by their elevated moment of inertia factors (e.g. Anderson et al. 2001; Iess et al. 2010; Gao and Stevenson 2013). In the absence of lithospheric strength and shell thickness variations, these satellites would adopt a perfectly hydrostatic shape, corresponding to a degree-two gravity field. On Titan, the existence of a non-negligible degree-three in the gravity field as well as significant topography suggest that non-hydrostatic effects may significantly affect the estimation of the moment of inertia factor (Iess et al. 2010; Gao and Stevenson 2013; Baland et al. 2014) and that the moment of inertia factor may be significantly smaller than the value estimated from the Radau–Darwin approximation. On Callisto, similar non-hydrostatic contributions originating in the lithosphere, which could not be tested with the Galileo spacecraft data, may also affect the estimation of its moment of inertia factor (McKinnon 1997; Gao and Stevenson 2013). On these two moons, the hydrostatic dynamical flattening is relatively small as they orbit relatively far from their respective planets, and therefore the non-hydrostatic contributions need to be correctly estimated in order to accurately infer the moment of inertia factor and the density profiles of their interior. Future measurements by the JUICE mission (Grasset et al. 2013) will allow us to test how far Ganymede and Callisto are from hydrostatic equilibrium.

5.2 Differentiation Process in Water-Dominated Interiors

Several scenarios have been proposed to explain the wide range of extents of differentiation among the icy moons that resulted from radioactive and accretional heating. O'Rourke and Stevenson (2014) showed that although rock–ice separation may be delayed by double-diffusive convection in the ice–rock interior, ice melting due to progressive radiogenic heating and subsequent differentiation cannot be prevented. Previous studies showed that it was

possible to avoid melting if the accumulation of accretion energy was inefficient, i.e. if the energy was radiated away at a rate comparable to the accretion rate (e.g., Schubert et al. 1981; Squyres et al. 1988; Kossacki and Leliwa-Kopystynski 1993; Coradini et al. 1995; Grasset and Sotin 1996). Based on these models, the accretion timescales should be longer than 1 Myr to avoid significant melting and hence differentiation of Callisto, while an accretion timescale as short as 10^3–10^4 yr may be possible for Ganymede. However, these timescales are dependent on the way heat deposition and cooling are treated. Barr and Canup (2010) proposed that the Ganymede–Callisto dichotomy can be explained through differences in the energy received during the Late Heavy Bombardment. Impacts would have been sufficiently energetic on Ganymede to lead to a complete ice–rock separation, but not on Callisto. More recently, Monteux et al. (2014) have developed a 3D numerical model that characterizes the thermal evolution of a satellite growing by multiple impacts, simulating the satellite growth and thermal evolution for a body radius ranging from 100 to 2000 km. Their results indicate that a satellite exceeding 2000 km in radius may accrete without experiencing significant melting only in case (i) its accretion history is dominated by small impactors (radius less than a few kilometers) and (ii) the conversion of impact energy into heat is unrealistically inefficient. In this context, they underlined that global melting for large bodies like Titan or Callisto is difficult to avoid.

Once the melting of the icy phase is initiated, ice–rock separation can proceed. This separation will lead to the accumulation of dense blocks of rock overlying a undifferentiated core consisting of a mixture of rock and ice (e.g., Friedson and Stevenson 1983; Kirk and Stevenson 1987). The dense layer of accumulated rock is gravitationally unstable, which leads to large-scale ice–rock separation. Friedson and Stevenson (1983) suggested that an increase in the silicate volume fraction from 44% for Callisto to 55% for Ganymede could have induced an increase in the internal viscosity of between 1 and 2 orders of magnitude. This increase in the internal viscosity of Ganymede might have led to a failure of its solid-state convection self-regulation. This failure would then have limited heat loss, favored partial melting of the ice and enhanced a catastrophic runaway differentiation (Kirk and Stevenson 1987). Similarly, Nagel et al. (2004) suggested that if Callisto accreted from a mixture of rock and ice and the average size of the rocks was of the order of meters to tens of meters, then the viscosity would range between 10^{13} and 10^{17} Pa s. For such viscosities, Callisto would have experienced a gradual, but incomplete unmixing of ice and rocks. This mantle/core separation potentially involves a large amount of heating due to the viscous dissipation of the potential energy (Flasar and Birch 1973). Contrary to terrestrial planets (Golabek et al. 2009; Ricard et al. 2009), this runaway separation has not yet been modeled.

5.3 Metal–Rock Separation

If a sufficient amount of native iron is present within the icy moon, an iron core may eventually form during or after the ice–rock separation. In this case, the deep interior would be comprised of a probably liquid iron core, and a convecting silicate mantle. Gravity measurements performed by the Radio Science System onboard the Cassini spacecraft suggest that the deep interior of Titan is not fully differentiated (Sotin et al. 2009a; Iess et al. 2010). However, the presence of an iron core cannot be definitely ruled out, and additional measurements are required to determine whether Titan possesses an iron core like Ganymede. On Ganymede, a second differentiation event likely occurred during or after the ice–rock separation since enough heat had been stored in the metal-silicate mixture leading to the formation of an iron core. The major observable feature of this metal-silicate separation is the presence of an intrinsic magnetic field generated in its deep interior (Kivelson

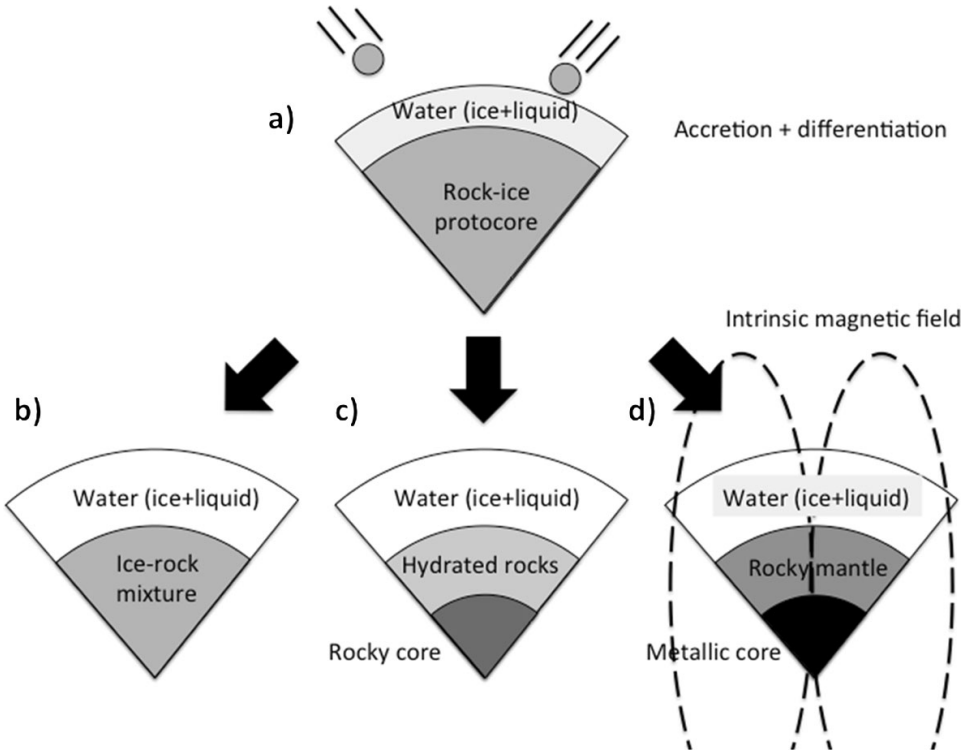

Fig. 13 Schematic representation of the structure of an icy moon (**a**) just after accretion and after differentiation leading to (**b**) a Callisto-like structure, (**c**) a Titan-like structure or (**d**) a Ganymede-like structure

et al. 1996). While the ice–rock separation has been extensively studied, the modalities of metal–rock separation on icy moons and, as a consequence, the modalities of the generation of intrinsic magnetic fields remain poorly constrained. Another major difficulty is to constrain the composition and size of the metallic core. Depending on whether the core is pure iron or a sulfur-iron alloy, it could represent 1 to 30% of the total mass of the icy moon (Anderson et al. 1996).

Although the interior of Ganymede is currently fully differentiated, the silicate rock and the iron likely coexisted and reacted with H_2O (as ice or water) before metal/silicate separation occurred. In this context, it is difficult to envision the formation of a pure iron core because oxidation of the iron would be unavoidable. This led Crary and Bagenal (1998) to suggest that Fe_3O_4-magnetite could maintain a strong remanent magnetic field within the rocky material of Ganymede. Scott et al. (2002) have shown that the presence of water could have enhanced the formation of low-density hydrated silicates and the alloying of iron with sulfur would have resulted in FeS-dominated cores. They performed high-pressure experiments that combined chondritic chemistry with water at a pressure of 1.5 GPa, temperatures between 300 °C and 800 °C and a range of oxygen fugacities. Their results indicate that sulfur may be a significant constituent of Ganymede's core but they did not observe the presence of either iron oxide species or metallic iron. Hence they concluded that magnetite is not a stable phase in the chondrite-water system in contrast with the suggestion of Crary and Bagenal (1998).

Hence, Ganymede's core probably contains not just pure iron but also lighter elements. As mentioned above a candidate for the dominant core-forming assemblage is an alloy of iron (Fe) and sulfur (S) (Hauck et al. 2006). Indeed sulfur is an element that was abundant in the proto-solar system (Hillgren et al. 2000). Within Ganymede, the core sulfur concentrations could range between 12 and 20 wt%. Under the pressure conditions of Ganymede's core (≈6–10 GPa) a mixture of iron and sulfur forms a binary, eutectic sys-

tem. A major consequence of adding sulfur to liquid iron is a depression of the liquidus (e.g., Usselman 1975; Fei et al. 1997). Upon freezing, nearly pure iron (Fe) (Li et al. 2001; Kamada et al. 2010) crystallizes on the Fe-rich side of the eutectic and iron sulfide (FeS) on the Fe-poor side. Various experiments have revealed that the eutectic composition of Fe–FeS becomes increasingly Fe-rich with increasing pressure (e.g., Chudinovskikh and Boehler 2007; Fei et al. 1997, 2000; Morard et al. 2008). Buono and Walker (2011) have suggested low and even negative gradients for the melting temperatures of Fe-rich Fe–FeS alloys in the pressure range of Ganymede's core. If the melting temperature has a lower gradient than the core temperature, iron will start to crystallize at the core-mantle boundary (CMB) and a growing snow zone will form during further cooling (McKinnon 1996; Hauck et al. 2006). However, the unknown oxidation state of the interior during differentiation limits our ability to constrain whether the composition of a sulfur-bearing core is on the Fe- or FeS-rich side of the eutectic composition (e.g., Scott et al. 2002; Breuer et al. 2015). Another important element could be hydrogen. The interaction of native iron with hydrated material could have led to the addition of hydrogen to the iron core resulting in the presence of iron hydride (Ohtani et al. 2005; Shibazaki et al. 2009).

5.4 Evidence for Active and Past Aqueous Processes

A range of geophysical evidence indicates that several moons of Jupiter (Europa, Ganymede, Callisto) and Saturn (Titan, Enceladus, Mimas) harbor extensive liquid water reservoirs beneath their cold icy surfaces (Khurana et al. 1998; Kivelson et al. 2000; Iess et al. 2014; Tajeddine et al. 2014; Thomas et al. 2016). Detection of ammoniated phyllosilicates on Ceres (de Sanctis et al. 2015) as well as the young age of some extensional features observed on Pluto (Hammond et al. 2016; Moore et al. 2016) suggest the existence of a subsurface ammonia-rich ocean, at least in the past, inside these two dwarf planets. Based on evolution models, many other icy bodies are also predicted to harbor internal oceans underneath their cold icy shells (Hussmann et al. 2006). These massive oceans constitute the greatest volumes of potentially habitable space in the Solar System. If chemical interactions with the rocky core and the irradiated surface provide nutriments and energy sources in sufficient amounts, the development of primitive life may be envisaged in these water-rich worlds. Several observational clues suggest that complex interactions between the subsurface oceans and their warm rocky interiors are presently occurring.

The most convincing evidence for active aqueous processes is provided by the surprising observations of eruptions of water vapor and salted icy grains at Enceladus' active south pole, indicating connections with a subsurface ocean (Postberg et al. 2009, 2011). The discovery of silicon-rich nano-particles further indicates that hydrothermal interactions are currently occurring in porous warm (100–200 °C) rock and that hydrothermal products are quickly transported to the plume source (Hsu et al. 2015; Sekine et al. 2015). Moreover, analysis of gravity, shape and libration data shows that the ice shell thickness at the south pole is thinner than 5 km, with a globally average value of not more than 21 km, requiring about 25–30 GW of internal power for such a configuration to be thermally stable (Cadek et al. 2016). This provides additional constraints in favor of a warm rocky core, powered by strong tidal dissipation. However, it remains unclear how Enceladus reached such a hyperactive state.

On Europa, although there is no direct evidence yet, the occurrence of hydrothermal processes at the seafloor, at present or in recent geological history (<100 Ma), is also likely. The observation of non-ice colored and hydrated materials in many disrupted areas on the surface of Europa points to exposure of oceanic species at the surface and to the possible

existence of suboceanic hydrothermal systems (Zolotov and Kargel 2009). The likelihood of presently active hydrothermal processes on Europa mostly depends on how much heat can be generated in the interior at present. Similarly to Enceladus and Io, tidal friction may contribute to Europa's internal budget, but in absence of observational constraints, it is still unclear if tidal friction in the rocky mantle is large enough at present to maintain active hydrothermal processes (Sotin et al. 2009b).

Despite the separation of the subsurface ocean from the rocky core by a thick high pressure ice mantle, water–rock interactions at the base of the thick ice mantle and the transport of brine through the ice mantle are still possible on the largest moons like Saturn's moon Titan and Jupiter's moon Ganymede (Vance and Brown 2013; Choblet et al. 2017). It is very likely that water–rock interactions occurred on these large moons in the past, especially during the differentiation stage when a large volume of water percolated throughout rock-dominated layers toward the surface (Tobie et al. 2013) (Fig. 13). The detection of ^{40}Ar, the decay product of ^{40}K initially contained in silicate minerals, in Titan's atmosphere (Niemann et al. 2010) as well as the likely presence of salts in the internal ocean of Titan (Béghin et al. 2012; Baland et al. 2014; Mitri et al. 2014), Ganymede (Saur et al. 2015) and Callisto (Khurana et al. 1998) indicate that water–rock interaction occurred during the evolution of these large icy moons. However, it is still unclear for how long these water–rock interactions lasted and what effects they had on the thermo-chemical evolution of their interiors.

5.5 Role of Volatile Compounds in the Aqueous Alteration Within Icy Bodies

During the early evolution of Pluto, impact heating, radiogenic heat sources (short- and long-lived) and tidal heating due to the interaction with Charon have likely been significant to induce a complete differentiation of Pluto's interior (Schubert et al. 2010, Sekine et al. 2017). At present-day, because of the rapid decay of short-lived radioisotopes and since the Pluto/Charon system has reached the "dual synchronous" state in which Charon's orbital period, spin period, and Pluto's rotation period are equal, these two major heat sources are probably too weak to maintain a current water ocean within Pluto's interior (Robuchon and Nimmo 2011; Barr and Collins 2015). The surprising discovery of two quasi-circular mounds on Pluto by New Horizons, suspected to be of cryovolcanic origin (Moore et al. 2016), suggests that the interior of the dwarf planet is more active than initially anticipated and that water–volatile–rock interactions may have operated during a long period of time in its interior. The presence of significant amounts of anti-freeze compounds, such as ammonia and methanol, together with gas compounds in the form of clathrate hydrates may explain the occurrence of such activity on Pluto. This hypothesis is consistent with the detection of ammonia-rich and methane-rich areas on Charon (Grundy et al. 2016). Although ammonia has not been identified on Pluto's surface, that is dominated by N_2 ices (Grundy et al. 2016), its presence on Charon indicates that it may have played a key role in the chemical evolution of the Pluto–Charon system, as well as in those of other Kuiper belt objects (Hussmann et al. 2006).

For decades, both ammonia and methanol, have been suspected to strongly affect the melting and crystallization process in icy bodies (e.g. Lewis 1971; Kargel 1992). The role of ammonia is expected to be particularly strong during the early stage in the evolution of icy bodies, when the first aqueous melts are generated during the post-accretional differentiation process and at the end of their evolution when the internal ocean becomes strongly concentrated in solutes by progressive crystallization of ice (Hussmann et al. 2006; Malamud and Prialnik 2015). Even in the absence of significant heat sources, the presence of ammonia, as well as methanol (both are present in comparable amount in comets, Cochran

et al. 2015) can sustain active aqueous processes for long periods of time. The recent detection of widespread ammoniated phyllosilicates across Ceres' surface (de Sanctis et al. 2015) may provide evidence for alteration of chondritic materials by N-bearing fluids. However, in absence of reliable experimental data on aqueous alteration by concentrated N-bearing fluids, it is difficult to investigate the conditions under which such ammoniated phyllosilicates may have formed.

6 Conclusions and Outlook

Water content and the internal evolution of terrestrial planets and icy bodies are closely linked. Indeed, the internal evolution and especially the formation time of the planetesimals and therefore the extent of radiogenic heating governs the amount of hydrous silicates and leftover rock–ice mixtures available in the late stages of their evolution. In turn, water content may affect the early internal evolution of the planetesimals and metal-silicate separation by favoring the sinking of metal diapirs over percolation processes. On the other hand, the absence of water could change the descent mode on larger terrestrial bodies from sinking diapirs to diking, thus affecting the heat partitioning between iron and silicates and modifying the thermal state of the accreting planet. Moreover, water content can contribute to an increase of f_{O_2} and thus affect the concentration of siderophile elements within the silicate reservoirs of the Solar System objects. Finally, the water content strongly influences the differentiation rate among the icy moons, controls their internal evolution and governs the alteration processes occurring in their deep interiors.

Partitioning of water between the mantle and the surface/atmosphere is also a key factor in regulating both planetary climate and internal dynamics. This partitioning is controlled by release of water by erupting melts, by hydrothermal alterations, mainly serpentinization, trapping some water in the form of hydrated minerals in the crust, and by recycling part of it deep into the mantle where it can be dissolved in nominally-anhydrous minerals. On Earth, where the water cycle is driven by plate tectonics, exactly how water partitions between surface and interior remains uncertain, but it is commonly thought to be of the order of 1. Parameterized models have recently been proposed to address the question of water cycle on other terrestrial planets, with different sizes and water contents (Crowley et al. 2011; Cowan and Abbot 2014; Schaefer and Sasselov 2015). These parameterized approaches enable some important characteristics of the water cycle to be understood, especially how surface gravity and the water volume at the surface influence the interior/surface exchange. However, they cannot describe the complexity of water transport in the mantle and its feedback on internal melting and crustal recycling. Describing correctly the coupled evolution of surface and internal reservoirs of water requires the use of thermo-chemical convection codes in 3D or at least 2D, including exchange of water between the crust and mantle, the convective transport in the mantle, its retroaction on viscosity, melting and associated outgassing.

Finally, with the discoveries of thousands of exoplanets, we are now entering a new era in comparative planetology. Even if the dataset is limited to the mass, radius and orbital characteristics of the planetary systems, it already offers a unique opportunity to test the models of planet formation and evolution. Model mass-radius relationships indicate a great diversity of interior compositions and atmospheric extents for the Super-Earth/Mini-Neptune-planet class (e.g. Howard et al. 2012), suggesting a wide range of volatile contents and compositions. Hence, planetary worlds are probably much more diverse than originally thought, with a wide range of water and other volatile contents.

Acknowledgements We thank L. Elkins-Tanton, A. Morbidelli and two anonymous reviewers for detailed and thoughtful comments that helped to improve the manuscript. D.C.R. was supported by the European Research Council Advanced Grant "ACCRETE" (contract number 290568) and additional support was provided by the German Science Foundation (DFG) Priority Programme SPP1833 "Building a Habitable Earth" (Ru 1323/10-1). J.M. was funded by the Auvergne Fellowship program. This is Laboratory of Excellence ClerVolc contribution no. 283. G.J.G. thanks Taras Gerya for providing the code I2MART. G.T. acknowledges support from the project ANR OASIS.

References

J.D. Anderson, R.A. Jacobson, T.P. McElrath, W.B. Moore, G. Schubert, P.C. Thomas, Shape, mean radius, gravity field, and interior structure of Callisto. Icarus **153**, 157–161 (2001)

J.D. Anderson, E.L. Lau, W.L. Sjogren, G. Schubert, W.B. Moore, Gravitational constraints on the internal structure of Ganymede. Nature **384**, 541–543 (1996)

P.J. Armitage, *Astrophysics of Planet Formation* (Cambridge University Press, Cambridge, 2010), 294 p.

Y. Asahara, T. Kubo, T. Kondo, Phase relations of a carbonaceous chondrite at lower mantle conditions. Phys. Earth Planet. Inter. **143–144**, 421–432 (2004)

X-N. Bai, J.M. Stone, Wind-driven accretion in protoplanetary disks. I. Supression of the magnetorotational instability and launching of the magnetocentrifugal wind. Astrophys. J. **769**, 21 (2013)

R.M. Baland et al., Titan's internal structure inferred from its gravity field, shape, and rotation state. Icarus **237**, 29–41 (2014)

A.C. Barr, R.M. Canup, Constraints on gas giant satellite formation from the interior states of partially differentiated satellites. Icarus **198**, 163–177 (2008)

A.C. Barr, R.M. Canup, Origin of the Ganymede–Callisto dichotomy by impacts during the Late Heavy Bombardment. Nat. Geosci. **3**, 164–167 (2010)

A.C. Barr, G.C. Collins, Tectonic activity on Pluto after the Charon-forming impact. Icarus **246**, 146–155 (2015)

C. Béghin, O. Randriamboarison, M. Hamelin, E. Karkoschka, C. Sotin, R.C. Whitten, J.-J. Berthelier, R. Grard, F. Simões, Analytic theory of Titan's Schumann resonance: constraints on ionospheric conductivity and buried water ocean. Icarus **218**(2), 1028–1042 (2012)

P.A. Bland et al., Why aqueous alteration in asteroids was isochemical: high porosity does not equal permeability. Earth Planet. Sci. Lett. **287**, 559–568 (2009)

R. Brett, P.M. Bell, Melting relations in the Fe-rich portion of the system Fe–FeS at 30 kb pressure. Earth Planet. Sci. Lett. **6**, 479–482 (1969)

D. Breuer et al., Iron snow, crystal floats, and inner-core growth: modes of core solidification and implications for dynamos in terrestrial planets and moons. Prog. Earth Planet. Sci. **2**, 39 (2015)

A.S. Buono, D. Walker, The Fe-rich liquidus in the Fe–FeS system from 1 bar to 10 GPa. Geochim. Cosmochim. Acta **75**, 2072–2087 (2011)

O. Cadek, G. Tobie, T. Van Hoolst, M. Massé, G. Choblet, A. Lefèvre, G. Mitri, R-M. Baland, M. Behounkova, O. Bourgeois, A. Trinh, Enceladus's internal ocean and ice shell constrained from Cassini gravity, shape, and libration data. Geophys. Res. Lett. **43**(11), 5653–5660 (2016)

J.C. Castillo-Rogez, J.I. Lunine, Evolution of Titan's rocky core constrained by Cassini observations. Geophys. Res. Lett. **37**, L20205 (2010)

J.C. Castillo-Rogez, E. Young, Origin and evolution of volatile-rich asteroids, in *Early Differentiation and Consequences for Planets*, ed. by L.T. Elkins-Tanton, B. Weiss. Cambridge Planetary Science (2017)

F. Cerantola, N. Walte, D.C. Rubie, Deformation of a crystalline olivine aggregate containing two immiscible liquids: implications for early core-mantle differentiation. Earth Planet. Sci. Lett. **417**, 67–77 (2015)

J.E. Chambers, Late-stage planetary accretion including hit-and-run collisions and fragmentation. Icarus **224**, 43–56 (2013)

E. Chiang, A.N. Youdin, Forming planetesimals in solar and extrasolar nebula. Annu. Rev. Earth Planet. Sci. **38**, 493–522 (2010)

G. Choblet, G. Tobie, C. Sotin, K. Kalousova, O. Grasset, Heat and melt transport in the high-pressure ice mantle of large icy moons. Icarus **285**, 252–262 (2017)

L. Chudinovskikh, R. Boehler, Eutectic melting in the system Fe–S to 44 GPa. Earth Planet. Sci. Lett. **257**(1), 97–103 (2007)

A.L. Cochran et al., The composition of comets. Space Sci. Rev. **197**(1–4), 9–46 (2015)

A. Coradini, C. Federico, O. Forni, G. Magni, Origin and thermal evolution of icy satellites. Surv. Geophys. **16**, 533–591 (1995)

A. Costa, L. Caricchi, N. Bagdassarov, A model for the rheology of particle-bearing suspensions and partially molten rocks. Geochem. Geophys. Geosyst. **10**, 3010 (2009)
N.B. Cowan, D.S. Abbot, Water cycling between ocean and mantle: super-Earths need not be waterworlds. Astrophys. J. **781**(1), 27 (2014).
F.J. Crary, F. Bagenal, Remanent ferromagnetism and the interior structure of Ganymede. J. Geophys. Res. **103**, 25757–25773 (1998)
J.W. Crowley, M. Gérault, R.J. O'Connell, On the relative influence of heat and water transport on planetary dynamics. Earth Planet. Sci. Lett. **310**, 380–388 (2011)
J.N. Cuzzi, K.J. Zahnle, Material enhancement in protoplanetary nebulae by particle drift through evaporation fronts. Astrophys. J. **614**, 490–496 (2004)
T.W. Dahl, D.J. Stevenson, Turbulent mixing of metal and silicate during planet accretion and interpretation of the Hf–W chronometer. Earth Planet. Sci. Lett. **295**, 177–186 (2010)
N. Dauphas, The isotopic nature of the Earth's accreting material through time. Nature **541**, 521–524 (2017)
M.C. de Sanctis et al., Ammoniated phyllosilicates with a likely outer solar system origin on Ceres. Nature **528**, 241–244 (2015)
J. de Vries, F. Nimmo, H.J. Melosh, S.A. Jacobson, A. Morbidelli, D.C. Rubie, Impact-induced melting during accretion of the Earth. Prog. Earth Planet. Sci. **3**, 7 (2016). https://doi.org/10.1186/s40645-016-0083-8
R. Deguen, M. Landeau, P. Olson, Turbulent metal–silicate mixing, fragmentation, and equilibration in magma oceans. Earth Planet. Sci. Lett. **391**, 274–287 (2014)
T. Encrenaz, Water in the solar system. Annu. Rev. Astron. Astrophys. **46**, 57–87 (2008)
Y. Fei, C.M. Bertka, L.W. Finger, High-pressure iron-sulfur compound, Fe_3S_2, and melting relations in the Fe–FeS system. Science **275**, 1621–1623 (1997)
Y. Fei, J. Li, C.M. Bertka, C.T. Prewitt, Structure type and bulk modulus of Fe_3S, a new iron–sulfur compound. Am. Mineral. **85**, 1830–1833 (2000)
F.M. Flasar, F. Birch, Energetics of core formation: a correction. J. Geophys. Res. **78**, 6101–6103 (1973)
A.J. Friedson, D.J. Stevenson, Viscosity of rock–ice mixtures and applications to the evolution of icy satellites. Icarus **56**, 1–14 (1983)
D.J. Frost, C. Liebske, F. Langenhorst, C.A. McCammon, R.G. Trønnes, D.C. Rubie, Experimental evidence for the existence of iron-rich metal in the Earth's lower mantle. Nature **428**, 409–412 (2004)
R.R. Fu, L.T. Elkins-Tanton, The fate of magmas in planetsimals and the retention of primitive chondritic crusts. Earth Planet. Sci. Lett. **390**, 128–137 (2014)
R.R. Fu, E. Young, R.C. Greenwood, L.T. Elkins-Tanton, Silicate melting and volatile loss during differentiation in planetesimals, in *Early Differentiation and Consequences for Planets*, ed. by L.T. Elkins-Tanton, B. Weiss. Cambridge Planetary Science (2017)
P. Gao, D.J. Stevenson, Nonhydrostatic effects and the determination of icy satellites' moment of inertia. Icarus **226**, 1185–1191 (2013)
T.V. Gerya, D.A. Yuen, Robust characteristics method for modelling multiphase visco-elasto-plastic thermomechanical problems. Phys. Earth Planet. Inter. **163**, 83–105 (2007)
G.J. Golabek, B. Bourdon, T.V. Gerya, Numerical models of the thermomechanical evolution of planetesimals: application to the acapulcoite-lodranite parent body. Meteorit. Planet. Sci. **49**, 1083–1099 (2014)
G.J. Golabek, T.V. Gerya, B.J.P. Kaus, R. Ziethe, P.J. Tackley, Rheological controls on the terrestrial core formation mechanism. Geochem. Geophys. Geosyst. **10**, Q11007 (2009)
O. Grasset et al., Jupiter ICy moons Explorer (JUICE): an ESA mission to orbit Ganymede and to characterise the Jupiter system. Planet. Space Sci. **78**, 1–21 (2013)
O. Grasset, C. Sotin, The cooling rate of a liquid shell in Titan's interior. Icarus **123**, 101–112 (1996)
O. Grasset, C. Sotin, F. Deschamps, On the internal structure and dynamics of Titan. Planet. Space Sci. **48**, 617–636 (2000)
L. Grossman, A.V. Fedkin, S.B. Simon, Formation of the first oxidized iron in the solar system. Meteorit. Planet. Sci. **47**, 2160–2169 (2012)
W.M. Grundy et al., Surface compositions across Pluto and Charon. Science **351**(6279), aad9189 (2016)
N.P. Hammond, A.C. Barr, E.M. Parmentier, Recent tectonic activity on Pluto driven by phase changes in the ice shell. Geophys. Res. Lett. **43**(13), 6775–6782 (2016)
L. Hartmann, in *Discs, Planetesimals, and Planets*, ed. by F. Garzon, C. Eiroa, D. de Winter, T.J. Mahoney. ASP Conf. Ser., vol. 219 (Astron. Soc. Pac, San Francisco, 2000), p. 95
T.I. Hasegawa, E. Herbst, C.M. Leung, Models of gas–grain chemistry in dense interstellar clouds with complex organic molecules. Astrophys. J. Suppl. Ser. **82**, 167 (1992)
S.A. Hauck, J.M. Aurnou, A.J. Dombard, Sulfur's impact on core evolution and magnetic field generation on Ganymede. J. Geophys. Res. **111**(E9), E09008 (2006)
V.J. Hillgren, C.K. Gessmann, J. Li, An experimental perspective on the light element in Earth's core, in *Origin of the Earth and Moon*, ed. by R.M. Canup, K. Righter (University of Arizona Press, Tucson, 2000), pp. 245–264

M.M. Hirschmann, Water, melting, and the deep Earth H_2O cycle. Annu. Rev. Earth Planet. Sci. **34**, 629–653 (2006)
G. Hirth, D.L. Kohlstedt, Water in the oceanic upper mantle: implications for rheology, melt extraction and the evolution of the lithosphere. Earth Planet. Sci. Lett. **144**, 93–108 (1996)
A. Holzheid, Sulphide melt distribution in partially molten silicate aggregates: implications to core formation scenarios in terrestrial planets. Eur. J. Mineral. **25**, 267–277 (2013)
A. Holzheid, M.D. Schmitz, T.L. Grove, Textural equilibria of iron sulphide liquids in partly molten silicate aggregates and their relevance to core formation scenarios. J. Geophys. Res. **105**, 13555–13567 (2000)
A.W. Howard et al., Planet occurrence within 0.25 AU of solar-type stars from Kepler. Astrophys. J. Suppl. Ser. **201**(2), 15 (2012)
H.H. Hsieh, D. Jewitt, A population of comets in the main asteroid belt. Science **312**, 561–563 (2006)
H.-W. Hsu, F. Postberg, Y. Sekine et al., Ongoing hydrothermal activities within Enceladus. Nature **519**, 207–210 (2015)
H. Hussmann et al., Subsurface oceans and deep interiors of medium-sized outer planet satellites and large trans-neptunian objects. Icarus **185**, 258–273 (2006)
H. Hussmann, C. Sotin, J.I. Lunine, Interiors and evolution of icy satellites, in *Physics of Terrestrial Planets and Moons Treatise on Geophysics*, vol. 10, 2nd edn. (Elsevier, Amsterdam, 2015), pp. 605–635
L. Iess et al., Gravity field, shape, and moment of inertia of Titan. Science **327**, 1367–1369 (2010)
L. Iess et al., The tides of Titan. Science **337**, 457 (2012)
L. Iess et al., The gravity field and interior structure of Enceladus. Science **344**, 78–80 (2014)
S.A. Jacobson, A. Morbidelli, S.N. Raymond, D.P. O'Brien, K.J. Walsh, D.C. Rubie, Highly siderophile elements in the Earth's mantle as a clock for the Moon-forming impact. Nature **508**, 84–87 (2014)
D. Jewitt, B. Yang, N. Haghighipour, Main-belt Comet P/2008 R1 (Garradd). Astron. J. **137**, 4313–4321 (2009)
A. Johansen, M.-M. Mac Low, P. Lacerda, M. Bizzarro, Growth of asteroids, planetary embryos, and Kuiper belt objects by chondrule accretion. Sci. Adv. **1**, 1500109 (2015)
S. Kamada, H. Terasaki, E. Ohtani, T. Sakai, T. Kikegawa, Y. Ohishi, N. Hirao, N. Sata, T. Kondo, Phase relationships of the Fe–FeS system in conditions up to the Earth's outer core. Earth Planet. Sci. Lett. **294**(1), 94–100 (2010)
S. Karato, V.R. Murthy, Core formation and chemical equilibrium in the Earth—I. Physical considerations. Phys. Earth Planet. Inter. **100**, 61–79 (1997)
J.S. Kargel, Ammonia±water volcanism on icy satellites: phase relations at 1 atmosphere. Icarus **100**, 556–574 (1992)
R.F. Katz, M. Spiegelman, C.H. Langmuir, A new parameterization of hydrous mantle melting. Geochem. Geophys. Geosyst. **4** (2003). https://doi.org/10.1029/2002GC000433
Y. Ke, V.S. Solomatov, Coupled core-mantle thermal evolution of early Mars. J. Geophys. Res. **114**, E07004 (2009)
J.D. Kendall, H.J. Melosh, Differentiated planetesimal impacts into a terrestrial magma ocean: fate of the iron core. Earth Planet. Sci. Lett. **448**, 24–33 (2016)
J.F. Kerridge, T.E. Bunch, in *Asteroids*, ed. by T. Gehrels (University of Arizona Press, Tucson, 1979), pp. 745–764
K.K. Khurana, M.G. Kivelson, D.J. Stevenson, G. Schubert, C.T. Russell, R.J. Walker, S. Joy, C. Polanskey, Induced magnetic fields as evidence for subsurface oceans in Europa and Callisto. Nature **395**, 777–780 (1998)
R.L. Kirk, D.J. Stevenson, Thermal evolution of a differentiated Ganymede and implications for surface features. Icarus **69**, 91–134 (1987)
M.G. Kivelson et al., Ganymede's magnetosphere: magnetometer overview. J. Geophys. Res. **103**, 19,963–19,972 (1998)
M.G. Kivelson, K.K. Khurana, C.T. Russell, M. Volwerk, R.J. Walker, C. Zimmer, Galileo magnetometer measurements: a stronger case for a subsurface ocean at Europa. Science **289**, 1340–1343 (2000)
M. Kivelson, K. Khurana, C. Russell, R. Walker, J. Warnecke, F. Coroniti, C. Polanskey, D. Southwood, G. Schubert, Discovery of Ganymede's magnetic field by the Galileo spacecraft. Nature **384**(6609), 537–541 (1996)
J. Korenaga, Scaling of plate-tectonic convection with pseudoplastic rheology. J. Geophys. Res. **115**, B11405 (2010)
K.J. Kossacki, J. Leliwa-Kopystynski, Medium-sized icy satellites: thermal and structural evolution during accretion. Planet. Space Sci. **41**, 729–741 (1993)
A.N. Krot et al., Progressive alteration in CV3 chondrites: more evidence for asteroidal alteration. Meteorit. Planet. Sci. **33**, 1065–1085 (1998)
A.N. Krot, B. Fegley, K. Lodders, Meteoritical and astrophysical constraints on the oxidation state of the solar nebula, in *Protostars and Planets IV*, ed. by V. Mannings, A.P. Boss, S.S. Russell (University of Arizona Press, Tucson, 2000), pp. 1019–1054

M. Küppers et al., Localized sources of water vapour on the dwarf planet (1) Ceres. Nature **505**, 525–527 (2014)
M. Landeau, P. Olson, R. Deguen, B.H. Hirsh, Core merging and stratification following giant impact. Nat. Geosci. **9**, 786–789 (2016)
J.S. Lewis, Satellites of the outer planets: their physical and chemical nature. Icarus **15**, 174–185 (1971)
J. Li, Y. Fei, H. Mao, K. Hirose, S. Shieh, Sulfur in the Earth's inner core. Earth Planet. Sci. Lett. **193(3)**, 509–514 (2001)
T. Lichtenberg, G.J. Golabek, T.V. Gerya, M.R. Meyer, The effects of short-lived radionuclides and porosity on the early thermo-mechanical evolution of planetesimals. Icarus **274**, 350–365 (2016)
C. Liebske, B. Schmickler, H. Terasai, B.T. Poe, A. Suzuki, K. Funakoshi, R. Ando, D.C. Rubie, Viscosity of peridotite liquid up to 13 GPa: implications for magma ocean viscosities. Earth Planet. Sci. Lett. **240**, 589–604 (2005)
U. Malamud, D. Prialnik, Modeling Kuiper belt objects Charon, Orcus and Salacia by means of a new equation of state for porous icy bodies. Icarus **246**, 21–36 (2015)
U. Mann, D.J. Frost, D.C. Rubie, Evidence for high-pressure core-mantle differentiation from the metal-silicate partitioning of lithophile and weakly siderophile elements. Geochim. Cosmochim. Acta **73**, 7360–7386 (2009). https://doi.org/10.1016/j.gca.2009.08.006
G.W. Marcy et al., Masses, radii, and orbits of small Kepler planets: the transition from gaseous to rocky planets. Astrophys. J. Suppl. Ser. **210**(2), 20 (2014)
T. Matsui, Y. Abe, Evolution of an impact-induced atmosphere and magma ocean on the accreting Earth. Nature **319**, 303–305 (1986)
M. Mayor, C. Lovis, N.C. Santos, Doppler spectroscopy as a path to the detection of Earth-like planets. Nature **513**, 328–335 (2014)
W.B. McKinnon, Core evolution in the icy Galilean satellites, and the prospects for dynamo-generated magnetic fields. Bull. Am. Astron. Soc. **28**, 1076 (1996)
W.B. McKinnon, Note: mystery of Callisto: is it undifferentiated? Icarus **130**, 540–543 (1997)
W.G. Minarik, F.J. Ryerson, E.B. Watson, Textural entrapment of core-forming melts. Science **272**, 530–533 (1996)
G. Mitri et al., Shape, topography, gravity anomalies and tidal deformation of Titan. Icarus **236**, 169–177 (2014)
J. Monteux, N. Coltice, F. Dubuffet, Y. Ricard, Thermo-mechanical adjustment after impacts during planetary growth. Geophys. Res. Lett. **34**, L24201 (2007)
J. Monteux, G. Tobie, G. Choblet, M. Le Feuvre, Can large icy moons accrete undifferentiated? Icarus **237**, 377–387 (2014)
J.M. Moore et al., The geology of Pluto and Charon through the eyes of New Horizons. Science **351**, 6279 (2016)
G. Morard, D. Andrault, N. Guignot, C. Sanloup, M. Mezouar, S. Petitgirard et al., In situ determination of Fe–Fe_3S phase diagram and liquid structural properties up to 65 GPa. Earth Planet. Sci. Lett. **272**, 620–662 (2008)
A. Morbidelli, B. Bitsch, A. Crida, M. Gounelle, T. Guillot, S. Jacobson, A. Johansen, M. Lambrechts, E. Lega, Fossilized condensation lines in the Solar System protoplanetary disk. Icarus **267**, 368–376 (2016)
I. Mosqueira, P.R. Estrada, Formation of the regular satellites of giant planets in an extended gaseous nebula. I: subnebula model and accretion of satellites. Icarus **163**, 198–231 (2003)
O. Mousis, A. Drouard, P. Vernazza, J.I. Lunine, M. Monnereau, R. Maggiolo, K. Altwegg, H. Balsiger, J.-J. Berthelier, G. Cessateur, J. De Keyser, S.A. Fuselier, S. Gasc, A. Korth, T. Le Deun, U. Mall, B. Marty, H. Rème, M. Rubin, C.-Y. Tzou, J.H. Waite, P. Wurz, Impact of radiogenic heating on the formation conditions of comet 67P/Churyumov–Gerasimenko. Astrophys. J. Lett. **839**, L4 (2017)
S. Mueller, W.B. McKinnon, Three-layered models of Ganymede and Callisto—compositions, structures, and aspects of evolution. Icarus **76**, 437–464 (1988)
K. Nagel, D. Breuer, T. Spohn, A model for the interior structure, evolution, and differentiation of Callisto. Icarus **169**, 402–412 (2004)
T. Nakamura, Yamato 793321 CM chondrite: dehydrated regolith material of a hydrous asteroid. Earth Planet. Sci. Lett. **242**, 26–38 (2006)
A. Nakato, T. Nakamura, F. Kitajima, T. Noguchi, Evaluation of dehydration mechanism during heating of hydrous asteroids based on mineralogical and chemical analysis of naturally and experimentally heated CM chondrites. Earth Planets Space **60**, 855–864 (2008)
H.B. Niemann et al., Composition of Titan's lower atmosphere and simple surface volatiles as measured by the Cassini–Huygens probe gas chromatograph mass spectrometer experiment. J. Geophys. Res. **115**, E12006 (2010)

F. Nimmo, D. O'Brien, T. Kleine, Tungsten isotopic evolution during late-stage accretion: constraints on Earth–Moon equilibration. Earth Planet. Sci. Lett. **292**, 363–370 (2010)
D.P. O'Brien, K.J. Walsh, A. Morbidelli, S.N. Raymond, A.M. Mandell, Water delivery and giant impacts in the 'Grand Tack' scenario. Icarus **239**, 74–84 (2014). https://doi.org/10.1016/j.icarus.2014.05.009
E. Ohtani, N. Hirao, T. Kondo, M. Ito, T. Kikegawa, Iron–water reaction at high pressure and temperature, and hydrogen transport into the core. Phys. Chem. Miner. **32**, 77–82 (2005)
T. Okuchi, Hydrogen partitioning into molten iron at high pressure: implications for Earth's core. Science **278**, 1781–1784 (1997)
H.St.C. O'Neill, D.C. Rubie, D. Canil, C.A. Geiger, C.R. Ross II., F. Seifert, A.B. Woodland, Ferric iron in the upper mantle and in transition zone assemblages: implications for relative oxygen fugacities in the mantle, in *Evolution of the Earth and Planets*, ed. by E. Takahashi, R. Jeanloz, D.C. Rubie. Geophysical Monograph, vol. 74, IUGG 14 (1993), pp. 73–88
P. O'Rourke, D.J. Stevenson, Stability of ice/rock mixtures with application to a partially differentiated Titan. Icarus **227**, 67–77 (2014)
R.T. Pappalardo, G.C. Collins, J.W. Head III., P. Helfenstein, T.B. McCord, J.M. Moore, L.M. Prockter, P.M. Schenk, J.R. Spencer, Geology of Ganymede, in *Jupiter: The Planet, Satellites and Magnetosphere*, ed. by F. Bagenal, T.E. Dowling, W.B. McKinnon. Cambridge Planetary Science (2004), pp. 363–396
C.C. Porco et al., Cassini observes the active South Pole of Enceladus. Science **311**, 1393–1401 (2006)
F. Postberg et al., Sodium salts in E-ring ice grains from an ocean below the surface of Enceladus. Nature **459**, 1098–1101 (2009)
F. Postberg, J. Schmidt, J. Hillier, S. Kempf, R. Srama, A salt-water reservoir as the source of a compositionally stratified plume on Enceladus. Nature **474**, 620–622 (2011)
D. Prialnik, G. Sarid, E.D. Rosenberg, R. Merk, Thermal and chemical evolution of comet nuclei and Kuiper belt objects. Space Sci. Rev. **138**, 147–164 (2008)
S.N. Raymond, A. Izidoro, Origin of water in the inner Solar System: planetesimals scattered inward during Jupiter and Saturn's rapid gas accretion. Icarus (2017). https://doi.org/10.1016/j.icarus.2017.06.030
S.N. Raymond, D.P. O'Brien, A. Morbidelli, N.A. Kaib, Building the terrestrial planets: constrained accretion in the inner Solar System. Icarus **203**, 644–662 (2009)
S.N. Raymond, T. Quinn, J.I. Lunine, Making other earths: dynamical simulations of terrestrial planet formation and water delivery. Icarus **168**, 1–17 (2004)
Y. Ricard, O. Šrámek, F. Dubuffet, A multi-phase model of runaway core-mantle segregation in planetary embryos. Earth Planet. Sci. Lett. **284**, 144–150 (2009)
G. Robuchon, F. Nimmo, Thermal evolution of Pluto and implications for surface tectonics and a subsurface ocean. Icarus **216**(2), 426–439 (2011)
L. Roth et al., Transient water vapor at Europa's South pole. Science **343**, 171 (2014)
D.C. Rubie, D.J. Frost, U. Mann, Y. Asahara, K. Tsuno, F. Nimmo, P. Kegler, A. Holzheid, H. Palme, Heterogeneous accretion, composition and core-mantle differentiation of the Earth. Earth Planet. Sci. Lett. **301**, 31–42 (2011). https://doi.org/10.1016/j.epsl.2010.11.030
D.C. Rubie, S.A. Jacobson, A. Morbidelli, D.P. O'Brien, E.D. Young, J. de Vries, F. Nimmo, H. Palme, D.J. Frost, Accretion and differentiation of the terrestrial planets with implications for the compositions of early-formed Solar System bodies and accretion of water. Icarus **248**, 89–108 (2015a)
D.C. Rubie, V. Laurenz, S.A. Jacobson, A. Morbidelli, H. Palme, A.K. Vogel, D.J. Frost, Highly siderophile elements were stripped from Earth's mantle by iron sulfide segregation. Science **353**, 1141–1144 (2016)
D.C. Rubie, H.J. Melosh, J.E. Reid, C. Liebske, K. Righter, Mechanisms of metal-silicate equilibration in the terrestrial magma ocean. Earth Planet. Sci. Lett. **205**, 239–255 (2003)
D.C. Rubie, F. Nimmo, H.J. Melosh, Formation of the Earth's core, in *Treatise on Geophysics*, ed. by D. Stevenson. Evolution of the Earth, vol. 9, 2nd edn. (Elsevier, Amsterdam, 2015b), pp. 43–79
J. Rudge, T. Kleine, B. Bourdon, Broad bounds on Earth's accretion and core formation constrained by geochemical models. Nat. Geosci. **3**, 439–443 (2010)
T. Rushmer, N. Petford, Microsegregation rates of liquid Fe–Ni–S metal in natural silicate-metal systems: a combined experimental and numerical study. Geochem. Geophys. Geosyst. **12** (2011). https://doi.org/10.1029/2010GC003413
H. Samuel, A re-evaluation of metal diapir breakup and equilibration in terrestrial magma oceans. Earth Planet. Sci. Lett. **313**, 105–114 (2012)
H. Samuel, P.J. Tackley, M. Evonuk, Heat partitioning in terrestrial planets during core formation by negative diapirism. Phys. Earth Planet. Inter. **290**, 13–19 (2010)
J. Saur et al., The search for a subsurface ocean in Ganymede with Hubble Space Telescope observations of its auroral ovals. J. Geophys. Res. Space Phys. **120** (2015)
L. Schaefer, D. Sasselov, The persistence of oceans on Earth-like planets: insights from the deep-water cycle. Astrophys. J. **801**(1), 40 (2015)

A. Scheinberg, R.R. Fu, L.T. Elkins-Tanton, B.P. Weiss, Asteroid differentiation: melting and large-scale structure, in *Asteroids IV*, ed. by P. Michel, F.E. DeMeo, W.F. Bottke (University of Arizona Press, Tucson, 2015), pp. 533–552

M. Schönbächler, R.W. Carlson, M.F. Horan, T.D. Mock, E.H. Hauri, Heterogeneous accretion and the moderately volatile element budget of Earth. Science **328**, 884–887 (2010). https://doi.org/10.1126/science.1186239

G. Schubert, H. Hussmann, V. Lainey, D.L. Matson, W.B. McKinnon, F. Sohl, C. Sotin, G. Tobie, D. Turrini, T. Van Hoolst, Evolution of icy satellites. Space Sci. Rev. **153**(1), 447–484 (2010)

G. Schubert, T. Spohn, R.T. Reynolds, Thermal histories, compositions and internal structures of the moons of the solar system, in *Satellites*, ed. by J.A. Burns, M.S. Matthews (University of Arizona Press, Tucson, 1986), pp. 224–292

G. Schubert, D.J. Stevenson, K. Ellsworth, Internal structures of the Galilean satellites. Icarus **47**, 46–59 (1981)

H.P. Scott, Q. Williams, F.J. Ryerson, Experimental constraints on the chemical evolution of large icy satellites. Earth Planet. Sci. Lett. **203**, 399–412 (2002)

Y. Sekine et al., High-temperature water–rock interactions and hydrothermal environments in the chondrite-like core of Enceladus. Nat. Commun. **6**, 8604 (2015)

Y. Sekine, H. Genda, S. Kamata, T. Funatsu, The Charon-forming giant impact as a source of Pluto's dark equatorial regions. Nat. Astron. **1**, 0031 (2017)

N.I. Shakura, R.A. Sunyaev, Black holes in binary systems. Observational appearance. Astron. Astrophys. **24**, 337–355 (1973)

Z.D. Sharp, F.M. McCubbin, C.K. Shearer, A hydrogen-based oxidation mechanism relevant to planetary formation. Earth Planet. Sci. Lett. **380**, 88–97 (2013)

Y. Shibazaki, E. Ohtani, H. Terasaki, A. Suzuki, K. Funakoshi, Hydrogen partitioning between iron and ringwoodite: implications for water transport into the Martian core. Earth Planet. Sci. Lett. **287**, 463–470 (2009)

J.B. Simon, P.J. Armitage, R. Li, A.N. Youdin, The mass and size distribution of planetesimals formed by the streaming instability. I. The role of self-gravity. Astrophys. J. **822**, 55 (2016)

F. Sohl et al., Subsurface water oceans on icy satellites: chemical composition and exchange processes. Space Sci. Rev. **153**, 485–510 (2010)

V.S. Solomatov, Magma oceans and primordial mantle differentiation, in *Treatise on Geophysics*, 2nd edn. (2015), pp. 81–104

C. Sotin, G. Mitri, N. Rappaport, G. Schubert, D. Stevenson, in *Titan from Cassini/Huygens*, ed. by R.H. Brown, J.P. Lebreton, J.H. Waite (2009a), pp. 61–73

C. Sotin, G. Tobie, J. Wahr, W.B. McKinnon, in *Tides and Tidal Heating on Europa*, ed. by R. Pappalardo et al., Space Science Series (University of Arizona Press, Tucson, 2009b), pp. 85–117

S.W. Squyres, R.T. Raynolds, A.L. Summers, F. Shung, Accretional heating of the satelites of Saturn and Uranus. J. Geophys. Res. **93**, 8779–8794 (1988)

D.J. Stevenson, Fluid dynamics of core formation, in *The Origin of the Earth*, ed. by H.E. Newsom, J.H. Jones (Oxford University Press, London, 1990), pp. 231–249

R. Tajeddine, N. Rambaux, V. Lainey, S. Charnoz, A. Richard, A. Rivoldini, B. Noyelles, Constraints on Mimas' interior from Cassini ISS libration measurements. Science **346**(6207), 322–324 (2014)

H. Terasaki, D.J. Frost, D.C. Rubie, F. Langenhorst, The effect of oxygen and sulphur on the dihedral angle between Fe–O–S melt and silicate minerals at high pressure: implications for Martian core formation. Earth Planet. Sci. Lett. **232**, 379–392 (2005). https://doi.org/10.1016/j.epsl.2005.01.030

H. Terasaki, D.J. Frost, D.C. Rubie, F. Langenhorst, Percolative core formation in planetesimals. Earth Planet. Sci. Lett. **273**, 132–137 (2008)

P.C. Thomas et al., Enceladus's measured physical libration requires a global subsurface ocean. Icarus **264**, 37–47 (2016)

G. Tobie, J.I. Lunine, J. Monteux, O. Mousis, F. Nimmo, The origin and evolution of Titan, in: *Titan: Surface, Atmosphere and Magnetosphere*, ed. by I. Mueller-Wodarg, C. Griffith, T. Cravens, E. Lellouch (Cambridge University Press, Cambridge, 2013)

K.A. Todd, H.C. Watson, T. Yu, Y. Wang, The effects of shear deformation on planetesimal core segregation: results from in-situ X-ray micro-tomography. Am. Mineral. **101**, 1996–2004 (2016)

T.M. Usselman, Experimental approach to the state of the core. Part I. The liquidus relations of the Fe-rich portion of the Fe–Ni–S system. Am. J. Sci. **275**, 278–290 (1975)

S. Vance, J.M. Brown, Thermodynamic properties of aqueous $MgSO_4$ to 800 MPa at temperatures from -20 to 100 °C and concentrations to 25 mol kg^{-1} from sound speeds, with applications to icy world oceans. Geochim. Cosmochim. Acta **110**, 176–189 (2013)

N. von Bargen, H.S. Waff, Permeabilities, interfacial areas and curvatures of partially molten systems: results of numerical computations of equilibrium microstructures. J. Geophys. Res. **91**, 9261–9276 (1986)

J.-B. Wacheul, M. Le Bars, J. Monteux, J.M. Aurnou, Laboratory experiments on the breakup of liquid metal diapirs. Earth Planet. Sci. Lett. **403**, 236–245 (2014)
J. Wade, B.J. Wood, Core formation and the oxidation state of the Earth. Earth Planet. Sci. Lett. **236**, 78–95 (2005)
K.J. Walsh, A. Morbidelli, S.N. Raymond, D.P. O'Brien, A.M. Mandell, A low mass for Mars from Jupiter's early gas-driven migration. Nature **475**, 206–209 (2011)
M.J. Walter, E. Cottrell, Assessing uncertainty in geochemical models for core formation in Earth. Earth Planet. Sci. Lett. **365**, 165–176 (2013)
K. Willacy, H.H. Klahr, T.J. Millar, Th. Henning, Gas and grain chemistry in a protoplanetary disk. Astron. Astrophys. **338**, 995–1005 (1998)
B.J. Wood, M.J. Walter, J. Wade, Accretion of the Earth and segregation of its core. Nature **441**, 825–833 (2006). https://doi.org/10.1038/nature04763
T. Yoshino, M.J. Walter, T. Katsura, Core formation in planetesimals triggered by permeable flow. Nature **422**, 154–157 (2003)
E.D. Young, The hydrology of carbonaceous chondrite parent bodies and the evolution of planet progenitors. Philos. Trans. R. Soc. Lond. A **359**, 2095–2110 (2001)
E.D. Young, R.D. Ash, P. England, D. Rumble III, Fluid flow in chondrite parent bodies: deciphering the compositions of planetesimals. Science **286**, 1331–1335 (1999)
E. Young, K. Zhang, G. Schubert, Conditions for pore water convection within carbonaceous chondrite parent bodies—implications for planetesimal size and heat production. Earth Planet. Sci. Lett. **213**, 249–259 (2003)
K. Zhang, K.M. Pontoppidan, C. Salyk, G.A. Blake, Evidence for a snow line beyond the transitional radius in the TW Hya protoplanetary disk. Astrophys. J. **766**, 82 (2013)
M.E. Zolensky, W.L. Bourcier, J.L. Gooding, Aqueous alteration on the hydrous asteroids: results of EQ3/6 computer simulations. Icarus **78**, 411–425 (1989)
M.Y. Zolotov, J.S. Kargel, On the composition of Europa's icy shell, ocean and underlying rocks, in *Europa*, ed. by R. Pappalardo, W.B. McKinnon, K. Khurana (University of Arizona Press, Tucson, 2009), pp. 431–457

9 Conclusion et intégration au Laboratoire Magmas et Volcans

Depuis le début de ma thèse, je me suis intéressé aux grandes étapes d'évolution primitive des planètes et lunes du système solaire. J'ai travaillé plus particulièrement sur la relation entre les impacts météoritiques, l'évolution thermique des jeunes planètes et les premiers épisodes majeurs de différenciation. Cette thématique de recherche m'a naturellement amené à travailler sur la dynamique d'évolution du champ magnétique des planètes telluriques mais aussi à considérer des objets tels que les satellites de glace. Pour cela, j'ai développé et j'adapté des modèles numériques afin d'obtenir les échelles caractéristiques de temps, de longueur et de température propres à ces événements qui ont grandement conditionné la structure thermo-chimique actuelle des planètes.

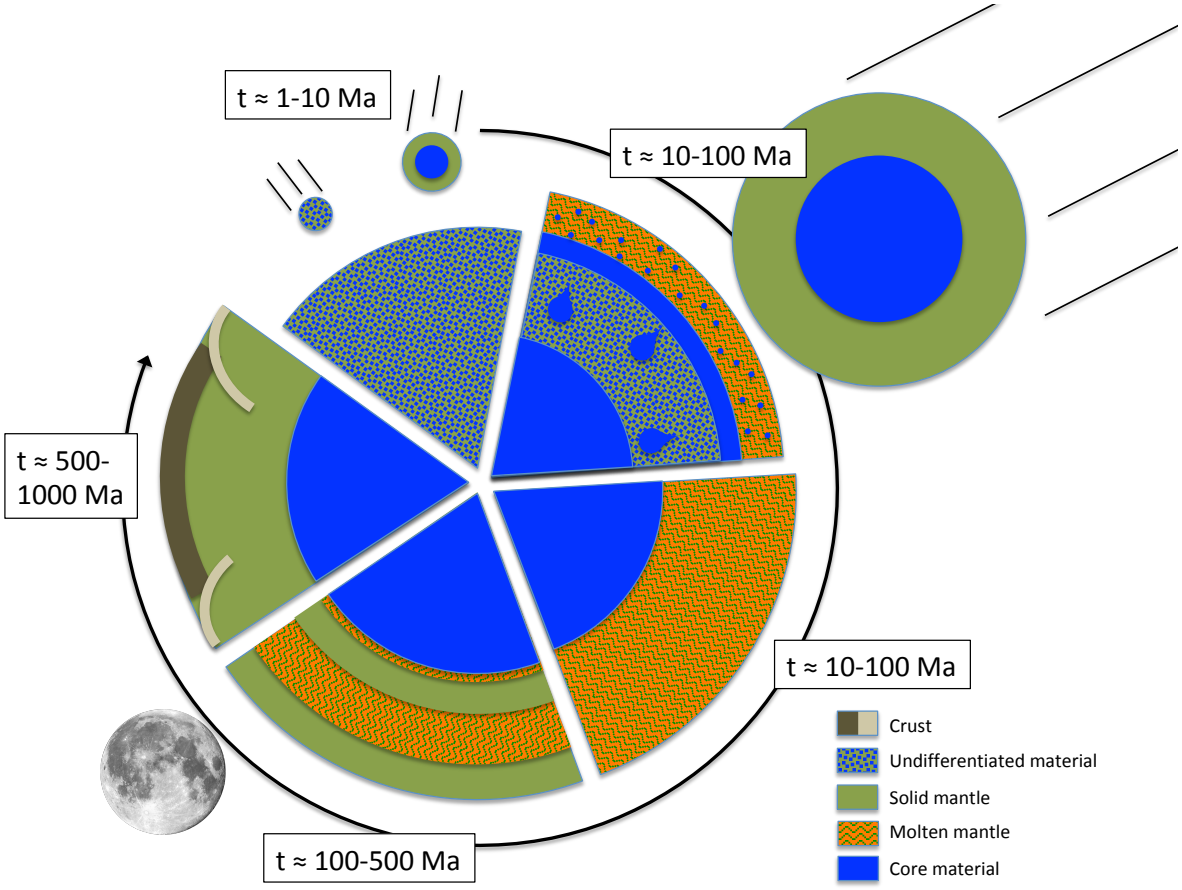

FIGURE 33 – *Représentation schématique de l'évolution de la structure interne de la Terre depuis la fin de son accrétion jusqu'à la mise en place d'une tectonique des plaques moderne.*

Au cours de mon parcours scientifique, j'ai utilisé des codes numériques (code d'analyse

de la déformation mécanique, code de convection, code de dynamo cinématique) et j'ai également modifié ces outils numériques afin de les adapter pour mieux comprendre comment évolue l'intérieur des jeunes planètes. J'ai ainsi transformé un code de convection 2D cartésien en un code de convection thermique axi-symétrique cylindrique puis en un code de convection thermo-chimique axi-symétrique sphérique afin de caractériser les conséquences d'un large impact météoritique sur une planète en croissance. J'ai modifié un code de convection thermique 3D sphérique pour inclure les effets de l'accrétion et de la différenciation des satellites de glace. Pour caractériser le refroidissement d'un océan magmatique impliquant tout le manteau terrestre j'ai développé une approche uni-dimensionnelle afin de pouvoir facilement implémenter des contraintes issues de la pétrologie expérimentale (courbes de fusion, adiabats, lois de viscosité...). Plus récemment, j'ai pris en main le logiciel COMSOL Multiphysics qui est un outil de modélisation en éléments finis permettant d'aborder différentes problématiques telles que les transferts thermiques, la mécanique des fluides et des solides ou les réactions chimiques. Il s'avère que cet outil est pertinent dans un laboratoire comme le LMV où les problématiques scientifiques sont très variées et où des progrès scientifiques majeurs nécessitants d'être envisagés d'un point de vue dynamique sont réguliers.

L'UMR 6524 Laboratoire Magmas et Volcans est une unité de recherche associée au CNRS. Ce laboratoire développe des programmes de recherche afin de comprendre l'ensemble des processus magmatiques et volcaniques, depuis la fusion dans le manteau terrestre jusqu'à l'éruption en surface en utilisant les méthodes et les outils les plus performants de différentes disciplines de la Pétrologie, de la Géochimie et de la Volcanologie et en s'appuyant sur un parc important d'appareillages expérimentaux et de caractérisations chimiques et physiques des roches et des minéraux. Mon arrivée au LMV en 2014 a permis d'apporter de nouvelles compétences en termes de modélisation numérique à ce laboratoire, en accord avec les évaluations AERES et HCERES qui avaient explicitement souligné le besoin du laboratoire en terme de modélisation géodynamique en complément, notamment, des approches transverses en pétrologie et géochimie isotopique sur les thématiques de la Terre interne et de l'origine du volcanisme.

Cette activité de recherche s'insère dans la thématique transverse «Terre primitive» du laboratoire (j'en suis l'animateur depuis 2022), et dont le but est de comprendre et caractériser les mécanismes géodynamiques, la structure interne et les signaux géochimiques des objets de la Terre primitive. Me concernant, ce laboratoire me permet de bénéficier d'expertises dans plusieurs domaines complémentaires, en particulier en géochimie et en pétrologie expérimentale qui apportent tous deux des contraintes majeures sur la séquence d'événements et les conditions dans lesquelles les processus d'accrétion et de différenciation planétaires se sont déroulées. Ainsi, ce projet est un élément charnière entre les membres de l'équipe Pétrologie (D. Andrault, A. Bouhifd, G. Manthilake) et ceux de l'équipe Géochimie dont plusieurs membres sont impliqués depuis longtemps dans l'analyse et la datation des éléments géochimiques traceurs des évènements terrestres primitifs (M. Boyet, M. Garçon, M. Guitreau). Ce projet permet ainsi de donner une autre dimension à ces deux équipes en apportant des contraintes sur la dynamique, les forces, la physique des mouvements que la géochimie et la

pétrologie expérimentale ne peuvent pas traiter.

Les moyens nécessaires pour mener à bien mon activité de recherche sont des instruments de calcul puissants permettant de lancer des codes numériques résolvant les équations de la dynamique des fluides que j'ai déjà développés ou que je souhaite adapter au quotidien. Ces instruments sont déjà présents au sein de l'UMR puisque celle-ci possède des moyens de calcul aux niveaux local (clusters), régional (Centre de Calcul Intensif Auvergrid) et bénéficie d'accès aux centres nationaux (le Centre Informatique National de l'Enseignement Supérieur et Institut du Développement et des Ressources en Informatique Scientifique).

Les neuf années que j'ai passées au Laboratoire Magmas et Volcans m'ont permis de voir quels étaient mes besoins pour aller plus loin dans mon activité de recherche mais aussi pour développer la modélisation numérique dans ce laboratoire. Tout d'abord, mon expérience d'encadrement des thèses de Baraa Qaddah (2017-2020) et de Tristan Engels (2021-2024) montrent qu'il est possible d'attirer et de conserver des étudiants motivés pour des travaux liés à la dynamique interne de le Terre Primitive alors que l'offre de formation attire plutôt des étudiants en volcanologie. Les étudiants formés à l'Université Clermont-Auvergne dans le parcours Magmas et Volcans sont sensibilisés à la mécanique des fluides, aux questions liées à la Terre primitive et à la dynamique de la Terre interne. J'envisage prochainement de déposer à l'École Doctorale un sujet lié aux effets de marées sur le refroidissement de la Terre primitive.

De plus, ces neuf années ont été jalonnées de projets et de publications avec des collègues qui souhaitaient renforcer leurs conclusions ou aller au-delà de leur expertise en s'appuyant sur des modèles numériques. Ainsi aujourd'hui il est courant que je développe des modèles avec des géochimistes (M. Guitreau, M. Boyet) et avec des spécialistes de la pétrologie expérimentale (D. Andrault, A. Bouhifd, G. Manthilake). Ces collaborations n'ont pas pour autant limité mes collaborations avec des chercheurs d'autres laboratoires que ce soit en France (M. Le Bars, G. Tobie, H. Samuel, P. Auclair-Desrotour) ou à l'étranger (J. Arkani-Hamed, S. Marchi).

Enfin, les collaborations récentes avec mes collègues pétrologues, géochimistes mais aussi volcanologues m'ont montré à quel point il fallait être réactif en terme de développement numérique afin de pouvoir apporter regard différent sur leurs résultats expérimentaux. Par exemple, je développe actuellement des modèles numériques en collaboration avec O. Roche afin de calibrer un dispositif expérimental permettant de caractériser la dynamique d'une chambre magmatique. Il s'agit notamment de caractériser l'effet d'injection de magmas sur la fusion et la remobilisation du matériel fondu pré-éxistant. Pour cela, O. Roche et moi avons travaillé sur le dimensionnement d'une expérience en laboratoire impliquant des matériaux analogues (liquides, volatils, particules). Notre collaboration a permis de designer au mieux le dispositif expérimental de cette étude. Mais pour développer ces modèles numériques, nous avons besoin de considérer des géométries et des rhéologies complexes et de tels modèles ne peuvent être développés que sur des échelles de temps courtes. Ainsi il semble qu'un outil tel que COMSOL Multiphysics soit particulièrement adapté dans ce laboratoire. Et au vu du nombre croissant des sollicitations, il serait à l'avenir intéressant d'avoir au LMV un Ingénieur

dédié au développement de tels modèles.

Références

Abe, Y., 1997. Thermal and chemical evolution of the terrestrial magma ocean. Physics of the Earth and Planetary Interiors 100, 27–39.

Abe, Y., Ohtani, E., Okuchi, T., Righter, K., Drake, M., 2000. Water in the Early Earth. Origin of the earth and moon, edited by R.M. Canup and K. Righter and 69 collaborating authors. Tucson : University of Arizona Press ; Houston : Lunar and Planetary Institute, c2000. (The University of Arizona space science series).

Acuña, M., Connerney, J., Ness, N., Lin, R., Mitchell, D., Carlson, C., McFadden, J., Anderson, K., Rème, H., Mazelle, C., Vignes, D., Wasilewski, P., Cloutier, P., 1999. Global distribution of crustal magnetization discovered by the mars global surveyor MAG/ER experiment. Science 284, 790–793.

Agnor, C. B., Canup, R. M., Levison, H. F., Nov. 1999. On the Character and Consequences of Large Impacts in the Late Stage of Terrestrial Planet Formation. Icarus 142, 219–237.

Agrusta, R., Morison, A., Labrosse, S., Deguen, R., Alboussiére, T., Tackley, P. J., Dubuffet, F., Mar. 2020. Mantle convection interacting with magma oceans. Geophysical Journal International 220 (3), 1878–1892.

Ahrens, T. J., Jan. 1993. Impact Erosion of Terrestrial Planetary Atmospheres. Annual Review of Earth and Planetary Sciences 21, 525–555.

Ahrens, T. J., Shen, A. H., Ni, S., Jul. 2004. Giant Impact Induced Atmospheric Blow-Off. In : Shock Compression of Condensed Matter. Vol. 706 of American Institute of Physics Conference Series. pp. 1419–1422.

Amit, H., Choblet, G., Olson, P., Monteux, J., Deschamps, F., Langlais, B., Tobie, G., 2015. Towards more realistic core-mantle boundary heat flux patterns : a source of diversity in planetary dynamos. Progress in Earth and Planetary Science 2 (1), 26.

Amit, H., Christensen, U., Langlais, B., 2011. The influence of degree-1 mantle heterogeneity on the past dynamo of Mars. Phys. Earth Planet. Int. 189, 63–79.

Anderson, J. D., Jacobson, R. A., McElrath, T. P., Moore, W. B., Schubert, G., Thomas, P. C., Sep. 2001. Shape, Mean Radius, Gravity Field, and Interior Structure of Callisto. Icarus 153, 157–161.

Andrault, D., Monteux, J., Le Bars, M., Samuel, H., Jun. 2016. The deep Earth may not be cooling down. Earth and Planetary Science Letters 443, 195–203.

Andrault, D., Pesce, G., Manthilake, G., Monteux, J., Bolfan-Casanova, N., Chantel, J., Novella, D., Guignot, N., King, A., Itié, J.-P., Hennet, L., Feb. 2018. Deep and persistent melt layer in the Archaean mantle. Nature Geoscience 11 (2), 139–143.

Andrault, D., Petigirard, S., Lo Nigro, G., Devidal, J.-L., Veronesi, G., Garbarino, G., Mezouar, M., 2012. Solid-liquid iron partitioning in Earth's deep mantle. Nature 487 (7407), 354.

Arkani-Hamed, J., Olson, P., Jul. 2010. Giant impacts, core stratification, and failure of the Martian dynamo. Journal of Geophysical Research (Planets) 115, 7012.

Asphaug, E., 2010. Similar-sized collisions and the diversity of planets. Chemie der Erde / Geochemistry 70, 199–219.

Ballmer, M. D., Lourenço, D. L., Hirose, K., Caracas, R., Nomura, R., Jul. 2017. Reconciling magma-ocean crystallization models with the present-day structure of the Earth's mantle. Geochemistry, Geophysics, Geosystems 18 (7), 2785–2806.

Barr, A. C., Canup, R. M., Nov. 2008. Constraints on gas giant satellite formation from the interior states of partially differentiated satellites. Icarus 198, 163–177.

Barr, A. C., Canup, R. M., Mar. 2010. Origin of the Ganymede-Callisto dichotomy by impacts during the late heavy bombardment. Nature Geoscience 3, 164–167.

Becker, H., Horan, M. F., Walker, R. J., Gao, S., Lorand, J.-P., Rudnick, R. L., Sep. 2006. Highly siderophile element composition of the Earth's primitive upper mantle : Constraints from new data on peridotite massifs and xenoliths. Geochimica et Cosmochimica Acta 70, 4528–4550.

Benson, D., Sep. 1992. Computational methods in Lagrangian and Eulerian hydrocodes. Computer Methods in Applied Mechanics and Engineering 99 (2-3), 235–394.

Benz, W., Slattery, W. L., Cameron, A. G. W., Jun. 1988. Collisional stripping of Mercury's mantle. Icarus 74, 516–528.

Boioli, F., Carrez, P., Cordier, P., Devincre, B., Gouriet, K., Hirel, P., Kraych, A., Ritterbex, S., Mar. 2017. Pure climb creep mechanism drives flow in Earth's lower mantle. Science Advances 3 (3), e1601958.

Boujibar, A., Andrault, D., Bolfan-Casanova, N., Bouhifd, M. A., Monteux, J., Sep. 2015. Cosmochemical fractionation by collisional erosion during the Earth's accretion. Nature Communications 6, 8295.

Boujibar, A., Andrault, D., Bouhifd, M. A., Bolfan-Casanova, N., Devidal, J.-L., Trcera, N., Apr. 2014. Metal-silicate partitioning of sulphur, new experimental and thermodynamic constraints on planetary accretion. Earth and Planetary Science Letters 391, 42–54.

Boyet, M., Carlson, R. W., 2005. ^{142}Nd Evidence for Early (>4.53 Ga) Global Differentiation of the Silicate Earth. Science 309, 576–581.

Brandenburg, J. P., Hauri, E. H., van Keken, P. E., Ballentine, C. J., Nov. 2008. A multiple-system study of the geochemical evolution of the mantle with force-balanced plates and thermochemical effects. Earth and Planetary Science Letters 276 (1-2), 1–13.

Buffett, B. A., 2002. Estimates of heat flow in the deep mantle based on the power requirements for the geodynamo. Geophys. Res. Lett. 29 (12), 1–4.

Běhounková, M., Tobie, G., Choblet, G., Čadek, O., 2010. Coupling mantle convection and tidal dissipation : Applications to Enceladus and Earth-like planets. Journal of Geophysical Research (Planets) 115, 9011.

Cameron, A. G. W., Ward, W. R., Mar. 1976. The Origin of the Moon. In : Lun. Planet. Inst. Conf. Abs. Vol. 7. pp. 120–122.

Canup, R. M., Apr. 2004. Simulations of a late lunar-forming impact. Icarus 168, 433–456.

Canup, R. M., Agnor, C. B., 2000. Accretion of the Terrestrial Planets and the Earth-Moon System. In : Origin of the Earth and Moon. Origin of the earth and moon, edited by R.M. Canup and K. Righter : University of Arizona Press, pp. 113–129.

Canup, R. M., Asphaug, E., Aug. 2001. Origin of the Moon in a giant impact near the end of the Earth's formation. Nature 412, 708–712.

Canup, R. M., Ward, W. R., 2002. Formation of the Galilean Satellites : Conditions of Accretion. aj 124, 3404–3423.

Caracas, R., Hirose, K., Nomura, R., Ballmer, M. D., Jun. 2019. Melt-crystal density crossover in a deep magma ocean. Earth and Planetary Science Letters 516, 202–211.

Castillo-Rogez, J. C., Lunine, J. I., Oct. 2010. Evolution of Titan's rocky core constrained by Cassini observations. Geophys. Res. Lett. 37, 20205.

Charlier, B., Namur, O., 02 2019. The Origin and Differentiation of Planet Mercury. Elements 15 (1), 9–14.

Chen, E. M. A., Nimmo, F., Sep. 2016. Tidal dissipation in the lunar magma ocean and its effect on the early evolution of the Earth-Moon system. Icarus 275, 132–142.

Choblet, G., Čadek, O., Couturier, F., Dumoulin, C., 2007. ŒDIPUS : a new tool to study the dynamics of planetary interiors. Geophysical Journal International 170, 9–30.

Christensen, U. R., Aubert, J., 2006. Scaling properties of convection-driven dynamos in rotating spherical shells and application to planetary magnetic fields. Geophys. J. Int. 166, 97–114.

Cížková, H., van den Berg, A. P., Spakman, W., Matyska, C., Jun. 2012. The viscosity of Earth's lower mantle inferred from sinking speed of subducted lithosphere. Physics of the Earth and Planetary Interiors 200, 56–62.

Clesi, V., Bouhifd, M. A., Bolfan-Casanova, N., Manthilake, G., Fabbrizio, A., Andrault, D., Nov. 2016. Effect of H_2O on metal-silicate partitioning of Ni, Co, V, Cr, Mn and Fe : Implications for the oxidation state of the Earth and Mars. Geochimica et Cosmochimica Acta 192, 97–121.

Clesi, V., Bouhifd, M. A., Bolfan-Casanova, N., Manthilake, G., Schiavi, F., Raepsaet, C., Bureau, H., Khodja, H., Andrault, D., Mar. 2018. Low hydrogen contents in the cores of terrestrial planets. Science Advances 4 (3), e1701876.

Clesi, V., Monteux, J., Qaddah, B., Le Bars, M., Wacheul, J. B., Bouhifd, M. A., Sep. 2020. Dynamics of core-mantle separation : Influence of viscosity contrast and metal/silicate partition coefficients on the chemical equilibrium. Physics of the Earth and Planetary Interiors 306, 106547.

Collins, G. S., Morgan, J., Barton, P., Christeson, G. L., Gulick, S., Urrutia, J., Warner, M., Wünnemann, K., Jun. 2008. Dynamic modeling suggests terrace zone asymmetry in the Chicxulub crater is caused by target heterogeneity. Earth and Planetary Science Letters 270, 221–230.

Coradini, A., Federico, C., Forni, O., Magni, G., Jul. 1995. Origin and thermal evolution of icy satellites. Surveys in Geophysics 16, 533–591.

Croft, S. K., 1982. A first-order estimate of shock heating and vaporization in oceanic impacts. Vol. 190. Geological Implications of Impacts of Large Asteroids and Comets on Earth, edited by T.L. Silver and P.H. Schultz,Spec. Pap. Geol. Soc. Am.

Ćuk, M., Stewart, S. T., 2012. Making the Moon from a Fast-Spinning Earth : A Giant Impact Followed by Resonant Despinning. Science 338, 1047–1052.

Dahl, T. W., Stevenson, D. J., 2010. Turbulent mixing of metal and silicate during planet accretion and interpretation of the Hf-W chronometer. Earth and Planetary Science Letters 295, 177–186.

Davison, T. M., Collins, G. S., Ciesla, F. J., 2010. Numerical modelling of heating in porous planetesimal collisions. Icarus 208, 468–481.

Deguen, R., Olson, P., Cardin, P., Oct. 2011. Experiments on turbulent metal-silicate mixing in a magma ocean. Earth and Planetary Science Letters 310, 303–313.

Doglioni, C., Ismail-Zadeh, A., Panza, G., Riguzzi, F., Nov. 2011. Lithosphere-asthenosphere viscosity contrast and decoupling. Physics of the Earth and Planetary Interiors 189 (1), 1–8.

Dwyer, C., Nimmo, F., Ogihara, M., Ida, S., 2013. The influence of imperfect accretion and radial mixing on ice :rock ratios in the galilean satellites. Icarus 225 (1), 390 – 402.

Dwyer, C. A., Stevenson, D. J., Nimmo, F., 2011. A long-lived lunar dynamo driven by continuous mechanical stirring. Nature 479, 212–214.

Dyal, P., Parkin, C. W., Daily, W. D., 1974. Magnetism and the interior of the moon. Reviews of Geophysics and Space Physics 12, 568–591.

Estrada, P. R., Mosqueira, I., Lissauer, J. J., D'Angelo, G., Cruikshank, D. P., Sep. 2008. Formation of Jupiter and Conditions for Accretion of the Galilean Satellites. ArXiv e-prints.

Estrada, P. R., Mosqueira, I., Lissauer, J. J., D'Angelo, G., Cruikshank, D. P., 2009. Formation of Jupiter and Conditions for Accretion of the Galilean Satellites. University of Arizona Press, pp. 27–+.

Farhat, M., Auclair-Desrotour, P., Boué, G., Laskar, J., Sep. 2022. The resonant tidal evolution of the Earth-Moon distance. Astronomy and Astrophysics 665, L1.

Flasar, F. M., Birch, F., 1973. Energetics of core formation : A correction. J. Geophys. Res. 78, 6101–6103.

Foley, B. J., Bercovici, D., Elkins-Tanton, L. T., Nov. 2014. Initiation of plate tectonics from post-magma ocean thermochemical convection. Journal of Geophysical Research (Solid Earth) 119 (11), 8538–8561.

Freitas, D., Monteux, J., Andrault, D., Manthilake, G., Mathieu, A., Schiavi, F., Cluzel, N., Mar. 2021. Thermal conductivities of solid and molten silicates : Implications for dynamos in mercury-like proto-planets. Physics of the Earth and Planetary Interiors 312, 106655.

Frossard, P., Boyet, M., Bouvier, A., Hammouda, T., Monteux, J., 2019. Evidence for anorthositic crust formed on an inner solar system planetesimal. Geochemical Perspectives Letters, 28–32.

Frost, H. J., Ashby, M., 1982. Deformation-Mechanism Maps : The Plasticity and Creep of Metals and Ceramics. Pergamon, Oxford.

Funamori, N., Sato, T., 2010. Density contrast between silicate melts and crystals in the deep mantle : An integrated view based on static-compression data. Earth and Planetary Science Letters 295, 435–440.

Genda, H., Brasser, R., Mojzsis, S. J., Dec. 2017. The terrestrial late veneer from core disruption of a lunar-sized impactor. Earth and Planetary Science Letters 480, 25–32.

Golabek, G. J., Gerya, T. V., Kaus, B. J. P., Ziethe, R., Tackley, P. J., Nov. 2009. Rheological controls on the terrestrial core formation mechanism. Geochemistry, Geophysics, Geosystems 10, 11007.

Gomi, H., Ohta, K., Hirose, K., Labrosse, S., Caracas, R., Verstraete, M. J., Hernlund, J. W., Nov. 2013. The high conductivity of iron and thermal evolution of the Earth's core. Physics of the Earth and Planetary Interiors 224, 88–103.

Grasset, O., Sotin, C., Sep. 1996. The Cooling Rate of a Liquid Shell in Titan's Interior. Icarus 123, 101–112.

Halliday, A. N., Feb. 2004. Mixing, volatile loss and compositional change during impact-driven accretion of the Earth. Nature 427 (6974), 505–509.

Hansen, C. J., Esposito, L., Stewart, A. I. F., Colwell, J., Hendrix, A., Pryor, W., Shemansky, D., West, R., Mar. 2006. Enceladus' Water Vapor Plume. Science 311, 1422–1425.

Hartmann, W. K., Davis, D. R., Apr. 1975. Satellite-sized planetesimals and lunar origin. Icarus 24, 504–514.

Honda, R., Mizutani, H., Yamamoto, T., 1993. Numerical simulation of Earth's core formation. J. Geophys. Res. 98, 2075–2090.

Hood, L. L., Zakharian, A., Halekas, J., Mitchell, D. L., Lin, R. P., Acuña, M. H., Binder, A. B., 2001. Initial mapping and interpretation of lunar crustal magnetic anomalies using Lunar Prospector magnetometer data. J. Geophys. Res. 106, 27825–27840.

Hutcheon, I. D., Hutchison, R., Jan. 1989. Evidence from the Semarkona ordinary chondrite for Al-26 heating of small planets. nat 337, 238–241.

Iess, L., Jacobson, R. A., Ducci, M., Stevenson, D. J., Lunine, J. I., Armstrong, J. W., Asmar, S. W., Racioppa, P., Rappaport, N. J., Tortora, P., Jul. 2012. The Tides of Titan. Science 337, 457–.

Iess, L., Rappaport, N. J., Jacobson, R. A., Racioppa, P., Stevenson, D. J., Tortora, P., Armstrong, J. W., Asmar, S. W., Mar. 2010. Gravity Field, Shape, and Moment of Inertia of Titan. Science 327, 1367–.

Jackson, M. G., Carlson, R. W., Kurz, M. D., Kempton, P. D., Francis, D., Blusztajn, J., Aug. 2010. Evidence for the survival of the oldest terrestrial mantle reservoir. Nature 466 (7308), 853–856.

Jacobson, S. A., Morbidelli, A., 2014. Lunar and terrestrial planet formation in the Grand Tack scenario. Royal Society of London Philosophical Transactions Series A 372, 174.

Javoy, M., Kaminski, E., Guyot, F., Andrault, D., Sanloup, C., Moreira, M., Labrosse, S., Jambon, A., Agrinier, P., Davaille, A., Jaupart, C., May 2010. The chemical composition of the Earth : Enstatite chondrite models. Earth and Planetary Science Letters 293, 259–268.

Jones, C., 2015. Thermal and compositional convection in the outer core, Treatise of Geophysics. Vol. 8. Olson, P. editor in Chief, Elsevier.

Jutzi, M., Asphaug, E., 2011. Forming the lunar farside highlands by accretion of a companion moon. Nature 476, 69–72.

Karato, S.-I., Murthy, V. R., 1997. Core formation and chemical equilibrium in the Earth-I. Physical considerations. Physics of the Earth and Planetary Interiors 100, 61–79.

Karki, B. B., Stixrude, L. P., May 2010. Viscosity of $MgSiO_3$ Liquid at Earth's Mantle Conditions : Implications for an Early Magma Ocean. Science 328 (5979), 740.

Kaula, W. M., Mar. 1979. Thermal evolution of earth and moon growing by planetesimal impacts. J. Geophys. Res. 84, 999–1008.

Ke, Y., Solomatov, V. S., 2009. Coupled core-mantle thermal evolution of early Mars. Journal of Geophysical Research (Planets) 114 (13), 1–12.

Kendall, J. D., Melosh, H. J., Aug. 2016. Differentiated planetesimal impacts into a terrestrial magma ocean : Fate of the iron core. Earth and Planetary Science Letters 448, 24–33.

Kervazo, M., Tobie, G., Choblet, G., Dumoulin, C., Běhounková, M., Jun. 2021. Solid tides in Io's partially molten interior. Contribution of bulk dissipation. Astronomy and Astrophysics 650, A72.

Kirk, R. L., Stevenson, D. J., Jan. 1987. Thermal evolution of a differentiated Ganymede and implications for surface features. Icarus 69, 91–134.

Kivelson, M. G., Warnecke, J., Bennett, L., Joy, S., Khurana, K. K., Linker, J. A., Russell, C. T., Walker, R. J., Polanskey, C., Sep. 1998. Ganymede's magnetosphere : Magnetometer overview. J. Geophys. Res. 103, 19963–19972.

Kleine, T., Münker, C., Mezger, K., Palme, H., 2002. Rapid accretion and early core formation on asteroids and the terrestrial planets from Hf-W chronometry. Nature 418, 952–955.

Kleine, T., Rudge, J. F., 2011. Chronometry of Meteorites and the Formation of the Earth and Moon. Elements 7, 41–46.

Kleine, T., Touboul, M., Bourdon, B., Nimmo, F., Mezger, K., Palme, H., Jacobsen, S. B., Yin, Q.-Z., Halliday, A. N., 2009. Hf-W chronology of the accretion and early evolution of asteroids and terrestrial planets. Geochimica et Cosmochimica Acta 73, 5150–5188.

Koker, N. d., Steinle-Neumann, G., Vl*f*çek, V., 2012. Electrical resistivity and thermal conductivity of liquid Fe alloys at high P and T, and heat flux in Earth,Äôs core. Proceedings of the National Academy of Sciences 109 (11), 4070–4073.

Kokubo, E., Ida, S., Jan. 2000. Formation of Protoplanets from Planetesimals in the Solar Nebula. Icarus 143, 15–27.

Konôpková, Z., McWilliams, R. S., Gómez-Pérez, N., Goncharov, A. F., Jun. 2016. Direct measurement of thermal conductivity in solid iron at planetary core conditions. Nature 534 (7605), 99–101.

Kossacki, K. J., Leliwa-Kopystyński, J., Oct. 1993. Medium-sized icy satellites : thermal and structural evolution during accretion. Planet. Space Sci. 41, 729–741.

Kuang, W., Jiang, W., Roberts, J., Frey, H. V., Nov. 2014. Could giant basin-forming impacts have killed Martian dynamo ? Geoph. Res. Lett. 41 (22), 8006–8012.

Kurosaki, K., Inutsuka, S.-i., Jan. 2019. The Exchange of Mass and Angular Momentum in the Impact Event of Ice Giant Planets : Implications for the Origin of Uranus. The Astronomical Journal 157 (1), 13.

Kutzner, C., Christensen, U. R., 2002. From stable dipolar towards reversing numerical dynamos. Physics of the Earth and Planetary Interiors 131, 29–45.

Labrosse, S., Hernlund, J. W., Coltice, N., Dec. 2007. A crystallizing dense magma ocean at the base of the Earth's mantle. Nature 450, 866–869.

Laneuville, M., Hernlund, J., Labrosse, S., Guttenberg, N., Mar. 2018. Crystallization of a compositionally stratified basal magma ocean. Physics of the Earth and Planetary Interiors 276, 86–92.

Lange, M. A., Ahrens, T. J., Jul. 1982. The evolution of an impact-generated atmosphere. Icarus 51 (1), 96–120.

Lange, M. A., Ahrens, T. J., Apr. 1986. Shock-induced CO_2 loss from $CaCO_3$; implications for early planetary atmospheres. Earth and Planetary Science Letters 77 (3-4), 409–418.

Langenhorst, F., Deutsch, A., 02 2012. Shock Metamorphism of Minerals. Elements 8 (1), 31–36.

Langlais, B., Lesur, V., Purucker, M. E., Connerney, J. E. P., Mandea, M., 2010. Crustal Magnetic Fields of Terrestrial Planets. Spa. Sci. Rev. 152, 223–249.

Langlais, B., Purucker, M. E., Mandea, M., 2004. Crustal magnetic field of Mars. Journal of Geophysical Research (Planets) 109, 2008.

Le Bars, M., Wieczorek, M., Karatekin, O., Cébron, D., Laneuville, M., 2011. An Impact-Driven Dynamo for the Early Moon. Nature 479, 215–218.

Lebrun, T., Massol, H., Chassefière, E., Davaille, A., Marcq, E., Sarda, P., Leblanc, F., Brandeis, G., Jun. 2013. Thermal evolution of an early magma ocean in interaction with the atmosphere. Journal of Geophysical Research (Planets) 118, 1155–1176.

Lee, D.-C., Halliday, A. N., Dec. 1996. Hf-W Isotopic Evidence for Rapid Accretion and Differentiation in the Early Solar System. Science 274 (5294), 1876–1879.

Lillis, R. J., Frey, H. V., Manga, M., 2008. Rapid decrease in Martian crustal magnetization in the Noachian era : Implications for the dynamo and climate of early Mars. Geoph. Res. Lett. 35, 14203–+.

Lock, S. J., Stewart, S. T., Petaev, M. I., Leinhardt, Z., Mace, M. T., Jacobsen, S. B., Cuk, M., Apr. 2018. The Origin of the Moon Within a Terrestrial Synestia. Journal of Geophysical Research (Planets) 123 (4), 910–951.

Lorand, J.-P., Alard, O., Luguet, A., in press 2012. Platinum-group elements systematics and petrogenetic processing of the continental upper mantle :a review. Invited Review Paper, Lithos. 70, 4528–4550.

Lorand, J.-P., Luguet, A., Alard, O., 2008. Platinum-group elements : a new set of key tracers for the Earth,Äôs interior. Elements 4, 247–253.

Manthilake, G., Chantel, J., Monteux, J., Andrault, D., Bouhifd, M. A., Bolfan Casanova, N., Boulard, E., Guignot, N., King, A., Itie, J. P., Sep. 2019. Thermal Conductivity of FeS and Its Implications for Mercury's Long-Sustaining Magnetic Field. Journal of Geophysical Research (Planets) 124 (9), 2359–2368.

Marchi, S., Black, B. A., Elkins-Tanton, L. T., Bottke, W. F., Sep. 2016. Massive impact-induced release of carbon and sulfur gases in the early Earth's atmosphere. Earth and Planetary Science Letters 449, 96–104.

Marinova, M. M., Aharonson, O., Asphaug, E., 2008. Mega-impact formation of the Mars hemispheric dichotomy. Nature 453, 1216–1219.

Marounina, N., Tobie, G., Carpy, S., Monteux, J., Charnay, B., Grasset, O., Sep. 2015. Evolution of Titan's atmosphere during the Late Heavy Bombardment. Icarus 257, 324–335.

Marty, B., Jan. 2012. The origins and concentrations of water, carbon, nitrogen and noble gases on Earth. Earth and Planetary Science Letters 313, 56–66.

Maurice, M., Tosi, N., Samuel, H., Plesa, A.-C., Hüttig, C., Breuer, D., Mar. 2017. Onset of solid-state mantle convection and mixing during magma ocean solidification. Journal of Geophysical Research (Planets) 122 (3), 577–598.

McDonough, W. F., Å rámek, O., Wipperfurth, S. A., Jul. 2020. Radiogenic Power and Geoneutrino Luminosity of the Earth and Other Terrestrial Bodies Through Time. Geochemistry, Geophysics, Geosystems 21 (7), e08865.

McKinnon, W., 2013. The shape of Enceladus as explained by an irregular core : Implications for gravity, libration, and survival of its subsurface ocean. J. Geophys. Res (Planets) 118, 1–14.

Meyer, B. S., Clayton, D. D., Apr. 2000. Short-Lived Radioactivities and the Birth of the sun. Space Science Reviews 92, 133–152.

Moffatt, H., 1978. *Magnetic field generation in electrically conducting fluids*. Cambridge University Press, Cambridge, UK.

Monteux, J., Amit, H., Choblet, G., Langlais, B., Tobie, G., Mar. 2015. Giant impacts, heterogeneous mantle heating and a past hemispheric dynamo on Mars. Physics of the Earth and Planetary Interiors 240, 114–124.

Monteux, J., Andrault, D., in press. Chapter 2 - Dynamique et evolution thermique du manteau terrestre primitif. In : Dynamique du manteau terrestre. ISTE collections, pp. 1–40.

Monteux, J., Andrault, D., Guitreau, M., Samuel, H., Demouchy, S., May 2020. A mushy Earth's mantle for more than 500 Myr after the magma ocean solidification. Geophysical Journal International 221 (2), 1165–1181.

Monteux, J., Andrault, D., Samuel, H., Aug. 2016a. On the cooling of a deep terrestrial magma ocean. Earth and Planetary Science Letters 448, 140–149.

Monteux, J., Arkani-Hamed, J., Mar. 2014. Consequences of giant impacts in early Mars : Core merging and Martian dynamo evolution. Journal of Geophysical Research (Planets) 119, 480–505.

Monteux, J., Arkani-Hamed, J., Jan. 2016. Scaling laws of impact induced shock pressure and particle velocity in planetary mantle. Icarus 264, 246–256.

Monteux, J., Arkani-Hamed, J., Oct. 2019. Shock wave propagation in layered planetary interiors : Revisited. Icarus 331, 238–256.

Monteux, J., Collins, G. S., Tobie, G., Choblet, G., Jan. 2016b. Consequences of large impacts on Enceladus' core shape. Icarus 264, 300–310.

Monteux, J., Coltice, N., Dubuffet, F., Ricard, Y., 2007. Thermo-mechanical adjustment after impacts during planetary growth. Geophys. Res. Lett. 34, 24201–24205.

Monteux, J., Golabek, G. J., Rubie, D. C., Tobie, G., Young, E. D., Feb. 2018. Water and the Interior Structure of Terrestrial Planets and Icy Bodies. Space Science Reviews 214 (1), 39.

Monteux, J., Jellinek, A. M., Johnson, C. L., 2011. Why might planets and moons have early dynamos ? Earth and Planetary Science Letters 310, 349–359.

Monteux, J., Jellinek, A. M., Johnson, C. L., 2013. Dynamics of core merging after a mega-impact with applications to Mars' early dynamo. Icarus 226, 20–32.

Monteux, J., Qaddah, B., Andrault, D., May 2023. Conditions for Segregation of a Crystal-Rich Layer Within a Convective Magma Ocean. Journal of Geophysical Research (Planets) 128 (5), e2023JE007805.

Monteux, J., Ricard, Y., Coltice, N., Dubuffet, F., Ulvrova, M., 2009. A model of metal-silicate separation on growing planets. Earth and Planet. Sci. Lett. 287, 353–362.

Monteux, J., Schaeffer, N., Amit, H., Cardin, P., 2012. Can a sinking metallic diapir generate a dynamo ? Journal of Geophysical Research (Planets) 117 (16), 10005.

Monteux, J., Tobie, G., Choblet, G., Le Feuvre, M., Jul. 2014. Can large icy moons accrete undifferentiated ? Icarus 237, 377–387.

Mosqueira, I., Estrada, P. R., May 2003. Formation of the regular satellites of giant planets in an extended gaseous nebula I : subnebula model and accretion of satellites. Icarus 163, 198–231.

Mueller, S., McKinnon, W. B., Dec. 1988. Three-layered models of Ganymede and Callisto - Compositions, structures, and aspects of evolution. Icarus 76, 437–464.

Nakajima, M., Golabek, G. J., Wünnemann, K., Rubie, D. C., Burger, C., Melosh, H. J., Jacobson, S. A., Manske, L., Hull, S. D., Aug. 2021. Scaling laws for the geometry of an impact-induced magma ocean. Earth and Planetary Science Letters 568, 116983.

Nakajima, M., Stevenson, D. J., Oct. 2015. Melting and mixing states of the Earth's mantle after the Moon-forming impact. Earth and Planetary Science Letters 427, 286–295.

Nimmo, F., Hart, S. D., Korycansky, D. G., Agnor, C. B., 2008. Implications of an impact origin for the martian hemispheric dichotomy. Nature 453, 1220–1223.

Nimmo, F., Kleine, T., 2007. How rapidly did Mars accrete ? Uncertainties in the Hf W timing of core formation. Icarus 191, 497–504.

Nomura, R., Ozawa, H., Tateno, S., Hirose, K., Hernlund, J. W., Muto, S., Ishii, H., Hiraoka, N., 2011. Spin crossover and iron-rich silicate melt in the Earth's deep mantle. Nature 472, 199–202.

Ogilvie, G. I., Lesur, G., May 2012. On the interaction between tides and convection. Monthly Notices of the Royal Astronomical Society 422 (3), 1975–1987.

Ohta, K., Kuwayama, Y., Hirose, K., Shimizu, K., Ohishi, Y., Jun. 2016. Experimental determination of the electrical resistivity of iron at Earth's core conditions. Nature 534 (7605), 95–98.

O'Keefe, J. D., Ahrens, T. J., 1977. Impact-induced energy partitioning, melting, and vaporization on terrestrial planets. In : Merril, R. B. (Ed.), Lun. Planet. Sci. Conf. Vol. 8. pp. 3357–3374.

Olson, P., 2007. Overview on core dynamics. In : Olson, P. (Ed.), *Treatise on Geophysics*. Vol. 8. Elsevier Science, pp. 1–30.

Pappalardo, R. T., Collins, G. C., Head, III, J. W., Helfenstein, P., McCord, T. B., Moore, J. M., Prockter, L. M., Schenk, P. M., Spencer, J. R., 2004. Geology of Ganymede. Jupiter. The Planet, Satellites and Magnetosphere, edited by Bagenal, F. and Dowling, T. E. and McKinnon, W. B., Cambridge Planetary Science, pp. 363–396.

Pierazzo, E., Artemieva, N., Asphaug, E., Baldwin, E. C., Cazamias, J., Coker, R., Collins, G. S., Crawford, D. A., Davison, T., Elbeshausen, D., Holsapple, K. A., Housen, K. R., Korycansky, D. G., Wünnemann, K., 2008. Validation of numerical codes for impact and explosion cratering : Impacts on strengthless and metal targets. Meteoritics and Planetary Science 43, 1917–1938.

Pierazzo, E., Vickery, A. M., Melosh, H. J., 1997. A Reevaluation of Impact Melt Production. Icarus 127, 408–423.

Pierru, R., Pison, L., Mathieu, A., Gardés, E., Garbarino, G., Mezouar, M., Hennet, L., Andrault, D., 2022. Solidus melting of pyrolite and bridgmanite : Implication for the thermochemical state of the Earth's interior. Earth and Planetary Science Letters 595, 117770.

Porco, C. C., Helfenstein, P., Thomas, P. C., Ingersoll, A. P., Wisdom, J., West, R., Neukum, G., Denk, T., Wagner, R., Roatsch, T., Kieffer, S., Turtle, E., McEwen, A., Johnson, T. V., Rathbun, J., Veverka, J., Wilson, D., Perry, J., Spitale, J., Brahic, A., Burns, J. A., Del Genio, A. D., Dones, L., Murray, C. D., Squyres, S., Mar. 2006. Cassini Observes the Active South Pole of Enceladus. Science 311, 1393–1401.

Pozzo, M., Davies, C., Gubbins, D., Alfè, D., May 2012. Thermal and electrical conductivity of iron at Earth's core conditions. Nature 485, 355–358.

Qaddah, B., Monteux, J., Clesi, V., Bouhifd, M. A., Le Bars, M., Apr. 2019. Dynamics and stability of an iron drop falling in a magma ocean. Physics of the Earth and Planetary Interiors 289, 75–89.

Qaddah, B., Monteux, J., Le Bars, M., May 2020. Thermal evolution of a metal drop falling in a less dense, more viscous fluid. Physical Review Fluids 5 (5), 053801.

Ray, R. D., Eanes, R. J., Lemoine, F. G., Feb. 2001. Constraints on energy dissipation in the Earth's body tide from satellite tracking and altimetry. Geophysical Journal International 144 (2), 471–480.

Raymond, S. N., Quinn, T., Lunine, J. I., 2006. High-resolution simulations of the final assembly of Earth-like planets I. Terrestrial accretion and dynamics. Icarus 183, 265–282.

Reali, R., Van Orman, J. A., Pigott, J. S., Jackson, J. M., Boioli, F., Carrez, P., Cordier, P., Feb. 2019. The role of diffusion-driven pure climb creep on the rheology of bridgmanite under lower mantle conditions. Scientific Reports 9, 2053.

Reese, C. C., Orth, C. P., Solomatov, V. S., 2010. Impact origin for the Martian crustal dichotomy : Half emptied or half filled ? Journal of Geophysical Research (Planets) 115 (14), 5004–+.

Ricard, Y., Šrámek, O., Dubuffet, F., 2009. A multi-phase model of runaway core-mantle segregation in planetary embryos. Earth and Planet. Sci. Lett. 284, 144–150.

Riley, G. N., Kohlstedt, D. L., Aug. 1991. Kinetics of melt migration in upper mantle-type rocks. Earth and Planetary Science Letters 105 (4), 500–521.

Roberts, J. H., Lillis, R. J., Manga, M., 2009. Giant impacts on early Mars and the cessation of the Martian dynamo. J. Geophys. Res. (Planets) 114 (13), 4009–+.

Roche, P.-E., Jul. 2020. The ultimate state of convection : a unifying picture of very high Rayleigh numbers experiments. New Journal of Physics 22 (7), 073056.

Roe, P. L., 1986. Characteristic-based schemes for the Euler equations. Annual Review of Fluid Mechanics 18, 337–365.

Roscoe, R., Aug. 1952. The viscosity of suspensions of rigid spheres. British Journal of Applied Physics 3 (8), 267–269.

Rubie, D. C., Melosh, H. J., Reid, J. E., Liebske, C., Righter, K., 2003. Mechanisms of metal-silicate equilibration in the terrestrial magma ocean. Earth and Planet. Sci. Lett. 205, 239–255.

Safronov, V. S., 1978. The heating of the Earth during its formation. Icarus 33, 3–12.

Salvador, A., Massol, H., Davaille, A., Marcq, E., Sarda, P., Chassefière, E., Jul. 2017. The relative influence of H_2O and CO_2 on the primitive surface conditions and evolution of rocky planets. Journal of Geophysical Research (Planets) 122 (7), 1458–1486.

Samuel, H., Tackley, P. J., Evonuk, M., 2010. Heat partitioning in terrestrial planets during core formation by negative diapirism. Earth and Planetary Science Letters 290, 13–19.

Schenk, P. M., McKinnon, W. B., Aug. 2009. One-hundred-km-scale basins on Enceladus : Evidence for an active ice shell. Geophys. Res. Lett. 36, 16202.

Schramm, D. N., Tera, F., Wasserburg, G. J., Dec. 1970. The isotopic abundance of ˆ26Mg and limits on ˆ26Al in the early Solar System. Earth and Planetary Science Letters 10, 44–59.

Schubert, G., Anderson, J. D., Travis, B. J., Palguta, J., 2007. Enceladus : Present internal structure and differentiation by early and long-term radiogenic heating. Icarus 188, 345–355.

Schubert, G., Stevenson, D. J., Ellsworth, K., Jul. 1981. Internal structures of the Galilean satellites. Icarus 47, 46–59.

Scott, T., Kohlstedt, D. L., Jun. 2006. The effect of large melt fraction on the deformation behavior of peridotite. Earth and Planetary Science Letters 246 (3-4), 177–187.

Sekine, Y., Genda, H., Apr. 2012. Giant impacts in the Saturnian system : A possible origin of diversity in the inner mid-sized satellites. Plan. Space Sci. 63, 133–138.

Sekine, Y., Genda, H., Sugita, S., Kadono, T., Matsui, T., 2011. Replacement and late formation of atmospheric N_2 on undifferentiated Titan by impacts. Nature Geoscience 4, 359–362.

Senshu, H., Kuramoto, K., Matsui, T., 2002. Thermal evolution of a growing Mars. J. Geophys. Res. 107, 1–13.

Shannon, M. C., Agee, C. B., May 1998. Percolation of Core Melts at Lower Mantle Conditions. Science 280, 1059–+.

Showman, A. P., Han, L., Hubbard, W. B., Nov. 2013. The effect of an asymmetric core on convection in Enceladus' ice shell : Implications for south polar tectonics and heat flux. Geophys. Res. Lett. 40, 5610–5614.

Shuvalov, V., 2009. Atmospheric erosion induced by oblique impacts. Meteoritics and Planetary Science 44, 1095–1105.

Siggia, E. D., Jan. 1994. High rayleigh number convection. Annual Review of Fluid Mechanics 26, 137–168.

Sleep, N. H., Zahnle, K. J., Lupu, R. E., Aug. 2014. Terrestrial aftermath of the Moon-forming impact. Philosophical Transactions of the Royal Society of London Series A 372 (2024), 20130172–20130172.

Sohl, F., Choukroun, M., Kargel, J., Kimura, J., Pappalardo, R., Vance, S., Zolotov, M., Jun. 2010. Subsurface Water Oceans on Icy Satellites : Chemical Composition and Exchange Processes. Space Sci. Rev. 153, 485–510.

Solomatov, V., 2007. Magma Oceans and Primordial Mantle Differentiation, Treatise of Geophysics. Vol. 9. Schubert, G. editor in Chief, Elsevier.

Solomatov, V. S., 2000. Fluid Dynamics of a Terrestrial Magma Ocean. In : Origin of the Earth and Moon. edited by R.M. Canup and K. Righter and 69 collaborating authors. Tucson : University of Arizona Press., p.323-338, pp. 323–338.

Solomatov, V. S., Olson, P., Stevenson, D. J., 1993. Entrainment from a bed of particles by thermal convection. Earth and Planetary Science Letters 120 (3-4), 387–393.

Solomatov, V. S., Stevenson, D. J., Mar. 1993. Suspension in convective layers and style of differentiation of a terrestrial magma ocean. jgr 98, 5375–5390.

Spencer, J. R., Nimmo, F., 2013. Enceladus : An Active Ice World in the Saturn System. Annual Review of Earth and Planetary Sciences 41, 693–717.

Spencer, J. R., Pearl, J. C., Segura, M., Flasar, F. M., Mamoutkine, A., Romani, P., Buratti, B. J., Hendrix, A. R., Spilker, L. J., Lopes, R. M. C., 2006. Cassini Encounters Enceladus : Background and the Discovery of a South Polar Hot Spot. Science 311, 1401–1405.

Squyres, S. W., Reynolds, R. T., Summers, A. L., Shung, F., Aug. 1988. Accretional heating of the satellites of Saturn and Uranus. J. Geophys. Res. 93, 8779–8794.

Sreenivasan, B., Mark Jellinek, A., Oct. 2012. Did the Tharsis plume terminate the Martian dynamo ? Earth and Planetary Science Letters 349, 209–217.

Stacey, F. D., Loper, D. E., Apr. 2007. A revised estimate of the conductivity of iron alloy at high pressure and implications for the core energy balance. Physics of the Earth and Planetary Interiors 161 (1-2), 13–18.

Stanley, S., Elkins-Tanton, L., Zuber, M. T., Parmentier, E. M., 2008. Mars' Paleomagnetic Field as the Result of a Single-Hemisphere Dynamo. Science 321, 1822–.

Stegman, D. R., Jellinek, A. M., Zatman, S. A., Baumgardner, J. R., Richards, M. A., 2003. An early lunar core dynamo driven by thermochemical mantle convection. Nature 421, 143–146.

Stevenson, D. J., 1981. Models of the earth's core. Science 214, 611–619.

Stevenson, D. J., 2003. Planetary magnetic fields. Earth and Planetary Science Letters 208, 1–2.

Stickle, A. M., Bruck Syal, M., Cheng, A. F., Collins, G. S., Davison, T. M., Gisler, G., Güldemeister, N., Heberling, T., Luther, R., Michel, P., Miller, P., Owen, J. M., Rainey, E. S. G., Rivkin, A. S., Rosch, T., Wünnemann, K., Mar. 2020. Benchmarking impact hydrocodes in the strength regime : Implications for modeling deflection by a kinetic impactor. Icarus 338, 113446.

Svetsov, V. V., 2007. Atmospheric erosion and replenishment induced by impacts of cosmic bodies upon the Earth and Mars. Solar System Research 41, 28–41.

Tarduno, J. A., Cottrell, R. D., Watkeys, M. K., Hofmann, A., Doubrovine, P. V., Mamajek, E. E., Liu, D., Sibeck, D. G., Neukirch, L. P., Usui, Y., 2010. Geodynamo, Solar Wind, and Magnetopause 3.4 to 3.45 Billion Years Ago. Science 327, 1238–.

Tobie, G., Lunine, J., Monteux, J., Mouzis, O., Nimmo, F., 2013. The origin and evolution of Titan. In : Mueller-Wodarg, I., Griffith, C., Cravens, T., Lellouch, E. (Eds.), Titan : Surface, Atmosphere and Magnetosphere. pp. 29–62.

Tobie, G., Čadek, O., Sotin, C., Aug. 2008. Solid tidal friction above a liquid water reservoir as the origin of the south pole hotspot on Enceladus. Icarus 196, 642–652.

Tonks, W. B., Melosh, H. J., 1992. Core formation by giant impacts. Icarus 100, 326–346.

Tonks, W. B., Melosh, H. J., Mar. 1993. Magma ocean formation due to giant impacts. J. Geophys. Res. 98, 5319–5333.

Touboul, M., Kleine, T., Bourdon, B., Palme, H., Wieler, R., 2007. Late formation and prolonged differentiation of the Moon inferred from W isotopes in lunar metals. Nature 450, 1206–1209.

Touboul, M., Puchtel, I. S., Walker, R. J., 2012. W-182 Evidence for Long-Term Preservation of Early Mantle Differentiation Products. SCIENCE 335 (6072), 1065–1069.

Ulvrová, M., Labrosse, S., Coltice, N., Råback, P., Tackley, P. J., Sep. 2012. Numerical modelling of convection interacting with a melting and solidification front : Application to the thermal evolution of the basal magma ocean. Physics of the Earth and Planetary Interiors 206, 51–66.

Šrámek, O., Ricard, Y., Dubuffet, F., 2010. A multiphase model of core formation. Geophysical Journal International 181, 198–220.

Wacheul, J.-B., Le Bars, M., Monteux, J., Aurnou, J. M., Oct. 2014. Laboratory experiments on the breakup of liquid metal diapirs. Earth and Planetary Science Letters 403, 236–245.

Waite, J. H., Combi, M. R., Ip, W.-H., Cravens, T. E., McNutt, R. L., Kasprzak, W., Yelle, R., Luhmann, J., Niemann, H., Gell, D., Magee, B., Fletcher, G., Lunine, J., Tseng, W.-L., Mar. 2006. Cassini Ion and Neutral Mass Spectrometer : Enceladus Plume Composition and Structure. Science 311, 1419–1422.

Watters, W. A., Zuber, M. T., Hager, B. H., 2009. Thermal perturbations caused by large impacts and consequences for mantle convection. Journal of Geophysical Research (Planets) 114, E02001.

Wiechert, U., Halliday, A. N., Lee, D.-C., Snyder, G. A., Taylor, L. A., Rumble, D., Oct. 2001. Oxygen Isotopes and the Moon-Forming Giant Impact. Science 294, 345–348.

Willbold, M., Elliott, T., Moorbath, S., Sep. 2011. The tungsten isotopic composition of the Earth's mantle before the terminal bombardment. Nature 477 (7363), 195–198.

Williams, G. E., Jan. 2000. Geological constraints on the Precambrian history of Earth's rotation and the Moon's orbit. Reviews of Geophysics 38 (1), 37–60.

Williams, J., Nimmo, F., 2004. Thermal evolution of the Martian core : Implications for an early dynamo. Geology 32.

Wood, B., Jan. 2011. The formation and differentiation of Earth. Physics Today 64 (12), 40.

Wünnemann, K., Collins, G. S., Melosh, H. J., Feb. 2006. A strain-based porosity model for use in hydrocode simulations of impacts and implications for transient crater growth in porous targets. Icarus 180, 514–527.

Zhang, Y., 2014. 6.2 - degassing history of earth. In : Holland, H. D., Turekian, K. K. (Eds.), Treatise on Geochemistry (Second Edition), second edition Edition. Elsevier, Oxford, pp. 37–69.

10 Annexes

10.1 Annexe 1 : Curriculum Vitae

Julien MONTEUX

Chargé de Recherche CNRS Classe Normale
Qualifié en sections 35 et 36
Laboratoire Magmas et Volcans
Campus universitaire des Cézeaux,
6 Avenue Blaise Pascal,
63170 Aubière

RENSEIGNEMENT PERSONNELS :

Date de naissance : 8 Juin 1982
Lieu de naissance : Saint-Etienne
Nationalité : Française
Statut marital : Marié, 3 enfants

INTERÊTS SCIENTIFIQUES :

- Modélisation numérique de la dynamique des fluides: convection thermo-chimique pour différentes géométries.
- Impacts météoritiques et différenciation des planètes
- Initiation/évolution du champs magnétique des planètes
- Accrétion et évolution thermo-chimique des planètes

FORMATION :

Septembre 2000-Juin 2002
Classe Préparatoire aux Grandes Ecoles, option Biologie Chimie Physique et Sciences de la Terre.
Lycée C. Fauriel, Saint-Etienne, France

Septembre 2002-Juin 2003
Licence en Géosciences - Géophysique,
Ecole Normale Supérieure de Lyon, Université Lyon 1, France

Septembre 2003-Juin 2005
Master en Géosciences - Géophysique,
Physique Chimie de la Terre et de Planètes
Ecole Normale Supérieure de Lyon, Université Lyon 1, France

Octobre 2005-Janvier 2009
Doctorat en Sciences de la Terre, Laboratoire des Sciences de la Terre, École Normale Supérieure de Lyon, Université Lyon 1, France

EXPÉRIENCES EN RECHERCHE:

Janvier 2003-Juillet 2003
Stage de Licence : *Évolution du champ de gravité terrestre et observation du rebond post-glaciaire.*
Encadrants : F. Chambat, Laboratoire des Sciences de la Terre, École Normale Supérieure de Lyon, CNRS.

Janvier 2004-Juillet 2004

Stage de M.2R. : *Modélisation mécanique de la déformation de la croûte océanique sous les volcans d'Hawaii.*
Encadrants : J.-L. Got et R. Hassani (Laboratoire de Géophysique Interne et de Tectonophysique de Chambéry, Université de Savoie.)

Octobre 2005-Janvier 2009

Thèse : *Modélisation numérique de la formation du noyau terrestre*
Financement Bourse M.R.T. (allocataire moniteur)
Encadrants : N. Coltice, Y. Ricard et F. Dubuffet, (Laboratoire des Sciences de la Terre, Université de Lyon, École Normale Supérieure de Lyon, Université Claude Bernard Lyon 1, CNRS).

Février 2009-Septembre 2010

Post-Doctorat : *Modélisation numérique de l'initiation du champ magnétique des objets du système solaire.*
Financement Bourse Lavoisier
Encadrants : M. Jellinek et C. Johnson (Earth and Ocean Sciences Laboratory, University of British Columbia, Vancouver, Canada).

Septembre 2010-Avril 2014

Jeune Chercheur : *Accrétion et Différenciation des Satellites de Glace, Évolution des dynamos planétaires.*
Financement A.N.R. Retour Post-doc *(projet Accrétis)*
Collaborateurs : G. Tobie, G. Choblet, H. Amit, B. Langlais (Laboratoire de Planétologie et de Géodynamique de Nantes).

Mai 2014- Octobre 2016

Jeune Chercheur : *Évolution thermo-chimique d'un océan magmatique*
Financement A.N.R. Oxydeep + Auvergne Fellowship
Collaborateurs : Denis Andrault, Ali Bouhifd (Laboratoire Magmas et Volcans de Clermont-Ferrand), Henri Samuel (IRAP, Toulouse).

Depuis Octobre 2016

Chargé de Recherche CNRS CN : *Accrétion et différenciation de la Terre primitive ; Évolution thermochimique jusqu'à aujourd'hui.*
Collaborateurs : Denis Andrault, Ali Bouhifd, Geeth Manthilake, Maud Boyet (Laboratoire Magmas et Volcans de Clermont-Ferrand), Henri Samuel (IRAP, Toulouse), Gabriel Tobie (LPG, Nantes), Michael Le Bars (IRPHE, Marseille).

PRINCIPAUX FINANCEMENTS

2023 Origines/INSU : *Deep Earth-MOon TIdal Coupling: a signature in the geochemical record and in the current orbital configuration?* 11 000 €

2021 LABEX ClerVolc : *Formation des atmosphères primitives des planètes : Le comportement des volatils (C, H, N, O et S) durant les impacts,* 108 000 €

2020 PNP/INSU : *Modélisation du rôle des impacts sur la composition en éléments volatils de la Lune,* 5 500 €

2020 UCA-WOW Mobilité sortante : *Modélisation du rôle des impacts sur la composition en éléments volatils de la Lune,* 5541 €

2020 LABEX ClerVolc : *Modélisation du rôle des impacts sur la composition en éléments volatils de la Lune*, 8 200 €

2017 PNP/INSU : Modélisation numérique de l'équilibration thermochimique pendant la ségrégation du fer dans un océan magmatique, 7 000 €

2017 LABEX ClerVolc : *Plate-forme de modélisation numérique multi-utilisateurs* COMSOL Multiphysics, 29 000 €

2015 Auvergne Fellowship , LMV – 2 year-project
Évolution thermo-chimique d'un océan magmatique, 100 000 €

2010 ANR Retour Post-doc Fellowship (PI), LPG Nantes, France –
Accrétion et évolution thermique des satellites de glace
3 year-project, 154 000 €
20 projects funded in France for 150 applications
https://anr.fr/Project-ANR-10-PDOC-0001

2009 Fellowship of excellence Lavoisier (PI) UBC, Canada – 1 year-project, 15 000 €
1980 laureates for 5,500 candidates in 2009.

ENCADREMENT :

2016-2017 1 post-doctorant : **Vincent Clési** (LMV, France)
Numerical modelling of core mantle separation (2 publications)

2016-2023 3 Étudiants en thèse
• **Tristan Engels** (2021-2024) (LMV France)
Formation des atmosphères primitives des planètes : Le comportement des éléments volatils (C, H, N, O et S) durant les impacts
• **Remy Pierru** (2018-2021) (LMV France)
Deep mantle melting and consequences for the Early Earth dynamics
• **Baraa Qaddah** (2017-2020) (LMV France)
Numerical modelling of the dynamics and thermal evolution of a metal drop in free fall in a viscous medium (4 publications)

2012-2023 3 Étudiants en Master

Tristan Engels (LMV, France), **Laura Clodoré** (LMV-LPGN), **Nadejda Marounina** (LPG, Nantes)

2020-2024 3 Étudiants en Licence
Anaëlle Antunes (LPG, Nantes), **Yoan Luzy** (LMV, France) et **Tristan Bablin** (LMV, France)

ENSEIGNEMENT

2014	Université Clermont-Auvergne, France CM : Modélisation numérique de la dynamique interne de la Terre (3h/an) CM et TD: Petrologie (Licence, 30h)
2010 – 2014	Université de Nantes, France TD et CM (Master, 80h)
2009 – 2010	University of British Columbia, Vancouver, Canada Responsable administratif du cours "Natural disaster" (1100 élèves)
2005 – 2009	Université Claude Bernard Lyon 1, France TD et CM (Licence+Master, Monitorat + ½ ATER : 290h)

ORGANISATION DE CONGRÈS SCIENTIFIQUE

2018 Membre du comité d'organisation de l' EMPG 16 (Clermont-Ferrand, France): International Symposium on Experimental Mineralogy, Petrology and Geochemistry (212 participants).

ANIMATION ET MANAGEMENT DE LA RECHERCHE

2022-	Membre du conseil scientifique du Programme National de Planétologie (domaines A.A. et TS de l'INSU)
2022-	Responsable de l'axe transverse « Géodynamique de la Terre Primitive » au Laboratoire Magmas et Volcans
2022-	Responsable du thème «Origin of Volcanoes and of the Earth» du Labex Clervolc.
2017-	Membre élu du conseil du Laboratoire Magmas et Volcans
2017- 2023	Membre de la Cellule Communication du Laboratoire
2017- 2023	Correspondant de la Commission Diffusion de la Culture Scientifique, Technique et Industrielle (DCSTI) au sein de l'Université Clermont−Auvergne
2017- 2023	Membre de la commission «Modélisation et concepts connexes» à l'Université Clermont-Auvergne

DIFFUSION SCIENTIFIQUE

- Membre du conseil scientifique (CS) et Participation au festival Nuées Ardentes
- Membre du CS et Participation au festival Rencontres Montagnes et Sciences
- Membre du CS d'Astusciences
- Organisation de la Fête de la Science au Laboratoire Magmas et Volcans

ACTIVITIES EDITORIALES

2005 – present	Reviewer pour Nature, Nature Geosciences, Earth and Planetary Science Letters, Physics of the Earth and Planetary Interiors, Icarus, Journal of Geophysical Research, Monthly Notices of the Royal Astronomical Society, Planetary and Space Science.

10.2 Annexe 2 : Valorisation des travaux

LISTE DES PUBLICATIONS

•[35] Bouhifd M.A., M. Boyet, N. Bolfan-Casanova, G. Manthilake, **J. Monteux,** M. Roskosz, F. Gaillard and D. Andrault, Water budget on Earth and its early reservoirs: Bulk Silicate Earth and Core, subm. to Geochem. Persp. Lett.

•[34] Engels. T., **Monteux J.,** Boyet M., Bouhifd M.A., Large impacts and their contribution on the volatile budget of the Early Moon. In revision for Icarus

•[33] **Monteux J.,** Qaddah B., Andrault D., Conditions for segregation of a crystal-rich layer within a convective magma ocean. In revision for J. Geophys Res.

•[32] Pierru R., Andrault D., Manthilake G., **Monteux J.,** Devidal J.L., Guignot N., King A., Henry L. Deep mantle origin of large igneous provinces and komatiites, Accepted in Science Advances.

•[31] Freitas D., **Monteux J.**, Andrault D., Manthilake G., Mathieu A., Schiavi F., Cluzel N. (2021). Thermal conductivities of solid and molten silicates: Implications for dynamos in mercury-like proto-planets. Physics of the Earth and Planetary Interiors vol.312, p.106655

•[30] B. Qaddah, **J. Monteux,** M. Le Bars, Thermal evolution of a metal drop falling in a less dense, more viscous fluid, (2020) Phys. Rev. Fluids, 5, 053801.

•[29] V. Clési, **J. Monteux,** B. Qaddah, M. Le Bars, J.B. Wacheul, M. A. Bouhifd, Dynamics of core-mantle separation: Influence of metal and silicate viscosity on the chemical equilibrium, (2020) Phys. Earth Planet. Int. Volume 306, 106547.

•[28] **Monteux J.,** Andrault D., Guitreau M., Samuel H., Demouchy S. (2020). A mushy Earth's mantle for more than 500 Myr after the magma ocean solidification. Geophys. J. Int. vol.221, p.1165-1181.

•[27] Frossard P., Boyet M., Bouvier A., Hammouda T., **Monteux J.** (2019). Evidence for anorthositic crust formed on an inner solar system planetesimal. *Geochemical Perspectives Letters* vol.11, p.28-32, DOI:10.7185/geochemlet.1921 .

•[26] Manthilake G., Chantel J., **Monteux J.**, Andrault D., Bouhifd A., Bolfan-Casanova N., Boulard E., Guignot N., King A., Itie J.P. (2019). Thermal Conductivity of FeS and Its Implicationsfor Mercury's Long-Sustaining Magnetic Field. *Journal of Geophysical Research - Planets* vol.124, DOI:10.1029/2019JE005979 .

•[25] **Monteux J.**, Arkani-Hamed J. (2019). Shock wave propagation in layered planetary interiors: Revisited. *Icarus* vol.331, p.238-256, DOI:10.1016/j.icarus.2019.05.016 .

•[24] Qaddah B., **Monteux J.**, Clesi V., Bouhifd A., Le Bars M. (2019). Dynamics and stability of an iron drop falling in a magma ocean. *Physics of the Earth and Planetary Interiors* vol.289, p.75-89, DOI:10.1016/j.pepi.2019.02.006 .

•[23] Andrault D., Pesce G., Manthilake G., **Monteux J.**, Bolfan-Casanova N., Chantel J., Novella D., Guignot N., King A., Itié J.P., Hennet L. (2018). Deep and persistent melt layer in the Archaean mantle. *Nature Geoscience* DOI:10.1038/s41561-017-0053-9 .

•[22] **Monteux J.**, Golabek G.J., Rubie D.C., Tobie G., Young E.D. (2018). Water and the interior structure of terrestrial planets and icy bodies. Space Science Reviews. ISSN: 0038-6308 (Print) 1572-9672 (Online).

•[21] Andrault D., Bolfan-Casanova N., Bouhifd A., Boujibar A., Garbarino G., Manthilake G., Mezouar M., **Monteux J.**, Parisiades P., Pesce G. (2017). Toward a coherent model for the melting behavior of the deep Earth's mantle. *Physics of the Earth and Planetary Interiors* vol.265, p.67-81, DOI:10.1016/j.pepi.2017.02.009 .

•[20] Bouhifd A., Clesi V., Boujibar A., Bolfan-Casanova N., Cartier C., Hammouda T., Boyet M., Manthilake G., **Monteux J.**, Andrault D. (2017). Silicate melts during Earth's core formation. *Chemical Geology* vol.461, p.128 - 139, DOI:10.1016/j.chemgeo.2016.12.035 .

•[19]Andrault D., **Monteux J.,** LeBars M., Samuel H. (2016). The deep Earth may not be cooling down. *Earth and Planetary Science Letters* vol.443, p.195-203, DOI:10.1016/j.epsl.2016.03.020 .

•[18] Guillaume B., Pochat S., **Monteux J.,** Husson L., Choblet G. (2016). Can eustatic charts go beyond first order? Insights from the Permian–Triassic. *Lithosphere* DOI:10.1130/L523.1 .

•[17] **Monteux J.**, Andrault D., Samuel H. (2016). On the cooling of a deep terrestrial magma ocean. *Earth and Planetary Science Letters* vol.448, p.140-149, DOI:10.1016/j.epsl.2016.05.010 .

•[16] **Monteux J.** Arkani-Hamed J. (2016). Scaling Laws of Impact Induced Shock Pressure and Particle Velocity in Planetary Mantle. *Icarus* vol.264, p.246-256, DOI:10.1016/j.icarus.2015.09.040 .

•[15] **Monteux J.**, Collins G.S., Tobie G., Choblet G. (2016). Consequences of large impacts on Enceladus' core shape. *Icarus*vol.264, p.300-310, DOI:10.1016/j.icarus.2015.09.034 .

•[14] Amit H., Choblet, G., Olson P., **Monteux J.**, Deschamps F., Langlais B., Tobie G. (2015). Towards more realistic core-mantle boundary heat flux patterns: a source of diversity in planetary dynamos. *Progress in Earth and Planetary Science* p.2-26, DOI:10.1186/s40645-015-0056-3 .

•[13] Boujibar A., Andrault D., Bolfan-Casanova N., Bouhifd A., **Monteux J.** (2015). Cosmochemical fractionation by collisional erosion during the Earth's accretion. *Nature Communications* vol.6, p.8295, DOI:10.1038/ncomms9295 | www.nature.com/naturecommunications .

•[12] Marounina N., Tobie G., Carpy, **Monteux J.**, Charnay B., Grasset O. (2015). Evolution of Titan's atmosphere during the Late Heavy Bombardment. *Icarus* vol.257, p.324-335, DOI:10.1016/j.icarus.2015.05.011 .

•[11] **Monteux J.**, Amit H., Choblet G., Langlais B., Tobie G. (2015). Giant impacts, heterogeneous mantle heating and a past hemispheric dynamo on Mars. *Physics of the Earth and Planetary Interiors* vol.240, p.114-124, DOI:10.1016/j.pepi.2014.12.005 .

•[10] Wacheul, J.B., Le Bars, M., **Monteux, J.**, Aurnou, J.M., (2014) Laboratory experiments on the breakup of liquid metal diapirs, Earth and Planet. Sci. Lett, Volume 403, Pages 236-245

•[9] **Monteux, J.**, G., Tobie, G., Choblet, M., Le Feuvre, (2014) Can large icy Moons accrete undifferentiated, Icarus, Volume 237, 15 July 2014, Pages 377-387

•[8] **Monteux, J.**, J., Arkani-Hamed (2014), Consequences of giant impacts in early Mars: Core merging and Martian dynamo evolution, J. Geophys. Res. (Planets), Volume 119, Issue 3, pages 480–505

•[7] Tobie, G., J.I. Lunine, **J. Monteux,** O. Mousis, F. Nimmo (2013), The Origin and Evolution of Titan, Titan: Surface, Atmosphere and Magnetosphere edited by I. Mueller-Wodarg, C. Griffith, T. Cravens and E. Lellouch for Cambridge University Press.

•[6] **Monteux, J.**, M. Jellinek, C .J., Johnson, (2013) Dynamics of core merging after a martian mega-impact, Icarus, 226, Issue 1, Pages 20–32.

•[5] **Monteux, J.**, N. Schaeffer, H. Amit, P. Cardin, (2012) Can a sinking metallic diapir generate a dynamo? J. Geophys. Res. (Planets), 117, E10005, 14 PP.,doi:10.1029/2012JE004075

•[4] **Monteux, J.**, M. Jellinek, C .J., Johnson (2011), Why might planets and moons have early dynamos?, Earth and Planet. Sci. Lett., 310, 349-359.

•[3] **Monteux, J.**, Y. Ricard, N. Coltice, F. Dubuffet, M. Ulvrova (2009), A model of Metal-Silicate separation on Growing Planets, Earth and Planet. Sci. Lett., 287,353-362.

•[2] Got, J.L., V. Monteiller, **J. Monteux**, R. Hassani, P. Okubo (2008), Deformation and rupture of the oceanic crust may control growth of hawaiian volcanoes, Nature, 451, 453-456.

•[1] **Monteux, J.,** N. Coltice, F. Dubuffet, Y. Ricard (2007), Thermo-mechanical adjustment after impacts during planetary growth, Geophys. Res. Lett, 34, L24201.

CHAPITRES D'OUVRAGES:

- Monteux J., Andrault, D., (2023). Dynamique et évolution thermique du manteau terrestre primitif. In Dynamique du manteau terrestre (resp. J. Monteux). Encyclopédie ISTE. Thème Terre interne (ed. N. Bolfan-Casanova).

- Monteux J., Golabek G.J., Rubie D.C., Tobie G., Young E.D. (2018). Water and the interior structure of terrestrial planets and icy bodies. In The Delivery of Water to Protoplanets, Planets and Satellites, Space Science Series of ISSI. ISSN: 0038-6308 (Print) 1572-9672 (Online).

- Andrault D., Bolfan-Casanova N., Bouhifd A., Boujibar A., Boyet M., Cartier C., Clesi V., Doucelance R., Hammouda T., Laubier M., Manthilake G., Marin-Carbonne J., Martin H., Moine B., Monteux J., Moyen J.F., Paquette J.L. (2017). Environnement de la Terre primitive: Comment construire une planète habitable ? Groupe de Recherche : ''Mécanismes géodynamiques de la Terre primitive''. Revue d'Auvergne vol.262-263, p.7-40.

- Tobie, G., J.I. Lunine, J. Monteux, O. Mousis, F. Nimmo (2013), The Origin and Evolution of Titan, Titan: Surface, Atmosphere and Magnetosphere edited by I. Mueller-Wodarg, C. Griffith, T. Cravens and E. Lellouch for Cambridge University Press.

PARTICIPATION À DES CONGRÈS SCIENTIFIQUES INTERNATIONAUX

- [46] Andrault D., **Monteux J.** (2023). Thermochemical modelling of chemical segregation in a crystallizing magma ocean . Goldschmidt conference, Lyon, France (2023).

- [45] **Monteux J.,** Qaddah B., Andrault D. (2023). Conditions for segregation of a crystal-rich layer within a convective magma ocean. Goldschmidt conference, Lyon, France (2023).

- [44] Engels T., **Monteux J.,** Boyet, M., Bouhifd A. (2023). Large impacts and their contribution on the volatile budget of the Early Moon. Goldschmidt conference, Lyon, France (2023).

- [43] Engels T., **Monteux J.,** Bouhifd A. (2022). Large impacts and their contribution on the volatile budget of the Early Moon. Programme National de Planétologie, Lyon (2022).

- [42] **Monteux J.**, Qaddah B., Andrault D. (2022). Stability of a thin mushy layer within a convecting magma ocean. Programme National de Planétologie, Lyon (2022).

- [41] Andrault D., **Monteux J.** , Pison L., Mathieu A. (2022). New measurements of Fe thermal conductivity and implications for the thermal history of the Earth's core. Programme National de Planétologie, Lyon (2022).

- [40] Frossard P., Boyet M., Bouvier A., Hammouda T., **Monteux J.** (2020), The diversity of early planetesimals crusts: Insights from NWA 7325/8486 and NWA 11119, École d'été des Houches.

- [39] Pierru R., Andrault D., Manthilake G., **Monteux J.**, Devidal J.L., Guignot N., King A. Mantle Origin of the Large Igneous Provinces. AGU fall meeting, New Orleans, USA, (2021).

- [38] **Monteux J.,** Qaddah B., Andrault D. (2021). Stability of a crystallizing layer within a (convecting) magma ocean. AGU fall meeting, New Orleans, USA, (2021).

- [37] Andrault D., Pison L., **Monteux J.,** Mathieu A., Thermal history of the Earth's core: new measurements of Fe thermal conductivity. AGU fall meeting, New Orleans, USA, (2021).

- [36] **Monteux J.,** Qaddah B., Andrault D. (2021). Stability of a crystallizing layer within a (convecting) magma ocean. Goldschmidt conference, Lyon, France (2021).

- [35] Frossard P., Boyet M., Bouvier A., Hammouda T., **Monteux J.** (2019). Magma cean-dervied anorthositc crust on early (<5 Ma) planetesimals. 50th Lunar and Planetary Conference, Houston, USA.

- [34] **Monteux, J.**, Andrault, D., Guitreau, M., Samuel, H., Demouchy, S., The influence of the Earth's early mantle viscosity on its cooling dynamics, EPSC-DPS Joint Meeting 2019.

- [33] Manthilake G., Chantel J., Andrault D., **Monteux J.,** Bouhifd A., Bolfan-Casanova N., Boulard E., Guignot N., King A., Itie J.P. (2018). Electrical conductivity of Fe−S alloys at high pressure and high temperature: Implications for Mercury's weak and long−lived magnetic field. EMPG XVI conference abstract, Clermont-Ferrand, 17-21 juin 2018.

- [32] **Monteux J.,** Andrault D., Samuel H. (2018). On the cooling of a deep mushy mantle. EMPG XVI Conference abstract, Clermont-Ferrand, 17-21 juin 2018.

- [31] Qaddah B., **Monteux J.,** Le Bars M., Clesi V., Bouhifd A. (2018). The breakup of liquid iron diapirs within the magma ocean. EMPG XVI Conference abstract, Clermont-Ferrand, 17-21 juin 2018.

- [30] Qaddah B., **Monteux J.**, Le Bars M., Clesi V., Bouhifd A. (2018). The breakup of liquid iron diapirs within the magma ocean. Study of the Earth Deep Interior (SEDI 2018), Edmonton (Canada), 8-13 Jul 2018.

- [29] Arkani−Hamed J., **Monteux J.** (2017). Shock Wave Propagation in Layered Planetary Interiors: Revisited. AGU Fall Meeting abstrac, New Orleans, USA.

- [28] **Monteux J.,** Arkani-Hamed J. (2017). Shock Wave Propagation in Layered Planetary Interiors: Revisited. AGU Fall meeting, New Orleans.

- [27] Samuel H., Michaut C., Baratoux D., **Monteux J.**, Andrault D., Kurita K. (2017). The Early Thermal Evolution and Delamination of Mars' Crust. Goldschmidt, Paris.

- [26] Drummond Mc.G., Thieulot C., **Monteux J.** (2016). The effect of giant impactors on the magnetic field energy of an early Martian dynamo. EGU General Assembly 2016.

- [25] Guillaume B., **Monteux J.**, Pochat S., Husson L., Choblet G. (2016). Can eustatic charts go beyond first-order? Insights from the Permo-Triassic. EGU General Assembly 2016.

- [24] **Monteux J.,** Andrault D., Samuel H. (2016). On the cooling of a deep terrestrial magma ocean. SEDI, Nantes, 24-29 Juillet 2016.

- [23] Andrault D., **Monteux J.**, Le Bars M., Samuel H. (2015). A steady thermal state for the Earth's interior. AGU Fall Meeting, San Francisco, 14-18 décembre 2015.

- [22] **Monteux J.**, Amit H., Arkani-Hamed J., Choblet G., Langlais B., Tobie G., Johnson C.L., Jellinek M. (2015). Consequences of Giant Impacts on the Martian dynamo. AGU Fall Meeting, San Francisco, 14-18 décembre 2015.

- [21] **Monteux J**., Amit H., Choblet G., Langlais B., Tobie G. (2015). Giant impacts, heterogeneous mantle heating and a past hemispheric dynamo on Mars. vol.17, p.EGU2015-1723-2, Geophysical Research Abstracts, EGU General Assembly 2015.

- [20] **Monteux J.,** Andrault D., Samuel H. (2015). On the cooling of a deep terrestrial magma ocean. European Planetary Science Congress 2015, Nantes, France, 27 September - 2 October, 2015.

- [19] **Monteux J.**, Andrault D., Samuel H. (2015). On the cooling of a deep terrestrial magma ocean. AGU Fall Meeting, San Francisco, 14-18 décembre 2015.

- [18] **Monteux J.**, Arkani-Hamed J. (2015). Scaling Law of Impact Induced Shock Pressure in Planetary Mantle. 46th Lunar and Planetary Science Conference (2015).

- [17] **Monteux J.,** Arkani-Hamed J. (2015). Scaling Law of Impact Induced Shock Pressure

in Planetary Mantle. vol.17, p.EGU2015-3785, Geophysical Research Abstracts, EGU General Assembly 2015.

- [16] **Monteux J.,** Collins G. S., Tobie G., Choblet G. (2015). Consequences of large impacts on Enceladus' core shape. European Planetary Science Congress 2015, Nantes, France, 27 September - 2 October, 2015.

- [15] Pesce G., Manthilake G., Andrault D., **Monteux J.,** Bolfan-Casanova N., Novella D., Guignot N., Chantel J. (2015). On the cooling of a deep terrestrial magma ocean: Experimental perspective. AGU Fall Meeting.

- [14] Pesce, G., Andrault D., Manthilake G., **Monteux J.**, Bolfan-Casanova N., Novella D., Guignot N., Chantel J. (2015). On the cooling of a deep terrestrial magma ocean: Experimental perspectives. AGU Fall Meeting, San Francisco, 14-18 décembre 2015.

- [13] **Monteux, J.,** Arkani-Hamed (2014) Thermal Consequences of Giant Impacts and Core Merging in Early Mars, Accrete Workshop, Nice (France).

- [1]2 Amit, H., Choblet, G., Olson, P., **Monteux, J.**, Deschamps, F., Langlais. B, Tobie, G. (2014) Planetary dynamos features driven by exotic models of core-mantle boundary heat flux, SEDI, Kanagawa (Japon)

- [11] Wacheul, J.B., Le Bars, M., Aurnou, J.M., **Monteux, J.** (2013), Experiments on the stability of metal diapirs, American Geophysical Union, Fall Meeting 2013.

- [10] **Monteux, J.**, G. Tobie, G. Choblet, M. Le Feuvre (2012), Can Large Icy Moons Accrete Undifferentiated, American Geophysical Union, Fall Meeting 2012.

- [9] **Monteux, J.**, M. LeBars, O. Aubert (2012), Influence of the viscosity contrast on the metal diapir breakup in primitive magma oceans, American Geophysical Union, Fall Meeting 2012.

- [8] **Monteux, J.**, N. Schaeffer, H. Amit, P. Cardin (2012), Can a sinking diapir generate a dynamo?, American Geophysical Union, Fall Meeting 2012.

- [7] **Monteux, J.**, G. Tobie, G. Choblet, M. Le Feuvre (2012), Can Large Icy Moons Accrete Undifferentiated, EPSC, 2012.

- [6] **Monteux, J.**, N. Schaeffer, H. Amit, P. Cardin (2011), Can a sinking diapir generate a dynamo?, EPSC-DPS, 2011.

- [5] **Monteux, J.,** M. Jellinek, C.J. Johnson (2010), Why might planets and moons have early dynamos?, Lunar and Planet. Sci. Conf., 2010.

- [4] **Monteux, J.,** M. Jellinek, C.J. Johnson (2009), Why might planets and moons have early dynamos?, American Geophysical Union, Fall Meeting 2009.

- [3] **Monteux, J.,** N. Coltice, F. Dubuffet, Y. Ricard (2008), Thermo-mechanical adjustment after impacts during planetary growth, European Geosciences Union 2008.

- [2] J.-L. Got, **J. Monteux**, V. Monteiller, R. Hassani, P. Okubo (2007), Better understanding of Hawaiian volcanoes through double-difference tomography and

mechanical modelling, European Geosciences Union 2007.

- [1] **Monteux, J.,** N. Coltice, F. Dubuffet, Y. Ricard (2006), Dynamics of magma ocean formation after large impacts, American Geophysical Union, Fall Meeting 2006, abstract#V11D-0609.

VALORISATION ET DIFFUSION SCIENTIFIQUE

- Nuées ardentes
- Communication LMV
- Fête de la Science (Nantes, Clermont...)
- 150 ans OPGC
- Exposition la Science des Minéraux
- Des chiffres et vous
- Expos'Sciences
- Littérature au Centre
- 70 ans CNRS
- Courts de Science
- Une année avec le CNRS

10.3 Annexe 3 : Publications dans d'autres thématiques

Got, J.L., V. Monteiller, **J. Monteux***, R. Hassani, P. Okubo (2008), Deformation and rupture of the oceanic crust may control growth of hawaiian volcanoes, Nature, 451, 453-456.* **LIEN HAL**.

Guillaume B., Pochat S., **Monteux J.***, Husson L., Choblet G. (2016). Can eustatic charts go beyond first order ? Insights from the Permian–Triassic. Lithosphere - DOI :10.1130/L523.1.* **LIEN HAL**.